IntechOpen

Advances in Composite Materials

Analysis of Natural and Man-Made Materials

Edited by Pavla Těšinová

ADVANCES IN COMPOSITE MATERIALS - ANALYSIS OF NATURAL AND MAN-MADE MATERIALS

Edited by **Pavla Těšinová**

Advances in Composite Materials - Analysis of Natural and Man-Made Materials
http://dx.doi.org/10.5772/728
Edited by Pavla Těšinova

Contributors

Eko Marsyahyo, Siswi Astuti, Iftitah Ruwana, Roberto Caputo, Luciano De Sio, Alessandro Veltri, Nelson V. Tabiryan, Andrey V. Sukhov, Cesare P. Umeton, Mauricio V. Donadon, Sérgio Frascino Muller de Almeida, Tulio Hallak Panzera, André L. Christoforo, Paulo H.R. Borges, Chris R. Bowen, Fábio P. Paiva Cota, Elisa Pietropaoli, Joao Eurico Eurico Fonseca, Maria Fatima Vaz, Helena Canhao, Alexandre Piche, Ivan Revel, Gilles Peres, Yongfeng Li, Tran Doan Hung, Petr Louda, Dora Kroisová, Oleg Bortnovsky, Nguyen Thang Xiem, João Silva, António Torres Marques, Carlos A. Bernardo, João Nunes, Salah M. ElHaggar, Mokhtar A. Aly Kamel, Shilko Serge, Milena Koleva, Anka Zheglova, Venceslav Vassilev, Emilija Fidančevska, Mohini - Saxena, Asokan Pappu, Anusha Sharma, Ruhi Haque, Sonal Wankhede, Mohammad S. Qatu, Mehdi Hajianmaleki, Chia-Chin Chiang, Parvez Alam, Alessandra de Almeida Lucas, José Donato Ambrósio, Baltus Cornelius Bonse, Sílvia Helena Prado Bettini, Mervi Puska, Allan J. Aho, Pekka Vallittu, Dessi A. Koleva, Klaas Van Breugel, João A. Oliveira, Joaquim Pinho-da-Cruz, Filipe Teixeira-Dias, Pengwan Chen, Zhongbin Zhou, Fenglei Huang, John Cuppoletti, Danuta H. Malinowska

Notice

First published in Croatia, 2011 by INTECH d.o.o.
eBook (PDF) Published by IN TECH d.o.o.
Place and year of publication of eBook (PDF): Rijeka, 2019. IntechOpen is the global imprint of IN TECH d.o.o.
Printed in Croatia

Legal deposit, Croatia: National and University Library in Zagreb

Additional hard and PDF copies can be obtained from orders@intechopen.com

Advances in Composite Materials - Analysis of Natural and Man-Made Materials
Edited by Pavla Těšinova

p. cm.

ISBN 978-953-307-449-8

eBook (PDF) ISBN 978-953-51-4440-3

Meet the editor

Ing. Pavla Těšinová Ph.D. studied textile material engineering at the Faculty of Textile Engineering, Technical University of Liberec with specialisation in textile reinforced composites and engineering pedagogy at the same University. She followed with Dissertation on the multi-scale modelling of mechanical properties of woven composites in Liberec where she cooperated on various research projects on textile structure not only for composite usage. The dissertation was defended in November 2008. Since that, she is a postdoc and a lecturer at the Department of Textile Evaluation, Faculty of Textile Engineering at Technical University of Liberec. She is a co-ordinator of the short EU mobility programme for students. Her main research interests include the mechanical properties of textiles (fibres, yarns, fabrics and composites), testing and modelling of mechanical properties of various structures of textile materials, knowledge of textile goods (technical textiles and smart textiles), maintenance of textiles and lifetime of textiles.

Contents

Preface

Nature creates the best material constituents and combines them as composite materials. Thus inspired people compose new designs for their purpose of utilization. We make new constructions, new types of man-made materials and evaluate them before use. Composites are made up of constituent materials with high engineering potential. This potential is wide as wide is the variation of materials and structure constructions when new updates are invented every day. Technological advances in composite field are included in the equipment surrounded us daily; our lives are getting safer, hand in hand with economical and ecological advantages.

This book collects original studies concerning composite materials, their properties and testing from various points of view. Chapters are divided into five groups according to their main aim: Material properties, Natural sources, Manufacturing, Testing and Modelling. Each part includes chapters with interesting topics. Worldwide spread authors were addressed so we are glad that this book represents research in high variety of outlooks.

Material properties are described in innovative ways either for standard components or biomaterials and natural sources materials. Commonly used materials as glass, carbon, epoxy resins, concrete, etc. were described with improved properties or constructions. Waste material using and recycling is the next step and it is an important way how to save our sources and environment. Renewable natural sources are on the top position for saving environment and we have to do our best to find proper applications for them.

Manufacturing processes are represented by moulding methods; lamination process includes monitoring during process. Innovative testing procedures are described in electrochemistry, ultrasonic pulse velocity, fracture toughness in macro-micro mechanical behaviour and more. Synergy between components, laminas and construction parts are tested by different principles. Modelling offers relatively cheap option how to observe long time processes in special conditions before actual production. Experimental testing with software modelling and computation are important to work together for deep description of composite properties.

All original contributions included in this book present knowledge and research in very special field. Big progress in composite engineering started in the second part of

the last century and is still growing. Study of composite materials has future when questions which we consider now are going to be answered and limitations which we see will be overcome.

I would like to thank Romina Krebel for her invaluable help in the organisation of the editing process.

Pavla Těšinová
Technical University of Liberec
Czech Republic

Part 1

Material Properties

1

Composites Containing Waste Materials

Milena Koleva[1], Anka Zheglova[1],
Venceslav Vassilev[2] and Emilija Fidancevska[3]
[1]*Technical University of Gabrovo*
[2]*University of Chemical Technology and Metallurgy, Sofia*
[3]*"St. Cyril and Methodius" University, Skopie*
[1,2]*Bulgaria*
[3]*Republic of Macedonia*

1. Introduction

In the development of new materials, apart from the properties of the materials, the economic and ecological aspects are also of considerable importance. Traditional products whose manufacture requires expensive raw materials are being replaced with composite materials with alternative properties which display better qualities and perform in a better way. Composite materials are obtained from much cheaper components and possess significantly lower relative weight.

Over the last few years different kinds of waste materials have been successfully utilized as filler in polymer composites with various applications. This not only reduces the production costs but also offers an opportunity for utilization of waste materials thereby reducing environmental pollution. Among them a large number of insulation composite materials with different practical application have been developed.

Many of the composites are thermal, electrical or noise insulating materials based on thermosetting polymers (polyester and epoxy resins) which combine the required physical characteristics with good processing properties. For example polyester resins have a series of valuable properties - suitable viscosity, ability to solidify at both room and high temperatures, high electric strength and dielectric ratings, high chemical stability and etc. Experimental research shows that the properties of the composites in this case are a function of both the curing degree of the polymer and the kind and properties of the filler.

At the same time there are organic or inorganic waste materials generated by the industrial processes or human activity, which could successfully replace or at least reduce the amount of raw materials used as components in insulation materials.

This chapter presents the outcomes of the experimental work aimed to evaluate the possibility for utilization of organic and inorganic industrial waste as fillers in polymer composites with thermal- and electrical insulation and sound damping properties.

2. Inorganic composite materials based on industrial wastes

2.1 Metallurgical slag

Recycling whereby metallurgical wastes are decreased is one of the most important processes for environmental protection. Metallurgical slag (ferronickel, ferrochromium,

calcium ferrite, etc.) is the main waste of ore processing in metallurgy. It is a multicomponent system characterized by high percentage content of Si-, Ca-, Fe- and Mg-oxides with high porosity related to the presence of glassy phase (5-30 %). In this sense the usage of metallurgical slag as raw base for production of new materials is useful for many other productions.

At controlled thermal treatment metallurgical wastes and glass can be used to obtain compact and porous glass-ceramic materials, which are used for production of electronic elements, catalysts, membranes, composite materials, etc. Metallurgical slag rich in Si- and Al-oxides can be used as material for ceramic filters, aerators and diffusers for treatment of industrial gases and waste waters purification. The obtained glass-ceramic products are resistant to harsh thermal changes and possess good chemical, physical, microbiological and mechanical properties.

The aim of this experimental work was to study the possibility for utilization of metallurgical ferronickel (Fe-Ni) slags. Two types of metallurgical slags are used: from the "refining" (Slag-R) and from the "melting" (Slag-M) processes. By their chemical composition these are multicomponent silicate systems with high content of Fe_2O_3, FeO, SiO_2, CaO and MgO. The grain size analysis shows that the highest is the fraction with particles size <0.045 mm. The Slag-R phase composition includes escolite (Cr_2O_3) and amorphous phase, while the Slag-M is consisted of hematite (Fe_2O_3), diopside ($CaMgSi_2O_6$), olivine ($MgFeSiO_4$) and amorphous phase.

Both slags possess different thermal characteristics: Slag-R has wider sintering interval (1250-1500°C) than this of Slag-M (1260-1370°C). The glass-transition and the melting temperatures of Slag-R (1500 and >1500°C) are higher than these of Slag-M (1370 and 1480°C), which is due to the higher content of hard melting oxides in it.

The green density of Slag-R and Slag-M are 5,04 g/cm^3 and 3,58 g/cm^3, respectively.

The thermomechanical properties of the Fe-Ni-slag are investigated on pressed samples with the shape of rectangular prism (60x5x5 mm^3), as fraction with particles size <0.045 mm; pressing pressure of 30 MPa; plastifyer - 1 % solution of polyvinyl alcohol (PVA) is used. Synthesis is conducted at T=900÷1200°C (Δ 50°C) in chamber furnace (air atmosphere; heating rate of 10°C/min; isothermal hold at the final temperature of 2 h). Slag-R increases its geometrical stability when the synthesis temperature is increased up to 1200°C whereas Slag-M samples are deformed at T>1150°C as a result of gas removal from their volume.

The technical coefficient of linear thermal expansion (α_{tech}) for both types of slagis in the interval 20-600°C is: 12,9.10^{-6} °C^{-1} (Slag-R) and 11,6.10^{-6} °C^{-1} (Slag-M) (Fidancevska et al., 2006).

Synthesis temperature influences the main properties of the compacts produced from the two slag types which is due to their different reactivity and significant differences in their chemical and phase composition - Table 1.

2.2 Waste glass

Waste glass (from windows, packages and TV sets) is used as initial material for production of glass-ceramic materials in many European countries. The waste window glass is recycled (≈ 26 %) and returned for secondary melting. The packages glass is recycled depending on its color: 82,0 % green, 44,5 %brown and 43,8 % white glass. From ecological point of view the windows and containers glass are harmless and can be used as initial material for blocking of harmful and dangerous for the environment elements.

Waste glass from TV monitors, windows and packages is used as source of glassy phase in the experiments for production of "glass-ceramic" composites. The TV-glass differs from the other two types by the presence of PbO (8,18 %) and K_2O (6,4 %). Glass from window panes has higher CaO content than the package glass: 8.96 versus 0,21 %, while the package glass has higher concentration of K_2O, MgO and B_2O_3 than this of the windows glass: 2,31, 7,34 and 4,00 versus 0,19, 3,62 and 0,00 %, respectively.

Window panes and package glass are subject to direct crushing and milling and the TV-glass is preliminary treated with 12 % HF solution for the purpose of removing the chemical components deposited on the TV screen. TV-glass has lower glass-transition temperature (700°C) than the other types of waste glass: (850°C) which is due to the presence of PbO and K_2O in it. For this reason TV-glass is appropriate for usage in composite systems. The complete melting temperature of the TV-glass (800°C) is lower than this of the window panes (950°C) and the package glass (960°C). To strengthen waste glass a powder fraction with particles sizes <45 μm is used as is the case with metallurgical slag. The compacts are produced in a way identical to that of the slag , however, it is carried out at lower synthesis temperature (600-800°C) and holding at the maximum temperature for 1 h (Vassilev et al., 2007a).

The main properties of the sintered compacts from the three types of waste glass are presented in Table 1. Linear thermal expansion coefficient (α_{tech}) in the interval 20-600°C is: $10{,}6.10^{-6}$ °C^{-1} (TV-glass); $10{,}1.10^{-6}$ °C^{-1} (window panes glass) and $10{,}8.10^{-6}$ °C^{-1} (package glass).

TV-glass is the most appropriate for production of glass-ceramic composites because of its sintering temperature, mechanical properties and technical coefficient of linear thermal expansion.

Waste	Synthesis temperature, °C	Density (d), g/cm^3	Porosity (θ), %	Young modulus (E), GPa	Bending strength (σ), MPa
Slag-R	1100	3,21	36,3	27,3	41,5
	1150	3,25	35,5	29,0	47,8
	1200	3,28	34,9	39,4	48,7
Slag-M	900	2,25	37,2	6,1	11,5
	950	2,36	34,1	6,2	14,0
	1000	2,38	33,5	6,7	17,8
	1050	2,48	30,7	16,1	26,0
	1100	2,76	22,9	25,2	49,9
	1150	2,93	18,2	29,1	51,0
TV-glass	600	2,61	-	72,0	136,0
Windows glass	750	2,66	-	50,0	125,0
Packages glass	800	2,54	-	52,0	127,0

Table 1. Density, porosity and mechanical properties of metallurgical slags: Slag-R and Slag-M and waste glass: TV, windows and packages

2.3 Composites based on Fe-Ni slag and waste glass

Environmental protection from the huge quantities of metallurgical and glass wastes by utilizing them as ingredients of different composites with wide range of possible application is a subject matter of proper addressing a challenge of urgent actuality. Here is shown one of the possibilities for production of composites based on metallurgical slag (Slag-R and Slag-M) and waste glass.

Composites based on metallurgical slag and waste glass are produced by mechanically mixing the two components as the glass content in them varies from 10 to 50 wt. %. The conditions at which the composites are obtained are similar to these used for obtaining compacts from the initial components (slag and glass).

Composites (Slag-R+10 % TV-glass) and (Slag-R+20 % TV-glass) are sintered at T = 1100, 1150 and 1500°C/2h. They show significant deformation even at 1100°C which increases with the rise of temperature. With composites (Slag-R+20 % windows glass) is observed deformation at sintering temperature ≥1200°C/2h, caused by the significantly lower melting temperature of the TV-glass compared to this of the windows. Their properties are shown in Table 2.

Composition	Synthesis temperature, °C	Bending strength (σ), MPa	Young modulus (E), GPa	Density (d), g/cm^3	Porosity (θ), %
Slag-R + 10% TV-glass	1100	43,5	33,1	3,20	33
Slag-R + 20% TV-glass	1100	45,0	37,6	3,33	27
Composite (Slag-R + 20% TV-glass) → α = 10,9.10^{-6} °C (20-600 °C)					
Slag-R + 20% TV-glass	1100	45,0	37,6	3,33	27
Slag-R + 20% TV-glass	1150	49,2	42,2	3,60	21

Table 2. Bending strength, Young modulus, density and porosity of composite Slag-R+glass depending on the composition and the synthesis temperature

The real density, porosity, elasticity modulus and bending strength of these composites are presented in Table 3 (depending on the composition) and in Table 4 (depending on the composition and the synthesis temperature).

Composition	Synthesis temperature, °C	Bending strength (σ), MPa	Young modulus (E), GPa	Density (d), g/cm^3	Porosity (θ), %
Slag-M + 10% TV-glass	900	16,67	10,47	2,28	36
Slag-M + 20% TV-glass	900	27,06	15,10	2,26	35
Slag-M + 30% TV-glass	900	27,25	15,12	2,23	34
Slag-M + 40% TV-glass	900	30,13	16,69	2,14	34
Slag-M + 50% TV-glass	900	31,08	20,07	2,11	33

Table 3. Bending strength, Young modulus, density and porosity of composite Slag-M+glass depending on the composition

The composites (Slag-M+waste glass), synthesized at 1150°C/2h, are completely melt at the sintering temperature if one of the waste glasses participates in their composition in

concentrations of 30, 40 or 50 wt. %. This means that the composites with such waste glass concentrations are practically inapplicable and that is why they are not included in Table 4.
As seen from Tables 2, 3 and 4 when waste glass concentration is increased the bending strength and the elasticity modulus increase by absolute value regardless of the slag composition. The influence of the synthesis temperature is the same, however, at significantly higher degree. Meanwhile the composites' porosity decreases with the increase of their density.

Composition	Synthesis temperature, °C	Bending strength (σ), MPa	Young modulus (E), GPa	Density (d), g/cm^3	Porosity (θ), %
Slag-M+20% TV-glass (α_{tech} = 11,1.10^{-6} °C) (20-600°C)	900	27,06	15,10	2,26	35
	950	28,58	16,07	2,31	34
	1000	35,37	17,05	2,36	32
	1050	53,97	23,06	2,42	30
	1100	57,05	40,10	2,75	21
	1150	64,08	47,95	3,34	4
Slag-M+20% windows glass (α_{tech} = 11,5.10^{-6} °C) (20-600°C)	900	18,06	10,23	2,03	42
	950	19,33	11,15	2,14	39
	1000	19,76	11,65	2,20	37
	1050	42,34	17,59	2,35	33
	1100	53,65	22,41	2,57	26
	1150	60,98	34,39	2,98	15
Slag-M+20% containers glass (α_{tech} = 11,4.10^{-6} °C) (20-600°C)	900	12,34	7,14	2,11	39
	950	20,44	8,80	2,14	38
	1000	28,31	15,28	2,14	38
	1050	48,73	20,43	2,34	33
	1100	56,92	24,71	2,58	26
	1150	77,41	39,93	2,92	16

Table 4. Bending strength, Young modulus, density and porosity of composite Slag-M+glass depending on the composition and the synthesis temperature

If the mechanical properties (σ and E), density (d), porosity (θ) and technical coefficient of linear thermal expansion (α_{tech}) are taken as criterion for selection of composite then the best qualities are displayed by the composite (Slag-M+20 % TV-glass) sintered at 1150°C/2h. It is characterized by porosity of 4 %, i.e. 96 % of the theoretical density and the best mechanical properties at the same time. According to the microstructural analysis the slag's particles are capsulated by melted glassy, partially crystallized phase (Fidancevska et al., 2007).

2.4 Porous composites based on Fe-Ni slag and waste glass

For the production of porous composites metallurgical Fe-Ni slag and waste TV-glass were used. The values of the composite properties are presented in Table 1 (shaded rows).

2.4.1 Porous composites based on coarse-grained slag

A liquid glass layer is formed around the slag's particles by this method. If the slag is with larger grain size, the possibility for formation of contact between them is smaller and there is more free space between them. At temperatures higher than the complete melting temperature of the glass liquid bridges along with liquid glass film are also formed between the particles which dry up during sintering. The magnitude and the shape of the obtained pores depend on the slag's particles sizes.

Slag-M, preliminary milled in ball grinder, is divided to fractions with different particles sizes. For the production of porous composites are used: slag with particles size between -1,0+0,5 mm; -0,50+0,25 mm and -0,250+0,125 mm and powder from TV-glass with particles size <0.045 mm. The content of the TV-glass in the composites is 20, 30 and 40 wt. %, respectively. From the composite press-powder (Slag-M+TV-glass+plastifyer PVA) are pressed samples with different shape at pressure of 30 MPa. The press-samples are sintered in air atmosphere at temperatures of 900, 950 or 1000°C during 2 h (heating rate of 10°C/min).

With the increase of the sintering temperature, the composites containing Slag-M with larger grains (fraction -1,0+0,5) show salient tendency to melting and deformation. Conversely, the composites containing Slag-M with smaller grains (fraction -0,250 +0,125) are steady to thermal treatment up to T≥1000°C.

From the produced row of porous composites only those which possess optimal mechanical characteristics are selected. The density, porosity and mechanical properties taken as selection criterion determine as optimal the composite (Slag-M+ 40 % TV-glass) with slag's particles size -0,250+0,125 mm, sintered at 950°C/2h. It shows the lowest porosity of 26.8 % and the best mechanical characteristics - Table 5.

Composite	$T_{synth,}$ °C	ρ, g/cm³	θ, %	σ, MPa	E, GPa
Slag-M -0,250+0,125 mm +40 % TV-glass	900	2,27	30,5	29,47	17,51
Slag-M -0,250+0,125 mm +40 % TV-glass	950	2,39	26,8	29,28	21,25
Slag-M -0,250+0,125 mm +40 % TV-glass	1000	2.26	30.8	33.19	21.22

Table 5. Density, porosity and mechanical properties of composite [Slag-M (fraction -1.0+0.5) + 20% TV-glass] depending on the synthesis temperature

Solubility in aggressive media (0,1 mol/dm³ HCl and 0,1 mol/dm³ Na_2CO_3) is low and varies between 0,02-0,20 %.

The cross-section of this composite shows presence of closed type micro-pores with sizes of 5-10 μm, which are formed during sintering, and opened pores with sizes of 250-500 μm, connected to the voids between the slag grains soldered with the glassy phase. These macro-pores are interconnected through the whole composite volume, due to which it can be used as diffuser for air aeration (Vassilev et al., 2007b).

2.4.2 Porous composites with gradient (multilayer) structure

These types of composites are characterized by linear porosity gradient. They are formed by 2(3) layers with different porosity. The upper layer is composite slag+glass with slag's particles ≤45 μm. The porosity of this layer is controlled by the sintering conditions. The second (third) layer is composite with slag's fractions -1,0+0.5, -0,50+0,25 and -0,250+0,125 mm and glass fraction <45 μm. The porosity of these layers is significantly higher than this of the first layer since one works with larger particles of the metallurgical slag. Three

sintering temperatures are investigated: 900, 950 and 1000°C (pressing pressure of 30 MPa, air atmosphere).
Composites (Slag-M+TV-glass) in which the slag is with particles size of -1,0 + 0.5 mm do not yield thermal treatment above 950°C/2h since deformation of samples occurs. For samples with smaller slag particles (-0,50+0,25 and -0,250+0,125 mm) availability of TV glass concentration will have a limiting influence during thermal treatment .At waste glass concentration of 40+ % a deformation of compacts occurs and at synthesis temperature ≥ 1000°C (40 % TV-glass and slag particles size -1,0+0.5 mm or -0.50+0.25 mm (-0.25+0.125 mm) the composites melt.

Composite	T, °C	ρ, g/cm³	θ, %	σ, MPa	E, GPa
Slag-M (-1,0+0,5 mm) + 40 % TV-glass	950	2,23	31,60	25,07	16,87
Slag-M (-0,50+0,.25 mm) + 40 % TV-glass	950	2,25	30,98	33,70	21,82
Slag-M (-0,250+0,125 mm) + 40 % TV-glass	950	2,29	29,75	40,88	25,68

Table 6. Density, porosity and mechanical characteristics of double layered Slag-M+TV-glass composites

The composite Slag-M+40 % TV-glass (Table 6), sintered at 950°C/2h is suitable for practical application. It has porosity of 29,75-30,98 % and possesses the best mechanical properties (σ = 40,88-33,70 MPa; E = 25,68-21,82 GPa). The upper layer of this double layered composite, formed by the larger particles fraction, has porosity of 30-40 % and pores size of 350-500 μm. The pores of the lower layer are with significantly smaller sizes - 50-100 μm and the integrated porosity is 29-31 % (Vassilev et al., 2007b).

2.4.3 Porous composites with gradient (multilayer) structure formed with carbon and coarse-grained slag

The composite is formed by two layers with different integrated porosity, size, shape and orientation of the pores. The particles of the glass and the slag in the first layer are with sizes <45 μm. Carbon dust (3, 5, 7 or 10 %) with particles sizes <1 μm is used as pore-creator. Slag grains in the II^d layer are with size -1,0+0,5mm, -0,50+0,25 mm or -0,250+0.125 mm and these of the glass are <45 μm.
Compacts are pressed at pressure of 50, 100, 150 and 200 MPa. and sintering is carried out at T=950°C/2 h; air atmosphere, heating rate of 5°C/min. CO_2 produced during thermal treatment creates pores which determines high integrated porosity: I-layer - 35-40 % and II-layer - 30-40 %. The relationship between the porosity (θ) of the composite's upper layer, formed by the pore-creator (carbon dust) and its percentage (x) is described by the expression: $\theta=28,26 \exp(0,033 x)$. Lower layer porosity (at x=0) is 28,26 %.
Diffusers for waste water aeration can be produced from the porous composites which are thermodynamically stable and possess good mechanical characteristics, interconnected porous structure and chemical inertness in aggressive media. The low concentration of carbon dust (≤ 3-5 %) guarantees air bubbles with smaller sizes (Vassilev et al., 2007b).

2.5 About a possibility for application of metallurgical slag and waste glass

2.5.1 Obtaining of composites with controlled porosity

The possibility for application of glass-ceramic composite based on metallurgical slag and waste glass with controlled porous structure as diffuser for water aeration is examined by Fidancevska et al. (Fidancevska et al., 2009).

Permeability of the porous matrix is determined by measurement of the gas bubbles pressure through the porous medium and the resulting gas flow rate
For lowering of the temperature interval of the composites sintering waste glass from TV monitors was used. For obtaining of composites with high mechanical indices, Slag-R (fraction -0,125+0,063 mm) and concentration of the TV-glass 20 % with particles size <0,045 mm. The sintering temperatures (T_s) and the main properties of the compacts are shown in Table 7.

Composite	T_s, °C	ρ, g.cm^{-3}	θ, %	E, GPa	σ, MPa
Slag-R (-0,125+0,063 mm) + 20 % TV-glass	850	2,24	43	9,6	36
Slag-R (-0,125+0,063 mm) + 20 % TV-glass	900	2,25	42	10,0	39
Slag-R (-0,125+0,063 mm) + 20 % TV-glass	950	2,26	43	11,0	41
Slag-R (-0,125+0,063 mm) + 20 % TV-glass	1 000	2,28	45	9,9	38

Table 7. Sintering temperature (T_s), density (ρ), porosity (θ), elasticity modulus (E) and bending strength (σ) of composite Slag-R+TV-glass

The composite Slag-R(-0,125+0,063 mm) +20 % TV-glass (sintered at 950 °C/2h) has optimal properties (Table 7) and the technical coefficient of linear thermal expansion (α_{tech}) of this composite is within the interval 20-600°C is 10,9.10^{-6} °C^{-1}.
This composite is used for the following experiments. Its SEM-microphotography is shown on Fig. 1.

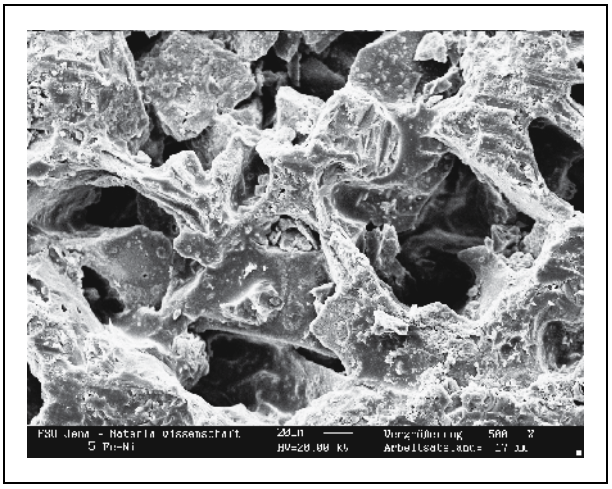

Fig. 1. SEM micrograph of the composite Slag-R(-0,125+0,063 mm) + 20 % TV-glass, sintered at 950°C/2h, (bar 20 μm)

The integrated porosity of the obtained composite is 43 %. Micropores of closed type with sizes of 5-10 μm are present in the composite as well as opened pores with sizes of 250-500 μm connected with the voids between the slag's grains and soldered with the glassy phase. Fractures among the pore walls were not evident.
Stability tests of the same composite in 0,1 M HCl and in 1 M Na_2CO_3 show that the weight loss after 24, 168 and 720 h varies between 0,02 and 0,6 wt. %, i.e. the composite is stable in aggressive media (Fidancevska et al., 2009).

2.5.2 Diffuser for water aeration

The permeability of the porous matrix is one of the most important characteristics determining its possible application. Pressure drop through the composite Slag-R (-0,125+0,063 mm) + 20 wt. % TV-glass as a function of the volumetric flow rate per unit of cross sectional area is shown in Fig. 2.

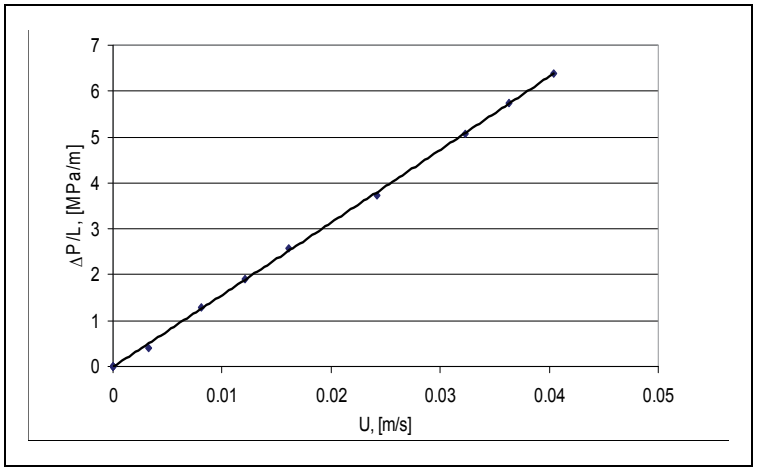

Fig. 2. Dependence of the volumetric flow rate per cross sectional area unit on the air pressure drop

Air permeability through the porous medium and the shape coefficient of the porous composite Slag-R (-0,125+0,063 mm)+20 % TV-glass are K_o=0,42 Da (1 Da=0,987.10^{-12} m^2) and C_o=5,82.10^6 m^{-1}, respectively. The mean cross sectional Darcy rate of the fluid, when the flow changes from Darcy's to quadratic flow regime, is 4,3 m/s.

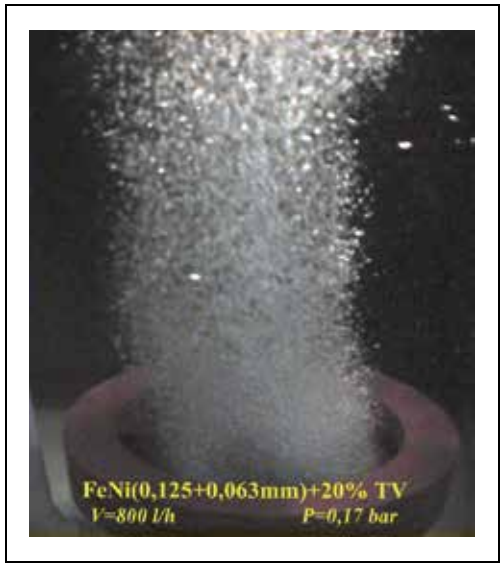

Fig. 3. Diffuser for water aeration (air flow V=800 l/h, air pressure P=0,17 bar)

This composite with controlled porosity is used for construction of diffuser for water aeration. The composite Slag-R (-0,125+0,063 mm)+20 wt. % TV-glass is built in plastic polyamide holders supplied with gaskets and inlet for air feeding. The diffuser has the following dimensions: ø=30 cm; h=6 cm. It is tested with working liquid water. Air flow is changed between 2.10^{-3}-7.10^{-2} $m^3/(m^2.s)$ and the air pressure – from 0,05 to 1,00 bar (Fig. 3).

The size of air bubbles depends on the air pressure in the aerator as the finest bubbles are obtained at low air pressure: at 0,05 bar their diameter is 300±100 μm. When the air pressure is increased up to 0,1 bar their diameter becomes 1,5-2,0 mm. A partial junction of bubbles is observed during their appearance from the diffuser's pores. At air pressure of 0,2 bar their diameter slightly increases and is about 2,5±0,5 mm. At pressure of 0,3 bar the bubbles change their geometry and possess diameter of 4±1 mm, which at 1 bar pressure reaches sizes 5±1 mm as a result of their instantaneous coalescence.

The diffusion air compression on the diffuser, the bubbles size, the air pressure, etc., show that the investigated composites based on industrial wastes (FeNi-Slag and TV-glass) can be used as diffusers for water aeration (Fidancevska et al., 2009).

3. Organic composite materials containing waste

3.1 Polymer composites containing organic waste

3.1.1 Polymer composites containing waste rubber

Although rubber wastes constitute a small portion of all world solid waste, their overall amount steadily increases as the number of disposed worn out tyres grows. For many years incineration and landfill were and, in some parts of the world, still are the main methods of their disposal. In the last years the rubber waste is applied in pavement of roads (Khalid & Artamendi, 2004), in the production of asphalt concrete mixtures (Tunsan, 2003; Zhan Ding et al., 2010), for production of activated carbons (Ko et al., 2004) but mostly as a fuel in cement production factories and kilns. Last few years waste rubber and mainly scrap tires were considered as one of the alternative energy sources (Stelmachowski & Słowiński, 2009, 2010). In addition grinded rubber waste and obtained granulate, fine rubber particles or rubber dust offer possibility for production of new composite materials with valuable properties – in (Aules, 2011; Sathiyamoorthy et al., 2011), for concretes with enhanced thermal insulation properties (Siddique& Naik, 2004; Yesilata et al., 2009), for sound insulation materials (Asdrubali, 2006) etc.

With regard to what has been said so far this topic of investigation combines naturally low thermal and electrical conductivity of UP in combination with rubber particles as a filler to find a way for waste rubber utilization as a component of polymer composites with electrical-, thermal- and sound insulation properties.

Experimental composites are based on unsaturated polyester resin (UP) "Vinalkid 550 P"(Orgachim Ltd, Bulgaria). The commercial product was a 66.8 w. % solution of the base polyester in styrene and was used as supplied by the producer. Polyester solidification was performed with cyclohexanon peroxide as initiator and cobalt-naphtenate as accelerator – both in concentration 2 w. % related to the UP weight. Rubber particles from ground rubber waste, 0.2-0.4 mm of size, previously dried are used as filler. Maximum concentration of the filler was determined as 12 w. % because of the sharp rise of viscosity at higher waste concentration.

Simple blending technology was used to prepare experimental samples: the resin and rubber particles were mixed thoroughly using a high-speed stirrer (700 rpm), cast in open polypropylene moulds and then cured at room temperature for 24 h. Post curing at 80 °C for 2 h was further applied.

In order to specify processing parameters flow behavior of UP/rubber particles polymer system was studied using rotational viscosimeter RHEOTEST (Germany), measuring device "cylinder - cylinder" (shear rate 0.2 - 1.3 10^3 s^{-1}, temperature range 25 - 85°C). Rheological experiments showed that "UP/rubber particles" polymer system could be characterized as suspensions of solid particles in Newtonian liquid. According to Utracki (Covas et al.,1995) the most common type of flow for suspensions is pseudoplastic, characterized by upper (η_0) and lower (η_∞) Newtonian viscosity. Results obtained by measurements confirmed that the presence of rubber particles changes the rheological behavior of the UP, depending on the rubber content from Newtonian at low concentrations, to dilatant at 10 w. % and pseudoplastic at 12 w.% (Fig.4).

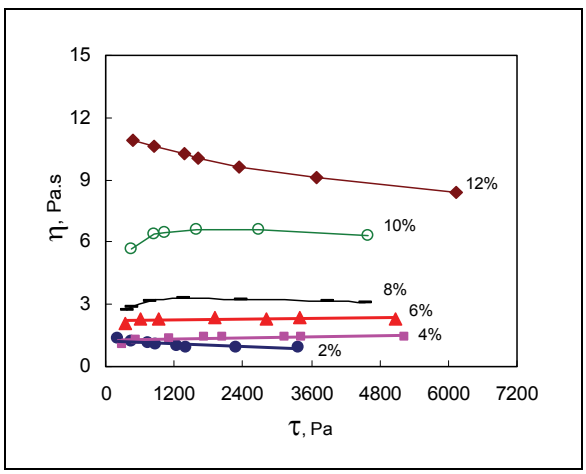

Fig. 4. Viscosity (η) - shear stress (τ) dependence for UP/rubber particles suspension (t = 25°C)

The possible reason for system flow behavior peculiarities was investigated applying optical microscopy (magnification x100). Rubber particles' optical micrographs demonstrated a very irregular shape and high-developed particles surface. Perhaps the close contacts between rubber particles at high concentration create a specific structure like pseudo-set and in this way the polyester resin turns out immobilized. Because of the highly developed particles' surface the quantity of the resin at 12 w. % rubber concentration is not enough to fully wet the filler and there is not really existing inter-phase layer between the two phases. It is known that the thickness of this layer is in high degree responsible for mechanical and strength properties of the composite. Based on these results, rubber particles content was limited up to 10 w. %.

As chemically inert composite component rubber particles were expected to not influence chemically the polyester curing reaction. The influence of the rubber particles on the process of solidification and mechanical behaviour of the composition were studied by mechanical impedance measurement on liquid-state samples (Petkov et al., 1999). The change of the mechanical impedance during the chemical solidification process follows the usual S-shaped

line (Fig. 5) but the increasing amount of waste particles leads to slow down of the curing reaction.

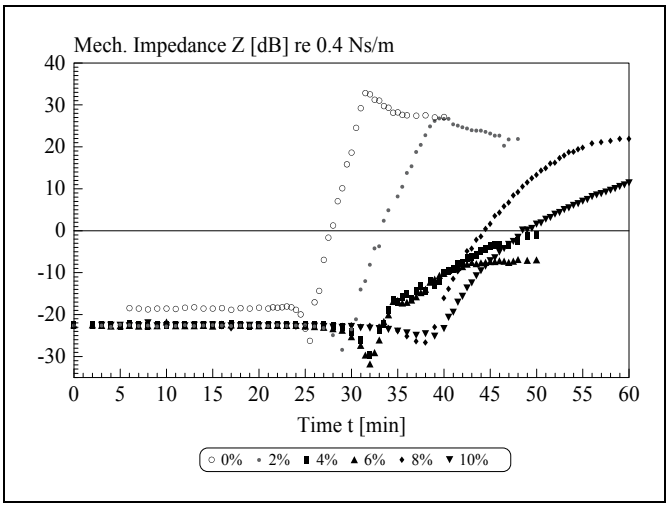

Fig. 5. Summarized plot of the experimental results for the mechanical impedance Z vs. the time for different concentration (w.%) of rubber particles

Strength properties of the polymer composite as impact strength, tensile breaking strength, compressing and bending strength were evaluated because these are the key properties most likely to be affected by incorporation of rubber particles. Experimental and measuring procedures are based on standard methods: *Tensile strength at break* was measured on ZD-20 all-purpose testing machine on standard dumbbell – shaped specimens, cut from 2 mm thick sheet, at room temperature, 100 mm/min speed; *Charpy impact tests* were carried out on notched specimens (pendulum power of 1.0 J, span of 40 mm); *Bending and compressing* tests were performed on universal ZD 10/90 testing machine, at 0,2 mm/s plates moving rate, at room temperature (accuracy ±1%) (Koleva, 2005).

Experimental results showed that tensile strength at break, bending strength and compression strength decrease with the rubber content increasing. This effect could be logically explained having in mind the structure peculiarities mentioned above. Because of the close interaction and aggregation at low concentrations, rubber particles act more like "defects" than as a toughening agent and increase the defectiveness of the matrix. At higher rubber concentration the effect of high developed particles surface and, as a result of that, pure wetting also takes place. The negative effects of the particles shape on the flow behavior and strength characteristic of composite could be eliminated in high degree by using rubber particles obtained by cryogenic grinding – in this case particles are geometrically shaped, with well formed sharp edges. Thus the particles' aggregation could be avoided and composite properties could be significantly improved (Rodriguez, 1998).

Based on the analysis of flow behavior and composite strength properties the content of rubber waste in the further experimental work was limited to 10 w. %. It was concluded also that the possible application of studied polymer composites should be limited for products, working in conditions without loading because of their insufficient strength characteristics. Thermo-physical characteristics of the composites were performed on ALAMBETA

measuring device (Czech Republic) at 25 ± 1°C. Thermal conductivity λ, thermal absorption *b*, thermal resistance *r* and thermal diffusivity coefficient *a* were calculated (Koleva et al., 2003).

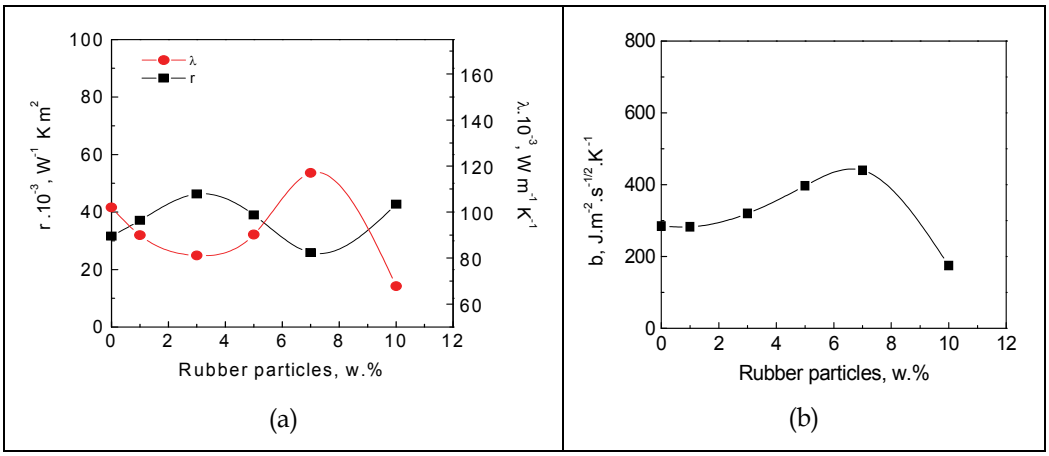

Fig. 6. Thermal conductivity (λ), thermal resistance (r) and thermal absorption (b) vs. rubber particles concentration, w. %

Data collected from experiments showed that the rubber particles content influences thermo-physical properties of the composition decreasing the thermal conductivity (Fig.6a) and increasing respectively the thermal resistance and thermal absorption of studied compositions (Fig.6b). An opposite tendency marks the changing of thermal absorption coefficient. The composition with 7 w. % shows lowest thermal conductivity and thermal diffusivity, and at the same time – high thermal absorption, therefore, it is suitable for thermal isolation materials.

When studying the electric characteristics of polymer materials two groups of properties are of great interest: the properties specified by the polymer characteristics in weak electric fields (dielectric permeability, tangent of dielectric losses, electrical conductivity) and those specified in strong electric fields (breakdown voltage, durability). The properties of the first group are closely related to the polymer chemical composition and structure. The evaluation of the second group is influenced by the presence of polar or non-polar ingredients as well as by the methods used for determining these properties.

RLC bridge and brass electrodes are used to measure the relative dielectric permeability (ε_r) and the tangent of the dielectric losses angle (tgδ), at 1 kHz frequency and room temperature. The dependences of these quantities on the frequency are determined by means of a Q-meter and by using a resonance method within the 8-25 MHz frequency range. A terra-ohmmeter was used for the specific volume resistance measurements at room temperature. To measure the electric strength high-voltage devices AII-70 at a constant rate of voltage increase are used.

Dependences of the dielectric permeability ε_r and dielectric losses tgδ on the rubber content are similar as a trend. The more considerable change in the tgδ values could be explained with the presence of electric conductivity losses. Frequency dependence of ε_r showed well expressed dispersion of values at the resonance frequencies – at high waste amounts new maximum values due to the rubber polarization occur (Fig. 7a). The tangent of the dielectric

losses angle decreases when the frequency increases for all materials studied since electric conductivity losses and polarization losses decrease (Fig. 7b). The highest tgδ values observed at frequency 9 MHz are due to resonance losses and they are more considerable at higher waste content. The specific volume resistance decreases with increasing the rubber content. The values of the electric strength are commensurate with those of the pure unsaturated polyester resins.

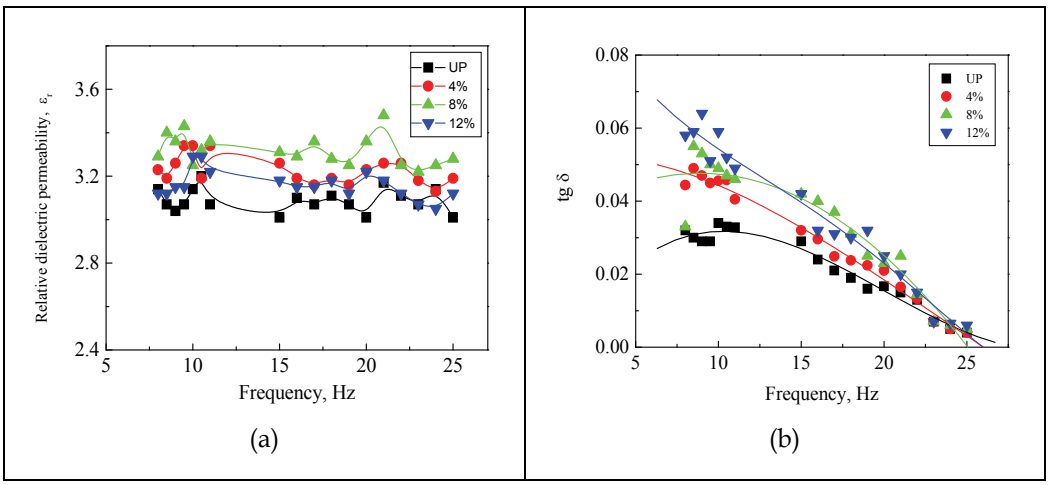

Fig. 7. Frequency dependence of the relative dielectric permeability (a) and tg δ (b) at various rubber contents

It was found by preliminary studies that the composition containing waste rubber particles demonstrates a good combination of elastic and viscose properties (Petkov et al., 1999). That offers possibilities for utilising the composition studied as a vibration dumping material.

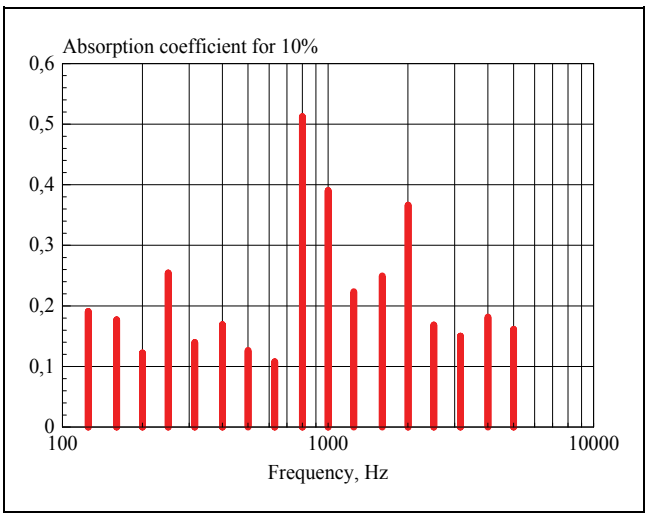

Fig. 8. Absorption coefficient α vs. frequency in 1/3 octave intervals for 10 wt. % rubber particles concentration

For estimation of the sound absorption properties of the composition a standard standing wave method was applied (Heckl & Mueller, 1995). The method is based on sound pressure level measurement in a tube of Kundt. As a result two parameters were calculated: acoustic impermeability R and absorption coefficient α (Petkov et al., 2001). The values of the absorption coefficient were measured for all 1/3 octave frequency bands in the range 125 - 5000 Hz (Fig.8). It is known that the frequency of 1000 Hz is a 0 dB level in the dB (A)-weighting filtering characteristics i.e. the isolation materials frequency response is supposed to be invers. Interesting results were obtained for the composition containing 10 wt. % of waste in the whole investigated frequency range, with very high values of absorption coefficient ($\alpha > 0.5$) around 800 - 1000 Hz. The same composition shows also very high stability and repeatability of results obtained by preliminary held experiments. The obtained high values for the absorption coefficient α, offer possibilities for practical application of the composite as an acoustical isolation material ($\alpha > 0{,}5$).

3.1.2 Polymer composites containing Gypsum-fiber waste

In the production of gypsum-fiber boards, gypsum-fiber powder is obtained as waste material. The usage of both gypsum and fiber as fillers of polymer composite materials is well known. The usage of waste material as a component of a composite material results in reduction of its cost, and in a positive environmental effect in view of the ecological problems (Pemikis, 1998; Zheglova, 2001).

Composite materials based on unsaturated polyester resin and epoxy resin as matrix and waste gypsum-fiber power – technological scrap as filler were studied in order to their possible application for electric insulation materials. The composites based on UP-PS5323 resin were solidified using iniciator Arrcoper 20 and Pitt-Consol 640 accelerator. The gypsum-fiber powder is processed up to 50°C within 10 hours, to remov the absorbed moisture. Simple blending technology, described above was used to prepare the experimental samples. The maximum quantity of gypsum-fiber powder has been defined to not exceed 40 w. % (Zheglova& Rashev, 2003).

Physical characteristics of the obtained composite material as density and hardness, strength and electric properties were measured as a function of the filler content. It was established that by increasing the filler quantity in the composition the composite density (Fig. 9a) and the hardness (measured with Brinell methods) (Fig. 9b) increased.

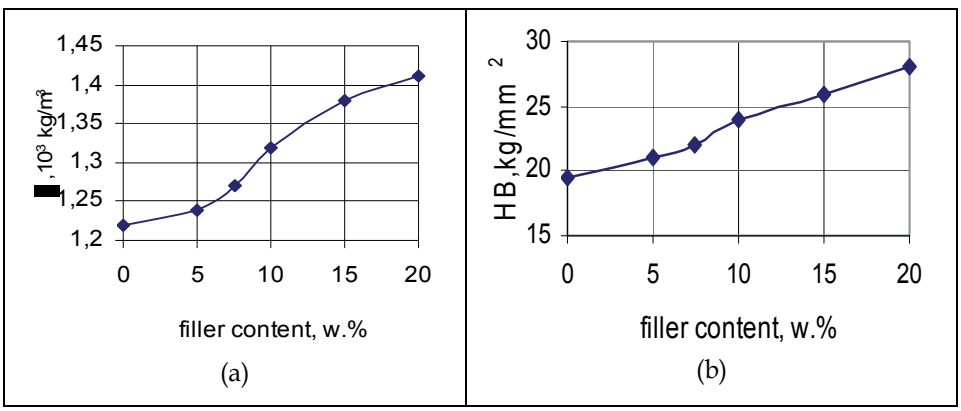

Fig. 9. Dependence of the composite density (a) and hardness (b) on the quantity of gypsum-fiber waste for UP-based composites

Strength characteristics of the composition also depend on the filler's amount in the composition. When the filler content increases, both tensile and compressive strengths decrease sharply at contents up to 7 (Fig. 10). The impact strength increases for composites containing up to 10%, then it gradually decreases while the gypsum-fiber content increases.

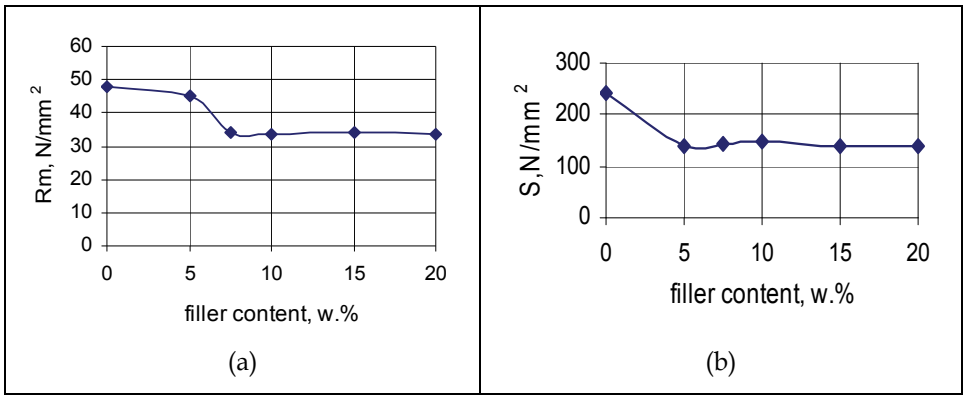

Fig. 10. Dependence of the composite tensile strength R (a) and compressive strength (b) on the gypsum-fiber concentration, w.% for composite based on UP

These trends considering the composite strength characteristics should be related first to the properties of its components (polyester resin and gypsum-fiber powder) on the one hand, and to the intensity of adhesion between the two phases on the other. The presence of microscopic particles of gypsum-fiber powder hinders the development of the dislocation planes of skidding in the process of determination and research of strength characteristics, influencing the process of destruction of the sample bodies (Zheglova& Rashev, 2003).

The influence of filler's amount on the electric properties of the composition as relative dielectric permeability ε_r and tgδ was studied. The relative dielectric permeability of complex dielectrics, which are compounds of chemically non-interacting components of different permeability values and with chaotic distribution of the components, as is the case with the composite materials under investigation, may be approximately described by the Lichtenekker equation (Pasinkov, 1986).

$$\ln\varepsilon_r^x = \theta_1 \ln\varepsilon_{r1}^x + \theta_2 \ln\varepsilon_{r2}^x \quad (1)$$

Using this equation (1), the values of ε_r of the obtained materials are calculated and compared with the experimentally measured values of ε_r for frequencies of 1kHz and 10MHz (Fig. 11).

A certain difference is observed between the calculated and measured values, but that is due to the fact that the composite material is assumed to consist of resin and filler only. In reality, it contains a small amount of gas inclusions in which moisture with great relaxation polarizations permeates.

Increasing the gypsum-fiber contents leads to increase of tgδ as the gypsum-fiber has greater losses due to both polarizations and conductivity. When the frequency increases, tgδ decreases because the slow polarizations disappear (Pasinkov, 1986; Zheglova, 2002).

The composite materials based on epoxy resins and gypsum-fiber were produced the same way as those based on UP and gypsum-fiber, using DER 331 epoxy resin (USA) with accelerator BDMA (Ciba-Switzerland) and hardener HY 917.

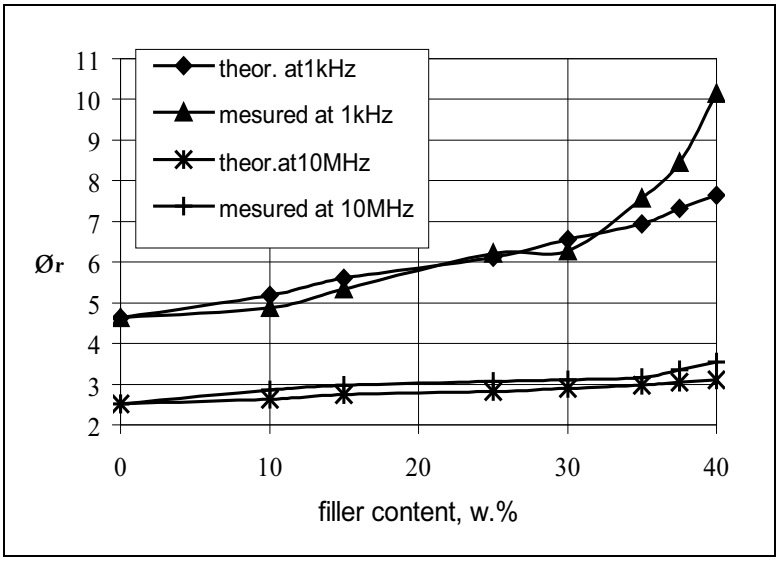

Fig. 11. Dependence of the composite relative dielectric permeability on the gypsum-fiber concentration

When comparing the properties of the composite materials with a gypsum-fiber filler based on unsaturated polyester resins and those of the materials based on epoxy resins, it could be concluded that the epoxy composite has a lower density and a hardness, but have a higher compressive strength (Fig. 12a), and impact strength (Fig. 12b).

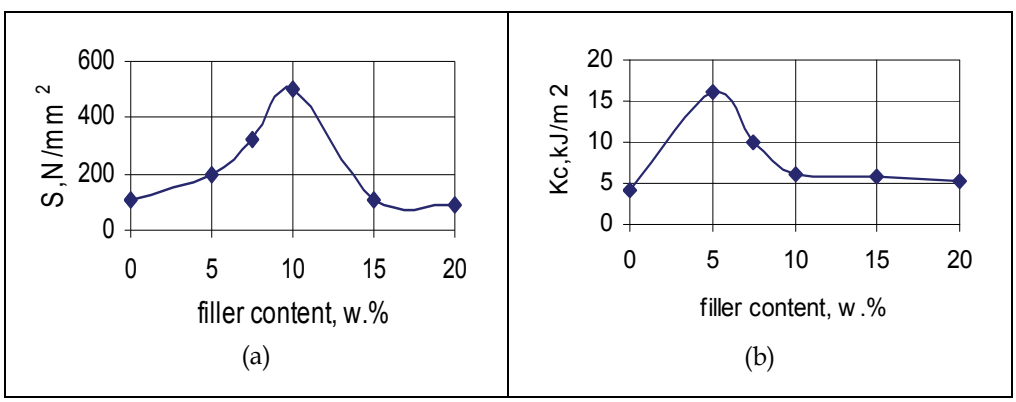

Fig. 12. Strength characteristics of epoxy resin-based composite containing gypsum-fiber waste as a function of the waste content: (a) compressive strength; (b) impact strength

The values of the tangent of the dielectric losses angle are comparable, but their dielectric permeability is lower due to their lower density. The electrical strength of the materials based on epoxy resins increases (Fig. 13a) when the quantity of the filler increases, whereas the electrical strength of the materials based on unsaturated polyester resins decreases under the same conditions (Fig. 13b).

Despite all this, all analyzed materials based on epoxy resins have a higher electrical strength than the materials based on unsaturated polyester resins. (Zheglova & Rashev, 2002).

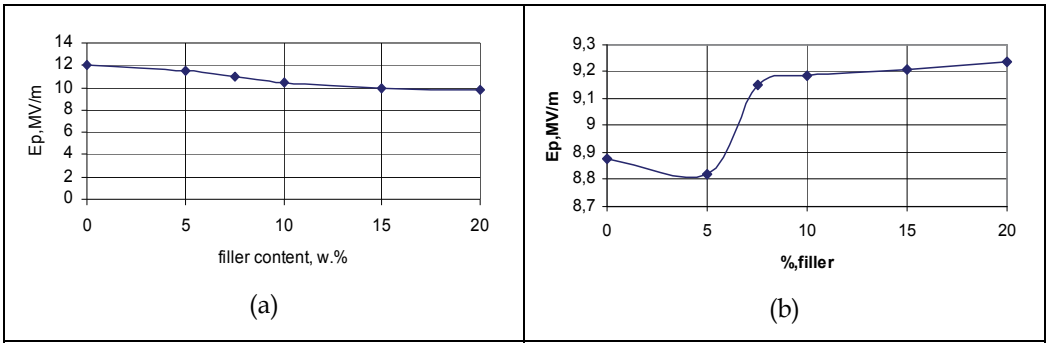

Fig. 13. Dependence of the electric strength on the gypsum-fiber quantity: (a) for UP – based composites; (b) for epoxy- based composites

3.2 Polymer composites containing inorganic waste

3.2.1 Organic composites containing waste dust from power production

Producing energy from coal and oil releases a wide range of pollutants into the environment. Moreover generation of sulphuric dioxide and nitrogen oxides, power production industry is one of the main sources of particulate matter in the air - industrial combustion plants and processes (17 %), commercial and residential combustion (16 %) and public power generation (15 %).

Ion based or electric filters are used to trap solid particles emission produced by burning in furnaces. Dust accumulated in these filters is deposited at dump sites. However, the chemical composition of captured electric filter dust is in fact a mixture of mineral oxides which could be used as fillers in both organic or inorganic composites intended for various applications. In this connection there has been studied the possibility of using waste dust from electric filters as filler in polymer compositions featuring electric insulation properties.

Unsaturated polyester resin "Vinalkid 550 PE - R" (Orgahim, Bulgaria) was used as matrix for the polymer composition. Waste dust collected by electro filters of thermal power station Maritza-Iztok 2 (Bulgaria) was used as filler. The filler was first fractionated - the largest fraction obtained after t fractioning was defined to be 125 – 250 μm. Following fractionating the waste has been processed by three consequent thermal processes: at 110, 600 and 800 °C until constant weight has been reached. Waste chemical composition was determined by combination of classical silicate analysis and atomic-absorption spectroscopy. Chemical analysis showed that it is composed by mixture of oxides, among them more than 50% is inert SiO_2, followed by Al_2O_3, some quantity of ferrous oxide and some other oxides. The mixture also consists of heavy metals' oxides and alkaline oxides in traces.

X-ray diffraction analysis was also processed on DRON-3 automatic powder diffractometer using filtered CuKα irradiation. The analysis showed the presence of the following phases (vol. %): quartz – 35.68; CaAl2Si2O8 – 28.03; mullite (3Al2O3.2SiO2) – 25.95; magnetite (Fe3O4) – 7.06; cristobalite – 3.27 (Koleva et al., 2008a).

Waste has been dried in electrically heated in thermal camera at 80°C for 24 hours for the sake of removing absorbed moisture before using it in the polymer composition. The waste content in the composition was limited up to 25 w. % as it was established that amounts greater than 25 w. % bring to a sharp increase in the viscosity thereby deteriorating of composition processability.

In order to investigate the influence of the waste on the composite's properties following composites were prepared and studied: composites containing mixed (not fractionated) not treated waste; composites containing activated waste with 125 – 250 μm size of particles and composits based on modified with high impact polystyrene (HIPS) polyester resin containing mechanically activated waste with 125 – 250 μm size of particles.

Strength and electrical characteristics of the material were tested to prove the suitability of experimental composites for electrical insulation materials. Strength characteristics as shock-resistance, compressive strength, and bending strength were determined using standard techniques described above. (Koleva et al., 2007). Specific electrical characteristics of the material as relative dielectric permeability, tangent of dielectric losses angle, electric strength and specific volume resistance were tested by methods and measuring devices described earlier (Zheglova et al., 2007).

Results obtained by experiments for composites containing mixed (not fractionated) waste showed that the presence of waste influences the studied strength characteristics and this influence depends on the amount of the waste in the composition. Into the studied concentration range the waste lowers the impact strength up 20 w. % waste content – then the impact strength values increase but the processing properties become worse. The waste also causes a drop of bending and compressive strength values compared to the neat polyester resin (Koleva, 2007).

According to Lipatov (Lipatov, 1986) the possible reason for this negative effect could be the poor interaction between the composition components. The main way to improve the interaction between phases and thus to improve the properties of the composite is to modify the filler and/or the polymer matrix. Two approaches were experimented: waste mechanical activation and modifying of polyester with polymer additive.

Waste mechanical activation was performed by dry processing in ball crusher with agate balls at room temperature for 15, 30, 45, 60, 120 and 180 minutes. During the milling process the particles surface energy increases constantly, but in a certain moment the geometric factor of activity (the specific surface) starts to exert influence. From this moment on the specific surface decreases, so this corresponds to the optimal milling time. In this particular case the optimal results were obtained at milling time of 30 minutes. Following mechanical processing the waste was again fractioned and chemically tested to determine some possible changes in particle size and chemical composition.

Chemical tests did not show significant changes in the waste chemical composition as the waste treatment was purely physical. But some changes in particles' size distribution compared to the one before treatment were observed (Fig. 14) - the amount of particles with largest size above 500 μm was reduced in half while the amount of the smallest particles (under 45 μm) doubled in the same time. The amount of 250 – 500 μm fraction increased and those of 125 – 250 μm decreased with one and the same amount so the quantities of two main fractions in the waste dust become almost equal. Decreasing in amount of largest particles and increasing the amount of smallest ones leads to more uniform and larger size distribution of waste particles so some changes in mechanical and strength properties of the studied composites could be expected (Koleva et al., 2008a).

Optical microscopy (magnification ×110) was applied to evaluate possible changes in waste particle shape and surface after activation. The irregularly shaped waste particles become more regular and round after activation. This effect, combined with the effect of particles size changing, could be a prerequisite to enhance the interaction between the polymer and the filler and thus the composite strength characteristics.

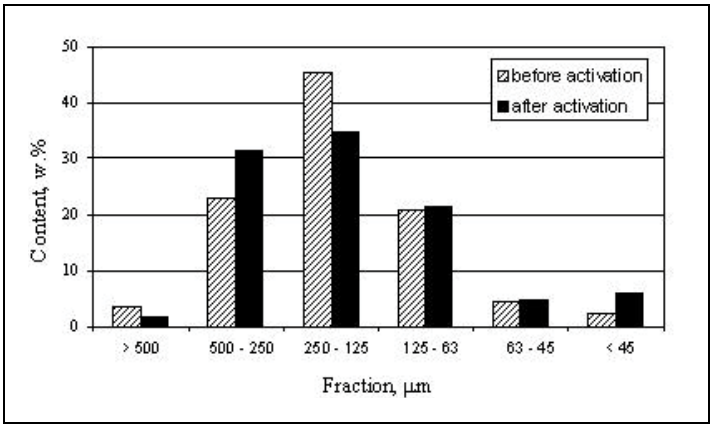

Fig. 14. Size distribution of waste dust particles before and after mechanical activation

Having in mind the effect of activation process on the size and shape of the waste, activated waste fraction 125 - 250μm was used in further experiments.
Based on the experimental results it could be concluded that the waste activation slightly influences the composite strength characteristics; in general, the type of the dependences does not change, but "activated" composites show higher bending and compressive strength (Fig. 15a and 15b) and lower impact strength compared to the "non- activated" ones (Koleva, 2008a, 2008b).

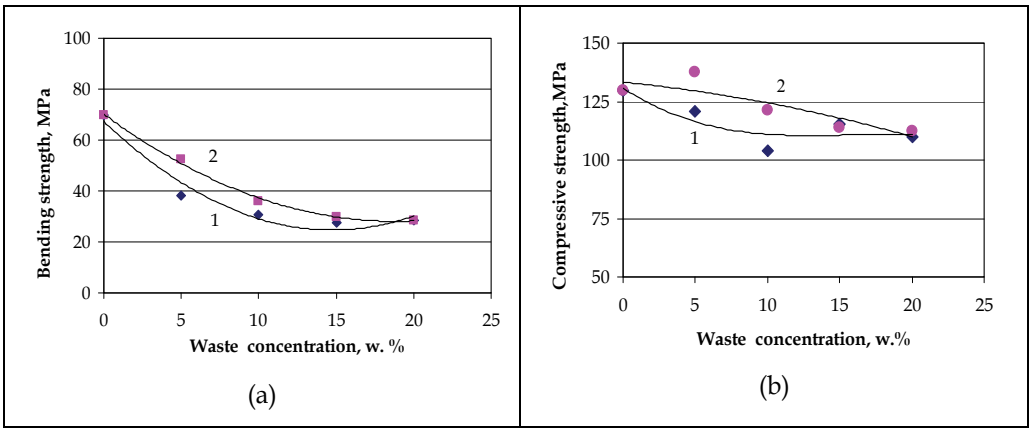

Fig. 15. Effect of waste dust content on bending (a) and compressive (b) strength of polymer composites containing not activated (1) and activated waste (2)

Electrical characteristics of the experimental composites were also influenced by waste mechanical activation. After the activation electrical strength increases and has its maximum at 10 w. % of waste (Fig. 16a) most probably due to the more uniform shape and size of the waste particles. Relative dielectric permeability increases also because of the dropping out of slow polarizations (Fig. 16b). The effect of activation is more clearly expressed at high frequency because of the stronger interaction between the waste particles and the polymer after activation – due to reduced molecules' mobility their polarization in the electric field becomes more difficult.

When the dielectric permeability decreases, tg δ values increase (Fig.17a) – this is caused by the increment of conductivity losses. This effect was proved by the specific volume resistance values (Fig.17b), which are in greatest degree changed after the activation (Koleva et al., 2008c).

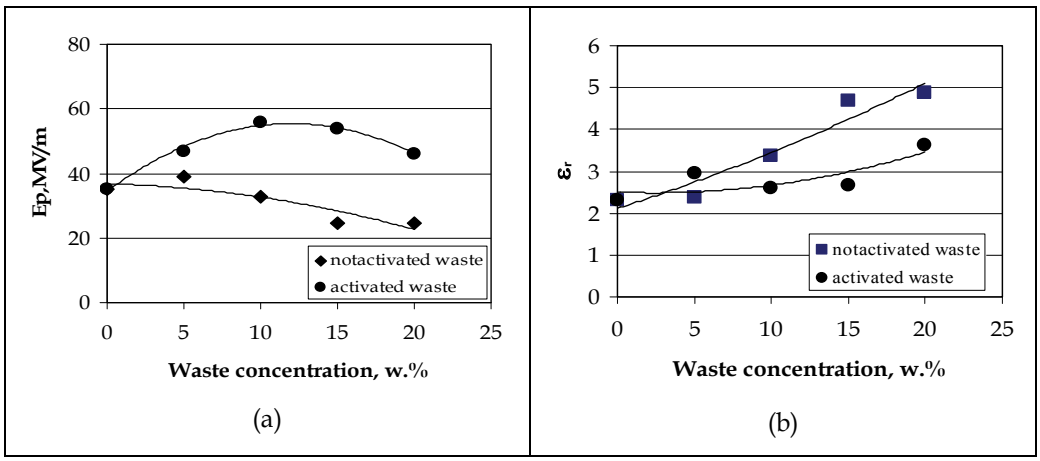

Fig. 16. Dependence of composite electrical strength (a) and relative dielectric permeability (b) on waste amount

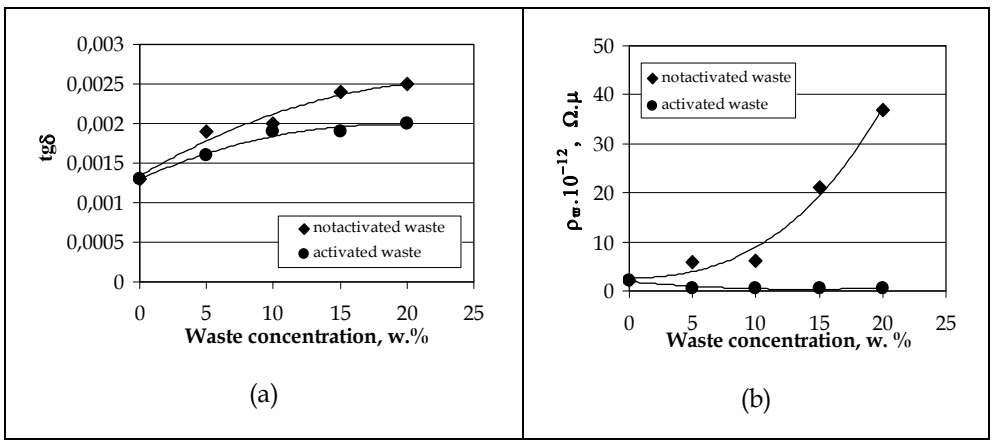

Fig. 17. Dependence of tgδ at frequency 8 MHz (a) and specific volume resistance values (b) on activated waste amount

In order to improve mainly the composite impact strength modification of UP with polymer additive was experimented. Based on previous studies (Koleva et al., 2005) high impact polystyrene (HIPS, Neftohim, Bulgaria) as a 40 w. % solution in styrene was used as modifier. From these investigations the optimal HIPS concentration was determined as 10 w. % from UP weight.

Positive effect of HIPS on composite strength properties was clearly expressed not only with regard to the composite's impact strength (Fig. 18a), but bending and compressive strength as well even though their values decrease with the increase in waste amount (Fig. 19b).

Lower strength characteristics at higher waste amounts probably result from some processes of filler sedimentation observed at concentrations of more than 10 w% that causes some anisotropy of strength properties (Koleva et al., 2008d).

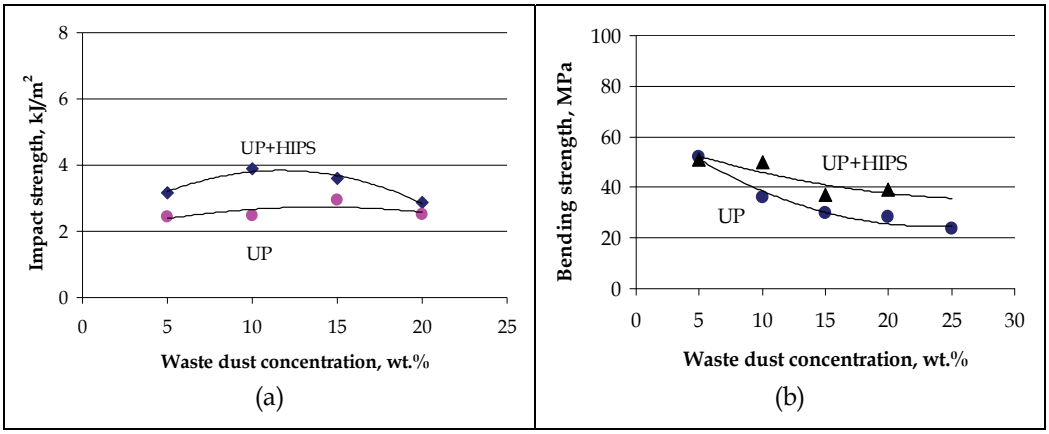

Fig. 18. Strength characteristics of composition based on UP/HIPS: impact strength (a) and bending strength (b) as function of waste amount

The presence of HIPS influences composite electric properties also – for example electric strength becomes slightly lower compared to the composite based on UP (Fig. 19a) – an effect caused by the structural nonhomogeny of the multiphase polymer system UP/HIPS (Koleva et al., 2008) but increases with the increase of waste amount in the composition.

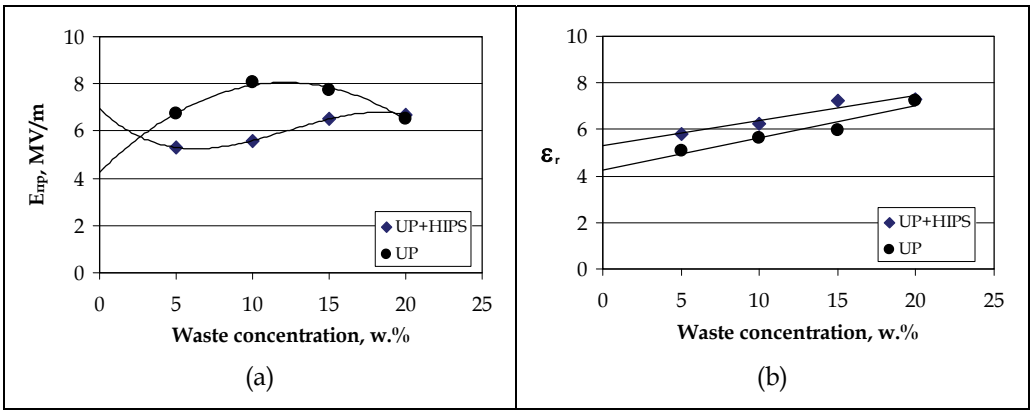

Fig. 19. Changing of electric strength E (a) and relative dielectric permeability ε_r (frequency 1 kHz) (b) values vs. the waste concentration for composites based on UP and UP/HIPS polymer system

The relative dielectric permeability increases also, because polarizations caused by HIPS superimpose on these ones generated by the polyester (Fig. 19b). Relative dielectric permeability values increase (especially at higher frequency) because of additional polarizations generated by the HIPS.

Values of tg δ and specific volume resistance ρ_v are higher for composites based on UP/HIPS, especially at lower frequency (Fig. 20a) because of dropping out of the slow

polarizations. At the same time the values of conductivity for these composites decrease, that means the losses caused by conductivity decrease also.

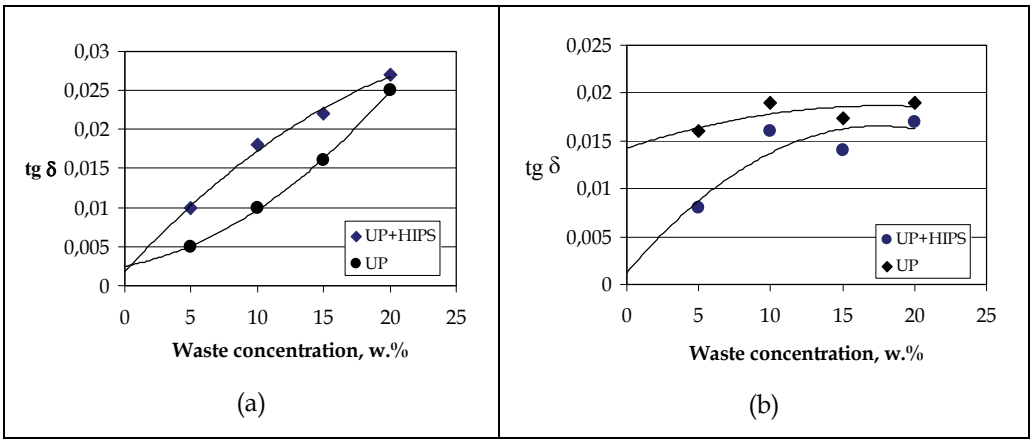

Fig. 21. Dependencies of tgδ on the waste content for composites based on UP and UP/HIPS at frequencies 1 kHz (a) and 8 MHz (b)

Dielectric losses become greater at higher waste concentration both at low and high frequency because of the part of them due to the waste increases – that is very well expressed at low frequency (Fig. 20b) (Koleva, 2008e).

4. Conclusions

A large number of waste materials have been studied as possible component of inorganic and organic polymer composites with specific characteristics and application. The tests carried out and the analysis of the results obtained considering the composite properties allow us to draw the following conclusions:

1. The waste ferronickel slag generated from the "refining" and "melting" processes, and waste glass from windows, containers and TV-monitors are suitable for wide application: direct - as filters with various application, glazes, etc., and indirect - as raw material for production of new materials useful for other productions (aerators, diffusers, ceramic filters, catalyst carriers, compact and porous glass-ceramics, etc.). The industrial waste slag and glass allow the production of composites with preassigned properties by the classical techniques of the ceramic technology. By using fractions of slag and glass with different ratio and grain size, as well as by addition of pore-creator, the production of composites with controlled microstructure and porosity (unilayer and multilayer (gradient)) is possible.
2. The composite materials developed on the basis of unsaturated polyester resins and gypsum-fiber filler show relatively good strength characteristics and can find application in the machine-building industry for the production of housings and other parts, replacing other materials with similar parameters, but of higher cost. The materials based on epoxy resins are better electro insulators and could be successfully used for electrical insulation compounds with application in electrical constructions, radio-electronics circuitry and other types of electrical equipment and appliances.

3. Grinded rubber waste could be used as filler in polymer composite materials based on unsaturated polyester resins. Filler's content should not exceed 12 w. % - otherwise the engineering properties of the resin deteriorate. The composition with 7 w. % shows optimal thermal characteristics and could be applied for thermal insulation materials. Although the values of some electric characteristics fall down, the compositions obtained keep their electric strength and specific volume resistance enough high, and the values of the relative dielectric permeability and the tangent of the dielectric losses angle low, which makes their use possible in electric insulating materials. The acceptable values of the absorption coefficient offer a good possibility for application of the composites containing rubber waste materials for noise isolation products (walls, plates, cylinders etc.).
4. The presence of waste dust from power production influences the strength and electric characteristics of the polymer compositions based on UP. This influence depends on the amount of the waste in the composition. The waste improves the electric strength, but lowers the relative dielectric permeability. Although this effect the composite possess enough good electric characteristics and could be used for electric insulation materials.

5. Acknowledgments

The authors extend their grateful acknowledgement to prof. Milosav Milosevski for his support in the synthesis and characterization of the inorganic composites.

6. Reference

Asdrubali, F. (2006). Survey on the acoustical properties of new sustainable materials for noise control, *Euronoise 2006*, Tampere – Finland, June 2006, pp 1-10.

Aules, W. A. (2011). Utilization of Crumb Rubber as Partial Replacement in Sand for Cement Mortar. *European Journal of Scientific Research*, Vol.51, No.2, pp.203-210.

Covas, J. A. et al. (1995). *Rheological Fundamentals of Polymer Processing*, Kluwer Academic Publishers, Niederland.

Ding, Z. et al.(2010). Research on Comprehensive Utilization of Waste Rubber and Aged Asphalt. *Applied Mechanics and Materials*, Vol. 34-35, pp.1526

Electric Power Industry: Largest US Toxic Polluter (n. d.) In source: http://www.mindfully.org/Energy/Power-Industry-Polluter.htm

Fidancevska, E.; Vassilev, V.; Milosevski, M.; Parvanov, S.; Milosevski, D. & Aljihmani, L. (2006). Composites on the base of industrial wastes. I. Physicochemical properties of Fe-Ni slag, *Journal of the University of Chemical Technology and Metallurgy*, Vol.41, No.4, pp. 431-438, ISSN 1311-7629.

Fidancevska, E.; Vassilev, V.; Milosevski, M.; Parvanov, S.; Milosevski, D. & Aljihmani, L. (2007). Composites based on industrial wastes III. production of composites of Fe-Ni slag and waste glass, *Journal of the University of Chemical Technology and Metallurgy*, Vol.42, No.3, pp. 285-290, ISSN 1311-7629

Fidancevska, E.; Vassilev, V.; Hristova-Vasileva, T. & Milosevski, M. (2009). On a possibility for application of industrial wastes of metallurgical slag and TV-glass, *Journal of the University of Chemical Technology and Metallurgy*, Vol. 44, No.2, pp. 189-196, ISSN 1311-7629.

Heckl, M. & Mueller, H.A.(1995). *Taschenbuch der Technischen Akustik*. Springler-Verlag, Berlin.

Khalid, H. A.; Artamendi, I. (2004). Mechanical Properties of Used – Tyre Rubber. *Engineering Sustainability,* 157, pp. 37 – 43.

Koleva, M., Betchev, Ch. & Zheglova, A. (2003). Rubber Waste /Polyesters Compositions for Insulation Materials. *Proceedings of 10 th International Conference on Mechanics and Technology of composite Materials*, Sofia, September, 2003.

Koleva, M., & Boyadjiiski, G. (2005). Influence of the mixing conditions on the physicomechanical properties of the polymer system NPES/UPS, *J. Techn. Univ. – Gaborovo.* Vol. 32, pp. 9–13, ISSN 1310-6686

Koleva, M. (2005). Rubber waste/UP polymer systems for insulation materials. *Proceedings of 6th International Scientific Conference "Advances in plastics technology" APT'05*, pp. 2005, ISBN 83-917693-4-8, Katowice, Poland, November 2005.

Koleva, M., Zheglova, A., Vassilev, V., Fidancevska, E., Milosevski, M., Vassilev, G. (2007). Strength characteristics of polymer composites with waste dust from power production. *Proceedings of International Scientific Conference UNITEH'07*, ISSN 1313-230X, Gabrovo, Bulgaria, November 2007.

Koleva, M., Vassilev, V., Vasilev, G.(2008). Polymer composites containing waste dust from power production. I. Influence of particles' mechanical activation on composition's strength characteristics. *Macedonian Journal of Chemistry and Chemical Engineering*, Vol.27, N 1, pp 41-46, ISSN 1857 – 5552.

Koleva, M., Vassilev, V., Vasilev, G.(2008). Polymer composites containing waste dust from power production. II. Strength characteristics of composites based on UP/HIPS polymer system. *Macedonian Journal of Chemistry and Chemical Engineering*, Vol.27, N 1, pp 47-52, ISSN 1857 – 5552

Koleva, M., Zheglova, A. & Vassilev, V.(2008). Polymer composites containing waste dust from power production. I. Impact of waste mechanical activation on electric properties of the polymer composite. *Journal of the Technical University of Gabrovo,* Vol. 36, pp. 64-69.

Koleva, M., Zheglova, A. & Vassilev, V.(2008). Polymer composites containing waste dust from power production. II. Electrical properties of polymer composites based on UP/HIPS polymer system. *Journal of the Technical University of Gabrovo*, Vol. 36, pp. 70-74.

Koleva, M., Zheglova, A. & Vassilev, V. (2008). Strength characteristics of polymer composites with mechanically activated waste dust from power production. *Proceedings of International Scientific Conference UNITECH'08,* Vol.2, Gabrovo, Bulgaria, November, 2008.

Lipatov, Y.S. (Ed.). (1986). *Physical chemistry of multicomponent polymer systems*. Naukova dumka, Kiev, Ukraine.

Pasinkov V.V.& Sorokin V.S. (1986).*Electronics Materials*, Vishaia shkola, Moskow, 1986.

Pemikis R. & Apsite B., (1998). Cellulose ether ionotropic gelsq their properties and applications.*Chemistry and Technology*, Vol.32, No 5-6, pp. 397-403.

Petkov, S., Koleva, M & V. Lazarova. (1999). Mechanical characteristics of rubber filled polyester. *Proceedings of International Conference TECHNOMER '99*, ISBN 3-00-0012510-8, Chemnitz, Germany, November 1999.

Petkov, S., Koleva, M. & V. Lazarova. (2001). Sound Dumping and Thermal Isulation properties of Plyester- Rubber aste Compositions. *Proceedings of International*

Conference TECHNOMER '2001, ISBN 3-00-008212-3, Chemnitz, Germany, September, 2001.

Rodriguez, E. L. (1988). The effect of cryogenically ground rubber on some mechanical properties of an unsaturated polyester resin. *Polym. Eng. Sci*., Vol. 28 N 22, pp. 1455-1461.

Sathiyamoorthy, M.; Thanappan, S.& Senthilkumar M. (2011). Utilization of waste rubber tires as an additional ingredient of concrete mixtures. *International J. of Engg. Research & Indu. Appls*. Vol.4, No. I (February 2011), pp. 335-350.

Siddique R. & Naik, T. R.. (2004). Properties of concrete containing scrap-tire rubber – an overview. *Waste Management,* Vol 24, N 6, pp. 563-569.

Soontaranum, W., Higgins, J. S. & Papathanasiou, T. D. (1996). Rheology and thermodynamics in partially miscible polymer blends. *J. Non-newtonian Fluid Mech*., vol. 67, N 1-3, pp. 191-212.

Stelmachowski, M. & Słowiński K. (2009). Conversion of waste rubber as an alternative rout to renewable fuel production. In: *Energy and Sustainability II,* Edited By: Mammoli, A.A.; Brebbia, C.A. & Popov, V., pp 489 – 499, WIT Press, London, UK.

Stelmachowski, M. & Słowiński, K. (2010). Feedstock recycling of plastic wastes and scrap rubber via thermal cracking. In: *Environmental Engineering III*. Edited by Pawłowski, A., Taylor & Francis Group, London, pp. 317–324.

Trofimov N.N.& Konovich M.Z. (1999). *Principles of the Creation of Polimer Compositions*, Nauka, Moscow, Russia.

Tunsan, M. (2003). The Use of Waste Materials in Asphalt Concrete Mixtures. *Waste Management and Research, Vol.* 21, № 2, pp. 83 – 92.

Vassilev, V.; Fidancevska, E.; Milosevski, M.; Parvanov, S.; Milosevski, D. & T. Hristova-Vasileva. (2007). Composites based on industrial wastes. IV. Production of porous composites from Fe-Ni slag and waste glass, *Journal of the University of Chemical Technology and Metallurgy*, Vol.42, No.4, pp. 369-376, ISSN 1311-7629.

Vassilev, V.; Fidancevska, E.; Milosevski, M.; Parvanov, S.; Milosevski, D. & T. Hristova-Vasileva. (2007). Composites on the base of industrial wastes. II. Physicochemical properties of waste glass, *Journal of the University of Chemical Technology and Metallurgy*, Vol.42, No.2, pp. 175-180, ISSN 1311-7629

Yesilata, B., Isıker, Y., Turgut, P. (2009). Thermal insulation enhancement in concretes by adding waste PET and rubber pieces. *Construction and Building Materials,* Vol. 23, pp. 1878–1882

Zheglova, A. & Rashev, G. (2001). Properties of Composite Materials from Unsaturated Polyester Resin, *Zbornik radova proceedings*, p. 141 – 146, 2001.

Zheglova A.& Rashev G.(2002). Properties of Composite Materials from Unsaturated Polyester Resins, *5th International Conference on Accomplishments of Electrical and Mechanical Industries*, Banja Luka, Republic of Srpska, 2002.

Zheglova A.; G. Rashev. (2003). Mechanical and Electrical Properties of Composite Materials based on Polyester Resins and Gypsymfiber. *Proceedings of International Conference* TECHNOMER'2003, (ISBN 3-00-008212-3) Chemnitz, Germany, November 2003,

Zheglova, A., Koleva, M., Vassilev, G., Boycheva, S. & Parvanov, S. (2007). Electrical characteristics of polymer composites containing waste dust from power production. *Proceedings of International Scientific Conference UNITECH'07*, vol.2, Gabrovo, November, 2007, ISSN 1313-230X

2

Porous Particle-Polymer Composites

Parvez Alam
Centre for Functional Materials, Abo Akademi University
Finland

1. Introduction

Composite materials designed to retain porosity usually have pore-structure specific application. Common man-made materials that exploit porosity include paper coatings, superconductors, nano-silicates and hydroxyapatite. Typical characteristics sought after include; capabilities of mass transfer and liquid retention, improved opacity, lighter weight, enhanced gloss, controlled spread and imbibition, and control of heat conduction. Though required for the enhancement of specific properties, porosity also has the drawback of reducing mechanical strength and stiffness. This chapter serves as an introduction to porous particulate-based composites. Included are the physical properties of minerals and their raw sources for excavation. Also described are the structures of packed particles and the physics of polymer spreading and dispersion. When combined, these effectively govern the geometrical characteristics of the resulting pore structures. Variations in polymer structure that arise through the presence and influence of particles are also explained. Following this section is a review on surface science, adsorption and wetting and the mechanisms of adhesion. To conclude the chapter, is a short discussion on the environmental footprint of particle-polymer composites such as are commonly designed to retain porosity. The primary focus in this chapter is on mineral-particle polymer-matrix composites with porosity.

2. Common mineral particles found in porous composites

This section introduces mineral particles oft used in porous composites. The particulate families of interest are the calcium carbonates, the kaolins, the talcs and the titanium dioxides.

2.1 Calcium carbonates

Calcium carbonates ($CaCO_3$) exist naturally in different forms. There are three crystal structures (aragonite, calcite and vaterite) though calcite, with a rhombohedral structure, is the most commonly used. Substantial calcite deposits can be found around the world. What differentiates chalk from limestone and marble (sources of calcite) are the levels of pressure and temperature to which they have been exposed. When calcite is close to the surface of the earth, a method of surface mining called "quarrying" is used. Otherwise, "underground mining" is used to extract calcite sources. The surface of calcite is reactive to acids, especially stearic acid, which improves its dispersion in polymers. Dispersed calcites usually have enhanced hydrophobic properties as compared to un-dispersed equivalents. Stearic acid

molecules react with carboxylate ions and organic chains on the surface of the calcite. Typical uses of calcium carbonates include rubber and plastic applications and they are predominantly utilised for financial benefit. Calcites are widely used in paper as a filling agent and as the main component of paper coatings. The typical types of calcium carbonates used are ground calcium carbonates (GCC) and precipitated calcium carbonates (PCC). PCC requires a three stage chemical conversion. The first is calcination, $CaCO_3$ + heat → CaO + CO_2; which is followed by hydration, $CaO + H_2O \rightarrow Ca(OH)_2$; and the final stage is the precipitation, $Ca(OH)_2 + CO_2 \rightarrow CaCO_3 + H_2O$ (Kemperl 2009).

2.2 Kaolins

Kaolin (Clays) ($Al_2O_3.2SiO_2.2H_2O$) are high aspect ratio particles with both anionic and cationic surface properties. Close to a thousand deposits are still commercially mined. The most noteworthy resources are in Cornwall, UK; South Carolina, USA; Georgia, USA and in Brazil. Hydraulic mining techniques are used at the Brazilian and Cornwall mines. Generally kaolin is dry mined, crushed and milled. This is the cheapest route from mining to processing. Particle size distributions are routinely expressed as an equivalent spherical diameter, esd. The highest (top) cut is typically at 75μm and refined clays range between 20μm-10μm. Kaolin can be used in an even finer size range using air-float or de-gritting methods. Most kaolin clays contain 50-99% kaolinite, some contain as little as 25% kaolinite. Mica, quartz and feldspar impurities make up most of the rest of kaolin.

2.3 Talcum

Talcum ($MgO.4SiO_2.H_2O$) is the softest mined mineral with a Mohs hardness value of 1. Like the calcium carbonates, talc exists prolifically around the world with particularly large deposits in Western Australia and France. Talc has been mined extensively using underground mining techniques, however in more recent decades, surface mining and open pit mining methods have become more widespread (Kennedy 1990). Talc particles tend to be within the 300-500nm size range though both fines and nano-talcum are receiving greater attention as reinforcing fillers for polymer (DePolo and Baird 2009). Talc is commonly used in paper making/coatings, as reinforcing in plastics and rubbers, in paints and in ceramics.

2.4 Titanium dioxide

Titanium dioxide (TiO_2) based composites normally comprise two of the three forms of TiO_2, these being anatase and rutile. Major TiO_2 mining operations are found in South Africa, Sierra Leone, Canada, Norway Australia and Ukraine. Open pit mines are typical for TiO_2 extraction and much of the mining is directed towards ore conversion to pure titanium. Both anatase and rutile have high energy surfaces and chemisorptions are common bonding mechanisms to these crystals (Andruszkiewicz 1990, Harris, 2004).

2.5 Table of physical properties of common mineral particles

Table 1 provides some rudimentary information on the physical characteristics of the mineral particulates described above.

3. Particle packing theory

The arrangement and distribution of particles will influence the properties of the composite and the structure of the pore space. Particle packing in nature is often found to be ordered

Particle	Shape	Density/ gcm^{-3}	Hardness (Mohs)
GCC*	Blocky, Cuboidal	2.7	3
Kaolin Clay	Platy, Hexagonal	2.6	2-2.5
PCC**	Acicular	2.7	3
Talcum	Platy	2.7	1
Anatase (TiO_2)	Acicular	3.82-3.97	5.5-6.0
Rutile (TiO_2)	Elongated to prismatic	4.23-5.5	6.5-7.0

*Ground Calcium Carbonate. **Precipitated Calcium Carbonate.
From (Besra et al 2000 , Broz et al 2006, Hauserman 1984, Holik 2006, Lam et al. 2009, Lerchenthal 1977, Meinhold 2010, Peters 1998)
Table 1. Physical properties of commonly used mineral particles

(Allen 1985). Particles used in composites are of different shapes, sizes, and surface chemistries. As a result, they interact differently with each other and with matrix materials. Particle packing theory has predominantly employed spheroids. Moreover, packing theory is generally restricted to pure particulate systems. Nevertheless, particles will tend to arrange within a composite according to the process arrangements and material properties/characteristics. Particles may pack more loosely than in compact packings but in a similar geometrical arrangement. Two classifications are oft used for random packings. These are loose and dense, and are in essence self explanatory (Cumberland and Crawford 1987). Dense packings are essentially those in which particles cannot easily move past each other, whereas loose packings are loose fit, easily moving particle packings.

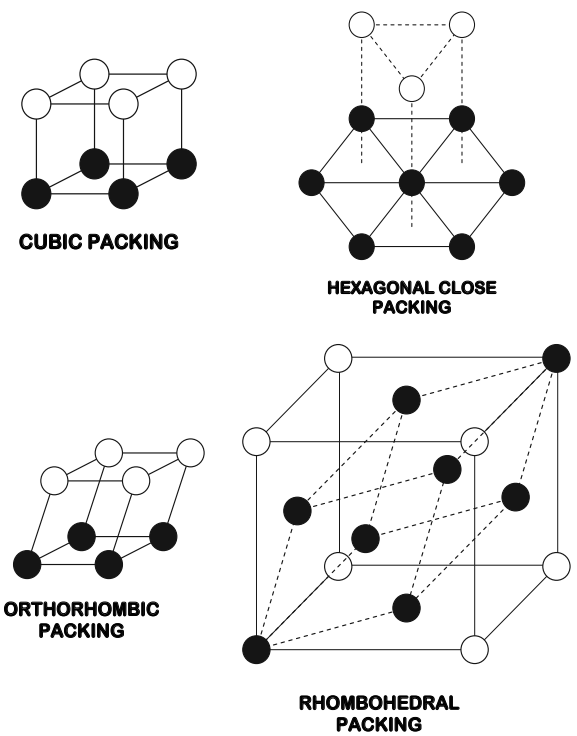

Fig. 1. Typical but idealised monodisperse packing arrangements

3.1 Idealised monodisperse sphere packings

A few idealised packing arrangements common to monodisperse spherical packings are shown in Figure 1. Particles in a packing occupying these positions and arrangements should be imagined as having larger particle diameters (almost touching) but are shown at distances in Figure 1 for diagrammatic clarity. Generally, the lower the matrix concentration, the closer the particles will pack and the more distinct the packing arrangement will be. Face centred cubic arrangements (not illustrated) are the tightest with a maximum packing fraction of 0.74. Hexagonal single layers are the tightest single layer arrangements. Porosity will arise when the matrix concentration is sufficiently low. Paper coatings are classic examples where the matrix concentration is so low that the pore fraction is often at around 30%. The highest possible coordination number for monodisperse spherical packings is 12. The coordination number can be defined as the integer sum of nearest neighbours, Figure 2. Nearest neighbours in powders and ceramics refer to those in a state of contact. In porous particle-polymer composites, the nearest particle neighbours can be considered as those that are conjoined by matrix material. In this sense, nearest neighbour definitions for such porous systems are simpler than those for filled system since in filled systems the particles may not actually be in contact.

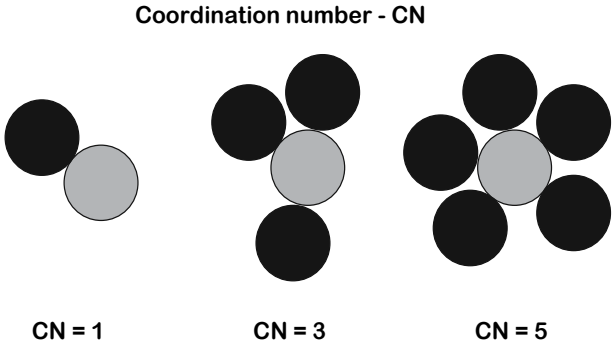

Fig. 2. Particle coordination numbers for particle systems are conceptually the same as for porous particulate-polymer composites. In both cases there must be contact between the particles, either directly or through a polymer matrix bridge

3.2 Polydisperse sphere packings

Polydisperse particle systems tend to have higher packing densities and average coordination numbers than monodisperse systems (Al-Raoush and Alsaleh 2007), Figure 3. A graph showing idealised packing density functions of monodisperse and binary packings is provided in Figure 4. In this figure, the binary packing refers to a two-particle polydisperse system. The secondary particle phase is considered an 'inclusion' therefore to an otherwise monodisperse system. One large particle in a polydisperse system may be surrounded by tens, hundreds or even thousands of contacting smaller particles, depending on the breadth of the particle size distribution. Volumes between larger particle contacts, depending on the size distribution, may act as particle-free volumes since particles can become trapped in regions close by, or the volumes are sufficiently small to prevent particle migration (Zok and Lang 1991). This is easiest to illustrate for binary particle systems, Figure 5. An idealised but typical graph comparing the coordination number frequencies for monodisperse and polydisperse systems is shown in Figure 6.

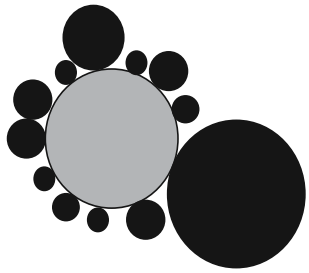

Fig. 3. Particle coordination numbers tend to be higher for polydisperse systems. The numerical value will depend on the breadth of the size distribution and the distribution of the particles and matrix material

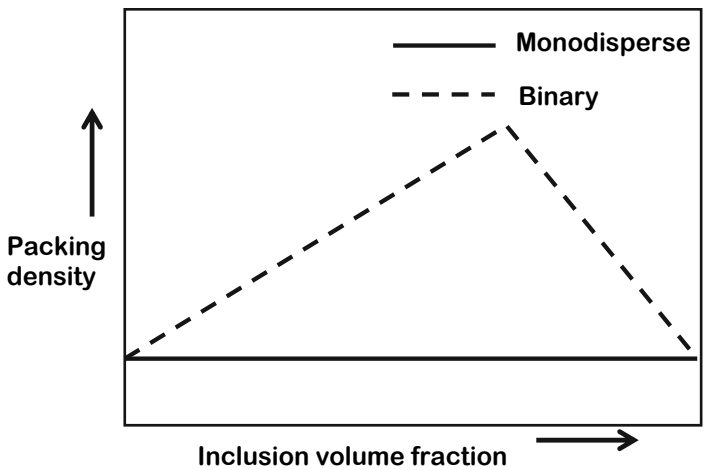

Fig. 4. Idealised packing density functions of monodisperse and binary packings

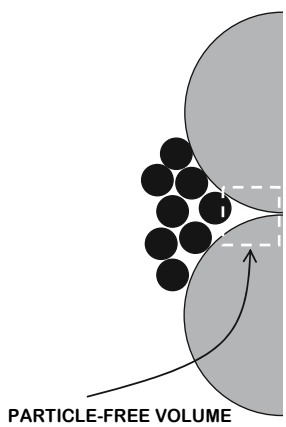

Fig. 5. Particle free volumes may arise through particle trapping as a function of the particle sizes

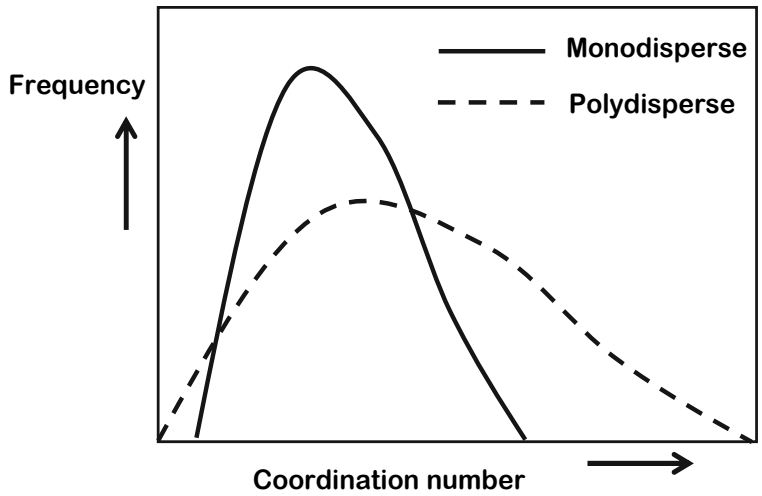

Fig. 6. Idealised but typical graph comparing the coordination number frequencies for monodisperse and polydisperse systems

3.3 Particle shapes

Many particle types used in porous composites are not spherical and cannot be justifiably approximated as such. Amongst the earlier classifications of particle shapes are those of Zingg (1935) who characterised four effectively cuboidal structures defined in Euclidean space according to a Cartesian coordinate system. The shape and orientation of particles distinctly impacts the properties of the composite material (Yamamoto and Matsuoka 1999, Abdul-Rashid and Akil 2008) and especially so with respect to the modes of failure and the fracture paths (Head and Rogers 1999). An ellipsoid for example may have the same sphericity as a sphere with surface protrusions, however, its influence on stress distributions and fracture, or indeed wetting and flow will differ considerably (Davis 1999). Typical particle geometries are shown in Figure 7. Of these particles, acicular particles exhibit the highest levels of microstructural heterogeneity (Alam et al. 2009) and platy particles laid relatively parallel pack very densely (Coulson 1949).

3.4 Computational packings

There have been numerous methods by which particles have been packed for computational and statistical analysis. For the most part computational packings have been made up of spheres or circles (Powell 1980, Scoppe 1990, Nolan 1992), often involving Monte Carlo methods; though, analytical shapes such as ellipsoids and spheroids have also been packed through discrete element methods (Ting et al., 1993; Lin and Ng, 1995). More recently, voxel digitisation has been used to successfully model arbitrary shaped random packings (Jia and Williams 2001, Byholm et al. 2004), which can subsequently be used for statistical, mass transfer and continuum mechanics simulations. The following are usually taken as minimal output requirements for computational packings (Davis 1999):

- Volume fractions of particles, polymer matrix and pores
- Dense and loose close packing fractions
- Coordination numbers
- Various distribution functions

- Particle and pore size distributions
- Distributions of various measures of surface curvature

In addition, the following should be deemed important further output parameters (Alam 2010):

- Anfractuosity (windiness of the solid state continuum)
- Tortuosity (windiness of the pore space continuum)
- Geometrical characteristics of the polymer matrix bridges
- Geometrical characteristics of the pore and neck space

The following section details briefly some of these parameters in respect of microstructure, influence and computation.

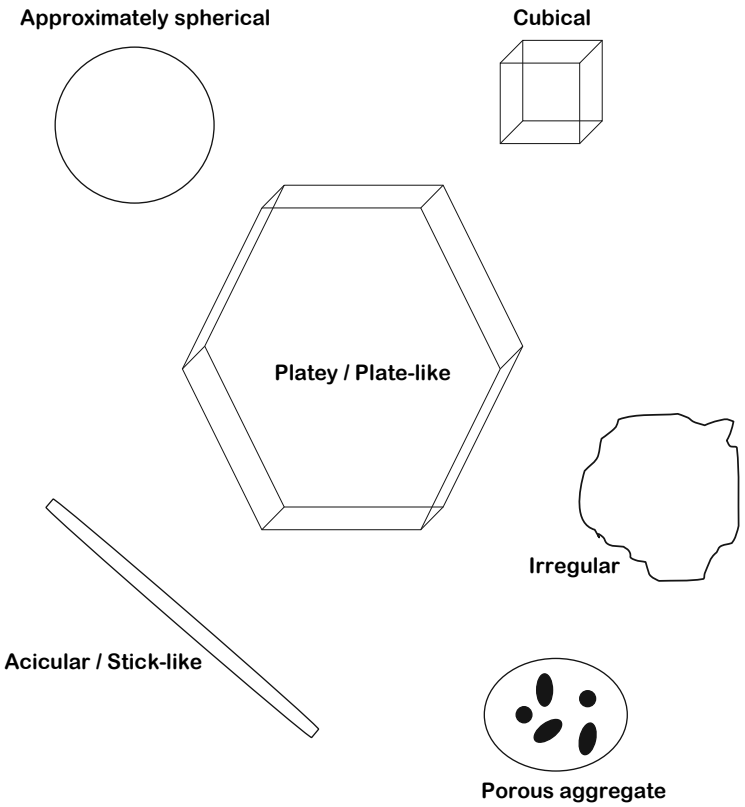

Fig. 7. Commonly applied approximations of particle geometries

4. Network connectivity in porous particle-polymer composites

There are essentially two 'networks' in any porous composite. These are the solid state network and the pore-neck network. This section outlines a few relevant issues pertaining to these networks.

4.1 The effects of pore space on microstructure and properties

Pore space dissociates the solidity of the composite. The levels of porosity, the pore size distribution and the pore-space connectivity may have both desirable and undesirable

effects on the properties of particle-polymer composites. Pore size and porosity can to some extent be controlled however; very often pore-space characteristics are heterogeneous causing irregular properties throughout the body of material.

Porosity is a necessary characteristic for imbibition (mass transfer), breathability, heat insulation and opacity. It is for these reasons amongst others, that composites are often manufactured to have porosity. Provided the materials and the manufacturing methods are suitable, evenly sized and spaced pores can be incorporated into materials. Particle-polymer composites are different, since the particles tend to pack 'quasi-randomly' and packing arrangements are seldom regular. The most homogenous pore space and size distributions arise through using monodisperse particles. Varying the polymer content inevitably changes the packing arrangement and indeed, polymer clustering can occur in some cases, which further increases the heterogeneity of the porous microstructure.

The characterisation of pore space is as much philosophical as it is statistical. Should necks that are larger than pores be counted as necks or as pores for example? How should one define the beginning of a neck and the end of a pore? Can pores be reticulate and if so, at which geometry do they become porous networks? For reasons such as these, the simpler statistical methods of analysing pore space can be better, especially in view of comparative studies. Even small alterations in the throat geometry can have noticeable effects on the properties of mass transfer (Ridgeway et al. 2001) and the levels of statistical deviation (Yanuka et al. 1986). The simplest parameter to determine is usually the porosity itself, Equation 1.

$$p = 1 - V_s \tag{1}$$

Where p is porosity and V_s is the volume fraction of the solid state. There are various experimental methods and computational methods for determining this parameter. Amongst the more prominent experimental techniques are the direct methods (weighing comparison with volume), intrusion methods such as mercury porosimetry, water evaporation methods, optical methods (often coupled to image analysis/computational science) and gas expansion methods. Mercury porosimetry, optical methods and gas sorption methods can furthermore be used to calculate pore surface areas. Surface area values are useful in common permeability equations such as the Kozeny-Carman relation (Kozeny 1927, Carman 1937, Carman 1956).

4.2 Characterisation of pore space

Pore circularity is a statistical parameter that is of relevance to porous composites, especially since pore aspect ratios can significantly affect composite properties (for e.g. conductance, mechanical). Circularity, *C*, is calculated for 2-dimensional slices according to Equation 2.

$$C = 4\pi\left(A / \mathrm{P}^2\right) \tag{2}$$

Where A is the area of a pore and P is the pore perimeter. Circularity is essentially a measure of how close to a circle the pore is. The value lies between 0 and 1. A value of 1 indicates a perfect circle and as the value approaches 0, the pore is understood to have an increasing aspect ratio. Even if porosity is low, if a pore has a high aspect ratio and lies perpendicular to, for example, a loading direction, it will considerably reduce the load carrying capacity of the composite (Alam 2010).

Other useful statistical parameters include the Feret diameter and the pore coordination number. The Feret diameter is the longest diametral distance that can be found about the extents of a pore. The coordination number can itself be taken to be the number of pores that are connected to a single pore. Combining the coordination number as a product with the neck area/total pore area ratio yields a numerical value that indicates the level of differential permeability, and hence pore space disorder, within a composite structure (Alam 2009).

Tortuosity, τ, is a parameter which indicates the levels of delineation of a pore network through a composite. The simplest model of tortuosity (Epstein 1989) is calculated as,

$$\tau = h/h_e \tag{3}$$

where h is the shortest length through the measured section of composite and h_e is the shortest length through the pore network across the same stretch of material. Numerical values of 1 indicate that the pore network runs linearly through the composite. As this value increases, so too does the running distance through the pore network. The value of tortuosity for packed media is not constant. Increasing the size of particles for example, whilst retaining a constant porosity, may lead to reduced tortuosity (Petford and Koenders 2001). Decreasing the particle size also decreases tortuosity, provided the porosity also increases (Attia 2005). Typically, porosity increases as particle packings use finer particles (Cumberland and Crawford 1987). Models developed for spherical packings since the 1880's substantiate that tortuosity decreases non-linearly as a function of increasing porosity (Boudreau 1996). Dias et al. (2006) further consider the function to be that of an inverse power law, but primarily for granular and spherical packings within the range of porosity 0.4-0.5. Moreover, the non-linear trend between tortuosity and porosity is found to be true for both systematic and random packings (Kim and Chen 2006, Zalc et al. 2004, Moldrup et al. 2001). Non-spherical models, such as those of Koponen (1998) and Alam et al. (2006) suggest inverse linear proportionality between the two parameters. Ultimately, decreasing tortuosity is usually coupled to increasing porosity; however, changing the aspect ratio and shape of particulates will further alter this tendency. Moreover, complex pore space geometries can be the cause of unpredictable mass transfer behaviour and hence, values for tortuosity, due to the existence of cavities and 'nests' (Alam et al. 2006). Armatas (2006) has also suggested that tortuosity is more closely linked to the standard deviation of the pore size distribution and less so to the connectivity.

4.3 Anfractuosity of the solid state continuum

The structural stability of any porous composite will depend upon the network connectivity of the solid-state. A higher and more scattered volume of porosity tends to break up the solid state network continuum and increases anfractuosity; A. Anfractuosity can be taken to be the 'tortuosity' of the solid state. In that sense,

$$A = l/l_e \tag{4}$$

where l is the shortest length through the measured section of composite and l_e is the shortest length through the solid-state network across the same stretch of material. Higher values of anfractuosity result in lowered load carrying capabilities of the composite (linear

load transfer being considered as 'ideal'). Conductance times are also increased as a result of greater anfractuosity in the solid-state. That coupled with porosity can sometimes give porous particle composites better insulating properties when compared with fully filled particle composites.

4.4 Polymer film formation

Mineral based particle composites with porosity will be bound by polymers. These polymers are normally added to slurry in fractions of weight. Properties worth considering before adding such polymers (e.g. styrene-butadiene latexes, acrylate-based latexes, starch-based polymers) include; polymer composition, colloidal properties (surface charges), rheological properties, mechanical properties, thermal and viscoelastic properties and surface energetics (Thümmes et al. 2009). When in contact with mineral particle surfaces, latex particles (often < 0.15μm) will spread. Subsequent film formation through further contact of latex particles (with each other) arises through a combination of compaction, cohesion and polymer chain inter-diffusion (coalescence). The formation of a defect free film will in turn depend on the temperature the latex particles coalesce under. The minimum film forming temperature (ASTM O 2354-68) should be reached for defect free film formation. Water must also evaporate for film formation to be complete. The procedure for drying such composites is governed to some extent by the properties of the composite components (such as solids content and burning temperatures), cross-linking characteristics and the dimensions of the material. Low solids content films dry much faster than high solids content films as there is less water to evaporate (Bierwagon 1979). Drying such composites too quickly can leave polymer films in a brittle state. Time should be allowed for the formation of polymer chain entanglements, which give rise to greater ductility within the cohered film (Gauthier et al. 1996). Film formation can be summarised accordingly (Steward et al. 2000):

- Evaporation, particle concentration and ordering
- Particle deformations, compaction and cohesion
- Polymer chain diffusion across particle boundaries

Mineral particle surfaces, following surface treatments with dispersing agents or surfactants, may comprise carboxylate groups. Such groups encourage interfacial cross linking not only between mineral (or dispersant) and polymer matrix, but also between latex particles. The formation of hydrogen bonds or ionic dipolar interactions eventuates in improved viscoelastic cohesive strengths of latex films and adhesive strengths at interfaces (Richard and Maquet 1992).

5. Polymer structure variations in porous particle-polymer composites

The presence of particulates may alter the structure and properties of the polymeric matrix within which it is held. Interfacial pinning for example, is an immobilisation of polymer chains at particle interfaces. This is true for interfaces that are purely particle-polymer as well as in cases where a layer of polar molecules (such as dispersants/surfactants) encapsulates the particle.

5.1 Polymer chain pinning

Polymer chain pinning can be considered as analogous to adhesion. Since many properties of composites rely on strong intermolecular forces of attraction between polymer and

particle, pinning is to an extent, a desired characteristic (Lepoutre 1994, Nielson 1966). Pinned polymer molecules are unable to move at one end and as a result have different characteristics to bulk polymer molecules. The thickness of this immobilised layer is difficult to predict or calculate. This immobilised layer is likely to be thinner in composites containing porosity because polymer molecules have more freedom to relax and orient to a lower energy state when there is less ambient resistance. Evidence and theory underlying the effects of polymer pinning on the dynamic properties can be found in Touaiti et al. (2010). The immobilised layer thickness in most particulate composites is generally in the range 1-50nm, (Rothan 2003) and varies as a function of particle size (Tan & McHugh 1996). The presence of particulates and the pinning of polymer molecules to particle interfaces may also restrict movement of polymer molecules as effectively, space limitations exist. Polymer molecules will moreover, orient according to lowest energy state principles and the presence of particles alongside pinning effects will guide somewhat the state of molecular orientation. For this reason, particles can act as nucleation sites and polymer crystallinity and orientation becomes a function of particle presence (Cho et al. 2002). Smaller particles (especially of the nano-scale) are highly effective as nucleating sites and can easily disrupt existing crystal structures (Bhimaraj et al. 2007, Yuan et al. 2006). Polymer chain pinning affects properties such as fracture strain, stiffness, and hardness (Akinci 2010). These are all in turn related to changes in activation energies for fracture, and energy that can be stored by pinned chains as compared to free moving chains. Interparticulate distances and particle surface areas will furthermore hinder to a greater or lesser degree, the polymer chain mobility. Smaller interparticulate distances and higher surface areas restrict mobility more effectively (Traina 2008). Porosity within the composite promotes 'free movement' of chains at free surfaces and reverses somewhat, the effects of pinning on the mechanical and viscoelastic properties of the composite (Mansfield & Theodorous 1991, Baschnagel & Binder 1995). Pores can thus act as 'relaxation' zones, which allow for increased free surface areas of the inter-pore polymer confinements.

5.2 Changes in the molecular weight through degradation and cross linking

Polymeric material degrades in the presence of particles thus reducing the molecular weight. This degradation may be onset by mechanical, thermal or chemical means. Degradation is often exacerbated in process operations such as moulding, extrusion, compounding and through the application of heat and pressure. Chemical interactions at the interface may deactivate stabilisers and antioxidants in the polymer, or, may simply be chemical species that degrade polymers such as surface-present enzymes in biodegradable composites (Cooper et al. 1995). Thermo-mechanical degradation that can occur during processes such as extrusion, is a result of highly localised interfacial frictions resulting in micro-scale mechanisms of erosion. Degradations, whether thermal, mechanical or chemically instigated, have a quite direct impact on the properties of the final composite (Traina 2008, Choi et al. 2005). However, the contribution to the overall properties through the particles themselves, result in mechanical enhancement even though there may be considerable evidence of polymer degradation (DePolo 2009). Mechanical work is probably the greatest contributing factor to degradation and the effects of particulates on polymer degradation is most pronounced when polymer viscosities are high. It should be noted that particle degradation also occurs (Fisa et al. 1984) during the processing stage with polymer. The level of mechanical degradation to the particle will however, be highly dependent on the properties and characteristics of the particle relative to the process conditions and the properties of the polymer. The molecular weight and crosslinking characteristics of the

polymer can also change during curing. The curing process determines the eventual molecular structural details of free-radical cured polymers, which in turn influence the polymer properties. Particles create variations in the curing process and thence the final properties of the polymer. These variations include; (a) lowering of the overall exotherm thus reducing the cure temperature and kinetics of curing and (b) particle surface chemistry altering the stability of the polymer at the interfaces (Rothan 2003).

5.3 Additives – for modification to surfaces and to polymer structures

Additives such as dispersants, surfactants, coupling agents, plasticisers and stabilisers will often adsorb more readily to a particulate surface than a polymer matrix material. This creates polymeric regions close to the particle interfaces with a lower molecular weight than the virgin polymer matrix. Without these additives, process and manufacture of porous particle-polymer composites with sufficient homogeneity is almost impossible (most notably due to particle agglomeration). In the cases of typical carbonate-latex coatings, dispersing agents used bind preferentially to calcite surfaces and the latex is effectively adhered to the surface of the dispersing agent. In such a case, there are essentially two interfaces in place of one, the calcite-dispersant interface, and the dispersant-latex interface. In some cases, surfactant adhesion to particulate surfaces can in fact improve the overall strength of the composite, provided the polymer-surfactant bond strength is superior to that of the polymer with the particle. A short list of common polymer additives from Stevens (1993) is provided in Table 2.

Additive	*Purpose*
Additives for the modification of surface properties	
Antistatic agents	Prevention of build up of static charges
Coupling agents	Interfacial bonding agents (for better bonding)
Release agents	Prevention of particulate sticking
Additives for the modification of chemical properties	
Antioxidants	Prevention of oxidative degradation
Additives for aesthetic pleasure	
Colouring agents	Optical/colour properties
Nucleating agents	Optical properties
Additives for process control	
Cross linking agents	In the curing process
Emulsifiers	Stabilisation of polymer emulsions
Heat stabilisers	Prevention of thermal degradation
Plasticisers	Lower the melt viscosity
Release agents	Prevention of particulate sticking
Thickeners	Increase the viscosity of the polymer

Table 2. List of common additives

6. Composite models for porous particulate materials

The most common engineering models for composites cannot be satisfactorily applied to porous particle-polymer composites. Various models suggested for porous two-phase particulate ceramics provide a good starting block for understanding how porosity affects particulate composites. The simplest of these models is that occupied by Voigt bounds such that the elastic modulus of the porous material, E, is inversely proportional to porosity, φ. In this model, E_c is the composite elastic modulus (assuming isotropy and no porosity).

$$E = E_c\left(1-\phi\right) \tag{5}$$

This model, though simple, has drawbacks in that it does not usually yield sound predictions for porous composites. Generally, non-linear models are found to be more accurate. Phani et al. (1988), Maitra and Phani (1994) and Wagh et al. (1993) have suggested the use of the following relationship, Equation 6, which is essentially an exponential modification of the linear expression (Equation 5). In this equation, a and b are constants, or, fitting parameters.

$$E = E_c\left(1-a\phi\right)^b \tag{6}$$

For the most part models used to predict the non-linear elastic modulus characteristics of multi-phase materials use such fitting parameters. This is often expressed by including a numerical exponent such as is shown in Equation 7, (Brown et al. 1964) and refer to Phani et al. (1988), Maitra and Phani (1994) and Wagh et al. (1993). The elastic modulus can also be expressed as being a product of the composite elastic modulus and e^m, Equations 8 and 9, (Rice 1977, Knudsen 1959).

$$E = E_c\left(1-a\phi^{2/3}\right) \tag{7}$$

$$E = E_c e^{-a\varphi} \text{ for } \phi \le 0.5 \tag{8}$$

$$E = E_c e^{-a(1-\varphi)} \text{ for } \phi \ge 0.5 \tag{9}$$

Further modified non-linear expressions for the elastic modulus of multiphase porous composites include fitting parameters that are a function of the pore aspect ratios, A_r, Equations 10 and 11 (Janowski and Rossi 1967, Boccaccini et al. 1993).

$$\begin{aligned} E &= E_c\left(1-a\phi\right) \text{ for } \phi \le 0.5 \\ a &= \mathrm{f}\left(\mathrm{A_r}\right) \end{aligned} \tag{10}$$

$$\begin{aligned} E &= E_c\left(1-\phi^{2/3}\right)^{1.21a} \text{ for } \phi \le 0.5 \\ a &= \mathrm{f}\left(\mathrm{A_r}\right) \end{aligned} \tag{11}$$

Equations of the generic form (Hashin 1962, Ramakrishnan and Arunachalam 1993),

$$E = E_c \frac{(1-\phi)^n}{1+k\phi} \tag{12}$$

include an additional parameter k that incorporates Poisson's ratio effects of the solid state into the model. These models have for the most part, been taken into consideration for two-phase (particle-air) composites. Models concerned with the prediction of three-phase (air-particle-polymer) composites are generally derivatives of the classical mixture's models (Voigt 1889, Reuss 1929, Halpin-Tsai 1969). These models shown in Equations 13, 14 and 15 respectively, are such that the volume fractions, F, of matrix, $_m$, and particle, $_p$, must be fractions of the composite including the extra air that exists through porosity.

$$E = E_p F_p + E_m F_m \tag{13}$$

$$E = \left(\frac{F_p}{E_p} + \frac{(1-F_p)}{E_m} \right)^{-1} \tag{14}$$

$$E = \frac{E_m (1+\xi\eta F_p)}{(1-\eta F_p)} \tag{15}$$

where $\eta = \dfrac{(E_p / E_m) - 1}{(E_p / E_m) + \xi}$ and $\xi = 1$

Needless to say, none of the classical models have shown they can be successfully used to predict the elastic modulus of porous particle-polymer composites. The Reuss and Halpin-Tsai models being "lower boundary" definitions usually yield the closest predictions, though these are still usually far out (Xu 2006). Alternative models specifically for fully-filled particle-polymer systems have been suggested by Eilers (1941), Brinkman (1952), Nielsen (1969), Narkis (1976) and Thomas and Muthukumar (1991). These being contemporary non-porous models, will not be reviewed herein.

McAdam (1951) modified the Reuss model to include a linearly proportional reduction of the elastic modulus as a function of increasing porosity, Equation 16.

$$E = \left(\frac{F_p}{E_p} + \frac{(1-F_p)}{E_m} \right)^{-1} \cdot (1-\phi) \tag{16}$$

Bert (1985), preferred to modify the Halpin-Tsai model with a slightly more complex reduction term. The Bert model includes a composite term that takes into consideration the relative pore space and the pore shape. This model, Equation 17, assumes K_0 = 2 for spherical pores.

$$E = \frac{E_m (1+\xi\eta F_p)}{(1-\eta F_p)} \cdot \left(1 - \frac{\phi}{(1-F_p)} \right)^{K_0 (1-F_p)} \tag{17}$$

A comprehensive model suggested by Alam (2010), Equation 18, factors into the mixtures' model of Voigt; an 'effective' binder fraction, a stress transfer, s_t, aspect ratio, L_p/d_p, product for the particles, an anfractuosity parameter, A, and an effective pore width ratio, $w_{p,\max}\, w^{-1}$. When compared with the Voigt, Reuss, Bert and McAdams models, against both experimental and simulation results, this model was found to yield the most accurate predictions.

$$E = \left(E_p F_p \left(\frac{\overline{L_p}}{d_p} \cdot \frac{1}{s_t} \right) + E_m F_{c,eff} \right) \cdot \frac{1}{\overline{A}} \cdot \left(1 - \frac{w_{p,\max}}{w} \right) \tag{18}$$

If there are no pores then $A = 1$ and $w_{p,\max} = 0$.

7. Surface science

The utility of any composite will be influenced by the strength and intimacy of the bond between the components. Many factors affect the bonding between components in a composite. These include at least wetting, roughness and the mechanisms of adhesion, all of which are interconnected.

7.1 Adsorption and wetting

The spreading of liquid across a solid surface and its ability to maintain contact is wetting. Wetting is a function of the intermolecular forces of attraction at the contacting surfaces. The extent of wetting is determined by the balance between adhesive (interfacial forces) and cohesive forces of attraction within the body of fluid. Higher adhesive forces encourage spreading while higher cohesive forces make the body of liquid curl into a ball. The droplet contact angle is the angle at which three phases meet (solid, liquid and gas). The droplet contact angle is an indicator of the level of wetting, and hence the relative strengths of the adhesive and cohesive interactions. Very low contact angles indicates high wetting favourability while very low contact angles mean the liquid does not wet the solid surface very well. Figure 8 shows examples of non-wetting, wetting and high (near-perfect) wetting surfaces.

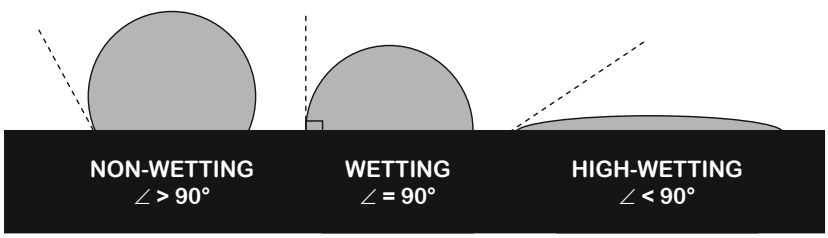

Fig. 8. Examples of non-wetting, wetting and high-wetting

Other factors that influence wetting include the liquid viscosity, the surface roughness and ambient pressures. The 'equilibrium' state of a droplet on a surface, Figure 9, is represented by Young's equation, Equation 19,

$$\gamma_{SG} = \gamma_{SL} + \gamma_{LG} \cos\theta \tag{19}$$

where γ is the surface energy between two phases.

Interactions at the interface of polymer and particle govern the spreading characteristics and ultimately the strength of the adhesive bond between the two. Ingress of polymer matrix into particle bodies is possible when the particles have holes, defects or micro-/meso-pores. Ingress such as this increases the number of interfacial interactions and mechanical interlocking, and consequently improves adhesion (Van Meer et al. 2009). Polymer droplet spreading/ingress behaviour is however, further complicated by factors such as the topography of the particle surface and external influences that may alter the flow and properties of the polymer matrix (pressure, temperature). The properties of the polymer (e.g. viscosity) relative to the topography and surface energies are paramount in wetting.

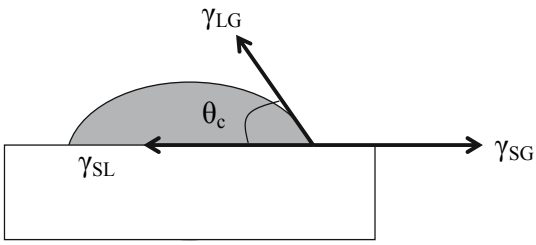

Fig. 9. The equilibrium state of a droplet is represented by Young's equation, Equation 19

7.2 Roughness

Packham (2003) justifies that the forces of attraction between two surfaces may be enhanced by increasing roughness, provided that the topographical profile does not reduce the total area of contact. A commonly employed roughness parameter is the R_a roughness. This is effectively a measure of the mean protruding to intruding height differentials about the average height. It is expressed as,

$$R_a = \frac{1}{L}\int_0^L |z(x)|\,\mathrm{d}x \tag{20}$$

where $z(x)$ is the local height of the surface and L is the sample length. R_a roughness is a deficient parameter in that it only measures the height differentials about the topography and high scatter that is often coupled to the use of the R_a roughness comes down to the lack of topographical detail defined within this parameter (Range and Feuillebois 1998).

Wenzel roughness (Wenzel 1936) is another oft used approximation for roughness. The Wenzel roughness, r_w, is defined as,

$$r_w = \frac{A_T}{A} \tag{21}$$

where A is the nominal surface area and A_T is the true area of cross section. This parameter works adequately for low levels of roughness (Packham 2003) and is quite easy to modify (McHale and Newton 2002) since it is an inherently simple model. Alam (2007) suggested the Wenzel roughness be used as part of a more explicatory topographical definition of roughness, φ, (Equation 22) which when compared against Wenzel roughness, was found to generate less scatter in droplet spreading simulations. In this equation, A_r is a ratio of mean

protuberance height to a square root of the protuberance cross section, and F is a normalised protuberance frequency term. There are numerous mathematical definitions of roughness (Stout et al. 1994) which have been compared in Bernardin and Mudawar (1996).

$$\varphi = \frac{r_w \times A_r}{e^F} \tag{22}$$

Roughness coupled to increased or decreased surface energies are ways by which coupled interactions can be amplified or diminished (Miwa et al 2000, Zhang et al. 2006, McHale et al. 2004). Particles exhibit roughness and particle shape specifications based on fractals have been suggested (Kaye 1989). On solid materials free of porosity, such as ceramic crystallite particles, a Tanner's law tendency is typically accepted as descriptive of droplet spreading behaviour and has been experimentally verified (Landry and Eustathopoulos 1996). Accordingly, Tanners law is $D_n \sim t^n$ where D_n is the diameter of spread, t is time and n is a constant. This law has also been found to hold true on porous solids (Holman et al. 2002) irrespective of the fluid imbibition that may take place within the first moments of contact, and indeed, irrespective of 'pinning' to the droplet protuberances (Raiskinmäki et al. 2000). Flow into porous media, and hence particle, is taken to be capillary driven (Alleborn and Raszillier 2004) however interfacial pressure pulsations (Toivakka 2003) may also give rise to increased volume ingress of polymer into particulates.

7.3 Surface energies

A final point that shall be made with regard to wetting is that of high and low energy surfaces. Metals and ceramics have what is said to be high energy surfaces. These materials are metallically or covalently bonded (primary bonds) and high levels of energy are required to break such bonds. Low energy surfaces are usually found on materials such as polymers, where the body of material is held together by weak secondary bonds (Van der Waals). The lower the value of γ_{LG} and θ, the more wetting a liquid is likely to be.

7.4 Mechanisms of adhesion

There are a number of interdependent mechanisms that govern the strength of bonding between individual composite materials.

Mechanical interlocking is one such mechanism. This is essentially a topography based effect, with specific topographical profiles yielding superior interlocking characteristics. Surface preparation/treatment is nonetheless important in its own right and the effectiveness of mechanical interlocking will to a great extent; depend upon the ease of permeation into valleys, holes and general topographical irregularities. This is a function of both the liquid/matrix material and the shape of the protuberances. A mechanically roughened substrate has the benefit of increasing the surface area available for adhesion, however if there is insufficient intimate contact, adhesion may in fact be lowered. Additionally, the shapes of certain surface irregularities may in fact increase the local stress concentrations when the composite, or the interface, is in any way strained. There are many possible surface shapes and configurations for surface irregularities. Biomimetic 'mushroom shaped' protuberances show great potential in enhancing the strength of adhesion. Porous materials such as wood, paper and certain large-pore ceramics have tortuous pore networks. Permeation and setting of adhesive/matrix into these networks will heighten the effects of mechanical interlocking. **Molecular entanglements** of polymer molecules at interfaces also

have the effect of improving the strength of interlocking. **Secondary force interactions** are perhaps the dominating interactions within *adsorption theory* of adhesion. The adsorption theory proposes that materials will adhere so long as there is sufficiently intimate contact between them for intermolecular forces of attraction to develop. Generally Van der Waals bonds dominate interface interactions between materials, however hydrogen bonds can also develop. **Electrostatic attraction** is a secondary bonding mechanism where oppositely charged surfaces interact. This can be dipole-dipole interaction, or, cationic-anionic couplings. **Chemical bonding** (primary bonding) may also occur across the interface; however '*chemisorptions*' as they are so called, are not as common and normally require special techniques during the process of manufacture. Bond energies for primary bonds can range from 60-1100 kJ/mol and 0.08-40kJ/mol for secondary bonds. **Polymer diffusion** and migration between contacting interfaces (*diffusion theory*) are means by which polymers adhere to each other (autohesion). This theory deems essential, high molecular chain mobility at interfaces for diffusion to take place alongside similar levels of solubility. Generally, long chain segments maintain position in the host polymer and chain ends will diffuse into adjacent polymeric material. The consequence is that the short segment of chain effectively 'anchors' itself into adjacent polymer and if this process repeats sufficiently, polymer-polymer adhesion occurs. **Molecular entanglements** may form when chain segments are sufficiently mobile. **Interphase regions** are regions of contacting materials that have combined local composite properties of both materials. Familiar day-to-day materials with interphase regions include "adhesive-wood" in jointed wood composites, "binder-paper" in coated paper composites and polymer-polymer in joined polymers (joined through polymer chain diffusion). The extent of influence such interphase regions will have on the composite properties will depend on a number of factors including but not limited to; depth of penetration relative to depth of composite, properties of penetrated/adsorbed material relative to substrate, intimacy of bonding between materials within the interphase, and the topographical profile. There are various tests that are used to determine the **strength of bonding** between two materials. The most ideal situation of bonding is one where failure occurs within one of the materials as opposed to at the interface between them. This means that the bond strength is not the limiting factor for strength, and that the materials are being used to their fullest potential. Typical bond strength measurements are done using fibre pull out tests, fibre push out tests, peel tests and shear tests.

8. Environmental footprint of mineral particle-polymer composites

Considerable effort and money is expended on issues related to, and for the improvement of, the environment. Materials, excavation, manufacturing routes and ultimately waste management are all matters that should be considered when designing composites. Since focus in this chapter is essentially on mineral pigment-latex composites, it is appropriate to begin with a small section on raw sources of materials.

8.1 Raw sources of mineral particles and conversion

Mining is currently the dominant method for excavating mineral ores. Different mining approaches to excavation have been mentioned in sections 2.1 to 2.4. Mining from start to finish is a 5 stage process. These stages in chronological order are; prospecting, area exploration, mine construction, mining and dismantling of mines with environmental restoration. The main types of mining used for excavating minerals/mineral ores are

quarrying, open pit mining, surface mining and underground mining. The main negative effects mining has on the environment can be summarised as follows:

- **Air pollution:** dust particles through explosions, release of sulphur dioxide, release of greenhouse gases
- **Damage to ecosystems:** destruction of animal habitat, leeching of chemicals foreign to the host environment
- **High energy consumption:** mine construction, maintenance of mine safety and temperature, use of machinery, transportation
- **Land pollution:** felling of forests to create mines, generation of large underground fault lines, exacerbation of land erosion
- **Water pollution:** sulphides released acidify local water supplies, aquatic life affected

Mining is however indispensible if the intention is to maintain a high standard of living. The mining industry creates jobs and generates money locally, nationally and globally. The ecological effects are usually short term and environmental rehabilitation is a legal requirement in most countries. The extent to rehabilitation does nevertheless vary. Mining has also become far safer, with a fifteen fold drop in mortalities and a four fold drop in injuries since the late 1930's. Mine debris can moreover be disposed of inside the mine, making rehabilitation easier.

There are several energy-intensive operations in converting the mineral ore to mineral particles readied for use. For kaolin particles, these include; high pressure water pumps, clay mica thickening tanks, clay fractionation or centrifugation and the separation of clay particles based on size.

8.2 Raw source and conversion of polymers used in particle-polymer composites

The origin of many polymers used in composite materials is crude oil. Similarly to mineral ores, crude oil is a finite resource. The numerous environmental issues brought on by the oil exploration and production industries include habitat protection and biodiversity, air emissions, marine and fresh water discharge, soil and groundwater contamination and oil spills (Visser and Larderel 1997). The route to styrene butadiene latex is process-intensive. Naptha is one of the many products that is output from heating crude oil. Naptha then needs to be reformed for benzene, which is used to produce ethylbenzene and subsequently styrene. Styrene, through the procedure of alkylation and combination with acrylonitrile is transformed to styrene butadiene latex polymer. Production of latex generates both recycle oil and white water. These are considered hazardous wastes that are capable of contaminating ground water supplies, rivers and lakes. Moreover, short-term inhalation of styrene is a respiratory hazard, irritates eyes and causes gastro-intestinal problems.

8.3 Disposal and recycling

Ordinarily incineration is the preferred method of disposal since the particles are not always deemed worth retrieving and the volumes of polymer in the systems are normally very low. If there is a concerted effort to actually recycle the polymeric phase of composites, this is then possible by acid treatment. Acid treatment has the added benefit of removing dispersing agents from particle surfaces. The use of biodegradable polymers is one possible means by which the environmental footprint can be decreased. These can be produced from both renewable sources (gluten, starches, corn based thermoset polyester, soy protein resin), and from crude oil sources (polybutylene succinate (PBS), polycaprolactone (PCL), polyvinyl alcohol (PAV/PVOH)). Many biodegradable polymers undergo photobiodegradation, which

is onset by UV light. Others degrade through mineralisation. This is effectively, the use of specialised bacteria to break down polymer to lower molecular weight species followed by a conversion to CO_2 and H_2O. Prodegradants such as catalytic metal compounds based on iron, cobalt and manganese may also be used to trigger and/or accelerate polymer degradation. Biolatexes are biodegradable polymers that can be derived from both petroleum (Figliolino and Rosso 2009) or natural sources such as starches (Bloembergen et al. 2010). These polymers are considered carbon neutral (Figliolino and Rosso 2009, Bloembergen et al. 2008) and are often also biodegradable. Carbon neutral polymers take generally 10^4 less time to convert carbon within their natural cycle of conversion than fossil carbon, thus remaining for considerably shorter times in the atmosphere.

9. Conclusions

There are a great many considerations in designing, manufacturing and engineering particulate-polymer composites with porosity. Accurately predicting strength and stiffness, and designing to improve durability is no trivial task. Models are continually being updated to reflect new theories on the more prominent and influential features of microstructure, in relation to properties. Mass transport issues also require manufacturing routes through which pore microstructures can be controlled and perhaps even manipulated. Surfaces may be designed to have improved brightness, opacity and wetting control. These issues again, rely on the ability to control the geometrical and chemical makeup of such composites. Porosity is a desired property when weight, optical properties and flux properties are of primary concern. The presence of pores does however negatively affect the mechanical properties and durability of the composite. Moreover, the extractions of raw materials, their processing and ultimately composite manufacture are all energy intensive ecologically damaging and environmentally polluting stages prior to use and disposal of the final product. There are a few ways by which the environmental footprint left over the life-cycle of these composites could be minimised, though to implement these would require that damages to the economics and finances at each stage are negligible.

10. References

Abdul-Rashid, E. & Akil, K. (2008). Mechanical and Thermal Properties of Polymer Composites for Electronic Packaging Application. *Journal of Reinforced Plastics and Composites*, Vol.27, No.15, pp. 1573-1584.

Akinci, A. (2010). The Determining Role of Inorganic Particles on Physical and Mechanical Properties of Reinforced Polyethylene Composites. *Journal of Reinforced Plastics and Composites*, Vol. 29, No.7, pp. 957-963.

Al-Raoush, R. & Alsaleh, M. (2007). Simulation of Random Packing of Polydisperse Particles. *Powder Technology*, Vol.176, pp. 47-55.

Alam, P. (2010). A Mixtures' Model for Porous Particle-Polymer Composites. *Mechanics Research Communications*, Vol.37, pp. 389-393 and (Erratum) pp. 672.

Alam, P., Toivakka, M., Backfolk, K. & Sirviö, P. (2007). Impact Spreading and Absorption of Newtonian Droplets on Topographically Irregular Porous Materials. *Chemical Engineering Science*, Vol.62, pp. 3142-3458.

Alam, P.; Byholm, T. & Toivakka, M. (2006). Calculating Tortuosity in Quasi-Random Ansiotropic Packings. *Nordic Pulp and Paper Research Journal*, Vol.21, No.5, pp. 670-675.

Alam, P.; Byholm, T.; Kniivilä, J.; Sinervo, L. & Toivakka, M. (2009). Calculating the Permeability of Model Paper Coating Structures Comprising Incongruent Particle Shapes and Sizes. *Microporous and Mesoporous Materials*, Vol.117, pp. 685-688.

Alleborn, N. & Raszillier, H. (2004). Spreading and Sorption of a Droplet on a Porous Substrate. *Chemical Engineering Science*, Vol. 59, pp. 2071-2088.

Allen, J. (1985). *Principles of Physical Sedimentology*, George Allen, Unwin, London.

Andruszkiewicz, B. & Pysiak, J. (1990). Chemisorption Capabilities of Anatase Surface. *Journal of Thermal Analysis,* Vol.36, pp. 2119-2124.

ASTM O 2354-68 (1993). Standard Test Method for Minimum Film Formation Temperature of Emulsion Vehicles. *American Society for Testing Materials*, Philadelphia, PA.

Attia, A. (2005). Effects of Petrophysical Rock Properties on Tortuosity Factor. *Journal of Petroleum Science and Engineering*, Vol.48, No.3-4, pp. 185-198.

Baschnagel, J. & Binder, K. (1995). On the Influence of Hard Walls on Structural Properties in Polymer Glass Simulation. *Macromolecules*, Vol.28, pp. 6808-6818.

Bernardin, J. & Mudawar, I. (1996). Experimental and Statistical Investigation of Changes in Surface Roughness Associated with Spray Quenching. *International Journal of Heat and Mass Transfer*, Vol.39, No.10, pp. 2023-2037.

Bert, C (1985). Prediction of Elastic Moduli of Solids with Oriented Porosity. *Journal of Materials Science*, Vol.20, pp. 2220-2224.

Besra. L.; Sengupta, D. & Roy, S. (2000). Particle Characteristics and their Influence on Dewatering of Kaolin, Calcite and Quartz Suspensions. *International Journal of Mineral Processing*, Vol.59, pp. 89-112.

Bhimaraj, P., Yang, H., Siegel, R. & Schadler, L. (2007). Crystal Nucleaetion and Growth in Poly(ethylene terephthalate)/Alumina-Nanoparticle Composites. *Journal of Applied Polymer Science*, Vol.106, pp. 4233-4240.

Bierwagon, G. (1979). Film Formation and Mud Cracking in Latex Coatings. *Journal of Coating Technology*, Vol.51, No.658, pp. 117-126.

Bloembergen, S., Lee, D., McLennan, I., Wildi, R. & Van Egdom, E. (2010). Process for Producing Biopolymer nanoparticle Biolatex Compositions having Enhanced Performance and Compositions Based Thereon. *Patent Application Publication*, Pub. No. US 2010/0143738 A1.

Bloembergen, S., McLennan, I., Lee, D., Van Leeuwen, J. (2008). Paper Binder performance with Biobased Nanoparticles. *Paper360º*, September 2008, pp. 46-48.

Boccaccini, A.; Ondracek, G.; Mazilu, P. & Windelberg, D. (1993). On the Effective Young's Modulus of Elasticity for Porous Materials: Microstructure Modelling and Comparison between Calculated and Experimental Values. *Journal of the Mechanical Behavior of Materials*, Vol.4, pp. 119-128.

Boudreau, B. (1996). The Diffusive Tortuosity of Fine-Grained Unlithified Sediments, *Geochimica et Cosmochimica Acta*, Vol.60, No. 16, pp. 3139-3142.

Brinkman, H. (1952). The Viscosity of Concentrated Suspensions and Solutions. *Journal of Chemical Physics*, Vol.20, No.4, pp. 571.

Brown, S.; Biddulph, R. & Wilcox, P. (1964). A Strength-Porosity Relation Involving Different Pore Geometry and Orientation. *Journal of the American Ceramics Society*, Vol.47, 320-322.

Broz, M.; Cook, R. & Whitney, D. (2006). Microhardness, Toughness, and Modulus of Mohs Scale Minerals. *American Mineralogist*, Vol.91, No.1, pp. 135-142.

Byholm, T., Alam, P., Sinervo, L., Stoor, C. & Toivakka, M. (2004). The Use of 3-Dimensional Image Analysis and Computer Simulation for Gathering Statistical Data and Physical Constants for Paper Coating. *Proceedings: PTS Coating Symposium*, Baden-Baden, Germany 2004.

Carman, P. (1937). Fluid flow through granular beds. *Transactions, Institution of Chemical Engineers*, Vol.15, pp. 150-166.

Carman, P. (1956). *Flow of gases through porous media*, Butterworth Scientific Publications.

Cho, K., Yang, H. & Byoungil, K. (2002). Influence of Crystalline Microstructure Near the Particle/Matrix Interface on Toughening Behavior of Toughened Semi-Crystalline Polymers. *Polymeric Materials: Science & Engineering*, Vol.86, pp. 421-422.

Choi, B., Zhou, Z., Chudnocsky, A., Stivila, S., Sehanobish, K. & Bosnyak, C. (2005). Fracture Initiation associated with Chemical Degradation: Observation and Modelling. *International Journal of Solids and Structures*, Vol.42, 681-695.

Cooper, S., Bamford, C. & Tsuruta, T. (1995). *Polymer Biomaterials in Solution, as Interfaces and Solids: a Festschrift Honoring the 60th Birthday of Dr. Allan S. Hoffman*, VSP BV, ISBN 90-6764-180-4.

Coulson, J. (1949). The Flow of Fluids Through Granular Beds: Effect of Particle Shape and Voids in Streamline Flow. *Transactions of the Institute of Chemical Engineering*, Vol.27, pp. 237-257.

Cumberland, D. & Crawford, R. (1987). *The Packing of Particles*, Elsevier ISSN 0617-3785.

Davis, I. (1999). Particle Pack Influence on Highly Filled Material Properties. *Current Opinion in Solid State and Materials Science*, Vol.4, pp. 505-513.

Depolo, W. & Baird, D. (2009). Particulate Reinforced PC/PBT Composites. I. Effect of Particle Size (Nanotalc Versus Fine Talc Particles) on Dimensional Stability and Properties. *Polymer Composites,* Vol.30, pp. 188-199.

Dias, R., Teixeira, J., Mota, M. & Yelshin, A. (2006). Tortuosity Variation in a Low Density Binary particulate Bed. *Seperation and Purification Technology*, Vol.51, pp. 180-184.

Eilers, H. (1941). Die giskosit/it yon Emulsionen hochviskoser Stoffe als Funktion der Konzentration. *Kolloid-Z*, Vol.97, pp. 313.

Epstein, N. (1989). On Tortuosity and the Tortuosity Factor in Flow and Diffusion through Porous Media. *Chemical Engineering Science*, Vol.44, No.3, pp. 777-779.

Figliolino, F. & Rosso, F. (2009). Suzano Experiences with Biolatex in Brazil. *Paper360º*, August 2009.

Fisa, B., Sanschagrin, B. & Favis, B. (1984). Mechanical Degradation of Mica During Processing with Polypropylene. *Polymer Composites*, Vol.5, No.4, pp. 264-276.

Gauthier, C., Guyot, A., Perez, J. & Sindt, O. (1996). Film Formation and Mechanical Behaviour of Polymer Latexes. *International Symposium Series No. 648, Film Formation in Waterborne Coatings*, pp. 163-178.

Halpin, J. & Tsai, S. (1969). Effects of Environmental Factors on Composite Materials. *AFRL-TR*, Vol.67, pp. 423.

Hashin, Z. (1962). Elastic Moduli of Heterogeneous Materials. *Journal of Applied Mechanics*, Vol.29, pp. 143-150.

Harris, L. & Quong, A. (2004). Molecular Chemisorption as the Theoretically Preferred Pathway for Water Adsorption on Ideal Rutile TiO_2(110). *Physical Review Letters,* Vol.93, No.8, (August 2004), pp. 086105-1-086105-4.

Hauserman, W. (1985). Hardness of Fine Ground Coals and Mineral Residues to Predict Slurry Erosion. *Powder Technology*, Vol.43, pp. 75-87.

Head, D. & Rogers, G. (1999). Stretched Exponentials and Power Laws in Granular Avalanching. *Journal of Physics A*, Vol.32, pp. 1387-1393.

Holik, H. (2006). *Handbook of Paper and Board*, WILEY-VCH Verlag GmbH & Co., ISBN 3-527-30997-7.

Holman, R., Cima, M., Uhland, S. & Sachs, E. (2002). Spreading and Infiltration of Inkjet-Printed Polymer Solution Droplets on a Porous Substrate. *Journal of Colloid and Interface Science*, Vol.249, pp. 432-440.

Janowski, K. & Rossi, R. (1967). Elastic Behaviour of MgO Matrix Composites. *Journal of the American Ceramics Society*, Vol.50, pp. 599-603.

Jia, X. & Williams, R. (2001). A Packing Algorithm for Particles of Arbitrary Shapes. *Powder Technology*, Vol.120, pp. 175-186.

Kaye, B. (1989). *A Random Walk Through Fractal Dimensions*, Wenheim VCH. ISBN 0895738880.

Kemperl, J. & Macek, J. (2009). Precipitation of Calcium Carbonate from Hydrated Lime of Variable Reactivity, Granulation and Optical Properties. *International Journal of Mineral Processing*, Vol.93, pp. 84-88.

Kennedy, B. (1990). *Surface Mining 2nd Edition*, Society for Mining, Metallurgy, and Exploration, Inc., ISBN 0-87335-102-9.

Kim, A. & Chen, H. (2006). Diffusive Tortuosity factor of Solid and Soft Cake Layers: A Random Walk Simulation Approach. *Journal of Membrane Science*, Vol.279, pp. 129-139.

Knudsen, F. (1959). Dependence of Mechanical Strength of Brittle Polycrystalline Specimens on Porosity and Grain Size. *Journal of the American Ceramics Society*, Vol.45, pp. 452-453.

Koponen, A. (1998). *Simulations of Fluid Flow in Porous Media by Lattice-Gas and Lattice-Boltzmann Mathos*, Ph.D. Thesis, University of Jyväskylä, Jyväskylä, Finland, ISBN 951-39-0219-6.

Kozeny, J. (1927). Ueber kapillare Leitung des Wassers im Boden. *Sitzungsber Akad*, Vol.136, No.2A, pp. 271-306.

Lam, T; Hoang, T.; Quang, D. & Kim, J. (2009). Effect of Nanosized and Surface-Modified Precipitated Calcium Carbonate on Properties of $CaCO_3$/Polypropylene nanocomposites. *Materials Science and Engineering A*, Vol.501, pp. 87-93.

Landry, K. & Eustathopoulos, N. (1996). Dynamics of Wetting in Reactive Metal/Ceramic Systems: Linear Spreading. *Acta Materialia*, Vol.44, No.10, pp. 3923-3932.

Lin, X. & Ng, T. (1995). Contact Detection Algorithms for 3-Dimensional Ellipsoids in Discrete Element Modelling. *International Journal for Numerical and Analytical Methods in Geomechanics*, Vol.19, pp. 653-659.

Maitra, A. & Phani, K. (1994). Ultrasonic Evaluation of Elastic Parameters of Sintered Powder Compacts. *Journal of Materials Science*, Vol.29, pp. 4415-4419.

Mansfield, K. & Theodorou, D. (1991). Molecular Dynamics Simulation of a Glassy Polymer Surface. *Macromolecules*, Vol.24, pp. 6283-6294.

McAdam, G. (1951). Some Relations of Powder Characteristics to the Elastic Modulus and Shrinkage of Sintered Ferrous Compacts. *Journal of the Iron Steel Institute,* Vol.168, No.4, pp. 346-358.

McHale, G. & Newton, M. (2002). Frenkel's Method and the Dynamic Wetting of Heterogeneous Planar Surfaces. *Colloids and Interfaces A: Pysicochemical and Engineering Aspects*, Vol.206, pp. 193-201.

McHale, G., Shirtcliff, N., Aqil, S., Perry, C. & Newton, M. (2004). Topography Driven Spreading. *Physical Review Letters*, Vol.93, No.3, pp. 036102(4).

Meinhold, G. (2010). Rutile and its Applications in Earth Sciences. *Earth.Science Reviews*, Vol.102, pp. 1-28.

Miwa, M., Nakajima, A., Fujishima, A., Hashimoto, K. & Watanbe, T. (2000). Effects of the Surface Roughness on Sliding Angles of Water Droplets on Superhydrophobic Surfaces. *Langmuir*, Vol.16, pp. 5754-5760.

Moldrup, P., Olesen, T., Komatsu, T., Schønning, P. & Rolston, D. (2001). Tortuosity, Diffusivity and Permeability in the Soil Liquid and Gaseous Phases. *Soil Science Society of America Journal*, Vol.65, pp. 613-623.

Narkis, M. (1976). Some Mechanical Properties of Particulate-Filled Thermosetting and Thermoplastic Polymers. *Journal of Applied Polymer Science*, Vol.20, pp. 1597-1606.

Nielsen, L. (1966). Simple Theory of Stress-Strain Properties of Filled Polymers. *Journal of Applied Polymer Science*, Vol.10, pp. 97-103.

Nolan, G. & Kavanagh, P. (1992). Computer Simulation of Random Packing of Hard Spheres. *Powder Technology*, Vol.72, pp. 149-155.

Packham, D. (2003). Surface Energy, Surface Topography and Adhesion. *International Journal of Adhesion and Adhesives*, Vol.23, pp. 437-448.

Peters, S. (1998). *Handbook of Composites 2nd Edition*, Chapman & Hall, ISBN 0-412-54020-7

Petford, N. & Koenders, M. (2000). Consolidation Phenomena in Sheared Gigantic Magma: Effects of Grain Size and Tortuosity. *Physics and Chemistry of the Earth, Part A: Solid Earth and Geodesy*, Vol.26, No.4-5, pp. 281-286.

Phani, K.; Niyogi, S. & De, A. (1988). Porosity Dependence of Fracture Mechanical properties of Reaction Sintered Si_3N_4. *Journal of Materials Science Letters*, Vol. 7, pp. 1253-1256.

Powell, M. (1990). Computer-Simulated Random Packing of Spheres. *Powder Technology*, Vol.25, pp. 45-52.

Raiskinmäki, P., Koponen, A., Merikoski, J. & Timonen, J. (2000). Spreading Dynamics of Three-Dimensional Droplets by the Lattice-Boltzmann Method. *Computational Materials Science*, Vol.18, pp. 7-12.

Range, K. & Feuillebois, F. (1998). Influence of Surface Roughness on Liquid Drop Impact. *Journal of Colloid and Interface Science*, Vol.18, pp. 7-12.

Reuss A. (1929). Berechnung der fliebgrenze von mischkristallen auf grund der plastizitätsbedingung für einkristalle. *ZAMM*, Vol.9 pp. 49-58.

Rice, R. (1993). Evaluating Porosity Parameters for Porosity-Property Relations. *Journal of the American Ceramics Society*, Vol.76, pp. 1801-1808.

Richard, J. & Maquet, J. (1992). Dynamic Micromechanical Investigations into Particle Particle Interfaces in Latex Films. *Polymer*, Vol.33, No.19, pp. 4164-4173.

Ridgeway, C., Schoelkoph, J., Matthews, G., Gane, P. & James, P. (2001). The effects of void geometry and contact angle on the absorption of liquids into porous calcium carbonate structures. *Journal of Colloid and Interface Science*, Vol.239, pp. 417-431.

Rothan, R. (2003). *Particulate-Filled Polymer Composites 2nd Edition*, Rapra Technology Ltd., ISBN 1-85957-382-7.

Scoppe, W. (1990). Computer Simulation of Random Packing of Hard Spheres. *Powder Technology*, Vol.62, pp. 189-196.

Stevens, M. (1993). Polymer Additivews Part I. Mechanical Property Modifiers. *Journal of Chemical Education*, Vol.70, No.6, pp. 444-448.

Steward, P., Hearn, J. & Wilkinson, M. (2000). An Overview of Polymer Latex Film Formation and Properties. *Advances in Colloid and Interface Science*, Vol.86, pp. 195-267.

Stout, K, Sullivan, P, Dong, P., Mainsah, E., Luo, N., Mathia, T. & Zahouani, H. (1994). The Development of Methods for the Characterization of Roughness on Three Dimensions. *Publication No. EUR 15178 EN of the Commission of the European Communities,* Luxembourg, ISBN 1857180232.

Tan, L. & McHugh, A. (1996). The Role of Particle Size and Polymer Molecular Weight in the Formation and Properties of and Organo-Ceramic Composite. *Journal of Materials Science*, Vol.31, pp. 3701-3706.

Thomas, C. & Muthukumar, M. (1991). Three-Body Hydrodynamic Effects on Viscosity of Suspensions of Spheres. *Journal of Chemical Physics*, Vol.94, pp. 5180-5189.

Thümmes, J., Lawrence, D. & Kröner, H. (2009). *Latex*, In: *Pigment Coating and Surface Sizing of Paper*, Ed. Paltakari, J., ISBN 978-952-5216-27-1.

Ting, J., Kwaja, M., Meachum, L. & Rowell, J. (1993). An Ellipse-Based Discrete Element Model of Granular Materials. *International Journal for Numerical and Analytical Methods in Geomechanics*, Vol.17, pp. 603-623.

Toivakka, M. (2003). Numerical Investigation of Droplet Impact Spreading in Spray Coating of Paper. *TAPPI Eighth Advanced Coating Fundamentals Symposium*, Atlanta USA, TAPPI Press.

Touaiti, F.; Alam, P., Toivakka, M. & Bousfield, D. (2010). Polymer chain pinning at interfaces in CaCO3–SBR latex composites. *Materials Science and Engineering: A*, Vol.527, No.9, April 2010, pp. 2363-2369.

Traina, M. (2008). *Preparationand Properties of Micro- and Nanocomposites based on High Density Polyethylene*, Ph.D. Thesis, Department of Materials Engineering and Industrial Technology, University of Trento, Italy.

Van Meer, M., Narasimhan, B., Shanks, B. & Malapragada, S. (2009). Effect of Mesoporosity on Thermal and Mechanical Properties of Polystyrene/Silica Composites. *Applied Materials and Interfaces*, Vol.2, No.1, pp. 41-47.

Visser, J. & Larderel, J. (1997). *Environmental Management in Oil and Gas Exploration and Production*, Words and Publications, ISBN 92-807-1639-5.

Voigt W. (1889). Über die beziehung zwischen den beiden elasticitätsconstanten isotroper körper. *Annals of Physical Chemistry*, Vol.38 pp. 573-587.

Wagh, A.; Singh, J. & Poeppel, R. (1993). Dependence of Ceramic Fracture Properties on Porosity. *Journal of Materials Science*, Vol.28, pp. 3589-3593.

Wenzel, R. (1936). Resistance of Solid Surfaces to Wetting by Water. *Industrial and Engineering Chemistry*, Vol.28, pp. 988.

Xu, Q. (2006). *Mechanical Properties of Paper Coatings*, M.Sc. Thesis, Abo Akademi Univeristy, Finland.

Yamamoto, S. & Matsuoka, T. (1999). Dynamics Simulation of Rod-Like and Plate-Like Particle Dispersed System. *Computational Materials Science*, Vol.14, pp. 169-176.

Yanuka, M., Dullien, F. & Elrick, D. (1986). Percolation processes and porous media: I. Geometrical and topological model of porous media using a three-dimensional joint pore size distribution. *Journal of Colloid and Interface Science*, Vol.112, No.1, pp. 24-41.

Yuan, Q., Awate, S. & Misra, R. (2006). Nonisothermal Crystallization Behavior of Polypropylene-Clay Nanocomposites. *European Polymer Journal*, Vol.43, pp. 1994-2003.

Zalc, J, Reyes, S. & Iglesia, E. (2004). The Effects of Diffusion Mechanism and Void Structure on Transport rates and Tortuosity Factors in Complex porous Structures. *Chemical Engineering Science*, Vol.59, pp. 2947-2960.

Zhang, J., Huang, W. & Han, Y. (2006). A Composite Polymer Film with both Superhydrophobicity and Superoleophilicity. *Macromolecular Rapid Communications*, Vol.27, pp. 804-808.

Zingg, T. (1935). *Beitrag zur Schotteranalyse*, Ph.D. Thesis, Eidhenössischen Technischen Hochschule, Zürich.

Zok, F. & Lange, F. (1991). Packing Density of Composite Powder Mixtures. *Journal of the American Ceramic Society*, Vol.72, No.8, pp. 1880-1885.

3

Polymer Composites for Bone Reconstruction

Mervi Puska, Allan J. Aho and Pekka Vallittu
University of Turku, Turku Clinical Biomaterials Centre – TCBC
Finland

1. Introduction

The need for reconstructive surgery of bones is continuously increasing along with the ageing of the population as well as the increase of traumatologic injuries. In the United States, the number of bone grafts was 350,000 in 2001. Nowadays, over 500,000 bone graft procedures are performed annually, and approximately 2.2 million worldwide (Giannoudis et al., 2005). The estimated cost of these procedures approaches US$2.5 billion per year. Hence, the considerable demand for these replacement procedures cannot be met solely by using donor material. Therefore, superior synthetic orthopaedic materials and techniques should be available on the market for clinical practice. Adjustable porosity, bioactivity, identical biomechanics, as well as all the other tissue-friendly properties to bone are central for achieving a durable, bonding-like, interface between the synthetic material and bone (Aho et al., 2004). Actually, modern material technology would have all the know-how for preparing excellent synthetic orthopaedic materials. Autografts are still regarded as optimal reconstruction material, because of the lack of good enough synthetic materials. However, in orthopaedics, the demands for synthetic materials could be fulfilled by using composite structures. In fact, it is possible to mimic better the structures of living materials, like bone, cartilage or teeth using composite structures. Therefore, there is still a constant need to search for better synthetic bone substitute materials for tissue engineering (Chung et al., 2007).

2. Clinical background

Typically, the synthetic bone substitute materials have traditionally been in the form of blocks, granules, mass, or gel. Although these kinds of materials are commercially available under several different trademarks, only a few defects are so far repaired using synthetic bone substitutes in clinical practice, in ca. 10% of cases (Stevens et al., 2008). Table 1 shows different types of materials that are employed as bone substitutes. Basically, only metallic materials, of the commercially available synthetic biomaterials, are mechanically good enough to reconstruct large cortical bone defects. Of donor materials, autograft is bone that is removed from the patient's own body, whereas allograft is bone that is removed from the same species (i.e. other humans). In addition, xenograft is also of biological origin; it is extracted from the inorganic phase of mammal bone but of some other species, typically e.g. that of neat. In fact, the use of autograft is drastically limited, because of the lack of availability and donor site morbidity limits. On the other hand, the risk of infection

transmission is a major concern that restricts the use of allografts and xenografts (Kappe et al., 2010; Tadic & Epple, 2004).

In the bone reconstructions, polymeric materials, such as, e.g. polymethylmethacrylate (PMMA) or polyethylene (UHMWPE), have been employed as PMMA-based bone cements or as acetabular cups of hip prostheses, for several years. In fact, their use will further increase in tissue engineering (Boyer et al., 2009; Gasser, 2000; Wang, 2003). Therefore, synthetic polymers used as biomaterials have sometimes even been called biopolymers. However, the concept of biopolymers has been traditionally reserved for the polymers, i.e. macromolecules that living organisms produce, e.g. cellulose, proteins, chitin, RNA and DNA. Therefore, biopolymers are also polymers that are employed in biomedical applications (Fukushima et al., 2011; Vieira et al., 2011).

ALLOGRAFT	**AUTOGRAFT**
Infection risk Management of bone bank is difficult Expensive	Lack of availability Damage to healthy bone tissues Secondary surgical procedure needed
METALLIC MATERIALS	**POLYMER-BASED MATERIALS**
Metal-bone interface mechanical Loosening risk Stress shielding High elasticity moduli not optimal for bone Release of nanoparticles	Residual toxic monomers, e.g. Risk of exothermic effects, hypotonia, or heart and lung complications Risk of wear debris
BIOCERAMICS AND BIOACTIVE GLASSES	**OTHER, e.g. Xenografts**
Brittleness Stress shielding High modulus of elasticity	Infection risk Low strength

Table 1. The main material categories to reconstruct bone, and some of their typical disadvantages

3. Methods to study materials for bone reconstruction

Biomaterial research is focused on the design and development of synthetic materials for surgery. Therefore, a multidisciplinary research environment, i.e. combining medical sciences and biotechnology with chemistry, biology and physics, is needed. More precisely, the required testing categories include (1) chemical analysis, (2) biomechanical engineering, (3) biological testing (biomimetic biomineralization, cell culture and in vivo studies), and (4) advanced imaging technology. In fact, in order to develop synthetic materials for bone reconstruction, a well-equipped biomaterial research laboratory has a wide range of instruments, such as microcomputed tomography (micro-CT), nuclear magnetic resonance (NMR) and fourier transform infrared spectroscopy (FTIR) spectrometers, and thermoanalytical techniques: e.g. differential scanning calorimeter (DSC) or thermomechanical analyzer (TMA), high performance liquid chromatography (HPLC), scanning electron microscope (SEM) or transmission electron microscope (TEM), and material testing machines (e.g. Lloyd LRX or Instron equipments). In addition, facilities for the synthesis of

organic molecules and biopolymers are needed. To carry out biological testing, the cell culture and histological laboratory, standard stainings and molecular biology techniques should be available, as well as several light microscopes and a computer-based histomorphometric analysis system (e.g. Aho et al., 2004; Meretoja et al., 2006; Puska et al., 2003; Silva Nykänen et al., 2011).

4. Composites for bone reconstruction

Modern synthetic chemistry has reached the point where it is possible to prepare molecules in almost any structure. Methods are available to produce a wide variety of useful materials, such as bioactive or chiral self-assembled polymer structures (Cui et al., 2010; Wang, 2008). For example, phosphorus-containing biopolymers have been synthesized and developed as polymeric candidates for potential tissue engineering applications (e.g. poly[bis(methacrylate)]phosphazene, PMAP) (Silva Nykänen et al., 2011). In the polymeric structure, the presence of phosphorus may improve the biocompatibility of polymers by enhancing their tissue contact. Actually, phosphorus is an essential element in all living systems, e.g. as a key part of the phosphodiester bonds in DNA and RNA.
In addition, in the form of thermosets and thermoplastics, both biostable and biodegradable polymers (e.g. polycaprolactone, PCL and PMMA) have been studied, largely for tissue engineering (Aho et al., 2004; Middleton & Tipton, 2000; Morita et al., 1998; Puska et al., 2003; Wang, 2003). Structurally, the form of these polymers can be linear, cross-linked or interpenetrated polymer networks (IPNs). IPNs are three-dimensional physically or chemically cross-linked polymeric materials that include two independent networks without any covalent bonds between them (Feng et al., 2004; Sperling 1994). Polymer composites are combinations of two or more components, usually containing an inorganic phase and a polymer phase that are essentially insoluble in each other (Gasser, 2000). Polymers have typically lower modulus and deformation resistance than the inorganic phase. Thus, attempts are made to adjust the mechanical properties of polymeric materials to approximate those of bone, using a composite structure. In fact, the matrix polymer-containing filling components result in a complicated interaction between the properties of every constituent phase, i.e. (a) the matrix, (b) filling components, and (c) the interfacial region between the filling components and the matrix polymer (Wang, 2003).

4.1 Chemistry of PMMA-based bone cements

For over 40 years, the best known polymeric material or "biopolymer" has been PMMA-based bone cement. Typically, PMMA-based bone cements are employed in many orthopaedic operations, e.g. in total joint replacement surgery, substitutes in vertebroplasty/kyphoplasty, or as filling material in trauma surgery (Boyd et al., 2008; Lewis, 2009). Commercially available bone cements are made of (a) a powder component consisting of PMMA polymer or related block copolymers and (b) a liquid component made of methylmethacrylate (MMA) or related monomer liquids. Just before the clinical procedure, bone cement is fabricated by combining the powder and the liquid component together. In fact, the monomer phase dissolves the powder component and, thereafter, it autopolymerizes within 10 – 15 min, resulting first in a mouldable viscous dough after 3-7 min, and then a very dense cured PMMA-based bone cement. More precisely, the powder component contains PMMA or related block copolymer beads (diameter 50 μm), an initiator, and radio-opaque substances. The liquid is methylmethacrylate (MMA) monomer or related

methacrylic monomers that polymerise in the presence of the initiator. Structurally, PMMA-based bone cements are formed of typical linear polymers. However, PMMA-based bone cement can also be modified in the form of a semi-IPN structure by adding small amounts of cross-linking monomers (e.g. 2-30 wt% of ethylene glycol dimethacrylate, egdma) to the liquid phase (Lewis, 2009; Puska et al., 2003, 2004). In future tissue reconstruction applications, the acrylic polymer matrix will most probably also be modified using dendritic macromonomers.

In joint replacement surgery, the main function of PMMA-based cement is to transfer body weight in order to increase the load-bearing and fixation capacity of the reconstruction area. On the other hand, PMMA-based cement is morphologically very dense, thus not allowing bone ingrowth. In addition, the exothermal polymerization of MMA in vivo might cause a risk of thermal and chemical necrosis of bone. However, in most cases, PMMA-based cements have been successfully utilized in orthopaedic surgery for many decades (Lewis 2009; Puska et al., 2003). Therefore, interest has arisen in developing more biocompatible PMMA-based cements. In fact, their weakest link is the dense non-bioactive cement-bone interface that is a barrier to direct fracture healing. Basically, it is possible to make the properties of PMMA-based bone cements more tissue-friendly, as an example of a functional active composite structure that is porous and bioactive. The porosity and bioactivity are created by filling components in both powder and liquid components, thus slightly changing the content.

In terms of bioactivity, PMMA-based cements are combined with inorganic substances, i.e. bioactive glasses, hydroxyapatite. In the literature, a number of bioactive PMMA cements are presented. Bioactive bone cements are normally successfully obtained when the PMMA matrix contains an appropriate concentration of bioactive ceramics. For example, Shinzato et al. have reported that bioactive PMMA cements containing bioactive substances have significantly higher bone-bonding strength than plain PMMA cement (Shinzato et al., 2001). However, the presence of fairy large concentrations of ceramics in PMMA can disfavour the mechanical properties. Especially if adhesion between the PMMA matrix and the particles of ceramics is missing, particles often behave like voids as crack nucleation (Abboud et al., 2000).

4.2 Bifunctional acrylic resins as matrix components

Bifunctional acrylic resins contain monomers with two active bonding positions. Originally, they were developed for dental applications (Schweikl et al., 2006), but nowadays these monomers have also been investigated for orthopaedic surgery. The best known bifunctional methacrylates are bisphenol-A-glycidyldimethacrylate (BisGMA) and triethylene glycol dimethacrylate (TEGDMA), Fig. 1. BisGMA-based bone cements are developed to reduce the problems encountered with bioactive PMMA cements (Boyd et al., 2008; Smit et al., 2008). Actually, highly cross-linked polymers, such as the BisGMA-based, are the only polymers that are strong enough (e.g. compression strength: >100 MPa) to withstand the different types of stresses of cortical bone (Gheduzzi et al., 2006). Especially Japanese researchers have been very active in studying BisGMA-based cements (Kobayashi et al., 1999).

One commercially available highly cross-linked biostable cement is Cortoss® (Orthovita, Malvern, USA) that comprises three main resins: BisGMA and ethoxylated bisphenol A dimethacrylate (BisEMA) and TEGDMA as a viscosity modifier. In addition, Cortoss® contains reinforcing particles of silica, barium boro-aluminosilicate glass and combeite glass

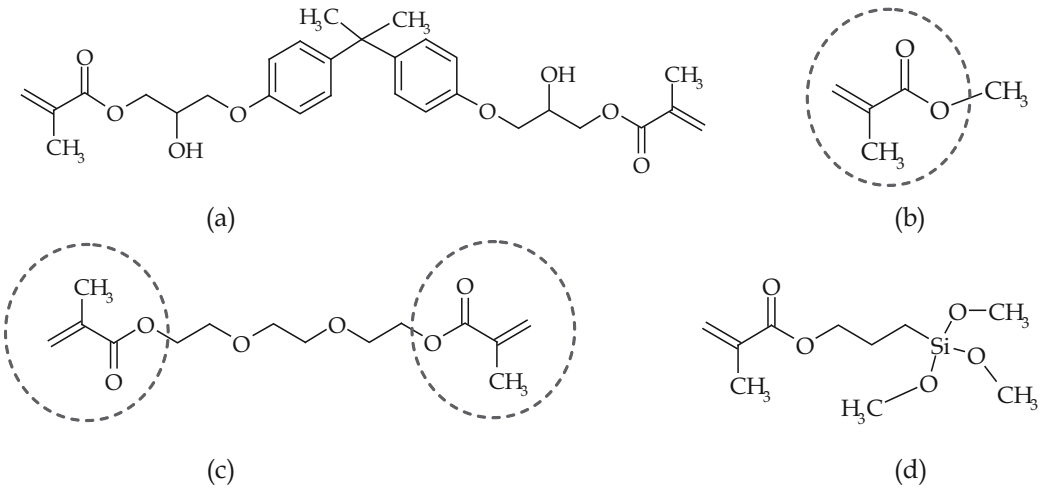

Fig. 1. The molecule structures of compounds containing methacrylate group: (a) bisphenol-A-glycidyldimethacrylate, BisGMA, (b) methylmethacrylate, MMA, (c) triethylene glycol dimethacrylate, TEGDMA, and (d) methacryloyloxypropyltrimethoxysilane, MPS. The circles show active bonding positions that are able to react with other monomers, i.e. necessary for the curing/hardening of acrylic bone cement

ceramic, as well as a silane coupling agent (Boyd et al., 2008; Gheduzzi et al., 2006; Smit et al., 2008). The setting time of Cortoss® cement is reported to be between 4 and 8 min, thus very suitable for bone reconstruction. The main drawbacks of Cortoss® are its missing porosity and, in some cases, the biodegradation of matrix polymer. In addition, the cements that are mechanically very strong may introduce stress shielding that is observed if the material exhibits much greater stiffness compared to the modulus of cortical bone. Another potential problem occurs if BisGMA-based cements are employed in vertoplasty. The extreme strengthening of one vertebra may potentially cause a fracture in the neighbouring osteoporotic vertebra. In fact, these acrylic monomers are also identified as being harmful in mammalian cells. Some of these substances can induce, e.g. gene mutations, probably because of the covalent binding to DNA via Michael addition (Schweikl et al., 2006).

4.3 Biodegradable polymers as matrix polymers

Since the mid-1990s, biodegradable polymer composites appear to have been studied for the applications of tissue engineering (Aho et al., 2004; Meretoja et al., 2006; Middleton & Tipton, 2000; Törmälä, 1992; Wang, 2003). In these, the typical matrix polymers are polylactide (PLA), polycaprolactone (PCL), polypropylenefumarate (PPF) or any of their copolymers. Basically, biodegradable polymer composites are prepared by mixing bioactive compounds in a certain fragment volume with melt/dissolved polymer (Rezwana et al 2006, Wang 2003). Typically, matrix polymers in these biocomposites are delivered as viscous liquids or mouldable pastes. The intermediate phase of the biodegradable polymer composites is a soft mouldable mass that hardens relatively fast in 20 s – 1 min. The compression strength of these biodegradable composites is rather low, between 10 and 50 MPa. However, the biodegradable composites containing bioactive compounds are osteoconductive and easy to handle. Therefore, they are very suitable as bone grafting substitutes for small cancellous bone or cartilage defects (Aho et al., 2004; Meretoja et al., 2006; Wang, 2003).

Some years ago, Aho et al. reported one injectable biodegradable composite that contains particles of bioactive glass embedded in poly(caprolactone-co-D,L-lactide) matrix. The glass particles in matrix polymer resulted in osteoconductivity (Aho et al., 2004). In addition, Leeuwenburgh et al. have developed a nanoceramic (CaP) polymer composite consisting of oligo(poly(ethylene glycol)fumarate) as matrix (Leeuwenburgh et al., 2007). Kim et al. have investigated an injectable PPF that is porous after injection. The porous structure is created in situ by CO_2 bubbles that are generated in a reaction of bicarbonate salt and weak acid (Kim et al., 2009). Łukaszczyk et al. have introduced a poly(3-allyloxy-1,2-propylene)succinate-based biodegradable bone cement that would have a tendency to set in situ in vivo by cross-linking poly(3-allyloxy-1,2-propylene)succinate (PSAGE) with MMA and methacrylic anhydride (Lukaszczyk et al., 2007). In fact, injectable PPF and methacrylated polyanhydrides have aroused much interest; one reason is their in situ curing capacity.

5. Biomechanics of composites for bone reconstruction

In terms of filling particles, the properties of matrix polymers, such as stiffness, thermal expansion, creep resistance or fracture toughness, can be changed. If particles are incorporated in polymers, it makes the final material stiffer or harder. On the other hand, the tensile strength decreases with an increasing amount of inorganic particles. Therefore, it is important to know the type and shape of the filling particles to be able to make the right choice. In fact, the shape of the component, e.g. particles vs. fibres, depends on the application to which the load-bearing forces are directed (Garoushi et al., 2006; Puska et al., 2004; Wang, 2003).

5.1 Reinforcing components

The properties of composites are dependent on the type, volume fraction and orientation of the filling substance. In the case of isotropic 3D reinforcing, it can be obtained using spheres, granules or short fibres (Wang 2003). Table 2 shows some typical categories of osteogenetic composites for bone reconstruction. In terms of fibre-reinforced composites (FRCs), reinforcing fibres are employed in two forms: (a) continuous unidirectional or (b) chopped. The other main parameters affecting mechanical properties of FRC include: (1) the exact composition of fibres and polymer matrix, (2) the orientation and quantity of fibres, (3) the adhesion between fibres and polymer matrix, and (4) the impregnation of the fibres by the resin matrix. Moreover, the fibre length also significantly influences the mechanical properties (Behr et al., 2000; Thomason, 2007). In fact, the reinforcing effect of fibres can be predicted using the so-called Krenchel's factor. In the Krenchel's analysis, the orientation of the fibres and the applied load depend on each other. Continuous unidirectional fibres give the highest mechanical properties, but only anisotropically, matching the direction of the fibres (Krenchel, 1963). In tissue engineering, the reinforcing fibres of composites can be made of E-glass, bioactive glass, polyethylene, the family of aromatic amides (i.e. aramid), carbon, graphite, titanium, or fibres of natural origin.

5.2 Interfacial aspects

To understand the reinforcing phenomenon of polymer composites, it is very important to understand the adhesion between the matrix polymer and the reinforcing substances. It requires a lot of information to understand, e.g. how materials interact with each other, what kinds of coupling systems there are, the interface, and the failure mechanism. Failures

often occur within the polymer or at the interface. To be precise, the surface of fillers can be modified either using (1) surface treatment or (2) chemical grafting. In fact, the surface roughness also has a significant effect on wettability by monomers or coupling agents. Using some kind of chemical surface treatment, e.g. using MPS-silane (Fig.1), a covalent bonding can be obtained between the polymer matrix and inorganic fillers at molecular level (Fig. 2) (Vallittu, 1995, 1998; Puska et al., 2009b).

Type of polymer composite	**Compression strength**	**Advantages**
Biodegradable matrix polymer with bioactive glasses or ceramics, Refs1	Low degree, weak ~10-50 MPa	Osteogenic and bone ongrowth
Biostable matrix polymer with calcium ceramics, Ref2	Moderate strength ~80 MPa	Slightly porous, osteogenic and bone on- and ingrowth
Modified PMMA-based bone cement, Ref3	Moderate strength ~70 MPa	Interconnected porosity, osteogenic and bone on- and in-growth
Fibre-reinforced and highly crosslinked acrylic polymer, Ref4	High degree, strength adjustable >150 MPa	Non-porous, optimal strength for cortical bone, tailor-made elasticity, osteogenic

Refs1: Aho et al., 2004; Rezwana et al., 2006; Wang, 2003;
Ref2: Puska et al., 2009a; Ref3: Puska et al., 2004; Ref4: Garoushi et al., 2006

Table 2. As bone substitutes, the osteogenic composites grouped according to their composition and biomechanics

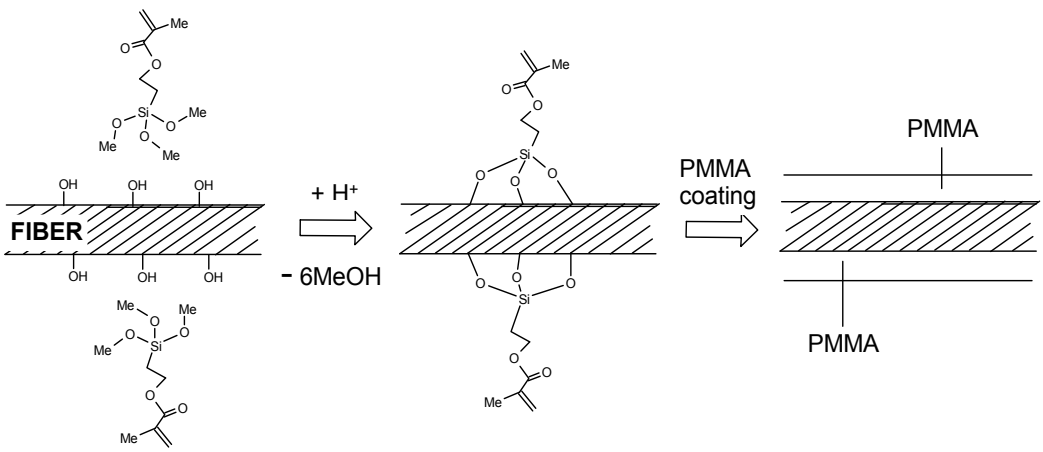

Fig. 2. Simplified presentation of glass fibre pre-impregnation with PMMA; these thin PMMA layers can be covalently bonded to the glass surface. (a) A plain tiny glass fibre strand and MPS (b) The formation of silanized layer (siloxane layer) (c) The deposition of PMMA layer

6. Osteoconductivity and porosity of synthetic biomaterials

Osteoconduction is a characteristic of bone reconstructive materials that favours the spread of osteogenetic cells, i.e. osteoblasts and osteocytes, on the surface of the material. Bioactive materials are designed to induce a specific biological activity (Einhorn, 1995; Hench & Wilson, 1984). In fact, the bioactive properties of composites can be altered by embedding the biologically active substances, such as drugs, bisphosphonates, antimicrobial agents, proteins, growth factors, enzymes and DNA into either pore-generating filler or into reinforcing components. In the case of tissue engineering, the matrix polymer could also imply bioactivity or it could contain biologically active components. In this context, bioactivity is surface reactivity that has the ability to bond with both bone and subcutaneous tissue. Basically, bioactive materials have been shown to form a direct connection to living bone through a Ca-P-rich layer. The main categories of bioactive compounds that are utilized as filling components are: (a) bioactive glasses (BAG) or apatite wollastonite glass ceramics (AW-GC), (b) calcium phosphates, and (c) calcium sulphates. Bioactive bone substitutes are normally successfully obtained when the matrix polymer contains appropriate concentrations of bioactive fillers, often more than 50 wt%. For example, bioactive PMMA-based bone cements containing AW-GC or BAG have significantly higher bone-bonding strength than plain PMMA cement (Kenny & Buggy, 2003).

6.1 Bioactive glasses

The most important feature for producing bioactive glasses is based on the specific composition of the glass, where the amount of oxides is: SiO_2 < 60 wt%, a high Na_2O and CaO content, and a high CaO/P_2O_5 ratio (Gomez-Vega et al., 2000; Zhang et al., 2010; Hench & West, 1996). Bioactive glasses can be produced in various shapes, e.g. as granules, spheres or in fibre form. In the case of PMMA-based bone cements, the biostable matrix polymer can be easily incorporated using bioactive glass substances. Namely, the bioactive substances used as fillers in the composite structure of inert polymer stimulate bone ingrowth into the outermost porous structure, thus accelerating the overall healing process.

6.2 Calcium-phosphate (CaP)-based fillers

The family of calcium phosphates (CaP), such as tricalcium phosphate (TCP) and hydroxyapatite (HA), are osteoconductive materials. In mammals, hydroxyapatite $Ca_{10}(PO_4)_6(OH)_2$, is the main mineral of hard tissues (Jarcho et al., 1976). Natural HA isolated from mammal bone has very good chemical and biological affinity to bone tissue. However, HA is nowadays prepared synthetically. In fact, natural and synthetic HA are only two compounds in the category of CaP cements (Tadic & Epple, 2004). Other compounds are tricalcium phosphate (TCP), tetracalcium phosphate (TTCP), and calcium pyrophosphate (CPP), dicalcium phosphate anhydride (DCPA) and dicalcium phosphate dehydrate (DCPD) (Chen et al., 2009; Heini & Berlemann, 2001). The manufacturing of CaP cements involves sintering at high temperatures with exclusion of H_2O.

6.3 Calcium-sulphate-based fillers

Calcium-sulphate ($CaSO_4$)-based materials have been utilized in the treatment of bone cavities for many decades (Abramo et al., 2010). Some alternatives of calcium-sulphate powders set in contact with water and the solid form contains two molecules of crystal water. Compared to CaP cements, $CaSO_4$-based materials imply biodegradation capacity.

Actually, plain $CaSO_4$-based cements disappear from the body in one year (Jung et al., 2010). Therefore, $CaSO_4$ cements are utilized as bone graft substitute in reconstruction in the distal radius. In terms of osteconductivity, $CaSO_4$-based materials seem to be good filling components when incorporated in inert polymer matrices (Fig. 3) (Puska et al., 2009a).

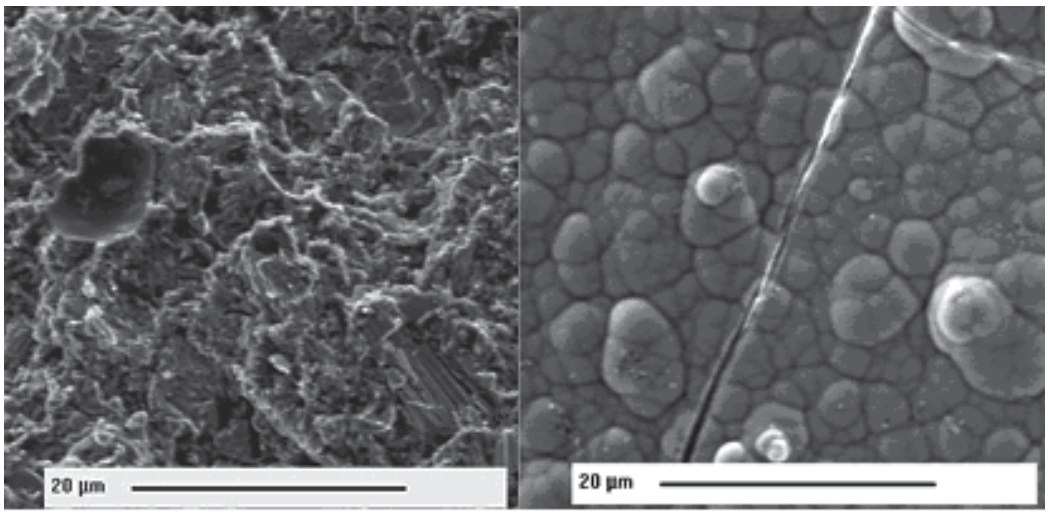

Fig. 3. On the left, structure of plain bifunctional polymer composite containing $CaSO_4$-based materials (50wt%) before SBF soaking. On the right, the effect of biomimetic mineralization (in SBF solution), i.e. the formation of hydroxyl apatite is significant. The length of the measuring rod is 20 µm (Ref. Puska et al., 2009a)

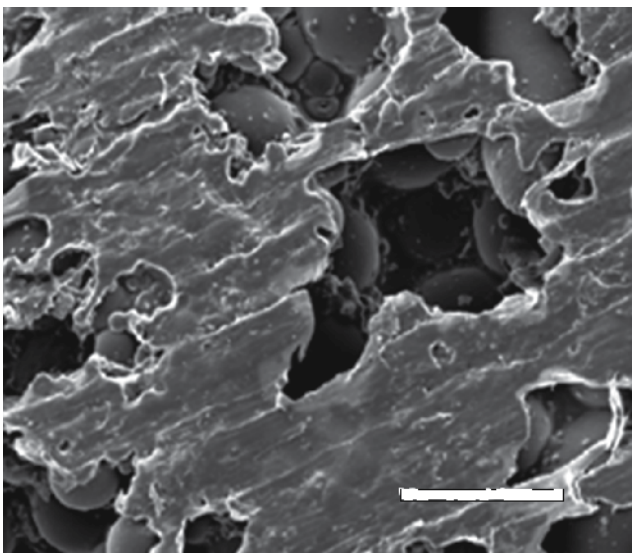

Fig. 4. The porosity of the outermost surface, i.e. in the modified PMMA-based bone cement structure after the specimen has been soaked in SBF solution. The length of the white measuring rod is 100 µm

6.4 Porosity in biocomposites

In biomaterials, the function of porosity is to provide a scaffold for new bone tissue ingrowth. In particular, the porosity should be continuous and interconnected, where most of the pores should be large enough (100 - 500 μm) (Deville et al., 2006; Itälä et al., 2001). Figure 4 shows the outermost surface of modified PMMA-based bone cement. In fact, porosity formation will increase the contact surface between the living tissue and the scaffold, thus holding the implant much more tightly in place. The porous structure can be created in situ in vivo using so-called pore-generating fillers that are bioabsorbable particles embedded inside non-resorbable matrix polymer. After the implantation, these fillers will degrade in contact with body fluid. Ideally, porosity should develop fast enough after the material has been implanted into living tissue, i.e. within the first few days. However, the porosity formation also decreases the mechanical properties of the cured bone cement (Puska et al., 2003, 2004).

7. Clinical demands

Most biological materials (e.g. bone, dentin, or cartilage) also tend to be composites. Natural composites quite often have extremely hierarchical structures, in which particulate, porous, and fibrous structures are present. In fact, the aim of composite technology for bone reconstruction is to tailor the properties of biomaterials closer to those of repaired hard tissue (e.g. cartilage or cortical bone). Therefore, optimal reconstruction of large-size bone damages is very challenging, because bone as a biological composite is porous, thus allowing constant circulation of fluids and different types of bone cells, minerals etc. (Aho et al., 2004; Itälä et al., 2001; Meretoja et al., 2006; Puska et al., 2003). In addition, if artificial materials are implanted into bone, there is a constant risk of infections. The properties of bone vary, i.e. depending on the anatomic location in the skeleton and the bone (Fig. 5). More precisely, biological criteria for reconstruction materials are classified according to the size, form and quality of bone (Ritchie et al., 2006). In addition, cortical bone as load-bearing sites of the skeleton also has specific elastic, anisotropic and heterogeneous structural properties that differ significantly from cancellous bone. More precisely, the compression strength of cortical bone is reported to be between 100 and 200 MPa, whereas the compression strength of cancellous bone is only between 2 and 12 MPa (Reilly & Burstein, 1974, Lotz et al., 1991).

In the case of bone reconstruction, the choice of the best available biomaterial has to be decided from among the alternatives of the categories presented in Table 1. Therefore, the clinician has to make the decision according to information based on the availability of materials *versus* the condition of the patient that depends on his/her age, physical size (height/ weight), health, and genotype, as well as the shape, size and location of the defect. After operation, when biomaterials are in very close contact with bone, the new bone formation occurs as an osteoconductive growth, i.e. osseointegration on the surface of the material (ongrowth) or into the material (ingrowth) if there is a suitable amount of porosity and bioactivity (Aho et al., 2004). In terms of osteoinduction, biomaterial also accelerates new bone formation by chemical means (e.g. bioactive glasses) (Hench & Wilson, 1984; Hench & West, 1996).

Sometimes, bone does not create a durable ongrowth to the biomaterial's surface, e.g. in the case of encapsulation, when a so-called foreign body reaction takes place. In order to avoid this, the employed biomaterial should have bioactivity and porosity, thus allowing a tight

osseointegration or even bone ingrowth into the interconnected 3D porous interfaces. On the other hand, in the case of totally or partially biodegradable biomaterials, the remodelling of new bone and the degradation of biomaterial should occur simultaneously.

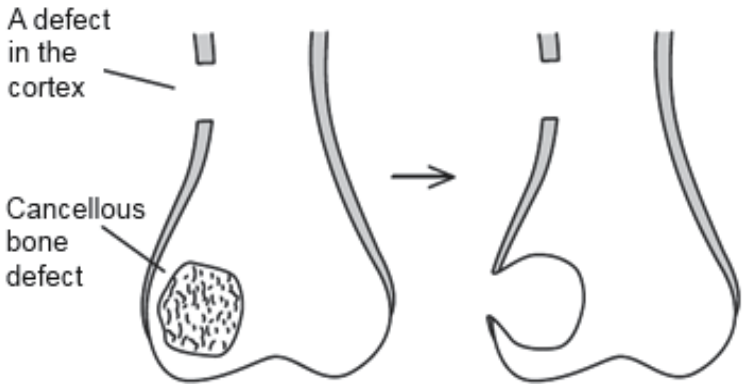

Fig. 5. Biomechanically, the highest load-bearing capacity of bone is needed on the outermost sites of bone. Therefore, if these parts of bone are reconstructed, the mechanical properties of the synthetic bone substitute should be similar to those of bone

7.1 Biological function: Bone grafting

Bone grafting is a surgical procedure, in which the bone defect or the missing bone is replaced with natural or artificial substitutes. More precisely, these are substitutes of natural origins (donor materials) or synthetic bone substitutes, i.e. inorganic compounds, polymeric materials, or biocomposites.

In fact, a highly sophisticated synthetic bone substitute should have:

1. porosity allowing new bone ongrowth and ingrowth,
2. bioactivity (i.e. osteoconductivity and/or osteoinductivity),
3. suitable mechanical properties (i.e. elasticity and weight-bearing capacity), and
4. physical form permitting application by injection as a paste or gel.

If these properties could be achieved, bone reconstruction surgery would most probably be more cost-effective in the long run; especially because improvement in the patients' quality of life would also be achieved.

In fact, an optimal synthetic bone substitute should be structurally and biomechanically as close to surrounding bone as possible. Typically, synthetic bone substitutes are employed in the treatment of broken bones in the vertebra, wrist or hip, often due to osteoporosis. In this disease, the progressive loss of bone tissue has made the skeleton weaker and more prone to fractures, because the amounts of collagen and calcium salts are depleted. In vertebroplasty/kyphoplasty, low viscosity bone substitutes are injected into the collapsed spinal vertebra in order to stabilize and strengthen the crushed bone (Erbe et al., 2001; Gisep et al., 2006).

As a superior composite (Fig. 6), the synthetic bone substitute would have: (1) tailor-made biomechanics, i.e. elasticity and weight-bearing capacity, (2) non-toxicity, (3) bioactivity (i.e. osteoconductivity and/or osteoinductivity), (4) porosity of ca. 20-40 vol%, allowing new bone ongrowth and ingrowth, (5) possibility to attach/incorporate other substances (bioactive glass, growth factor, mesenchymal stem cells, etc.), and (6) physical form permitting application by injection/kneading as a paste or gel, and in some cases (7) highly

controlled biodegradation by surface erosion mechanism, if the matrix polymer is biodegradable and remodelling of new bone is assumed to be sufficient (Aho et al., 2004).

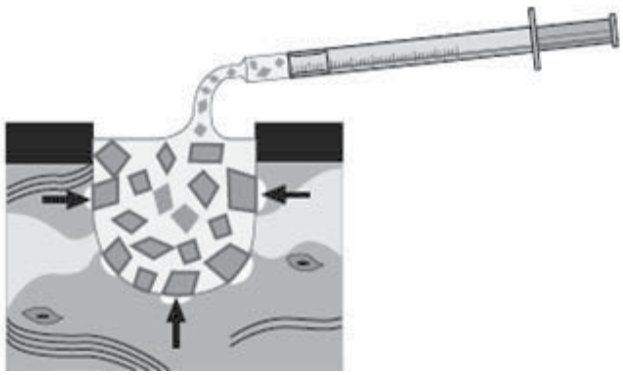

Fig. 6. In more sophisticated cases, bone defects can be reconstructed with a mouldable mass that is injected into the bone. This kind of dough-like substitute should also contain the bioactive substances and pore-generating fillers (Ref. Aho et al., 2004)

7.2 Challenges of artificial materials for bone reconstruction of arthritic disorders

Arthritis is a joint disorder featuring inflammation. The two most common types of arthritis are osteoarthritis and rheumatoid arthritis that usually involve various joints such as those in fingers, spine, legs or arms. Rheumatoid arthritis is an autoimmune inflammatory disease, whereas osteoarthritis is mostly related to ageing, but can also be caused by a disease. In the case of very severely damaged bone, the only treatment is joint replacement surgery. In this, a joint is amputated and replaced with a metallic prosthesis, e.g. in hips or knees (Boyer et al., 2009).

The artificial parts of the prosthesis are often cemented into place by PMMA-based bone cement (Lewis 2009). The PMMA-based bone cement layer adheres tightly to the prosthesis in the skeleton and acts as an intermediate bumper. Therefore, the patients can normally walk with their newly implanted knees or hips very soon after the operation. As medical devices, metallic implants, made of stainless steel or titanium, are most frequently used in total joint replacements. However, metals exhibits much greater stiffness compared to the elasticity of bone. In the fixation of the prosthesis, the large elasticity difference between these two materials can cause stress shielding that leads to an increase in bone porosity and atrophy. In addition, there are some other clinical problems such as the activation of periprosthetic connective tissue, macrophage activation, and bone resorbtion, as well as wear and corrosion problems (Santavirta et al., 1998, 1999). Release of nanosized particles of metal may also have undesired effects on the biology of tissues.

The main disadvantage associated with the use of traditional PMMA-based bone cement is the anchoring effect that happens only as a mechanical locking, because the surface of the polymerised bone cement is of a dense structure that does not allow the bone to grow into the cement (i.e. mechanical locking). Therefore, new bone formation is limited only to the surface between the bone cement and the bone. If the fixation is only mechanical, the micromotion between the bone and the implant interface can lead to resorbtion of bone and then the failure and the final loosening of the prosthesis (Santavirta et al., 1998, 1999). Therefore, some re-operations of total knee/hip replacement systems have been required even within four to eight years after the primary operation (Hooper et al., 2009), although all

the prostheses should last for the rest of the patients' life. To avoid re-operations, these prosthetic implant materials should be developed to approximate more closely to the properties of bone (e.g. elasticity).

8. Clinical applications

A wide range of porous composites for tissue engineering has been studied. In fact, if porous scaffolds are utilized effectively in load-bearing applications, the mechanical properties of materials with porosity and void spaces should be known. In clinical applications, the tailor-made composite structure materials could be employed as follows: (1) in osteoarthrosis, (2) in the treatment of osteoporotic fractures, (3) in the controlled filling of defects, and (4) as bone grafting materials (Fig. 7).
In vertebroplasty/kyphoplasty, low viscosity cements, e.g. modified PMMA-based bone cements, could be injected into the collapsed spinal vertebra in order to stabilize and strengthen the crushed bone (Hulme et al., 2006). Actually, the optimal setting/curing time for biomaterials in vertebroplasty is still under investigation. For the application of tissue engineering, it should be possible to tailor the curing of materials. In fact, according to our studies, this is possible using a specific type of wave energy that increases the polymerization of matrix polymer. Thus, the ultimate strength of the substitute can be achieved in a couple of minutes after mixing the components. In the fixation of fractures of the radius, the better curing would also improve the quality of bone reconstruction. In arthroscopic surgery, the injection of bone substitute with controlled curing would probably allow the possibility of operating without opening the joint using a micro-invasive technique.

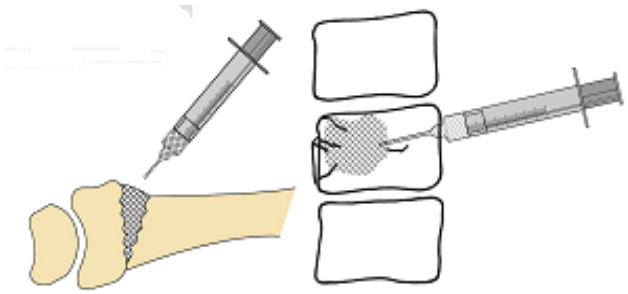

Fig. 7. Synthetic bone substitutes can be utilized in typical surgical defects of fractured bone. Typically, bone defects are reconstructed in the distal radius or vertebra

Bone fractures and tumour defects often locate in long bone. In the reconstruction of bone, autograft bone is assumed to be the best alternative. However, bone defects could also be reconstructed using synthetic materials that can interact with biological systems (Lindfors et al., 2009). In the case of composites, tailor-made structures could serve as an alternative for the traditional implant devices. In contact with living hard tissues, the composite structures are able to adapt according to the biological and mechanical requirements. The authors of this book chapter have developed new materials and techniques, where the composite material will meet the clinical demands including the adjustability and highly controlled setting of the material (Aho et al., 2004; Puska et al., 2003, 2004, 2009a). Figure 8 shows one example of our experimental materials for bone reconstruction. In our coming papers, these new alternatives that have properties like putty form, easy handling and good filling, but

are also biomechanically suited to bone tissue, will be presented. In fact, it is predicted that a number of autografts will in future be replaced by the more sophisticated biomaterials. From the patient's point of view, this would be a huge improvement. Thus, the mutilation of bone and secondary operation would be avoided.

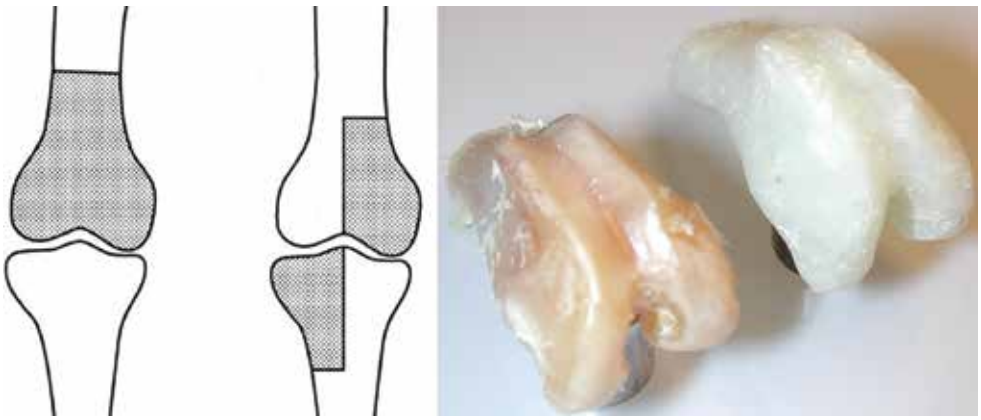

Fig. 8. Synthetic reconstruction materials can be utilized as osteoarticlular graft for bone tumour surgery. On the right, the image presents a natural rabbit knee joint and beside it an artificial joint made of bifunctional polymer composite (Aho et al., 2007)

9. Summary

In the biological environment, the demands of biomaterials are challenging. Typically, in the reconstruction of bone defects, clinicians use autograft bone, based on the fact that the commercially available synthetic materials are not optimal for the reconstruction of bone. Nevertheless, calcium-based compounds are generally marketed under several trade names. In fact, they are only suitable in a few fixations of bone defect, e.g. to fill the defects in cancellous bone. On the other hand, in the case of artificial joint reconstruction, the biomechanical properties of inorganic compounds or metallic materials do not respond to the demands of bone. In terms of composite structures, bone substitutes can be adjusted to be closer to the demands of bone. Thus, polymer composites mimic the structures of bone better, because they can be tailor-made to be both osteoconductive and strong enough to withstand weight-bearing. These better synthetic bone substitutes will most probably be commercially available for orthopaedic applications in the near future.

10. Acknowledgments

In terms of our own studies presented in this book chapter, the research has partly been funded by the Academy of Finland (grant number: 128636) and the Finnish Dental Society APOLLONIA. Prof. Antti Yli-Urpo is acknowledged for his encouragement in the topic of functionally active bone cements and substitutes.

11. References

Abboud, M.; Casaubieilh, L.; Morvan, F.; Fontanille, M.; Duguet, E. (2000). PMMA-based composite materials with reactive ceramic fillers: IV. Radiopacifying particles

embedded in PMMA beads for acrylic bone cements. *Journal of Biomedical Materials Research*, Vol.53, No.6, pp. 728-736, ISSN 1552-4973

Abramo, A.; Geijer, M.; Kopylov, P.; Tägil, M. (2010). Osteotomy of distal radius fracture malunion using a fast remodeling bone substitute consisting of calcium sulphate and calcium phosphate. *Journal of Biomedical Materials Research Part B: Applied Biomaterials*, Vol.92B, No.1, (January 2010), pp. 281–286, ISSN 1552-4973

Aho, A.J.; Tirri, T.; Kukkonen, J.; Strandberg, N.; Rich, J.; Seppälä, J.; Yli-Urpo, A. (2004). Injectable bioactive glass/biodegradable polymer composite for bone and cartilage reconstruction: concept and experimental outcome with thermoplastic composites of poly(epsilon-caprolactone-co-D,L-lactide) and bioactive glass S53P4. *Journal of Materials Science: Materials in Medicine*, Vol.15, No.10, pp. 1165-1173, ISSN 0957-4530

Aho, A.J.; Puska, M.; Vallittu, P. (2007) A New Calcium Salt-Resin Composite for Bone Crafting. *16th International Congress of the European Association of Tissue Banks (EATB 2007)*, p. 39, Budapest, Hungary, October 17-20, 2007

Behr, M.; Rosentritt, M.; Lang, R.; Handel, G. (2000). Flexural properties of fiber reinforced composite using a vacuum/pressure or a manual adaptation manufacturing process. *Journal of Dental Research*, Vol.28, No.7, pp. 509-514. ISSN 0022-0345

Boyd, D.; Towler, M.R.; Wren, A.; Clarkin, O.M. (2008). Comparison of an experimental bone cement with surgical Simplex® P, Spineplex® and Cortoss®, *Journal of Materials Science: Materials in Medicine*, Vol. 19, No. 4, pp. 1745-1752, ISSN 0957-4530

Boyer, P.; Lazennec, J.-Y.; Poupon, J.; Rousseau, M.-A.; Ravaud, P.; Catonné, Y. (2009). Clinical and biological assessment of cemented titanium femoral stems: an 11-year experience. *International Orthopaedics*, Vol.33, No.5, pp. 1209-1215, ISSN 0341-2695

Chen, W.C.; Ju, C.P.; Tien, Y.C.; Lin, J.H. (2009). In vivo testing of nanoparticle-treated TTCP/DCPA-based ceramic surfaces. *Acta Biomaterialia*, Vol.5, No.5, pp. 1767-1774, ISSN 1742-7061

Chung, U.; Itaka, K.; Nishiyama, N.; Takato, T.; Kawaguchi, H.; Nakamura, K.; Kataoka, K. (2007). Scaffolds for Skeletal Regeneration. *NanoBioTechnology*, Vol.3, No.2, pp. 104-106, ISSN 1550-7033

Cui, H.; Pashuck, E.T.; Velichko, Y.S; Weigand, S.J; Cheetham, A.; Newcomb, C. J.; Stupp, S. I. (2010) Spontaneous and X-ray–Triggered Crystallization at Long Range in Self-Assembling Filament Networks. *Science*, Vol.327, No.5965, pp. 555-559, ISSN 0036-8075

Deville, S.; Saiz, E.; Tomsia, A.P. (2006) Freeze casting of hydroxyapatite scaffolds for bone tissue engineering. *Biomaterials*, Vol.27, No.32, pp. 5480-5489, ISSN 0142-9612

Einhorn, T.A. (1995). Enhancement of fracture-healing. *Journal of Bone and Joint Surgery - American Volume*, Vol.77, No.6, pp. 940-956, ISSN 1535-1386

Erbe, E.; Clineff, T.; Gualtieri, G. (2001) Comparison of a new bisphenol-a-glycidyl dimethacrylate-based cortical bone void filler with polymethyl methacrylate. *European Spine Journal*, Vol.10, Suppl, pp. S147–S152, ISSN 0940-6719

Feng, X.Q.; Tian, Z.; Liu, Y.H.; Yu, S.W. (2004). Effective Elastic and Plastic Properties of Interpenetrating Multiphase Composites. *Applied Composite Materials*, Vol.11, No.1, pp. 33-55, ISSN 0929-189X

Fukushima, K.; Tabuani, D.; Abbate, C.; Arena, M.; Rizzarelli, P. (2011). Preparation, characterization and biodegradation of biopolymer nanocomposites based on fumed silica. *European Polymer Journal*, Vol.47, No. 2, pp. 139–152, ISSN 0014-3057

Garoushi, S.K.; Lassila, L.V.; Vallittu, P.K. (2006). Short fiber reinforced composite: the effect of fiber length and volume fraction. *Journal of Contemporary Dental Practice*, Vol.7, No.5, pp. 10-7, ISSN 1526-3711

Gasser, B. (2000). About composite materials and their use in bone surgery. *Injury*, Vol.31, Suppl. No. 4, pp. S48-S53, ISSN 0020-1383

Gise, A.; Curtis, R.; Hänni, M.; Suhm, N. (2006). Augmentation of implant purchase with bone cements: An in vitro study of injectability and dough distribution. *Journal of Biomedical Materials Research Part B: Applied Biomaterials*, Vol.77B, No.1, pp. 114–119, ISSN 1552-4973

Giannoudis, P.V.; Dinopoulos, H.; Tsiridis, E. (2005). Bone substitutes: an update. *Injury*, Vol.36, Suppl. No. 3, pp. S20-S27, ISSN 0020-1383

Gheduzzi, S.; Webb, J.J.C.; Miles, A.W. (2006). Mechanical characterisation of three percutaneous vertebroplasty biomaterials. *Journal of Materials Science: Materials in Medicine*, Vol.17, No. 5, pp. 421–426, ISSN 0957-4530

Gomez-Vega, J.M.; Saiz, E.; Tomsia, A.P.; Marshall, G.W.; Marshall, S.J. (2000). Bioactive glass coatings with hydroxyapatite and Bioglass particles on Ti-based implants. 1. Processing. *Biomaterials*, Vol.21, No.2, pp. 105-111, ISSN 0142-9612

Heini, P.; Berlemann, U. (2001). Bone substitutes in vertebroplasty. *European Spine Journal* Vol.10, Suppl, pp. S205–S213, ISSN 0940-6719

Hench, L.L.; Wilson, J. (1984). Surface-active biomaterials. *Science*, Vol.226, No.4675, pp. 630-636, ISSN 0036-8075

Hench, L.L.; West, J.K. (1996). Biological applications of bioactive glasses. *Life Chemistry Reports*, Vol.13, No.3, pp. 187-241, ISSN 0278-6281

Hooper, G.J.; Rothwell, A.G.; Stringer, M.; Frampton, C. (2009). Revision following cemented and uncemented primary total hip replacement. *Journal of Bone and Joint Surgery - British Volume*, Vol.91B, No. 4, pp. 451-458, ISSN 0301-620X

Hulme, P.A.; Krebs, J.; Ferguson, S.J.; Berlemann, U. (2006). Vertebroplasty and Kyphoplasty: A Systematic Review of 69 Clinical Studies. Spine, Vol.31, No.17, pp. 1983-2001, ISSN 0362-2436

Itälä, A.I.; Ylänen, H.O.; Ekholm, C.; Karlsson, K.H.; Aro, H.T. (2001). Pore diameter of more than 100 micrometer is not requisite for bone ingrowth in rabbits. *Journal of Biomedical Materials Research*, Vol.58, No.6, pp. 679- 683, ISSN 1552-4973

Jarcho, M.; Bolen, C.H.; Thomas, M.B.; Bobick, J.; Kay, J.F.; Doremus, R.H. (1976). Hydroxylapatite synthesis and characterization in dense polycrystalline form. *Journal of Materials Science*, Vol.11, No.11, pp. 2027-2035, ISSN 0022-2461

Jung, H.-M.; Song, G.-A.; Lee, Y.-K.; Baek, J.-H.; Ryoo, H.-M.; Kim, G.-S.; Choung, P.-H.; Woo, K.M. (2010). Modulation of the resorption and osteoconductivity of alfa-calcium sulfate by histone deacetylase inhibitors, *Biomaterials*, Vol.31, No. 1, pp. 29–37, ISSN 0142-9612

Kappe, T.; Cakir, B.; Mattes, T.; Reichel, H.; Flören, M. (2010). Infections after bone allograft surgery: a prospective study by a hospital bone bank using frozen femoral heads from living donors. *Cell Tissue Bank*, Vol.11, No.3, pp. 253-259, ISSN 1389-9333

Kenny, S.M.; Buggy, M. (2003). Bone Cements and Fillers: A Review. *Journal of Materials Science: Materials in Medicine*, Vol.14, No.11, pp. 923-938, ISSN 0957-4530

Kim, J.; Yaszemski, M.J.; Lu, L. (2009). Three-Dimensional Porous Biodegradable Polymeric Scaffolds Fabricated with Biodegradable Hydrogel Porogens. *Tissue Engineering, Part C: Methods*, Vol.15, No.4, pp. 583-594, ISSN 1937-3384

Kobayashi, M.; Nakamura, T.; Tamura, J.; Kikutani, T.; Nishiguchi, S.; Mousa, W.F.; Takahashi, M.; Kokubo, T. (1999) Osteoconductivity and bone-bonding strength of high- and low-viscous bioactive bone cements. *Journal of Biomedical Materials Research*, Vol.48, No.3, pp. 265-276, ISSN 1552-4973

Krenchel, H. (1963). Fibre Reinforcement (PhD Thesis). Copenhagen, Technical University of Denmark

Lewis, G. (2009). Properties of Antibiotic-Loaded Acrylic Bone Cements for Use in Cemented Arthroplasties: A State-of-the-Art Review. *Journal of Biomedical Materials Research Part B: Applied Biomaterials*, Vol.89B, No. 2, pp. 558–574, ISSN 1552-4973

Leeuwenburgh, S.C.G.; Jansen, J.A.; Mikos, A.G. (2007). Functionalization of oligo(poly(ethylene glycol)fumarate) hydrogels with finely dispersed calcium phosphate nanocrystals for bone-substituting purposes. *Journal of Biomaterials Science, Polymer Edition*, Vol.18, No.12, pp. 1547-1564. ISSN 0920-5063

Lindfors, N.; Heikkilä, J.; Koski, I.; Mattila, K.; Aho, A.J. (2009). Bioactive Glass and Autogenous Bone as Bone Graft Substitutes in Benign Bone Tumors. *Journal of Biomedical Materials Research Part B: Applied Biomaterials*, Vol.90B, No. 1, pp. 131–136, ISSN 1552-4973

Lotz, J.C.; Gerhart, T.N.; Hayes, W.C. (1991). Mechanical properties of metaphyseal bone in the proximal femur. *Journal of Biomechanics*, Vol.24, No.5, pp. 317-329, ISSN 0021-9290

Lukaszczyk, J.; Smiga-Matuszowicz, M.; Jaszcz, K.; Kaczmarek, M. (2007). Characterization of new biodegradable bone cement compositions based on functional polysuccinates and methacrylic anhydride. *Journal of Biomaterials Science, Polymer Edition*, Vol.18, No.7, pp. 825-842, ISSN 0920-5063

Meretoja, V.V.; Helminen, A.O.; Korventausta, J.J.; Haapa-aho, V.; Seppalä, J.V.; Närhi, T.O. (2006). Crosslinked poly(.epsilon.-caprolactone/D,L-lactide)/bioactive glass composite scaffolds for bone tissue engineering. *Journal of Biomedical Materials Research, Part A*, Vol.77A, No.2, pp. 261-268, ISSN 1549-3296

Middleton, J.C.; Tipton, A.J. (2000). Synthetic biodegradable polymers as orthopedic devices. *Biomaterials*, Vol.21, No.23, pp. 2335-2346, ISSN 0142-9612

Puska, M.; Kokkari, A.; Närhi, T.; Vallittu, P. (2003). Mechanical properties of oligomer-modified acrylic bone cement. *Biomaterials*, Vol.24, No. 3, pp. 417-425, ISSN 0142-9612

Puska, M.; Närhi, T.; Aho, A.; Yli-Urpo, A.; Vallittu, P. (2004). Flexural properties of crosslinked and oligomer-modified glass-fibre reinforced acrylic bone cement. *Journal of Materials Science: Materials in Medicine*, Vol.15, No.9, pp. 1037-1043, ISSN 0957-4530

Puska, M.; Korventausta, J.; Garoushi, S.; Seppälä, J., Vallittu, P., Aho, A. (2009a). Preliminary in vitro biocompatibility of injectable calcium ceramicpolymer composite bone cement, *Key Engineering Materials*, Vols.396-398, Bioceramics, pp. 273-276, ISSN 1013-9826

Puska, M.; Lassila, L.; Vallittu, P.; Seppälä, J.; Matinlinna, J. (2009b). Evaluation of bis-GMA/MMA resin adhesion to silica-coated and silanized titanium. *Journal of Adhesion Science and Technology*, Vol.23, No. 7-8, pp. 991-1006, ISSN 0169-4243

Reilly, D.T.; Burstein, A.H. (1974). The mechanical properties of cortical bone. *Journal of Bone and Joint Surgery - American Volume*, Vol.56A, No.5, pp. 1001-1022, ISSN 1535-1386

Rezwana, K.; Chena, Q.Z.; Blakera, J.J.; Boccaccinia, A.R. (2006). Biodegradable and bioactive porous polymer/inorganic composite scaffolds for bone tissue engineering. *Biomaterials*, Vol.27, No.18, pp. 3413–3431, ISSN 0142-9612

Ritchie, R.O.; Kinney, J.H.; Kruzic, J.J.; Nalla, R.K. (2006). Cortical Bone Fracture. In: *Wiley Encyclopedia of Biomedical Engineering*, M. Akay, (Ed.), John Wiley & Sons, ISBN 978-0-471-24967-2, Hoboken, USA

Santavirta, S.; Xu, J.W.; Hietanen, J.; Ceponis, A.; Sorsa, T.; Kontio, R.; Konttinen, Y.T. (1998). Activation of periprosthetic connective tissue in aseptic loosening of total hip replacements. *Clinical Orthopaedics and Related Research*, Vol.352, pp. 16-24, ISSN 0009-921X

Santavirta, S.; Takagi, M.; Gomez-Barrena, E.; Nevalainen, J.; Lassus, J.; Salo, J.; Konttinen, Y.T. (1999). Studies of host response to orthopedic implants and biomaterials. *Journal of long-term effects of medical implants*, Vol.9, No.1-2, pp. 67-76, ISSN 1050-6934

Schweikl, H.; Spagnuolo, G.; Schmalz, G. (2006). Genetic and cellular toxicology of dental resin monomers. *Journal of Dental Research*, Vol.85, No.10, pp. 870-877, ISSN 0022-0345

Silva Nykänen, V.P.; Nykänen, A.; Puska, M.; Silva, G.; Ruokolainen J. (2011). Dual-responsive and super absorbing thermally cross-linked hydrogel based on methacrylate substituted polyphosphazene, Soft Matter, Vol.7, No.9, pp.4414-4424, ISSN 1744-683X

Shinzato, S.; Nakamura, T.; Kokubo, T.; Kitamura, Y. (2001). A new bioactive bone cement: effect of glass bead filler content on mechanical and biological properties. *Journal of Biomedical Materials Research*, Vol.54, No.4, pp.491-500, ISSN 1552-4973

Smit, R.S.; van der Velde, D.; Hegeman, J.H. (2008). Augmented pin fixation with Cortoss® for an unstable AO-A3 type distal radius fracture in a patient with a manifest osteoporosis. Archives of orthopaedic and trauma surgery, Vol.128, No.9, pp. 989-993, ISSN 0936-8051

Sperling, L.H. (1994). Interpenetrating Polymer Networks: An Overview. In: *Interpenetrating Polymer Networks*. D. Klempner, L.H. Sperling and L.A. Utracki, (Eds), 1-38, Advances in Chemistry Series 239, American Chemical Society, ISBN 0841225281 Washington, D.C., USA

Stevens, B.; Yang, Y.; Mohandas, A.; Stucker, B.; Nguyen, K.T. (2008). A review of materials, fabrication methods, and strategies used to enhance bone regeneration in engineered bone tissues. *Journal of Biomedical Materials Research Part B: Applied Biomaterials*, Vol.85B, No.2, pp. 573–582, ISSN 1552-4973

Tadic, D.; Epple, M. (2004). A thorough physicochemical characterisation of 14 calcium phosphate-based bone substitution materials in comparison to natural bone, Biomaterials. Vol.25, No.6, pp. 987-994, ISSN 0142-9612

Thomason, J.L. (2007). The influence of fibre length and concentration on the properties of glass fibre reinforced polypropylene: 7. Interface strength and fibre strain in injection moulded long fibre PP at high fibre content. *Composites, Part A: Applied Science and Manufacturing*, Vol.38A, No.1, pp. 210-216, ISSN 1359-835X

Törmälä, P. (1992). Bioabsorbable surgical composite materials. *Advanced Materials*, Vol.4, No.9, pp.589-591, ISSN 0935-9648

Vallittu, P.K. (1995). Impregnation of glass fibers with poly(methyl methacrylate) using a powder-coating method. *Applied Composite Materials*, Vol. 2, No.1,pp.51-58, ISSN 0929-189X

Vallittu, P. (1998). Polymer-fibre prepreg, a method for the preparation thereof as well as the use of said prepreg. *International Patent,* No. US005846640A, pp. 10

Vieira, M.G.A.; Altenhofen da Silva, M.; Oliveira dos Santos, L.; Beppu, M.M. (2011). Natural-based plasticizers and biopolymer films: A review. *European Polymer Journal,* Vol.47, No.3, pp. 254-263, ISSN 0014-3057

Wang, M. (2003) Developing bioactive composite materials for tissue replacement. Biomaterials, Vol.24, No.13, pp. 2133-2151, ISSN 0142-9612

Wang, V,; Misra, G.; Amsden, B. (2008). Immobilization of a bone and cartilage stimulating peptide to a synthetic bone graft. *Journal of Materials Science: Materials in Medicine*, Vol.19, No.5, pp. 2145-2155, ISSN 0957-4530

Zhang, D.; Leppäranta, O.; Munukka, E.; Ylänen, H.; Viljanen, M.K.; Eerola, E.; Hupa, M.; Hupa, L. (2010). Antibacterial effects and dissolution behavior of six bioactive glasses. *Journal of Biomedical Materials Research, Part A*, Vol.93A, No.2, pp. 475-483. ISSN 1549-3296

4

New Generation of Geopolymer Composite for Fire-Resistance

Tran Doan Hung[1], Petr Louda[2],
Dora Kroisová[2], Oleg Bortnovsky[3] and Nguyen Thang Xiem[2]
[1]*Nha Trang University, Faculty of Mechanical Engineering,*
[2]*Technical University of Liberec, Faculty of Mechanical Engineering, Department of Material Science, Liberec,*
[3]*Research Institute of Inorganic Chemistry, Inc., Revoluční 84, 400 01 Ústí nad Labem,*
[1,2]*Viet Nam*
[3]*Czech Republic*

1. Introduction

The most popular matrix used for fiber-reinforced industrial composites is organic polymer. The nature flammability of the organic polymer matrix (Marsh, 2002), however, limits the use of these materials in ground transportation (Hathaway, 1991), submarine and ships (Demarco, 1991), and commercial aircraft (Davidovits, 1991), where restricted egress of fire hazard is an important design consideration, although traditional fibers, such as carbon and glass fibers or new developed, high temperature, thermal-oxidative stable fibers from boron, silicon carbide and ceramic are inherently fire resistant (Papakonstantinou et al., 2001). In other word, most of organic matrix composites cannot be used in applications that require more than 200 ^{o}C of temperature exposure. In these cases of applications, composites based on carbon matrix or ceramic matrices are being exploited. However, use of these materials is even strongly limited, due to high cost accompany with special and high-thermal processing requirements (Papakonstantinou et al., 2001; Papakonstantinou & Balaguru 2005).
In 1978, Joseph Davidovits proposed that binders could be produced by a polymeric reaction of alkaline liquids with the silicon and the aluminum in source materials of geological origin or by-product materials such as fly ash and rice husk ash (Davidovits, 1999). These binders have been coined as term geopolymers since 1979; they are inorganic polymeric materials with a chemical composition similar to zeolites but without defined crystalline structure and possessing ceramic-like features in their structures and properties. The amorphous to semi-crystalline three dimensional of sialate network consists of tetrahedral SiO_4 and AlO_4 which are linked alternately by sharing all the oxygens to create polymeric Si-O-Al bonds (Davidovits & Sawyer 1985; Davidovits, 1991). Geopolymers are still considered as a new material for coatings and adhesives, a new binder for fiber composites, and a new cement for concrete (Davidovits, 2008). They are mineral polymers and the essence of all mineral polymers is never burn (Davidovits, 2008). Therefore, we can state that geopolymer materials are ideal for high temperature and fire applications.
Fiber-reinforced composites based on geopolymer matrix (geocomposite) have been well-known for over 20 years, since the first Davidovits' patent was filed (Davidovits et al., 1989).

These new materials can be fabricated and cured at room temperature or thermoset in a simple autoclave. After approximately several hours of curing, these materials exhibit excellent features such as lightweight and high strength but are also ideally fire resistant, with non toxic fumes and smokes, and resist all organic solvents (Lyon et al., 1997; Davidovits, 2002, 2005, 2008; Duxson et al., 2007). These special properties permit us to use geopolymer matrix composites more efficiently in high-tech technologies such as aerospace, naval architecture, ground transportation or automotive industry, especially for those applications that require high temperature resistance (Lyon et al., 1997; Papakonstantinou et al., 2001; Davidovits, 2002, 2008). Geopolymer composites can efficiently replace lightweight, high strength composites which are made from carbon or glass fibers and ceramic matrices or organic matrices due to high costs associated with special ceramic processing requirements and impossibility of the application of most organic matrix composites at temperatures above 200 °C (Papakonstantinou et al. 2001; Papakonstantinou & Balaguru, 2005). In addition, wide scale of reinforcement fibers can be used, and special matrices can protect carbon from oxidation (Papakonstantinou et al., 2001; Sheppar, 2007).
In order to study the fire-resistant properties of materials in general and geopolymer composites, three following groups of specifications of materials should be investigated, including: Ignitability, heat release and smoke for the first group; the second group includes flame spread index and the last one is residual flexural strength (Lyon et al., 1996, 1997). Among these parameters, Richard E. Lyon and his colleagues determined that perhaps the most important fire behaviour parameter for structure applications is the strength retention of the composite after fire exposure (Lyon et al., 1996).
In this chapter, two formulations of geopolymer matrices, abbreviated as 'M1' and 'M2', based on thermal silica with fine size-particle and main molar ratio Si/Al ≈ 10, potassium hydroxide solution and further minor admixtures for improving application features, were created and synthesized. Thermal silica-based geopolymer resin is better than convensional geopolymer resins based on metakaolin, fly-ash and similar materials which contain rather large size-particles and marked with high viscosity and therefore hardly used effectively for fiber impregnation or very high pressure must be applied to penetrate the resin into the spaces between single filament fibers (Bell et al., 2005). The properties of six geopolymer composites based on M1, M2 and approximately 45, 53 or 60 vol.% of unidirectional carbon fiber HTS 5631 1600tex 24K, basalt roving BCF13 - 2520tex - KV12 Int. or Saint-Gobain - Vetrotex E-glass E2400P192, which were fabricated under simplified pultruded home-made impregnation machine and cured at optimal range of curing conditions, were studied. The effects of severe thermal exposure in a furnace at high temperatures up to 1000°C for 1 hour on the thermal-mechanical properties of the geocomposites were evaluated. The flexural properties of the resulting composites were determined on a universal testing machine under three-point bending mode in accordance with ASTM C 1341 – 06 and DIN V ENV 658-3:1993-02. The microstructure of concerned composites M1/Carbon and M2/Carbon were analyzed by means of Scanning Electron Microscope (SEM). Moreover, Energy Dispersive X-ray Analysis (EDX) was used to determine whether initial reaction layer on the fibers and was presented as well.

2. Experimental design

2.1 Initial materials

The formulations of two geopolymer matrices (M1 and M2), consisted of thermal silica, potassium hydroxide solution or potassium water glass, and further minor admixtures for

improving application features. The difference between these two was in the nature of additives: alkali borate addition to M1 and alkali phosphate addition to M2. Details of chemical composition of two used geopolymer matrices expressed as main elements molar ratios are showed in Table 1.

Matrix	Si/Al	K/Al	K/Si	K/P	Si/P	K/B	Si/B	H_2O/K
M1	11.3	3.1	0.27	-	-	4.9	18.7	4.7
M2	9.7	2.4	0.24	4.2	17.5	-	-	5.2

Table 1. Chemical composition of geopolymer matrices M1 and M2 expressed as main elements atomic ratios

The reinforcement used in the composites discussed in this paper were continuous fibers (rovings) that came from carbon HTS 5631 1600 tex, TohoTenax; basalt roving BCF13 - 2520tex - KV12 Int. or Saint-Gobain - Vetrotex E-glass E2400P192. The mechanical properties of single filament was tested on Universal Tensile Testing machine LaborTech 2.050 (maximum load of sensor: 5 N) at ambient conditions in accordance with Japanese Industrial Standard (JIS R 7601) before and after heat treatment at different temperatures in a furnace for 3 hours, Table 2 contains information of the properties (Tran et al., 2008; Nguyen et al., 2009).

Kind of fiber	d_0	20 °C			200 °C			400 °C			700 °C		
		ε	σ	E	ε	σ	E	ε	σ	E	ε	σ	E
Carbon HTS 5631 1600tex 24K	7	1.84	3120	170	1.33	2340	176	1.66	2861	172	Fibers were destroyed totally (nearly disappeared)		
Basalt BCF13 - 2520tex - KV12 Int	13	3.98	2563	64	3.44	2111	61	1.7	1281	75	The fibers still remained in the furnace, but too brittle		
E-glass E2400P192	24	4.72	1504	32	3.26	1106	34	2.08	995	48	1.03	575	56

d_0 - Average diameter of fiber filament [μm]; σ - Tensile strength [MPa];
E - Tensile module [GPa]; ε - Failure strain [%]

Table 2. Estimated properties of applied fibers after treatment at different temperature

2.2 Method for geocomposite fabrication

Continuous fibres (rovings) were impregnated ("wetted-out") with geopolymeric resin on an impregnation machine – Fig. 1. The equipment has been designed based on simulating the real pultrusion or filament winding technique of a current composite manufacture. Pulling velocity 34 m/h of the fiber during impregnation process was chosen to achieve the best penetration of geopolymer resin into the fiber.

Impregnated cut-up rovings were laid manually into a silicon rubber mould 3×9×150 mm, layer by layer. Series of five samples were prepared from a batch, 16 bunches of pre-preg carbon fiber, 18 bunches of impregnated basalt fiber, or 20 bunches of geopolymer saturated E-glass fiber were needed for each specimen. The mold with pre-pregs was then covered by a peel ply fabric and suction tissue and placed into a sealed plastic bag.

Fig. 1. Details of pultrusion technique used for the preparation of geocomposites

The specimens were cured under optimal procedure of 3 stages by help of currently used technique of vacuum bagging (abbreviated by 1:1:5), in the first stage at room temperature for 1 hour under vacuum bagging, and then 1 hour in oven at optimal temperature, 80 °C for M1 system and 85 °C for M2 system with hot vacuum bagging. Finally, the specimens were released from bags, dried open in the oven at the same temperature for another 5 hours, and one long specimen (3x9x150 mm) was cut into two samples in dimension 3x9x85 mm and 3x9x65 mm for suit the planned spans. Only rough surface treatment with emery paper was applied.

2.3 Testing setup

Specimens were tested for flexural properties before and after the fire exposure up to high temperature to determine the residual properties of the composites. Generally, for testing the residual properties, the specimens are exposed to a 25 kW/m^2 radiant heat source for a duration of 20 minutes according to ASTM E-662 protocol for smoke generation in a flaming mode, after that they are tested in flexure for mechanical properties. Since the geopolymer composites would not burn, they are not subjected to the ASTM E-662 protocol (Lyon, Balaguru et al., 1997). As a replacement, the samples were tested at room temperature (20 °C) or subjected to temperatures of 200 °C, 400 °C, 600 °C, 800 °C and 1000 °C (1000 °C for carbon fiber reinforced geocomposites only) for 60 minutes of soaking time and at the oxidizing environment in a forced air furnace. The ramp of temperature was 10 K.min^{-1} and samples then were cooled in the furnace with opening gate for 24 hours. At 400 °C of the furnace exposure is comparable to the equilibrium surface temperature of a vertically oriented, unit-emissivity surface exposed to 25 kW/m^2 of radiant energy in quiescent air for the same time period as the ASTM E-662 protocol (Foden et al., 1996).

2.4 Mechanical measurement

The residual mechanical properties of composites after exposing up to high temperature were measured on Universal Tensile Testing machine Instron Model 4202 with a mid-span deflection rate of 2 mm/min at two different outer support span-to-depth ratios

L/H = 20 to 1 in DIN V ENV 658-3:1993-02 and L/H = 16 to 1 as in accordance with ASTM C 1314 – 06. Virtual flexural values were evaluated in agreement with the size-independent method and presented as a visual presentation as well (Tran et al., 2010).

3. Preliminary results and discussion

Fig. 2. presents photographs illustrating of the typical condition of the specimens before and after thermal exposure.

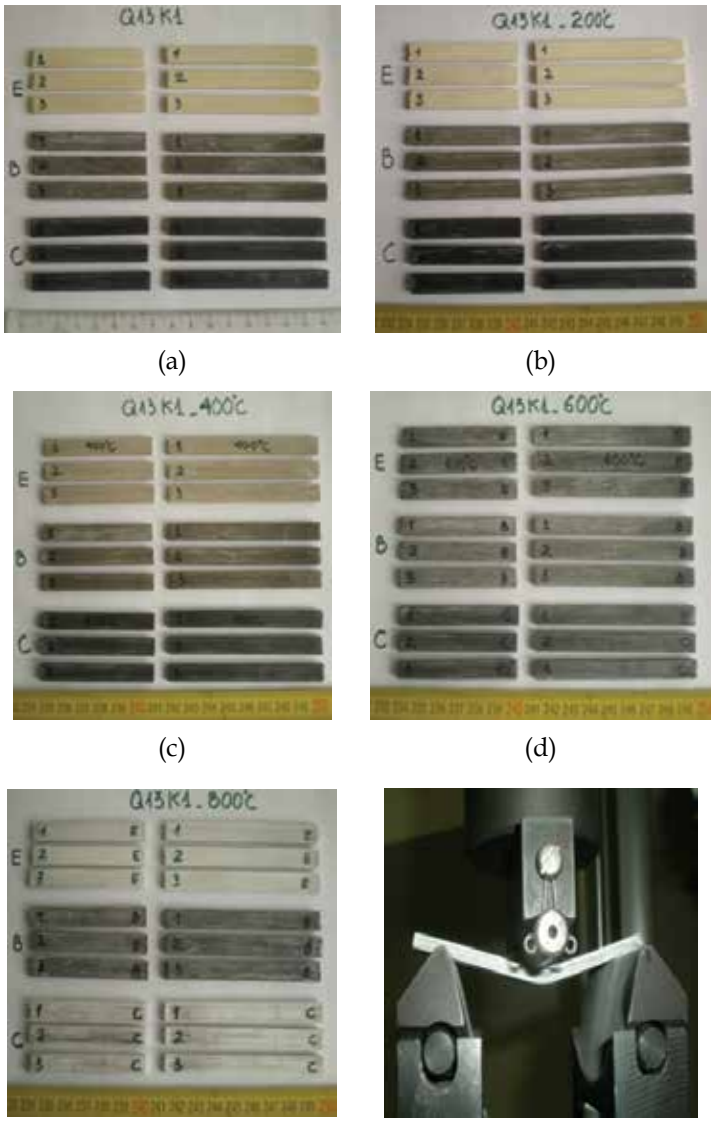

(a) (b) (c) (d) (e) (f)

Fig. 2. Geocomposite specimens (M2 system) before (a) and after thermal exposure (b, c, d, e) and typical failure pattern of M2-Carbon after calcination at 800 °C (f)

Mechanical properties of the geocomposites after thermal exposure up to high temperature were evaluated by equations in agreement with DIN EN 658-3:2002 (L/H = 20 to 1) and ASTM C 1314 – 06 (L/H = 16 to 1). The degradation of specimen weight was also concerned. Residual flexural strength (σ_m), modulus (E), strain in the outer surface (ε_m) and weight lost (Δm) are presented in Table 3 to 8. Visual demonstrations are exhibited on Fig. 3 to Fig. 8 respectively. In order to make the figures clearly, no error of measurements are shown on the figures.

M1/Carbon	L/H = 16 to 1			L/H = 20 to 1			Δm
	σ_m [MPa]	E [GPa]	ε_m [%]	σ_m [MPa]	E [GPa]	ε_m [%]	[%]
20 °C	401.1 ±18.5	65.2 ±3.8	0.90	470.9 ±6.5	92.3 ±6.9	0.74	0.0
200 °C	316.3 ±14.0	62.5 ±1.6	0.77	437.3 ±19.1	88.7 ±5.3	0.72	4.1
400 °C	198.6 ±26.3	39.9 ±6.6	1.00	275.8 ±21.6	49.4 ±2.4	1.06	8.8
600 °C	111.8 ±2.1	11.3 ±1.1	1.43	173.5 ±33.5	19.1 ±3.9	1.69	15.5
800 °C	266.6 ±29.5	38.3 ±4.8	1.35	255.2 ±26.0	37.5 ±2.6	1.04	17.4
1000 °C	154.9 ±21.6	43.4 ±9.2	1.06	222.2 ±57.5	59.4 ±8.5	0.66	18.1

Δm – percentage of weight lost

Table 3. Flexural properties of geocomposites M1 reinforced by Carbon fibers cured at 80 °C after thermal exposure for 60 minutes at different L/H ratios

M1/Basalt	L/H = 16 to 1			L/H = 20 to 1			Δm
	σ_m [MPa]	E [GPa]	ε_m [%]	σ_m [MPa]	E [GPa]	ε_m [%]	[%]
20 °C	371.0 ±14.4	42.7 ±3.0	1.10	451.7 ±12.2	68.2 ±1.3	0.86	0.0
200 °C	291.4 ±20.0	45.9 ±1.8	0.84	307.9 ±7.1	55.5 ±1.4	0.72	5.3
400 °C	222.9 ±4.6	39.0 ±1.0	0.76	257.5 ±27.5	51.2 ±1.5	0.64	4.9
600 °C	94.4 ±8.2	39.9 ±2.3	0.27	84.4 ±1.5	48.1 ±0.7	0.21	5.1
800 °C	52.5 ±6.2	26.2 ±2.9	0.30	45.1 ±5.7	26.8 ±5.6	0.25	4.7

Table 4. Flexural properties of geocomposites M1 reinforced by Basalt fibers cured at 80 °C after thermal exposure for 60 minutes at different L/H ratios

M1/E-glass	L/H = 16 to 1			L/H = 20 to 1			Δm
	σ_m [MPa]	E [GPa]	ε_m [%]	σ_m [MPa]	E [GPa]	ε_m [%]	[%]
20 °C	109.2 ±13.3	32.6 ±4.0	0.59	144.5 ±11.2	44.0 ±2.3	0.53	0.0
200 °C	69.8 ±5.0	21.3 ±2.5	0.64	82.0 ±10.0	30.8 ±1.7	0.50	1.9
400 °C	42.7 ±0.6	9.7 ±2.0	0.71	54.9 ±6.0	18.2 ±4.0	0.52	4.0
600 °C	40.0 ±3.3	10.8 ±1.4	0.58	42.9 ±2.6	20.2 ±1.3	0.29	4.3
800 °C	41.0 ±4.8	11.8 ±1.3	0.75	24.9 ±0.4	6.9 ±1.2	0.48	4.5

Table 5. Flexural properties of geocomposites M1 reinforced by E-glass fibers cured at 80 °C after thermal exposure for 60 minutes at different L/H ratios

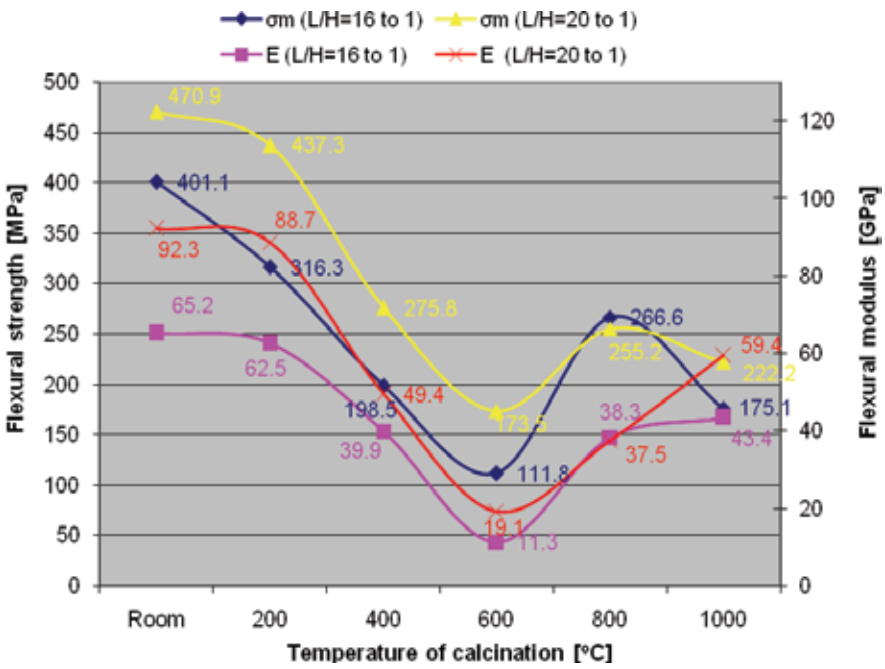

Fig. 3. Residual mechanical properties of geocomposites M1/Carbon fibers

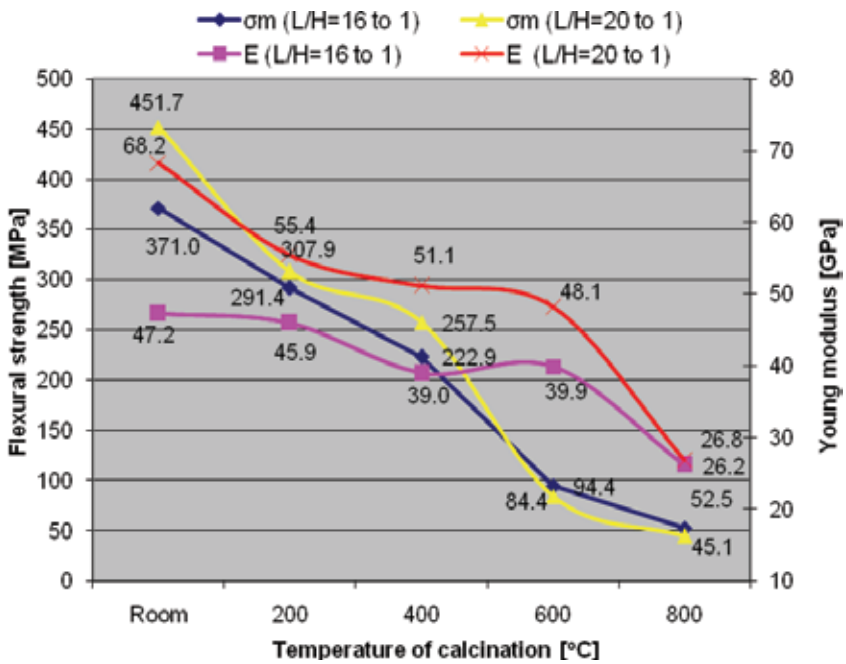

Fig. 4. Residual mechanical properties of geocomposites M1/Basalt fibers

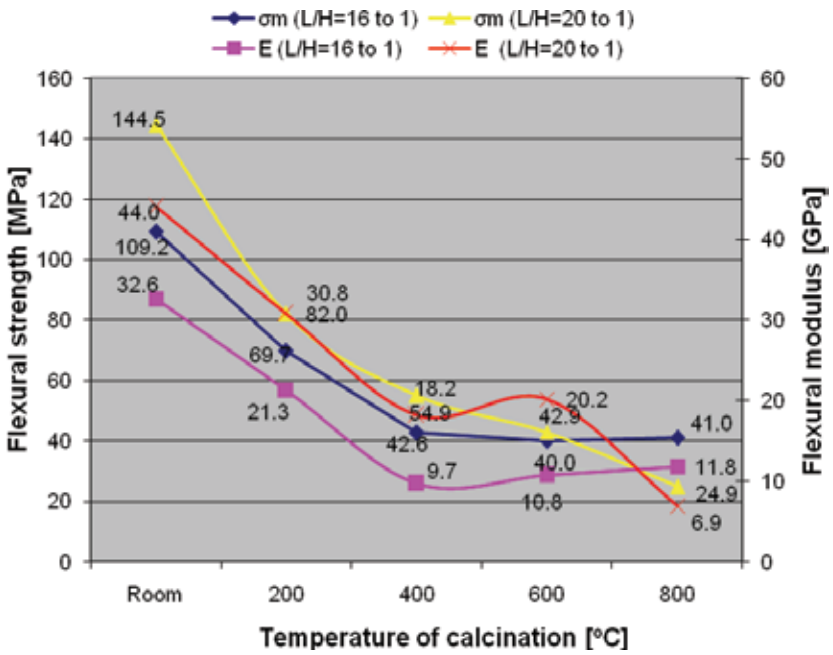

Fig. 5. Residual mechanical properties of geocomposites M1/E-glass fiber

M2/Carbon	L/H = 16 to 1			L/H = 20 to 1			Δm
	σ_m [MPa]	E [GPa]	ε_m [%]	σ_m [MPa]	E [GPa]	ε_m [%]	[%]
20 °C	290.9 ±15.7	85.3 ±1.4	0.49	355.7 ±10.8	106.6 ±5.7	0.40	0.0
200 °C	283.4 ±2.5	69.3 ±7.1	0.84	322.4 ±19.7	99.7 ±13.8	0.56	4.0
400 °C	259.1 ±17.9	64.0 ±1.2	0.86	269.4 ±6.8	77.4 ±4.1	0.87	5.8
600 °C	184.0 ±7.5	36.0 ±1.5	1.11	204.9 ±7.5	47.2 ±1.5	0.80	11.6
800 °C	173.6 ±10.0	28.9 ±1.1	1.25	211.7 ±11.8	35.3 ±3.8	1.24	18.6
1000 °C	190.1 ±13.3	28.9 ±1.1	1.11	206.1 ±8.9	36.6 ±1.5	0.98	18.5

Table 6. Flexural properties of geocomposites M2 reinforced by Carbon fibers cured at 85 °C after thermal exposure for 60 minutes at different L/H ratios

M2/Basalt	L/H = 16 to 1			L/H = 20 to 1			Δm
	σ_m [MPa]	E [GPa]	ε_m [%]	σ_m [MPa]	E [GPa]	ε_m [%]	[%]
20 °C	220.5 ±11.4	53.5 ±3.5	0.58	273.1 ±2.0	65.9 ±1.4	0.49	0.0
200 °C	221.3 ±12.4	48.9 ±4.4	0.78	250.3 ±13.5	58.7 ±2.1	0.61	2.3
400 °C	211.8 ±7.0	52.4 ±5.0	0.55	221.0 ±10.5	55.8 ±2.0	0.57	3.0
600 °C	152.6 ±15.1	56.2 ±1.5	0.35	153.6 ±19.7	68.3 ±2.7	0.28	4.4
800 °C	44.9 ±26.3	46.3 ±4.1	0.12	47.0 ±8.6	56.4 ±5.0	0.07	5.0

Table 7. Flexural properties of geocomposites M2 reinforced by Basalt fibers cured at 85 °C after thermal exposure for 60 minutes at different L/H ratios

M2/E-glass	L/H = 16 to 1			L/H = 20 to 1			Δm
	σ_m [MPa]	E [GPa]	ε_m [%]	σ_m [MPa]	E [GPa]	ε_m [%]	[%]
20 °C	158.1 ±8.8	51.9 ±5.0	0.46	202.0 ±6.9	56.6 ±4.6	0.40	0.0
200 °C	128.2 ±11.8	42.5 ±4.6	0.42	165.6 ±2.8	57.2 ±0.6	0.40	2.7
400 °C	140.8 ±15.5	51.1 ±8.8	0.35	133.8 ±5.4	64.0 ±2.6	0.23	3.3
600 °C	95.9 ±7.6	46.8 ±8.2	0.37	126.0 ±25.1	66.0 ±3.7	0.28	4.0
800 °C	56.1 ±5.0	51.1 ±5.3	0.14	61.8 ±1.9	63.7 ±3.8	0.07	4.0

Table 8. Flexural properties of geocomposites M2 reinforced by E-glass fibers cured at 85 °C after thermal exposure for 60 minutes at different L/H ratios

In general, the mechanical properties of geocomposites reinforced by carbon, basalt or E-glass fibers remained approximately around 90% after sustaining up to 400 °C for 1 hour. Almost all composites remained over 50% of strength after calcination at 600 °C, for carbon fiber reinforced geocomposites the temperature can be over 1000 °C; exceptionally, geocomposite M1/E-glass, due to degradation in alkaline medium and by themselves at high temperature.

The shear strength could even take an important role in the failure pattern of fiber reinforced geocomposites after exposing up to high temperature. For both geocomposites reinforced by basalt fibers, however, after calcinating to over 400 °C their flexural strengths of testing at different L/H ratios were nearly similar (see Fig. 4 and 7). Some unusual behavior of elastic moduli of geocomposites M2/basalt and M2/E-glass were determined (Fig. 7 and 8). It may need more experiments for explaining the mechanism of these behaviors.

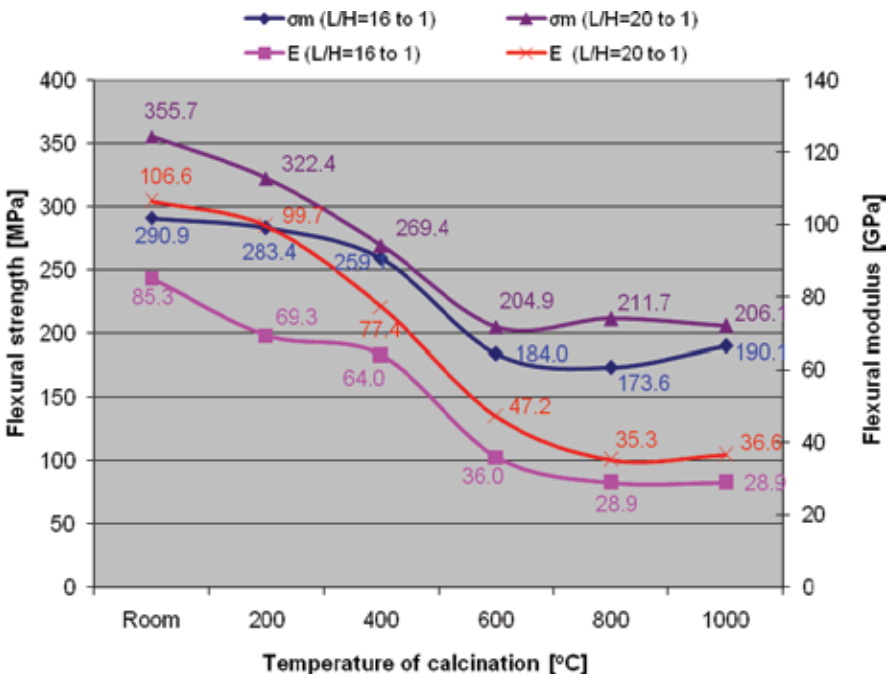

Fig. 6. Residual mechanical properties of geocomposites M2/Carbon fiber

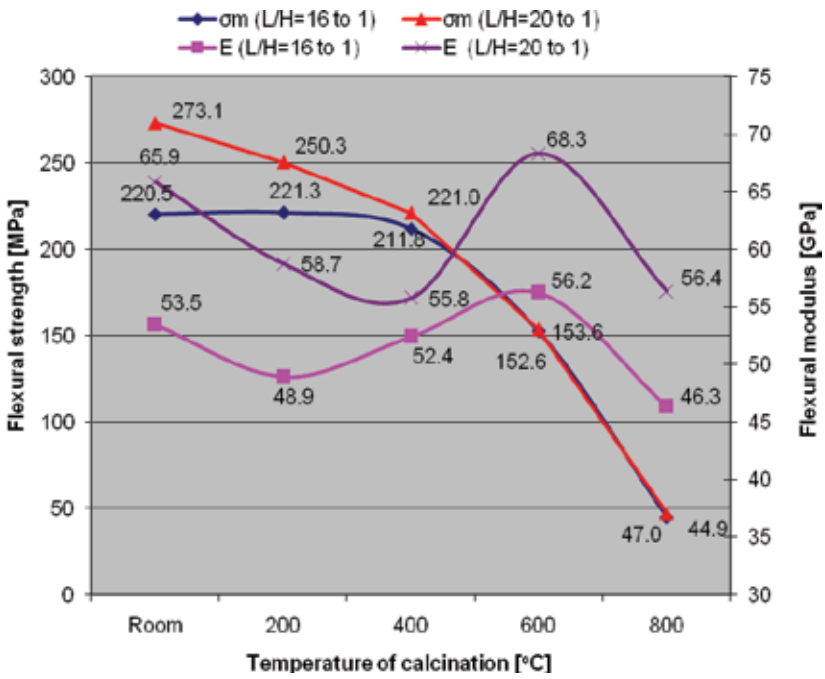

Fig. 7. Residual mechanical properties of geocomposites M2/Basalt fiber

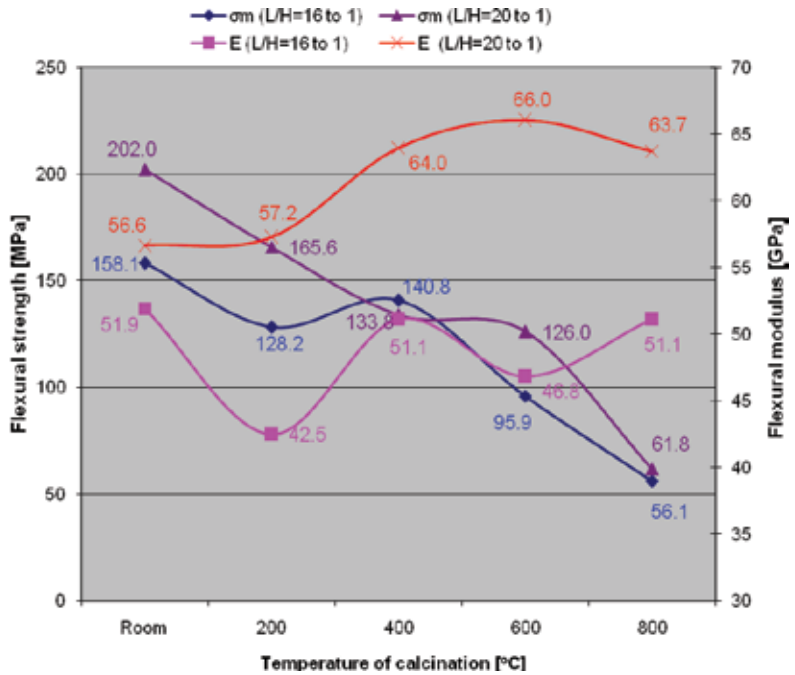

Fig. 8. Residual mechanical properties of geocomposites M2/E-glass fiber

Meanwhile the major weight lost of geocomposites reinforced by basalt or E-glass during the calcination is assumed that from evaporation of free water of 4.5 to 5.0 wt.%, the value can be reached after the composites are exposed up to over 400 °C. The value of carbon fiber reinforced geocomposites must be caused by not only free water evaporation but also partial carbon fiber oxidizing of the outer layers at temperature higher 400 °C, it was estimated that approximately 14 wt.% of carbon fibers is disappeared (see the last columns of Table 3 to Table 8).

Experimental findings show that composites based on geopolymer matrix M2 were very good at thermal dimensional stability, the composites exhibited no thermal expansion even they were calcinated up to 800 °C for basalt and E-glass reinforcements and 1000 °C for carbon fiber reinforcement. On the contrary, the geocomposites based M1 and carbon, basalt and E-glass have different expansion under thermal conditions. Meanwhile dimensional stability was recorded up to 600 °C for M1/basalt, the temperature for M1/carbon and M1/E-glass remain dimensional stability is 400 °C and 200 °C respectively. After exposing up to 600 °C, the expansion of M1/C and M1/E-glass were 40.7 vol.% and 30.8 vol.% in comparison with values at room temperature. After exposing to 800 °C, expansion of M1/E-glass was 135.2 vol.% and M1/basalt was 53.1 vol.%. Moreover, over 800 °C of thermal exposure, white outer calcinated layer of the composite is formed (Fig. 2 and 9).

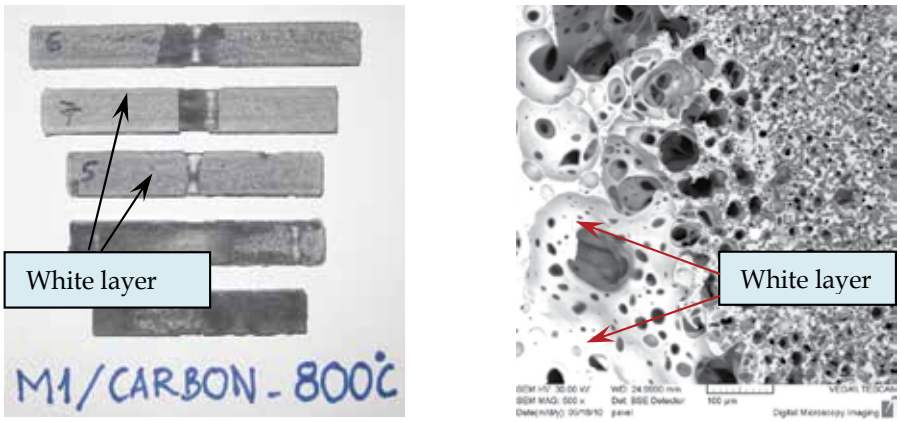

(a) (b)

Fig. 9. Outer calcinated layer of composite M1 after exposing up to 800 °C at macro structure (a) and micro-structure (b at 500x)

The most advantages of geopolymer materials are they possess ceramic-liked properties, meanwhile they can be fabricated at room or very low temperature (in our research, 65-85 °C is recommended) and special ones can protect carbon fiber from oxidation. Among three kinds of commercial selected roving fibers, carbon (HTS 5631 1600tex 24K, TohoTenax), advanced basalt (BCF13-2520tex KV12 Int, Basaltex) or electrical grade glass (E-glass: E2400P192, Saint-Gobain, Vetrotex) which used to reinforce geopolymer composites, the combination between geopolymer and carbon fiber reinforcement attracted much more our attention. The materials have a great expectation for applying into high-tech applications.

Mechanism of mechanical behavior of geocomposite M1/Carbon was very special (Table 3 and Fig. 3). At support span-to-depth ratios L/H = 20 to 1, the properties of the composites

seem to be constant when the samples are exposed up to 200 °C. It was easy to notice that the properties went down drastically after exposing up to higher than 200 °C of calcination, when these composites were exposed up to 600 °C, the flexural strength remained only 37% and elasticity modulus approximately 20% compared to the original ones. It can be seen from Fig. 10 that the interaction of the fiber reinforcement and geopolymer matrix is so loose, it seems no connection between them. The reason is assumed that the difference of relative thermal expansion of these two component parts could be maximum around 600 °C of calcination, this problem should be next investigations.

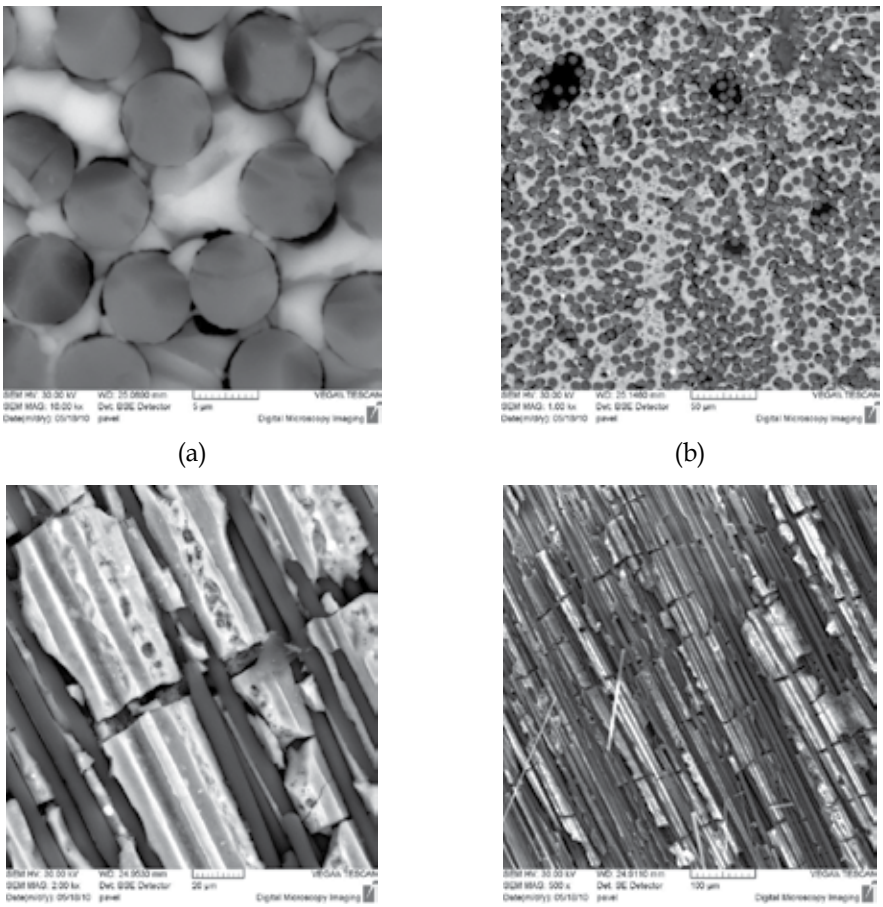

(a) (b)

(c) (d)

Fig. 10. SEM images of M1/carbon after exposing up to 600 °C on sections perpendicular to fibers (a) 10kx and (b) 1.0 kx and surfaces of composite (c) 2.0 kx and (d) 500x

When the temperature of calciantion was higher than 600 °C, the mechanical properties of the composites were shown better, because the adhesion was improved and initial reaction layer might be created, so the flexural strength gained 54% and remained around 50% after calcination up to 800 °C and 1000 °C respectively, meanwhile the flexural modulus could be 65 % compared to those of composites at room temperature (Fig. 11a and c). In addition, after exposing up to higher 800 °C, at low magnification 500x (Fig. 11b and d), the

microstructure of geocomposite looked like foam structure. Fig. 12 shows many micro-cracks in the composites M1/Carbon after high temperature exposing.

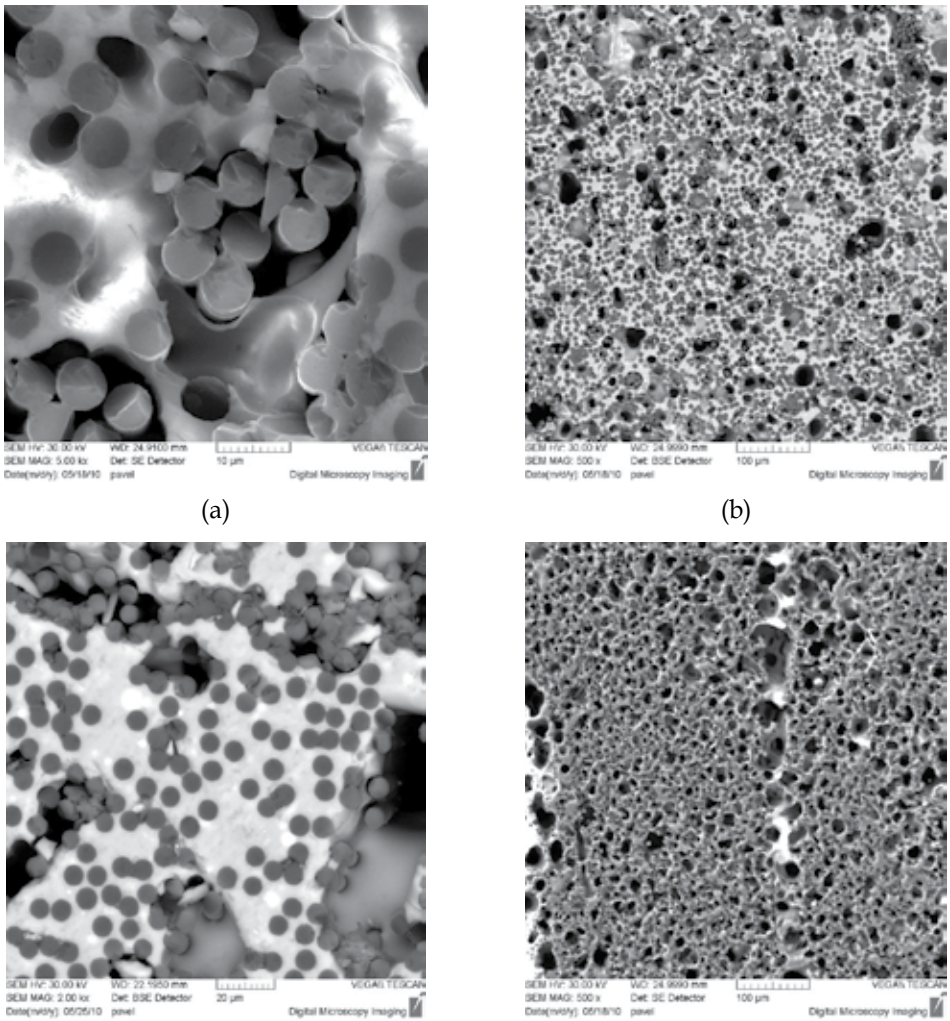

(a) (b)

(c) (d)

Fig. 11. SEM of M1/carbon after exposing up to 800 °C (a) 5.0kx and (b) 500x and 1000 °C (c) 2.0kx and (d) 500x on sections perpendicular to fibers

For M2/carbon fiber composites (Table 6 and Fig. 6), with the span of testing was 64 mm (L/H = 20 to 1), the flexural strength and modulus of elasticity seemed to go down quite dramatically when the temperature of calcination increased from 200 to 600 °C, retained around 57 % of flexural strength (204,9 MPa compared to 355,7 MPa) and 45% of elastic modulus (47,2 MPa in contrast with 106,6 MPa). However, the flexural properties seemed constant even when the composites were exposed up to 800 °C and 1000 °C. Microstructure of the composites is also presented on Fig. 13, as can be seen from this figure that after exposing the composite at 600 °C, the adhesion between carbon fiber and M2 matrix was

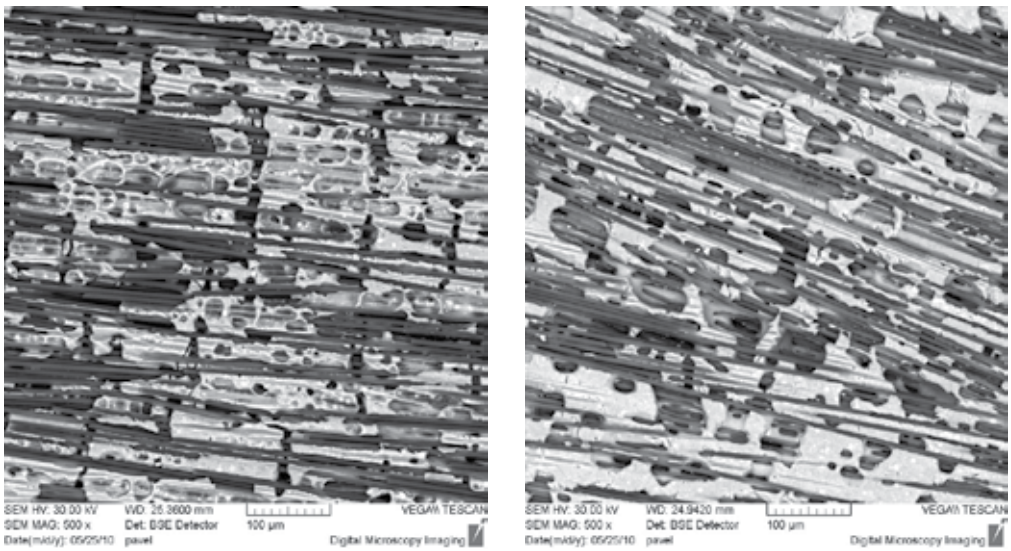

(a) (b)

Fig. 12. SEM of M1/carbon after exposing up to 800 °C (a) and 1000 °C (b) on the surfaces of composite at magnification 500x

also not very good (Fig. 13a and b) and shown better after 1000 °C of exposure (Fig. 13c and d). The behaviors looked like the same as composites M1/carbon. However, for M2/carbon nearly non difference of flexural strength, modulus and dimensional stability were determined in range of 600 to 1000 °C of thermal exposure. Furthermore, the microstructure of geocomposite M2/carbon after exposing high temperature was exhibited on Fig. 14.

It seemed quite interesting when both M1/carbon and M2/carbon possess nearly the same flexural strength around 220 MPa after thermal exposing up to 800 °C and 1000 °C, although their microstructures were presented differently on Fig. 12 and Fig. 14. For composite M2/carbon (Fig. 14), it is visible to the naked eye that not so many cracks and porosities were determined in comparison with composites M1/carbon. This means that the composites based on geopolymer matrix M2 with phosphoric acid as functional additive, the chemical and physical properties of this matrix were stable at high temperature and the thermal dimensional stability was determined as unavoidable results.

With the hypothesis that at high temperature a chemical reaction between interface of carbon fiber and derivative silicon of geopolymer matrix might be taken place to generate SiC which could prevent carbon fiber from oxidation in turn, the Energy Dispersive X-ray Analysis (EDX) was used. Fig. 15b and 15c show minor change of silicon and carbon atoms on the interface of fiber and matrix when compared with original one shown on Fig. 15a. These results show that it is very difficult to confirm at temperature higher than 800 °C the carbon fiber could be protected from oxidization by the initial reaction layer on the fiber (Fig. 15d). Until now the mechanism of geopolymer for protection carbon fiber from oxidation is not identified clearly. The mechanism would be assumed that at high temperature the slowly continuous free water evaporation could create a vapor that can protect carbon fiber and with an special medium the SiC would be create at lower temperature instead of over 1400 °C as usual. Many investigations must be taken place to explain these assumptions.

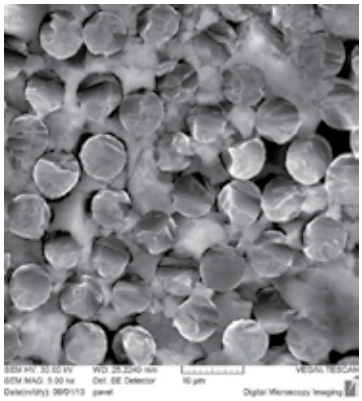

(a)

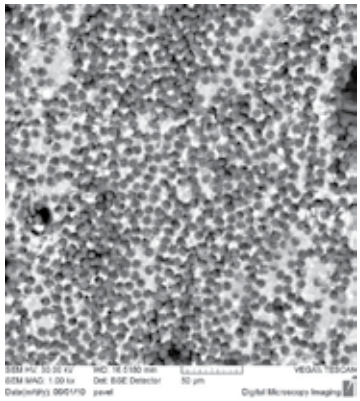

(b)

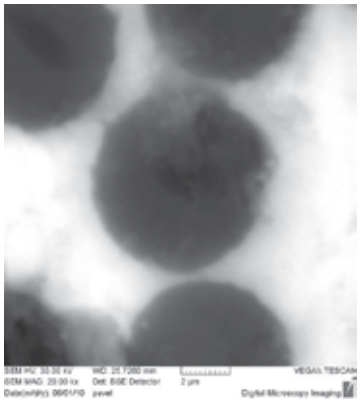

(c)

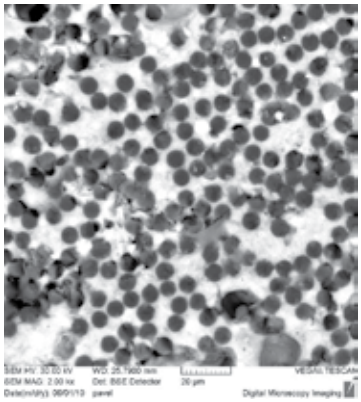

(d)

Fig. 13. SEM of M2/carbon after exposing up to 600 °C (a) 5.0kx and b) 1.0kx and 1000 °C (c) 20.0kx and (d) 200x on sections perpendicular to fibers and surfaces of composite

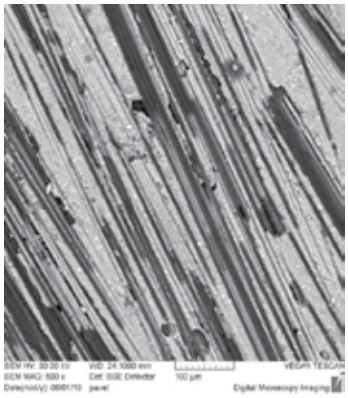

(a)

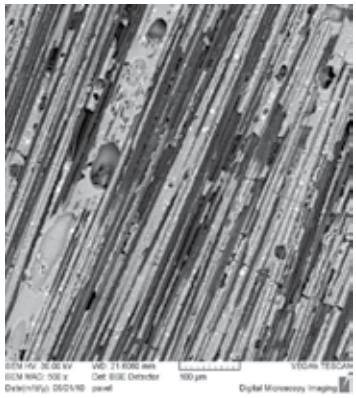

(b)

Fig. 14. SEM of M2/carbon after exposing up to 600 °C (a) and 1000 °C (b) on the surfaces of composite at 500x

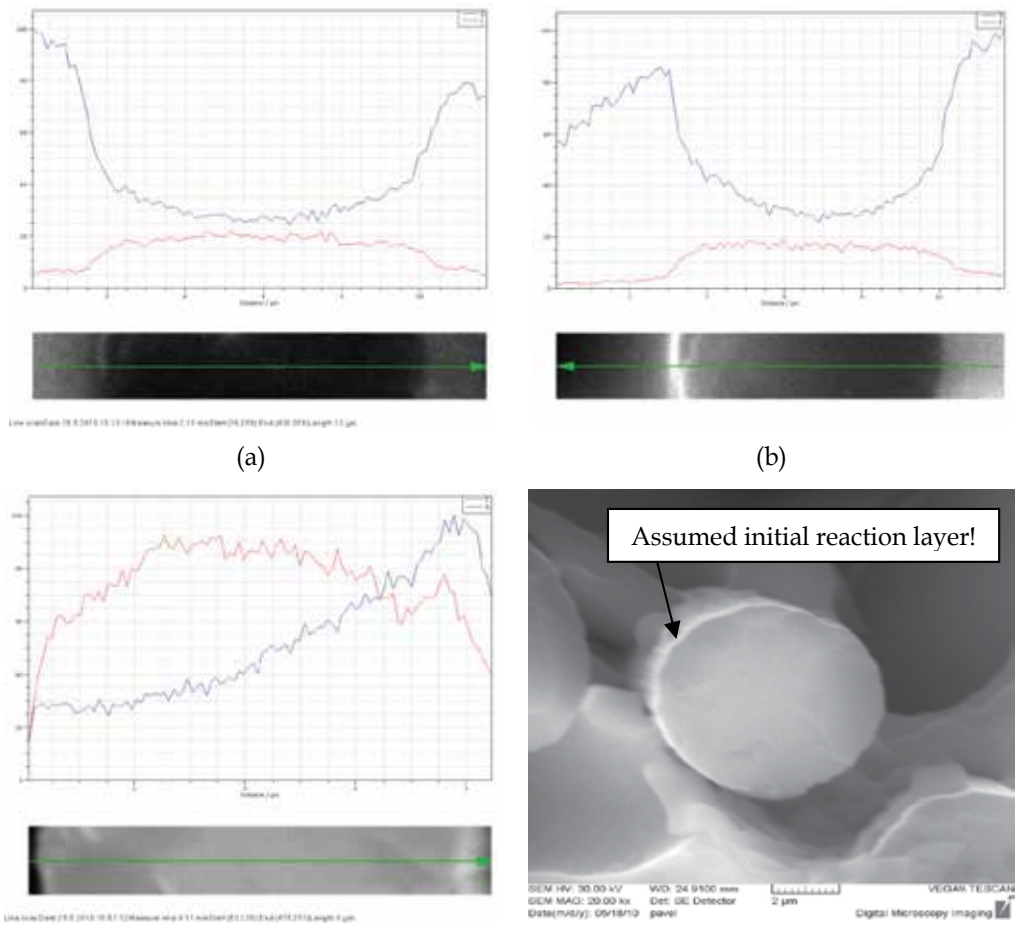

Fig. 15. EDX of line profiles through cross-section of filament fiber in the composite M1-carbon after calcination at (a) room temperature, (b) 800 °C, (c) 1000 °C and (d) SEM after exposing up to 800 °C (at 20kx)

Comparison of the composite resin categories on the basis of percent residual flexural strength retained after the fire exposure is shown in Fig. 16. They are exhibited a combined average for the thermoset (vinyleste, epoxy), advanced thermoset (BMI, PI), phenolic, and engineering thermoplastic (PPS, PEEK) (Lyon et al. 1996, 1997). A big notice should be taken into account is the values here just evaluated after the materials are exposed to a 25 kW/m^2 radiant heat source (equivalent to thermal exposure at 400 °C) for 20 minutes according to ASTM E-662 protocol. In our case of study all the geocomposites were subjected to a much more severe thermal condition (example 800 °C equivalent to 75 kW/m^2) but geocomposites retained 50 to 60% of their original strength at room temperature after exposing up to 600 °C for one hour for M2/basalt and M2/E-glass. Especially the temperature for M1/carbon and M2/carbon can be higher than 1000 °C.

In comparison with the fiber reinforced ceramic matrix composites, the residual flexural strength of SiC/SiC composite retained about 80% of the room temperature at 800 °C and

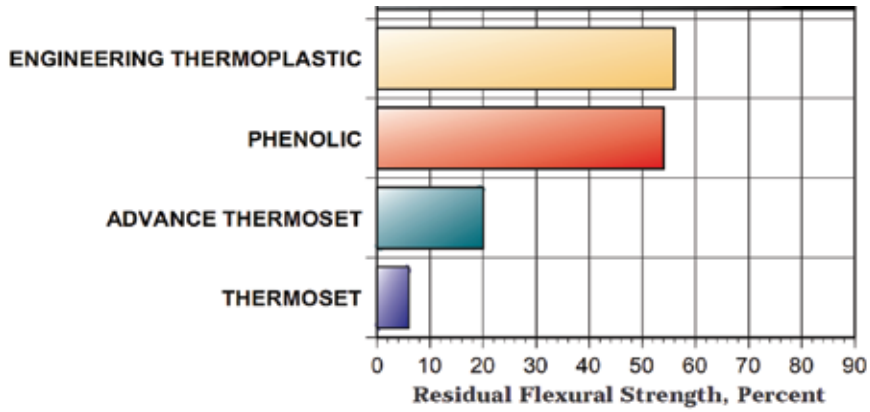

Fig. 16. Residual flexural strength of some commercial composites after fire exposure at a 25 kW/m² radiant heat source for 20 minutes (Lyon, Usman et al. 1996; Lyon, Balaguru et al. 1997)

dropped almost linearly to 55% at 1200 °C (Gomina et al. 1991). For alumina/glass and alumina/tin/glass composites behaved comparably well up to 400 °C, and retaining almost 75% of their strength, but at 600 °C the glass matrix softened (Papakonstantinou, Balaguru et al. 2001). Meanwhile in oxidizing environments, typical carbon/carbon composites oxidized at 400 °C (Luo, Yang et al. 2000); at 1000 °C the carbon/carbon composites retained only 20% of the room temperature strength and even optimal anti-oxidative fillers ($MoSi_2$) was added, the strength of the composites could increase up to only 41% of origins at room temperature (Park and Cho, 2000).

Material	Density	Tensile Modulus	Specific Modulus	Flexural Strength	Specific Flexural Strength	T_{MC}
	[kg/m³]	[GPa]	[MPa.m³/kg]	[MPa]	[MPa.m³/kg]	[°C]
Fiber-Reinforced Concrete	2300	30	13.0	14	0.006	400
Structural Steel	7860	200	25.4	400	0.053	500
7000 Series Aluminium	2700	70	25.9	275	0.102	300
Phenolic-Carbon Fabric Laminate	1550	49	31.6	290	0.187	200
Phenolic-E-glass Fabric Laminate	1900	21	11.0	150	0.074	200
M1/Carbon	2000	x	x	471	0.236	≥1000
M1/Basalt	2400	x	x	452	0.188	≥400
M2/Carbon	2000	x	x	356	0.178	≥1000
M2/Basalt	2400	x	x	273	0.114	≥600
M2/E-glass	2400	x	x	202	0.084	≥600

T_{MC} - Maximum Temperature Capacity

Table 9. Typical properties of structural materials (Lyon, Balaguru et al. 1997)

Table 9 presents the thermomechanical properties of fiber reinforced concrete, structural steel, 7000-series alminium used in aircraft structures, phenolic - carbon fabric laminate,

phenolic – E-glass fabric laminate (Lyon et al. 1997) and fiber reinforced geocomposites based on thermal silica geopolymer matrices M1 and M2. Maximum temperature capacity is defined as the temperature in air at which the nominal tensile or flexural strength falls to one-half of its room temperature value. The results show that the composites based on geopolymer matrices and fiber reinforcements are much better in both specific flexural strength and maximum temperature capacity.

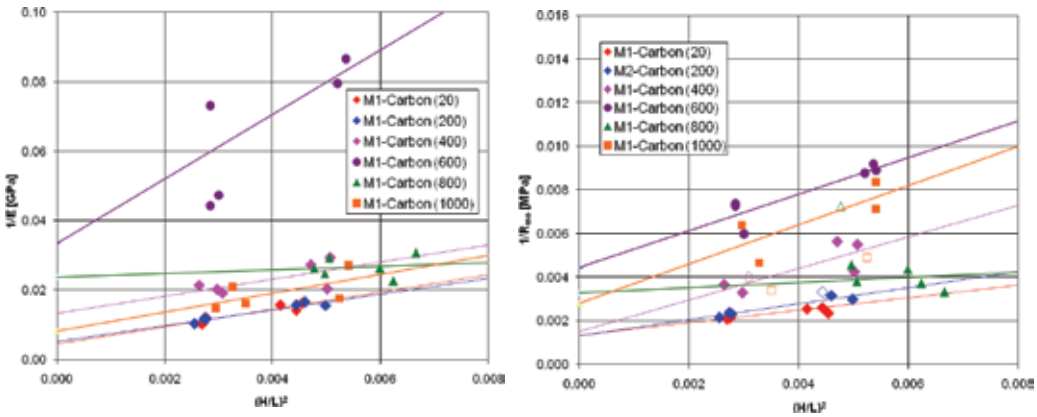

(a) (b)

Fig. 17. Reciprocal effective flexural properties vs. $(H/L)^2$ ratio a) elasticity modulus, b) flexural strength of M1/Carbon after thermal exposure

In order to estimate the virtual flexural strength (σ^*_m) and virtual modulus (E^*) of the geocomposites when support span-to-depth ratios $L/H \rightarrow \infty$ to 1. The novel size-independent method was utilized and the typical of reciprocal effective flexural properties vs. $(H/L)^2$ ratio of geocomposites M1/Carbon after thermal exposure are presented on Fig. 17. However, the linear regressions are created on two series of H/L ratios so large error could be involved in extrapolation. In some cases, the error can reach nearly 100%, it is supposed that the results from these calculation are not enough accurate and no detailed presentation in our works.

4. Conclusions

Thermal silica-based geopolymer reinforced composites possessing ceramic-like properties can be fabricated with simple process (using pultrusion technique, 1 hour at room temperature and 1 hour in oven at only 80 °C for M1 and 85 °C for M2 under vacuum-bagging technique and post-cured by drying at the same temperature for 5 hours more).
Generally, all the geocomposites reinforced by 45, 53 or 60 vol.% of unidirectional carbon fiber HTS 5631 1600tex 24K, basalt roving BCF13 - 2520tex - KV12 Int. or Saint-Gobain - Vetrotex E-glass E2400P192 exhibit very good thermal-mechanical properties, retain nearly 50% of flexural strength even after severe thermal exposure up to 600 °C for basalt and E-glass fiber reinforced geocomposites and 1000 °C for geocomposites with carbon fiber reinforcement for 1 hour in oxidation environment. The geopolymer resins can protect carbon fibers from oxidation; however, approximately 14 wt.% of carbon fibers is oxidized after the composites are exposed higher 800 °C. In addition, experimental findings show that

composites based on geopolymers are very good at thermal dimensional stability, especially for matrix M2, the composites exhibit no thermal expansion even they are calcinated up to 800 °C for basalt and E-glass reinforcements and 1000 °C for carbon fiber reinforcement.
The adhesion between geopolymers and carbon fibers shows very good after curing and even exposing up to over 800 °C, after calcination at higher temparature the morphology of composite look like foam and initial reaction layer of SiC may be created as well. Around 600 °C, however, the loose interaction of fiber and matrix is detected, that causes low mechanical properties. In addition, non toxic fumes and smokes are generated during thermal exposure.
Base on the preliminary results, fiber reinforced geopolymer composites open a nice view of a new generation of fire-resistant materials which possess ceramic like properties while fabricated under very simple procedures and at low temperature.

5. Acknowledgements

This work was supported by Ministry of Industry and Trade of Czech Republic under the project #FT-TA4/068 and by Ministry of Education and Youth of Czech Republic under project MSMT 4674788501.

6. References

Davidovits, J. (1991). Geopolymers: Inorganic Polymeric New Materials. *Thermal Analysis* 37: pp. 1633-1656.

Davidovits, J. (1999). Chemistry of Geopolymeric Systems, Terminology. *Geopolymere '99 International Conference*, Saint-Quentin, France, pp. 9-22.

Davidovits, J. (2002). 30 Years of Successes and Failures in Geopolymer Applications - Market trends and Potential breakthroughs. *Geopolymer 2002 Conference*, Melbourne, Australia, Geopolymer Institute, pp. 1-16.

Davidovits, J. (2005). Geopolymer chemistry and sustainable Development - The Poly(sialate) terminology: a very useful and simple model for the promotion and understanding of green-chemistry. *Geopolymer 2005 World Congress*, Saint-Quentin (North of Paris), France, Geopolymer Institute, pp. 9-16.

Davidovits, J. (2008). *Geopolymer Chemistry & Applications*, Istitute Geopolymer.

Davidovits, J. and J. L. Sawyer (1985). Early high-strength mineral polymer U. S. Patent. United States. 4,509,985.

Davidovits, N. et al. (1989). Ceramic-ceramic composite material and production method. U. S. Patent. United States. 4,888,311.

Demarco, R. A. (1991). Composite applications at Sea: Fire Ralated Issues. Proc. 36th Int'l. SAMPLE Sumposium.

Duxson, P. et al. (2007). Geopolymer technology: the current state of the art. *Journal of Materials Science* 42(9): pp. 2917-2933.

Foden, A. et al. (1996). High Temperature Inorganic Resin for Use in Fiber Reinforced Composites. *The 1st International Conference on Composites in Infrastructure (ICCI'96)*, Tucson, Arizona; United States. pp. 166-177.

Gomina, M. et al. (1991). High temperature mechanical behaviour of an uncoated SiC-SiC composite material. *Journal of Materials Science* 26(7): pp. 1891-1898.

Hathaway, W. T. (1991). Fire Safety in Mass Transit Vehicle Materials. *36th International SAMPE Symposium and Exhibition*, San Diego Convention Center, San Diego, California.

Bell, J.L. et al. (2005). Graphite Fiber Reinforced Geopolymer Molds for Near Net Shape Casting of Molten Diferrous Silicide. *GGC 2005: International Workshop On Geopolymers And Geopolymer Concrete*, Perth, Australia: Curtin University of Technology.

Luo, R. et al. (2000). Effect of additives on mechanical properties of oxidation-resistant carbon/carbon composite fabricated by rapid CVD method. *Carbon* 38(15): pp. 2109-2115.

Lyon, R. E. et al. (1997). Fire-resistant aluminosilicate composites. *Fire and Materials* 21(2): pp. 67-73.

Lyon, R. E. et al. (1996). Fire response of geopolymer structural composites. *The First International Conference on Composites in Infrastructure (ICCI' 96)*, Tuscon, Arizona, United States. pp. 972-981.

Marsh, G. (2002). Fire-safe composites for mass transit vehicles. *Reinforced Plastics* 46(9): pp. 26-30.

Nguyen T.X. et al. (2009). Effects of temperature and plasma treatment on mechanical properties of ceramic fibres. *Achievements in Materials and Manufacturing Engineering* 37(2): pp. 526-531.

Papakonstantinou, C. G. et al. (2001). Comparative study of high temperature composites. *Composites Part B: Engineering* 32(8): pp. 637-649.

Papakonstantinou, C. G. and P. N. Balaguru (2005). Use of geopolymer matrix for high temperature resistant hybrid laminates and sandwich panels. *Geopolymer 2005 World Congress*. Saint-Quentin (North of Paris), France, Geopolymer Institute: pp. 201-207.

Park, S.-J. and M.-S. Cho (2000). Effect of anti-oxidative filler on the interfacial mechanical properties of carbon-carbon composites measured at high temperature. Carbon 38(7): pp. 1053-1058.

Sheppar, L. M. (2007). "Geopolymer Composites: A Ceramics Alternative to Polymer Matrices." The 105th Annual Meeting and Exposition of the American Ceramic Society Retrieved 30 September, 2009, from http://composite.about.com/library/weekly/aa030529.htm.

Tran, D.H et al. (2008). Effect of curing condition on mechanical properties of fibers and composites based on geopolymer matrices. *The 2nd International Student Conference of Material Science*. Liberec - Czech Republic.

Tran, D.H. et al. (2010). Mechanical Properties of Silica-Based Geopolymer Composites Cured at Ambient Conditions in Accordance with Size-Independent Method. *The 2nd RMUTP International Conference: Green Technology and Productivity*, Bangkok (Thailand). pp 134-141.

5

POLICRYPS Composite Materials: Features and Applications

R. Caputo[1], L. De Sio[1], A. Veltri[1],
A. V. Sukhov[2], N. V. Tabiryan[3] and C. P. Umeton[1]
[1]LICRYL (Liquid Crystals Laboratory, IPCF-CNR), Center of Excellence (CEMIF.CAL) and Department of Physics, University of Calabria, Arcavacata di Rende, 87036 Cosenza,
[2]Institute for Problems in Mechanics, Russian Academy of Science, Moscow 119526,
[3]Beam Engineering for Advanced Measurements Company, Winter Park, Florida 32789,
[1]Italy
[2]Russia
[3]USA

1. Introduction

In recent decades, great attention has been devoted to the realization of electrically switchable holographic gratings in liquid crystalline composite materials. It has been shown, indeed, that devices based on holographic polymer dispersed liquid crystals (HPDLCs) are of low cost and can exhibit good diffraction efficiency (DE) [Margerum et al, 1992; Sutherland et al, 1996]. However, application oriented utilization of these devices is limited, in general, by their strong scattering of light, due to the circumstance that the droplet size of the nematic liquid crystal (NLC) component inside the polymer matrix is comparable to the wavelength of the impinging light. In this framework, we have recently proposed a new kind of holographic grating called POLICRYPS, made of polymer slices alternated to films of regularly aligned NLC. These structures do not present those optical inhomogeneities that are due to the presence of NLC droplets in usual HPDLC samples [Sutherland et al, 1994], and can therefore exhibit good optical characteristics, with values of the diffraction efficiency as high as 98%.
This chapter is devoted to give an overview of the POLICRYPS as a composite material, along with a description of its main applications. After a short presentation of the structure, in terms of its fabrication process, we present the POLICRYPS as the device it was initially designed for: a switchable diffraction grating. We also demonstrate that, by suitably choosing the sample thickness and geometrical parameters, a POLICRYPS put perpendicular to the impinging light can behave as a switchable optical phase modulator, where the retardation between ordinary and extraordinary waves can undergo a fine electrical regulation. It is very interesting to show how by adding dye materials to the initial chemical mixture, necessary for obtaining POLICRYPS, can change the way we control its functionalities. In this case, such control can be obtained by using a laser beam of the right colour and power. This fact allows the realization of completely new applications like an optically controlled tunable beam splitter.

New intriguing sceneries open when using different materials to realize POLICRYPS. In particular, if a dye-doped cholesteric liquid crystal (instead of a nematic liquid crystal) is used, the POLICRYPS polymeric channels become mirrorless optical cavities where a distributed feedback (DFB) lasing effect (with a very low threshold) can be obtained. Another challenging opportunity is offered in case a tiny concentration of metallic nanoparticles is included in the initial POLICRYPS mixture. By doing so, we obtain a new device whose frequency spectrum is dependent on the probe light polarization. This last possibility is still in progress and is oriented to the realization of a POLICRYPS structure with meta-material properties.

2. The POLICRYPS structure

The morphology of the POLICRYPS is quite different from the HPDLC one. Optical microscope and scanning electronic microscope (SEM) investigations have shown that the structure consists of rigid slices of almost pure polymer alternated to films of almost pure NLC. The polymeric slices are well glued to two glasses that confine and contain the POLICRYPS. These slices represent a rigid frame that, somehow, 'stabilizes' the NLC component and, therefore, the whole sample. Separation interfaces between polymer slices and NLC films are quite regular and sharp; furthermore, there is convincing evidence that, at these interfaces, the NLC director is everywhere perpendicular to them, thus inducing a good, uniform alignment of the director in the whole NLC film standing between two polymeric slices. This circumstance represents one of the main features that determine the overall characteristics of the whole structure. The uniform and regular alignment of the director in the NLC films of the structure determines the main optical and electro-optical properties of the POLICRYPS. From the optical point of view, losses due to the scattering of the visible light (which is eventually brought to impinge onto the POLICRYPS) are reduced to less than 2%, thanks to the absence of droplets, which exist in HPDLC samples, with an average size comparable to the light wavelength and an arbitrary director alignment. From an electro-optical point of view, the fact that the NLC molecules are confined (and well aligned) in a uniform film, rather than in a small droplet, allows a suitably oriented electric field of the order of a few V/μm to uniformly 'reorient' the NLC director in a millisecond timescale. Afterwards, by suitably choosing the values of the refractive index of the polymer and the ordinary/extraordinary refractive index of the NLC, this director reorientation can be exploited to vary the spatial modulation of the refractive index of the POLICRYPS.

2.1 Fabrication process and set-up

The standard procedure that enables the realization of a good POLICRYPS structure exploits the high diffusivity of NLC molecules in the isotropic state, which avoids the formation and separation of the nematic phase (as NLC droplets) during the curing process [Caputo et al, 2000, 2004, 2007]. The main fabrication steps can be illustrated as follows. By means of a hot stage, a syrup of NLC, monomer and photo-initiator is heated up to a temperature which is above the nematic–isotropic transition point of the NLC component; the sample is then 'cured' with the interference pattern of a UV radiation. After the curing process has come to an end, the sample is brought below the isotropic–nematic transition point by means of a controlled, very slow, linear cooling down to room temperature. The experimental set-up exploits an active system for suppression of vibrations [De Sio et al, 2006, 2008a] and is presented in Fig. 1. An Ar-ion laser is the source of a single-mode radiation at the

wavelength λ_B = 351 nm. The beam is broadened up to a diameter of about 25 mm by the beam expander BE, and divided into two beams of almost equal intensity by the beam splitter BS. These two beams overlap and give rise to the 'curing' interference pattern at the entrance plane of the sample cell S, whose temperature is controlled by the hot stage. Depending on the required nano/microscale dimensions of the structure, the spatial period of the interference pattern can be varied in the range Λ = 0.2–15 μm by adjusting the total interference angle $2\theta_{cur}$. A commercial, metal-coated, reflective diffraction grating (Edmund Optics) placed above the sample is used as a test element for the interferometric monitoring of vibrations. Part of each of the curing beams is reflected and diffracted by this grating. The set-up is adjusted to make the reflected part of one beam spatially coincident with the diffracted part of the second one. These two radiations are wave coupled by the test grating and their interference pattern is detected by an additional photodiode PD3. The signal of this photodiode is sent to a computerized active feedback system, which exploits a software that is based on a proportional–integral–derivative (PID) protocol; this drives a mirror-holder whose position can be controlled by a piezoelectric mechanism, used in feedback configuration. This control system has proved to be able to continuously compensate for changes in the optical path length due to vibrations as well as variations in environmental conditions such as room pressure, temperature or humidity; residual fluctuations are of the order of 6–7 nm, which correspond to the sensitivity of the piezo-system used.

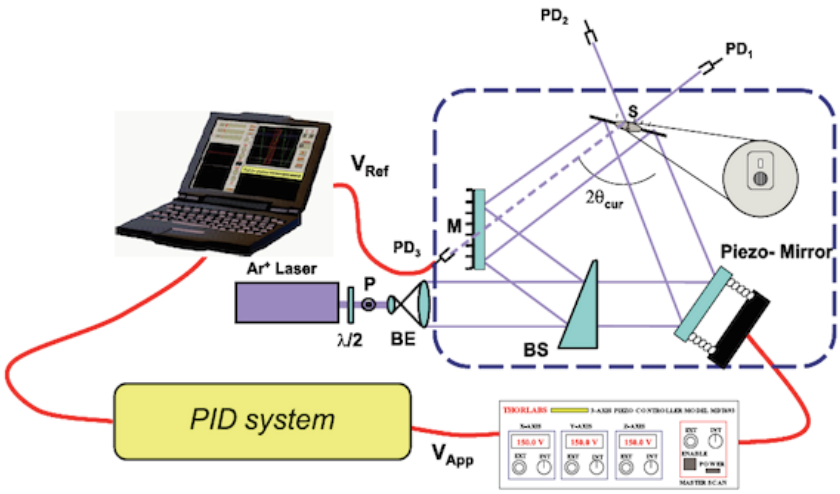

Fig. 1. Optical holographic set-up for UV curing of gratings with stability check. P, polarizer; λ/2, half-wave plate; BE, beam expander; BS, beam splitter; $2\theta_{cur}$, total curing angle; M, mirrors; S, sample; PD1, first beam photo-detector; PD2, second beam photo-detector; PD3, diffracted/reflected beam photo-detector. In the insertion the reference grating is shown (put immediately below the sample area) which enables the stability check

3. The POLICRYPS grating/phase modulator

3.1 POLICRYPS as a high quality, switchable, diffraction grating

The basic device that can be realized by using electrically switchable holographic gratings in liquid crystalline composite materials is an electro-optical switch [Sutherland et al, 1994].

Such a device should, in principle, completely diffract or transmit an impinging light beam, depending on the application of an external voltage (Fig. 2).

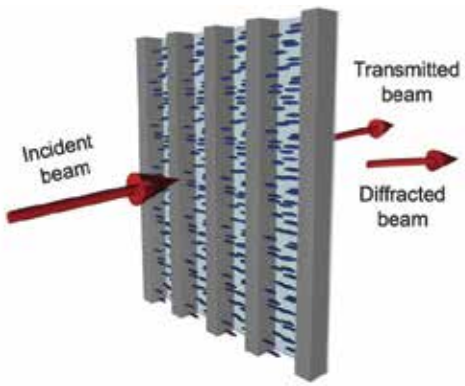

Fig. 2. Sketch of a POLICRYPS grating in transmission configuration

PDLCs have been actively utilized in the past in order to realize working prototypes of this kind of device; unfortunately, they still show issues that affect their performances. One of the main reasons that brought us to design POLICRYPS systems was the possibility of overcoming most of these issues. In the following, we report the results of an experimental comparison between an HPDLC and a POLICRYPS grating, in order to put into evidence how microscopic features of the structure can influence the overall performance of the macroscopic device. We have realized a standard HPDLC and a POLICRYPS grating, both with a fringe spacing Λ=1.5 μm. Sample cells, 16 μm thick, made with indium tin oxide (ITO)-coated glass slabs, were filled with the same initial chemical syrup. This was prepared by diluting the NLC 5CB (Merck, ≈30 wt%) in the prepolymer system Norland Optical Adhesive NOA-61. The POLICRYPS grating was cured by a total UV intensity of 11 mW/cm², acting on the sample for $\tau \approx 1000$ s at high temperature (e.g. above the nematic–isotropic transition point of the 5CB liquid crystal), these being the optimal conditions for achieving a high diffraction efficiency and a morphology of good quality [Caputo et al, 2001]. Almost the same UV intensity and curing time proved also to be adequate for the realization of the PDLC grating, but in this case the sample was cured at room temperature. In order to explore the performances of both gratings, we used a weak (P≈1mW) He–Ne laser radiation (λ_R=633 nm), with its angle of incidence adjusted for satisfying the Bragg condition for the first-order diffracted beam. With the aim of performing a comparison in the same experimental conditions, before starting the curing process of each sample, we measured the intensity I_{in} of the impinging probe beam (before the sample) and the transmitted intensity I_{tr}. Then, once the curing process had been completed and the UV light switched off, we measured both the intensity I_0 of the zero-order (direct transmitted) probe beam and the intensity I_1 of the first-order diffracted probe beam. In this way we were able to calculate the zero-order transmittivity $T_0=I_0/I_{in}$, the first-order transmittivity $T_1=I_1/I_{in}$, the total transmittivity $T_{tot}=T_0+T_1$ and the first-order diffraction efficiency, which is usually calculated as $\eta_1=I_1/I_{tr}$. During all the experiments, the intensity of the probe beam was maintained at a fixed value (the value of the initial impinging intensity before the curing process started). We measured the first-order diffraction efficiency at room temperature

both for POLICRYPS and HPDLC gratings, obtaining $\eta^1_{POLICRYPS}$ = 88% and η^1_{HPDLC} = 41.2%. We stress that the value of $\eta^1_{POLICRYPS}$ is not the highest that we can get since, by using other POLICRYPS gratings (not involved in comparisons with HPDLC ones), we have obtained $\eta^1_{POLICRYPS}$ values as high as 98%. The electro-optic response of the two gratings was investigated by exploiting a low frequency (500 Hz) square-wave voltage, and results are reported in Fig.3.

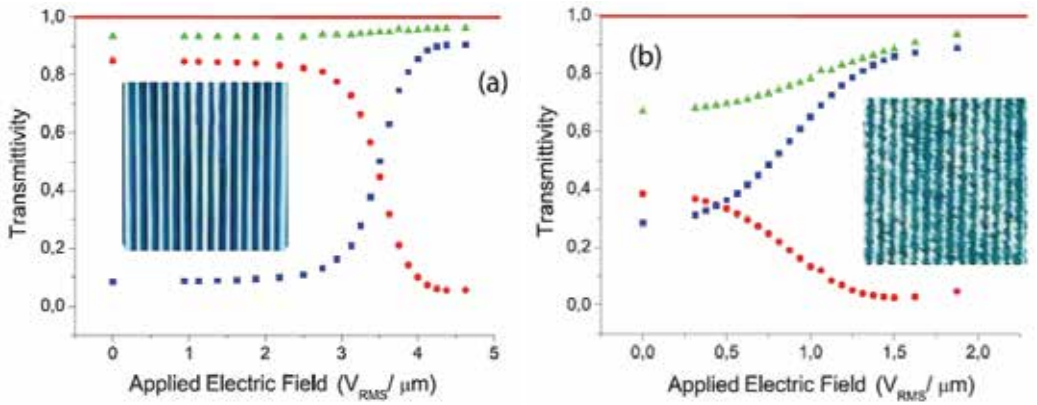

Fig. 3. Dependence on applied voltage of the zero-order transmittivity T_0 (squares), first-order transmittivity T_1 (circles) and total transmittivity T_{tot} (triangles) for (a) a POLICRYPS grating and (b) an HPDLC grating at room temperature. Error bars are of the order of the dot size. The pictures in the inset show respectively a typical POLICRYPS and HPDLC grating morphology observed under a polarizing optical microscope

Fig. 3a represents the switching curve of the POLICRYPS grating: the behaviour of the first-order transmittivity T_1 (circles), zero-order transmittivity T_0 (squares) and total transmittivity T_{tot} (triangles) is reported versus the root mean square applied electric field.

	$\tau_{fall}\,(\mathrm{ms})$	$\tau_{rise}\,(\mathrm{ms})$
POLICRYPS	1.12 ± 0.03	0.88 ± 0.03
HPDLC	10.53 ± 0,18	1.36 ± 0.04

Table 1. Measured values of the switching times for a POLICRYPS and an HPDLC grating obtained from the same initial mixture

It is worth noting that T_{tot} is only slightly lower than 1 and remains approximately the same for all values of the applied field; this indicates that the grating exhibits negligible scattering losses. The situation is quite different for the HPDLC grating (Fig. 3b): the total transmittivity is well below 1 and increases as the applied field increases. We also note that the switching efficiency $h_{sw} \equiv \frac{T^1_{on} - T^1_{off}}{T^1_{on}}$, where T^1_{on} and T^1_{off} are the first-order transmittivities in the switch-on and switch-off condition respectively, is almost the same (93.3%) for both gratings. Where the switching fields are concerned, the first diffracted beam is almost completely switched off by a field of about 1.5V/μm applied to the HPDLC grating, while a value of about 4.3V/μm is needed to obtain the same effect in the

POLICRYPS one. This particular difference can be due to the average size of NLC droplets in the HPDLC; evidently, this size is large enough to enable low switching fields. This is confirmed by the values of the switching times shown in table 1: both the rise and fall times of the HPDLC grating are longer than those of the POLICRYPS; this suggests a very large average size of PDLC droplets. Here, we stress that the electro-optic behaviour shown in Fig. 3a, and its noticeable difference with the one of Fig. 3b, represents the best evidence of the good performances of POLICRYPS gratings; indeed, people working with HPDLCs of nanosized droplets also find for these materials behaviours that are comparable to the one shown in Fig. 3a, but for values of the switching fields which are about four-fold higher [Lucchetta et al, 2003].

3.2 POLICRYPS as an optical phase modulator

The preferential orientation and the good alignment assumed by the molecular director **n** of the LC material within a POLICRYPS structure recently suggested a possible use of these systems as switchable phase modulators [De Sio et al, 2008b]. Examples of such devices are already present in literature. A basic embodiment is obtained by enclosing a NLC with a positive dielectric anisotropy in a cell made of two ITO-coated glasses, treated to give a planar alignment to the NLC director. Since the liquid crystal is birefringent, light with wavelength λ, propagating through the structure, is separated into an ordinary and an extraordinary component. If L is the thickness of the sample and Δn_{LC} indicates its birefringence, the phase difference δ_{LC} between these two waves, measured at the exit of the sample, depends on the value of Δn_{LC}: $\delta_{LC}=2\pi L\Delta n_{LC}/\lambda$. By applying an external electric field **E** with direction perpendicular to the glass slabs of the cell, **n** tends to reorient along the same direction as **E**, thus producing a change in the phase difference. However, this simple device presents some drawbacks. The orientation of **n** is, indeed, sensitive to temperature changes [de Gennes, 1993]. This can represent a serious limit for an eventual device when the power of the impinging radiation is high. Moreover, the switching times of such devices are usually quite long (2–8 ms), thus limiting the field of possible applications. In order to overcome the above-mentioned problems, the NLC layer is often stabilized by means of polymeric chains [Wu et al, 2004]; their presence improves the response times of the device but, unfortunately, drastically increases the operating voltages (due, probably, to the torque exerted by the polymer on the nematic director). Moreover, due to the irregularity of morphology induced by the presence of polymeric chains, visible light is strongly scattered. Therefore, these systems are suitable only for wavelengths in the infrared range. Several features of POLICRYPS structures make them an attractive alternative to the discussed system. First of all, they exhibit limited scattering losses when illuminated by visible light. Second, the polymer slices confine and stabilize the NLC molecules, thus also influencing their alignment, and third, POLICRYPS structures can be driven by low voltages exhibiting short switching times. We expect that the better the alignment of the NLC director in the nematic layer of the POLICRYPS, the higher the value of Δn_{LC}; then, the phase retardation introduced by the grating will depend on the angle that the polarization vector of the impinging light forms with the nematic director within the LC layers Fig. 4.

It is important to underline that, because of the diffractive nature of a POLICRYPS structure, the light impinging on the device will not only experience a phase modulation but will also undergo a dichroic absorption as explained in [Caputo et al, 2010]. This double behaviour can be taken into account by considering the POLICRYPS, in terms of the Jones matrix formalism, as both a retardation plate and a dichroic absorber. This is done by multiplying the Jones Matrix of the generic phase retarder by a new matrix L given by:

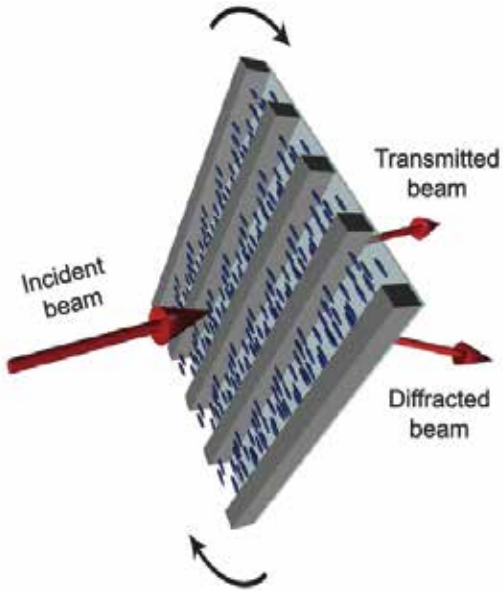

Fig. 4. Sketch of a POLICRYPS grating in transmission configuration used as a phase modulator

$$L = \begin{pmatrix} H & 0 \\ 0 & V \end{pmatrix} \tag{1}$$

where H and V parameter values depend on the considered material and can reflect a broad range of situations. The POLICRYPS used for experiments as a phase modulator has a thickness L=3.03μm and a fringe spacing Λ=1.22μm. In order to check the phase retardation properties of this structure, we used the experimental set-up reported in Fig. 5. The POLICRYPS is put between a polarizer P and an analyzer A, with its optical axis oriented at an angle θ=π/4 with respect to the first polarizer; in this position, the field components have the same amplitude ($E_{||}=E_{\perp}$) and the sample introduces the maximum retardation.
During experiments, the position of the sample remains fixed while the analyzer is rotated (in steps of 10°) around the axis of propagation of the probe light (z axis in Fig. 5). We define β as the angle between directions of analyzer and incident polarization (therefore β=0 when the analyzer A is parallel to the polarizer P). If we indicate with I_{inc} the intensity of the impinging beam, by means of eqs (2) and (3) (derived in [Caputo et al, 2010]), it is possible to calculate the complex electric field $\tilde{E}_{out}(\beta)$ and hence the intensity $I_{out}(\beta)$ of light transmitted by the analyzer A in our experimental geometry.

$$\tilde{E}_{out}(\beta) = \frac{\sqrt{2}}{2}\sqrt{I_{inc}} \begin{pmatrix} -He^{i\frac{\delta}{2}}\sin^2\beta - Ve^{-i\frac{\delta}{2}}\sin\beta\cos\beta \\ He^{i\frac{\delta}{2}}\sin\beta\cos\beta + Ve^{i\frac{\delta}{2}}\cos^2\beta \end{pmatrix} \tag{2}$$

$$I_{out}(\beta) = \tilde{E}_{out}(\beta)\cdot\tilde{E}^{*}_{out}(\beta) = \frac{I_{inc}}{2}\left[H^2\sin^2\beta + V^2\cos^2\beta + HV\sin 2\beta\cos\delta\right] \tag{3}$$

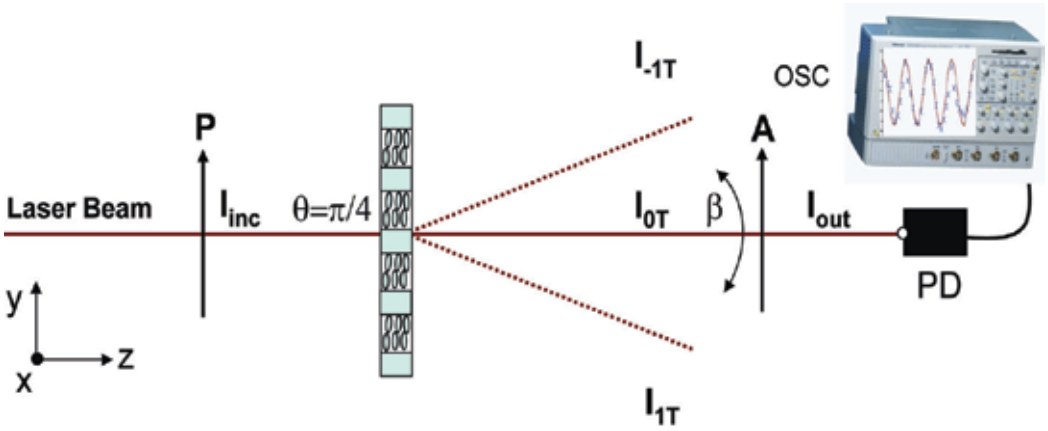

Fig. 5. Experimental geometry utilized for measuring the intensity transmitted by the system composed of a birefringent/dichroic sample put between two polarizers. P polarizer, A analyzer, I_{inc} total incident intensity, I_{out} output intensity, I_{0T} and $I_{\pm 1T}$ zeroth and first order transmitted intensities, respectively. θ is the angle between the light polarization direction (y axis) and the grating optical axis (laying in the xy plane), PD Photo-detector, OSC oscilloscope. The probe beam is from a He-Ne laser at the wavelength λ=632.8 nm. S is the POLICRYPS sample

Parameters H and V are given by:

$$H = \sqrt{\frac{2I_{out}\left(\beta = \pi/2\right)}{I_{inc}}} \tag{4}$$

$$V = \sqrt{\frac{2I_{out}\left(\beta = 0\right)}{I_{inc}}} \tag{5}$$

While the phase retardation δ introduced by the sample can be calculated as:

$$\cos\delta = \frac{1}{HV}\left[\frac{2I_{out}\left(\beta = \pi/4\right)}{I_{inc}} - \frac{H^2 + V^2}{2}\right] \tag{6}$$

By substituting obtained data in eqs. (4), (5) and (6), we obtain: H=0.727, V=0.406 and δ=1.26rad. In Fig. 6, the experimental value of I_{out} as a function of the angle β (crosses) is compared with the theoretical behavior predicted by eq. 3 (solid line).

The different values of H and V show that, even at normal incidence, the diffraction efficiency of the POLICRYPS grating is significant. As for the birefringence of the structure, the obtained value of δ yields Δn=0.042. By considering that the periodicity of the grating is much larger than the probe wavelength we can exclude that this considerably high value is due to form birefringence and hence to the geometrical features of the grating. We are confident, instead, that this value indicates that the stabilizing and confining action exerted by polymer slices on the NLC molecules has a direct influence on their alignment.

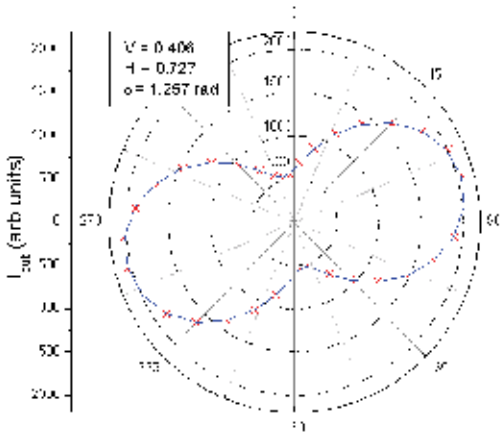

Fig. 6. Behaviour of the intensity transmitted by the analyzer put after a POLICRYPS grating as a function of the angle β between the electric field of the impinging wave and the axis of the analyzer itself. Two segments in the graph evidence output intensity values for the analyzer positions β=0 and β=π/2 respectively

3.2.1 Tunability of the phase retardation

In order to verify the functionalities of POLICRYPS as a tunable phase retarder, we prepared another sample whose thickness had a wedge shaped profile [Caputo et al, 2011a]. As discussed above, by applying an external electric field we can change the birefringence and hence the phase retardation introduced by the structure. However, the phase retardation also depends on the thickness of the layer in which the light propagates. This explains the choice of a wedge shaped cell: by combining the application of the electric field and the possibility to shift the sample to get the desired thickness, it is possible to achieve a very fine tunability for our device. The realized wedge-shaped structure has a thickness varying in the interval (3.00÷5.00 μm) and has been experimentally characterized by means of the setup shown in Fig. 5. The check of the electro-optical tunability of the sample birefringence, has been performed by probing the fabricated sample in the area corresponding to a thickness L=4.35μm. This and other thickness values have been measured before filling the cell by means of an Agilent spectrophotometer and considering the cell as a Fabry-Perot etalon. The applied electric field is a bipolar square wave with frequency ν=1 kHz and a peak-to-peak amplitude varying in the interval (0÷9 Volts/μm). Measurements of the intensity $I_{out}(\beta)$ of light transmitted by the analyzer A have been performed by changing β in the interval 0≤β≤2π, for different values of the applied electric field. Obtained results show that the application of an electric field produces a tuning action of the phase retardation from 1.64rad to 1.07 rad. In each curve of Fig. 7, dots represent experimental values whereas solid lines indicate theoretical predictions; it is evident that the agreement is very good. The plot of both the birefringence value Δn (red dots) and the phase retardation δ (blue dots) of the structure, calculated considering a thickness L=4.35μm, are reported in Fig. 8 as a function of the applied electric field. Phase retardation variations yield, in this case (λ=632.8nm), to a birefringence value varying in the interval (0.024÷0.038). The phase retardation/birefringence properties of our POLICRYPS structure can be also varied by shifting the probed area of the sample along the wedge direction. Several positions have been probed. Experimental results and corresponding theoretical curves are shown in Fig. 9.

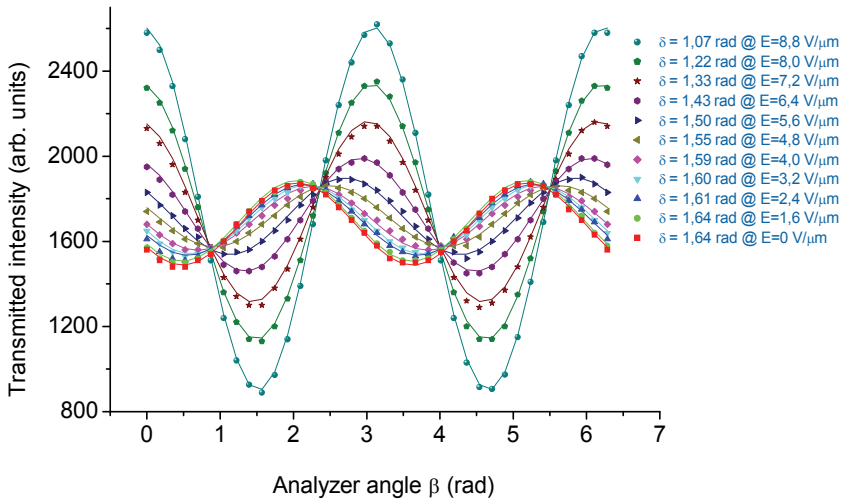

Fig. 7. Behavior of the intensity transmitted by the analyzer put after the POLICRYPS grating obtained by changing the amplitude of the applied electric field. For each amplitude, the output intensity has been measured by varying β between 0 and 2π. Solid lines are theoretical fits while dots represent experimental data. Experimental errors are of the order of the dot size

Also in this case, results confirm the possibility of tuning the phase retardation at will by just probing the sample in the position where it has the right thickness.The thickness value L=4.10μm corresponds to a phase retardation δ=1.55rad (orange curve in Fig. 9) which is close to the condition of quarter wave plate for the He-Ne laser wavelength. This curve is almost constant for every β angle, as expected for this particular value of the phase retardation.

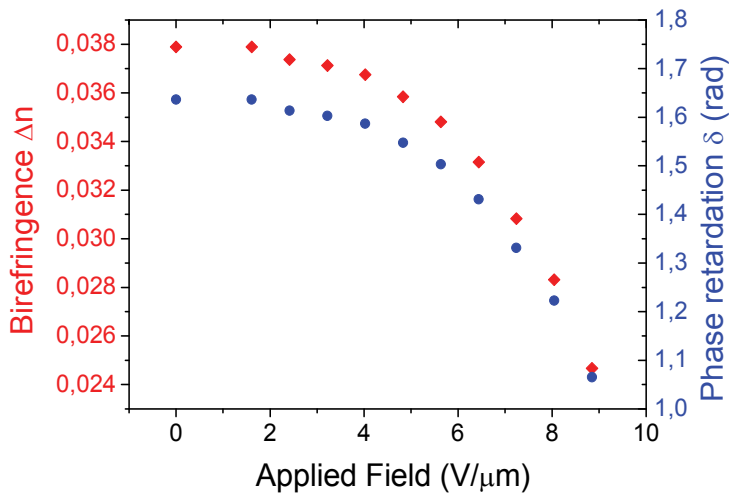

Fig. 8. Plot of birefringence Δn (red dots) and phase retardation δ (blue dots) of the POLICRYPS structure versus the amplitude of the applied electric field

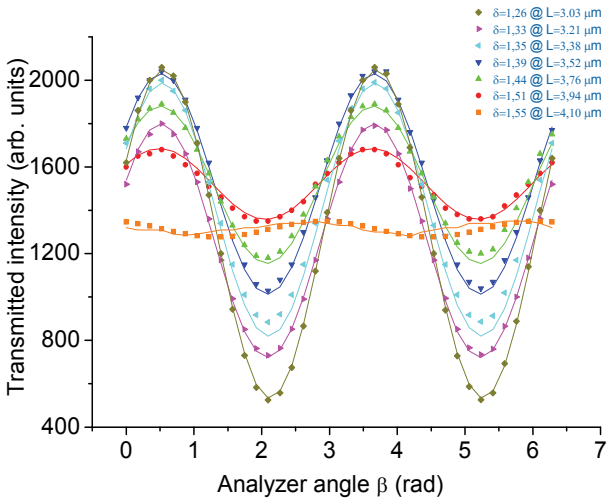

Fig. 9. Behavior of the intensity transmitted by the analyzer put after a POLICRYPS grating obtained by shifting the sample along the wedge direction and probing it in areas with different thickness. For each thickness, the output intensity has been measured by varying β between 0 and 2π. Solid lines are theoretical fits while dots represent experimental data. Experimental errors are of the order of the dot size

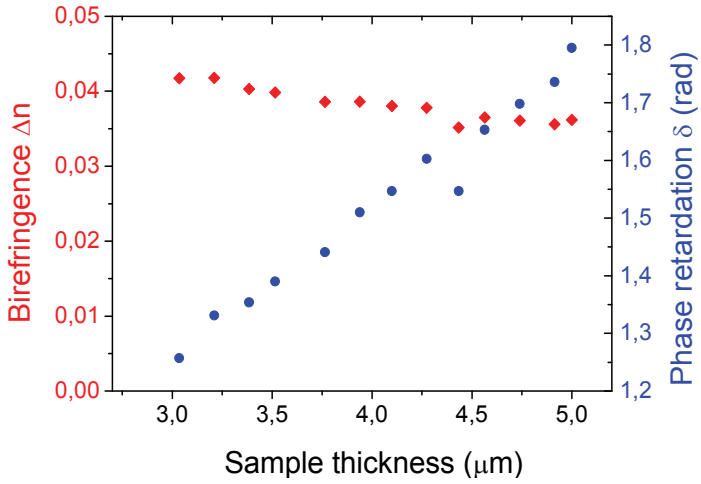

Fig. 10. Plot of birefringence Δn (red dots) and phase retardation δ (blue dots) of the POLICRYPS structure measured by shifting the sample along the wedge direction and probing it in areas of different cell thickness

This result confirms the possibility of finely tuning the phase retardation introduced by the structure by playing both with the amplitude of the applied electric field and the position of the sample for finding the area corresponding to the optimal thickness.
Birefringence and corresponding phase retardation values, measured by shifting the sample along the wedge direction, are reported in Fig. 10. We can notice that, by increasing the thickness L in the interval (3.0÷5.0μm), Δn remains almost constant, as expected if we

consider that the POLICRYPS grating exhibits a quite homogeneous morphology. On the contrary, the phase retardation δ shows a linear increase with values varying in the interval (1.25÷1.80 rad).

4. Photoresponsive POLICRYPS structures

As discussed above, a fundamental advantage provided by holographic structures containing liquid crystal materials is the possibility of tuning their optical properties by applying external electric or thermal fields. Some years ago, Tondiglia et al. have proposed another fascinating possibility: the use of light for switching the optical properties of gratings [Bunning et al, 2000]. Indeed, azobenzene liquid crystals enable to access, optically and isothermally, a nematic to isotropic (NI) transition that changes the refractive index of the liquid crystal films, thus modifying the refractive index modulation of the whole structure. The exploited mechanism is that, upon UV (λ=360 nm) irradiation, azo-LC molecules undergo a conformational change (from rodlike trans to cis) which drives the LC through an isothermal NI phase transition; this process can be driven in the reverse direction by converting the cis-azobenzene moieties back to their rodlike *trans* state via exposure to a radiation of a suitable wavelength [Tsutsumi & Ikeda, 1995]. The decision to adopt these materials in the initial POLICRYPS mixture brought to the realization of the so-called azo-POLICRYPS: optically controlled POLICRYPS structures. Samples have been realized by means of the typical setup for POLICRYPS fabrication (reported in Fig. 11). Preliminary attempts, performed on different sample cells, have shown that the best performances are exhibited by the one of L=11.4μm thickness, with a grating pitch Λ=1.6μm, this value being such that the highest diffraction efficiency is obtained with the actual cell thickness. Samples have been prepared by using the following mixture: 25 wt % of NLC (E7 by Merck), 5 wt % of azo-LC (1005 by BEAM Co.), and 70 wt % of monomer (NOA61 by Norland). A qualitative characterization, made with an optical microscope, shows that this azo-POLICRYPS exhibits a stable structure, made of alternated layers of pure polymer and pure LC, with the apparent absence of PDLC droplets (inset of Fig. 11).

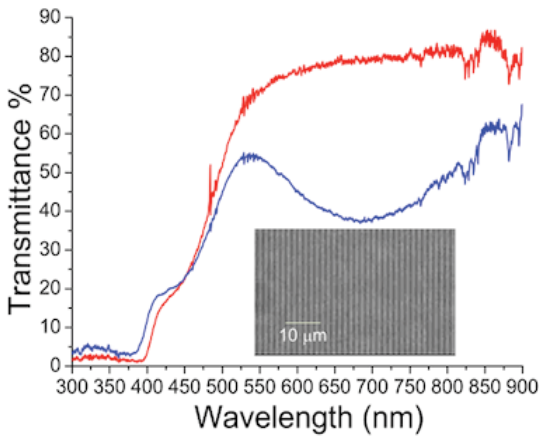

Fig. 11. Transmission spectra of both the uncured mixture (red curve) and the realized grating (blue curve). Inset: photo of a POLICRYPS grating taken with a 20x objective equipped Olympus microscope

Transmission spectra reported in Fig. 11 have been obtained with the aid of a fiber optic spectrometer, using light beams of arbitrary polarization at normal incidence. The mixture exhibits a high absorption in the λ=300–400 nm range, while the grating gives rise to a relative minimum in the transmission around λ=650 nm.

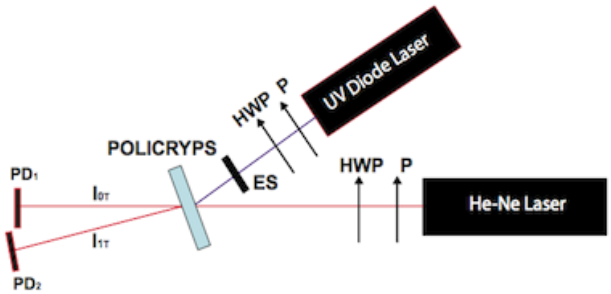

Fig. 12. Experimental setup for the observation of all-optical processes in azo-POLICRYPS. $PD_{1,2}$: photodetectors; HWP: half-wave plate; P: polarizer; ES: electronic shutter

Thus, the setup utilized for the characterization of the sample (Fig. 12) makes use of an UV diode pump laser emitting at λ=409 nm (in the high absorption range of the mixture spectrum) and a He–Ne probe beam of λ=633 nm (in the range that is of high efficiency for the grating); this beam impinges at the Bragg angle θ=11.5°. For experimental simplicity, we have used an unfocused pump beam with a power of only 4.4 mW, which exhibits an oval shape on the sample of about 2-3 mm^2. Fig. 13 shows that a pump irradiation of duration τ=20 s, operated by opening the electronic shutter (ES), reduces the diffraction efficiency of the azo-POLICRYPS grating to less than 75% of its initial value in a time of a few seconds; a slow increase toward the initial value is then observed when the shutter closes the pump beam.

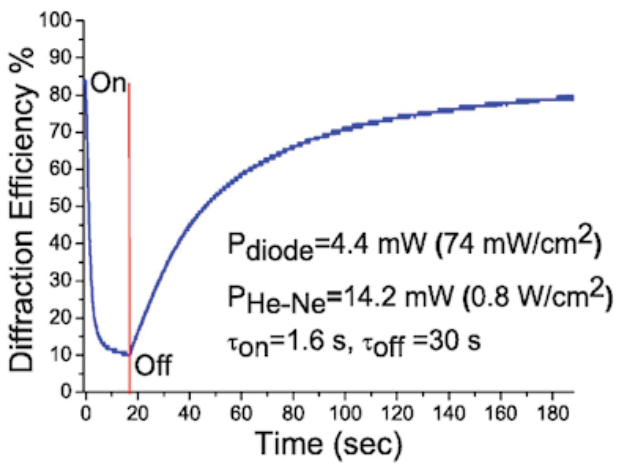

Fig. 13. Dynamics of the diffraction efficiency of the probe first order diffracted beam. The diffraction efficiency of the grating is de- fined as the diffracted intensity divided by the sum of the diffracted and transmitted intensities

We have investigated this dynamics by varying the pump power from 0.1 mW to 14.6 mW, while the probe power is kept constant: (inset of Fig. 14).

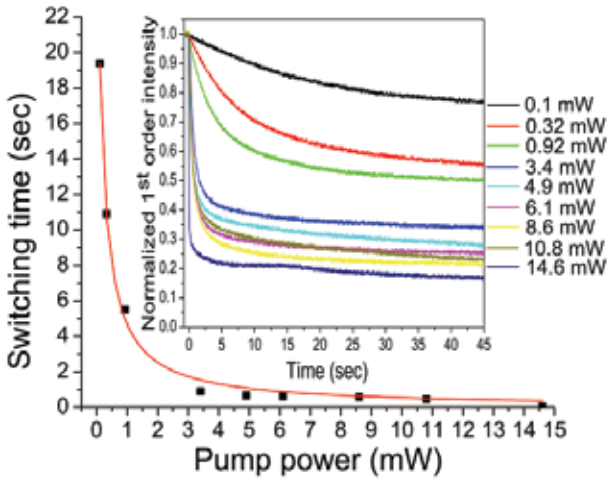

Fig. 14. Response time of the azo-POLICRYPS grating vs the power of the pump beam; the error bar is of the order of the square dimension. Diffraction efficiency values in the inset are normalized to the initial ones

The switching time (sw) of each curve is reported in Fig. 14 as a function of the impinging pump power P: when this power exceeds a minimum value $P_{min}\cong 0.1$ mW (below which the effect is very small and it is almost impossible to get a good signal), data are well fitted by the negative exponential red curve,

$$\tau_{sw} = \tau_0 e^{-(P-P_{\min})/P_0} \tag{7}$$

where τ_0=19.4 s and P_0=1.8 mW; this behavior can be explained by assuming the rate of concentration of photoisomerized azo-LC molecules proportional to the impinging intensity.Taking into account that in the actual experiment the pump beam is not focused, we foresee that much shorter switching-off times can be achieved in systems irradiated by a focused beam, where a high power density is obtained with power levels even lower than the actual ones.

4.1 azo-POLICRYPS as an optically controlled beam-splitter

The possibility to realize an optically controlled POLICRYPS structure is of particular interest for applications, since fast light responsive devices represent an innovative way to realize an on-chip technology. A fundamental element of an optical set-up is the beam-splitter. This element splits an incident light beam into two or more beams, which may or may not have the same intensity. These devices are usually passive in the sense that the intensity of the splitted beams is fixed or it can be eventually varied by changing the angle of incidence of the light impinging on the device. POLICRYPS diffraction grating can combine the capability of "dividing" beams (typical of periodic structures) with the effects of an adjustable birefringence, typical of nematic liquid crystals, which influences the intensities of the diffracted beams.

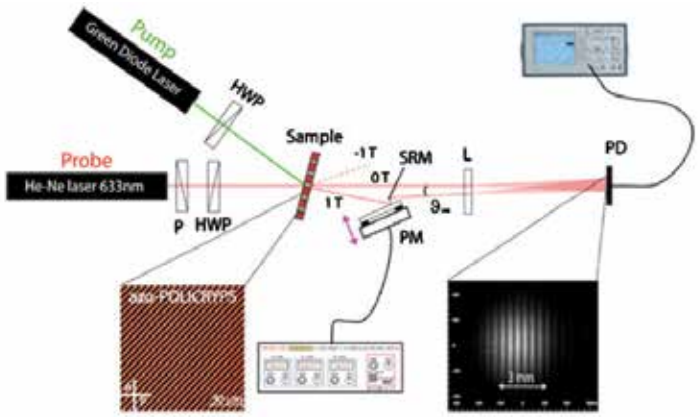

Fig. 15. All-optical OBS and interferometer setup: P, polarizer; HWP, half-wave plate; SRM, semireflective mirror; θ_{int}, interference angle; PM, piezomirror; PD, photodetector; L, lens

By using an azo-POLICRYPS as an optical beam splitter (OBS) it is possible to obtain a tunable optical element, where we can choose, at will (turning a knob), the portion of initial intensity which remains to the transmitted beam and the amount which is transferred to the splitted (diffracted) one. For the experiment, we have fabricated an azo-POLICRYPS structure whose geometrical parameters are L=6.95μm in thickness and Λ=1.57 μm in fringe spacing; according to Kogelnik's theory, [Kogelnik, 1969] this grating operates in the Bragg regime with a characteristic parameter $\rho=\Lambda^2/\lambda L=0.56$ at λ=0.633 nm. The experimental setup utilized to exploit the azo-POLICRYPS as a finely adjustable, optically controlled OBS is reported in Fig. 15. The impinging probe light is split into two beams (the transmitted and the diffracted orders, 0T and 1T respectively) by the azo-POLICRYPS grating. These are recombined in Mach–Zehnder interferometer geometry; this part of the setup is actually used to monitor the functionality of the OBS. The diffraction efficiency change of the azo-POLICRYPS is driven by an external pump source green diode laser. On application of the pump laser, the index contrast of the grating vanishes and the structure becomes transparent to the impinging probe light. Fig. 16a shows the evident change in the diffraction efficiency induced by switching ON the pump green light.

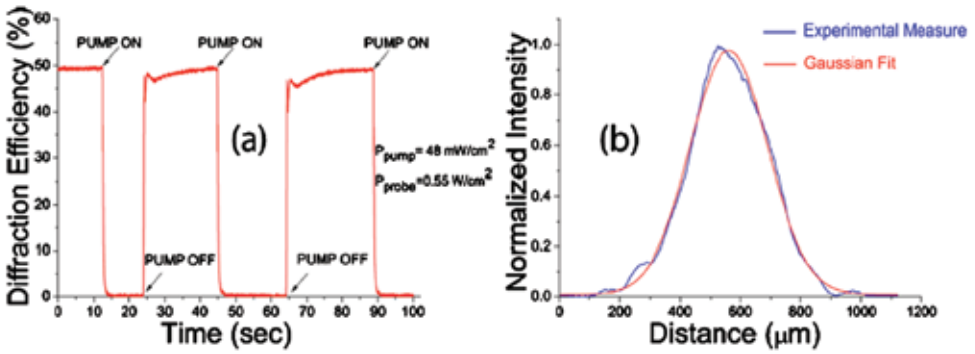

Fig. 16. (a) Reversible and repeatable changes of the azo-POLICRYPS diffraction efficiency induced by a pump green light. Power density values are reported in the figure; (b) Typical intensity profile of the transmitted intensity trough the structure

The switching response of the azo-POLICRYPS OBS is detected by using a sequence of ON-OFF pump beam irradiance P_{pump}=48 mW/cm² while the intensity of the probe red beam is kept ON at all times P_{probe}=0.55 W/cm².
As for the quality of the transmitted (0T) and diffracted (1T) beams outgoing from our OBS, we have detected their transverse intensity profiles with a charge-coupled device CCD camera for different increasing values of the incident probe power; we had the evidence that the grating does not modify the typical Gaussian shape of both beams, which remains almost unchanged for any value of the impinging probe power density in the range 0.1 to 0.7 W/cm²; Fig. 16b shows the Gaussian profile of the transmitted beam detected for the value P_{probe}=0.7 W/cm². The ratio $R=I_{1T}/I_{0T}$ of the intensities of 1T and 0T beams is related to the diffraction efficiency of the azo-POLICRYPS through the equation

$$\eta = \frac{I_{1T}}{I_{0T} + I_{1T}} = \frac{R}{1+R} \tag{8}$$

For the aim of the actual work, the polarization of the probe beam and its incident angle have been adjusted to obtain a maximum diffraction efficiency value max=50%, that is to say R_{max}=1, when the pump beam is off [De Sio et al, 2010]. In order to characterize and exploit the azo-POLICRYPS as a variable OBS, we have used the interferometer setup reported in Fig. 15. The interference pattern reported in the dark insets of Fig. 15 produced by overlapping 0T and 1T beams is monitored by means of the detector PD, which is provided of a small aperture 500 μm on top of the active area. The pattern periodicity can be easily controlled by varying the orientation of the semireflecting mirror, thus the angle θ_{int}. In our experiment, θ_{int} was relatively small 0.04°, and the scale is reported in the same dark inset of Fig. 15. The fringe visibility, defined as $\nu=(I_{max}-I_{min})/(I_{max}+I_{min})$, (where I_{max} and I_{min} are the measured maximum and minimum intensity values of the interference pattern) strongly depends on R. Indeed, for our geometry, it is easy to see that

$$\nu = \frac{2\left(I_{0T}I_{1T}\right)^{1/2}}{I_{0T} + I_{1T}}|\gamma| = \frac{2R^{1/2}}{1+R}|\gamma| \tag{9}$$

Here, γ (the degree of coherence of the two beams [Yariv, 1989] is related to the difference Δl of the optical path lengths of the two beams and to the coherence length lc of the probe laser beam, which in our case is of the order of 10 cm (HRP050 Thorlabs). We can assume that Δl does not exceed few micrometer even when the piezomirror (PM) is shifted back and forward of few micrometer, therefore $|\gamma|=(1-\Delta l/l_c)\approx 1$. Relating η to R by the equation $R=\eta/(1-\eta)$ and substituting it into eq. (9) we obtain:

$$\nu = 2\left(\frac{\eta}{1-\eta}\right)^{1/2} \tag{10}$$

Since in our azo-POLICRYPS grating η varies with the impinging pump power P_{pump}, we have investigated the behavior of our tuneable OBS by detecting the fringe visibility ν versus P_{pump}. Measurements have been performed by applying a linear voltage to the piezomirror PM included in the interferometric part of the setup of Fig. 15. In this way, we were able to modify the optical path length of one of the two arms, thus allowing a scrolling of the fringe pattern on the PD and a measurement of I_{max} and I_{min} values, without shifting

the PD from the top of the impinging Gaussian beams. Indeed, a linear movement of the piezomirror in the direction normal to the mirror plane corresponds to a shift of the fringe pattern along a direction parallel to the PD surface; therefore, the output signal from the PD exhibits the sinusoidal behavior shown in Fig. 17.

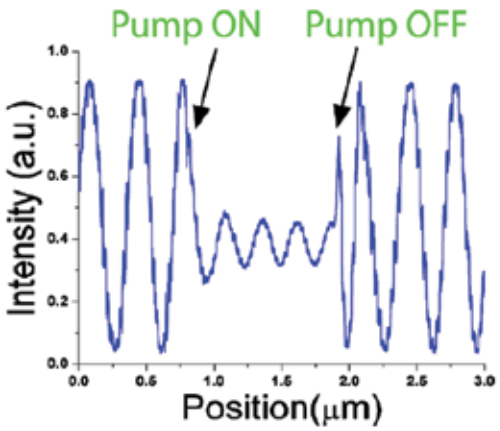

Fig. 17. Intensity profile of the interference pattern vs the piezomirror position. A reversible change of oscillation amplitude, obtained by switching ON and OFF the external pump can be well observed

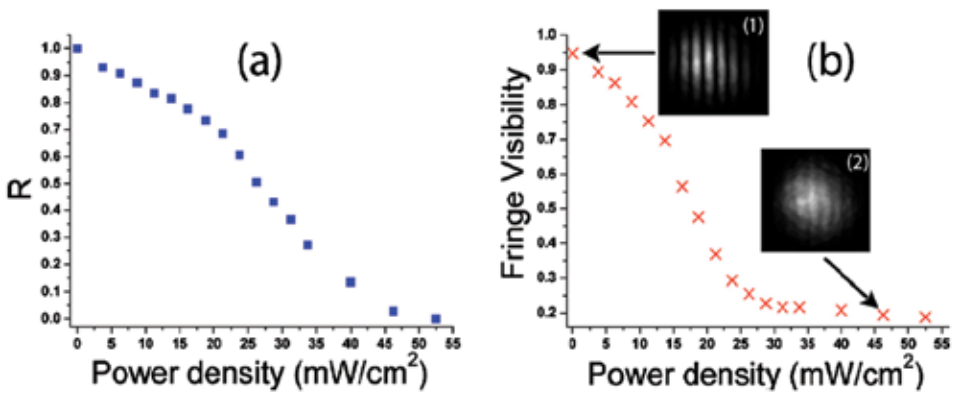

Fig. 18. Beam splitting (a) and fringe visibility (b) vs the pump power density. Interference pattern acquired with a CCD camera is reported for ν=0.94 (1) and ν=0.2 (2). Experimental errors are the order of dot and cross dimensions

The amplitude of the sinusoidal modulation is strongly attenuated when irradiating with a green pump laser (P_{pump}=48 mW/cm²) over the spot of the red light; oscillation amplitude is restored to its initial value in some milliseconds by turning off the external pump. The behavior of ν versus fine variations in P_{pump} is reported in Fig. 18b, along with measured values of R. Curves can be explained by considering that the rate of the trans–cis isomerization process depends on the number of excited molecules; therefore, the rate of concentration of photoisomerized azo-LC molecules is proportional to the pump power

density. This phenomenon directly affects R and therefore ν, which varies from 0.94 to 0.20. Fig. 18a shows that R values can be finely adjusted between 1 (transmitted and diffracted beams of the same intensity) and 0 (no diffracted beam, the whole impinging intensity is transmitted).
As for the measured ν values, following eq. (9), also ν should vary between 1 (when R=1) and 0 (when R=0). The observed discrepancy (0.92 instead of 1 and 0.2 instead of 0) can be explained by taking into account that, due to the birefringence of the grating [Caputo et al, 2010] the transmitted beam is elliptically polarized, with an ellipticity of the order of $a/b \approx 10/1$ where a and b are the major and minor axes of the polarization ellipse, respectively. The weak component polarized perpendicularly to the diffracted field is responsible for the small discrepancy between measured and predicted ν values.

5. The POLICRYPS as an array of optical resonators

A new intriguing scenario of applications emerges if we explore the possibility of obtaining a lasing action in POLICRYPS structures. Indeed, in recent years, many efforts have been spent in research for the realization of lasing devices based on organic systems: good candidate materials for achieving this result are cholesteric liquid crystals (CLCs). It is well known that CLC materials possess a helical periodic superstructure which provides a 1D spatial modulation of the refractive index [de Gennes, 1993]. This system behaves as a photonic band gap (PBG), i.e. it exhibits a window in the electromagnetic spectrum where wave propagation is forbidden. This is due to a mechanism known in literature as distributed feedback (DFB), and has the consequence that the system behaves as a mirrorless optical resonator. If the CLC material is doped with fluorescent guest molecules, a gain enhancement of the radiation, propagating in the structure, is possible. Kogelnik and Shank [Kogelnik & Shank, 1971] were the first to report laser action in mirrorless periodic Bragg DFB structures, while laser action in chiral liquid crystals was predicted by Goldberg and Schnur [Goldberg & Schnur, 1973]. There are many advantages in using POLICRYPS as a host structure for dye doped CLC helices. The sharp and parallel channels of POLICRYPS can behave as an array of optical resonators, each of them working as a microlaser. The length of the single channel is not limited by the sample geometry; in principle the single cavity can be several centimetres long, thus containing thousands of periods of the CLC helices. At the same time, its volume can be reduced at will by changing the periodicity of the structure. Optical resonators with these two features present a high quality factor Q and correspond to very efficient microcavity lasers. Such an array of microlasers has been experimentally realized in a POLICRYPS structure [Strangi et al, 2005]. A slightly different chemical mixture was used: a small amount (0.7 wt%) of Irgacure 2100 and Darocur 1173 photoinitiators (1:1 wt%, Ciba Specialty Chemicals) was used to reinforce the polymeric network and a 0.09 wt% of pyrromethene dye (Exciton) was added, which represented the gain medium of our system. Other components were 29.9 wt% BL088 cholesteric liquid crystal (Merck), and 69.3 wt% of NOA-61 monomer (Norland). The mixture was introduced by capillarity between ITO-coated glass plates separated by 13.5 μm thick mylar spacers. The sample was then prepared by following the typical recipe for obtaining POLICRYPS. The only difference is that the curing temperature was sensitively higher in order to bring the CLC material in the isotropic phase during curing. At the end of the whole process, an almost complete phase separation was obtained, giving rise to helixed liquid crystal

channels periodically separated by polymer walls. A scanning electron microscopy analysis of the sample showed a periodicity of 5 μm with the microcavity width of about 1.5 μm. The system was optically pumped with the second harmonic (λ = 532 nm) of a Nd:YAG laser. The laser beam was focused onto the sample by means of a cylindrical lens (f = 100 mm) and linearly polarized perpendicularly to the microchannels. The long axis of the section was oriented perpendicularly to the orientation of the polymeric walls; therefore, the profile obtained (long axis of approximately 5 mm) ensured the simultaneous excitation of multiple microchannels. Above a certain pump power, stimulated emission was achieved, emerging from the microcavities in a direction parallel to the glass plates and along the microchannels. At their end highly sensitive emission measurements were performed in a restricted cone angle of about 0.1 rad. The sketch in Fig. 19 shows this lasing scenario of the microlaser array.

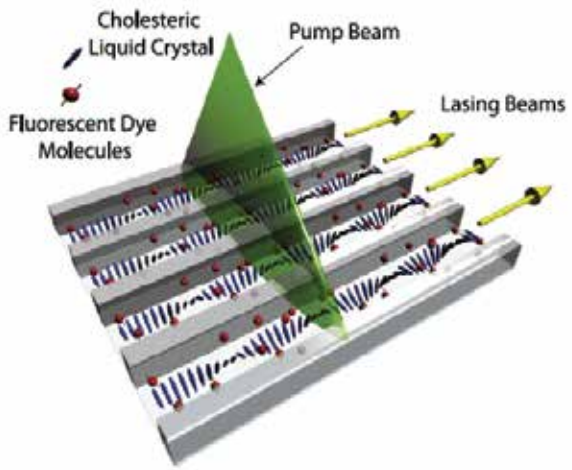

Fig. 19. Sketch of a multilaser array realized in a POLICRYPS structure

The stimulated emission emerging from the microchannels was circularly polarized, demonstrating that the distributed feedback mechanism due to the CLC helices is the cause of the observed phenomenon. The dependence of the emitted intensity and spectral linewidth (FWHM) on the input pump energy are reported in Fig. 20.

At low excitation energies, both the emission intensity and the linewidth show a quasilinear dependence on the pump energy. Above a characteristic threshold (the pump energy per excited sample area was about 5 mJ/cm^2, which corresponds to about 25 nJ/pulse), the emitted intensity suddenly starts to increase nonlinearly. Also, above this threshold, the emission linewidth breaks off from the previous trend and begins to decrease significantly. The observed pump energy value at which the power explosion and line narrowing effects occur (25 nJ/pulse) is one order of magnitude lower than in the case of other conventional dye-doped systems in a similar environment and under the same pumping conditions.

A striking scenario is presented in Fig. 21, showing the spatial distribution of the laser emission emerging from the microcavity laser array. A high sensitivity and resolution (1390 × 1024 12-bit PixelFlyQe, PCO) imaging CCD camera was employed in order to check the near-field modal profile of the stimulated emission. Images were acquired by scanning in the proximity of the output edge of our sample cell, in a direction perpendicular to the

microchannels. The mapped intensity profile hereby obtained indicates that the maxima of lasing intensities have a spatial recurrence, with a periodicity that is found to be about 5 μm; this value is in perfect agreement with the initial tailoring configuration (i.e. the distance between the polymeric walls).

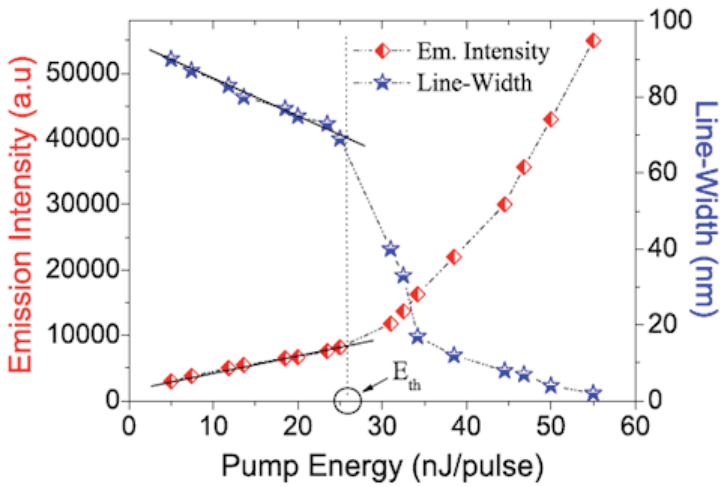

Fig. 20. Emitted intensity and linewidth dependence on input pump energy. Above a threshold of 25 nJ/pulse the reported curves change from initial regimes while lasing occurs

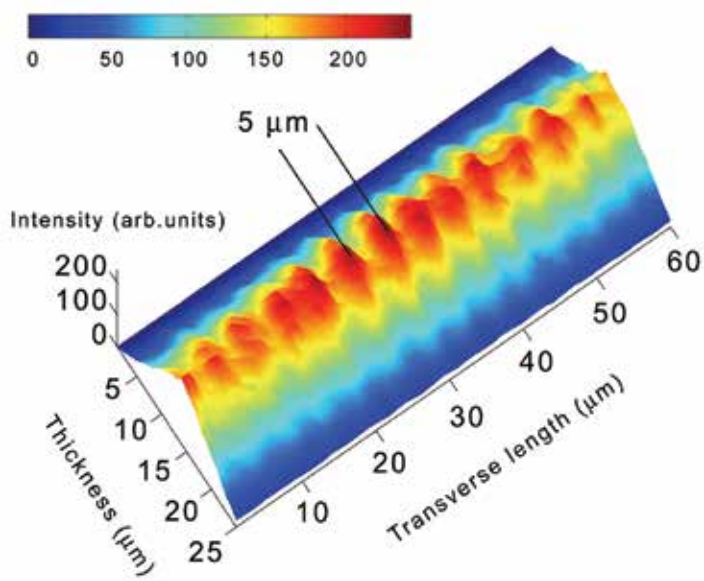

Fig. 21. Spatial distribution of the laser emission emerging from the mirrorless microcavity laser array. The periodicity of maximum intensities is 5 μm. This value is in agreement with the tailoring distance between the polymeric microchannels

Therefore we can definitely conclude that POLICRYPS microchannels act as miniaturized mirrorless cavity lasers, where the emitted laser light propagates along the liquid crystal helical axis, which behaves as a Bragg resonator.
This level of integration can lead to new photonic chip architectures and devices, such as a zero-threshold microlaser, phased array, discrete cavity solitons, filters, and routers. Furthermore, tailoring a proper array of electrodes, which enables the application of a local electric field, would give rise to electrically programmable phase holograms with interesting light polarization properties. Then, by including different dyes in neighbour channels, and by using proper microfibres connected at the exit, the result should be a multi-colour microlaser array with the possibility to control the intensity of each channel separately.

6. POLICRYPS with metallic nanoparticle inclusions

Noble metal nanoparticles (NPs) exhibiting plasmonic properties attract wide interest in research for the possibility they offer to realize metamaterials [Rockstuhl et al, 2007]. These have been predicted in 1969 by Veselago [Veselago, 1968] and they are materials that gain peculiar electromagnetic properties (e.g. negative refractive index) from their structure, rather than from their chemical composition. Thanks to recent advances in nanofabrication, first examples of such materials, which exhibit particular functionalities at optical frequencies, have been realized [Valentine et al, 2008]. However, the success of these results is limited by the typical size of devices that can be fabricated, which is actually very small (few square millimetres). Alternative approaches are emerging, which propose the use of self-assembling materials in order to overcome this issue and obtain the sought for greater structures, with less difficulty [Nanogold, (2009-2012; Metachem (2009-2013)]. An ambitious project is to combine metallic units with host materials whose dielectric properties can be tuned by an external control; indeed, a modification of the dielectric behavior of the host could correspond to a tuning action of the plasmon resonance frequency [Kossyrev et al, 2005]. In this regard, by combining the tunability of POLICRYPS structures with the plasmonic response of metallic NPs could give rise to novel metamaterial devices with tunable properties.

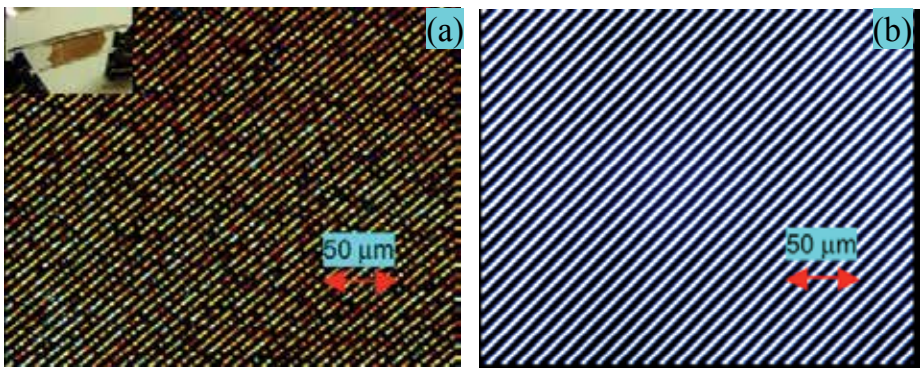

Fig. 22. Polarizing optical microscope images of (a) POLICRYPS diffraction grating with Ag NP inclusions; (b) typical POLICRYPS diffraction grating. In the inset of Fig.1a, a photograph which shows the brownish color of the realized new sample

In order to obtain a POLICRYPS structure that includes metallic NPs, we have used the Harima Silver nanopaste NPS-J (from Harima Chemicals, Inc.) that is generally involved with other applications (e.g. ink-jet printing and laser sintering) [Niizeki et al, 2008].
After some difficulties encountered for mixing this Harima material with the standard POLICRYPS precursor [Caputo et al, 2011b], we obtained a new mixture composed by: NOA61, 68.5 wt%; NPS-J, 3.5 wt%; E7, 28.0 wt%. The experiment followed the same procedure used for fabricating a standard POLICRYPS structure [Caputo, 2004]: the mixture has been sandwiched by capillarity in a 13μm thick glass cell and then, by keeping it at high temperature (about 70°C), it has been exposed to a UV interference pattern with a periodicity of 6μm. A microphotograph of the fabricated sample, observed between crossed polarizers at the polarizing optical microscope (POM), is reported in Fig. 22a along with the picture of a typical POLICRYPS structure without NPs (Fig. 22b) reported for comparison aims. Some morphological differences between the two structures are evident which are obviously due to the presence of metal nano-particles in the new sample.
A SEM micrograph of the same sample (Fig. 23) reveals that the NPs are organized in clusters (the typical size ranging between 0.3μm and 1μm), homogeneously distributed all over the grating area, and visible as bright spots. Of course, those clusters that are trapped in the LC films locally disturb the order of the nematic director but, nevertheless, large LC domains, with the director aligned perpendicularly to the polymer slices of the structure, are still present. This feature, which is typical of a standard POLICRYPS grating, is evident by rotating the sample between crossed polarizers.

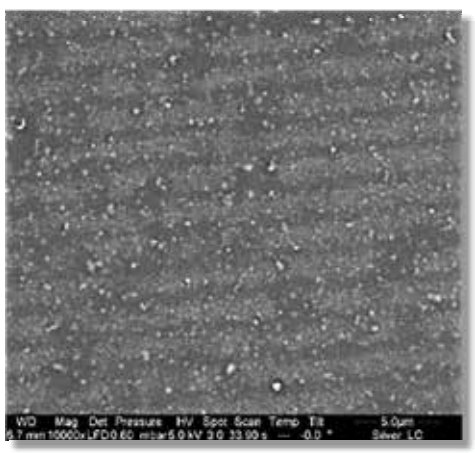

Fig. 23. scanning electron microscope image of the POLICRYPS diffraction grating with Ag NP inclusions; Ag clusters (with size ranging between 0.3μm and 1μm) are visible in the picture as bright spots

6.1 Spectroscopical characterization

As a consequence of considerations in paragraph 3.2, if we illuminate a POLICRYPS structure (not including metallic NPs) with linearly polarized white light (wavelength in the range 350-1100nm, at normal incidence), we expect a behaviour that is strongly dependent on the incident polarization state. In particular, we can expect that the polarization parallel to the nematic director **n** (p-type) is diffracted by the grating and hence the light

transmission is almost suppressed. On the other hand, the orthogonal polarization (s-type) is, instead, highly transmitted in the whole analyzed range (350-1100nm), because the experienced refractive index modulation is limited and the grating is almost absent. By repeating the same experiment with the NP doped POLICRYPS sample, new features come out. As in the case of a standard POLICRYPS, the p-polarized light is diffracted by the structure and the transmission of the grating is negligible for almost all the visible part of the spectrum (Fig. 24, GPP curve). For the orthogonal polarization (s-type), we observe instead a highly transmitted intensity, whose spectrum exhibits a peculiar behaviour (Fig. 24, curve GSP). The polarization sensitivity of the grating is further on demonstrated by the GNP curve reported in the middle of Fig. 24, obtained by probing the grating with unpolarized light: the behaviour of this spectrum represents a kind of "average" of the two, differently polarized, ones. A comparison of the GSP curve (Fig. 25, top curve) with the spectrum transmitted by a mixture of Harima NPs dissolved in Chloroform (Fig. 25, bottom curve) can help to interpret above results. Indeed, the shape of this curve has particular features, exhibiting a transmission minimum at $\lambda \approx 520$nm. The typical plasmonic response of Harima NPs (20-50nm in diameter) is peaked around $\lambda = 400$nm; in presence of Ag clusters (0.3-1μm), not perfectly diluted in Chloroform, we can expect a shift of the Ag plasmonic resonance to the observed value [Mock et al, 2002]. A similar minimum, can also be noted in the GSP curve (500÷570nm) of the NP doped POLICRYPS sample. Given that the grating is almost absent for the s-polarized light (the diffraction pattern can hardly be seen in this condition), our guess is that the shape of the GSP curve of Fig. 24 reveals the presence of Ag clusters within the structure.

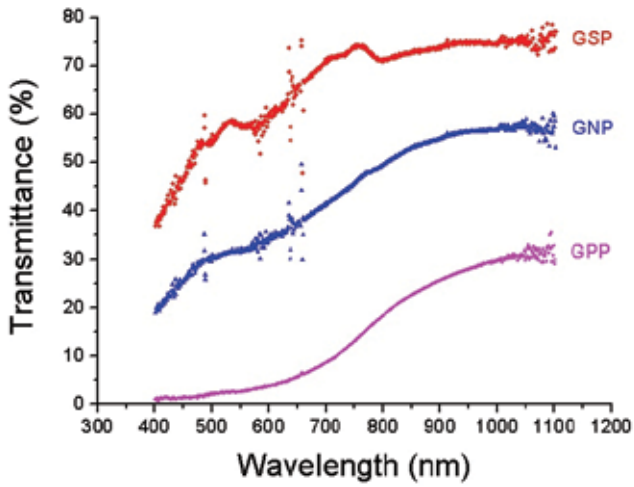

Fig. 24. Spectral response of the newly realized POLICRYPS structure containing Ag NPs. Top and bottom curves have been obtained by probing the sample with s-polarized light (GSP) or p-polarized light (GPP) respectively; In the middle, the curve obtained by probing the grating with unpolarized light (GNP)

Above considerations can just give a qualitative proof of that guess and, as such, further investigations are essential in order to provide a quantitative confirmation. However, in case of a positive outcome, these novel structures could reveal quite promising for the realization of polarization sensitive plasmonic devices.

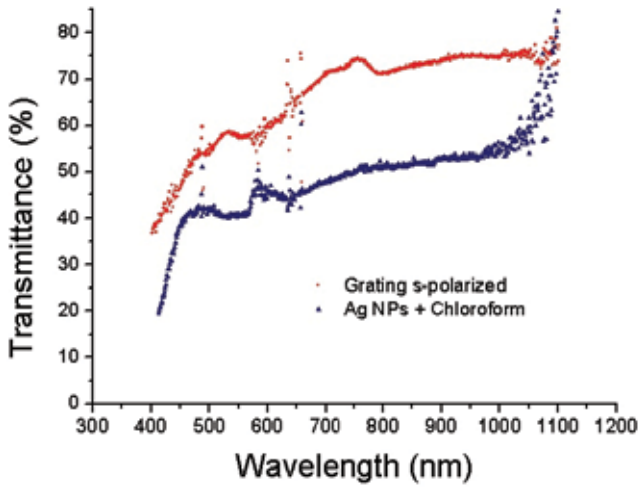

Fig. 25. Comparison between the spectral response of pure Ag NPs in Chloroform (bottom curve, 5x factor) and that of Ag NPs inclusions in a POLICRYPS structure (top curve, sample probed with s-polarized white light)

7. Conclusion

In the field of electrically switchable devices, exploiting liquid crystalline composite materials, POLICRYPS represents a very promising nano/microstructure with several possibilities of application. Indeed, few main features of this system act as a common denominator for these applications: the sharpness of the structure and the uniformity of the LC films minimize light scattering losses, while the application of a suitable, relatively low, external voltage can determine, in a millisecond timescale, a reorientation of the LC director and hence the tunability of the device. Depending on the way a light beam propagates through, the POLICRYPS can be used as a switchable diffraction phase grating, for light impinging at a given angle with the structure; a switchable optical phase modulator (with a light beam impinging almost perpendicularly to the structure); an all-optical switchable device, an array of mirrorless optical micro-resonators devoted to obtain a tuneable lasing effect (if the NLC is substituted with a mixture of dye-doped CLC and the system is optically pumped) and a plasmonic device with polarization sensitive properties (when metallic nanoparticles are included in the chemical mixture). Performances exhibited in all the above applications are very interesting and stimulate further investigations in the different fields.

8. Acknowledgment

Our sincere thanks go to Dr. Giuseppe Strangi and his group for the fruitful collaboration in the realization and characterization of microlaser arrays in POLICRYPS structures and to Dr. Nelson Tabiryan and his group for the possibility offered in realizing Azo-materials doped POLICRYPS structures.
Finally, the research leading to these results has received funding from the European Union's Seven Framework Programme (FP7/2007-2013) under grant agreement n°228455.

9. References

Bunning, T.J.; Natarajan, L.V.; Tondiglia, V.P. & Sutherland, R.L. (2000). *Holographic polymer-dispersed liquid crystals (H-PDLCs)*, Annu. Rev. Mater. Sci. Vol. 30, pp. 83-115

Caputo, R.; Sukhov, A.V.; Umeton, C.P. & Ushakov, R.F. (2000). *Formation of a grating of submicron nematic layers by photopolymerization of nematic-containing mixture*, J. Exp. Theor. Phys. Vol. 91 pp. 1190–1197

Caputo, R.; Sukhov, A.V.; Tabyrian, N.V.; Umeton, C.P. & Ushakov, R.F. (2001). *Mass transfer processes induced by inhomogeneous photo-polymerisation in a multicomponent medium*, Chem. Phys. Vol. 271, pp. 323–335

Caputo, R.; De Sio, L.; Sukhov, A.V.; Veltri, A. & Umeton, C.P. (2004). *Development of a new kind of switchable holographic grating made of liquid crystal films separated by slices of polymeric material (policryps)*, Opt. Lett. Vol. 29, pp. 1261-1263

Caputo, R.; Umeton, C.P.; Veltri, A.; Sukhov, A.V. & Tabiryan, N. (2007). *Holographic diffraction grating,process for its preparation and opto-electronic devices incorporating it*, European Patent Request 1649318; US Patent Request 2007/0019152A1

Caputo, R.; Trebisacce, I.; De Sio, L. & Umeton, C.P. (2010). *Jones matrix analysis of dichroic phase retarders realized in soft matter composite materials*, Opt. Express Vol. 18, pp. 5776-5784

Caputo, R.; Trebisacce, I.; De Sio, L. & Umeton, C.P. (2011a). *Phase modulator behavior of a wedge-shaped POLICRYPS diffraction grating*, Mol. Cryst. Liq. Cryst. (accepted)

Caputo, R.; De Sio, L.; Dintinger, J.; Sellame, H.; Scharf, T. & Umeton, C.P. (2011b). *Realization and characterization of POLICRYPS-like structures including metallic subentities*, Mol. Cryst. Liq. Cryst. (submitted)

de Gennes, P.G. (1993). *The Physics of Liquid Crystals* (Oxford: Clarendon)

De Sio, L.; Caputo, R.; De Luca, A.; Veltri, A.; Sukhov, A.V. & Umeton, C.P. (2006). *In situ optical control and stabilization of the curing process of policryps gratings*, Appl. Opt. Vol. 45, pp. 3721-3727

De Sio, L.; Veltri, A.; Tedesco, A.; Caputo, R.; Sukhov, A.V. & Umeton C.P. (2008a). *Characterization of an active control system for holographic set-up stabilization*, Appl. Opt. Vol. 47, pp. 1363-1367

De Sio, L.; Tabiryan, N.; Caputo, R.; Veltri, A. & Umeton C.P. (2008b). *Policryps structures as switchable optical phase modulators*, Opt. Express Vol. 16, pp. 7619–7624

De Sio, L.; Serak, S.; Tabiryan, N.; Ferjani, S.; Veltri, A. & C. Umeton, (2010). *Holographic Gratings Containing Light-Responsive Liquid Crystals for Visible Bichromatic Switching*, Adv. Mater. Vol. 22, pp. 2316-2319.

EU Project: "Self-organised nanomaterials for tailored optical and electrical properties (Nanogold)", FP7-NMP-SMALL-2008-228455, nanogold.epfl.ch, (2009-2012); EU Project: "Nanochemistry and self-assembly routes to metamaterials for visible light (Metachem)", FP7-NMP-SMALL-2009-228762, www.metachem-fp7.eu, (2009-2013).

Goldberg, L.S. & Schnur, J.M. (1973). *Tunable internal-feedback liquid crystal laser*, US Patent Specification 3 771 065

Kogelnik, H. (1969). *Coupled Wave Theory for Thick Hologram Gratings*, Bell Syst. Tech. J. Vol. 48, pp. 2909-2948

Kogelnik, H. & Shank, C.V. (1971). *Stimulated emission in a periodic structure*, Appl. Phys. Lett. Vol. 18, pp. 152-154

Kossyrev, P.A.; Yin, A.; Cloutier, S.G., Cardimona, D.A.; Huang, D.; Alsing, P.M. & Xu, J.M.; (2005) *Electric Field Tuning of Plasmonic Response of Nanodot Array in Liquid Crystal Matrix*, Nano. Lett. Vol. 5, pp. 1978-1981.

Lucchetta, D.E.; Criante, L. & Simoni, F. (2003) *Optical characterization of polymer dispersed liquid crystals for holographic recording*, J. Appl. Phys. Vol. 93, pp. 9669-9675

Margerum J.D.; Lackner, A.M.; Ramos, E.; Smith, G.W.; Vaz, N.A.; Kohler, J.L. & Allison, C.R. (1992). *Polymer dispersed liquid crystal film devices*, US Patent Specification 5,096,282, March 17, 1992

Mock, J.J.; Barbic, M.; Smith, D.R.; Schultz, D.A. & Schultz, S. (2002). *Shape effects in plasmon resonance of individual colloidal silver nanoparticles*, J. Chem. Phys. Vol. 116, 6755-6759

Niizeki, T.; Maekawa, K.; Mita, M.; Yamasaki, K.; Matsuba, Y.; Terada, N. & Saito, H.; (2008) *Laser Sintering of Ag Nanopaste Film and Its Application to Bond-Pad Formation*, Proc. ECTC 2008.

Ozaki, M.; Kasano, M.; Ganzke, D.; Haase, W. & Yoshino, K. (2002) *Mirrorless lasing in a dye-doped ferroelectric liquid crystal*, Adv. Mater. Vol. 14, pp. 306-309

Rockstuhl, C.; Lederer, F.; Etrich, C.; Pertsch, T & Scharf, T.; (2007). *Design of an Artificial Three-Dimensional Composite Metamaterial with Magnetic Resonances in the Visible Range of the Electromagnetic Spectrum*, Phys. Rev. Lett. Vol. 99, 017401.

Strangi, G.; Barna, V.; Caputo, R.; De Luca, A.; Versace, C.; Scaramuzza, N.; Umeton, C.P. & Bartolino, R. (2005) *Color-tunable organic microcavity laser array using distributed feedback*, Phys. Rev. Lett. Vol. 94, 063903

Sutherland, R.L.; Tondiglia, V.P.; Natarajan, L.V.; Bunning, T.J. & Adams W.W. (1994). *Electrically switchable volume gratings in polymer-dispersed liquid crystals*, Appl. Phys. Lett., Vol. 64, pp. 1074–1076

Sutherland R.L., Tondiglia V.P., Natarajan L.V., Bunning T.J. & Adams W.W. (1996). *Electro-optical switching characteristics of volume holograms in polymer dispersed liquid crystals*, J. Nonlinear Opt. Phys. Mater., Vol. 5, pp. 89–98

Tsutsumi, O. & Ikeda, T.; (1995). *Optical switching and image storage by means of azobenzene liquid-crystal films*, Science Vol. 268, pp. 1873-1875

Yariv, A. (1989). *Quantum Electronics* (Wiley, New York)

Valentine, J.; Zhang, S.; Zentgraf, T.; Ulin-Avila, E.; Genov, D.A.; Bartal, G. & Zhang, X.; (2008). *Three Dimensional Optical Metamaterial Exhibiting Negative Refractive Index*, Nature, vol. 455, 376.

Veselago, V.G.; (1968). *The electrodynamics of substances with simultaneously negative values of* ε *and* μ, Sov. Phys. Usp, Vol. 10, 4, 509-514 (1968).

Wu, Y.H.; Lin, Y.H.; Lu, Y.Q.; Ren, H.; Fan, Y.H.; Wu, J. & Wu, S.T. (2004). *Submillisecond response variable optical attenuator based on sheared polymer network liquid crystal*, Opt. Express Vol. 12, pp. 6382–6389

Part 2

Natural Sources

6

Composite Materials from Natural Resources: Recent Trends and Future Potentials

Mohini Saxena, Asokan Pappu,
Anusha Sharma, Ruhi Haque and Sonal Wankhede
CSIR- Advanced Materials and Processes Research Institute,
Council of Scientific & Industrial Research,
Habibganj Naka, Bhopal,
India

1. Introduction

Composites are combinations of two or more than two materials in which one of the materials, is reinforcing phase (fibres, sheets or particles) and the other is matrix phase (polymer, metal or ceramic). Composite materials are usually classified by type of reinforcement such as polymer composites, cement and metal- matrix composites (Chemical and Materials Engineering Department, home Page 2011; About.com, home page, 2011). Polymer matrix composites are mostly commercially produced composites in which resin is used as matrix with different reinforcing materials. Polymer (resin) is classified in two types thermoplastics (polyethylene (PE), polypropylene (PP), polyether ether ketone (PEEK), polyvinyl chloride (PVC), polystyrene (PS), polyolefin etc.) and thermosets (epoxy, polyester, and phenol–formaldehyde resin, etc.) which reinforces different type of fibre like natural (plant, animal, mineral) and man-made fibre for different application. In metal matrix composites, metal is one of important part of element and other part may be metal, ceramic or organic compounds. Cement matrix composites are made up of cement and with aggregate and basically used in building applications.

Due to increase in population, natural resources are being exploited substantially as an alternative to synthetic materials. Due to this, the utilization of natural fibres for the reinforcement of the composites has received increasing attention. Natural fibres have many remarkable advantages over synthetic fibres. Nowadays, various types of natural fibres (Taj et al., 2007) have been investigated for use in composites including flax, hemp, jute straw, wood, rice husk, wheat, barley, oats, rye, cane (sugar and bamboo), grass, reeds, kenaf, ramie, oil palm, sisal, coir, water hyacinth, pennywort, kapok, paper mulberry, banana fibre, pineapple leaf fibre and papyrus. Natural fibres are largely divided into three categories depending on their origin: Mineral based, Plant based, and Animal based. In general, a mineral based composite is asbestos and is only a naturally occurring mineral fibre (silicate based mineral). In 2006, 2.3 million tones of asbestos were mined worldwide. Russia was the largest producer with about 40.2% world share followed by China (19.9%), Kazakhstan

(13.0%), Canada (10.3%), and Brazil (9.9%) (Wikipedia, home page, 2010). The main properties of asbestos fibres are their thermal, electrical, and sound insulation; inflammability; matrix reinforcement (cement, plastic, and resins), adsorption capacity, wear and friction properties (friction materials), brake linings and chemical inertness (except in acids). Asbestos fibres are often mixed with cement or woven into fabric or mats/ sheets (Britannica home page, 2011; Wright, 2005).

Plant-based natural fibres are ligno-cellulosic in nature composed of cellulose, hemicellulose, and lignin, whereas animal based fibres are of proteins, e.g., silk and wool. Natural fibre-reinforced polymer composites have attracted more and more research interests owing to their potential as an alternative for synthetic fibre composites such as glass or carbon fibre composites (Bledzki & Gassan, 1999). Natural fibre composites posses the advantages such as easy availability, renewability of raw materials, low cost, light weight and high specific strength, and stiffness. It is expected that in the near future biodegradable polymers will replace synthetic polymers, at least in some specific applications where a short life of the product will be more desirable. Natural polymers are considered suitable to replace synthetic ones in some specific applications where a long span life is not required. Natural fibre thermoplastic composites are relatively new family of composite materials. In such composites, a natural fibre/filler (such as kenaf fibre, wood fibre, hemp, sisal etc.) is mixed with a thermoplastic (e.g., polyethylene, polypropylene, PVC etc.) to produce the composite. In the last few years, thermoplastics as well as thermoset-based natural fibre composites (NFCs) have experienced a tremendous growth in the auto industry due to environmentally friendliness, renewability of these fibres, good sound abatement capability, and improved fuel efficiency resulted from the reduced weight of the components. These composite materials have received much commercial success in the semi-structural as well as structural applications. For example, interior parts such as door trim panels from natural fibre polypropylene (PP) and exterior parts such as engine and transmission covers from natural fibre-polyester resins are already in use in auto industry. Advantages of thermoplastic NFC over thermoset-based NFC include the greater design freedom as they are suitable for injection molding and extrusion processing in addition to the recycling possibilities.

2. Classification of natural fibres

Natural fibres are classified into three categories. These are plant fibres, animal fibres and mineral fibres (Fig. 2.1) (FAO home page, 2010). Plant fibres are important types of natural fibres and these are generally comprised mainly of cellulose, hemi-cellulose, lignin, pectin. Prominent natural fibers are cotton, jute, flax, ramie, sisal and hemp. Cellulose fibres are mainly used in manufacturing of paper and cloth. This fibre is categorized into seed fibres, leaf fibres, bast fibre/ stem fibre, fruit fibre, stalk fibre (Table 2.1 and Fig. 2.1.1).

2.1 Animal fibre and their sources

Animal fibres generally comprise proteins. Examples are wool, silk, human hair and feathers etc. Wool has several qualities that distinguish it from hair or fur; it is crimped, it is elastic, and it grows in staples (D'Arcy, 1986). Fibre taken from animals or hairy mammals e.g. sheep wool, goat hair (cashmere, mohair), alpaca hair, horse hair etc. Wool is the textile fibre.

Silk fibre: Silk is a natural protein fibre, some forms of which can be woven into textiles. The best-known type of silk is obtained from the cocoons of the larvae of the mulberry silkworm. The shimmering appearance of silk is due to the triangular prism-like structure of the silk fibre, which allows silk cloth to refract incoming light at different angles, thus producing different colours.

Human hair: The human body, apart from its skin, is covered by follicles which produce thick terminal and fine hair. Hair is a filamentous biomaterial that grows from follicles found in the dermis. Most common interest in hair is focused on hair growth, hair types and hair care but hair is also an important biomaterial primarily composed of protein, notably keratin. Hair is a non homogenous complex material which can be associated with a polymer. It is made up 95% of Keratin.

Feathers: Feathers are among the most complex integumentary structure found in vertebrates and are formed in tiny follicles in the epidermis, or outer skin layer, that produce keratin proteins (Schor & Krimm, 1961; Linus Pauling & Robert, 1951; Hornik et al., 2005). Feathers are one of the epidermal growths that form the distinctive outer covering or plumage on birds. They are considered the most complex integumentary structures found in vertebrates, (Prum & Brush, 2002, 2003; Pettingill, 1970). Fig 2.1.2 shows different species of feathers.

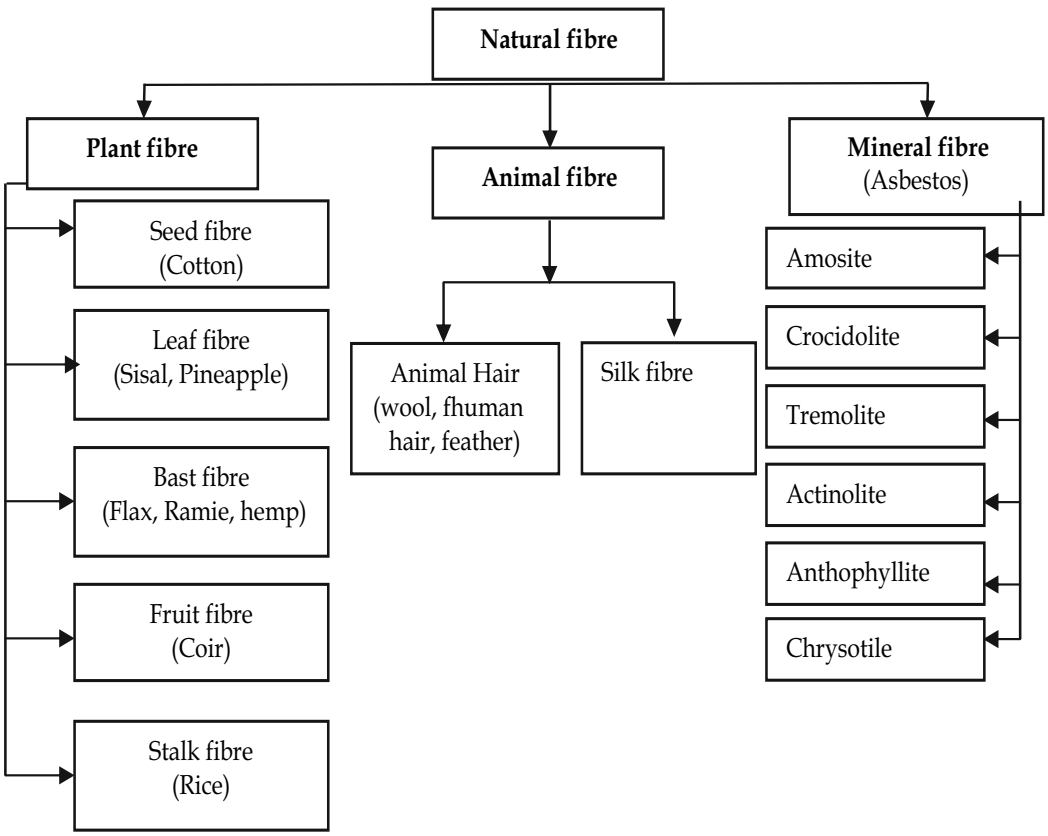

Fig. 2.1 Classification of natural fibre

S. No.	Category	Plant fibre
1.	**Bast fibre / stem fibre**	**Jute fibre:** Generally jute fibres are extracted from the ribbon of the stem. It is used as packaging material (bags), carpet backing, ropes, and yarns (Fig 2.1.1a) and in many other decorative items.
2.	**Leaf fibre**	**Sisal:** Sisal plant belongs to the agave family (Agavaceae). The plant looks like giant pineapples. The soft tissue is scraped from the fibres by manually or machine (Fig 2.1.1b). It is mainly used for mats, carpets and many other reinforcement materials.
3.	**Seed fibre**	**Hemp:** Hemp fibres have long been valued for their high strength and long fibre length, and have been used extensively in the fabrication of ropes and sails, as well as for paper and textiles. Hemp is a hardy plant, and grows well in a moderately cool climate. Hemp fibres are mainly composed of cellulose, hemicellulose, and lignin and pectin (Fig 2.1.1c).
		Ramie: Ramie is an expensive and durable fibre. The ramie plant can easily grow in fabrics. It is widely used in making of furniture covers and wall paper etc.
		Cotton: Cotton is the most important fibre used in the textile industry. Cotton is generally collected by picking which is generally carried out by hand. Comparison with other natural fibres, cotton is mainly used in the manufacturing of clothes, blankets, carpets (Fig 2.1.1d).
		Flax: Flax fibre one of the strongest fibre among natural fibre. Flax has good heat conducting properties. However, constant creasing in the same place in sharp folds tends to break the fibre. Flax is used for the production of linen, canvas, ropes and sacks.
4.	**Fruit fibres**	**Coir:** Generally coconut fibres (Fig 2.1.1e) are obtained from the husk of the fruit of the coconut palm. These coconut fibres are strong, light and easily withstand heat and salt water.
5.	**Stalk fibre**	These fibres are actually extracted from the stalks of the plant. For example, rice, barley, straws of wheat, bamboo and grass.

Table 2.1 Plant fibre and their sources

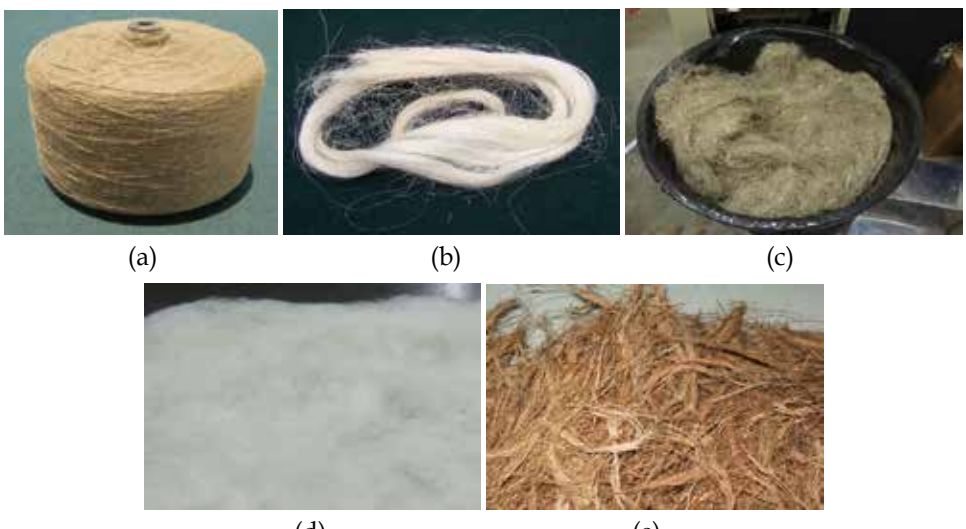

Fig. 2.1.1 (a) Jute yarn (b) Sisal fibre (c) Hemp fibre (d) Cotton fibre (e) Coir fibre

(a)

(b)

Fig. 2.1.2 Feathers picture of different species (a) Bird feather, (b) Chicken feather

2.2 Mineral fibres and their sources

Mineral fibres are mainly naturally occurring fibre or slightly modified fibre processed from minerals, can be defined into the following forms. Asbestos is the group of minerals that occur naturally in the environment as bundles of fibres. These fibres are resistant to heat, fire and bad conductor of electricity. Asbestos mineral are silicate compound, contain silicon and oxygen in their molecular structure. Asbestos minerals are divided into two major group's serpentine asbestos and amphibole asbestos (ATSDR home page, 2011). Asbestos is mainly divided into six fibrous minerals. The six types include (1) Amosite asbestos, (2) crocidolite asbestos, (3) tremolite asbestos, (4) actinolite asbestos (5) anthophyllite asbestos and chrysotile asbestos.

Amosite asbestos is the second most prevalent type of asbestos found in building materials. It is also known as brown asbestos and sometimes "grey" asbestos. Its colour comes from the natural presence of magnesium and iron. Generally amosite was used as a fire retardant in thermal insulation product (Maacenter, home page, 2011). Crocidolite also known as blue asbestos was the least used in commercial products (Britannica home page, 2011). Generally tremolite forms by metamorphism of sediments rich in dolomite and quartz. Mainly pure magnesium tremolite is creamy white in colour, but due to the increasing iron content colour grades to dark green. At high temperature it is toxic and converts to diopside (Mesorfa, home page, 2011). Another type is actinolite is derived from the Greek word aktis, meaning beam or ray. Actinolite is normally found in metamorphic rocks like cooled intrusive igneous rocks, aureoles. Anthophyllite also known as amphibole mineral occurs of metamorphism of magnesium-rich rocks and dolomite shales. It is an amphibole mineral. Chrysotile asbestos also known as white asbestos. It is a very soft, fibrous silicate mineral of phyllosilicates. It is the most widely used forms of a member of serpentine asbestos family. This fibre is long, hollow cylinders and very strong.

3. Extraction and processing of plant fibre

3.1 Jute fibre

Retting is the process of extracting fibre from the long lasting life stem or bast or the bast fibre plants. The retting process of jute fibre can be classified as: mechanical retting (hammring), chemical retting (boiling & applying chemicals), steam/vapor/dew retting and water or microbial retting. Availability of water and the cost of retting process is main parameter to select type of retting. To extract fine fibres from jute plant, first observation were require that if the fibre can easily be removed from the jute hurd or core, then the crop is ready for harvesting. Jute stalks after harvesting are submerged in soft running water in bundles for 20 days, and is grabbed in bundles and hit with a long wooden hammer to make the fibre loose from the jute hurd or core. Afterwards, the extracted fibres is further washed with fresh water and allowed to dry. Finally, obtain dry processed fibre for different application.

3.2 Sisal fibre

Sisal fibre can be extracted from its leaves by Retting, Boiling and Mechanical extraction methods. Water retting is a traditional biodegradation process involving microbial decomposition (breaking of the chemical bonds) of sisal leaves, which separates the fiber from the pith. The fibers are washed and processed further. This process takes 15–21 days for a single cycle of extraction and degrades the quality of fiber. Retting is a very slow, water intensive process, unhygienic, and not eco-friendly. Fiber extracted by this method is poor in quality. Boiling is another extraction method, in which leaves of sisal plant are boiled, subsequently beating is done then after washing and sun drying we may get the usable clean fiber. This method is not suitable for large-scale extraction. Mechanical extraction involves inserting leaves into a machine "raspador machine "and pulling the raw material out (Fig 3.2.1). This process does not deteriorate fiber quality and is suitable for small-scale operations and is efficient, versatile, cost effective and eco-friendly process. Residues produced during and after extraction of fiber are about 96% which is useful for biogas

Fig. 3.2.1 Mechanical process of sisal fibre extraction using raspador machine

generation, composting, and isolation of a steroid, ecogenin, making paper, biodegradable polymer and wax.

3.3 Flax fibre

Flax fibres were collected from diverse sources with the intention to provide characteristically different physical and chemical properties. The fibre bundles are located just under the skin and embedded in bast tissue. Harvested the plants are spread over the ground for retting, in which the pectin layer that binds the fibres to the bast tissue and the flax stem is broken down. In past, retting (water retting) was usually performed by immersing bundles of flax stem into running water or in standing water in ponds Fermentation by anaerobic bacteria degrades the pectins and other substances that bind the fibres to the stem. After the fibres have been loosened from the stem, the stem is broken on a roller; afterwards these broken stem parts fibres are removed. The total process to remove the wooden stem from the fibres is also called decortications. These fibre bundles are still relatively coarse and thick which are then processed in the hackling process for further application.

3.4 Cotton fibre

Fifteen percent of world cotton production is ginned on roller gins and almost all the rest of cotton is seeing ginned in most countries. Cotton is a shrubby plant belongs to Mallow family. Its name refers to the cream-colored fluffy fibers surrounding small cotton seeds called a boll. The small, sticky seeds are separated from the wool in order to process the cotton for spinning and weaving. De-seeded cotton is cleaned, carded (fibers aligned), spun, and woven into a fabric that is also referred to as cotton. The harvested cotton is cleaned to separate dirt, seeds, and short lint from the cotton. At the gin, the cotton enters module feeders that fluff up the cotton before cleaning. Some gins use vacuum pipes to send fibers to cleaning equipment where trash is removed. After cleaning, cotton is sent to gin stands where revolving circular saws pull the fiber through wire ribs, thus separating seeds from the fibre (Madehow, home page, 2010).

4. Processing of animal fibre

4.1 Wool

Wool is considered to be a protein called keratin. Its length usually ranges from 2 to 35 centimetres depending on the breed of sheep. Each piece is made of three essential components; the cuticle, the cortex, and the medulla. The cuticle is the outer layer. The cortex is the inner structure made up of millions of cigar-shaped cortical cells. In wool processing, wool straight off a sheep contains a high level of grease which contains valuable lanolin, as well as dirt, dead skins and vegetable matter. This semi grease wool can be worked into yarn and knitted into particularly water-resistant sweaters. Processing of wool is shown in following Fig. 4.1.1.

The major steps to process wool from the sheep to the fabric are shearing, cleaning and scouring, grading, sorting, carding, spinning, weaving and finishing. In wool shearing process, sheep are sheared once a year-usually in the springtime. The fleece recovered from a sheep can weigh between 2.7 and 8.1 kilograms. While most sheep are still sheared by hand, now a days many new techniques have been developed for this (Table 4.1).

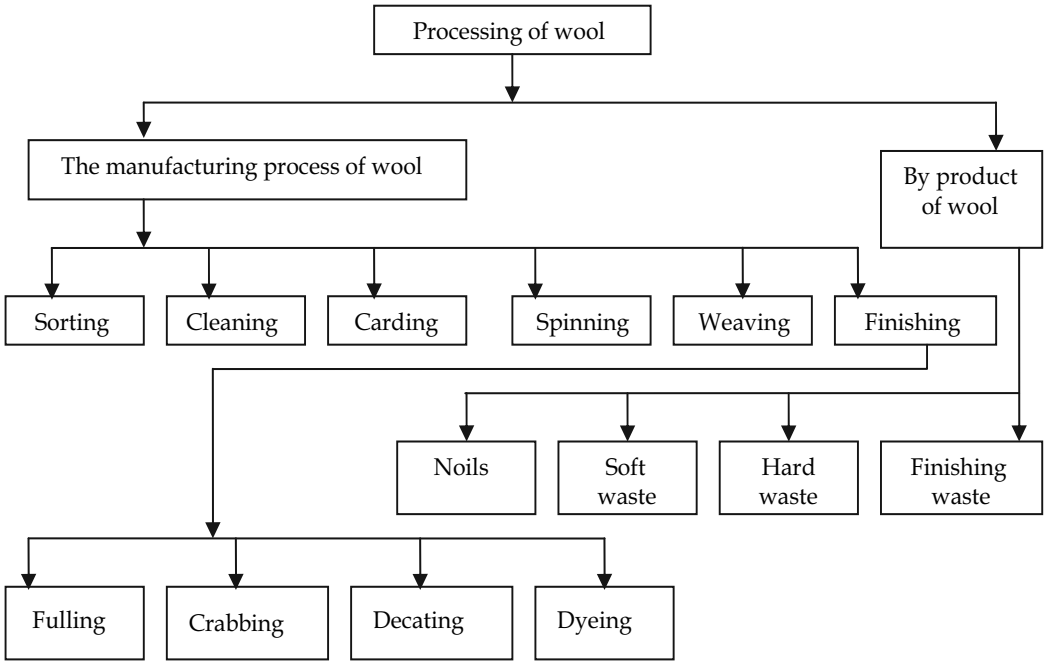

Fig. 4.1.1 Wool processing

1.	Sorting	In the process of sorting, the wool is broken up into sections of different quality fibres. The best quality of wool comes from the shoulders and sides of the sheep which is used for clothing.
2.	Cleaning	Raw wool contains dirt, grease and sand. To remove these contaminants, the wool is scoured in a series of alkaline baths containing soap, water and soda ash.
3.	Carding	In the process of wool carding the wool fibres are passed through a series of metal teeth. Carding also removes residual dirt and other matter left in the fibres. Carded wool intended for worsted yarn. Carded wool to be used for woollen yarn is sent directly for spinning.
4.	Spinning	Thread is formed by spinning in wool spinning process. The fibres together to form one strand yarn. Spinning for woollen yarn is typically done on a mule spinning machine. When yarn is spun, it is wrapped around bobbins and cones.
5.	Weaving	The next step is wool weaving. In this process the wool yarn is woven into fabric usually manufacturers use two basic weaves for weaving; the plain weave and the twill. Plain weave used for the woollen yarns which are made into fabric. Worsted yarn can create fine fabric with delicate patterns using a twill weave. So the results are more smooth fabric and more tightly woven.
6.	Finishing	After the process of weaving both worsted and woollens undergo a series of finishing procedure such as: Fulling (immersing the fabric in water to make the fibres interlock), Crabbing (permanently setting the interlock), Decating (shrink- proofing), Dyeing.

Source: Madehow, home page, (2011)

Table 4.1 Wool processing

4.2 Silk

Making of silk is different from that of other natural fibres. There are many steps involved in silk manufacturing as shown in Fig. 4.2.1.

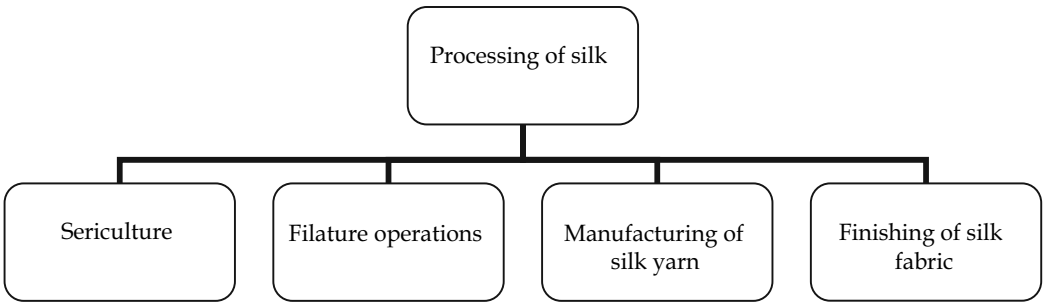

Fig. 4.2.1 Silk processing

Sericulture

The major steps of silk processing are sericulture in which cultivation of cocoons has been done for their filaments. Raw silk is obtained from the species of moth called Bombyx mori. The female moth lays around 355 to 405 eggs and the moth die soon after. Larva of about 3 mm is hatched from the eggs. They are carefully nurtured and are fed five times a day on chopped mulberry leaves. After transforming into caterpillar, they are ready to spin cocoon for which racks, clusters of twigs or straw are provided. This caterpillar have small openings this is known as spinnerets through which they secret a substance like protein. This substance when it comes in contact with air solidifies and the filament thus formed a spun around the silk worm. In three days the cocoon gets completed which is about a peanut shell size. The filament is held together by sericin or silk yarn.

Filature operations

The raw silk is unwound from cocoons in the factories known as filature and the process known as filature operations. Here the cocoons are sorted based on their colour, size, texture and shape. After that immersed in hot and cold water to soften the sericin. In this process whole seracin is not removed as it protects the delicate filament in further operations.

Silk yarn manufacturing

The next process is "reeling" (unwinding the filament from the cocoon). This reeled silk is formed into silky yarn or silk thread through the process called 'throwing.' The raw silk skeins are sorted according to their physical properties like colour, length quantity, and size and washed in warm water with soap for softening the seracin. After drying, placed in reel from where the silk is wound on bobbins. During winding, the silk strands are given desired amount of twist. To get equal diameter throughout the length, the yarn is run through rollers. Following kinds of silk yarns are obtained: Thrown singles (Three to eight silk filaments are twisted together in only one direction, Tram (a slight twist is given to two to four untwisted singles), Crepe (individual raw silk filaments are twisted together), and Organize (a raw-silk thread, usually used as a warp thread).

Finishing of silk fabric

Calendering (a finishing process), cireing and singeing (a process applied to yarns and fabrics to produce an even surface) finishing process are applied to different silk fabric in

order to improve their appearance, durability and to make them smooth and with fine texture. Processing and lustering removes wrinkles from the finished fabric. One finish that is unique to silk fabric is 'weighting.' The weight of silk is lost during the process of degumming. Weighting is done during the dyeing process. This weighted silk is less compactly woven when compared to the unweighted silk. This weighting gives it crispness, and luster (Teonline, home page, 2011).

4.3 Human hair

Washing

In the process of washing hairs, fibres were bleached using a solution of hydrogen peroxide (7 %) in the presence of respective surfactants. pH 10 of bleaching solution was adjusted with NH4OH and the treatment was carried out for1 hour at 60 °C. The tress was then rinsed with 2 % aqueous acetic acid solution and then with demineralised water until pH was neutral. The excess water was removed by placing the tress onto a paper towel. The tress was dried up under ambient temperature in open air (20± 2 °C).

4.4 Feather

Processing of feather start by scrapping the inner part of feathers quill. Then start cutting the feather from the bottom to the top at the centre. After that remove the excess from the front and back. Then put the feather into the feather holder. Sand the quill with 36 grit paper to thin it out after; make sure the other side is thin sand the quill for final processing (Legionnaire Archery, home page, 2011).

5. Processing of mineral fibres

Asbestos is found in the nature, due to natural weathering of rocks, mining. Asbestos fibres are released into the environment through erosion and carried by the wind. Magnetic sensor (magnometer) is used to locate the deposition of asbestos in earth crust. After asbestos is removed from the crust, it is processed and divided into groups according to fibre length. Longer fibres are separated out for weaving into a cloth-like material.

5.1 Mining

Asbestos fibres are separated from the rocky ore using physical methods because chemical composition of ore is similar to the fiber, so chemical methods are not used. Mining process is first step used in processing of asbestos fiber from ore. Most asbestos mining operations are conducted in an open-pit mine and branch drilling technique. Open pit type mining is a surface mining method; it is used for those asbestos containing ore which lies near the surface of ore.

5.2 Milling

The second main step after mining is milling of ore using different series of crushing machine with vacuum and vibrating plate. In milling process two type of milling are used (i) dry and (ii) wet milling operations. Wet ore is collected from bottom of stock pile (where ore is store after mining) and dry ore present in upper part of mine ore. The dry ore is goes to rotating cylinder dryer and then different crushing was done to fine the ore size. Using

vacuum aspiration vibrating screen, under aerodynamic nature of asbestos fibre readily collects in the vacuum area. Rock circuit is used for separating fiber according to length of fiber and then fiber is compressing and packaged in bags (Madehow, home page, 2011; Virta, 2002). Asbestos processing is shown in Fig 5.2.1.

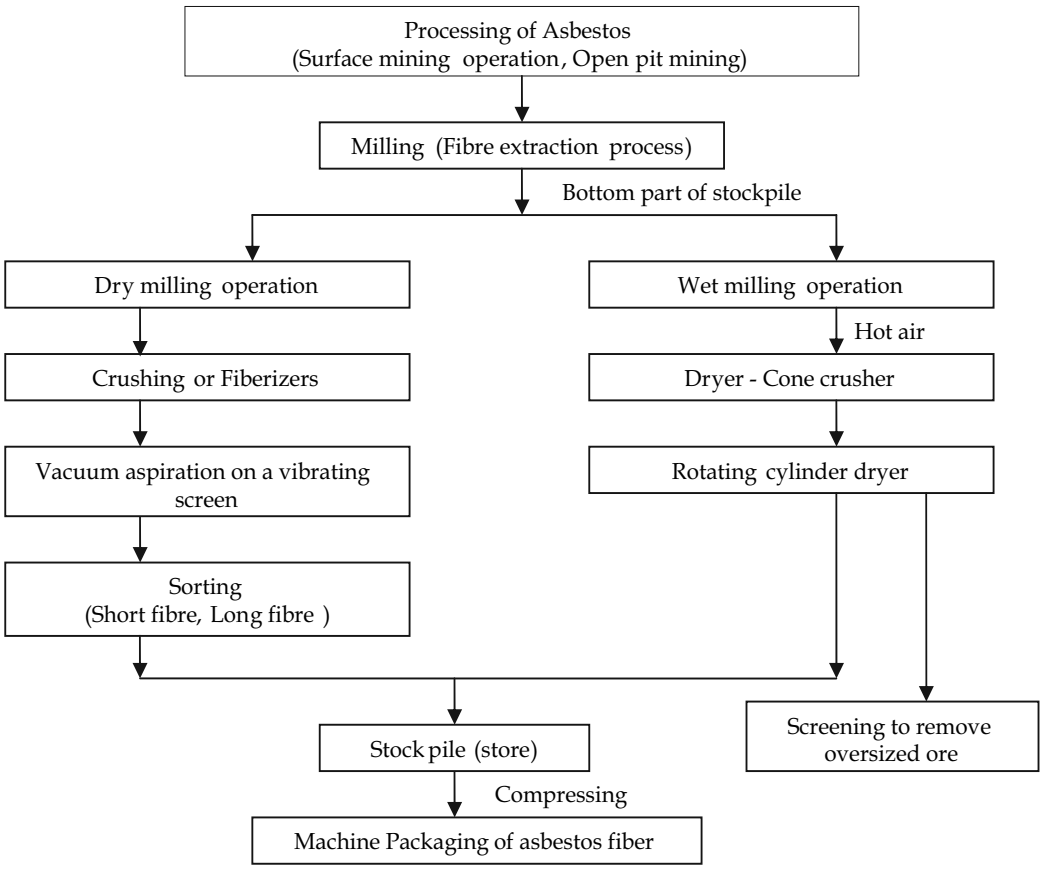

Fig. 5.2.1 Flow chart of asbestos processing

6. Properties of natural fibre

6.1 Characteristics of plant fibre

Plant fibres are a composite material designed by nature. The fibres are basically a rigid, crystalline cellulose micro fibril-reinforced amorphous lignin and/or with hemicellulosic matrix. Most plant fibres are composed of cellulose, hemicellulose, lignin, waxes, and some water-soluble compounds. The percentage composition of each of these components varies for different fibres. Generally, the fibre contains 60-80 % cellulose, 5-20% lignin and up to 20 % moisture (Taj et al., 2007; Wang et al., 2008). During the biological synthesis of plant cell walls, polysaccharides such as cellulose and hemicellulose are produced simultaneously. Lignin fills the space between the polysaccharide fibres, cementing them together. This lignifications process causes a stiffening of cell walls and the carbohydrate is protected from chemical and physical damage (Taj et al., 2007). The chemical composition of natural fibres

varies depending upon the type of fibres. The chemical composition as well as the structure of the plant fibres is fairly complicated. Hemicellulose is responsible for the biodegradation, micro absorption and thermal degradation of the fibre as it shows least resistance, whereas lignin is thermally stable but prone to UV degradation. The details of different plant fibre such as sisal, flax, cotton and jute fibre are discussed as follows.

Sisal fibre varies in their quality. The large variations in its chemical compositions are because of its different sources, age, extraction methods, etc. (Chand, 1988). As reported by Wilson, (1971) sisal fibre contains 78% cellulose, 8% lignin, 10% hemicelluloses, 2% waxes, and about 1% ash by weight, whereas Rowell et al., (1992) reported that sisal contains 43–56% cellulose, 7–9% lignin, 21–24% pentosan, and 0.6–1.1% ash. The work carried out by Chand and Hashmi (1993) showed that the cellulose and lignin contents in sisal vary from 49.62 to 60.95% and 3.75 to 4.40%, respectively. According to Mohanty et al., (2005) sisal fibre contain 66–78% cellulose, 10–14% hemicellulose, 10–1% lignin, 10% pectin, 10–22% moisture content, and 2% waxes (Mohanty, 2005). It is apparent from the above studies that chemical composition and other characteristics of sisal fiber depends on various agro-climatic conditions under which sisal is grown, age of the sisal plant and extraction process (Saxena et al., 2011).

Flax fibres budles are isolated from the plant by breaking and scutching processes. The isolated fibres are composed of a few fibres, bonded together by a relatively weak pectin and lignin interphase, which is at some places along the fibres virtually absent. The fibres are composed of elementary fibres of diameters around 15 mm and lengths between 20 and 50 mm. The fibre consists of about 10–40 elementary fibres in cross section. The elementary fibres are bound together by a pectin interphase. This interphase is much stronger than the interphase between the technical fibres (Oever, 2000). Flax fibre contain 71% Cellulose, 18.6-20.6 % Hemicelluloses, 2.2% Lignin, 2.3% Pectin, 8-12 Moisture Content, 1.7% Waxes and 5-10° Microfi brillar Angle (Taj et al., 2007; Saxena et al., 2011). Cotton fibre contains 85-90% Cellulose, 5.7% Hemicelluloses, 0-1 % Pectin, 7. 85- 8.5 moisture Content, 0.6 % Waxes (Taj et al., 2007; Saxena et al., 2011). Jute fibre contain 61.1-71.5 % Cellulose, 13.6-20.4% Hemicelluloses, 12-13% Lignin, 0.2% Pectin, 12.5-13.7 Moisture Content, 0.5% Waxes and 8°Microfi brillar Angle (Taj et al., 2007; Saxena et al., 2011).

Fibre	Density (g/cm^3)	Tensile strength (MPa)	Elongation at Break (%)	Tensile Modulus (GPa)	Reference
Jute	1.3	393-773	7.0 – 8.0	5.5-12.6	Taj et al., (2007)
	1.3 – 1.46	345 - 1500		2.7 - 3.2	Baiardo et al., (2004)
Flax	1.29	663	5.0	160	"
	1.5	345-1035	2.7-3.2	27.6	Taj et al., (2007)
	1.4-1.5	600-1100	1.5-2.4	45-100	Saxena et al., (2011)
Cotton	1.5-1.6	287-597	7.0-8.0	5.5-12.6	"
	1.5	200- 40	6-7	8.0	Saxena et al., (2011)
Sisal	1.45	468 - 640	3-7	9.4 - 22	Lamy & Pomel, (2002); Saxena et al., (2011)
	1.35	550 ± 100	24 ± 0.4	4±0.6	Baiardo et al., (2004)

Table 6.1.1 Physical and Mechanical properties of different plants fibre

Engineering properties of plant fibre

The mechanical properties and physical properties of natural fibres vary considerably depending on the chemical and structural composition, fibre type and growth conditions. Mechanical structure of plant fibres is much lower when compared to those of the most widely used competing reinforcing glass fibres. However, because of their low density, the specific properties (property-to-density ratio), strength, and stiffness of plant fibres are comparable to the values of glass fibres (Taj et al., 2007; Saxena et al., 2011). Table 6.1.1 shows some of the engineering properties of natural fibre.

6.2 Characteristics of animal fibre

Physicochemical properties of wool fibre

Wool fibres have a low tenacity which have excellent elongation and elastic recovery. Wool fabric is durable with moderate resistance. Wool is a poor conductor of heat. These fibres are more hygroscopic than any other fibre. They have excellent resiliency. Wool generally retains its shape fairly well during normal use. Wool garments required to be handled carefully when they are hand washed in order to avoid shrinkage. Wool fibre is very sensitive to some alkalis due to keratin which break down its disulfide linkages and weaken the fibre properties. At the burning, wool fibre burns slowly with a slight sputtering when a flame is presented. The residue from burning is brittle, black bead that crushes when squeezed. Generally, Wool fibres are fairly resistant to bacteria (Composite Fabrics, home page, 2010).

Physicochemical properties of silk

Durability of silk fibre is very strong. Its strength is excellent in relation to its fineness. It may lose up to 20 percent of its strength in wet state. Silk has moderate abrasion resistance. Silk cannot return to its original shape even when it is stretched in a small amount, it remains slightly stretched. Therefore, fabrics made of cultivated silk have a smooth appearance and luxurious hand. Silk fibre is a poor conductor of heat just like wool, it is comfortably warm in the winter. Silk fibres do not shrink as the molecular chains in fibres are not distorted easily. Silk swells only a small amount when wet and it has moderate resistance to wrinkling. Silk have higher tensile strength than glass fibre or synthetic organic fibres, good elasticity, and excellent resilience. The chemical compositions are, in general, silk fibroin of 75–83%, sericin of 17–25%, waxes of about 1.5% and others of about 1.0% by weight. The densities of silk fibres are in the range of 1320–1400 kg/m^3 with sericin and 1300–1380 kg/m^3 without sericin (Sang & Donghwan, 2005). Silk is resistant to most mineral acids but will dissolve in sulfuric acid. It is resistant to dilute mineral acids and organic acids. Silk is resistant to attack by bacteria and fungi. Sunlight accelerates silk decomposition which is more susceptible to ultraviolet damage than wool (Neste & Shaker, 2001; Lewis, 1989; Wei et al., 2005).

Mechanical properties of Silk

Silk is one of the strongest natural fibres but loses up to 20% of its strength when wet. It has a good moisture regain of 11%. Its elasticity is moderate to poor, if elongated even a small amount it remains stretched. It can be weakened if exposed to too much sunlight. Generally Silk fibres have a triangular cross section with rounded corners. This reflects light at many different angles, giving silk a natural shine. It has a smooth, soft texture that is not slippery,

unlike many synthetic fibres. Its denier is about 4.5 g/d when dry and 2.8-4.0 g/d when moist. The physico mechanical properties of wool and silk are as shown in Table 6.2.1.

S. No	Properties	Wool	Silk	Reference
1.	Type	Natural	Natural	Quazi et al., (2010)
2.	Melting temperature (°C)	570-570	-	Matbase, (2010) home page, (2010)
3.	Service temperature (°C)	100-400	-	"
4.	Density (Kg/m^3)	1.3	1.3-1.38	"
5.	Tensile strength (MPa)	125-200	650-750	"
6.	Elongation (%)	20-40	-	"
7.	Polarity	-	Hygroscopic	Quazi et al., (2010)
8.	Young's modulus (MPa)	-	16	"
9.	Elongation at failure (%)	-	18-20	"
10.	Crystalinity (%)	-	65 -70	"

Table 6.2.1 Physico-mechanical properties

Physicochemical properties of human hair

Hair is surprisingly strong. Cortex keratin is responsible for this property and its long chains are compressed to form a regular structure (Valeria et al., 2009). The physical proprieties of hair involve, stretching, elasticity and hydrophilic power. Generally physical proprieties of hair depend on its geometry (Kolar & Miller, 1972; Juez & Gimier, 1983; Valeria et al., 2009). Due to elasticity, hair can resist forces that could change its shape, its volume or its length. Elasticity is one of the most important properties of hair. Hair fibre has an elastic characteristic and it may undergo moderate stretching. The elasticity of hair depends on the long keratin fibres in the cortex. Both natural sunlight and artificial ultraviolet light break down chemicals in the hair and damage its elasticity. The texture of hair depends mainly on average diameter of the individual hairs. There are different chemical components present in the human hair it is an "integrated" system. The different chemical components in human hair act together to maintain the normal flow of functions. The chemical composition of hair fibre includes essential functional elements like amino acids, keratin, melanin, and protein. Proteins are present also within the cuticle which provides elasticity to the hair. Hair, from its growth under the skin of the scalp, is filled with a fibrous protein called keratin. The keratin protein found in hair is called hard keratin. It is made up of eighteen amino acids. The lipid content of the hair is not constant but varies with age and other factors. In the hair structure, lipids are present in Inner Root Sheaths and hair shaft lipids provide sheen to the hair and contribute towards its tensile properties.

Melanin is the hair pigment which gives color to the skin and hair. The size, type and distribution of the melanosomes will determine the natural color of the hair (Hair dressing home page, 2011; Juez & Gimier, 1983). Amino acids are the principle building block of the keratin proteins found in hair fibres, and approximately 20 different amino acids are present in these proteins. The chemical composition of hair fibres is dominated by carbon, which comprises about 45% of the atomic structure of hair. Oxygen accounts for approximately 28%, nitrogen 15%, hydrogen 7%, and sulfur 5%. Several essential trace elements are also

present in hair fibres including iron (20 - 220 ppm), copper (10-20 ppm), zinc (190 ppm), and iodine (0.6 ppm) (Wella, 1999).

Mechanical properties of hair

The mechanical properties of α-keratin fibres such as hair fibres and wools are primarily related to the two components of the elongated cortical cells, the highly ordered intermediate filaments (microfibrils) which contain the α-helices, and the matrix in which the intermediate filaments are embedded (Feughelman, 2002). Chemical treatment, bleaching and dyeing is known to be one of hair cuticle and cortex damage producing and properties impairing factors (Neste & Shaker, 2001; Lewis, 1989; Wei et al., 2005). Mechanical properties such as elasticity and durability are governed by the interactions of proteins in the cortex. The cortex is a complicated, disulfide cross-linked polymer system comprising the crystalline low-sulfur proteins and the globular matrix of high-sulfur proteins.

Physicochemical properties of feather

The moisture content of processed feathers can vary depending upon processing and environmental conditions. The moisture content of feather fibre is an important variable that can have implications ranging from transportation costs to mechanical properties. Hong and Wool, (2005) reported a typical value of 8 mm for fibre length. Barone and Schmidt, (2005) measured the density of chicken feather fibre, obtained from feather fibre Corporation, by displacing a known volume and weight of ethanol with an equivalent amount of fibre. Density of solid keratin was studied by Arai et al., (1989) and also Barone and Schmidt, (2005) reported an apparent density of feathers and reported fibre lengths of 3.2-13 mm for the feather fibre. Hong and Wool (2005) have reported that the density of feather fibre is 0.8 g/cm^3. However, Barone and Schmidt's (2005) reported a value of 0.89 g/cm^3 and is relatively similar to the value (0.80 g/cm^3) cited by Hong and Wool (2005) when compared with a value of 1.3 g/cm^3 reported by keratin (Arai et al., 1989). Barone and Schmidt, (2005) reported fibre lengths of 3.2-13 mm. The structure of keratin, affects its chemical durability which is the primary constituent of feathers. Keratin shows good durability and resistance to degradation.

Mechanical properties of feather

The first step in exploring the mechanics of feathers in birds was to investigate how variable the properties of keratins are between species. While examining the stiffness (Young's modulus) properties of a wide range of bird species, it has been found that there is a very little evidence of systematic differences in properties between species. Hence, the mechanical performance of feathers were therefore, controlled more by shape than by material properties The fracture toughness of β-keratin has proved to be very high, around 10 kJm (Reading, home page, 2011). The mechanical properties of feather fibre are related to the structure of keratin. The mechanical properties of bird's feathers are highly related to their function (Bonser & Purslow, 1995). Further, work carried out by Cameron et al., (2003) confirmed that the mechanical properties of feather keratin vary appreciably along the length of the rachis. Using x-ray diffraction, Cameron et al., (2003) discovered that, moving from calamus to tip, the keratin molecules become more aligned than at the birds skin before returning to a state of higher disorder towards the rachis tip. George et al., (2003b) studied turkey feather fibre properties for fibres at different positions along the rachis. It was found that both the tenacity and modulus of turkey feather fibre, measured in g/denier,

increased with the distance from the calamus. Purslow and Vincent (1978) measured the elastic modulus of feather rachis from pigeons with and without inner quill. Dehydrated feather rachises were tested in bending. Taylor et al., (2004) studied the affect of moisture content on mechanical properties.

6.3 Characteristics of mineral fibre

Asbestos was formerly known as a 'miracle mineral' due to its special properties that include strength, flexibility, low electrical conductivity, and resistance to heat and chemicals. Asbestos does make construction better in many ways. It has been used for thousands of products in innumerable workplaces.

Physicochemical properties of asbestos fibre

Asbestos almost has become a superstar in the world of industrial chemistry due to its physical properties however manufacturing and utility of asbestos has been banned in many developing and developed countries. It has remarkable thermal stability, resistance for thermal and electrical and non-flammable. Asbestos fiber can be split up into fine fibres, and these fibers are enough strong and flexible material and are use for thermal and electrical insulator, flame retardant, chemically inert, insulating purpose. Asbestos fibres are odourless and tasteless. Asbestos group fibers are insoluble in water, air and soil. Its colour will depend on type, and metallic composition. Crocidolite is the most colourful elements, which have iron and sodium and its colour shades are lavender, blue and green. The colours of other type of asbestos are depending on amount of iron. Asbestos is divided into two major groups: amphiboles and serpentines. Both amphibole and serpentine asbestos are fibrous. The amphiboles group are double-chain silicates (inosilicates). The basic structural unit is $(Si_4O_{11})^{-6}$ with side groups that are responsible for the overall amphibole structure. The quantity and positioning of metal atoms (sodium, calcium, manganese, magnesium, iron (II), iron (III) and aluminium) differentiate amphiboles from one another (Virta, 2002). The serpentine group of minerals have the formula $Mg_3Si_2O_5$ $(OH)_4$. Serpentine structure is a bending sheet. Chrysotile is very elastic. Asbestos is easily turned into a dust with finger pressure this properties called friability. Due to this nature asbestos fibres releases into the atmosphere and cause health problems (Virta, 2002; Burdeti, 2007).

Mechanical properties of asbestos fibre

The tensile strength of a single asbestos fibre, based on the strength of silicon oxygen bonds (Si-O-Si) in the silicate chain. Industrial fibres have lower tensile strength, because of the presence of different types of structural or chemical defects. For higher tensile strength measurements short and thin fibres have used. The tensile strengths of amosite and crocidolite are equivalent to that of chrysotile. Tensile strength is very much influenced by iron content in amphiboles, the since iron-oxygen bonds located in the fibre axes, are strong. Iron content of asbestos fibres effect the tensile strength this is as observed increasing trend tensile strength in the order amphiboles ‹ tremolite‹ amosite ‹ crocidolite. The tensile strength of asbestos fibres is change with temperature and sharply distinguishes chrysotile and amphiboles. In chrysotile when temperature is increased up to 500˚C slightly increase in tensile strength is observed, which the beginning of due to dehydroxylation reaction is. In the case of amphiboles, when temperature increases more than 200˚C decreases tensile strength is observed at 350˚C Crocidolite has lost 50% of its initial tensile strength. Physical, chemical and mechanical properties of asbestos are shown in Table 6.3.1.

Group	Type	Chemical formula	Diameter µm	Specific gravity	Tensile strength (MPa)	Reference
Serpentine	Chrysotile (white colour)	$Mg_3(Si_2O_5)(OH)_4$	0.1–1	2.2-2.9	1100-4400	Wikipedia, home page, (2011); Virta, (2002)
Amphibole	Amosite/ Grunerite (Brown colur)	$Fe_7Si_8O_{22}OH)_2$		3.4 -3.5	1500-2600	"
	Crocidolite/ Richter Ite (Blue)	$Na_2Fe^{2+}{}_3Fe^{3+}{}_2Si_8O_{22}(OH)_2$	0.1-2	3.0-3.5	1400-1600	USEPA, home page 2011; CDCP, home page, (2010); Maacenter, home page, (2010); Virta, (2002)
	Tremolite	$2CaO.5MgO.8SiO_2.H_2O$		2.9-3.2	< 500	Virta, (2002)
	Anthophyllite	$7.MgO.2SiO_2.2H_2O$			-	"
	Actinolite.	$Ca_2(Mg,Fe)_5Si_8O_{22}(OH)$		3.00	-	"

Table 6.3.1 Physical, chemical and mechanical properties of asbestos group

7. Composite fabrication

7.1 Plant fibre composite

There are several method for making of natural fibre composites. Most of the techniques commonly used for making glass fibre composites are applicable for making natural fibre composites. However, the well known method for composites making are as followings: Hand Lay-up/Spray up is one of the cheapest and most common processes for making fibre composite products. In this process, the mold is waxed and sprayed with gel coat and cured in a heated oven. In the spray up process, catalyzed resin is sprayed into the mold, with chopped fibre where secondary spray up layer imbeds the core between the laminates resulting a composite. In hand layup processing, both continuous fibre strand mat and fabrics are manually placed in the mold. Each ply is sprayed with catalyzed resin and with required pressure compact laminate is made. Resin transfer molding (RTM) provides high quality finished surface on both the sides of composites with a relatively low energy makes perfect shapes. The fabricator generally gel coats the mold halves, then lays continuous or chopped strand mat and closes the mold. Resin transfers into mold through injection pressure, vacuum pressure, or both. Cure temperature depends on the resin system. Compression molding is a molding technique for making composite materials with low unit cost with faster cycle times. Sheet molding compounds (SMC) is a sheet that sandwiches fibre between two layers of resin paste. Fibre/Fabric drop onto the paste and a second film carrier faces with another layer of resin. When the SMC is ready for molding, the mold is closed, clamped, and between 500 and 1,200 psi pressure is applied. After curing, mold is opened and the sheets were removed manually or through an injector system and ready for use.

Automated injection molding of thermoset bulk molding compound (BMC) has increasingly taken over markets previously held by thermoplastics for application in electrical and automotive components, housing appliances, and motor parts. BMC is a low-profile (nearly zero shrinkage) formulation of a thermoset resin mix with 15–20% chopped fibre. Injection molding is a fast, high volume, low pressure, and closed process. Injection speeds are typically 1–5 s and nearly 2,000 small parts can be produced per hour. A ram or screw type plunger forces a material shot through the machine's heated barrel and injects it into a closed, heated mold. Heat build-up is carefully controlled to minimize curing time. After cure and injection, parts need only minimal finishing. Filament winding is an automated, high volume process that is ideal for manufacturing pipe, tank, shafts and tubing, pressure vessels, and other cylindrical shapes. The winding machine pulls dry fibres from supply racks through a resin bath and winds the wet fibre around a mandrel. Pultrusion is the continuous, automated closed-molding process that is cost effective for high volume production of constant cross sectional parts. Pultruded custom profiles include standard shapes such as channels, angles, beams, rods, bars, tubing and sheets (Saxena et al., 2008).

7.2 Animal fibre composite: Fabrication of the wool fibre composites

As a composite, wool fibres have been combined with polyester fibres and spun into multistrand yarn as threads, again for use in garments. Traditionally, wool fibres have been spun into multilayer fibres in the form of threads, which are then knitted into cloth and utilized for the manufacture of garments. The composite matrix was prepared from polyester resin with 1% hardener (methyl ethyl ketone peroxide). Samples of composite sheets were prepared in the laboratory from skeins of wool laid alternatively with layers of resin mixture, and placed in a rectangular mould. The top of the mould was sealed and hydraulic pressure of 1.2 MPa was applied for a period of 24 h. The pressure was then reduced to 0.6 MPa, the sample sheet was removed and excess solid resin trimmed. The composite so obtained was cured in air. This process was repeated for sample sheets containing wool by mass of 40, 30, 20 and a control sheet of polyester resin. Fabrication of different types of silk fibre composites, human hair composites and feather fibre composites can be made with hand lay up technique and compression molding which has been already described in fabrication of plant fibre composites.

7.3 Mineral fibre composite

The Hatschek process: Mineral fiber composites are made through Hatschek and Magnani processes which are commonly used for making mineral fibre cement composites. The Hatschek process (or wet process) is the most widely used method of fabrication of asbestos composites. About 7-10% solids by weight of aqueous slurry of asbestos and cement matrix is used to a holding tank which has a number of rotating screen cylinders. The cylinders select solid matter removing some of the water. A continuous felt group travels over the surfaces of the cylinders and select a thin layer of formulation from each cylinder. The formulation is the gash up on a steel calendar, or incorporation roll, need of thickness of product. The material is now compressed by pressure rolls, which are direct contact with the assimilation rolls. For sheet manufacture, the layer built up on the assimilation roll is mechanically cut off and drops onto a conveyor to be transferred for curing. For making of corrugated roofing, the flat sheet is removed to a corrugating station and put on oiled steel moulds for shaping.

The Magnani (or semi-dry) process: The Magnani (or semi-dry) process is used to prepare corrugated sheet and pipes. In this process, thickness of material can be increased at the peaks and troughs of the corrugations sheet and hence the bending strength is greater. About 50% solids of the thick slurry materials of this process can flow equivalently and directly onto a felt conveyor which goes through numerous vacuum boxes to dewater the formulation. The corrugated roofing is compressed over a corrugated past by a shaped roller. Pipe formation is similar to the Mazza process. The formulation of the matrix, and hence the cure of the product, has varied from country to country and between companies within a country. The formulations remain confidential to the company or its licensees and only general details will be discussed here. The autoclaved curing process has always been favored in Australia and the USA and in some European countries. In the autoclave process, the matrix is usually a mixture of ordinary Portland cement (OPC) and finely ground sand (silica), or lime and silica. The product, after an initial pre-cure period in air, is cured in an autoclave in a steam environment say 8 hours at 170-180 °C. The cured sheets are virtually at full strength after autoclaving and can be dispatched from the factory in a short time. By contrast the more traditional air-cured products require 14-28 days of air curing before they can be dispatched involving considerable stock inventory. The air-curing process is lower in capital outlay as no high-pressure autoclaves and steam raising plant are required; however, cement is more expensive than silica, and therefore material costs are higher (Shah et al., 1981). Attempt were made at AMPRI-CSIR Bhopal to make asbestos substitute composites replacing asbestos fiber with sisal fiber, though hand lay-up method Fig 7.3.1 show corrugated sisal cement roofing sheets and plan sheet prepared at AMPRI, Bhopal using hand lay up technique.

(a) (b)

Fig. 7.3.1 Sisal composites: (a) Sisal fiber cement roofing sheet (b) Sisal pulp cement composites panel

8. Properties of composite

8.1 Properties of plant fibre composites

Increased importance of renewable resources for raw materials and recyclability or biodegradability of the product at the end of the useful life is demanding a shift to natural fibers such as cotton, flax, kenaf, hemp, sisal etc in applications in addition to there exist technical advantages like strength, lightweight, and noise absorption etc.

8.1.1 Jute composite

Jute fibre possesses moderately high specific strength and stiffness which make it suitable for reinforcement in composite. Development of cheap high performance composite from jute has always been a major concern area due to the easy availability, low cost, high strength (tensile strength).Various composites were developed with different thermoplastic and thermo set polymers. Jute reinforced polyester, epoxy composite and jute reinforced polypropylene, polystyrene thermoplastic composite were developed from very long time and research were focused on its mechanical performance which is summarized here.

8.1.1.1 Jute-polyester composite

Dynamic mechanical properties of jute composite were found to be very high. Dash et al., (1999) processed and analyzed the mechanical properties of jute reinforced polyester composite. Tensile and flexural properties were investigated in terms of bleached and control jute composite at various fibre loading. Composites mechanical properties such as tensile, flexural strain, toughness and moduli were compared and found that 60% fibre loading showed highest tensile strength (90.52±8.83). In between control and bleached jute polyester composite, control jute polyester composite (JPH(C)) showed highest tensile property whereas bleached jute polyester (JPH (B)) composite showed highest flexural strength as shown in table 8.1.1.1 (Dash et al., 1999). Jute polyester hot curing (Bleached) composites showed 18440MPa flexural modulus and 171MPa flexural strength whereas Jute polyester hot curing (Control) composites showed 140MPa flexural strength and 13850MPa flexural modulus (Dash et al., 1999). Composite made from bleached fibre showed higher flexural properties due to the increase in the extent of chemisorptions of bleached jute fibre surface (Dash et al., 1999).

Composite	Fibre Volume (%)	Tensile Strength (MPa)	Ult Strain (%)	Tensile modulus (MPa)
Jute Polyester Hot curing (Control)	60	132± 6.33	5.83± 0.68	2956± 774
Jute Polyester Hot curing (Bleached)	60	117± 21.32	6.687± 0.82	2106± 229
Jute Polyester Hot Curing	55	78.15± 7.45	5.04± 0.72	2535± 884
Jute Polyester Hot Curing	60	90.52± 8.83	3.82± 0.12	4189± 403
Jute Polyester Hot Curing	66	80.6± 12.5	3.27 ± .40	4072± 402
Jute Polyester Hot Curing	71	70.31± 6.89	2.85± 0.25	4328± 358

Source: Dash et al., (1999)

Table 8.1.1.1 Mechanical properties of jute polyester composite

8.1.1.2 Jute vinyl ester composite

Ray et al. (2001) used a solution of NaOH (5%) to treat the jute fibre for 0, 2, 4, 6 and 8 hours at 30ºC. For the vinyl ester resin composites reinforced by 35 wt% jute fibre treated for 4 h,

an improvement of 20% for the flexural strength, 23% for the flexural modulus and 19% for the laminar shear strength was observed (Ray et al., 2001). Results are summarized in Table 8.1.1.2.

% Fibre volume	Flexural Strength (MPa)	Flexural Modulus (GPa)	Breaking Energy (J)
0	2.120	2.951	0.8227
8	106.30	4.220	0.2948
15	128.60	5.544	0.3399
23	145.70	7.355	0.3531
30	180.60	10.030	0.4799
35	199.10	11.890	0.5543

Source: Ray et al., (2001)

Table 8.1.1.2 Flexural properties of jute vinyl ester composite

8.1.1.3 Jute epoxy composite

After Jute polyester analysis, Mishra et al., (2000) investigated the effect of 50 % fibre loading of (control and Bleached) jute fibre reinforced epoxy composite on mechanical performance and found that bleached composite showed better flexural and impact strength whereas controlled jute epoxy composite showed higher tensile strength at 50 % fibre loading which are summarized in Table 8.1.1.3 (Mishra et al., 2000). In bleaching, fibre delignified and dewaxed and cell separated with each other and surface becomes clean with increased micro roughness which enhances the fibre matrix mechanical interlocking. Gassan & Bledzki, (1997) also investigate the effect of coupling agent between fibre and matrix and observed enhancement in mechanical performance. Table 8.1.1.3 showed that tensile strength (131MPa) and tensile modulus (2.35GPa) of 50% fibre loaded bleached jute reinforced epoxy composite is lesser than the corresponding 148 MPa and 3.18GPa of unbleached jute epoxy composite. In contrary, flexural strength (155MPa) and flexural modulus (14.232GPa) of raw jute epoxy composite is lesser than the corresponding 196MPa and 20.4GPa of bleached jute reinforced composite. Impact strength of bleached jute epoxy composite (107.94 J/K) is higher than the control jute epoxy composite (94.46 J/K) (Mishra et al., 2000). Mishra et al. (2000) also studied the effect of chemical modification on the impact energy of jute/Flax/hemp epoxy composite and concluded that the modified surfaces can further bond with epoxy resin and enhanced good bonding which resulted in increased impact strength (Mishra et al., 2000).

Also observed 60 % enhancement in strength on increasing fibre volume Vf from 0.15 to 0.22 in hemp/ interfacial adhesion, through chemical bonds between the fibre and coupling agent/film former and the coupling agent/ film former and matrix. 1 wt% NaOH for 4 hours was found to be the optimal condition for the fibre surface treatment. In the combination of the silane with epoxy, the dispersion is efficient with an aliphatic silane (3-Aminopropyl-triethoxy-silane), but not with an aromatic silane (Phenylaminopropyl-trimethoxy-silane. The transverse tensile strengths of unidirectional jute/epoxy composites increased by 29%, and the transverse bending strength increased by 17% for NaOH treated

jute/epoxy composites. However, the fibre surface treatment did not significantly influence the tensile and bending modulus because of same fibre volume contents. The water absorption of the jute/epoxy composites also follows a Fickian model. The fibre surface treatments decrease the water uptake and the diffusivity of the composites compared to the untreated state (Gassan & Bledzki, 1997; Maschinenwesen et al., 2006). Mishra et al., 2000) studied the tensile, flexural and impact properties of control and bleached jute reinforced epoxy composite (JEH 50 (C) and JEH 50 (B) respectively), in which JEH 50 (B) possess a higher (107.94 j/m) Izod impact strength than that of JEH 50 (C) (94.46 j/m); that means JEH 50 (B) composite has more toughness, and hence, can resist the fracture under stress applied at high speed. JEH 50 (B) showed higher impact strength (14,701.38 j.m^2) than the JEH 50 (C) (11482.14 j/m^2). High impact value attributed to the better bonding between the bleached fibre and matrix. Thus, the composite becomes more hydrophobic and tougher due to delignification. Here resin replaces the role of the lignin in jute fibre epoxy composite, but jute epoxy composite showed the contrary as the impact strength decrease on further increase in volume e fraction (Mishra et al., 2000). For the epoxy matrix, fibre surface treatment by alkali, organo silane, epoxy dispersions and the combinations lead to better interfacial adhesion. Especially, the presence of coupling agent or epoxy film former, incorporated into the composites to tailor the chemical structure, leads to improved.

8.1.1.4 Jute polypropylene/ polystyrene thermoplastic composite

Earlier work on jute polypropylene composite developed using different coupling agent like Maleic anhydride grafted polypropylene (2% wt MAHgP) showed enhanced tensile strength. The interfacial shear strength increases 91% for PP1-jute composite and 68% for PP2 jute composite (jute polypropylene). Concluded that the intrinsic tensile properties of jute fibre are propositional to fibre cross sectional area associated with its perfect circle shape, the measured fibre tensile strength actually increase with jute cross sectional area at a constant gauge length. An increase of the tensile strength occurs for jute/pp composites in humidity aging conditions which are attributed to the improvement in both polymer and interfacial adhesion strength (Doan et al., 2006). Coupling agent MAHgPP (2%) in jute PP composite increases the storage modulus at 19.8% fibre content, which indicate the enhanced adhesion between fibre and matrix due to the coupling agent, leading to the better transfer of stress from matrix to the fibre (Doan et al., 2007).

Interfacial Sher Stress (IFSS) between fibre and matrix is much lower (3.49MPa) than the synthetic fibre and thermo sets. This IFSS is mainly depends on the chemical and mechanical interlocking. Untreated jute have less compatibility with matrix due to hydroxyl group presence, hence IFSS is mainly attributed to irregularity of jute fibre surfaces. Treatment improved the compatibility, hence IFSS increases. The IFSS with 2 wt% NaOH and 2 wt % KH 550 treated jute PP composite increases approximately 51%,39% and 22% than untreated Jute PP composite (Liu & Dai, 2007). In another study, effect of coupling agents on both interfacial and bulk mechanical properties of jute fibre/polypropylene composites were investigated with three kinds of maleic anhydride grafted polypropylene (MAHgPP), namely Exxelor PO 1020 (Ex), Polybond 3200 (PO) and TPPP 8012 (TP) were used as matrix modifier. Ex was found to achieve the best mechanical properties at a content of 2 wt%.

Higher molecular weight polypropylene (PP) with less melt flow rates improved the mechanical properties to a greater extent than lower molecular weight polypropylene. The

tensile modulus of jute/PP composites increased with increasing fibre content and showed less sensitivity to the variation of interfacial adhesion. Thermal behavior of the jute, PP and composites was determined differently under nitrogen and air flows. The thermal resistance of PP (High m.wt.) composites decreased with increasing fibre content in nitrogen atmosphere. However, the TG curves of these composites in air shift towards a lower temperature region and the thermal resistance of composites was found to increase with increasing fibre content. The diffusion process of water in jute/polypropylene composites followed Fickian model. An increase in moisture absorption was observed with increasing fibre content. An increase of the tensile strength occurred for jute/PP composites after humidity aging, which is attributed to the improvement in both polymer and interfacial adhesion strength. Using jute fibre as the reinforcement increased the storage modulus with increasing fibre content. However, the moisture uptake caused a decrease in the storage modulus for most temperatures and also in glass-transition temperature at the same fibre content.

Composite	**Fibre Volume (%)**	**Ult Strength (Mpa)**	**Ult strain (%)**	**Tensile modulus (MPa)**	**Flexural strength (MPa)**	**Flexural Modulus (MPa)**	**Izod Impact strength (J/K)**	**Charpy Impact strength (J/K)**
Jute Epoxy (control)	50	148.3± 6.94	6.29± 0,93	3184± 620	155.82± 13.59	14232± 2216	94.46	11482.14
Jute Epoxy (Bleached)	50	131.09± 23,563	7.41± 0.90	2348±261	196.12± 18.99	20445± 2240	107.94	14701.38
Jute epoxy	40	139.8± 4.59	7.32± 0.69	2826±146	-	-	-	-
Jute Epoxy	50	148.3± 6.94	6.29± 0.93	3184±185	-	-	-	-
Jute Epoxy	57	143.36± 4.06	5.98± 0.92	3060±185	-	-	-	-

Source: Mishra et al., (2000)

Table 8.1.1.3 Mechanical properties of Jute Epoxy composite

Generally, 10% fibre loading can increase the tensile strength of polystyrene/pp blend. Jute reinforcement increases the tensile strength as compared to coconut reinforcement, PP/PS composite, which is due to the single fibre property; means tensile strength of jute is higher than the single coconut fibre. Tensile strength of PP/PS blend (24.73 MPa) increases up to 30.99MPa after jute fibre loading explained in Table 8.1.1.4. Youngs modulus of composites with 10 % fibre loading are higher than the PP/PS composite which shows that stiffness increases after fibre addition (1.2163 GPa to 1.2244GPa). But charpy impact strength of jute addition to PP/PS blend decreases from 3.89 KJ/m^2. The failure mechanism of these composite was mainly by fibre pull out due to the weakness of interfacial strength between fibre and matrix. Impact energy is dissipated by deboning, fibre and matrix fracture and fibre pull out (Hatta et al., 2008).

Type of Composite	Fibre Volume (%)	Tensile Strength (MPa)	Youngs Modulus (Gpa)	Impact strength	Flexural Strength (MPa)	Reference
Jute fibre Mat polypropylene Composite		28.4±0.90	-	65±3.2 j/m	35.1±1.2	Liu & Dai, (2007)
Pure Polypropylene + pure Polystyrene (50/50)	0	24.73±0.99	1.1745	3.89 KJ/M^2	-	Hatta et al., (2008)
Pure Polypropylene + pure Polystyrene (50/50) + 10% fibre	10	30.99±0.85	1.2163	3.11 KJ/M^2	-	"

Table 8.1.1.4 Mechanical properties of jute –Polypropylene/Polystyrene composite

8.1.2 Sisal composite

8.1.2.1 Sisal polyester composite

Most of the physico-mechanical properties of composites made from fibres are shown in Table 8.1.2.1. The density of these composites is 0.99 to 1.12 g/cm^3. The results indicate that there is no appreciable change in density with respect to the surface- modifying agents. The void contents of surface treated fibre samples are lower than those of untreated ones; silane-treated samples are the lowest. It has been reported that voids, even in small amounts, are detrimental to the mechanical properties of polymer composites. The surface modification of sisal fibres caused a modest improvement of 15 to 33% in tensile strength, 45 to 79% in tensile modulus and 21 to 29% in both flexural strength and flexural modulus (silane-treated samples showed an improvement of 62% in flexural properties). This improvement indicates improved fibre-matrix adhesion (Felix et al., 1993). The interface formed is much less stiff than the resin matrix and provides a deformation mechanism to reduce interfacial stress concentration. Further, it may also prevent fibre-fibre contacts, which are sources of high stress concentrations in the final composites (Kardos et al., 1985).

Composite	Fibre Vol (%)	Density g/cm^3	Tensile strength (MPa)	Elongation (%)	Tensile Modulus (GPa)	Flexural Strength (MPa)	Flexural Modulus (Gpa)	Reference
Sisal Polyester composite	50	0.99	29.66	9.52	1.15	59.57	11.94	Singh et al., (1996)
Polyester neat composite	-	-	22.5	1.8	1.39	-	-	Fonseca et al., (2004)

Table 8.1.2.1 Physico Mechanical Properties of Sisal-Polyester composite

Elongation at break of silane-treated composites is lower than that of the others. The high energy to break off surface-treated composites indicates that the matrix is controlling the growth of cracks as fracture proceeds. Work carried out by Fonseca et al., (2004) showed that sisal polyester composites resulted a tensile strength, tensile modulous, impact strength of 7 MPa, 1.7GPa and 328±65 respectively. However, the elongation at break (1.7%) found to be higher than that of the similar polyester sisal composites as reported by Singh et al., (1996). A 69% decrease on tensile strength and a 46% decrease on elongation at break were

observed with sisal addition for the polyester– sisal composites. A weak fibre–matrix interface was expected for this composite, since no fibre treatment or matrix modification was performed. The weak interface and the low fibre volume fraction employed are held responsible for the low mechanical properties and premature failure of that composite (Fonseca et al., 2004).

8.1.2.2 Sisal epoxy composite

Incorporation of the sisal fibre significantly increase the tensile strength and Young's modulus of the epoxy resin composite (46% (v/v) and is summarized in Table 8.1.2.2. As reported by sisal epoxy composite showed a Young's modulus of about 20GPa and tensile strength of 210 MPa. Flexural modulus of unidirectional sisal– epoxy composites showed 16GPa (40%v/v) (Bisanda & Ansell, 1991) and flexural strength was 266 MPa. For nonwoven sisal mats, Singh et al., (1996) reported that sisal–polyester composites (50% v/v) had a tensile strength of 30 MPa and a tensile modulus of 1.15 GPa for which composites were manufactured by impregnation of the nonwoven sisal mats and then compression moulded during 2 h (Oksman et al., 2002). The tensile behavior of the sisal reinforced composites is illustrated by Fonseca et al., (2004). Sisal addition increased (20%) young's modulus of unmodified polyester (SP) with the respective matrices. This behavior was expected, since sisal fibres have higher young's modulus than both the unmodified and the flame retardant modified matrices. The uniform increases in modulus values for these two composites are in accordance with the fact that the volume fraction of fibres in both composites was equivalent. Another important mechanical property i.e. impact strength of sisal epoxy composite were analyzed by Rong et al., (2002) and it was found in the range of 65 – 80 Kj/m^2. Silane treated matrix (SM) composites resulted caused a marked increase on its tensile modulus. This behavior is thought to be due to an enhancement on fibre/matrix adhesion, caused by the incorporation of the silane coupling agent.

S. No.	Composite	Fibre Volume (%)	Tensile strength (MPa)	Elongation at break (%)	Tensile Modulus (GPa)
1.	Epoxy	0	76	7.3	3.1 - 3.2
2.	Sisal Epoxy composite	28	169±23	2.3	14.2±1.6
3.	Sisal Epoxy composite	35	183±16	2.2	14.5±1.6
4.	Sisal Epoxy composite	46	211±12	1.9	19.7±1.5

Source: Oksman et al., (2002)

Table 8.1.2.2 Mechanical Properties of Sisal Epoxy Composite

8.1.2.3 Sisal Urea formaldehyde composite

Mechanical properties of Sisal fibre reinforced urea-formaldehyde resin composites were investigated by Zhong & Wei, (2007), Table 8.1.2.3. The composite with 50% (w/w) sisal fibre showed optimal charpy impact strength (9.42kJ/m^2). Whereas the flexural strength, wear resistance and water absorption properties are proved to be excellent in the composite with 30% (w/w) sisal fibre under the present experimental conditions adopted. The fibres

themselves possess a higher wear resistance than the matrix and should protrude from the SEM surface that these composites in fibre board can be expanded (Zhong & Wei, 2007).

S.No.	Fibre volume (%)	Charpy Impact strength (Kj/m^2)	Flexural Strength (MPa)	Flexural Modulus (Gpa)	Density (g/cm^3)
1.	30	5.75	58.58	7.63	1.53
2.	40	6.5	55.80	5.27	1.52
3.	50	9.5	53.07	4.93	1.48
4.	60	7	37.73	4.09	1.44
5.	70	6.8	15.28	1.59	1.22

Source: Zhong & Wei, (2007)

Table 8.1.2.3 Mechanical Properties of Sisal – Urea formaldehyde composite

8.1.2.4 Sisal polystyrene / polypropylene composite

Polystyrene with maleic anhydride (PSMA), toluene diisocyanate (T'DI), methyl triethoxy silane and triethoxy octyl silane) on sisal fibre were tried to improve its efficiency as reinforcement in polystyrene-sisal fibre composites. All fibre modifications improve the tensile properties of the composite. The decreased in hydrophilicity of the treated fibre and increased thermodynamic compatibility of the treated fibre with the polymer matrix are responsible for the improvement in the mechanical properties (Nair et al., 2003). The maximum improvement in tensile properties was observed with PSMA coating (Table 8.1.2.4). In all cases except PSMA coating, fibre modification decreases the impact strength of the composites and PSMA coating showed an improvement in the impact strength. Flexural strength of treated composites exhibits an improvement in all cases except benzoylation. Flexural modulus showed a decrease in both benzoylated and toluene diisocyanate treated fibre composites and an improvement in the case of silane treated fibre composite. PSMA treated fibre composite, however, shows no considerable variation in flexural modulus. Flexural strain also showed no considerable variation with fibre modification (Nair et al., 2003).

Composite	Fibre volume (%)	Tensile strength (MPa)approx	Flexural Strength (Mpa)	Impact strength (J/m)	Reference
Polystyrene	0	35	48	-	Nair & Thomas, (2003)
Untreated sisal PS composite	0	43	72	-	
Sisal-PP	0	17.80	19.60	23.25	
Sisal-PP	6.8	24.17	34.83	40.50	
Sisal-PP	10.3	26.11	46.35	46.10	Mohanty et al., (2004)
Sisal-PP	21.0	29.25	48.96	51.79	
Sisal-PP	31.0	23.21	43.41	39.83	

Table 8.1.2.4 Mechanical properties of sisal Polypropylene (PP)/Polystyrene (PS) Composite

The mechanical and dynamic mechanical properties of PP–sisal fibre composites have been investigated and summarized in Table 8.1.2.4. It was observed that the composites prepared with 21% fibre content with 1% MAPP concentration showed optimum mechanical strength. Storage modulus versus temperature plots showed an increase in the magnitude of the peaks with the addition of fibres and MAPP. The damping properties of the composites, however, decreased with the addition of the fibres and MAPP. Based on these studies, it can be concluded that sisal fibres could reinforce the PP matrix when used in optimal concentration of fibres and coupling agents (Mohanty et al., 2004).

8.1.3 Flax composite

8.1.3.1 Flax polyester composite

The mechanical properties of short fibre reinforced composites are expected to depend on the intrinsic properties of both matrix and fibre, on aspect ratio, content, length and fibre-matrix adhesion that is responsible for the efficiency of load transfer in the composite. In flax polyester composite, tensile modulus E increase with fibre content as shown in Table 8.1.3.1. Tensile strength of polyester composite tends to 20 MPa to 21 MPa at 12.5 % flax loading, 19.4 MPa at 25% flax loading and decreases at 37.5% loading (16.2%). Critical fibre length also affect the stress transfer from fibre to matrix, means critical fibre length is inversely proportional to the interfacial strength (Baiardo, 2004). Bledzki et al., (2008) studied the effect of acetylation on mechanical properties and found tensile and flexural strength of composite increase with increasing the degree of acetylation and contrary to it, Charpy impact strength of composite were found to decreased with increasing degree of acetylation (Bledzki, 2008). Marais et al., (2005) worked out the cold plasma treatments on mechanical properties of unsaturated polyester composite. The mean value of tensile modulus, tensile specific modulus, breaking strength, breaking strain of untreated pure resin and composite were determined. The value of the tensile specific modulus and breaking strength of the reinforced composite higher than for the polyester, matrix (Marais, 2005).

S. No.	Composite	Fibre volume (%)	Breaking strength (MPa)	Breaking strain (%)	Youngs Modulus (MPa)
1.	Polyester	0	20.0	19.6	435
2.	Flax polyester	12.5	21.7	14.1	760
3.	Flax polyester	25	19.4	6.1	1112
4.	UPR	-	70	2.2	3.7
5.	Flax composite	-	1150	3	70

Source: Baiardo et al., (2004)

Table 8.1.3.1 Mechanical properties of flax Polyester composite

8.1.3.2 Flax epoxy composite

Modulus of epoxy resin is 2909MPa whereas the flax fibre has low modulus. The mechanical properties depend on defects and dispersion in geometry of fibres. The fibre has a polygonal cross section that contains many defects along their length. Lamy & Pomel, (2002) determine the modulus E1 of unidirectional flax epoxy composite using equation below for a fibre

volume fraction 40% and compared with experimental results (Table 8.1.3.2). Longitudinally flexural modulus E1 is 12000 MPa, for unidirectional composite and measured modulus of the woven flax reinforced composite is 3500 MPa (Lamy & Pomel, 2002).

S.No.	Composite	% Fibre	Thickness (mm)	Flexural stiffness (J)	Flexural Modulus
1.	Flax Epoxy	34	2.28±0.01	82900±1800	3500±150
2.	Glass Epoxy	50	1.03±0.01	41800±900	19000±1000

Source: Lamy & Pomel, (2002)

Table 8.1.3.2 Flexural strength of flax epoxy composite

8.1.3.3 Flax Polystyrene composite

Tensile strength of a material is the maximum amount of tensile stress that can be subjected to before it breaks. Polystyrene blend show tensile strength (125N/mm^2) enhancement of raw flax fibre loading to 175 N/mm^2 and extension increases up to 4.3 mm shown in Table 8.1.3.3. Grafting with MMA on flax increases the water resistance because MMA has less water affinity (Kaith et al., 2008).

Composite	Compressive strength (N/mm^2)	Compression	Tensile strength (N/mm2)	Extension
PS	100±5.5	00.27±0.02	125±3.6	0.42±0.05
Flax PS composite	400±3.6	0.9±0.04	175±4.6	4.3±0.01

Source: Kaith et al., (2008)

Table 8.1.3.3 Mechanical properties of Flax Polystyrene (PS) composite

8.1.3.4 Flax polypropylene composite

MAPP (Maleic Anhydride polypropylene) treatment were done and it was found that flexural strength of flax pulp and fibre PP composite is higher than that for neat polypropylene blend because the fibres have higher stiffness than polymer. Flax fibre always has higher mechanical properties than the fibre pulp and treatments vary the modulus, this is due to the –OH adsorption bands. Neat PP blends have less flexural strength than the all composite containing fibre shown in the results of Table 8.1.3.4. MAPP containing polypropylene chain smooth the different surface energy values of matrix and fibre, increases better wetting of fiber and the interfacial adhesion. Composites made with a 10 wt % MAPP treated fibre have the highest flexural and tensile strength (Cantero et al., 2003).

Composite	Tensile strength (MPa)	Tensile Modulus (MPa)	Charpy Impact strength (mj/mm^2)	Flexural strength (MPa)	Flexural Modulus (MPa)	Reference
PP	27	700	-	35	1400	Cantero et al., (2003)
Flax PP	19	17500	-	48	3400	
Flax PP	39	4200	19	56	3800	Bledzki et al., (2008)

Table 8.1.3.4 Mechanical properties of Flax Polypropylene (PP) composite

8.1.4 Cotton composite

The work done by Gohil & Shaikh, (2010) discussed the variation in composite strength as a function of fibre volume (*v/v)* for longitudinally placed cotton fibre with polyester resin. The composite strength with polyester resin is summarized in Table 8.1.4. It is observed that composite strength in the range of 27.94 MPa to 71.16 MPa for longitudinally placed cotton fibre with 10.41% to 35.27%. The variation in composite elastic modulus as a function of *f v* for longitudinally placed cotton fibre with polyester resin is observed in the range of 2.70GPa to 4.04GPa for longitudinally placed cotton fibre adjacent to the *f v* range of 10.41% to 35.27%. The experimental investigation indicates that, as the fibre volume fraction increases the strength as well as longitudinal elastic modulus increases linearly. This is inline with the rule of mixture which predicts the linear increase in composite strength with increase in volume fraction of fibres holds true for longitudinally placed fibre composite for all the fibre matrix combination (Gohil & Shaikh, 2010) (Table 8.1.4).

S. No.	% Fibre volume	Tensile Strength (MPa)	Elastic Modulus (GPa)
1.	10	28	2.8
2.	20	45	3
3.	25	53	3.4
4.	28	62	3.6
5.	35	72	4

Source: Gohil & Shaikh, (2010)

Table 8.1.4 Tensile properties of Cotton polyester composite

8.2 Properties of animal fibre composite

8.2.1 Wool composite

Results indicate that there is little influence on the tensile stress or modulus of elasticity with increasing fraction of wool content. However, when the fibres were laid in a transverse position to the tensile load, the tensile stress was increased. The modulus of elasticity of the transverse samples was similar to that of the parallel fibre samples. The influence of apparent fibre orientation is again indicated where the transverse toughness values are one-third of the longitudinal values. This implies that wool may be able to provide reinforcement in multi-axial situations (Blicblau, 1997). The mechanical properties of raw wool polyester resin composite are shown in Table 8.2.1.

S. No.	Wool (wt %)	Tensile strength (MPa)	Tensile modulus (MPa)	Flexural strength (MPa)	Izod impact toughness
1.	0	33.7 ± 4.2	0.7 ± 0.2	-	-
2.	22	35.9 ± 3.3	3.2 ± 0.2	76.2 ± 6.3	9.2 ± 1.3
3.	37	34.6 ± 2.6	2.7 ± 0.3	72.1 ± 6.2	46.7 ± 15.8
4.	51	39.1 ± 1.7	1.6 ± 0.2	75.4 ± 6.3	49.9 ± 10.4
5.	54	40.7 ± 1.2	1.8 ± 0.1	7.5.1 ± 1.3	58.1 ± 9.3
6.	54	17.1 ± 1.2	1.3 ± 0.1	54.7 ± 0.9	25.1 ± 0.6

Source: Quazi et al., (2010)

Table. 8.2.1 Mechanical properties of raw wool–polyester resin composites

8.2.2 Silk composites

Silk fibre reinforced composite materials comprising a thermoplastic polymer matrix, which are relatively light whilst having a high impact resistance. Due to the high impact resistance of the fibrous composite material, panels or shells comprising such composites are particularly useful for the manufacture of objects which in the course of their life cycle are subject to shocks or at risk of penetration (Patent; Silk fibre composites, Washington, DC, US, 2010). There is a growing interest in the use of composite materials. Silk fibre/ gelatin bio-composites were fabricated using compression molding. Bombyx mori woven natural silk is among the strongest fibres produced in nature. It has high specific-strength and high specific-stiffness; extremely elastic and resilient (Bledzki & Gassan, 1999). Perez-Rigueriro et al., (2000) showed that Bombyx mori silk is better than Kevlar or steel in terms of elongation at failure. It has a good capacity to absorb energy and to dissipate this energy in a very controlled manner as the silk deforms (Perez-Rigueriro et al., 2000). The interlacing of fibre bundles in woven fabrics composites prevents the growth of damage and hence provides an increase in impact toughness compared with unidirectional composites.

Silk woven fabrics composites are easy to handle and have excellent formability (Dasgupta & Agarwal, 1992). The tensile strength (TS) and bending strength (BS) with varying silk content of the composite. TS and BS increased with the increase of fibre content and were found maximum in this experiment for 30% fibre. TS and BS of composite with 30% silk content showed 54 MPa and 75 MPa, respectively, whereas the 0% silk content gelatin film showed the TS and BS of 32 MPa and 47 MPa, respectively. At low fibre content, the composites showed poor TS and BS. This is because of higher matrix content and attribution of low load transfer capability by low fibre content. With the increase of fibre content from 10 to 30%, load transfer capability also increases and greater TS and BS results. The tensile modulus (TM) and bending modulus (BM) of the composites were found to increase on increasing silk content signifying that the stress transfers from the gelatin matrix to the stiffer fibre occurred.

8.2.3 Human hair composites

Investigations on the mechanical properties of human hair and its composites are inadequate. The most important mechanical property of hair is its elasticity. According to Hooke's law, when an elastic fiber is pulled, the change in length is proportional to the force applied. The elasticity of wet and dry hair is directly proportional to shaft diameter. Hair diameter is the most important factor for hair mechanics (Franbourg et al., 2003; Dawber & Messenger, 1997). The physical properties of hair can be divided into elastic deformations including stretching, bending, stiffness, torsion, cross sectional area and shape, density, friction and static charge (Dawber & Messenger, 1997). Bleaching alters the elasticity of hair, and decreases its tensile properties by up to 25% (Dawber & Messenger, 1997). The hairs were dyed or un-dyed did not affect the mechanical properties of hairs. If there is a connection between the mechanical properties of human hair and its durability, it is possible to alter the properties of hair. The mechanical properties of human hairs would effects on protein structure, a-keratin fibres and microfibril– and matrix composite behaviours (Berivan et al., 2008). So there is lot of scope for new studies on composites development using human hair which may result in a new materials with better performance leading to effective recycling/ utilization of human hair for value added engineering application.

8.2.4 Feather fibre composites

Hong and Wool (2005), studied the bulk density of feather fibre soy resin matrix composites. Composite bulk density of 1.08 g/cm^3 was higher than expected (1.001 g/cm^3) for the composite containing 30% wt feather fibre. The higher bulk composite density could also be explained by a higher value for the apparent density of feather fibre. However, yet very limited work has been reported on feather fibre composites. The effects of various blends of cement and feather on the hygroscopicity and dimensional stability were measured using water absorption and thickness swelling tests. These tests were determined by submerging specimens horizontally in water at room temperature for two and 22 hours. After each submersion period, samples were drained of excess water and measured for change in thickness and amount of water absorbed. Thickness swelling was measured from two marked points along the length of each sample with a digital sliding caliper. Water absorption and thickness swelling were expressed as a percentage of the original weight and thickness, respectively (Menandro & Acda, 2010). The effects of different formulations on board stiffness and flexural strength were evaluated using a three point bending test, with some modifications.

8.3 Properties of Mineral fibre composites

Many building product have been made from asbestos fiber such as tiles, sheet, corrugated roofing element, sheets, pipes, etc., mostly these materials were made using asbestos fiber with cement. Asbestos cement products contain 8-16 % of asbestos fibre by volume. Shah, 1981 used two type of asbestos fibre Chrysotile and Crocidolite for comparison of their strength and found crocidolite asbestos cement composites strength was more than chrysotile cement composites. Asbestos mechanical properties of cement composites are shown in Table 8.3.1. Sung et al., (1975) was studied on asbestos reinforced with phenolic resin which resulted flexural strength of 93.76MPa, flexural modulus of 159.96GPa and impact strength of 64.08j/m. Akers & Garrett, (1983) studied on the failure process of asbestos-cement composites and calculates the flexural strength (35-37 MPa). Lee et al, (2004) used different orientation of asbestos fiber in phenolic composites and reported that in axial position of fiber in composites showed maximum tensile strength but of compressive strength was maximum in radial position. Asbestos mechanical properties of cement composites are shown in Table 8.3.2. Akers & Garrett, (1986) has reported that when fibre mass fraction increased modulus of rapture is also increase up to 15 %. Addition of more than 20 % asbestos fiber decreased the modulus of rapture but decreased the density from 1.65 g/cm3 to 1.23 g/cm3 when 35 % fiber was added, however the impact strength was increased with increased in fiber content. Asbestos mechanical properties of cement composites are shown in Table 8.3.3 and Table 8.3.4. When water cement ratio varies in

S. No.	Type of composites	Tensile strength (MPa)	Young's Modulus of elasticity (GPa)	Density	Elongation of break(%)
1.	Chrysotile Asbestos cement composites	3100	16.4	2.55	2-3
2.	Crocidolite Asbestos cement composites	3500	19.6	3.37	2-3

Source: Shah, (1981)

Table 8.3.1 Physico- mechanical properties of Asbestos cement composites

asbestos cement composites, modulus of rupture (MOR) also varied and it is maximum at 0.33 water cement ration but when water cement ratio increase from 0.33, the mechanical properties is also decreased. Optimum water-cement ratio need to be maintained about 0.33, where maximum strength can be achieved (Akers & Garrett, 1986).

S.No.	Orientation of fibre	Tensile strength (MPa)	Tensile modulus (GPa)	Compressive strength (MPa)
1.	Hoop	82	13.3	86.2
2.	Radial (orientation of fibre)	11.1	3.0	105.3
3.	Axial (orientation of fibre)	15.6	3.5	75.3

Source: Lee & Kim, (2004)

Table 8.3.2 Mechanical properties of Asbestos Phenolic Composite

S. No.	% Fibre mass fraction	Modulus of rapture (N/mm^2) (no pressure)	Impact resistance (KJ/m^2)	Density (g/cm^3)
1.	5	20-24	0.6- 1.4	1.65
2.	10	35-40	2.0 -2.4	1.55
3.	15	37-42	2.2 – 3.0	1.45
4.	20	33-37	3.0 – 3.5	1.3
5.	25	25-30	3.5-3.8	1.25
6.	30	25-30	3.5-3.8	1.23

Source: Akers & Garrett, (1986)

Table 8.3.3 Physico Mechanical properties of asbestos fibre cement composites (Different % fibre content)

S. No.	Water cement ratio	Modulus of rapture (N/mm^2) (no pressure)	Impact resistance (KJ/m^2)	Density (g/cm^3)
1.	0.30	30-32	0.8-1.2	1.65
2.	0.33	32-35	1.2-1.4	1.55
3.	0.35	25-30	1.0-1.3	1.45
4.	0.37	23-25	1.2-1.4	1.3
5.	0.40	20-25	0.8-1.2	1.25
6.	0.45	15-20	0.4-0.8	1.23
7.	0.50	10-15	0.2-.06	-

Source: Akers & Garrett, (1986)

Table 8.3.4 Physico Mechanical properties of asbestos fibre cement composites (Variation in water cement ratio)

9. Opportunities and challenges

Natural fibres have gained much interest among technologists and scientist for applications in civil, military, industrial, space craft and biomedical sectors (Saheb & jog, 1999). In the past two decades, growing interest for natural fibres composites has resulted in extensive research. The driving forces are (i) cost reduction, (ii) weight reduction and (iii) marketing (application of renewable materials). Technical requirements were of less importance; hence application remained limited to non-structural parts for a long time. The reason for this is the traditional shortcomings of NF composites, the low impact resistance and moist degradation. Recent research however showed that significant improvements of these properties are possible. The scope of different natural fiber composites and feature challenges and discussed with following section.

9.1 Plant fiber

The use of plant fibres as reinforcement in composite materials is finding increasing interest in the automotive and building industry, and the properties of plant fibre composites have been addressed in numerous research studies. New composite materials based on plant fibres and polymers are being increasingly used in the building industry and in automotive industry. Plant fibres, such as sisal, jute, hemp, flax, palm etc can be used as reinforcement for Epoxy, polyester, PVC, PE or PP-type polymers in place of synthetic fibres (glass, Kevlar, carbon, etc.). This substitution offers many benefits:

- Economic: lower costs on account of significantly reduced cycle times, energy savings.
- Technical: mechanical properties identical to those of traditional reinforcements, reduced tool wear and tear, high geometric stability of the manufactured parts, good insulation characteristics;
- Environmental: renewable resource, easy to recycle, no material toxicity, reduced fossil fuels content, CO_2-neutral materials.

Natural fiber composite materials are being used for manufacturing many components in the automotive sector (Taj et al., 2007; Karus & Gahle, 2006; Saxena et al., 2008, 2011; Mohanty et al., 2005; Xin et al., 2007). Like glass, the natural fibers combine readily with a thermoplastic or thermosetting matrix to produce commodity goods (Brouwer, 2002). Typical market specification natural fibre composites includes ultimate breaking force and elongation, impact strength, flexural properties, acoustic absorption, fogging characteristics, flammability, and suitability for processing: temperature and dwell time, odor, water absorption, dimensional stability, and crash behavior (Mohanty et al., 2005). Plant fibers are mainly used in the interior parts making of passenger cars and truck cabins. Such insulating materials, mainly based on cotton fibers recycled from textiles, have relatively high fiber content of more than 80% by weight. Brazilian trucks trim parts were made of a mixture of jute, coffee bag wastes, and polypropylene bags show that recycling sometimes can lead to advanced applications (Bledzki & Gassan, 1999). The use of plant fiber based automobile parts such as trim parts, various panels, shelves, and brake shoes are attracting automobile industries worldwide because of its reduction in weight of about 10%, energy production of 80%, and cost reduction of 5%. Conservative estimates indicate that about 6,000 TPA plant fiber-based composite parts can find their way into passenger cars and multi-utility vehicles (Saxena et al., 2005, 2011).

Prospects for the use of plant fiber in Automotive locomotive, aerospace, construction industry has long way to go to meet the societal area. In railways, the gear case, main doors,

luggage racks, floor/roof panels, berths, chair backings, interior panels and partitions, interior furnishing and seating, modular toilets, and lightweight coaches are made from different natural fiber composites and their combinations. Composite materials offer some significant advantages to metals in many structural applications in railways to the effect that they are lightweight, cost-effective, corrosion resistant, energy saving (Saxena et al., 2011). Development of biodegradable materials as an alternative to synthetic materials such as glass fiber-reinforced plastics and other synthetic plastics is the challenge for the present and future generations in the context of global climate change. Moreover, there are various problems associated with synthetic polymer composites due to the inherent problem of life cycle assessment and waste management at the end of its service life. At this juncture, biodegradable materials offer significant advantages provided they are techno-economically viable. Worldwide, considerable work is being done by several researchers for the development of biodegradable polymers leading to manufacturing of biodegradable polymer composites for various engineering applications (Lu, 2004; Oudshoorn, 1995).

9.2 Animal fibre

Applications of animal fibres in composites have not yet been exploited fully. But yet no precise method available to identify and differentiate the fibres quantity. They are often adulterated during marketing. Animal based natural fibres can also be used as alternatives for producing composite materials which may have great scope in value added application including bio-engineering and medical applications. The contents of these fibres are mainly made by proteins, like wool, spider and silkworm silk. Wool is the most popular natural material. In the textile industries, a lot of waste wool fibres and their products induce actions which lead to the regeneration of wool keratin materials. However, the most significant limitations may be the poor fracture resistance of neat keratin materials. Rock Wool Composite panel (rock wool sandwich board) is one such example for animal fiber composites. It has good fire-resistance and noise-absorbing properties. The silk fibres are environmentally stable as compared to the proteins because of their extensive hydrogen bonding. Silk fibre composites is expected to be light weight and very tough with good impact strength bearing materials. It can be shaped into complex shapes with suitable matrix. Though formed to that of synthetic fiber composites.Improvement of interface needs attention, mechanical performance.

Animal fibre reinforced composite materials have found applications in the automotive, aerospace and sports equipment industries. Compared to most metals and unreinforced plastics, animal fiber composites may offer a high strength-to-weight ratio, corrosion and termite resistant. Advantage of animal fiber composite materials is that they can be tailored to meet the specific structure. Composites may expect to be cost competitive and a very attractive alternative to conventional materials. Further the feathers take up a lot of space in landfills and take a long time to decay because of the keratin proteins that make up the feathers. There is also the fear of bird flu, which makes converting feathers into animal feeds undesirable. The cement-bonded feather board developed is more resistant to decay and termite attack due to the keratin, Feather boards could be used for paneling, ceilings and as insulation but not for weight-bearing building components like walls or pillars. Thus use of feather in composites would be an attractive and better alternative for safe management especially in value added engineering.

9.3 Mineral fibre

Asbestos fibres have been used for the fabrication of corrugates roofing, sheet, pipeline wrapping, electrical insulation, etc. Asbestos textiles, comprising yarn, thread, cloth, tape, or rope, also found broad application in thermal and electrical insulation and friction products in brake or clutch pads. Chrysotile has been used in asbestos-cement generally because it is cost-effective and has good mechanical properties. Asbestos has been durable and heat and oil resistant so it is incorporated into friction materials (e.g. brake linings). The asbestos fibres combine with various types of natural or synthetic resins to the development of a variety of products and applications. In asbestos fibres mainly chrysotile was used into rubber matrices yields materials that were used fabrication of packings and gaskets and heavy task insulation components as a compressed board with or without silicone resin impregnation.

Asbestos fibres also have found broad application as reinforcing agents in coatings and adhesive formulations. In the United States, the major use of asbestos fiber in roofing compounds (62%), gaskets (22%), and friction products (11%). Some quantity of asbestos also is used for manufacture insulation products and woven and plastic products (Encyclopedia of Earth home page, 2011). Asbestos composites have a broad range of applications in various industries (marine, railway, and automotive, aerospace and general engineering industries). Asbestos cloth or fibre impregnated with resins and cured under heat and pressure to fabricate sheets, rods, tubes and shaped mouldings. Asbestos causes serious health hazards, which include a range of lung, eye, and skin diseases. Thousands of deaths in the twentieth century cause by Asbestos. In many developed countries today, asbestos-related deaths are the occurred at the place of work. Asia, being the largest consumer of asbestos concern (Handbook of composites reinforced, wiley-vch, 1993). In recent years, use of asbestos in many applications has decreased, due to various environmental concerns.

Asbestos Product	Substitute Products
Asbestos-Cement Corrugated Roofing	• Vegetable fibres in asphalt Slate
Asbestos-Cement Flat Sheet (ceilings, facades, partitions)	• Fibre-cement using vegetable/cellulose fibres • Softwood frame with plasterboard or calcium • silicate board facing
Asbestos-Cement Pipe	• Cellulose/PVA fibre-cement pipe • Cellulose-cement pipe
Asbestos-Cement Water Storage Tanks	• Cellulose-cement • PVA-cellulose fibre-cement

Source: Castleman, (2009); Soyouwanna, home page, (2011).

Table 9.3.1 Asbestos Substitute Products

10. Conclusions

Due to various environmental concerns natural fibre has been gaining special attention of technologist, engineers, industrial and manufacture for its enormous potential for

application in different engineering utility in the area of building constuction, railway, automotive, packaging, defence etc. Further, natural fibre composite is cost effective, low density, renewable material, environment friendly and reduces CO_2 evolution. These natural fibres have been in use as reinforcing agent in polymeric, cement, matrix to increase the physical, mechanical/engineering properties. Plant, animal and asbestos fibre are the main class of natural fibres which are extensively used in product development and manufacturing. Among them, plant fibres percentage use is much higher than the animal and asbestos fibres, due to its renewability, recyclabilty, availability, environment friendliness. Utilization of animal fibre in composite making is an emerging area, because waste animal fibre can be utilized in useful technical application, whereas asbestos fibre has attractive mechanical, thermal, acoustic properties which can enhance its use in engineering application. But due to its carcinogenic nature many developed and developing country prohibited its use because this causes various types of diseases. So researchers are eager to develop alternative to traditional asbestos reinforced composite materials.

Animal fibres are not yet been exploited and can be used as a reinforcing medium for composite making. Composite manufacturing in this area is limited due to availability of fibre but it is emerging area of feather research. Moreover the resultant products will leads to convert the waste into wealth. Tensile strength of wool and silk is 125-200 MPa and 650-750 MPa respectively and its composite showed tensile strength 30-55 MPa. Huge range of plant fibre with wide variation in their physical, chemical and mechanical properties were found in nature and can be enhanced by different genetic and biotechnological route. Tensile strength of different plant fibres were found in the range of about 650MPa with varying density from 0.2-2 g/cm^3. Series of composite of different plant fibre with different matrix has been made and utilized in different applications. Advantage of using natural fibre in composites is that they would be sustainable, biodegradable and bio-derived. It is therefore suggested that biodegradable / bio-derived matrix should be developed to meet the future challenges to safeguard nonrenewable resources and comply with Kyoto protocol for sustainable environmental sound management and save our mother earth.

11. Acknowledgement

The authors are thankful to Dr. Anil K. Gupta, Director, Advanced Materials and Processes Research Institute (AMPRI) Bhopal, Council of Scientific and Industrial Research (CSIR) India, for the support and permission to publish this article. The moral support and contribution of Mr. Pavan K. Srivastava at various levels is thankfully acknowledged. Thanks to Mr. Dharam Raj Yadav and other staff of the Building Materials Development Group AMPRI, Bhopal for their valued contribution. Authors are also grateful to CSIR, New Delhi, India for the valued support.

12. References

[1] ATSDR, home page, accessed on 10-11-2010, http://www.atsdr.cdc.gov

[2] Akers, S. A. S., & Garrett, G. G. (1983). Observations and predictions of fracture in asbestos-cement composites. Journal of Materials Science, Vol. 18, pp. (2209-2214)

[3] Akers, S. A. S., & Garrett, G. G. (1986). The influence of processing parameters Lee on the strength and toughness of asbestos cement composites, Longman group ltd

[4] Arai, K., Sasaki, N., Naito, S., & Takahashi, T. (1989). Crosslinking structure of keratin. determination of the number of crosslinks in hair and wool keratins from mechanical properties of the swollen fibre. *Journal of Applied Polymer Science*, Vol. 38, pp. (1159-1172)

[5] ATSDR, home page accessed on 03/04/2011, http://www.atsdr.cdc.gov/toxprofiles/tp61.pdf

[6] Baiardo M., Zini E., & Scandola, M. (2004). Flax fibre–polyester composites. *Composites: Part A*, Vol. 35, pp. (703–710)

[7] Barone, J.R., & Schmidt, W.F. (2005). Polyethylene reinforced with keratin fibres obtained from chicken feathers. *Composites Science and Technology*, Vol. 65, pp. (1173-181)

[8] Berivan, Erik, Hasan, H., Sebnem A., & Nuriye, K. (2008). Biomechanical properties of human hair with different parameters. *Skin Research and Technology*, Vol. 14, pp. (147–151)

[9] Bisanda E.T.N., & Ansell M.P. (1991). The effect of silane treatment on the mechanical and physical properties of sisal-epoxy composites. *Compos Sci Technol,* Vol. 41, pp. (165–178)

[10] Bledzki, A., & Gassan, J. (1999). Composites reinforced with cellulose-based fibres. *Progress in polymer Science*, Vol. 24, pp. (221- 274)

[11] Bledzki, A.K., Mamun, A.A., Lucka-Gabor, M., & Gutowski, V.S. (2008). The effects of acetylation on properties of flax fibre and its polypropylene composites. *Express Polymer Letters,* Vol.2, No.6, pp. (413–422)

[12] Blicblau, A.S. (1997). Novel composites utilizing raw wool and polyester resin, *Journal of Materials Science C Letters,* Vol. 16, pp. (1417–1419)

[13] Bonser, R.H.C., & Purslow, P.P. (1995). The Young's modulus of feather keratin. *Journal of Experimental Biology,* Vol. 198, pp. (1029-1033)

[14] Braaten, & Ann, W. (2005). Wool, In Steele, Valerie. *Encyclopedia of Clothing and Fashion*, pp. (441–443)

[15] Britannica, home page, accessed on 2011 http://www.britannica.com, 2011

[16] Burdeti, G. (2007). Investigation of the chrysotile fibres in an asbestos cement simple, Harper hill, buxton derbyshire, www.hst.gov.uk

[17] Cameron, G., Wess, T., & Bonser, R. (2003). Young's modulus varies with differential orientation of keratin in feathers. *Journal of Structural Biology*, Vol. 143, No. 2, pp. (118–23)

[18] Cantero, G., Arbelaiz, A., Llano-Ponte, R., & Mondragon, I. (2003). Effects of fibre treatment on wettability and mechanical behavior of flax/polypropylene composites. *Composites Science and Technology,* Vol. 63, pp. (1247–1254).

[19] Castleman, B. (2009). Substitute for asbestos cement construction products, http://ibasecretariat.org/bc_subst_asb_cem_constr_prods.php

[20] CDCP, home page, accessed on 2010 http://www.cdc.gov/niosh/topics/asbestos

[21] Chand, N., Tiwary, R.K., & Rohatgi, P.K. (1988). Bibliography resource structure properties of natural cellulosic fibers –an annotated bibliography. *J Mater Sci*., Vol.23, No. 2, pp. (381–387)

[22] Chand N., & Hashmi S. (1993). Effect of plant age on structure and strength of sisal fiber. Met Mater Process,Vol. 5, pp. (51–57)

[23] Chand, N., & Joshi, S.K. (1994). Temperature dependence of dielectric behavior of sisal fiber. J Mater Sci Lett., Vol. 13, pp. (156–158)

[24] Composite Fabrics, home page, accessed on Dec 2010, http://218.189.210.187/ Apparel Key/Document

[25] Craven, J. P., Cripps, R., & Viney, C., (2000). Evaluating the silk/epoxy interface by means of the Microbond Test. *Composites Part A: Applied Science and Manufacturing*, Vol. 31, pp. (653-660)

[26] D'Arcy, J.B. (1986). *Sheep Management & Wool Technology*. NSW University Press, Kensington, ISBN 0 86840 106 4

[27] Dasgupta, A., & Agarwal, R. K. (1992). Orthotropic Thermal Conductivity of Plain-weave: Fabric Composite Using a Homogenization Technique. *Journal of Composite Materials,* Vol. 26, No.18, pp. (2736-2758)

[28] Dash, B.N., Rana, A.K., Mishra, H.K., Nayak, S.K., Mishra, S.C., & Tripathy, S.S. (1999). Novel, low-cost jute-polyester composites. Part 1: processing, mechanical properties, and SEM analysis. *Polymer Composites*, Vol. 20, No. 7, pp. (62-71)

[29] Dawber, R. P. R., & Messenger, A. G. (1997). Hair follicle structure, keratinization and the physical properties of hair. In: Dawber RPR, ed. Physical properties of hair. *Oxford: Blackwell Science*, pp. (45–50)

[30] Doan, T.L., Brodowsky, H., & Mader, H. (2007). Jute fibre/polypropylene composites II. Thermal, hydrothermal and dynamic mechanical behavior. *Composites Science and Technology,* Vol. 67, pp. (2707–2714)

[31] Doan, T.L., Gao, S., & Mader, E. (2006). Jute/polypropylene composites. Effect of matrix modification. *Composites Science and Technology*. Vol. 66, pp. (952 -963)

[32] Encyclopedia of Earth home page, accessed on 04/03/2011, http://www.eoearth.org

[33] Felix, J. M., & Gatenholm, P. (1993). *J. Appl. Polym. Sci.*, pp. (699)

[34] Feughelman, M. (2002). Natural Fibres, *Journal of Applied Polymer Science,* 83, pp. (489 – 507),

[35] Fonseca, V.M., Fernandes, V.J., Carvalho, L.H., & Almeida, J.R.M. (2004). Evaluation of the mechanical properties of sisal–polyester composites as a function of the polyester matrix formulation. *Journal of Applied Polymer Science*, Vol. 94, pp. (1209–1217)

[36] FAO, home page, accessed on 12/12/2010, http://www.fao.org

[37] Franbourg, A., Hallegot, P., Baltenneck, F., Toutain, C., & Leroy, F. (2003). Current research on ethnic hair. *J Am Acad Dermatol, Vol.* 48, pp. (115–119)

[38] Gassan, J.,& Bledzki, A.K. (1997). Effect of Moisture Content on the Properties of Silanized Jute-Epoxy Composites. *Polym Compos.,* Vol.18, No. 2, pp. (179-184)

[39] George, B.R., Bockarie, A., McBride, H., Hoppy, D., & Scutti, A. (2003b). Keratin Fibre Nonwovens for Erosion Control. Natural Fibres, Plastics, and Composites – Recent Advances. Kluwer Academic Publishers, pp. (67-81)

[40] Gohil, P.P., & Shaikh, A.A. (2010). Experimental investigation and micro mechanics assessment for longitudinal elastic modulus in unidirectional cotton-polyester composites. *International Journal of Engineering and Technology*, Vol. 2, No.2, pp. (111-118)

[41] Hair Dressing, home page, accessed on 12/03/2011, http://www.hair-dressing.com, 2011

[42] Hatta, N., & Akmar, N. (2008). Mechanical properties of polystyrene/polypropylene reinforced coconut and jute fibers, *Proceedings of CUTSE International Conference 2008*, Miri, Sarawak, Malaysia, 24-27 November 2008.

[43] Hong, C.K., & Wool, R.P., (2005). Development of Bio-Based Composite Materials from Soybean Oil and Keratin Fibres. *Journal of Applied Polymer Science*, Vol. 95, pp. (1524-1538)

[44] Hornik, C., Krishan, K., Yusuf, F., Scaal, M., & Brand-Saberi, B. (2005) Dermo-1 misexpression induces dense dermis, feathers, and scales. *Developmental Biology,* Vol. 277, No. 1, pp. (42–50)

[45] Juez, J.L., & Gimier, L. (1983). Ciencia cosmética. 2. ed. Madrid: Soc. Espanhola de Quim. Cosmet, pp. (98-119)

[46] Kaith, B.S., Singha, A.S., Kumar, S., & Kalia, S. (2008). Mercerization of flax fiber improves the mechanical properties of fiber-reinforced composites. *International Journal of Polymeric Materials*. Vol. 57, pp. (54–72)

[47] Kardos, J.L. (1985). *Molecular Characterisation of Composite Interfaces (*Plenum Press), H. Ishida and G. Kumar, eds., New York

[48] Karus, M., & Gahle, G.C. (2006). Use of natural fibers in composites for the German automotive production from 1999 till 2005. Slowed growth in the past two year's new production techniques arising. Nova-Institut, Hurth.

[49] Kolar, G., & Miller, A. (1972). Hair straightness. In: BALSAM, M.S.; SAGARIN, *E. Cosmetics science and technology*. 2. Ed. New York Interscience, cap.22, pp. (150-277)

[50] Lamy, B., & Pomel, C. (2002). Influence of fiber defects on the stiffness properties of flax fibers-epoxy composite materials. *Journal of materials science letters*. Vol. 21, pp. (1211 – 1213)

[51] Lee, D. G. & Kim, S.S. (2004) Failure analysis of asbestos–phenolic composite *journal bearing, Composite Structures,* Vol. 65, pp. (37–46)

[52] Legionnaire Archery home page. Accessed on 10/05/2011, http://www.legionnairearchery.com

[53] Lewis, D. M. (1989). Damage in Wool Dyeing, *Review of Progress in Coloration.* Vol. 19, pp. (49 – 55)

[54] Linus Pauling, & Robert, B. C. (1951). The Structure of Feather Rachis keratin. *Proceedings of the National Academy of Sciences of the United States of America,* pp. (256–261)

[55] Liu, X.Y., & Dai, G.C. (2007). Jute fibre/polypropylene composites II. Thermal, hydrothermal. *Express. Polym. Lett*., Vol. 1, pp. (299)

[56] Lu, X., (2004). Environmental degradability of self-reinforced composites made from sisal. Compos Sci Techno, Vol. l64, pp. (1301–1310)

[57] Maacenter, home page, accessed on 05/04/2011, http://www.maacenter.org/asbestos

[58] Madehow, home page, accessed on 2010, http://www.madehow.com/Volume-6/Cotton.html

[59] Madehow, home page, accessed on 25/04/2011, http://www.madehow.com

[60] Marais, S., Gouanve, F., Bonnesoeur, A., Grenet, J., Poncin-Epaillard, F., Morvan, C., & Metayer, M. (2005). Unsaturated polyester composites reinforced with flax fibers: effect of cold plasma and autoclave treatments on mechanical and permeation properties. *Composites: Part A.* Vol. 36, No. 7 pp. (975–986)

[61] Maschinenwesen, D.F. (2006). Investigation on jute fibres and their composites based on polypropylene and epoxy matrices. PhD Dissertation, University of Dresden Vietnam

[62] MATBASE, home page, accessed on 16/12/2010, http://www.matbase.com

[63] Menandro, N. A. (2010). Waste Chicken Feather as Reinforcement in Cement-Bonded Composites, Philippine Journal of Science, Vol. 139, No. 2, pp. (161-166)

[64] Mesothelioma Research Foundation of America (MESORFA), home page, accessed on 15/04/2011, http://www.mesorfa.org

[65] Mishra, H.K., Dash, B.N., Tripathy, S.S., & Padhi, B.N. (2000). A Study on mechanical performance of jute –epoxy composites. *Poly.-Plast.Technol. Eng*., Vol. 39, No. 1, pp. (187–198)

[66] Mohanty, A.K., Misra, M., & Drzal, L.T. (2005). *Natural fibers biopolymers and biocomposites* (1 edition), CRC press, ISBN 084931741X

[67] Mohanty, S., Verma, S.K., Nayak, S.K., & Tripathy, S.S. (2004). Influence of fiber treatment on the performance of sisal–polypropylene composites. *Journal of Applied Polymer Science*. Vol. 94, pp. (1336–1345)

[68] Nair, K.C.M., & Thomas, S. (2003). Effect of Interface modification on the mechanical properties of polystyrene-sisal fiber composites. *Polymer Composites*, Vol. 24, No. 3, pp. (332- 343)

[69] Neste, D. V., & Shaker, G. (2001). Specific Action of Hair Cosmetics in Hair Surface (Cuticula), Cortex, and Medulla. *Handbook of Cosmetic Science and Technology*. Marcel Dekker, Inc., pp. (577– 580)

[70] Oever, M.J.A.V., BOS, H.L., & Vankemenade, M.J.J.M. (2000). Influence of the Physical Structure of flax fibres on the mechanical properties of flax fibre. *Applied Composite Materials.Vol.* 7, pp. (387–402)

[71] Oksman, K., Wallstro, L., Berglund, L.A., & Filho, R.D.T. (2002). Morphology and mechanical properties of unidirectional sisal–epoxy composites. *Journal of Applied Polymer Science*, Vol. 84, pp. (2358–2365)

[72] Oosthuizen, D., & Kruger, D. (1994). The use of Sisal Fiber as natural geotextile to control erosion. In: Rao GV, Balan K (eds) *proceeding of the fifth international conference on geotextiles, geomembranes and related products*, *Singapore, coir geotextiles – emerging trends.* The Kerala State Coir Corporation, Kerala, India

[73] Oudshoorn, K. (1995). Biogas from sisal waste – a new opportunity for the sisal industry in Tanzania. Energy Sustain Dev, Vol. 2, No.4, pp. (46–49)

[74] Patent: Ignace Verpoest Aart Willem Van Vuure Nedda El Asmar Jan Vanderbeke. (2010). Silk fibre composites, 20100040816, Washington, DC, US

[75] Patra, A., Bisoyi, & D.K. (2010). Dielectric and impedance spectroscopy studies on sisal fiber–reinforced polyester composite. *J Mater Sci,* Vol.45, No.21, pp. (5742–5748)

[76] Perez-Rigueiro, J., Viney, C., Llorca, J., & Elices, M., (2000). Mechanical properties of singlebrin silkworm silk. *Journal of Applied Polymer Science*, Vol.75, pp. (1270-1277)

[77] Pettingill, O.S. Jr. (1970). Ornithology in Laboratory and Field. Fourth edition. Burgess Publishing Company, pp. (29–58)

[78] Prum, R. O., & Brush, A. H. (2002). The evolutionary origin and diversification of feathers. *The Quarterly Review of Biology,* Vol. 77, No. 3, pp. (261–295)

[79] Prum, R.O., & Brush, A. H. (2003). Which Came First, the Feather or the Bird? Scientific American, Vol. 288, No. 3, pp. (84–93)

[80] Purslow, P. P., & Vincent, J. F. V. (1978). Mechanical properties of primary feathers from the pigeon. *J. exp. Bid*., Vol. 72, pp. (251-260)

[81] Quazi, T. H., Shubhra, A. K. M. M., Alam, M. A., Gafur, Sayed M., Shamsuddin, Mubarak A., Khan, M., Dipti Saha, M. A., Quaiyyum, J. A., Khan., M. D., &

Ashaduzzaman, M.D. (2010). Characterization of plant and animal based natural fibers reinforced polypropylene composites and their comparative study, *Fibers and Polymers*, Vol. 11, PP. (725-731)

[82] Ray, D., Sarkar, B. K., Rana, A. K. & Bose, N. R. (2001). Effect of alkali treated jute fibres on composite properties. *Bulletin of Materials Science.* Vol. 24, No. 2, pp. (129-135)

[83] Reading, home page, accessed on 20/04/2011, http://www.reading.ac.uk

[84] Roberta, B. C. (2004). Asbestos, its Chemical and Physical Properties; Second in a series of articles on asbestos: Its history, chemical and physical properties, uses, health hazards and the legal implications of asbestosis & mesothelioma

[85] Rong, M.Z., Zhang, M.Q., Liu, Y., Yan, H.M., Yang, G.C., & Zeng, H.M. (2002). Interfacial interaction in sisal epoxy composites and its influence on impact performance. *Polymer Composites,* Vol. 23, No. 2, pp. (182-192)

[86] Rowell R.M., Schultz T.P., & Narayan R. (1992). Emerging technologies for materials and chemicals for biomass. *Series of ACS Symp*, ISBN 13 : 9780841221710, Washington, D.C., August 26-31, 1990 Saheb, D. N. & Jog, J. P. (1999). Natural fiber polymer composites: A Review., Advances in Polymer Technology, Vol. 18, No. 4, (351–363)

[87] Sang Muk Lee, & Donghwan, Cho. (2005). Department of Polymer Science and Engineering, Kumoh National Institute of Technology, Korea

[88] Saxena, M., Asokan, P., & Bakshi, P. (2008). Sisal potential for engineering application–an overview. In: Sisal fiber technologies for sustainable rural employment generation. Allied Publications, New Delhi, pp. (112–154)

[89] Saxena, M., Murali, S., & Nandan, M.J. (2005). Sisal Potential for employment generation and rural development. In: 3rd International Conference Rural India, pp. (208–212)

[90] Saxena, M., Pappu, A., Haque, R., & Sharma, A. (2011). Sisal Fiber Based Polymer Composites and Their Applications Cellulose Fibers: Bio- and Nano-*Polymer Composites.* Springer Book ISBN 13 783642173691

[91] Schor, R. & Krimm, S. (1961). Studies on the Structure of Feather Keratin II. A β-Helix Model for the Structure of Feather Keratin. *Biophys J,* Vol. 1, No. 6, pp. (489–515)

[92] Shah, S. P. (1981). Fibre reinforced concretes, a review of capabilities publication C810261. The Aberdeen Group

[93] Shukla, J.P., Ram, R., & Peters, E. (2008). Scope of sisal based geotextile application. In: Sisal fiber technologies for sustainable rural employments generation. Allied Publication, New Delhi, pp. (45–59)

[94] Singh, B., Gupta, M., & Verma, M. (1996). Influence of fiber surface treatment on the properties of sisal-polyester composites. *Polymer Composites* Vol. 17, No. 6, pp. (910-918)

[95] Soyouwanna, home page, accessed on 2011, http://www.soyouwanna.com/asbestos-substitutes-21197.html

[96] Standards Association Of Australia, Australian Standard AS 1146.1-1990 "Methods for impact tests on plastics" (Standards Association of Australia, Sydney.

[97] Sung H.N., Churchill, B. G., & Suh, N. P. (1975). Studies of the flexural properties of asbestos reinforced phenolic composites. *Journal of material science* , Vol. 19, pp. (1741-1750)

[98] Taj S., Munawar, M.A., & Khan, S.U. (2007). Review: Natural fiber-reinforced polymer composites. Proc Pakistan Acad Sci , Vol 44, No.2 , pp. (129–144)

[99] Taylor, A. M., Bonser, R. H. C., & Farrent, J. W. (2004). The influence of hydration on the tensile and compressive properties of avian keratinous tissues. *J. Mater. Sci,*, Vol. 39, pp. (939-942)

[100] Textile Exchange (Teonline), home page. Accessed on 06/03/2011 http://www.teonline.com

[101] US Environmental Protection Agency, home page, accessed on 2011, http://www.epa.gov/asbestos

[102] Valeria, M., Velasco, R., Cristina de Sá Dias, T., Zanardi de Freitas, A., Dias Vieira Júnior, N., Sales de Oliveira Pinto, C.A., Kaneko, T. M., & Baby, A. R. (2009). Hair fiber characteristics and methods to evaluate hair physical and mechanical properties. *Brazilian Journal of Pharmaceutical Sciences*, vol. 45, No. 1, pp. (153-162)

[103] Virta, R. L. (2002). Asbestos: Geology, Mineralogy, Mining, and Uses U.S. Department of The Interior U.S. Geological Survey, Open-File Report 02-149 USGS Science for a changing world

[104] Wang, W., Cai, Z., & Yu, J. (2008). Study on the chemical modification process of jute fiber. *Journal of Engineered Fibers and Fabrics*, Vol. 3, No. 2 pp. (1-11)

[105] Wei, G., Bhushan, B., & Torgerson, P. M. (2005). Nanomechanical Characterization of Human Hair Using Nanoindetation and SEM. Ultramicroscopy, Vol. 105, No. 1–4, pp. (248 – 266)

[106] Wella, A.G. (1999). Wella Hair Structure, Annette Schwan-Jonczyk, Darmstadt, Germany, 1st edition

[107] Wikipedia, home page, accessed on Dec 2010 http://en.wikipedia.org

[108] Wilson, P.I. (1971). Sisal, vol 2. In: Hard fibers research series. Vol. 8, FAO, Rome

[109] Wright, H. (2005). Asbestos, Instructor Dr. Eckhert EHS201, UCLA

[110] Xin, X., Xu, C. G., & Qing, L. F. (2007). Friction properties of sisal fiber reinforced resin brake composites. Wear, Vol. 262, pp. (736–741)

[111] Zhong, J. B., & Wei, J.L.C. (2007). Mechanical properties of sisal fibre reinforced urea formaldehyde resin composites. Express Polymer Letters, Vol. 1, No.10, pp. (681–687)

7

Natural Fiber Polymer Composites Technology Applied to the Recovery and Protection of Tropical Forests Allied to the Recycling of Industrial and Urban Residues

Alessandra de Almeida Lucas[1], José Donato Ambrósio[2], Baltus Cornelius Bonse[3] and Sílvia Helena Prado Bettini[1]
[1]*Universidade Federal de São Carlos, UFSCar*
[2]*Centro de Caracterização e Desenvolvimento de Materiais, CCDM-UFSCar*
[3]*Centro Universitário da FEI*
Brazil

1. Introduction

*"Often when pursuing research into green composites we say we are protecting the environment, that we are working for nature. We may as well stop kidding ourselves – nature will be fine; nature will work out OK and adapt to changes. It´s humans that will cease to exist if we continue the way we are at present. Some scientists and engineers have realized that they need to take responsibility for the outcome of their work. Researching ways of creating faster machines and bigger toys, without due consideration of the effects on the environment or on people, is irresponsible… We need to consider the impact that our material choice and design will have on the society and the environment"**

Generation of residues is inherent to human activities. After the Industrialization Period, with modernization of the society, the amount of industrial and postconsumer residues, together with the associated environmental problems, has been increasing at alarming levels. Residue management has become a major problem in modern society. The search for innovative solutions for the reuse of solid residues increased in the late 20th century and has intensified with growing urgency for environmental preservation. Many residue management solutions aim to add value to residue through the development of new materials and processes.

Natural fiber polymer composites basic technologies are already relatively well established. Excellent textbooks can be found on this theme (Klyosov, 2007; Niska & Sain, 2008; Mohanty et al., 2005). Its concepts can be extended to the reuse of solid industrial and urban residues. In these composites the matrix is a polymer, and wood, vegetable or animal fibers are used as fillers or reinforcements. Both polymer and fiber may have been generated as an industrial or postconsumer residue.

Another environmental problem that must be accounted for is the huge amount of deforested areas worldwide, also a consequence of human activities. Important research has

* Baillie (2004)

been carried out on the possibility of recovering forests using modern concepts of Short Cycle Agrosilviculture, which allow generation of wood, fibers, food, biofuels, oils, pharmaceuticals etc, creating synergy between the recovery and protection of the environment and the development of new materials.
Within this context, the main purpose of this text is to present case studies where wood and natural fiber polymer composites technologies are applied to the recovery and protection of tropical forests allied to the recycling of industrial and urban residues.

1.1 Natural fiber composites

Natural fibers can be classified according to their origin: vegetable, animal or mineral. Vegetable fibers include wood flour (or sawdust) from a huge variety of softwood and hardwood specimens and plant fibers, such as hemp, kenaf, curaua, coir, jute, sisal, bamboo, among others. Animal fibers include silk and leather. The most well-known mineral fibers are glass, boron and asbestos; the latter in disuse nowadays as it has been found to be harmful to humans.
Over the past years sustainable eco-efficient practices and products have gained increasing attention and the use of natural fibers as reinforcement for polymers has been rapidly expanding (Bettini et al., 2010; Bonse et al., 2010; Kalia et al. 2009; Mohanti, 2005; Saheb & Jog, 1999; Sanadi et al, 1994). In certain composite applications biofibers have shown to be competitive in relation to glass fiber (Sudell & Evans, 2005). Advantages of biofibers over synthetic ones include the fact that they are renewable and biodegradable, present low cost, light weight, low energy consumption, carbon dioxide sequestration, low abrasiveness and excellent strength to weight ratio [Sanadi et al, 1994]. Limitations of biofibers as reinforcement in polymers are: difficulties in maintaining homogenization of fiber properties; processing temperature, which should not exceed the degradation temperature of these fibers of around 200°C; and high moisture absorption, which may impair mechanical properties as well as facilitate fungus growth (Kalia et al. 2009). Typical thermoplastic polymers that can be easily processed at temperatures up to 200-220°C, and thus may be used as matrix, include: polypropylene (PP), polyethylene (PE), polystyrene (PS) acrylonitrile-butadiene-styrene (ABS), PVC and more recently polyvinyl butyral (PVB) (Ambrósio et al., 2011).
Vegetable or lignocellulosic fibers consist mainly of cellulose, hemicelluloses and lignin, at major levels and pectin and waxes, at lower levels. In these fibers hollow cellulose fibrils are maintained united by lignin and cellulose. The fibrils have a thin primary wall surrounding a secondary wall, which consists of three layers (S1, S2 and S3). The S2 layer is usually thicker and determines fiber strength. This layer contains helical cellulose microfibers which form a certain angle in relation to fiber orientation. The various types of lignocellulosic fibers (coir, curauá, sisal, sawdust, bamboo etc) present significantly different contents of lignin, cellulose and hemicellulose, rendering very different adhesion and mechanical properties to the composites, as fibers containing higher lignin content tend to present improved compatibility towards non-polar polymers, since lignin is the most non-polar constituent of the fiber. Fiber properties may be altered by this microfibrillar angle, as well as by constituent concentration. Climatic and soil conditions also tend to affect fiber properties.
These fibers are not necessarily cultivated for polymer reinforcement purposes. In many cases the source of natural fibers used as reinforcement is waste or residues from other industries, such as architectural, furniture, wood manufacturing etc. When a commercial product is intended to be developed it is necessary to guarantee a continuous and homogeneous source of wood or fibers.

There are many residue materials generated in great quantities for which no large-scale application has yet been found, such as chromium-treated leather. The treatment of leather with products made of heavy metals such as chromium (chromium oxide) is still allowed in several countries. Leather treated with chromium oxide during the tanning process is used on a large scale in the footwear, automotive, garment and personal protective equipment (PPE) industries, generating a large amount of residue (Ambrósio et al., 2011). Leather fibers are mainly constituted of collagen.

Incorporation of natural fibers into polymers will result in composites with adequate properties only when a set of factors are judiciously controlled in their manufacture, such as moisture and particle size which may adversely affect composite properties. Fiber moisture should not exceed the 1 to 2% range, since excessive moisture can cause internal bubbles in the composites and fiber degradation. On the other hand if the fiber is completely dried, firing explosions can be caused during transport and feeding processing operations. Particle size studies indicate that very small particles may burn during processing, leading to degradation of the thermoplastic composites. Another important factor in the manufacture of these composites is that mixing of the polymer and the fibers should preferably be carried out in twin-screw extruders, which provide high level of mixing and homogeneity resulting in the production of high performance materials. A smooth screw elements profile, a high enough length to diameter ratio (L/D) and degassing zones are factors that must be accounted for. The feed process may also be a problem since the non-homogeneity of fiber surface topography may cause bridging in hoppers. In addition to temperature during extrusion and injection molding, other processing conditions must be carefully chosen to avoid excessive shearing of the fiber: low screw speed, flow rates and back pressure levels. Tools (molds and dies) should also be correctly designed to avoid excessive shear and stagnation regions. Excessive shearing will cause shear heating which consequently can cause fiber degradation.

It is necessary to create an adequate interface between the polymer matrix and the fibers, as in all composites, to generate good stress transfer during loading. Chemical polarity of the matrix will favor interaction with the fibers, since cellulose has a large number of –OH groups on the surface. When the polymer is non polar, such as PP and PE, compatibilizers and coupling agents must be used to improve adhesion between matrix and fibers. They are bifunctional molecules that can interact or even react with both the non polar matrix and with the very polar fiber. Another alternative is to promote chemical attack of the fiber surface, rendering it more irregular to facilitate adhesion to the polymer matrix. Among these the use of compatibilizer has shown to be more efficient in improving interface adhesion.

It should be pointed out that the polymer and the fibers are not the only components in the formulation of these composites. Depending on the final application and the composite, different levels of additives are incorporated: compatibilizers or coupling agents, internal and external lubricants, UV stabilizers, antioxidants, mineral fillers (such as talc, calcium carbonate and mica), flame retardants and smoke suppressants, biocides, acid scavengers, blowing agents, among others (Klyosov, 2007; Niska & Sain, 2008).

1.2 The Amazonian Phoenix Project concept

The Amazonian Phoenix Project is a very clever compilation of an integrated system of sustainable enterprises in Amazon lands, elaborated by Dr. Antonio Donato Nobre, during

his long periods of research in the Rain Forest. Further details can be obtained from the author (Nobre, 2006). The concept of recovery and protection of the Amazon Rainforest of the Phoenix Project can be better viewed in figure 1. The fibers and wood collected from plantations in already deforested areas could be used for biocomposite production in association with polymers from urban and industrial residues. The protection of the Forest would come from the demand for seeds of pioneer, thorny and noble specimens. It should be mentioned that exploitation of the Forest would not be stopped, but it would be done in a very sustainable and well-planned manner.

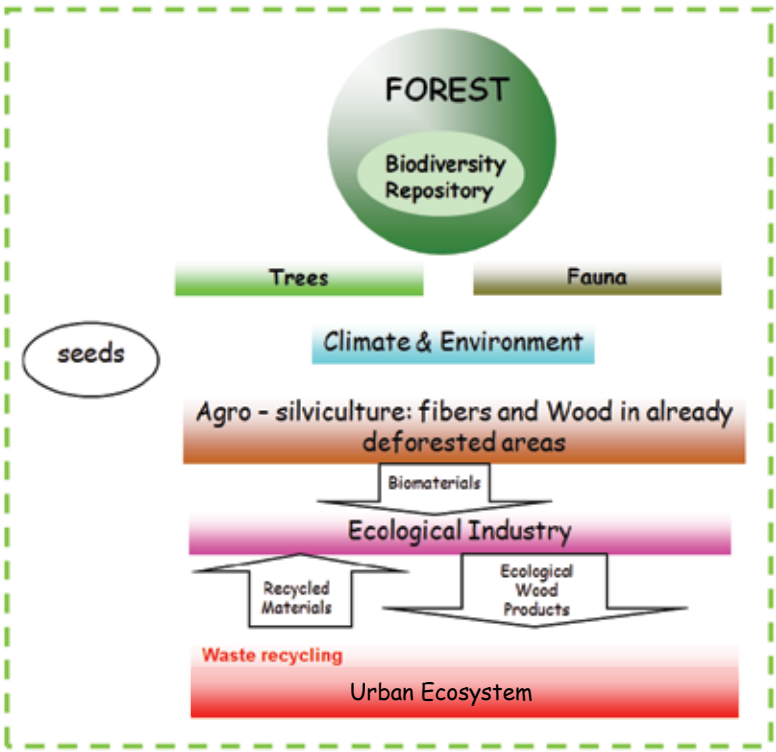

Fig. 1. Principal components of one of the production systems of the Amazonian Phoenix ecosystem (Nobre, 2006)

In the last decades, the Amazon Rain Forest has attracted worldwide attention due to its effect on the water cycles in America, the green house gas emissions caused by burnings, as well as the deforestation caused by the exploitation of timber, grain agriculture and more recently cattle ranching. It is known that deforestation in the Amazon Forest occurs naturally on a very limited scale as a consequence of storms and the Forest has developed very smart self-recovery mechanisms. There are pioneer plant specimens that grow very fast, under very extreme environmental conditions, such as direct sunlight and rain, forming a dense, secondary forest and creating protective conditions for the complex, diverse, massive and long lasting forest that needs this protection for recovery. The pioneer trees have the ability to close the gaps in the forest canopy. Unfortunately, this natural recovery process cannot keep pace with the very high rates of destruction caused by human activities.

Recent studies (Barbosa et al., 2003) have shown that a clever Short Cycle Agrosilviculture System can be used in deforested areas. These pioneer plants can be cultivated with the purpose of collecting fibers and wood of commercial interest, to be used, for example, in wood flour and fiber polymer composites. These pioneer trees include balsawood (*Ochrama Pyramidale*), marupa (*Simarolba amara*) and caroba (*Jacaranda copaia*), surucucumira (Spathelia excelsa). To protect these plantations from young herbivores, they are surrounded by thorny plants such as curaua (*Ananas erectifolius*), pupunha palm (*Bactris gasipae*) and tucum palm (*Astrocaryum vulgare*), just to cite a few among dozens of specimens that can be planted. The planted pioneer trees can be harvested after 2-3 years and be used in several applications including furniture, structural and architectural buildings, biofuels, papers; most of these of very high value added. All these industrial processes will generate residues and byproducts which can be used as fillers and reinforcement in plastics.
As materials engineers and scientists, our role in this project is to evaluate the use of the aforementioned useful specimens in the development of polymer biocomposites. The basic idea is to mimic the regenerative dynamics of the natural ecosystem in Short Cycle Agrosilvicultural Production areas, utilizing a variety of technologies to transform raw wood and fibers from these fast growth native plants into a variety of of high value added materials.

2. Case studies

2.1 Balsa wood polymer composites

As mentioned before, balsa wood (BW) is one of the very fast growing pioneer native species in a plantation on degraded pastureland near Manaus, AM, Brazil (Barbosa et al., 2003). Balsa wood is a very light weight wood and the residues from the processing of sticks, blocks and sheets for model airplanes and building models were used. In this context, balsa wood fiber composites were produced with two polypropylenes as matrices: a virgin (vPP) and a recycled one (rPP), both with MFI = 3.5 g/10min. The BW content was varied from 10 to 30 wt%.
Polypropylene is used as matrix in lignocellulosic fiber composites because of its relatively low melt temperature (165 °C) which allows processing within the limits imposed by the fibers. However, PP is incompatible with these fibers, because of its non polar character against the polar character of the fiber constituents. These differences result in poor adhesion between the phases, with high surface tension, rendering an incompatible system. As compatibilizer Orevac C100, a 1% maleic anhydride grafted polypropylene from Atofina, was used at 2 wt% fixed level.
Mixing was performed in a corotating twin-screw extruder from Imacom, Brazil, (L/D = 40 and a diameter of 30 mm) with a screw profile adequate for natural fiber polymer composites.
The thermal stability of the fiber was evaluated by Thermo Gravimetric Analysis (TGA), where the weight of the sample was monitored as a function of the temperature at a heating rate of 20 °C/min. Figure 2 presents the TG curve and its derivative (DTG). It can be observed that the degradation process of balsa starts at around 200 - 220°C. Therefore, the temperature profile throughout the extruder screw zones was set from 140 °C to 185 °C, from the feed to the metering zone.
The morphology of balsa wood flour can be seen in figure 3, parallel and normal to tree growth. The Scanning Electron Microscopy used was a Zeiss Model Stereoscan 440. A very opened cell structure can be seen, which explains the very low density of balsa wood.

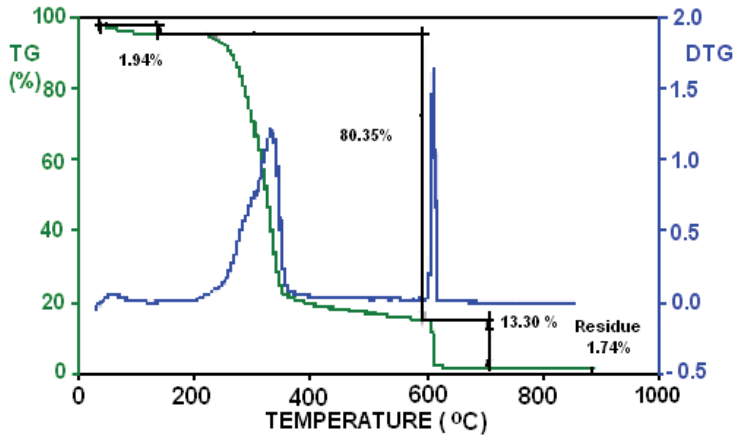

Fig. 2. Thermo gravimetric analysis of balsa wood (Marinelli et al., 2008)

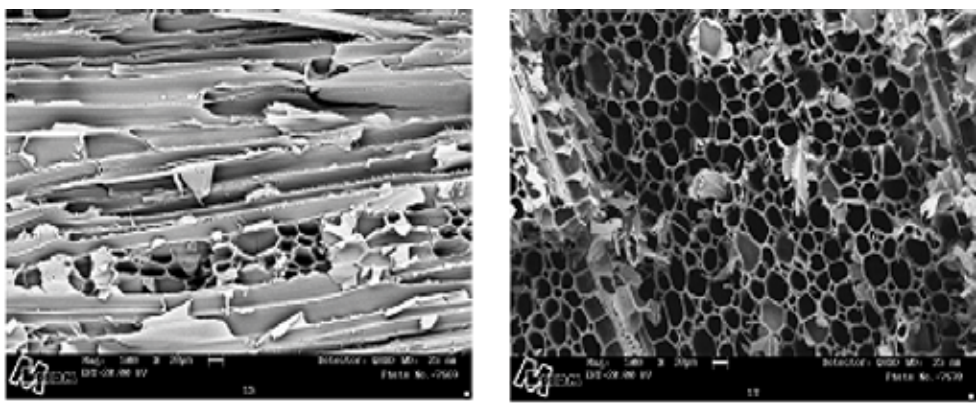

Fig. 3. SEM observation of (b) Longitudinal and (c) Transversal morphology (Marinelli et.al, 2008, Branciforti et al., 2009, Nobre et al., 2009)

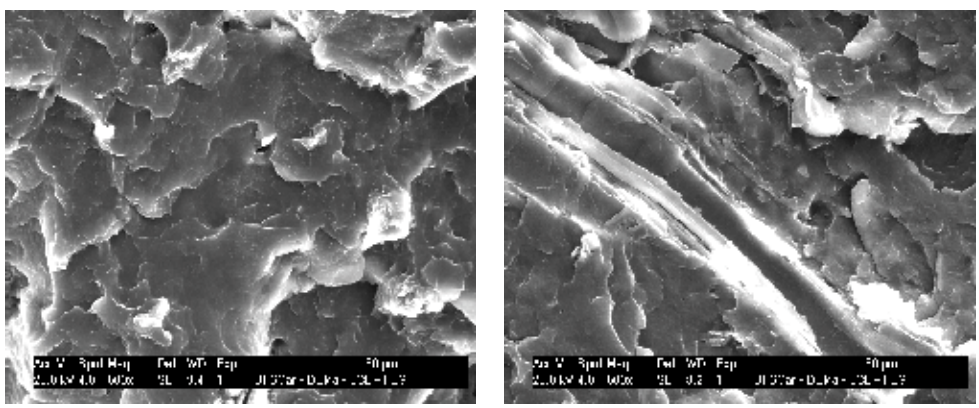

Fig. 4. SEM characterization of the transversal and longitudinal surface of the compatibilized PP/Balsa Wood Composites (80/20) showing the good interface between the fiber and the polymer matrix (Nobre et al., 2009)

Figure 4 presents the SEM morphology of the composite sample vPP/PPgMA/BW (78/2/20), cryogenically fractured and sputtered with gold. The SEM used was FEG from Phillips, model XL30. A very good interface between the fibers and the PP matrix can be observed, since no gaps are seen. This is a very interesting result, especially if we consider that the sample was cryogenically fractured.

Figure 5a and 5b show the mechanical properties of the PP/BW composites under flexural and tensile loading. Both flexural and tensile moduli increase with fiber content. The same trend is observed for flexural strength. The tensile strength of the samples did not change very much. A decrease in this property would be expected if no compatibilizer were used. The amount used was only enough to keep this property similar to that of pure PP. Higher amounts of PPgMa should be used if higher values are desired. Further discussion on compatibilizer level effects is presented in the next case studies.

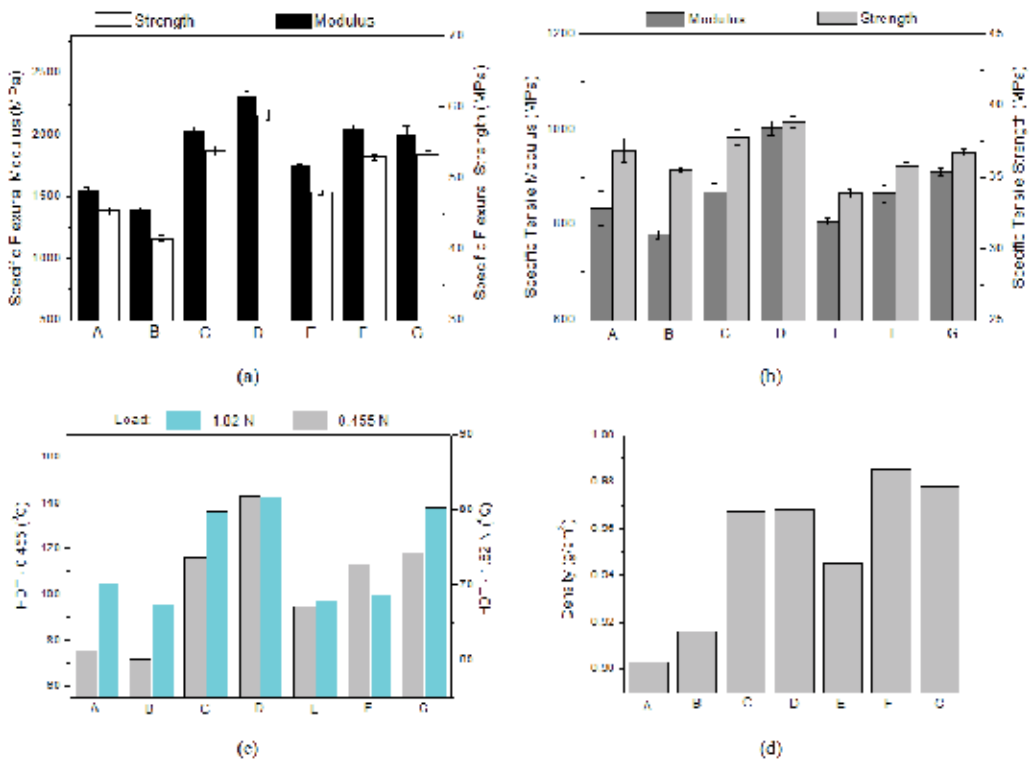

Fig. 5. (a) Flexural Properties; (b) Tensile Properties; (c) Heat Deflection Temperature and (d) Density of the PP/BW composites. Legend: **A**- vPP; **B** – rPP; **C** – vPP/PP-g-AM/BW (78/2/20); **D** - vPP/PP-g-AM/BW (68/2/30); **E** - rPP/PP-g-AM/BW (88/2/10); **F** - rPP/PP-g-AM/BW (78/2/20); G –vPP/rPP/PP-g-AM/BW (39/39/2/20), (Nobre et al., 2009)

Figures 5c and 5d present the Heat Deflection Temperature (HDT) and the density of the composites. HDT is related to the thermal and dimensional stability of the composite under load. At the lower load (0.455 N) HDT of both vPP and rPP increased with increasing BW content. At the upper load (1.82 N) the same behavior was observed for vPP and blend composites, but no changes were observed for the composites containing rPP. All the density values of the samples remained lower than 1g/cm^3, even though a good interface of

the composite phases was observed. Wood flour polymer composites may present density near the density of the cell walls of the wood flour, 1.45 -1.50 g/cm^3, since the wood and fibers are compressible during processing due to the high levels of shear and pressure, causing the hollow cell fibers to collapse or the hollow cells may become filled with polymer or low molecular weight additives. This increase in density was not observed and the low density character of balsa wood fibers was predominant.
Three results must be underlined in this case study: 1) the recycled PP reinforced with 20 wt% balsa wood fibers has presented the same properties of virgin PP reinforced with the same fiber content; 2) all the samples presented a density lower than 1g/cm^3 associated with a very good interface between the fibers and PP matrices and 3) The 30 wt% BW composites have mechanical properties comparable to wood flour PP composites (Niska & Sain, 2008). These results reflect important contributions of recovering recycled PP properties producing light weight composites using balsa wood residues.

2.2 PP/Sawdust composites

Sawdust is a wood processing residue from consumer good manufacture, which is commonly very little used or disposed of. The most common method of disposal is burning, which is economically little feasible as well as environmentally unfriendly. Some countries, mainly European, have therefore created laws that limit burning of cellulose residues.
Incorporation of sawdust in polymers has become a feasible possibility in obtaining products with suitable characteristics for use as a substitute for wood or in applications of important ecological appeal. The sawdust used in this study was waste from a sawmill "indústria Madeireira Uliana Ltda" (Tietê, Brazil) and despite the fact that this waste was ground in a grinder equipment with a 0.8 mm screen to adjust particle size, large dispersion in particle shape and size was observed. Micrographs of the sawdust particles are shown in Figure 6, which shows they are very non-homogeneous in shape and size (Bettini et al., 2008).
Sawdust was collected from a storage silo containing a mix of several Brazilian timber types: pink cedar (*Cedrela* sp), arana cedar (*Cedrelinga cateniformis*), ipê (*Tabebuia* spp), angelim (*Hymenolobiem petroeum*), marupá (*Simarolba amara*), loro vermelho (*Nectanda rubra*), cumarú (*Dipterysa odorata*), and jatobá (*Hymenoea* sp). The relative amounts of the timber types have not been determined.

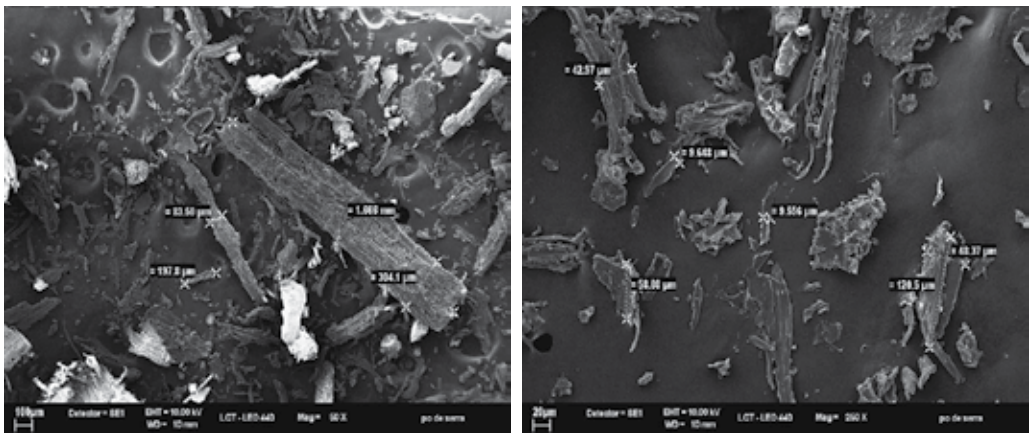

Fig. 6. SEM micrographs of sawdust particles

If we consider that sawmill activities in Amazon lands have a very low productivity level, this study also reflects a very important contribution to the Amazonian Phoenix Project concept, since there are huge sawdust amounts as byproducts of wood exploitation and sawmill activities in the Amazon Forest that may be used for the production of wood polymer composites.
Several studies have been undertaken by our group for better insight into the role of compatibilizers and coupling agents on the adhesion in PP/lignocellulosic composites, as well as the interaction with processing additives, such as lubricants.
Treating the fibers with silane coupling agents has shown little effect on mechanical properties. The main contribution showed to be related to water absorption.

2.2.1 Processing and compatibilizer levels effects

Figure 7 presents micrographs of PP/sawdust composites, with no compatibilizer and containing 3 wt% compatibilizer (PPgMA), extruded in a twin-screw extruder coupled to a Haake torque rheometer in the presence of lubricants.

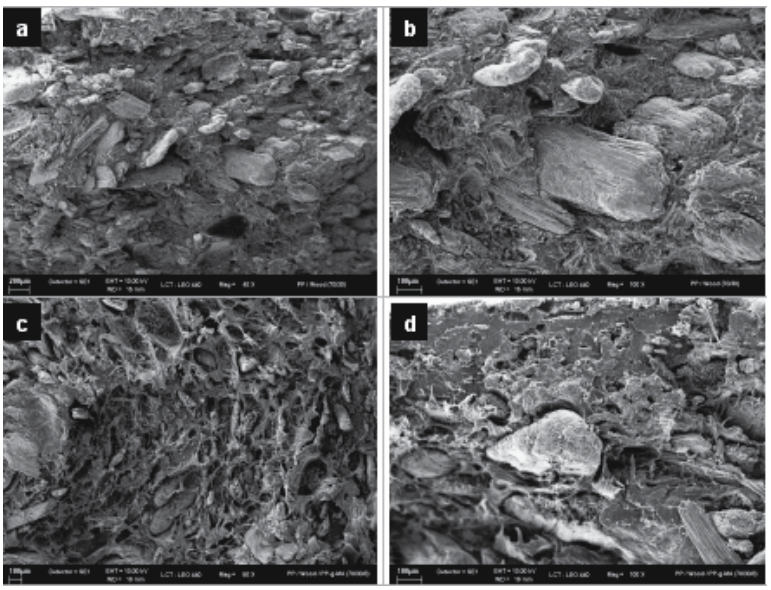

Fig. 7. SEM micrographs of the fractured surfaces of the PP/sawdust/PPgMA compounds: a) and b) 70/30/0, c) and d) 67/30/3 (Bettini et al., 2008)

Figures 7a and 7b show fiber pull-out of the matrix, observed throughout almost the entire sample, indicating poor adhesion between the fibers and the polypropylene. The fractured surfaces in Figures 7c and 7d show pronounced deformation of the polymer matrix and significant reduction in fiber pull-out, indicating the compatibilizer likely affects interface, reducing interfacial tension and improving adhesion.
During Haake extrusion, samples without compatibilizer were difficult to process as they broke easily on exiting the die. Furthermore, these samples presented white spots when injection molded.
Composites were prepared according to a central composite design in which sawdust and PPgMA contents were varied and tensile and flexural properties were assessed. Superior

and inferior concentration levels were 40 and 60 wt% for sawdust and 3 and 5 wt% for PPgMA, respectively.

Multivariate analysis of the properties flexural modulus, tensile strength and % tensile elongation at break of samples, processed in the Haake torque rheometer showed that incorporated sawdust content (independent variable) was the only variable affecting these properties.

The fact that increasing PPgMA content did not affect the dependent variables indicates that PPgMA did not act as compatibilizer, contradicting the preliminary tests, as well as previous investigations (Keener et al., 2004; Oksman & Clemon, 1998; Suarez et al., 2003).

This behavior might arise from two factors: the presence of retained moisture in the pellet, which might have settled at the PP/sawdust interface, impairing compatibilizer effectiveness, and inadequate mixing of the compound. The first factor might be explained by the lack of a degassing zone in the extruder coupled to the Haake rheometer as well as the fact that the extrudate was cooled in a water bath. With regard to inadequate mixing, this might have occurred because of the low L/D ratio (about 28) of the Haake rheometer for composite processing.

It was therefore decided to reprocess the composite pellets in a ZSK 25 Werner & Pfleiderer extruder with two degassing zones. The results were, then, submitted to multivariate analysis and the investigated dependent variables (tensile strength, % elongation at break and flexural modulus) could be fitted in relation to the independent variables (sawdust and compatibilizer content). The results showed that both sawdust and compatibilizer content affected the investigated dependent variables.

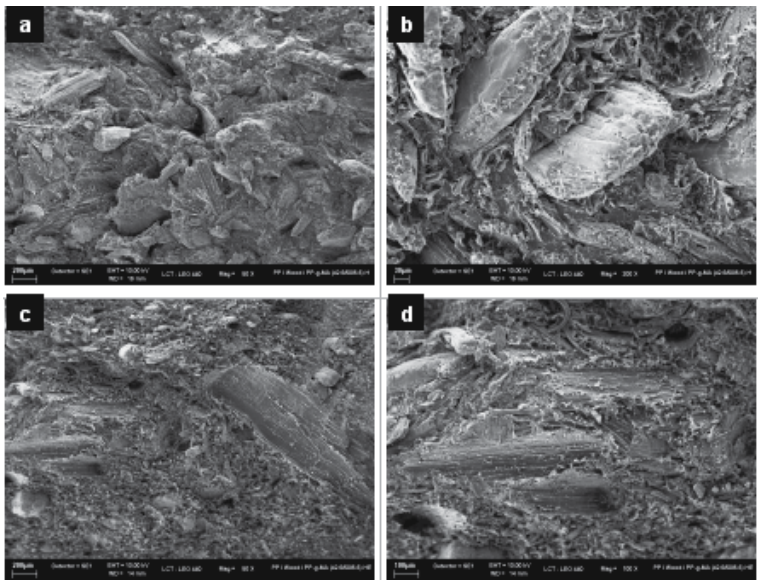

Fig. 8. SEM micrographs of the fractured surfaces of the PP/sawdust/PPgMA compounds (42.5/50/5.5): a) and b) processed in the Haake torque rheometer only (H); c) and d) processed in the Haake torque rheometer and subsequently in the Werner Pfleiderer Extruder (HE) (Bettini et al., 2008)

SEM analysis was performed on the surface of tensile fractured samples PP/Sawdust/PPgMA, 42.5/50/5.5, processed in the twin-screw extruder coupled to the

Haake torque rheometer (H), extruded in the Haake and reextruded in the Werner Pfleiderer Extruder (HE). Figure 8 shows analyses of samples 10H and 10HE.
Comparison between samples H and HE, shown in Figure 8, shows increased deformation of the matrix of the samples reprocessed in the extruder, as well as improved fiber adhesion. The samples processed in the Haake torque rheometer only, showed a less deformed matrix, a greater amount of voids, as well as poor fiber adhesion. This behavior is an indication of the improved adhesion brought about by reprocessing in the extruder due to more adequate mixing and moisture removal.
Analyses of the fractured surfaces (Figure 8) and mechanical properties (Figure 9) show the importance of processing conditions on composite properties. As can be seen both PPgMA and sawdust content influenced mechanical properties. The highest tensile strengths occurred at low sawdust and high compatibilizer contents, indicating that at higher sawdust contents the amount of incorporated compatibilizer should exceed the investigated levels.

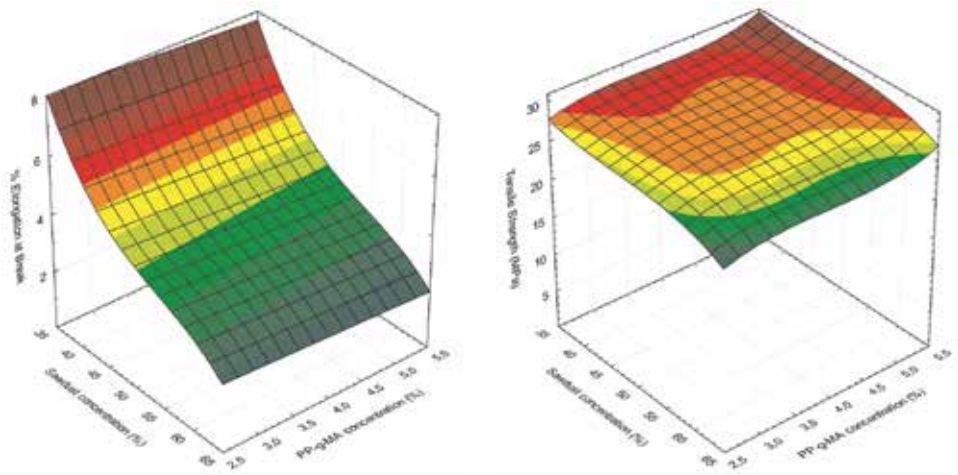

Fig. 9. Effect of sawdust and compatibilizer (PPgMA) concentrations on % elongation at break and tensile strength (Bettini et al., 2008)

2.2.2 Interactions between compatibilizer and lubricants

The wood plastic industry, due to economical reasons, uses expressive loading levels of sawdust, as high as 60 wt%. Hence, a drawback in the processing of these composites is the very high viscosities and, consequently, also very high pressures required, which sometimes can become impracticable.
The addition of lubricants may overcome this difficulty. There are a few works in the literature evaluating lubricants for HDPE based wood composites (Harper and Wolcott, 2003; Li and Wolcott, 2004, 2005, 2006; Santi el al., 2009). In these works, there is some evidence that the compatibilizer, which was maleic anhydride grafted polyethylene (PE-g-MA), acted not only as a compatibilizer, but also as an internal lubricant. Though, depending on the nature of the lubricant, the compatibilization effect may be reduced, Li and Wolcott (2006) did not observe a decrease in compatibilizer efficiency when an ester-based lubricant was used. On the other hand, zinc stearate lubricant reduced PE-g-MA activity.
In a previous study, Bettini et al. (2008) observed that conventional PPgMA concentrations in PP/sawdust composites, when in the presence of ester-based lubricants, were insufficient

to achieve the required mechanical properties. Santi et al. (2009) also noticed that the mechanical properties of HDPE/sawdust composites can be reduced when ester-based lubricant and PE-g-MA compatibilizer are used simultaneously.

The influence of an ester-based lubricant on the compatibilization effect of PP/sawdust composites, both in the presence and absence of PPgMA, were assessed through the analysis of mechanical and rheological properties (Bettini et al., 2010b).

Table 1 presents tensile strength and elongation at break results. Polymer and sawdust contents were maintained at 70 and 30 wt%, respectively, and the sawdust used was ground pinus wood. Increase in sawdust content, without the presence of the compatibilizer, resulted in decrease in both properties, due to the incompatibility between polypropylene and sawdust.

With the introduction of lubricant in the polymer/sawdust system (formulations 10 and 11) tensile strength also decreased. This behavior was expected, since the lubricant does not act as a compatibilizer. Furthermore, the remaining lubricant in the polymer matrix after processing might contribute to the decrease in composite strength due to its low molar mass.

On the other hand, introduction of compatibilizer PPgMA in the composites (formulations 8 and 9) resulted in a noticeable increase in tensile strength in comparison to the non-compatibilized composite. However, at PPgMA contents exceeding 6 wt%, this trend was not observed, indicating that this concentration might be the optimum for the investigated system.

The unexpected decrease in tensile strength when compatibilizer was increased to 8 wt% might be an indication that this additive has reached a limit in the system and is in excess, leading to the formation of an extra PPgMA phase, thus reducing its efficiency.

These results imply that the introduction of compatibilizer in these composites is crucial for the achievement of high tensile strength. However, addition of lubricant to the compatibilized system reduces tensile strength. This suggests that, possibly, the lubricant interacts with the compatibilizer and reduces its efficiency.

The response surface plot of the influence of compatibilizer and lubricant concentrations on tensile strength is presented in Figure 10.

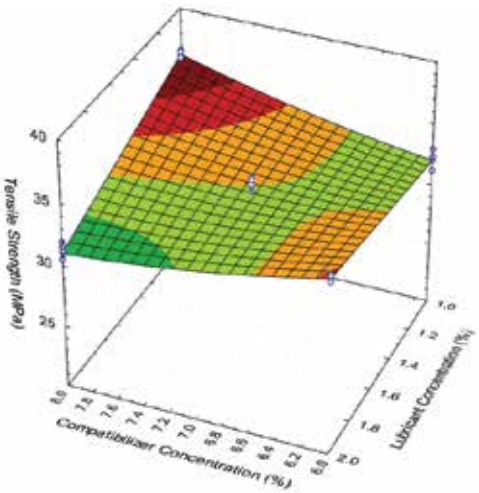

Fig. 10. Effect of compatibilizer (PPgMA) and lubricant (Struktol TPW 113) concentrations on tensile strength (Bettini et al., 2010b)

As can be seen in Figure 10 and Table 1, tensile strength is affected by all variables. For instance, at the lower lubricant level, increasing the amount of the compatibilizer leads to an improvement in tensile strength. However, an opposite trend is observed at higher lubricant level. Despite the assumption that the lubricant could decrease compatibilization efficiency, the higher its amount, the greater are the chances of anhydride or acid groups to interact with sawdust hydroxyl groups. The lowest tensile strength of the composite is achieved when both additives are at their highest level (i.e. 8 wt% compatibilizer and 2 wt% lubricant). As mentioned earlier in this text, there is evidence that when at high concentration levels, the compatibilizer may form a distinct phase in the composite, decreasing compatibilization efficiency.

	C_C (%)	C_{TPW} (%)	Tensile Strength (MPa)	Elongation at break (%)
1	6	1	32.15 ± 0.64	2.76 ± 0.29
2	8	1	36.32 ± 0.26	2.99 ± 0.24
3	6	2	34.33 ± 0.24	3.19 ± 0.20
4	8	2	31.16 ± 0.62	3.24 ± 0.43
5	7	1.5	33.41 ± 0.30	3.11 ± 0.26
6	7	1.5	32.12 ± 0.44	3.22 ± 0.48
7	0	0	30.55 ± 0.71	2.57 ± 0.40
8	6	0	40.35 ± 0.78	4.53 ± 0.48
9	8	0	38.68 ± 0.36	4.28 ± 0.51
10	0	1	28.90 ± 0.42	5.40 ± 1.07
11	0	2	27.91 ± 0.12	4.28 ± 0.78
12	0	0	31.42 ± 0.3	> 500

Table 1. Tensile test results of PP/30 wt% pinus sawdust composite with varying contents of compatibilizer (Cc) and lubricant (C_{TPW}) (Bettini et al., 2010b)

Therefore, if there is less compatibilizer available, due to the formation of a new phase, and if lubricant concentration is at its highest level, which increases the chances of reaction between these additives, then a decrease in compatibilization is expected. This may be a result of the reduced availability of the PPgMA anhydride and/or acid group to interact with the sawdust hydroxyl groups, which might explain the low tensile strength shown by Formulation 4.

Despite the adverse effects of lubricants on the adhesion in PP/sawdust composites, problems encountered at the die exit when high levels of sawdust are incorporated can be overcome by adding external lubricants. Compatibilizer should therefore be used at amounts suited to the required purpose.

2.3 PP/Coir composites

As mentioned, disposal of green coconut husks after consumption of coconut water has great impact in tropical countries like Brazil and has become a sanitation and a public health

problem. Coir is extracted from the green coconut husks and may be used in a wide spectrum of applications such as car seat stuffing, mats, brushes, rope, insulation, as well as reinforcement in polymers.

Coir consists of lignocellulosic fibers, obtained from the mesocarp of the coconut fruit and makes up about 25 % of the nut. Some characteristics of coir are that the fibers are more flexible than glass fiber, nontoxic and can be chemically modified (Tomczak et al., 2007).

The use of coir fiber as reinforcement in polymers has been the object of several works. The most commonly used matrixes include polypropylene (Bettini et al., 2010, 2011; Haque et al., 2009; Ishizaki et al., 2006 Islam et al., 2010; Leblanc et al., 2006; Rozman et al., 2000; Santos et al., 2008; Wambua et al., 2003), natural rubber (Geethamma et al., 1995, 2005) and polyester resins (Monteiro et al., 2006; Prasad et al., 1983; Rout et al., 2001).

Extracted coir usually consists of long fibers and has therefore improved reinforcement potential, as final size may be controlled by grinding. Figure 11 contains micrographs of coir used in our research.

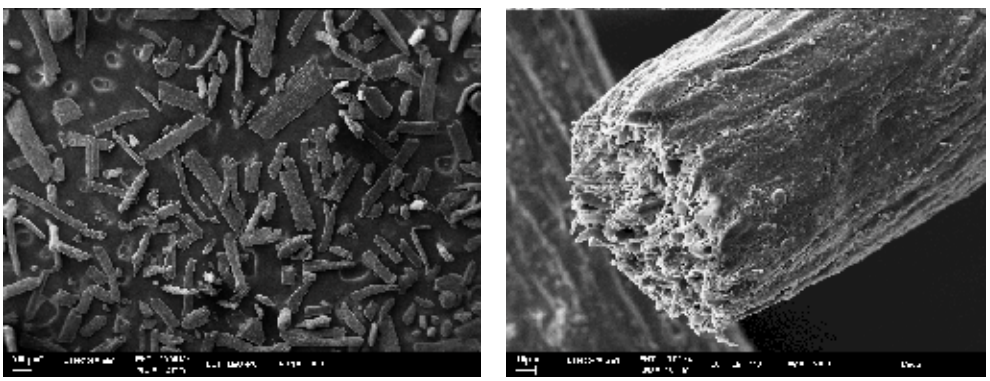

Fig. 11. SEM micrograph of coir fibers (Bettini et al., 2010)

PP/coir fiber composites present the same difficulties regarding adhesion as other lignocellulosic fibers due to the chemical differences between matrix and fiber. Therefore, compatibilizers should be incorporated into these composites. One of the most commonly used compatibilizer in PP/natural fiber composites is maleic anhydride grafted polypropylene (PPgMA).

The effect of lignin as compatibilizer in PP/coir fiber composites has also been investigated by Rozman et al. (2000). This investigation showed that the presence and increase in lignin content increased flexural properties; however no significant increase was seen in tensile properties when compared to the composites without this compatibilizer. For comparison sake PPgMA was also used as compatibilizer in this work and the composites compatibilized with PPgMA showed better mechanical properties than those compatibilized with lignin.

Based on the investigations regarding PP reinforced with sawdust, PP/coir composites were prepared according to a central composite design, employing coir levels of 20 and 40 wt%, and PPgMA levels of 4 and 8 wt%. Adhesion was only achieved in the presence of PPgMA as shown in the SEM micrographs (Figure 12). Figure 13a and Figure 13b present the surface responses of tensile strength and elongation at break, when the independent variables, coir content and compatibilizer content, were varied (Bettini et a., 2010).

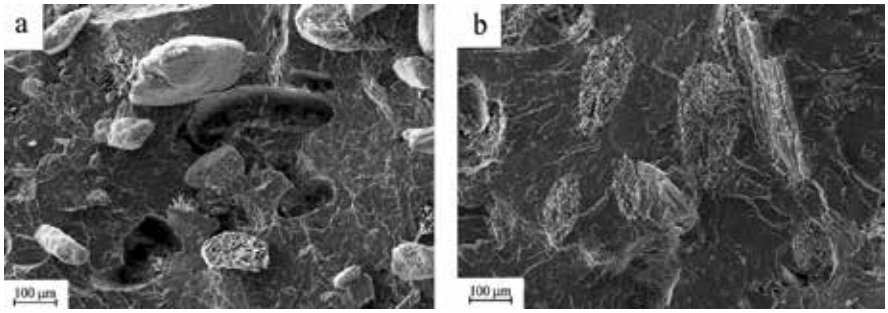

Fig. 12. SEM micrographs of tensile fractured surfaces of 30 wt% CF composites with (a) no PPgMA and (b) 6 wt% PPgMA (Bettini et al., 2010)

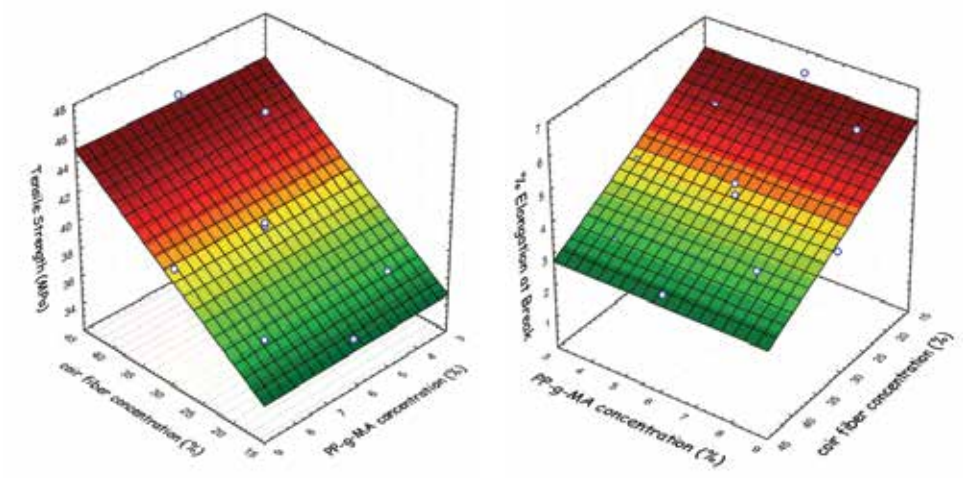

(a) (b)

Fig. 13. Effect of fiber and compatibilizer content (PPgMA) on (a) tensile strength and (b)% elongation at break of the composites (Bettini et al., 2010)

It can be seen in these figures that in the presence of compatibilizer increase in coir fiber content results in increase in tensile strength and a reduction in elongation at break and that the increase in amount of compatibilizer (PPgMA) does not alter the investigated properties. This analysis shows the addition of compatibilizer is important for reducing interfacial tension, with consequent increase in adhesion between the phases. When coir fibers were added to PP without the presence of compatibilizer, tensile strength was seen to reduce with increasing fiber content. So, although the effect of compatibilizer content was not observed, its presence is necessary. It is also verified that for the investigated coir fiber contents and processing used the lower level of PPgMA content would be sufficient to achieve good adhesion.

Compatibilizer did not affect the properties in the investigated range, which means that smaller amounts of compatibilizer could have been used in the PP/coir composites. Some factors may affect this analysis in relation to the concentration of the same compatibilizer in PP/sawdust composites. Different fibers have different contents of lignin, cellulose and

hemicellulose, as well as different structures. Moreover, no ester lubricant, which has already shown to reduce compatibilizer efficiency, was added to the PP/coir composites.
Compatibilized and non compatibilized polypropylene/coir fiber composites were also submitted to fatigue testing. Fatigue life of these composites was also compared with that of pure polypropylene.
Fatigue tests were performed in an MTS 810A servo hydraulic universal testing machine at a testing frequency of 6 Hz. S-N curves were obtained with maximum applied force varying from 1400 N to 850 N; considering that compressive loads could not be applied due to occurrence of buckling, minimum force was maintained at 50 N, resulting in cyclic loadings with the ratio between minimum and maximum stress (R) approximately zero. The results allowed calculating the applied maximum stress as a function of number of cycles to failure. When no fracture occurred, failure was considered when specimen displayed plastic deformation (Bettini et al., 2011).
The data obtained from the fatigue tests allowed the construction of S-N curves presented in Figure 14, which shows that the fatigue behavior of pure PP is different from the behavior of the two composites. These composites exhibit similar behavior, but the compatibilized composite presented longer fatigue life at a same loading.
Results from Figure 14 indicate that incorporation of coir fiber reduces fatigue life of the composite when compared to pure PP, and that the compatibilized composite presents a higher number of fatigue cycles for the same applied stress amplitude, evidencing the need to use compatibilizer.

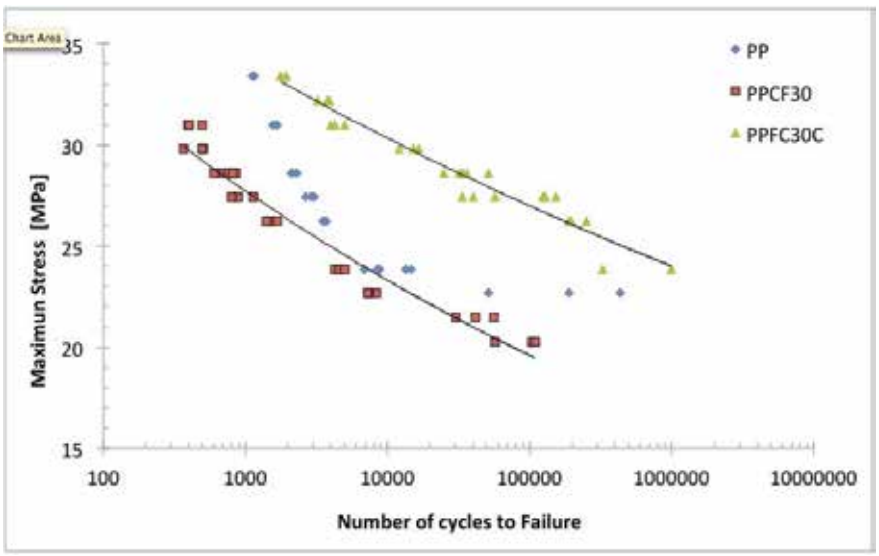

Fig. 14. S-N curves obtained in the fatigue tests, for pure polypropylene (PP), polypropylene /coir fiber composites without compatibilizer (PPFC30) and with compatibilizer (PPFC30C) (Bettini et al., 2011)

An optical pyrometer allowed observing that during the fatigue tests PP heated up to approximately 50°C and failed by yielding instead of rupturing. Initially the center of the specimen whitened, indicating polymeric chain alignment and microfibriling, followed by necking and finally yielding.

This phenomenon was observed in all fatigue tests on PP, however yielding was considerably less at the lowest tested stress (22.67 MPa), where the material, besides yielding, also fractured and the maximum temperature in this test was approximately 30°C.
Specimen heating at higher stresses can be explained by the low thermal conductivity of the polymer. In each cycle the heat generated by molecular friction is not readily dissipated. However, at lower loadings the generated heat is less in each cycle and therefore accumulated heat is less. This indicates that at higher stresses the main failure mechanism in pure polypropylene is thermal fatigue and at low stresses mechanical failure predominates. This change in behavior of the failure mechanisms is also noticed by the inflection of the fatigue curve of pure PP (Figure 14).
The compatibilized and non compatibilized polypropylene/coir fiber composite specimens displayed fracture without macroscopic plastic deformation. The maximum temperature recorded during the fatigue tests of the composites was 30°C, indicating preferential mechanical failure mode. This behavior might be explained by the reduced mobility of the polymer chains due to the presence of fibers, which leads to lower hysteresis and consequently less heat generation compared to pure PP.

2.4 PP/Bamboo fiber composites

Bamboo plantations are another abundant source of natural fibers. Bamboo has a very high strength/weight ratio. Brazil has the largest native giant bamboo plantations in the world, located in Acre, a State in the Southwest region of the Amazon. Approximately every 30 years these plants bloom and die, opening a clearing in the forest, which serves as a source of fires under lightning, contributing to the emission of greenhouse gases. The use of bamboo fibers in composites and laminates, before plant death, not only would avoid the emission of greenhouse gases to the atmosphere but would also serve as an alternative sustainable activity for the local population. There are about 300 different specimens of bamboo in Brazil, around 400 in the whole world. All these populations present the same natural cycle characteristic of flowering followed by death.
In this context an investigation was carried out regarding the effect of fiber size, compatibilizer (maleic anhydride grafted PP) and bamboo fiber content on the physical properties of polypropylene/bamboo fiber composites. Bamboo fibers used were ground waste generated during cutting, milling and finishing operations from a small bamboo laminating mill. Bamboo fiber levels of 20 and 40 wt% were employed and PPgMA levels of 1 and 4 wt%, against the 4 and 8 wt% levels used with coir fibers. As can be inferred from figures 15a and 15b, which show SEM micrographs of 20 wt% bamboo fiber composites with no compatibilizer and with 4 wt% compatibilizer, adequate adhesion could be obtained at 4 wt%. Lack of adhesion in composites without compatibilizer is evidenced in the SEM micrograph of Figure 15a, whereas in Figure 15b the fibers in the composite containing compatibilizer are seen to be well adhered to the matrix.
Except for impact strength, the behavior of all mechanical properties showed similar trends when comparing bamboo and coir fiber composites. Impact strength of coir composites with no compatibilizer increased at increasing coir contents above 20 wt%, whereas that of bamboo fiber composites decreased. It should however be mentioned that depending on composite nature (different fibers with different stiffness) and type of impact test, apparent impact strength may either increase or decrease with fiber content (Nielsen & Landel, 1994).

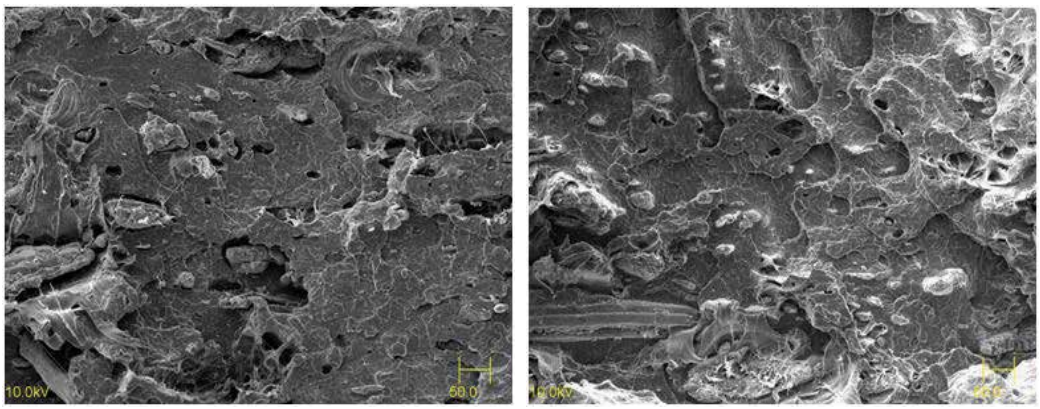

(a) (b)

Fig. 15. SEM micrographs of tensile fractured surfaces of 20 wt% BF composites with (a) no PPgMA and (b) 4 wt% PPgMA. (Bonse et al., 2010)

Comparing tensile strength of 40 wt% compatibilized with non-compatibilized bamboo fiber composite showed increase in tensile strength of 66% and with pure PP an increase of 34%. These values are similar to those obtained with the same amounts of coir fiber and compatibilizer (63% and 35%, respectively), despite the higher reported tensile strength and modulus of bamboo fiber (BF) in relation to coir (Suddell & Evans, 2005). When the same analysis is applied to flexural modulus the compatibilized BF composite showed an increase of 114% in relation to pure PP, against 78% obtained with coir. Thus fiber stiffness seems to have a stronger effect on composite flexural properties than on tensile properties.

In addition to compatibilizer and bamboo fiber content, the effect of fiber size on the physical properties of the composites was also assessed according to a 2x2x2 factorial design. Physical properties assessed were tensile and flexural modulus, tensile and impact strength, percent elongation at break, fatigue life and heat deflection temperature (HDT).

As-received bamboo waste fibers were first submitted to screening after which size distribution measurements by optical microscopy revealed an average equivalent diameter for the inferior and superior level fibers of 0.94 mm and 2.19 mm, respectively.

To assess the effect of fiber size, bamboo fiber and PPgMA content - and possible interactions - on the mechanical properties of the composites, multiple regression analysis was performed by means of software Statistica® on all data used to generate Table 2. The encountered R^2 values indicate that, except for impact strength, the model fits the data reasonably well. Results of the 2x2x2 experimental design are presented in Table 3.

Analyzing Table 3 and the statistically significant effects obtained, it can be concluded that the effect of bamboo fiber size showed to be significant on tensile strength, however to a lesser extent than compatibilizer and BF content, whose effects have already been discussed. Increasing fiber length is expected to increase tensile strength. Fiber ends support less load than the remaining parts of the fiber, so the longer the fiber, the higher its ability to support load. However, reinforcement effect will be small when fiber length is smaller than a certain critical length. This might have been the case here. Fibers were apparently also randomly distributed in the matrix with no preferential orientation in relation to applied load. Fiber size would be more efficient in distributing and transferring applied tensile stress if fibers were aligned parallel to the applied load.

independent variables			dependent variables						
D_{eq} (mm)	BF (wt%)	PPgMA (wt%)	TS (MPa)	ε_{break} (%)	E (GPa)	IS (J/m)	FM (GPa) 0.5%	σflex (MPa)	Fatigue (log cycles to failure)	HDT (°C)
0.94	20	1	37.5±0.3	5.6±0.5	3.15±0.11	11.2±1.6	1.96±0.11	40.8±1.0	2.84±0.03	88.3±0.7
0.94	20	4	40.1±0.2	9.0±0.9	3.33±0.12	11.6±0.3	2.15±0.06	42.6±0.5	3.06±0.05	93.0±0.6
0.94	40	1	38.6±0.1	2.4±0.2	4.64±0.06	10.4±0.6	3.45±0.14	52.8±0.8	2.66±0.19	113.4±1.4
0.94	40	4	46.6±0.5	5.0±0.2	4.68±0.09	10.6±1.8	3.28±0.19	53.1±1.8	4.07±0.11	115.3±.3
2.19	20	1	38.8±0.3	6.6±0.6	3.25±0.12	9.3±0.2	2.42±0.08	37.1±1.1	2.85±0.06	82.8±3.8
2.19	20	4	40.2±0.3	8.7±1.1	3.16±0.08	12.3±0.2	2.51±0.10	40.3±1.3	3.08±0.07	82.7±0.6
2.19	40	1	40.9±0.2	2.8±0.3	4.63±0.07	10.0±0.9	3.27±0.05	46.1±0.7	3.01±0.08	115.3±1.8
2.19	40	4	45.0±0.2	4.3±0.2	4.52±0.09	13.4±0.6	3.57±0.09	54.0±1.1	3.82±0.09	112.8±3.5
neat PP			34.1±0.3	>500	2.22±0.11	12.8±1.3	1.80±0.06	31.4±0.5	3.11±0.03	64.0±0.2

D_{eq}: equivalent diameter; TS: tensile strength; ε_{break}: strain at break; E: tensile modulus;
FM: flexural modulus at 0.5% strain; σflex: flexural stress at 2% strain; IS: notched Charpy impact strength

Table 2. Results of the different tests: average of five specimens, except for fatigue and HDT (three specimens). (Bonse et al, 2011)

	a_0	a_1	a_2	a_3	a_4	a_5	a_6	a_7	R^2
TS (MPa)	40.97	0.26	1.81	1.99	--	-0.65	1.02	-0.34	0.99
ε break (%)	5.55	--	-1.91	1.21	--	--	-0.30	--	0.935
E (GPa)	3.92147	-0.03186	0. 69766	--	--	-0.0518	--	--	0.9815
FM (GPa)	2.8256	0.11715	0.056539	0.05339	-0.088.01	0.04659	--	0.07203	0.9653
σflex (MPa)	45.85	-1.46	5.64	1.66	--	1.13	0.41	0.77	0.9692
Fatigue (Log_{10} cycles to failure)	3.18	--	0.24	0.34	--	-0.08	0.23	-0.08	0.9634
HDT(°C)	100.44	-2.05	13.77	--	1.89	-1.15	--	--	0.9803

TS: tensile strength; ε_{break}: strain at break; E: tensile modulus; FM: flexural modulus at 0.5% strain; σflex: flexural stress at 2% strain

Table 3. Coefficients of the regression model $\mathbf{a_0+a_1x_1+a_2x_2+a_3x_3+a_4x_1x_2+a_5x_1x_3+a_6x_2x_3+a_7x_1x_2x_3}$ used for the different properties (x_1: fiber size; x_2: BF content; x_3: PPgMA content). (Bonse et al., 2011)

The effect of BF size on strain at break, i.e. ductility, was not significant. As expected and already discussed increasing BF content reduces ductility, as fibers impose restraint on molecular mobility. Not surprisingly this variable also showed to be the most important for the apparent elastic modulus. On the other hand compatibilizer has no significant effect on elastic modulus and tends to increase ductility. The interactions promoted by PPgMA likely allowed improved molecular mobility and flow.

Properties obtained in bending mode (HDT, flexural modulus and strength) are strongly affected when fibers are perpendicular to the applied load. The bamboo fibers however were apparently randomly distributed and the effect of BF size was hence less pronounced than the effect of BF content on the flexural properties.

With regard to fatigue life fiber size showed no significant effect, in contrast to fiber and compatibilizer content which tend to maximize fatigue life with increasing contents, similar to their effect on tensile strength. It should be mentioned that fatigue tests were performed in tensile mode.

It can thus be concluded that incorporation of compatibilizers is essential for achieving higher tensile and flexural strength than those of the pure polymer; however, increase in stiffness, proportional to elastic modulus, is obtained even for the non compatibilized composites.

2.5 PVB/wood flour composites

The composites developed with the aforementioned thermoplastics matrixes are usually rigid and generally have low flexibility due to the characteristics of the matrix. Nevertheless, some natural fiber composite applications require rubbery behavior or high flexibility, such as curved coatings, soles and insoles for shoes.

A thermoplastic matrix that fulfills this requirement is an amorphous random copolymer from poly(vinyl butyral) (PVB), produced from the condensation reaction of polyvinyl

alcohol with n-butyraldehyde in the presence of an acid catalyst (Dhaliwal & Hay, 2002; Valera & Demarquette, 2008). The properties of this copolymer, such as elasticity, toughness and adhesion to different substrates depend on the ratio between the monomers in the copolymer. The main application of PVB is in laminated safety glass, particularly in the automotive, aerospace and architectural glass sectors. PVB used in sandwiched laminated glass has between 10% and 35% alkyl phthalate, dibutyl sebacate, triethylene glycol bis (2-ethylhexanoate) or dihexyl adipate plasticizer (El-Din & Sabaa, 1995; Jeong et al., 1998; Saflex®, 2010; Valera & Demarquette, 2008). Due to its molecular structure and the presence of plasticizers, PVB used in automotive glass has properties similar to those of an elastomer (Cha et al., 1998). The production of PVB laminated glass generates large volumes of residues that have not yet been widely destined for recycling.

2.5.1 Preparation of the composites

Prior to extrusion, the leather fibers, wood flour and PVB flakes were dried in an oven at 70°C for 4 hours to remove moisture and prevent degradation. The two composites (PVB/leather and PVB/wood flour) were mechanically mixed in the solid state at three mass proportions and processed in an extruder equipped with a 45-mm diameter Maillefer screw, L/D = 25, and a pineapple mixing element in the metering zone. A flat die (150.0 mm wide, 2.0 mm thick) was used to obtain flexible sheets. The temperature profile was 170/170°C/175°C in the extrusion barrel and 180°C in the extrusion head. After extrusion, the composite sheets were compression-molded at a temperature of 180°C and pressure of 20 ton to improve surface finishing. A final thickness of 3.50 mm was obtained for the samples to be used in mechanical tests. Figure 15 shows a schematic drawing of the extruder screw used for preparing the flexible PVB/leather and PVB/wood flour composites.

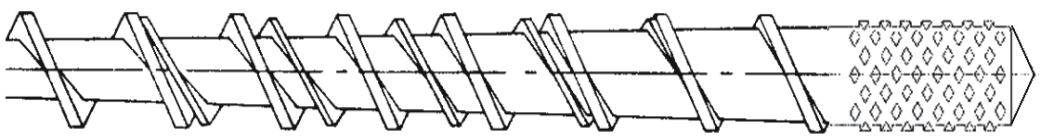

Fig. 15. Maillefer screw with pineapple mixing element in the metering zone (Rauwendaal, 2001)

Results of mechanical properties obtained with flexible composites of PVB/leather and PVB/wood flour, for application as coatings in products such as shoes, cars and architectural design, are presented next.

Figure 16 presents a micrograph of a cryogenically fractured surface of the PVB/wood flour composite sample. Sites exhibiting good interfacial adhesion with continuity of the interface are observed. As previously mentioned it is usually difficult to achieve good adhesion between a nonpolar thermoplastic matrix and natural fibers. One way to improve interfacial adhesion and obtain continuous surfaces in thermoplastic composites containing wood fibers is to use coupling agents or compatibilizers such as maleic anhydride grafted PP (PPgMA) (Oksman & Clemons, 1998). The good adhesion at the interface of the PVB/wood flour composites without the addition of coupling agents or compatibilizers may be due to improved interaction between the PVB matrix and the wood fibers. Just as in the leather fibers, some molecules that compose the chemical structure of the various components of wood contain -OH groups, which may have created hydrogen bonds with PVB molecules.

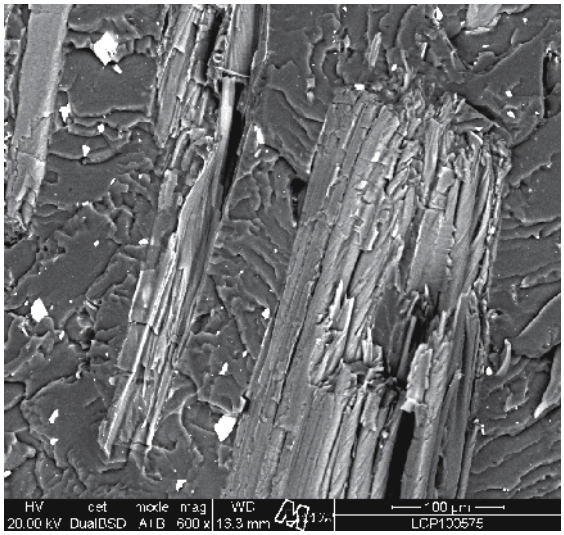

Fig. 16. Cryogenically fractured surface micrographs of the PVB/wood flour (60/40) composite

Figure 17 shows the results of the tensile tests for PVB/wood flour composites. The graph in Figure 17a shows that the tensile strength values of the composites are significantly lower than those found for neat PVB. However, the tensile strength tends to increase when the amount of wood flour in the composites increases from 25% to 55%. The mechanical properties of fiber-reinforced composites depend not only on the characteristics of the polymer matrix and the reinforcement fibers but also on the interface between the matrix and the fiber, which is important for the transfer of interfacial stress (George, 2001; Madera-Santana et al., 2002; Saheb & Jog, 1999). A reduction in tensile strength is a general phenomenon that occurs in the case of thermoplastics filled with natural fillers as the filler loading increases, thereby increasing the interfacial area. The increase in tensile strength with increasing wood flour content observed in the PVB/wood flour composite without the addition of coupling agents or compatibilizers is unusual for thermoplastic composites with natural fibers. This behavior may be related to the good interfacial adhesion observed by the continuity of the wood flour with the PVB matrix shown in Figure 16.

Figure 17b shows the decrease in elongation at break with increasing wood flour content as usually expected in composites where the disperse phase is stiffer than the continuous phase. This behavior is also observed in Figure 17c which presents the tensile modulus as a function of wood fiber content. The increase in Young's modulus show that wood fiber increased composite stiffness.

The low standard deviation and the increase in mechanical properties with leather fiber and wood flour content show that the mixing process in a single screw extruder with Maillefer type screw and pineapple mixing element in the metering zone can produce homogeneous composites.

The PVB/wood flour composites were obtained from fully recycled raw materials, resulting in innovative flexible composite sheets, as seen in figure 18, which can be used as coatings on curved surfaces, allowing freedom of creation and design. The composites showed a good interface between fiber and polymer, observed by Electron Microscopy (SEM).

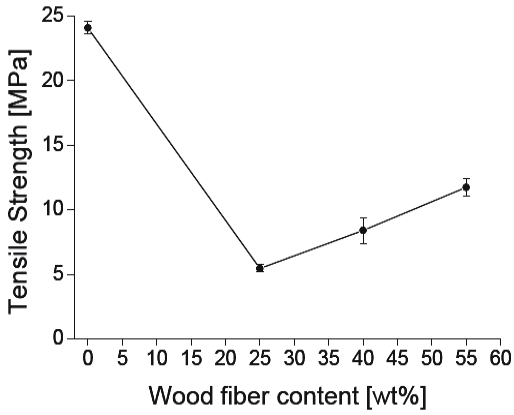

(a)

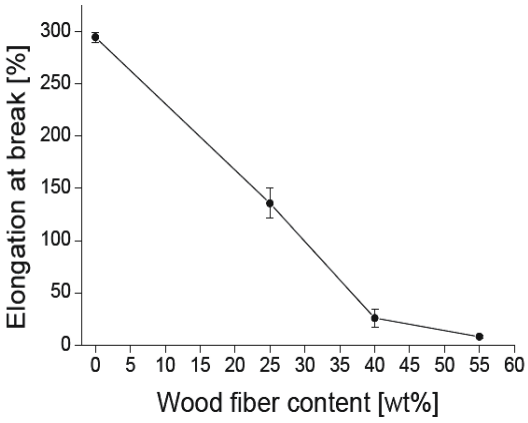

(b)

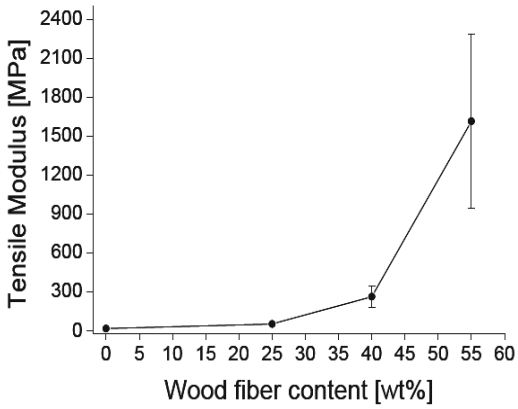

(c)

Fig. 17. Tensile tests results of PVB/wood composites fiber. a) Tensile strength, b) Elongation at break and c) Tensile modulus

Fig. 18. Flexible sheet of PVB/wood flour (60/40) composite

2.6 PVB/Leather composites

Due to the presence of chromium in leather fibers, relatively low processing temperatures must be used, which makes PVB a very interesting polymer matrix for the development of PVB/leather composites.

Figure 19 presents SEM micrographs of cryogenically fractured surfaces of the PVB/leather composite samples, where leather fiber agglomerates appear distributed in the PVB matrix. These composites were obtained by the same process used to prepare PVB/wood flour composites. Although there are some voids in the matrix, possibly due to defibrillation and pull-out of the leather fiber agglomerates, good interfacial adhesion can be observed by the continuity of the leather fiber agglomerates with the PVB matrix (Ambrósio et al., 2011). As mentioned before, good adhesion is usually difficult to achieve between nonpolar thermoplastic matrix and natural fibers due to the polarity differences between the hydrophilic fibers (composed of collagen macromolecules) and the hydrophobic thermoplastic matrices. PVB copolymer contains vinyl alcohol hydroxyl groups which may interact with the OH and -C(=O)-OH groups of the collagen macromolecules in the leather fibers . The interaction of these groups may have created an interface which managed to transfer stress from the PVB matrix to the leather fibers upon cryogenic fracture (Ambrósio et al., 2011).

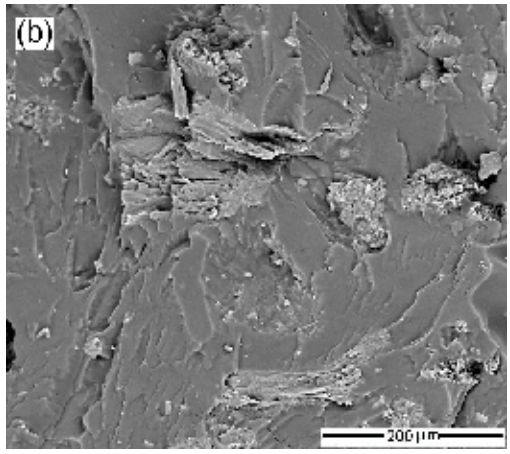

Fig. 19. Cryogenically fractured surface micrographs of the PVB/leather fiber (70/30) composites (Ambrósio et al., 2011)

Figure 20 shows the results of the tensile tests for PVB composites with recycled leather fibers. The elastic modulus increases considerably with increasing amounts of leather fiber in the composite. The elastic modulus increased from 4 MPa for neat PVB to 270 MPa for the composite with 70 wt% leather fiber. Such a rapid and nonlinear increase of the elastic modulus with fiber content is not commonly observed in thermoplastic composites reinforced with natural fibers. As previously discussed, the PVB contains plasticizer, which imparts improved flexibility to the composites (Ambrósio et al., 2011).

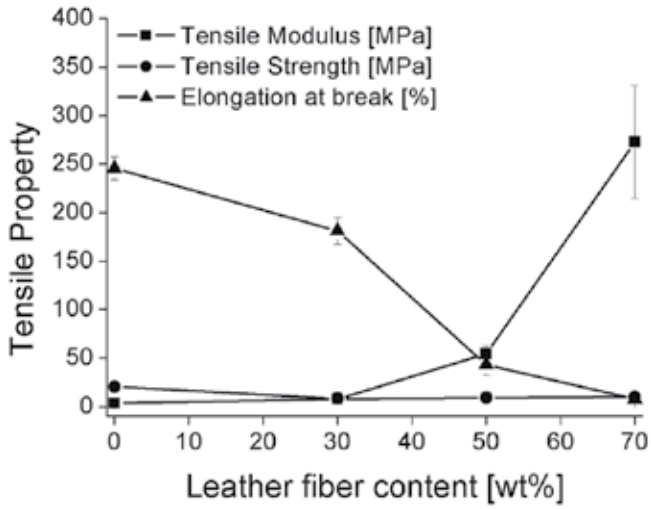

Fig. 20. Variation in tensile mechanical properties of the composites as a function of leather fiber content

There are some studies in the literature on thermoplastic composites containing leather fibers. Matrices include highly plasticized PVC (pPVC) (Madera-Santana et al., 1998), acrylonitrile-butadiene-styrene terpolymer (ABS) (Ramaraj, 2006) and poly(methyl methacrylate) (PMMA) (Madera-Santana & Moreno, 1999), where the elastic modulus has shown different behavior. While ABS/leather and PMMA/leather composites exhibit decrease in elastic modulus or a slight increase as leather fiber content increases, p-PVC/leather composites show similar behavior to PVB/leather composites, i.e., the elastic modulus is strongly influenced by fiber content, especially at compositions exceeding 30 wt% leather fibers. It should be pointed out that both polymer/leather composites where the elastic modulus increases considerably with increasing amounts of leather fiber, had plasticized thermoplastic matrices, i.e., p-PVC and PVB used in this study. The reduction in tensile strain of the PVB/leather composites may be attributed to a reduction in the deformation ability of the matrix due to the concentration of leather fiber agglomerates (Ambrósio et al., 2011).

It should be mentioned that, despite the fact that the mechanical properties of this composite did not show great improvement, this material has presented all the adequate standard properties for its use in shoe soles and insoles: abrasion resistance, hardness, tear resistance, adhesion to commercial glues, flexibility or folding ability, appearance etc. and is currently being tested in shoe factories with success. By means of a simple and cheap processing technique, i.e., a harvest feed extrusion equipped with a Maillefer single screw, composites

were manufactured with suitable properties for use as shoe soles, to be returned as a raw material to the shoe industry chain, facilitating approval of the recycled products by the regulatory agencies.

3. A few words on life cycle assessment (LCA) of natural fiber polymer composites

There are many methodologies in use to determine the LCA of a final product. Whatever the methodology adopted, the following characteristics may impact positively on the environmental impact of natural fiber polymer based products, if adequately handled: resources, production, distribution, use, disposal and re-use.

With regard to the recyclability of these composites, Tajvidi & Takemura (2009) have shown that these composites can be reprocessed many times, even with gain in stiffness, water absorption, and no effect on thermal stability, as a consequence of an observed improvement of the interface quality of the composites.

According to Murphy (2004) as cited in Patel *et al*. (2003) at least in the context of bio-based polymers, reductions of the order of 20% in most environmental impacts (and specifically a saving of 20 MJ per kg of polymer and avoidance of 1 kg CO_2 per kg of polymer) would be a useful guide for a good environmental improvement target.

Pervaiz & Sain (2003) have performed a comparative life cycle analysis focused on nonrenewable energy consumption of natural and glass fiber composites. Their analysis shows that a net saving of 50 000 MJ (3 ton CO_2 emissions) per ton of thermoplastic can be achieved by replacing 30% glass fiber reinforcement with 65% hemp fiber. It is further estimated that 3.07 million ton CO_2 emissions (4.3% of total USA industrial emissions) and 1.19 million m^3 crude oil (1.0% of total Canadian oil consumption) can be saved by substituting 50% fiber glass plastics with natural fiber composites in North American auto applications. However, to compete with glass fiber effectively, further research is needed to improve natural fiber processing, interfacial bonding and control moisture sensitivity in longer run.

Joshi et al. (2004) performed extensive studies comparing life cycle environmental performance of natural fiber composites with glass fiber reinforced composites and found that natural fiber composites are environmentally superior in the specific applications studied, that means, each case or application must be studied separately.

When dealing with leather residues, the benefits go beyond: the leather scraps may be used as shoe soles in the shoe making chain itself, avoiding land fill of tons of scraps. This might generate economy in the correct disposal of this residue (which must be very well controlled and then paid for), and in the energy used for its production, also serving as a cheaper raw material for new recycled shoe soles and insoles. From an environmental point of view, tons of chrome may be kept inside the polymer as Cr^{3+}, without the risk of oxidizing to Cr^{6+} under the action of sun light and heat, reducing the risk of water and soil contamination. Regarding balsa wood, wood flour, saw dust, bamboo and coir polymer composites we also have to consider the CO_2 sequestration capacity of these composites during their useful life.

Of course, the use of industrial and postconsumer residues and the recovery of forests must be stimulated by public policies and programs, in addition to education of the people, who will be the major beneficiaries. Research studies may point out solutions and alternatives. However, adequate waste management and recycling programs are required to make these materials become reality.

4. Concluding remarks

From the few case studies presented in this text, we may conclude that high value added natural fiber reinforced polymer composites can be developed from different industrial and postconsumer urban residues or waste, with positive impact on the environment by reducing contamination and sequestering CO_2 from the atmosphere, contributing to the recovery of not only the Amazon Rainforest, but also any forest worldwide.

5. Acknowledgment

Acknowledgements are due to Quattor and Braskem for donating the polypropylenes used in the composites, Tiva-Design in Bamboo, Projeto Coco Verde, Empresa Pinho Pó and Orion Madeira Balsa for donating the bamboo fibers, coir fibers, pinus wood and balsa wood waste, respectively; as well as CCDM-UFSCar, FINEP and CNPq for the financial support.

6. References

Ambrósio, J. D.; Lucas, A. A.; Otaguro, H. & Costa, L. C. (2011). Preparation and characterization of poly(vinyl butyral)-leather fiber composites. *Polymer Composites*, in press, ID: 823786-701370 (accepted - Feb/2011), ISSN 1548-0569

Baillie, C. (2004). Why Green Composites?, In: *Green composites - Polymer composites and the environment*, Edited by Caroline Baillie, pp. 1 -8 , Woodhead Publishing Ltd & CRC Press LLC, ISBN 0-8493-2576-5 Cambridge, England and Boca Raton, FL, USA

Barbosa, A.P.; Campos, M. A. A.; Sampaio, P. T. B.; Nakamura, S. & Gonçalves, C. Q. B. (2003). O Crescimento de duas espécies florestais pioneiras, pau-de-balsa (*Ochroma lagopus* Sw.) e caroba (*Jacaranda copaia* D. Don), usadas para recuperação de áreas degradadas pela agricultura na Amazônia Central, Brasil. *Acta Amazônica,* Vol.33, No3, 2003, pp. 477-482, ISSN 0044-5967

Bettini, S.H.P.; Uliana, A.T.& Holzschuh, D. (2008). Effect of Process Parameters and Composition on Mechanical, Thermal, and Morphological Properties of Polypropylene/Sawdust Composites. *Journal of Applied Polymer Science*, Vol. 108, pp. 2233-2241, ISSN 0021-8995

Bettini, S.H.P.; Bonse, B.C.; Melo, E.A. & Muñoz, P.A.R. (2009). Effect of Sawdust Surface Treatment and Compatibilizer Addition on Mechanical Behavior, Morphology, and Moisture Uptake of Polypropylene/Sawdust Composites. *Polymer Engineering Science*, Vol. 50, pp. 978-985, ISSN 0032-3888

Bettini, S. H. P.; Bicudo, A. B. L. C.; Augusto, I. A.; Antunes, L. A.; Morassi, P. L.; Condotta, R. & Bonse, B. C. (2010). Investigation on the Use of Coir Fiber as Alternative Reinforcement in Polypropylene. *Journal of Applied Polymer Science*, Vol. 118, pp. 2841–2848, ISSN 1359-835X

Bettini, S.H.P.; Josefovich, M. P. P. M. & Lotti, C. (2010). Effect of the Presence of Lubricants on the Mechanical Properties of PP-g-Ma Compatibilized Polypropylene/Sawdust Composites. *Proceedings of the Polymer Processing Society 26th Annual Meeting*, PPS-26, Banff, Canada, July 4-8, 2010

Bettini, S.H.P.; Antunes, M.C. & Magnabosco, R. (2011). Investigation on the Effect of a Compatibilizer on the Fatigue Behavior of PP/Coir Fiber Composites. *Polymer Engineering Science, in press*, ISSN 0032-3888

Bonse, B. C.; Mamede, M. C. S.; da Costa, R. A. & Bettini, S. H. P. (2010). Effect of Compatibilizer and Bamboo Fiber Content on the Mechanical Properties of PP-g-MA Compatibilized Polypropylene/Bamboo Fiber Composites, *Proceedings of the Polymer Processing Society 26th Annual Meeting*, PPS-26, Banff, Canada, July 4-8, 2010

Bonse, B.C.; Caranti, L.R.A.; Josefovich, M.P.P.M.; da Costa, R.A.; Magnabosco, R. & Delijaicov, S. (2011). Effect of Fiber Size, Compatibilizer and Bamboo Fiber Content on Physical Properties of PP-g-MA Compatibilized Polypropylene/Bamboo Fiber Composites, *Proceedings 27th World Congress of the Polymer Processing Society PPS-27*, Marrakech, Morocco, May 10-14, 2011

Brahmakuma, R. M.; Pavithran, C. & Pillai, R. M. (2005) Coconut Fibre Reinforced Polyethylene Composites: Effect of Natural Waxy Surface Layer of the Fibre on Fibre/Matrix Inferfacial Bonding and Strength of Composites. *Composites Science and Technology* Vol. 65, pp. 563-569

Branciforti, M.C., Marinelli, A. L. ., Kobayashi, M., Ambrosio, J. D. , Monteiro, M. R., Nobre A. D. (2009), Wood Polymer Composites Technology Supporting the Recovery and Protection of Tropical Forests: The Amazonian Phoenix Project, *Sustainability, 1*, 1431-1443, ISSN 2071-1050

Dhaliwal, A. K. & Hay, J. N. (2002). The characterisation of polyvinyl butyral by thermal analysis. *Thermochimica Acta*, Vol. 391, N° 1-2, pp. 245-255. ISSN 0040-6031

El-Din, N. M. S. & Sabaa, M. W. (1995). Thermal degradation of poly(vinyl butyral) laminated safety glass. *Polymer Degradation and Stability*, Vol. 47, N° 2, pp. 283-288, ISSN 0141-3910

Gauthier, R.; Joly, C; Coupas, A.C.; Gauthier, H. & Escoubes, M. (1998). Interfaces in polyolefin/cellulosic fiber composites: Chemical coupling, morphology, correlation with adhesion and aging in moisture. *Polymer Composites*, Vol. 19, N° 3, pp. 287-300, ISSN 0272-8397

Geethamma, V. G.; Reethamma, J. & Thomas, S. (1995) Short Coir Fiber-Reinforced Natural Rubber Composites: Effects of Fiber Length, Orientation, and Alkali Treatment. *Journal of Applied Polymer Science,* Vol. 55, pp. 583-594, ISSN 0021-8995

Geethamma, V. G.; Kalaprasad, G.; Groeninckx, G. & Thomas, S. (2005) Dynamic Mechanical Behavior of Short Coir Fiber Reinforced Natural Rubber Composites. *Composites: Part A*, Vol. 36, pp. 1499-1506, ISSN 1359-835X

George, J.; Sreekala, M. S. & Thomas, S. (2001). A review on interface modification and characterization of natural fiber reinforced plastic composites. *Polymer Engineering and Science*, Vol. 41, N° 9, pp. 1471–1485, ISSN 1548-2634

Haque, Md. M.; Hasan, M.; Islam, Md. S. & Ali, Md. E. (2009). Physico-Mechanical Properties of Chemically Treated Palm and Coir Fiber Reinforced Polypropylene Composites. *Bioresource Technology*, Vol. 100, pp. 4903-4906, ISSN 09608524

Harper, D. & Wolcott, M. (2004). Interaction between coupling agent and lubricants in wood-polypropylene composites. *Composites – Part A*, Vol. 35, pp. 385-394, ISSN 1359-835X

Herrera-Franco, P. J. & Valadez-Gonzalez, A. (2004). Mechanical Properties of Continuous Natural Fibre-Reinforced Polymer Composites. *Composites: Part A*, Vol. 35, pp. 339-345, ISSN 1359-835X

Hristov, V. N.; Lach, R. & Grellmann W. (2004). Impact Fracture Behavior of Modified Polypropylene/Wood Fiber Composites. *Polymer Testing*, Vol. 23, pp. 581-589, ISSN 0142-9418

Ichazo, M.N.; Albano, C.; González, J.; Perera, R. & Candal, M.V. (2001). Polypropylene/Wood Flour Composites: Treatments and Properties. *Composites Structure*, Vol. 54, pp. 207-214, ISSN 0263-8223

Ishizaki, M. H.; Visconte, L. L. Y.; Furtado, C. R. G.; Leite, M. C. A. M. & Leblanc, J. L. (2006). Caracterização Mecânica e Morfológica de Compósitos de Polipropileno e Fibras de Coco Verde: Influência do Teor de Fibra e das Condições de Mistura, *Polímeros*, Vol. 16, pp. 182-186, ISSN 0104-1428

Islam, Md N.; Rahman, Md R.; Haque, Md M. & Huque, Md. M. (2010). Physico-Mechanical Properties of Chemically Treated Coir Reinforced Polypropylene Composites. *Composites Part A: Applied Science and Manufacturing*, Vol. 41, pp. 192-198, ISSN 1359-835X

Jeong, H. K.; Rooney, M.; David, D. J.; MacKnight, W. J.; Karasz, F. E. & Kajiyama, T. (2000). Miscibility and characterization of the ternary crystalline system: poly(vinyl butyral)/poly(vinyl alcohol)/nylon6. *Polymer*, Vol. 41, N° 17, pp. 6671-6678. ISSN 0032-3861

Joshi, S.V.; Drzal, L.T.; Mohanty A.K. & Arorac, S. (2004). Are natural fiber composites environmentally superior to glass fiber reinforced composites? *Composites: Part A Applied Science and Manufacturing*, Vol. 35, pp. 371–376. ISSN 1359-835-X

Kalia, S.; Kaith, B.S. & Kaur, I. (2009). Pretreatments of natural fibers and their application as reinforcing material in polymer composites – A review. *Polymer Eng. and Science*, Vol.49, pp. 1253-1272, ISSN 0032-3888

Karmarkar, A.; Chauhan, S.S.; Modak, J.M. & Chanda, M. (2007). Mechanical Properties of Wood–Fiber Reinforced Polypropylene Composites: Effect of a Novel Compatibilizer with Isocyanate Functional Group. *Composites: Part A*, Vol. 38, pp. 227-233, ISSN 1359-835X

Keener, T.J.; Stuart, R.K.; Brown, T.K. (2004). Maleated Coupling Agents for Natural Fibre Composites. *Composites: Part A*, Vol. 35, pp. 357-362, ISSN 1359-835X

Klyosov, A.A. (2007). *Wood-Plastic Composites*, John Wiley & Sons, Inc., ISBN 978-0-470-14891-4, Hoboken, New Jersey, USA

Leblanc, J. L.; Furtado, C. R. G.; Leite, M. C. A. M.; Visconte, L. L. Y. & Ishizaki, M. H. (2006). Investigating Polypropylene–Green Coconut Fiber Composites in the Molten and Solid States Through Various Techniques. *Journal of Applied Polymer Science*, Vol. 102, pp. 1922-1936, ISSN 0021-8995

Li, T. Q. & Wolcott, M. P. (2004). Rheology of HDPE-wood composites. I. Steady state shear and extensional flow, *Composites: Part A*, Vol. 35, pp. 303-311, ISSN 1359-835X

Li, T. Q. & Wolcott, M. P. (2005). Rheology of Wood Plastics Melt. Pat 1. Capillary Rheometry of HDPE Filled with Maple, *Polymer Engineering Science,* Vol. 45, pp. 549-559, ISSN 0032-3888

Li, T. Q. & Wolcott, M. P. (2006). Rheology of Wood Plastics Melt, Part 2: Effects of Lubricating Systems in HDPE/MAPLE composites, *Polymer Engineering Science*, Vol. 46, pp. 464-474, ISSN 0032-3888

Madera-Santana, T. J.; Torres, A. C. & Lucero, A. M. (1998). Extrusion and mechanical characterization of PVC-leather fiber composite. Polymer Composites, Vol. 19, N° 4, pp. 431–439, ISSN 0272-8397

Madera-Santana, T. J. & Moreno, F. V. (1999). Graft polymerization of methyl methacrylate onto short leather fibers, Polymer Bulletin, Vol. 42, N° 3, pp. 329-336, ISSN 0170 – 0839

Madera-Santana, T. J.; Veja, M. J. A.; Márquez, A. M.; Moreno, F. V.; Richardson, M. O. W. & Machin, J. L. C. (2002). Production of leather-like composites using short leather fibers. II. Mechanical characterization, Polymer Composites, Vol. 23, Nº 6, pp. 991–1002, ISSN 0272-8397

Mano, B.; Spinacé, M. A. S.; De Paoli, M. A. (2007). Polypropylene Composite Reinforced with a Natural Fiber: Processing and Coupling Agent Effect. *The Polymer Processing Society 23rd Annual Meeting*. Salvador, Brazil, 2007

Marcovich, N. E.; Reboredo, M. M.; Aranguren, M. I. (1998). Dependence of the mechanical properties of woodflour–polymer composites on the moisture content. *Journal of Applied Polymer Science*, Vol. 68, 2069-2076, ISSN 0021-8995

Marinelli, A.L.; Monteiro, M.R.; Ambrósio, J.D.; Branciforti, M.C.; Kobayashi, M. & Nobre, A.D. (2008). Desenvolvimento de compósitos poliméricos com fibras vegetais naturais da biodiversidade, *Polímeros: Ciência e Tecnologia*, Vol. 18, nº 2, pp. 92-99, ISSN 0104-1428

Mohanty, A. K.; Misra, M.; Drzal, L. T. (Editors) (2005). *Natural fibers, biopolymers, and biocomposites*, Taylor & Francis Group, LLC, ISBN 0-8493-1741-X, Boca Raton, FL, USA

Monteiro S. N.; Terrones L. A. H.; Carvalho E. A.; D'Almeida, J. R. M. (2006). Efeito da Interface Fibra/Matriz Sobre a Resistência de Compósitos Poliméricos Reforçados com Fibras de Coco. *Revista Matéria*, Vol. 11, pp. 395-402, ISSN 1517-7076

Murphy, R. (2004). Life Cycle Assessment, In: *Green composites - Polymer composites and the environment*, Caroline Baillie, pp. 23 - 48, Woodhead Publishing Ltd & CRC Press LLC, ISBN 0-8493-2576-5, Cambridge, England and Boca Raton, FL, USA

Nielsen, L. E. & Landel, R. F. (1994). *Mechanical Properties of Polymers and Composites*, chapter 8, 2nd Edition, Marcel Dekker Inc, New York, ISBN 0-8247-8964-4

Niska, K.O. & Sain, M. (Ed.) (2008). *Wood Polymer Composites*, Woodhead Publishing Ltd & CRC Press LLC, ISBN 1-85573-739-6, Cambridge, England and Boca Raton, FL, USA

Nobre, A.D. (2006). *Fênix Amazônico Project: Renascendo das Cinzas da Destruição*; Um projeto para a construção de um ecossistema de empreendimentos sustentáveis na Amazônia; Instituto Nacional de Pesquisas da Amezônia (INPA): São José dos Campos, Brazil, (mail to: anobre@ltid.inpe.gov.br).

Nobre, A.D.; Marinelli, A.L.; Monteiro, M.R.; Ambrósio, J.D.; Branciforti, M.C. & Kobayashi, M. (2009). The development of Bio-fibre polymer composites: a contribution to the Amazon Rain Forest Sustainability – The Amazon Fenix Project, *Proceedings of 10th International Conference on Wood and Biofiber Plastic Composites and Nanotechnology in Wood Composites Symposium*", Madison, WI, USA, May 2009.

Oksman, K. & Clemons, C. (1998) Mechanical Properties and Morphology of Impact Modified Polypropylene-Wood Flour Composites. *Journal of Applied Polymer Science*, Vol. 67, 1503-1513, ISSN 0021-8995.

Pervaiz, M. & Sain, M.M. (2003). Carbon storage potential in natural fiber composites. *Resources, Conservation and Recycling*, Vol. 39, pp. 325 - 340. ISSN 0921-3449.

Pickering, K.L.; Abdalla, A.; Ji, C.; McDonald, A.G. & Franich, R.A. (2003). The Effect of Silane Coupling Agents on Radiata Pine Fibre for Use in Thermoplastic Matrix Composites. *Composites: Part A*, Vol. 34, pp. 915-926, ISSN 1359-835X.

Prasad, S. V.; Pavithran, C., Rohatgi, P. K. (1983) Alkali Treatment of Coir Fibres for Coir-Polyester Composites. *Journal Material Science*, Vol. 18, pp. 1443-1454, ISSN 0022-2461

Ramaraj, B. (2007). Crosslinked poly(vinyl alcohol) and starch composite films: Study of their physicomechanical, thermal, and swelling properties, *Journal of Applied Polymer Science*, Vol. 103, N° 2, pp. 1127–1132, ISSN 0021-8995.

Rauwendaal, C. (2001). *Polymer Extrusion* (4th edition), Hanser Gardner Publications, Inc. ISBN 3-446-21774-6, New York (USA).

Rout, J.; Mishra, M.; Tripathy, S. S.; Nayak, S. K. & Mohanty, A. K. (2001) The Influence of Fibre Treatment on the Performance of Coir-Polyester Composites. *Composites Science and Technology*. Vol. 61, pp. 1303-1310, ISSN 0266-3538.

Rozman, H. D.; Tan, K. W.; Kumar, R. N.; Abubakar, A.; Mohd Ishak, Z. A., Ismail H. (2000) The effect of lignin as a compatibilizer on the physical properties of coconut fiber–polypropylene composites. *European Polymer Journal*, Vol. 36, pp. 1483-1494, ISSN 0014-3057.

Saflex ® - Solutia, In: Material Safety Data Sheet available, (07/13/2010). Available from <https://team.solutia.com/sites/msds/Lists/MSDS%20Search%20Tool/WebByProduct.aspx>

Saheb, D. N. & Jog, J. P. (1999). Natural fiber polymer composites: A review. *Advances in Polymer Technology*, Vol. 18, N° 4, pp. 351–363, ISSN 1098-2329.

Sanadi, A. R.; Caulfield, D. F. & Rowell, R. M. Reinforcing Polypropylene With Natural Fibers. *Plastics Engineering*, Vol.50, pp. 27-28, 1994, ISSN 0091-9578.

Santi, C. R.; Hage Jr., E; Vlachopoulos, J., Correa, C. A. (2009) Rheology and Processing of HDPE/Wood Flour Composites, *International Polymer Processing*, Vol. 4, pp. 346-353, ISSN 0930-777X.

Santos, E. F.; Mauler, R. S. & Nachtigall S. M. B. (2008). Effectiveness of Maleated- and Silanized-PP for Coir Fiber-Filled Composites. *Journal of Reinforced Plastics and Composites*, Vol. 28, pp. 2119-2129, ISSN 07316844.

Santos, P. A.; Spinacé, M. A. S.; Fermoselli, K. K. G. & De Paoli, M. A. (2007). Polyamide-6/Vegetal Fiber Composite Prepared by Extrusion. *The Polymer Processing Society 23rd Annual Meeting*. Salvador, Brazil, 2007.

Satyanarayana, K. G.; Sukumaran, K.; Mukherjee, P. S. & Pillai, S. G. K. (1986). Materials Science of Some Lignocellulosic Fibers, *Metallography,* Vol. 19, pp. 389-400, ISSN 0026-0800.

Suarez, J.C.M.; Coutinho, F.M.B. & Sydenstricker, T.H. (2003). SEM Studies of Tensile Fracture Surfaces of Polypropylene-Sawdust Composites, *Polymer Testing*, Vol. 22. pp. 819-824, ISSN 0142-9418.

Suddell, B. C. & Evans, W. J. (2005). Chapter 7 Natural Fiber Composites in Automative Applications, In: *Natural Fibers, Biopolymers and Biocomposites*, Mohanty, (Ed.), Taylor &Francis Group, Florida, pp. 237–297, ISBN 084931741X.

Tajvidi, M. & Takemura, A. (2009). Recyclability Index: a measure to determine how recyclable natural fiber plastic composites are. *Proceedings of 10th International Conference on Wood and Biofiber Plastic Composites and Nanotechnology in Wood Composites Symposium*", Madison, WI, USA, May 2009.

Tomczak, F.; Sydenstricker, T.H.D.& Satyanarayana, K.G. (2007) Studies on lignocellulosic fibers of Brazil. Part II: Morphology and properties of Brazilian coconut fibers. *Composites: Part A*, Vol. 38, pp. 1710-1721, ISSN 1359-835X.

Towo, A.N. & Ansell, M.P. (2008) Fatigue of Sisal Fibre Reinforced Composites: Constant-life Diagrams and Hysteresis Loop Capture. *Composites Science Tecnology*, Vol. 68, pp. 915-924, ISSN 0266-3538.

Valadez-Gonzalez, A.; Cervantes-Uc, J. M.; Olayo, R. & Herrera-Franco, P. J. (1999) Chemical Modification of Henequén Fibers with an Organosilane Coupling Agent. *Composites: Part A*, Vol. 30, 321-331, ISSN 1359-835X.

Valera, T. S. & Demarquette, N. R. (2008). Polymer toughening using residue of recycled windshields: PVB film as impact modifier. *European Polymer Journal*, Vol. 44, N° 3, pp. 755-768, ISSN 0014-3057

Wambua, P.; Ivens, J. & Verpoest, I. (2003). Natural fibres: can they replace glass in fibre reinforced plastics? *Composite Science and Technology*, Vol. 63, pp. 1259-1264, ISSN 0266-3538.

Yang, H.S., Qiao P. & Wolcott M.P. (2010). Fatigue Characterization and Reliability Analysis of Wood Flour Filled Polypropylene Composites. *Polymer Composites.* Vol. 31, pp. 553-560, ISSN 0272-8397.

8

Bone: A Composite Natural Material

Maria Fátima Vaz[1], Helena Canhão[2] and João Eurico Fonseca[2]
[1]*ICEMS and Mechanical Engineering Department, Instituto Superior Técnico,Technical University of Lisbon,*
[2]*Rheumatology Research Unit, Instituto de Medicina Molecular, Faculty of Medicine, University of Lisbon and Rheumatology Department, Santa Maria Hospital, Lisbon, Portugal*

1. Introduction

Composite materials are solids with two or more distinct constituents at a larger scale than an atomic one (Hull, 1981). In accordance to this definition, materials or biological tissues such as wood, dentin and bone are regarded as composite natural materials (Cowin, 2001; Lakes, 2003; Park & Lakes, 1992). Bone is regarded as a natural composite material, which appears as it is in nature, rather than the artificial or man made composites.

As for other composite materials, the mechanical properties of bone are dependent on its composition and structure, which includes the arrangement of the components and the bond between fibers and matrix. For example, the arrangement of fibers is different in several types of bones, gives rise to distinct properties.

An understanding of the mechanical behavior of bone is extremely important for the evaluation of fracture risk. Some types of bones, like vertebrae are constantly submitted to compressive loads and have an increased risk of fracture. Most bones are composed by outer cortical bone and an inner trabecular bone. Fractures on vertebrae, hip and wrist tend to start the global structural failing process in the regions of trabecular bone with decreased bone mass and microarchitecture changes (Fratzl & Weinkamer, 2007; Gibson & Ashby, 1999).

The emphasis of this chapter will be on the structure and mechanical properties of bone and how some diseases affect the material's characteristics. This chapter has two main sections. Firstly, we will describe the structure of bone at different scales, including the two different types of bone, cortical and trabecular. As growth and remodeling are key processes in the continuous renewal of bone, the issue will be also focused in this section. Several techniques can be used to characterize the hierarchical structure of bone. A particular emphasis will be given to transmission electron microscopy, scanning electron microscopy, second-harmonic generation imaging with a two-photon microscope, microcomputed tomography, quantitative backscattered electron imaging, atomic force microscopy, small angle X-ray scattering and neutron scattering.

The remaining part of the chapter will be devoted to the mechanical behavior of bone. As bones are often submitted to different types of external loadings, several types of tests will be reviewed namely compression, tension, bending, fatigue, creep, torsion and nanoindentation. Compression tests on femoral epiphysis of patients submitted to total hip

replacement surgery will also be discussed. Some aspects of the bone deformation mechanisms will also be approached.
Subsections will be devoted to the effect of a) metabolic bone diseases and b) inflammatory diseases on both structural and mechanical properties. Animal models are useful to reproduce human bone behavior on an experimental controlled environment and will be adressed. Besides the animal model, relevance will also be given in both subsections to human bone characterization. These issues will be discussed and illustrated using results from studies performed by the authors.
In summary, in this chapter, the authors will review the principal concepts of bone structure, microarchitecture and biomechanics in physiologic and pathologic states and will enrich this state of the art with a discussion of their own original results.

2. Structure

This section will be dedicated to the description of the structure of the bone at different scales, as well as, to the techniques used for structural characterization.

2.1 Structure at different scales

Bone has a complex hierarchical structure which will be analysed at different scales, in different subsections. In a continuous upsizing analysis we will address the molecular level (molecular structure of the constituents), the nanometer scale (fibril arrays of collagen and mineral phases), the submicrostructure scale (the intrinsic lamellae structure), the microstructural point of view (Harversian systems, osteons and trabeculae) and the macrostructural (cortical and trabecular bone).

2.1.1 Structure from the molecular to the nanometer scale

Bone has a hierarchical ordered structure, and at a nanometer-scale can be compared to a composite material, composed by type I collagen fibers reinforced with calcium phosphate crystals (Fratzl et al., 2004; Park & Lakes, 1992). Water constitutes around 25% of the weight of fresh bone, essentially localized inside blood vessels in Harversian canals (Weiner & Wagner, 1998). The inorganic phase is composed essentially by carbonated apatite ($Ca_5(PO_4,CO_3)_3(OH)$), which presents as small crystals. In dry bone it accounts for almost two-thirds of bone weight. The remaining weight corresponds to organic material, which is essentially collagen, but there are also non-collagen proteins and lipids (Fratzl & Weinkamer, 2007).
Collagen is related to the capacity of bone to absorb energy, *i.e.* to the toughness, while the mineral phase plays an important role on the stiffness of the tissue (Viguet-Carrin et al., 2006).
Collagen is the most abundant protein in mammals and is formed by molecules that have a length around 280 to 300 nm and a diameter of 1.5 nm (Buehler, 2006; Fratzl et al., 2004; Fratzl & Weinkamer, 2007; Weiner & Wagner, 1998). The collagen molecule is composed by three polypeptide chains, which form a triple helix molecule (Figure 1a)) (Fratzl & Weinkamer, 2007; Weiner & Traub, 1992).
Collagen molecules are staggered, but there is a gap zone or spacing between them in the order of 35nm (Fratzl et al., 2004; Fratzl & Weinkamer, 2007; Weiner & Traub, 1992). Changes on the spacing, orientation, length of collagen molecules and the strength of intermolecular interactions, may give rise to different mechanical responses of the collagen

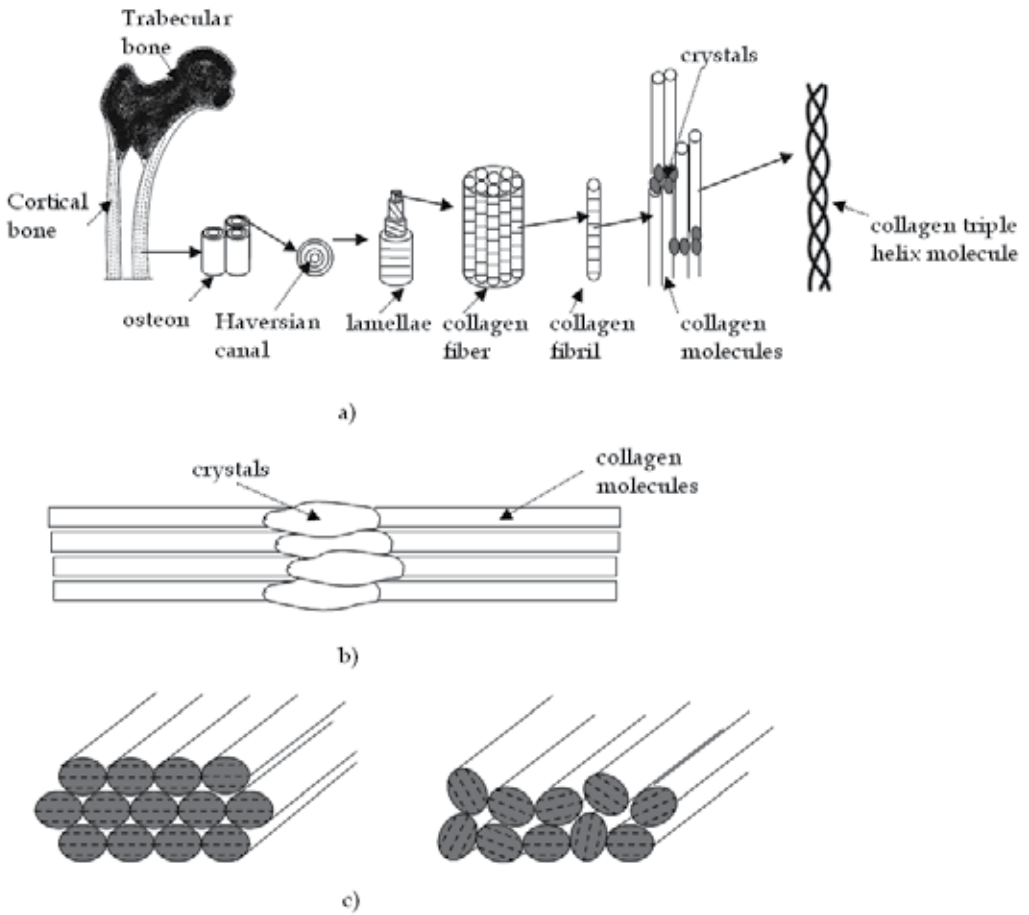

Fig. 1. a) Scheme of bone at different scale ranges (adapted from (Rho, et al., 1998)), b) arrangement of the apatite crystals which are aligned with the longitudinal direction of collagen fibers, c) inside one fiber, the fibrils may be aligned with respect to crystal axes and fibril axes, or the fibrils may have only an alignment of the fibril axes (adapted from (Weiner & Wagner 1998))

fibrils array (Buehler, 2006). The gaps between collagen molecules are sites for the nucleation of the calcium crystals (Fratzl & Weinkamer, 2007; Viguet-Carrin et al., 2006). Crystal size and orientation are influenced by collagen organization (Viguet-Carrin et al., 2006). However, the interface between collagen and apatite crystals is not well known (Weiner & Wagner, 1998). Mineral crystals of calcium phosphate particles deposit on the collagen array in the form of flat plates (Weiner & Traub, 1992). The crystals are essentially parallel to each other and to the axis of the collagen fibrils and occur at regular intervals along the fibrils at distances corresponding to the distances between collagen molecules (Figure 1b)). The arrangement of apatite crystals which are aligned with the longitudinal direction of collagen fibers is responsible for the anisotropic properties of bone, giving rise to higher values of stiffness and strength in that direction (Gibson & Ashby, 1999). The size, shape, arrangement and volume fraction of the crystals influence the mechanical behavior of bone (Fratzl et al., 2004). The distribution of crystals is not uniform in bone due to several

factors which involve bone remodeling, with zones with different degrees of mineralization, which are important in crack initiation and propagation (Fratzl et al., 2004). Mineral crystals have a plate shape with a wide range of dimensions. The thickness of the crystals is around 2-7 nm, while the length varies from 15 to 200 nm and the width from 10 to 80 nm (Fratzl et al., 2004; Fratzl & Weinkamer, 2007; Weiner & Traub, 1992; Weiner & Wagner, 1998). In the early stages of mineralization, crystal growth is limited by the collagen fibers, keeping the crystals separated. However, as growing progresses, crystals continue to grow and eventually join, which influences the mechanical properties of the fibrils (Giraud-Guille, 1988). In such conditions crystals maintain their plate-like shape but become very thin (Fratzl & Weinkamer, 2007).
Finally collagen molecular arrangement, cross-linking and molecular packing are important factors for bone properties (Fratzl et al., 2004; Viguet-Carrin et al., 2006).

2.1.2 Structure from the submicrostructure to the microstructure scale

The molecules of mineralized collagen form fibrils by a self assembling process with dimensions of 0.5 to 1 μm (Fratzl et al., 2004; Weiner & Wagner, 1998). A mineralized collagen fibril has a higher stiffness, strength and energy until failure comparing to a pure collagen fibril showing that mineralization is a crucial step for normal bone properties (Buehler, 2007).
Fibrils also assemble parallel to each other into fibers (circa 10 μm) (Buehler, 2006; Fratzl et al., 2004; Fratzl, & Weinkamer, 2007). Inside each fiber, fibrils may be aligned following both crystal axes and fibril axes, or on the contrary the fibrils may have only an alignment of the fibril axes, as can be seen in Figure 1c (Weiner & Wagner, 1998). In the first case, the structure will have orthotropic symmetry, while the other organization will exhibit transversal isotropy.
Fibers may arrange at a lamellar type or at a woven type. The mineralized collagen fibers can arrange in a defined configuration giving rise to lamellar bone, or may be disposed with no particular pattern, which originates woven bone (Rho et al., 1998). Woven bone is found at early stages of mineralization (Weiner & Wagner, 1998). Cortical bone can exist on the form of woven or lamellar, but is mostly lamellar.
As the name suggests, the lamellar bone is made of lamellae at a micrometer range (Fratzl et al., 2004; Fratzl, & Weinkamer, 2007; Rho et al., 1998; Weiner & Traub, 1992; Weiner & Wagner, 1998). Lamellae are planar arrangements (3-7 μm) formed by bundles of collagen fibers (Weiner & Traub, 1992). Lamellae, lacunae, canaliculi and cement lines are present in the bone at the same structural level. Lamellar arrangements can be found in plexiform or osteonal bones in the cortical aspect. Plexiform bone has the appearance of a brick structure, with the lamellae sandwiched between nonlamellar bone layers (Weiner & Wagner, 1998). Plexiform bone is rarely present in humans, but can be found in animals (Weiner & Wagner, 1998).
In osteonal cortical bone, the lamellae in the sheet form, wrap into concentric layers of 3 to 8 lamellae around a canal filled with a blood vessel, giving rise to an osteon (Rho et al., 1998).
It is classic to distinguish between primary and secondary osteons (Weiner & Wagner, 1998). Primary osteons contain a less amount of lamellae and smaller vascular channels in comparison with secondary osteons. Secondary osteons appear due to the replacement of bone by remodeling. Haversian systems or secondary osteons have a cylindrical shape (diameter 200 to 250 μm) and run parallel to the long axis of bone (Rho et al., 1998; Weiner & Wagner, 1998).

Lamellae, around an osteon, can be classified according to the Ascenzi group (Boyde et al., 1984) into a orthogonal plywood organization with alternate lamellae containing fiber orientation parallel and perpendicular to the axis of the osteon or into a unidirectional plywood for which the fiber orientation on the lamellae is longitudinal or transverse to the osteon axis (Fratzl, & Weinkamer, 2007). The Giraud-Guille model (Giraud-Guille, 1988) suggests that there is a change in the orientation of fibers, inside each lamellae (Figure 2), with angles that can reach 90º. Experimental observations suggest that inside each lamella, there are layers of sublamella (Weiner et al., 1999). The collagen fibers within the same sublamellae are essentially parallel to each other, while the orientation of collagen fibers between adjacent sublamellae may change (Fratzl, & Weinkamer, 2007), as seen in Figure 2c)).

According to this model, adjacent lamellae have different orientations as they can be arranged longitudinally to the collagen fibers that are parallel to the axis of the arrangement or transversal to the collagen fibers, which run perpendicularly to the long axis (Rho et al., 1998).

The trabecular bone has a different arrangement of the lamellae in comparison with cortical bone, which are organized longitudinally along the trabeculae instead of concentrically (Fratzl, & Weinkamer, 2007). However, the several layers of lamellae may have different mineral contents (Fratzl, & Weinkamer, 2007).

Osteocyte lacunae and canaliculi are holes present in bone, containing osteocytes. These mature cells evolved from the osteoblasts and were trapped during the mineralization process (Bonewald, 2011). The diameter of the lacunae is around 10 to 20 μm (Bonewald, 2011). Canaliculi are channels that connect the lacunae and represent the entrapment of cytoplasmic extensions that interconnect osteocytes. Cement lines result from remodeling and have a thicknesses ranging from 1 to 5 μm (Nicolella et al., 2011).

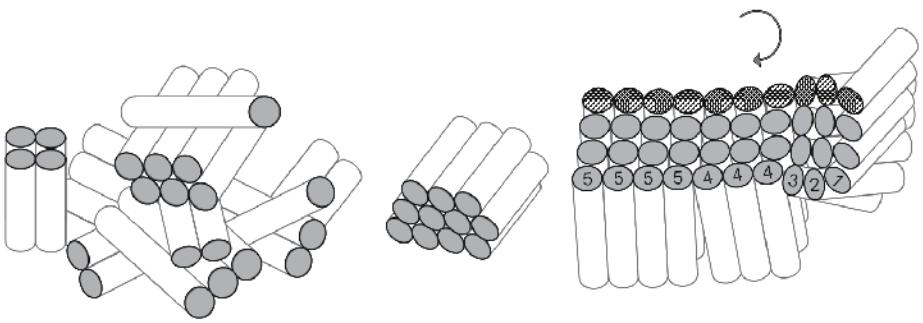

a) b) c)

Fig. 2. Orientation of the fibers inside a lamellae: a) woven, b) parallel fibers (lamellar), c) plywood lamellar showing change in the orientation of fibers, inside one lamellae, with angles that can reach 90º (adapted from (Weiner & Wagner, 1998; Weiner et al., 1999))

2.1.3 Structure at microscopic level

The cortical bone structure is characterized by concentric layers around a blood vessel, which are denoted by osteons or Haversian systems. The Volkmann's canals are channels that connect transversely the blood vessels that are inside the Haversian canals (Fratzl, & Weinkamer, 2007).

The trabecular bone has a cellular structure made of an interconnected network of rods and plates forming an open cell foam (Gibson & Ashby, 1999; Gibson, 2005). The walls of the cell foam are limited by trabeculae which have a thickness around 200 μm (Fratzl, & Weinkamer, 2007). Trabeculae are surrounded by bone marrow and living cells.
The trabeculae exhibit some osteocyte lacunae which connect to each other and to the exterior by the channels called canaliculi (Fratzl, & Weinkamer, 2007).

2.1.4 Structure at a macrostructure scale

Taking a femur as an example of a long bone, at a macroscopic structural level, one can observe distinct parts with different characteristics, with trabecular (or cancellous or spongy) zones surrounded or protected by a cortical (or compact) shield (see Figure 3a)). Vertebra (Figure 3b) and c)), have also a shell of cortical bone that surrounds the trabecular area.
Trabecular bone has a porosity around 80% (Figure 3d)) while cortical bone is denser and has a porosity of less than 6% (Figure 3e)) (Fratzl & Weinkamer, 2007; Gibson & Ashby, 1999; Gibson, 2005).

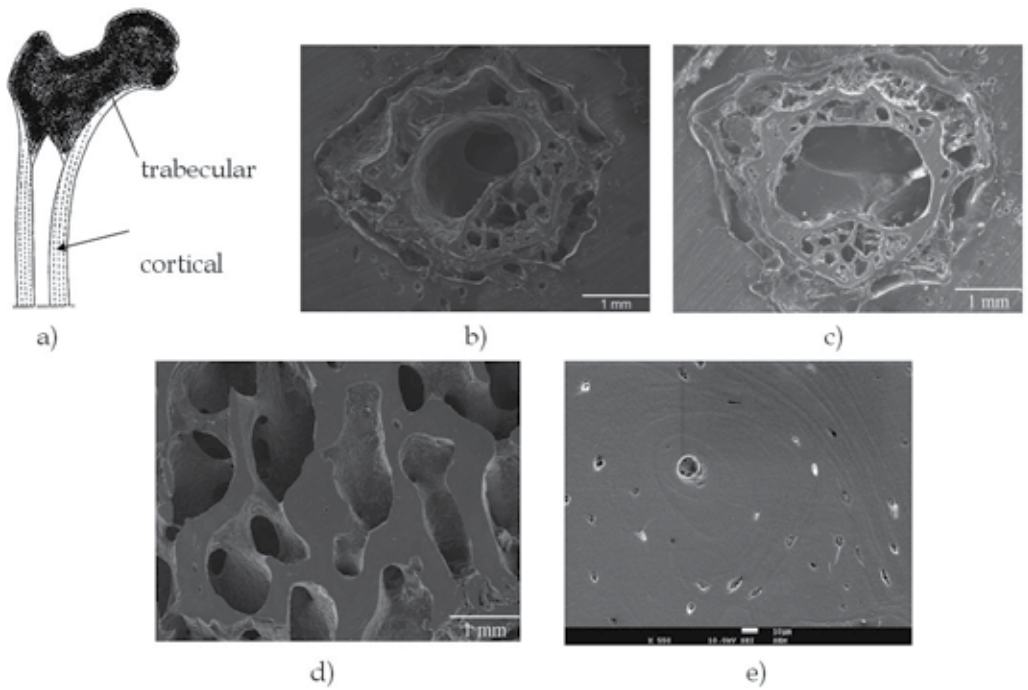

Fig. 3. a) Scheme of a femoral head with indication of trabecular and cortical zones. SEM pictures of: b) arthritic mouse vertebra, c) control mouse vertebra, d) human trabecular bone and d) of cortical equine bone

2.2 Chemical composition and density

Compact bone and trabecular bone have almost the same elemental composition. Even arthritic bone, in an animal model, has a similar composition compared to control, with calcium=73% and phosphorus=27% (Caetano-Lopes et al., 2009a).

The density of the compact bone is in the range of 1800-2000 kg/m^3, while the density of each trabeculae is 1820 kg/m^3. The porosity however is much higher in trabecular bone, reaching 80%. As for other cellular materials, density of trabecular bone is usually calculated as the ratio between the density of bone and the density of a single trabeculae (Gibson & Ashby, 1999).

2.3 The effect of growth and remodeling on the structure of bone

Natural materials, such as bone, have a growing process that is continually responding and adapting to environmental requirements. Bone is modified either by cellular activity during growth, as a response to systemic hormones, by the response to mechanical stress applied to the skeleton and by other environmental and genetic factors.
Bone is a dynamic structure under permanent remodeling. During childhood and adolescence, bone remodeling contributes to linear growth and to bone mass increase. Peak bone mass is attained around 25-30 years old. After this age bone starts slowly to change the metabolic activity, leading to progressive bone loss. The growth and remodeling process allow a renewal of the material. During bone remodeling, both osteoclast-mediated bone resorption of old material and osteoblast-mediated new bone matrix production occurs.
Cancellous bone is remodeled more often than the cortical bone (Rho et al., 1998).
As a consequence of bone remodeling, collagen fibers align along the direction of the load of the mature bone, which provides an increase in the mechanical strength (Caetano-Lopes et al., 2010).

2.4 Techniques for structure characterization

Image techniques have attracted much interest lately and provide important insights on the characterization of bone structure. For example, the size and shape of mineral particles can be analyzed by transmission electron microscopy (Weiner & Traub, 1992). In this section, emphasis will be also given to scanning electron microscopy, second-harmonic generation imaging with a two-photon microscope, microcomputed tomography, quantitative backscattered electron imaging and atomic force microscopy. The techniques of small angle X-ray scattering and neutron scattering will be briefly mentioned.

2.4.1 Transmission electron microscopy, TEM

Transmission electron microscopy uses an electron beam that is transmitted through the specimen, generating an image by the interactions beam-sample. TEM requires extremely thin samples (Goodhew & Humphreys, 2000).
Transmission electron microscopy is used to image the nanostructure of bone, such as, collagen fibrils and apatite crystals and to analyze the size and shape of bone mineral particles (Fratzl et al., 2004; Rubin et al., 2004; Weiner & Traub, 1992; Weiner et al., 1999). TEM can be used in human (Fratzl et al., 2004; Weiner & Traub, 1992; Weiner et al., 1999) and in animal bone (Rubin et al., 2004; Weiner et al., 1999). Collagen organization can be studied by TEM, after the mineral removal (Weiner et al., 1999).
While the majority of studies describe mineral particles with a plate shape, some refer to needle shape (Fratzl et al., 2004). The dimensions of platelets range from 2 to 7nm in thickness, 15 to 200 nm in length and 10 to 80 nm of width (Fratzl et al., 2004).

2.4.2 Scanning electron microscopy, SEM

Scanning electron microscopy (SEM) uses an electron beam to scan the surface of a sample (Goodhew & Humphreys, 2000). Different interactions can be obtained when the electron

beam hits the material, including secondary electrons (SE), back-scattered electrons (BSE), characteristic X-ray and others (Goodhew & Humphreys, 2000). Secondary electrons have lower energy as they result from inelastic collisions between the incident beam and the sample, but produce very high resolution images with a large field depth. Back-scattered electrons consist of high energy electrons that are produced from elastic collisions among incident beam and material (Goodhew & Humphreys, 2000). BSE are used to detect contrast between regions with different chemical compositions as the intensity of the BSE signal depends on the atomic number of the specimen.

The preparation of bone samples to be observed in SEM is simple. If the bone sample is small, it does not need any previous procedure, but if it is large, a sample of dimensions of 1 cm of length must be obtained by cutting or drilling. After this procedure and completely deffated, the sample is mounted in resin, polished with grid papers and coated with a gold layer (Caetano-Lopes et al., 2009a, 2010).

SEM is a powerful tool to characterize the superficial structure of bone. SEM can be used at the macroscopic scale, from the submicrostructure to the microstructure scale, for example to observe the trabeculae distribution (Rubin et al., 2004) or the lamellae arrangement (Fratzl et al., 2004; Weiner & Traub, 1992; Weiner et al., 1999).

An example of a healthy mouse vertebrae imaged with scanning electron microscopy is presented in Figure 3c). For trabecular bone some structural parameters can be defined such as the area occupied by trabeculae, inter-trabecular distance and the trabecular thickness. Image analysis software, as Sigma ScanPro or Image J, can be used to determine the parameters mentioned (Caetano-Lopes et al. 2009a, 2010).

While the images of Figure 3b) to e) were obtained with secondary electrons (SE), backscattered electrons (BSE) can also be used and images of Figure 4 are an example. Figure 4a) and b) are respectively images from control and from osteoporotic vertebral L4 trabecular bone mice. The arrangement of lamellae can be observed (Figure 4).

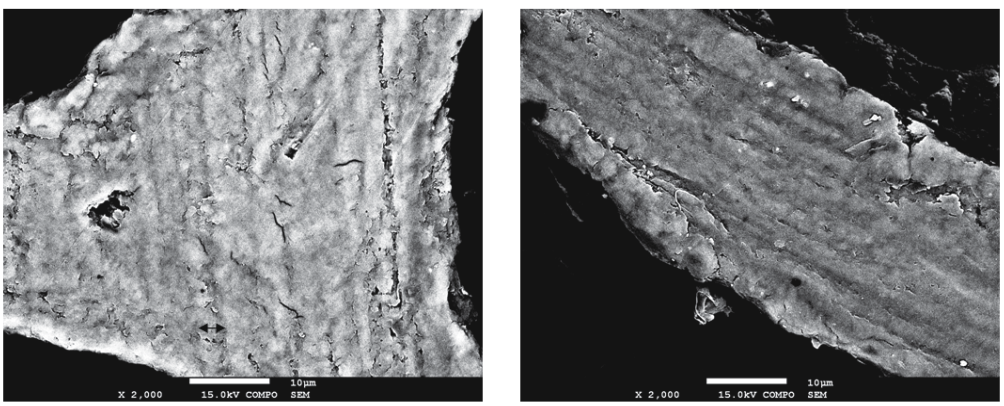

a) b)

Fig. 4. Images of SEM with backscattered electrons: a) from a control and b) from an osteoporotic mice vertebral L4 trabecular bone. Lamellae can be observed, and on figure a) a black arrow indicates a lamellae

2.4.3 Second-harmonic generation SHG and two-photon excitation microscopy

Second-harmonic generation (SHG) and two-photon excitation microscopy is used to evaluate the collagen organization of bone (Caetano-Lopes et al., 2009a, 2010). Collagen is

able to generate a second-harmonic signal due to the nonsymmetrical arrangement (Cox et al., 2003; Cox & Kable, 2006). When an electric field is able to deform a molecule, a second-harmonic generation occurs. With collagen, an asymmetrical molecule, an oscillating field is generated at twice the frequency (second-harmonic). Prior to observation, bone samples are decalcified, embedded in paraffin, cut in a microtone and deparaffinized. With this technique it is possible to distinguish the mature polymerized collagen from the immature collagen, indicating fibrillogenesis. The backward-SHG channel detects the backscattered-SHG signal associated to a green image, representing a less dense and immature collagen network, while the forward-SHG channel captures forward-SHG signal originating a blue image, associated with presence of a more dense and polymerized collagen matrix. Image analysis software is used to determine the amount of mature and immature collagen on a given area. The relative distributions of mature and immature collagen were found to be equivalent in the arthritic and control groups of 5 months old SKG mice (Caetano-Lopes et al., 2009a). However, in the 8 months old SKG mice, we have observed that the ratio of the forward to backward signal was higher in arthritic animals than in control, which revealed a lower collagen density and organization (Caetano-Lopes et al., 2010). As an example, Figure 5 shows two multiphoton microscopy images from a) SKG mouse vertebrae and b) BALB/c mouse vertebrae. The collagen component is strongly affected by the inflammatory disease which was eventually reflected on the mechanical performance of bone.

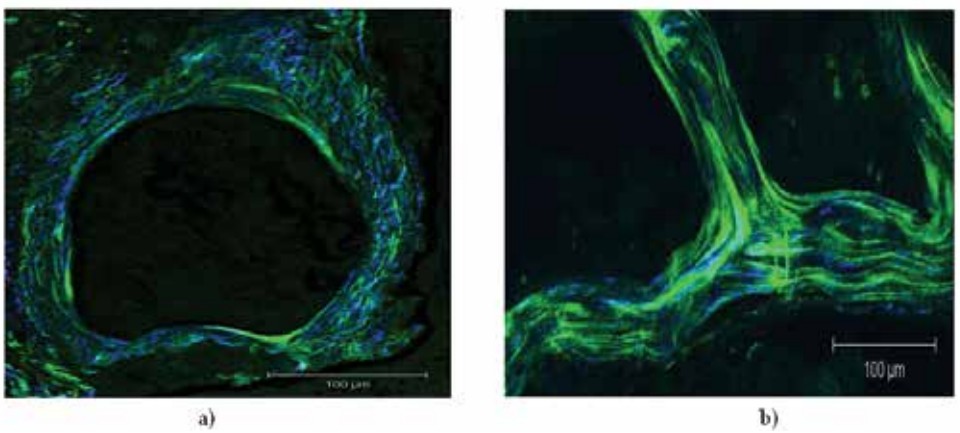

Fig. 5. Multiphoton microscopy images from 5 months old a) arthritic and b) control vertebrae of mice. Green and blue colors correspond respectively to the backward- and forward-SHG channels

2.4.4 Microcomputed tomography (micro-CT or μ -CT)

Microcomputed tomography (micro-CT) is a technique that enables to characterize bone microstructure. It has been used to evaluate bone volume fraction or apparent density, as well as the architectural bone arrangement (Cory et al., 2010; Nazarian et al., 2007). Micro-CT has becoming a leading technique on non-destructive structural evaluation.

Three-dimensional (3D) micro-CT has been applied to the visualization and quantification of the 3D structure of trabecular bone (Bevill et al., 2009; Chappard et al., 2008; Chevalier et al., 2007; Diederichs et al., 2009; Ding et al., 1999; Djuric et al., 2010; Homminga et al., 2002; Jiang et al., 2003; Link et al., 1998; Macho et al., 2005; Teo et al. 2006; Teo et al. 2007). Micro-

CT may be used to evaluate differences of trabecular microstructure, for example between several age groups (Djuric et al., 2010; Macho et al., 2005) at different femoral regions (Bevill et al., 2009; Djuric et al., 2010), or on vertebral bodies (Teo et al. 2006).

The identification of the optimal micro-CT parameters for human trabecular bone characterization has been performed by the authors of this chapter (Pereira et al.). Acquisition (voltage, intensity), resolution (voxel size), and especially image analysis (threshold values) parameters, were adapted in order to optimize the experimental procedures. Our experience has been centred in samples from patients with osteoarthritis and osteoporosis, who were submitted to total hip arthroplasty. The removed hip epiphysis were subjected to drilling, fixation, dehydration, cleaning and, in some of the cases, impregnation.

Micro-CT procedure involves three main steps: acquisition, reconstruction and image analysis. During the acquisition step, scans are performed in order to obtain, for each sample, a stack of about 500 images. On the reconstruction phase, the binarization is carried out, that is, to separate bone from regions without bone tissue and thresholding or other segmentation methods may be used for the definition of Bone Volume of Interest (BVI). To reconstruct the images, a 3D reconstruction software is used to generate an assemblage of virtual cross section slices through the object. Figure 6 shows the scanned image, the Bone Volume of Interest (BVI), the binarized region, and the 3D rendering (*i.e*, manipulation in a virtual space) of a sample of a human trabecular bone. Figure 7 exhibits a 3D reconstruction image of an equine cortical bone.

On the third phase, the image data is interpreted with 3D analysis software, which enables the quantification of the parameters that characterize the trabecular bone structure (Parfitt et al., 1987): Percent bone volume (BV/TV, %), Bone specific surface (BS/BV, mm^{-1}), Bone surface density (BS/TV, mm^{-1}), Structure Model Index (SMI, none), Trabecular thickness (Tb.Th, mm), Trabecular number (Tb.N, mm^{-1}), Trabecular separation (Tb.Sp, mm) and Degree of anisotropy (DA, none).

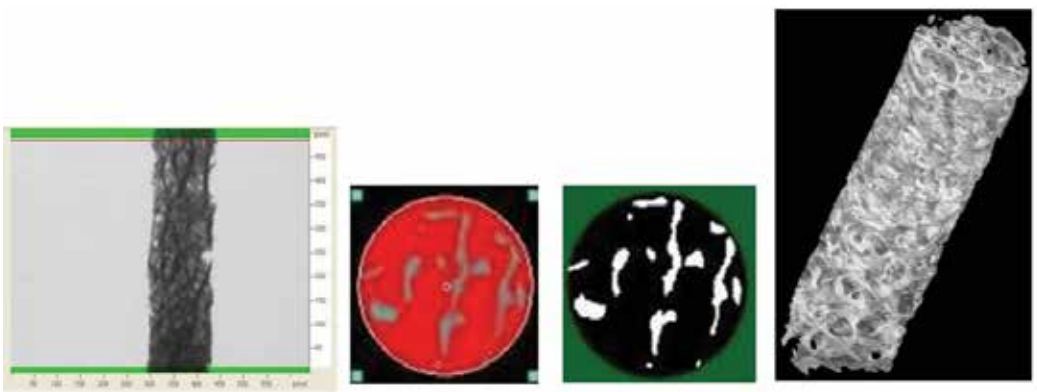

Fig. 6. a) Projection Image, b) Bone Volume of Interest (BVI), c) Binarized BVI, d) 3D rendering

Although most of the work on the application of micro-CT is for trabecular bone, cortical bone has also been studied (Basillais, 2007; Cooper et al., 2007a, 2007b; Wachter et al., 2001). For cortical bone characterization, the used parameters are (Parfitt et al., 1987): Canal volume fraction (Ca.V/TV), Pore volume fraction (Po.V/TV), Surface to volume ratio

(Ca.S/Ca.V), Mean diameter of pores (Ca.Dm), Mean pore separation (Ca.Sp) and Degree of anisotropy (DA).

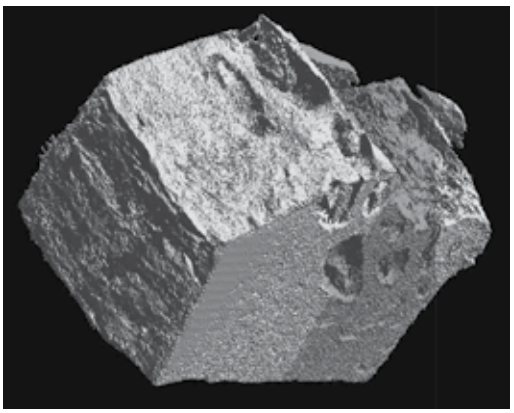

Fig. 7. Three-dimensional (3D) reconstruction image of an equine cortical bone

2.4.5 Quantitative backscattered electron imaging, qBEI

The mineralized component of bone is directly related to the fragility of bone. In this way, it is extremely important to determine the volume fraction of mineral particles, their shape and arrangement (Fratzl et al., 2004). The average mineral content of bone is in the range of 30 to 55%, but the trabeculae in the trabecular bone or the osteons in the compact bones do not exhibit a uniform mineralization. In fact, they have a regional variation (Fratzl et al., 2004). Two factors contribute to this difference in the degree of mineralization (Fratzl et al., 2004). One factor is remodeling as the old matrix is continuously resorbed and replaced by new bone. The other factor is related to the fact that mineralization of the matrix follows a certain time course, including a rapid mineralization within a few days combined with a mineralization that takes years. As a result, bone is formed by different zones which have distinct mineral characteristics, with the lower mineralized zones corresponding to fresh bone formation (Fratzl et al., 2004). The mineral content in different zones may be determined by quantitative backscattered electron imaging, qBEI (Fratzl et al., 2004) as explained schematically with the help of Figure 8a). The qBEI method is used to obtain the bone mineralization density distribution (BMDD), which can be represented by the scheme of Figure 8b) (Fratzl et al., 2004). BMDD provide complementary data to BMD (bone mineral density) for osteoporosis diagnosis and management.

The qBEI is based, on the detection of backscattered electrons, using SEM. As previously mentioned the intensity of backscattered electrons increases with the atomic number. Bone is essentially formed by the organic matrix, which is composed by the elements H, C, N, O, P, S and by a mineral phase, which has Ca, P, O, H, C and Mg as components (Roschger et al., 1998). From these elements, Ca is the one with the highest atomic number and as a result it dominates the intensity of the backscattered beam.

The sample preparation involves dehydration and embedding the bone sample into polymethylmethacrylate, followed by polishing (Roschger et al., 1998).

In qBEI technique, different gray levels are correlated with different calcium contents (Fratzl-Zelman et al. 2009; Roschger et al., 1998, 2008, 2010). To achieve this effect, first, the backscattered signal is calibrated using the atomic number contrast of the reference

materials, carbon and aluminum. Secondly, calibrated gray levels must be converted into calcium concentration, taking 0% of Ca for osteoid and 39.86% Ca for pure hydroxyapatite (Roschger et al., 1998). From the bone mineralization density distribution (BMDD) curves (see Figure 8b)), the following parameters can be determined: Ca_{mean} (the weighted mean calcium concentration), Ca_{peak} (the peak of the calcium concentration), Ca_{width} (the width at half of the calcium distribution), Ca_{low} (the percentage of bone area that is mineralized below 5%) and Ca_{high} (the percentage of bone area that is mineralized above 95%) (Roschger et al., 2008, 2010). Patients with pathological remodeling disturbances present different parameters in comparison with healthy individuals (Roschger et al., 1998).

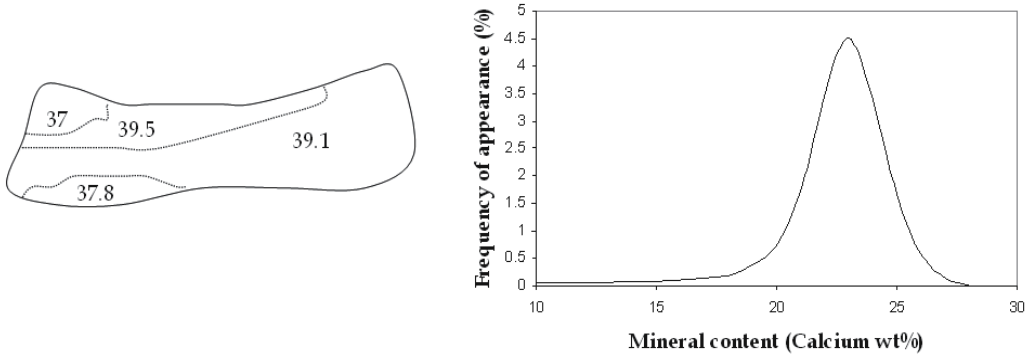

Fig. 8. a) Different zones with different mineral content, b) bone mineralization density distribution (adapted from (Fratzl et al. 2004))

2.4.6 Atomic force microscopy AFM

Atomic force microscopy (AFM) can be used to assess the structure and the topology of bone (Bozec et al., 2005; Fantner et al., 2004; Hassenkam et al., 2004) and also to evaluate the mechanical properties of the constituents by nanoindentation, which will be described in section 3.

AFM is based into a piezo mechanism, on which the deflection of an arm, due to van der Waals forces between the atom of the tip and the atom at the surface, is measured.

The sample preparation procedure is simple and only involves bone marrow removal and dehydration. The sample is glued to metal disks (Fantner et al., 2004; Hassenkam et al., 2004).

Studies on structural or morphological characterization of bone with AFM were carried out either for trabecular (Fantner et al., 2004; Hassenkam et al., 2004, 2006; Hengsberger et al., 2001) and for cortical bone (Bozec et al., 2005; Hengsberger et al., 2001). For example, AFM imaging of the surface of trabecular bone reveals the arrangement of either the collagen fibres as well as the crystals distribution, which can be used to assess the role of the two components at the nanoscale level (Hassenkam et al., 2004). The mineral phase was found to have a platen shape and lies flat on the fibrils (Hassenkam et al., 2004). In animals, AFM showed that on the surface of a trabecula there is a woven layer of less mineralized fibrils in comparison with the trabecular interior where the mineral phase is higher (Hassenkam et al., 2004). Also, the arrangement of mineralized collagen around an osteon can be observed by AFM (Bozec et al., 2005).

2.4.7 Small angle X-ray scattering, SAXS

The thickness of bone mineral plates is difficult to evaluate from X-ray diffraction data, but can be extracted from small-angle X-ray scattering. In this method, the scattering of X-rays by a sample is recorded at low angles. The technique is used to analyze the size and shape of mineralized particles, as well as their distribution (Bunger et al., 2010; Fratzl et al., 2004; Fratzl-Zelman et al. 2009; Roschger et al., 2010).

The scattered intensity and the scattering vector are obtained and converted into shape parameters (Bunger et al., 2010; Fratzl et al., 2004; Roschger et al., 2010). In bone analysis, the SAXS parameter $T = 4\Phi(1 - \Phi) / \sigma$, where Φ is the mineral bone volume fraction and σ is the bone surface per unit volume is used to estimate the average mineral particles thickness (Fratzl et al., 2004; Fratzl-Zelman et al. 2009; Roschger et al., 2010). It is assumed that the mineral particles have the shape of platelets. A shape function G(x) can also be derived from the SAXS data to characterize the mineral particle shape, size distribution and arrangement (Fratzl et al., 2004). The shape function exhibits differences between different species, like human and rat (Fratzl et al., 2004). Another example is the examination of bone from normal and ovariectomized rats by SAXS which found that the mineral plates were thicker in old bone in comparison with new bone (Bunger et al., 2010).

2.4.8 Neutron scattering

The mineral-matrix arrangement has an extremely important impact on the bone properties and some of the matrix properties can be extracted from neutron scattering experiments.

The fibrils, *i.e.*, the molecules of mineralized collagen are arranged in a banded structure as previously stated. Neutron scattering experiments can be used to determine the spacing between adjacent collagen molecules or adjacent fibrils. It was shown that the spacing between collagen molecules was 1.6 nm and 1.1 nm respectively for non-mineralized wet and dry molecules, while for the mineralized wet bone, the distance between adjacent fibrils was 1.25nm (Fratzl et al., 2004; Fratzl & Weinkamer, 2007).

2.5 The effect of disease on the bone's structure

Metabolic bone diseases and inflammatory rheumatic diseases will be considered.

2.5.1 Metabolic bone diseases

Osteoporosis (OP) is a bone disease defined as a systemic skeletal disease characterized by a reduction in bone mass and microarchitectural deterioration of bone tissue, which leads to an increased bone fragility and susceptibility to fracture (Kanis et al., 2005).

Bone microarchitecture deterioration occurs due to changes in organic matrix and a decrease in the mineralized component of bone (Boyle et al., 2003). This effect occur when the balance between bone formation and bone resorption is disrupted by increased resorption (*i.e.* menopause) or decreased formation (*i.e.* aging).

Bone mass loss is not due to exactly equal mechanisms in men and women. While in men, bone loss predominantly occurs by trabecular thinning and reduced bone formation, in women there is an earlier loss of connectivity between trabeculae and earlier cortical thinning (Seeman, 2007).

The comparison of normal with osteoporotic human bone shows a decrease in the trabeculae thickness and a deficiency in the trabecular structure with breakage of trabeculae (Rubin et al., 2004).

It was found that the removal of struts or loss of connectivity reduces more severely the modulus of elasticity and the strength than the uniform thinning (Fratzl, & Weinkamer, 2007; Gibson, 2005).
The techniques described above can detect differences between normal and osteoporotic bones and are very useful as research tools to study animal model and human bone samples.

2.5.2 Inflammatory rheumatic diseases

Inflammatory systemic diseases like rheumatoid arthritis (RA) are characterized by chronic inflammation, which induces synovium proliferation, increasing local and systemic bone resorption and ultimately structural damage and secondary OP (Alamanos & Drosos, 2005; Caetano-Lopes et al., 2009b; Orstavik et al., 2004; van Staa et al., 2006). Osteoimmunology is a new research field, which bridges the concepts of inflammation and bone.
The study of the effect of rheumatoid arthritis (RA) on the structure of bone is not a simple task. In fact patients who suffer from RA are submitted to medications which may contribute to bone fragility. In this way, the use of a mice model to study the effect of chronic inflammation on the structure of bone is useful (Caetano-Lopes et al., 2009a, 2010) and recently we have studied the inflammation on bone using the SKG mice model, which behaves like human RA (Caetano-Lopes et al., 2009a, 2010). SKG mice were obtained from BALB/c mice, with a point mutation in the ZAP-70 gene, which triggered by a zymosan injection developed a chronic arthritis (Caetano-Lopes et al., 2009a, 2010). BALB/c can be used as control for SKG mice.
In five months (Caetano-Lopes et al., 2009a) and eight months (Caetano-Lopes et al., 2010) arthritic SKG mice, we have evaluated the bone structure by scanning electron microscopy and found that it was affected by the inflammatory disease. For example, the trabecular thickness was reduced from 70.91 ± 23.66 to 57.18 ± 16.78 μm in arthritic animals (Caetano-Lopes et al., 2009a). The vertebrae from arthritic mice have a higher inter-trabecular distance and a decreased trabeculae thickness (Caetano-Lopes et al., 2009a, 2010).
At higher magnifications, the structure of lamellae can be observed by SEM with backscattered electrons (Figure 4). Comparing Figures 4a) and b), respectively from control and osteoporotic mice, no particular differences can be detected with this technique, at this scale range.
In an inflammatory process the lack of collagen matrix repair affects the mineral crystal deposition, which will contribute to the decreasing of mechanical strength (Caetano-Lopes et al., 2010).

3. Mechanical properties

This chapter gives an emphasis on the relationship between the complex hierarchical structure of bone and its mechanical properties. Bone is a complex but ordered composite material having the function of resisting to mechanical forces and fractures.
With regard to the assessment of the bone stiffness, strength and toughness, there are different tests such as compression, tension, bending, fatigue, creep, torsion and nanoindentation.
In addition, these tests can be performed under different loading conditions, alone or in combination, and can be applied either cyclically or monotonically, short- or long-term, and at several loading rates. At a more microscopic level, atomic force microscopy may be used

for nanoindentation, which measures the mechanical properties of the bone units, trabeculae or osteons, respectively for trabecular and cortical bone.

In the mechanical tests, it is possible to obtain data that enables the assessment of parameters like the elastic or Young's modulus, the yield stress, and energy until yield which are used to evaluate respectively the stiffness, strength and toughness of bone. An example of a stress-strain compression curve is given in Figure 9c), where an indication of these parameters is shown. The Young's modulus is the slope of the stress-strain curve in the elastic regime. The yield stress is the stress attained at the end of elastic deformation and the energy until yield is evaluated by the area under the curve before yielding (Viguet-Carrin et al., 2006).

Several factors affect the mechanical properties of bone, such as, age (Sun et al., 2008; Wang et al., 2002, 2005; Woo et al., 2010), sex (Duan et al., 2005; Seeman, 2003, 2007; Wang et al., 2005), anatomical location (Morgan & Keaveny, 2001; Morgan et al., 2003; Nazarian et al., 2007), load orientation (Fratzl, & Weinkamer, 2007; Gibson & Ashby, 1999; Gibson, 2005), geometry/architecture (Ammann & Rizzoli, 2003; Rho et al., 1998; Silva, 2007), arrangement of collagen fibers and mineral particles (Viguet-Carrin et al., 2006), bone density (Ammann & Rizzoli, 2003; Cory et al., 2010; Kopperdahl & Keaveny, 1998; Mueller et al., 2009; Silva, 2007), and bone diseases (Caetano-Lopes et al., 2009a; Ciarelli et al., 2000; Homminga et al. 2002; Li & Aspden, 1997; Sun et al., 2008; Woo et al., 2010).

The arrangements of bone trabeculae, the orientation of collagen fibres and carbonated apatite crystals in relation to load have an important role in determining bone strength (Viguet-Carrin et al., 2006). Carbonated apatite crystals are very stiff and strong, but not very tough, with a Young's modulus around 165 GPa, while collagen has much more toughness but is not very stiff, and exhibits a modulus of 1.24 GPa. The mechanical properties of bone depend on the arrangement of collagen fibers which condition the deposition of mineral crystals and influences bone strength (Viguet-Carrin et al., 2006). The composite, remarkably combines, the properties of the two components, the stiffness and the toughness. As for any other composite material, the elastic modulus of the bone will have an intermediate value between the ones of its components.

Woven bone composed by unorganized collagen fibers has lower mechanical properties than lamellar bone with a well defined arrangement of mineralized collagen fibers, which reveals the importance of the collagen disposition (Viguet-Carrin et al., 2006).

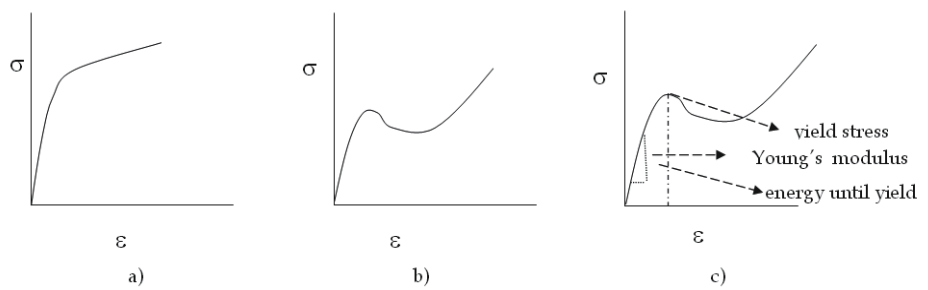

Fig. 9. Schematically compressive stress-strain curves for healthy a) cortical and b) trabecular bone (adapted from (Gibson & Ashby, 1999)), c) typical stress-strain curve with the indication of the Young's modulus, yield stress and energy until yield (adapted from (Viguet-Carrin et al., 2006))

While cortical bone has a Young's modulus in the range of 10 to 20 GPa, the trabecular bone has a lower value of the stiffness, with values that can vary between 0.3 and 3000 MPa (Fung, 1993).

It is widely accepted that the relative density of trabecular bone depends on the load that it suffers, with low density structures developing where the stress is low. In this sense, the trabecular architecture adapts to the external loading (Fratzl, & Weinkamer, 2007; Gibson & Ashby, 1999; Gibson, 2005; Keaveny et al., 2001). If the loads are equivalent in the three directions of bone, a structure with equiaxed cells is obtained. However, if load is higher in one direction, the trabeculae tend to align in the load direction, adopting an anisotropic structure (Gibson & Ashby, 1999; Keaveny et al., 2001).

In cortical bone the mechanical properties depend on the porosity, degree of mineralization and organization of bone (Rho et al., 1998) and at a macroscopic level properties vary from one bone region to another (Rho et al., 1998). In human trabecular bone, the mechanical properties change from the periphery to the center of the bone (Rho et al., 1998). The intrinsic mechanical properties of isolated osteons and individual trabeculae can be determined. The elastic modulus of single trabeculae was found to be similar to the one of the cortical tissue (Rho et al., 1998).

Although sometimes it is not taken into account, hydration is also an important factor which has to be considered when performing mechanical tests of bone. It is known that dry bone has a higher Young's modulus, but the strength and strain to failure decrease significantly (Gibson & Ashby, 1999). Thus, the mechanical tests are generally performed with wet bones.

This section will be divided in subsections, for specific types of mechanical tests. The influence of some parameters on those types of tests will be also addressed. Some issues related with bone deformation mechanisms will be discussed in section 3.8, while the effect of aging and disease on the bone's mechanical properties will be handled on section 3.9.

3.1 Compression

The compression tests are the most frequently performed tests to determine the bone's mechanical properties, due to their simple procedure and to the fact that bones are often submitted to compression loads (Cory et al., 2010; Kopperdahl & Keaveny, 1998; Li & Aspden, 1997; Morgan & Keaveny, 2001; Morgan et al., 2003; Sun et al., 2008; Woo et al., 2010).

The mechanical behaviour of cortical bone is quite different from the behaviour of trabecular bone, as schematically presented in the stress-strain curves of Figure 9a) and b) (Gibson & Ashby, 1999). The cortical bone tested in the longitudinal direction exhibits an elastic region up to strains of 0.7% and a plastic deformation until 3% (Gibson & Ashby, 1999). Bone has an anisotropic performance, as when is tested along the transversal direction is less stiff and strong (Gibson & Ashby, 1999).

In the present chapter, more relevance will be given to trabecular bone, due to its importance from the clinical point of view. Trabecular bone is included in the class of open cellular materials or foams. The compressive stress-strain curves of healthy trabecular bone are characterized by three distinct regions (Figure 9b)) (Gibson & Ashby, 1999; Gibson, 2005). The initial elastic response is due to the bending of trabeculae, while the second region is associated with elastic buckling, plastic yielding or brittle fracture of trabeculae (Gibson & Ashby, 1999). Finally the third regime occurs when cell walls or trabeculae touch each other (Gibson & Ashby, 1999). It is generally accepted that the mechanical properties of

trabecular bone are related to their density. For example, the Young's modulus is proportional to the square of the relative density (Gibson & Ashby, 1999; Gibson, 2005).
Several works can be found on the compression of trabecular bone, using vertebrae (Ammann & Rizzoli, 2003; Kopperdahl & Keaveny, 1998; Matsuura et al., 2008; Morgan & Keaveny, 2001; Morgan et al., 2003; Silva, 2007; Woo et al., 2010), tibia (Fonseca & Ward, 2004; Morgan & Keaveny, 2001; Morgan et al., 2003), femur (Cory et al., 2010; Fonseca & Ward, 2004; Morgan & Keaveny, 2001; Morgan et al., 2003) and femoral heads (Ciarallo et al., 2006; Knoob et al., 2007; Li & Aspden, 1997; Matsuura et al., 2008; Morgan & Keaveny, 2001; Morgan et al., 2003; Sun et al., 2008). For example, it was found that for a given density, samples from tibia had higher Young's modulus than the ones from vertebrae (Morgan et al., 2003).
Experimentally, the compression of bone can be performed either in animal model or in human samples.
We have used a mice model, the SKG arthritic mice, to evaluate the effect of chronic inflammation on the biomechanical properties of the bone (Caetano-Lopes et al., 2009a). Compression tests on the vertebral bodies of SKG mouse chronic arthritis model were performed (Caetano-Lopes et al., 2009a, 2010). In this case, a load cell of 500N and a cross-head speed of 0.01 mm/s were used. Samples were kept wet during the test. From the load F – displacement ΔL curves, stress an strain are calculated, respectively, as

$$\sigma = F/A \tag{1}$$

$$\varepsilon = \Delta L/L \tag{2}$$

where A is the sample area and L is the length. The stress-strain curves of Figure 10 were calculated assuming that the vertebrae have a cylinder body. Figure 10a) and b) shows the stress-strain curves obtained on the compression of arthritic and control female 5 months mice vertebrae. A photograph with the vertebrae can be observed in Figure 10c). Parameters like the elastic modulus, yield stress, maximum stress, energy until yield and the energy until maximum stress were determined. SKG mice vertebrae were found to exhibit lower stiffness, strength and toughness in comparison with the results obtained on the compression of control BALB/c mice, aged 5 and 8 months (Caetano-Lopes et al., 2009a, 2010).
Compression of trabecular bone samples from femoral epiphyses collected from patients with osteoporosis and osteoarthritis was performed by this chapter's authors (Vale et al.). Figure 11 shows a cylinder of trabecular bone, the compression set-up used and the stress-strain curve obtained on the compression test of a human sample from a patient with osteoporosis.
The methodology of the compression tests is not always the same and variables like the geometry, dimensions of the samples and type end supports can vary. The shape of the samples may be cubic (Diamant et al., 2007; Sun et al., 2008) or cylinder (Li & Aspden, 1997; Matsuura et al., 2008; Morgan & Keaveny, 2001). In general, cylinders are more used as they are easily obtained by drilling. From several studies, it is suggested that cylinder specimen with a length: diameter ratio between 1.5 and 2 provides accurate results (Li & Aspden, 1997; Matsuura et al., 2008; Morgan & Keaveny, 2001). The sample in Figure 11 is in this range of ratio, with a diameter of 15 mm.

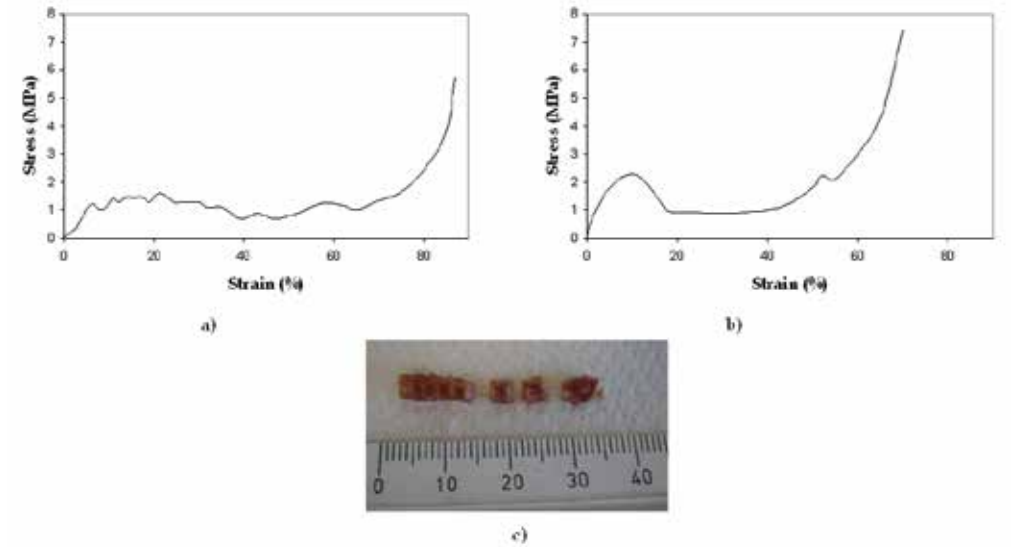

Fig. 10. a) Stress-strain curves obtained on the compression of a) arthritic and b) control female 5 month mice vertebrae. c) Photograph of mice vertebras

While in some publications, it is not clear the type of end support used, on other cases it is mentioned the platen technique and the end-cap technique. In the platen method the samples are placed inside metallic platens (Helgason et al., 2008; Morgan & Keaveny, 2001), while with the end-cap method the samples are embedded into polymeric end-caps (Helgason et al., 2008; Matsuura et al., 2008; Morgan & Keaveny, 2001). Both methodologies intend to minimize the side effects, but it is not consensual which the most reliable procedure is. We have used a metallic platen for the upper extremity of the sample, while the bottom was left free.

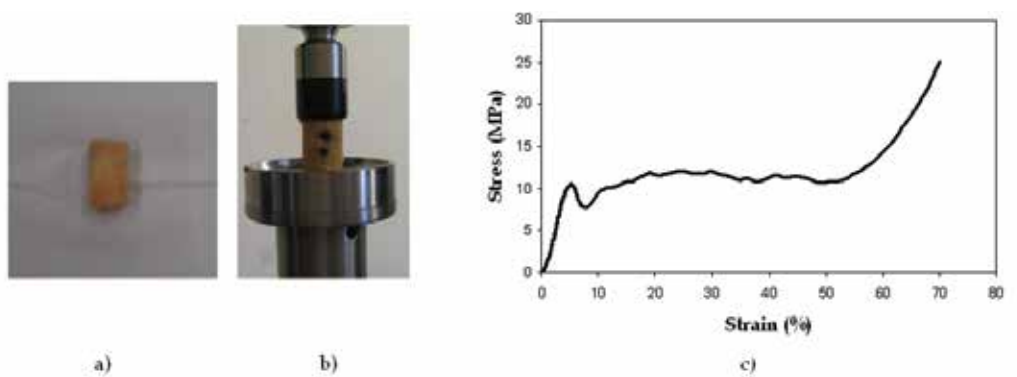

Fig. 11. a) Cylinder of trabecular bone, b) compression set-up and c) stress-strain curve for a human sample from a male patient with osteoporosis

3.2 Tension

The preparation of specimens to perform tensile tests is not simple; probably this is one of the reasons why the studies on bone traction are rarer. For example, the extremities of a

mice femur may be inserted in brass fixtures and glued with dental cement, followed by bone micromachining (Ramasamy & Akkus, 2007). Other authors mentioned that cylindrical specimens from human trabecular bone were embedded into polymeric end-caps to fit into the grips of the testing machine (Morgan & Keaveny, 2001).

Tensile stress- strain curves for healthy trabecular bone are characterized by an initial linear elastic region, followed by a non-linear deformation until a maximum is achieved which corresponds to crack initiation (Gibson & Ashby, 1999). In tension, the Young's modulus of the compact bone increases with the mineral content (Giraud-Guille, 1988).

The tensile-compressive yield strength ratio is around 0.62 for trabecular bone (Bayraktar et al., 2004). This means that the strength is asymmetric, with a higher strength in compression than in tension. The difference between tensile and compression curves can be observed in the plots of Figure 12, for mice femur, for which the compression strength is greater than the tensile strength (Ramasamy & Akkus, 2007). The Young's modulus is also higher in compression than in traction, either in vertebrae, tibia and femoral heads (Morgan & Keaveny, 2001).

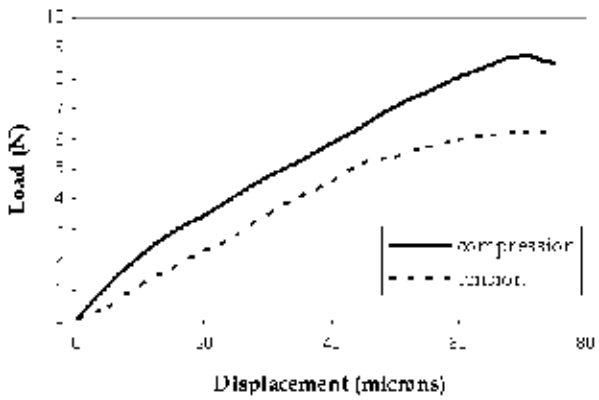

Fig. 12. Comparison of the load-displacement curves obtained in tension and in compression for mice femur (adapted from (Ramasamy & Akkus, 2007))

3.3 Bending

The mechanical performance of the entire bone is of much interest from the clinical point of view and bending tests are the most common methods used to analyze long bones as a whole (Sharir et al., 2008).

Bending tests can use three or four point bending devices (Sharir et al., 2008). In a three point bending test, the bone is placed on two supports, while only one support contacts the opposite surface, exactly at the mid point between the two supports. In this case, the maximum load occurs at the middle point and the bone will fracture in this location (Sharir et al., 2008).

On the four point bending procedure, there are two upper and two lower supports. The advantage is that the section of the bone is submitted to a uniform moment, without shear effects (Sharir et al., 2008). However, as bones have an irregular geometry, it is difficult to have two supports contacting bone at the same time. In addition, samples may have a size too small for this technique. Due to these reasons, the three point bending procedure is the most used for bone (Sharir et al., 2008).

To calculate the stresses and strains during the test, it is assumed that bones are cylinders and the diameter of their cross section is d. The applied load is denoted by F, S is the distance between lower supports and Δl is the elongation of the sample. Therefore the stress and the strain are given respectively by (Beer et al., 1992)

$$\sigma = \frac{FS}{\pi\left(\frac{d}{2}\right)^3} \tag{3}$$

$$\varepsilon = \frac{12\left(\frac{d}{2}\right)\Delta l}{S^2}. \tag{4}$$

Bending tests may be performed with animal radius, femurs and tibias (Akhter et al., 2001; Bensamoun et al., 2006; Schriefer et al., 2005; Shahnazari et al., 2007) to determine bone strength. For the evaluation of bending data, it is usual to define yield stress, Young's modulus, ultimate stress, ultimate strain and energy until the maximum stress (Akhter et al., 2001; Bensamoun et al., 2006; Schriefer et al., 2005).

We have performed three point bending tests with femoral bones of SKG and BALB/c mice at a cross-head speed of 0.01 mm/s and a load cell of 500N (Caetano-Lopes et al., 2009a, 2010). Figure 13 shows stress-strain curves obtained from the bending of arthritic and control female mice femurs, as well as the experimental set-up for three point bending of mice femur. The distance between supports is 5mm. From the stress-strain curves it was possible to obtain the above mentioned parameters. The results obtained showed that arthritic femurs had, in comparison with control animals, lower elastic modulus, yield stress, ultimate stress and energy until ultimate stress.

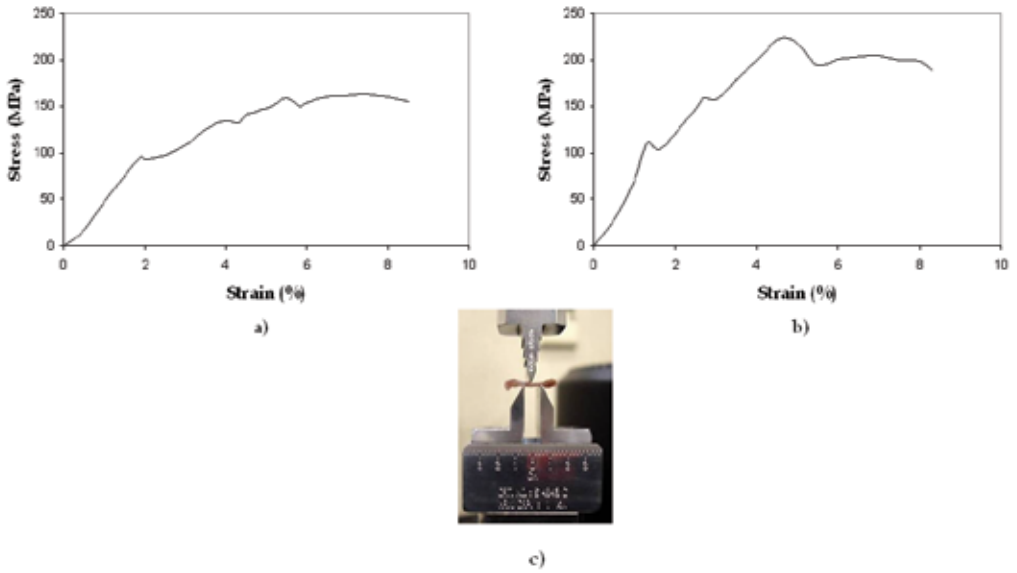

Fig. 13. a) Stress-strain curves obtained on the bending of a) arthritic and b) control female 5 month mice femurs, c) experimental set-up for three point bending of mice femur

3.4 Fatigue

Bones are subjected to fatigue due to the action of cyclic loading. Some studies can be found in the literature on fatigue of human trabecular bone (Dendorfer et al., 2008; Haddock et al., 2004; Rapillard et al., 2006; Yamamoto et al. 2006), but the majority of the works describe results from animal testing (Dendorfer et al., 2008, 2009; Ganguly et al., 2004; Haddock et al., 2004; Moore et al., 2003; Moore & Gibson, 2003).

A material under cyclic loading fails at stresses below the values that the material can bear under static loading. Bones are subjected to fatigue loading as a result of daily activity or prolonged exercise, which occurs for instance in athletes (Ganguly et al., 2004; Moore et al., 2003; Moore & Gibson, 2003). Fatigue loading is one of the primary causes of human bone failure (Ganguly et al., 2004). Therefore, it is important to characterize the residual strains that occur after cyclic loading (Yamamoto et al., 2006).

Fatigue fractures may occur in young adults (failure due to stress concentration, known as stress fractures). Failures due to stress concentration result from prolonged exercise and occur more frequently at the tibia and metatarsal bones, while fragility or osteoporotic fractures of elderly individuals take place on the proximal femur and on vertebrae where the trabecular bone supports most of the load (Ganguly et al., 2004).

Fatigue damage results from accumulation of micro-cracks (Fratzl & Weinkamer, 2007; Moore et al., 2003; Taylor, 1998). Micro-cracks are repaired through bone remodeling. However, if micro-cracks are not repaired, they accumulate and coalesce, leading to a decrease in bone stiffness and to an increase of fracture risk (Dendorfer et al., 2008; Moore et al., 2003; Moore & Gibson, 2003; Taylor, 1998).

The preparation of bone samples to perform fatigue tests includes an initial defatting of cylinder specimens, followed by a press-fit into brass end caps of the sample extremities (Dendorfer et al., 2008; Ganguly et al., 2004; Moore et al., 2003; Moore & Gibson, 2003; Yamamoto et al., 2006). The extension may be measured by extensometers attached to the brass caps (Ganguly et al., 2004; Moore et al., 2003; Moore & Gibson, 2003) or by the displacement of the cross-head (Dendorfer et al., 2008). As fatigue tests may take a long time, samples must be kept wet with soaked gauze or using a saline bath (Dendorfer et al., 2008; Ganguly et al., 2004; Moore et al., 2003; Moore & Gibson, 2003).

Fatigue tests consist on the application of a certain number of cycles of compressive loading and unloading. As an initial step, samples are subjected to a small number of cycles (10 cycles) with low stress and strain. The initial secant elastic modulus E_0 is determined from the slope of the 10^{th} cycle (Ganguly et al., 2004; Moore et al., 2003; Moore & Gibson, 2003; Yamamoto et al. 2006). The initial modulus is used to normalize the applied stress. The following step is the definition of $(\Delta\sigma/E_0)$ where $\Delta\sigma$ is the interval of applied stress, *i.e.*, $\Delta\sigma=\sigma_{max}-\sigma_{min}$. If high values of $(\Delta\sigma/E_0)$ are imposed it is expected that the material fails at a small number of cycles. The frequency of the cycles varies from 1 to 2 Hz (Dendorfer et al., 2008; Ganguly et al., 2004; Moore et al., 2003; Moore & Gibson, 2003) and values of $(\Delta\sigma/E_0)$ =0.008 or lower can be used (Moore & Gibson, 2003). It is considered that on a test, failure occurs when the modulus reduction is 10% (Ganguly et al., 2004; Moore et al., 2003; Moore & Gibson, 2003).

From fatigue tests, stress-strain curves are obtained and it is possible to measure the secant modulus (from the slope of each cycle), changes in the plastic strain for a single cycle $\Delta\varepsilon_{pl}$, residual strain on unloading ε_{res} and maximum strain ε_{max} (Dendorfer et al., 2008; Ganguly et al., 2004; Moore et al., 2003; Moore & Gibson, 2003).

The fatigue behavior of trabecular bone is characterized by an increase on ε_{res}, a broadening of the hysteresis loops, and by a decrease of the secant modulus. The strains, ε_{max} or ε_{res} plotted against the number of cycles, exhibit the typical fatigue curve with three stages. There is an initial increase of the strains with the number of cycles, a zone where the strain rate is almost constant and finally a third zone characterized by a rapid increasing of strains until failure (Dendorfer et al., 2008, Ganguly et al., 2004; Moore et al., 2003; Moore & Gibson, 2003).
An example of fatigue curves of trabecular bone from a femoral head of a patient with osteoporosis is given in Figure 14. Figure 14 a) shows the initial preconditioned with 10 cycles, while Figure 14b) presents σ/E_0 versus the strain ε in a test with 1000 cycles. The modulus E_0 is calculated from the slope of the 10th cycle. The ratio of ($\Delta\sigma/E_0$) was 0.002. The strains ε_{max} or ε_{res} increased with the number of cycles. However, the modulus (E_{sec}/E_0) was kept almost constant. This is probably due to the application of very small values of stress and a reduced number of cycles.

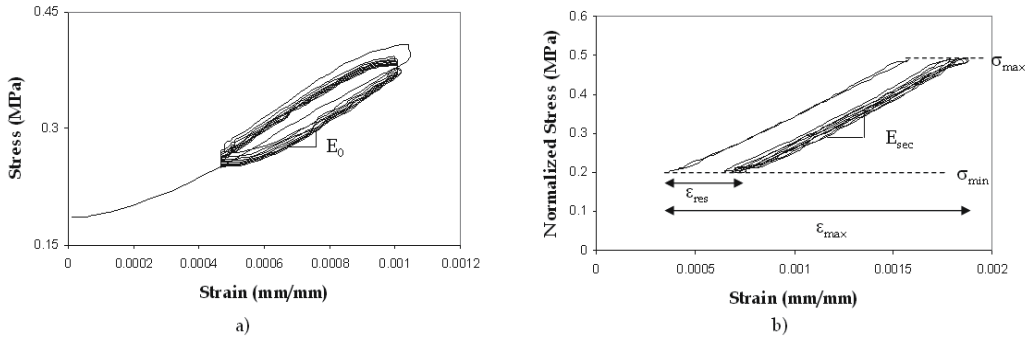

Fig. 14. Fatigue curves of trabecular bone from a femoral head of a patient with osteoporosis: a) initial preconditioned with 10 cycles, b) σ/E_0 versus the strain ε in a test with 1000 cycles: only cycles n^o 1, 200, 400, 600, 800 and 1000 are represented

3.5 Creep

Like other biological materials, bone exhibits a time-dependent damage or creep (Keaveny et al., 2001). Vertebral fractures present deformations on the vertebrae which indicate a time dependent failure mode, due to irreversible residual strains (Yamamoto et al., 2006). It is suggested that the trabecular bone does not have time to recover from creep deformations accumulated by static loading (Yamamoto et al., 2006).
Creep tests can be made on human vertebral trabecular bone, with cylindrical specimens. Prior to tests, samples were defatted and placed into brass end caps (Yamamoto et al., 2006). First, the samples go through a preconditioned stage, similar to the one performed in fatigue tests, composed by 10 cycles. The initial modulus is recorded. The specimen is then subjected to a static loading for 35h, after which is unloaded for a period of 35h (Yamamoto et al., 2006). Figure 15 presents the strains measured over the loading and unloading stages.
Depending on the applied loads, the creep curve may have a different shape from the one of Figure 15, and may exhibit an initial rapid response, a steady state at a constant speed, followed by a rapid increase in deformation before fracture (Keaveny et al., 2001).
Particular attention is given to the residual strains which remain at the end of the unloading phase. Although loads were applied only for 35h, it was found that deformations only

disappear after 1 month (Yamamoto et al., 2006). As vertebrae had no time to recover from prolonged loading, long time effects may contribute to vertebral fractures.

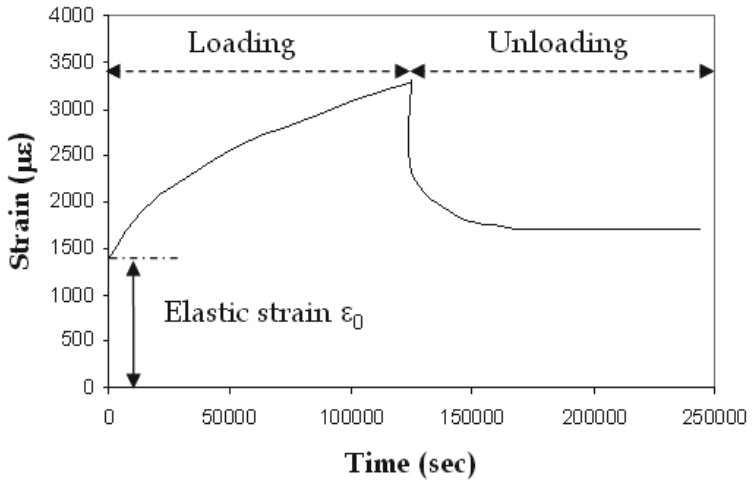

Fig. 15. Typical strain-time curve obtained on a creep test from a vertebral trabecular bone (adapted from (Yamamoto et al., 2006))

3.6 Torsion

Bone can be submitted to multiaxial stresses due to bone pathologies, to accidental loads or to a joint replacement (Garnier et al., 1999).

Torsional tests are less frequently used than compression or bending (Sharir et al., 2008). The extremities of the bone sample are embedded in blocks of polymer material which fit the grips of the testing device (Nazarian et al., 2009; Sharir et al., 2008). Deformation rates from 0.01 to 0.36 rad s^{-1} may be applied (Kasra & Grynpas, 2007).

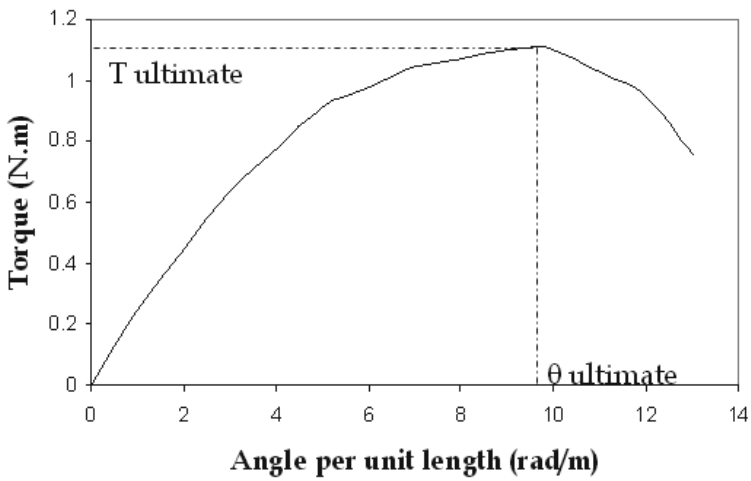

Fig. 16. A typical torque-angular deformation curve from a torsion test with trabecular femoral head bone (adapted from (Garnier et al., 1999))

During a test, the specimen is subjected to a torque that originates its torsion (Sharir et al., 2008). The torque-angular deformation curve is recorded and the shear modulus is calculated from the slope of the linear region (Kasra & Grynpas, 2007; Nazarian et al., 2009; Sharir et al., 2008). The shear stress is also calculated from the data of the torque-angular deformation curve (Garnier et al., 1999). A typical torque deformation curve is shown on Figure 16.

The shear modulus increases with the strain rate, which reveals the viscoelastic nature of the bone tissue (Kasra & Grynpas, 2007). On human femoral trabecular bone, the mean shear modulus was found to be 289 MPa (Garnier et al., 1999), which is similar to the values obtained for animal trabecular bone (Kasra & Grynpas, 2007).

3.7 Nanoindentation

Besides structural assessment, AFM can operate to perform nanoindentation, which is used to measure the intrinsic mechanical properties, such as, the bone tissue modulus of trabecular bone (Chevalier et al., 2007) and cortical tissue (Bembey et al., 2006), or the mechanical properties of the bone structural units, *i.e.*, the osteon for cortical bone and the trabeculae wall for trabecular bone (Hengsberger et al., 2001; Rho et al., 1997; Rho et al., 1999; Zysset et al., 1999). Nanoindentation measures the elastic modulus or the stiffness, as well as, the hardness of the bone tissue (Hengsberger et al., 2001).

The combination of AFM and nanoindentation has the possibility of investigating the elastic properties of bone structural units (BSU) associated to a surface characterization, which provides high resolution to the position of the tip on the structure of interest (Hengsberger et al., 2001). The combination of AFM with nanoindentation allows obtaining a surface topography of constant contact force and a force-displacement curve in nanoindentation (Hengsberger et al., 2001).

The procedure to prepare the bone samples includes, besides bone marrow removal by distilled water, and subsequent dehydration, an embedment in a resin and polishing with 1200, 2400 and 4000 grade silicon carbide papers and with alumina suspension (Chevalier et al., 2007; Hengsberger et al., 2001).

Nanoindentation is performed in three phases, which include a loading phase where the tip is pressed into the material up to a maximum force, an holding period where the tip penetrates into the material (Figure 17a)) leaving indentation marks (Figure 17b)) followed by an unloading step. Load-displacement curves are obtained (Figure 17c)). As during loading and holding phases, both elastic and plastic deformation occur, it is only possible to determine the elastic modulus on the unloading phase, where the elastic recovery is the only mechanism present (Hengsberger et al., 2001). The stiffness is determined by the slope of the unloading curve between 40% and 90% of the maximum load (Hengsberger et al., 2001). To determine the contact area the procedure derived by Oliver & Pharr (Oliver & Pharr, 1992) is followed. The hardness is obtained by dividing the maximum load by the contact area (Hengsberger et al., 2001).

The experimental Young's moduli for the bone units vary from 0.76 GPa to 20 GPa for trabecular bone and from 5 GPa to 27 GPa for cortical bone. Hardness presents values of 0.6±0.11 GPa for compact bone and 1.1±0.17 GPa for trabecular bone (Hengsberger et al., 2001).

Other studies propose the combination of AFM with SEM to measure the properties of collagen fibrils (Hang & Barber, 2011) or the combination of AFM with qBEI (Fratzl-Zelman

et al. 2009) to evaluate if a reduced mineral content determined by qBEI is associated with a reduction of the stiffness and hardness of the bone.

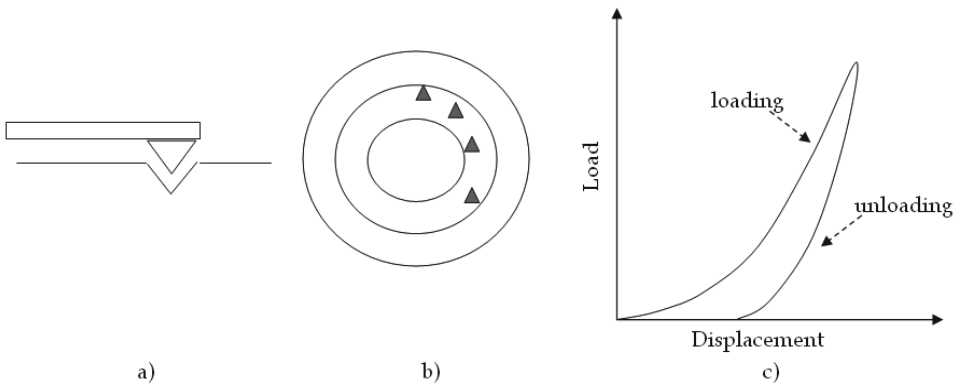

Fig. 17. Schematically nanoindentation a) tip, b) indentation marks on an osteon and c) curve load-displacement (adapted from (Hengsberger et al., 2001))

3.8 Bone deformation mechanisms

Several attempts have been made to predict the mechanical properties of bone including the composite rule of mixtures (Rho et al., 1998). As mentioned in Section 2, bone is a composite material formed by mineral crystals of carbonated apatite in a matrix of collagen. As the apatite is a rigid, brittle material, collagen must play an important role on the bone deformation (Fratzl et al., 2004; Fratzl & Weinkamer, 2007). It is assumed that the elastic behavior of bone is dominated by the mineral phase, while the plastic deformation is governed by a combination of the elastic-plastic behavior of the mineral with pure elastic deformation of the collagen matrix (Fratzl et al., 2004; Fratzl & Weinkamer, 2007). The matrix between the mineral particles has the role of dissipating energy, by deviating or creating barriers to crack propagation (Fratzl et al., 2004; Fratzl & Weinkamer, 2007). It has been proposed that the bonds within or between collagen molecules have the ability to recover after load removal, being responsible for the toughness of the bone (Fratzl et al., 2004; Fratzl & Weinkamer, 2007). Bone deformation, for example by tensile loading, induces shear stresses on the matrix, which means that the mechanical performance of bone is controlled by the shear stiffness, strength and toughness of the matrix (Fratzl et al., 2004; Fratzl & Weinkamer, 2007). Following this analysis, within a fibril, the organic matrix should be thin to withstand shear stress and the mineral particles must be thin to reduce the brittleness of the tissue (Fratzl et al., 2004; Fratzl & Weinkamer, 2007). As a result, the mechanical behavior of the bone, as a composite material, depends on its components, collagen and mineral particles and on the interaction between them.

3.9 The effect of aging and disease on the bone's mechanical properties

There is some uncertainty in the prediction of mechanical behavior of bone influenced by aging or bone disease.

Aging, is associated with changes in bone structure and microarchitecture, decreased bone strength and increased the risk of fragility fractures, due to a decrease in bone volume formed, continued resorption and high remodeling (Seeman, 2007, 2008). In post menopause

women, increased remodeling induces cortical thinning, higher porosity, trabecular thinning as well as loss of trabeculae connectivity (Seeman, 2007, 2008). High remodeling also decreases the bone mineral content, which is reflected on a reduction of stiffness (Seeman, 2007).
It was found that with aging, a significant loss on the mechanical strength is observed, as the yield stress is reduced by 10% per decade, from the 2nd decade to the 10th decade (Keaveny et al., 2001).

3.9.1 Metabolic bone diseases

There are some studies on the effect of osteoporosis on the mechanical properties of bone (Ciarelli et al., 2000; Homminga et al. 2002; Sun et al., 2008; Woo et al., 2010). Osteoporotic individuals have worse mechanical properties, evaluated by the Young's modulus and yield stress, in comparison with controls (Ciarelli et al., 2000). Differences were also detected in the other methods performed.

3.9.2 Inflammatory rheumatic diseases

The effect of arthritis in the mechanical deformation either in compression and bending were previously described in sections 3.1 and 3.3, for SKG mice (Caetano-Lopes et al., 2009a). In fact, arthritic mice vertebrae were found to have lower stiffness, strength and toughness in comparison with the results obtained on the compression of control BALB/c mice (Caetano-Lopes et al., 2009a, 2010). Moreover we have also observed in these mice degradation of mechanical properties studied by femur bending tests.
Compression tests performed on human osteoporotic samples and on osteoarthritis samples revealed that specimens with osteoporosis had lower Young's modulus and yield stress than the ones with osteoarthritis (Li & Aspden, 1997; Sun et al., 2008).

4. Conclusions

This chapter gave a general approach of the bone as a composite material with particular emphasis on the bone structural and mechanical properties. Essentially the line followed was to focus on the experimental procedures and on the techniques used for bone assessment. Some aspects were not covered as the finite element modeling, which the authors considered to be out of the scope of the chapter. Results from research studies performed by the authors, namely in a mice model of arthritis and in human bone samples obtained from patients submitted to total hip replacement surgery were presented to illustrate the impact of the inflammation on bone and also whether the bone mechanical and structural properties can be affected in primary and secondary osteoporosis.

5. References

Akhter, M.; Cullen, D.; Gong, G. & Recker, R. (2001). Bone biomechanical properties in Prostaglandin EP1 and EP2 knockout mice. *Bone*, Vol. 29, pp.121-125, ISSN 8756-3282.

Alamanos, Y. & Drosos, A. (2005). Epidemiology of adult rheumatoid arthritis. *Autoimmunity Reviews*, Vol.4, No.3, pp. 130-136, ISSN 1568-9972.

Ammann, P. & Rizzoli, R. (2003). Bone strength and its determinants. *Osteoporosis International*, Vol.14, pp. S13-S18, ISSN 0937-941X.

Basillais, A.; Bensamoun, S.; Chappard, C.; Brunet-Imbault, B.; Lemineur, G.; Ilharreborde, B.; Ho Ba Tho, M. & Benhamou, C. (2007). Three-dimensional characterization of cortical bone microstructure by microcomputed tomography: validation with ultrasonic and microscopic measurements. *Journal of Orthopaedic Science*, Vol.12, No.2, pp. 141-148, ISSN 0949-2658.

Bayraktar, H.; Morgan, E.; Niebur, G.; Morris, G.; Wong, E. & Keaveny, T. (2004). Comparison of the elastic and yield properties of human femoral trabecular and cortical bone tissue. *Journal of Biomechanics*, Vol.37, No.1, pp. 27-35, ISSN 0021-9290.

Beer, F.; Johnston, E. & DeWolf, J. (1992). *Mechanics of Materials* (2nd Ed.). McGraw-Hill, ISBN0-070-04340-X, New York, USA.

Bembey, A.; Bushby, A.; Boyde, A.; Ferguson, V. & Oyen, M. (2006). Hydration effects on the micro-mechanical properties of bone. *Journal of Materials Research*, Vol.21, No.8, pp. 1962-1968, ISSN 0884-2914.

Bensamoun, S.; Subramaniam, M.; Hawse, J.; Ilharreborde, B.; Bassillais, A.; Benhamou, C.; Fraser, D.; Oursler, M.; Amadio, P.; Na, K. & Spelsberg, T. (2006). TGF-β inducible early gene-1 knockout mice display defects in bone strength and microarchitecture. *Bone*, Vol.39, No.6, pp. 1244-1251, ISSN 8756-3282.

Bevill, G.; Farhamand, F. & Keaveny, T. (2009). Heterogeneity of yield strain in low-density versus high-density human trabecular bone. *Journal of Biomechanics*, Vol.42, No.13, pp. 2165-2170, ISSN 0021-9290.

Bonewald, L. (2011). The amazing osteocyte. *Journal of Bone and Mineral Research*, Vol. 26, pp. 229-238, ISSN 1523-4681.

Boyde, A; Bianco, P.; Barbos, M. & Ascenzi, A. (1984). Collagen orientation in compact-bone. A new method for the determination of the proportion of collagen parallel to the plane of compact-bone sections. *Metabolic Bone Disease and Related Research*, Vol.6, No.6, pp. 299-307, ISSN 0221-8747.

Boyle, W.; Simonet, W. & Lacey, D. (2003). Osteoclast differentiation and activation. *Nature*, Vol.423, pp. 337-342, ISSN 0028-0836.

Bozec, L.; de Groot, J.; Odlyha, M.; Nicholls, B. & Horton, M. (2005). Mineralised tissues as nanomaterials: Analysis by atomic force microscopy. *IEE Proceedings Nanobiotechnology*, Vol.152, No.5, pp.183-186, ISSN 1478-1581.

Buehler, M. (2006). Nature design tough collagen: explaining the nanostructure of collagen fibrils. *Proceedings of the National Academy of Sciences of the United States of America*, Vol.103, No.33, pp.12285-12290.

Buehler, M. (2007). Molecular nanomechanics of nascent bone: fibrilar toughening by mineralization. *Nanotechnology*, Vol.18, No.29, pp. 295102, ISSN 0957-4484.

Bunger, M.; Oxlund, H.; Hansen, T.; Sørensen, S.; Bibby, B.; Thomsen, J.; Langdahl, B.; Besenbacher, B; Pedersen, J. & Birkedal, H. (2010). Strontium and Bone Nanostructure in Normal and Ovariectomized Rats Investigated by Scanning Small-Angle X-Ray Scattering. *Calcified Tissue International*, Vol.86, No.4, pp.294-306, ISSN 0171-967X.

Caetano-Lopes, J.; Nery, A.; Henriques, R.; Canhão, H.; Duarte, J.;Amaral, P.; Vale, M.; Moura, R.; Pereira, P.; Weinmann, P.; Abdulghani, S.; Souto-Carneiro, M.; Rego, P.; Monteiro, J.; Sakagushi, S.; Konttinen, Y.; Graça, L.; Queiroz, M.; Vaz, M. &

Fonseca, J. (2009a). Chronic arthritis directly induces quantitative and qualitative bone disturbances leading to compromised biomechanical properties. *Clinical and Experimental Rheumatology*, Vol.27, No.3, pp.475-482, ISSN 0392-856X.

Caetano-Lopes, J; Canhão, H. & Fonseca, J. (2009b). Osteoimmunology - The hidden immune regulation of bone. *Autoimmunity Reviews*, Vol.8, No.3, pp. 250-255, ISSN 1568-9972.

Caetano-Lopes, J.; Nery, A.; Canhão, H.; Duarte, J.; Cascão, R.; Rodrigues, A.; Perpétuo, I.; Abdulghani, S.; Amaral, P.; Sakaguchi, S.; Konttinen, Y.; Graça, L.; Vaz, M. & Fonseca, J. (2010). Chronic arthritis leads to disturbances in the bone collagen network. *Arthritis Research & Therapy*, Vol.12, R9, ISSN 1478-6362.

Chappard, C.; Marchadier, A. & Benhamou, L. (2008). Interindividual and intraspecimen variability of 3-D bone microarchitectural parameters in iliac crest biopsies imaged by conventional micro-computed tomography. *Journal of Bone and Mineral Metabolism*, Vol.26, No.5, pp. 506-513, ISSN 0914-8779.

Chevalier, Y.; Pahr, D.; Allmer, H.; Charlebois, M. & Zysset, P. (2007). Validation of a voxel-based FE method for prediction of the uniaxial apparent modulus of human trabecular bone using macroscopic mechanical tests and nanoindentation. *Journal of Biomechanics*, Vol.40, No.15, pp. 3333-3340, ISSN 0021-9290.

Ciarallo, A.; Barralet, J.; Tanzer, M. & Kremer, R. (2006). An approach to compare the quality of cancellous bone from the femoral necks of healthy and osteoporotic patients through compression testing and microcomputed tomography imaging. *McGrill Journal of Medicine*, Vol.9, No.2, pp. 102-107, ISSN 1201-026X.

Ciarelli, T.; Fyhrie, D.; Schaffler, M. & Goldstein, S. (2000). Variations in Three-Dimensional Cancellous Bone Architecture of the Proximal Femur in Female Hip Fractures and in Controls. *Journal of Bone and Mineral Research*, Vol.15, No.1, pp. 32-40, ISSN 0884-0431.

Cooper, D.; Turinsky, A.; Sensen, C. & Hallgrimsson, B. (2007a). Effect of voxel size on 3D micro-CT analysis of cortical bone porosity. *Calcified Tissue International*, Vol.80, No.3, pp. 211-219, ISSN 0171-967X.

Cooper, D.; Thomas, C.; Clement, J.; Turinsky, A.; Sensen, C. & Hallgrimsson, B. (2007b). Age-dependent change in the 3D structure of cortical porosity at the human femoral midshaft. *Bone*, Vol.40, No.4, pp. 957-965, ISSN 8756-3282.

Cory, E.; Nazarian, A.; Entezari, V.; Vartanians, V.; Muller, R. & Snyder, B. (2010). Compressive axial mechanical properties of rat bone as functions of bone volume fraction, apparent density and micro-CT based mineral density. *Journal of Biomechanics*, Vol.43, No.5, pp. 953-960, ISSN 0021-9290.

Cox, G. & Kable, E. (2006). Second-harmonic imaging of collagen. *Methods in Molecular Biology*, Vol.319, pp.15-35, ISSN 1064-3745.

Cox, G.; Kable, E.; Jones, A.; Fraser, I.; Manconi, F. & Gorrell, M. (2003). 3-dimensional imaging of collagen using second harmonic generation. *Journal of Structural Biology*, Vol.141, No.1, pp. 53-62, ISSN 1047-8477.

Cowin, S. (2001). *Bone mechanics handbook* (2nd Ed.), CRC Press, ISBN 0-8493-9117-2, Boca Raton, USA.

Dendorfer, S.; Maier, H.; Taylor, D. & Hammer J. (2008).Anisotropy of the fatigue behaviour of cancellous bone. *Journal of Biomechanics*, Vol.41, No.3, pp. 636-641, ISSN 0021-9290.

Dendorfer, S.; Maier, H. & Hammer, J. (2009). Fatigue damage in cancellous bone: An experimental approach from continuum to micro scale. *Journal of the Mechanical Behavior of Biomedical Materials*, Vol. 2, No. 1, ISSN 1751-6161.

Diamant, I.; Shahar, R.; Masharawi, Y. & Gefen, A. (2007). A method for patient-specific evaluation of vertebral cancellous bone strength: In vitro validation. *Clinical Biomechanics*, Vol.22, No.3, pp. 282-291, ISSN 0268-0033.

Diederichs, G.; Link, T.; Kentenich, M.; Schwieger, K.; Huber, M.; Burghardt, A.; Majumdar, S.; Rogalla, P. & Issever, A. (2009). Assessment of trabecular bone structure of the calcaneus using multi-detector CT: Correlation with microCT and biomechanical testing. *Bone*, Vol.44, No.5, pp. 976-983, ISSN 8756-3282.

Ding, M.; Odgaard, A. & Hvid, I. (1999). Accuracy of cancellous bone volume fraction measured by micro-CT scanning. *Journal of Biomechanics*, Vol.32, No. 3, pp. 323-326, ISSN 0021-9290.

Djuric, M.; Djonic, D.; Milovanovic, P.; Nikolic, S.; Marshall, R.; Marinkovic, J. & Hahn, M. (2010). Region-Specific Sex-Dependent Pattern of Age-Related Changes of Proximal Femoral Cancellous Bone and Its Implications on Differential Bone Fragility. *Calcified Tissue International*, Vol.86, No.3, pp. 192-201, ISSN 0171-967X.

Duan, Y.; Wang, X.-F.; Evans, A. & Seeman, E. (2005). Structural and biomechanical basis of racial and sex differences in vertebral fragility in Chinese and Caucasians. *Bone*, Vol.36, No.6, pp. 987-998, ISSN 8756-3282.

Fantner, G.; Birkedal, H.; Kindt, J.; Hassenkam, T.; Weaver, J.; Cutroni, J.; Bosma, B.; Bawazer, L.; Finch, M.; Cidade, G.; Morse, D.; Stucky, G. & Hansma, P. (2004). Influence of the degradation of the organic matrix on the microscopic fracture behavior of trabecular bone. *Bone*, Vol.35, No.5, pp. 1013-1022, ISSN 8756-3282.

Fonseca, D. & Ward, W. (2004). Daidzein together with high calcium preserve bone mass and biomechanical strength at multiple sites in ovariectomized mice. *Bone*, Vol.35, No.2, pp. 489-497, ISSN 8756-3282.

Fratzl, P.; Gupta, H.; Paschalis, E. & Roshger, P. (2004). Structure and mechanical quality of the collagen-mineral nano-composite in bone. *Journal of Materials Chemistry*, Vol.14, No.14, pp. 2115-2123, ISSN 0959-9428.

Fratzl, P. & Weinkamer, R. (2007). Nature's hierarchical materials. *Progress in Materials Science*, Vol.52, No.8, pp. 1263-1334, ISSN 0079-6425.

Fratzl-Zelman, N.; Roschger, P; Gourrier, A.; Weber, M.; Misof, B.; Loveridge, N.; Reeve, J.; Klaushofer, K. & Fratzl, L. (2009). Combination of nanoindentation and quantitative backscattered electron imaging revealed altered bone material properties associated with femoral neck fragility. *Calcified Tissue International*, Vol.85, No.4, pp. 335-343, ISSN 0171-967X.

Fung, Y. (1993). *Biomechanics: mechanical properties of living tissues* (2nd Ed.), Springer Verlag, ISBN 0-387-97947-6, New York, USA.

Ganguly, P.; Moore, T.; Gibson, L. (2004). A Phenomenological Model for Predicting Fatigue Life in Bovine Trabecular Bone. *Journal of Biomechanical Engineering*, Vol.126, No.3, pp. 330-339, ISSN 0148-0731.

Garnier, K.; Dumas, R.; Rumelhart, C. & Arlot, M. (1999). Mechanical characterization in shear of human femoral cancellous bone: torsion and shear tests. *Medical Engineering & Physics*, Vol.21, No.9, pp. 641-649, ISSN 1350-4533.

Gibson, L. & Ashby, M. (1999). *Cellular Solids, Structure and Properties* (2nd Ed.), Cambridge University Press, ISBN 0-5214-9911-9, Cambridge, UK.

Gibson, L. (2005). Biomechanics of cellular solids. *Journal of Biomechanics*, Vol.38, No.3, pp. 377-399, ISSN 0021-9290.

Giraud-Guille, M. (1988). Twisted plywood architecture of collagen fibrils in human compact bone osteons. *Calcified Tissue International*, Vol.42, No.3, pp. 167-180, ISSN 0171-967X.

Goodhew, P. & Humphreys, F. (2000). *Electron Microscopy and Analysis* (3rd Ed.). Taylor and Francis, ISBN 0-748-40968-8, London, UK.

Haddock, S.; Yeh, O.; Mummaneni, P.; Rosenberg, W. & Keaveny, T. (2004). Similarity in the fatigue behaviour of trabecular bone across site and species. *Journal of Biomechanics*, Vol.37, No.2, pp. 181-187, ISSN 0021-9290.

Hang, F. & Barber, A. (2011). Nano-mechanical properties of individual mineralized collagen fibrils from bone tissue. *Journal of the Royal Society Interface*, Vol.8, No.57, pp. 500-505, ISSN 1742-5689.

Hassenkam, T.; Fantner, G.; Cutroni, J.; Weaver, J.; Morse, D. & Hansma, P. (2004). High-resolution AFM imaging of intact and fractured trabecular bone. *Bone*, Vol.35, No.1, pp. 4-10, ISSN 8756-3282.

Hassenkam, T.; Jorgensen, H. & Lauritzen, J. (2006). Mapping the imprint of bone remodelling by atomic force microscopy. *The Anatomical Record. Part A, Discoveries in Molecular, Cellular and Evolutionary Biology*, Vol.288A, No.10, pp.1087-1094, ISSN 1552-4884.

Helgason, B.; Perilli, E.; Schileo, E. & Taddei, F. (2008). Mathematical relationships between bone density and mechanical properties: A literature review. *Clinical Biomechanics*, Vol.23, No.2, pp. 135-146, ISSN 0268-0033.

Hengsberger, S.; Kulik, A. & Zysset, P. (2001). A combined atomic force microscopy and nanoindentation technique to investigate the elastic properties of bone structural units. *European Cells & Materials*, Vol.1, pp. 12-17, ISSN 1473-2262.

Homminga, J.; McCreadie, B.; Ciarelli, T.; Weinans, H.; Goldstein, S. & Huiskes, R. (2002). Cancellous Bone Mechanical Properties from Normals and Patients with Hip Fractures Differ on the Structure level not on the Bone Hard Tissue Level. *Bone*, Vol.30, No.5, pp. 759-764, ISSN 8756-3282.

Hull, D. (1981). *An introduction to composite materials* (1st Ed.), Cambridge University Press, ISBN 0-521-38190-8, Cambridge, UK.

Jiang, Y.; Zhao, J.; Mitlak, B.; Wang, O.; Genant, H. & Eriksen, E. (2003). Recombinant Human Parathyroid Hormone (1-34) [Teriparatide] Improves Both Cortical and Cancellous Bone Structure. *Journal of Bone and Mineral Research*, Vol.18, No.11, pp. 1932-1941, ISSN 0884-0431.

Kanis, J.; Cooper, C.; Burlet, N.; Delmas, P.; Reginster, J.-Y.; Borgstrom, F. & Rizzoli, R. (2005). European guidance for the diagnosis and management of osteoporosis in post menopausal women, Available from: <http://www.shef.ac.uk/FRAX>.

Kasra, M. & Grynpas, M. (2007). On the shear properties of trabecular bone under torsional loading: effects of bone marrow and strain rate. *Journal of Biomechanics*, Vol.40, No.13, pp. 2898-2903, ISSN 0021-9290.

Keaveny, T.; Morgan, E.; Niebur, G. & Yeh, O. (2001). Biomechanics of Trabecular Bone. *Annual Review of Biomedical Engineering*, Vol.3, pp. 307-333, ISSN 1523-9829.

Knoob, T.; Pringle, D.; Gedbaw, E.; Meredith, J.; Berrios, R. & Kim, H. (2007). Biomechanical properties of bone and cartilage in growing femoral heads following ischemic osteonecrosis. *Journal of Orthopaedic Research*, Vol.25, No.6, pp. 750-757, ISSN 0736-0266.

Kopperdahl, D. & Keaveny, T. (1998). Yield strain behavior of trabecular bone. *Journal of Biomechanics*, Vol.31, No.7, pp. 601-608, ISSN 0021-9290.

Lakes, R. (2003). Composite Biomaterials, In: *Biomaterials: Principles and Applications*, J. B. Park & J. D. Bronzino, (Ed.), CRC Press, ISBN 0-849-31491-7, Boca Raton, USA.

Li, B. & Aspden, R. (1997). Composition and mechanical properties of cancellous bone from the femoral head of patients with osteoporosis or osteoarthritis. *Journal of Bone and Mineral Research*, Vol.12, No.4, pp. 641-651, ISSN 0884-0431.

Link, T.; Majumdar, S.; Lin, J.; Augat, P.; Gould, R.; Newitt, D.; Ouyang, X.; Lang, T.; Mathur, A. & Genant, H. (1998). Assessment of trabecular structure using high resolution CT images and texture analysis. *Journal of Computer Assisted Tomography*, Vol.22, No.1, pp. 15-24, ISSN 0363-8715.

Macho, G.; Abel, R. & Schutkowski, H. (2005). Age Changes in Bone Microstructure: Do They Occur Uniformly? *International Journal of Osteoarchaeology*, Vol.15, No.6, pp. 421-430, ISSN 1047-482X.

Matsuura, M.; Eckstein, F.; Lochmuller, E. & Zysset, P. (2008). The role of fabric in the quasi-static compressive mechanical properties of human trabecular bone from various anatomical locations. *Biomechanics and Modeling in Mechanobiology*, Vol.7, No.1, pp. 27-42, ISSN 1617-7959.

Moore, T. & Gibson, L. (2003). Fatigue Microdamage in Bovine Trabecular Bone. *Journal of Biomechanical Engineering*, Vol.125, No.6, pp. 769-776, ISSN 0148-0731.

Moore, T. & Gibson, L. (2003). Fatigue in Bovine Trabecular Bone. *Journal of Biomechanical Engineering*, Vol.125, No.6, pp. 761-768, ISSN 0148-0731.

Morgan, E. & Keaveny, T. (2001). Dependence of yield strain of human trabecular bone on anatomic site. *Journal of Biomechanics*, Vol.34, No.5, pp. 569-577, ISSN 0021-9290.

Morgan, E.; Bayraktar, H. & Keaveny, T. (2003). Trabecular bone modulus-density relationships depend on anatomic site. *Journal of Biomechanics*, Vol.36, No.7, pp. 897-904, ISSN 0021-9290.

Mueller, T.; van Lenthe, G.; Stauber, M. & Gratzke, C. (2009). Regional, age and gender differences in architectural measures of bone quality and their correlation to bone mechanical competence in the human radius of an elderly population. *Bone*, Vol.45, No.5, pp. 882-891, ISSN 8756-3282.

Nazarian, A.; Muller, J.; Zurakowski, D.; Muller, R. & Snyder, B. (2007). Densitometric, morphometric and mechanical distributions in the human proximal femur. *Journal of Biomechanics*, Vol.40, No.11, pp. 2573-2579, ISSN 0021-9290.

Nazarian, A.; Meier, D.; Muller, R. & Snyder, B. (2009). Functional dependence of cancellous bone shear properties on trabecular microstructure evaluated using time-lapsed micro-computed tomographic imaging and torsion testing. *Journal of Orthopaedic Research*, Vol.27, No.12, pp. 1667-1674, ISSN 0736-0266.

Nicolella, D.; Ni, Q. & Chan, K. (2011). Non-destructive characterization of microdamage in cortical bone using low field pulsed NMR. *Journal of the Mechanical Behavior of Biomedical Materials*, Vol.4, No.3, pp.383-391, ISSN 1751-6161.

Oliver, W. & Pharr, G. (1992). An improved technique for determining hardness and elastic modulus using load and displacement sensing indentation experiments. *Journal of Materials Research*, Vol.7, No.6, pp. 1564-1583, ISSN 0884-2914.

Orstavik, R.; Haugeberg, G.; Mowinckel, P.; Hoiseth, A.; Uhlig, T.; Falch, J.; Halse, J.; McColskey, E. & Kvien, T. (2004). Vertebral deformities in rheumatoid arthritis: a comparison with population-based controls. *Archives of Internal Medicine*, Vol.164, No.4, pp. 420-425, ISSN 0003-9926.

Parfitt, A.; Drezner, M.; Glorieux, F.; Kanis, J.; Malluche, H.; Meunier, P.; Ott, S. & Recker, R. (1987). Bone histomorphometry: standardization of nomenclature, symbols, and units. *Journal of Bone and Mineral Research*, Vol.2, No.6, pp. 595-610, ISSN 0884-0431.

Park, J. & Lakes, R. (1992). *Biomaterials: an introduction* (2nd Ed.), Plenum Press, ISBN 0-306-43992-1, New York, USA.

Pereira, M.; Mauricio, A.; Vale, A.; Vidal, B.; Rodrigues, A.; Caetano-Lopes, J.; Fonseca, J. E.; Canhão, H.; Vaz, M.F.; paper in preparation

Ramasamy, J. & O. Akkus, O. (2007). Local variations in the micromechanical properties of mice femur: the involvement of collagen fibre orientation and mineralization. *Journal of Biomechanics*, Vol.40, No.4, pp. 910-918, ISSN 0021-9290.

Rapillard, L.; Charlebois, M & Zysset, P. (2006). Compression fatigue behavior of human vertebral trabecular bone. *Journal of Biomechanics*, Vol.39, No.11, pp. 2133-2139, ISSN 0021-9290.

Rho, J.; Tsui, Y. & Pharr, G. (1997). Elastic properties of human cortical and trabecular lamellar bone measured by nanoindentation. *Biomaterials*, Vol.18, No.20, pp. 1325-1330, ISSN 0142-9612.

Rho, J.; Kuhn-Spearing, L. & Zioupos, P. (1998). Mechanical properties and the hierarchical structure of bone. *Medical Engineering & Physics*, Vol.20, No.2, pp. 92-102, ISSN 1350-4533.

Rho, J.; Roy, M.; Tsui, T. & Pharr, G. (1999). Elastic properties of microstructural components of human bone tissue as measured by nanoindentation. *Journal of Biomedical Materials Research*, Vol.45, No.1, pp. 48-54, ISSN 0021-9304.

Roschger, P.; Fratzl, P.; Eschberger, J. & Klaushofer, K. (1998). Validation of Quantitative Backscattered Electron Imaging for the Measurement of Mineral Density Distribution in Human Bone Biopsies. *Bone*, Vol.23, No.4, pp.11-20, ISSN 8756-3282.

Roschger, P.; Paschalis, E.; Fratzl, P. & Klaushofer, K. (2008). Bone mineralization density distribution in health and disease. *Bone*, Vol.42, No.3, pp.456-466, ISSN 8756-3282.

Roschger, P.; Lombardi, A.; Misof, B.; Maier, G.; Fratzl-Zelman, N.; P Fratzl, P. & Klaushofer, K. (2010). Mineralization Density Distribution of Postmenopausal Osteoporotic Bone Is Restored to Normal After Long-Term Alendronate Treatment: qBEI and sSAXS Data From the Fracture Intervention Trial Long-Term Extension (FLEX). *Journal of Bone and Mineral Research*, Vol.25, No.1, pp. 48-55, ISSN 0884-0431.

Rubin, M.; Rubin, J. & Jasiuk, I. (2004). SEM and TEM study of the hierarchical structure of C57BL/6J and C3H/HeJ mice trabecular bone. *Bone*, Vol.35, No.1, pp.11-20, ISSN 8756-3282.

Schriefer, J.; Robling, A.; Warden, S.; Fournier, A.; Mason, J. & Turner, C. (2005). A comparison of mechanical properties derived from multiple skeletal sites in mice. *Journal of Biomechanics*, Vol.38, No.3, pp. 467-475, ISSN 0021-9290.

Seeman, E. (2003). The structural and biomechanical basis of the gain and loss of bone strength in women and men. *Endocrinology and Metabolism Clinics of North America*, Vol. 32, No.1, pp. 25-38, ISSN 0889-8529.

Seeman, E. (2007). Bone's material and structural strength. *Journal of Bone and Mineral Metabolism*, Vol.26, No.1, pp. 1-8, ISSN 0914-8779.

Seeman, E. (2008). Structural basis of growth-related gain and age-related loss of bone strength. *Rheumatology*, Vol.47, No.4, pp. iv2-iv8, ISSN 1462-0324.

Shahnazari, M.; Lang, D.; Fosmire, G.; Sharkey, N.; Mitchell, A. & Leach, R. (2007). Strontium administration in young chickens improves bone volume and architecture but does not enhance bone structural and material strength. *Calcified Tissue International*, Vol.80, No.3, pp.160-166, ISSN 0171-967X.

Sharir, A.; Barak, M. & Shahar, R. (2008). Whole bone mechanics and mechanical testing. *Veterinary Journal*, Vol.177, No.1, pp. 8-17, ISSN 1090-0233.

Silva, M. (2007). Biomechanics of osteoporotic fractures. *Injury*, Vol.38, No.3, pp. 69-76, ISSN 0020-1383.

Sun, S.-S.; Ma, H.-L.; Liu, C.-L.; Huang, C.-H.; Cheng, C.-K. & Wei, H.-W. (2008). Difference in femoral head and neck material properties between osteoarthritis and osteoporosis. *Clinical Biomechanics*, Vol.23, pp. S39-S47, ISSN 0268-0033.

Taylor, D. (1998). Fatigue of Bone and Bones: An Analysis Based on Stressed Volume. *Journal of Orthopaedic Research*, Vol.16, No.2, pp.163-169, ISSN 0736-0266.

Teo, J.; Teo, E.; Shim, V. & Teoh, S. (2006). Determination of Bone Trabeculae Modulus—An Ultrasonic Scanning and MicroCT (μCT) Imaging Combination Approach, *Experimental Mechanics*, Vol.46, No.4, pp. 453-461, ISSN 0014-4851.

Teo, J.; Si-Hoe, K.; Keh, J. & Teoh, S. (2007). Correlation of cancellous bone microarchitectural parameters from microCT to CT number and bone mechanical properties. *Materials Science & Engineering*, Vol.27, No.2, pp. 333-339, ISSN 0928-4931.

Vale, A.C.; Aleixo, I.P.; Lúcio,M.; Saraiva, A.; Caetano-Lopes, J.; Rodrigues, A.; Amaral, P. M.; Rosa, L. G.; Monteiro, J.; Fonseca, J. E.; Vaz, M. F.; Canhão, H.; paper in preparation.

van Staa, T.; Geusens, P.; Bijlsma, J.; Leufkens, H. & Cooper, C. (2006). Clinical assessment of the long-term risk of fracture in patients with rheumatoid arthritis. *Arthritis and Rheumatism*, Vol.54, No.10, pp. 3104-3112, ISSN 0004-3591.

Viguet-Carrin, S.; Garnero, P. & Delmas, P. (2006). The role of collagen in bone strength. *Osteoporosis International*, Vol.17, No.3, pp. 319-336, ISSN 0937-941X.

Wachter, N.; Augat, P.; Krischak, G.; Mentzel, M.; Kinzl, L. & Claes, L. (2001). Prediction of cortical bone porosity in vitro by microcomputed tomography. *Calcified Tissue International*, Vol.68, No.1, pp. 38-42, ISSN 0171-967X.

Wang, X.; Shen, X.; Li, X. & Agrawal, C. (2002). Age-related Changes in the Collagen Network and Toughness of Bone. *Bone*, Vol.31, No.1, pp. 1-7, ISSN 8756-3282.

Wang, X.-F.; Duan, Y.; Beck, T. & Seeman, E. (2005). Varying contributions of growth and ageing to racial and sex differences in femoral neck structure and strength in old age. *Bone*, Vol.36, No.6, pp. 978-986, ISSN 8756-3282.

Weiner, S. & Traub, W. (1992). Bone-structure – from angstroms to microns. *Journal of the Federation of American Societies for Experimental Biology*, Vol.6, pp. 879–885, ISSN 0892-6638.

Weiner, S. & Wagner, H. (1998). The material bone: structure mechanical function relations. *Annual Review of Materials Science*, Vol.28, No.1, pp. 271-298, ISSN 0084-6600.

Weiner, S.; Traub, W. & Wagner, H. (1999). Lamellar Bone: Structure–Function Relations. *Journal of Structural Biology*, Vol.126, No.3, pp. 241-255; ISSN 1047-8477.

Woo, D.; Kim, C.; Lim, D. & Kim, H. (2010). Experimental and simulated studies on the plastic mechanical characteristics of osteoporotic vertebral trabecular bone. *Current Applied Physics*, Vol.28, No.3, pp. 729-733, ISSN 1567-1739.

Yamamoto, E.; Crawford, R.; Chan, D. & Keaveny, T. (2006). Development of residual strains in human vertebral trabecular bone after prolonged static and cyclic loading at low load levels. *Journal of Biomechanics*, Vol.39, No.10, pp. 1812-1818, ISSN 0021-9290.

Zysset, P.; Guo, X.; Hoffler, C.; Moore, K. & Goldstein, S. (1999). Elastic modulus and hardness of cortical and trabecular bone lamellae measured by nanoindentation in the human femur. *Journal of Biomechanics*, Vol.32, No.10, pp. 1005-1012, ISSN 0021-9290.

9

Wood-Polymer Composites

Yongfeng Li
Key Laboratory of Bio-based Material Science and Technology of Ministry of Education, Northeast Forestry University, Harbin 150040, P. R. China

1. Introduction

Wood has been an essential material for human survival since the primitive state, for its wide abundance, renewable and environmentally benign nature, relative ease of working it, and outstanding mechanical properties. With the development of technology, wood came to be used for shelter, fuel, tools, boats, vehicles, bridges, furniture, engineering materials, weapons, and even raw materials for energy (Li et al., 2011a). Now, wood is widely used in various corners of human life.

Wood possesses porous structures consisting of various cell walls, which are mainly composed of biopolymers, i.e., carbohydrate polymers of cellulose and hemicelluloses and phenolic polymers of lignin. The cellular structure of wood endows it with high strength-to-weight ratio. Because of this, some high-quality wood can be used as structural materials. However, wood components are easy to be degraded by microorganisms, and susceptible to damage by fire (Fuller et al., 1997). Besides, as the most abundant functional group in wood cell walls is the hydroxyl group, the hygroscopic character of these groups can render wood with poor dimensional stability. In other words, wood will shrink as it dries, while conversely swell when it is wetted (Alfered, 1977). All these disadvantages limit the application of wood as high-quality materials.

Furthermore, with the development of society, the consumption of wood has been rapidly increasing year by year. In contrast, however, the production of high-quality wood has been fleetly decreasing. The prominent contradiction has driven researchers to look for alternative low-quality resources for value-added applications. To achieve these goals, suitable technologies are needed to improve low-quality resources (especially specific wood quality) attributes (e.g., mechanical properties, dimensional stability, decay resistance and thermal stability) in order to meet end-use requirements (Wang et al. 2007; Zhang et al. 2006).

As the above unfavorable behaviors of wood are fundamentally ascribed to the presence of numerous hydroxyl groups (reactive sites) in the wood major components and various cell cavities (major paths for moisture movement) within wood (Couturier et al. 1996; Yildiz et al. 2005), blocking these reactive sites or plugging the cavities could not only make the wood more resistant to moisture, but also improve its dimensional stability and physical as well as biodegradation properties. Consequently, treatment of wood to modify its structure and thus improve its physical and mechanical properties, as well as durability, has been carried out via chemical modification, chemical impregnation, compression during heating, and heating at high temperature (Handa et al.1976).

One of the techniques used to improve the properties of wood, which has received considerable attention in the past few decades, is the fabrication of wood-polymer composites (WPC) through in-situ formation of polymer from unsaturated monomers within wood pores (vessels, tracheids, capillaries and ray cells). The resultant polymer can both strength the mechanical properties of wood and defer or stop wood matrix from being attacked by water or microorganisms (Baysal et al. 2007; Hashizume et al. 1988; Yalinkilic et al. 1999). Such multifunctional treatment can help avoid the potential damage of leached preservatives from chemically treated wood on environment (Obanda et al. 2008), strengthen the wood (Souloungangа et al. 2004), avoid dimensional deformation of compressed wood (Ellis et al. 1999) and color change of heat-treated wood (González-Peña et al. 2009). Thus, such treatment became an environmentally friendly wood modification process.
On the consideration of importance of such wood modification and development of researches on wood-polymer composite, this article presents an overall review on preparation, performance and application of wood-polymer composites. Prior to the detailed introductions, general knowledge on wood structure and components are first given for readers clearly understanding the principle of formation of wood-polymer composites.

2. Wood structure and components

Wood is, perhaps, nature's most wonderful gift to humanity, which versatile character providing unlimited scope for property manipulation and product development to suit diverse applications. In today's world, parallel to the technological developments, the number of fields where the raw material of wood is usage increased and it has not lost its importance as a raw material. The reason for the diversity of why the fields where wood is used too much is related to its anatomical structure, physical and mechanical properties and its chemical composition. The properties which make wood important among other raw material sources are its widespread occurrence, stability, hardness, lightness, elasticity and being a renewable source (Şolpan & Güven, 1999a).

2.1 Wood structure

2.1.1 Macro structure of wood

The three dimensional section of a tree trunk (Fig. 1) shows well defined concentric subdivisions. From the outside to the center: periderm, bark, vascular cambium, sapwood, heartwood and the pith. In a tree trunk, all the tissue inside the cambium layer to the center of the tree is xylem or wood. The wood of a tree trunk is mostly dead xylem tissue. The darker, scentral region is called heartwood. The lighter, younger region of wood closer to the cambium is called sapwood. Wood in most species is clearly differentiated into sapwood and heartwood. Softwood (Fig. 2a), which have needle-like or scale-like leaves, belongs to gymnosperms and hardwoods (Fig. 2c), which have broad leaves, belongs to angiosperms. Distinct anatomical differences exist between the gymnosperms (softwoods) and angiosperms (hardwoods) (Peydecastaing, 2008). The softwoods are fairly homogeneous as they consist basically of only two cell types, the longitudinal tracheids and ray cells. Hardwoods, on the other hand, are composed of mixtures of four or five cell forms and are thus relatively heterogeneous in structure (Patrice, et al. 1997; Stubičar, et al. 1998). The different cells that comprise xylem are alive when they are initially produced by the meristematic cambium, but when they actually become functioning water-conducting cells (tracheids and vessels), they lose their cell contents and become hollow, microscopic tubes with lignified walls.

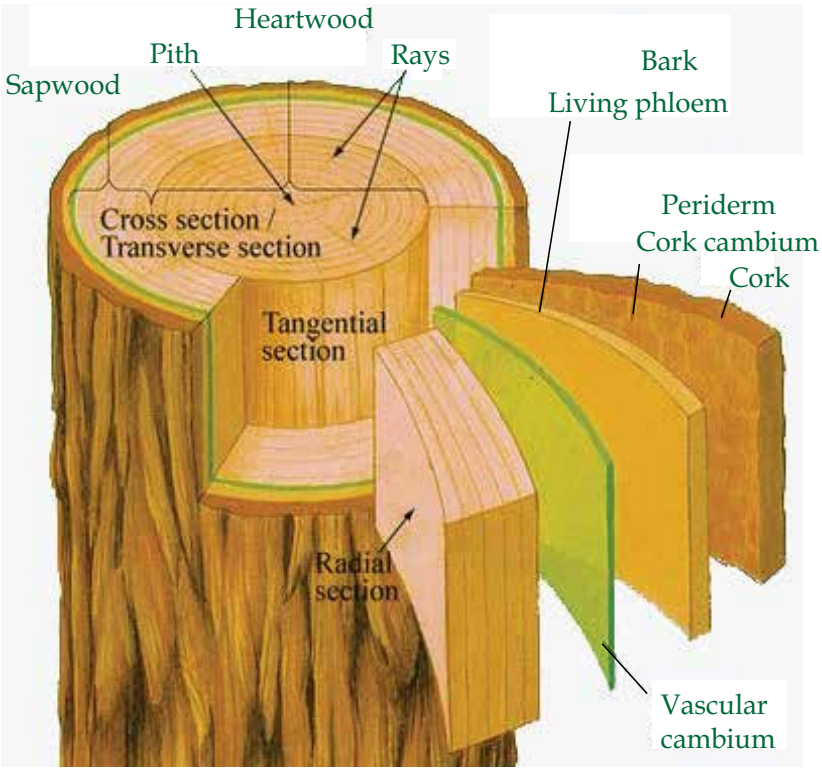

Fig. 1. The three dimensional section of a tree trunk

2.1.2 Micro structure of wood

Wood is composed of millions of individual units called cells, which differ in shape and size, depending on the tree's physiological function (Young & Rowell, 1986). The cells that make up the xylem of conifers have structures simpler than those of the dicotyledons. Conifers are composed mainly of cells that are tubular, elongated, pointed and closed at the ends, called tracheids (Hon, 1996). The dicotyledons, on the other hand, are composed of cells of more varying shapes and sizes. Most dicotyledon cells are long and narrow, with pointed and closed ends – the fibers. The tracheids in conifers and the fibers in dicotyledons constitute the greatest part of the cell wall and can be credited with most of the wood's physical and chemical properties (Hon, 1996). Other important constituents are the parenchyma and, in relatively small quantities, the vessels that, in transversal cuts, are called pores (Plackett & Dunningham, 1992). These cells have open ends and are usually shorter than fibers, varying considerably in shape and size.

Wood cells are connected to each other through a cemented substance called intercellular layer or medium lamella. A mature cell is made up of two layers: the primary wall (P)– a thin external layer, and the secondary wall (S)– a thicker internal layer composed of three other layers. The interior of the cell contains the cellular lumen which, in most mature cells, is completely empty (Young & Rowell, 1986). Thus, in whole, wood is a very porous material, about 70% of the volume is made up of air-filled cells. The remaining 30% is wood substance, or cell walls (wood constituents) (Fig. 2b and 2d). Although wood is considered a

highly porous material, it is not always highly permeable and shows great variability in permeability both within and between species. Important existing processes that are strongly influenced by wood permeability are seasoning, wood preservative, wood chemical modification and fire retardant treatments as well as pulping. The efficiency of these treatments, which in turn is related to cost, is largely controlled by the anatomical structure of the wood.

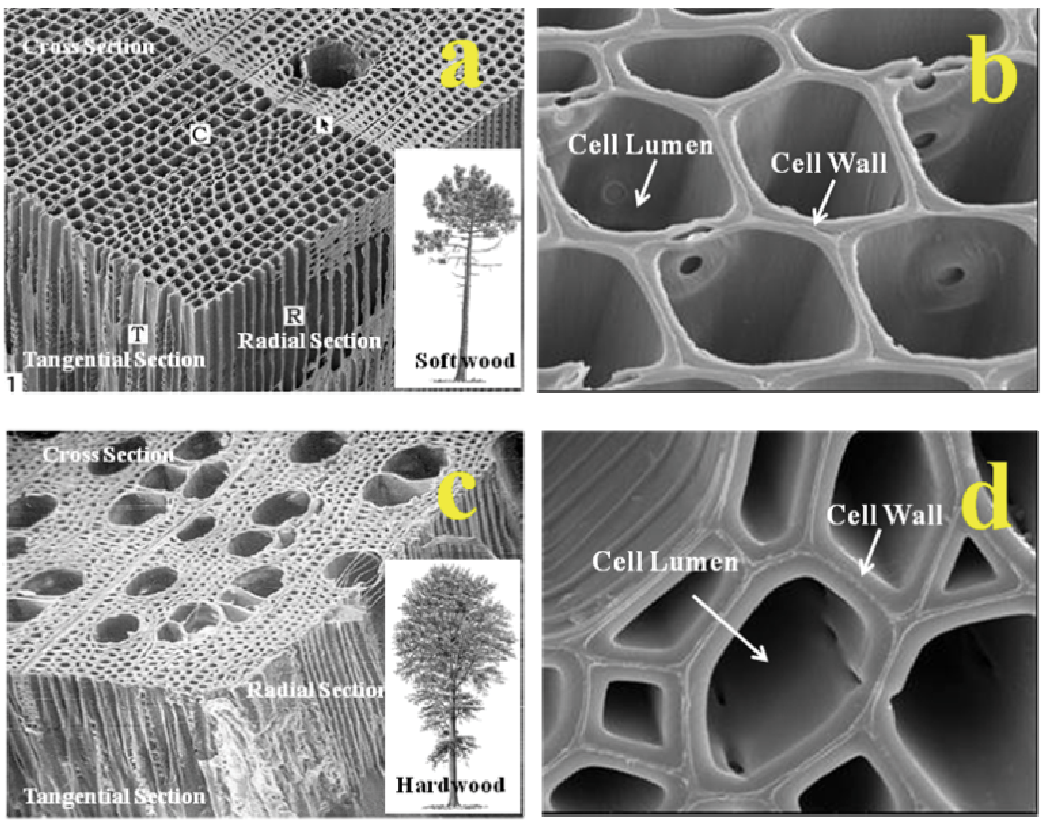

Fig. 2. SEM morphologies of wood porous structure: a) three-dimensional micrograph of softwood, b) the corresponding cross-section micrograph of softwood; c) three-dimensional micrograph of hardwood, d) the corresponding cross-section micrograph of hardwood

In detail, as Fig. 3 shown, the primary layer is the first to be laid down when the cell is formed and is composed of microfibrils, which have an essentially random orientation that allows expansion as cell growths. The secondary layer is subsequently formed, with each of the sub-layers exhibiting different patterns in the microfibrils orientation. From these, the S2 layer occupies the greatest volume of the wall. Consequently it has the greatest influence on the properties of the cell and hence of the wood. The S2 layer exhibits a definite microfibrillar orientation, and is itself composed of many lamellae consisting of numerous closely associated microfibrils that exhibit a helical winding pattern. The space between the cell fibers is occupied by the middle lamella. But micropores are still present permitting under certain conditions accessibility to the cell wall.

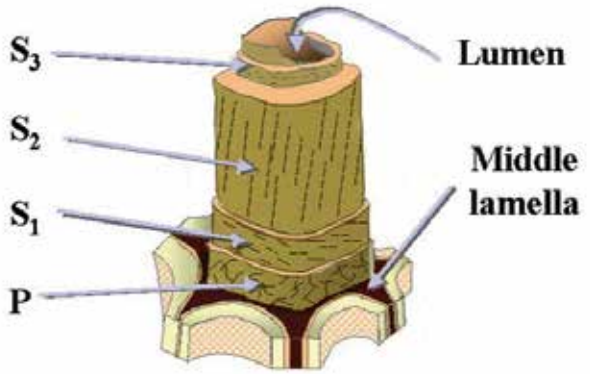

Fig. 3. Ultrastructure of the wood cell wall

2.1.3 Nanodimensional structure and chemical components of wood

Wood is a cellular hierarchical biocomposite (Fig. 4) made up of cellulose, hemicellulose, lignin, extractives and trace elements. Cellulose is the major carbohydrate component of wood along with the hemicelluloses (20–35% by weight). Lignin, extractives, and trace amounts of other materials make up the remaining portion of wood. Wood like many other biological tissues including bones and teeth are hierarchically structured composites in order to provide maximum strength with a minimum of material. Many of the physical, chemical and biological properties of wood can be understood by referring to the polymeric chemical constituents of the cell wall. At the nanoscale level, wood is a cellulosic fibrillar composite. Wood is approximately 30–40% cellulose by weight with about half of the cellulose in nanocrystalline form and half in amorphous form (Fig. 4g).

The hierarchical structure of wood, based on its elementary nanofibrilar components, leads to the unique strength and high performance properties of different species of wood. While a great deal of valuable study has led to an understanding of many mechanisms relating to the properties of wood, the overall complexity of wood's structure has limited discovery. Today we have the tools used in other areas of nanotechnology to look at structures down to the atomic scale. While this is fueling discovery in a wide range of biomimetic materials, studies on wood are only now beginning (Lucia & Rojas, 2009).

2.2 Wood components

2.2.1 Cellulose

The cellulose is a polymer of D-glucopyranose units (Fig. 4h). These monomeric units (anhydroglucose units, AGU) are alternately inverted in the plane of the ring. The AGU are linked together by β(1→4) glucosidic bonds forming the linear polymer cellulose. Cellulose is expressed from enzyme rosettes as 3–5 nm diameter fibrils that aggregate into larger microfibrils up to 20 nm in diameter (Figure 4g and 4f). These fibrils self-assemble in a manner similar to liquid crystals leading to nanodimensional and larger structures seen in typical plant cell walls (de Rodriguez et al. 2006). The theoretical modulus of a cellulose molecule is around 250 GPa, but measurements for the stiffness of cellulose in the cell wall are around 130 GPa. This means that cellulose is a high performance material comparable with the best fibers technology can produce (Vincent, 2002). Due to its crystallinity, cellulose

is relatively unreactive and thermally stable. It is difficult to isolate cellulose from wood in a pure form because it is intimately associated with lignin and hemicelluloses.

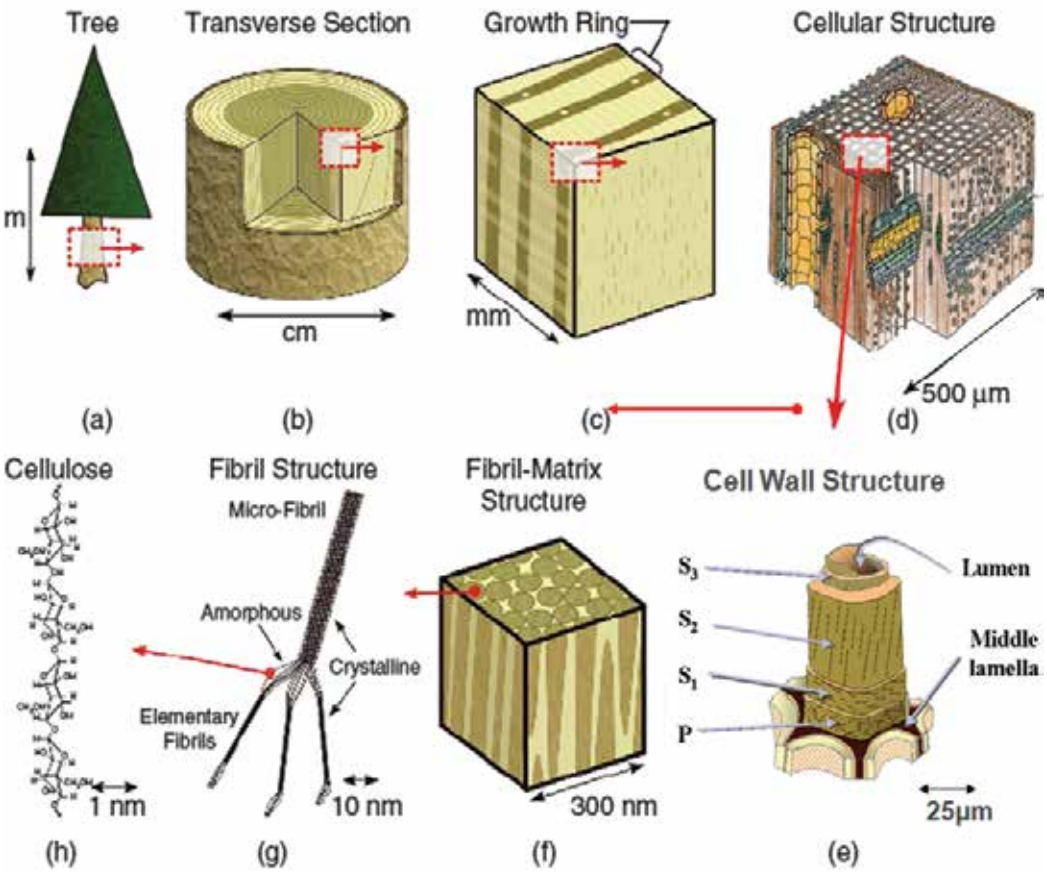

Fig. 4. Wood hierarchical structure: from tree to cellulose (Moon, 2008)

2.2.2 Hemicelluloses

Hemicelluloses are heteropolysaccharides with a lower DP than cellulose of about 100-300. They are also less ordered than cellulose, although some can form crystalline units. Hemicelluloses are referred to by the sugars they contain. The hemicelluloses also may contain carboxyl, acetyl- and methyl-substituted groups. The detailed structures of most wood hemicelluloses have not been determined, only the ratios of sugars that these polysaccharides contain have been determined. Hemicelluloses appear to act as interfacial coupling agents between the highly polar surface of the microfibrils and the much less polar lignin matrix.

2.2.3 Lignin

Lignin is a complex amorphous phenolic polymer of intermediate molecular weight. It is responsible for providing stiffness to the cell wall and also serves to bond individual cells

together in the middle lamella region. The precursors of lignin biosynthesis are p-coumaryl alcohol, coniferyl alcohol and sinapyl alcohol (Fig. 5).

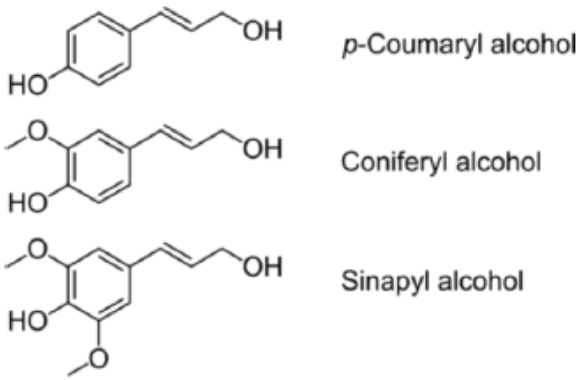

Fig. 5. Monolignol structures

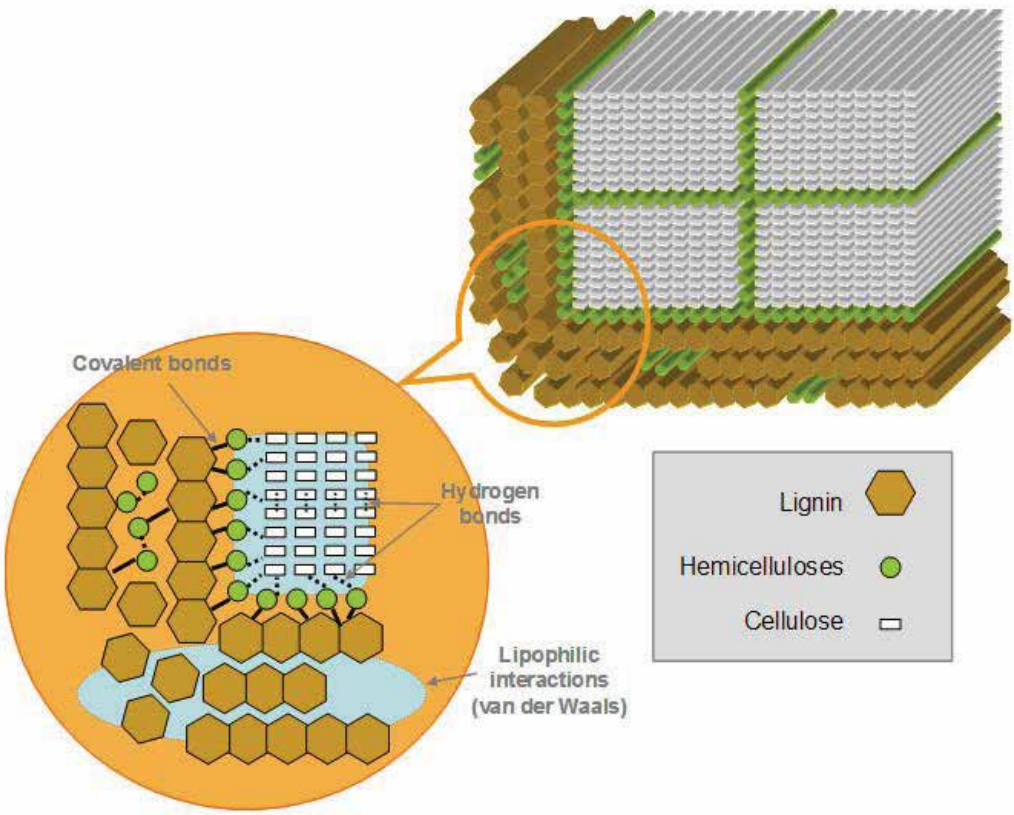

Fig. 6. Schematic representation of the lignin-carbohydrate complex (LCC) and its interaction with cellulose microfibrils

There is a wide variation of structures within different wood species. The lignin content of hardwoods is usually in the range of 18-25%, whereas its content in softwoods varies between 25 and 35%. Lignin from softwoods is mainly a polymerization product of coniferyl alcohol and is called guaiacyl lignin. Hardwood lignin is mainly syringyl-guaiacyl lignin, because they are a copolymer of coniferyl and sinapyl alcohols.
Lignin is associated by covalent bonding (ester and ether) with hemicelluloses forming lignin-carbohydrate complexes. There is no evidence that lignin is associated with cellulose but hydrogen bonds are certainly established within hemicelluloses (Fig. 6) (Peydecastaing, 2008).
In conclusion, for wood cell wall, the hydroxyl groups they contain are the most abundant reactive chemical sites. For the cell lumen, it can be viewed as bulk storage reservoirs for chemicals. For example, the void volume of southern pine springwood or earlywood with a density of 0.33 g/cm^3 is 0.77 cm^3 voids/cm^3 wood or 2.3 cm^3/g. For summer-wood or latewood with a density of 0.70 g/cm^3, the void volume is 0.52 cm^3/ cm^3 wood or 0.74 cm^3/g. The cell wall can also swell and act as a chemical storage reservoir. For southern pine the cell wall storage volume from oven dry to water swollen is 0.077 cm^3/cm^3 wood (Rowell & Ellis, 1981). On the basis of the abundant hydroxyl groups and various pores with partly permeable, wood chemical modification can be commonly achieved.

3. Wood-polymer composites

A composite is any combination of two or more materials in any form and for any use. Composites take advantages of the beneficial characteristics of each component material, and often have more useful properties than any of the constituents on its isolation (Haque, 1997).
Progress in the field of polymer chemistry led to the development of a new class of wood products with substantially improved physical, chemical, mechanical, and biological properties. Aesthetic superiority, uniform finish, property enhancement, and reduced maintenance also made modified wood attractive for large-scale application in many industrial uses as substitutes for costly metals and alloys (Deka & Saikia, 2000).
Just under such background, the term Wood-Polymer Composite (WPC) emerges, as the times require. WPC can be any combination of wood and polymer, from polymer filled with wood fiber to solid pieces of wood filled with polymer. This chapter denotes the material formed when wood is impregnated with unsaturated monomers which are then polymerized (Fig. 7). The polymerization may be initiated by treatment with high energy radiation, either from a cobalt source or from an electron accelerator, or by the action of polymerization catalyst and heat (Haque, 1997).

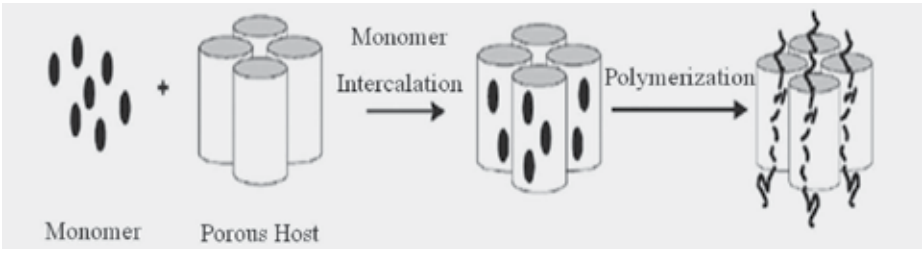

Fig. 7. Schematic view of production process of Wood-Polymer Composite

Generally, WPC involved bulk polymerization of vinyl type monomer(s) in the void spaces of solid wood. The void places (Fig. 8) include vessels, capillaries, ray cells etc., and perhaps to some extent in the cell wall through the assistance of swelling agents (Persenaire et al., 2004). The WPC production necessarily goes through two different phases: monomer(s) is(are) first introduced into the wood pores by various methods depending on the properties of the wood being treated, followed by its(their) polymerization inside the wood (Din, 1989). The resulting product resembles natural wood, and its properties are a combination of wood and polymer material, i.e., applied to the wood components: improved hardness, abrasion resistance, compressive and bending strength, dimensional stability, resistance to biological degradation and others (Schaudy & Proksch, 1982). Such WPC typically find applications in high value wood products where their use may be justified in spite of their higher cost relative to wood. In general, WPC are made from hardwoods and low-cost monomers such as styrene and methyl methacrylate (MMA), but other wood species and chemicals have also been used successfully (Noah & Foudjet, 1988; Couturier et al., 1996). This material has been known and available in small quantities for years since the 1960s. Among them, some specialty products have found commercial applications.

Over the years, several review articles on wood-polymer composites have been published (Stamm, 1977; Witt, 1977; Hamed & Coran, 1978; Meyer, 1977, 1981, 1982, 1984; Rowell & Konkol, 1987; Schneider, 1994; Youngquist, 1995; Ellis, 2000; Persenaire et al., 2004; Schneider & Witt, 2004). These reviews cover from chemical modification, treatment of wood, plastics to production technologies and applications for various types of wood-polymer composites (table 1). This chapter is intended as an overall review for materials, production, properties, application and history of wood-polymer composite and an update and extension of reviews on WPC. The developing trend of wood-polymer composites in future is also recommended in the end.

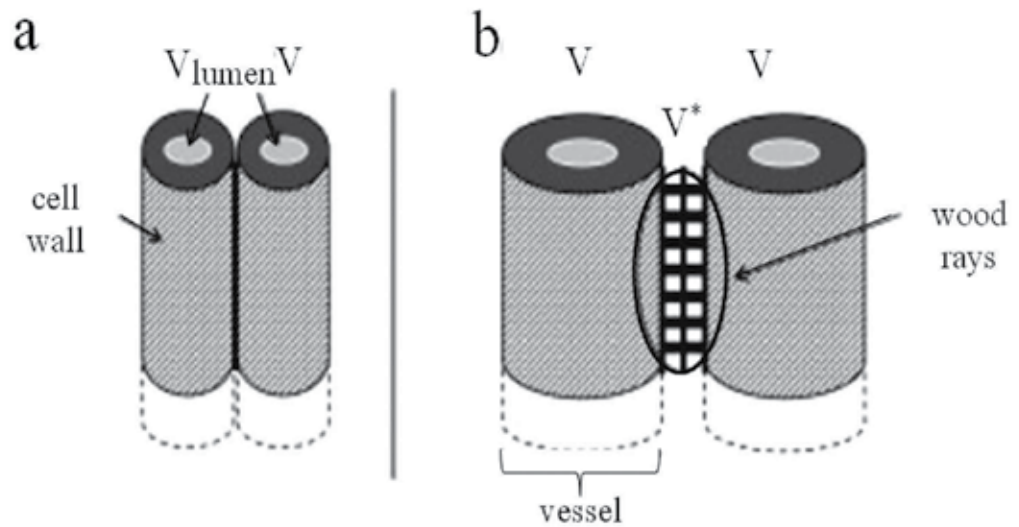

Fig. 8. Representation of two adjacent wood vessels in untreated wood (a) compared to WPC (b) and localization of the fracture propagation V and V*

Authors	Title	Wood Species	Properties	Monomers	Initiators	Treating Conditions	Journal
Ergun Baysa, Mustafa Kemal Yalinkilic, Mustafa Altinok, Abdullah Sonmez, Hüseyin Peker, Mehmet Colak	Some physical, biological, mechanical, and fire properties of wood polymer composite (WPC) pretreated with boric acid and borax mixture	Sapwood of Scots pine (*Pinus sylvestris L.*) in Turkey	Some physical properties including ASE, specific gravity (SG), reduced WA, MOE and MOR; biological resistant against decay fungi, *Tyromycetes palustris* and *Coriolus versicolor* and fire resistance were evaluated	Styrene (St), methylmethacrylate (MMA), and their mixture (50:50; volume:volume); Boric acid (BA) and borax (BX) mixture at 1% concentration prior to monomer treatment. Divinyl benzene was used as a cross-linker	Benzoyl Peroxide	1% Boric mixture of aqueous solution was impregnated into wood. After dring, styrene, methylmethacrylate and their mixture (50/50; volume/volume) were impregnated under a vacuum of 760 mmHg^{-1} for 30 min, followed by an oven dry with aluminum foil at 90°C for 4 h.	Construction and Building Materials 21 (2007) 1879–1885
Ergun Baysal, Abdullah Sonmez, Mehmet Colak, Hilmi Toker	Amount of leachant and water absorption levels of wood treated with borates and water repellents	Douglas fir (Pseudotuga menziesii var. viridis) in Turkey	The amount of leachant and water absorption levels of wood after boron treatment was determined.	Vinyl monomers: styrene (St) and methyl methacrylate (MMA) containing divinyl benzene as a crosslinker	Benzoyl Peroxide	Boric acid and borax mixture (7:3; weight to weight) were prepared with their aqueous solutions at 7% concentration and suspensions in polyethylene glycol-400 (PEG-400), prior to water repellent treatments with vinyl monomers: styrene (St), methyl methacrylate (MMA) and isocyanate (ICN). Wood specimens were evacuated for 30 min at 760 mm Hg to accelerate absorption. The soaking period was 30 min. Impregnated wood specimens were then wrapped in aluminum foil before in situ polymerization process in an oven at 90°C for 4 h	Bioresource Technology 97 (2006) 2271–2279
Kartal, S.; Yoshimura, T. & Imamura, Y.	Decay and termite resistance of boron-treated and chemically modified wood by in situ co-polymerization of allyl glycidyl ether (AGE) with methyl methacrylate (MMA)	Sugi wood (*Cryptomeria japonica* D. Don)	Dimensional stability, leachability, decay resistance, termite resistance	MMA+ allyl glycidyl ether (AGE) polymer mixtures (1:1, v:v)	2,2'-azobis-(isobutyronitrile) (AIBN)	In the single processes: blocks were treated with 1.0, 0.5 or 0.1% boric acid equivalent (BAE) DOT solutions or with MMA+AGE polymer mixtures (1:1, v:v). In sequential processes: wood specimens were firrst treated with DOT solutions, dried at 60°C for 1 day, and then 100°C for 3 days. The blocks were then treated either with MMA or with MMA+AGE (1:1).	International Biodeterioration & Biodegradation 53 (2004) 111–117
J. N. Noah, A. Foudjet	Wood-polymer composites from some tropical hardwoods	Three diffuse porous wood species: Movingui (*Distemonanthus benthamianus*), Bilinga (*Nauclea diderrichii*) and Sapelli (*Entandrophragma cylindricum*) in Cameroon	The fractional volumetric retentions of monomer and polymer were determined and expressed in terms of the fraction of voids filled by the impregnant. According to these, the treatability of the three species was evaluated, respectively.	Methyl methacrylate (MMA) monomer containing 5% ethylene glycol dimethacrylate as crosslinker	2% benzyl peroxide	A vacuum of 5 mm Hg for 30min; then, a positive pressure of 61 psi was applied using nitrogen gas over a period ranging from 0 to 8 hours. After wrapped in aluminum foil, polymerization was allowed to occur at 65°C during 24 hours.	Wood Science and Technology 22 (1988) 115-119

Table 1. List of literatures of WPC

Authors	Title	Wood Species	Properties	Monomers	Initiators	Treating Conditions	Journal
Ümit C. Yildiz, Sibel Yildiz, Engin D. Gezer	Mechanical properties and decay resistance of wood–polymer composites prepared from fast growing species in Turkey	Maritime pine (*Pinus pinaster* Ait.) and poplar (*Populus x. euramericana cv.* I-214) in Turkey	Compression strength parallel to grain, static bending strength, decay resistance against *Coniophora puteana* and *Coriolus versicolor*	Styrene (St), methyl methacrylate (MMA) and styrene/methyl methacrylate (ST/MMA, 65/28 (w/w) %) mixture and 5% divinyl benzene as cross-linker (the cross-linker to adjust the three different polymer loading levels in WPCs)	2% benzyl peroxide	A full vacuum (<70mmHg) for 30min and then soaked in monomer solution for 24h under ambient conditions. Afterward, the impregnated samples were wrapped in aluminum foil and heated to 90°C for 24h to polymerize the monomer.	Bioresource Technology 96 (2005) 1003–1011
Rashmi R. Devi, Ilias Ali, T.K. Maji	Chemical modification of rubber wood with styrene in combination with a crosslinker: effect on dimensional stability and strength property	Rubber wood (*Hevea Brasiliensis*) in India.	Anti-shrink efficiency (ASE), water absorptivity (WA), modulus of rupture (MOR) and modulus of elasticity (MOE) as well as biodegradability	Styrene in combination with a crosslinker, Glycidyl Methacrylate (GMA)	2,2′-azobis-(isobutyronitrile) (AIBN)	Vacuum Impregnation with a followed immersion in solution at room temperature for another 4 h after attaining atmospheric pressure. Then, the samples were wrapped in aluminum foil and cured at 90°C for 24 h in an oven, followed by another drying at 105°C for 24 h.	Bioresource Technology 88 (2003) 185–188
Rashmi R. Devi, T. K. Maji, A. N. Banerjee	Studies on dimensional stability and thermal properties of rubber wood chemically modified with styrene and glycidyl methacrylate	Rubber wood (*Hevea brasiliensis*) in India	Water uptake, water vapor exclusion, water-repellent effectiveness, and dimensional stability.	Styrene in combination with a crosslinker, Glycidyl Methacrylate (GMA)	2,2′-azobis-(isobutyronitrile) (AIBN)	Vacuum Impregnation with a followed immersion in solution at room temperature for another 4 h after attaining atmospheric pressure. Then, the samples were wrapped in aluminum foil and cured at 90°C for 24 h in an oven, followed by another drying at 105°C for 24 h.	Journal of Applied Polymer Science, Vol. 93, 1938–1945 (2004)
Rashmi R. Devi, T. K. Maji	Chemical modification of simul wood with styrene–acrylonitrile copolymer and organically modified nanoclay	Simul wood (*Salmalia malabarica*) in India	Physical properties including weight percent gain, density, hardness, water uptake, water-repellent effectiveness (WRE), chemical resistance)	Styrene–acrylonitrile copolymer (SAN), glycidyl methacrylate (GMA), and organically modified nanoclay	2,2′-azobis-(isobutyronitrile) (AIBN)	A mixture of monomers, styrene and acrylonitrile (molar ratio, 2:3) in the presence of 0.05 phr of AIBN were polymerized for approximately 30 min in an oil bath at 70–80°C. The heat-catalyst treatment was applied at 90°C for 24hrs, followed by 105°C for 24hrs and finally soxhlet-extracted using chloroform	Wood Science and Technology, 2011, DOI 10.1007/s00 226-011-0406-2.

Table 1. (continues) List of literatures of WPC

Authors	Title	Wood Species	Properties	Monomers	Initiators	Treating Conditions	Journal
Shane B. Elvy, Gary R. Dennis, and Loo-Teck Ng	Effects of coupling agent on the physical properties of wood-polymer composites	Australian commercial popular timbers, radiate pine (*pinus radiata*)-a soft wood and fast growing plantation timber, and blackbutt (*eucalyptus pilulüaris*)-a hard and plantation timber.	Hardness and compression tests as well as dimensional stability	Methyl methacrylate (MMA) containing benzoyl peroxide (1%) (BPO), lauroyl peroxide (0.5%) (LPO) and the accelerator-N, N-dimethylaniline (0.5%) (DMA). Vinyltriacetoxysilane (H_2C=CHSi ($OOCH_3$)$_3$) was used as a silane coupling agent	1% BPO	Vinyltriacetoxysilane (1.3% v/v in methanol) was introduced into the wood samples under a vacuum of 5 mmHg for 30 min, and then continued to soak the samples overnight, followed by an oven dry under 70°C for 1hr. After that monomer/catalyst mixture were introduced under vacuum, followed by a continue immersion at room temperature for 90 minutes. Finally, curing the samples at 70°C for 5 hr and at 103°C overnight.	Journal of Materials Processing Technology 48 (1995) 365-372
Dilek Şolpan, Olgun Güven	Preparation and properties of some wood/(co)polymer composites	Beech (*Fagus Orientalis* Lipsky) and Spruce (*Picea Orientalis* Lipsky) in Turkey	The dimensional stabilization (water uptake and artificial acid rain) and decay resistance against the biological attacks of microorganisms like mould and bacteria	Monomers-acrylonitrile (AN), methyl methacrylate (MMA), allyl glycidyl ether (AGE), and monomer mixtures-AGE + AN, AGE + MMA	Gamma radiation	The impregnated samples via vacuum-pressure process were wrapped in aluminum foils and then irradiated by a ^{60}Co γ-source.	Die Angewandte Makromolekulare Chemie 269 (1999a) 30–35
Dilek Şolpan, Olgun Güven	Preservation of beech and spruce wood by allyl alcohol-based copolymers	Beech (*Fagus Orientalis* Lipsky) and Spruce (*Picea Orientalis* Lipsky) in Turkey	Compressional strength, brinell hardness and water uptake capacity as well as biodegradation	Monomers-acrylonitrile (AN), methyl methacrylate (MMA), allyl glycidyl ether (AGE), and monomer mixtures-AGE + AN, AGE + MMA	Gamma irradiation	Vacuum of less than 25 mmHg for 15min, and then irradiated by a ^{60}Co-γ source at a dose rate of 0.85 kGy/h	Radiation Physics and Chemistry 54 (1999b) 583–591
C. Roussel, V. Marchetti, A. Lemor, E. Wozniak, B. Loubinoux and P. Gérardin	Chemical modification of wood by polyglycerol/ maleic anhydride treatment	Pine Wood (*Picea abies*) and Beech Blocks (*Fagus sylvatica*) in France	Dimensional stability, compression, MOE and decay resistance against fungi (*Poria placenta* and *Coriolus versicolor*)	Synthesied PG/MA	Methylethyl ketone peroxide (2 wt%, MEKP), cobalt naphthenate (2 wt%)	Vacuum-pressure treatment and heat-catalyst method	Holzforschung 55 (2001) 57-62
Denise Ortigosa Stolf, Francisco Antonio Rocco Lahr	Wood-polymer composite: physical and mechanical properties of some wood species impregnated with styrene and methyl methacrylate	Pine (*Pinus caribaea*) classified as a conifer and Eucalyptus (*Eucalyptus grandis*) within the class of the dicotyledons in Brazil	Most of the physical and mechanical properties and dimensional stability	Styrene and methyl methacrylate	Benzoyl peroxide (BPO)	Vacuum-pressure treatment (a pressure of 0.66 MPa for 30 min), and then at 60°C for 48h in aluminum foil, finally, unwrapped at 50°C for 72h	Materials Research, 7 (2004) 611-617

Table 1. (continues) List of literatures of WPC

Authors	Title	Wood Species	Properties	Monomers	Initiators	Treating Conditions	Journal
W. Dwianto, M. K. Yalinkilic	Fixation of compressive deformation of wood by vinyl polymerization	Sugi (*Cryptomeria Japonica* D. Don.) sapwood	Specific Gravity (ρ) and Weight Gain (WG) and their relationship with MOR and MOE	MMA, St and MMA+St(7:3 in weight)	AIBN, 1%	Compressing the samples in R direction to 50% of their initial thickness at 100°C for 4h by a hot press, then vacuum for 30min, followed by heat treatment at 90°C for 4h	Prosiding Symposium Fisika Nasional XVIII, April 2000: 73-80
L. H. L. Chia, P. H. Chua, E. E. N. Lee	A Preliminary study on the thermal conductivity and flammability of WPC based on some tropical woods	Kapur, Kempas, Keruing, Light Red Meranti, Seraya, and Chengal in Singapore	Thermal conductivity, flammability and the correlation of thermal conductivity to flammability.	Acrylonitrile (AN), 60% styrene-40%-acrylonitrile (STAN), MMA, 95% MMA--5% dioxane (MD), and vinylidene chloride (VDC).	BPO, 1%	Vacuum-pressure process and heat-catalyst treatment	Radiation Physics and Chemistry 26 (1985) 423-432
G. Scurfield, S. R. Silva, M. B. Wold	Failure of wood under load applied parallel to grain: A study using scanning electron microscopy	Wood of *Gonystylus sp.* in Australia	Compression and strain frature under load with SEM	MMA	γ-irradiation with a Co60 source	Impregnated with methyl methacrylate under nitrogen at 25psi for 3hr. The monomer was polymerised by exposing the impregnated specimens to γ-irradiation from a ^{60}Co γ-source.	Micron, 3 (1972) 160-184
Jorge A. Duran, John A. Meyer	Exothermie heat released during catalytic polymerization of basswood-methyl methaerylate composites	Basswood (*Tilia americana* L.) in American	Effect of vazo catalyst and crosslink on exothermic heat of WPC	MMA containing trimethyl propane trimethacrylate (TMPTMA) as a crosslinker	Vazo	Vacuum was applied to the oven dried wood for 30 minutes, and the wood was soaked in the monomer under atmospheric pressure for one hour. Polymerization was processed at 60°C in an air oven	Wood Science and Technology 6 (1972) 59-66
M. H. Alma; H. Hafizolu; D. Maldas	Dimensional stability of several wood species treated with vinyl monomers and polyethylene glycol-1000	Black alder (*Alnus glutinosa* Mill, Gaertn.), scotch pine (*Pinus sylvesfris* L.), oriental spruce (*Picea orientalis* L.), and Caucasian fir (*Abies nordmanniana* L.) in Turkey	ASE and SEM observation	Styrene (St), and a mixture (5:2 weight ratio) of styrene and methylmethacrylate, (St-MMA), and 30% aqueous solution of PEG-1000 were used as bulking agents.	2,2'-azobisisobutyronitrile (AIBN) , 0.1wt%	The vinyl monomers containing 0.1wt% AIBN were introduced into wood under vacuum (25-cm Hg) condition for 30 min at ambient temperature, followed by thermally polymerized at 60-70°C for 24 h, finally with oven-dry at 50°C for 12 h (PEG1000 with 30% concentration were impregnated stepwise under pressure.)	International Journal of Polymeric Materials, 32 (1996) 93-99
Wan Asma Ibrahim & Abdul Razak Mohd. All	The effect of chemical treatments on the dimensional stability of oil palm stem and rubberwood	Oil palm stem and solid rubberwood in Malaysia	Relationship between WPG and ASE	Analytical grade acetic anhydride, methyl methacrylate and glycidyl methacrylate	2,2'-Azobisisobutyronitrile (AIBN)	The samples were impregnated by monomers under 3 to 6 mm Hg for 1 hr, and then filled with nitrogen gas, sealed and cured in the oven at 120°C and 80°C for acetic anhydride and monomers respectively. The curing time for methyl methacrylate and glycidyl methacrylate was 20 h.	Journal of Tropical Forest Science 3 (1991) 291 - 298

Table 1. (continues) List of literatures of WPC

Authors	Title	Wood Species	Properties	Monomers	Initiators	Treating Conditions	Journal
N. Sheikh and F. Afshar Taromi	Radiation induced polymerization of vinyl monomers and their application for preparation of wood-polymer composites	Beech and Hornbeam in Iran.	Physical and mechanical properties	Vinyl acetate, acrylic acid and acrylic acid/styrene mixture	Radiation source-a γ-ray from ^{60}Co with a dose rate of 4-5 kGy/hr	Vacuum time was 1 hour, thereafter, the samples were allowed to soak in monomer solution for a predetermined period of time.	Radiation Physics and Chemistry 42 (1993) 179-182
M. F. Couturier, K. George, M. H. Schneider	Thermophysical properties of wood-polymer composites	Red maple in Canada	Theoretical models for the longitudinal and transverse thermal conductivities of wood-polymer composites prepared from maple boards	Styrene, methyl methacrylate or polyfurfuryl alcohol.	AIBN	Vacuum-pressure treatment and heat-catalyst method	Wood Science and Technology 30 (1996) 179-196
Marc H. Schneider, Keith I. Brebner and Ian D. Hartley	Swelling of a Cell Lumen Filled and a Cell-wall Bulked Wood Polymer Composite in Water	Sugar maple (*Acer saccharum* Marsh.) in Canada	Ultimate swelling, moisture diffusion coefficient and fiber saturation points (FSP)	A nonswelling monomer similar to methyl methacrylate and the second monomer (FA) that swells the wood	AIBN	Vacuum-pressure treatment and heat-catalyst method	Wood and Fiber Science 23 (1991) 165-172
M. H. Schneider	New cell wall and cell lumen wood polymer composites	Sugar maple (*Acer saccharum* Marsh.) sapwood in Canada	Properties (density, hardness, anti swelling efficiency) gradients	FA containing 5% $ZnCl_2$ and 5% water; MMA containing 0.3% AIBN and 3% ethylene glycol dimethacrylate as a crosslinker	AIBN	The formulation containing 90% MMA monomer and 10% polymerizable, polar monomer (FA) was added to the wood samples under vacuum (about 98 kPa) for 1 hr and then a pressure of about 8 atm (120 psig or 827 kPa) was applied for 2 hr, followed by a heat-catalyst treatment.	Wood Science and Technology 29 (1995) 121-127
Howal-d N. Rosen	Moisture adsorption and swelling in polyethylene glycol and polymethyl methacrylate treated wood at high relative humidity	Yellow-poplar (*Liriodendron tulipifera* L.) sapwood and silver inaple (*Acer saccharinum* L.) heartwood in America	ASE and swelling efficiency	MMA monomer (0.2% Vazo catalyst) or 30% and 50% concentration of PEG-1000 treated wood	Vazo	A full cell pressure treating method (150 psi with pressure applied for 90 min at 22°C) was used. Cylinders treated with MMA were cured at 67°C for 5 h.	Wood and Fiber Science 7 (1976) 249-255

Table 1. (continues) List of literatures of WPC

Table 1. (continues) List of literatures of WPC

Authors	Title	Wood Species	Properties	Monomers	Initiators	Treating Conditions	Journal
Wesleye. Loos, Morgantown, West Virginia	Dimensional stability of wood-plastic combinations to moisture changes	loblolly pine (*Pinus taeda* L.) and yellow-poplar (*Liriodendron tulipifera*, L.) in America	Anti-shrinking efficiency (ASE)	Methyl methaerylate (MMA), and Styrene-Aerylonitrile (ST-ACN) (60%-40%)	WPC	Vacuum-pressure treatment and heat-catalyst method	Wood Science and Technology 2 (1968) 308--312
M. H. Schneider and J. G. Phillips	Elasticity of wood and wood polymer composites in tension compression and bending	Sugar maple (*Acer saccharum* Marsh.) and basswood (*Tilia americana* L.) in Canada	The values in bending, tension and compression and the ratio of tensile to compressive modulus of elasticity	MMA	0.2% Vazo	Vacuum-pressure treatment and heat-catalyst method	Wood Science and Technology 25 (1991) 361-364
Loo-Teck Ng, John L. Garnett, Shahroo Mohajerani	Role of additives in wood-polymer composites. Relationship to analogous radiation grafting and curing processes	Australian softwood, Pine wood (*Pinus radiata*) in Australian	Tensile strength and dimensional stability as well as comparising effect of radiation and heat-catalyst treatment on curing consolidation	MMA containing diethy-leneglycol dimethacrylate (DEGDMA) and divinyl benzene (DVB) as crossing-linkers, and urea for improving PL of WPC as well as oxygen scavenger (N,N-diethylaminoethyl methacrylate (DEAEMA)	Azobisisobutyronitrile (AIBN)	γ-radiation or the catalyst-accelerator method	Radiation Physics and Chemistry 55 (1999) 633-637
H. Matsuda, M. Ueda and H. Mori	Preparation and crosslinking of oligoesterified woods based on maleic anhydride and allyl glycidyl ether	Red pine (*Pinus densiflora* Sieb. et Zucc.) in Japan.	heat distortion temperature (> 165°C) and compressive strength, flexural strength, Impact strength and hardness as well as water absorption	maleic anhydride and allyl glycidyl ether	2 wt-% of dicumyl peroxide (DCP) as initiator	Heat-catalyst treatment at 120°C for 8 h.	Wood Science and Technology 22 (1988) 21-32
Baki Hazer, Yalcin Ors and M. Hakki Alma	Improvement of wood properties by impregnation with macromonomeric initiators (Macroinimers)	Scotch pine (*Pinus sylvestris* L.) , eastern spruce (*Picea orientalis* L.) , and eastern beech (*Fagus orientalis* L.) in Turkey	PAE was prepared by synthesis of azobisisobutyronitrile and polyethylene glycols (PEG-200) with molecular weight of 200	The mixture, containing 140 g PAE, 80 ml TDI, 70 ml HEMA, 400 ml St, and 5 ml SO as a catalyst	Synthetic macromonomeric initiator	A vacuum impregnation (< 3 mm Hg) at 40-50°C for 1 hr, and then the wood samples were wrapped in aluminium foil and thermally polymerized at 105°C for 2 h. After unwrapping, the samples were dried in a vacuum oven at 30°C overnight.	Journal of Applied Polymer Science 47 (1993) 1097-1103

Authors	Title	Wood Species	Properties	Monomers	Initiators	Treating Conditions	Journal
J. R. Wright and L. J. Mathias	New wood-polymer composites containing ethyl α-hydroxymethyl acrylate polymers	Southern pine in America	ASE, Compressive Strength	Ethyl acrylate, styrene, tetraethyleneglycol diacrylate (TEGDA), and 1,6-hexanediol diacrylate as well as 4-(N,N-dimethylamino) pyridine as catalyst.	AIBN	The samples were put under vacuum of ≤3 mm Hg) for 20~25 min, and then the monomer or comonomer mixture containing crosslinking agent and initiator was introduced to soak for 18 to 24 h at 25 to 30°C. After impregnation, each sample was wrapped in aluminum foil and cured at 50 to 60°C (AIBN) or 70 to 80°C (V-30) for different lengths of time varying from 36 to 48 h.	Polymer Engineering and Science 32 (1992) 370-375
Aikfei Ang, Zaidon Ashaari, Edi Suhaimi Bakar & Mohd Hamami Sahri	Enhancing the properties of mahang (*Macaranga* spp.) wood through acrylic treatment in combination with crosslinker	Mahang, *Macaranga* spp. in Malaysia	Mechanical strength containing specific strength (strength to density ratio), MOR, compressive stress and hardness, stiffness (MOE) as well as dimensional stability	Methyl methacrylate (MMA) in combination with a crosslinker-trimethylolpropane trimethacrylate (TMPTMA)-1~5 wt%	2% BPO	Vacuum-pressure treatment: a 15-min initial vacuum of 85 kPa, followed by a pressure of 340 kPa for 30 min at ambient temperature. The samples were then heated in an oven maintained at 65°C±1°C for 2 h, then at 103±2°C to constant weight.	Modern Applied Science 3 (2009) 2-10
Elias Hanna Bakraji, Numan Salman	Properties of wood–plastic composites: effect of inorganic additives	White poplar (*Populus alba*), cypress (*Cupressus sempervirens*), and white willow (*Salix alba*) in Syrian	Polymer loading and compression strength as well as dimensional stabiltiy	The bulk monomers, AM and BMA, and the additives $LiNO_3$, $CuSO_4$ and H_2SO_4	γ-irradiation	γ-irradiation with a ^{60}Co source	Radiation Physics and Chemistry 66 (2003) 49–53
Zaki Ajji	Preparation of pinewood/polymer/composites using gamma irradiation	White poplar, cypress tree, and white willow	Tensile and compression strength	Butyl acrylate, butyl methacrylate, styrene, acrylamide, acrylonitrile, and unsaturated polyester styrene resin	^{60}Co gamma source	The wood samples were put into a vacuum oven for 30 min at 60°C and a pressure lower than 20 kPa in order to remove air and the free water. The monomer/polymer solutions were introduced into the oven where the wood samples were covered with the compound solution, then the samples were left at room temperature for 24 h.	Radiation Physics and Chemistry 75 (2006) 1075–1079

Table 1. (continues) List of literatures of WPC

3.1 Polymerization mechanism

The key point of WPC production is the in-situ formation of polymer from monomer(s) within wood pores. The polymerizing process is completed by monomer(s) on the basis of mechanism of free radical polymerization. It is a method of polymerization by which a polymer is formed from the successive addition of free radical building blocks. The free radicals (R•) are commonly generated in two ways: by temperature-sensitive catalysts or by radiation curing. However, despite of the two different sources, the polymerization mechanism is the same after the free-radical creation, which can be presented as the following three steps:

$$\text{Chain Initiation Step: } R\bullet + M \text{ (monomer)} \rightarrow R\text{-}M \tag{1}$$

Chain initiation is the first step of the polymerization process. During initiation, an active center is created from which a polymer chain is generated. After which, it is the propagation step:

$$\text{Chain Propagation Step: } R\text{-}(M)_n\text{-}M\bullet + M \rightarrow R\text{-}(M)_{n+1}\text{-}M \tag{2}$$

Once a chain has been initiated, the chain propagates until there is no more monomer (living polymerization) or until termination occurs. During the polymerization, a polymer spends most of its time in increasing its chain length.
In the final process of the polymerization, chain termination occurs as follow:

$$\text{Chain Termination Step: } R\text{-}(M)_n\text{-}M\bullet + R\text{-}(M)_n\text{-}M\bullet \rightarrow R\text{-}(M)_n\text{-}M\text{-}M\text{-}(M)_n\text{-}R \tag{3}$$

After this step, the polymer is resulted. For free radical polymerization, it is a key synthesis route for obtaining a wide variety of different polymers and material composites. The relatively non-specific nature of free radical chemical interactions makes this one of the most versatile forms of polymerization available and allows facile reactions of polymeric free radical chain ends. The free radical polymerization was an improvement over the condensation polymerization reaction because the free radical catalyst was neither acidic nor basic, nor does the reaction leave behind a reaction product, such as water, that must be removed from the final composite. The acid and base catalysts used with the other treatments degrade the cellulose chain and cause brittleness in the composite. Thus, on the basis of the free radical polymerization mechanism and wood porous structure, the wood-polymer composites were created by vinyl type monomers on 1960s. As the above mentioned two generation ways of free radicals in the WPC production, each process for generating free radicals has its own peculiarities, though the vinyl polymerization mechanism is the same after free-radical generation. Chemical curing is a more economical method for small-scale production, whereas gamma radiation is more economical on a larger scale (Ibach and Ellis 2005). However, both of them place an important role in the production of WPC.

3.1.1 Radiation-initiated polymerization

There are two main radiation-initiated polymerization methods used to cure monomers in wood (table 1): gamma radiation and electron beam.

3.1.1.1 Gamma radiation

When γ-radiation passes through a material such as wood or a vinyl monomer it leaves behind a series of ions and excited states as the energy of the γ-ray is absorbed through photoelectric, Compton, and pair production collisions (Fig. 9). (Cobalt-60 produces two γ-rays of 1.17 and 1.33 MeV. Approximately 30eV is required to rupture a covalent bond and to cause ionization.) The ions and excited states generated in the absorbing material immediately rearrange to form free radicals, which in turn initiate the polymerization process.

$$\underset{\text{Excited State}}{(\text{Monomer})^*} \rightarrow \underset{\text{Free Radicals}}{R\bullet + H} \qquad (4)$$

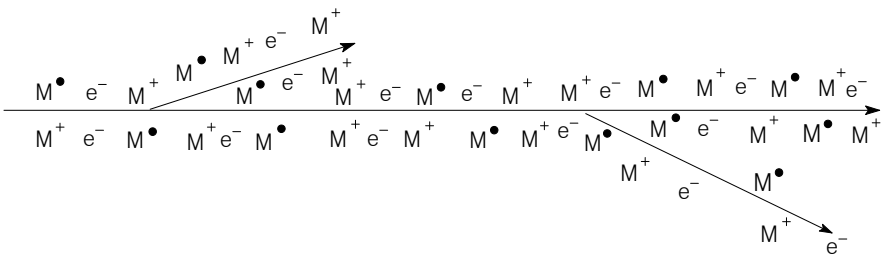

Fig. 9. Ionized and excited molecules along the path of a γ -ray

The free radicals usually consist of H* and the radical monomer. Once the free radical is generated, the polymerization reaction is the same as that o f the above normal free-radical-catalyzed, vinyl monomer bulk polymerization (Meyer, 1984).

With gamma radiation, polymerization rate and extent of polymerization within wood pores are dependent on the type of monomer, other chemical additives, wood species, and radiation dose rate. An example of radiation polymerization of the vinyl type monomer, MMA using cobalt 60 γ-ray dose rates of 56, 30, and 9 rad/s produced exotherms at 120˚C, 90˚C, and 70˚C, respectively, with reaction times of 5, 7, and 12 h, respectively, produced 70–80% wood weight gain. A 1.5–2.5 Mrad dose of gamma irradiation from a cobalt-60 source of isotope activity 20,000 Ci can be used to polymerize MMA in wood. Polymerization rate of vinyl compounds in wood, by gamma-ray irradiation, decreases in the presence of oxygen giving 50–90% conversion for styrene, methyl-, ethyl-, propyl-, and butyl methacrylates, and 4–8% conversion of vinyl acetate. Radiation polymerization of the vinyl monomers butyl methacrylate and styrene in different wood species, using cobalt 60 γ-ray radiation at various doses at a dose rate of 100 rad/s exotherms with different monomer concentrations, produced 5–140 % polymer retention (Bakraji et al., 2001). The radiation dose required for complete conversion during polymerization in an inert atmosphere was 1.5–2 Mrad for spruce and 2.0–2.5 Mrad for pine, polar and beech (Ding, 2009; Pointing, 1998).

Wood as a mixture of high-molecular-weight polymers, when exposure to high-energy radiation, it will depolymerize the polymers by creating free radicals along the C-C backbone to initiate polymerization. If two free radicals are created on separate chains in close proximity, cross-linking will take place. Thus, when radiation exposure reaches 1.0 Mrad, some slight increase in mechanical properties and a decrease in hygroscopicity

normally take place. If the free radical is created near a reactive or functional group, other types of reactions, not cross-linking reaction, normally take place. When the free radical is on a tertiary carbon, disproportionation will occur with chain scission. The effect on wood properties was negligible up to a dose of 10.0 Mrad, but higher radiation doses led to strength and toughness losses (Šimunková et al. 1983). When radiation doses achieve 3×10^8 rd, the wood will be completely soluble (Meyer, 1984). Consequently, the theoretical radiation doses for polymerization of monomers and graft of wood consequents are normally below 10 Mrad.

However, as the vinyl monomers are normally nonpolar and the wood's cell wall structure is not swollen by the monomers, there is little opportunity for the monomer to reach the free-radical sites, generated by the γ-radiation on the cellulose, to form a vinyl polymer branch, and there is little if any interaction with the hydroxyl groups attached to the cellulose molecule. Consequently, in general, most vinyl polymers simply bulk the wood structure by filling the capillaries, vessels, and other voids within wood.

3.1.1.2 Electron beam

High-energy electrons are another way of generating free radicals to initiate polymerization, and have been used with some success. Electron-beam irradiation was used to make WPCs of beech sapwood veneers with styrene, MMA, acrylonitrile, butyl acrylate, acrylic acid, and unsaturated polyesters (Handa et al., 1983; Doss et al., 1991; Şolpan & Güven, 1995; 1996; Tang & Xu, 2004). Increasing the wood moisture content has a positive effect on electron curing. For example, the monomer conversion in the electron beam-induced polymerization of MMA pre-impregnated in beech veneer increases with increases of moisture content in the wood up to 20–30% moisture, and is proportional to the square root of the electron dosage. The polymerization of styrene and acrylonitrile in veneer is also affected similarly by moisture content (Ibach & Ellis, 2005).

Some studies have indicated that curing of monomer systems in wood causes some interaction of the polymer with the wood. WPCs made with MMA, MMA–5% dioxane, and vinyl acetate impregnation into the wood cellular structure, followed by electron-beam irradiation show an increase in the compressive and bending strength, indicating some interaction at the wood-polymer interface (Boey et al., 1985). A recent study (Tang & Xu, 2004) used resins including styrene alone, styrene/unsaturated polyester mixture, and styrene/acrylic epoxy ester mixture, respectively, with the help of electron irradiation of a dose of 56 kGy, to prepare a series of wood/polymer composites (WPCs) (Matsuda et al., 1988). The results showed that the curing degree of the impregnated resins could be greater than 90 % with the aid of electron irradiation; and the WPCs possessed much higher hardness and compression strength, and much lower water absorption, compared to untreated wood .

3.1.2 Heat-catalyst-initiated polymerization

As the radiation method has drawbacks such as safety concerns, cost considerations as well as special regulations, and certain monomers (e.g. MMA, St, acrylonitrile) with low boiling points, need low curing temperature to avoid significant monomer loss during their curing process, method of initiators sponsored polymerization as catalysts which can generate free radicals by self-decomposition under lower temperatures were developed.

Two kinds of initiators as catalysts are commonly used in the heat-catalyst-initiated polymerization: Vazo series and Peroxide catalysts.

3.1.2.1 Peroxides

The commonly used peroxides for the polymerization of monomers in wood include dicumyl peroxide (DCP), t-butyl hydroperoxide (TBPB), methyl ethyl ketone peroxide (MEKP), lauroyl peroxide (LPO), isopropyl hydroperoxide (ISO-HPO), cyclohexanone peroxide (CHPO), hydrogen peroxide (HPO), and benzoyl peroxide (BPO) (table 1). Each of the radicals generated from these peroxides has a different reactivity. The phenyl radical is more reactive than the benzyl radical, and the allyl radical is unreactive. Thus, benzoyl peroxide is one of the most commonly used peroxides initiator. Usually the amount of peroxide added ranges from 0.2–3% by weight of monomer (Ibach & Ellis, 2005). Excess peroxide may adversely affect the mechanical properties of the composite because molecular chain scission of the polymer and cellulose occurs when peroxide is too abundant (Maldas and Kokta 1991a).

3.1.2.2 Vazo catalysts

Vazo or 2,2' -azobisisobutyronitrile series catalysts are solvent soluble and have a number of advantages over organic peroxides (Rowell, 2009). The catalysts are more stable than most peroxides, so they can be stored under milder conditions, and are not shock-sensitive. They decompose with first-order kinetics, resulting in faster polymerization in the presence of AIBN than with benzoyl peroxide; are not sensitive to metals, acids, and bases; and are not susceptible to radical-induced decompositions. The Vazo catalysts produce less energetic radicals than peroxides, so there is less branching and cross-linking. They are weak oxidizing agents, which allows them to be used to polymerize unsaturated amines, mercaptans, and aldehydes without affecting pigments and dyes. The catalysts are white crystalline solids that are soluble in most vinyl monomers. Upon thermal decomposition, the catalysts decompose to generate two free radicals per molecule. Nitrogen gas is also generated (5). The rate of decomposition is first-order and is unaffected by contaminants such as metal ions. This first-order reaction is independent of the concentration of vazo and the type of monomer (Meyer 1984).

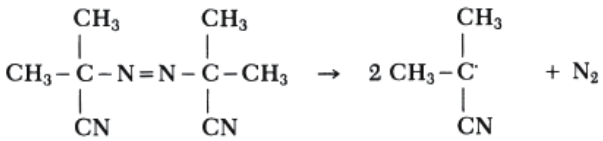

(5)

The rapid decomposition of vazo catalyst with an increase in temperature (Table 2) can be used to advantage in the bulk vinyl polymerizations in wood. A moderate temperature of 60 °C can be used to initiate the reaction, and, because the half-life is more than 40,000,000 min or about 20 years at 0 °C, the catalyzed monomer can be stored safely for months. Catalyzed monomers have been stored for over a year at 5 °C. The cost of vazo catalyst is in the range of $1-$10 a pound depending upon the amount ordered. Theoretically, 1g will produce 7.4 x 10^{21} free radicals and at $10/lb; this is 3.3 x 10^{23} free radicals per dollar, or about $0.02/g (Meyer 1984). Consequently, the reaction of vazo-initiated polymerization is easier to control and cheaper than the radiation process.

Dupont manufactures a series of Vazo catalysts that are substituted azonitrile compounds. The grade number is the Celsius temperature at which the half-life in solution is 10 hours. The series consists of the following compounds (Ibach & Ellis, 2005):

Vazo®52, the low-temperature polymerization initiator (2,2′-azobis-2,4-dimethylvaleronitrile),

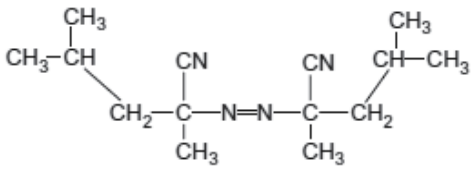

(6)

Vazo®64 (2,2′-azobisisobutyronitrile), also known as AIBN (toxic tetramethylsuccinonitrile (TMSN) is produced, therefore better to substitute Vazo 67),

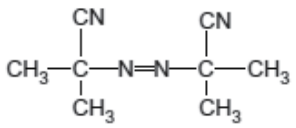

(7)

Vazo®67 (2,2′-azobis-(2-methylbutyronitrile)), best solubility in organic solvents and monomers,

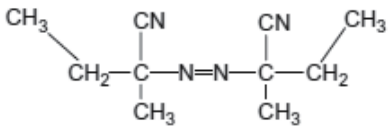

(8)

and Vazo®88 (1,1′-azobis-cyclohexanecarbonitrile),

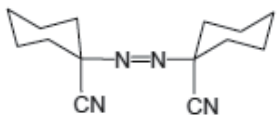

(9)

Temperature (°C)	$T_{1/2}$ (min)
0	4×10^{7}
7	1×10^{7}
18	1×10^{6}
30	1×10^{5}
46	1×10^{4}
70	270
100	5.5

Table 2. Half-life of Vazo Catalyst vs. Temperature

In addition to the Vazo series initiators, some macromonomeric initiators are also synthesized, which behave as macroinitiator, macromonomer and macrocrosslinker in thermal polymerization by themselves or copolymerization with vinyl monomers (Hazer, 1989; Matsumoto et al., 1989; Yamamoto et al., 2003). For example, a new macroinimers (Fig. 10) was prepared from the mixture of polyazoester (PAE-200), toluene diisocyanate (TDI) and hydroxyethyl methacrylate (HEMA) in the mol ratio of 1 : 2 : 2, respectively.

(Hazer et al., 1993). Such macromolecular initiator works more stable and normally has higher conversion rate as well as multifunction (Zhu & Guo, 1998).

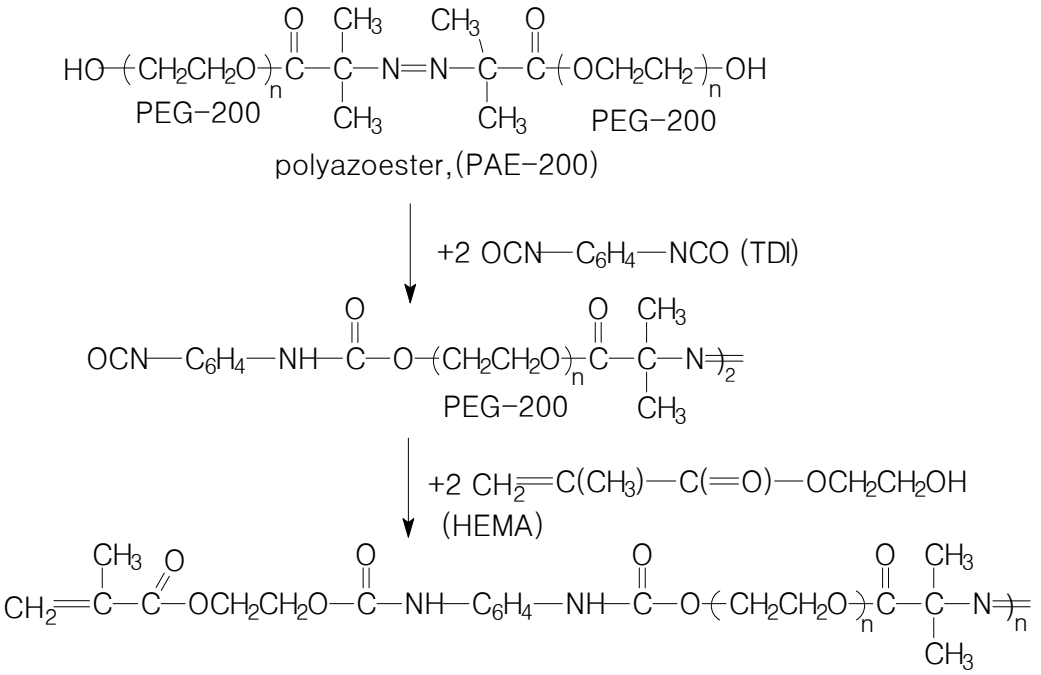

Fig. 10. Scheme of synthesis of the new macroinimer from mixture of PAE-200, TDI and HEMA

Vazo catalysts are most frequently used in concentrations of 1% or less by weight of the monomers. The rate of free radical formation is dependent on the catalyst used and is controlled by regulating the temperature. For Vazo 52, the temperature range is 35–80˚C; for Vazo 64 and 67, 45–90˚C; and for Vazo 88, 80–120˚C (Ibach & Ellis, 2005). Benzoyl peroxide were used as initiators for beech wood impregnated with trimethylolpropane trimethacrylate (TMPTA) and polyethylene glycol dimethacrylate (PEGDMA), and cyclohexanone peroxide were used to initiate the polymerization of styrene in birch wood (Ibach & Ellis, 2005; Ang et al., 2009). AIBN was used as an initiator under 80~110°C to initiate the polymerization of methyl methacrylate (MMA), styrene (St), glycidyl methacrylate (GMA) within poplar wood (Li et al., 2009; 2010a, 2010b; 2011a, 2011b).

3.2 Wood species

Many different wood species in the world have been reported to prepare WPC, e.g., maple (*acer pseudoplatanus*), spruce (*picea abies*), beech (*fagus silvatica*), white ash (*Fraxinus amerixans L*), white fir (*Abies alba*), lime (linden), abachi (*Triplochitin scleroxylon*), niangon (*Heritiera trifoliolata*), mutenye (*Guibourtia regia*), alder (*Alnus spp.A.cordata*), birch (*Betula pendula*), walnut (*Juglans nigra*), pear (*Pyrus sorotina*), hornbeam (*Acercarpinifolium*), larch (*Larix olgensis Henry*), ramin (*Gonystylus* spp.), redwood (*Seqyiua senoervurebs Endl*), red lauan (*Shorea* spp.), African rosewood (*Dalbergia melanoxylon Guill. & Perr.*), Brazilian rosewood (*Dalbergia Nigra*) and iroko (*Chorophora excelsa*) (Schaudy and Proksch, 1982).

Theoretically, both hardwood and softwood can be prepared into wood-polymer composites. However, most researches for WPCs mainly focused on hardwood. And in application, WPCs are traditionally made from hardwoods. Several reasons may contribute to this situation. One reason is that WPC is used for finished products, which are traditionally made from hardwoods. Another is that sapwood of most species (hardwoods and softwoods) treats well, but heartwood treatability is species-dependent. In hardwoods, pores (vessels) provide major longitudinal flow paths for fluids, while in softwoods, pits between pores and fibers, fiber lumens, and rays also play important roles in fluid flow, which commonly results in the poor impregnation of softwoods. Also, softwoods usually have lower density than hardwoods, requiring more treating chemical for comparable properties (Schaudy & Proksch, 1982; Schneider, 1994; Stolf & Lahr, 2004; Witt et al., 1977, 1981). In other words, most of hardwoods have the common denominator that they have a relatively open pore structure and minimum anmunt of pore blockage so that impregnant can be forced into the cell structure in a cost effective time frame. However, over all, a great many wood species in the world containing North America, South America, Asia, Europe, Africa and Australia, from softwoods to hardwoods even tropical woods, have been extensively investigated to be sutiable for WPCs Production (table 1).

In total, with the decrease of wood availability and the increase of less durable, younger and faster-growing trees, it seems a good way to replace expensive hardwoods with less expensive softwoods and low-quality faster-growing woods by producing WPCs, but to use wood to its best advantage and most effectively in structural or nonstructural applications, specific characteristics or physical properties must be considered.

3.3 Monomers

In WPCs, vinyl type monomers are polymerised into the solid polymer by means of a free radical mechanism, like the polymerisation of pure monomers. This vinyl polymerization is an improvement over the condensation polymerization reaction because the free radical catalyst was neither acidic nor basic which degrades the cellulose chain and causes brittleness of the composite, nor does the reaction leave behind a reaction product that must be removed from the final composite, such as water (Meyer, 1977). Vinyl polymers have large range of properties from soft rubber to hard, brittle solids depending upon the groups attached to the Carbon-Carbon backbone. Some examples of vinyl monomers used in WPC are styrene, vinyl chloride, vinyl acetate, ethylene oxide, many of the acrylates especially methyl methacrylate, acrylonitrile, t-butyl styrene and cholorostyrene. Since vinyl monomers are non-polar there is little if any interaction with the OH groups attached to the cellulose molecule. In general, vinyl polymers simply fill the capillaries, vessels and other void spaces in the wood structure (Meyer, 1981). However, there are cases where vinyl polymers bulk and graft with cell wall components (Li et al., 2011a). Vinyl monomers were used to stabilise wood in the presence of moisture and to increase the mechanical properties, while at the same time retaining the aesthetic qualities of wood that make it so desirable. Unlike deep coloured PF based thermosetting polymers, the vinyl polymers are clear, colourless and hard thermoplastic materials. The process of polymerising the vinyl monomers is the void spaces of wood does not discolour the wood or alter in any way its eye appealing nature (Haque, 1997)

Most of vinyl monomers are lised in table 1. Some of them are shown below:

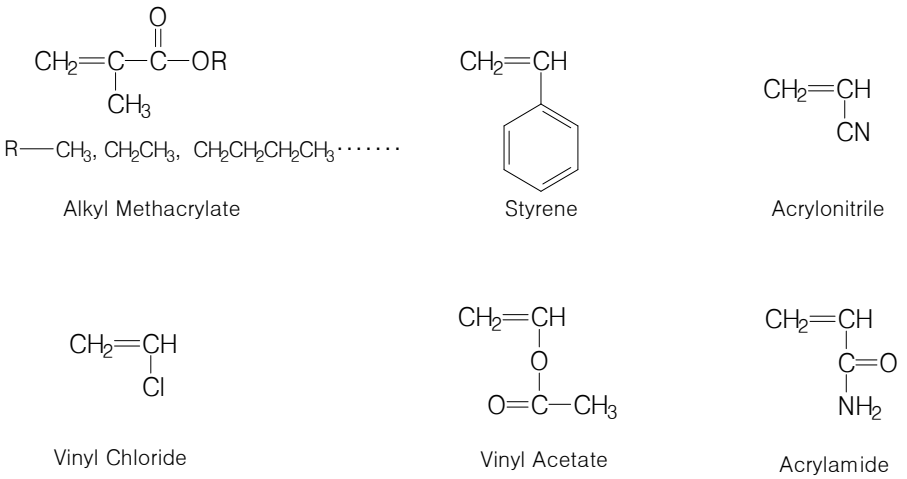

Fig. 11. Structure of the commonly vinyl monomers for WPCs

3.3.1 Methyl methacrylate

Methyl methacrylate (MMA) is shown in Fig. 11. It is one of the least expensive and most readily available monomers and is used alone or in combination with other monomers to crosslink the polymer system (Li et al., 2011b). MMA has a low boiling point (101˚C) that can result in significant loss of monomer during curing and it is mostly cured in an inert atmosphere. The PMMA is resistant to aliphatic hydrocarbons, cycloaliphatic compounds, fats and oils, and also to weak acids and bases at temperatures of up to 60 ºC. The resistance to weathering of PMMA is very good. PMMA has good insulating properties, a high dielectric strength and high tracking resistance. PMMA is naturally transparent and colorless. The transmission for visible light is 92%. The refractive index is 1.492 for PMMA. There are types that transmit UV rays, and types that absorb it almost completely, as a result of which sensitive dyes on painted surfaces behind are protected from fading. Consequently, it is the most commonly used monomer for WPCs (Ibach & Ellis, 2005). MMA shrinks about 21% by volume after polymerization, which results in some void space (seen in Fig. 12a) at the interface between the cell wall of the wood and the polymer (Li et al., 2010a, 2011a). Adding crosslinking monomers such as di- and tri-methacrylates decreases the shrinkage of the polymer, which improves the compatibility between the polymer and cell walls (Fig. 12b).
Oak and maple are often dyed to resemble walnut.

3.3.2 Styrene

Styrene (Fig. 11) is another monomer that is commonly used for WPCs (Ibach & Ellis, 2005). It normally relusts in poor interaction between polymer and wood cell walls because of its lower polarity (Fig. 13a). Other monomers are commonly added to control the polymerization rate, extent of polymerization, and to crosslink the styrene for improved physical properties of the WPCs (Fig. 13b) (Li et al., 2009; 2011a).
Hardness, compression and shear strength, wearability and bending strengths of styrene-treated wood are better than those of untreated samples. However, commonly, its impact strength sharply decreases over untreated wood, as seen of the clear cracks (Fig. 14a) and smooth fracture section (Fig. 14b) in the SEM morphologies of styrene-treated wood (Razi & Raman, 2000; Li et al., 2009; 2011a).

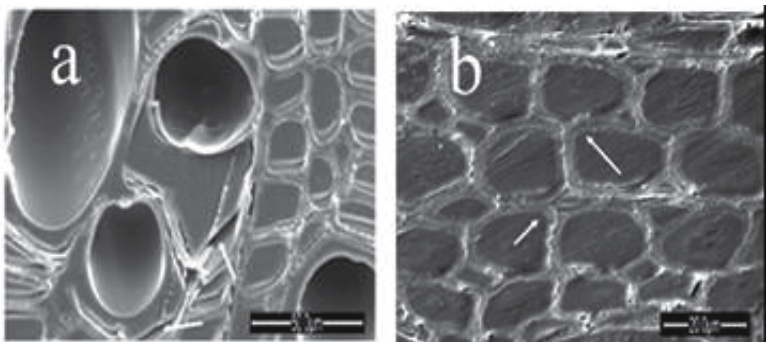

(a) (b)

Fig. 12. SEM morphologies of WPCs prepared from MMA monomer(s) (a) WPC made with MMA monomer (b) WPC made with MMA with GMA or/and anhydride as cross-linker

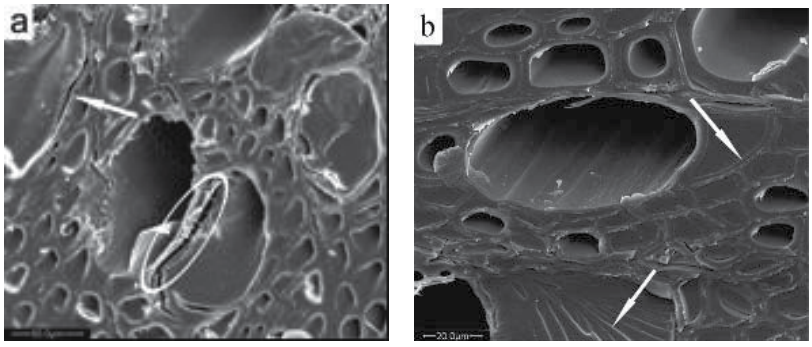

(a) (b)

Fig. 13. SEM morphologies of WPCs prepared from St monomer(s) (a) WPC made by St monomer (b) WPC made by St with GMA or/and anhydride as cross-linker

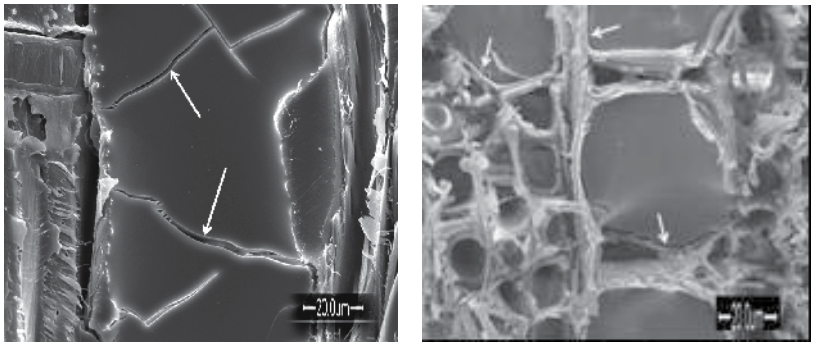

(a) (b)

Fig. 14. SEM morphologies of impact fracture section of styrene treated wood (a) Vertical section of styrene treated wood after impact fracture (b) Cross section of styrene treated wood after impact fracture

3.3.3 Acrylonitrile

Acrylonitrile (Fig.11) is used in the production of WPCs mostly in combination with other monomers because the polymer does not improve properties by itself (Persenaire et al., 2004; Şolpan & Güven, 1999b). It is most frequently used with styrene, and less frequently with MMA, methyl acrylate, unsaturated polyester, diallyl phthalate, and vinylidene chloride. WPCs made with MMA-acrylonitrile or styrene-acrylonitrile mixtures were cured using either gamma radiation or catalyst (table.1), and the resultant composites were found to be very similar (Yap et al. 1990; Yap et al. 1991a, b, c).

Acrylonitrile is highly toxic and is a carcinogen; therefore attempts have been made to find chemicals that can be substituted for acrylonitrile in the treating solutions. These attempts have been only partially successful. N-vinyl carbazol can be used as a partial replacement of acrylonitrile. Several other compounds including acryloamide, N-hydroxy acryloamide, and 1-vinyl-2-pyrrolidone were tried unsuccessfully (Bakraji et al., 2001; Ibach & Ellis, 2005).

3.3.4 Vinyl chloride

Vinyl chloride is the organochloride with the formula CH_2-CHCl, which has a sickly sweet odor at ambient pressure and temperature. It is also called vinyl chloride monomer, or VCl. This colorless compound is an important vinyl monomerl chiefly used to produce the WPC because of its high reactivity (Calleton et al., 1970). However, recently, it has been rarely used in the production of WPC for its highly toxic and carcinogenic characteristic.

3.3.5 Vinyl acetate

Vinyl acetate (VAc) monomer with the formula $CH_3COOCH=CH_2$ is a versatile and economically important chemical building block used in a wide variety of industrial and consumer applications, such as: Plastics, films, lacquers, elastomers, inks, water-based emulsion paints, adhesives, finishing and impregnation materials, paper coatings, floor tiling, safety glass, building construction, acrylic fibers, glue, cosmetics and personal care products, textile finishing and non-wovens and so on. Among, about 83% of the VAc manufactured is used to produce polyvinyl acetate emulsions and resins for its lower toxicity and good reactivity. Thus, vinyl acetate is often used as active vinyl monomer to produce WPCs. However, it is commonly used in combination with other monomers such as methyl methacryalte, styrene, acrylonitrile, vinyl chloride, glycidyl methacrylate and so on (Baysal et al., 2007; Deka & Saikia, 2000; Li et al., 2010c). The resultant WPCs exhibit excellent mechanical properties and good durability (Sheikh & Taromi, 1993).

3.3.6 Acrylamide

Acrylamide (or acrylic amide) is a chemical compound with the chemical formula C_3H_5NO. It is a white odourless crystalline solid, soluble in water, ethanol, ether, and chloroform. Acrylamide is incompatible with acids, bases, oxidizing agents, iron, and iron salts. Acrylamide is prepared on an industrial scale by the hydrolysis of acrylonitrile by nitrile hydratase.

As the conjugated effect of acrylamide, it is one of the most active acrylic-based monomers. Thus, it is universally used by itself or in combiniation with other vinyl monomers to prepare WPCs (Bakraji et al., 2001, 2002, 2003). The resultant physical and mechanical properties of acrylamide treated wood were significantly improved for the higher polymer loading in the presence of acrylamide (Bakraji & Salman, 2003).

3.4 Additives

Additive is a substance added to another substance or material to improve its properties or impart functions to it in some way. Additives are often present in small amounts and are used for a variety of purposes, as in preventing corrosion, stabilizing and strengthing polymers, preserving and coloring material, promoting reaction, controlled release of biocides, repellenting water or other functions.

Additives designed or suitable for wood-polymer composites are wholly classified two categories. One is normal additives, including crosslinkers, coupling agents and curatives. The other is functional additives, including fungicides, fire retardants, hydrophobic agents, pigments and UV stabilizers.

3.4.1 Normal additives

The normal additives are commonly used to improve the properties of polymer for wood-polymer composites.

3.4.1.1 Crosslinkers

Crosslinkers are additives used to enhance crosslinking or bonding between polymer chains, so that the resultant polymer mainly exists in a 3D network form in wood pores, which could increase reaction rate and significantly improve the mechanical properties of WPCs. The studied crosslinkers in WPCs include glycidyl methacrylate (GMA), ethylene glycol dimethacrylate (EGDMA), polyethylene glycol dimethacrylate (PEGDMA), 1,6-hexanediol diacrylate (HDDA), trimethylene glycol dimethacrylate (TMEGDMA), tetraethylene glycol dimethacrylate (TTEGDMA), trimethylolpropane triacrylate (TMPTA), trimethylolpropane trimethacrylate (TMPTMA), triallyl phosphate (TAP), trivinyl isocyanurate (TVI), unsaturated polyester (UP) and divinylbenzene (DVB) (table 1). The crosslinking agents are normally used with MMA, St, or other vinyl monomers. The addition of 1.0% divinylbenzene, triallyl phosphate, or trimethylolpropane trimethacrylate crosslinking agent to styrene results in an increased polymerization rate, with divinylbenzene having the most pronounced effect on the polymerization rate (Lawniczak & Szwarc 1987). Generally 10% or more crosslinking agent is needed to give the best improvement in physical or mechanical properties, such as hardness, abrasion resistance, and compression strength as well as bend strength. Composite materials obtained by evacuation of wood (beech, spruce, ash, and tropical wood *Pterocarpus vermalis*) followed by its impregnation with an unsaturated polyester-MMA-styrene mixture or unsaturated polyester-acrylonitrile-styrene mixture and gamma irradiation-induced curing exhibit decreased water vapor absorption and improved dimensional stability, hardness, compression strength, and wear resistance, compared to untreated wood (Ibach & Ellis, 2005; Ng et al. 1999).

WPCs with only MMA show a void space at the interface between cell wall and polymer (Fig. 12a). With addition of polar crosslinking esters, such as EGDMA, PEGDMA, the shrinkage (and hence void spaces) of the polymer during polymerization is reduced (Fig. 15), suggesting better adhesion of the polymer to the inner surface of cell wall.

In addition, some crosslinkers in certain contents can also improve the impact strength. In theory, the embrittlement may be due to the short inflexible unit of polymer in WPCs. If the inner unit of polymer has more flexibility, the embrittlement should be reduced. For example, wood-polystyrene composite has lower impact strength for the stereo-hindrance effect of bezene ring of polystyrene, as evidenced by the smooth impact fracture section (Fig. 14b). However, it would be useful to reduce the brittleness by addition of reactive

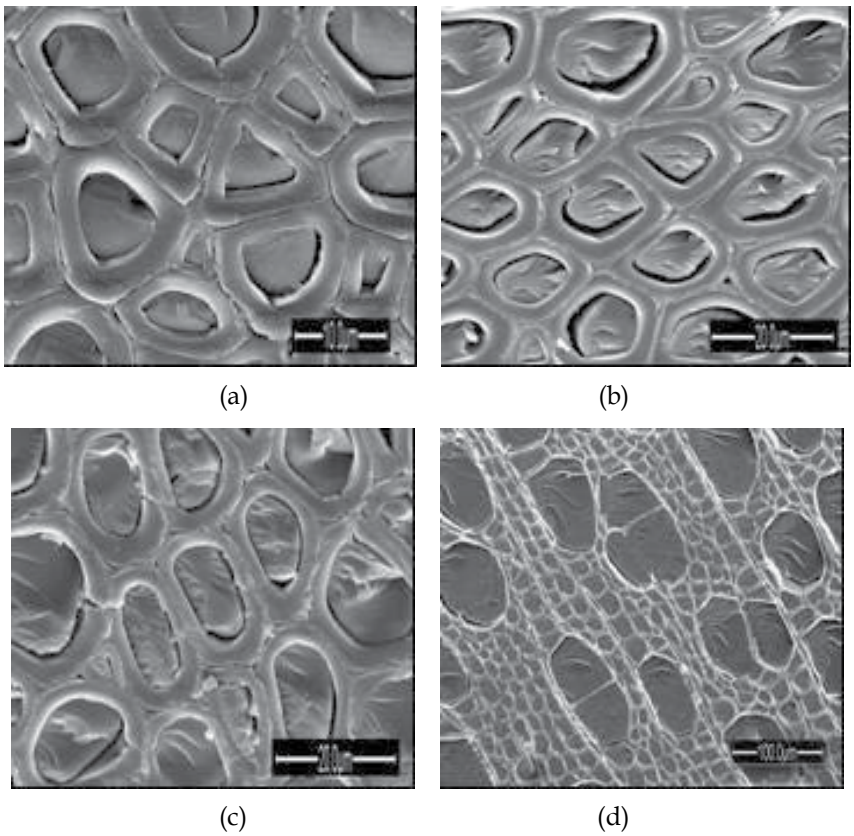

(a) (b)

(c) (d)

Fig. 15. SEM morphologies of WPCs prepared with addition of crosslinkers (a) WPC made by MMA and EGDMA (b) WPC made by St and EGDMA (c) WPC made by EGDMA (d) WPC made by PEGDMA

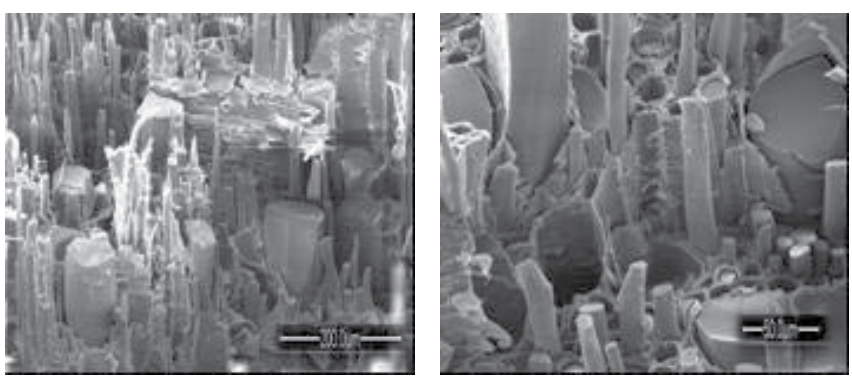

(a) (b)

Fig. 16. SEM morphologies of impact fracture section of WPCs with PEGDMA as crosslinker (a) Cross-section suface of WPCs with PEGDMA after impact fracture (b) Cross-section of WPCs with PEGDMA and St after impact fracture

difunctional chemicals with long ether chains. For example, the addition of EGDMA or PEGDMA containing 4 to 10 units of ethelene glycol can help wood-polystyrene composite achieving good toughness, as evidenced by the rough impact fracture section (Fig. 16). The addition of isocyanate compounds with acrylic monomers reduces the brittleness of WPCs consisting only of acrylic compounds (Schaudy & Proksch, 1982). The toughness of Wood-Polystyrene Composites modified by GMA and anhydride as crosslinkers and other mechanical properties as well as dimensional stability were all improved (Li et al. 2011a).

3.4.1.2 Coupling agents

Coupling agents are substances that are used in small quantities to treat a surface so that bonding occurs between it and other surfaces, e.g., wood and polymer resulted in WPCs (Chen et al. 1998). Generally, coupling agents act as bridges that link wood matrix and resulting polymers by one or more of the following mechanisms: covalent bonding, polymer chain entanglement, and strong secondary interactions as in the case of hydrogen bonding (Lu et al. 2000).

Over forty coupling agents have been used in WPCs, which are classified into organic, inorganic, and organic-inorganic groups. Organic agents include isocyanates, anhydrides, acrylates, epoxides, organic acids, monomers, polymers, and copolymers. Only a few inorganic coupling agents, such as silicates, are used in WPC. Organic-inorganic agents include silanes and titanates (Lu et al. 2000).

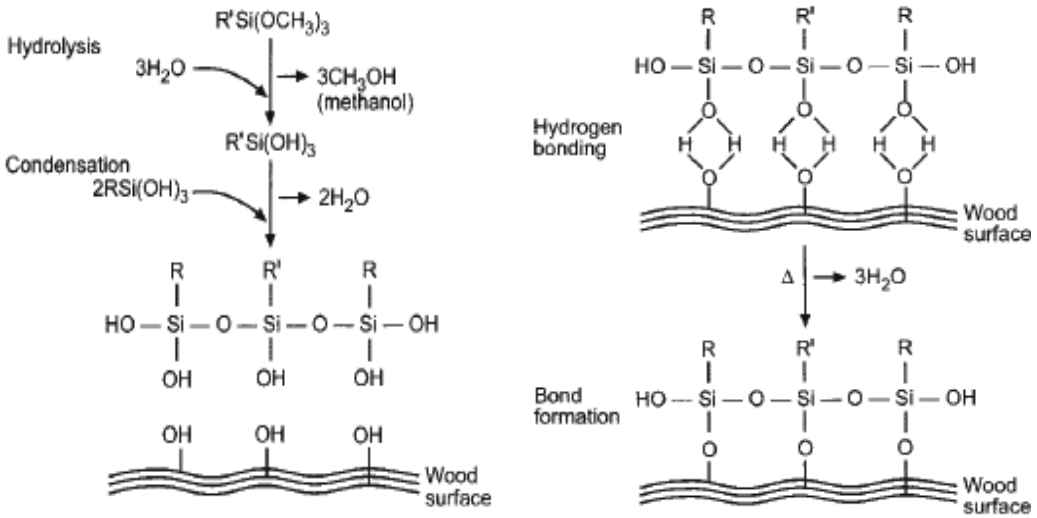

Fig. 17. Scheme for chemical coupling of alkoxysilane onto wood surface

Organic coupling agents in WPCs normally have bi- or multifunctional groups in their molecular structure. These functional groups, such as (-N=C=O) of isocyanates, [-(CO),O-] of maleic anhydrides, and (-C1-) of diclorotriazine derivatives, interact with the polar groups [mainly hydroxyl groups (-OH)] of cellulose and lignin to form covalent or hydrogen bonding (Lu et al. 2000). Alternatively, organic coupling agents can modify the polymer matrix by graft copolymerization, thus resulting in strong adhesion, even crosslinking, at the interface. The normally used organic coupling agents include glycidyl methacryalte (GMA) (Li et al. 2009a; Westin et al. 2006), allyl glycidyl ether (AGE) (Şolpan &

Güven, 1999a), isopropyl glycidyl ether (IPG) (Chang & Chang, 2006), hexanediol diacrylate (HDDA) (Ibach & Ellis, 2005), hydroxyethyl methacrylate (HEMA) (Hazer et al. 1993; Zhang et al. 2006), maleic anhydride (MA) (Li et al. 2011a; Mohamad et al. 2007) and N-vinyl pyrrolidone (NVP) (Husain et al. 1995; 1996; Bakraji et al. 2002). In principle, the acrylic coupling agents commonly bear similar structure with the chief components of wood, i.e. cellulose and lignin, thus such coupling agents have been played an important role in wood-polymer composites (Baysal et al. 2007).

Inorganic coupling agents possibly act as dispersing agents to counteract the surface polarity of wood and improve the conlpatibility between wood and polymer (Lu et al. 2000; Mai & Militz, 2004a). Organic-inorganic agents are hybrid compounds in structure. For example, titanates usually contain a titanium center and an organic part surrounding this inorganic atom. The functionality of the organic part in these agents determines their coupling effectiveness in WPCs (Bengtsson et al. 2007). Organic-inorganic coupling agents are between organic and inorganic agents in function (Lu et al. 2000; Mai & Militz, 2004b). One of most important organic-inorganic coupling agents is silicone organic silicon compound (Brebner & Schneider, 1985; Elvy et al. 1993; Mai & Militz, 2004b; Schneider & Brebner, 1985; Sèbe & Brook, 2001). The mechanism of such organic coupling agent for wood modification is schemed as Fig. 17 (Tshabalala et al. 2003). For example, wood fiber surface was effectively modified by triethoxyvinylsilane (TEVS) (Fig. 18) (Gwon et al. 2010). The normally used organic silicone coupling agents included triethoxyvinylsilane (TEVS), γ-Aminopropyltriethoxysilane (KH550), γ-Glycidoxypropy1 trimethoxysilane (560), γ-Methacryloxypropyl trimethoxysilane (KH570), 3,3,3-trifluoropropyltrimethoxysilane (TFPTMOS), 2-heptadecafluorooctylethyltrimethoxysilane (HFOETMOS) and decyltrimethoxysilane (DTMOS) (Mai & Militz, 2004b; Hansmann et al., 2005).

3.4.1.3 Catalysts

Catalysts normally play an important role in proceeding reaction or activating chemicals. Some catalysts have been reported in accelerating reactions of monomers or activating wood components in wood-polymer composites. For example, N, N-dimethylaniline is used as an accelerator to improve the reaction of monomers within wood under lower temperature (Hazer et al. 1993). When Maleic anhydride (MAN) is used as a coupling agent of WPCs, adding a moderate amount of MgO can improve the performance of MAN because MgO reacts with water and the acid group to yield carboxylate ions (-COO-). Concurrently, Mg^{2+} interacts with two carboxylate ions as a crosslinking agent and yields ionomer systems (Lu et al. 2000). Lithium nitrate ($LiNO_3$), copper sulfate ($CuSO_4$) and sulfuric acid (H_2SO_4) are found to be useful for improving the polymer loading and partly enhanceing the mechanical properties (Bakraji et al. 2002; Bakraji & Salman, 2003; Husain et al. 1996).

3.4.2 Functional agents

3.4.2.1 Fungicides

Fungicides are designed to kill and prevent the growth of fungi. There are two normal ways favorating the decay resistance of wood-polymer composites. One is inorganic compounds like boron compounds as wood preservatives being added into wood pores before formation of WPCs (Kartal et al., 2004; Baysal et al. 2007). Boron mixture of Boric acid (BA) and borax (BX) are used as preservatives for its sufficient protection against wood destroying organisms, low mammalian toxicity, and low volatility as well as colorless and

odorless characteristic. The polymerization of monomers in wood cell lumen further improves the leachability of the boron compounds. Thus, the combination treatment synergeticly improves the mechanical properties, dimensional stability, decay resistance and fire resistance (Baysal et al. 2007). The other way is fabrication of bioactive wood-polymer composites. The basic approach is still in situ polymerization of vinyl monomers in wood, with the appropriate choice of a bioactive, toxic, functional group incorporated in the monomer, and with other modifications based on wood-polymer reactions (Subramanian, 1984). Organotin monomers carrying the bioactive tributyltin group are considered to be the effective monomers for bioactive wood-polymer composites. Tri-n-butyltin methacrylatemaleic anhydride and tri-n-butyltin methacrylate—glycidyl methacrylate are examples of suitable monomer combinations for in situ copolymerization. SEM-EDX proves that a detectable portion of tin copolymer is located in cell walls, and the test results indicate that the treated wood is effective in providing resistance against white rot and brown rot

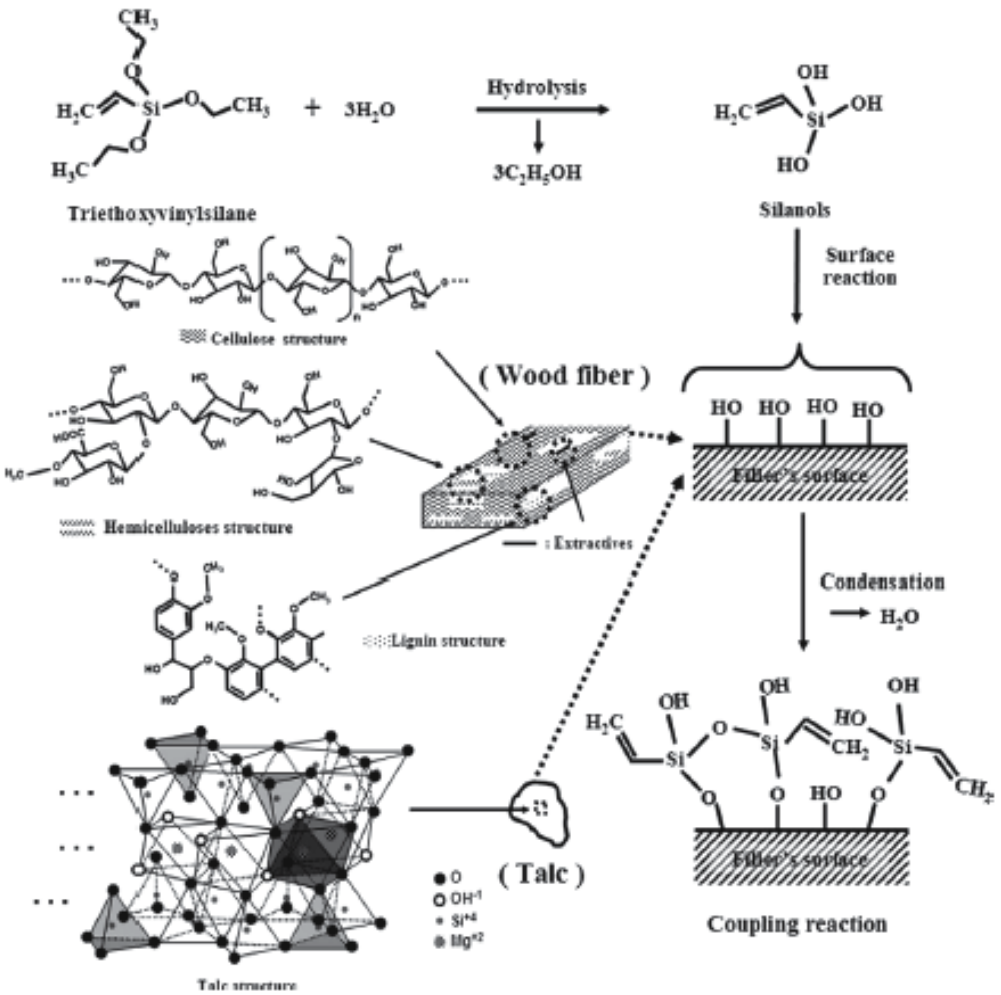

Fig. 18. Schematics of the triethoxyvinylsilane coupling reactions on the wood matrix

fungi as well as marine organisms; notable improvements in flexural and impact strength and significant reduction in moisture absorption are also observed (Subramanian, 1984). Such bioactive monomers are normally synthesized before impregnated into wood pores, thus, the additives here refer to the tin materials.

3.4.2.2 Fire retardants (thermal stabilizer)

Fire retardants (thermal stabilizer) are additives added to improve fire resistance (or thermal stability) of wood-polymer composites. They are normally applied to pretreat wood or mixed into monomers before impregnating wood. Such additives include silicone dioxide (SiO_2), alumina trihydrate ($Al(OH)_3$), magnesium oxide (MgO), boric acid (H_3BO_3), or/and borax ($Na_2B_4O_7$), tributyl phosphate and alkenyl esters of phosphorus acids (Baysal et al. 2007; Ibach & Ellis, 2005; Lu et al. 2000). The addition of magnesium oxide and boron compounds can protect wood fiber from thermal decomposition and degradation during high-temperature composite processing (Lu et al. 2000).

Addition of a solid organic halogen-compound with a high content of Cl or Br, accelerates the polymerization (Pesek et al. 1969). Addition of tributyl phosphate accelerates the polymerization rate of MMA 2.5 times and decreases the required radiation dosage. Addition of alkenyl phosphonates or alkenyl esters of phosphorus acids increases the polymerization rate and imparts fire resistance and bioresistance to the resultant WPC (Schneider et al., 1994).

3.4.2.3 Hydrophobic agents

Hydrophobic agents are substances that are used in small quantities to impart hydrophobicity to materials so that the contact angle is biger than 90° (Baysal et al. 2006; Sèbe & Brook, 2001; Tshabalala et al. 2003). The normal ways to endow wood-polymer composites with hydrophobic property include pretreatment of wood substance by organic silicone compounds (Fig. 19) and in situ polymerization of special monomers bearing fluorin (F) element within wood pores (Fig. 20). From the figures, it can be known that both methods impart hydrophobic property to wood. The hydrophobic agents, i.e. water repellent agents are organic silicone compound and 2,2,3,3,4,4,5,5,6,6,7,7-Dodecafluoroheptyl methacrylate (G04), respectively.

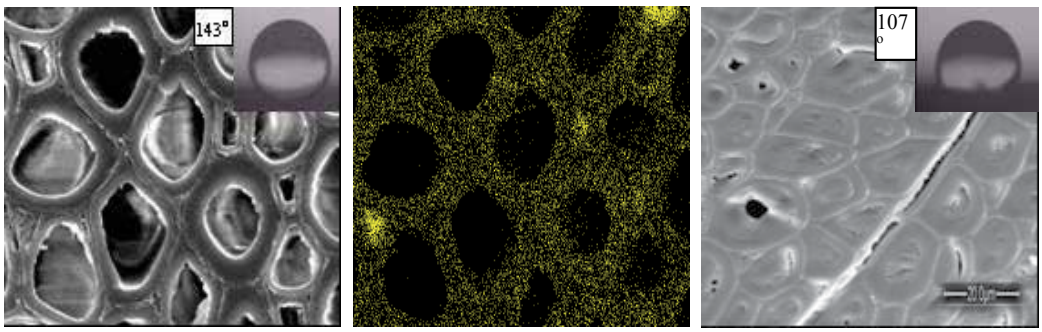

(a) (b) (c)

Fig. 19. SEM morphologies of silicone compounds pretreated wood with contact angle (a) Wood pretreated with organic silicone compound (b) Si element distribution corresponding to micrograph (a) (c) WPC pretreated with silicone compound

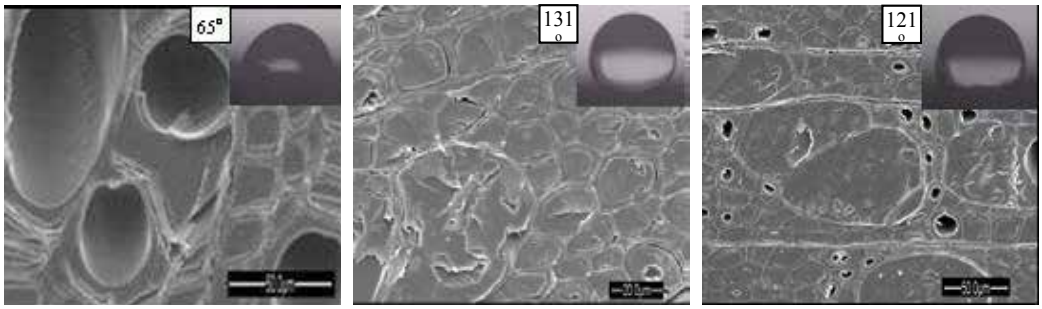

(a) (b) (c)

Fig. 20. SEM morphologies of wood-polymer composites with contact angles (a) WPC prepared by MMA (b) WPC prepared by G04 (c) WPC prepared by G04 and GMA

3.4.2.4 Pigments

Pigment additives, i.e. dyes, are substance being used to impart color to materials (WPCs). They can be added to change the color of the impregnated wood with the darker browns the most popular (Fig. 21). Oak and maple are often dyed to resemble walnut. Veneers can be treated with MMA and a dye to give veneers of different colors which are laminated into custom knife handles (Fig. 22) (Rowell, 2009).

Fig. 21. Comparison of the colors of WPCs with different dyes

Fig. 22. Colored knife handles from veneers with MMA monomer and dyes

3.4.2.5 UV Stabilizers

UV stabilizing agents are used to increase the ultraviolet (UV) and sunlight exposure resistance of plastics, elastomers, paints, coatings, adhesives and other polymeric materials (e.g. WPCs). The normal ways also contain pretreatment with inorganic additives (Fig. 19c) and in-situ polymerization of inorganic additives with monomers (Fig. 23) (Li et al. 2009b).

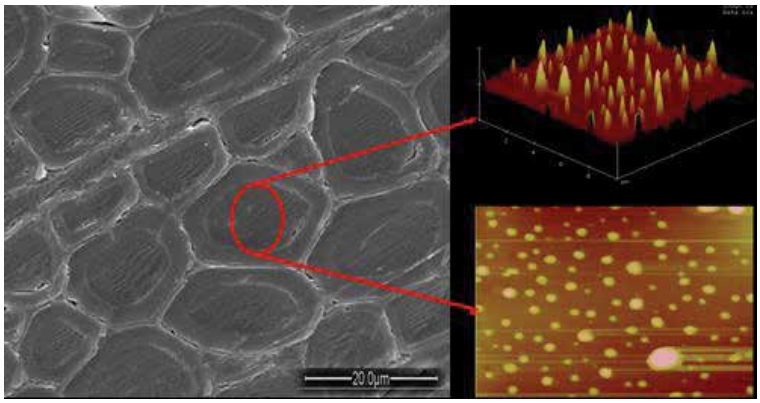

Fig. 23. WPC added with nano-SiO_2

3.5 Impregnation style

Wood is impregnated by various monomers, which can be done by diffusion, vacuum immersion and vacuum-pressure (Husain et al. 1996). The final way can be conducted depending on the variation in permeability of wood, containing the broadly variation between species, between sapwood and heartwood, variation in wet and dry condition, and the availability of facilities as well as the experimenter's preferences. Vacuum or/and pressure is usually applied during impregnation because simple diffusion of wood in a treating solution under normal atmospheric pressure requires a lengthy time and usually leads to incomplete absorption. Vacuum immersion of monomer consists of evacuating the air and moisture from wood vessels and lumens using a vacuum pump and then introducing the monomer from a reservoir maintained at atmospheric pressure (Fig. 24). Vacuum-pressure method uses a combination of vacuum and pressure (Zhang et al. 2006). Both the vacuum immersion and vacuum-pressure treatments are widely used in preparation of WPCs (Fig.25) (Ding, 2009).

3.6 Polymerization style

The impregnated monomer can be polymerized through two different processes: by the incidence of radiation or by the thermal decomposition of initiators, which have been introduced above (Meyer, 1984).

The U.S. Atomic Energy Commission sponsored research that used gamma radiation to make WPCs in the early 1960s. The cobalt-60 radiation process does have some distinct advantages in making WPCs, such as the monomer can be stored at ambient conditions, as long as inhibitor is included, and the rate of free radical generation is constant for cobalt-60 and does not increase with temperature; terilization can be achieved simultaneously by gamma irradiation; the gamma radiation technique can be applied to any size of material due to its high penetration; natural wood grain and colour are retained, or an artificial, uniform colouring the material is possible.(Şolpan & Güven, 1999a; 1999b). However, drawbacks include safety concerns, cost considerations and regulations needed when using radiation. Safety requirements must be satisfied before a cobalt-60 source can be installed and licensed. Radiation-trained personnel must be on the staff before a license can be issued. At least 500,000-1,000,000, Ci (curies) of cobalt-60 are required in a production source for making wood-polymer composites, and at $1.00 or more per curie, a considerable investment must be made before production can begin (Ibach & Ellis, 2005).

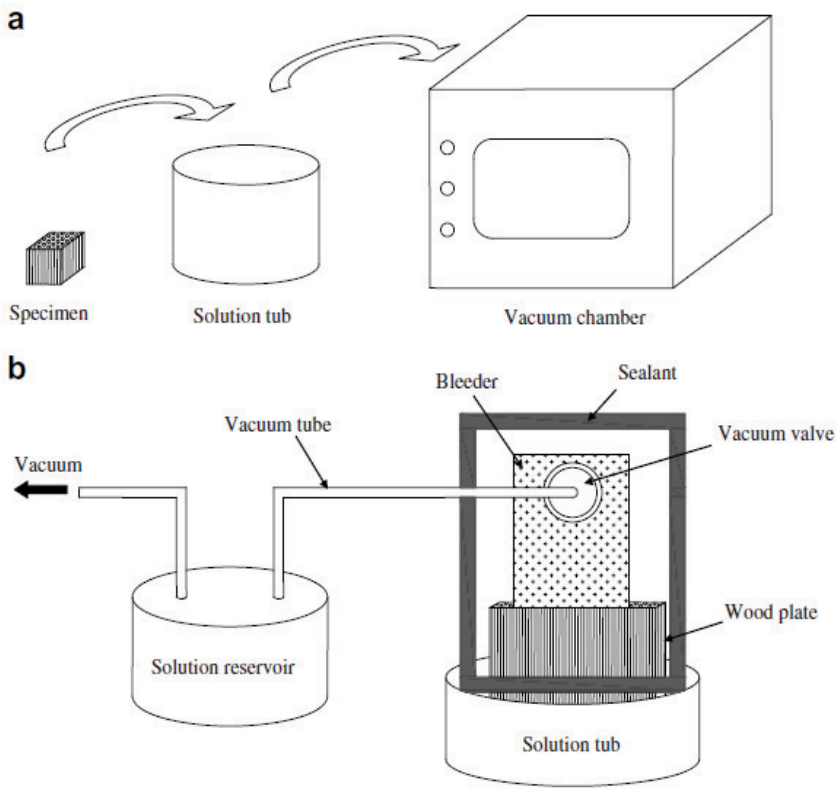

Fig. 24. Impregnating methods for wood-polymer composites: (a) natural soaking method, and (b) vacuum bag method (Kim et al. 2008)

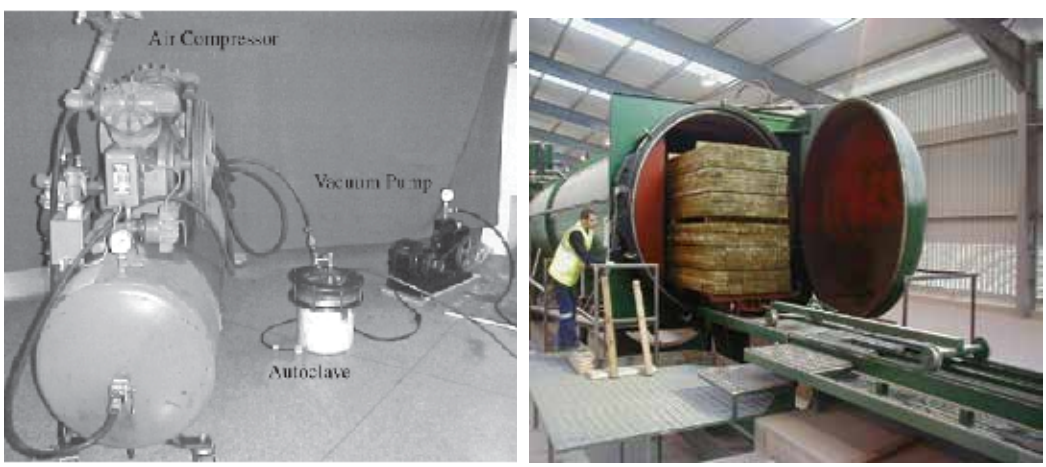

(a) (b)

Fig. 25. Systems used to impregnate the wood (a) impregnating equement in experimental use (b) impregnating equement in plant use

The heat-catalyst-initiated method is now widely used by researchers (El-Awady 1999; Yildiz et al. 2005; Zhang et al. 2006; Li et al., 2009; 2010a; 2011a, 2011b) and in industrial production, for it is less cost and easier operation; and the improvements in the physical and mechanical properties of wood species combined with anti-shrink efficiency make this method preferable to the γ-radiation method (El-Awady 1999). But, it also has some shortcomings such as longer reaction time over gamma radiation, sealed container requirement and releasing nitrogen during decomposition which normally results in void spaces in the resultant polymers within wood pores and thus decreases by the mechanical properties of wood-polymer composites. However, despite all that, during the past 50 years the industrial development has been slow but steady for bothγ-radiation and catalyst-heat processes.

3.7 WPC types

There are two orders of porosity in wood: cavities for the cell lumen and micropores within the cell walls. Normally, as the monomers are nonpolar, they maninly exist in cell lumen, and the resulting WPC belongs to cell-lumen WPC. While the cell lumen and cell wall being combinely treated by monomer with other chemical reagents, the resulting WPC belongs to combined cell-wall-lumen WPC. However, there is another treatment for WPC which is different from the above two WPC types. It is considered to be compressed WPC for the wood being compressed before or after the monomers penetrating wood.

3.7.1 Cell-lumen WPC

If a chemical introduced into dry wood does not cause swelling, the chemical remains in cell lumens. Most ofthe common vinyl monomers (such as styrene and methyl methacrylate) are in the nonswelling or little-swelling category over normal treating times (Schneider, 1994) and so produce essentially cell-lumen WPC. When a nonswelling chemical is changed into a polymer, the polymer will occupy the cell cavities but not the cell walls. Since the cell cavities are a major path for moisture movement in wood (Li et al, 2011c), plugging them with a polymer makes the wood more resistant to rapid changes in moisture content, especially along the grain. The effect is greater dimensional stability over the short term. There is speculation that physical restraint by polymers in cell lumens reduces swelling at a given moisture condition (Schneider et al. 1994). This would contribute to dimensional stability. Similar to this, by adding bulk vinyl monomers to the void spaces in wood; compression strength, hardness, and abrasion resistance greatly improved In the homo-polymerization process, the polymer is located almost completely in the lumen; only minor amounts are polymerized in the cell wall. Thus, most of the WPCs are cell-lumen type WPCs (Schneider et al., 1994).

3.7.2 Combined cell-wall-lumen WPC

Cell-wall micropores are transient. They are at maximum volume in fully water-swollen wood and disappear nearly linearly with moisture content as wood dries below the fiber saturation point. They can be largely (there is some hysteresis) restored by re-exposing to moisture or another polar fluid. The cyclic moistening and drying wood undergoes in use, increasing and decreasing micropore volume, are the reason for its dimensional instability. If a chemical reagent can bulk and/or react with wood cell wall, it may inhibit the cell wall from swelling and slow down the movement of moisture into wood cell wall, particularly in the liquid form. Consequently, the combined treatment of bulking wood cell wall and filling

wood cell lumen may impart both improved mechanical properties and durability to wood. The bulking reagents include silicon compound, maleic anhydride, PEG1000 and so on (Fig. 19 and Fig. 26); and the filling reagents could be most of vinyl monomers and functional monomers, such as GMA, EGDMA, PEG(200)DMA and so on (Keskin et al., 2008; Persenaire et al., 2004; Rodrigues et al., 2004; Roussel et al., 2001; Schneider et al.; 1991; 1995; WallstroÈm & Lindberg, 1999)

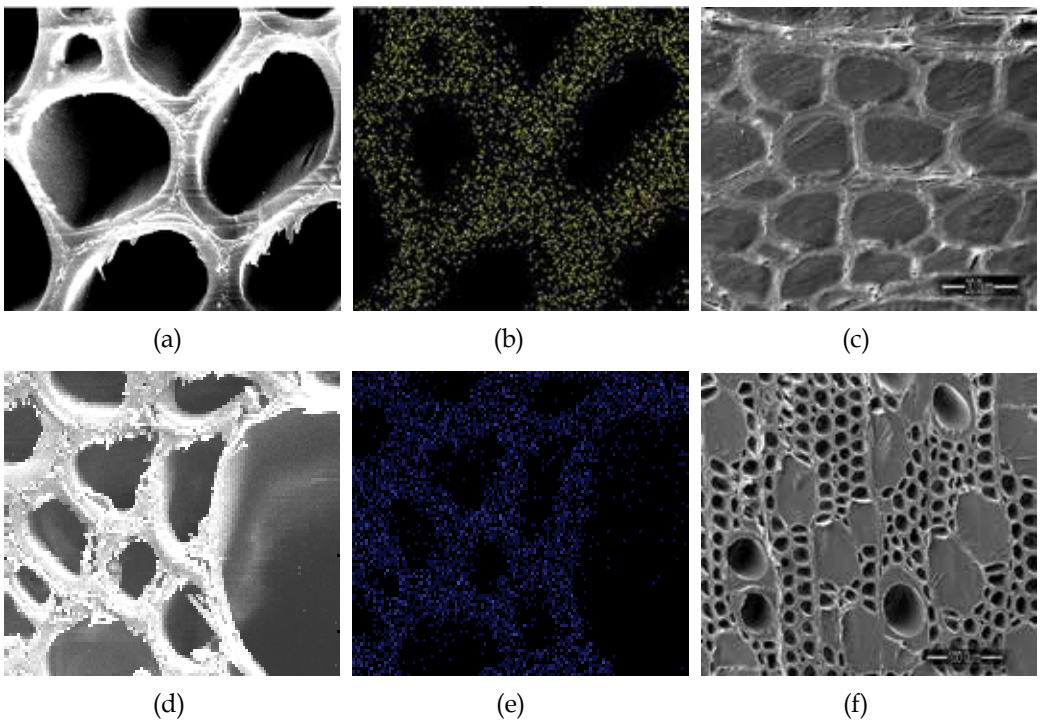

Fig. 26. SEM morphologies of wood and bulked wood as well as cell-wall-lumen WPC (a) Wood (b) Wood bulked with maleic anhydride marked by Diacetone acrylamide (DAAM) (c) Combined cell-wall-lumen WPC (d) Wood (e) Wood bulked with PEG1000 marked by silicon element (f) Combined cell-wall-lumen WPC

For the bulking treatment, one way is the bulking agents in liquid form directly move into and thus swell the cell wall; another way is the bulking agents as nonpolar or weak polar molecules swell the cell wall by diluting in polar solvents, such as methanol acetone, tetrahydrofuran (THF), ethanol, dimethyl sulfoxide and so on (Meyer, 1981). The solvents evaporate during cure, which limits solids retention. Cell-wall followed by cell-lumen treatments, neat (100% active ingredient), swelling monomers or mixtures of swelling and nonswelling monomers (Rowel1 et al., 1982) and silane coupling agents combined with nonswelling monomers have shown improved dimensional stability over cell-lumen treatments (Brebner & Schneider, 1985; Schneider & Brebner, 1985). Considering the large number of chemicals available, combination formulations that develop desirable properties of both cell-wall and cell-lumen treatments have promise (Schneider et al., 1994).

3.7.3 Compressive WPC

The compressive-wood polymer composite (CWPC) was developed based on combination of compression technique and vinyl polymerization. One way is compressing wood followed by vinyl polymerization; the other way is one-step combination of compressing wood and vinyl polymerization. For the prior way, vinyl monomers such as MMA, St, combination of MMA and St, are impregnated into a drying set of deformed wood and further polymerized to fix the compressive deformation. Resultantly, increasing MOR and MOE as well as superior dimensional stability are finally obtained (Dwianto & Yalinkilic, 2000). For the latter way, vinyl monomers with functional groups, such as GMA, AGE, Maleic Anhydride (MAN) are impregnated into wood and then the impregnated wood (or veneer) are further hot-compressed under temperature of 70~120^{o}C depending on the activity of monomers (Fig. 27).

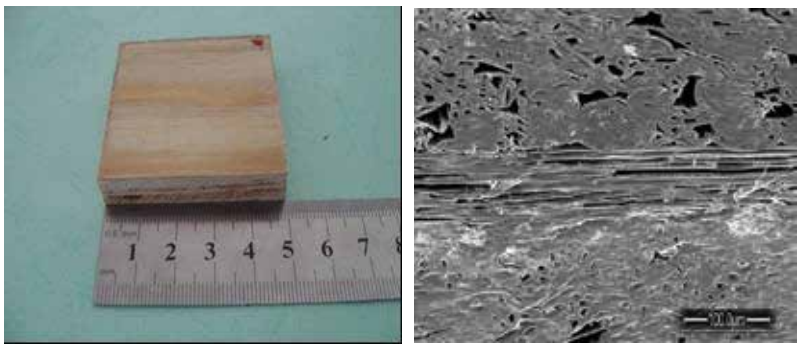

(a) (b)

Fig. 27. Compressive WPC veneer covered plywood and its SEM morphology (a) Compressive WPC veneer covered plywood (b) SEM morphology of sample (a)

3.8 WPC properties

In-situ formation of polymer within wood pores improves the physical properties of the wood, allowing the composite to be tailored for specific applications. Frequently targeted properties are most mechanical properties, hardness, dimensional stability and resistance to abrasion, decay, weather and fire. Other important propertics are toughness, strength, thermal conductivity and appearance.

3.8.1 Mechanical properties

It was found that most of the mechanical properties of WPC are improved over untreated wood. The normal including properties are MOE, MOR and compressive strength (Li et al. 2009a; 2010a; 2011a). The mechanical properties of WPC are almost the same for Cell-lumen WPC and Cell-wall-lumen WPC. But where WPC is impregnated into the cell wall it imparts better dimensional stability than in a lumen only treatment. In addition, the toughness and impact strength of WPCs are variable depending on the style of monomers. Increasing the toughness of wood with polymer increases the crack resistance and brittleness at room temperature. Impact strength and toughness are closely related; both refer to the ability of WPCs to resist fracturing. Measurements of impact strength are made using the Izod and the Charpy impact test instruments. The test involves striking the specimen with a

pendulum and measuring the impact energy necessary to initiate fracture. Microscopy indicates brittle polymer fracture extends across lumens but stops at the polymer and cell wall interface (Schneider, 1994). Brittleness of a composite can be severely increased by increasing the amount of a crosslinker such as ethylene glycol dimethacrylate even to as little as 1.5% in MMA. WPCs with high toughness (low brittleness) have been prepared by using a treating mixture consisting of MMA and an isocyanate that has an acrylic functionality. This treating mixture increased the impact bending strength of the WPC by about 100% (Ibach & Ellis, 2005).
WPCs formed by St, GMA monomers possess decreased toughness and impact strength. While WPCs impregnated with MMA or/with EGDMA or PEGDMA as crosslinkers, normally has improved impact strength (Fig. 14 and Fig. 16). Figure 28 shows different fracture pattern between control and MMA treated wood. The control samples break deep within the sample and it looks more like a brittle failure. In the case of the MMA treated wood, the break is confined to the outer surface and failure is more in the longitudinal direction. This indicates that the MMA polymer is acting as a reinforcing element in the longitudinal direction (Rowell, 2009).

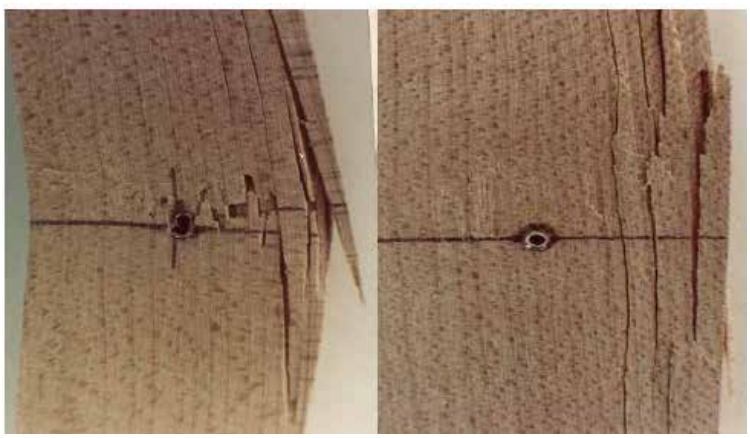

(a) (b)

Fig. 28. Failure pattern of control (a) and MMA treated wood (b) for toughness

3.8.2 Hardness

Hardness implies the ability of a material to resist deformation. There is a wide variety of hardness assessment procedures available, including static indentation, scratch, plowing, rebound, damping, cutting, abrasion and erosion tests. Recently, nanoindentation techniques have also been used for the investigation of hardness of wood. Hardness is a routinely measured mechanical characteristic that is sensitive to structural parameters as well as to mechanical behavior. A classical method used to measure hardness is the static indentation test, which involves forcing a hard tool of known geometry into the sample body. The hardness of the sample is then defined as the ratio of the applied force to the size of the resulting indentation. Brinell hardness is defined as the ratio of the applied force to the actual area of surface contact, whereas Meyer hardness is the ratio of the applied force to the projected contact area (Zhang et al., 2006).

Hardness of a WPC depends on polymer hardness and loading. Polymer hardness is affected by the type of polymer, presence of crosslinking chemicals, and method and extent of polymerization. Polyner loading is affected by wood porosity and density; porous, low-density wood requires a high polymer load. Conversely, dense wood, such as the latewood of oak, accepts a very low polymer load. In general, the higher the polymer load the greater the WPC hardness. Polymer loading is also affected by impregnation method and monomer properties, such as viscosity, boiling point (evaporation during cure), polarity, molecular weight, and shrinkage with polymerization (Ellis, 2000). However, all WPC samples tested in these studies were found to be harder than their corresponding untreated wood samples (Şolpan & Güven, 1999b; Li et al., 2009a, 2010a, 2011a).

3.8.3 Abrasion resistance

Abrasion resistance is determined by the Taber wear index, which is the weight loss (mg/1000 cycles) caused by an abrasive wheel turning on a specimen. The lower the weight loss value, the better the resistance to wear. In general, abrasion resistance increases with increasing polymer content in the wood. Softwood species such as birch, gray and black alder, and spruce when made into a composite with polystyrene have abrasion resistance comparable to that of natural oak wood. Alder wood and birch wood impregnated with MMA had up to 85% less weight loss than untreated wood (Ibach & Ellis, 2005). In our previos studies, the poplar wood impregnated with MAN and GMA as well as MMA has significant improvement of abrasion resistance over untreated poplar wood (Li et al, 2009a, 2011a).

3.8.4 Dimensional stability

Dimensional stability is the property of wood that allows it to resist changes in dimensions when exposed to various moisture conditions. Dimensional stability is reported as percent volumetric swelling, moisture exclusion efficiency (MEE) or as antishrink efficiency (ASE). ASE is the percent reduction in volumetric swelling of treated wood compared to untreated wood at equilibrium water- or moisture-saturated conditions. Moisture exclusion efficiency, the ability to exclude moisture, is related to the rate at which the composite absorbs moisture and swells and not to the maximum extent of swelling or moisture uptake. MEE has been used to represent dimensional stability when the composite reached equilibrium with respect to moisture or water. In WPC, the large void volume of wood filled with polymer reduces pathways for entrance of water and moisture; thus, ASE and MEE are normally used to represent dimensional stability.

As many vinyl monomers are just confined in cell lumen for polymerization without reacting with wood cell wall, they are rarely dimensionally stable so that with time in water or high humidity, they will swell to the same amount as untreated wood (Li et al., 2009a; 2010b; 2011a). While the monomers possessing functional groups (e.g. hydroxylethyl acrylate, glycidyl methacrylate, isocyanate acrylate) or some reactive chemicals (e.g. anhydride, isocyanates, epoxides, alkoxysilane coupling agents) being incorporated with vinyl monomers, the resulting WPCs will hve excellent dimensional stability (Deka & Saikia, 2000; Ibach & Ellis, 2005; Li et al., 2011a).

3.8.5 Decay resistance

Brown-, white-, and soft-rot fungi all contribute to the decay of wood. The conditions essential for fungal growth in wood are food, sufficient oxygen, suitable temperature, and

adequate moisture. Wood itself provides the necessary food, and oxygen is readily available in the environment. A wood moisture content of approximately 20% is required for decay. Below this level degradation due to fungal attack will not occur, and fungi that may have already begun to grow will cease growing (Şolpan & Güven, 1999a). As a general rule, if wood is kept dry, i.e. moisture content below 20% then fungi typically will not attack wood. However, in unprotected outdoor or marine exposures, wood can be exposed to high levels of moisture that provide the necessary conditions for biological attack. Although, many poisonous chemicals are effective for biological resistance of wood, their toxicity to environment is normally questionable. Increased public concern on the environmental effect of many wood preservatives has rendered a special importance to wood-polymer composite as an environmentally friendly way for wood protection. Several reasons contribute to the effectiveness of WPCs on wood protection against microorganisms. It is speculated that the biological resistance of chemically modified wood by in-situ polymerization of monomers is due to chemical alteration of cellulosic substrate so that the very specific hydrolytic enzymatic reactions cannot take place. Resistance may also be due, in part, to reducing the available cell wall moisture to below a level required for biological attack. The decrease in swelling of wood in contact with moisture--that is, dimensional stability--which results from chemical modification of wood is due to the bulking action of the added chemical to the cell wall or the reduced availability of hydroxyl groups on cell wall. The bulked wood cell walls are kept in a swollen state as long as the bonded chemical is retained. In this swollen condition, wood cannot expand in response to water. And the chemical modification of hydroxyl groups increases the repellency of wood against water (Rowell & Ellis, 1981).

WPCs prepared by vinyl monomers are not decay-resistant because the polymer merely fills the lumens and does not enter the cell walls, which makes the cell walls accessible to moisture and decay organisms. WPCs prepared using vinyl monomers and several kinds of crosslinking monomers (e.g. ethylglycol dimethacrylate, polyethylglycol dimethacrylate, trimethylolpropane trimethacrylate) and polar monomers (2-hydroxyethyl methacrylate and glycidyl methacrylate) added at 5–20% concentration have excellent resistance to brown rot decay (Ibach & Ellis, 2005). Actually, the crucial point of WPCs for wood protection is the selection of a monomer which can protect and consolidate the wood. In principle, the consolidating action can best be obtained if a polymer is fully compatible with the chemical constituents of the wood. The structures of cellulose and lignin, chief constituents of wood, led us to select glycidyl methacrylate, allyl glycidyl ether (AGE), ethylglycol dimethacrylate and polyethylglycol dimethacrylate as potential monomers for the conservation of wood. Due to resonance stability of allylic radicals, chain polymerization of allyl monomers does not take place efficiently and products obtained have very low molecular weight. Thus, these functional monomers are normally used with MMA, St and other monomers (Yildiz et al., 2005; Şolpan & Güven, 1999a).

In addition, using methanol with MMA or St allows the polymer to penetrate the cell walls. The amount of polymer in the cell wall is important for decay resistance. Some protection against biological degradation is possible at cell wall polymer contents of 10% or more. Acrylate monomers with various bioactive moieties such as boron compounds, can also effectively improve decay resistance of wood (Baysal et al. 2007).

Another basic, effective approach to bring about simultaneous improvements in decay resistance, dimensional stability, and mechanical behavior of wood is in situ polymerization and copolymerization of organotin monomers carrying the bioactive tributyltin group. Tri-n-butyltin methacrylatemaleic anhydride and tri-n-butyltin methacrylate-glycidyl

methacrylate are examples of suitable monomer combinations for in situ copolymerization. Comonomers that carry anhydride or epoxy functional groups graft to wood through esterification or etherification of wood hydroxyls. Pentachlorophenol acrylate and Fyrol 6 acrylate polymers provided no protection against decay, whereas tributyltin acrylate, 8-hydroxyquinolyl acrylate, and 5,7-dibromo-8-hydroxyquinolyl acrylate were found to be resistant to the brown-rot fungus, *Gloeophyllum trabeum,* at low polymer loading of 2–5% retention (Matsuda , 1987; Subramanian, 1984; Ibach & Ellis, 2005; Matsuda et al., 2003).

3.8.6 Weather resistance

WPCs made with birch and pine impregnated with MMA or styrene-acrylonitrile were exposed in a weatherometer for 1000 hours and became more resistant to surface checking than untreated controls. Wood-polymer composites made with styrene and acrylonitrile performed better than those made with MMA. A combination of cell wall-modifying treatments (butylene oxide or methyl isocyanate) with MMA lumen-filled treatments results in a dual treatment that resists the degradative effects of accelerated weathering in a weatherometer. The use of MMA in addition to the cell wall-modifying chemical treatments provides added dimensional stability and lignin stabilization and has a significant effect on weatherability (Rowell, 1981). The combination use of monomers of MANwith GMA or AGE and compression treatment for WPC can impart wood excellent weather resistance (Timara et al., 1999). The combination treatment of inorganic compounds such as silicon compounds, titanic compounds, aluminous compounds with monomers can also remarkably improve the weather resistance of wood (Fig. 19 and 23).

3.8.7 Fire resistance

Wood and wood-polymer composites consist of organic compounds are composed mainly of carbon and hydrogen, for this reason, they are combustible. It is impossible to make wood and WPCs incombustible but it is possible to make it fire retardant. It is well known that boron compounds work efficiently as fire retardant chemicals for cellulosic materials. Boric acid and borax mixtures have some efficacy in retarding flame spread on wood surfaces. In addition to the usual char-forming catalytic effect, they have a rather low melting point and form glassy films when exposed to high temperatures in fires. Borax tends to reduce flame-spread but can promote smoldering or glowing. On the other hand, boric acid suppresses smoldering but has little effect on flame spread. Therefore, these compounds are usually used together to pretreat wood, followed by polymerization of monomers within woor pores for fire resistant improvement of WPCs (Baysal et al. 2007; Couturier et al., 1996; Deka & Saikia, 2000).

There are several methods of measuring different aspects of the property of fire retardancy. Thermogravimetry measures char formation and decomposition temperatures by heating small specimens in an inert atmosphere. More char generally indicates greater fire retardancy. The oxygen index test measures the minimum concentration of oxygen, in an oxygen and nitrogen atmosphere, that will just support flaming combustion. Highly flammable materials are likely to have a low oxygen index. Flame spread tests are those in which the duration of flaming and extent of flame spread are measured. The results of any of the test methods that use small specimens often do not correlate with the actual performance of materials in a real fire situation. The surface burning characteristics of WPCs used as building materials are best measured by flame spread tests that use large specimens,

such as the ASTM E84 test that requires specimens approximately 514 mm wide by 7.3 m long. The test chamber in this test also has a photometer system built in to measure smoke and particulate density. Smoke evolution is very important because many fire deaths are due to smoke inhalation.
Bis(2-chloroethyl)vinyl phosphonate with vinyl acetate or acrylonitrile improves the fire retardancy, but is less effective than poly(dichlorovinyl phosphate) or poly(diethyl vinyl phosphonate). Wood impregnated with dimethylaminoethyl methacrylate phosphate salt and then polymerized in the presence of crosslinking agents has high fire retardancy as does trichloroethyl phosphate. The addition of chlorinated paraffin oil to monomer systems imparts fire retardancy to composites. The limiting oxygen index values of the MMA-bis(2-chloroethyl)vinyl phosphonate copolymer and MMA-bis(chloropropyl)-2-propene phosphonate copolymer wood composites are much higher than that of untreated wood and other composites, indicating the effectiveness of the phosphonates as fire retardants (Yap et al. 1991). WPC specimens made with MMA are smoke-free, but styrene-type monomers create dense smoke. The presence of aromatic polymers, such as poly(chlorostyrene), and fire retardants having aromatic benzene rings in wood increase the smoke evolution, flame spread, and fuel contribution in a modified tunnel furnace test. In all specimens tested, the smoke evolution increased markedly after the flame is extinguished (Ibach & Ellis, 2005). The addition of magnesium oxide and boron compounds can protect wood fiber from thermal decomposition and degradation during high-temperature composite processing (Lu et al. 2000). Addition of alkenyl phosphonates or alkenyl esters of phosphorus acids increases the polymerization rate and imparts fire resistance and bioresistance to the resultant WPC (Schneider et al., 1994).

3.8.8 Thermal conductivity

Thermophysical properties such as thermal conductivity and thermal diffusivity which influence the insulating and fire retardant characteristics of wood-polymer composites have received comparatively little attention. In a preliminary study, researchers found that wood-polymer composites prepared using tropical woods have a lower longitudinal thermal conductivity than untreated woods (Chia et al., 1985). While another research (Couturier et al., 1996) made different conclusions: the addition of polystyrene and polymethyl-methacrylate to red maple boards increased the thermal conductivity of the boards in both the longitudinal and transverse directions. However because the increase in the thermal conductivity was less than the increase in the volumetric heat capacity, the thermal diffusivity of the wood-polymer composites was in all cases less than that of the parent wood. The proposed theoretical models (Fig. 29) for the longitudinal and transverse thermal conductivities of wood polymer composites have been shown to give reliable predictions. The models apply to both cell-wall and cell-lumen composites and the inputs of the model are simply the thermal conductivity of the constituent materials, the fractional volumetric expansion observed during treatment and the porosities of the composite and parent wood. On average the thermal diffusivity of the composites was 26% smaller than that of the parent wood.

3.9 Application of WPC

The potential uses for WPC fall into four main categories: construction materials, traffic materials, military materials and furniture materials (Fig. 30). Wood-polymer composites are becoming more accepted in advanced engineering applications. The latest generation of

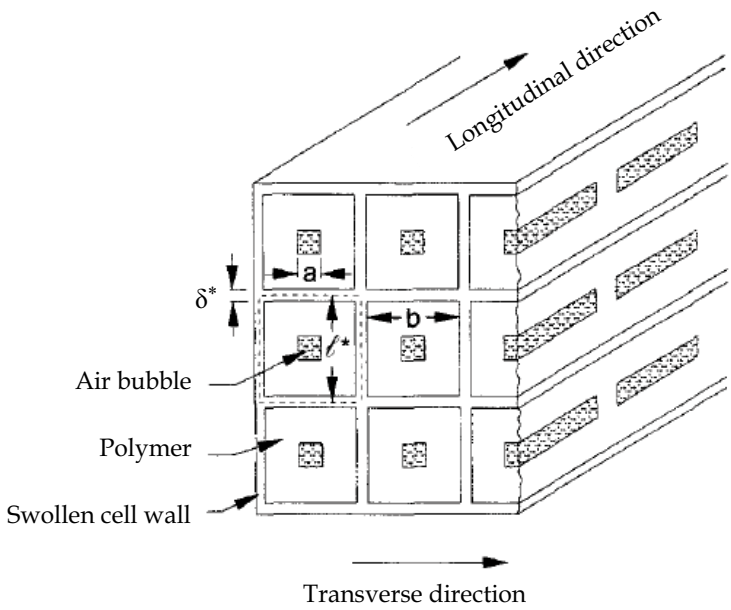

Fig. 29. Geometrical model for the cellular structure of wood-polymer composites

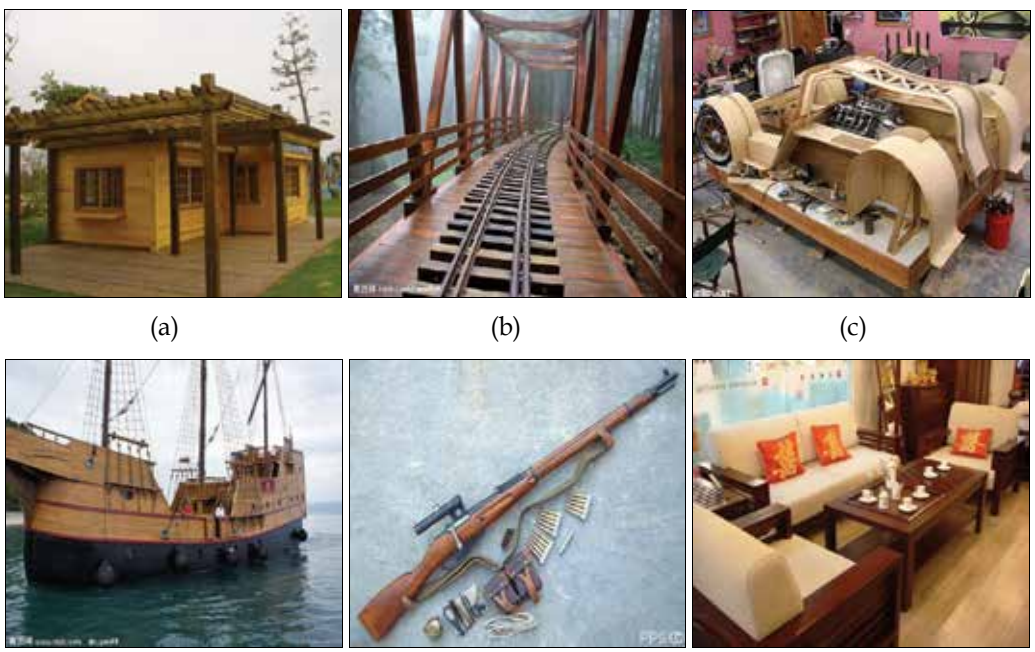

Fig. 30. Major uses for WPCs (a) Construction Material (b) Traffic Material- Crosstie (c) Traffic Material for car beds (d) Traffic Material for ship uses (e) Military Materials (f) Furniture Materials

wood-polymer composites is being used in automotive, civil and marine engineering. Advances in durability, mechanical properties and materials used in their production have allowed a significant increase in their use in outdoor applications such as decking, fencing, utility poles and exterior woodwork on buildings. Wood-polymer composites also benefit from being more sustainable than other, traditional, composites and possess a consistency in quality that cannot be achieved by wood alone. Flooring, the largest volume use for WPC, includes solid plank flooring, top veneers of laminated flooring, and fillets for parquet flooring (Rowell, 2009). The major raw materials for the above floorings have been primarily red oak, ash, maple, and walnut. As for sports equipment, patents have been issued for golf club heads, bows, baseball bats, hockey sticks, and parts of laminated skis, gun stocks. WPC is used for wind instruments, bagpipe chanters, mouthpieces of flutes and trumpets and finger boards of stringed instruments. Another huge potential use is veneer laminates for scratch resistant furniture (such as desk writing surfaces, tabletops), decorative products (knife handles, clock faces, plaques) and recreational equipment (Ellis, 2000). Another smaller application, in relation to volume, would be handrails. These handrails are used primarily for commercial type installations, such as malls, department stores, and airports, for their strength improvements, aesthetics, as well as the ease of maintenance (Schaudy & Proksch, 1982; Kim et al. 2008).

3.10 History

This material has been known and available in small quantities for years made from lumber since 1960s. After the Second World War, the United States government worked very hard to erase the atomic bomb from peoples' minds. One result was President Eisenhower's Atoms for Peace program designed to find peaceful uses of nuclear energy. A project under that program impregnated vinyl-group-containing monomers into wood and cured them using gamma radiation from Cobalt 60 produced in nuclear fission reactors. The process dramatically improved some wood properties. Initial work was done at Brookhaven National Laboratories in the early 1960s. A pilot plant funded by the program was set up at Lockheed to run test materials for anyone that made a wood product. Then the program funded a multiyear project at West Virginia Technological University to study the properties of WPCs. This work started around 1963. The Research Triangle Institute in North Carolina was awarded funds to summarize all of the work in a report. Considerable money and effort went into developing the product. The project was the beginning of the new material: solid-wood-based WPCs. The low viscosity of the treating monomer allowed lumber and other solid wood products to be made into WPCs. The virtually 100 percent solids of the vinyl monomers used (all of the treating solution except that lost through evaporation became solid polymer) allowed very high wood loadings. Since no solvent was needed for the treating solution, dry wood was the preferred raw material. Thus wood could be dried and pre-shaped before treatment (Schneider & Witt, 2004).

During the 1960's support for making wood-plastics by the radiation process was available from the various Atomic Energy Agencies. This support resulted in a great amount of research in Canada, Finland, Sweden, Japan, and South America, and commercial amounts of wood-plastic flooring were produced for airport terminals and office buildings. Today there is no known commercial gamma radiation production of wood-plastics outside of the United States.

The catalyst-heat system for making wood-plastics is used on a commercial scale in Japan, Germany and Italy. Few details are available on the German production of shuttle cocks for the textile industry. In Italy a plant in the Bologna area is producing about three cubic meters a day using styrene monomer. This polystyrene wood-plastic is used for buttons, desk sets and other high cost low volume items. The same organization is planning a future plant in Spain. The Japanese have been very active in research and the production of wood-plastics using the catalyst-heat system with MMA and styrene mixtures. Applications research at the Government Forest Experiment Station in Tokyo has been carried through to production by the Iwaso Company, Ltd. in Ishikawa, Japan. Iwaso Ltd. produces a range of wood-plastic colors for industry including the Pilot Pen Co. Pilot pen and pencil sets with solid dyed wood-plastic bodies are available in U.S.A. at most stationery stores. Iwaso Ltd. produces wood-plastics for vases, bowls, desk caddies, unusual paper weights, letter holders and the ancient abacus.

Over the years wood has been treated with variety of chemicals to change its physical characteristics. A great deal of effort has been put into attempts to make wood plastics or structural board from comminuted wood. Now the physical properties of wood-polymer composites are better known, specific commercial products are being produced which take the advantage of the desirable aesthetic appearance, the high compression strength, increased hardness and abrasion resistance, and improved dimensional stability as well as decay resistance. In total, recent interest in environmentally friendly biodeterioration-resistant wood products has caused new interest in WPC material, which may lead to more use of it. This material, a composite of wood and polymer, can be considered a "value-added" product of wood. However, compared to the amount of wood and plastic products used, WPC sales are small for its higher price (Schneider & Witt, 2004). Future use of wood-polymer composites will depend upon the imagination of the producer and the market place.

4. Conclusion and future recommendation

With the demand of environmentally benign nature and good value-added uses for wood material, WPC are likely to be found applications in broad fields. However, considering its high cost, the market for WPCs may continue to grow slowly in a long term (Schneider & Witt, 2004). In addition, there are much more fundamental works remaining to be done before more satisfactory processes being practiced in the industries. There is yet to be learned about chemical formulations, treating and curing, and their relationships to property enhancements, WPC recyclability, and chemicals from renewable sources for making WPC. Consequently, with the purpose of enhancing the cost effectiveness of WPCs, some technologies need to be further incorporated with in-situ polymerization of monomers within wood pores: foaming technology, nanotechnology and organic-inorganic hybrid technology.

4.1 Wood-polymer composite foams

Foamed solid polymers, also referred as microcellular composites or expanded composites or sponge materials are a class of materials that are extensively used in everyday applications because of their outstanding cost-to-performance and favorable strength-to-weight ratios. Recently, nanocomposite foams produced by introducing nanometer-sized

elements such as layered silicates, carbon nanofibers, or metal nanoparticles to the cell walls of the foam have received a great deal of attention for their large specific surface area and high aspect ratio, which will impart materials good thermal properties, sound insulation properties, excellent strength-to-weight ratio, and energy-absorbing capacity as well as some functional properties. According to some estimates, the market of foam products in the world stands at 14 billion US Dollars and is expected to grow at a phenomenal rate of 14% for the next 5 years. Thus, this kind of polymer exhibits promising and wide applications in future (Svagan et al., 2008).

The foam style is normally classified as two categories: physical foam and chemical foam. Physical foaming agents including water, argon, nitrogen, and carbon dioxide are compounds that liberate gases as a result of physical processes (evaporation, desorption) at elevated temperatures or reduced pressures; Chemical foaming agents (CFAs) such as azodicarbonamide and sodium bicarbonate are substances that decompose at processing temperatures thus liberate gases like CO_2 and/or nitrogen. Despite of all, combination of polymer foam and wood-polymer composite has been rarely reported (Faruk et al., 2007). One of successful reports on wood-polymer composite foams showed that in-situ foaming polyurethane resins within wood pores remarkably improved the mechanical properties and dimensional stability of wood without high density (Gao & Li, 2007). Consequently, wood-polymer composite foams or combinating with nanotechnology seems a novel promising field for development of WPCs in future.

4.2 Wood-nanofiller reinforced polymer composites

Nanocomposite technology with silicon dioxide or layered silicate nanoclays as in situ reinforcement has been intensively investigated in recent years (Fig. 23). Essential improvements of physical and mechanical properties including tensile modulus and strength, flexural modulus and strength, thermal stability, flame resistance, and barrier resistance have been observed for various thermoplastic and thermoset nanocomposites at low silicate content (Kiliaris & Papaspyrides, 2010). Barrier properties, fire resistance and mechanical properties are of great importance for the successful application of selected wood products. However, few efforts based on such technology have been made in the formation of wood polymer composite (WPC), to improve such properties so as to meet specific end-use requirements (Cai et al., 2008; Devi & Maji, 2011). It seems to be a promising way to further improve the comprehensive performance of wood.

4.3 Wood-organic-inorganic hybrid nanocomposites

Hybrid organic–inorganic nanomaterials with remarkable improvement in properties such as mechanical, thermal, electrical, and magnetic compared to pure organic polymers, are promising systems for a variety of applications due to their extraordinary properties based on the combination of the different building blocks and synergism between the properties of the components, and thus are attracted a lot of attention during the last years. The most commonly employed preparation procedures for these materials are the use of the sol–gel process for the formation of interpenetrating networks (IPNs) between inorganic and organic moieties (Kickelbick, 2003).

We recently used sol-gel approach to form organic-inorganic nanopolymer within wood pores and successfully improved the thermal stability and mechanical properties as well as

dimensional stability of wood. Consequently, it also seems to be a wonderful way to form wood to be a novel value-added composite-Wood-organic-inorganic hybrid nanocomposites (Fig. 31).

In addition, recently, with much attention payed on bionanocomposites, incorporation of bioactive wood-polymer composites (Subramanian, 1984) with nanotechnology seems to be a potential and promising direction for value-addition of wood-polymer composites.

In conclusion, a new generation of hybrid nanostructured materials signifies an emerging field in the frontier between chemistry, nanotechnology and biomass materials. An expanding exploration with the novel interdisciplinary technology may be advisable for development of wood-polymer composites so that it can continue to find a place in the commercial market where the improved and novel conveyed functional properties justify the additional cost.

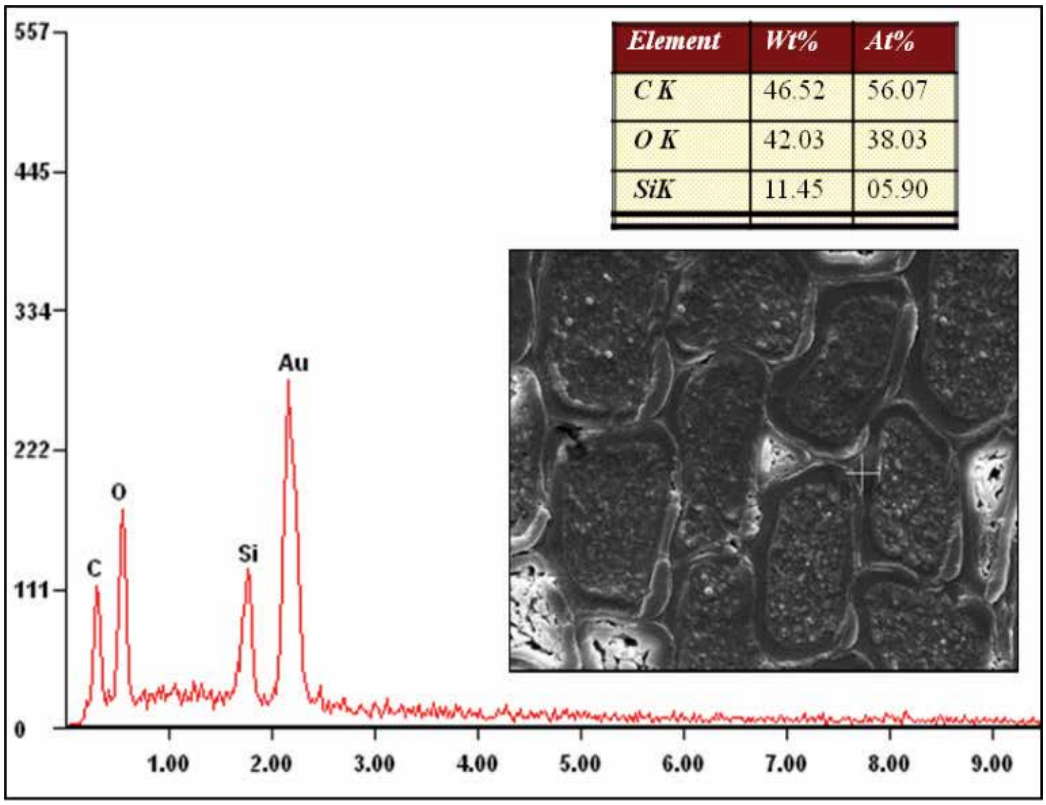

Fig. 31. SEM-EDX of wood-organic-inorganic hybrid nanocomposites

5. Acknowledgements

The authors would like to acknowledge the financial supports of the Breeding Plan of Excellent Doctoral Dissertation of Northeast Forestry University (OPTP10-NEFU), and an Opening Program of the Breeding Lab of Central South Fast-Growing Wood of the State Forestry Administration (KF(2009)- 04).

6. References

Ang, A.; Ashaari, Z.; Bakar, E. & Sahri, M. (2009). Enhancing the properties of Mahang (*Macaranga* spp.) wood through acrylic treatment in combination with crosslinker, Modern Applied Science Vol.3 (No.11): 2-10

Alfred, J. (1977). Wood Technology: Chemical Aspects, American Chemical Society, Washington, DC, pp. 115-140.

Bakraji, E., Salman N. & Al-kassiri H. (2001). Gamma-radiation-induced wood–plastic composites from syrian tree species, *Radiation Physics and Chemistry* Vol.61 (No.2): 137-141.

Bakraji, E.; Salman, N. & Othman, I. (2002). Radiation-induced polymerization of acrylamide within Okoume (*Aucoumea klaineana pierre*), *Radiation Physics and Chemistry* Vol.64: 277-281

Bakraji, E. & Salman, N. (2003). Properties of wood-plastic composites: effect of inorganic additives, *Radiation Physics and Chemistry* Vol.66: 49-53

Baysal, E.; Sonmez, A.; Colak, M. & Toker, H. (2006). Amount of leachant and water absorption levels of wood treated with borates and water repellents, *Bioresource Technology* Vol. 97: 2271–2279

Baysal, E.; Yalinkilic, M.; Altinok, M.; Sonmezc, A.; Pekerd, H. & Colaka, M. (2007). Some physical, biological, mechanical, and fire properties of wood polymer composite (WPC) pretreated with boric acid and borax mixture, *Construction and Building Materials* Vol.21 (No.9): 1879–1885

Bengtsson, M.; Stark, N. & Oksman, K. (2007). Durability and mechanical properties of silane cross-linked wood thermoplastic composites, *Composites Science and Technology* Vol.67: 2728-2738

Schneider M. & Brebner, K. (1985). Wood-polymer combinations: The chemical modification of wood by alkoxysilane coupling agents, *Wood Science and Technology* Vol.19: 67-73

Brebner, K. & Schneider, M. (1985). Wood-polymer combinations: bonding of alkoxysilane coupling agents to wood, *Wood Science and Technology* Vol.19: 75-8l

Boey, F., Chia, L. & Teoh, S. (1985). Compression, bend, and impact testing of some tropical wood-polymer composites. *Radiation Physics and Chemistry* Vol.26 (No.4): 415-421

Cai, X.; Riedl, B; Zhang, S.; Wan, H. (2008). The impact of the nature of nanofillers on the performance of wood polymer nanocomposites, *Composites: Part A* Vol. 39: 727–737

Chia, L.; Chua, P.; Lee, E. (1985). A Preliminary study on the thermal conductivity and flammability of WPC based on some tropical woods, *Radiation Physics and Chemistry* Vol.26 (Vol.4): 423-432

Calleton, R.; Choong, E. & McIlhenny, R. (1970). Treatments of southern pine with vinyl chloride and methyl methacrylate (MMA) for radiation-produced wood-plastic combinations, Journal Wood Science and Technology Vol.4 (No.3): 216-225

Chen, M.; Meister, J.; Gunnells, D. & Gardner, D. (1995). A process for coupling wood to thermoplastic using graft copolymers, *Advances in Polymer Technology* Vol. 14 (No. 2): 97-109

Chang, H. & Chang, S. (2006). Modification of wood with isopropyl glycidyl ether and its effects on decay resistance and light stability, Bioresource Technology Vol.97: 1265–1271.

Couturier, M.; George, K. & Schneider, M. (1996). Thermophysical Properties of Wood-Polymer Composites, *Wood Science and Technology* Vol.30 (No.3): 179-196.

Deka, M.; Saikia, C. (2000). Chemical modification of wood with thermosetting resin: effect on dimensional stability and strength property. *Bioresource Technology* Vol.73 (No.2): 179-181

Devi, R. & Maji, T. (2011). Chemical modification of simul wood with styrene–acrylonitrile copolymer and organically modified nanoclay, *Wood Science and Technology* DOI 10.1007/s00226-011-0406-2: 1-17

Din, R. (1989). Wood Polymer Composites: Their Properties and Applications. MSc Thesis. Univeristy of Wales, Bangor, 60-63.

Ding, W. (2009). Study of physical and mechanical properties of hardened hybrid poplar wood. Master Degree Paper. 1-24.

Doss, N; Elawady, M.; Ela, W., et al. (1991). Impregnation of white pine wood with unsaturated polyesters to produce wood-plastic combinations, *Journal of Applied Polymer Science* Vol. 42: 2589-2594.

Dwianto, W. & Yalinkilic, M. (2000). Fixation of compressive deformation of wood by vinyl polymerization, *Prosiding symposium Fisika Nasional* Vol.XVIII: 73-80

Noah, J. & Foudjet, A. (1988). Wood-polymer composites from some tropical hardwoods, *Wood Science and Technology* Vol. 22: 115-119

El-Awady, N. (1999). Wood polymer composites using thermal and radiation techniques. *Journal of Reinforced Plastics and Composites* 18 (15): 1367–1374

Ellis, D.; O'Dell, J. (1999). Wood–Polymer Composites (WPC) Made with Acrylic Monomers, Isocyanate, and Maleic Anhydride, *Journal of Applied Polymer Science* Vol.73 (No.2): 2493–2505.

Ellis, W. (2000). Wood-polymer composites: Review of processes and properties. *Molecular Crystalsand Liquid Crystals* Vol.353: 75-84

Elvy, S.; Dennis, G. & Ng, L. (1995). Effects of coupling agent on the physical properties of wood-polymer composites, *Journal of Materials Processing Technology* Vol.48: 365-372

Faruk, O.; Bledzki, A. & Matuana, L. (2007). Microcellular foamed wood-plastic composites by different processes: a review, *Macromolecular Materials and Engineering* Vol. 292: 113–127

Fuller, B.; Ellis, W.; Rowell, R. (1997). Hardened and Fire Retardant Wood Products. US Patent 5605767.

Gao, Z. & Li, D. (2007). Chemical modification of poplar wood with foaming polyurethane resins, *Journal of Applied Polymer Science* Vol.104 (No. 5: 2980–2985

González-Peña, M.; Curling, S. & Hale, M. (2009). On The Effect of Heat on The Chemical Composition and Dimensions of Thermally-Modified Wood, *Polymer Degradation and Stability* Vol.94 (No.12): 2184-2193.

Gwon, J.; Lee, S.; Chun, S., Doh, G. & Kim, J. (2010). Effects of chemical treatments of hybrid fillers on the physical and thermal properties of wood plastic composites, *Composites: Part A* Vol.41: 1491-1497

Hamed, P. & Coran, A. (1978). Reinforcement of Polymers Through Short Cellulose Fibers. Pages 29-50 in *Seymour, R. B.* ed. Additives for plastics, vol. 1. State of the art. Academic Press, New York, NY.

Handa, T., Seo, I., Ishii, T., & Hashizume, Y. (1983). Polymer-performance on the dimensional stability and the mechanical properties of wood-polymer composites prepared by an electron beam accelerator. *Polymer Science and Technology* Vol.20 (No.3):167–190

Handa, T.; Yoshizawa, S.; Ikeda, Y.; Saito, M. (1976). Characterization of Polymers and Their Mechanical Performance in Wood-Polymer Composite (WPC), *Kobunshi Ronbunshu* Vol.33 (No.3): 147-154.

Hansmann, C.; Weichslberger, G. & Gindl, W. (2005). A two-step modification treatment of solid wood by bulk modification and surface treatment, *Wood Science and Technology* Vol. 39: 502-511

Haque, N. (1997). A Literature Review of Research into Wood-Plastic Composites. MSc Thesis. University of Wales, Bangor, UK, 1-11.

Hashizume, Y.; Yoshizawa, S.; Nakamura, T.; Yajima, H.; Ishii, T. & Handa, T. (1988). Dimensional Stability of Wood-Polymer Composite (WPC) Using the Pretreatment of Liquid Anhydrous Ammonia, *Kobunshi Ronbunshu* Vol.45 (No.8): 617-624.

Hazer, B. (1989). Handbook of polymer science and technology, vol. 1, N. P. Cheremisinoff (Ed.), Marcel Dekker, New York, pp. 133-176.

Hazer, B.; Örs, Y. & Hakkialma, M. (1993). Improvement of wood properties by impregnation with macromonomeric initiators (macroinimers). *Journal of Applied Polymer Science* Vol.47 (No.6): 1097-1103

Hon, D. (1996). Chemical Modification of Lignocellulosic Materials, In: *CRC Press*, 1-370, ISBN: 0824794729

Husain, M.; Khan, M.; Idriss Ali, K. & Hasan, A. (1995). Wood plastic composite at different urea concentrations, *Radiation Physics and Chemistry* Vol.45 (No.4): 623-627

Husain, M.; Khan, M.; Idriss Ali, K. & Mustafa, A. (1996). Effect of sulfuric acid in wood plastic composite, *Radiation Physics and Chemistry* Vol.47 (No.1): 149-153

Husain, M.; Khan, M.; Ali, M.; Ali, K. & Mustafa, A. (1996). Impregnation mode in wood plastic composite, *Radiation Physics*
and Chemistry Vol.48 (No.6): 781-786

Ibach, R. & Ellis, W. (2005). Lumen modifications, *in* Roger M. Rowell of Editors (ed.), *Handbook of Wood Chemistry and Wood Composites*, CRC Press, Washington, D.C., pp. 421-446

Kartal, S.; Yoshimura, T. & Imamura, Y. (2004). Decay and termite resistance of boron-treated and chemically modified wood by in situ co-polymerization of allyl glycidyl ether (AGE) with methyl methacrylate (MMA), *International Biodeterioration & Biodegradation* Vol. 53: 111-117

Kickelbick, G. (2003). Concepts for the incorporation of inorganic building blocks into organic polymers on a nanoscale, *Progress in Polymer Science* Vol. 28: 83-114

Keskin, H.; Atar, M. & Togay, A. (2008). Impacts of impregnation with imersol-aqua on the compression strength of some solid wood materials, *Construction and Building Materials* Vol.22: 1402-1408

Kiliaris, P. & Papaspyrides, C. (2010). Polymer/layered silicate (clay) nanocomposites: An overview of flame retardancy, *Progress in Polymer Science* Vol. 35: 902-958

Kim, S.; Yu, H.; Hwang, I. & Lee, D. (2008). Characteristics of wood–polymer composite for journal bearing materials, *Composite Structures* Vol.86: 279-284

Lawniczak, M.; Melcerova, A. & Melcer, I. (1987). Analytical characterization of pine and alder wood polymer composites, *Holzforschung und Holzverwertung* Vol.39 (No.5): 119–121

Li, Y.; Liu, Y.; Yu, H. & Sun, Q. (2009a). Property improvement of wood-polymer composites with glycidyl methacrylate. *Acta Materiae Compositae Sinica* Vol.26 (No.5): 1-7

Li, Y.; Liu, Y.; Wang, F. & Wang, X. (2009b). Structure and property of nano-SiO2-PMMA/Wood composite, *Proc SPIE Int Soc Opt Eng* Vol. 7493 74935U

Li, Y.; Liu, Y.; Wang, F. & Wang, X. (2010a). Structure and Properties of Polymer Reinforced Wood-based Composites. *Acta Materiae Compositae Sinica* Vol.27 (No.5): 7-12

Li, Y.; Meng, X.; Li, J. & Liu, Y. (2010b). Performance of Wood-Polymer Composite Prepared by In-situ Polymerization of Styrene. *Applied Mechanics and Materials* Vols. 26-28: 181-185

Li, Y.; Liu, Y.; Li, J.; Lv, D. & Fan, X. (2010c). Fabrication of a novel wood-based composite by in-situ polymerization of functional monomers, *Proceedings of the 2010 International Conference on Measuring Technology and Mechatronics Automation* Vol.2: 208-211

Li, Y.; Liu, Y.; Wang, X.; Wu, Q.; Yu, H. & Li, J. (2011a). Wood-Polymer Composites Prepared by In-situ Polymerization of Monomers within Wood, *Journal of Applied Polymer Science* Vol.119(No.6): 3207–3216

Li, Y.; Li, J.; Wang, X.; Liu, Y. & Wang, B. (2011b). Thermoforming of polymer from monomers in wood porous structure and characterization for wood-polymer composite. *Materials Research Innovations* Vol.15 (S1): S446-S449

Li, Y.; Liu, Y.; Yu, H. & Liu, Z. (2011c). Theory of fluids penetrating wood and its researching method, *Scientia Silvae Sinicae* Vol.47 (No.2): 134-144

Lu, J.; Wu, Q. & McNabb, H. (2000). Chemical coupling in wood fiber and polymer composites: a review of coupling agents and treatments, *Wood and Fiber Science* Vol.32 (No.1): 88-104

Lucia, L.; Rojas, O. (2009). The Nanoscience and Technology of Renewable Biomaterials, In: *Wiley-Blackwell*, 1-366, ISBN: 978-1-4051-6786-4, Washington, D.C .

Mai, C. & Militz, H. (2004a). Modification of wood with silicon compounds, inorganic silicon compounds and sol-gel systems: a review, *Wood Science and Technology* Vol.37: 339-348

Mai, C & Militz, H. (2004b). Modification of wood with silicon compounds, treatment systems based on organic silicon compounds-a review, *Wood Science and Technology* Vol.37: 453-461

Matsuda, H. (1987). Preparation and utilization of esterified woods bearing carboxyl groups, *Wood Science and Technology* Vol. 21: 75-88

Matsuda, H., Ueda, M. & Mori, H. (1988). Preparation and crosslinking of oligoesterified woods based on phthalic anhydride and glycidyl methacrylate, *Wood Science and Technology* Vol. 22: 335-344

Matsuda, H. (1993). Preparation and properties of ofigoesterified wood blocks based on anhydride and epoxide, *Wood Science and Technology V*ol. 27: 23-34

Matsumoto, A.; Ando, H. & Oiwa, M. (1989). Gelation in the copolymerization of methyl methacrylate with trimethylolpropane trimethacrylate, *European Polymer Journal* Vol. 25 (No. 4): 385-389

Meyer, J. (1977). Wood-Polymer Composites and Their Industrial Applications. In Wood Technology: Chemical Aspects; *Goldstein, I. S.*, ed.: ACS Symposium Series; American Chemical Society; Washington DC

Meyer, J. (1981). Wood-Polymer Materials: State of the Art. *Wood Science* Vol.14 (No.2): 49-54.

Meyer, J. (1982). Industrial Use of Wood Polymer Materials: State of the art. *Forest Product Journal* Vol.32 (No.1): 24-29.

Meyer, J. (1984). Wood-polymer materials. Pages 257-289 in *Rowell, R. M.* ed. The Chemistry of Solid Wood, ACS Advances in Chemistry Series 207. American Chemical Society, Washington, D.C.

Mohamad, S.; Rozman, H. & Rahim, S. (2007). Rubberwood-polymer composites: the effect of chemical impregnation on the mechanical and physical properties, *Malaysian Polymer Journal* Vol. 2 (No. 2): 1-11

Moon, R. (2008). Nanomaterials in the forest products industry. McGraw-Hill Yearbook in Science & Technology, 226–229, Chicago, IL.

Ng, L.; Garnett, J. & Mohajerani, S. (1999). Role of additives in wood-polymer composites, relationship to analogous radiation grafting and curing processes, *Radiation Physics and Chemistry* Vol. 55: 633-637

Obanda, D.; Shupe, T. & Barnes, H. (2008). Reducing Leaching of Boron-based Wood Preservatives –A Review of Research, *Bioresource Technology* Vol.99 (No.15): 7312–7322.

Patrice, A.; Véronique, L.; Ana, T. & Alessandro G. (1997). An Apparatus for The Ccharacterization of The Static and Dynamic Wettability of Complex Interfaces, *Review of Scientific Instruments* Vol.68 (No.4): 1801-1808.

Persenaire, O.; Alexandre, M.; Degée, P.; Pirard, R.; Dubois, P. (2004). End-Grained Wood-Polyurethane Composites, 1. Synthesis, Morphology and Characterization Olivier Persenaire. *Macromolecular Materials and Engineering* Vol.289 (No.10): 895–902.

Persenaire, O.; Alexandre, M.; Degée, P. & Dubois, P. (2004). End-grained wood-polyurethane composites, 2a: dimensional stability and mechanical properties, *Macromolar Materials and Engineering* Vol.289: 903-909

Peydecastaing, J. (2008). Chemical Modification of Wood by Mixed Anhydrides. Université de Toulouse. Doctoral dissertation

Plackett, D. & Dunningham, E. (1992). Chemical Modification of Lignocellulosics, In: *Forest Res Inst Bull*, 33-40, Rotorua, New Zealand

Pointing, S.; Jones, E.; Jones, A. (1998). Decay prevention in waterlogged archaeological wood using gamma irradiation, *International Biodeterioration & Biodegradation* Vol. 42: 17-24.

Razi, P. & Raman, A. (2000). Studies on impact fracture properties of wood-polymer composites, *Journal of Composite Materials* Vol.34 (No. 12): 980-997

Rodriguez, N.; Thielemans, W. & Dufresne, A. (2006). Sisal cellulose whiskers reinforced polyvinyl acetate nanocomposites, *Cellulose* Vol.13 (No.3): 261–270.

Rowell, R.; Ellis, W. (1981). Bonding of Isocyanates to Wood, In: Urethane Chemistry and Applications, K.N. Edwards, (Ed.), 263–284, ACS Symposium Series, ISBN 9780841206649, Washington, D.C .

Rowell, R. & Konkol, P. (1987). Treatments That Enhance Physical Properties of Wood. U.S. Forest Products Laboratory General Technical Report FPL-GTR-55. 12 pp.

Schaudy, R.; Proksch, E. (1982). Wood-Plastic Combinations with High Dimensional Stability. *Industrial & Engineering Chemistry Research and Development* Vol.21 (No.3): 369-375.

Schneider, M. (1994). Wood Polymer Composites. *Wood and Fiber Science* Vol.26 (No.1): 142-151.

Schneider, M.; Witt, A. (2004). History of Wood Polymer Composite Commercialization. F*orest Products Journal* Vol.54 (No.4): 19-24

Sèbe, G. & Brook, M. (2001). Hydrophobization of wood surfaces: covalent grafting of silicone polymers, *Wood Science and Technology* Vol.35: 269-282

Sheikh, N. & Taromi, F. (1993). Radiation induced polymerization of vinyl monomers and their application for preparation of wood-polymer composites, *Radiation Physics and Chemistry* Vol.42 (No.1-3): 179-182

Şolpan, D. & Güven, O. (1995). Radiation initiated copolymerization of allyl 2,3 epoxy propyl ether with acrylonitrile and methyl methacrylate and their potential use in the preservation of wooden objects, *Radiation Physics and Chemistry* Vol.46 (No. 4-6): 889-892.

Şolpan, D. & Güven, O. (1996). Radiation initiated copolymerization of allyl alcohol with acrylonitrile, *Radiation Physics and Chemistry* Vol.48 (No. 1): 55-60.

Şolpan, D. & Güven, O. (1999a). Preparation and properties of some wood/(co)polymer composites, *Die Angewandte Makromolekulare Chemie* Vol.269 (No.1): 30-35.

Şolpan D.; & Güven, O. (1999b). Preservation of beech and spruce wood by allyl alcohol-based copolymers, *Radiation Physics and Chemistry* Vol.54: 583-591.

Soulounganga, P.; Loubinoux, B.; Wozniak, E.; Lemor, A. & Gérardin, P. (2004). Improvement of wood properties by impregnation with polyglycerol methacrylate, *European Journal of Wood and Wood Products* Vol.62 (No.4): 281-285.

Svagan, A.; Samir, M. & Berglund, L. (2008). Biomimetic Foams of High Mechanical Performance Based on Nanostructured Cell Walls Reinforced by Native Cellulose Nanofibrils, *Advanced Materials* Vol. 20: 1263-1269.

Stamm, A. (1977). Dimensional Changes of Wood and Their Control. Pages 115-139 in *Goldstein, I.S.*, ed. Wood Technology: Chemical Aspects. ACS Symposium Series 43. American Chemical Society, Washington, DC.

Stolf, D. & Lahr, F. (2004). Wood-polymer composite: physical and mechanical properties of some wood species impregnated with styrene and methyl methacrylate, *Materials Research* Vol. 7(No. 4): 611-617

Stubičar, N.; Šmit, I.; Stubičar, M.; Tonejc, A.; Jánosi, A.; Schurz, J. & Zipper, P. (1998). An X-Ray Diffraction Study of the Crystalline to Amorphous Phase Change in Cellulose During High-Energy Dry Ball Milling, *Holzforschung* Vol.52 (No.5): 455-458.

Tang, H. & Xu, X. (2004). Research of wood/polymer composites based on the electron beam curing. *China Plastic* Vol.18 (No.1): 50-54

Timara, M.; Pitmanb, A. & Mihai, M. (1999). Biological resistance of chemically modified aspen composites, *International Biodeterioration & Biodegradation* Vol. 43:181-187

Tshabalala, M.; Kingshott, P.; VanLandingham, M. & Plackett, D. (2003). Surface chemistry and moisture sorption properties of wood coated with multifunctional alkoxysilanes by sol-gel process, *Journal of Applied Polymer Science* Vol. 88: 2828-2841

Vincent, J. (2002). Survival of the cheapest, *Materials Today*, Vol.5 (No.12): 24–41.

Wallstro Èm, L. & Lindberg, K. (1999). Measurement of cell wall penetration in wood of water-based chemicals using SEM/EDS and STEM/EDS technique, *Wood Science and Technology* Vol. 33: 111-122

Wang, Y.; Minato L. & Iida, I. (2007). Mechanical Properties of Wood in An Unstable State due to Temperature Changes and Analysis of The Relevant Mechanism III: Effect of Quenching on Stress Relaxation of Chemically Modified Wood, *Journal of Wood Science* Vol.53 (No.2): 94-99.

Westin, M.; Rapp, A. & Nilsson, T. (2006). Field test of resistance of modified wood to marine borers, *Wood Material Science and Engineering* Vol.1: 34-38

Witt, A. (1977). Applications in Wood Plastics. *Radiation Physics and Chemistry* Vol.9 (No.1-3): 271-288

Witt,. A.E.; Henise, P.D. & Griest, L.W. (1981). Acrylic woods in the united states, *Radiation Physics and Chemistry* Vol.18 (No.1-2): 67-80

Yalinkilic, M.; Gezer, E.; Takahashi, M.; Demirci, Z.; Ilhan, R. & Imamura, Y. (1999). Boron Addition to Non- or Low-Formaldehyde Cross-linking Reagents to Enhance Biological Resistance and Dimensional Stability of Wood. *European Journal of Wood and Wood Products* Vol.57 (No.5): 351-357.

Yamamoto, Y.; Nakao, W.; Atago, Y.; Ito, K. & Yagci, Y. (2003). A novel macroinimer of polyethylene oxide: synthesis of hyper branched networks by photoinduced H-abstraction process. *European Polymer Journal* Vol.39 (No.3): 545–550

Yap, M.; Chia, L. & Teoh, S. (1990). Wood-polymer composites from tropical hardwoods I: WPC properties, *Journal of Wood Chemistry and Technology* 10(1):1–19.

Yap, M.; Que, Y. & Chia, L. (1991a). Dynamic mechanical analysis of tropical wood polymer composites, *Journal of Applied Polymer Science* Vol.43(No.11):1999-2004

Yap, M.; Que, Y.; Chia, L. & Chan, H. (1991b). Thermal-properties of tropical wood polymer composites, *Journal of Applied Polymer Science* Vol.43 (No.11):2057-2065

Yap, M.; Que, Y. & Chia, L. (1991c). FTIR characterization of tropical wood-polymer composites, *Journal of Applied Polymer Science* Vol.43:2083-2090

Yildiz, Ü; Yildiz, S & Gezer, E. (2005). Mechanical Properties and Decay Resistance of Wood-Polymer Composites Prepared from Fast Growing Species in Turkey, *Bioresouce Technology* Vol.96 (No.9): 1003-1011.

Young, R., Rowell, R. (1986). Cellulose: Structure, Modification and Hydrolysis, In: *Young, R.*; Rowell, R.(Ed.), In: *Wiley Interscience*, 3-50, ISBN 0471827614, New York

Youngquist, J. (1995). The Marriage of Wood and Nonwood Materials. *Forest Product Journal* Vol.45 (No.10): 25-30.

Zhang, Y.; Zhang, S. & Chui, Y. (2006). Water vapor adsorption and volumetric swelling of melt-impregnated wood–polymer somposites, *Journal of Applied Polymer Science* Vol. 102: 2668-2676

Zhang, Y.; Zhang, S.; Yang, D.; Wan, H. (2006). Dimensional Stability of Wood-Polymer Composites, *Journal of Applied Polymer Science* Vol.102 (No.6): 5085-5094.

Zhu, W. & Guo, F. (1998). Recent developments on the studies of wood-polymer compoxites (In Chinese). *Journal of Northwest Forestry College* Vol.13 (No.4): 82-91

10

Engineered Membranes and Transporters for Useful Devices

John Cuppoletti and Danuta H. Malinowska
Department of Molecular and Cellular Physiology,
University of Cincinnati,
Cincinnati OH, 45267-0576
USA

1. Introduction

Biological membranes consist of lipid bilayers which are permeant to gases and water and some hydrophobic substances, but are impermeant to charged materials such as ions. Biological membranes in cells contain a variety of proteins (ion transporters, ion channels, pumps and other types of pore proteins) to facilitate the transport of ions and other molecules such as glucose and even large molecules such as proteins. The present chapter describes our studies to form bilayers on artificial porous supports and solid supports, and incorporate transporters and ion channels into such artificial membranes in functional form. We were then able to remove ion channels from cells, and place them onto a wide variety of solid and permeant synthetic supports without loss of function. While the above studies involved native ion transport proteins, we also have undertaken studies to modify ion channels to give useful properties. Starting with ion channels of known sequence and crystal structures, these studies outlined the structural basis for functional and regulatory properties. The approaches taken to prepare the engineered composite membranes are generally applicable to the development, design and prediction of properties of a wide variety of materials such as selectively permeable membranes or functionalized thin films with desired chemical, electrical or optical properties. ClC-2 Cl^- transporting channels, potassium ion channels, and transporters were used for this work. The following major developments have facilitated this phase of the work. First, the primary structure of the ion channels was known from cloning. Second, the X-ray crystal structure and additional NMR structures of a ClC Cl^- channel have been published. Our group was been able to use both the primary structure and the structural information to develop experiments to engineer new properties into the channels. Recent NMR and X-ray crystal structural studies have given important new information regarding the structure of the intracellular C-terminal region of ClC-2, and this information helped to explain the structural basis for our findings that this same region is involved in phosphorylation-dependent regulation of the channel. Dissection and reconstitution of this region has already been carried out, raising our level of confidence that we can exploit this regulatory region further in future studies, such as

engineering this region to produce ion channel-based sensors which recognize a wide variety ligands by inserting aptamers.

2. Materials and methods

2.1 Formation of bilayers on porous supports

Bilayers can be formed across a small hole in a hydrophobic support, and ion channel proteins can be incorporated into those membranes (1, 2). We expanded this approach to form bilayers on a variety of porous and solid supports containing either single holes in wells, or many holes in a single well (3). Methods were also developed for constructs on solid supported membranes (4). A variety of useful devices were developed using these approaches (please see John Cuppoletti's patents and patent applications at http://patft.uspto.gov/).

2.2 Formation of lipid bilayers

For solid supported membrane studies please see (4) and for porous supports, please see (3). In most studies, we used a 3:1 mixture of palmitoyl-oleoyl-phosphatidylserine (POPS) and palmitoyl-oleoyl-phosphatidylethanolamine (POPE) lipids (Avanti Polar Lipids, Birmingham, Ala), 10 mg/ml and 3.33 mg/ml in n-decane for formation of the bilayer on porous supports. This preparation appeared to work well for most studies. In the case of the anthrax protective antigen studies, we used 3% (w/w) 1,2-diphytanoyl-sn-glycero-3-phosphocholine in n-decane (Avanti Polar Lipids, Birmingham, Ala). 10 µl of lipid solution was added to the membranes. Buffered salt solution was then added to both sides of the membrane and left for 30 min. A multimeter (Epithelial Volt-ohm-meter, World Precision Instruments, Sarasota, Fl) and Ag/AgCl reference electrodes were used to measure the resistance across the phospholipid-coated membranes. When gramicidin D was used to verify that a bilayer was formed (gramicidin is only large enough to cross one leaflet of the bilayer), it was mixed with the lipids to a final concentration of 1 µg/ml. 10 µl of the lipid/gramicidin mixture was added to the membranes. Alternatively, gramicidin can be added to both sides of the membrane. With gramicidin present in both bilayer leaflets, the resistance of the bilayer decreased, verifying the presence of a lipid bilayer.

2.3 Measurement of ion currents

Currents were then measured using an Ag/AgCl reference electrode inside the well and a Dri-Ref™ reference electrode in the outside solution. These were connected to an HS-2A headstage which was connected to a Gene Clamp 500 amplifier (Molecular Devices, Inc. Sunnyvale, California) (3, 4). Channel currents were filtered at 60 Hz. Voltages ranging from −80 to +70 mV were applied in 10-mV increments for 200 ms, and electrical currents were recorded. pCLAMP version 5.5 was used to acquire data and Clampfit 8.0 (Axon Instruments) was used to compare current recordings. Whole cell currents were measured as described for potassium channels (3, 4) and chloride channels (5).

2.4 Types of supports used in these studies

Solid supported membranes were prepared as described in (4). Commercially available porous membranes were used for most studies. Multiscreen-MIC (10 µm thick) filter plates

were obtained from Millipore Corporation (Bedford, MA.) that contained inserts with polycarbonate membranes with 3, 5 and 8 µm pores at the bottom. Micro porous 9 µm thick PETE membranes with 3 µm pores were obtained from GE Osmonics, Inc. (Minnetonka, MN). Individual wells were excised from the plates for use in these studies. Porous supports were also prepared from various polymers (3). A diagram of the experimental setup is shown in (3).

3. Results

Preparation of a device for measurements of the effects of inhibitors on Kv1.5 potassium channels.

Polycarbonate membranes at the base of 0.3 cm^2 polystyrene inserts or wells of Millipore Multiscreen-MIC filter plates were used. 10 µl of 3:1 POPS: POPE (40 mg/ml) in n-decane as described above was added to the membranes and left for 30 min. 100 mM KCl/10 mM HEPES (pH 7.4) was then added to both sides of the membrane. An ohmmeter and Ag/AgCl reference electrodes were used to measure the resistance across the phospholipid-coated membranes. Solutions containing either potassium or N-methyl glutamine were used to determine ion selectivity. In some cases gramicidin (at a final concentration of 1 µg/ml) was included in the lipid to demonstrate that a bilayer was obtained (since two head to tail gramicidin molecules is only large enough to form a leak across a bilayer). With gramicidin and potassium solutions, the resistance decreased, indicating that the presence of a bilayer. Membrane vesicles from cells containing Kv1.5 K^+ channels or without Kv1.5 K^+ channels were prepared as described (3), and incubated with the lipid bilayers across the holes in the membranes. Current across the bilayer was measured as described in the methods. The ion channels in these devices were selective for K^+, and were sensitive to a pharmacological compound, an inhibitor of Kv1.5 K^+ channels, showing that these devices containing reconstituted Kv1.5 K^+ channels on porous supports were useful for screening of drug candidates (3). (See also US Patent 7833805).

4. Development of detectors for bacterial pore forming peptides

Many bacterial pore proteins including α-hemolysin from *Staphylococcus aureus* and the *Bacillus anthracis* protective antigen 635 (PA63) are secreted and bind to a cell receptor on the host, which then inserts into the membrane. Both proteins have been previously reconstituted, but without receptors (6). A lipid bilayer was formed on a porous support with appropriate receptors (CHO-K1 as a substitute for the normal human receptor) (7), membrane proteins and human red cell membranes. It was then determined whether such membranes could serve as an anthrax detector or α-hemolysin detector (see US patent application 20080138839). Lipid bilayers were formed on porous supports as described in the methods. In a control test experiment, ion solutions were then added to the well followed by the addition of varying concentrations of α-hemolysin from 0 to about 500 mg/ml. Once the α-hemolysin solution was added, current flow across the membrane as a function of α-hemolysin concentration, was measured using standard electrophysiological equipment (Materials and Methods). The experiment was repeated for the same range of α-hemolysin concentrations, except that the lipids forming the bilayer membrane were

mixed with membranes from red blood cells (which include the receptor protein for α-hemolysin). Red blood cell membranes were obtained by lysis in 0.15 M NH_4Cl, 10 mM K_2CO_3, and 0.1 mM EDTA and centrifugation. 1 ml of packed red blood cell membranes was resuspended in the solutions above and added into each well. After 1 hr the ion solutions were added, followed closely by the range of α-hemolysin concentrations as used in the control experiment. The current across the membrane was measured as before. We found that α-hemolysin inserted into the bilayers with red cell membrane proteins in a concentration dependent manner, and that the red cell membrane proteins shifted the concentration dependence of pore formation to lower concentrations.

To examine whether anthrax proteins could be similarly detected, 3% (w/w) 1,2-diphytanoyl-sn-glycero-3-phosphocholine (7) lipid solution was placed into wells of the porous support. Varying concentrations of protective antigen 635 were added to the bilayer and allowed to incubate for 30 min. Then 100 mM KCl/10 mM $CaCl_2$/10 mM Tris, pH=7.1-7.4 (neutral salt solution) was added. The plate was then placed into a bath which contained the same neutral salt solution buffer and allowed to incubate for an additional 60 min. Current was measured using pCLAMP software. The experiment was then repeated with CHO-K1 cell membrane vesicles added to the lipid bilayer and a dose response to protective antigen 635 was again determined. Interaction of the bilayer and vesicles was allowed to occur over 1 hr and salt solution was then added to the wells. The bilayers were first tested for stability and to see if the bilayers were formed. Then protective antigen 635 was added and allowed to incubate for 1.5 hr. Salt solutions were added and the current was again measured at each concentration of protective antigen 635. We found that the concentration of protective antigen 635 which caused a leak current (prevented by the inhibitor tetrabutylammonium chloride) was greatly reduced by the presence of CHO-K1 membranes. This device is thus useful as an anthrax protein detector.

5. Use of gramicidin as a proton pore for fuel cell membranes

Gramicidin is a small molecular weight molecule which is available commercially, and which has the property of transporting ions, including protons. We have shown that gramicidin can be easily incorporated into porous membranes using the techniques described above. While having large surface areas of porous membranes is useful for such uses, it appears that high temperatures are required to maintain the integrity of the catalysts which are used in fuel cell membranes. We have found in single channel studies that gramicidin can function at very high temperatures, therefore providing a potential use of these techniques to prepare fuel cell membranes which can function at very high temperatures (95^{o}C or greater) (unpublished data).

6. Solid supported membranes reconstituted with Kv1.5 potassium channels

There have been several reports of fusion of membrane fragments containing electrogenic ion pumps with solid supported membranes, with a resultant functionally relevant ion current upon concerted activation of the ion pumps (8, 9). Building on these studies, we examined whether it would be possible to form solid supported membranes with ion channels (4). However, it was our intent to insert the ion channels directly into a lipid

bilayer on a solid supported membrane. In these studies, gold coated glass slides with a chromium undercoat and a silver wire added as a ground were reacted with 1-octadecanethiol (4, 8, 9). Over this layer was placed an epoxy resin which coated most of the surface, but left some surface voids. The expoy resin was then treated with a 3:1 mixture of palmitoyl-oleoyl-phosphatidylserine (POPS) and pamitoyl-oleoyl-phosphatidylethanolamine (POPE) lipids, 10 mg/ml and 3.33 mg/ml in hexane respectively, and used to form a Langmuir monolayer, which was then deposited on the thiol-treated gold slide using the Langmuir-Blodgett technique. Experimental wells of known area were then constructed by placing plastic ring on the surface with silicon grease and sealed with a coating of clear nail polish around the inner edge. Then, membrane vesicles from cells over-expressing Kv1.5 potassium ion channels (or vesicles from cells without Kv1.5 vesicles), were then applied. K^+ dependent currents were measured when Kv1.5 K^+ channels were present and these were inhibited by known Kv1.5 K^+ channel inhibitors (4).

7. High temperature studies of naturally occurring ion channels

The question of whether devices containing ion channels can remain active under harsh conditions that may be necessary to use is often raised. Biological transport proteins have potential for use in many biotechnology applications. However, high temperatures or harsh chemical environments could limit their use. In the case of the apical ion channels of gastric parietal cells, these channels are routinely exposed to very low pH (pH 3), and are actually activated by low pH (1, 3). We sought to study ion channels which might be active at elevated temperatures. As stated unpublished studies using gramicidin showed H^+ transport at temperatures as high as 96°C. In another study (10) a ClC-like channel from the archeobacter hyperthermophile, *Methanococcus jannaschii* (mj) which grows at a temperature optimum of 85-90°C, was cloned from mj genomic DNA. It was ligated into pcDNA3.1/V5-His TOPO and stably expressed in HEK293 cells. Cl- currents were studied by patch clamp electrophysiology. ClCmj-expressing HEK293 cells (but not mock transfected cells) exhibited voltage activated Cl^- currents which were inhibited by 500 μM $CdCl_2$. When membranes were isolated from ClCmj-expressing HEK293 cells and fused to planar lipid bilayers, single Cl- channels were evident at room temperature (25°C) and they persisted at elevated temperatures up to at least 96°C. No channels were evident with membranes from mock transfected HEK293 cells. These studies demonstrated that ion channels from these organisms are functional at elevated temperatures as required for applications in biotechnology.

8. Manipulation of the properties of ion channels

Total flow of ions through an ensemble of channels is equal to the number of channels (N), multiplied by the open probability (Po), multiplied by the unit conductance of the channels (γ). Up-regulation of the number of channels by insertion into the membranes being studied, or by increasing the copies of the ion channels are straightforward ways of increasing N. The time spent in the closed or open state can be manipulated by drugs, covalent modification, or by physiological regulation such as phosphorylation or binding of

endogenous ligands such as fatty acids. The unit conductance of ion channels is generally constant, thereby contributing to the unique signature of the ion channel, although there may be apparent changes to the measured unit conductance when certain drugs are present which modify the open or closed time.

ClC-2 chloride channels are the major focus of study of our laboratory (1, 2, 5, 11, 12). Early studies showed that these channels from human and rabbit (in contrast to rat ClC-2) were activated by treatments which raised the levels of intracellular cAMP. The rabbit form of ClC-2 was cloned and shown to contain sites which were predicted to be sites for phosphorylation by cAMP dependent protein kinase (PKA) (12). This suggested that ClC-2 was regulated by phosphorylation. The human ClC-2 protein sequence was shown to contain similar sites (13). In order to explore further regulation by protein kinase, we used programs which identified potential phosphorylation sites on the human (and rabbit) ClC-2 protein amino acid sequence, and compared these with those present on the rat ClC-2 protein. Both human and rabbit ClC-2 sequences contained in the C-terminus, two potential phosphorylation sites that were absent from the rat ClC-2 channel. The two sites on the human ClC-2 channel were then probed by site-directed mutagenesis, where the amino acids responsible for accepting the phosphate serine and threonine in the two predicted sites, were changed to alanine. In both cases, the single site mutant channels could be activated by phosphorylation, albeit with slightly different properties (5). However, when both sites were simultaneously changed to alanine, the channel could not be activated by phosphorylation, demonstrating that the two sites were important to regulation of the channel by phosphorylation (5). Moreover, when one of the sites was changed to aspartate, a mimetic of phosphorylation, the channel was constitutively open, and could not be further activated by phosphorylation. This approach has practical implications in generating channels which are constituently active and thus useful for studies of inhibitors of the channel, which is normally inactive in the absence of activators or PKA phosphorylation. This approach can also generate a ClC-2 channel that cannot be activated by cAMP or activators that act through PKA phosphorylation, which would be useful when searching for direct activators of this ion channel.

9. Covalent chemical modifications of ion channels

The rabbit and human forms of the ClC-2 chloride channel are also activated by low extracellular pH. Thus the channel is more active at pH 3.0 than at pH 7.4. To identify the charged residues on ClC-2 which lead to activation by low extracellular pH, an analysis of the predicted topology of the channel was first carried out, and a charged region of the channel was identified that was thought to be glycosylated and therefore exposed to the outside of the cell. Site directed mutagenesis and analysis of channels can be very time consuming. An alternative approach was first taken to determine whether acidic amino acids were indeed involved in the pH activation seen in rabbit ClC-2. We used water soluble carbodiimide to catalyze the amidation of the channel protein (1). The carbodiimide would only access the outer surface of the channel. We found that treatment with the amidation reagents led to activation of the channel to levels similar to that seen with acidic pH. We then carried out site directed mutagenesis of the putative amino acids and showed that changes of a single glutamate to glutamine led to loss of activation by low extracellular pH,

while other changes did not affect pH activation. This approach has practical applications in that the channel can be activated constitutively by amidation without the need of low extracellular pH. As one approach the amidation reagents might be used to activate the channel when it is available to the environment such as in the lung or in devices (see US patent 6,159,698).

Other approaches to covalent modification were also carried out. We have studied chloride transport in the stomach for many years in the context of gastric acid secretion. It was known that the gastric H^+/K^+ ATPase was a target of proton pump inhibitors, such as omeprazole. Omeprazole, when acid activated, will react with a large number of proteins, but generally acts mostly in the stomach, where acid activation is robust. Thus, it was not known whether the chloride transport channel (thought to be ClC-2) was also affected by omeprazole. The ClC-2 channel in bilayers was found to be activated by acid activated omeprazole (11). This provided another potential way to activate the ClC-2 channel, such as in the lung or in devices (see US patent 6,015,828).

10. Search for drug binding sites

The ClC-2 channel is known to be activated by a drug, lubiprostone, that is currently used in treatment of constipation (14, 15) and by a large variety of fatty acids, including arachidonic acid (13). In ongoing work, we have been searching for the binding region for lubiprostone and other fatty acids. Preliminary data (not shown) suggest that certain amino acids play a major role in activation of the channel by lubiprostone. The amino acid mutagenesis and chemical modification studies described above have provided information which can be compared with known X-ray and NMR structures of the ClC channels. For example, the crystal structure of parts of several ClC channels have appeared (16, 17), and NMR studies have described organized regions of the cytosolic C-terminus of the channel which cannot be crystallized (18). These structures, in conjunction with site directed mutagenesis studies provide a roadmap for understanding how various structures within the channel might lead to regulation of the channels.

11. Discussion

We have described our studies of reconstitution of potassium channels on solid and porous supports for pharmacological studies, reconstitution of the anthrax pore protein and α-hemolysin with their respective membrane protein receptors, preparation of membranes with gramicidin which might be useful for fuel cells, and reconstitution of other membrane proteins, including ion pumps and channels. The work described in this chapter produced unique new materials with the ability to "sense" the environment and at the same time send an electrical signal reporting changes in the chemical or physical environment. These devices can sense chemicals and toxins and even shrink and swell events or produce or transduce energy from biochemicals. Indeed, the present work contributes to a new field of engineering which can produce materials with unprecedented properties. In living cells, these ion channels and other chemi-osmotic transport proteins use electrochemical gradients formed by light and chemical substrates to produce and interconvert energy, mechanical work, electrical work, osmotic work, chemical work and heat. Using the described approaches, composite materials will be developed to do the same in the future.

The approaches described are general. They can also be used for other channels. None of these techniques absolutely require that the ion channels be highly purified from cells and will work even if the ion channels represent a very small fraction of the total membrane protein. The reason for this is that ion channels have unique electrophysiological properties which allow them to be identified by ion selectivity, responses to drugs, unit conductance, voltage responses, and whether they act as single or double barreled channels. However, in some cases it is necessary to alter the source of ion channel protein. Thus, it is possible to increase the complement of ion channel proteins by over expression, to purify and even crystallize the proteins, or, as described above, prepare ion channel proteins with altered amino acid sequence. Purification of these proteins generally requires that the membranes in which they are embedded must be disrupted by detergents. Detergent disruption, subsequent purification and reconstitution into membrane vesicles disrupts the orientation of the membrane proteins into inside out and outside out configurations. This is in contrast to ion channels isolated from native membrane that are normally in one configuration, e.g. inside out. Nevertheless, it is possible to purify membrane vesicles containing a single ion channel in a single configuration by chromatography or free flow electrophoresis. These can then be reconstituted in a single configuration.

The techniques for insertion of ion channels (and other transporters) into porous supports are straightforward and generally applicable. The formation of the lipid bilayer and insertion of the proteins into the bilayer occur by self assembly. The procedure can be scaled from a few hundred square angstroms to square meters. It is also possible to expand upon the geometries of these devices, perhaps placing one type of protein on one side of a compartment, and another on the other side of a compartment, as occurs in living cells. Such studies can be understood within the context of the chemiosmotic theory (19), and can be best understood and driven in the future by that theory. Possible criticism of the approach is that the devices may not be sufficiently robust to function in harsh environments. However, as described in this chapter, some ion channels have been shown to be active at extremes of pH and at high temperatures.

12. References

[1] Stroffekova K., Kupert E. Y., Malinowska D. H., Cuppoletti J. (1998) Identification of the pH sensor and activation by chemical modification of the ClC-2G Cl^- channel. *Am J Physiol 275*: C1113-C1123.

[2] Sherry A. M., Stroffekova K., Knapp L. M., Kupert E. Y., Cuppoletti J., Malinowska D. H. (1997). Characterization of the human pH- and PKA-activated ClC-$2G_{2\alpha}$ Cl^- channel. *Am J Physiol* 273: C384-C393.

[3] Dhoke M. A., Ladha P. J., Boerio F. J., Lessard L. B., Malinowska D. H., Cuppoletti J., Wieczorek D. S. (2005). Porous membranes for reconstitution of ion channels. *Biochim Biophys Acta 1716*: 117-125.

[4] Matsuno N., Murawsky M., Ridgeway J., Cuppoletti J. (2004). Solid support membranes for ion channel arrays and sensors: application to rapid screening of pharmacological compounds. *Biochim Biophys Acta 1665*: 184-190.

[5] Cuppoletti J., Tewari K. P., Sherry A. M., Ferrante C. J., Malinowska D. H. (2004) Sites of protein kinase activation of the human ClC-2 Cl^- channel. J Biolll Chem 279: 1849-21856.

[6] Shenoy D. K., Barger W. R., Singh A., Panchal R. G., Misakian M., Stanford V. M., Kasianowicz J. J. (2005) Functional reconstitution of protein ion channels into planar polymerizable phospholipid membranes. *Nano Lett* 5: 1181-1185

[7] Wolfe J. T., Krantz B. A., Rainey G. J., Young J. A., Collier R. J. (2005) Whole-cell voltage clamp measurements of anthrax toxin pore current. *J Biol Chem* 280: 39417-39422.

[8] Pintschovius J., Fendler K., Bamberg E. (1999) Charge translocation by the Na^+/K^+-ATPase investigated on solid supported membranes: cytoplasmic cation binding and release. *Biophys J* 76: 827-836.

[9] Pintschovius J., Fendler K. (1999) Charge translocation by the Na^+/K^+-ATPase investigated on solid supported membranes: rapid solution exchange with a new technique. *Biophys J* 76: 814-826.

[10] Cuppoletti, Birn S. S., Tewari K. P., Chakrabarti J., Malinowska D. H. (2008) Studies of Ion transport at extreme temperature. Experimental Biology, 2008.

[11] Cuppoletti J., Tewari K. P., Sherry A. M., Kupert E. Y., Malinowska D. H. (2001) ClC-2 Cl^- channels in human lung epithelia: activation by arachidonic acid, amidation, and acid-activated omeprazole. *Am J Physiol* 281: C46-C54.

[12] Malinowska D. H., Kupert E. Y., Bahinski A., Sherry A. M., Cuppoletti J. (1995) Cloning, functional expression, and characterization of a PKA-activated gastric Cl^- channel. *Am J Physiol* 268: C191-C200.

[13] Tewari K. P., Malinowska D. H., Sherry A. M., Cuppoletti J. (2000) PKA and arachidonic acid activation of human recombinant ClC-2 chloride channels. *Am J Physiol Cell Physiol* 279: C40-C50.

[14] Cuppoletti J., Malinowska D. H., Tewari K. P., Li Q. J., Sherry A. M., Patchen M. L., Ueno R. (2004) SPI-0211 activates T84 cell chloride transport and recombinant human ClC-2 chloride currents. *Am J Physiol Cell Physiol* 287: C1173-C1183.

[15] Bao H. F., Liu L., Self J., Duke B. J., Ueno R. and Eaton D. C. (2008). A synthetic prostone activates apical chloride channels in A6 epithelial cells. *Am J Physiol Gastrointest Liver Physiol* 295: G234-G251.

[16] Dutzler R., Cambell E. B., Cadene M., Chalt B. T., MacKinnon R. (2002). X-ray structure of a ClC chloride channel at 3.0 Å reveals the molecular basis of anion selectivity. Nature (Lond) 415: 287-294.

[17] Meyer S., Dutzler R. (2006). Crystal structure of the cytoplasmic domain of the chloride channel ClC-0. Structure 14: 299-307.

[18] Alioth S., Meyer S., Dutzler R., Pervushin K. (2007). The cytoplasmic domain of the chloride channel ClC-0: Structural and dynamic characterization of flexible regions. J Mol Biol 369: 1163-1169.

[19] Mitchell P. (1978) Nobel Lecture: 8 David Keilin's respiratory chain concept and its chemiosmotic consequences.
http://livingwaterusa.com/documents/mitchell-lecture%20chemiosmosis.pdf

Part 3

Manufacturing

11

Mechanical Improvement of Ramie Woven Reinforced-Starch Based Biocomposite Using Biosizing Method

Eko Marsyahyo, Siswi Astuti and Iftitah Ruwana
Mechanical Engineering, Faculty of Industrial Engineering,
National Institute of Technology Malang
Indonesia

1. Introduction

Biocomposite materials have been developed that offer certain mechanical and environmental advantages and also renewable-abundant resources. Biocomposite are defined as composite materials that build up by natural cellulose fibers as reinforcement fibers and starch or biopolymer as natural matrix. Biocomposites also called as green composites.

Based on previous paper (Marsyahyo *et al*, 2008), the density of ramie fibers is much less than that of synthetics fibers such as E-glass fibers but ramie fibers has surface characteristic to be applied as superior renforcement in composite material. The specific strength and specific modulus of natural fibres are comparable or even superior to E-glass fibres. Hence, there is an opportunity for using the natural fibres such as ramie) to replace the E-glass fibre for a composite reinforcement (Drzal *et al*. 2004). Drzal et al (2004) suggested that in order to develop biocomposites with better mechanical properties, it is necessary to solve the problems by suitable treatments to enhance the compatibility between fibers and the matrix. Natural fibers are inexpensive, abundant and renewable, lightweight, degradable and abrasive to processing equipments (Alvarez, Vazquez, & Bernal, 2006).

According to Kalambur and Rizvi (2006), starch as biodegradable polimer to replace synthetic polymer has still needed to improve because of complex disadvanteges including brittleness in the absence of suitable plasticizers, hydrophilic nature of starch and poor water resistance, deterioration of mechanical properties upon exposure to environmental conditions like humidity, and soft and weak nature of starch in the presence of plasticizers. Starch as an inexpensive material and renewable source is biodegradable and biocompatible. Its small granule size makes it as good particulate filler in many polymer blending systems (Ning *et al* , 2010). Also starch has its stiffness, tensile strength, and gas permeability are comparable to those of synthetic polymers from fossil fuels as a matrix in composite. Torres *et al* (2007) reported that starch processing method was not so complicated compare to synthetic polymers and can be produced from a wide variety natural resources and also compatible to plasticizer to improve their properties. Because of their mechanical performances, natural fiber and natural starch, as a composite system, were used intensively for components subtitution in automotive and engineering structures

(Chen *et al*, 2005; Muller and Krobjilowski, 2003). Moreover, Rochardjo *et al* (2009) also utilised ramie fiber for high impact resistant panel for body armours. Figure 1 shows teoritical background on how the composite laminated to be made including stacking squence, the number of ply and also fiber volume fraction embedded in matrix as a composite system.

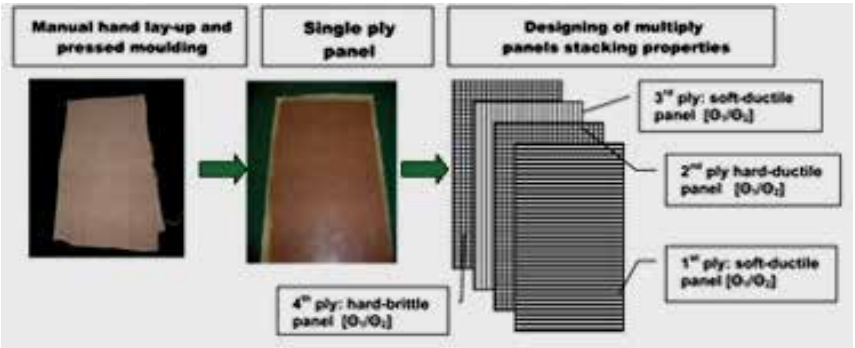

Fig. 1. Laminated composite system (Rochardjo *et al*, 2009)

(a) Ramie yarns in cones

(b) Rami woven

(c) Ramie yarns 12s/3 (mag. 25x)

(d) Plain weave ramie woven (mag.10x)

Fig. 2. Ramie woven structure

2. Materials and methods

Ramie (*Boehmeria nivea*) woven in plain weave structures with double warp and weft orientation was treated by biosizing materials. Dextrin was prepared and used as biosizing materials and matrix to build-up for biocomposites were made from starch based materials obtained form gelatinized garut (*Maranta arundinacea)* and tapioka (*Manihot esculenta*). **Appendix 1** shows FTIR group function identification of dextrin, garut and tapioka starches. All biosizing material was processed in boiling water with mixing in one part starch and 3 parts water in kilograms/litters. Ramie woven was hot-dipped into the mixtures of dextrin and boiled water for 30 minutes and drained in room temperature for 6 hours before used as reinforcement material in biocomposite system. All biosized ramie woven was tested to obtained mechanical strength in laminate forms or multi layer ramie woven biocomposite. The ramie woven structure as a reinforcement material was design in plain weaving with double warp and weft of ramie yarn structure as seen on Figure 2.
Figure 2(a) and (c) are pure ramie yarn. The yarns to be designed in woven form with double warp and weft as shown in Figure 2(b) and (d). Spesification of the woven structure is showed in Table 1.

Specifications ramie woven#	
a. Tensile strength (cN/tex)	45 – 75
b. Elongation (%)	7 - 12
c. Bursting strength (MPa)	8,5 - 16
d. Tearing strength (N)	300 - 550

Yarn dimension is 12/3s and containing 100% ramie fiber. The woven structure is plain weave double warp/weft.

Table 1. Ramie woven specifications

Ramie woven material for tensile testing showed in Figure 3(a) and bending Figure 3(b). All specimen was prepared and cut into standard size for mechanical testing before laminated to build up biocomposite system.

(a) Ramie woven for tensile testing (b) ramie woven for bending test

Fig. 3. Ramie woven as fiber reinforcement material

The number of each group of the specimens to be tested is 15 samples. Testing was conducted according to ASTM standards. The standards used in this test were D 638 for tensile testing, D790 for bending testing and D 256 for impact test.

Figure 4 shows the biosizing methode to processing rami woven. Both garut (*Maranta arundinacea)* and tapioka (*Manihot esculenta)* boiled in 3 parts of water until reached gelatinised starch for biosizing and applied to ramie woven surfaces.

(a) (b) (c)

Fig. 4. Making biosizing for matrix in biocomposite system. (a) starch based material for sizing; (b) Gelatinised starch; (c) biosizing ready to use

Figure 4(a) is starch based from garut (*Maranta arundinacea)* and tapioka (*Manihot esculenta*) to be processed into gelatinised starch becoming biosizing material which had a capability to bond the ramie woven in laminated composite and to fill the gap between ramie yarn in double warp and weft as woven palin weave structure.

3. Results and discussions

3.1 Tensile strength

Tensile strength of biocomposite ramie without treatment showed has a lower strength about 14.45 MPa for ramie-garut biocomposite and 12.81 for ramie-tapioka biocomposite. In certain voleme fraction, the optimum tensile strength was 19.47 MPa for 60% containing fiber embedded in garut as composite matrix but for tapioka matrix showed 70% fiber content has optimum tensile strength 16.84 MPa in average. Figure 5 shows ramie-garut biocompossite relatively has higher tensile strength than ramie-tapioka.

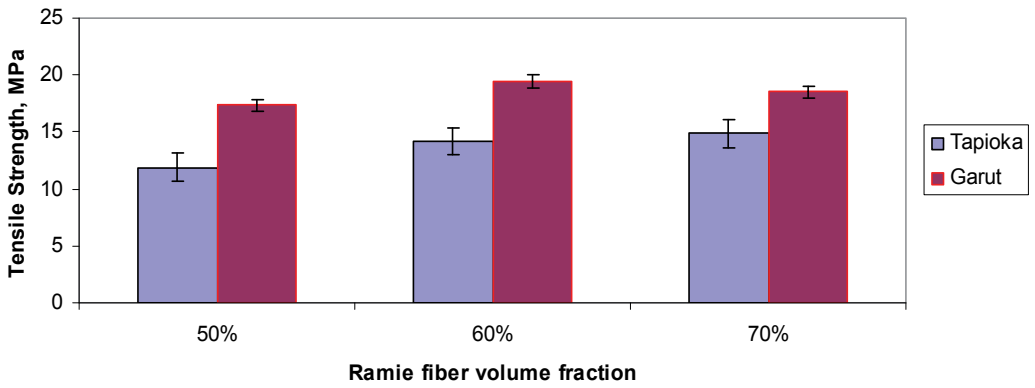

Fig. 5. Tensile strength ramie-garut and ramie –tapioka biocomposite

From figure 6 it can be showed that without biosizing, spesimen damage after tensile testing mostly dominated by debonding interlayer because low bonding mechanism between the woven and the matrix and affected to debonding failure easily.

(a) without biosizing treatment

(b) with biosizing 50:50

(c) biosizing 70:30

Fig. 6. Failure in biocomposite with different fiber volume fraction

Figure 6 also shows that fiber broken dominate biocomposte failure especially for 60% and 70% ramie content embedded in the matrix both tapioka and garut.

3.2 Bending strength

The result of bending test showed that ramie woven treated by dextrin biosizing had bending strength higher than without treatment. Biocomposite 60% fiber volume frcation embedded in garut matrix showed bending strength 18.2 MPa and relatively higher than other combinations (Figure 7). The function of the 60% ramie woven fiber in garut matrix indicated effective load transfer during flexuring or deflection.

Deformation after bending test in Figure 8 showed that ramie woven composite in stacking still bonding together. There was no debonding between each plies of the stacking woven both fiber volume fraction 70/30 and 50/50. It was indicate that ramie woven biosized using garut and tapioca had capability to resist debonding during deflection in bending load test.

3.3 Impact strength

Untreated ramie or without sizing using dextrine media shows that the value of their impact strength did not differ sharply. Ramie-garut biocomposite had 4-6 % higher than ramie-tapioka biocomposite as seen in figure 9. Varied in fiber volume fraction both for ramie-tapioka and ramie-garut biocomposite also shows a little difference and it can be understood that the fibers function more effectively absorbed impact energy than the matrix.

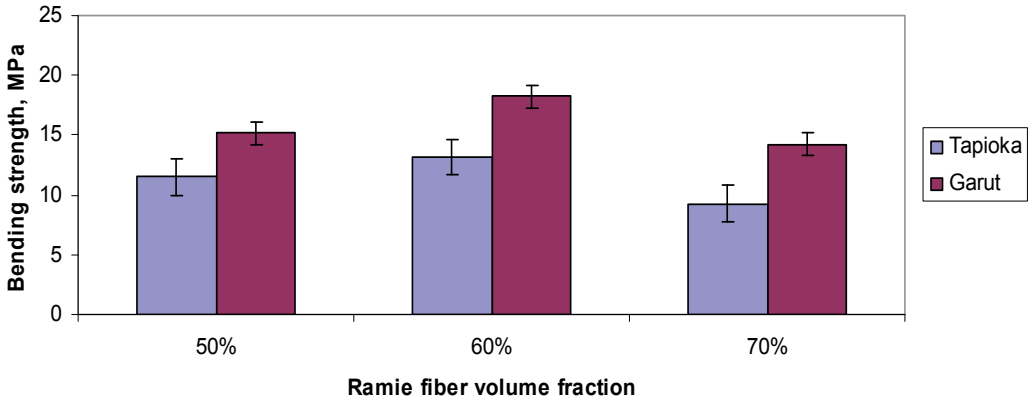

Fig. 7. Bending strength comparison between ramie-tapioka and ramie-garut biocomposite

(a) bending spesimens biosized 70:30 (b) biosized 50:50

Fig. 8. Bending failure of the specimens

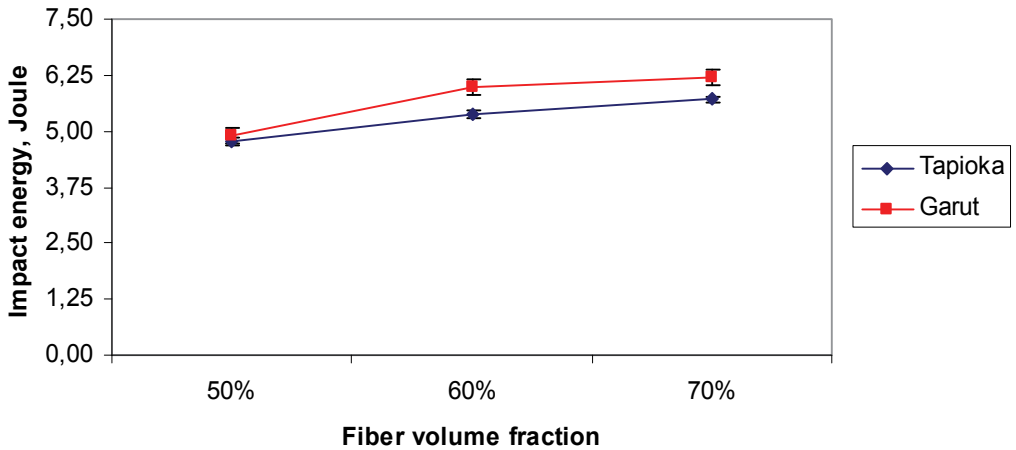

Fig. 9. Impact strength untreated ramie-tapioka and ramie-garut biocomposite

Increasing the impact strength of treated ramie by dextrin showed in figure 10. Ramie-garut biocomposite had impact strength higher than ramie-tapioka. Impact strength between 60% and 70% ramie fiber volume fraction embedded in both for garut and tapioka matrix showed little difference due to rigidity of the fiber remain uniform and did not affected by the matrix very much.

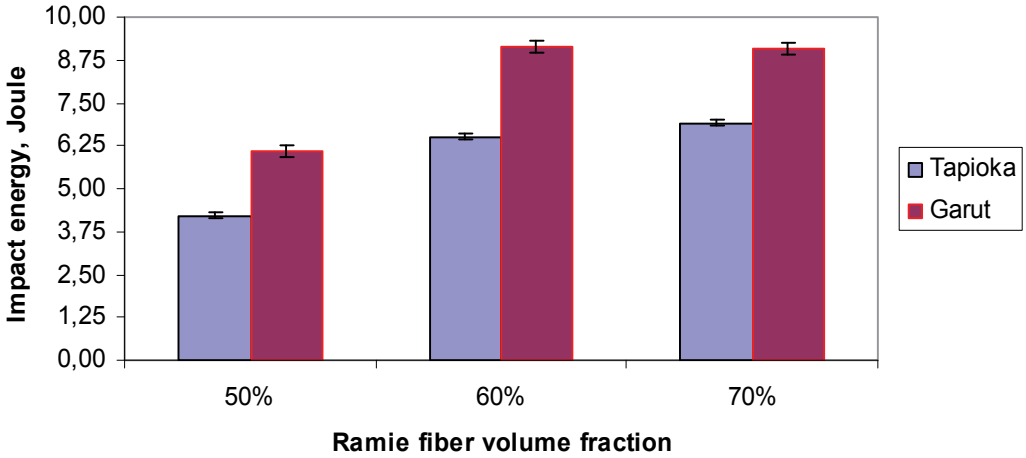

Fig. 10. Impact strength treated ramie-garut and ramie-tapioka biocomposite

For further development of some extent of application for low impact resistant biocomposite product, ramie-garut biocomposite system was also tested for especially safety helmets as shown in figure 11. This preliminary safety helmets were designed for low compressive load.

Fig. 11. Preliminary design safety helmet ramie-garut biocomposite

The helmets were designed in laminated biocomposite with 4 plies or layers of ramie woven. Fiber volume fraction of the ramie woven was about 60%. Garut as material for matrix was blended with antibacterial (see Appendix 1) media to protect from environment such as moisture and tropical fungis. The helmets were tested in 2 direction (figure 12) of compressive load. The test speed was set-up about 10 mm/sec.

(a) Loading in y-direction (down arrow)

(b) Loading in x-direction (down arrow)

Fig. 12. Compressive testing of the helmets

The load application of the compressive testing resulting a compressive strength in y-direction was 1026 N in average and in x-direction was 483 N. From the point of view, abundant supply and low cost of ramie woven will further promote in engineering applications and also market worldwide.

4. Conclusions

Improving mechanical properties of the ramie woven by sizing method using dextrin media showed the enhancement 40 % to 50 % of tensile strength, flexural strength and impact strength of the ramie-garut and ramie-tapioka biocomposite system. Ramie-garut biocomposite had more optimum mechanical strength than ramie-tapioka due to efective adhesive bonding mechanism between fiber and matrix. Ramie fiber volume fraction 60% potentially the best choice for renforcement in garut as a matrix to build up biocomposite system to meet mechanical and fully biodegradable criteria for further engineering applications.

5. Acknowledgement

The authors would like to acknowledge financial aid from the Ministry of National Education of Republic of Indonesia, Directorate General of Higher Education for research grant competition (Hibah Bersaing DP2M-DIKTI) in 2009-2010.

Appendix 1. FTIR group function of garut (*Maranta arundinacea*) and tapioka (*Manihot esculenta*) biosizing starches

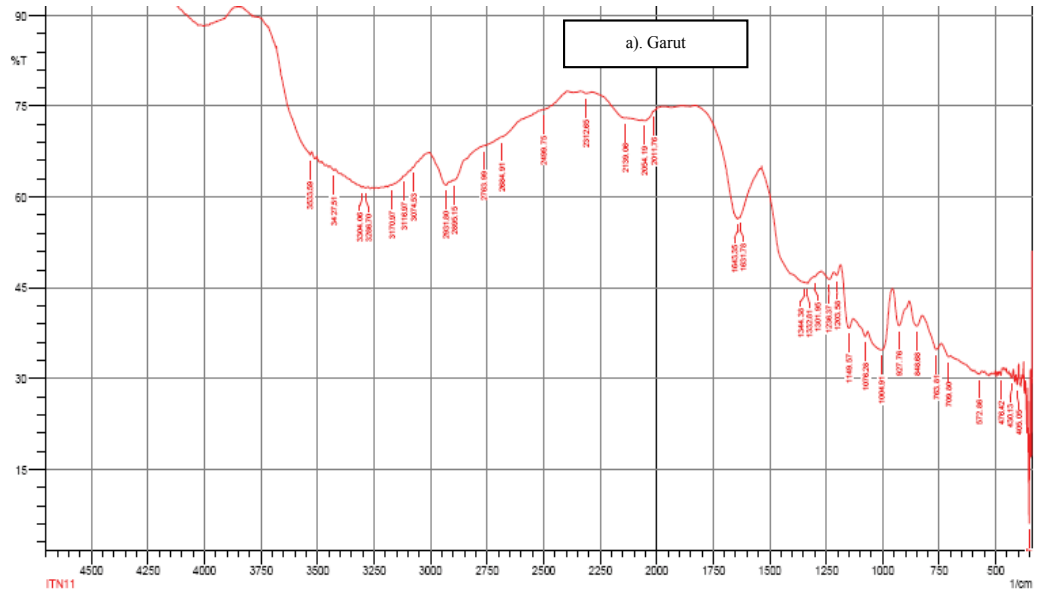

(a) FTIR group function of Garut (*Maranta arundinacea)*

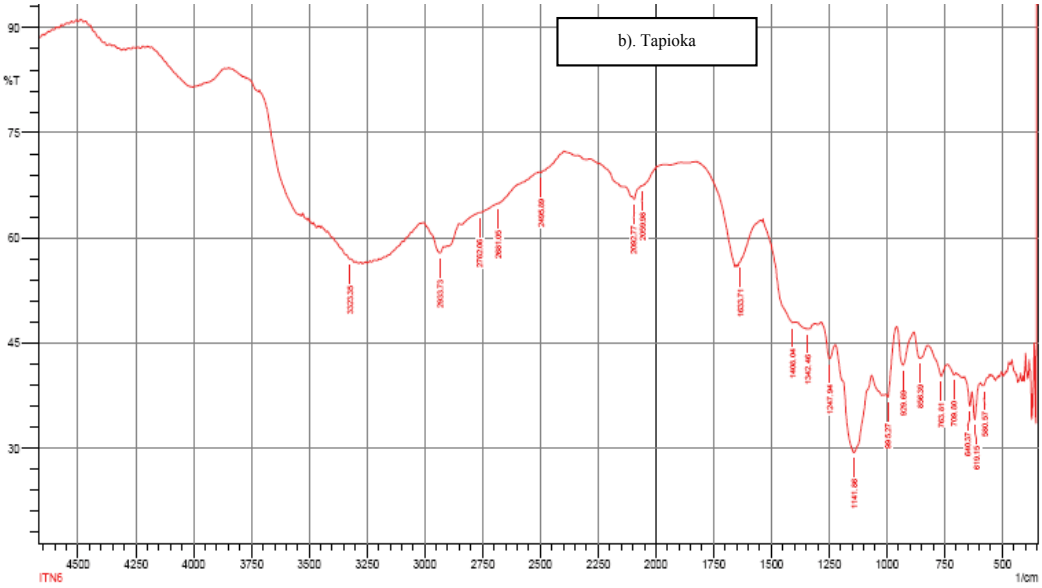

(b) FTIR group function of tapioka (*Manihot esculenta*)

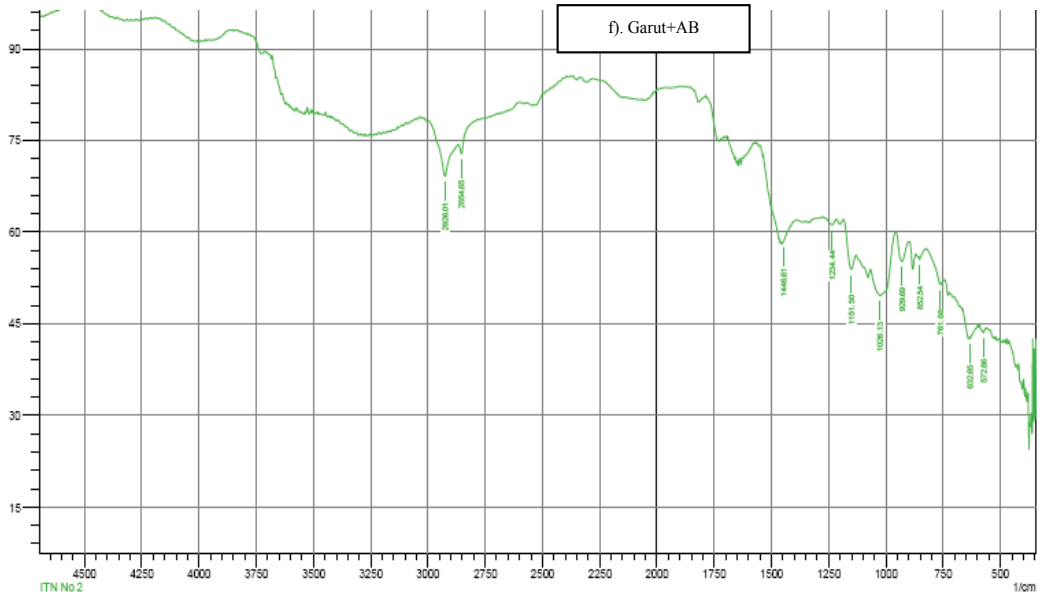

(c) FTIR group function of garut blended antibacterial agent (AB)

6. References

Alvarez, V., Vazquez, A., & Bernal, C. (2006). Effect of Microstructure on the Tensile and Fracture Properties of Sisal Fiber/Starch-based Composites Journal of Composite Materials. *Processing*.

Chen, O. Chiparus, L. Sun, I. Negulescu, D. V. Parikh and T. A. Calamari. (2005) Natural Fibers for Automotive Nonwoven Composites, Journal of Industrial Textiles, vol.35

Drzal, L., Mohanty, D., Burgueno, R. & Misra, M. 2004. Biobased structural composite materials for housing and infrastructure applications: opportunities and challenges. *Proceedings of the NSF Housing Research Agenda Workshop* 2: 129-140.

Kalambur, S. and Rizvi, S.S.S., 2006, An overview starch based plastic blends from reactive extrusion, J. Plastic Film and Sheetings, vol. 22, Sage publ.

Ning, W., Xingxiang,Z.,Na, H., and Jianming, F, (2010). Effects of Water on the Properties of. Thermoplastic Starch Poly(lactic acid) Blend Containing Citric Acid *Journal of THERMOPLASTIC COMPOSITE MATERIALS*, vol. 23

Marsyahyo, E., Soekrisno, Rochardjo, H.S.B., Jamasri.,(2008), *Identification of Ramie Single Fiber Surface Topography Influenced by Solvent Based Treatment*, Journal of Industrial Textiles, vol.38, no.2, Sage Publ.

Muller, D.H., Krobjilowski, A., (2003), *New Discovery in the Properties of Composite Reinforced with Natural Fibers*, Journal of Industrial Textiles, vol.33, no.2, pp.111-130 Sage Publ.

Rochardjo, H.S.B., Marsyahyo, E., Soekrisno and Jamasri., (2009), Preliminary investigation on Bulletproof Panels Made from Ramie Fiber Reinforced Composites for NIJ Level II, IIA, and IV, Journal of Industrial Textiles, vol. 39, no.1, Sage Publ.

Torres, F. G., Arroyo O. H., and Gomez, C. (2007). Processing and Mechanical Properties of Natural Fiber Reinforced Thermoplastic Starch Biocomposites, Journal of Thermoplastic Composite Materials, vol. 20.

12

Thermoplastic Matrix Composites from Towpregs

João Silva[1], João Nunes[2], C. A. Bernardo[2] and António Marques[3]
[1]*Institute for Polymers and Composites/I3N, ISEP*
[2]*Institute for Polymers and Composites/I3N, University of Minho*
[3]*FEUP/ University of Porto*
Portugal

1. Introduction

In recent years, continuous fibre reinforced thermoplastic matrix composites have been successfully employed in the aircraft, military and aerospace industries due to the excellent properties (Brandt et al. 1993 & Nunes et al 2005a). In these and many other commercial engineering applications, they can replace other materials, such as thermosetting matrix composites. However, the high cost of the impregnation of continuous fibre thermoplastic composites, arising from the melting of the polymer or the use of solvents, still restricts their use in commercial applications. Hence, cost reduction largely depends on developing more efficient methods for impregnating fibres with high-viscosity thermoplastics and for processing final composite parts.

This chapter summarizes the development of new technologies to fabricate long and continuous fibre reinforced composite structures from thermoplastic matrix semi-products (towpregs and PCT – pre-consolidated tapes) for commercial and highly demanding markets.

The production of continuous fibre reinforced thermoplastic matrix towpregs and PCT's was done using a recently developed coating line (Nunes et al. 2008, 2010 & Silva, R.F. et al. 2008).

Using this prototype equipment, it was possible to produce glass fibre polypropylene (PP) and polyvinylchloride (PVC) towpregs for commercial markets and towpregs from carbon fibres and Primospire®, an amorphous highly aromatic material developed by Solvay Advanced Polymers, for application in advanced markets (Nunes et al. 2005, 2009 & Silva, J. F. et al. 2010).

To process these thermoplastic pre-pregs into composite structures, conventional thermosetting equipments were adapted to fabricate thermoplastic matrix composites. Filament winding, pultrusion and hot compression moulding were the studied technologies. The mechanical properties determined on the final composites were compared with the theoretical predictions and have shown to be acceptable for the targeted markets.

As applications, filament wound pressure vessels prototypes for gas and incompressible fluids were produced from towpregs and submitted to internal pressure burst tests [Silva, J. F. et al. 2008 & Velosa et al. 2009). These prototypes have accomplished all requirements of the applicable European standards.

2. Experimental

2.1 Powder coating equipment

The prototype powder coating equipment used to produce glass and carbon fibre reinforced towpregs is schematically depicted in Figure 1. It consists of six main parts: a wind-off system, a fibres spreader unit, a heating section, a coating section, a consolidation unit and a wind-up section. In order to produce the towpregs, the reinforcing fibres are wound-off from their tows and pulled through a pneumatic spreader. After, they are heated in a convection oven and so made to pass into a polymer powder vibrating bath to be coated. A gravity system keeps constant the amount of polymer powder. The oven of the consolidation unit allows softening the polymer powder, promoting its adhesion to the fibre surface. Finally, the thermoplastic matrix towpreg is cooled down and wound-up on the final spool.

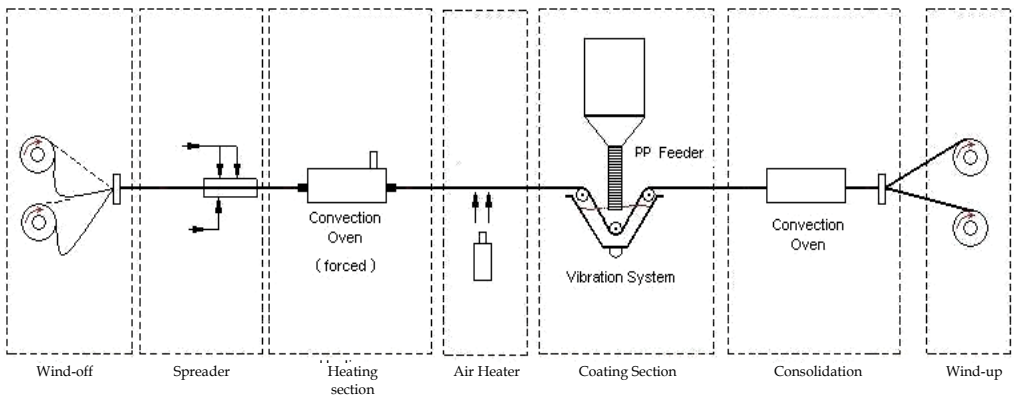

Fig. 1. Schematic diagram of the powder-coating line set-up

The photograph depicted in Figure 2 shows a general overview of the developed powder coating equipment.

2.2 Raw materials

2400 Tex type E glass fibre rovings, from Owens Corning, polypropylene, from ICO Polymers France (Icorene 9184B P), and polyvinyl chloride, supplied by CIRES (PVC - PREVINIL AG 736), powders were used to produce GF/PP and GF/PVC towpregs to be applied in common composite engineering parts. Table 1 summarises the most relevant properties of these materials.

Property	Units	Glass fibres	Polypropylene	PVC
Density	Mg/m^3	2.56	0.91	1.4
Tensile strength	MPa	3500	30	55
Tensile modulus	GPa	76	1.3	3.0
Average powder particle size	μm	-	440	150
Linear roving weight	Tex	2400	-	-

Table 1. Properties of raw materials used in towpregs for common applications

Fig. 2. Powder coating equipment

A new polymer developed by Solvay Advanced Polymers (Primospire® PR 120) and carbon fibre tows from TORAYCA (760 Tex M30SC) were used to produce towpregs for highly demanding markets. Table 2 presents the most relevant properties determined on these raw materials.

Property	Units	Carbon fibres	Primospire®
Density	Mg/m^3	1.73	1.21
Tensile strength	MPa	2833	104.3
Tensile modulus	GPa	200	8.0
Average powder particle size	μm	-	139.4
Linear roving weight	Tex	760	-

Table 2. Properties of the raw materials used in towpregs for advanced applications

This new polymer was also characterised in terms of other relevant properties, such as thermal, reheological and flame and smoke characteristics. The glass transition temperature (Tg) of the polymer was determined, by using a Diamond Pyris Perkin Elmer DSC, as 158.0 which is the value supplied by it manufacturer (158.0 ºC).

The rheological characteristics of the Primospire® PR 120 were determined in oscillatory regimen using a parallel plate rheometer TA Instruments Weissenberg. The dependence of the elastic and dissipative modulli with the oscillatory frequency was obtained at 3 different

temperatures: 320 ºC, 330 ºC and 340 ºC. Polymer discs with 25 mm of diameter produced by compression moulding were used in these tests. The Cox-Merz rule was used to establish the relation between the dynamic viscosity (function of the angular frequency) and the shear viscosity (function of the shear rate).
Figures 3 and 4 show the results obtained for the dependence of the viscosity on shear rate values at different temperatures using linear and logarithm scales, respectively.

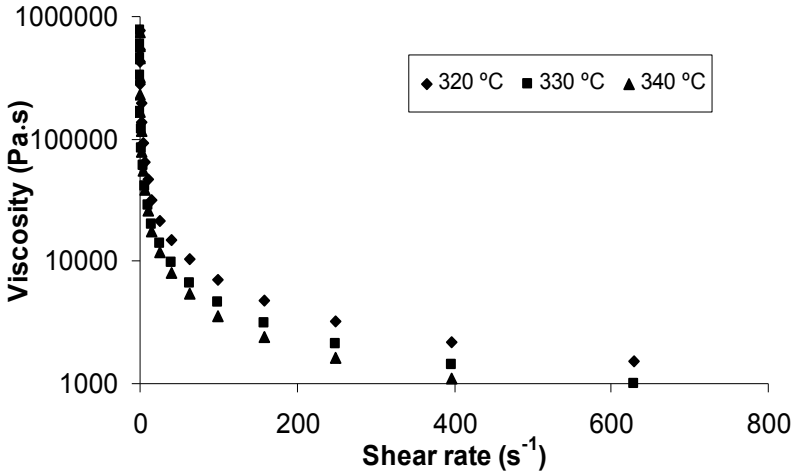

Fig. 3. Dependence of the Primospire® viscosity on shear rate at different temperatures

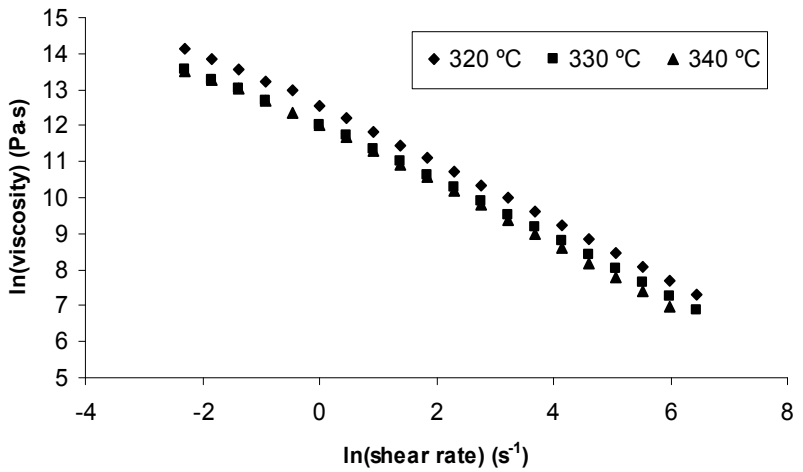

Fig. 4. Dependence of the viscosity on shear rate at different temperatures in a ln-ln scale

To obtain the flame and smoke characteristics of the Primospire® tests were carried out, according to ASTM E 1354:2004, in a cone calorimeter using a constant external heat flux of 50 kW/m² and an exhaust duct flow rate 0.025 m³/s. Heated compression moulded square plates with approximately 100 x 100 x 4 (mm) and 50g of weight were horizontally tested.
Table 3 summarises the results obtained in the cone calorimeter tests.

Property	Units	Value		
Time to ignition	s	163		
Total heat	kJ	574		
Mass loss	g	21.8		
	%	44.1		
		Peak	**Time** (s)	**Average**
Heat release rate	kW/m²	119.4	265	34.7
Effective heat of combustion	MJ/kg	45	370	26.3
Specific extinction area	m²/kg	242.6	190	102.5
Carbon monoxide	kg/kg	0.6438	1740	0.2722
Carbon dioxide	kg/kg	1.54	310	0.78

Table 3. Cone calorimeter results (ASTM E 1354)

Table 4 compares the obtained Primospire PR120 fire characteristics with those of other current polymers and composites. As can be seen, the study material seems to exhibit excellent fire characteristics.

	MATERIAL	Time to ignition (s)	Heat release rate peak (kW/m²)	Effective Heat of Combustion (MJ/kg)	Total heat release (MJ/m²)	Residue (%)
Thermo-plastics	Primospire PR 120	163	119.4	26.3	57.4	55.9
	HDPE a)	71	2021	43.8	-	-
	PC a)	125	725	19.5	-	-
	PA a)	86	1489	29.7	-	-
	POM a)	37	571	13.6	-	-
Thermo-settings b)	PF (phenol/ formaldehyde= 1:2)	102	174	-	23	76.6
	PF (phenol/ formaldehyde= 2:1)	59	79	-	5	95.1
Composites c)	Graphite/ phenolic (1103)	104	177	-	50	72
	Graphite/ PPS (1085)	173	94	-	26	84
	Graphite/ Epoxy (1093)	94	171	-	-	76
	Graphite/ PEEK (1086)	307	14	-	3	98

Notes: a) (Panagiotou 2004); b) (Nyden et al. 1994); c) (Sorathia & Beck 1995)]

Table 4. Fire properties of current polymers and composites

2.3 Optimising the processing conditions of the towpregs

Figure 5 shows the polymer mass fraction of the glass fibre reinforced polypropylene (GF/PP) towpregs by varying the coating line oven temperature at different fibre pull-speeds. The polymer fractions were determined by cutting and weighting 1 m length of the towpreg strips produced in the coating line.

As expected, the polymer mass fraction decreased with increasing fibre pull-speed, maxima polymer depositions being obtained for oven temperatures range between 400 ºC and 450 ºC.

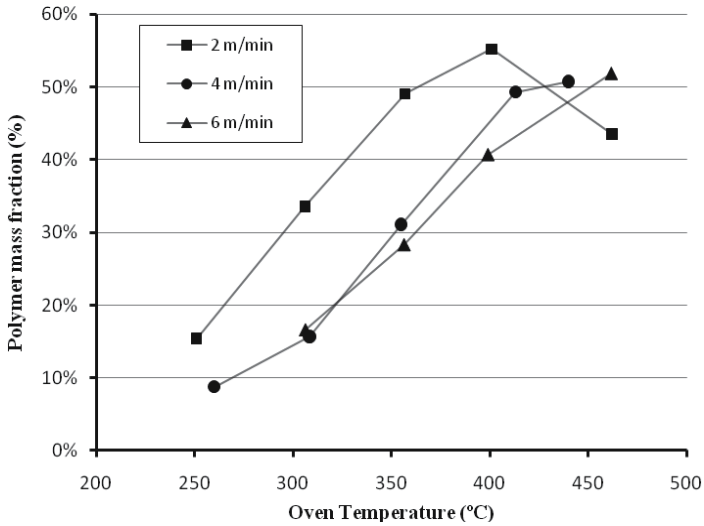

Fig. 5. Variation of the polymer mass fraction with oven temperature and fibre pull-speed

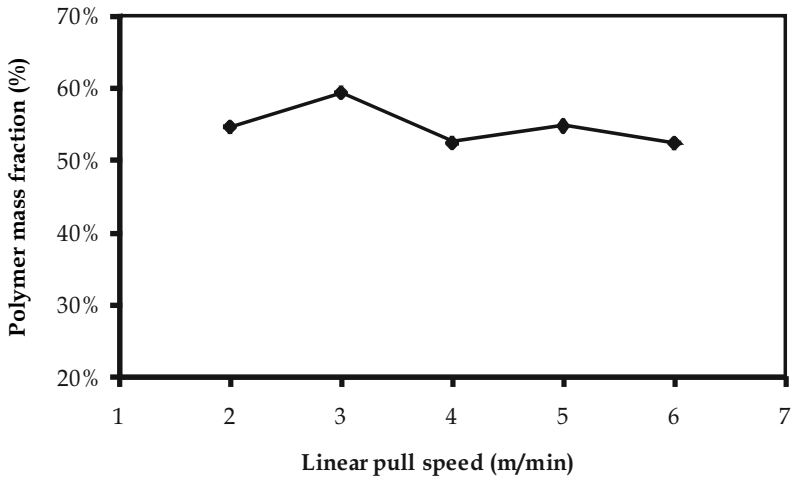

Fig. 6. Influence of production speed on the polymer content of the GF/PVC towpregs

Figure 6 presents the same type of results for the glass fibre reinforced polyvinyl chloride (GF/PVC) towpregs produced in the coating line using oven temperatures in the range between 260 ºC and 315 ºC. In this case, it was observed that only in such small range gap of temperatures it was possible to produce enough good GF/PVC towpregs. A deep decrease in the amount of polymer was verified when lower oven temperatures were used and considerably polymer degradation (great changes in PVC colour) was observed at higher oven temperatures.

As it may be seen, a good and almost constant level of PVC mass content was obtained by using fibre pull-speeds between 2.0 and 6.0 m/min.
Figures 7 to 9 show the variation of the polymer mass fraction in the Primospire®/Carbon towpregs with fibre pull speeds at three constant oven temperatures. It may be concluded that the polymer mass fraction decreases with the fibre pull speed at the lower oven temperature (600 °C). At the higher oven temperatures, the amount of polymer in the towpregs seems to keep an approximately constant value of 40% at all fibre pull speeds.

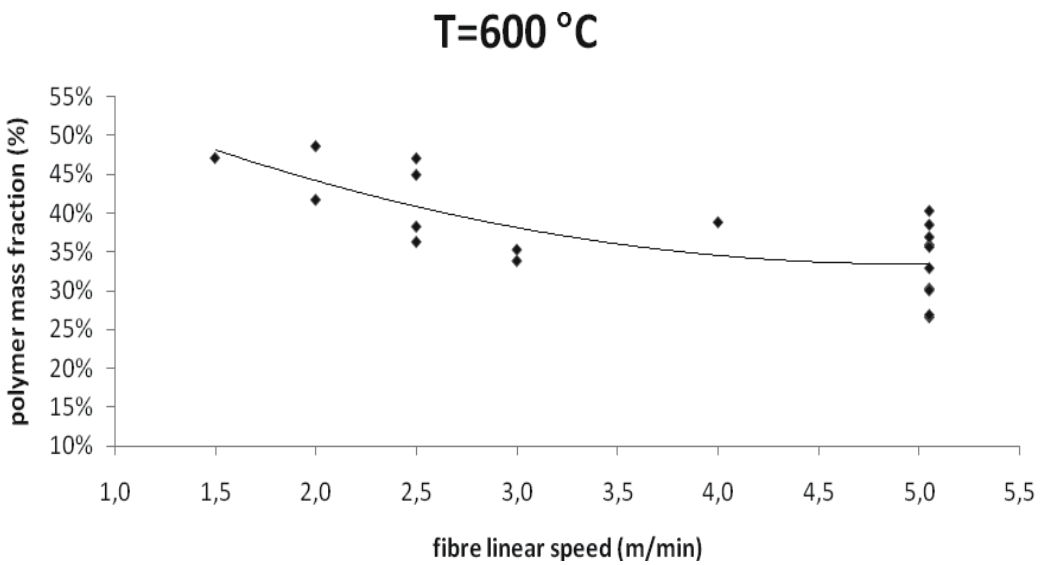

Fig. 7. Polymer mass fraction variation with fibre pull speed for 600 °C oven temperature

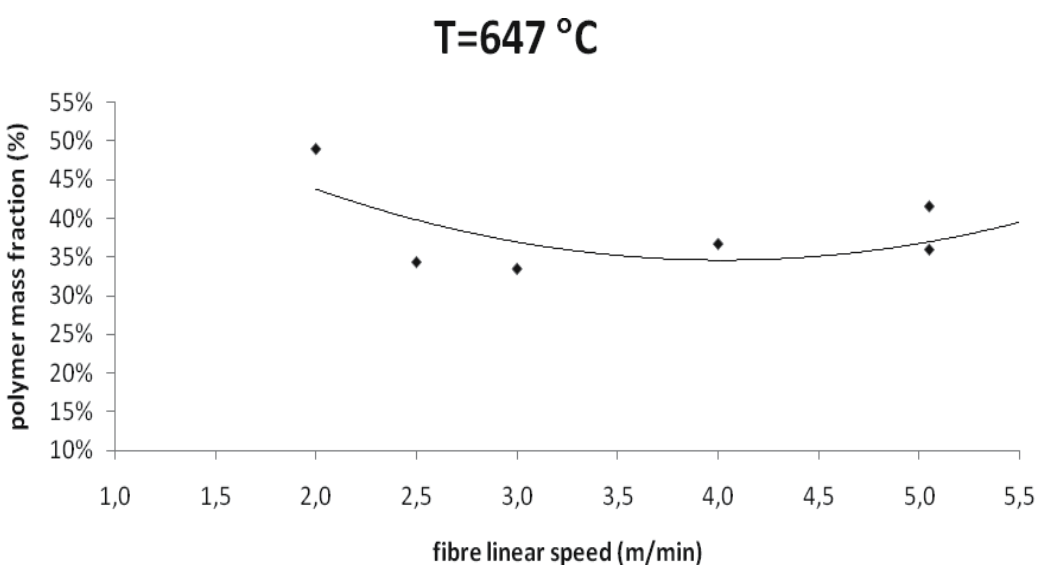

Fig. 8. Polymer mass fraction variation with fibre pull speed for 647 °C oven temperature

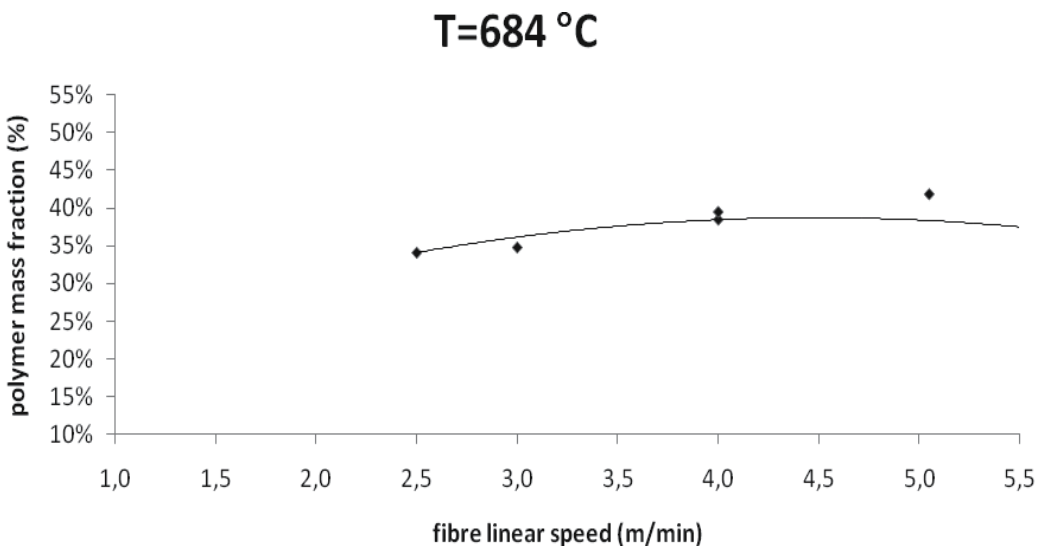

Fig. 9. Polymer mass fraction variation with fibre pull speed for 684 ºC oven temperature

2.4 Characterization of towpregs by SEM

Several samples of the GF/PP towpregs were analysed under a Nova NanoSEM 200 scanning electron microscope to evaluate the polymer powder distribution and its adhesion to the fibres. Figure 10 shows a SEM micrograph of a towpreg sample produced in the dry coating line using an oven temperature around 400 ºC and a fibre pull-speed of 4 m/min.
As it may be seen in Figure 10, at these optimised coating line operating conditions a good polymer melting and adhesion to glass fibres seems to have been achieved.

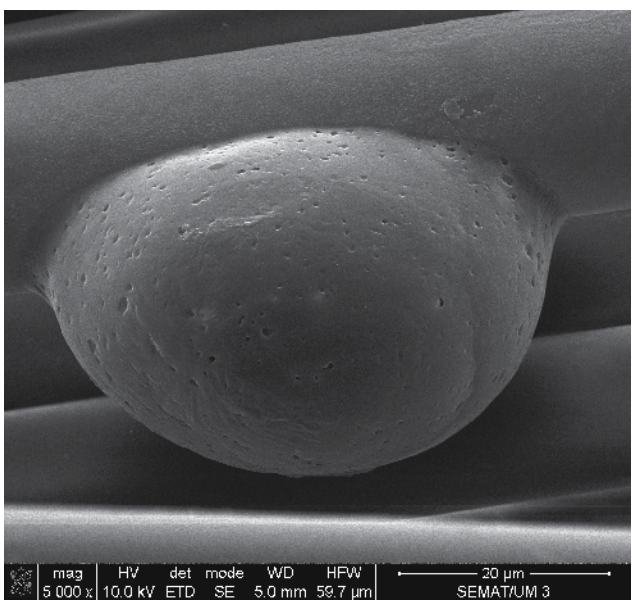

Fig. 10. SEM micrograph of GF/PP towpreg (magnification of 5000×)

A Leica S360 scanning electron microscope was also used to observe the typical aspect of the GF/PVC towpregs. As it is shown in the SEM micrograph depicted in Figure 11, a good adhesion was also obtained between PVC particles and glass filaments in the samples processed at the optimised oven temperatures from 260 ºC to 315 ºC.

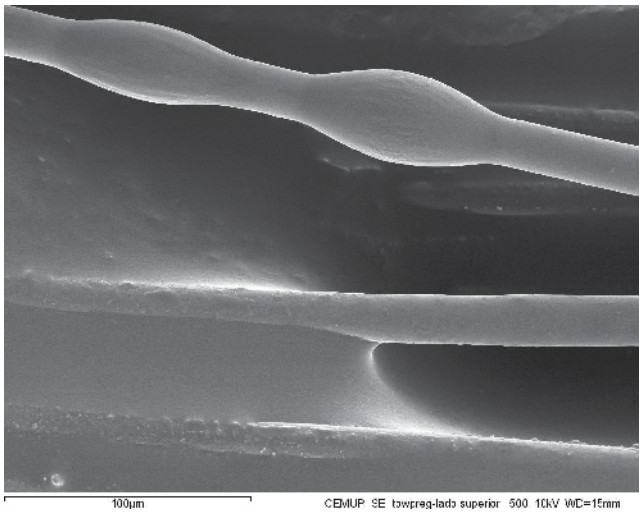

Fig. 11. SEM micrograph of GF/PVC towpreg (magnification of 1000×)

The same Leica S360 scanning electron microscope equipment was used to evaluate the polymer powder distribution and its adhesion to the fibres in several Primospire®/carbon towpreg samples. Figure 12 shows two representative SEM micrographs of samples produced using an optimised 650ºC oven temperature in the dry coating equipment.
As can be seen, in the case of this highly demanding market towpregs most of the polymer particles exhibit bigger sizes than the fibre diameter and, even after heating, polymer particles present an irregular shape. It is also possible to observe a enough good degree of adhesion between fibres and polymer powder.

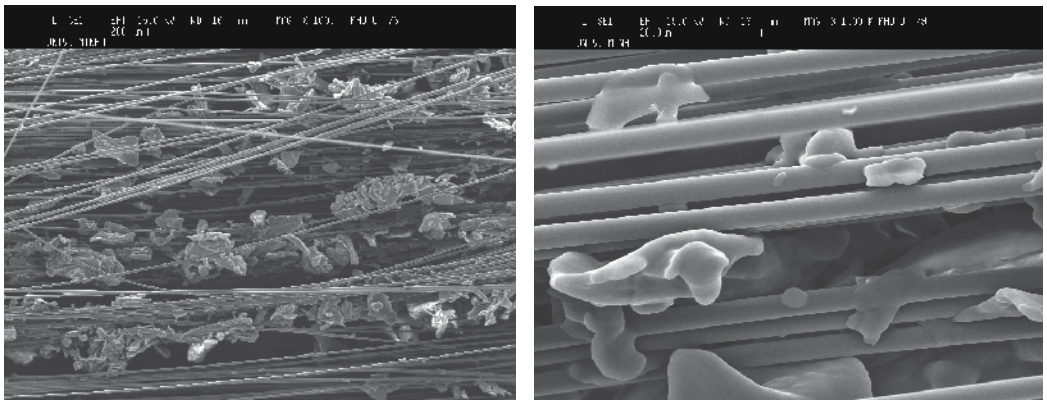

a) Magnification: 100× b) Magnification: 1000×

Fig. 12. Micrographs of Primospire®/carbon towpreg under SEM

2.5 Composite processing technologies

2.5.1 Compression moulding

SATIM and MOORE hot plate presses with capacity of 400 kN were used to process the produced towpregs into composite plates by compression moulding using a technique described elsewhere (Klett et al. 1992). First, the towpregs were wound over a plate with appropriate dimensions and the resultant pre-form then conveniently placed in the cavity of a heated mould. After that, the press is closed, to obtain the desired pressure during the consolidation time. Then, the mould is cooled down to room temperature and, finally, the laminate composite plates are removed. Table 5 summarizes the compression moulding cycle parameters.

Composite	Temperature (°C)	Pressure (MPa)	Consolidation time (min)
GF/PP	250	20	15
GF/PVC	210	15	15
CF/Primospire®	320	20	30

Table 5. Compression moulding cycle parameters

In the case of CF/Primospire towpregs, plain woven fabrics were also produced from towpreg tows using a manual weaving loom. This pre-preg material has shown to be easier to process by compression moulding than unidirectional pre-forms.

2.5.2 Filament winding

Figure 13 depicts schematically the filament winding system developed to produce GF/PP pipes and plates from towpregs. This system was tested with a laboratory CNC 6 axes conventional PULTREX filament winding machine. The equipment consists on a pre-heating furnace, a hot-air heater and a pneumatic controlled consolidation roll.

Before being wound onto the mandrel, the GF/PP towpregs are guided, at controlled and constant tension, through the pre-heating furnace at the desired temperature. Final consolidation is achieved in the mandrel, at a required pressure, using a consolidation head,

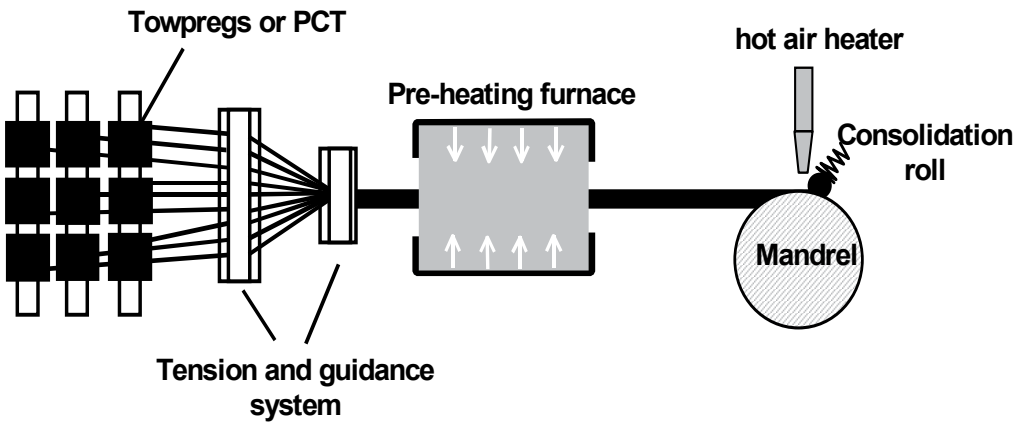

Fig. 13. Schematic representation of the filament winding system

assisted by a hot-air heater. A thermocouple allows the temperature to be adjusted during the consolidation.
GF/PP pipes with dimensions of ∅ 80×2 (mm) were produced using the typical filament winding conditions presented in Table 6.

Variable		Units	Value
Mandrel rotational speed		rpm	5-30
Temperature	Pre-heating Air heater	°C	200 300-350
Consolidation force		N	80-100
Tow tension		N	10

Table 6. Typical filament winding parameters

In the case of GF/PVC ∅ 80×3 (mm) filament wound pipes were produced by using a conventional wet fibre impregnation route. A low viscosity vinyl chloride homopolymer past obtained from an emulsion polymerization was used. By using this PVC type, it was only necessary to incorporate a heating system in the conventional filament winding machine eye-feed mechanism to process good quality continuous fibre reinforced pipes.

2.5.3 Pultrusion

A pultrusion head was used mounted on a conventional 60 kN pultrusion line. This head allowed the adaptation of the line, designed for thermoset matrix composites, to the production of continuous profiles made from thermoplastic matrix towpregs. The concept for the pultrusion head, as shown in Figure 14, includes three main parts: i) the pre-heating furnace; ii) the pressurization and consolidation die and, iii) the cooling die.

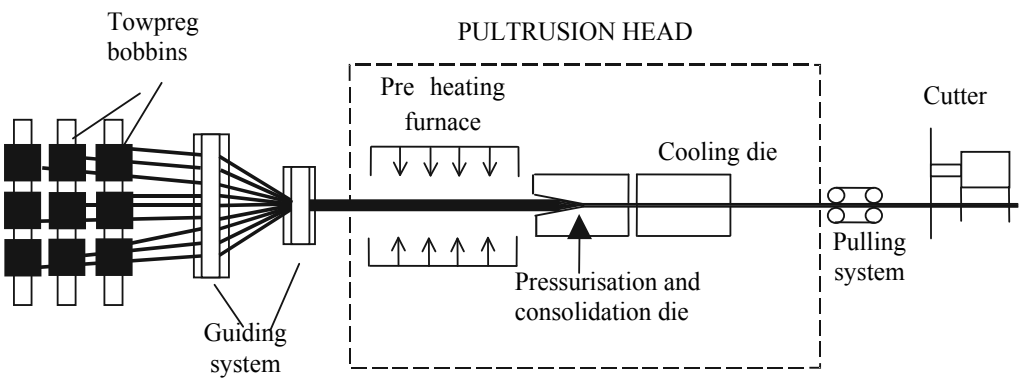

Fig. 14. Schematic diagram of the pultrusion line

The process involves three phases. First, the GF/PP towpregs are guided into the pre-heating furnace. Then, they pass through the first part of the pultrusion head where the consolidation occurs. The consolidated material then enters the cooling die where it cools down to a required temperature. Finally, after leaving the pultrusion head, the profile is cut to specified lengths. Table 7 reports the operating conditions typically used in tests with the pultrusion line.

Variable	Units	Value
Pultrusion pull speed	m/min	0.5-0.8
Pre-heating furnace temperature	°C	200-250
Die temperature	°C	300-320
Cooling die temperature	°C	60

Table 7. Typical pultrusion operating conditions

GF/PP U-shape profiles with 24 × 4 mm² cross-section, 2 mm thick were fabricated, with well-defined forms and smooth surfaces.

2.6 Final composites mechanical properties

The fibre mass fraction, flexural and tensile properties of the continuous fibre reinforced composites fabricated by the different technologies were determined in accordance to ISO 1172, ISO 178 and EN 60, respectively. The split disk test method according to ASTM 2290 was employed to determine the circumferential strength and modulus on the filament winding pipes.

Table 8 summarises the final results obtained for CF/Primospire® composite specimens. The theoretical values presented in this Table were calculated from the raw materials properties by using the rule of mixtures (ROM).

Property		Units	Determined Values	
			Average	Stand. Dev.
Flexural modulus (Unidirectional composite)	Experimental	GPa	30.0	5.0
	Theoretical		103.8	
Flexural modulus (woven fabrics)	Experimental		26.8	2.2
	Theoretical		53.8	
Flexural strength (Unidirectional composite)	Experimental	MPa	124.3	15.0
	Theoretical		867.0	
Flexural strength (woven fabrics)	Experimental		160	56
	Theoretical		459.0	
Fibre mass fraction	Experimental	%	59.7	0.3
Fibre volume fraction	Calculated		51	

Table 8. Flexural properties of composites made from CF/Primospire® towpregs

As can be seen, the composites manufactured from the woven fabrics presented mechanical properties in better agreement with the theoretical expected ones than those reinforced with unidirectional fibres. The major causes for the differences found in these mechanical tests between the experimental and theoretical flexural stiffness and strength values have been attributed to a low fibre/matrix adhesion and also to fibre misalignments observed in the composite plates.

Figure 15 and 16 show the results from tensile and flexural tests, respectively, obtained from GF/PP towpregs produced in the coating line with different parameters and processed by compression moulding.

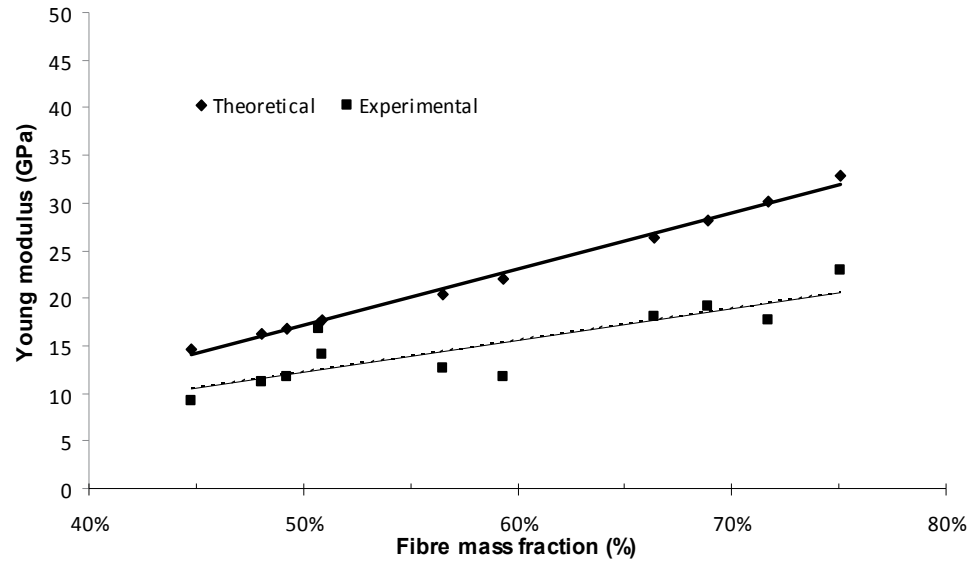

Fig. 15. Tensile test results from compression moulded GF/PP towpregs

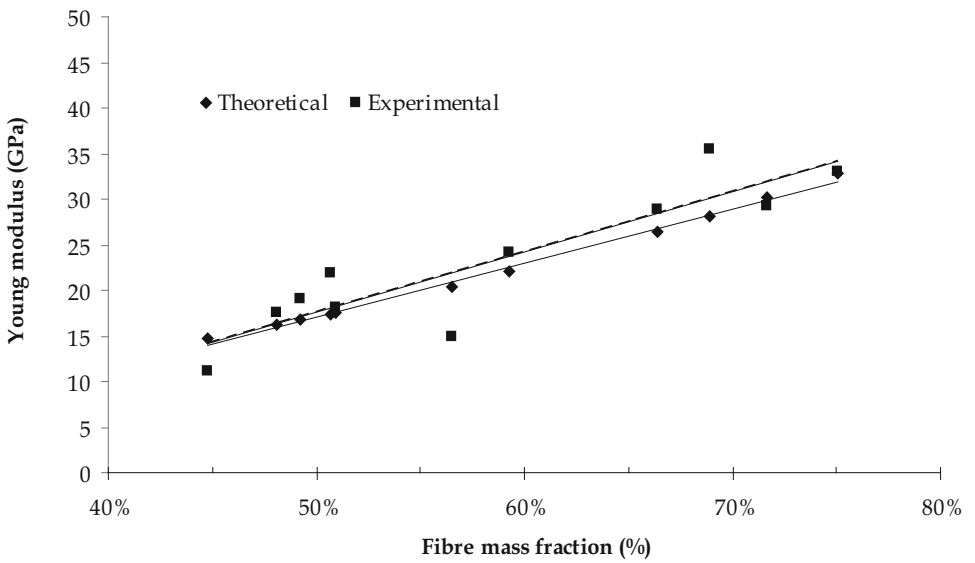

Fig. 16. Flexural test results from compression moulded GF/PP towpregs

As can be seen from the previous figures, the experimental results for the Young modulus are in accordance with the theoretical expected ones. Also, as expected, the value of that mechanical property increases with the fibre mass fraction.

The average (Av.) and standard deviation (SD) of all results from GF/PP towpregs consolidated by pultrusion or filament winding are summarised in Table 9.

As can be seen from Table 9, experimental strength results lower than the theoretical ones were obtained. In any case, such strength results seem to be compatible with the major

commercial applications expected for GF/PP composites. However, the experimentally obtained modulli results present good agreement with the theoretical ones.

Production technique	Kind of Data	Properties											
		Tensile strength (MPa)		Tensile modulus (GPa)		Flexural strength (MPa)		Flexural modulus (GPa)		Fibre mass fraction (%)		Fibre volume fraction (%)	
		Av.	SD	Av.	SD	Av.	ST	Av.	SD	Av.	SD	Av.	SD
Pultrusion	Determined	305	26	29.9	3.5	>117	4.3	22.5	0.3	78.4	1.4	56.2	2.8
	Theoretical	661.6	219	35.6	7.4	661.6	219	35.6	7.4				
Filament winding	Determined	431.0	37.6	31.0	2.8	-	-	-	-	80.2	1.5	59.0	2.8
	Theoretical	693.7	229	37.3	7.7	-	-	-	-				

Table 9. Mechanical properties of GF/PP composites

Tables 10 summarizes the experimental mechanical properties obtained on GF/PVC compression moulded plates and compares them with the theoretical ones predicted by the Classical Lamination Theory (CLT), by using the rule of mixtures and the raw materials properties shown in Table 1.

Property		Units	Determined values GF/PVC plates	
			Average	St. dev.
Flexural strength	Experimental	MPa	62.2	6.9
	theoretical		500.0	
Flexural modulus	Experimental	GPa	17.6	0.9
	Theoretical		26.7	
Fibre fraction	Mass	%	57.7	1.1
	Volume		42.7	

Table 10. Properties of composite plates made from towpreg

As may be seen, the composite flexural strength value is considerably lower than the theoretically expected one. This could be attributed, at least partially, to fiber misalignments found in the composite plates and fiber/polymer adhesion losses. In spite of the lower than expected flexural modulus values obtained, they may be considered sufficiently high to allow composites being applied in almost all commercial engineering applications.

Each GF/PVC pipe, produced by using the conventional wet fibre impregnation route previously described in the paragraph 2.5.2, was also tested in order to determine the circumferential tensile strength and fiber mass content accordingly to ASTM 2290 and EN 60, respectively.

For evaluating the consolidation quality, specimens with dimensions of $10 \times 7 \times 4$ mm^3 were also cut from the filament wound pipes and submitted to interlaminar shear tests using a testing device based on the one described elsewhere (Lauke et al. 1992 & Nunes et al. 2005b).

After mounting this device in an universal INSTRON 4505 testing machine, simple supported specimens were submitted to shear tests using a cross-head speed of 1 mm/min.
Table 11 shows the experimental results obtained. Such results are also compared with the CLT theoretical predictions calculated in the above referred conditions. As may be seen, the strengths obtained in the GF/PVC filament wound pipes present a good approximation to the calculated theoretical values.

Property		**Units**	**Determined values GF/PVC pipes**	
			Average	St. dev.
Tensile strength	Experimental	MPa	114.7	9.5
	theoretical		236.3	
Interlaminar shear strength	Experimental	MPa	1.7	0.1
Fibre fraction	Mass	%	31.7	2.1
	Volume		20.2	

Table 11. Properties of composite pipes made from PVC paste

3. Applications of thermoplastic matrix towpregs

Figures 17 to 22 show different applications successfully developed using the thermoplastic towpregs produced in this work. Figure 17 and 18 show a GF/PP pressure vessel with capacity of 0,06 m^3 for incompressible fluids able to withstand an internal burst pressure up to 40 bar and a GF/PVC pipe having an internal diameter of 80 mm, respectively.

Fig. 17. Filament wound GF/PP pressure vessel processed from towpregs

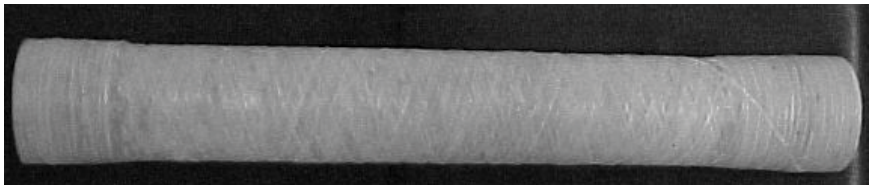

Fig. 18. Filament wound GF/PVC pipe

Figures 19 and 20 show a U-shaped $24 \times 4 \times 2$ (mm) GF/PP profile obtained by using the towpreg pultrusion and LFT compression moulded plates also processed from GF/PP towpregs. Such plates were stamped using cut towpregs mixed together at low shear stress to avoid fibre breakage.

Fig. 19. U-Shape GF/PP pultruded profile made from towpregs

Fig. 20. GF/PP LFT plates made from towpregs

Finally, a woven fabric manufactured from CF/Primospire® towpregs and suitable to be processed into a composite part by compression moulding is shown in Figure 21.

Fig. 21. Primospire/carbon woven fabric

4. Conclusions

The new powder-coating equipment has shown to be suitable to produce towpregs adequate for common and advanced engineering markets. From the tests made, it was found that all of those different towpregs can be easily and continuously produced at industrial production speeds between 2 a 6 m/min.

For common engineering markets glass fibre reinforced polypropylene and polyvinyl chloride matrix were studied. For these materials the optimised processing oven temperatures were in the ranges of 400ºC to 450ºC and 260ºC to 315ºC respectively.

Carbon fibre reinforced Primospire® towpregs were also studied envisaging possible applications in advanced composite structural markets. In such case, the optimised processing oven window was found to be located a much higher temperature range from 640 ºC to 690 ºC.

The mechanical properties of the composites processed from these towpregs by major different processing technologies were also found to be adequate either for structural as for common engineering applications.

This work also demonstrated the large potential of polymer powder deposition techniques to fabricate continuous fibre thermoplastic matrix towpregs that can be easily processed into composites with adequate engineering properties. By using efficient processing technologies different composite parts were already manufactured with success.

5. Acknowledgment

Authors wish to acknowledge the European Space Agency (ESA) for the financial support given to the present work through the project contract ESTEC/16813/0/NL/PA-ccn3.

6. References

Brandt, J., Drechsler, K. and Richter, H. (1993). The Use of High-Performance Thermoplastic Composites for Structural Aerospace Applications, *9th Int. Conf. on Composite Materials (ICCM-9), Vol. 6,* pp. 143-150, Madrid, Spain, July 1993.

Klett, J. W., Albiger, J., Edie, D. D. and Lickfield, G. C. (1992). Production and Evaluation of a Polyimide/Carbon Fibre Powder-Coated Towpreg, *Proceedings of the Seventh Inter. Conference on Carbon, Carbon '92,* p. 683, Essen, Germany, June 1992.

Lauke, B., Schneider, K and Friedrich, K. (1992). Interlaminar shear Measurement of Thin Composite Rings Fabricated by Filament Winding, *Proceedings of ECCM 5*, Bordeaux, France, pp. 313-318, April 1992.

Nunes, J. P., van Hattum, F.W. J., Bernardo, C. A., Brito, A. M., Pouzada, A. S., Silva, J. F. e Marques, A. T. (2005a). Part III: Chapter 11- Production of Thermoplastic Towpregs and Towpreg-based Composites, In: *Polymer Composites – From Nano- to Macro-Scale*, Eds K. Friedrich, S. Fakirov and Z. Zhang, pp. 189-214, Springer Science+Business Media, Inc., New York/USA.

Nunes, J. P, Silva, J. F., Marques, A. T.(2005b). Using Additives to Improve the Properties of Composites Made from Towpregs, *Proceedings of the ANTEC'05*, Boston/Massachusetts, USA, May 2005.

Nunes, J. P., Silva, J. F., Velosa, J. C., Bernardo, C. A. and Marques, A. T. (2008). Production of New Thermoplastic Matrix Composites For High Demanding Applications, *13th European Conference on Composite Materials –ECCM 13*, Stockholm, Sweden, June 2008.

Nunes, J. P., Silva, J. F., Velosa, J. C., Bernardo, C. A. and Marques, A. T. (2009). New Thermoplastic Composites for Demanding Applications. *Plastics, Rubber & Composites: Macromolecular Engineering*, Vol. 38: 2/3/4, pp. 167-172.

Nunes, J. P., Amorim, L., Velosa, J. C. and Silva, J. F. (2010). Optimizing the Continuous Dry Impregnation of Thermoplastic Matrix Fiber Reinforced Materials, *14th European Conference on Composite Materials – ECCM 14*, Budapest, Hungary, June 2010.

Nyden, M. R., Brown, J. E. and Lomakin, S. M. (1994). Chapter 16: Flammability Properties of Honeycomb Composites and Phenol–Formaldehyde Resins, In: *Fire and Polymers II: Materials and Test for Hazard Prevention*, ACS Symposium Series 599, American Chemical Society, Washington, DC, USA.

Panagiotou, J. (2004). *A Methodology for Flammability Diagrams*, MSc Thesis, University of Maryland..

Silva, J. F., Nunes, J. P., Vieira. P. and Marques, A. T. (2008). GF/PP Towpregs Production Testing and Processing. *Int. Journal Mec. Maters Des. 4*, pp. 205-211.

Silva, J. F., Nunes, J. P. and Bernardo, C. A. (2010). Determining the Final Properties of Thermoplastic Matrix Composites Produced from Towpregs, *14th European Conference on Composite Materials – ECCM 14*, Budapest, Hungary, June 2010.

Silva, R. F., Silva, J. F., Nunes, J. P., Bernardo, C. A. and Marques, A. T. (2008). New Powder Coating Equipment to Produce Continuous Fibre Thermoplastic Matrix Towpregs, in "Materials Science Forum", Trans Tech Publications, Vol. 587-588, pp. 246-250.

Sorathia, U. and Beck, C. (1995) Chapter 6: Fire-Screening Results of Polymers and Composites. In: *Improved Fire- and Smoke-Resistant Materials for Commercial Aircraft Interiors: A Proceedings*, pp. 93-114, National Materials Advisory Board, USA.

Velosa, J. C., Nunes, J. P. , Antunes, P. J., Silva, J. F. and Marques, A. T. (2009) Development of a New Generation of Filament Wound Composites Pressure Cylinders. *Composites Science and Technology*, 69:; pp. 1348-1353.

13

Wood Plastic Composites

El-Haggar, Salah M. and Kamel, Mokhtar A.
The American University in Cairo
Egypt

1. Introduction

Plastic and wood wastes have been a main environmental concern. Plastic is the biggest problem due to its high amount of waste generated, non biodegradability and the fastest depletion of natural resources regarding its short life cycle, therefore increased amount of material utilized in its production, and waste generated. The same applies to wood with lesser degree where it is depleting trees and forests and the wastes mainly are either burned or disposed; resulting in extra consumption, depletion, and pollution of nature. Several worldwide attempts have been adopted; especially in the developed countries, to take advantage of these types of waste especially with the raised need for alternatives to virgin materials (Winandy, et al. 2004). Wood plastic composite (WPC) is a product which could be obtained from plastic and wood. WPC is a composite with a rapid growing usage consisting of a mixture of wood waste and polymeric material (Soury, et al. 2009). Many trials of obtaining a WPC product were basically built on the concept of a Cradle to Cradle approach where the material is recycled at the end of its life cycle to produce a Cradle (new) product and thus close the loop and imitate the natural ecosystem (McDonough and Braungart 2002) & (El-Haggar 2007). As a consequence, this minimizes the solid waste content and conserve the natural resources. Therefore, costs, energy, and depletion of virgin materials are reduced. In addition, it assures the sustainability over the incoming years for future generations' use (Youngquist, et al. 1992).

WPC has become currently an important address of research that gained popularity over the last decade especially with its properties and advantages that attracted researchers such as: high durability, Low maintenance, acceptable relative strength and stiffness, fewer prices relative to other competing materials, and the fact that it is a natural resource (Bengtsson and Oksman 2006) & (Winandy, et al. 2004). Other advantages have been strength points including (Wechsler and Hiziroglu 2007): the resistance in opposition to biological deterioration especially for outdoor applications where untreated timber products are not suitable, the high availability of fine particles of wood waste is a main point of attraction which guarantees sustainability, improved thermal and creep performance relative to unfilled plastics where It can be produced to obtain structural building applications including: profiles, sheathings, decking, roof tiles, and window trims.

On the other hand, WPCs are not nearly as stiff as solid wood; however, they are stiffer than unfilled plastics. In addition, they do not require special fasteners or design changes in application as they perform like conventional wood (Clemons and Caufield 2005).

As mentioned, the reasons for using WPC are many; however, there are other causes that enforced many countries to tend for using alternative sources to virgin materials. In the United States, for example, the U.S. Environmental Protection Agency, by the beginning of 2004, has phased out the usage of wood treated with chemicals such as the chromated copper arsenate (CCA) to prevent environmental and microbial degradation (Yeh and Gupta 2008). As this type of wood was used in the building products' market concerned with residential applications such as decking, the need for the alternative survived the WPC market (Yeh and Gupta 2008). In Europe, environmental concerns are focused on limiting the use of finite resources and the need to manage waste disposal; therefore, the tendency to recycle materials at the end of their useful life has increased tremendously (Yeh, et al. 2009). Recycling polymers in Europe was less preferred than other types of materials such as metal; however, illegality of land filling and waste management priority in many European countries were the motive to do so (Yeh, et al. 2009). In addition to the enforced environmental policies, the growth of environmental awareness led to a new orientation to use wasted natural materials for different applications and industries such as the automotive, packaging and construction industries (Yeh, et al. 2009).

2. Market potential

The awaiting market for WPC is huge due to the high production of plastics and wood which constitutes a significant amount of solid waste which is mostly disposed not recovered (Adhikary, et al. 2008). Najafi, et al. 2007, mentioned that WPC presents a promising raw material source for new value added products due to the large amount of daily waste generation and low cost (Najafi, et al. 2007). WPC commercial products are increasingly replacing many products in many applications especially the construction related ones (Yeh, et al. 2009). WPCs have gained an ever larger share; especially for decks and other outdoor structures (Youngquist, et al. 1992). Other production lines of fencing, roofing, and siding have started to get a noticeable market share (Winandy, et al. 2004). WPC usage is extensively spread especially in strips; where wood peel layers are tilted in the same direction, used in furniture industry (Augutis 2004). WPC is also used in producing panels where it is produced by mixing wood flour and plastics giving a material which can be processed similar to 100% plastic-based products (Wechsler and Hiziroglu 2007). Approximately one-half of all industrial materials used in the United States are wood-based; thus, the finding that the WPC market is increasing is not a surprise (Falk 1997). The growth of WPC decking in the U.S. has started from less than 1 % in mid-90's to over 10% today with growth projected by several studies to reach 20% before the end of 2010 (Winandy, et al. 2004). Two large sectors, the decking and fencing sector, the siding and roofing sector started to use the WPCs commercially in the U.S. (Winandy, et al. 2004). Concerning the decking and fencing in the U.S., a study was done in 2002 which showed that there were 1.4 million new houses constructed (for single families) and 0.3 million new houses for multi-families; where the house averaged about 215 m^2 made from wooden decks (Winandy, et al. 2004). Winandy, et al. 2004, concluded that all this huge amount of consumed wood could be substituted by WPC. The U.S. decking market alone uses a sum total of nearly 18.5 million m^3 of wood where 90% uses natural treated wood and 10% WPC (Winandy, et al. 2004). In addition, the U.S. fencing market was divided into 45% wood, 44% metal, 7% plastic and 5% other material (Winandy, et al. 2004). It was calculated at $US 2.6 billion in 2002 and was expected to grow approximately 5% per year and therefore a great potential of WPC domination was expected (Winandy, et al. 2004).

3. Applications

Advantages, desired properties, environmental regulations, and awareness have led to the substitution of using conventional woods with the WPC. Its production is growing over time due to its several applications (Adhikary, et al. 2008). Main motives include:

- It can be molded in any particular mold with a variety of shapes and angles, so it can give any desired design (Takatani, et al. 2007).
- It can be treated in the same manner as the conventional wood using the same cutting and sawing equipment (Winandy, et al. 2004).

Therefore, it is easy to use any conventional wood workshop with WPC products which have proven to give the same functionality as conventional wood in many areas (Wechslera and Hiziroglu 2009). Various WPC products are available in the US market substituting some of the conventional wood products such as outdoor deck floors (Winandy, et al. 2004). It is also used for railings, fences, landscaping timbers, siding, park benches, molding and trim, window and door frames, panels and indoor furniture (Winandy, et al. 2004).
In addition, Wood plastic composites can also substitute neat plastics in applications where the need for an increase in stiffness is an addition; where the wood fiber elasticity is almost 40 times higher than that of polyethylene and the overall strength is approximately 20 times greater (Bengtsson and Oksman 2006). It has also higher thermal and creep performance compared to plastics and thus could be used in many structural building applications (Wechslera and Hiziroglu 2009).
A high potential of using WPC in a large scale to produce pallets is raised by Soury, et al. 2009; whereas the amount of consumed wooden pallets is huge (400 million pallets) accounting for about 86% of all pallets sold worldwide. In addition, product degradation due to environmental factors, which is one of the main disadvantages of wood, made WPC as an best alternative option (Soury, et al. 2009).
WPC started to be utilized in siding market in 2003 based on studies done in 2002 that revealed that wood occupied about 17% of the materials share of the U.S. siding market (960 million square meters) (Winandy, et al. 2004). Therefore, a promising market was opened for WPC products which gave a promising performance over other materials such as aluminum and vinyl and similar to wood (Winandy, et al. 2004).

4. Material

4.1 Material utilized in WPC

Wood and plastics (virgin or recycled) with various types, grades, sizes, and conditions are the main materials utilized in WPC production. WPC is composed mainly from a plastic matrix reinforced with wood and other additives sometimes are added using the appropriate processing procedures. Several ingredients of WPC are found in literature. Najafi, et al. 2007, mentioned that WPC is a composite composed from a natural fiber/filler (such as kenaf fiber, wood flour, hemp, sisal etc.) which is mixed with a thermoplastic. They added that virgin thermoplastic materials (e.g. high and low density polyethylene (LDPE and HDPE), polypropylene (PP), polyvinyl chloride (PVC)) are commonly utilized. In addition, any recycled plastic which can melt and be processed in a temperature less than the degradation temperature of the wood filler (200 C) could be used to produce WPC (Najafi, et al. 2007). Morton and Rossi 2003, said that the huge majority of WPC utilizes polyethylene and they classified the types of plastic used in WPC as follow: polyethylene

(83%), polyvinyl chloride (9%), polypropylene (7%), others (1%) (Morton and Rossi 2003). Clemons and Caufield added that wood flour is obtained from wood wasted from wood processors. They said also that it should be from high quality and free of bark, dirt, and other foreign matter. Moreover, species are mainly selected based on regional availability of high quality flour and color. Pine, oak, and maple are the most common used in the United States (Clemons and Caufield 2005). Adhikary, et al. 2008, used recycled and virgin high density polyethylene (HDPE) with wood flour (Pinus radiata) as filler. The HDPE utilized was obtained from a plastics recycling plant and sawdust was collected from a local sawmill (Adhikary, et al. 2008).

4.2 Advantage of WPC ingredients over other materials

The fact that WPC ingredients are mainly composed from wood and plastic has led to the rapid worldwide growth of its production due to the high availability of non-utilized plastic and wood wastes. Dividing the subject into two main sub-subjects, the plastic waste has the highest contribution regarding its huge available quantities which gives a strong advantage to WPC. The market potential regarding the usage of plastic waste into other utilizations is huge due to the high amounts of its disposition which constitutes the largest share of the global municipal and industrial solid waste. Kikuchi, et al. 2008, mentioned that the plastic waste constitutes more than 60% of the total MSW, 22% was recovered and 78% disposed (Kikuchi, et al. 2008). In United States, the waste of plastics; in 2005, was calculated as 11.8% of the 246 million tons of MSW generated (USEPA 2006). In India, Plastic in municipal solid waste makes up to 9–12% by weight of the total in addition to other wastes which may contain much higher proportions of plastics (Panda et al. 2010). The majority of the plastic wastes generated are disposed (Kikuchi, et al. 2008). However, the continuous growth of worldwide plastic consumption due to its short life cycle compared to other products; roughly 40% have duration of life cycle smaller than 1 month, and the legislations of many countries concerned with minimizing landfills content and incinerators have led to a necessity of recovering plastic waste instead of disposing (Kikuchi, et al. 2008) & (Panda et al. 2010). Incineration and land filling alternatives were rejected by several countries due to their potential danger to the environment either by polluting air or land; which results in not closing the loop of Cradle to Cradle and therefore depleting natural resources. As a consequence, the tendency towards recycling has increased (Jayaraman and Bhattacharyya 2004). Some attempts for plastic recovery resulted during 2004 in a recovery of almost 8.25 million tons (39% of total amount of plastics consumed) in Western Europe; 35,000 tons (13.48% of total imported virgin plastics) in New Zealand (Adhikary, et al. 2008). While in 2005, the United States recycled around 5.7% of the total plastics generated (USEPA 2006). On the other hand, some states in the US like Michigan have a recycling rate that is close to 100% (Beg and Pickering 2008). In Brazil, some potential in recycling have been raised where around 15% of all plastics consumed are recycled and returned to industry (Beg and Pickering 2008).

Therefore, the tendency towards recycling plastic instead of other options made it better for the sake of WPC production increase in the future. On the other hand, wood waste has a significant contribution to the total amount of waste especially that it comes from various commercial, industrial, and residential activities; which could include scrap lumbers, pallets, sawdust, tree stumps, branches, twigs, wooden crates and pallets, building construction and demolition, furniture manufacturing, and many others. In addition, it is one of the main

environmental concerns stated by many countries. In the United States, a report that was written in 1995 by CIWMB (California Integrated Waste Management Board) tells that severe problems concerned with landfill disposing were revealed (CIWMB 1995). It tells that the construction and demolition of buildings; which are mainly wood waste, generates almost twelve percent of all solid waste in California. Furthermore, the average fee for disposing of a ton of waste in a California landfill is about $30 to $35, but disposing of a ton of wood at a wood processing facility may only cost $10. In addition, the amount of wasted wood disposed in landfills in some regions in California reaches 90 percent of the total wood waste (CIWMB 1995). Adhikary, et al. 2008, stated that a large amount of wood waste is generated from wood industry at different stages of the processing of wood; which is disposed mostly in landfills; Besides, the hazardous content of the wood waste are numerous and takes time to decompose (Adhikary, et al. 2008). The Department of Environmental Quality (DEQ) in the United States reported that the other alternative; that used to be used, to get rid of wood wastes instead of disposing was burning (DEQ 2009). Wood burners were used at first and as a result of their environmental hazards; represented in huge amount of smoke & ash generated directly to the atmosphere polluting air and ambient, were shut down and prohibited from being used (DEQ 2009). Currently, a tremendous shift is done in the area of wood burning especially with the developed ideas of avoiding the environmental hazards. Therefore, the use of wood waste in WPC helps to overcome disposal and burning hazards and costs (Adhikary, et al. 2008).

4.3 Virgin or recycled (non-virgin) material in WPC production

The issue of producing WPC using virgin or recycled (non-virgin) material is been controversial. When searching in literature, various opinions were found regarding the practicality of usage, mechanical properties, physical properties, and even final product look or appearance.

Various comparisons were done between virgin and recycled materials using many conditions have shown agreements of authors with the use of recycled material and other times disagreements. However, studies based on recycled products are very limited (Adhikary, et al. 2008) and almost all producers of the commercial scale WPC are using virgin materials (Klyosov 2007). This tendency could be due to the fear of obtaining a product with non controllable properties resulted from impurities as justified by Yeh, et al. 2009, on research scale (Yeh, et al. 2009). Conversely, Adhikary, et al. 2008, used in their study post-consumer HDPE which was collected from plastics' recycling plant and sawdust was obtained from a local sawmill. They have shown in their study the feasibility of making composite panels from recycled HDPE using hot-press molding technique. They added that the obtained product has proven superior dimensional stability when compared to virgin HDPE and equivalent tensile and flexural properties of the composites. On the other hand, Yeh, et al. 2009, showed that wood with recycled ABS resulted in poor and variable mechanical properties as compared to the relevant virgin ABS. They added that unlikable odor is obtained from recycled material which could be avoided by adding a thin layer of virgin polymer (Yeh, et al. 2009).

Regarding physical properties, Adhikary, et al. 2008, showed that the panels gave very low water absorption and thickness swelling thus the products was considered stable in humid environment (Adhikary, et al. 2008). In contrast, Najafi, et al. 2007, have tested water absorption and thickness swelling of WPC obtained from sawdust and recycled and virgin plastic; HDPE and PP. The test consisted of 2 hr and 24 hr submersion tests.

The results showed that recycled WPC absorbed more than virgin, PP absorbs water more than HDPE, and the mix of recycled HDPE and PP absorbed the maximum (Najafi, et al. 2007).

Yeh, et al. 2009, and Adhikary, et al. 2008, have found variable performance of their final product. It was justified by Adhikary, et al. 2008, by the different grades and colors of waste stream used and the material contaminants. They said also that the impact is still not fully understood which calls for further investigations and opens a new area of research (Adhikary, et al. 2008). Moreover, the problem was addressed by Yeh, et al. 2009, as the reuse of polymers obtained from post-consumer application caused unpleasant outcomes many times. They justified by basing their claim on the impurities contained within the material; which led to decrease the mechanical and thermal behavior. The authors added that; based on their findings, impurities would affect the product impact strength and ductility negatively to the extent even if it was of 1 % of amount. Another problem accompanied with impurities in polymers is that the cost of its disposal will be more than using virgin material (Yeh, et al. 2009). Therefore, it could be concluded that the main problem lies in the variable performance or different outcomes of the same material settings when tested. This issue was also discovered in findings of the new proposed technology in this chapter as the main cause of variability was due to impurities and contaminants agreeing with authors; as mentioned above. However, the environmental savings from using non-virgin material, availability, high properties, and almost no-cost should be the stimuli behind using recycled material instead of virgin.

4.4 Additives

Additives should be added to the mix because the majority of the WPC physical and mechanical properties are depending mostly on the interaction developed between wood and the plastic which is increased by additives (Wechslera and Hiziroglu 2009). Generally, the additives enhance the compatibility between hydrophilic wood and hydrophobic plastic allowing the formation of single-phase composite (Wechslera and Hiziroglu 2009). The two main families of additives which are used with WPC are mineral additives and coupling agents. The most famous coupling agent utilized in literature by many researchers is the maleated polypropylene (MAPP); on the other hand, the most famous mineral additive utilized is the talc and calcium carbonate (Klyosov 2007), (Adhikary, et al. 2008), and (Fabiyi, et al. 2008). Maleated polyolefins, organosilanes, and acrylic-modified polytetrafluoroethylene (PTFE) are the most famous family of coupling agents which are added to the composite with minimal percentages; typically less than 5% (Klyosov 2007), (Adhikary, et al. 2008), (Bengtsson and Oksman 2006), and (Fabiyi, et al. 2008). Typically, coupling agents act to provide better flowability of the molten composite, therefore better compatibility obtained, and strength enhanced (Klyosov 2007). However, many arguments were raised mentioning that coupling agents do not provide strong adhesion between fiber and plastic; which is the main intended function (Klyosov 2007). The main mineral additives adopted in literature are talc ($Mg_3Si_4O_{10}(OH)_2$), calcium carbonate, silica, glass fiber, kaoline clay (Al_2O_3, $2SiO_2$, $2H_2O$), wollastonite ($CaSiO_3$) (Klyosov 2007). Talc and calcium carbonate are most common additives used in WPC production due to their good outcome in enhancing mechanical properties, availability, and cheap cost (Klyosov 2007). Additionally, talc is the most additive used in literature due its good absorption of water; to minimize the wood moisture, its natural similarity to oil in addition to its distinct platy shape (non uniform layered

composition) making it a good filler for hydrophobic plastic (Klyosov 2007). In addition, talc was utilized by many researchers because it has proven that it enhances WPC mechanical properties (Fabiyi, et al. 2008, Klyosov 2007).

5. Manufacturing

5.1 WPC manufacturing techniques

Various techniques were adopted in literature to manufacture WPC, however; the two main adopted techniques are extrusion and injection molding.

Typically, the extrusion process produces continuous linear profiles via forcing a melted thermoplastic through a die; on the other hand, the injection molding process produces three-dimensional items with minimizing the stages of post-manufacturing (Migneault, et al. 2009).

The manufacturing techniques adopted by Bengtsson and Oksman 2006, were based on drying wood flour at 100 C to reach a moisture content of 0.3%. The dried wood and plastic granules were then fed to the cororating twin-screw extruder at temperatures varying from 165 to 200 C. A rectangular die was used at the extruder end and the extrudates were then cooled at ambient temperature. Silane was added during extrusion to enhance the product properties. Bengtsson and Oksman 2006, showed that adding silane resulted in superior increase in toughness, impact strength and creep properties in comparison to those without silane; However, The flexural modulus was lower (Bengtsson and Oksman 2006). Yeh, et al. 2009, divided the WPC manufacturing process into two main parts. The first part consisted of compounding the material; using a twin-screw extruder. The second part was to obtain profiles via single-screw extruder or use injection molding to obtain a product resembling to wood in look and properties (Yeh, et al. 2009). Bouafif, et al. 2009, produced WPC in a two-stage process. In the first stage, a co-rotating twin-screw extruder was used to compound wood particles with HDPE into pellets at temperatures from 180 C to 190 C. In the second stage, a reciprocating screw injection molding machine was used to inject WPC test specimens (Bouafif, et al. 2009). Soury, et al. 2009, manufactured WPC pallets by firstly producing profiles; utilizing counter-rotating twin screw extruder, and then assembling them by using nails, rivets and screws. The authors found an advantage of adopting extrusion instead of injection molding represented in the high challenge of producing one piece pallet in injection molding which could make the wood; in the composite, burn. This is due to the high shear rate in the rapid injection speed and therefore excessive heat generated causing burn to the product. On the hand, extrusion generates much less shear and therefore heat; in addition, it is more flexible in terms of adoption of various die designs (Soury, et al. 2009). Migneault, et al. 2009, conducted a comparison between extrusion and injection molding for producing WPC, common steps found in both include melting, shaping, and cooling; in addition, they both use screws to convey, pump, and blend the mixed component. However, they added that process parameters such as residence time, temperature, pressure, shear rate, shear stress, and cooling rate are different. Moreover, they concluded that pressure and shearing in injection molding are higher than en extrusion regardless the process parameters mentioned (Migneault, et al. 2009). Stark, et al. 2004, compared WPC samples; composed from 50% wood flour and HDPE, obtained from extrusion and injection molding and found that they gave the same flexural modulus; however, the flexural strength and density of injected parts were higher. The authors justified that this could be resulted from the better interfacial contact in injection molding

between wood and polymer; totally encapsulated wood particles within polymer matrix, resulting in higher density and therefore more strength (Stark, et al. 2004).
However, Bledzki and Faruk 2004, have shown that WPC made from 30% hardwood particles and polyethylene resulted in similar specific bending modulus of elasticity and density for both injection molding and extrusion techniques. Conversely, injection molded WPC have shown higher specific tensile strength (Bledzki and Faruk 2004).
Concerning physical properties, Clemons and Ibach conducted sorption behavior comparison for WPC; composed from 50% of 40-mesh pine flour and HDPE, and concluded that water-soaked extruded samples absorbed and swelled more water than injection molded samples (Clemons and Ibach 2004).

5.2 WPC reprocessing

Another important point that should be addressed is the reprocessing of the wood plastic composite itself. Although literature did not emphasize much on this point, however; Beg and Pickering, 2008, have shown that mechanical properties of WPC samples composed from 50% fiber; reprocessed two times, increased respectively by 13.5% and 33% for tensile strength and yield modulus. In addition, after the second reprocessing time, the properties decreased till reaching the 8th reprocessing when tensile strength and yield modulus; of a WPC with 40% fiber, was reduced to 25% and 16% respectively (Beg and Pickering 2008).

6. WPC new manufacturing technology

6.1 Experimental stages

Most of the WPC techniques mentioned in the literature are very expensive and require high technology which called for developing a simple, reliable, cheap technique to produce WPC. A new suggested technology in this section utilizes extrusion technique which was decided based on a local market survey that was performed. The technology was applied at The American University in Cairo (AUC) Technology and Innovation Labs. It showed high availability of extrusion technologies; manufactured locally, and relative cheap cost. Conversely, injection molding machines mainly are less available and more expensive than extruders. Therefore, the decision was made to use the extrusion method. In addition, Special procedures were presented to manufacture WPC that showed satisfying outcomes. All the processes have gone through several **pilot, prerequisite, stage 1, 2, and 3** experimentations till reaching the required manufacturing processes which will be explained in details within this section.

Pilot experimentations

These experiments are called the pilot or baseline experiments (Elsayed, 2009). It is consisting of running initial experiments to get more experience and knowledge about the factors included, determine the important ones to be investigated further, and exclude the unimportant i.e. getting the feeling of interconnected components. In addition, its outcomes give the necessary data to set bounds and constraints on factors involved. As well, it is the key which gives the guidelines for the necessary manufacturing techniques; as it was shown in this work. Moreover; based on results obtained from pilot experiments, sequential modifications were done leading to the final adopted manufacturing technology. These experiments were run in random patterns to estimate the general behavior of factors; however, extreme settings of factors should be experimented to be able to add boundaries and restrictions.

Prerequisite stage

This stage consisted of making assumptions to start the experiments with. It was based on literature review and a local market survey. The first experimental settings were built based on this stage; where literature was the first key giving the way for a manufacturing technology. Two methods for the manufacturing of wood plastic composites were suggested: injection molding method and extrusion and compression molding method (Klyosov, 2007). Then, a local market survey was conducted to check the availability of machines needed for these two technologies. It showed high availability of single extrusion technologies; manufactured locally, and relative cheap cost. Conversely, injection molding machines and twin extruders are not manufactured locally, less available and more expensive than extruders. Therefore, the decision was made to use the extrusion method.

Stage 1

The main target of this stage was to check the adequacy of the chosen technology via its applicability using virgin plastic and wood waste. Virgin plastic was used to block any effect that could be accompanied with plastic waste. As a result, the three manufacturing steps; extrusion, heating, and compression have proven efficiency and gave a feasible product.

Stage 2

Plastic waste was utilized within WPC instead of virgin within experimentations. Several problems appeared in this stage regarding wood and plastic wastes. As a consequence, the product which was obtained suffered in many cases from a non homogenous grains' distribution in the final product i.e. plastic and wood weren't distributed evenly in the product. Therefore; it was suspected to obtain non consistent properties if large WPC sheets were decided to be produced. This problem was avoided in stage 3 when meshing and shredding process were added. The main problem accompanied with plastic waste was the formation of volatile organic compounds which affected the product negatively and called for adding bounds and constraints for this factor. On the other hand, wood waste has caused problems concerning the formation of water bubbles; due to its hydrophilic nature, and the uneven grain distribution within the product which allowed the formation of water bubbles and voids within the wood plastic matrix.

Stage 3

Stage 3 included many modifications that started by the introduction of shredding and meshing operations to avoid non homogenous products obtained in stage 2. Eight different sizes of sieves were adopted ranging from 400 to 1300 Micrometers to mesh the wood; where only 2 sizes; 500 and 1180 Micrometers, were decided to be used in the final experimental processes as they gave the highest flexural strength and modulus properties. The 500 Micrometers' sieve was selected from a range of sizes that is commonly used in literature for the production of WPC; ranging from 50 to 700 Micrometers (Klyosov, 2007), and the 1180's one was selected based on a claim that increasing in particle size would ameliorate properties (Klyosov, 2007). The second important modification was the need to do something concerning the wood humidity and tendency to absorb water; hydrophilic nature. Drying wood before usage was the first step to minimize wood water content and adding talc was the second. On the other hand, decisions concerned with process variables (furnaces' temperatures and extruder's temperatures and speed) were taken in this stage

also. Mainly, the limits' selection of all these variables was based on the product obtained; whereas, burned products will call for decreasing temperature; for example. Typically, it was required to obtain a well cooked product yet not burned with the minimum possible time. Therefore, Furnaces' temperature; used for wood drying and forming the paste, were set based on these main criteria. Extruder's temperature was decided to be set at a specific degree to avoid solidification or overheating of the product. Extruder's speed was set at 19 RPM; because when the speed was higher than 20 RPM, the product obtained wasn't coherent and well mixed. In other words, the time wasn't sufficient to merge plastic and wood where the plastic wasn't well heated. In contrast, when the speed was less than 18 RPM the product obtained was overheated; therefore the plastic liquidified and stuck within the extruder. Based on the previous justifications, levels of process variables were decided not to be included within the final experimental processes.

6.2 Factors affecting WPC

Four factors (ingredients) were used to produce WPC: plastic, talc, and wood waste with size of up to 1.18mm and 0.5mm. The wood waste utilized is formed from sawdust with fine particle sizes. This type of wood waste generally is a by-product of wood sawing which ranges from 20 to 5000 μm (Klyosov 2007). Based on literature, the common adopted sizes of wood utilized for the production of WPC range from 50 to 700 Micrometers; where increasing particle size results in better flow of molten composite, lower mold shrinkage, and higher flexural modulus (Klyosov 2007). In other words, better properties are obtained when the size approaches the 700 Micrometers. Based on this claim, it was decided; during pilot experimentations, to test 8 different sieves ranging from 300 to 1300 Micrometers for the sake of obtaining the best possible accepted product. Increasing the size more than 700 Micrometers intended to experiment the claim mentioned above of "the increase in size would ameliorate properties". As a result, two sieves were decided to be used with sizes of 500 Micrometers (0.5mm) and 1180 Micrometers (1.18mm) as they gave higher flexural strength and modulus in comparison with the other 6. Moreover, it was decided to use various mixtures of these two sizes during main experiments; as it was suspected that a mixture of two sizes may ameliorate properties. For illustration, these factors will be described as X1, X2, X3, and X4 respectively. Table 1 presents all the bounds and constraints in this technique. Bounds were the upper and lower limits of each factor that was adopted in this work.

	Upper and lower bounds	*Constraints*
X1 = Plastic	$40 \leq X1 \leq 70$	$15 \leq X3+X4 \leq 50$
X2 = Talc	$0 \leq X2 \leq 35$	
X3 = Wood (1.18mm)	$0 \leq X3 \leq 50$	$X1-X3-X4 \geq 0$
X4 = Wood (0.5mm)	$0 \leq X4 \geq 50$	

Table 1. Upper, lower bounds, and constraints of factors

All percentages, bounds, and constraints were based on pilot experimentations that showed these adopted percentages to be most appropriate using this technology.

X1 Factor

X1 is the percentage of plastic within the mix. It is a mix of HDPE and LDPE with ratios of 25% and 75% respectively. It is a waste product obtained from municipal waste and no

virgin materials were used. It is composed of shredded plastic waste obtained mainly from garbage plastic bags which are highly contaminated. The utilization of this type of plastic would save the environment as these bags are non biodegradable materials which are mostly thrown away in a dumpsite; therefore, it is a costless unutilized resource calling for investment. In addition, the highest percentage of WPC produced commercially worldwide is based on Polyethylene (Klyosov, 2007). X1 was utilized in this work with percentages varying from 40% to 70% (table 1). The higher bound of X1 was decided based on pilot experimentations. When the percentage exceeded 75% then, volatile organic compounds; resulted from melted plastic, were produced during extrusion in addition to unknown gases which could be resulted from the contaminations in plastic (bearing in mind it is a product obtained from black plastic bags used for garbage collection). The production of these gases caused a continuous blowing of the extruder; which called for shutting down several experiments for safety reasons and to avoid possible hazard. Therefore, it was decided afterwards not to exceed the amount of plastic more than 70%. On the other hand, the adoption of the lower bound was based on the non-coherent burned product obtained when the percentage of plastic was 35% or less during pilot experimentations. This could be due to the high wood (filler) amount not meeting enough plastic to be merged in a matrix.

X2 Factor

X2 is the percentage of talc ($Mg_3Si_4O_{10}(OH)_2$) within the mix. It is a part of the phyllosilicate minerals which is used as a mineral additive to this mix. It is characterized with its ability to absorb water; therefore, minimize the humidity of wood; which is characterized with its hydrophilic nature, as a consequence enhancing mechanical properties of WPC (Sun-Young Lee, et al. 2008). In addition, talc has a natural affinity to oil; therefore, it works as good filler for hydrophobic plastic (Klyosov, 2007). Also, talc is available with very low cost in Egypt and elsewhere. Before using talc; within pilot experimentations, water formation within the product was a major problem especially with mixtures containing high filler content; 45% or more. These products failed easily with minor load application when tested; flexural strength was 2 MPa or less and the modulus didn't exceed 250 MPa. However, results after using talc were far higher and the effectiveness of its usage was proven in this technique. The upper bound was based on literature recommendations; where talc gave highest flexural strength modulus at 27% talc (Noel and Clark, 2005) & (Klyosov, 2007). Therefore, it was decided to use an upper bound of 35%.

X3 and X4 Factors

X3 and **X4** are the percentage of meshed wood waste with size of up to 1.18mm and 0.5mm. X3 and X4 are sawdust wastes obtained from wood workshops; which are typically thrown away in dumpsites. The main problem of wood waste lies in its hydrophilic nature; unlike the contamination issue of plastic where wood is obtained from wood workshops. It absorbs water and humidity in an immense way. Two actions were taken to solve this problem; drying wood and adding talc. The upper bound of X3 and X4 was decided not to exceed 50% as the plastic should be at least 40% to produce coherent product and 10% would be considered as a basic percentage of talc to get rid of wood water content. However, runs with zero talc percentage were also conducted to measure its effect.

The first constraint tells that the total wood wastes percentage shouldn't be less than 15% and more than 50%. The lower bound was needed because there should be a minimum

amount of wood waste in the product to give the desired WPC properties which was obtained at a minimum of 15% wood waste content. The upper bound was added to make the total wood wastes acting less than or equal 50% in all cases to avoid burned products and get the desired properties. The second constraint says that the plastic percentage should be more than the total wood wastes percentage. It is an assurance condition for avoiding a case such as 40% plastic, 50% wood, 10% talc; where non-coherent product was suspected in this mix (containing high filler content).

6.3 Processes experimental settings

The processes start as shown in figure 1 by meshing the wood waste into 2 predetermined grades using sieves of sizes giving wood waste particles up to 0.5 mm and 1.18 mm to obtain a homogenous saw dust material. Based on pilot experimentations, these two sizes were used as they gave highest flexural properties (strength and modulus) of the final product in comparison with several sieves of different sizes utilized during trials. The meshed wood waste is then taken to be dried in a furnace for 4 hours to eliminate the moisture within wood waste particles up to almost 100%. The furnace temperature is set at 115 C. This temperature was decided not to be increased more than 115 C due to safety reasons as to avoid wood waste burning. After drying takes place, the wood waste is then mixed with plastic and talc (if any) in a jar (container) using a mixer and then the mix are fed into the single screw extruder. The talc is added as a mineral additive to enhance the properties of the final product. Two electric heaters are used at the beginning and end of the extruder. Temperatures were set at 120 C for the first and 150 C for the second heater. The resulted extrudates are left to be cooled at room temperature then taken to the shredder to form small particles with identical dimensions which will make the paste formed from the last process more homogenous. Then, the shredded particles are fed into the furnace to form a paste which is formed after about 15 min. Therefore, it is taken to the hydraulic compression molding machine to be pressed. A die with specific dimensions is used to satisfy the required application. Finally, trimming and cutting processes into the exact specified dimensions are done to make the product ready for testing in accordance with the requirements of the testing standards.

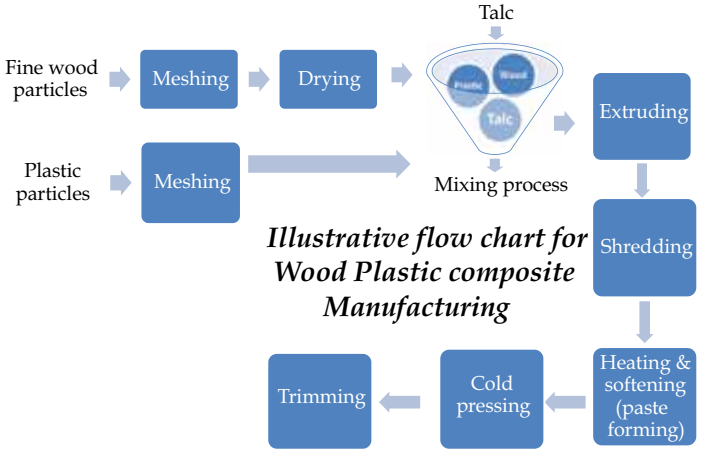

Fig. 1. Illustrative process flow chart of WPC manufacturing

6.4 Experimental processes

Wood waste meshing

The wood waste utilized is formed from sawdust with fine particle sizes. This type of wood waste generally is a by-product of wood sawing which ranges from 20 to 5000 µm (Klyosov, 2007). Based on literature, the common adopted sizes of wood utilized for the production of WPC range from 50 to 700 Micrometers; where increasing particle size results in better flow of molten composite, lower mold shrinkage, and higher flexural modulus (Klyosov, 2007). In other words, better properties are obtained when the size approaches the 700 Micrometers. Based on this claim, it was decided; during pilot experimentations, to test 8 different sieves ranging from 300 to 1300 Micrometers for the sake of obtaining the best possible accepted product. Increasing the size more than 700 Micrometers intended to experiment the claim mentioned above of "the increase in size would ameliorate properties". As a result, two sieves were decided to be used with sizes of 500 Micrometers (0.5mm) and 1180 Micrometers (1.18mm) as they gave higher flexural strength and modulus in comparison with the other 6. Moreover, it was decided to use various mixtures of these two sizes during main experiments; as it was suspected that a mixture of two sizes may ameliorate properties.

Wood waste drying

The dryer used was set at 115 C to avoid wood waste burning. The meshed wood waste is left for 4 hours in the dryer to get rid of the moisture (see figure 2). It was assured that the moisture was totally eliminated through a test that was done. The test consisted of taking two samples of wood waste; sizes of up to 0.5mm and 1.18mm, utilized within experiments and weighs it through a calibrated scale. Then, it was left in the dyer for 2 hours then weighed. Each hour after the second hour, it was weighed. At the 5th and 6th hour the weight was not changed for the two types. Therefore, it was concluded that 4 hours was sufficient to dry the meshed wood waste. The experiment was repeated 3 times to guarantee the results.

Fig. 2. Oven used to dry waste wood

Extruding

Before feeding the extruder (single screw extruder), the plastic is mixed; using a mixer, with wood waste and talc (if any). The plastic used; which is composed of a mix of HDPE and LDPE with 25 % and 75 % respectively, has the shape of small particles. This mix is composed of shredded plastic waste obtained mainly from garbage plastic bags which are highly contaminated. The talc is used as a mineral additive; to enhance mechanical properties, with percentages varying from 0 to 35 percent by weight of the total. The mix is then being fed into the hopper of the extruder and the process starts as shown in figure 3.

Fig. 3. Feeding the extruder with the mixture

Setting the two heaters at 120 C; for the first one, and 150 C; for the second, the extrudates are produced and the sample is accomplished and extrudates obtained within about 17 min for a 1.5 kg used (see figure 4 and 5). Intuitively, a warm up period for the heaters of about an hour was a prerequisite. The temperatures' settings were dependent mainly on the plastic utilized as it has major effects on the process and therefore the final product obtained. These effects were discovered during pilot experimentations; which were reflected when the temperature range of the extruder was increased to 135 C (1st one) and 165 C (2nd one), the melt was overheated, liquidified, then stuck around the screw as it turned with its rotation without flowing. This caused the process to stop as it prevented the flow to continue and jammed the whole process. In other instances, when the temperature was dropped to 105 C (1st one) and 135 C (2nd one), the melt was solidified causing the blockage of the flow. Therefore the settings of 120 C ± 5 and 150 C ± 5 were applied to obtain a well cooked product yet not burned with the minimum possible time. The difference in temperature is due to start with a primary heating then increase it to the final one as not to cause a sudden increase in temperature within the mix and therefore caused an incremental pressure resulted in exploding the mix from extruder outlet rather than flowing.

Fig. 4. The hot extrudates coming out of the extruder

Shredding

The extrudates (see figure 5) are crushed in the shredder (see figure 6) forming small particles with identical sizes to be fed into the furnace. The shredding operation was important as it avoided bad distribution of the mix during furnace heating within experimentation. As this process at first; during the pilot trials, was done without shredding which resulted in several cases of non homogenous final product. The main reason behind this that the extrudates have different sizes and the material's concentration within each extrudate wasn't distributed the same. Therefore, it was decided to use a shredder.

Fig. 5. The final shape of the extrudate

Fig. 6. The shredder adopted in crushing the extrudates

Drying

The furnace works for about 15 min at 140 C to form a paste which is then taken to be pressed (see figure 7). The temperature was decided based on pilot trials aimed at forming a homogenous paste without burning.

Fig. 7. The furnace used for heating the shredded particles to form a paste

Compression molding

The hydraulic compression molding machine used consists of a hydraulic press with parallel platens which apply the pressure of high amount (see figure 9). A pressure of 40 bars is applied. The steel die used is a custom made one with dimensions of 42 * 12 * 12 cm

(see figure 8) to accommodate the size required for the ASTM D 4761 test of flexural test. A sample obtained after pressing is show in figure 10.

Fig. 8. The custom made die

The required thickness is obtained via right weight selection for the mix and adjusted using thickness cutter.

Fig. 9. The hydraulic press used

Fig. 10. The sample obtained after pressing

Trimming and adjusting thickness

A trimming process is done for the sample giving final dimensions of 40 * 10 cm to be ready for the testing in accordance with the ASTM D 4761 requirements. The thickness is corrected via cutting the sample obtained to the 1 cm thickness required by the ASTM D 4761.

7. Conclusion

Plastic and wood wastes have been a major environmental concern because of high amount of waste generated which affect the sustainability of natural resources. Wood Plastic Composites (WPC) made out of wood waste and plastic waste has been a fast growing research area because of its wide range of applications such as fences, siding, park benches, landscaping timbers, windows and door frames, ponds, indoor furniture, pellets and many others. The fact that WPC ingredients are manly composed from wood and plastic wastes has led to the rapid increase of its production due to the high availability of non-utilized plastic and wood wastes. WPC will close the loop for conserving the natural resources, according to cradle-to-cradle concept. The use of plastic waste and wood waste in WPC helps to overcome disposal (through landfill) and burning hazardous material through incinerators and reduce the cost of environmental degradation as well as depleting the natural resources and the indirect cost of health hazardous material.

Various techniques were adapted in the literature to manufacture WPC, however, the two main adapted techniques were extrusion and injection moulding. This chapter provide a new technique based on moulding technology which is cheaper than extrusion & injection moulding and provide WPC with any dimensions and shapes according to the dimension and shapes of moulds.

8. Acknowledgment

The authors would like to acknowledge the support from technology and innovation labs available in the Mechanical Engineering Department at the American University in Cairo.

9. References

Adhikary, Kamal B., Shusheng Pang, and Mark P. Staiger. "Dimensional stability and mechanical behaviour of wood–plastic composites based on recycled and virgin high-density polyethylene (HDPE)." *Composites: Part B*, no. 39 (2008): 807–815.

Augutis, V., Gailius, D., Balčiūnas, G. "Testing system for composite wood based strips." *Measurement Technologies Laboratory* (Faculty of Telecomunications and Electronics), no. Issue 285 (2004).

Beg, M.D.H., and K.L. Pickering. "Reprocessing of wood fibre reinforced polypropylene composites. Part I: Effects on physical and mechanical properties." *Composites: Part A*, no. 39 (2008): 1091–1100.

Bengtsson, Magnus, and Kristiina Oksman. "Silane crosslinked wood plastic composites: Processing and properties." *Composites Science and Technology*, no. 66 (2006): 2177–2186.

Bledzki, Andrzej K, and Omar Faruk. "Extrusion and injection moulded microcellular wood fibre reinforced polypropylene composites." *Cellular polymers journal* 4, no. 23 (2004): 211-227.

Bouafif, Hassine, Ahmed Koubaa, Patrick Perré, and Alain Cloutier. "Effects of fiber characteristics on the physical and mechanical properties." *Composites: Part A*, 2009.

CIWMB. "CalRecycle." *CalRecycle Web site.* Department of Resources Recycling and Recovery. 1995. http://www.calrecycle.ca.gov/ (accessed February 2009, 2009).

Clemons, C.M., and R.E. Ibach. "Effects of processing method and moisture history on laboratory fungal resistance of wood-HDPE composites." *Forest Products Journal* 4, no. 54 (2004): 50-57.

Clemons, Craig M., and Daniel F. Caufield. "Wood Flour." In *Functional Fillers for Plastics*, by Craig M. Clemons and Daniel F. Caufield, edited by M. Xantos, 249-270. Federal Republic of Germany: The Forest Products Laboratory, 2005.

DEQ. The Department of Environmental Quality (DEQ). 2009. http://bluebook.state.or.us/state/executive/Environmental_Quality.htm (accessed February 10, 2009).

Fabiyi, James S., Armando G. McDonald, Michael P. Wolcott, and Peter R. Griffiths. "Wood plastic composites weathering: Visual appearance and chemical changes." *Polymer Degradation and Stability*, no. 93 (2008): 1405–1414.

Falk, H. "Wood recycling: Opportunities for the wood waste resource." *Forest Products Journal* 6, no. 47 (1997): 17-21.

Jayaraman, Krishnan, and Debes Bhattacharyya. "Mechanical performance of woodfibre–waste plastic composite materials." *Resources, Conservation and Recycling Journal* 41 , no. 4 (July 2004): 307-319.

Kikuchi, Ryunosuke, Jan Kukacka, and Raschman Robert. "Grouping of mixed waste plastics according to chlorine content." *Separation and Purification Technology* 61, no. 1 (2008): 75-81.

Klyosov, Anatole A. *Wood-Plastic Composites.* New Jersey: John Wiley & Sons, Inc., 2007.

McDonough, W., and M. Braungart. *Cradle to Cradle: Remaking the way we make things.* North point press, DuraBook, 2002.

Migneault, Sebastien, Ahmed Koubaa, Fouad Erchiqui, and Abdelkader Chaala. "Effects of processing method and fiber size on the structure and properties." *Composites: Part A*, no. 40 (2009): 80–85.

Morton, J., and L. Rossi. "Current and Emerging Applications for Natural and Wood Fiber Composites." *7th International Conference on Woodfiber-Plastic Composites* . Madison, WI: Forest Products Society, 2003.

Najafi, Saeed Kazemi, Mehdi Tajvidi, and Elham Hamidina. "Effect of temperature, plastic type and virginity on the water uptake of sawdust/plastic composites." *Holz Roh Werkst*, no. 65 (2007): 377–382.

Panda, Achyut K, RK Singh, and DK Mishra. "Thermolysis of waste plastics to liquid fuel: A suitable method for plastic waste management and manufacture of value added products - A world prospective." *Renewable and Sustainable Energy Reviews* 14, no. 1 (January 2010): 233–248.

Soury, E., A.H. Behravesh, E. Rouhani Esfahani, and A. Zolfaghari. "Design, optimization and manufacturing of wood–plastic composite pallet." *Materials and Design*, no. 30 (2009): 4183–4191.

Stark, N.M., L.M. Matuana, and C.M. Clemons. "Effect of processing method on surface and weathering characteristics of wood-flour/HDPE composites." *Journal of Applied Polymer Science*, no. 93 (2004): 1021-1030.

Sun-Young Lee, In-Aeh Kang, Geum-Hyun Doh, Ho-Gyu Yoon, Byung-Dae Park, Qinglin Wu. "Thermal and Mechanical Properties of Wood Flour/Talc-filled Polylactic Acid Composites: Effect of Filler Content and Coupling Treatment." *Journal of thermoplastic composite materials* 21 (May 2008): 209-223.

Takatani, Masahiro, Kohei Ikeda, and Kei Sakamoto. "Cellulose esters as compatibilizers in wood/poly(lactic acid) composite." *The Japan Wood Research Society*, no. 54 (2007): 54-61.

USEPA. *Municipal solid waste in the United States: 2005 facts and figures.* officail report, Municipal and industrial solid waste division, US Environmental Protection Agency, Washington, DC: US Environmental Protection Agency, 2006.

Wechsler, A., and S. Hiziroglu. *Building and Environment* 42 (2007): 2637–2644.

Wechslera, Andrea, and Salim Hiziroglu. "Some of the properties of wood–plastic composites." *Materials and Design*, no. 30 (2009): 4183–4191.

Winandy, J.E., N. M. Stark, and C. M. Clemons. "Consideration In Recycling Of Wood-Plastic Composites." *5th Global Wood and Natural Fiber Composites Symposium.* Kassel - Germany, 2004.

Yeh, Shu-Kai, and Rakesh K. Gupta. "Improved wood–plastic composites through better processing." *Composites: Part A* 39 (2008): 1694–1699.

Yeh, Shu-Kai, Sushant Agarwal, and Rakesh K. Gupta. "Wood–plastic composites formulated with virgin and recycled ABS." *Composites Science and Technology*, no. 69 (2009): 2225–2230.

Yeh, Shu-Kai, Sushant Agarwal, and Rakesh K. Gupta. "Wood–plastic composites formulated with virgin and recycled ABS." *Composites Science and Technology*, no. 69 (2009): 2225–2230.

Youngquist, J., G. Myers, and T. Harten. *Lignocellulosic – Plastic Composites from Recycled Materials.* American Chemical Society, 1992.

14

Curing Monitoring of Composite Material Using Embedded Fiber Bragg Grating Sensors

Chia-Chin Chiang
Department of Mechanical Engineering, National Kaohsiung University of Applied Sciences, 415 Chien Kung Road, Kaohsiung 807, Taiwan

1. Introduction

The composite materials with high specific stiffness and strength have been widely applied in various fields such as aerospace or industry. Simultaneously, curing methods for joining composite materials have also gone through development intensively, for examples Hot-press, Pultrusion, Resin Transfer Molding (RTM) and Vacuum Molding. During the curing process, internal damages and residual strain are the most considerable relevance to quality of product, and hence demanded careful treatment. Commonly, the internal damage of composite materials could be detected by using ultrasound scan and X-ray, but these methods, however, are significantly high cost and not on-line monitoring. It is not suitable for smart structure application.

Since several recent decades, optical fiber sensors have been utilized in composite material field popularly for their predominating advantages such as small size, low cost, and capability of avoiding electromagnetic influence. In 1988, Afromowitz proposed the polymer fiber embedded into composite materials to monitor the refractive index changes in the composite materials during curing process [Afromowitz, 1988]. And one year later the authors presented Fiber Optic Fresnel Reflection Technique for supervising the curing process [Afromowitz & Lam, 1990]. In late 1980s, Fiber Bragg Grating (FBG) sensor, one kind of optical fiber sensors, has attracted considerable attentions to the applications in aerospace, structural, medical and chemical spheres. FBG sensors are small and compatible with common polymeric materials, and thereby being easily embedded close to the internal sensing site in a composite structure without introducing significant defects.

In 1990, Dunphy et al. employed the Fiber Bragg Grating embedded into composite materials to monitor the vitrification during curing process [Dunphy et al., 1990]. Similarly, FBG sensors were also applied to measure strain and residual stress after curing [Dewynter-Marty et al., 1998 & Okabe et al., 2002a]. On the other hand, Kuang and collegues improved detecting effect of the sensors by embedding FBG into composite materials in different layers [Kuang et al., 2001b]. Alternatively, in 2002, Okabe et al. utilized small-diameter FBG to study residual stress with micro damage of inner structure of the composite [Okabe et al., 2002b]. Furthermore, FBG has been also used to monitor the epoxy curing, and found the glass transition temperature with intensity changes [Giordano et al., 2004 & Wang et al., 2007].

Recent studies [Okabe et al., 2002a & Kuang et al., 2001a] discovered that when FBG sensors are embedded in CFRP laminates, the reflection spectrum from the sensors splits into two peaks because of the non-axisymmetric thermal residual stresses. This deformation of the spectrum was considered defective as it would lead to misinterpretation in strain measurements or crack detection in the laminates [Menendez & Guemes, 2000; Murukeshan et al., 2000; Leng & Asundi, 2002].

According to our knowledge, most of the previous researches focus on measuring the mechanical properties of composite materials and damage evaluation, but lack of curing residual strain monitoring in different layers. The aim of current study is to apply Fiber Bragg Grating sensors to monitor the characteristics of the curing process in a Graphite/Epoxy composite. Four FBGs are embedded into different lamina of composite materials, and the curing development as well as internal residual strain during curing process would be measured.

2. Theory

2.1 Fiber Bragg Grating Sensor

Fiber Bragg Grating Sensor consists of thousands of short period refractive index modulation. When the broad band light source lunches at the FBG, the certain wavelength of the light will be reflected. The reflected wavelength of FBG can be expressed as following [Hill & Meltz, 1997]:

$$\lambda = 2n_{eff}\Lambda \tag{2-1}$$

where n_{eff} is the effective refractive index of optical fiber, Λ is the grating period which is about 1um. Fig. 1 illutrates the principle of FBG schematically.

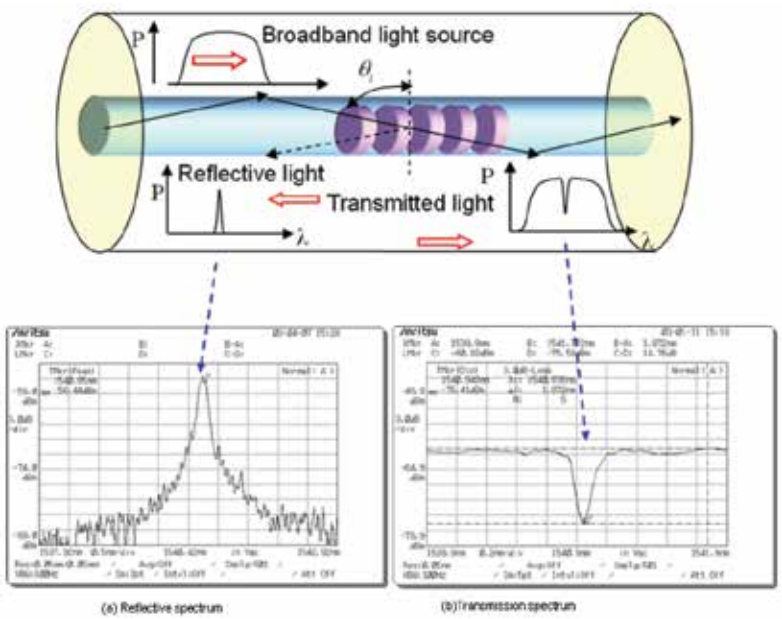

Fig. 1. Reflective and transmission spectra of single-mode fiber Bragg gratings

2.2 FBG wavelength shifts owing to temperature and strain

Because of thermo-optic effect and Photo-Elastic effect, the wavelength of FBG will be shifted with changes of temperature and strain. The FBG wavelength is a function of the temperature and strain and in form as following [Hill & Meltz, 1997]:

$$\frac{\Delta\lambda}{\lambda} = \left\{1 - \frac{n_{eff}^2}{2}\left[p_{12} - \nu\left(p_{11} - p_{12}\right)\right]\right\}\varepsilon + \left[\alpha + \frac{\left(\frac{dn_{eff}}{dT}\right)}{n_{eff}}\right]\Delta T$$

$$= \left(1 - p_e\right)\varepsilon + \left(\alpha + \xi\right)\Delta T = K_\varepsilon \varepsilon + K_T \Delta T \tag{2-2}$$

where ξ is the thermo-optical coefficient, α is the CTE of optical fiber, ΔT is the temperature change, K_ε is the strain sensitivity, and K_T is the temperature sensitivity.

2.3 FBG spectrum splitting with residual strain

Theoretically, the wavelength of FBGs shifted under two strain conditions including uniaxial and multiaxial strain. Following, discussion about the two kinds of wavelength shift is presented particularly.

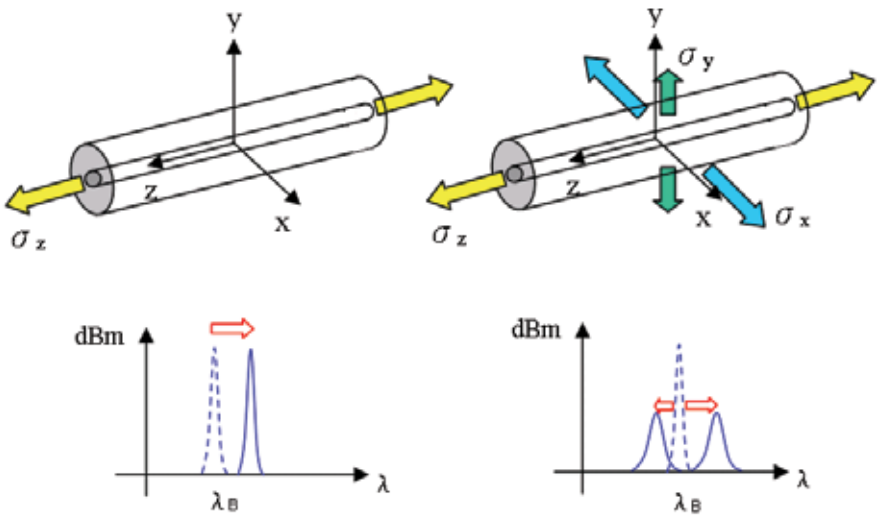

(a) (b)

Fig. 2. The optical fiber Bragg grating sensor is under an uniaxial strain (a) and a general multiaxial strain (b). [Lin, 2004]

(I) Wavelength shift due to uniaxial strain

When the fiber is suffered a uniaxial uniform strain ε_i along its axis (as shown in Fig. 2a), then $\varepsilon_x = \varepsilon_y = -\nu\varepsilon_z$ (ν is the Poisson ratio of optical fiber). As a result, the wavelength shift is related to the applied strain and temperature change as given by equations below:

$$\frac{\Delta\lambda_B}{\lambda_B} = K_\varepsilon \varepsilon \ + K_T \Delta T \tag{2-3}$$

where $K_T = \frac{\xi}{n_0} + [1 - \frac{n_0^2}{2}(p_{11} + p_{12})]\alpha$, $K_\varepsilon = 1 - \frac{n_0^2}{2}[p_{12} - (p_{11} + p_{12})]$.

Referring to work [Lin, 2004], p_{11} =0.113, p_{12} =0.252, and $n_{eff,0}$ ~1.458, ν ~0.17, α ~0.55×10-6, one can obtain the constants K_ε ~0.8 and K_T ~5.88×10-6. The strain is measured by the reflective wavelength shift of the fiber Bragg gratings.

(II) Wavelength shift due to multiaxial strain

When the FBGs are embedded in the composite laminate, the FBG will be suffered three dimensional loading. As the fiber is under a general multiaxial strain (Fig. 2 b), the Bragg wavelength shifts caused by refractive index changes in the x- and y- directions are dissimilar. As shown in the Fig. 2 b, the original Bragg reflection peak is shifted in two opposite directions, and thereby causing spectra to split [Lin, 2004]. This phenomenon is due to the birefringence effect.

The 3-D strain and wavelength effect is shown as following [Lin, 2004; Menendez & Guemes, 2000]:

$$\begin{Bmatrix} \frac{\Delta\lambda_x}{\lambda_x} \\ \frac{\Delta\lambda_x}{\lambda_x} \end{Bmatrix} = \begin{bmatrix} D_1 & D_2 \\ D_1 & D_3 \end{bmatrix} \begin{Bmatrix} \varepsilon_x \\ \varepsilon_y \end{Bmatrix} + K_T \Delta T \{I\} \tag{2-4}$$

where D_1, D_2 and D_3 are constant. $D_1 = 1 + \frac{n_0^2}{2}[\upsilon(p_{11} + p_{12}) - p_{12}]$, $D_2 = -\upsilon + \frac{n_0^2}{2}[2\upsilon p_{12} - p_{11}]$, $D_3 = -\upsilon + \frac{n_0^2}{2}[\upsilon(p_{11} + p_{12}) - p_{12}]$, $K_T = \frac{\xi}{n_0} + [1 - \frac{n_0^2}{2}(p_{11} + 2p_{12})]\alpha$, and $\{I\}$ is the unit matrix.

Therefore, the curing residual strain can be monitoring according to the spectra of the embedded FBGs. The Residual strain along the x-axial and y-axial are expressed in following [Menendez & Guemes, 2000]:

$$\varepsilon_y = \frac{\frac{\Delta\lambda_y}{\lambda_y} - \frac{\Delta\lambda_z}{\lambda_z}}{D_2 - D_3} \tag{2-5}$$

$$\varepsilon_x = \frac{1}{D_1}\left\{\left[\frac{\left(\frac{\Delta\lambda_y}{\lambda_y} - \frac{\Delta\lambda_z}{\lambda_z}\right)D_3}{D_2 - D_3}\right] - \frac{\Delta\lambda_z}{\lambda_z}\right\} \tag{2-6}$$

By monitoring the 3-dimemsional strain in the composite laminate, we can measure and evaluate the curing residual strain during the process.

3. Experimental results

3.1 Preparation of the composite laminate

The 16-layer thermosetting prepregs, Carbon/Epoxy composition T300/3501, are used for laying up the composite laminate in the sequence with four embedded FBGs [0(FBG-1)90/0(FBG-2)90/0(FBG-3)90/0(FBG-4)0/90/0/90/0/90/0/90/0]. The curing process is implemented by utilizing the Modified Diaphragm Forming (MDF) with the air compressor, vacuum pump, and heat chamber. The mod of MDF consists of two Teflon films to prevent adhesion, polyimide-diaphragm and o-ring for sealing, which is depicted in Fig. 3.

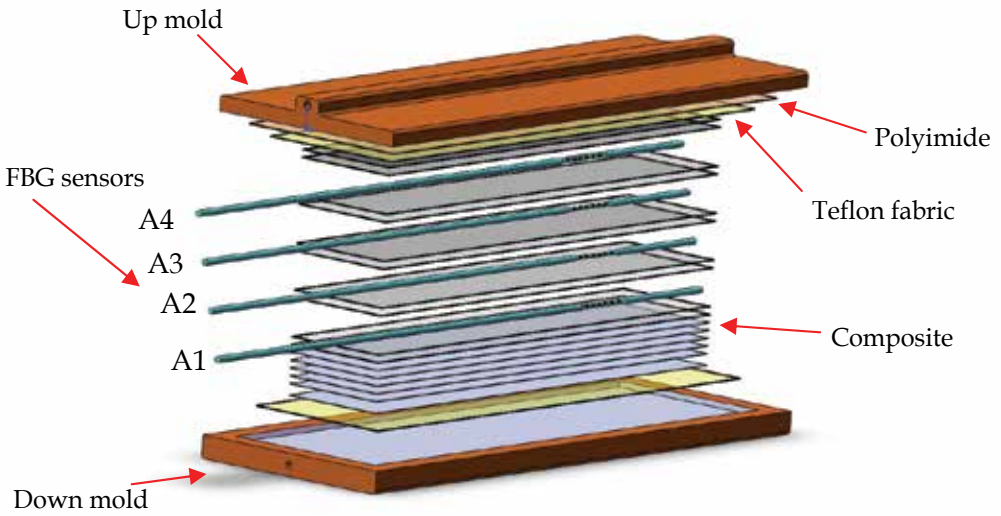

Fig. 3. Schematic of the diaphragm type forming mold for laminate curing process

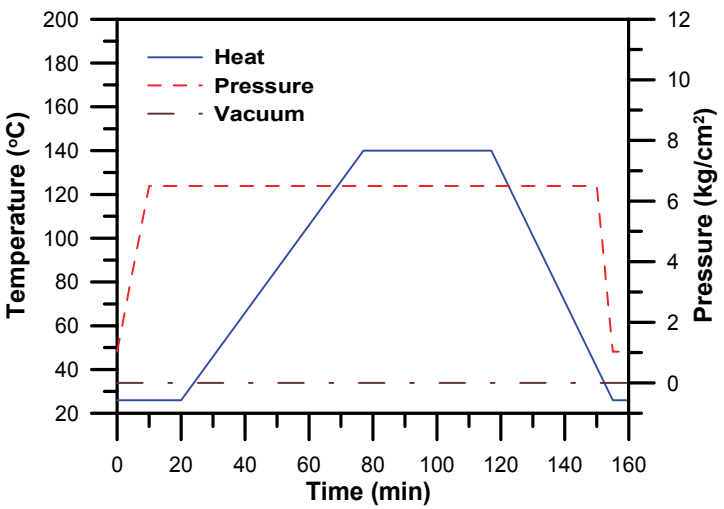

Fig. 4. Curing conditions of composite specimen

The prepregs in MDF will be closed by air pressure beyond the diaphragm, and removed excess gas in the laminate by vacuum pump simultaneously. The curing process is composed of three stages including heating, isothermal and cooling stage. The process starts at heating stage with 7 kg/cm^2 air pressure upon the diaphragm, and 6.5 kg/cm^2 vacuum in the mod. The heating rate is 2 °C/min from room temperature to 140 °C. Second state is isothermal stage at 140 °C in 40mins. During this stage, the resin viscosity is low and easy to flow. The vacuum condition assists avoiding the delamination due to the exhaust gas in the laminate. The third state is cooling to room temperature when the resin viscosity becomes large and stable. Moreover, the residual strain will occur at the end of this stage. The whole curing conditions are described in Fig. 4.

3.2 Experimental set-up and fabrication of FBG

The involved FBG was fabricated in the Ge-B co-doped single cladding photosensitive fiber by using the phase mask method. Meanwhile, the photosensitive fiber was manufactured by Fibercore Co. Ltd. (PS1250/1550).

A schematic diagram of photoimprinting FBGs in photosensitive optical fiber is illustrated in Fig. 5 particularly. The 248-nm UV radiation from a KrF Excimer laser is employed while the impulse frequency of laser is 10 Hz. To avoid burning the phase mask, the laser power should be <500 mJ/cm^2. Along the fiber core, the FBG has a periodic refractive index modulation with a period of 1.05~1.08 μm, obtained by using phase masks with different periods. This resulted in a peak Bragg reflecting wavelength of 1540~1564 nm. The reflectivity of the resulting FBG was about 99% and the FWHM (Full width Half Maximum) of the FBG is about 0.175 nm.

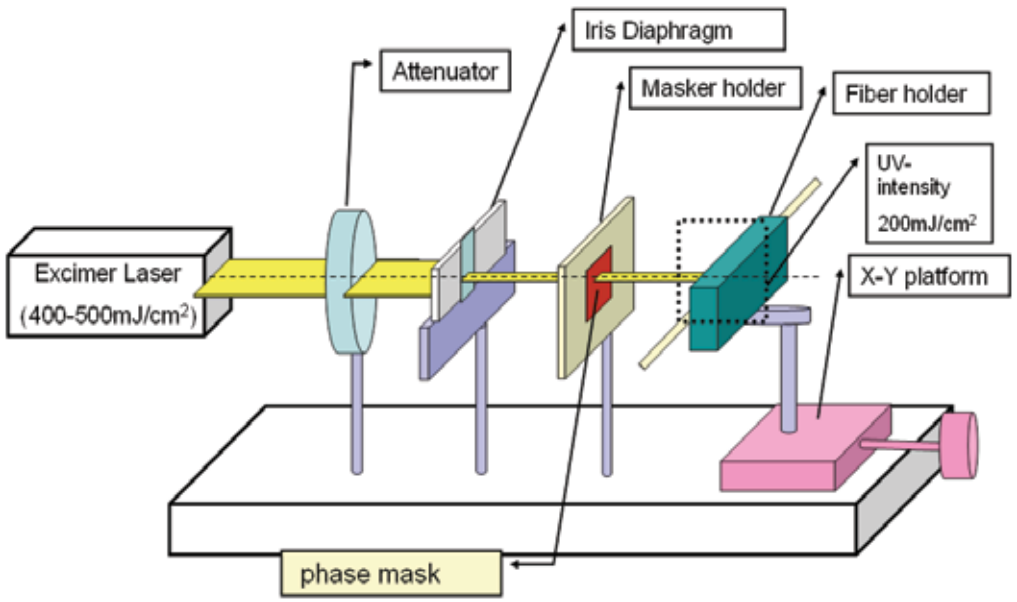

Fig. 5. A schematic diagram of the FBGs fabrication set-up

The experimental set-up for curing monitoring is shown in Fig. 6. The light source in the experiment is the broadband Super Luminescent Diode (SLED) with wavelength span is

1400nm~1600nm. The main objective of the system is to observe the reflective spectra from the embedded FBGs in the laminate.

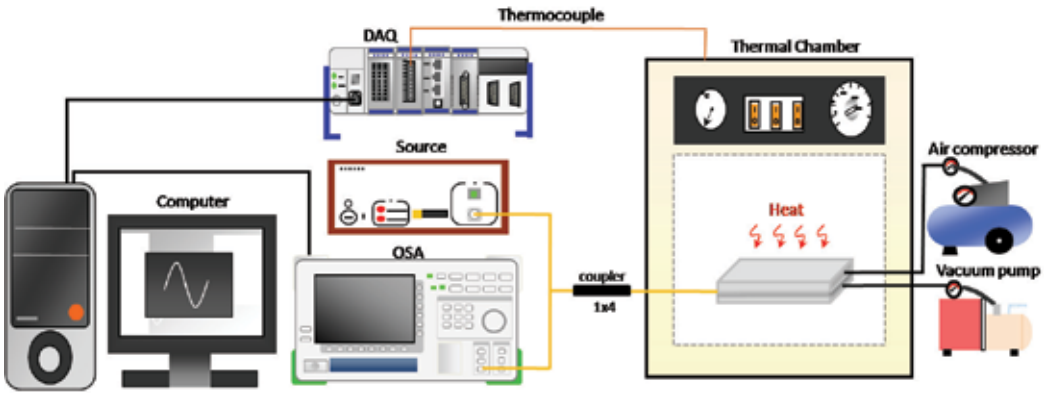

Fig. 6. Experimental set-up of curing monitoring

3.3 Results and discussion

We embedded four FBGs (FBG-A1:1541.13nm, FBG-A2:1552.85nm, FBG-A3:1554.61nm, and FBG-A4:1560.65nm) into the composite laminate. Fig. 7 depicts the temperature calibration (from room temperature to 180 °C) of FBGs before embedded in the laminate. The temperature sensitivity of FBG-A1, FBG-A2, FBG-A3 and FBG-A4 are 9.8, 9.5, 11.4 and 9.4, respectively. It could be observed that the variation of wavelength with temperature is quite linear with the average of R-squared is 0.997.

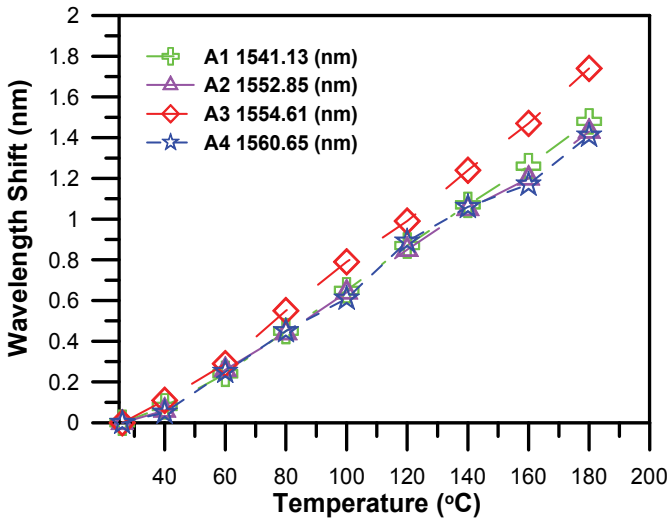

Fig. 7. FBG wavelength shift with the temperature raising

From the reflective spectrum of embedded FBG sensors, we can observe the peak wavelength of FBGs (FBG-A1:1540.81nm, FBG-A2:1552.6nm and FBG-A3:1554.79nm). The signal of FBG-A4 is very weak after raising the air pressure in the up-mod. The high

pressure could be the reason causing the breakage of FBG-A4. As shown in Fig. 8, which describes the change of spectra and the intensity in the heating stage of the curing process, the wavelength shifts to the right while intensity is increasing with temperature rising. The phenomenon is as a result of the diminished compression loading. As the temperature increases, the viscosity of the matrix materials (Epoxy) is decreasing gradually. Therefore, the embedded FBG will be adapted well in the carbon fiber lamina. The pressure loading will be then taken by the carbon fiber, and thereby reducing the loading on the embedded FBGs. In the Fig. 9, there are three transition points of the intensity-temperature curve at about 105 °C, which is near to the glass transition temperature of the epoxy matrix (95 °C).

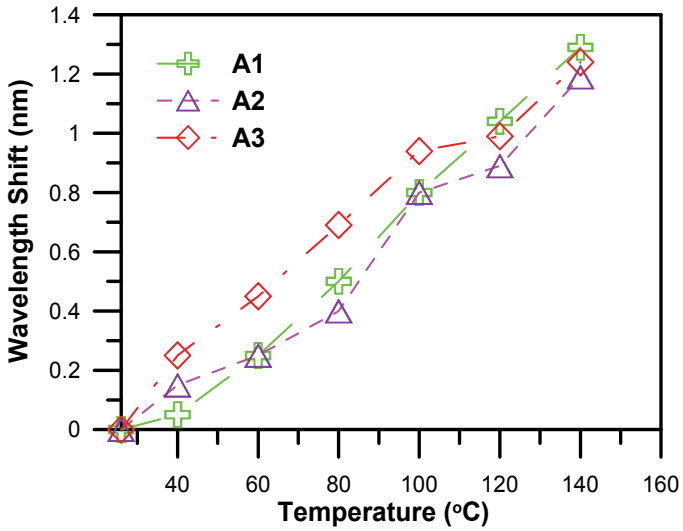

Fig. 8. FBG wavelength shift during heating stage during curing process

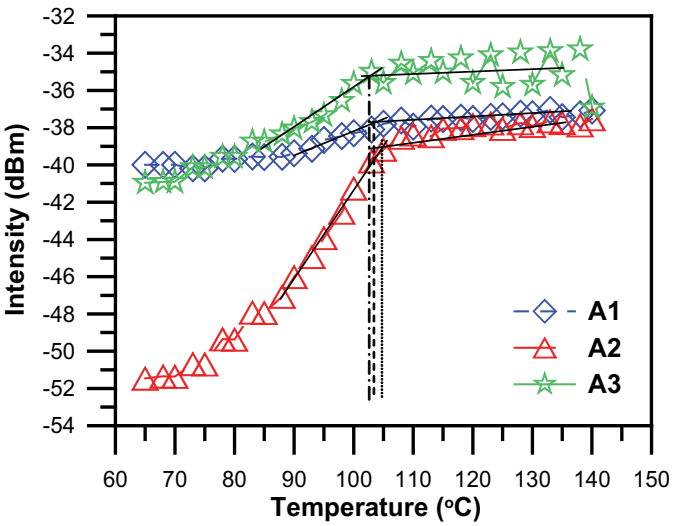

Fig. 9. The intensity changes of the embedded FBGs during the heating stage

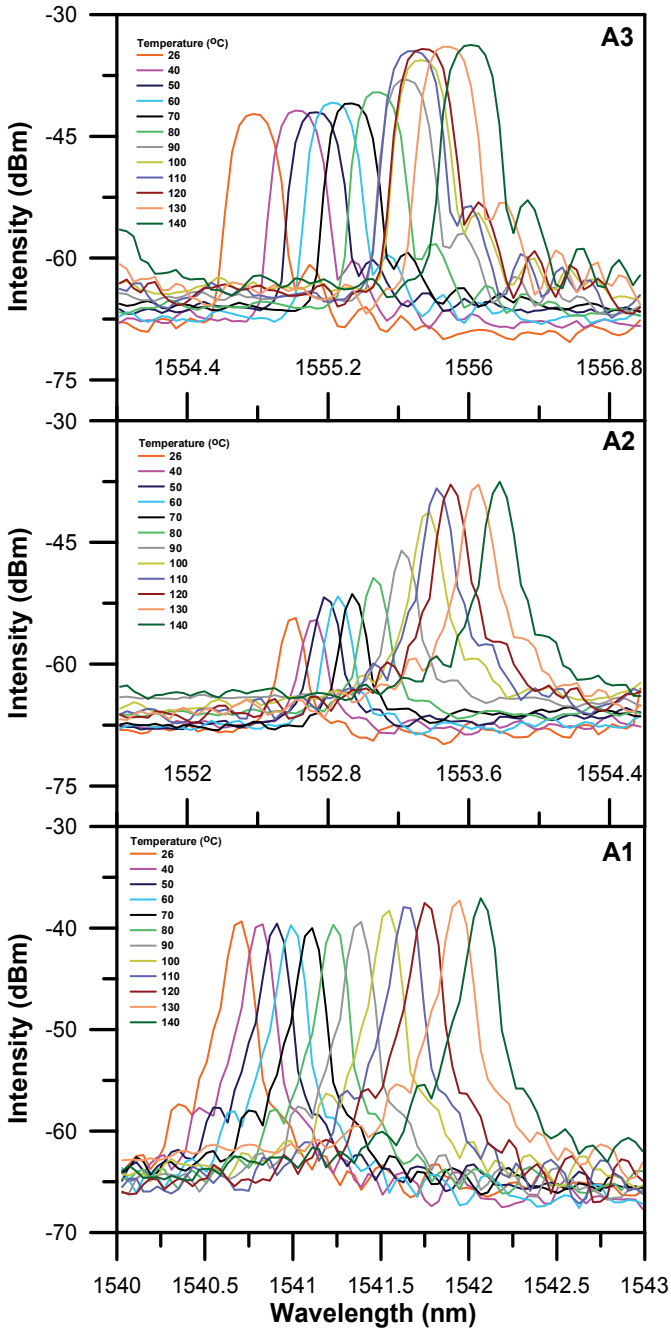

Fig. 10. Spectrum of change during the heating stage

The intensity and the spectrum shape of the FBGs do not change at the isothermal stage (holding at 140 °C). However, the resin viscosity is reducing gradually during cooling process. In cooling stage, the intensity of the embedded FBGs' spectra is linearly decreasing, and the spectrum width of FBGs is broadening with temperature cooling in Fig 10.

Fig. 11. illustrates the split of FBG spectra during cooling stage when the wavelength is shifted to left. The peak of FBG spectra (A1 and A2) gradually broadens at about 95 °C, and splitting into two peaks at 90 °C while the peak of FBG spectra (A3) broadens and splitting into two peaks at 50 °C.

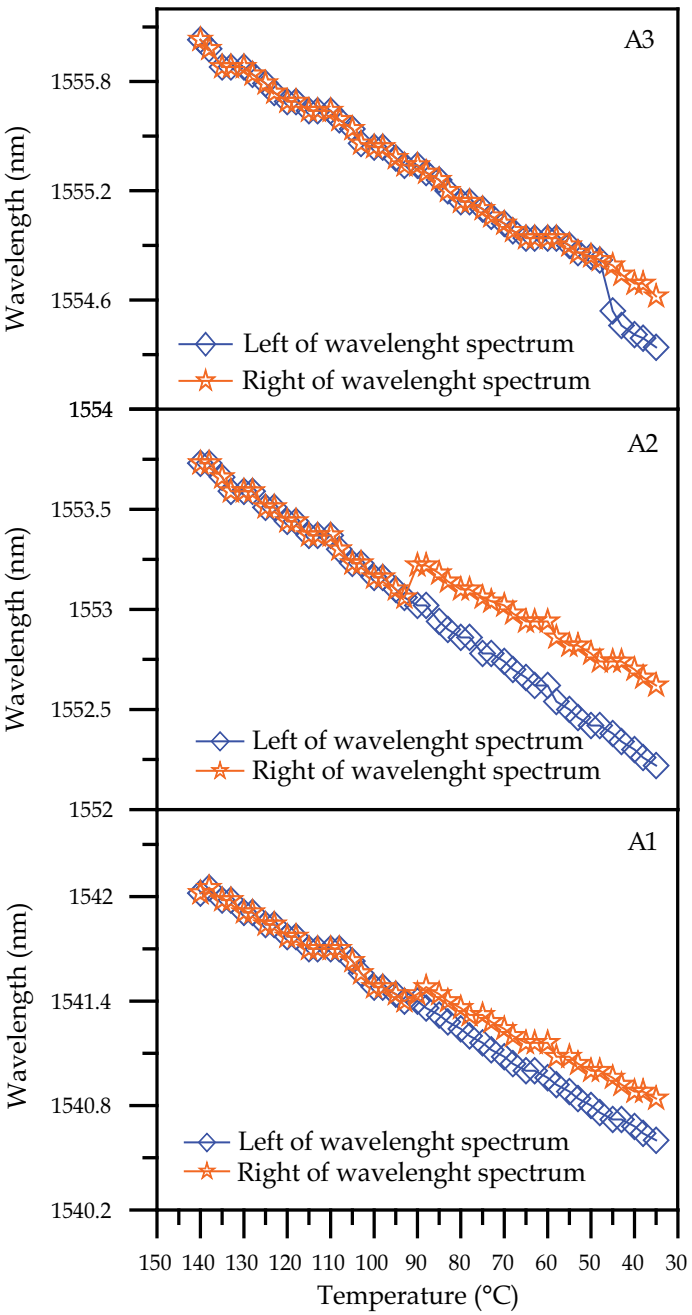

Fig. 11. The split of FBG spectra during the cooling stage

Fig. 12. depicts the variations of the intensity of FBG spectra during cooling stage. Below 90 °C, the spectra will split into two peaks, and, therefore, the intensity is decreasing with the occurrences of peak splitting.

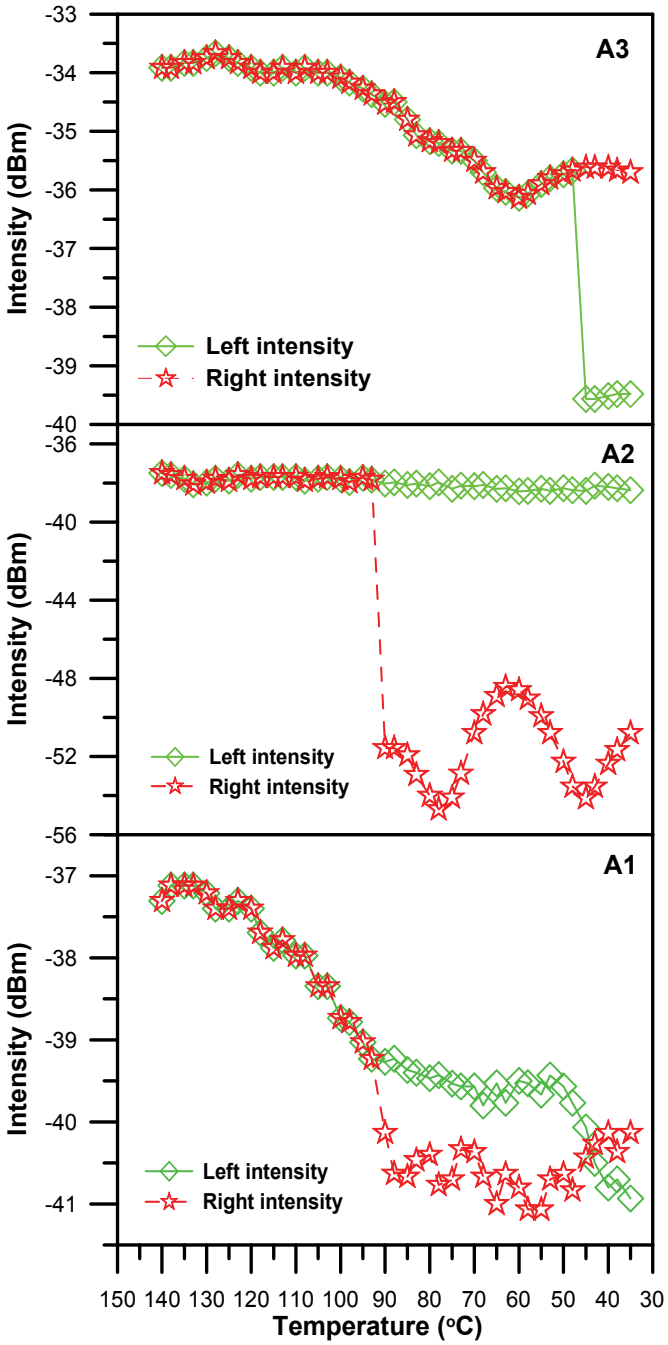

Fig. 12. Intensity of FBG Spectra during cooling stage

During the cooling process, we can observe the changes of intensity and wavelength in the FBGs' spectra. As shown in Fig. 13, the width of FBG spectra broadens below 100 °C. The spectra of FBG (A1 and A2) split into two peaks at about 90 °C whereas FBG (A3) splits at about 50 °C. In addition, splitting peaks of FBG (A3) are unobvious, and owing to smaller residual strain. This phenomenon may be caused by various residual strains from different layers of the laminated composites.

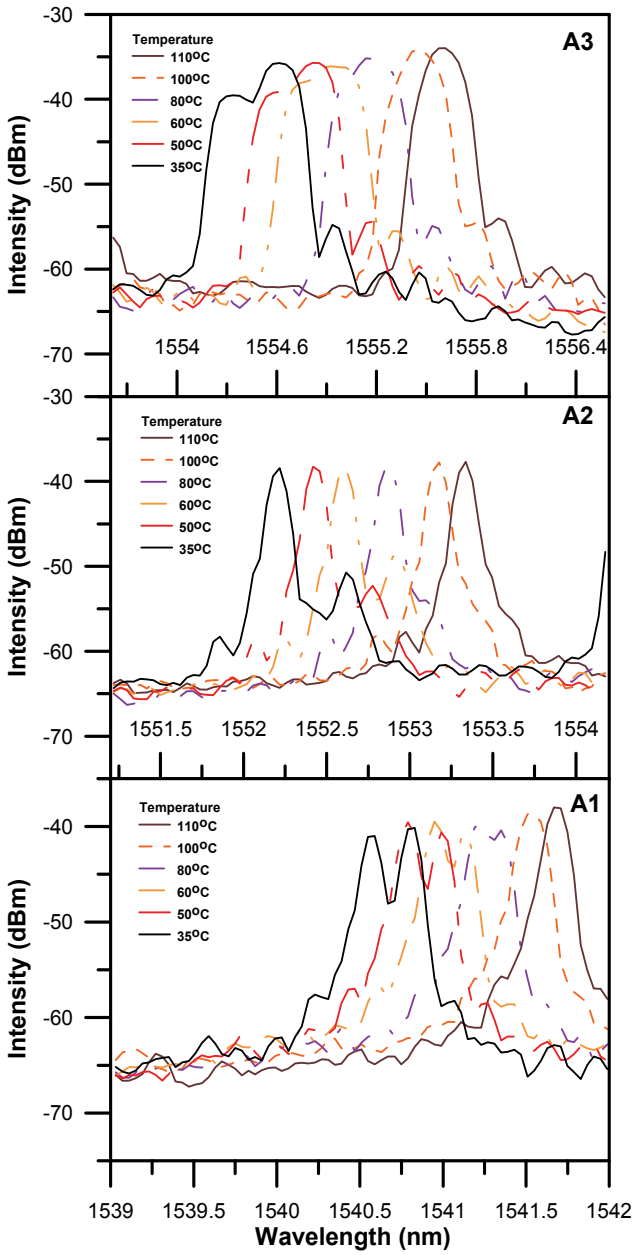

Fig. 13. FBG spectra monitoring during cooling stage

The comparison of the FBG spectra at before and after the curing process is illustrated in Fig. 14. After curing process, the spectra are shifted to left and splitting into two peaks owing to the transverse residual strain while the wavelengths of FBG (A1) and FBG (A2) shift to the left apparently. The wavelength shift is caused by the axial residual strain.

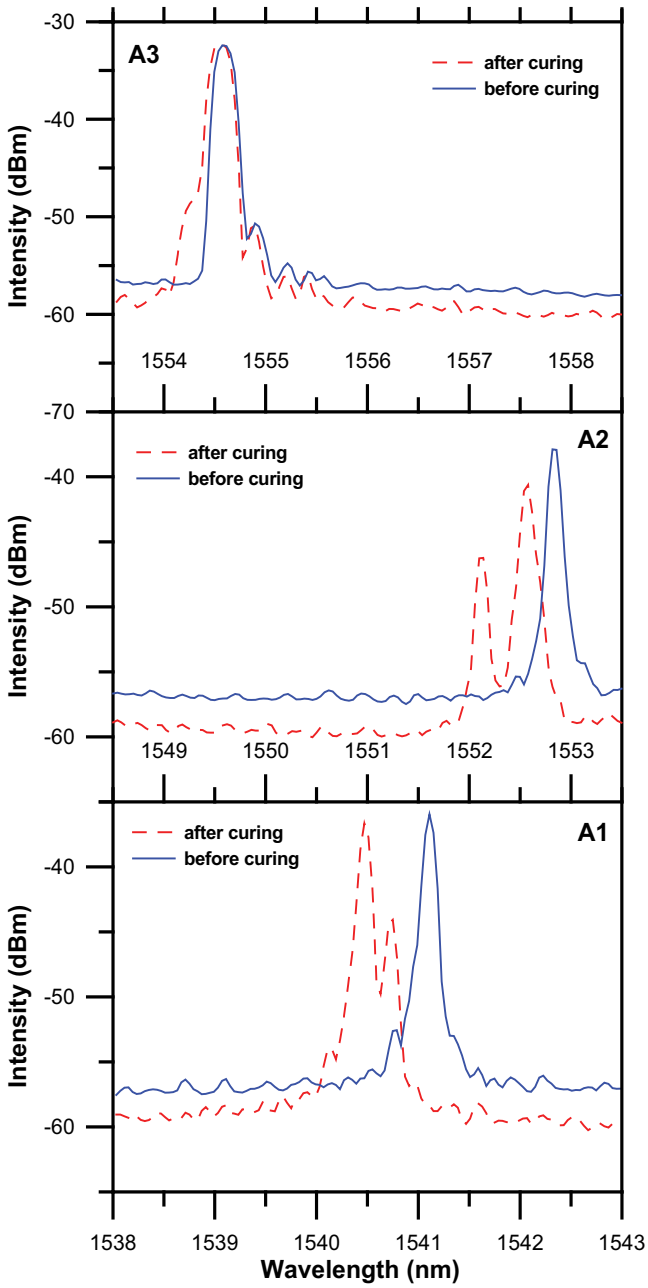

Fig. 14. Comparison of FBG spectra before and after curing

As shown in Fig.15, the residual strain of the FBG (A1) and FBG (A2) are -423με and -407με, respectively. Meanwhile, the residual strain of the FBG (A3) is -32με, much smaller than those of FBG (A1) and FBG (A2), could be considered as having no significant change after curing. Briefly, the residual strain of FBG (A1), FBG (A2) and FBG (A3) are compression strain although less residual strain could be detected at the outer layer of composite.

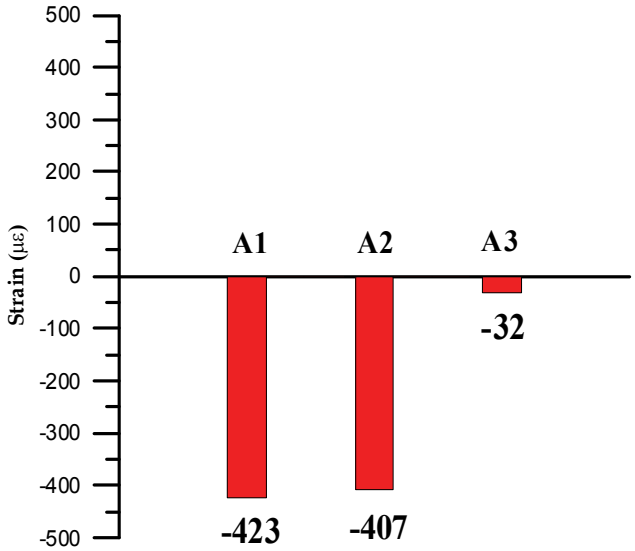

Fig. 15. Axis residual strain of FBG sensors in different layer of the composite laminate

5. Conclusions

We propose a method for monitoring the curing process of composite materials using four embedded FBGs in different layers in the composite laminate. The embedded FBGs are successful to supervise curing process including residual strain and glass transition temperature. The curing development and residual strain measurement are assessed through changes in the shape of the optical spectra, intensity attenuation and shifts in wavelengths of FBGs. The maximum curing residual strain was -423 με in the central laminate of the composite. The curing residual strain of FBG-1, FBG-2 and FBG-3 are -423, -407 and -32με, respectively. During the cooling stage, the spectra are shifted to left, broadening, and then splitting into two peaks owing to the transverse residual strain.

6. Acknowledgment

This work is supported by the National Science Council under contracts NSC 98-2221-E-151 -013 and NSC 99-2221-E-151-011.

7. References

Afromowitz, M. A. (1988). Fiber optic polymer cure sensor, *Journal of Lightwave Technology,* Vol. 6, No. 10, (August 2002), pp. (1591-1594), ISSN 0733-8724

Afromowitz, M. A. & Lam, K. Y. (1990). The optical properties of curing epoxies and applications to the fiber-optic epoxy cure sensor, *Sensors and Actuators A: Physical*, Vol. 23, No. 1-3, (April 1990), pp. (1107-1110), ISSN 0924-4247

Dewynter-Marty, V.; Ferdinand, P.; Bocherens, E.; Carbone, R.; Beranger, H.; Bourasseau, S.; Dupont, M. & Balageas, D. (1998). Embedded Fiber Bragg Grating Sensors for Industrial Composite Cure Monitoring, *Journal of Intelligent Material Systems and Structures*, Vol. 9, No. 10, (October 1998), pp. (785-787)

Dunphy, J. R.; Meltz, G.; Lamm, F. P. & Morey, W. W. (1990). Multifunction, distributed optical fiber sensor for composite cure and response monitoring, *Proceedings of Fiber Optic Smart Structures and Skins III*, San Jose, USA, September 1990

Giordano, M.; Laudati, A.; Nasser, J.; Nicolais, L.; Cusano, A. & Cutolo, A. (2004). Monitoring by a single fiber Bragg grating of the process induced chemo-physical transformations of a model thermoset, *Sensors and Actuators A: Physical*, Vol. 113, No. 2, (July 2004), pp. (166-173), ISSN 0924-4247

Hill, K. O. & Meltz, G. (1997). Fiber Bragg grating technology fundamentals and overview, *Journal of Lightwave Technology,* Vol. 15, No. 8, (August 2002), pp. (1263-1276), ISSN 0733-8724

Kuang, K. S. C.; Kenny, R.; Whelan, M. P.; Cantwell, W. J. & Chalker, P. R. (2001a). Residual strain measurement and impact response of optical fibre Bragg grating sensors in fibre metal laminates, *Smart Materials & Structures*, Vol. 10, No. 2, (April 2001), pp. (338-346), ISSN 0964-1726

Kuang, K. S. C.; Kenny, R.; Whelan, M. P.; Cantwell, W. J. & Chalker, P. R. (2001b). Embedded fibre Bragg grating sensors in advanced composite materials, *Composites Science and Technology*, Vol. 61, No. 10, (2001), pp. (1379-1387), ISSN 0266-3538

Lin, C.L. "Opto-Mechanical Applications of Microstructured Materials" PhD thesis, Joseph Fourier University /National Taiwan University, 2004.

Leng, J. S. & Asundi, A. (2002). Real-time cure monitoring of smart composite materials using extrinsic Fabry-Perot interferometer and fiber Bragg grating sensors, *Smart Materials & Structures*, Vol. 11, No. 2, (April 2002), pp. (249-255), ISSN 0964-1726

Menendez, J. M. & Guemes, J. A. (2000). Bragg-grating-based multiaxial strain sensing: its application to residual strain measurement in composite laminates, *Proceedings of Smart Structures and Materials 2000: Sensory Phenomena and Measurement Instrumentation for Smart Structures and Materials*, Newport Beach, CA, USA, March 2000

Murukeshan, V. M.; Chan, P. Y.; Ong, L. S. & Seah, L. K. (2000). Cure monitoring of smart composites using Fiber Bragg Grating based embedded sensors, *Sensors and Actuators A: Physical,* Vol. 79, No. 2, (February 2000), pp. (153-161), ISSN 0924-4247

Okabe, Y.; Yashiro, S.; Tsuji, R.; Mizutani, T. & Takeda, N. (2002a). Effect of thermal residual stress on the reflection spectrum from fiber Bragg grating sensors embedded in CFRP laminates, *Composites Part A: Applied Science and Manufacturing*, Vol. 33, No. 7, (July 2002), pp. (991-999), ISSN 1359-835X

Okabe, Y.; Mizutani, T.; Yashiro, S. & Takeda, N. (2002b). Detection of microscopic damages in composite laminates with embedded small-diameter fiber Bragg grating sensors,

Composites Science and Technology, Vol. 62, No. 7-8, (June 2002), pp. (951-958), ISSN 0266-3538

Wang, Y.; Han, B.; Bar-Cohen, A. & Cho, S. (2007). Fiber Bragg Grating Sensor to Characterize Curing Process-dependent Mechanical Properties of Polymeric Materials, *Proceedings of Electronic Components and Technology Conference, 2007. ECTC '07. Proceedings. 57th*, ISBN 0569-5503, June 2007

Part 4

Testing

15

The Synergy of Electrochemistry and Concrete Material Science in Evaluating Corrosion Resistance of Wastes-Containing Reinforced Cement-Based Systems

D. A. Koleva and K. van Breugel
Delft University of Technology, Faculty of Civil Engineering and Geosciences, Department Materials & Environment, Stevinweg 1, 2628CN Delft, Netherlands

1. Introduction

Next to water, concrete is the most used material on earth. Reinforced concrete has the potential to be durable and capable of withstanding a variety of adverse environmental conditions. One of the major difficulties in the engineering practice, however, is the multi-dimensional nature of reinforcement corrosion related issues. Nevertheless, materials and processes involved in the service life of a civil structure and their interaction are independently weighed and are seldom brought together. Very often the design of concrete mix proportions and the design of protective measures (such as the application of coatings or electrochemical techniques) are made in separate steps and (positive or negative) interactions among themselves are neglected. The most original aspect of this work is the integration of fundamental electrochemical techniques and concrete material science within monitoring and assessment of the corrosion performance of reinforced cement-based materials. Further, hereby discussed is the implementation of an eco-friendly approach of waste utilization for corrosion control and/or achieving superior properties and performance.

Reinforced cement-based systems (e.g. reinforced mortar and concrete) are multi-phase composite materials at different levels of aggregation. Hence, multi-phase interfaces are involved in their structural performance and material behaviour. The steel reinforcement is embedded (on meso-level, generally relevant to mm dimension) in supposedly homogeneous cement-based bulk matrix. However, on a lower structural level (micro-level, expressed in μm), the bulk material consists of cement paste and aggregate particles, with air voids and macro pores dispersed in the cement paste matrix. Further, the cement paste can be decomposed into un-hydrated cement, hydration products, and capillary pore structure. The latter is generally assumed to have significant relevance to permeability and other transport phenomena in concrete technology.

Both the reinforcement corrosion processes (i.e. electrochemical phenomena) and the development of the cement-based microstructure are influencing the material structure in reinforced cement-based materials (as mortar or concrete) on macro and micro/nano level. The corrosion process on one hand and hydration mechanisms on the other, determine changes in microstructural properties and ion transport, compared to rest conditions (in

non-corroding systems). Chloride penetration and further corrosion will induce structural alterations of the composite material in various aspects, e.g. modifying the pore structure and interfacial zones, inducing cracking at the steel–paste interface (as a result of volume expansion of corrosion products) and further crack propagation in the bulk matrix. These microstructure alterations are underlying the evolution of electrical behaviour of reinforced mortar (concrete) during the corrosion process (as previously investigated by the authors (Koleva et al., 2008) unfavourable pore structure alterations in cement-based materials yield non-uniform electrical properties and thereby possibly result in disturbance of the electrolytic path due to heterogeneities and instabilities inherent to the bulk matrix). The electrical properties and the material microstructure undergo continuous changes due to complicated cement hydration and steel corrosion process. The correlation of electrical properties, pore solution chemistry, local microstructure of the material (in terms of porosity, pore size distribution, pore connectivity, etc.) logically influence the corrosion resistance and electrochemical behaviour of the embedded steel reinforcement. Whereas the bulk matrix properties are generally separately evaluated via well known methods and techniques of concrete material science, the reinforcement behaviour is mostly considered separately as well, using the means of electrochemical and corrosion science. However, if a reinforced cement-based system (heterogeneous and non uniform at different levels) has to be evaluated in terms of corrosion resistance and therefore service life performance, a thorough and reliable investigation and recommendation is only possible if considering the integration of both concrete material science and electrochemistry.

In the framework of an extensive experimental study on corrosion, electrochemical protection (cathodic protection efficiencies) and novel approaches for corrosion control (employment of tailored nano-aggregates and wastes) the authors have investigated the electrochemical phenomena of steel reinforcement corrosion in aggressive environments by means of electrochemical techniques, e.g. Electrochemical Impedance Spectroscopy (EIS), Potentiodynamic polarization (PD), Cyclic voltammetry (CVA). Microscopic and image analysis techniques (e.g. Scanning electron microscopy (SEM) and Energy dispersive X-ray (EDX)) render possible quantitative characterization of the composite microstructure at various interfaces, including structural morphology of steel corrosion and cement hydration products, pore structure, as well as the interfacial transition zones between cement paste and aggregate or bulk cementitious matrix and steel. Steel surface properties for all investigated cases were (as generally) determined via X-ray analysis (X-ray diffraction (XRD) and X-ray photoelectron spectroscopy (XPS)).

This chapter will discuss and give examples for the integration of electrochemical methods and microstructural investigation in reinforced cement-based materials within conditions of chloride-induced corrosion. Further, the chapter will discuss an eco-friendly approach to corrosion control in reinforced cement-based systems, by involving waste utilization (slag, from the steel production and red mud, from the aluminum production), presenting material properties and materials interactions in the context of improved long-term service life in civil engineering applications.

2. OPC and BFS cement concrete: Correlation of electrochemical parameters and microstructural characteristics

This paragraph reports on the electrochemical behavior of construction steel (FeB500 HKM), correlated with microstructural characterization of the bulk matrix in reinforced concrete,

using Ordinary Portland cement (OPC), CEM I and Blast Furnace Slag (BFS) cement, CEM III/B. The corrosion initiating environment was 5% NaCl. Potential mapping, Electrochemical Impedance Spectroscopy (EIS) and Potentio-dynamic polarization (PDP) were employed to evaluate the corrosion performance of the embedded steel. The electrochemical parameters were further coupled with pore structure parameters, thus establishing the reason for the postulated higher corrosion resistance of reinforcing steel in BFS reinforced concrete.

Concrete (reinforced concrete respectively), using BFS cement, is widely used in practical applications in Northern European countries (Çopuroğlu O. et al. 2006b). Since BFS is a by product (within the process of steel production), it can be considered as an ecologically friendly manner of minimizing the usage of cement and CO_2 emissions respectively. From the view point of bulk cement matrix characteristics, a wide range of investigations are reported, discussing cementitious materials with BFS cement (Çopuroğlu O. et al. 2006b, Bouikni A. et al. 2009, Dehghanian C. et al. 1997, Thomas M. D. A. et al. 1999. Audenaert K., et al. 2010. Li S. et al. 1986). Steel behaviour in BFS concrete is also reported, although not as widely investigated, as the bulk cementitious matrix only (Dehghanian C. et al. 1997, Song Ha-Won, et al. 2006, Pal S.C., et al. 2002, Dinakar P., et al. 2007, Macphee D.E., et al. 1993, Baweja D., et al. 1998). Compared to OPC concrete, the major contribution of BFS has been identified to result in a denser pore structure (Bouikni A. et al. 2009, Giorv O. E., et al. 1979, Manmohan D., et al. 1981, Kumar A.D.M. 1986, Hooton R.D., 1986) and reduced global porosity (Copuroglu O., 2006a). These considerations are directly linked to eventual beneficial influence of BFS, related to chloride-induced steel corrosion in reinforced concrete. Studies have shown that the use of BFS may reduce the probability of steel corrosion due to decreased permeability (Ramezanianpour A.A., 1995, Osborne G.J., 1999, Irassar E. F., et al. 2000, Hossain K. M. A., et al. 2004, Gjorv O. E. 1995), low electrical conductivity and refined pore structure (Song Ha-Won, et al. 2006, Efes Y. 1980, Dehghanian C. 1999, Gu P., et al. 2000). Other studies, however, either report close and significant dependence of the corrosion rate on the BFS content [Song Ha-Won, et al. 2006, Pal S.C., et al. 2002], or report on decreased corrosion resistance in BFS concrete at early hydration stages (Song Ha-Won, et al. 2006) and higher corrosion rates in BFS due to limited oxygen availability and thus shift of the corrosion potential of the steel surface to a more negative (active) state (Dehghanian C. et al. 1997). To this end this paragraph aims to illustrate that a thorough evaluation of the reinforced concrete system (in this case when BFS is involved in comparison to ordinary OPC concrete), is only possible via the synergy of electrochemistry and concrete material science. The electrochemical behavior of the embedded steel is discussed in correlation with microstructural characterization of the bulk cementitious matrix (the full scale of this experiment, including more details on electrochemical performance and the properties of the steel/cement paste interface are reported in (Koleva D.A. 2010a)

2.1 Experimental materials and methods

2.1.1 Materials

Reinforced concrete cylinders (d = 700 mm, h = 200 mm) were cast according EN 196-1, using water to cement ratio 0.6 (effective 0.48), cement to sand to gravel ratio 1:2:4.

The steel reinforcement (construction steel FeB500 HKN, d=12mm, h=200mm; composition according NEN6008 (in wt.%): C < 0.12 wt.%, Si max 0.6, P max 0.05, S max 0.05, N max 0.012) was cast as received. Both ends of the steel bars were isolated (to avoid crevice corrosion) and the bar was positioned in the middle of the concrete specimens. Embedded in

the concrete cover was a Mixed Metal Oxide (MMO) titanium mesh, serving as a counter electrode; SCE electrode was used as a reference electrode. The experimental set-up and specimen's geometry are as previously used and reported in (Koleva D.A., et al. 2007a). Two main groups of specimens are discussed: 1) mixtures, using OPC CEM I 42.5N; and 2) mixtures, using BFS cement CEM IIIB 42.5N. Group 1) is denoted OPC, group 2) is denoted BFS. Table 1 summarizes the chemical composition of BFS and OPC cements, used in this study (supplier of the cements is ENCI, NL). All groups were cured for 28 days in fog room (20°C and 98% humidity) and then placed in lab conditions: lab air, 22°C and 1/3rd of height immersed in water (control groups) or 5% NaCl (corroding groups), 18 replicates per group and condition were monitored.

Chemical composition, wt.%		
Oxide	**OPC CEM I 42.5**	**BFS CEM III/B 42.5N**
CaO	63.90	48.20
SiO_2	21.00	30.10
Al_2O_3	5.03	10.10
SO_3	3.00	2.50
Fe_2O_3	2.83	1.00
MgO	2.00	6.80
Na_2O	0.24	0.30
K_2O	0.65	0.30
TiO_2	0.30	-
P_2O_5	0.16	-
Mn_2O_3	0.06	-

Table 1. Chemical composition of OPC and BFS (ENCI, NL)

2.1.2 Methods

Conventional monitoring: in terms of assessing corrosion initiation, a generally accepted method is half-cell potential mapping, hereby performed for the reinforced concrete cylinders according ASTMC876 and NACE RP0290-2000 respectively. Chemical analysis was performed for the cement paste adjacent to the steel surface in each technical condition according ASTM C1218 and ASTM C1152 for total chloride concentration in wt.% per dry cement weight (using Volhard titration method). The Electrochemical methods involved were electrochemical impedance spectroscopy (EIS) and potentio-dynamic polarization (PDP). The measurements were performed at open circuit potential (OCP) for all cells. PDP was performed in the range of -0.15 V to +0.75 V vs OCP at scan rate 0.5 mV/s. The EIS measurements were carried out in the frequency range of 50 KHz to 10 mHz by superimposing an AC voltage of 10 mV. The used equipment was a High performance Autolab PGSTAT302N, combined with FRA2 module, using GPES and FRA interface. Scanning electron microscopy, using ESEM Philips XL30, combined with energy dispersive X-ray analysis (EDX) has been employed for visualization and microstructural investigations directly on the steel surface and on cross sections of the steel/cement paste interface. Section images of the specimens were obtained in backscattered electron (BSE) mode, operating at an accelerating voltage of 20 to 25 kV for imaging and EDX analysis. Image analysis was performed using OPTIMAS software package. Further, the combination of ESEM images and quantitative image

analysis allows deriving structural information of pore space, such as the porosity and critical pore size of the bulk cementitious matrix. On the basis of mathematical morphology transformations, pore size distribution can be obtained by using a sequence of similarly shaped structuring elements of increasing size (Serra J. 1982). The results from image analysis are an average of 35 locations per sample of 20 × 20 mm for the bulk matrix in each specimen. The physical size of the reference region of each image is 226 μm in length and 154 μm in width, with resolution of 0.317 μm/pixel, corresponding to a magnification of 500x; the sample preparation and imaging procedures are as reported in (Serra J. 1982, Ye G. 2003, Hu J. et al. 2003, Koleva D. A., et al. 2010b, Koleva D. A., et al. 2007b).

2.2. Results and discussion

2.2.1 Potential mapping

Figure 1 presents the evolution of Open Circuit Potentials (OCP) for the corroding cells from groups OPC and BFS with time of conditioning (the OCP values for the identical in preparation and geometry, but immersed in water, control groups OPC and BFS were always more noble than -250 mV SCE).

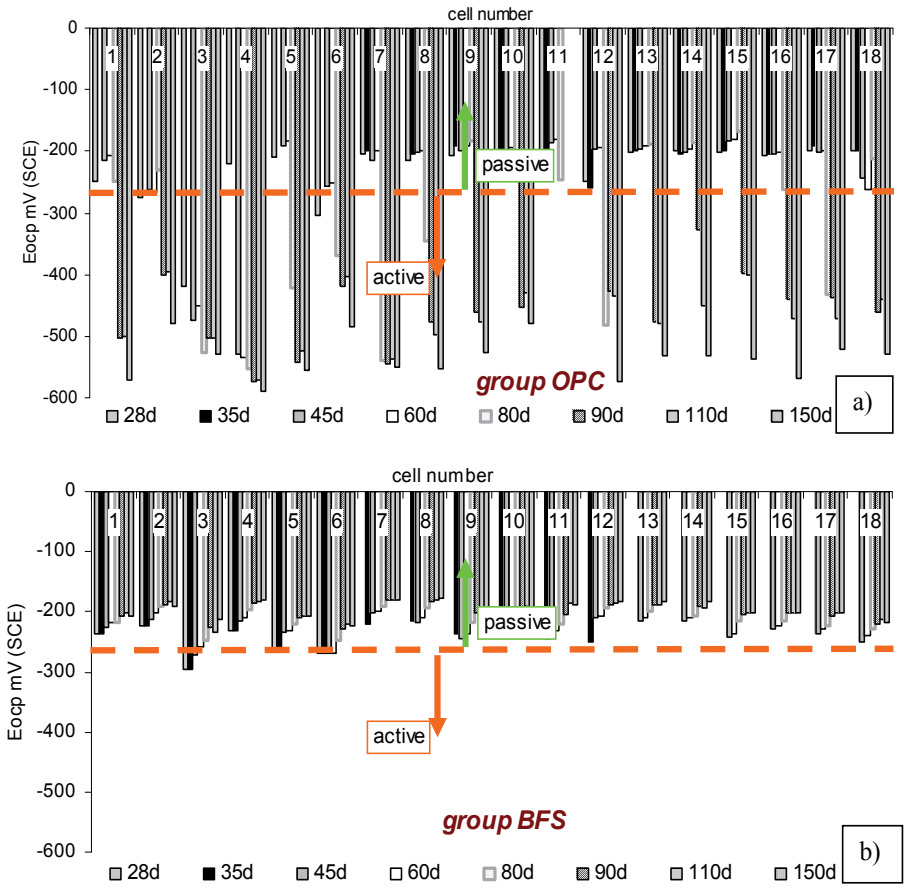

Fig. 1. Evolution OCP values for the corroding OPC and BFS specimens with time

Relevant to steel in reinforced concrete (and according ASTM C876) the evolution of OCP values gives information for the time to corrosion initiation, following the criteria: E_{ocp} > -270 (SCE) mV is interpreted as minimum probability for steel corrosion i.e. passive state, whereas E_{ocp} < -270 mV(SCE) means high probability for corrosion or active corrosion state. The OCP values in Fig. 1, refer to the stages from 28 to 150 days after immersion in 5% NaCl. As seen form the plots at the latest stage of 150 days, all OPC cells exhibit active corrosion behavior with OCP values between -500 to -600 mV (Fig.1a). In contrast, the "corroding" cells from BFS group (Fig. 1b) exhibit OCP values above the threshold for active corrosion i.e. all cells show no evidence of active corrosion (i.e. E_{ocp} > -270 mV SCE) for the hereby presented duration of test of 28 - 150 days.

2.2.2 Potentio-dynamic polarization (PDP)

Figure 3 depicts an overlay of PDP curves for all investigated cases (control and corroding OPC and BFS specimens) for 28 days (first recorded time interval) and 150 days (latest recorded time interval). As seen from the plots, at 28 days similar corrosion potentials (E_{corr}), anodic currents and corrosion current densities (I_{corr}) respectively are recorded for all cases, with a more active behaviour for the corroding OPC and BFS cells and the control BFS cells. At the stage of 150 days corrosion was observed only for the corroding OPC specimens, while all other groups behave similarly to the 28 days stage: the most significant anodic control in the region immediately after E_{corr} is observed for the control specimens OPC, followed by the control and corroding specimens BFS, whereas the corroding specimens OPC present significantly higher corrosion and anodic current densities and cathodically shifted corrosion potential i.e. at the stage of 150 days corrosion is still not initiated in the BFS corroding group. Corrosion current density values (I_{corr}, $\mu A.cm^{-2}$) for the control and corroding OPC and BFS groups were calculated after IR drop correction and using Tafel and Butler-Volmer equation fit of the Autolab interface. The I_{corr} values for the control groups (OPC and BFS) and for the corroding BFS group are very low (lower than 0.1 $\mu A.cm^2$), whereas active behaviour and corrosion current density of approximately 0.4 $\mu A.cm^2$ (and increasing) is relevant for the OPC corroding group.

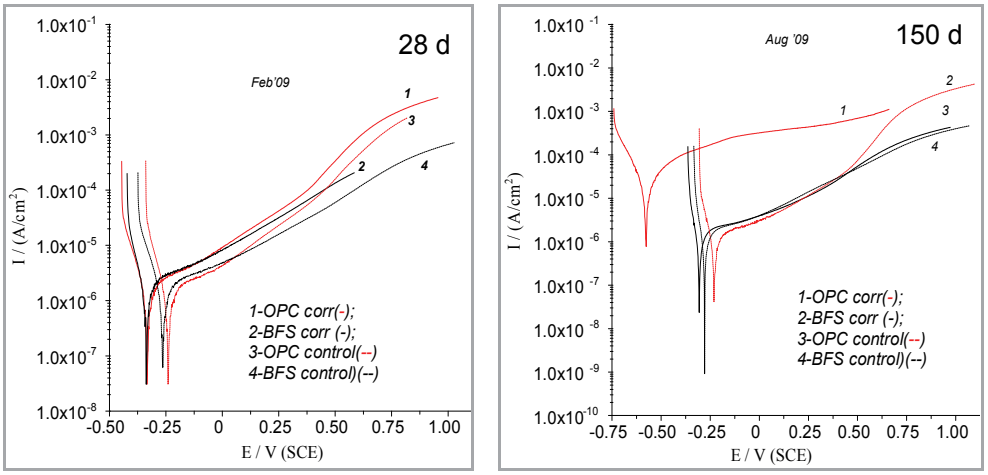

(a) (b)

Fig. 2. PDP curves for OPC and BFS control and corroding groups at 28 (a) and 150 (b) days

2.2.3 Electrochemical impedance spectroscopy (EIS)

EIS is a useful technique for obtaining knowledge of the steel/concrete system as it provides information for both the steel surface (electrochemical parameters) and the concrete bulk matrix (concrete bulk and pore network resistance) (Sagüés A. A., et al. 1995, Feliú V., et al. 2004). Figure 3 depicts the equivalent electrical circuit, used for interpretation and data fitting of the experimental EIS response (the circuit is as previously used and reported in (Koleva D.A., et al. 2007a, Koleva D. A., et al. 2009).

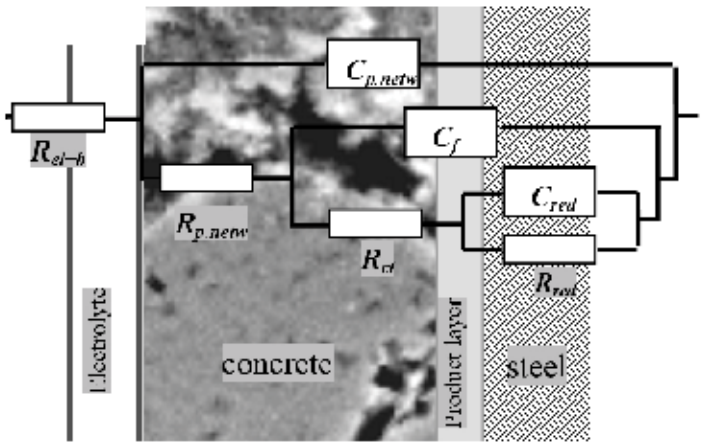

Fig. 3. Equivalent electrical circuit for fitting the experimental EIS response

The elements of the equivalent circuit present the following physical meaning: R_{el+b} is the concrete resistance including the contribution of electrolyte resistance, the latter being negligible compared to the concrete resistance. The first time constant ($R_{p.netw}$,$C_{p.netw}$) is attributed to the properties of the concrete matrix in terms of pore network; the second time constant (R_{ct} , C_f) deals with the electrochemical reaction on the steel surface; the third time constant (R_{red}, C_{red}) is attributed to redox processes, taking place in the product layers on the steel surface. An overlay of the experimental EIS response in Nyquist format for all groups is presented in Fig. 4 relevant to the time intervals of 28 (Fig. 4a) and 150 days respectively (Fig. 4b). Summarised data for the best fit parameters are presented in Table 2.

The high frequency response corresponds to the concrete bulk resistance, including the contribution of electrolyte resistance. The obtained ($R_{b+p.netw}$) values (Table 2) correspond to the overall concrete resistance. For deriving polarization resistance (R_p) from EIS measurements in reinforced concrete (R_{ct} and R_{red} respectively), the medium-low and low frequency limits of the impedance spectra are generally considered, as reported in (Montemor M. F., et al. 2002, Feliú V., et al. 1998, Wenger F., et al. 1990, Fedrizzi L., et al. 2005), previously discussed and reported for reinforced mortar and concrete in (Koleva D.A., et al. 2007a, Koleva D. A., et al. 2009) and used in the present study as well.

At the stage of 28 days similar EIS response in terms of electrochemical behavior was recorded for all cells, evidenced by the close to capacitive behavior at low frequencies (indicating situation of passivity). The result is in line with the PDP curves (Fig. 2a) for this time interval. The response for all OPC and BFS specimens (for all stages) differs in the high frequency domain, denoted to the bulk properties of the cement-based matrix in BFS, compared to OPC. The former matrix is generally reported to be denser compared to the

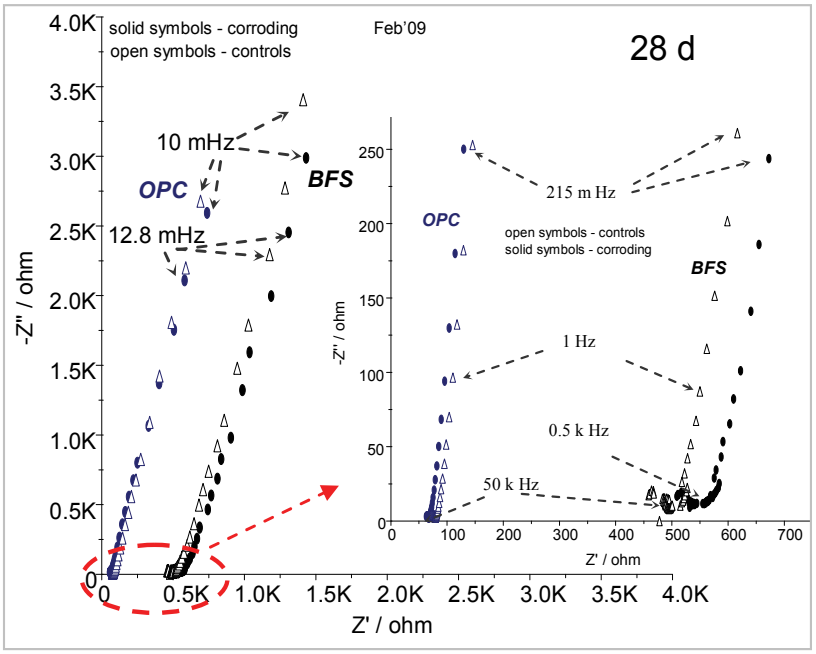

(a)

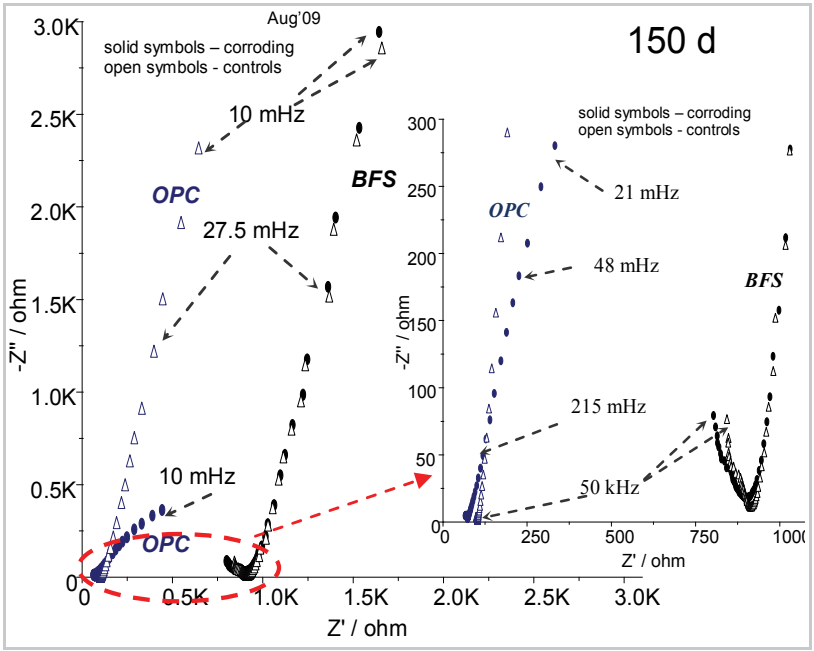

(b)

Fig. 4. EIS response at 28 days (a) for corroding OPC and BFS (solid symbols) and for control OPC and BFS (solid symbols); EIS response at 150 days (b) for corroding OPC and BFS (solid symbols) and for control OPC and BFS (solid symbols)

latter one (Bouikni A. et al. 2009, Giorv O. E., et al. 1979, Manmohan D., et al. 1981, Kumar A.D.M. 1986, Hooton R.D., 1986), which gives the difference in bulk matrix resistance, Table 2 (about 300 kOhm.cm^2 for the BFS groups, compared to approximately 50 kOhm.cm^2 for the OPC groups at stage 28 days). Figure 4b presents the latest stage of the experiment, 150 days, reflecting still passive state for the corroding BFS group and enhanced corrosion activity for the OPC corroding group only (reduced magnitude of |Z| and phase angle drop to below 40^o). Table 2 summarizes all best-fit parameters (for 28 and 150 days). The bulk matrix resistance ($R_{b+p.netw}$) for all specimens (corroding and control groups) increases with time as a result of cement hydration (NaCl slightly influencing the electrical resistivity values), the major difference being denoted to the type of cement i.e. OPC cells (corroding and control) presenting bulk matrix resistance in the range of 55 – 86 kOhm.cm^2, while for BFS cells, this range is 460 - 470 kOhm.cm^2 at 150 days.

Time interval	R_{el+b} kOhm.cm^2	$R_{p.netw.}$ kOhm.cm^2	$C_{p.netw.}$ μF/cm^2	$R_{ct.}$ kOhm.cm^2	C_f μF/cm^2	$R_{red.}$ kOhm.cm^2	C_{red} μF/cm^2	$R_{b+p.netw.}$ kOhm.cm^2
OPC corroding								
28 d	34.98	17.75	2.31	76.90	32.56	817.30	26.92	52.74
150 d	38.65	16.51	1.36	14.59	76.92	48.67	229.49	55.16
OPC control								
28 d	39.42	10.58	1.16	81.92	35.26	869.20	27.56	50.00
150 d	53.25	33.69	2.19	87.36	26.79	1237.40	25.00	86.95
BFS corroding								
28 d	275.03	26.99	3.88E-02	78.39	29.49	984.36	34.62	302.01
150 d	409.70	57.95	1.94E-03	59.28	21.15	1184.82	29.49	467.65
BFS control								
28 d	238.39	22.39	1.94E-03	55.38	22.95	889.78	31.41	260.79
150 d	423.12	51.34	1.94E-03	84.24	26.15	1224.60	27.31	474.46

Table 2. Best-fit parameters, derived on basis of experimental EIS results, using simulation and fitting procedures and the equivalent circuit: $R_{el+b}(C_{p.netw}(R_{p.netw}(C_f(R_{ct}(C_{red}R_{red})))))$ (relative error for each best-fitted parameter 0.2 to 3.0%)

The charge transfer resistance (R_{ct}) decreases for the OPC corroding cells only (attributed to enhanced corrosion activity in this group), whereas no active behaviour is observed for the BFS corroding group, the latter behaving as a control group (the best-fit parameters in Table 2 are an average of 18 replicates per group). Considering the investigated system, the proposed equivalent circuit (Fig. 3) and the derived best-fit parameters (Table 2) the following can be summarized: the first time constant ($R_{p.netw}C_{p.netw}$) is related to the pore network of the bulk matrix since the capacitance values are low (range 0.002 to 2.4 μF.cm^{-2}), hence can not be denoted to electrical double layer on the steel surface or to redox-reactions (Feliú V., et al. 2004, Dhoubi L., et al. 2002). The second time constant ($R_{ct}C_f$) is related to the charge transfer resistance and double layer capacitance at the steel surface, since the capacitance is more or less stable with time for the control groups and increases for the corroding groups, which is consistent with the drop in charge transfer resistance for the latter groups. The third time constant ($R_{red}C_{red}$) is relevant to the transformations and contribution of the product layers on the steel surface; capacitance vales for the corroding group OPC being significantly higher than the control groups, attributed to the spreading of corrosion damage on a larger steel surface area with time of conditioning.

The data derived from potential mapping, PDP and EIS tests of OPC and BFS corroding and control specimens denote for active corrosion state in the OPC corroding group only. In contrast, the BFS corroding group behaves as a control one. According to electrochemical behavior, steel corrosion in this group is still not initiated at the stage of 150 days. Obviously, the altered microstructural properties of BFS containing specimens play a significant role in corrosion delay. In order to verify this statement and elucidate the reasons for the observed electrochemical behavior, a bulk matrix investigation is required, which will be discussed in the following sections.

2.2.4 Bulk matrix properties

The previously discussed electrochemical behaviour is supported by wet chemical analysis for chloride concentration in the cement paste, adjacent to the steel surface. The analysis was performed in a way as schematically shown in Fig. 5 (bottom, middle and top of the cylinders). The result is approximately 5 times higher chloride concentration (in wt.% per dry cement weight) in the OPC corroding cells, compared to the BFS corroding cells. Two considerations are hereby relevant: on one hand, the matrix permeability of the BFS cells is most likely significantly lower; secondly, although low, the chloride concentration in the BFS cells is at the threshold for corrosion initiation (accepted to be between 0.2 and 2 wt%, (Petterson K. 1994, Page C. L. 2002, Vassie P.R.W. 1984, Glass G.K., et al. 1997), yet corrosion in the BFS cells was not observed. Apparently, not only chemical composition, but also the microstructural properties of the matrix play a distinctive role for the corrosion initiation (or lack thereof) and electrochemical behaviour of the embedded steel. The delay in corrosion initiation in the BFS specimens (as evidenced by potential mapping, PDP and EIS response) is attributed to a modified cement-based matrix. As a result, at 150 days of conditioning, chlorides are not yet present at the steel/cement paste interface and corrosion in the BFS specimens is still not initiated within the hereby investigated period.

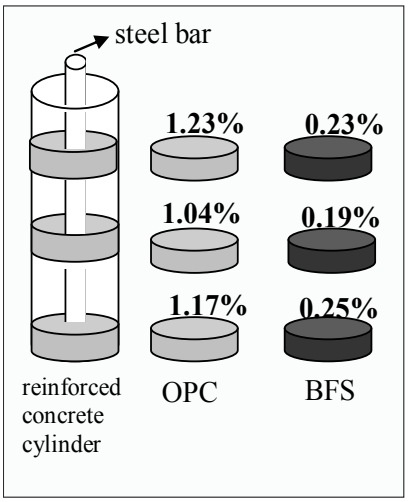

Fig. 5. Schematic presentation of the reinforced concrete cylinders and the location of the samples, taken from each investigated case for chloride wet chemical analysis and chloride concentration in wt.% per dry cement weight (for each specimen type, the samples are taken from identical locations of the cylinders)

With respect to microstructure of the bulk matrix, there are three main mechanisms/processes, influencing the microstructural properties: cement hydration with aging, the influence of NaCl, which accelerates cement hydration and causes initial densification of the bulk porosity (Suryavanshi A.K., et al. 1995, Díaz B., et al. 2006), and third – the corrosion process itself (volume expansion of corrosion products induces micro-cracking). Since reinforced concrete is a highly heterogeneous material and considering the variety and complexity of external influences in this study, it is inappropriate to claim absolute values for each parameter. Hence, the analysis would be better considered as comparative investigation between the different concrete mixtures and regimes of conditioning, based on the fact that all investigations were performed in exactly the same manner for each specimen.

2.2.5 Bulk matrix microstructure: fundamental aspects

The electrolytic path in reinforced cementitious systems is dependent on the kinetics of ion transport mechanisms. These mechanisms, in addition to the cement hydration and the morphological alterations, are affected by the pore size distribution and the pore connectivity of the bulk concrete material. The original BSE image (or a selected area, similar to the presented in Fig. 6a micrographs, provided the analysis should exclude the aggregate

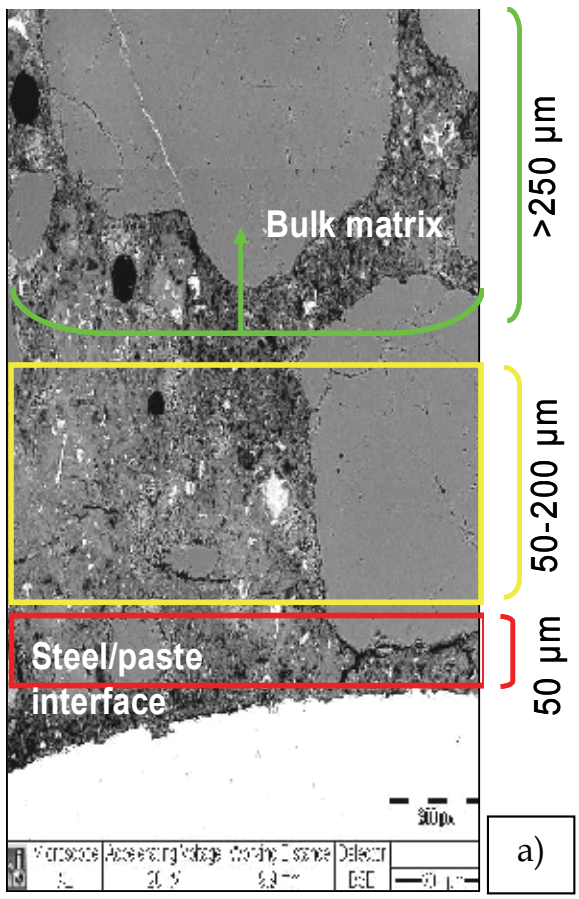

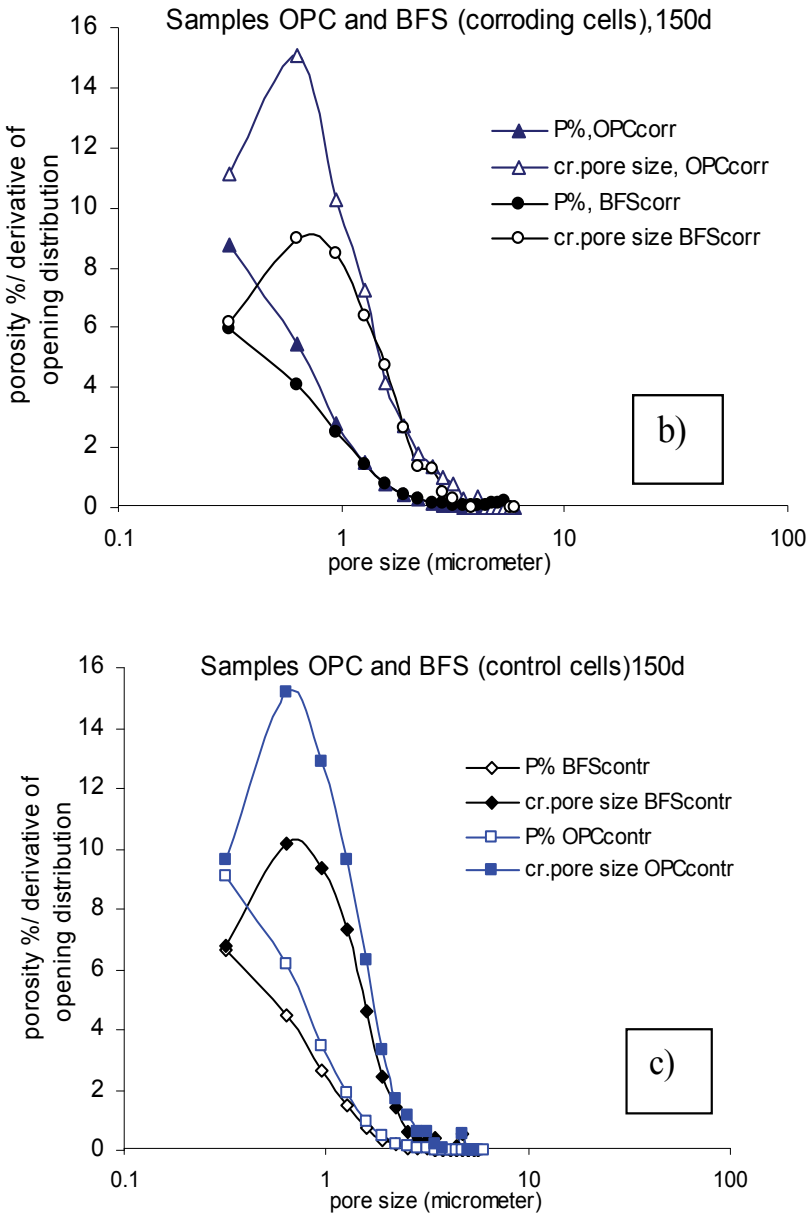

Fig. 6. SEM micrographs (mounted images) of the steel/cement paste interface and into the bulk matrix (a); porosity/pore size distribution for corroding groups OPC and BFS (b) and control groups OPC and BFS (c)

particles in the image, if any) is segmented by applying a gray-level threshold to create a binary image, reflecting the pore phase (Ye G. 2003). The binary image is then subjected to quantitative image analysis for derivation of structural parameters (pore size distribution, critical pore size, pore connectivity etc.). The "opening distribution" technique was used, whereby the binary image is opened by a series of squares of increasing size (Hu J. et al.

2003). The cumulative pore size distribution curve is obtained by plotting the pore area fraction after an opening operation versus linear dimension of the structuring element (as presented in Fig. 6b)c)). This gives a type of "size" classification in the case of an interconnected structure, like pore space in concrete. The critical pore size lc can be conceived as the diameter of the pore that completes the first interconnected pore pathway in a network, developed by a procedure of sequentially adding pores of diminishing size to this network. The critical pore size l_c is a unique transport length scale of major significance for permeability properties and can be associated with the inflection point of the cumulative pore size distribution curve (Fig. 6b)c)).
In this research, relevant to morphological aspects of the pore structure and ion transport, the pore interconnectivity (defined as the fraction of connected pores out of the total pore area) is used in terms of pore distribution density (PDD), as PDD contains information on both pore size and connectivity of pore space and gives the permeability of the matrix. For more details on the fundamental aspects and image analysis of cement-based materials, including mortar, plain concrete and reinforced concrete, please see (Serra J. 1982, Ye G. 2003, Hu J. et al. 2003, Koleva D. A. 2007c).

2.2.6 Correlation of pore structure characteristics and EIS parameters

A set of SEM images on polished sections were made and were further subject to image analysis. The hereby discussed porosity and pore size distribution refer to the bulk matrix only. The structural parameters were averaged from at least 35 locations in the bulk matrix (sample of 2x2 cm). The final data were considered after performing a statistical evaluation in terms of frequency of occurrence (% distribution) vs class (porosity in %) for the samples in each regime. The calculated pore size distribution and critical pore size are presented in Fig.6b)c) for the bulk matrix (> 250 μm away from the steel surface) for specimens groups OPC and BFS corroding (b) and OPC and BFS control (c). The highest bulk porosity was recorded for the control specimens OPC (9.06 %), followed by the corroding OPC specimens (8.78%). The lowest porosity was observed for the corroding specimens BFS (5.92%), the control BFS specimens exhibiting slightly higher porosity of 6.62%. The critical pore size for all investigated groups is similar (approximately 0.634 μm). The porosity difference between OPC and BFS corroding (and control) specimens (of 2-3%) could not be responsible for the significantly lower chloride concentration in the corroding BFS, compared to corroding OPC groups (Fig. 5). Apparently porosity alone is not the factor determining the significantly different electrochemical behavior (Figs. 1, 2 and 4), delayed chloride ingress and corrosion initiation respectively in the BFS corroding cells. What has to be considered is the pore interconnectivity in the cement-based matrix and thus the matrix permeability. Figure 7a) presents the derived from image analysis (for hydration stage 150 days) porosity and matrix permeability.
As seen from the plot, the almost equal porosity in specimens OPC control and OPC corroding (higher than both BFS groups) does not result in similar pore interconnectivity and permeability respectively. The specimens OPC corroding are characterized with lower permeability (8.02×10^{-10} m/s), compared to specimens OPC control (1.29×10^{-9} m/s). The result for the former case is denoted to the influence of NaCl, which initially accelerates cement hydration and leads to a larger portion of isolated and/or disconnected conductive paths (Koleva D. A., et al. 2007b, Suryavanshi A.K., et al. 1995, Díaz B., et al. 2006, Koleva D. A., et al. 2008b, Koleva D. A., et al. 2008c). At this stage steel corrosion is at a low to moderate stage (as evidenced by the derived corrosion current densities for the group OPC

corroding), hence a significant contribution of micro-cracking due to volume expansion of corrosion products at the steel/cement paste interface is not observed. Therefore, the permeability of the corroding specimens OPC ends up still lower than the control specimens OPC. Figure 7a) depicts the slightly lower porosity values for both control and corroding groups BFS, but significantly lower (than the OPC groups) permeability values (~ 4×10^{-10} m/s).

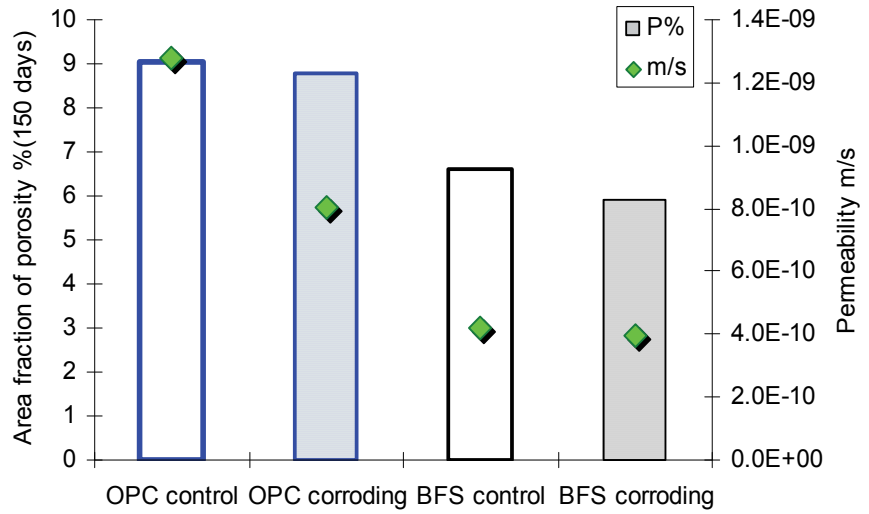

(a)

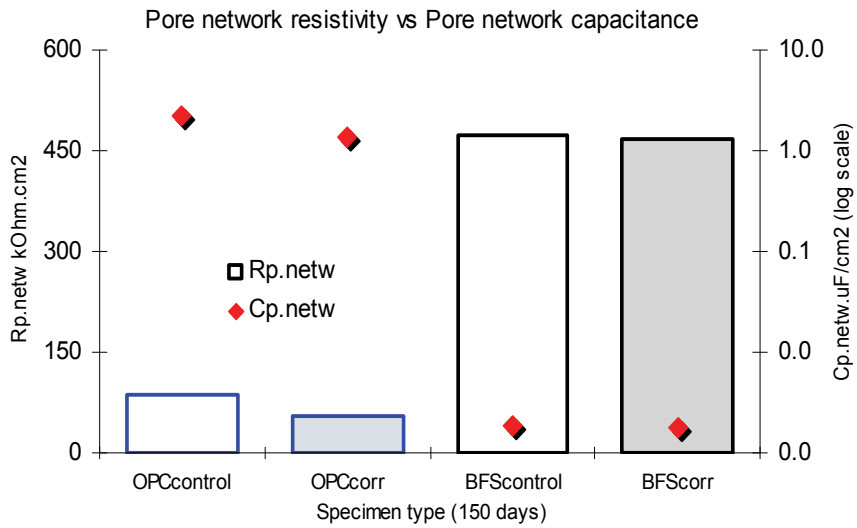

(b)

Fig. 7. (a) correlation of porosity (%) and permeability (m/s), derived from image analysis for all investigated groups at the stage of 150 days; (b) Pore network resistivity versus pore network capacitance (as derived by EIS) for all studied groups, stage 150 days

Further, a correlation can be made between pore network parameters (Fig. 7a) and electrochemical (EIS) parameters, mainly pore network capacitance ($C_{p.netw}$) and pore network resistance, $R_{p.netw}$ (Fig. 7b). The higher porosity (P%) and permeability (m/s) in OPC control and corroding cells (Fig. 7a) corresponds to the highest $C_{p.netw}$ and lowest $R_{p.netw}$ (Fig. 7b), the values being lower for OPC corroding cells, compared to OPC control cells (Fig. 7b). The lowest $C_{p.netw}$ (1.94×10^{-3} $\mu F.cm^{-2}$, Fig. 7b) corresponds to the lowest permeability values, derived for specimens BFS (both corroding and control groups, Fig. 7a). The result is very well in line with the derived global bulk electrical resistivity of the matrix in BFS as well (Table 2). Consequently, the BFS matrix in the corroding specimens would be characterized with a larger pore surface area but also increased portion of disconnected and isolated conductive pore pathways (increased pore network resistance). The capacitance values for BFS corroding cells are significantly lower than those for the OPC corroding cells, therefore a comparison of pore network permeability and interconnectivity between OPC and BFS specimens can be reliably derived on the basis of pore network capacitance and resistance. Consequently (and moreover, after verification with microstructural analysis), it can be stated that EIS is a powerful, non-destructive technique for evaluation of pore network parameters. Combined with the electrochemical parameters, derived for the embedded steel, EIS allows a thorough evaluation of a reinforced concrete system.

Summarizing, this paragraph discussed the corrosion behaviour of reinforcing steel in OPC and BFS concrete, subjected to chloride-induced corrosion (5% NaCl), in comparison with control cases for both concrete types. Additionally, the electrochemical parameters for the embedded steel were correlated with the microstructural parameters and properties of the bulk concrete matrix. After 150 days of conditioning, corrosion was not initiated in the BFS reinforced concrete, whereas active behavior was observed (starting at 40 – 45 days) for the steel in OPC concrete. The higher corrosion resistance in BFS reinforced concrete is denoted to decreased pore-network interconnectivity, evident from the significantly lower pore network capacitance and higher pore network resistance, as derived from EIS and verified on the basis of microstructural analysis. In that sense EIS appears to be a valuable tool for non-destructive and thorough evaluation of not only the electrochemical behavior of reinforcing steel, but also for detailed investigation of the bulk cement based matrix.

3. OPC reinforced mortar, using red mud as partial cement replacement

Corrosion in reinforced concrete is a major and costly concern, arising from the higher complexity of involved phenomena on different levels of material science (electrochemistry, concrete materials, etc.) and material properties (macro/micro/ nano). As previously introduced, for a thorough evaluation of a reinforced cement-based system (as reinforced concrete) an integrated approach of electrochemistry and concrete material science is necessary in order to thoroughly evaluate corrosion-related phenomena. Moreover, when a modified cement-based material is to claim superior performance, the synergy of various fundamental aspects and experimental tests is a must.

This paragraph deals with a brief introduction of a sustainable solution for corrosion control in reinforced concrete, by using a waste from the aluminium production (i.e. Red Mud), as partial replacement of the cement fraction in the reinforced concrete system (for the elaborated and complete work on red mud-containing mortar and concrete, please see (Koleva D.A. 2011)). The waste "red mud" (RM) is generated during aluminium production

from bauxite. The annual production of 1 tone of metallic aluminium generates about 2 tones of red mud (Ayres R.U, et al. 2001). The disposal of this alkaline waste is expensive (up to 1–2% of the alumina price); the enormous quantity of red mud generated every year (about 66 million tones) posses very serious and alarming environmental problems (Mymrin V., et al. 2003). Consequently, research on ways of making use of this residue is of significant importance.

Red mud is reported to increase steel passivity in alkaline solutions (pre-treatment procedure) (Collazo A.,et al.2007, Díaz B., et al. 2004); "red mud" additions to cement-based materials are reported to result in mixtures, shielding X-ray radiation or heavy metal (and other toxic substances) binding effects (Amritphale S.S, et al.2007, Cengeloglu Y, et al. 2007, Yong Liu, et al.2007), while maintaining sufficient mechanical properties (Tsakiridis P.E., et al. 2004).

To this end, the objective of an ongoing research project is to investigate the application of "red mud" as an additive for reinforced concrete, aiming to achieve corrosion protection on one hand, to eventually improve the concrete bulk microstructure on the other and thus to finally contribute to cement cost reduction and waste utilization in an ecologically friendly manner. This paragraph reports on the electrochemical behaviour of steel in red mud-modified mortar and the microstructural characteristics of the bulk matrix. Further, an illustration for the recorded superior steel corrosion performance in the presence of wastes is provided by means of microscopical analysis and x-ray techniques (the recorded parameters for the full duration of the test of 310 days, including X-ray tests (XRD and XRF) and a detailed presentation of the electrochemical measurements is reported in (Koleva D.A. 2011)). The aim of this paragraph is to add clarification and give another example (in addition to paragraph 2) for the implementation of electrochemistry and concrete material science in evaluating a reinforced cement-based system, particularly in the presence of wastes.

3.1 Experimental materials and methods

Materials: Reinforced mortar cylinders (d = 3.5 cm; h = 20cm) were cast from OPC CEM I 32.5, cement/sand ratio of 1:3 and water/cement ratio of 0.5. Four groups (5 replicates per group) were monitored: two control groups (non-corroding) with and without red mud, denoted as RMw and OPCw respectively, and two corroding groups, with and without red mud, denoted RMn and OPCn. All specimens were cured for 7 days in fog room (20 ^{o}C and 98% RH) and maintained in lab air further on. An external solution of 10 % NaCl was used as a chloride-induced accelerator for the corroding groups (the specimens were 1/3rd of height immersed in the solution; the control specimens were immersed in tap water). Red mud was added (after drying at 105^{o}C and grinding to cement finesse) as a 20% cement replacement for the RMw and RMn specimens. The chemical and mineralogical composition of red mud depends on the processed bauxite, the aluminium production process itself and the geographical location (Li L.Y 1998). The red mud used in this study was supplied from Suriname (XRF analysis of the received supply gives major contributions of: Al_2O_3 29.1 wt.%, Fe_2O_3 24.9 wt.%, Na_2O 14.3 wt.%, SiO_2 20.2 wt.%, CaO 3.5 wt.%). The steel re-bars (construction steel FeB500 HKN, d=0.8cm, h=10cm) were embedded "as received" i.e. there was no preliminary treatment of the bars before casting (casting procedures, cement composition (OPC CEM I) and steel properties are as previously described with relevance to paragraph 2). Methods: The electrochemical methods, microscopical investigation and

image analysis employed in this part of the study are as previously listed in paragraph 2, section 2.1.

3.2 Results and discussion

3.2.1. Electrochemical behaviour

Open circuit potential (OCP) mapping and steel response with external from 7 days (initial lab conditioning) until 136 days are presented as follows. Figure 8 depicts the potential/time history (data interpretation as previously discussed in paragraph 2 and according ASTM C876) for two of the 5 replicates per specimens' group.

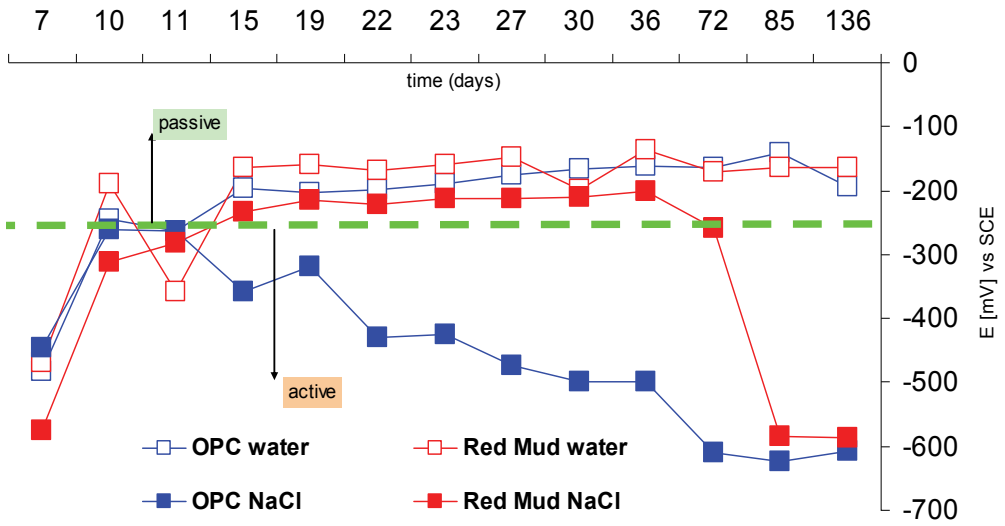

Fig. 8. OCP readings for corroding (OPC NaCl and RedMud NaCl) and control (OPC water and RedMud water) reinforced mortar from initial (7 days) until 136 days of treatment

As seen from the plot, an initially active behavior was observed for all cells (Fig. 8, 7 days stage), which actually corresponds to the end of the mortar "fog room" curing and the start of the lab conditioning (water for the control cells and 10% NaCl immersion for the corroding cells). Fundamentally this initial activity is due to the presence of galvanic micro-cells on the steel surface, formed as a result from steel heterogeneity (cathodic and anodic areas). Further, formation of the passive film takes place (starting 10-15 days) and as long as it remains intact, there will be no activity on the steel surface. In the event of chloride ions penetration through the mortar bulk matrix and arrival at the steel/cement paste interface (as in the case of specimens OPC NaCl, Fig. 8), corrosion will be initiated due to the disruption of the passive film in the presence of chlorides. What is interesting to note is the OCP evolution of the red mud containing corroding specimens (RM NaCl): in the period of 15 to 72 days of conditioning they behave as control (non corroding) cells, since their OCP values are more anodic than ~ -300 mV (SCE), whereas active corrosion was observed in the corroding OPC (OPC NaCl) specimens, which exhibit significantly lower (more cathodic) potentials. In other words, OCP evolution shows the significant corrosion delay in the presence of RM, which is further supported by the potentio-dynamic polarization (PDP) tests (Fig. 9).

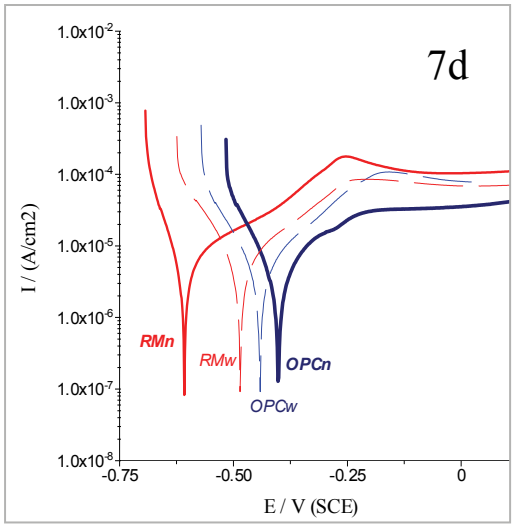

(a)

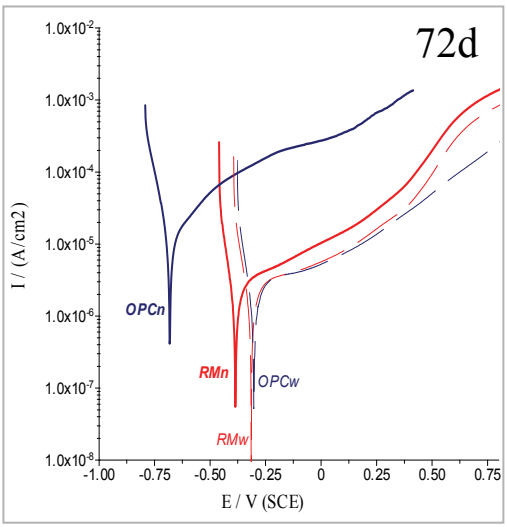

(b)

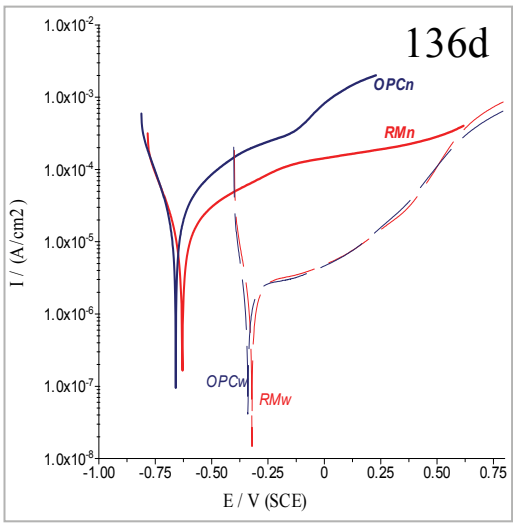

(c)

Fig. 9. PDP scans for all hereby investigated cells after 7 days (a), 72 days (b) and 136 days (c) of treatment

PDP was performed on intervals for all investigated specimens. Figure 9 depicts an overlay of PDP scans for all investigated groups at 7 days (a), 72 days (b) and 136 days (c). As seen from the plots, initially the RM containing groups present a slightly more active behaviour, corresponding to the initial alterations in the passive layer as previously discussed and recorded via OCP mapping (Fig. 8). Further and until 72 days (Fig. 9b) passive state was observed for the control OPCw and RMw cells, along with passive state for the corroding otherwise RMn(NaCl) specimens. The behaviour of the former two groups is as expected; for the latter group, although a transition from passive to active behaviour would be

expected at 72 days (via the recorded OCP values, Fig. 8), the response with external polarization shows performance close to the control cases. In contrast, for the corroding specimens OPCn(NaCl) significantly higher corrosion and anodic currents are recorded at 72 days of stage (Fig. 9b). For the latest hereby reported interval (136 days), the corroding RMn(NaCl) specimen is already active (Fig. 9c), but still exhibiting lower anodic currents, compared to identically conditioned, corroding specimen OPCn(NaCl).

As evident from the electrochemical measurements, 20% red mud as cement replacement results in corrosion delay of approximately 5 times in the very aggressive environment of 10% NaCl. Similarly to BFS (as discussed in paragraph 2), the presence of RM in reinforced mortar (and concrete respectively) will account for an increased corrosion resistance in the wastes-modified systems. In order to clarify the responsible mechanisms and related phenomena, microstructural analysis of the bulk cementitious matrix is performed and discussed in what follows.

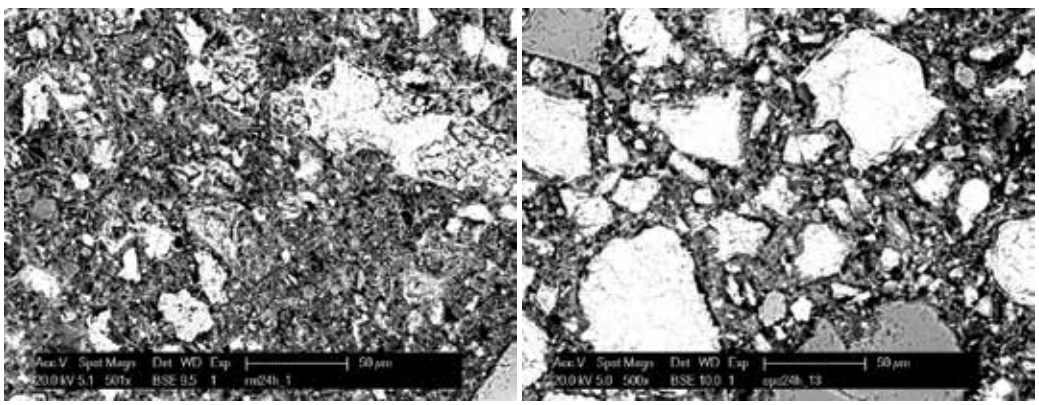

(a) (b)

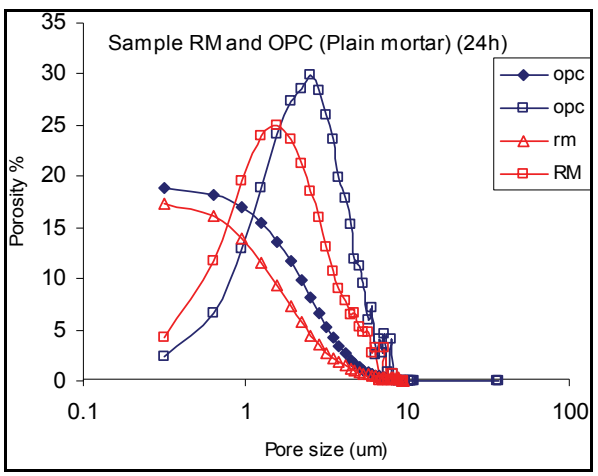

(c)

Fig. 10. Micrographs of the bulk cementitious matrix in OPC (a) and RM (b) plain mortar specimens after 24h hydration; porosity and pore size distribution for OPC and RM specimens at 24h hydration age (c)

3.2.2 Bulk matrix properties

Microstructural parameters (bulk matrix) were initially derived for plain (not-reinforced) mortar as a preliminary test (using identical to the reinforced mortar mixtures). Figure 10 depicts micrographs of the bulk matrix at 24h hydration age for a control OPC specimen (Fig. 10a) and control RM-containing specimen (Fig. 10b).

The recorded porosity and pore size distribution are shown in Fig. 10c). As seen from the plots, after 24h cement hydration the RM specimen presents slightly lower porosity (17.3%), compared to the OPC specimen (18.7%) and reduced pore size for the former, compared to the latter (compressive strength at 24h was also recorded as an average of three replicates per mortar type, resulting in similar values of 13 MPa at 24h). The above results are not entirely in line with the expectations i.e. since red mud is reported to have a pozolanic activity it was expected that the difference in porosity will be more substantial. Further, a reduced porosity and pore size would account for reduced permeability of the cementitious matrix i.e. reduced chloride penetration would delay corrosion initiation. Therefore, porosity alone is not the only factor, causing microstructural alterations in the red mud containing cells, which apparently resulted in inhibition of corrosion. Further, porosity and pore size distribution were recorded for the bulk mortar matrix of the reinforced mortar specimens at 136 days. Figure 11 presents summarized bulk porosity values (a) and pore size distribution (b) for non-corroding (Ow and Rw) and corroding (On and Rn) mortar cells without (designation O) and with (designation R) red mud. It is obvious that 20% addition of red mud to the cement based matrix induces reduction of porosity, but not as pronounced as expected. The corroding cells from both types (Rn and On) would normally have lower porosity, compared to the relevant control specimens (Rw and Ow), since chloride is known to be a hydration accelerating factor and thus initially reduces porosity of the bulk matrix (Koleva D. A. 2007c). However, when chloride-induced corrosion is involved, the corrosion-induced cracking in the matrix (as consequence from formation and volume expansion of corrosion products at the steel/cement paste interface) contributes to the pore structure performance.

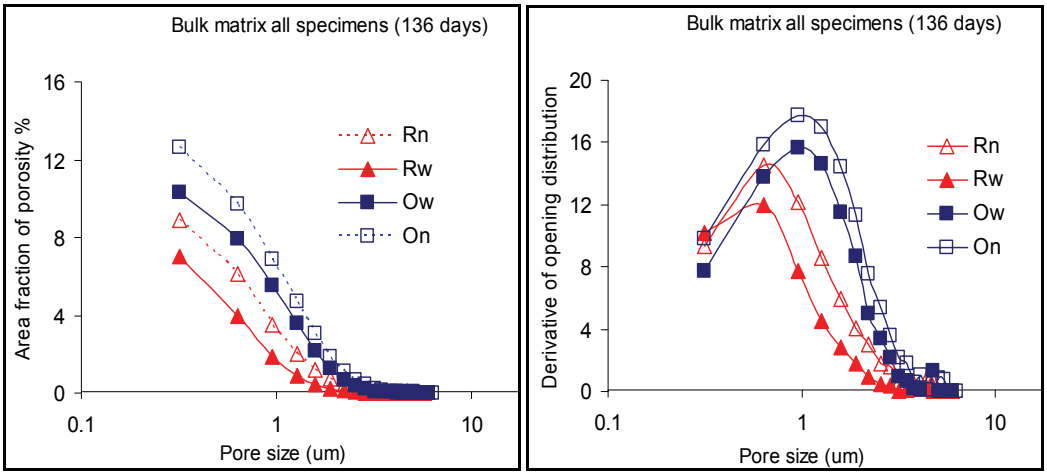

Fig. 11. Porosity (left) and pore size distribution (right) for reinforced mortar with and with and without red mud at 136 days of hydration age

Finally, if a comparison is made between all investigated specimens, the lowest porosity was recorded in the control specimens with red mud (Rw), almost equal to the corroding

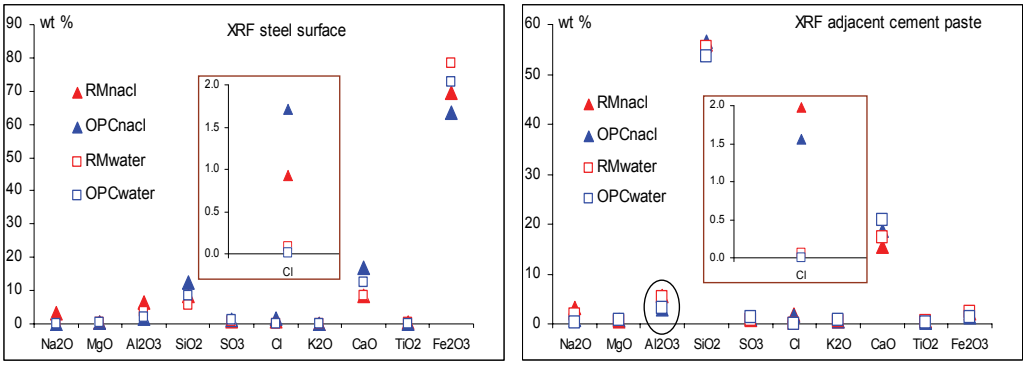

Fig. 12. XRF analysis of the product layers on the steel surface (left) and the adjacent cement paste (right) for all investigated specimens

specimen with red mud (Rn) i.e. red mud decreases bulk porosity in both cases. The highest recorded porosity (due to corrosion induced cracking) was in the corroding specimen without red mud (On), which was about 2% higher than the control one without red mud (Ow). Overall, it can be stated that the difference of 2.5 – 3% in porosity, relevant to all investigated conditions at 136 days of age, would not be the main and only factor, influencing to such a significant extent the corrosion resistance properties and behaviour.

The most plausible mechanism for the beneficial influence of red mud in terms of corrosion resistance is a combined effect of both red mud properties and microstructural changes: Red mud consists of a mixture of caustic insoluble minerals, originally present in bauxite, from which hematite (Fe_2O_3) has a major influence on the corrosion related phenomena (hematite is approximately 25% present in the used red mud) i.e. the presence of Fe^{3+} indicates a certain degree of redox activity (Ramanujan S. 1962, Skoulikidis T., et al.1992) on the steel surface and thus favours steel passivation. Furthermore, a possibly increased chloride binding mechanisms is relevant for the mixtures, containing red mud, as evidenced by XRF analysis on the steel surface and the adjacent cement paste (Fig. 12). As seen from the plots, the chloride concentration on the steel surface in corroding specimens RMNaCl is 1.5 times lower than the RM-free specimen OPCNaCl (Fig. 12, left), however, the chloride concentration in the cement paste, adjacent to the steel surface, is higher for the former (RMNaCl) and lower for the latter (OPCNaCl) case (Fig. 12, right).

Figure 13 presents light microscopy images of the steel surface (right column) and the immediately adjacent cement paste (left column) for OPC corroding (top row) and RM corroding (bottom roll) specimens after 136 days of conditioning. Well visible is the significant corrosion damage (localised corrosion) in the RM-free specimen OPC. The corrosion products in the corroding specimens OPC volume expanded and deposited (penetrated) the adjacent cement paste (Fig. 13 top left). In contrast, for the RM corroding specimens, at the stage of 136 days only minor corrosion product accumulation was observed on the steel surface (Fig. 13); the corrosion products did not yet propagate and deposit in the adjacent cement paste (Fig. 13. bottom left). Considering also the ESEM microscopical investigation (again, directly on the steel surface and the adjacent cement paste (after 136 days) - Fig. 14), showing a well adhered product layer for control conditions in the presence of red mud (compare Fig. 14 a) and b)) and minimum or non corrosion products for the red mud-corroding cases (compare Figs. 14c) and d) and Fig. 13 b) and d)), it is obvious that several aspects are responsible for the positive effect of red mud on

corrosion resistance in reinforced concrete. In addition to slightly altered microstructural properties and apparently increased chloride thresholds, the properties of red mud are playing a role in the observed corrosion mechanisms.

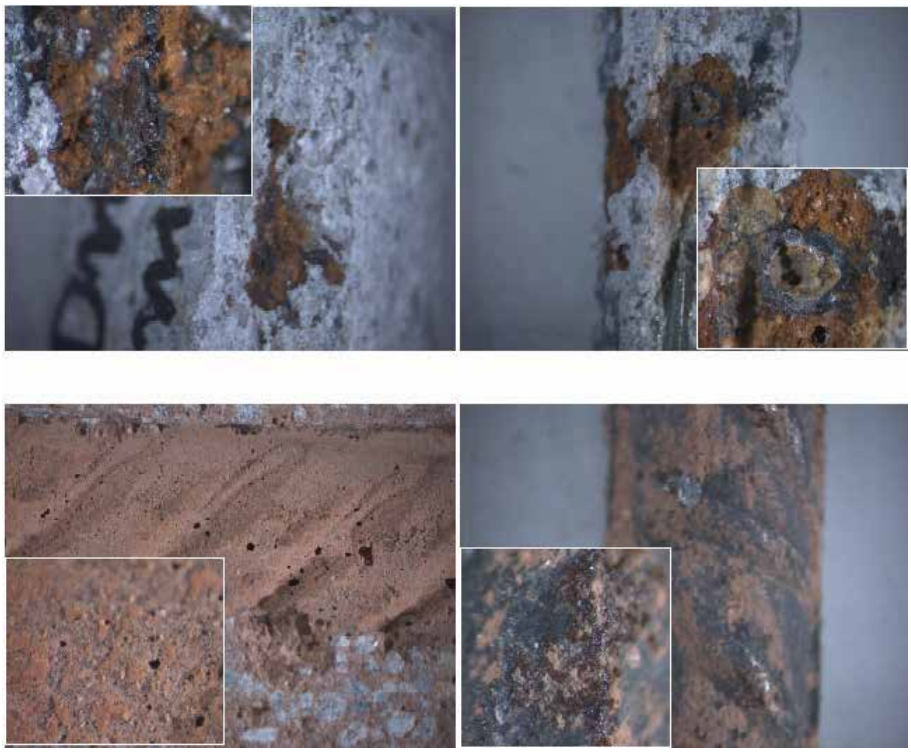

Fig. 13. Light microscopy of the cement paste, adjacent to the steel reinforcement (left) and steel surface (right) for corroding cells OPC (top row) and corroding cells RM (bottom row)

The surface charge of the RM particles is of significant importance for the chemical and physicochemical alterations in a cement-based matrix. As reported (Chvedov D., et al. 2001), there are ionized surface (OH^-) groups on the RM particles' surface allowing them to perform as active sites and thus favouring their adhesion on a metallic surface (Díaz B., et al. 2004, Koleva D.A., et al. 2008d, Collazo A., et al. 2005). Thus, the steel surface in the red mud containing corroding specimens will have increased corrosion resistance due to a simple barrier effect of the adhered RM layer. Additionally, the surface groups can acquire protons without changing the pH of the surrounding medium i.e. reported are buffering effects of the RM particles (Chvedov D., et al. 2001, Stumm W. 1995, Atun G., et al.2000). These latter effects will additionally delay corrosion initiation/corrosion propagation (as actually observed, no significant corrosion layer was formed on the steel surface (Figs. 13, 14d) or deposited in the adjacent cement matrix (Figs. 13, 14d) when red mud was admixed in reinforced mortar. Finally, the negatively charges RM particles can act as adsorption sites for Ca^{2+} or other positively charged ions, thus capture Cl^- (similar effect is also reported in (Collazo A., et al. 2005) as evident from XRF analysis (Fig. 12). Summarizing, this paragraph briefly discussed an eco-friendly approach to corrosion control via waste utilization, in particular a largely generated waste from the aluminum production (red mud). Reinforced

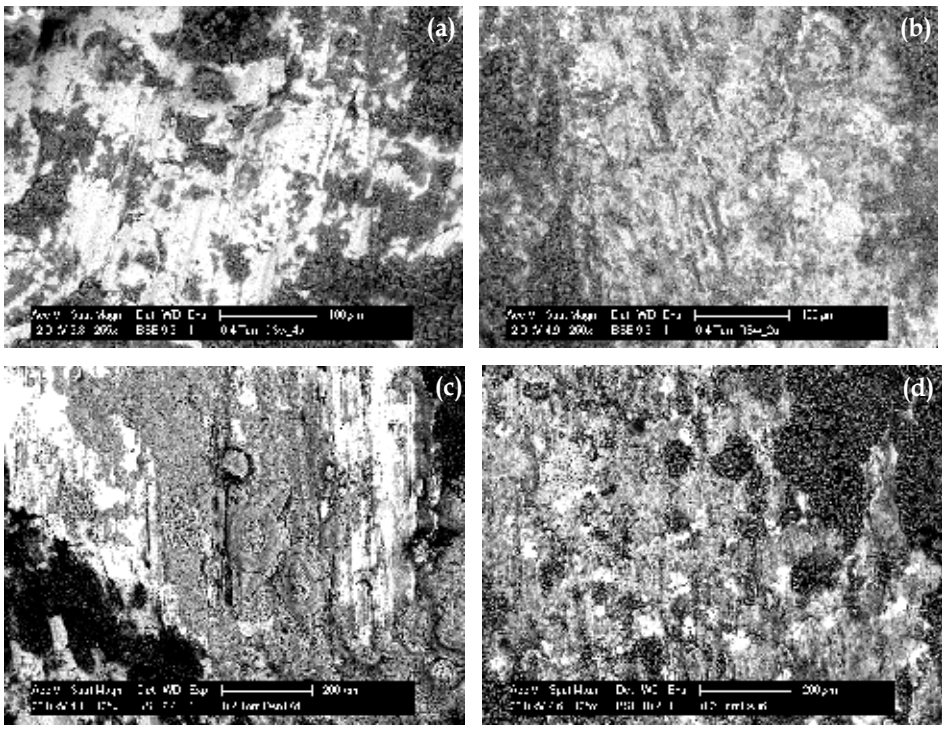

Fig. 14. ESEM micrographs for the steel surface (and product layers respectively) for control OPC and RM cells (a,b) and corroding OPC and RM cell (b,d)

mortar, using 20% cement replacement with red mud was evaluated in terms of steel corrosion behaviour and bulk matrix properties. The electrochemical monitoring (7 until 136 days) proves the higher corrosion resistance of Red Mud containing reinforced mortar in highly aggressive environment (10 % NaCl) i.e. 20% red mud (as cement replacement) leads to approximately 5 times delay in corrosion initiation (compared to red mud – free mixtures). Slightly lower porosity and pore size distribution was recorded for the bulk matrix of the red mud – containing mortar (without calcination of the red mud before admixing). The positive effect of red mud lies in the combined influence on microstructural properties, redox activity and thus favouring steel passivation and the peculiarities (as surface charge) of the red mud particles themselves. Similarly to BFS cement mortar/concrete (paragraph 2) this paragraph illustrated the importance of an integrated approach (electrochemistry and concrete material science) for a thorough investigation of a reinforced cement-based system and for clarifying the phenomena, responsible for the observed behaviour in the relevant conditions.

4. Conclusions

This chapter discussed and gave examples for the integration of electrochemical methods and microstructural investigation in reinforced cement-based materials within conditions of chloride-induced corrosion. An eco-friendly approach to corrosion control in reinforced cement-based systems, by involving waste utilization (slag, from the steel production and red mud, from the aluminum production) was also discussed, presenting material properties and materials interactions in the context of increased corrosion resistance.

For the hereby reported period of 28 to 150 days for reinforced concrete and 7 until 136 days for reinforced mortar, the specimens cast with OPC CEM I only exhibit active corrosion behaviour and reduced corrosion resistance, whereas passive state or minimal corrosion activity was recorded for the identically conditioned BFS (CEMIII) and RM (cement replacement with red mud) specimens.
For reinforced concrete (paragraph 2), in the BFS specimens corrosion at the stage of 150 days was still not initiated (corrosion medium of 5% NaCl) and they behave as "passive" (control) cells. The beneficial effect of BFS in terms of delay in corrosion initiation, is obvious: significantly higher corrosion resistance (impedance |Z| and derived Rct values respectively), no chlorides accumulated in the immediate vicinity of the steel surface, increased concrete resistivity. Apparently, the bulk cement matrix in the BFS specimens plays a significant role in the observed behaviour. Additionally, the electrochemical parameters for the embedded steel were correlated with the microstructural parameters and properties of the bulk concrete matrix. The higher corrosion resistance in BFS concrete is not related to the postulated lower porosity, or higher chloride binding capacity, but is denoted to significantly lower pore network capacitance and higher pore network resistance i.e. decreased pore-network interconnectivity and permeability, verified with microstructural analysis. In that sense EIS is proved to be a valuable tool for non-destructive and thorough evaluation of a reinforced concrete system.
For the series of reinforced mortar (paragraph 3) open circuit potential mapping of the embedded steel (corrosion medium of 10% NaCl) shows that 20% red mud as cement replacement in the mortar mixture, significantly delays corrosion initiation i.e. in the specimens containing red mud, corrosion starts after 70 to 85 days, while in the "control" (corroding) samples corrosion was initiated 10 to 15 days after immersion in NaCl. Polarization resistance values clearly show the increased corrosion resistance of the red mud containing corroding cells and the above stated delay in corrosion initiation. The addition of red mud slightly decreases porosity and critical pore size in the bulk cementitious matrix through increasing the chloride binding capacity of the latter, evidenced by the lack of free chlorides at the steel/paste interface in the specimens, containing red mud. Furthermore, the negatively charged red mud particles most likely act as adsorption sites for positively charged species (Ca^{2+}, Al-hydrates etc.) and thus result in "capturing" chloride ions. Further investigation is clearly necessary to provide firm evidence for the surface charge, absorption mechanisms and the positive influence of red mud particles in terms of favored passivation and/or buffering effects on the steel surface in reinforced cement-based materials.
In conclusion, EIS is a powerful and valuable tool for characterizing a reinforced concrete system, in terms of corrosion performance of the steel surface, but providing information for the properties of the bulk cement-based matrix as well. Thus, fundamental electrochemistry (in the sense of widely known and applied electrochemical techniques) is an essential part of studies related to reinforced concrete (and therefore applicable in the field of civil engineering). The proper evaluation of a reinforced concrete system is only possible via the application of electrochemical techniques and a thorough characterization of the involved phenomena can be achieved via the integrated approach of electrochemical science and concrete material science.

5. References

Amritphale S.S, Anshul A, Chandra N, Ramakrishnan N, (2007) A novel process for making radiopaque materials using bauxite—Red mud, Journal of the European Ceramic Society 27, 1945–1951

Atun G., Hisarli G., (2000) J. Colloid Interf. Sci. 228, 131.
Audenaert K., Yuan Q., De Schutter G., (2010) *Constr. Build. Mater. 24, 396.*
Ayres R.U, John H. and Bjorn A, (2001) Utilisation of wastes in the new millennium. MRSI Bull., 7, 477–480
Baweja D., Roper H., Sirivivatnanon V., (1998) *ACI Mater. J. 207.*
Bouikni A., Swamy R.N., Bali A., (2009) *Constr. Build. Mater. 23, 2836.*
Cengeloglu Y, Tor A , Arslan G, Ersoz M, Gezgin S, (2007) Removal of boron from aqueous solution by using neutralized red mud, Journal of Hazardous Materials, 142, 1-2, 412-417
Chvedov D., Ostap S., Le T., (2001) Colloids Surf. A 182, 131.
Collazo A., Fernandez D., Izquierdo M., Novoa X.R., Perez C., (2005) Progress in Organic Coatings, 52, 351–358.
Collazo A., Izquierdo M., Novoa X.R., Perez C., (2007) Surface treatment of carbon steel substrates to prevent cathodic delamination, El. Acta 52, 7513-7518.
Copuroglu O., (2006a) *PhD Thesis, Frost salt scaling of cement-based materials with a high slag content. TUD Technische Universiteit Delft.*
Çopuroğlu O., Fraaij A.L.A., Bijen J.M.J.M., (2006b) *Cem. Concr. Res. 36, 1475.*
Dehghanian C., Arjemandi M., (1997) *Cem. Concr. Res. 27, 937.*
Dehghanian C., (1999) *Corrosion 55, 291.*
Dhoubi L., Triki E., Raharinaivo A., (2002) *Cem. Concr. Comp. 24, 35.*
Díaz B., Joiret S., Keddam M., Nóvoa X. R., Pérez M. C., Takenouti H., (2004) Passivity of iron in red mud's water solutions, Electrochimica Acta, 49, 3039-3048.
Díaz B., Nóvoa X.R., Pérez M.C., (2006) *Cem. Concr. Comp. 28, 237.*
Dinakar P., Babu K.G., Santhanam M., (2007*) Cem. Concr. Comp. 29, 136*
Efes Y., (1980) *in: Betonwerk und Fertigtiel Technik (Wiesbaden) 46 (4) 224–229.*
Fedrizzi L., Azzolini F., Bonora P. L., (2005) *Cem. Concr. Res. 35, 551.*
Feliú V., González J. A., Andrade C., Feliú S., (1998) *Corr. Sci. 40, 975.*
Feliú V., González J. A. and Feliú S., (2004) *J. Electrochem. Soc. 151, B134.*
Giorv O. E., Vennesland O., (1979) *Cem. Concr. Res., 9, 229.*
Gjorv O. E., (1995) *ACI Mater. J. 92, 591.*
Glass G.K., Buenfeld N.R., (1997) *Corros. Sci., 39, 1001.*
Gu P., Beaudoin J.J., Zhang M.H., Malhotra V.M., (2000) *ACI Mater. J. 97, 254.*
Hooton R.D., (1986) *In: Frohnsdorff G, ed. Blended cement, ASTM STP 897; 128.*
Hossain K. M. A., Lachemi M., (2004) *Cem. Concr. Res. 34, 695.*
Hu J., Stroeven P., (2003) *Image Analysis Stereology, 22, 97.*
Irassar E. F., Gonzalez M., Rahhal V., (2000) *Cem. Concr. Compos. 22, 361.*
Koleva D.A., de Wit J.H.W., van Breugel K., van Westing E., (2007a) *J. Electrochem. Soc. 154, P52.*
Koleva D.A., Hu J., Fraaij A., van Breugel K., de Wit J.H.W., (2007b) *Cem. Concr. Res., 37, 604.*
Koleva D. A., (2007c) *Corrosion and Cathodic Protection in Reinforced concrete, PhD Thesis, Delft University of Technology, Delft.*
Koleva D.A., Copuroglu O., van Breugel K., Ye G., de Wit J.H.W., (2008a) Electrical resistivity and microstructural properties of concrete materials in conditions of current flow, Cem.Concr.Compos., 30, pp 731-744
Koleva D. A., de Wit J.H.W., van Breugel K., Veleva L.P., van Westing E., Copuroglu O., Fraaij A.L.A., (2008b) *Mater. Character. 59, 801.*
Koleva D. A., van Breugel K., de Wit J.H.W., van Westing E., Copuroglu O., Veleva L., Fraaij A.L.A., (2008c) *Mater. Character. 59, 290.*
Koleva D.A., Copuroglu O., van Breugel K., de Wit J.H.W., (2008d) "EIS and PDP of construction steel in cement extract, containing red mud and chloride

contamination", 214th Joint Meeting of the Electrochemical Society and the Electrochemical Society of Japan, Honolulu, Hawaii, US, 11th – 17th October 2008, www.electrochem.org

Koleva D. A., Guo Z., van Breugel K., de Wit J. H. W., (2009) *Mater. Corrosion 60, 344.*

Koleva D.A., (2010a) Corrosion resistance of construction steel in BFS and OPC concrete: correlation of electrochemical parameters and microstructural characteristics, Corr.Sci. submitted

Koleva D. A., Guo Z., van Breugel K., de Wit J. H. W., (2010b) *Mater. & Corrosion, In press, DOI: 10.1002/maco.200905423*

Koleva D.A., (2011), The significant delay of a chloride-induced corrosion in reinforced mortar, containing red mud as cement replacement, Submitted to J. Electrochem. Soc.

Kumar A.D.M. (1986), *In: Proc. 8th Conf. Chemistry of Cement, Brazil, 73.*

Li L.Y, (1998) Envirnmental Engineering 3, 254.

Li S., Roy Della M., (1986) *Cem. Concr. Res.16, 749.*

Macphee D.E., Cao H.T., (1993) *Mag. Concr. Res. 45, 63.*

Manmohan D., Mehta P.K., (1981) *Cem. Concr. Aggr. 3, 63.*

Montemor M. F., Cunha M. P., Ferreira M. G., Simões A. M., (2002) *Cem. Concr. Comp. 24, 45.*

Mymrin V., de Araujo P., Lopes H., Ferreira O., (2003) Environment friendly method of high alkaline bauxite's red mud and ferrous slag utilization as an example of green chemistry, Green Chem., 5, 357–360

Osborne G.J., (1999*) Cem. Concr. Compos. 21, 11.*

Page C. L., (2002) *in: Proc. 15th Intern.Corrosion Congress, Granada*

Pal S.C., Mukherjee A., Pathak S.R., (2002) *ACI Mater. J. 99, 1.*

Petterson K., (1994) *in: Corrosion and corrosion protection of steel in concrete, Ed. Swamy RN, Academic Press, Sheffield, 461.*

Ramanujan S., (1962) Paintindia 12, 22.

Ramezanianpour A.A., (1995) *Cem. Concr. Compos. 17, 125.*

Sagüés A. A., Kranc S. C., Moreno E.I., (1995) *Corr. Sci. 37, 1097.*

Serra J., (1982) *Image analysis and mathematical morphology. London: Academic Press.*

Skoulikidis T., Vassiliou P., Diamantis N., Tunturi P.J. (1992) (Eds.), Proc. of 12th Scand. Corros. Congr. Eurocorr'92, Corros. Soc. of Finland, p. 475.

Song Ha-Won, Saraswathy V., (2006) *J. of Hazardous Materials B138 226.*

Stumm W.,(1995) Chemistry of the Solid–Water Interface, Wiley, New York, (Chapters 2–6).

Suryavanshi A.K., Scantlebury J.D. , Lyon S.B., (1995) *Cem. Concr. Res. 25, 980.*

Thomas M. D. A., Bamforth P.B., (1999) *Cem. Concr. Res. 29, 487.*

Tsakiridis P.E., Agatzini-Leonardou S., Oustadakis P., (2004) Red mud addition in the raw meal for the production of Portland cement clinker Journal of Hazardous Materials, 116, 1-2, 103-110.

Vassie P.R.W., (1984) *Proc. Inst. Civ. Engnrs., 76, 713.*

Wenger F., Galland J., (1990) *Electrochim. Acta 35, 1573.*

Ye G., (2003) *Experimental Study and Numerical Simulation of the Development of the Microstructure and Permeability of Cementitious Materials, PhD thesis, Delft University of Technology, Delft.*

Yong Liu, Chuxia Lin, Yonggui Wu., (2007) Characterization of red mud derived from a combined Bayer Process and bauxite calcination method, J. of Hazardous Materials, 146, 255-261

16

Intralaminar Fracture Toughness Characterization of Composite Laminates

Maurício V. Donadon and Sérgio Frascino Muller de Almeida
Instituto Tecnológico de Aeronautica-ITA
Brazil

1. Introduction

The current emphasis within the composite design community is gradually shifting from achieving minimum weight designs at all costs to more cost-effective and damage tolerant structural designs. A damage tolerant structure must not only be able to effectively absorb energy locally at the point of damage initiation but must also be fail-safe. A very efficient way of designing a composite fail-safe structure is to provide it with the ability to arrest a potentially catastrophic crack by increasing its fracture resistance. The fracture behaviour of composites can be quantified by measuring its toughness and it can be broadly classified into interlaminar and intralaminar fractures. Most of the work reported in the recent literature has focused on the investigation of the interlaminar behaviour of composites with a limited number of works addressing the intralaminar fracture behaviour.

The measurement of intralaminar toughness requires a pre-cracked specimen and in most cases, particularly for CFRP materials. Its determination can be based on the Linear Elastic Fracture Mechanics (LEFM) approach. Different types of specimens and crack geometries are currently available in the literature to characterise the intralaminar fracture behaviour of composites under pure mode I (Cowley & Beaumont, 1997; Konstantinos et al., 2005), mode II and mixed-mode loading (Lin & Shetty, 2003), however none of them are standardised. The specimen selection depends on the material system under investigation and expected toughness values range from initiation to propagation. It is also worth mentioning that most of these specimens were originally designed for fracture in isotropic materials. The poor performance of composites in shear and compression loading, compared to tension loading in the fibre direction may lead to failure prior to crack growth. Such restrictions impose limitations on their applicability and alternative specimen designs are needed. For mode-I, the Overheight Compact Tension (OCT) specimen has the advantage of promoting a stable crack growth which eventually enables the evaluation of both initiation and propagation values for the intralaminar toughness.

Jose et al. (2001) investigated the mode I intralaminar toughness of carbon/epoxy cross-ply laminates using overheight compact tension specimens. The experimental results were compared with finite element simulations using a modified crack-closure integral method and a methodology for calculating the stress intensity factor associated with matrix cracking and fibre fracture was presented. Based on the work by Jose et al. (2001), Pinho et al. (2006a) investigated the intralaminar toughness associated with fibre breakage in tension and fibre kinking in compression in unidirectional pre-preg composites using Compact Tension (CT)

and Compact Compression (CC) specimens. A very consistent resistance curve (R-Curve) containing initiation and propagation values was obtained in tension, with a marked increase in the toughness values in compression due to fibre compression kinking. The authors attribute the increase in the toughness in compression to the contact in the crushed area. In fact, the contact is a problem even in tension, if the specimen is subjected to cyclic loading-unloading, due to debris effects which prevent the total crack closure, resulting in permanent displacements (Konstantinos et al., 2005). Kostopulos and co-workers (1998) proposed a modified compliance method to handle problems in which permanent displacements are an important issue. The method is based on the Non-Linear Fracture Mechanics (NLFM) approach and the resultant nonlinear fracture toughness is composed of elastic and non-elastic terms due to the presence of irreversible deformations. The method uses an effective crack length based on a semi-empirical equation.

The increasing computational resources combined with recent developments on advanced physically based failure models have allowed reliable prediction of progressive damage in composites by using the finite element method (Iannucci e al., 2006; Pinho et al., 2006b; Donadon et al., 2009). These models require, among others parameters, a number of intralaminar fracture energies as input parameters. For instance, for pure tensile failure in both transverse and longitudinal directions the fracture energy can be determined using the Overheight Compact Tension (OCT) specimen. In a similar way the Compact Compression (CC) specimen can be used to determine the fracture energy associated with fibre kinking (Pinho et al., 2006). The fracture energy associated with shear dominated failure modes can be measured using the Four Point End Notched Flexure (4ENF) specimens (Martin et al., 1998).

This chapter intends to present a detailed discussion on test methods and data reduction schemes for mode-I intralaminar fracture toughness characterization of composite laminates. Additionally, fracture mechanics based finite element models of all described tests were developed to confirm the experimental results. Details on specimen manufacturing and preparation for different pre-cracked geometries including Overheight Compact Tension (OCT), double edge notch (DEN) and centrally cracked four-point-bending (4PBT) test specimens are also presented and discussed. The limitations of the applicability of the standard data reduction schemes for the determination of intralaminar toughness of composite materials are also addressed in this chapter. A methodology based on the numerical evaluation of the strain energy release rate using the J-integral method is presented in details. This methodology was used to derive new geometric correction functions for the determination of the stress intensity factor for composites. The proposed method accounts for material anisotropy and finite specimen dimension effects regardless of the geometry. The approach has been validated for alternative non-standard specimen geometries. The chapter ends by showing a comparison between experimental results obtained using different data reduction schemes. A discussion on advantages, disadvantages and limitations of each method is also presented.

2. Specimen configurations and data reduction schemes

Strictly speaking, no data reduction scheme for the computation of the mode-I, mode II and mixed-mode loading intralaminar toughness as well as test standards are currently available in the literature for composite materials. Most researchers employ the same data reduction schemes and test standards as the one used for isotropic materials; however, their

applicability for composites and the reliability of the results are questionable. The standard data reduction schemes for isotropic materials are presented herein and it will be shown that in their original forms these expressions are not applicable for the material system investigated in this chapter.

2.1 Overheight Compact Tension (OCT)

The determination of the stress intensity factor for isotropic materials using OCT specimens is based on the ASTM E399-90 standard (Annual book of ASTM standards, 1993),

$$K_{IC} = \frac{P}{h\sqrt{w}} f(a/w) \tag{1}$$

where P is the applied load, h is the thickness and w is the distance from the loading line up to the crack tip, as shown in Fig. 1. $f(a/w)$ is the geometric function introduced to account for finite specimen dimension corrections, which is given by(Annual book of ASTM standards, 1993),

$$f(a/w) = \frac{2 + a/w}{(1-a/w)^{1.5}}\left[0.886 + 4.64(a/w) - 13.32(a/w)^2 + 14.72(a/w)^3 - 5.6(a/w)^4\right] \tag{2}$$

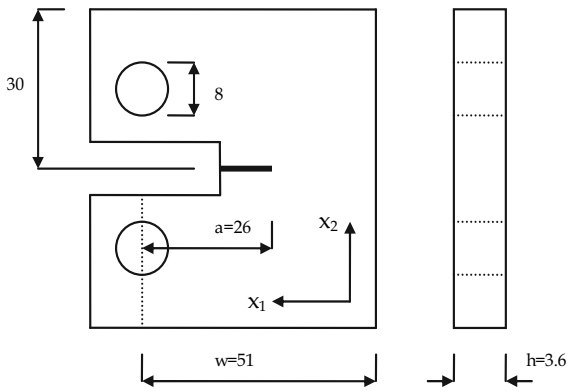

Fig. 1. Typical dimensions for the Overheight Compact Tension (OCT) specimen (dimensions in *mm*)

2.2 Double Edge Notch (DEN)

For the double edge notch (DEN) specimens the stress intensity factor is given by (Brown & Strawley, 1967),

$$K_{IC} = f(a/w)\sigma\sqrt{a} \tag{3}$$

where σ is the applied stress, w is the specimen width and a is the crack length, as depicted in Fig. 2. $f(a/w)$ is the finite dimension correction function given by (Brown & Strawley, 1967),

$$f(a/w) = 1.98 + 0.36(2a/w) - 2.12(2a/w)^2 + 3.42(2a/w)^3 \tag{4}$$

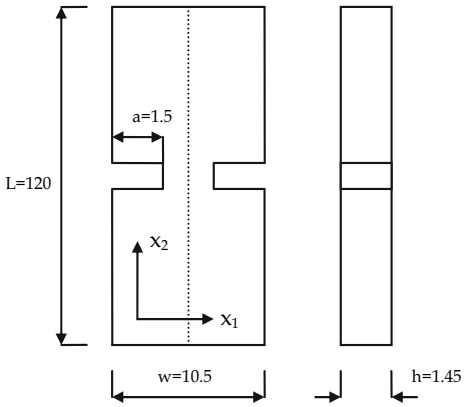

Fig. 2. Typical dimensions for the Double Edge Notch (DEN) specimen (dimensions in *mm*)

2.3 Four Point Bending (4PBT)

For the four point bending (4PBT) specimens the stress intensity factor is defined as (Rooke & Cartwright, 1976),

$$K_{IC} = \frac{6Pc\sqrt{\pi a}}{2wh^2} f(a/h) \tag{5}$$

where P is the total applied load, c is the distance between the edge of the specimen and the upper loading point (see Fig.3), w and h are the width and thickness of the specimen, respectively, and $f(a/h)$ is the geometric correction function given by (Rooke & Cartwright, 1976),

$$f(a/h) = 1.12 - 1.39(a/w) + 7.32(a/w)^2 - 13.1(a/w)^3 + 14.0(a/w)^4 \tag{6}$$

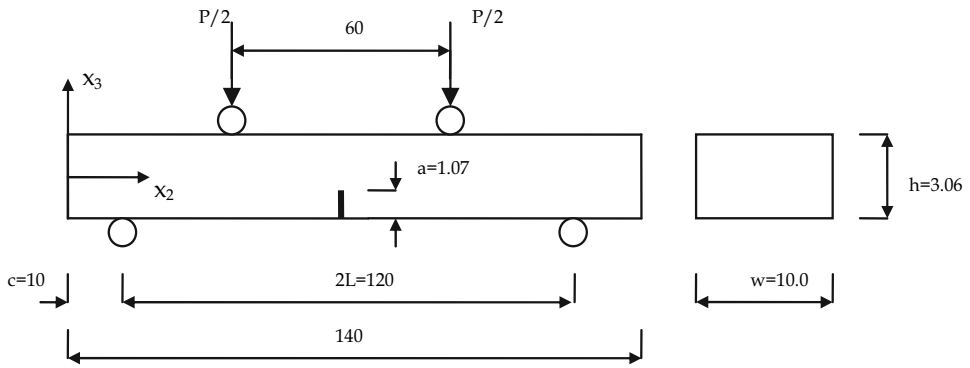

Fig. 3. Typical dimensions for the Four Point Bending (4PBT) specimen (dimensions in *mm*)

2.4 Intralaminar fracture toughness for composites

For an on-axis, plane stress, orthotropic plate with an initial crack subjected to in-plane loading, the fracture toughness values can be obtained from the Griffith's strain energy release rate functions as follow (Paris & Sih, 1960; Lin et al., 1997)

$$G_{Ic} = \frac{K_{IC}^2}{\sqrt{2\bar{E}_1\bar{E}_2}}\sqrt{\alpha+\beta} \tag{7}$$

with $\alpha = \sqrt{\bar{E}_1 / \bar{E}_2}$ and $\beta = \bar{E}_1 / 2\bar{G}_{12} - \bar{\nu}_{12}$, where $\bar{E}_1$, $\bar{E}_2$ are the effective Young's modulus in the longitudinal and transverse direction, respectively, and $\bar{\nu}_{12}$ is the effective in-plane Poisson´s ratio. $\bar{G}_{12}$ is the effective in-plane shear modulus. Equation 7 is valid for the OCT and DEN specimens. For the four point bending specimens the values of G_{Ic} associated with the fracture in the transverse direction can be determined as (Rooke & Cartwright, 1976),

$$G_{Ic} = \frac{K_{IC}^2}{\bar{E}_2} \tag{8}$$

where $\bar{E}_2 = E_2$ under plane stress and $\bar{E}_2 = E_2 / (1-\nu_{12}^2)$ under plain strain conditions.

3. Stress intensity factor for orthotropic materials

Experimental and numerical studies carried out by Donadon et al. (2007) have shown that the stress intensity factor for composites is significantly overestimated by the direct application of Eqs. (1), (3) and (5). The authors suggest that a possible source of error is the finite geometry correction factor, which was originally derived for isotropic materials. In order to tackle this problem, the authors proposed a methodology based on the numerical evaluation of the J-integral to derive new finite geometry correction functions for composite specimens. A detailed description on the methodology proposed by the authors is given in the following sections.

3.1 Theoretical aspects

The numerical evaluation of the strain energy release rate associated with intralaminar fracture was based on the J-integral method. For this purpose, ABAQUS Standard version 6.5 was used (ABAQUS, 2005). The software provides a calculation procedure for J-integral based on the virtual crack extension/domain integral methods (ABAQUS, 2005). Alternatively, the J-integral can be numerically evaluated by measuring the change in strain energy, ΔU of the specimen with a crack advance, Δa, where the J-integral is given as the negative differential of strain energy with respect to crack length that is,

$$J = -\frac{\partial U}{\partial A} \approx \frac{U(a) - U(a+\Delta a)}{h\Delta a} \tag{9}$$

where $U(a)$ and $U(a+\Delta a)$ are the strain energies associated with a crack length a and $a+\Delta a$, respectively. Δa is the crack increment and h is the thickness of the specimen. Although both methods provide the same results in the linear elastic regime, the latter requires extra data post-processing whilst in the former the J-integral values are obtained straightway. For a linear elastic orthotropic material under plane-stress assumption loaded in mode-I opening, $J = G_{Ic}$ and the stress intensity factor can be related to the J-integral values using (Lin et al., 1997),

$$K_{IC}^2 = \frac{J\sqrt{\bar{E}_1\bar{E}_2}}{\sqrt{(\alpha+\beta)/2}} \tag{10}$$

where α and β are orthotropic constants previously defined in Eq. (7). Eq. (10) is valid for OCT and DEN specimens. For the 4PBT specimens, the relationship between the stress intensity factor and J-integral values is obtained from Eq. (8) with $J = G_{Ic}$,

$$K_{IC}^2 = \bar{E}_2 J \tag{11}$$

By using Eqs. (1), (3), (5), (10) and (11), a new correction function which incorporates orthotropic effects may be obtained using the following procedure:

1. For the OCT and DEN specimens, compute J-integral values for different crack lengths and for each J-integral value ($J_i(a_i)$), compute the stress intensity factor using Eq. (10),

$$K_{Ic}^i = \frac{J_i^{0.5}(\bar{E}_1\bar{E}_2)^{0.25}}{(\alpha/2+\beta/2)^{0.25}} \tag{12}$$

   For the 4PBT specimen, compute J-integral values for different crack lengths and for each J-integral value ($J_i(a_i)$), compute the stress intensity factor using Eq. (11),

$$K_{Ic}^i = \sqrt{\bar{E}_2 J_i} \tag{13}$$

2. From Eqs. (1), (3) and (5) compute a new correction function $F(a_i)$. The new correction functions for OCT, DEN and 4PBT specimens are respectively given by,

$$F(a_i) = \frac{K_{Ic}^i h\sqrt{w}}{P_i} \quad \text{(OCT)} \tag{14}$$

$$F_i(a_i) = \frac{K_{IC}}{\sigma\sqrt{a}} \quad \text{(DEN)} \tag{15}$$

$$F(a_i) = \frac{K_{IC} w h^2}{3Pc\sqrt{\pi a_i}} \quad \text{(4PBT)} \tag{16}$$

3. The $F(a)$ values are plotted against their correspondent crack lengths and the new correction function is obtained by finding the best fit function which interpolates those points.

4. Materials and laminates manufacturing

The fabric used in the experimental part of this chapter consists of a hybrid plain weave fabric supplied by EUROCARBON® and PRIME 20LV® two part epoxy resin system, supplied by GURIT. The fabric is composed of T700-12K-50C carbon fibres in the warp direction and PPG EC09 34*2 S150 1383 glass fibres in the weft direction. The fabric configuration, material local axes and intralaminar cracking directions are illustrated in Fig. 4.

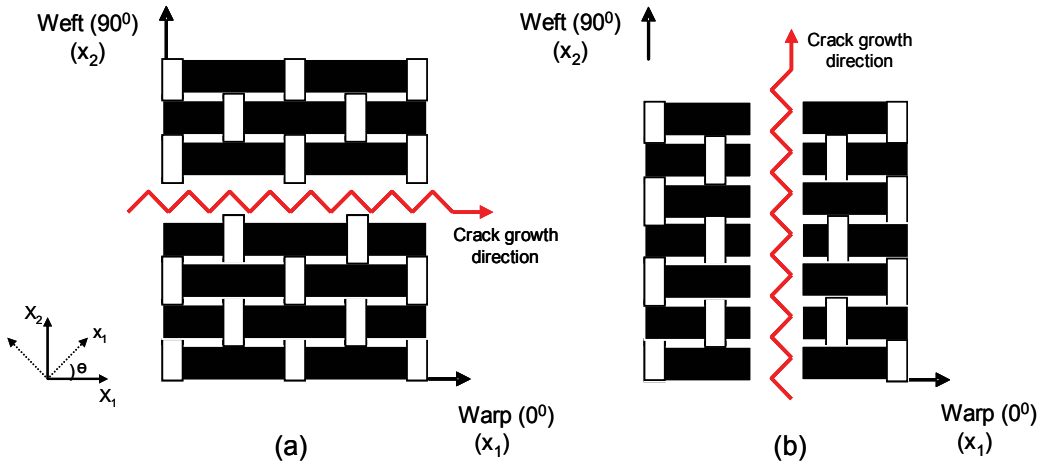

Fig. 4. Hybrid plain weave fabric: (a) Longitudinal crack growth direction, (b) Transverse crack growth direction

All laminates were manufactured using the Resin Infusion under Flexible Tooling (RIFT) process setup outlined in Fig. 5.

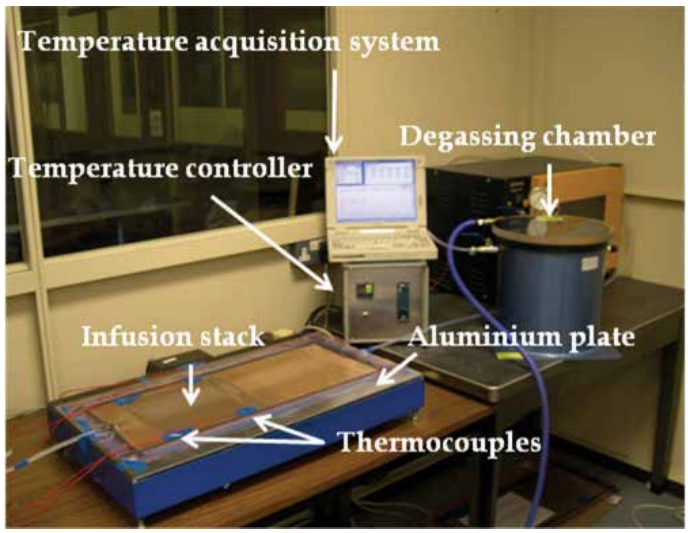

Fig. 5. Rift setup (Donadon, 2004a)

A flat 700mm x 400mm x 4 mm aluminium plate was used as a mould tool. Prior to laying up the fabric, the aluminium plate was covered with a melanex film and one peel ply layer, which aids the removal of the composite plates after cure. The fabrics were covered with a flow distribution medium on the upper and lower surfaces, in order to ensure complete fabric wetting-out. The resin flow medium was intentionally cut 30 mm shorter from the end of the preform near the vacuum vent to reduce the resin flow rate within the infusion stack. Subsequently, the infusion stack was bagged and placed on the hot platen. Next, vacuum drop tests were carried out by applying full vacuum into the infusion stack and

monitoring the pressure using a dial gauge connected to the degassing chamber for 30 minutes. This procedure ensures the vacuum integrity within the RIFT system. Vacuum integrity is possibly the most important manufacturing parameter for the RIFT process. Infusions were carried out at room temperature (25 °C), with panels cured for 7 hours at 65 °C. The temperature variation of the laminate during the curing stage was measured by attaching thermocouples on the upper surface of the stack. The temperature measurements were taken from five different positions, four of them were placed in each corner of the square plate, whereas the fifth was in the centre of the plate. The temperatures were recorded by means of a temperature data-logger connected to acquisition software. The point-to-point temperature variation was within +/-5 °C. In order to assess the final quality of the laminates, the panels were inspected by ultrasound generating C-scans. The fibre volume fraction and void content were measured using the acid digestion method. According to c-scan images the laminates were free of any major defect, with a typical value of 53% and 1% for the fibre volume fraction and void content, respectively.
The laminate mechanical properties were measured using standard test methods (Donadon, 2004b) and are summarised in Table 1.

Stiffnesses and strengths	
Young's modulus in the warp direction, E_{11}	100 GPa
Young's modulus in the weft direction, E_{22}	8.11 GPa
In-plane shear modulus, G_{12}	3.88 GPa
Major in-plane Poisson's ratio, ν_{12}	0.35
Tensile strength in the warp direction, $\sigma_{f,1}^{t}$	2005 MPa
Tensile strength in the weft direction, $\sigma_{f,2}^{t}$	63 MPa
Compressive strength in the warp direction, $\sigma_{f,1}^{c}$	750 MPa
Compressive strength in the weft direction, $\sigma_{f,2}^{c}$	170 MPa
In-plane shear strength, σ_{12}^{f}	60 MPa
Mode II interlaminar fracture toughness G_{II_c}	2.2 kJ/m^2

Table 1. Laminates mechanical properties

4.1 Crack tip preparation

A three step procedure was used to produce a sharp crack tip in the OCT specimens. Firstly a 30 mm length notch was inserted in the specimens using a 3.5mm thick dry diamond saw. Secondly a series of razor saws were used to further increase the crack length by 10mm; each razor saw employed had progressively increasing number of teeth in the blade, three types were used with each removing 3.3mm of material. The thickness of the razor saw blade was no more than 0.2mm. Lastly to produce an extreme sharp crack tip a 0.06mm thick razor blade was used lightly to improve the sharpness of the crack tip. A typical micrograph illustrating the quality of the crack tip is shown in Fig. 6.

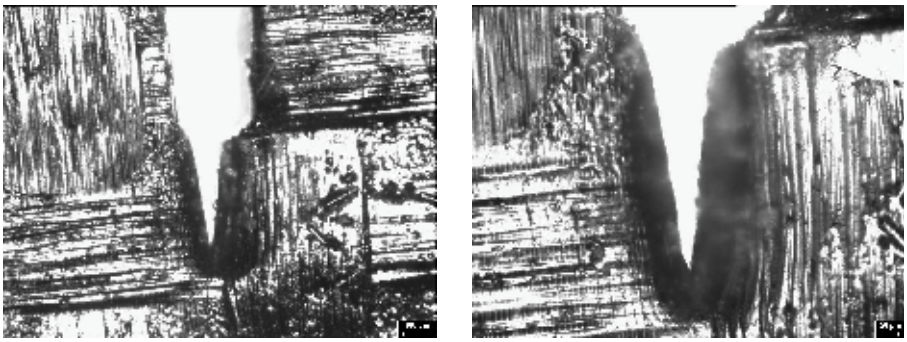

(a) 50 x (b) 100x

Fig. 6. Crack tip images of the OCT specimens

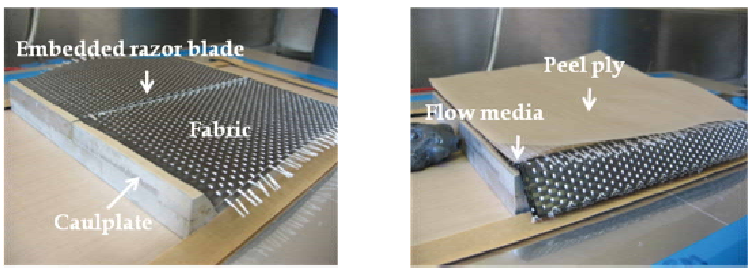

(a) (b)

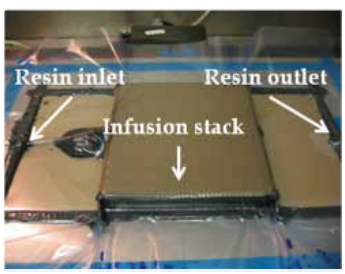

(c)

Fig. 7. Manufacturing steps for the 4PBT specimens

For the DEN specimens only the razor saws were used to insert two symmetrical 1.5 mm long notches in the middle of the specimens. In order to produce a pre-cracked four-point-bending specimen, the original RIFT setup had to be modified. A caulplate with a 0.06mm thick sharp razor blade embedded in the mid-plane was used as a tool to introduce the pre-crack. The two halves of the caulplate were covered with two strips of peel ply to aid the removal of the composite panel after cure. The blade had a protruding height of 1.07mm so three plies on each side of the blade had to be used so the crack tip was flush with the top surface of the stacked plies. The plies were cut in two halves along the warp direction (parallel to the carbon fibres) and the two halves were laid up on the top of the peel ply strips. The next step to produce the pre-cracked laminate was to stack more plies on the

bottom three plies. Since the blade tip was now flush with the bottom plies, any plies that were stacked did not require to be cut in half. Hence, seven additional plies were placed on top of the crack resulting in the fibre stack being ten-ply thick. The fabric was then covered with another continuous peel ply layer followed by the flow media and another peel-ply layer on top of the stack. Flow medium was not applied below the fibre stack due to the stack being thin and overall dimensions being small. Moreover, the use of a bottom flow media would have increased the overall rate of infusion to the extent that through thickness infusion of the stack would have been limited thus promoting the presence of voids. The inlet for resin transfer had to be raised to the same level as the fibre stack to maximise fibre wet-out. Any blunt and malleable platform can be employed for this purpose. In this study a ball of tack tape was used as it had the added advantage of securing a relatively large proportion of the inlet pipe. Subsequently, the infusion arrangement was bagged and vacuum tested, infusion and cure were carried out. The specimen manufacturing steps are shown in Figs. 7 (a), 7 (b) and 7 (c), respectively.

5. Experimental setup and data collection

5.1 OCT specimens

The mechanical tests for the OCT specimens were carried out using a 100 kN Instron testing machine equipped with 10kN and 100kN load cells to measure the initiation and propagation loads for growing the crack in the warp and weft directions, respectively. The crosshead displacement and load histories were recorded by using a data acquisition system. The tests were carried out with crosshead displacement rate of 1mm/min. Two different lay-ups were used, namely unidirectional $(0_2)_{2s}$ and cross-ply $(0,90)_{2s}$ for determination of the toughness in the warp and weft directions, respectively. The nominal thickness for both unidirectional and cross-ply panels was 3.6mm. Prior to testing, all specimens were prepared using a two stage painting procedure. This procedure is required by the digital speckle photogrammetry system in order to compute the strain field histories during the test. Firstly, one of the faces of the specimens was painted white in order to provide a white background for the black speckles introduced in the second stage. In the second stage, fine black speckles were uniformly sprayed into the white painted face of the specimen. After spraying the black speckles on the specimens, a 20 mm scale ruler equally divided into increments of 1mm was drawn parallel and ahead of the initial crack. A set of two cameras orientated at 12.5° with respect to the direction normal to the face of the specimen was used to record the displacement and strain field histories during the test. Additionally, an extra CCTV camera connected to a TV set was placed normal to the specimen to monitor the crack growth. By using this extra camera together with a crack event marker, it was possible to determine the load and displacements associated with a specific crack length. The experimental setup for measuring the intralaminar fracture toughness using OCT specimens is shown in Fig. 8.

5.2 DEN specimens

The same equipment described previously was used to measure the displacements and load histories during the test. 10kN and 100kN load cells were used to measure the load histories in the weft and warp directions, respectively. The specimens were loaded at a displacement rate of 0.5 mm/min. The specimen preparation followed the same steps as that for the OCT

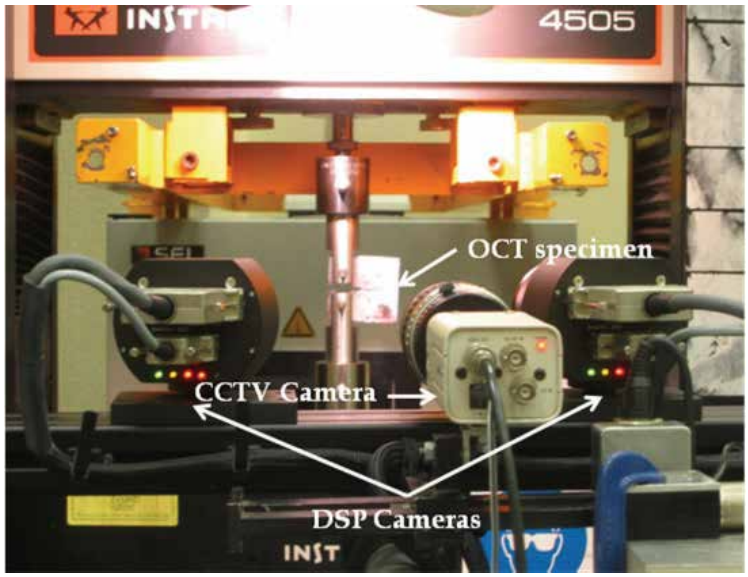

Fig. 8. Experimental setup for OCT specimens

specimens. The digital speckle photogrammetry system was used to identify the position of the crack tip. Prior to testing the specimens were end tabbed and fixed in the testing machine by means of the jaws as shown in Fig. 9.

Fig. 9. Experimental setup for DEN specimens

5.3 Four point bending specimens

Due to the unstable nature of the crack growth in this specimen geometry, only the initiation value could be experimentally obtained and hence no use was made of digital speckle

photogrammetry. A 10kN loading cell was used and the tests were carried out at 0.5mm/min. Crosshead displacements and load histories were recorded during the test using a data acquisition system. The specimens were loaded by means of the four point loading jig according to Fig. 10. A rubber film was placed between the specimens and the loading jig in order to prevent lateral sliding.

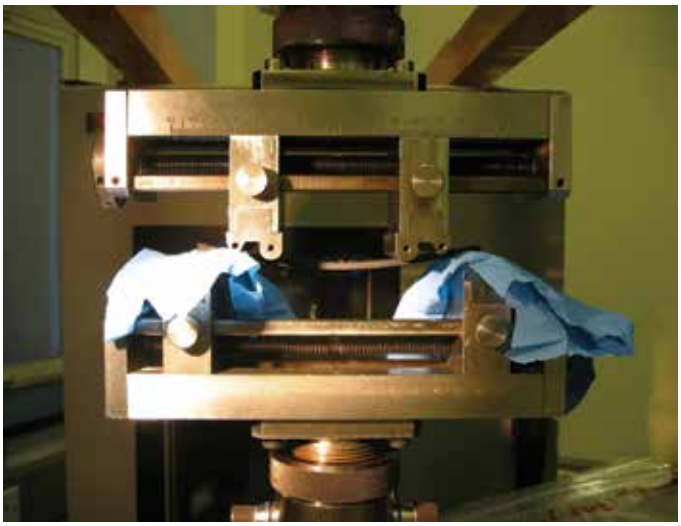

Fig. 10. Experimental setup for 4PBT specimens

6. Experimental results

Five unidirectional OCT specimens were tested and a typical load-displacement curve is shown in Fig. 11.

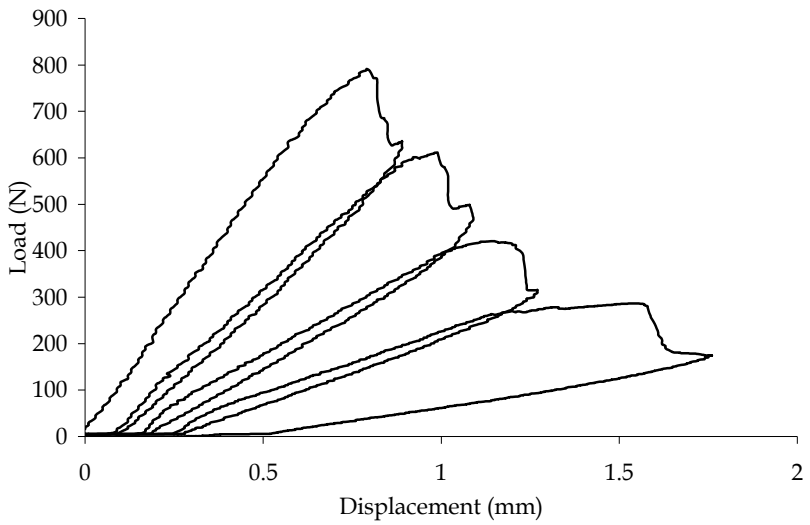

Fig. 11. Load-displacement curves for unidirectional specimens

All specimens were immediately unloaded for each crack increment and up to four cycles could be obtained before the crack reached the edge of the specimen.
The load displacement curve exhibits a stick-slipping behaviour which is attributed to the fracture of the transverse glass fibres normal to the crack growth direction. The spacing between two subsequent peak loads is fairly consistent from specimen to specimen and the interval is associated with the spacing between two consecutive normal glass fibre yarns. As a result, the toughness in the weft direction will be given by the sum of the toughness associated with matrix cracking plus the toughness associated with glass fibre fracture. The permanent displacements during the unloading stage are mainly due to micro-cracking damage (such as fibre/matrix debonding) and interaction between fragments of fractured glass fibres which results in partial crack closure. As an initial assessment, the toughness values were determined using the compliance method (Slepetz & Carlson, 1975). Additionally, numerical simulations were carried out in order to evaluate the compliance changes for different crack lengths. The crack tip position was identified by using the digital speckle photogrammetry system and a typical experimental strain contour is shown in Fig. 12. The experimental and numerical compliance variations with respect to the crack length are shown in Fig. 13.

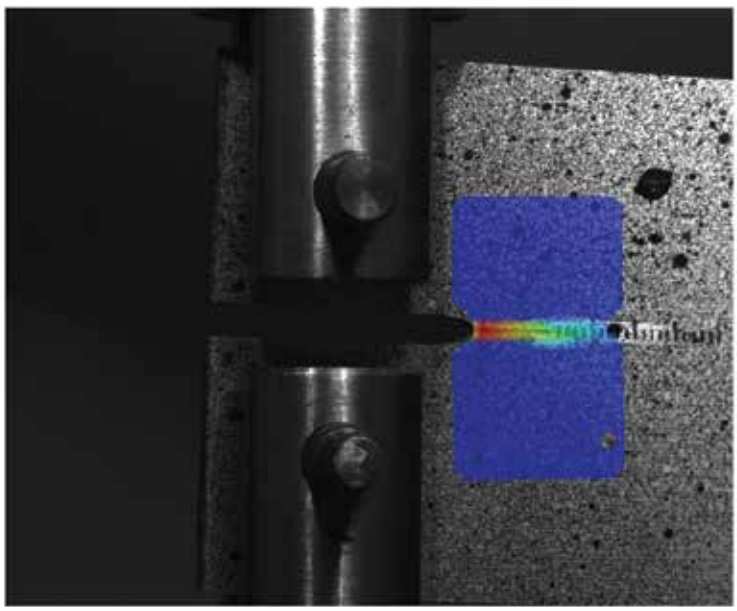

Fig. 12. Experimental strain field for the OCT specimens

Based on the correlation between numerical and experimental results a polynomial cubic relationship between compliance versus crack length was defined in the following form,

$$C(a) = c_1 a^3 + c_2 a^2 + c_3 a + c_4 \tag{17}$$

where the best fit coefficients were $c_1 = 3,4461.10^{-6}$, $c_2 = -3,2348.10^{-4}$, $c_3 = 1,0249.10^{-2}$ and $c_4 = -0.1080$, respectively. The toughness values for the unidirectional OCT specimens were computed using the following expression (Slepetz & Carlson, 1975),

$$G_{Ic} = \frac{P_c^2}{2h}\frac{\partial C}{\partial a} \tag{18}$$

where P_c is the critical load associated with a given crack length and h is the thickness of the specimen. The toughness values for the unidirectional specimens tested are presented in Fig. 14.

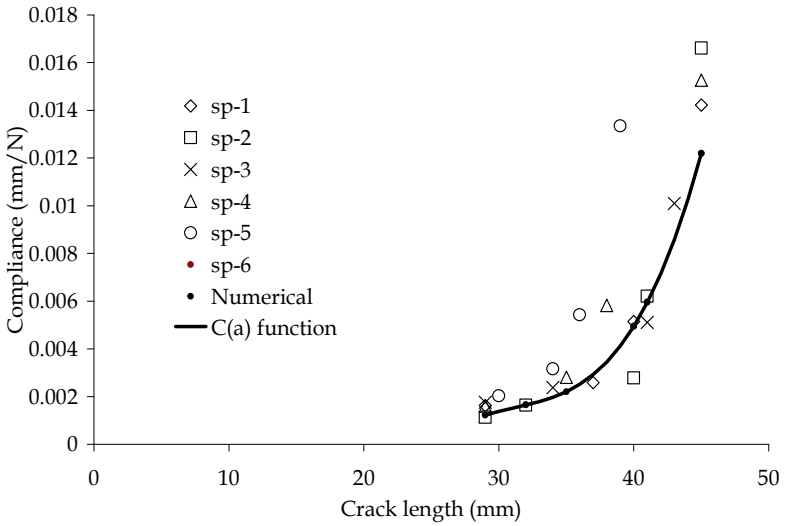

Fig. 13. Experimental compliance versus crack length for unidirectional OCT specimens

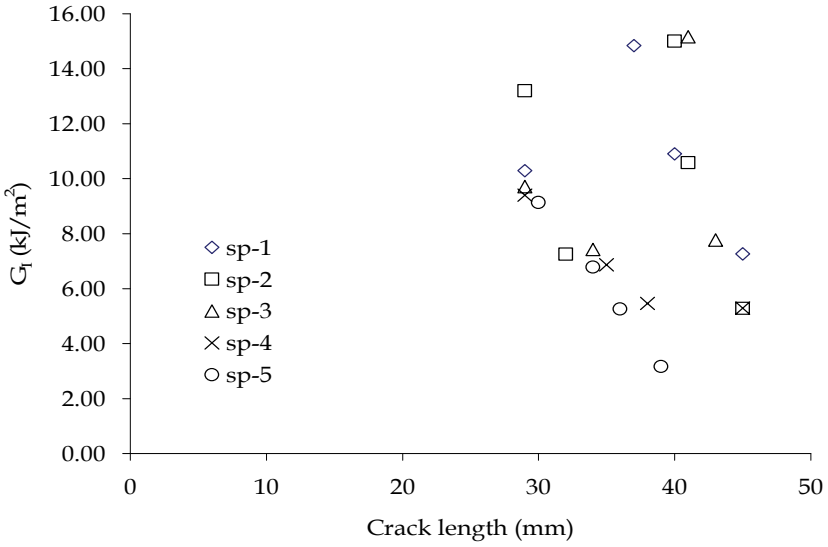

Fig. 14. Experimental toughness values for the unidirectional OCT specimens (R-Curve)

A large scatter for the toughness values was obtained, with a resultant mean value around 10 kJ/m² and standard deviation of 3.2 kJ/m². In fact this is not surprising since the fracture

process is very complex in fabrics of this nature. The variations in the initial values may be attributed to the intra-planar heterogeneities of the constituents and location of the initial crack tip which for some specimens was within the glass fibre yarns and for others only in resin rich areas. Fibre bridging was also observed which may explain the dispersion in results for higher crack length values. Also, the crack did not propagate in a perfect straight line as it was intended, but followed a tortuous path which may have resulted in coupling between different fracture modes (mode I and mode II for instance) (See Fig. 15). Crack bifurcation mainly in the regions close to the transverse glass fibres was also observed. Moreover, the number of glass fibre yarns normal to the fracture surface varied along the crack growth line from specimen to specimen due to the non-uniform distribution arising from the manual lay-up stage. These processes either together or individually introduce extra dissipation mechanisms during the fracture process which may explain such a variation. The low toughness values may be attributed to matrix cracking only whereas the high toughness values to the glass fibre fracture. It is very difficult to distinguish and attribute a particular toughness value to each fracture mechanism involved in the fracture process and one may assume the mean value as a reasonable one for design purposes.

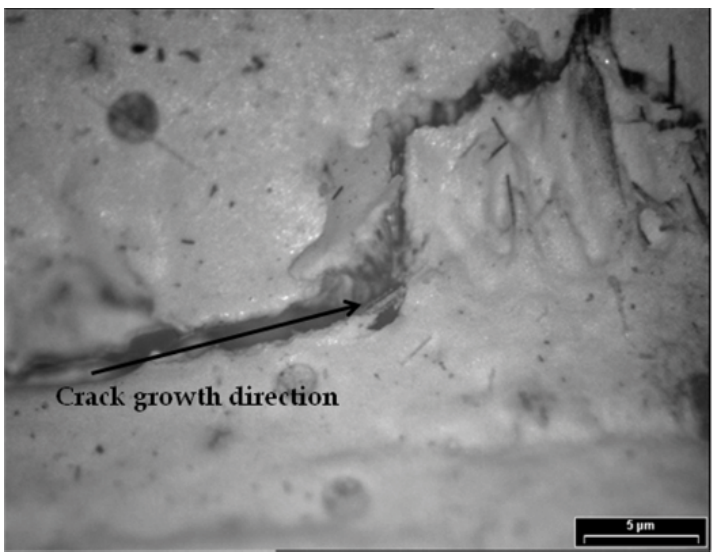

Fig. 15. Intralaminar crack growth path

For the DEN and Four-Point-Bending (4PBT) specimens only the initiation values could be experimentally obtained due to the unstable crack growth on those specimens. For the DEN specimens the applied tension stresses remote from the crack were computed by dividing the ultimate load by the cross-sectional area of the specimen. Having defined the stress, Eqs (3) and (4) were then applied to obtain the toughness values. For specimens loaded in the weft direction, failure took place within the pre-cracked region, as intended, but this was not the case for specimens loaded in the warp direction. A mean toughness value of G_{Ic} =2.50 ± 0.25 kJ/m² was found for the specimens loaded in the weft direction and Fig. 16 depicts the observed failures modes in each direction for DEN specimens.

For the 4PBT specimens the intralaminar fracture toughness values were computed using Eqs. (5), (6) and (8) and a mean toughness value of G_{Ic} = 2.20 ± 0.12 kJ/m² was found. It was

noticed that four point bending test specimens showed a lower scatter in results compared to the DEN specimens. In fact, having double pre-cracked specimens such as DEN specimens may introduce extra sources of errors and variations in the results such as asymmetrical crack tip sharpness and non-self-similar crack growth. The values obtained using the 4PBT specimens compare well with the one obtained from the DEN tests confirming the initiation toughness values in the weft direction.

(a)

(b)

Fig. 16. Failure modes for DEN specimens: (a) Warp direction, (b) Weft direction

7. Finite element modelling

7.1 FE model setup for the OCT specimen

The OCT specimen was modelled using 8-node quadratic plane stress elements available in ABAQUS/Standard. The dimensions for the virtual unidirectional coupon were 51x30x3.6 mm^3. Due to the symmetry of the problem, only one half of the specimen was modelled and a finer mesh was assigned to the region around the crack tip in order to obtain an accurate representation of the stress/strain fields on that region. A typical FE mesh is shown in Fig. 17.

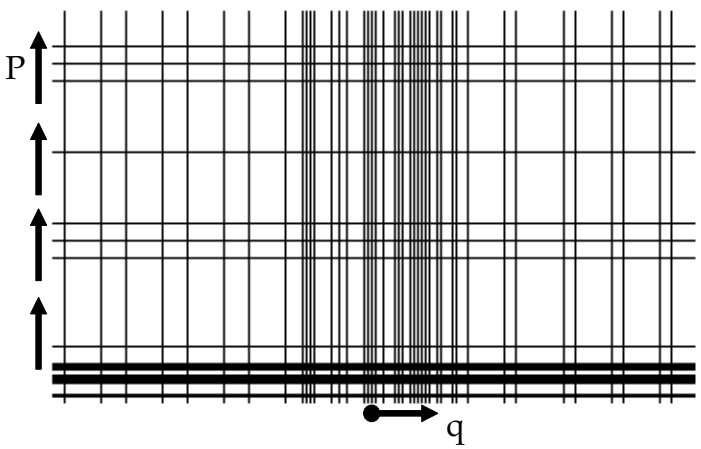

Fig. 17. FE mesh used for OCT simulations

In order to model the contact forces between the loading pins and composite specimen the load was assumed to be uniformly distributed along the loading line of the specimens as shown in Fig. 17. The material behaviour was modelled using linear orthotropic elastic material model available in ABAQUS/Standard with mechanical properties given in Table 1. The virtual crack extension direction was assumed to be normal to the loading direction and defined by a vector q = (1,0,0). The simulations were performed for crack lengths of 28mm, 37mm and 40mm and the J-integral values were evaluated on ten different integral contours for each crack length. Mean J-integral values of 9.91766 ± 0.015 kJ/m², 10.8025 ± 0.012 kJ/m² and 11.4708 ± 0.014 kJ/m² were obtained for the crack lengths of 28mm, 37mm and 40mm, respectively. The numerical results were very consistent confirming the path independency of the J-integral method and they correlate reasonably well with the average experimental toughness obtained using the compliance method. This correlation confirms that the values derived from the compliance method are representative of the toughness behaviour for the material under investigation. An extra evaluation was carried out using the expression from the ASTM E399-90 standard to verify the validity of the expressions for orthotropic materials. A comparison between ASTM, compliance, J-integral and results obtained using the proposed method described in section 3 are shown in Fig. 18. Fig. 19 shows a comparison between the original ASTM and modified correction function obtained using Eq. (14).

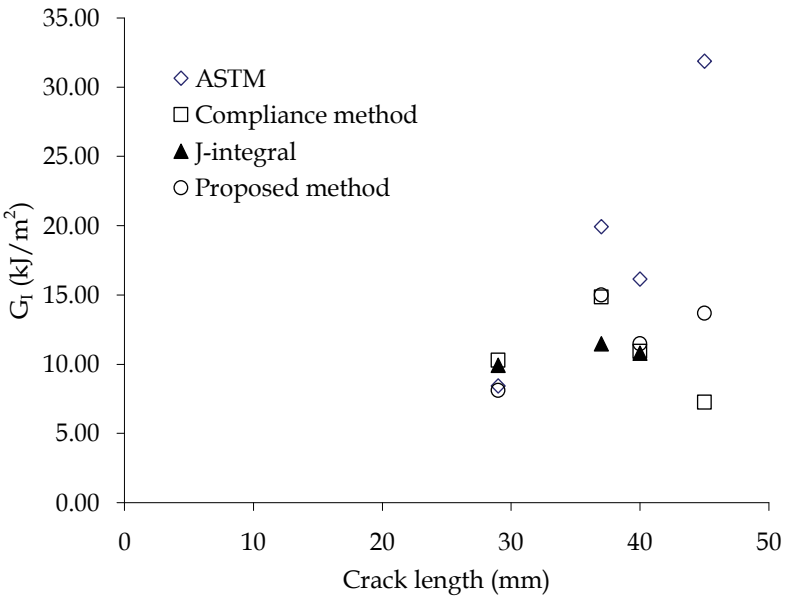

Fig. 18. Comparison between different methods for computing G_{Ic} using OCT specimens

It can be seen from Fig. 18 that there is a reasonably good agreement between the ASTM and compliance method for the initiation values of G_{Ic} however the propagation values are over predicted by the ASTM standard compared to the numerical values. On the other hand, despite these variations, the experimental values obtained using the compliance method varies consistently around the average numerical values.

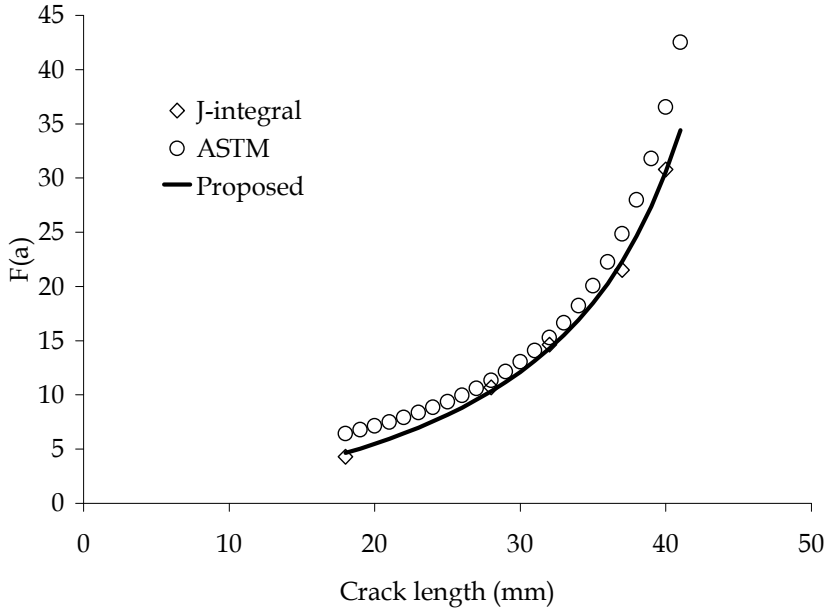

Fig. 19. Comparison between correction functions for determination of K_{Ic}

7.2 FE model setup for the DEN specimen

The DEN specimen was modelled using 8-node quadratic plane stress elements. Due to the symmetry of the problem, only one quarter of the specimen was modelled. A finer mesh was assigned to the region around the crack tip in order to obtain an accurate representation of the stress/strain fields on that region. The ultimate load was uniformly distributed along the top edge of the virtual specimen. A close look at the FE mesh around the crack tip is shown in Fig. 20.

The J-integral was evaluated on ten different integration contours with mean values of 2.2 ± 0.011 kJ/m^2 and 170 ± 0.013 kJ/m^2 for the specimens loaded in the weft and warp directions, respectively. The numerical results agree reasonably well with experimental ones which confirm the initiation values obtained using DEN specimens. It also confirms the values obtained using 4PBT specimens which were around 2.2 kJ/m^2. For the virtual DEN specimens loaded in the warp direction a value around 170 kJ/m^2 was numerically obtained which also agree very well with 165 kJ/m^2 obtained using the compliance method.

7.3 FE model setup for the 4PBT specimen

A three-dimensional orthotropic model was generated using ABAQUS/CAE to calculate the toughness values in the weft direction based on the J-integral method for the four point bending specimens. The specimen had a $(90^0)_{10}$ lay-up with dimensions given in Fig.3. The virtual specimen was discretised using 20-node quadratic brick elements. A finer mesh was assigned to the crack tip region in order to better represent the stress/strain field on that region. The crack front line and the virtual crack extension vector were defined through-the-thickness direction by taking the free sides of the elements at the crack tip and one half of the total load was uniformly distributed along the contact line between specimen and upper testing jig. Due to the symmetry of the problem only one fourth of the specimen was

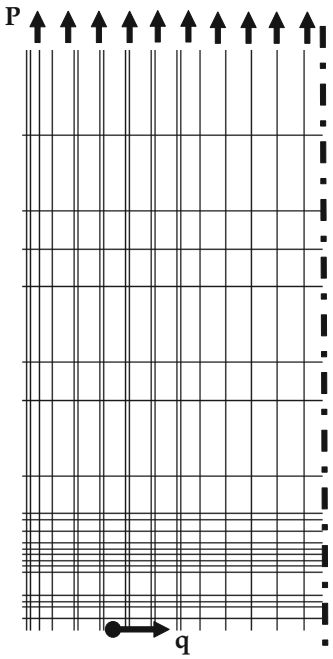

Fig. 20. FE mesh for the DEN specimens

modelled and a typical FE mesh is shown in Fig. 21. A mean value of 25 ± 0.01 kJ/m² was obtained for the J-integral and this result agrees well with the experimental values and numerical results obtained for DEN specimens. Unfortunately due to the unstable nature of crack growth it was not possible to derive a specific correction function for this specimen geometry and the validity of Eq. (6) remains questionable.

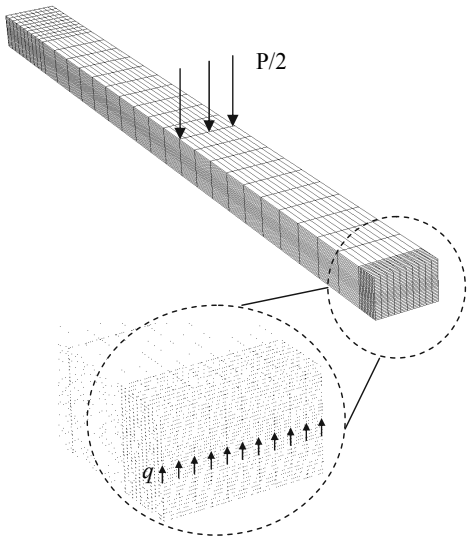

Fig. 21. FE mesh for the four point bending specimen (4PBT)

8. Concluding remarks

This chapter presented a detailed numerical and experimental study on the intralaminar fracture behaviour of hybrid plain weave laminates under mode I loading using different specimen geometries and data reduction schemes. Based on the numerical and experimental results the following conclusions were obtained:

- The fracture behaviour of hybrid plain weave laminates is far more complex than conventional UD laminates due to interactions between two different fibrous constituents and matrix which may result in a local coupling between different failure modes (mode I/mode II) during the fracture process;
- The class of material investigated exhibited much higher intralaminar toughness values compared to conventional UD laminates making them good candidates for designing damage resistant/tolerant composite aerostructures;
- A lower scatter in the toughness values was obtained using 4PBT specimens;
- Initiation and propagation toughness values around 2 kJ/m^2 and 10 kJ/m^2, respectively, were obtained in the weft direction;
- Initiation and propagation toughness values around 100 kJ/m^2 and 165 kJ/m^2, respectively, were obtained in the warp direction;
- The application of the ASTM E399-90 is questionable for composites in general and it can overestimate the toughness values by factors higher than three if used in its original form;

A methodology to derive a new correction function accounting for geometry and orthotropic effects was presented and discussed in this chapter. The methodology can handle different geometries giving better correlation with experimental results compared with standard methods.

9. References

ABAQUS 6.5-1. (2005). *Theoretical manual*.

Brown, W.F., Jr. and Strawley, J.E. (1967). Plane strain crack toughness testing of high strength metallic materials, *ASTM STP 410*, *American Society for Testing and Materials*.

Cowley D.K., Beaumont P.W.R. (1997). The interlaminar and intralaminar fracture toughness of carbon-fibre/polymer composites: The effect of temperature. *Composite Science and Technology,* Vol. 57, pp. 1433-1444, ISSN 0266-3538.

Donadon M.V., Hodgkinson J.M., Falzon B.G., Iannucci L. (2004a). The reliability of the resin infusion under flexible tooling process for manufacturing composites aerostructures. *Proceedings of the 13th Sicomp*, Sweden, September, 2004.

Donadon M.V., Hodgkinson J.M., Falzon B.G., Iannucci L., (2004b). The impact behaviour of composites manufactured using resin infusion: Mechanical and physical properties assessment, Internal report, Dept. of Aeronautics, Imperial College London.

Donadon M.V, Hodgkinson J.M., Falzon B.G., Iannucci L. (2004c). Impact damage in composite structures manufactured using resin infusion under flexible tooling (RIFT) process. *Proceedings of the ECCM-11*, Greece, 2004.

Donadon M.V, Hodgkinson J.M., Falzon B.G., Iannucci L. (2007). Intralaminar toughness characterisation of unbalanced hybrid plain weave laminates. *Composites Part A: Applied Science and Manufacturing*, Vol. 38, No. 6, pp. 1597-1611, ISSN: 1359-835X.

Donadon M.V, Almeida S. F. M., Arbelo M. A., de Faria A. R. (2009). A three-dimensional ply failure model for composite structures. *International Journal of Aerospace Engineering*, Vol. 2009, pp. 1-22, ISSN: 1687-5966.

Iannucci L., Willows M.L. (2006). An energy based damage mechanics approach to modelling impact onto woven composite materials—Part I: Numerical models. *Composites Part A: Applied Science and Manufacturing*, Vol. 37, No. 11, pp. 2041-2056, ISSN: 1359-835X.

Jose S., Kumar R.R., Jana M.K., Rao G.V. (2001). Intralaminar fracture toughness of a cross-ply laminate and its constituent sub-laminates. *Composite Science and Technology,* Vol. 61, pp. 1115-1122, ISSN: 0266-3538.

Konstantinos G. D, Kostopoulos V., Steen M. (2005). Intrinsic paramaters in the fracture of carbon/carbon composites. *Composite Science and Technology*, Vol. 65, pp. 883-897, ISSN: 0266-3538.

Kostopoulos V, Markopoulos Y.P., Pappas Y.Z., Peteves S.D. (1998). Fracture energy measurements of 2-D Carbon/Carbon composites. *Journal of European Ceramic Society* Vol. 18, pp. 69-79, ISSN: 0955-2219.

Lin G. Y., Shetty D. (2003). Transformation zones, crack shielding, and crack-growth resistance of Ce-TZP/alumina composite in mode II and combined mode II and mode I loading. *Engineering Fracture Mechanics,* Vol. 70, pp. 2569-2585, ISSN: 0013-7944.

Lin, S. T., Feng Z., Rowlands R.E. (1997). Thermoelastic determination of stress intensity factors in orthotropic composites using J-integral. *Engineering Fracture Mechanics,* Vol. 56, No. 4, pp. 579-592, ISSN: 0013-7944.

Pinho S.T, Robinson P., Iannucci L. (2004). Intralaminar fracture toughness of laminated composites: manufacture of specimens with sound pre-cracks. Internal Report, Dept. of Aeronautics, Imperial College London, 2004.

Pinho S.T, Robinson P., Iannucci L. (2006a). Fracture toughness of the tensile and compressive fibre failure modes in laminated composites. *Composite Science and Technology* , Vol. 66, No. 13, pp. 2069-2079, ISSN: 0266-3538.

Pinho S.T, Robinson P., Iannucci L. (2006b). Physically-based failure models and criteria for laminated fibre-reinforced composites with emphasis on fibre kinking: Part I: Development. *Composites Part A: Applied Science and Manufacturing*, Vol. 37, No. 1, pp.63-73, ISSN: 1359-835X.

Paris, P.C, Sih C. G. (1960). Stress analysis of cracks, fracture toughness and applications, *STP-381, ASTM 1960*; pp. 30-83.

Rooke D. P., Cartwright D.J. (1976). Compendium of stress intensity factors. London HMSO 1976.

Martin R. H., Elms T., Bowron S. (1998). Characterisation of mode II delamination using the 4ENF. Proceedings of the 4th European Conference on Composites: Testing and Standardisation, Lisbon Portugal, 31st August-2nd September 1998.

Standard test method for plane strain fracture toughness of metallic materials, ASTM E399-90, *Annual book of ASTM standards* 03.01 1993; pp. 407-528

Slepetz J.M., Carlson. (1975). Fracture of composite compact tension specimens, ASTM STP 593, *American Society for Testing and Materials* 1975.

17

Ultrasonic Pulse Velocity Evaluation of Cementitious Materials

T. H. Panzera[1], A. L. Christoforo[1],
F. P. Cota[1], P. H. R. Borges[2] and C. R. Bowen[3]
[1]*Department of Mechanical Engineering, Federal University of São João del Rei - UFSJ, Praça Frei Orlando, 170 São João Del Rei – MG,*
[2]*Department of Civil Engineering, Federal Centre for Technological Education of Minas Gerais, CEFET-MG,*
[3]*Materials Research Centre, Department of Mechanical Engineering, University of Bath, Bath BA2 7AY,*
[1,2]*Brazil*
[3]*UK*

1. Introduction

There is a growing interest at an international level in non-destructive testing of cement based materials, such as: impact-echo, pulse-echo, ultrasonic pulse velocity, wave reflection, resonant frequency, acoustic emission and microwave adsorption methods, along with techniques measuring the conductivity and resistance of the material (Demirboga et al., 2004; Panzera et al., 2008; Trtnik et al., 2008). The pulse velocity method has been shown, for some time, to provide a reliable means of estimating properties and offers a unique opportunity for direct, reliable, quick, safe, inexpensive and non-invasive quality control of buildings and other concrete constructions damaged by earthquake, fatigue, conflagration or other catastrophic scenarios (Leslie & Cheeseman, 1949; Elvery, 1973; Bungey, 1982).
The internal structure of concrete, mortar and cementitious composites is highly complex and can be considered to be composed of (a) cement paste, which in itself is a highly complex multiphase material, (b) mineral aggregates, which are also porous composite materials and (c) the interface between paste and aggregate particles. Thus, concrete can be aptly considered a composite at a range of scales and heterogeneous at both microscopic and macroscopic levels. This complexity makes the behaviour of ultrasonic waves in concrete highly irregular, which, in turn, hinders non-destructive testing (Prassianakis & Giokas, 2003). The velocity of ultrasonic pulses traveling in a solid depends on the density and elastic properties of the material. It is thought that ultrasonic pulse velocity can often be used to assess the overall quality of a material, as well as to determine their elastic properties (Marfisi et al., 2005).
Pulses of longitudinal, elastic stress waves are generated by an electro-acoustical transducer that is held in direct contact with the surface of the concrete under test (Komlos et al., 1996). After traversing through the material, the pulses are received and converted into electrical energy by a second transducer. This common principle is expressed in somewhat different

ways among the standards of various nations (see Table 1). There are also differences in how the standards discuss the factors that affect pulse velocity in cementitious composites. It is necessary to consider all factors and their correlation with physical properties, so that the measurement of pulse velocity is reproducible and exclusively dependent on the properties of the material under test (Castro & Carino, 1998).

Country	Designation	Year
Begium	NBN 15-229	1976
Brazil	ABNT 18:04.08.001	1983
Bulgaria	BDS 15013-80	1980
Czech republic	CSN 731371	1981
DDR	TGL 33437102	1983
Denmark	DS 423.33	1984
Germany	Draft. Same as ISOiDIS 8047	1983
Hungary	MI 07-3318	1994
International	ISO/DIS 8047	1983
Mexico	NOM-C-275-l 986	1986
Poland	PN-B-06261	1974
RILEM	NDT 1	1972
Romania	C-26-72	1972
Russia	COST 17624	1987
Scandinavia	NT BUILD 213	1984
Spain	UNE 83-308-86	1986
Sweden	SS 137240	1983
United Kingdom	BS 12504-4: Part 4	2004
USA	ASTM C 597	1983
Venezuela	COVENIN 1681-80	1980
Yugoslavia	JUS U.Ml.042	1982

Table 1. Standards for the determination of longitudinal ultrasonic pulse velocity in concrete (Castro & Carino, 1998)[1]

The direction in which the maximum energy is propagated is at right angles to the face of the transmitting transducer; however, it is possible to detect pulses travelling through concrete in some other direction. In other words it is possible, to make measurements of pulse velocity (BS 12504-4, 2004) by placing the two transducers on either:

a. opposite faces - direct transmission (Figure 1a),
b. adjacent faces - semi-direct transmission (Figure 1b);
c. the same face - indirect or surface transmission (Figure 1c).

[1] Local standards from EU countries may have been superseded by EN 12504-4 (2004)

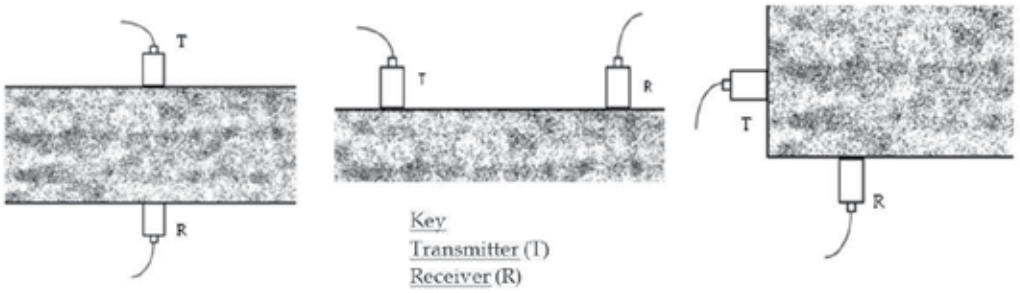

(a) Direct Transmission (b) Indirect or surface Transmission (c) Semi-direct Transmission

Fig. 1. Methods of propagation and receiving ultrasonic pulses (BS 12504-4, 2004)

Direct transmission is the most sensitive, and indirect transmission the least sensitive. Indirect transmission should be used when only one face of the concrete is accessible, when the depth of a surface defect or crack is to be determined or when the quality of the surface concrete relative to the overall quality is of interest. The velocity, v, is calculated from the distance, between the two transducers and the electronically measured transit time, t, of the pulse as:

$$v = \frac{l}{t} \tag{1}$$

Pulses are not transmitted through large air voids in a material. Therefore, if such a void lies directly in the pulse path the instrument will indicate the time taken by the pulse that circumvents the void by the quickest route. It is thus possible to detect large voids when a grid of pulse velocity measurements is made over a region in which these voids are located. A viscous material, such as a jelly or grease, is commonly used as a coupling agent to ensure that the vibrational energy enters the test object and can be detected by the receiving transducer (Pundit, 1990).

A number of researchers have developed theoretical models for the prediction of relationships between pulse velocity and physic-mechanical properties, such as modulus of elasticity, compressive strength, density, porosity and permeability. Other interests are focused on the correlation between pulse velocities and cement characteristics, such as water/cement ratio, aggregate particle size, hydration process and curing temperature effects. The correlation between ultrasonic pulse velocity (UPV) and the properties of cement-based materials will be presented in the following sections.

2. UPV and physical and durability properties

2.1 UPV and stiffness (modulus of elasticity)

It has been demonstrated that it is possible to measure the dynamic modulus of elasticity using established non-destructive test methods based on stress-wave propagation. The results have shown good agreement between average values of static and dynamic modulus. The dynamic values had less test variability than the static values (Castro & Carino, 1998; Vipulanandan & Garas, 2008).

Linear elastic, homogeneous and isotropic materials can be characterized by two material constants such as two elastic moduli. When there is shear deformation, the shear modulus

(G_p) controls the shear velocity. The equation relating the shear wave velocity (V_s) and shear modulus (G_p) is as follows (Leslie & Chessman 1949; Mantrala & Vipulanandan 1995):

$$G_p = (\gamma/g).V_s^2 \tag{2}$$

Where (γ/g) = mass density of the material.
If the deformation is axial (ε) and the wave velocity is controlled by the constrained modulus (M), the equation relating the constrained modulus (M) and P-wave velocity (V_p) is as follows (Leslie & Chessman 1949):

$$M = (\gamma/g).V_p^2 \tag{3}$$

For an elastic, homogenous, and isotropic material

$$M = \left[\frac{(1 - \nu)}{(1 + \nu)(1 - 2\nu)}\right]E \tag{4}$$

Where E= Young´s modulus of the material and ν = Poisson´s ratio
At small strain levels, the mortar system can be assumed linearly elastic homogeneous and isotropic and the dynamic Poisson´s ratio (ν_p) of different mortar composites can be found by combining Eqs (2) – (4) as follows:

$$\frac{V_p}{V_s} = \left[\frac{2(1 - \nu_p)}{(1 - 2\nu_p)}\right]^{1/2} \tag{5}$$

And the dynamic Young´s modulus (E_p) can be determined as follows:

$$E_p = \frac{(1 + \nu_p)(1 - 2\nu_p)}{(1 - \nu_p)}.(\gamma/g)V_p^2 \tag{6}$$

The pulse frequency used for testing cementitious materials range from about 20 kHz to 250 kHz, with 50 kHz being appropriate for field-testing of concrete. These frequencies correspond to wavelengths ranging from about 200 mm (for the lower frequency) to about 16 mm at the higher frequency (Pundit, 1990).
Hansen (1965) as cited in Nwokoye (1974) has given some practical equations for the prediction of elastic modulus of mortar and concretes. Dynamic moduli of concrete, mortar, quasi-mortar and cement past phases can be estimated from a consideration of the stiffness constant of the particular phases. For mortars in which the cement paste is considered as the matrix and sand as the particles:

$$\frac{1}{E_{ms}} = \frac{1}{2}\left(\frac{K_p}{E_p} + \frac{K_s}{E_s}\right) + \frac{1}{2}\left(\frac{1}{K_pE_p + K_sE_s}\right) \tag{7}$$

where K_p and K_s are volume fractions of cement paste and sand respectively and E_{ms} is the modulus of elasticity of mortar.
For concrete in which mortar is considered as the matrix and regular aggregate as the particles:

$$E_0 = \left(\frac{1}{\frac{1-\alpha}{E_{ms}} + \frac{\alpha}{E_a}} \right) \quad (8)$$

Where E_0 is the elastic modulus of concrete, E_{ms} is the elastic modulus of mortar, E_a is the elastic modulus of aggregate, α is the volume fraction of coarse aggregate and β is the volume fraction of fine aggregate (β = 1- α).

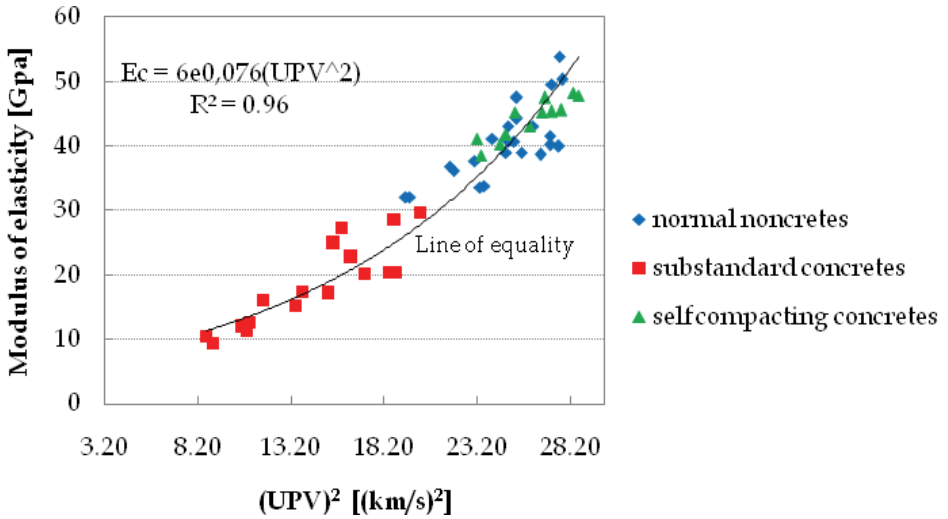

Fig. 2. Relationship between UPV and E_s (Yildirim & Sengul, 2011)

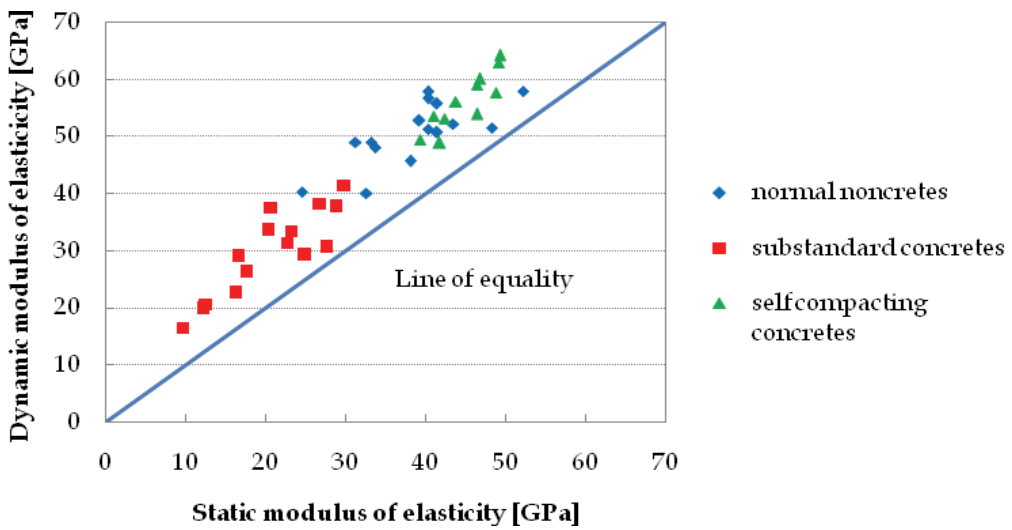

Fig. 3. Relationships between static and dynamic modulus of elasticity (Yildirim & Sengul, 2011)

Yildirim and Sengul (2011) investigated the effects of water/cement ratio, maximum size of the aggregate, aggregate type, and fly ash addition on the dynamic modulus of elasticity of low quality concrete with water/cement ratios close to 2.2. A strong relationship was obtained between the static modulus of elasticity and ultrasound pulse velocity (see Figure 2). The relationship indicates that the ultrasonic pulse velocity measurements can be used also for estimating the static modulus of elasticity of substandard concretes in existing structures where taking out cores from the structural elements is not preferred due to very low concrete strength or small dimensions of the elements. Figure 3 shows the correlation between static and dynamic modulus of elasticity. These results indicate that the dynamic modulus values are, approximately 30% higher than the static modulus obtained from compressive testing. The reason behind such a result may be that, since ultrasonic test is conducted at low stress levels, the test results more closely resemble an initial tangent modulus of the material (Yildirim & Sengul, 2011).
Trtnik et al. (2008) presented the relationships between V_p (UPV) and E_{stat}, E_{dyn} and G (Figure 4). Despite the dynamic modulus being higher than the static modulus, they exhibited the similar trends.

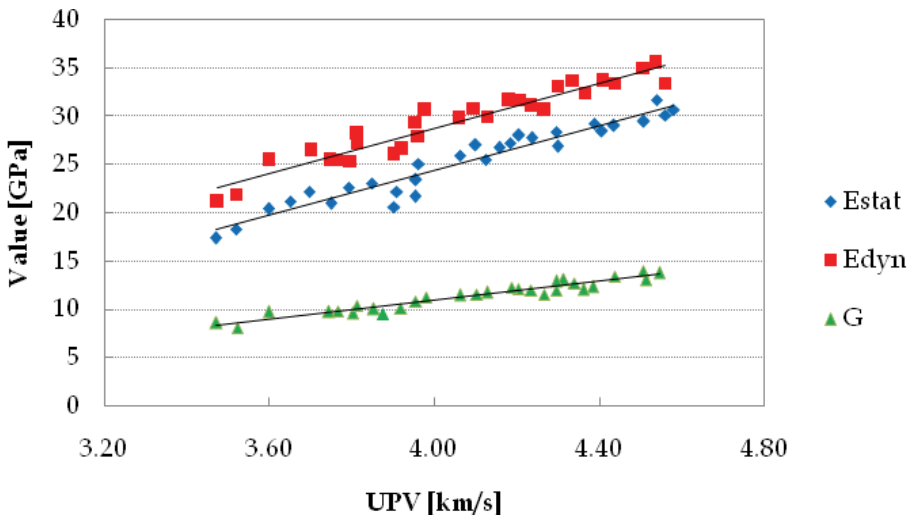

Fig. 4. Relationships between UPV and E_s, E_d and G (Trtnik et al., 2008)

2.2 UPV and strength

The ultrasonic pulse velocity in cement-based materials depends mainly on its elastic modulus and, since the latter is closely related to mechanical strength (how is elastic modulus related to strength, something can be stiff and weak (e.g. chalf)) or stiff and strong (e.g. carbon fibre), it is natural do believe the pulse velocity can be also correlated to compressive strength. The correlation, however, is not unique, but rather depends particularly on the mix proportions, cement type and type of aggregate used (Neville, 1996; Trtnik et al. 2009). Therefore, the UPV may be used to estimate compressive strength as long as a calibration curve exists for each assessed material (Mandandoust et al., 2010).
Numerous data and correlation relationships between the strength and pulse velocity of concrete have been presented and proposed. Galan (1967) reported a regression analysis to

predict the compressive strength of concrete based on acoustic characteristics such as UPV and the damping constant. Rajagopalan et al. (1973) reported a correlation between the UPV and compressive strength of concrete for some typical mixes. This particular study presented simultaneous measurements of pulse velocity and compressive strength made on 150 mm cubes at different ages from 1 to 28 days, indicating a linear relation between strength and velocity. Lin et al. (2003) carried out experiments to establish mathematical models for predicting concrete pulse velocity based on aggregate content and water–cement ratio. Tharmaratram & Tan (1990) provided an empirical formula of the combined UPV and ultrasonic pulse amplitude. Demirboga et al. (2004) found an exponential relationship between compressive strength and UPV for mineral-admixtured concrete. The equation most commonly used is (Trtnik et al. 2009):

$$S = a.\exp(b.V_p) \tag{9}$$

where a and b are empirical parameters determined by the least squares method. Table 2 presents some relationships between concrete compressive strength S and the ultrasonic pulse velocity of longitudinal waves V_p, together with the coefficients of determination R^2.

Equation	R^2	References
$S = 1.146\exp(0.77V_p)$	0.80	Turgut (2004)
$S = 1.19\exp(0.715V_p)$	0.59	Nashn't et al. (2005)
$S = 8.4 * 10^{-9}(V_p * 10^3)^{2.5921}$	0.42	Kheder (1999)[A]
$S = 1.2 * 10^{-5}(V_p * 10^3)^{1.7447}$	0.41	Kheder (1999)[B]
$S = \exp[(-3.3 \pm 1.8) + (0.0014 \pm 0.0004)\ (V_p * 10^3)]$	0.48	Rio et al. (2004)

[A]For wet concrete, [B]For dry concrete

Table 2. Relationships between concrete compressive strength and ultrasonic pulse velocity (Trtnik et al., 2009)

It can be seen from Table 1 that the coefficients of determination (R^2) are low because the concrete composition was not taken into account or, in other words, different concrete compositions were compared at a time. That is the reason why the exponential curve is also broad in Fig. 5. In fact, it is well known that many parameters or cement paste characteristics that influence the concrete strength also influence pulse velocity, though not necessarily in the same way or to the same extent (Popovics, 2007). The effect of different composite parameters on UPV results will be treated in Section 3. The results performed by Bernardo (2003) as cited in Trtnik et al. (2009) indicated a 40%increase in UPV measured after three years. The increase in the compressive strength during the same period is much higher, more than 500%.

Keating et al. (1989) investigated the correlation between UPV and strength for slurries often used in cementing oil well casings, where temperatures do not exceed 50 °C. It was shown that there is a correlation at atmospheric pressure, between pulse velocity and cube strength for the first 24 hours after mixing. A lower bound curve can be used to predict initial set and waiting on cement time, from pulse velocity (Fig. 6). The initial pulse velocity of about 1580m/s exhibited a relatively stable plateau region during the first two hours after mixing but after a period when it became possible to strip the cubes from their moulds and test them, the pulse velocity increased relatively rapidly for period up to about four hours and then at a progressively slower rate of increase for the remainder of the test. During this

period the cubes showed a steady rate of increase in strength. After six hours the pulse velocity ranged from 1850 m/s to 2000 m/s with cube strengths of about 2.4 MPa while at 24 hours the range was from 2200 m/s to 2600 m/s with cube strengths of about 12 MPa.

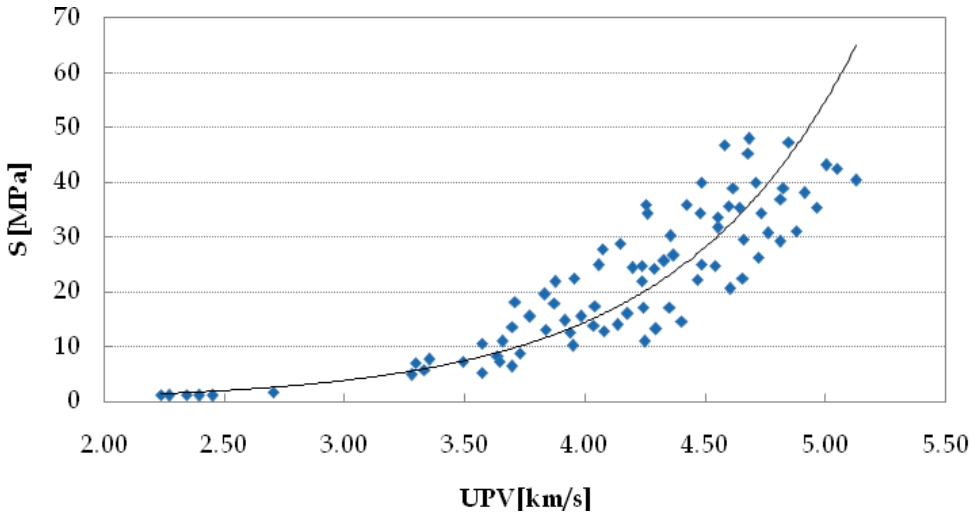

Fig. 5. Relationship between UPV and strength (Trtnik et al., 2009)

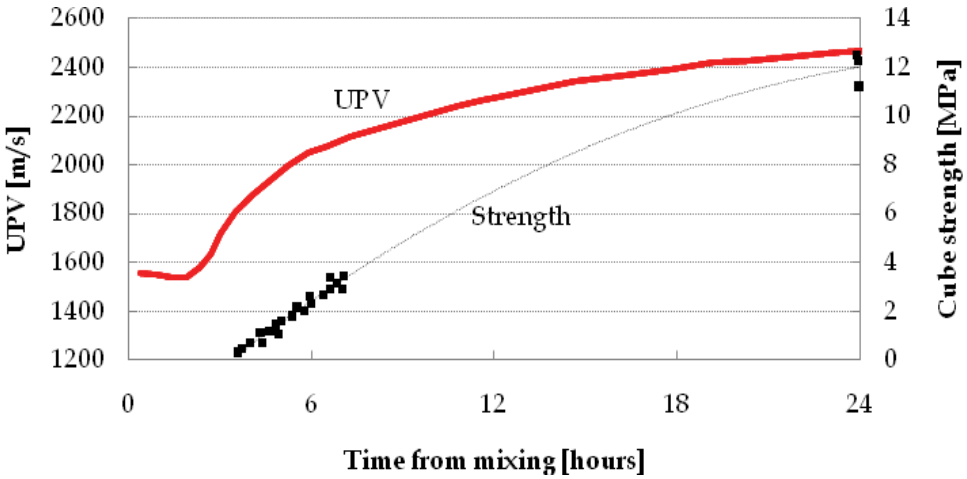

Fig. 6. Comparison between pulse velocity and cube strength at ages between 0 and 24 hours after mixing at 20 °C (Keating et al. 1989)

Ulucan et al. (2008) investigated the effect of silica fume (SF) and fly ash (FA) as mineral admixtures replacing Portland cement (PC) in self-compacting concrete (SCC). It can be seen from Fig. 7a that the UPV values decreased with increasing FA replacement of PC in SCCs at 3 and 7 days, while SCC containing 30% FA replacement had the highest UPV values at 28- and 130-day curing periods. The UPV values increased with increasing curing period at all levels of FA replacement in SCCs. The UPV values of SCCs containing FA were higher than

those of SCCs with SF replacement at all levels of replacement for all curing ages (see Fig. 7b), indicating the filling and packing capacity of FA particles. The correlation between UPV and compressive strength is also exponential for SCCs containing both FA and SF (Fig. 8). However, constants for each pozzolanic material were different for each level of replacement of PC in SCCs.

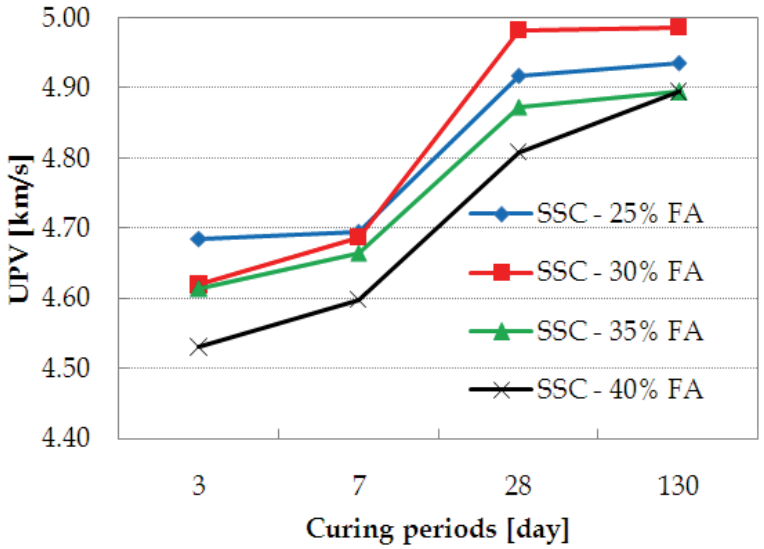

(a)

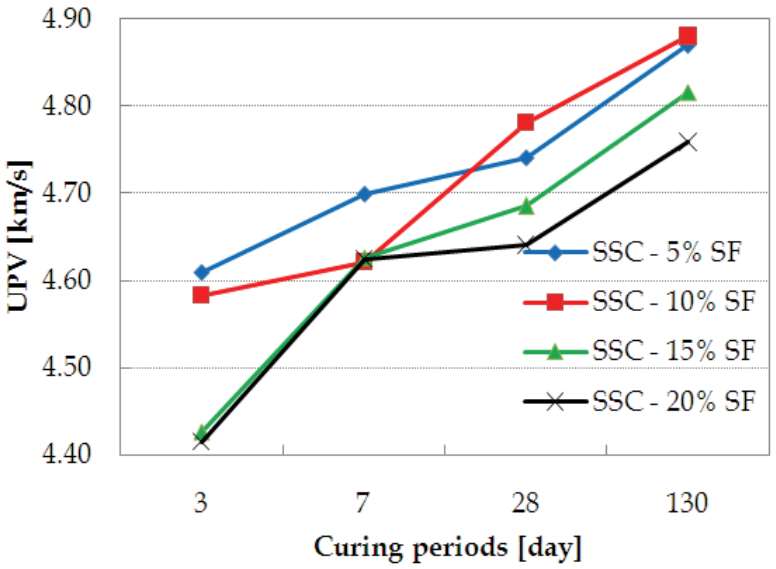

(b)

Fig. 7. UPV results for SCC with FA (a) and SF (b) for different curing periods

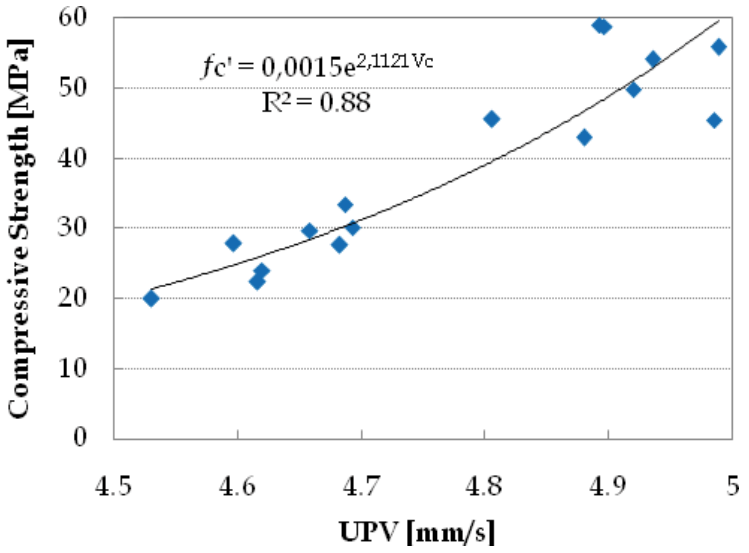

(a)

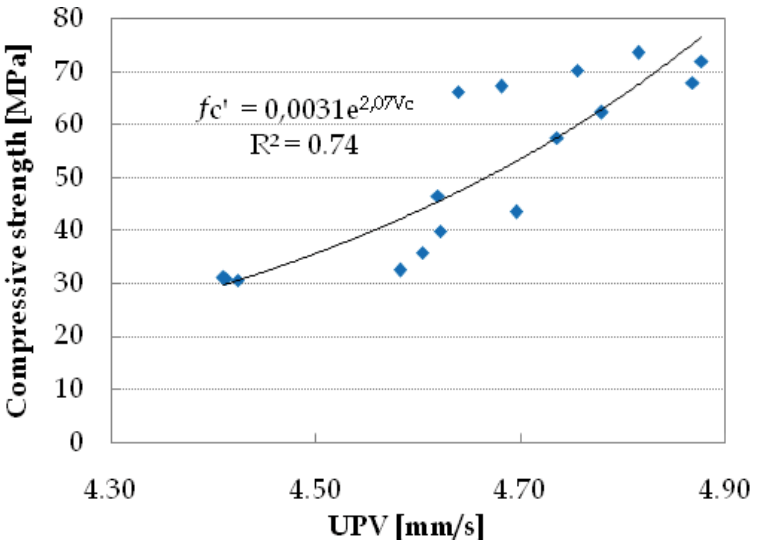

(b)

Fig. 8. Correlation between compressive strength and UPV for SCC with FA (a) and SF (b) (Ulucan et al., 2008)

Dmirboga et al. (2004) investigated the addition of 50%, 60% and 70% of FA as a replacement of PC. Both compressive strength and UPV were very low for all replacement levels at an early age of curing. However, with the increase of curing period, both compressive strength and UPV of all the samples increased, which confirm the findings of Ulucan et al. (2008).

Ikpong (1993) stated that the introduction of a pozzolanic material into concrete affect both the compressive strength and pulse velocity along the same direction. A unit volume of cement contributes more to the strength and pulse velocity through the concrete than does an equivalent volume of the ash. The primary products of hydration formed by the reaction between cement and water account for a greater proportion of each of these three quantities than do the secondary products of hydration resulting from the pozzolanic reaction involving the ash (Ikpong, 1993).

Mohammed (2011) studied the fresh and hardened properties of concrete containing crumb rubber (rubbercrete) as a replacement of fine aggregate. The utilization of the crumb rubber from scrap tires as a sustainable building materials in the construction industry help to preserve natural resources and maintain the ecological balance. The UPV values of the rubbercrete decrease with an increase in the percentage of the crumb rubber content and decreases with an increase in the water/cement ratio. The results also revealed that the UPV values increase as the curing age increases (Mohammed, 2011).

Other authors (Kewalramani & Gupta, 2006; Hola et al., 2005 and Trtnik et al., 2009) compared artificial neural networks and multiple-regression analysis to predict concrete compressive strength based on UPV and weight of concrete. They concluded that the prediction performed using ANN has a better degree of coherency with experimentally evaluated compressive strength than multiple-regression analysis.

Trtnik et al. (2009) studied the influence of aggregate content, nominal maximum aggregate size, type and shape of aggregate, and also the type of cement, initial concrete temperature, environmental temperature, and water–cement ratio on the strength–velocity relationship. They observed that the characteristics of the aggregate are very important to assess the compressive strength of concrete based on the measurement of ultrasonic pulse velocity. Therefore they employed some characteristics of aggregate (amount, nominal maximum size, type and shape) and UPV as input parameters to build an ANN model to accurately predict concrete compressive strength (Trtnik et al., 2009).

Despite the results presented above, some other authors did not find good correlation between strength and UPV for cementitious materials (Popovics & Rose, 1994; Qasrawi, 2000; Turgut & Kucuk, 2006; Panzera et al, 2008). The prediction of cementitious materials strength based on UPV technique depends not only on their constitution but also on the manufacturing process, which can occasionaly be a difficult and unreliable task (Zarandi, 2008). Calibration may be also an issue.

The factors influencing calibrations are so many that even under ideal conditions with a specific calibration it could be unlikely to achieve 95% confidence limits of better than ±20% for an absolute strength prediction of insitu concrete (Mandandoust et al., 2010).

2.3 UPV and porosity, permeability & density

Deterioration of concrete is generally caused by penetration of aggressive agents –sulfates, nitrates, chlorides, water, frost, CO_2 – into the material interior. The kinetics of reaction of concrete with those agents, hence its durability, is essentially determined by the transfer properties of the cover, i.e. the first few centimeters below the surface of the structure (Goueygou et al, 2009; Lafhaj et al., 2006).

The theoretical relationship between ultrasonic propagation and material durability parameters is based on a simple model proposed by Yaman et al. (2002). The longitudinal and shear wave velocities are related to the modulus of elasticity and density by well-known formulas (10) (Popovics, 2007):

$$V_p = \sqrt{\frac{E}{\rho}.\frac{1-\nu}{(1+\nu)(1-2\nu)}} \quad V_s = \sqrt{\frac{E}{\rho}.\frac{1}{2(1+\nu)}} \tag{10}$$

Next, the relationship between Young's modulus and porosity p is taken in the form of a power law (Popovics, 2007).

$$E = E_0(1-p)^c \tag{11}$$

where c is an empirical fitting parameter and E_0 is the Young's modulus of the material at zero porosity (in what follows, index "0" will refer to the zero-porosity material). As density is related to porosity by:

$$\rho = \rho_0(1-p) \tag{12}$$

and neglecting the influence of porosity on Poisson ratio, i.e. $\nu = \nu_0$ for a given value of water content, insertion of Eqs. (11) and (12) into Eq. (10) yields:

$$\begin{aligned} V_p &= V_{p_0}(1-p)^a \\ V_s &= V_{s_0}(1-p)^a \end{aligned} \tag{13}$$

Where, $V_{p_0} = \sqrt{\frac{E_0}{\rho_0}.\frac{1-\nu_0}{(1+\nu_0)(1-2\nu_0)}}$, $V_{s_0} = \sqrt{\frac{E_0}{\rho_0}.\frac{1}{2(1+\nu_0)}}$ and $a = \frac{c-1}{2}$

For low porosity values, Eq. (13) can by approximated by the following linear relationships:

$$\begin{aligned} V_p &= V_{p_0}(1-bp) \\ V_s &= V_{s_0}(1-bp) \end{aligned} \tag{14}$$

According to Shkolnik et al. (1997), parameter b is related to Poisson ratio at zero porosity by:

$$b = 15\left(\frac{1-\nu_0}{7-5\nu_0}\right) \tag{15}$$

Finally, the porosity (*p*) and permeability (*k*) relationship is derived from a simple model, assuming that for fluid flow, the system of open pores is equivalent to a set of parallel circular channel of diameter d directed along the macroscopic fluid flow (Udegbunam et al., 1999):

$$k = \frac{pd^2}{32} \tag{16}$$

Combining Eqs. (14) and (16), a linear relationship between permeability (*k*) and UPV can be derived:

$$k = \frac{d^2}{32b}.\frac{\Delta V_{p,s}}{V_{p,s_0}} \tag{17}$$

Where $\frac{\Delta V_{p,s}}{V_{p,s_0}}$ corresponds to the variation of UPV of longitudinal or shear wave relative to the zero-porosity value. Eqs. (13), (14) and (17) represent the theoretical model relating UPV with porosity and permeability.

The ultrasonic test has been used for nondestructive durability assessment to chloride ion penetration (Shkolnik et al., 1997; Udegbunam et al., 1999; Lafhaj et al., 2006). Three ranges of saturation were considered: full saturation (FS) when the water content is more than 85% of the fully saturated specimen; partial saturation (PS) when it is in between 45% and 55%; dry (D) when the saturation is less than 10%. The variation of ultrasonic parameters can be observed in Fig.9. Pulse velocity decreases with porosity and permeability, and it increases with water content. Such trends are in accordance with works published by other researchers (Winkler & Nur, 1982; Ohdaira&Masuzawa, 2000; Vergara et al., 2001). The dependence of permeability on porosity and water content is very significant. As a matter of fact, permeability does not depend only on porosity but also on tortuosity, specific surface, pore size distribution and connectivity of pores.

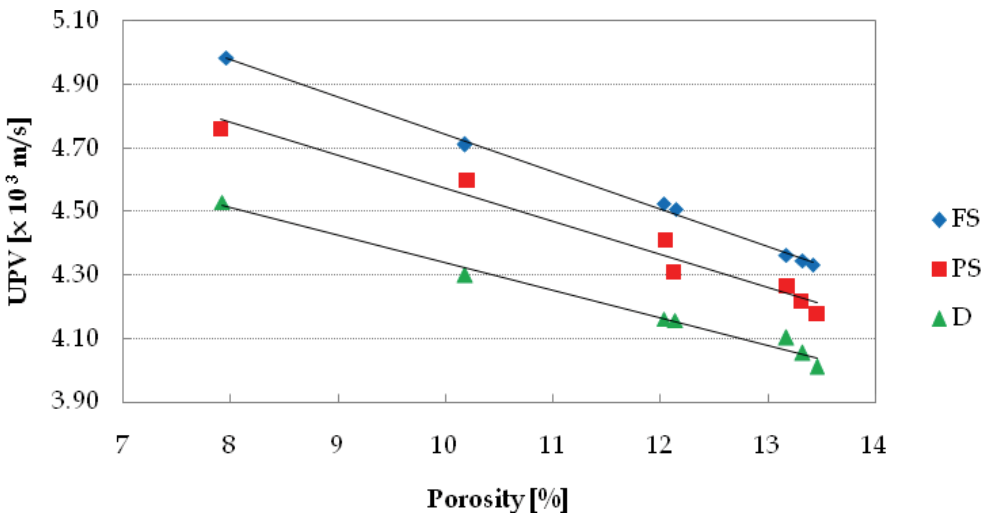

Fig. 9. Variation of UPV versus porosity (Lafhaj et al., 2006)

Panzera et al. (2008) investigated the effect of UPV of compacted cementitious composites based on ordinary Portland cement (OPC) and silica particles with a low water/cement ratio. The results reveal a significant correlation between the UPV and porosity (Fig. 10a) and oxygen permeability (Fig. 10b). A decrease of the pulse velocity corresponds to an increase of porosity and oxygen permeability, which confirms that a region of low compaction, voids or damaged material is present in the composites and leads to a reduction in the calculated pulse velocity.

A linear correlation between UPV and bulk density was found represented by the equation $y = 1506.9x + 541.7$ ($R^2 = 88.69\%$), where y is the pulse velocity and x the bulk density. As observed in Figure 11, the higher the pulse velocity the higher the bulk density of the cementitious composites (Panzera et al 2008).

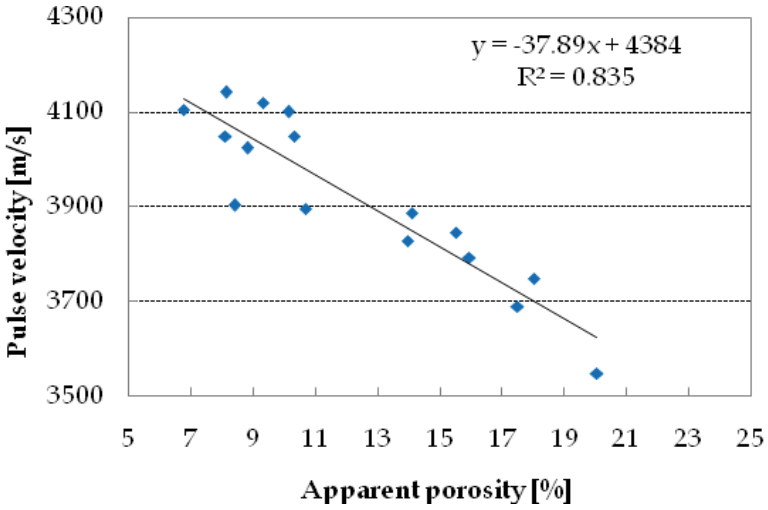

(a)

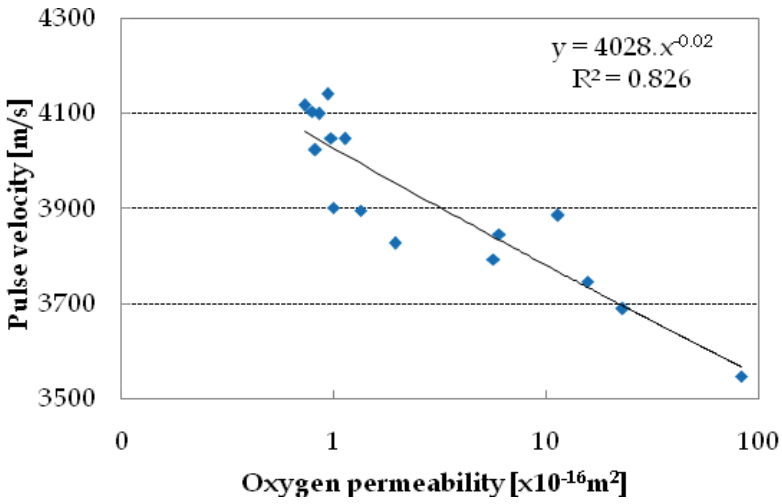

(b)

Fig. 10. Correlation plot between the apparent porosity (a) and (b) permeability versus UPV (Panzera et al., 2008)

3. Influence of paste / concrete parameters on UPV

As mentioned in section 2.2, several parameters affect strength of cement-based materials and consequently the UPV results. The following sections cover the most common parameters studied with UPV.

3.1 UPV and water content in cementitious composites

Ye et al. (2004) studied concretes with three different water/cements (w/c) ratios, 0.40, 0.50 and 0,55, and concluded that the mixes with lower w/c had higher values of UPV, which

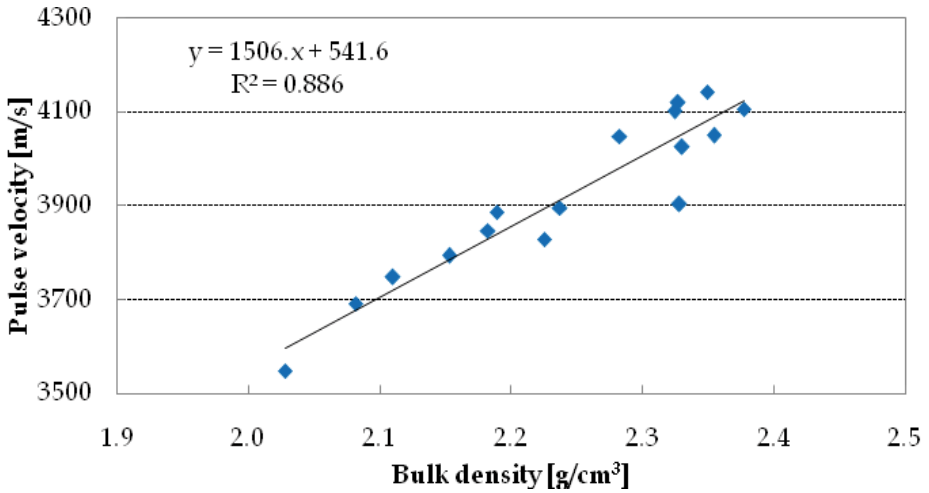

Fig. 11. Correlation plot between the bulk density and the pulse velocity (Panzera et al., 2008)

could be associated with higher amount of solids in those mixes (Fig. 12). In addition, mixes with lower w/c had more aggregate content, which also increases the pulse velocity. Some research (Trtnik et al., 2009; Madandoust, 2010) have pointed out that the influence of w/c on UPV results is more pronounced at later ages of hydration, when the volume of capillary pores is reduced. During the first three days of hydration, the ultrasonic velocity is significantly low due to the large amount of capillary pores, so that the sensitivity to w/c alterations is not noticed.

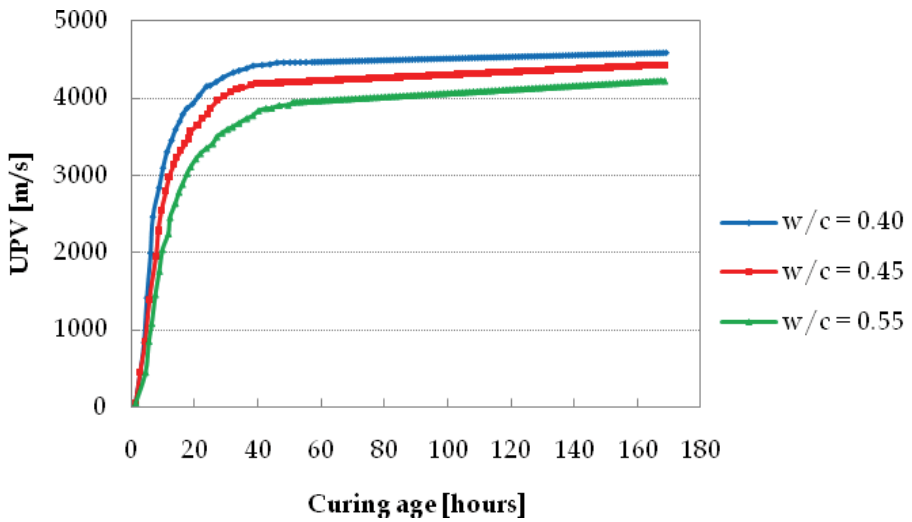

Fig. 12. Effect of the w/c ratio on UPV (Ye et al., 2004)

It is important to differentiate the effect of water content on UPV results. Mixing water, usually described in terms of w/c ratio, usually reduces UPV results as described in the last

paragraph. However, the amount of water present in the samples subjected to testing (i.e. cement paste or concrete moisture) has a different impact on pulse velocity. Ohdaira (2000) and Bernardo (2003) found that moisture content helps the propagation velocity in concrete. On the other hand, it affects compressive strength negatively. So, such dissimilarities may create ambiguity in the interpretation of UPV results (Li, 2004). Lajhaf (2006) summarizes as follows: for a given value of moisture, a significant decrease of velocity is observed with increasing porosity. As an example, the reduction of velocity for the fully saturated material is about 15% when porosity increases from 8% to 13.5%. On the other hand, for a given value of porosity, velocity increases with water content, which was also confirmed by Ohdaira and Masuzawa (2000). According to Yaman et al. (2001, 2002), the UPVchanges between the dry and the saturated state because moisture changes the shape of capillary pores, which significantly affects the mechanical properties of concrete. The shear wave appears to be less sensitive to water content than longitudinal wave velocity, especially when comparing partially (PS) and fully (F) saturated samples.
In general, the change of UPV response with water content opens new possibilities of studying the hydration process and hence to develop hydration models to cement-based materials.

3.2 UPV and cement hydration

UPV may be a valuable tool to assess the hydration of cementitious materials, including the early stages when the paste is not set. The determination of the initial setting of cement, for example, still relies on standard tests like the Vicat Neddle which cannot monitor the hydration continuously and often do not represent the characteristics of concretes (Trtnik, 2008). Therefore it makes sense to search for alternative methods to follow both the initial and later stages of hydration, such as those based on ultrasonic waves.
Keating et al. (1989) studied the hydration of oil well cement slurries using UPV and observed three stages as times elapsed after mixing: an initially constant regime, a rapidly increasing regime and a much more slowly increasing or almost constant regime. Later on, several other researchers (Popovics et al. 1993; Reinhardt et al., 2000, 2004; Lee et al. 2004, Trtnik, 2008, Zhang et al., 2009) have found similar patterns in mortar and concrete, which can be generalized as in Fig 13.
At the early stages of hydration, when the paste is not set, UPV is governed by the water/air phase in the cement paste, and the air bubbles present in the water acts as the dominant factor that determines the UPV (Ye et al., 2004). Stage 1 represents this stage, when increased tortuosity of the pore or air-filled space due to the formation of hydration products may even cause slight decrease in UPV (Lee et al., 2004). At very early ages in Stage 1, the presence of aggregates does not influence the pulse velocity, given that ultrasonic waves propagate through the phase of viscous suspension. Hence, mortars or concretes with same w/c will have approximately the same UPV results.
Stage 2 begins when there is a minimum quantity of hydration products filling the pores so the connection of particles leads to clusters that form a percolating solid network. Then, this step is marked by a switch of propagation path of ultrasonic pulse from the liquid to the solid phase, with a consequent rise in UPV. It is noticed that beyond this stage the influence of the solid phase becomes dominant instead of air bubbles on the UPV (Ye et al. and Lee et al., 2004). Finally, when all the solid phase was connected, the slow increase of the UPV followed the evolution of the total solid fraction (Step 3).

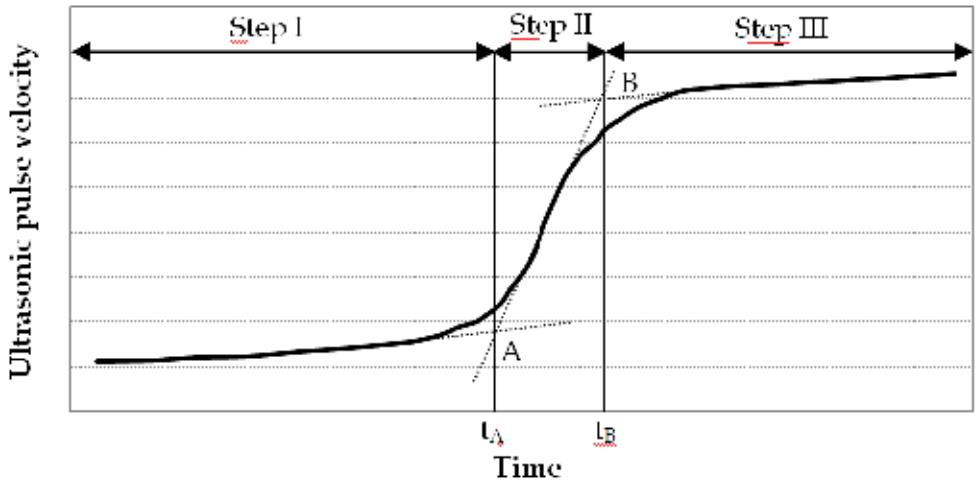

Fig. 13. Schematic representation of typical evolution of UPV in cement pastes (Lee et al., 2004)

Unlike Stage 1, the UPV profiles at later ages (Stages 2 and 3) have different shapes depending on the concrete mixtures. In other words, not only the w/c of the mixes but also the retarding effect of pozzolanic materials and the volume of coarse aggregates (which have higher stiffness than cement paste) affect the shape of the UPV with time curve.

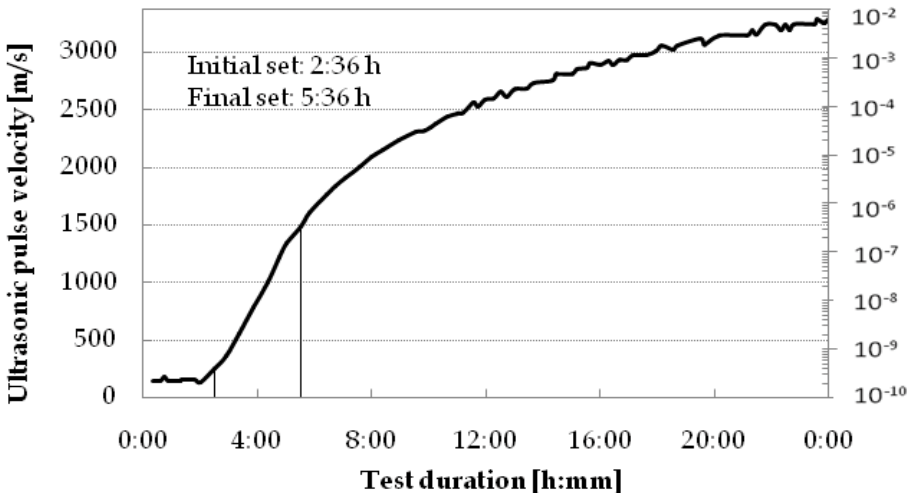

Fig. 14. Illustration of the beginning and end of setting for a mortar with CEM II 42.5 N and w/c = 0.6 (Reinhardt and Grosse, 2004)

It appears that both the onset and offset time of Stage 2 are closely related to setting of cement paste. Some authors (Reinhardt and Grosse, 2004; Chen et al., 2010) are convinced that the beginning of Stage 2 when the UPV transforms from a flat increase to a sharp one corresponds to the initial setting of cement pastes. Chotard et al. (2001) states that the duration of its sharp increase corresponds to the cement stiffening process and that the

beginning of Stage 3 is when the cement skeleton approaches its final stiffness, which is in accordance with results of Zhang (2009). Reinhardt and Grosse (2004), however, points out that the final setting is still under discussion and that a practical experience shows that the velocity of 1500 m/s could define it. This could be the case for curves without a clear step transitions, as in Fig. 14.

3.3 UPV and curing conditions

It is well known that the propagation velocity of ultrasonic pulse increases with the age of the concrete. This final section shows that the increase of UPV results with curing time is related to the change in the gel/space ratio that takes place with paste hydration. Since the pulse velocity through voids is less than that through solid matter, the greater the gel/space ratio (which increases with time) the lower the volume of pores and the greater the velocity of pulses propagated through concrete (Ikpong, 1993). Due to the changes of the structure with the age of cementitious materials, the standards recommend that changes in the properties which occur in time be determined by repeated measurements of pulse velocity at different ages, but always using the same transducers in the same position (Komlos et al. 1996).

Curing time will affect the UPV results; the curing regime may also play an important role. Kheder et al. (2003) studied mortars cured either in water or submitted to accelerated curing according to the BS 12504-4 (2004) method (20 hours water bath at 55°C). It has been found out that samples submitted to accelerated curing provided better correlation between strength and density and between strength and UPV.

Gesoglu (2010) studied concretes incorporating metakaolin and silica fume. Samples were either cured in water at 23°C and or steam cured at 70°C for 17 hours. Pulse velocity was determined at 1, 7 and 28 days. For the 1-day measurements, the steam cured concretes had slightly greater UPV values than the water cured concretes, in spite of a marked difference seen in the compressive strength. But in general, it has been concluded that there was no remarkable difference in the UPV values of the steam cured and water cured concretes for all testing. Krishna Rao et al. (2010) also has found no significant differences between UPV results from concrete samples subjected to membrane curing and conventional water curing.

On the other hand, Yasicioglu et al. (2006), has shown that self compacted concrete cubes provided best UPV results at all ages after curing in water at 20°C, when compared to cubes sealed (to prevent moisture loss) or air cured. This is in accordance to later results obtained by Tanyidizi (2008), which indicated that the highest compressive strength and ultrasonic pulse velocity values are obtained from water cured specimens followed by the sealed and air cured specimens regardless of the concrete types.

Not all authors agree on which curing method provides better UPV results (and this may depend on the material studied). However, there is a general agreement that the correlation between physical properties with UPV is much improved when all samples are cured the same way, irrespective of the method used (Kheder et al., 2003).

3.4 UPV and aggregate particle size and content

The presence of aggregate in cementitious composites affects the compressive strength, pulse velocity and relation between the two properties. Therefore the influence of aggregate is very important and cannot be neglected for accurate prediction of compressive strength of concrete based on ultrasonic pulse velocity (Trtnik, 2009). Researchers have found that for

the same strength level, concretes with the highest aggregate content will probably have the highest pulse velocity (Crawford, 1997; Trtnik, 2009). Berriman et al. (2004) has shown a strong positive linear correlation between aggregate content in concretes and speed of sound. Therefore the amount of aggregate does not affect UPV and strength to the same degree. In some cases, the higher aggregate content can cause an increase in the UPV results and at the same time decrease in compressive strength, which will depend on the mix design (Trtnik, 2009). Considering concrete as a two-phase composite material (aggregates plus cement paste), the increase of UPV with the increase of aggregate content can be represented as in Eq. 18 (Ye, 2003):

$$\frac{1}{UPV_{CONC}} = \frac{V_{CEM}}{UPV_{CEM}} + \frac{V_{AGG}}{UPV_{AGG}} \tag{18}$$

where V_{cem} and V_{agg} are the volume percentages of cement paste and aggregate in the concrete, respectively and UPV_{cem} and UPV_{agg} are the longitudinal ultrasonic velocities of the cement paste and aggregate, respectively.

Trtnik (2009) has carried out a comprehensive study of the influence of the aggregate content, type, shape and size on the determination of strength using ultrasonic pulse velocity. It has been concluded that:

a. Aggregates with low pulse velocity reduce both the strength and UPV of concretes, when compared to aggregates with high pulse velocity;
b. For the same UPV level, mixtures with the lowest and the highest nominal aggregate size have the highest and the lowest compressive strength S, respectively.
c. At the same UPV level, a mixture with the rounded aggregate grains has lower compressive strength than mixture with crushed aggregate shape, which can be explained by weaker contact between aggregate grains and cement paste in the case of rounded aggregate grains, leading to a reduction in the concrete strength.

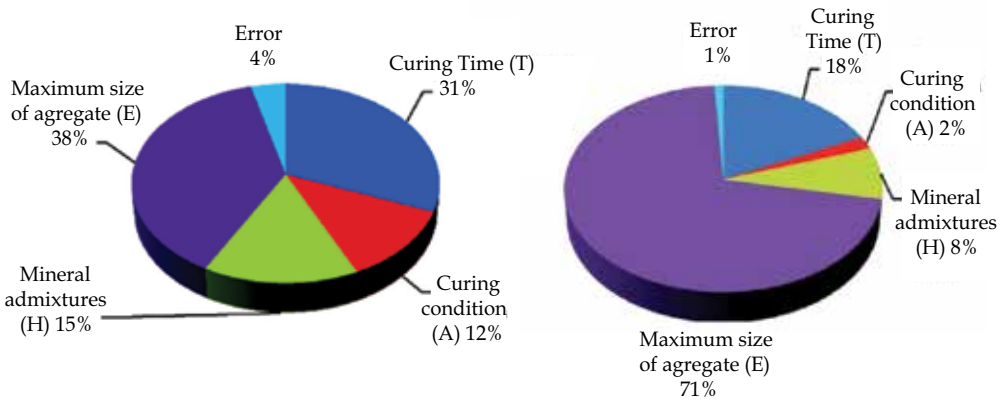

Fig. 15. The effect of experimental parameters on (a) ultrasonic pulse velocity and (b) compressive strength of lightweight concrete (Tanayidizi and Coskun, 2008)

Tanyidizi and Coskun (2008) used the analysis of variance (ANOVA) method to study the level of importance of four parameters – maximum size of aggregate, curing conditions,

mineral admixtures and curing time – on UPV and compressive strength of lightweight concrete. The results were summarized with the pie charts of Fig. 15. It is possible to see that the maximum size of aggregate is the main parameter governing both UPV results and compressive strength, being more significant for the first.
Despite the general agreement on the effect of the amount of aggregates on the correlation between UPV and strength, it is important to note that variations in the fine/coarse aggregate ratio may not affect the UPV – strength correlation (Lin et al., 2003; Madandoust et al., 2010), as shown in Fig. 16.

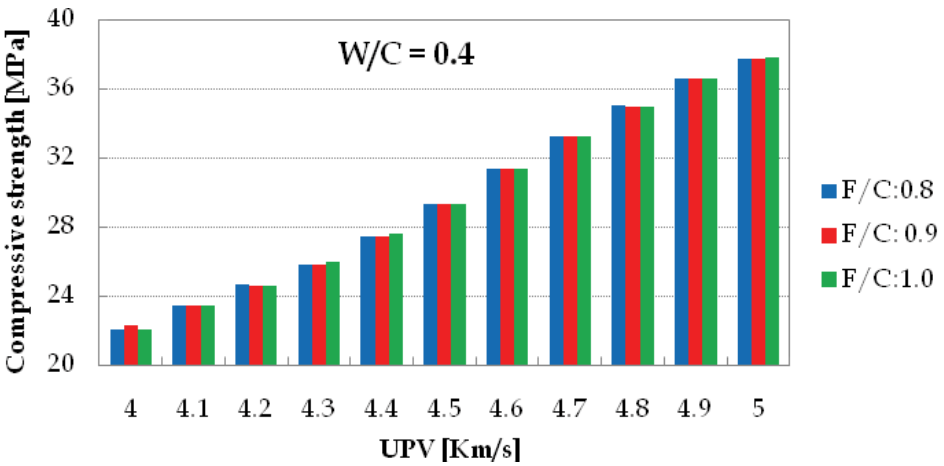

Fig. 16. Variarion of concrete compressive strength vs. UPV for different fine/coarse (F/C) aggregate ratios. Samples with w/c = 0.4 (Madandoust, 2010)

4. Special applications of UPV in cementitious composites

The objective of this section is to show a few practical examples of the utilization of ultrasonic pulse velocity as a non-destructive characterization technique for cementitious composites. It obviously does not cover all applications, but rather gives an overview of special or novel systems to where UPV can be employed. UPV has been largely used on the assessment of the uniformity of concrete, as well the detection of defects in concrete structures. The non-uniformity is indicated by the variation of the pulse velocities obtained from different points (Komlos et al., 1996). However, other examples below show that the application of this non-destructive technique goes beyond the original idea of detection of large voids or cavities in structural concrete.
UPV has been used to evaluate the strength of concrete exposed to elevated temperature. Results have shown the feasibility of using UPV for evaluation of the residual strength of fire-damaged concrete structures. UPV appears to be a qualitative (rather than quantitative) technique for determination of fire-damage in structures affected by fire (Cioni et al. 2001, Yang et al., 2009). A modified UPV test proposed by Colombo and Felicetti (2007) proved to be more effective to assess buildings affected by fire.
Lee et al (2004) used UPV to assess the early properties of high-performance concrete (HPC), which usually have a low water-to-cementitious materials (w/cm) ratio and also employ various chemical and mineral admixtures. HPC may be quite different from those of

ordinary concrete. An ultrasonic monitoring system has been used to successfully measure the UPV of both mortar and concrete beginning immediately after mixing. This method proved to be advantageous over the conventional method of conventional setting tests, as it could be conducted directly on concrete rather than on standard pastes that do not represent the rheology of HPC.

Shotcrete is employed in many situations, in particular for concreting in difficult locations, and the number of practical applications has continued to increase. The basic requirements of shotcrete are adequate adhesion to the substrate, satisfactory shooting stiffness and high early strength preventing dangerous fallout of fresh material from walls and overheads. A new generation of alkali-free accelerators has been used to achieve such properties. However, these chemicals significantly change the microstructure development during setting and hardening of mortar and concrete. UPV appears to be clearly sensitive to the effect of cement type, accelerator type and dosage on the setting behaviour of shotcrete. Apparently, stepwise increase of the accelerator dosage resulted in increasing values for the pulse velocity at early ages (Belie et al., 2005).

UPV may be successfully used to assess the changes in physical or mechanical properties when sustainable concretes are developed. Albano et al. (2005) used tyre tread scrap as a substitute for fine aggregates in concrete. When the weight proportion increased and particle size of the scrap rubber decreased (0.59 and 0.29 mm), flow and density of concretes in the fresh state decreased, as well as compressive strength and splitting tensile strength in the dry state. UPV has proved to be effective to describe the negative impact on mechanical and physical properties, as the percentage of rubber increased (Fig. 17). Mohammed and Abdullahi (2011) have found similar trends with "rubbercrete".

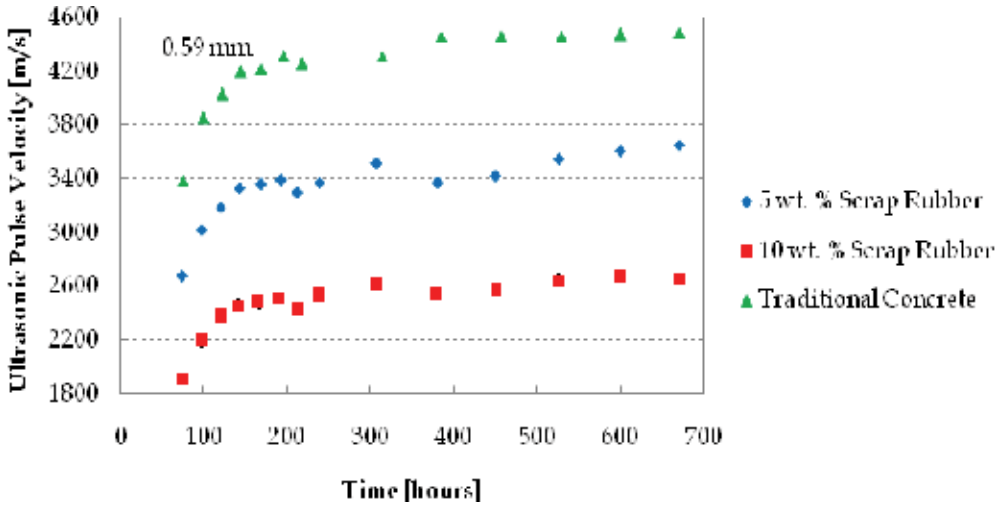

Fig. 17. Variation of ultrasonic pulse velocity with curing time for concrete-rubber mixes without coupling agent (scrap rubber particle size: 0.59 mm)(Albano et al., 2005)

As mentioned in the previous sections, UPV has been used to determine the setting time and hydration of cementitious materials. Keating et al. (1989) has studied oil well cement slurries and some of the important parameters of these cementitious systems. The parameters include the rate of development of static gel strength, the time to initial set, the volume

change and the 'waiting on cement' time for cement to reach a pre-determined strength before drilling operations can continue. These important measurements cannot all be made using a single test technique, and UPV has proved to be one of the satisfactory techniques.
More recently, UPV has been used to correlate physical and mechanical properties in novel cement systems, commonly referred as alkali-activated binders or "geopolymers" (Bondar et al., 2008, Gesoglu, 2010). This technique has the same applicability in geopolymer concretes than in conventional OPC concrete; however, due to its lower density, velocity of pulses in geopolymer concrete tend to be lower than OPC concrete.

5. Summary

Ultrasonic pulse velocity is a valuable technique for characterization of cement-based composites. This chapter shows that this technique has been used for different purposes over the years, e.g. setting and hydration of cement, detection of defects in structures, assessment of damage after high-temperature exposure, incorporation of different aggregates in concrete, among others. It continues to be an important non-destructive technique, which provides reliable results based on rapid measurements with relatively inexpensive equipment.

6. References

Berriman, J., Purnell, P., Hutchins, D.A., Neild, A. (2005). Humidity and aggregate content correction factors for air-coupled ultrasonic evaluation of concrete. *Ultrasonics,* Vol. 43, pp. 211–217.

Bondar, D., Lynsdale, C.J., Milestone, N., Hassani, N., Ramezanianpour, A.A. (2009). Engineering properties of geopolymer concrete based on alkali activated natural pozzolan. *Proceedings of the Third International Conference on Concrete and Development*, Tehran, April 2009.

British Standard BS EN 12504-4 (2004). Testing concrete. Determination of ultrasonic pulse velocity.

Bungey J. H. (1982). *The Testing of Concrete in Structures*. SUNY University Press, New York.

Castro P. F. and Carino N. J. (1998). Tensile and nondestructive testing of FRP bars. *Journal of composites for construction*, February, No. 17.

Cioni, P., Croce, P., Salvatore, W. (2001). Assessing fire damage to r.c. elements. *Fire Safety Journal,* Vol. 36, pp. 181-199.

Chen, W., Shui, Z., Li, W. (2010). Early age hydration of cement paste monitored with ultrasonic velocity and numerical simulation. *Journal of Wuhan University of Technology-Mat. Sci. Ed.*, Vol. 25, No. 4, pp. 704-707.

Chotard, T., Gimet-Breart, N., Smith, A., Fargeot, D., Bonnet, J.P., Gault, C. (2001). Application of ultrasonic testing to describe the hydration of calcium aluminate cement at the early age. *Cement and Concrete Research,* Vol. 30, pp. 405-412.

Colombo, M., Felicetti, R. (2007). New NDT techniques for the assessment of fire-damaged concrete structures. *Fire Safety Journal,* Vol. 42, pp. 461–472.

Demirboga R., Türkmen I. and Karako M.B. (2004). Relationship between ultrasonic velocity and compressive strength for high-volume mineral-admixtured concrete. *Cement and Concrete Research*, Vol. 34, No. 12, pp. 2329–2336.

Elvery R. H. (1973). Estimating strength of concrete in structures. Current Practice Sheet 10. *Concrete*, Vol. 11, No. 7, pp. 49–51.

Galan A. (1967). Estimate of concrete strength by ultrasonic pulse velocity and damping constant. *ACI J. Proceedings*, Vol. 64, No. 10, pp. 678–684.

Gesoglu, M. (2010). Influence of steam curing on the properties of concretes incorporating metakaolin and silica fume. *Materials and Structures,* Vol. 43, pp. 1123-1134.

Goueygou M., Lafhaj Z., Soltani F. (2009). Assessment of porosity of mortar using ultrasonic Rayleigh waves. *NDT&E International*, Vol. 42, pp. 353–360.

Hola J., Schabowicz K. (2005). Application of artificial neural networks to determine concrete compressive strength based on non-destructive tests. *Journal of Civil Engineering and Management*, Vol. 11, No. 1, pp. 23–32.

Hola J., Schabowicz K. (2005). New technique of nondestructive assessment of concrete strength using artificial intelligence. *NDT&E International*, Vol. 38, No. 4, pp. 251–259.

Ikpong A.A. (1993). The relationship between the strength and non-destructive parameters of rice husk ash concrete. *Cement and Concrete Research*, Vol. 23, pp. 387-398.

Keating J., Hannant D.J., Hibbert A.P. (1989). Correlation between cube strength, ultrasonic pulse velocity and volume change for oil well cement slurries. *Cement and Concrete Research*, Vol. 19, pp. 715-726.

Kewalramani M.A., Gupta R. (2006). Concrete compressive strength prediction using ultrasonic pulse velocity through artificial neural networks. *Automation in Construction*, Vol. 15, No. 13, pp. 374–379.

Kheder G.F. (1999). A two stage procedure for assessment of in situ concrete strength using combined non-destructive testing. *Materials and Structures,* Vol. 32, pp. 410–417.

Kheder, G.F., Al Gabban, A.M., Abid, S.M. (2003). Mathematical model for the prediction of cement compressive strength at the ages of 7 and 28 days within 24 hours. *Materials and Structures,* Vol. 36, pp. 693-701.

Komlos K., Popovics S., Niirnbergeroh T., Babd B. and Popovics J. S. (1996). Ultrasonic Pulse Velocity Test of Concrete Properties as Specified in Various Standards. *Cement and Concrete Composites*, Vol. 18, pp. 357-364.

Krishna Rao, M.V., Rathish Kumar, P., Khan, A.M. (2010). A sudy on the influence of curing on the strength of a standard grade concrete mix. *Facta Universitatis (Series Architecture and Civil Engineering)*, Vol. 8, No. 1, pp. 23-34.

Lafhaj Z., Goueygou M., Djerbi A., Kaczmarek M. (2006). Correlation between porosity, permeability and ultrasonic parameters of mortar with variable water / cement ratio and water content. *Cement and Concrete Research*, Vol. 36, pp. 625 – 633.

Law, D.W., Adam, A.A., Molyneaux, T.K., Patnaikuni, I. (2008). Durability Properties of Geopolymer Mortars. *Proceedings of the 11DBMC International Conference on Durability of Building Materials and Components*, Istanbul, May 2008.

Leslie J. R. and Cheeseman W. J. (1949). An ultrasonic method for studying deterioration and cracking in concrete structures. *American Concrete Institute Proceedings*, Vol. 46, No. 1, pp. 17–36.

Leslie J. R. and Chessman W. J. (1949). An ultrasonic method of studying deterioration and cracking in concrete structures. *Journal of American Concrete Institute*, Vol. 21, No. 1, pp. 17-35.

Lin Y., Lai C.P. and Yen T. (2003). Prediction of Ultrasonic Pulse Velocity in Concrete. *ACI Materials Journal*, Vol. 100, No. 1, pp. 21–28.

Madandoust R., Ghavidel R., Nariman-zadeh N. (2010). Evolutionary design of generalized GMDH-type neural network for prediction of concrete compressive strength using UPV. *Computational Materials Science,* Vol. 49, pp. 556–567.

Mantrala S. K. and Vipulanandan C. (1995). Nondestructive evaluation of polyester polymer concrete. *ACI Material Journal*, Vol. 92, No. 6, pp. 660-668.

Marfisi E., Burgoyne C. J., Amin M. H. G. and Hall L. D. (2005) The use of MRI to observe the structure of concrete. *Magazine of Concrete Research*, Vol. 57, No. 2, pp. 101–109.

Mohammed B.S., Azmi N.J., Abdullahi M. (2011). Evaluation of rubbercrete based on ultrasonic pulse velocity and rebound hammer tests. *Construction and Building Materials*, Vol. 25, pp. 1388–1397.

Nash't I. H., A'bour S. H., Sadoon A. A. (2005). Finding an united relationship between crushing strength of concrete and non-destructive tests, *Proceedings of Middle East Nondestructive Testing Conference & Exhibition*, Bahrain, 2005.

Neville A. M. (1996). *Properties of Concrete*, fourth ed., John Wiley and Sons, Inc., New York.

Nwokoye D.N. (1974). Assessment of the elastic moduli of cement paste and mortar phases in concrete from pulse velocity tests cement and concrete research. Vol. 4, pp. 641-655.

Ohdaira E., Masuzawa N. (2000). Water content and its effect on ultrasound propagation in concrete – the possibility of NDE. *Ultrasonics*, Vol. 38, pp. 546– 552.

Panzera T. H., Rubio J. C., Bowen C. R., Vasconcelos W. L., Strecker K. (2008). Correlation between structure and pulse velocity of cementitious composites. *Advances in Cement Research*, Vol. 20, No. 3, July, pp. 101–108.

Popovics J. S. and Rose L. J. (1994). A survey of developments in ultrasonic NDE of concrete. *IEEE Transactions on Ferroelectrics and Frequency Control*, Vol. 41, No. 1, pp. 140– 143.

Popovics S. (2007). Analysis of the Concrete Strength Versus Ultrasonic Pulse Velocity Relationship, In: *American Society for Nondestructive Testing*, 12th of December 2010, Available from: <http://www.asnt.org/publications/materialseval/basics/feb01basics/feb01basics. htm>.

Prassianakis I. N. and Giokas P. (2003). Mechanical properties of old concrete using destructive and ultrasonic non-destructive testing methods. *Magazine of Concrete Research*, Vol. 55, No. 2, pp. 171–176.

Pundit. (1993). Manual of Portable ultrasonic non destructive digital indicating tester, C. N. S. Instruments, London.

Qasrawi Y.H. (2000). Concrete strength by combined non-destructive methods simply and reliably predicted. *Cement and Concrete Research*, Vol. 30, No. 6, pp. 739–746.

Rajagopalan P.R., Prakash J. and Naramimhan V. (1973). Correlation between ultrasonic pulse velocity and strength of concrete. *Indian Concrete. Journal*, Vol. 47, No. 11, pp. 416–418.

Reinhardt, H.W., Grosse, C.U. (2004). Continuous monitoring of setting and hardening of mortar and concrete. *Construction and Building Materials*, Vol. 18, pp. 145–154.

Reinhardt, H.W., Große, C.U., Herb, A.T. (2000). Ultrasonic monitoring of setting and hardening of cement mortar – a new device. *Materials and Structures*, Vol. 33, pp. 580-583.

Rio L.M., Jimenez A., Lopez F., Rosa F.J., Rufo M.M., Paniagua J.M. (2004). Characterization and hardening of concrete with ultrasonic testing. *Ultrasonics*, Vol. 42, pp. 527–530.

Shkolnik I.E., Udegbunam O.C., Aktan H.M. (1997). Ultrasonic methods of evaluating concrete permeability. *Proceedings of the Conference on NDT in Civil Engineering, British Institute of NDT*, University of Liverpool, pp. 111 –120.

Tanyidizi, H. Coskun, A. (2008). Determination of the principal parameter of ultrasonic pulse velocity and compressive strength of lightweight concrete by using variance method. *Russian Journal of Nondestructive Testing,* Vol. 44, No. 9, pp. 639–646.

Tharmaratram K. and Tan B.S. (1990) Attenuation of ultrasonic pulse in cement mortar. *Cement and Concrete Research,* Vol. 20, pp. 335–340.

Trtnik G., Kavcic F., Turk G., (2009). Prediction of concrete strength using ultrasonic pulse velocity and artificial neural networks *Ultrasonics* Vol. 49, pp. 53–60.

Trtnik G., Turk G., Kavèiè F., Bosiljkov V. B. (2008). Possibilities of using the ultrasonic wave transmission method to estimate initial setting time of cement paste. *Cement and Concrete Research*, Vol. 38, pp. 1336–1342.

Turgut P. (2004). Evaluation of the ultrasonic pulse velocity data, *Proceedings of Fourth International Conference on NDE in Relation to Structural Integrity for Nuclear and Pressurised Components*, London, 2004.

Turgut P., Kucuk O. F. (2006). Comparative relationships of direct, indirect, and semi-direct ultrasonic pulse velocity measurements in concrete. *Russian Journal of Nondestructive Testing*, Vol. 42, No. 11, pp. 745–751.

Udegbunam O., Yaman I., Aktan H., Hohm T. (1999). Developing a rapid measure of concrete permeability for use in QA/QC specifications. Proceedings of Transportation Research Board, 78th Annual Meeting, January 10– 14, Washington D.C., 1999.

Ulucan Z. Ç., Türk K. and Karata M. (2008). Effect of mineral admixtures on the correlation between ultrasonic velocity and compressive strength for self-compacting concrete. *Russian Journal of Nondestructive Testing,* Vol. 44, No. 5, pp. 367–374.

Vergara L., Miralles R., Gosalbez J., Juanes F.J., Ullate L.G., Anaya J.J., Hernandez M.G., Izquierdo M.A.G. (2001). NDE ultrasonic methods to characterise the porosity of mortar. *NDT & E International*, Vol. 34, pp. 557–562.

Vipulanandan C. and Garas V. (2008) Electrical resistivity, pulse velocity and compressive properties of carbon fiber reinforced cement mortar. *Journal of material in Civil Engineering*, pp. 93-101.

Winkler K., Nur A. (1982). Seismic attenuation: effects of pore fluids and frictional sliding. *Geophysics*, Vol. 47, No. 1, pp. 1 – 15.

Yaman I.O., Hearn N., Aktan H.M., (2002). Active and non-active porosity in concrete: Part I. Experimental evidence. *Materials and Structures*, Vol. 35, No. 246, pp. 102– 109.

Yaman I.O., Aktan H.M., Hearn N. (2002). Active and non-active porosity in concrete: Part II. Evaluation of existing models. *Materials and Structures*, Vol. 35, No. 246, pp. 110–116.

Yazicioglu, S., Caliskan, S., Turk, K. (2006). Effect of curing conditions on the engineering properties of self-compacting concrete. *Indian Journal of Engineering & Materials Science,* Vol. 13, pp. 25-29.

Ye, G., van Breugel, K., Fraaij, A.L.A. (2001). Experimental study on ultrasonic pulse velocity evaluation of the microstructure of cementitious material at early age. *Heron,* Vol. 46, No. 3, pp. 161-167.

Yildirim H., Sengul O. (2011). Modulus of elasticity of substandard and normal concretes. *Construction and Building Materials*, Vol. 25, pp. 1645–1652.

Zhang, J., Qin, L., Li, Z. (2009). Hydration monitoring of cement-based materials with resistivity and ultrasonic methods. *Materials and Structures,* Vol. 42, pp. 15-24.

Zarandi M.H. F., Turksen I.B., Sobhani J., Ramezanianpour A.A. (2008). Fuzzy polynomial neural networks for approximation of the compressive strength of concrete. *Applied Soft Computing*, Vol. 8, No. 1, pp. 488–498.

18

Macro-Micro Mechanical Behavior of a Highly-Particle-Filled Composite Using Digital Image Correlation Method

Pengwan Chen, Zhongbin Zhou and Fenglei Huang
State Key Laboratory of Explosion Science and Technology, Beijing Institute of Technology, Beijing 100081, China

1. Introduction

Particle reinforced composites represent a large group of materials used in a variety of applications, such as concretes and solid rocket propellant. The mechanical behavior of these materials depends on properties of constitutes and any microstructural changes that may occur in the body under loading. Generally, particles are applied to high stress in these composites. Heterogeneity plays an important role in composite fracture. Because the mechanical properties of dispersed phase and matrix differ from each other, any one of the following micro-damage nucleation mechanisms has been observed during the deformation process, including cracking of particles, debonding at the particle-matrix interface and fracture of the matrix. In addition, failure also depends on the volume ratio of particles to matrix.

The polymer bonded explosive (PBX) is a highly filled composite material of crystalline high explosives (90%-95% by weight) in polymer binder. This matter is a kind of functionally energetic materials being used increasingly as energetic fillings in both civil and military applications when a very high performance is required. The mechanical properties of PBX subjected to a range of conditions are important criteria to determine a safe working life. The study on the mechanical properties and the failure mechanisms of PBX has drawn much attention in recent years [1-9]. Low strengths and safety concerns bring additional difficulties in preparing samples and conducting mechanical tests of PBX. Therefore, the fracture behavior and the failure mechanisms of PBX are not full understood, some beneficial works are still need to be done to bring some further insights into this issue.

There are many techniques to measure the deformation in experimental test. Strain gauge and extensometer are widely used, while the microstructure deformation can not be provided by these techniques. Significantly, the strain gauge measures the deformation at a single point, which only gives information at one point, and the gauge may provide local reinforcement causing error in the displacement measure. Several high resolution and non-contact optical techniques do have the advantages that they can measure the whole displacement and strain field providing deformation information, and it is enough to follow strains until failure. In recent years, many beneficial works have been reported from Cavendish Lab. The quasi-static deformation fields were measured by this technique. The influence of particles microstructure was found to be significant for its fracture behavior

[6-7, 10-12]. Rae et al. [13] used DIC to investigate the effect of thermal aging on a UK PBX containing nitrocellulose. And in Rae et al. [5], the method is described in detail including an extended discussion on error analysis. Specially, the deformation and fracture behavior of PBX was studied using the DIC technique at the micro-scale combined with an optical microscope or an SEM imaging system [8-9, 14]. Moreover, the DIC method was used to study the dynamic fracture behavior and mechanical properties of PBX at high-strain rate [15-17].

In this work, a series of quasi-static tests, including Brazilian test, semi-circular bending test, uniaxial compression and punch loading tests, were carried out to study the deformation and fracture behavior of a PBX simulation material, which is a highly-particle-filled composite in which the explosive particles are replaced by simulant particles at 90%-95% weight, with a few percent binder of fluorine rubber. The PBX simulant powder was hot pressed in a steel mold, and then a short, cylinder-shaped specimen can be obtained with 20 mm diameter. The test specimens were machined from the original cylindrical specimens. The DIC technique was used to digitally process the speckle's movement to determine the full displacement and strain fields. The vector field of displacement can be used to display the failure mechanisms of specimens, and the strains distribution can be used to predict the initiation and propagation of cracks. In addition, an SEM imaging system was used to in situ examine the microstructure of PBX simulant. The microscopic damages, such as debonding, particle's fracture, were observed. The method combing SEM imaging system with DIC technique was used to determine the strain fields of specimens at micro-scale, with the aim at predicting the propagation of cracks with possible developing paths in a splitting fracture of brittle failure.

2. Principle of digital image correlation

Digital image correlation (DIC) method is a rapidly developing technique of optical mechanics. It is worth noting that in recent years, it has been widely used to measure the surface deformation field in experimental mechanics for its advantages of no contacting, high accuracy, real time and full deformation field measurement. In the system, a random speckle pattern must need for DIC technique to calculate the deformation field. A CCD camera and a personal computer were used to capture the movement of speckles in situ before and after a deformation. By comparing the speckle pattern in the objective configuration with the speckle pattern in the initial configuration, the displacement and strain full-field can be determined. The algorithm of DIC technique has been developed by many authors [18-20]. The matching theory of this method is given in Fig. 1.

Quadrangle S (solid line) is a reference (or undeformed) sub image and quadrangle S_1 (dash line) is the corresponding deformed sub image. In order to obtain the displacement u_m and v_m of point M, sub image S_1 is matched with sub image S using a correlation operation. If subset S is sufficiently small, the coordinates of points in S_1 can be approximated by first-order Taylor expansion as fellows [21]

$$x_{n1} = x_m + u_m + (1 + \frac{\partial u}{\partial x}\Big|_M) \cdot \Delta x + \frac{\partial u}{\partial y}\Big|_M \cdot \Delta y \tag{1}$$

$$y_{n1} = y_m + v_m + (1 + \frac{\partial v}{\partial x}\Big|_M) \cdot \Delta x + \frac{\partial v}{\partial y}\Big|_M \cdot \Delta y \tag{2}$$

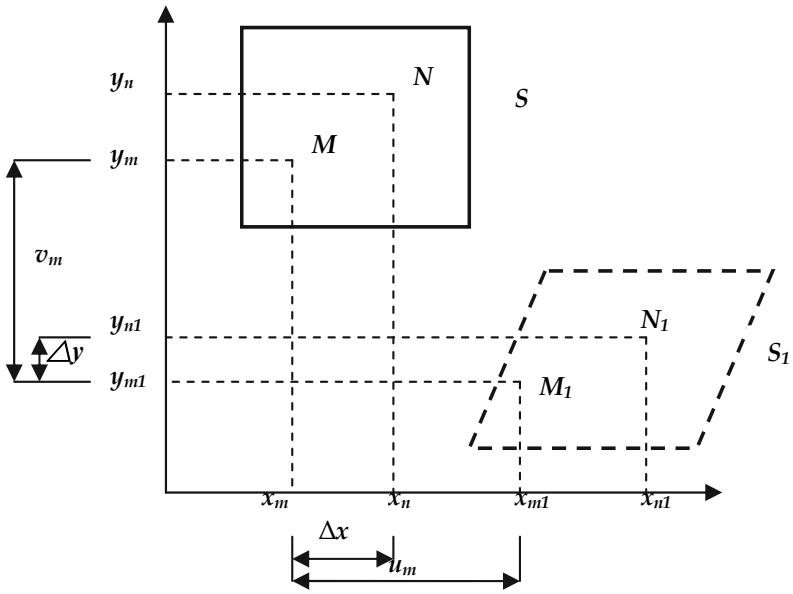

Fig. 1. Schematic diagram of deformed process for planar object

The criterion for comparing two images is commonly given by using the cross-correlation coefficient, which can be written in form as [22]

$$C = 1 - \frac{\sum f(x,y) \cdot \sum g(x^*,y^*)}{\sqrt{\sum f^2(x,y) \cdot \sum g^2(x^*,y^*)}} \tag{3}$$

where (x, y) and (x^*, y^*) are Cartesian Coordinates of a material point in the image of the undeformed and deformed patterns, respectively. $F(x, y)$ and $g(x^*, y^*)$ are light intensities at that point in the corresponding images. The correlation value C varies from 0 to 1, with 0 signifying a perfect match between the two images.

3. Experiments

3.1 Brazilian test

The Brazilian test is used for making the testing of uniaxial dumbbell specimens impractical. It is a biaxial method for estimating the tensile failure stress of a material by applying a pair of compressive loads P diametrically to a disc-shaped specimen. A vertical tensile failure is generated in the center region of the specimen along the loading axis, as shown in Fig. 2. According to simple elasticity theory, the tensile stress at the center of the disc is given by

$$\sigma_t = \frac{2P_m}{\pi D\delta} \tag{4}$$

where P_m is the maximum applied force. D is the diameter of the disc specimen and δ is the thickness.

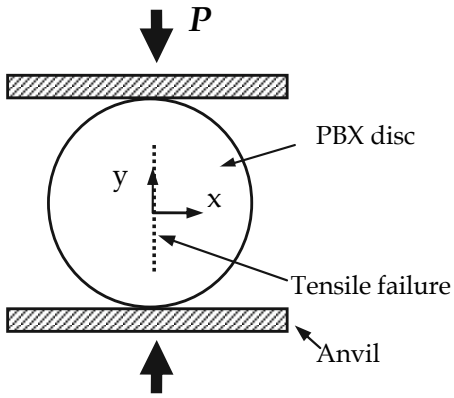

Fig. 2. Brazilian test geometry

3.2 Uniaxial compression

Quasi-static uniaxial compression tests were conducted on PBX simulants with the aim at understanding the different failure mechanisms and characterizing the material to allow a valid fracture computational model design. In compression, the cylindrical specimens with 20 mm diameter and 30 mm height were machined into block specimens with different aspect ratios. In this work, we focus on the study of the deformation and fracture behavior of block specimens under uniaxial compression action. Combining with the DIC technique, the full displacement and strain fields are to be obtained with significant interests to reveal the strain component distribution, which can be used to predict the propagation of the induced crack with possible failure path.

3.3 Semi-circular bending (SCB) test

Standard methods are available for determining the plane strain fracture toughness of metallic materials. The direct application of such standard methods to brittle materials, e.g. rocks and concretes, is also acceptable. However, it is difficult to machine the specimen because the brittle materials are low strength and low mechanical impendence. In order to determine the brittle material's behavior, a typical geometry of the specimen should be utilized for the testing. Since the material is weak in tension, tests should preferably be done with compressive loading where tensile fracture is induced. To satisfy this requirement, Chong and Kuruppu [23] proposed a bending test by using a semi-circular specimen with a pre-notch along the line of symmetry at the specimen's edge and oriented along the loading direction, subjected to a three-point bending load, as shown in Fig. 3. Considering the specimen's geometry, tensile crack (model I) is induced in SCB test.

Chong et al. [24] proposed a formula for determining K_I by using both the strain energy release rate method and the elliptical displacement approach, which is given by

$$K_I = \frac{P\sqrt{\pi a}}{D\delta} Y_K \tag{5}$$

where P is the applied force, D is the diameter of the SCB specimen and δ is the thickness. Y_K is the dimensionless stress intensity factor as a function of the dimensionless crack length, a/D. Y_K can be approximated by a third order polynomial as follows

$$Y_K = 4.47 + 7.4\frac{a}{D} - 106\left(\frac{a}{D}\right)^2 + 433.3\left(\frac{a}{D}\right)^3 \tag{6}$$

For $0.25 \le a/D \le 0.35$ and $S/D=0.4$ with $2S$ is the loading span.

For the stress state near the crack tip, the criterion of crack propagation can be given in the following form: $K_I \le K_{IC}$, which is extremely convenient for applications. Where K_I is the stress intensity factor, and K_{IC} is the static fracture toughness. We notice that K is not a local but an integral characteristic, depending on the energetic state of the whole construction. Thus, in the problem of static loading there are two fracture criteria: $P \le P_C$ for defectless media and $K_I \le K_{IC}$ for crack domains. In both cases, we are dealing with certain external stress attaining the given critical value, whereupon, according to the theory, a fracture occurs instantaneously. Therefore, fracture toughness K_{IC} under mode I condition can be possible calculated from the stress intensity factor solutions, is given by

$$K_{IC} = \frac{P_C\sqrt{\pi a}}{D\delta} Y_K \tag{7}$$

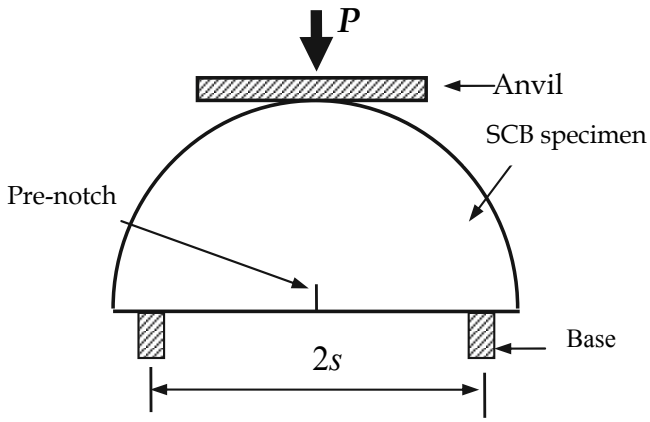

Fig. 3. Geometry of semi-circular bend test

3.4 Punch loading tests

PBX is increasingly used in decreased sensitivity munitions at low strain rate. Mechanical stimuli may affect the safe working life of explosives. In order to understand the mechanisms that lead to reaction or detonation, it is important to know the mechanical behavior of PBX. The punch loading test was proposed by Prandtl. In this method, a rigid object slowly penetrates the material to study the fracture process and failure mechanisms [25]. In literature [25, 26], the flat punch loading test has been carried out on a PBX mock material. In our work, two punch loading experimental patterns, including the flat punch and wedge-shaped punch test, were used to study the fracture behavior of PBX simulant. In this paper, only the flat punch loading results are shown providing some further insights into PBX fracture. The length, width and height of a specimen are 20 mm, 8 mm and 6 mm respectively. Contact surface size is 5 mm×5 mm for punch, which was used to impact the top of the specimen at a rate of 1.8 mm/minute.

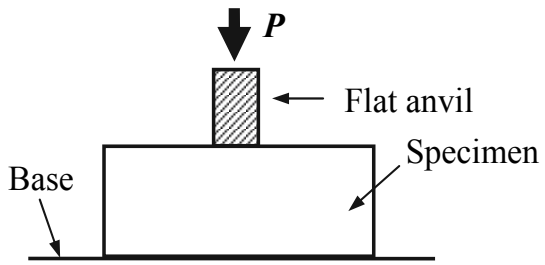

Fig. 4. Schematic diagram of a flat punch loading test

4. Results and discussion

4.1 Brazilian test

Following, a disc specimen with 20 mm diameter and 8 mm thickness was diametrically compressive loaded in a material test system (MTS). The loading velocity is 0.05 mm/minute. Images of evolving movement of the speckle pattern were recorded by using a CCD camera at a frame rate of 5 frames per-second, with a high resolution of 1624×1236 pixels^2 in each image. During the test, the applied compressive load P was normalized by the product of the specimen initial thickness δ and the radius R of the disc specimen, and the diameter change Δ along loading axis was normalized by the specimen initial diameter D. Fig. 5 shows the resulting relationship of the applied compressive load ($P/(\delta R)$) versus the displacement (Δ/D). It is obvious that the applied force firstly linearly increases with the deformation increases. The force reaches a maximum, and then rapidly decreases.

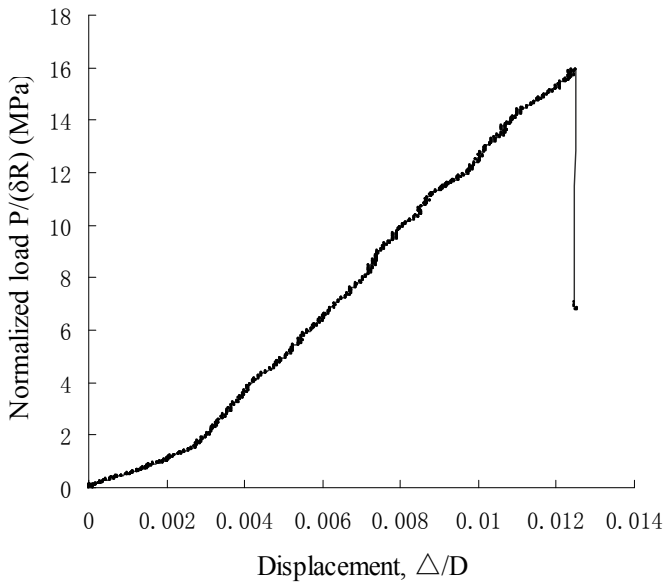

Fig. 5. Relationship of the applied compressive load and displacement

It is believed that the disc specimen fractures at the maximum load, indicating a brittle failure behavior. The tensile strength was calculated using Equation 4 from the applied

force, and the magnitude of tensile failure stress is about 5.07 MPa. Fig. 6 shows the strain field distribution which corresponds to the state that the fracture of specimen occurs. The image shows how the strain localizes along the loading axis, indicting the possible crack developing route. The largest strain occurred near the contact points of specimen and anvils, which is caused by the stress concentration, and premature failure occurs under shear stress action.

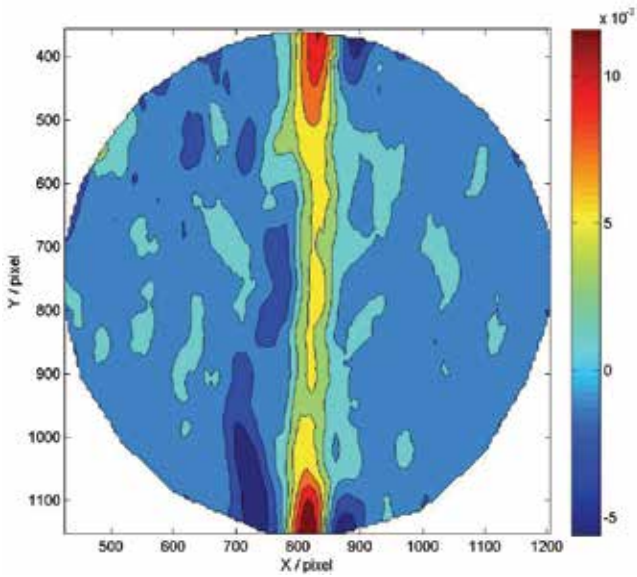

Fig. 6. Strain (ε_x) distribution

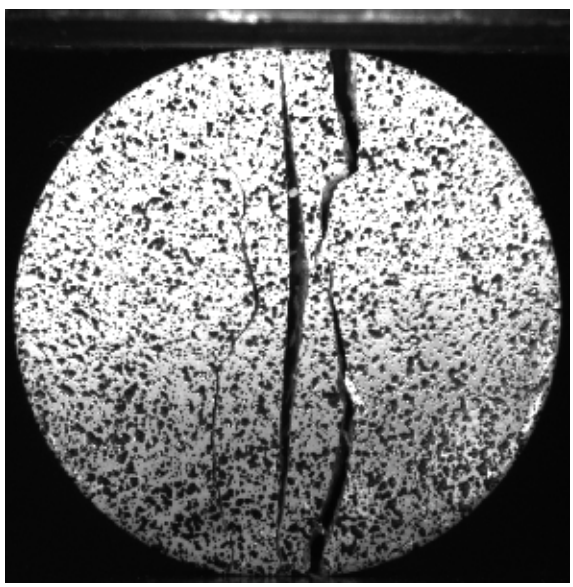

Fig. 7. Fracture morphology of PBX

The strain field calculated from the DIC can demonstrate the material damage underneath the specimen surface even though there were no differences between the surface topographies at different loading state for the specimen prior to total failure. Fig. 7 shows the typical fracture morphology of specimen in Brazilian test. The tensile failure path is along the loading axis and the crack opening displacement in the disc specimen center is largest. The principle crack initiated at the specimen center and evolved upward and downward along the loading line. Moreover, two sub-cracks occurred in specimen, which was due to shear stress at the contacts between specimen and anvils. The right sub-crack occurred and propagated into the specimen, but not run through.

4.2 Compression tests

Quasi-static compressive loads were performed on simulant specimens. A series of block specimens with aspect ratio of 1.8, 2.0 and 2.3 were used to study the different failure mechanisms. In order to discuss the deformation and fracture behavior of specimens under compressive load, the captured speckle images were computed by the DIC.

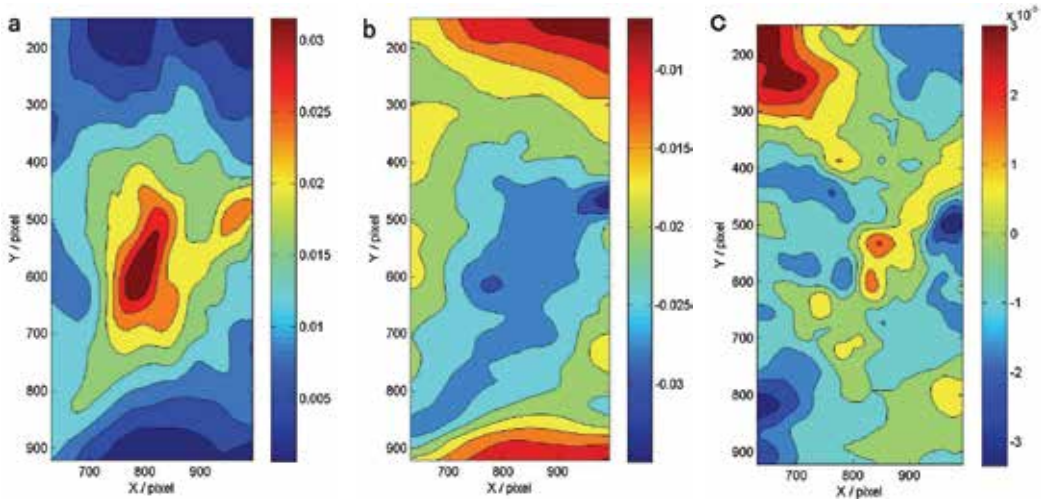

Fig. 8. Strain components distribution. a) Extensive strain (ε_x), b) Compressive strain (ε_y), and c) Shear strain

For a block specimen with size of 20 mm height by 10mm width by 10 mm thickness, a series of random speckle patterns were captured before and after load. Fig. 8 illustrates the computed strain field distribution for the block specimen just prior to total failure under compressive load. In Fig. 8a, it is obvious that a concentrated strain band localizes in an area along the load axis near the center of the specimen. Meanwhile, a localized shear strain band concentrated in the area near the diagonal line, as shown in Fig. 8c. From these strain maps, it can be seen that the extension strain is larger than the compression and shear strain in the center, demonstrating that the macroscopic fracture mode of the specimen is dominant caused by extension and shear action when under external force. The whole vector field of displacement distribution gives a quantitative measurement, as shown in Fig. 9. Two wedges of matters can be seen driven downward and upward into the material with shear regions clear visible, and the central materials moved to the left and right approximately

perpendicular to the loading axis. The vectors are scaled and can be used as a quantitative measurement. The result gives a clear indication of the failure mechanisms in the specimen more clearly than by observation.

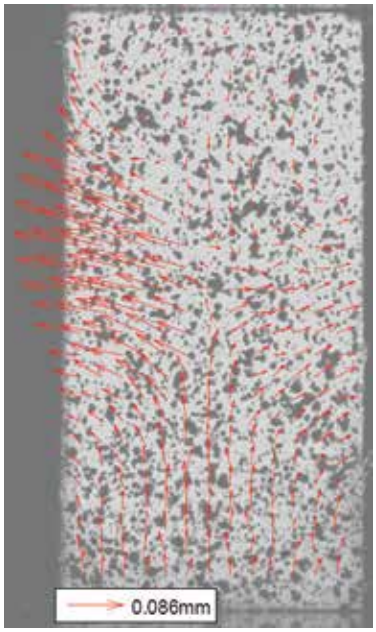

Fig. 9. Displacement vector with aspect ratio of 2.0

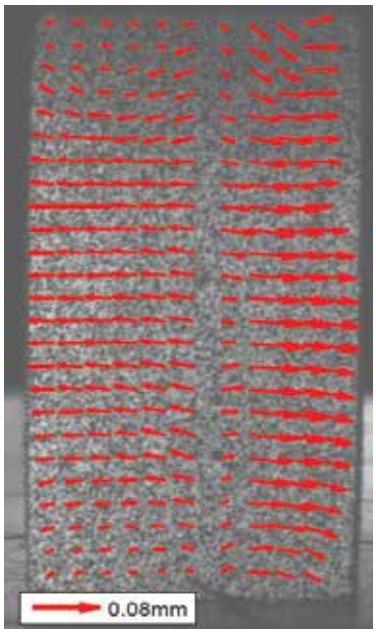

Fig. 10. Displacement vector with aspect ratio of 2.3

Fig. 10 shows the displacement vector pattern under a compressive force calculated by using the DIC. Here, it can be seen that the materials flow to the right and left approximately along the central loading axis. Meanwhile, a tensile crack can be seen on the specimen surface. Fig.s 11a-c show the whole strain field distribution of a specimen with the size of 10×10×23 mm^3 under compressive load. In Fig. 10a, it is obvious that a concentrated extensile strain band localizes along the load axis and extends from the top of specimen to the bottom. The maximum strain value is approximately 0.06 in tensile stress field near the center of the specimen. While the compressive and shear strain values are very small, the maximum value is less than 0.01, as shown in Fig.s 11b and c. Comparing this to Fig. 8,

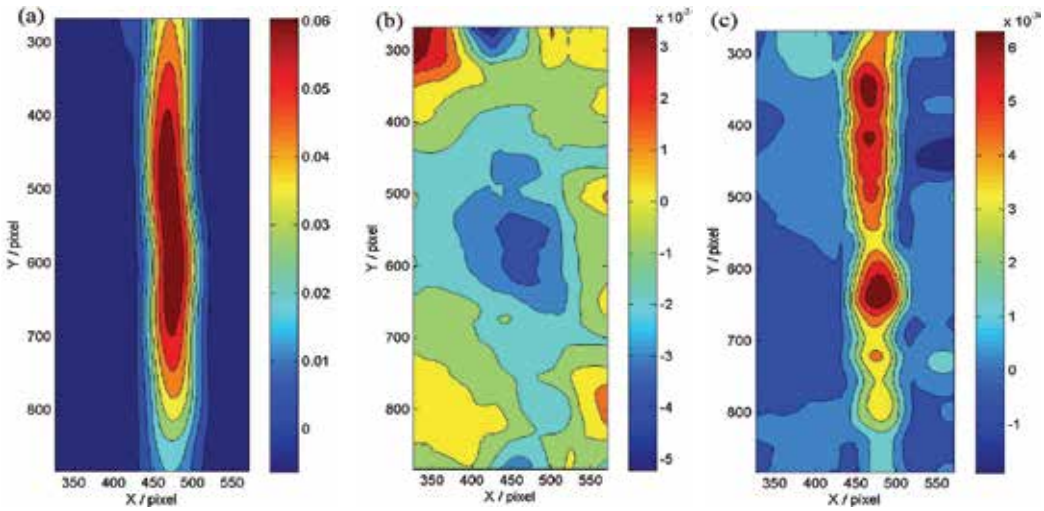

Fig. 11. Strain components distribution. a) Extensive strain (ε_x), b) Compression strain (ε_y), and c) Shear strain

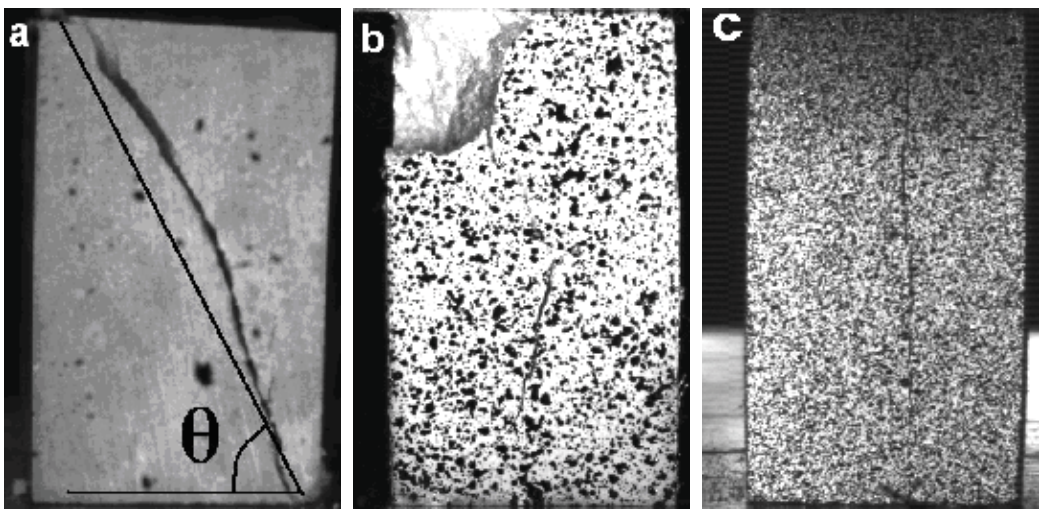

Fig. 12. Fracture morphology of specimens. (With different aspect ratio. a) 1.8; b) 2.0; c) 2.3)

results indicate that the fracture mechanism of block specimens under compressive loading is different significantly with aspect ratio changes. It is believed that the macroscopic fracture of specimen with aspect ratio of 2.3 is dominant caused by extension action.

The fracture monographs of specimen are evidently different shown in Fig. 12. Fig. 12a shows the post-failure specimen photography. It can be seen that the fracture path is nearly along the diagonal line, which was caused by shear stress action when subjected to compressive loads. With aspect ratio increased, the fracture mode is changed. Fig. 12b shows the fracture morphology of PBX simulation material with aspect ratio of 2.0. Fracture surface can be seen obviously at the top left corner, the main crack is running from the upper left corner to the lower left corner, and in the center of the specimen it is running along the vertical axis. Result shows the fracture mode is mainly caused by the extension and shear action. When the aspect ratio is up to a critical value such that the shear action disappeared, as shown in Fig. 12c, a single crack can be seen which is caused by the extension stress action, and the failure plane is parallel to the loading axis. Fracture photographs are in agreement with the results predicted from the strain fields.

Displacement and strain fields obtained in the experiments have examined the failure mechanisms of block specimen under compression load, to provide explanations for the observed failure behavior. The compression experiments carried out at an aspect ratio of 1.8 gave an ultimate compressive engineering stress of about 50.21 MPa. Based on the Mohr-Coulomb failure law [27], a quasi-static compression data has been obtained on a cylindrical specimen PBS9501[28], the shear stress τ can be given by $\tau=\mu\sigma_n+c$, where σ_n is the normal stress acting on failure plane, c is the cohesion and μ is the friction coefficient. The angle of internal friction of the material φ is relative to the friction coefficient through the relationship $\mu=tan\varphi$ and can be calculated by $\theta=\pi/4+\varphi/2$. Where θ is the angle made between the failure plane normal and the loading axis. From Fig. 12 (a) the value θ is approximately 61°, then the friction angle can be calculated and the value is about 32°. Given this information, a value for the coefficient of cohesion can be calculated to be about 13.47 MPa. Additionally, the tensile strength is approximately 14.93 MPa. Results can be conductive to understand the material fracture properties.

4.3 Semi-circular bending tests

Semi-circular specimens were pre-notched with a 0.2 mm thickness steel blade, the initial pre-notch of 1.0 mm length was along the line of symmetry at the specimen edge and oriented along the compression direction. Pre-notched specimens were sprayed with mists of black and white paints alternatively to create the random speckle patterns. A CCD camera was used to record decorated random speckles movement in situ. In order to investigate the fracture mechanism under mechanical loading, speckle images were digital processed using the DIC. The displacement and strain fields were calculated.

Fig. 13 shows the extensive strain field maps at two loading steps of P=105 N and P=479 N respectively. In Fig. 13a, it can be noted that a concentrated tensile strain band localizes in the vicinity of tip of the prefabricated notch. Meanwhile, it can also be noted that a localized strain presents in an area near the anvil, which is caused by the point-contact between anvil and specimen. As external force applied further, the localized extensive strain is evolving continuously along the pre-notch orientation, see Fig. 13b. It is believed that during this process the initial damages underneath the specimen surface may be activated and some new damages will generate. Results indicate that a possible fracture path will follow the concentrated strain band and the specimen will break into two parts eventually.

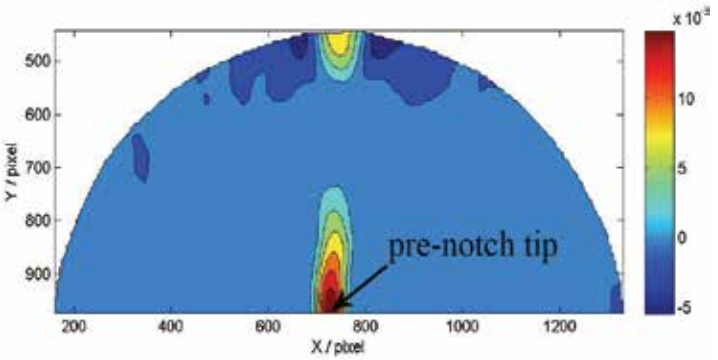

(a) P=105 N

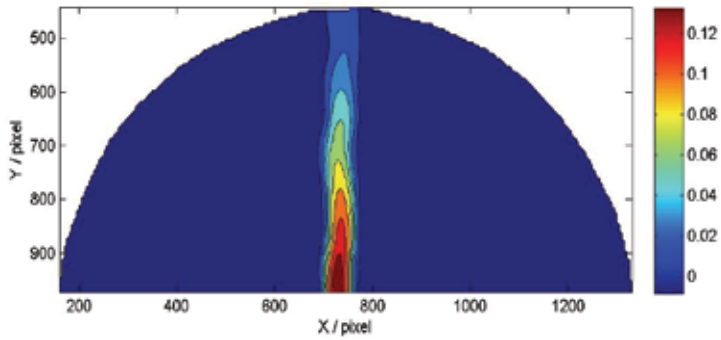

(b) P= 479 N

Fig. 13. Tensile strain field (ε_x) of SCB specimen at different load

Fig. 14 shows the vector distribution of displacement under a tensile stress calculated by the DIC. The vector arrows are scaled and can act as a quantitative measurement for discussing the failure behavior of semicircular specimen under compression loading. In Fig. 14, a single

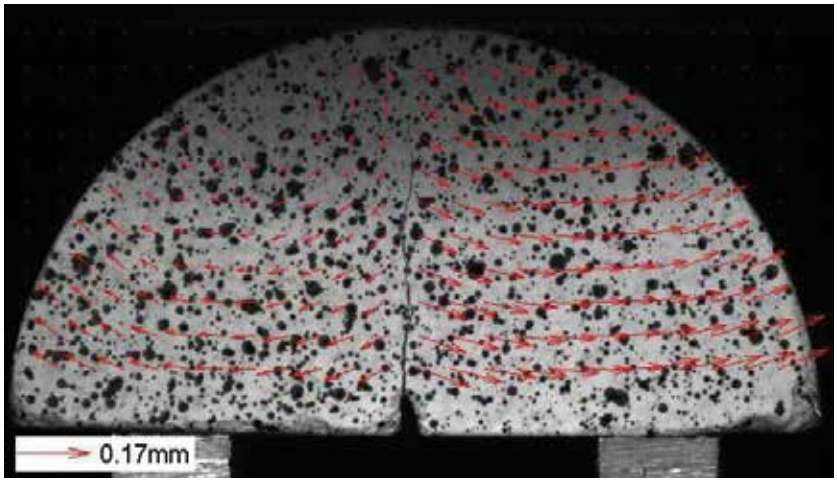

Fig. 14. Vector field of displacement for a post-failure SCB specimen

macroscopic crack can be observed on the specimen surface, this crack is just in the line with the orientation of pre-notch. Typically, it is obvious that the materials left and right of the failure path moved horizontal just perpendicular to the load axis. Result is in agreement with the prediction from the whole strain field. All the results indicate that the material is suffering from large extension stress under compressive loading.

Cracking is the most dominate mechanical failure mechanism in high explosives and could affect the mechanical performance and detonation of weapon systems. However, it is a challenge that the direct observation and quantitative measurement of the deformation field associated with the formation and extension of microcracks, because cracks are hard directly observed until they have grown large enough. Nevertheless, in recent years, a technique has been developed to quantitatively describe the initiation and propagation of cracks in explosive materials [29]. In DIC calculation, the correlation coefficient *C* is a function of two random speckle images captured before and after a deformation. When two small images match each other, the correlation coefficient reaches a minimum. However, when damage or cracks develop in the small region during deformation, the value of the coefficient *C* becomes bigger than other regions where no damage or cracks are present. In this work, based on the above discussion, we use the correlation coefficient to quantify the location and extent of cracks in SCB specimen.

Fig. 15 shows the contour plot of normalized correlation coefficient at four loading states. For PBX specimen, at moment A, the normalized correlation coefficient over the entire specimen surface is a constant, the magnitude of coefficient *C* is approximate 0, indicating that the two speckle images match each other very well, and no damage formed. In the subsequent moments, B, C and D, in some regions within the specimen surface the normalized correlation coefficient becomes bigger than other regions. In moment B, the small cracked region formed around the preset crack, and at the next moments C and D, the cracked region grows larger. Specially, at moment D, a single dominant crack is generated along the orientation of preset crack.

In addition, a set of SCB tests were carried out to determine the fracture toughness. Fig. 16 shows the typical relationship curve of load *P* and crack opening displacement *V*, in which the crack opening displacement was determined using DIC technique. Follow ASTM standard procedure E399, increment of crack extension was established by a 5 percent deviation from the linear portion of the record. A secant line through the origin of the test record with slope $(P/q) = 0.95(P/q)_0$ where $(P/q)_0$ was the slope of the tangent line 1 to initial linear part of the record was drawn. Load P_q was defined at the point of intersection of the secant line 2 and the curve. If P_m is taken as the maximum load achieved, the ratio P_m/P_q is found to be about 1.05 in most cases, but less than 1.1 in all tests satisfying the requirements for plane stain fracture toughness measurement. In this work, the critical failure load is determined by $P_m/P_q = 1.05$, given these information, combining Equations 6 and 7, the fracture toughness K_{IC} of SCB specimens are given in Table 1. The fifth column gives the critical failure force determined by Equation $P_m/P_q = 1.05$, the last column shows the plane strain fracture toughness of four semicircular specimens. Results show that the K_{IC} value is approximately 0.50 ± 0.02 MPa·$m^{1/2}$. Unfortunately, the study on the fracture toughness of real PBX materials is very rare in literature at present due to difficulties in experiments, so the method described in this paper may be provide some further insights into this issues.

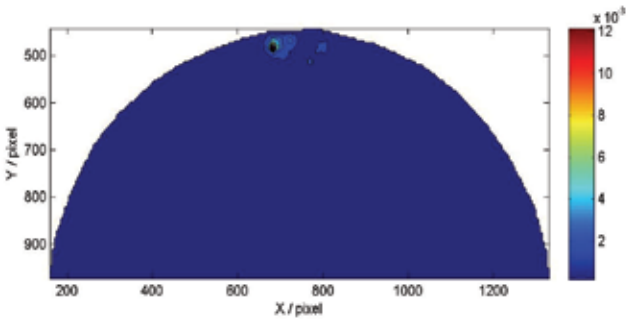

(a) P=360 N

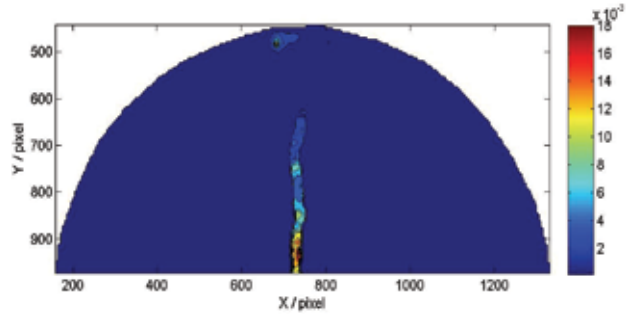

(b) P=385 N

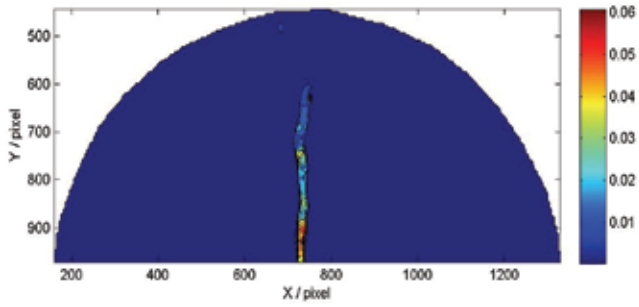

(c) P=410 N

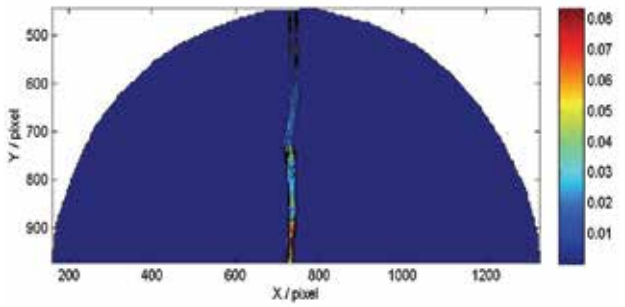

(d) P=435 N

Fig. 15. Contour plot of normalized correlation coefficient at four selected moments in SCB test

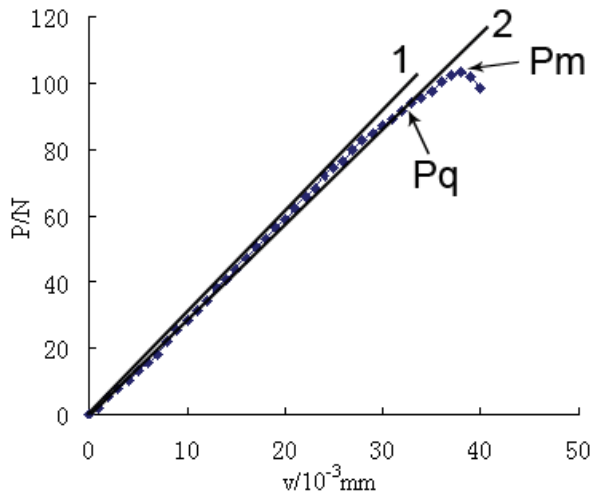

Fig. 16. Relationship of load versus crack opening displacement

a/mm	D/mm	B/mm	P_m/N	P_q/N	K_{IC}/MPa·m$^{1/2}$
4.9	20	9	119.58	113.89	0.49
5	20	9	116.27	110.73	0.50
5	20	9	122.18	116.36	0.52
5.1	20	9	107.55	102.43	0.48

Table 1. Specimen dimensional requirements for fracture toughness measurement

4.4 Punch loading test

Fig. 17 shows the displacement vector field of the specimen under the flat punch loading test prior to failure. Viscoelastic-plastic flow occurred in the specimen during punch penetration. The direction and magnitude of the plastic flow are represented by vector arrows which represent the relative degree of the displacement from the beginning of the experiment. The displacement quivers plot shown, as a quantitative measurement, gives a clear indication of the failure mechanisms in the specimen than visual observation. It is obvious that a triangular 'dead zone' has been completely formed in the specimen. In 'dead zone', the matter moves downward with the punch itself at the same velocity V, if not, the matter flows from the side of dead zone towards to the free surface at the velocity of $0.731V$. Fig. 18 illustrates the definite contour of tensile strain in horizontal direction when compression loading was applied to 6 seconds, just for the specimen prior to fracturing. This Fig. clearly shows the strains distribution on the specimen surface. It can be seen that strain contours are mainly concentrated underneath the flat punch and the maximum tensile strain is about 0.02. So it is believed that microcracks occur underneath the specimen surface, propagate and coalescence a large macrocrack, and finally induce cleavage rupture of the specimen with increasing of external force. It is also possible to generate full shear strain fields. As shown in Fig. 19, the strain concentration slip bands just localized underneath the punch and on the sides of the dead zone, where the highest shear strain rates and shear stresses produce and could cause fracture. Further SEM examination of this region can validate the shear fracture models.

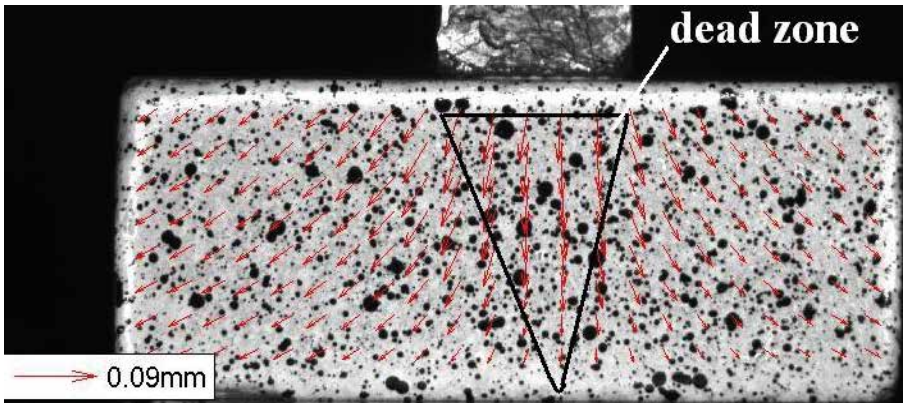

Fig. 17. Displacement vector field of the specimen under flat punch loading test

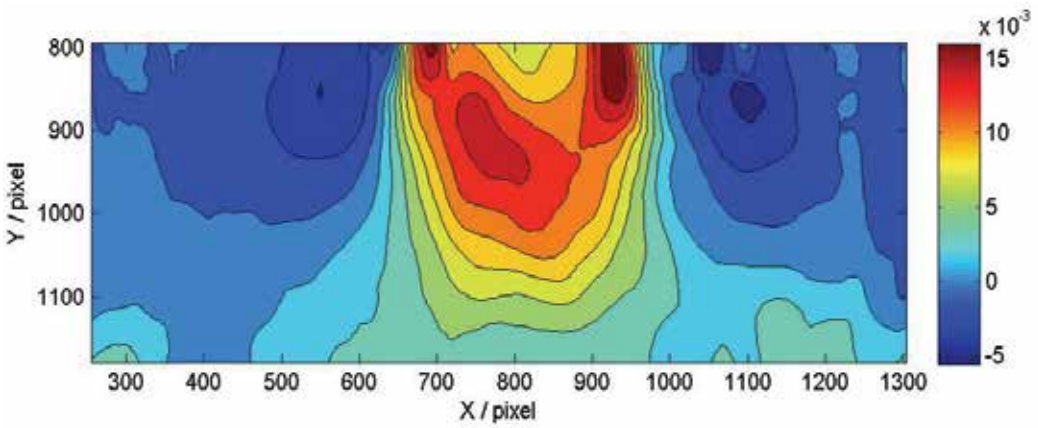

Fig. 18. Tensile strain field (ε_y) from a flat punch loading results prior to failure

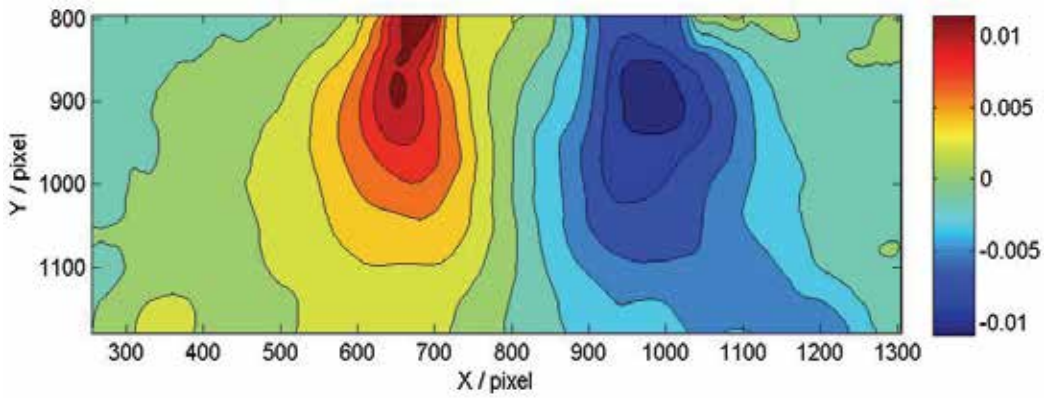

Fig. 19. Shear strain field from a flat punch loading result

4.5 Microstructure measurement

SEM was used to examine the microstructure of PBX. The observed surface should be polished before the testing. The experimental results show that the initial damages, such as microscopic voids may be caused by the small filler particles flowed and reset between large filler particles during hot compacting process and microcracks can be observed. Careful examination can see that deformed twinning occurred on the single particle surface. It's known that twinning allows particles to accommodate large strains without fracture, but fractures can develop through the particles with increasing of the external force, it is considered that the twin is forming a step at the surface that acts as a stress concentrator [30].

Real time microscopic examination reveals that different forms of failure including interfacial debonding and particle fracture can be observed. The failure generally starts at many independent sites, usually around the boundaries of the large filler particles before linking up into larger cracks, and finally induce cleavage rupture of the specimens. The initial damage, such as debonding generated during the pressing, is the origin of failure. Particle fracture was very rare, but may appear due to the orientation of a long crystal face lying perpendicular to an advancing crack path. Fig. 20 shows the results of real time microscopic examination of PBX simulation material in Brazilian test. Results show that cracks are extending along the boundaries of larger filler particles.

Real time SEM examination of a block specimen shows that different fracture modes can be seen. Fig. 21 shows that interfacial debonding is the dominate failure mode in compression test. In particular, the crack path mainly follows the boundaries of the filler particles. However, particle fractures do occur when the particle orientation impedes the crack growing path even this failure rare occurrences, see particle K. Moreover, microscopic cracks (indicated by arrows in Fig. 21) occurred within the filler particles, see particles M and N, which may be caused by initial damage activated and evolved under external force. The microcracks may coalescence and induce particle breakage finally. Therefore, both the interfacial debonding and the particle breakage indicate that the transgranular cracking and intergranular cracking are the significant failure modes.

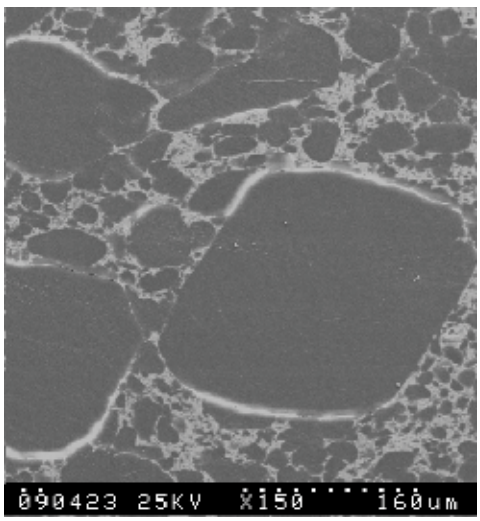

Fig. 20. Micrograph of a specimen in Brazilian test

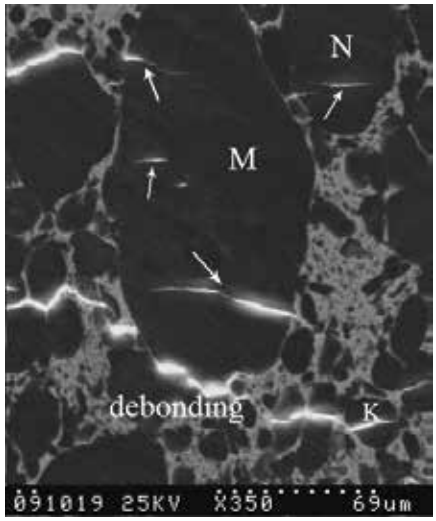

Fig. 21. Micrograph of a specimen in compression

The non-uniform strain field distribution in PBX simulant specimens calculated by the DIC offers basic information and can well predict the damage when specimen was loaded by compression. Moreover, as shown in this work, the deformation field obtained through DIC is also possible to reveal the strain singularity in particle-based composites and to predict the growing path of the cracks during the fracture process. A SCB specimen with a size of 20 mm in diameter and 10mm in thickness was machined from a disc specimen, and an edge pre-notch with 0.9mm length and 0.2 mm width was fabricated in the specimen perpendicular to the load direction, as shown in Fig. 22.

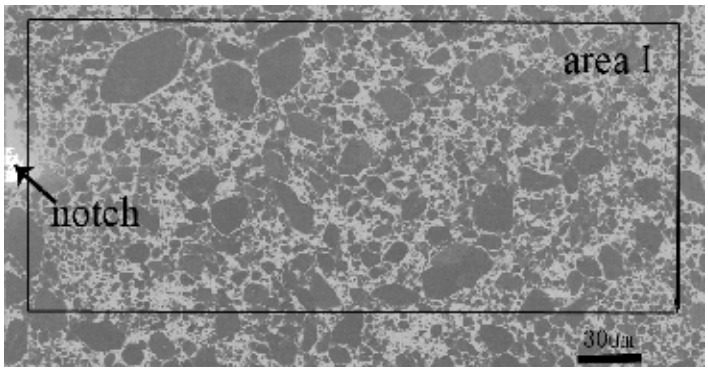

Fig. 22. Micrograph of a SCB specimen

The semicircular disc specimen was compressed by a flat steel anvil installed in SEM chamber. The near region (rectangular area I shown in Fig. 22) around the tip of the prefabricated crack was magnified by the SEM to real time observe the surface topography and to record the images during the quasi-static loading. For each loading step with a force increment about ΔP=50 N, the digital surface image was analyzed by DIC to match with the initial image recorded before deformation so as to obtain the displacement field and strains. This can show the deformation history by load steps to reveal the strain locality and to

predict the crack possible growing path. Fig. 23 illustrates the strain contours of a specimen in semicircular bend test at three loading steps of P=150 N, P=250 N and P=400 N, respectively. The extension strain field is not uniform. It can be noted that the maximum contours are concentrated around the tip of prefabricated crack, and it can also be seen that the localized strain is propagating and evolving along the pre-notch direction with external load increasing, so the primary failure route is following prefabricated crack orientation.

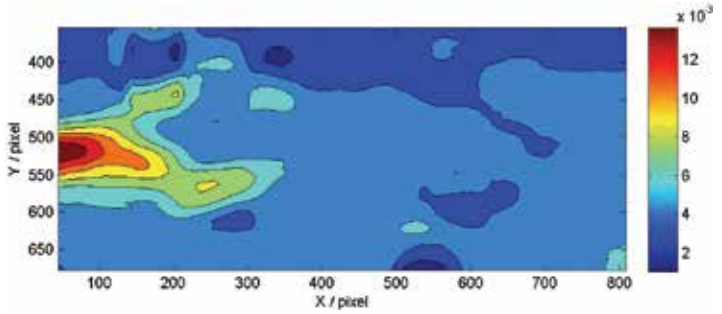

(a) P=150 N

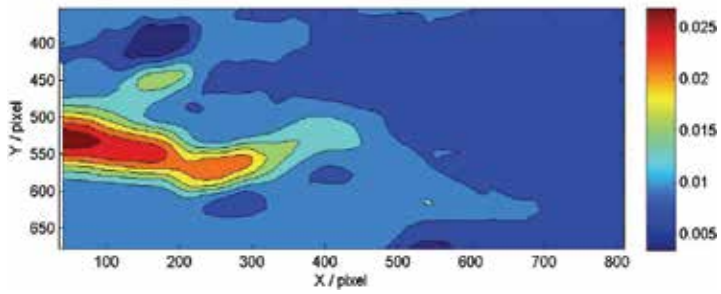

(b) P=250 N

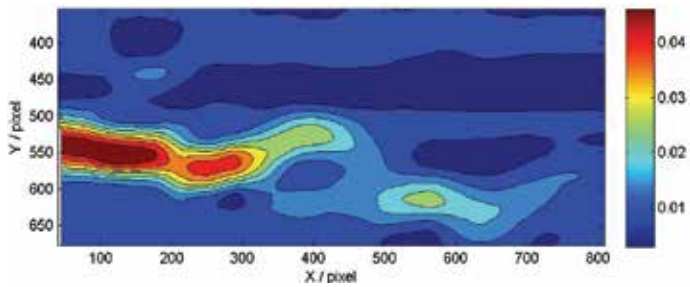

(c) P=400 N

Fig. 23. Strain contours of a specimen at different loads in SCB test

SEM was taken to examine the damage occurred in simulant materials. Fig. 24 indicates the SEM image of the fracture surface of a simulant specimen. The flat fracture morphology of specimen can be seen, demonstrating that the filler particles experienced transgranular fracture. Some microcracks can be seen on the large particles indicated by arrows, and interfacial debonding can be noted.

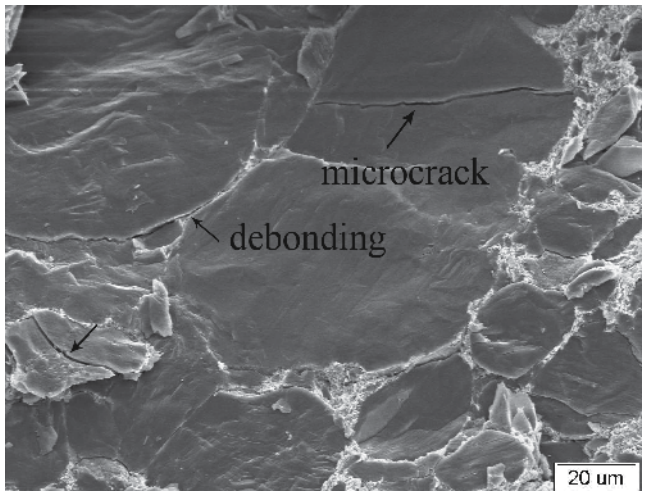

Fig. 24. Fracture morphology of PBX in Brazilian test

Fig. 25 shows the SEM image of the block specimen fracture surface under compression loading. It can be seen that the particles experienced fragmentation. A large number of smaller particles formed, which indicates the compression induces a lot of filler particle crushing. Typically, Fig. 25 clear reveals the presence of brittle particle and cleavage fracture, and the particle Q dislocation fracture (indicated by arrow) is obvious caused by particle to particle contact. It is believable that the particle fractures are mainly associated with particle to particle contact due to an extremely high density of filler particles in simulation material. Fig. 26 shows an image of shear slips in the hard particle directly to the side of intruding punch, demonstrating that large shear stresses occurred in this region of the specimen during punch penetration.

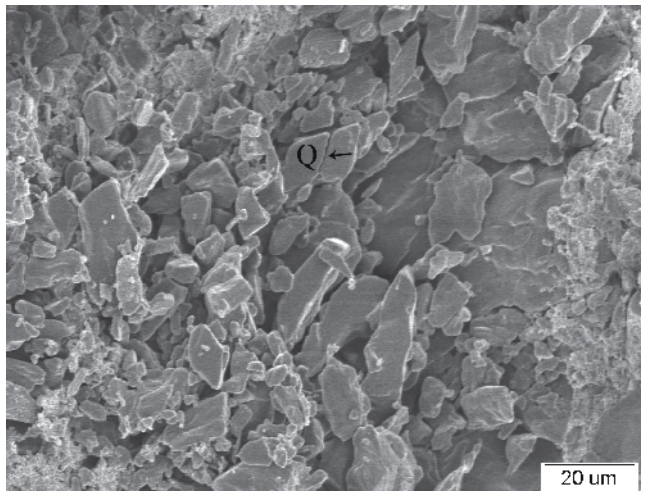

Fig. 25. Fracture morphology of PBX in compression

Previous studies in the literatures [4, 6, 31-32] shown that failure tends to start around the boundaries of large filler particles. Results show that the predominant failure mode of PBX

is interfacial debonding between explosive particles and binder under extension action. While further examples have been presented in this paper, the failure path in PBX simulant appears to follow unexpected routes. Our studies of PBX simulant under tensile stress field suggest that the transgranular cracking is the dominant fracture mode. It should be remembered that specimens are three-dimensional materials even only the exposed surface can be observed. Consequently, particles just below the observed surface may influence the measured behavior.

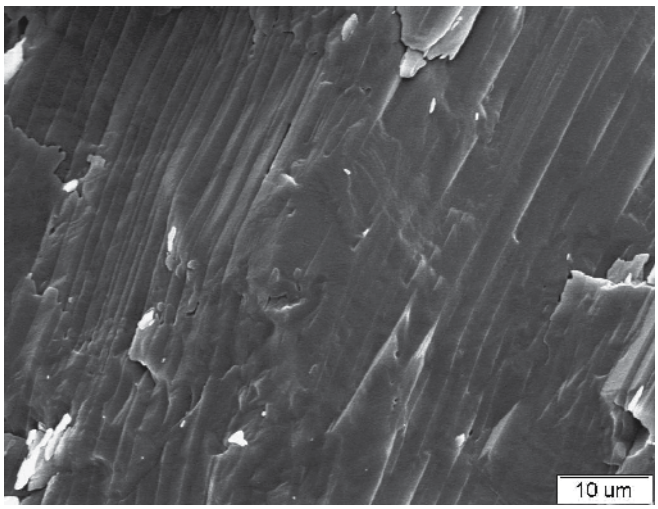

Fig. 26. Shear slips in a particle

5. Conclusions

As PBX systems becoming more widely used, the understanding of the damage and fracture mechanisms responsible for safety working life evolution is important. As discussed, DIC is an optical full-field measurement technique. Even though no information can be generated to investigate the internal material motion, the deformation and fracture behavior of PBX simulants can be studied according to the full strain field and displacement vector plots on specimen's surface. More important, the digital correlation processing of SEM images can provide the non-uniform deformation information in PBX simulants, demonstrating the microscopic damage evolution and predicting possible failure routes in specimen. In addition, the advantage of DIC described here is the ability to make tensile stress/strain measurements. Moreover, based on Mohr-Coulomb failure criteria, the fracture parameters, such as cohesion and friction angle etc, can be calculated. In addition, the fracture toughness can be determined by using the SCB test. The results are contributing to understand the fracture mechanical properties of specimens under compressive loading.

PBX simulant is a highly filled composite consists of up to 95% by weight particles coated by binder. Therefore, the coverage degree is less than 100%. Microstructures of PBX simulant were observed by using an SEM. Real time microstructure examinations show that decohesive failure of interface between particles and binder is the dominant fracture mode due to incomplete interfacial cohesion. In addition, particle cleavage fracture can also be seen evidently under the compression and shear stress action (Fig. 20 and Fig. 21). However,

the specimens are three-dimensional materials even only the exposed surface was observed. Particles just below the observation plane can influence the measured behavior. The fracture mode in our Brazilian test is evident transgranular cracking (Fig. 24). The result could demonstrate that the tensile failure strength of particles must be lower than cohensive strength between particles and binder. The authors think it is reasonable to demonstrate the failure mechanisms of PBX simulant by the fracture surface morphology.

6. Acknowledgements

The authors of this paper acknowledge the financial support from the National Natural Science Foundation of China (grant number 10832003), the National Basic Research Program of China (grant number 613830202), and the Program for New Century Excellent Talents (NCET-06-0159). The authors also thank Professor Nie Fude from Institute of Chemical Materials, Chinese Physical Academy for providing PBX simulation materials.

7. References

[1] S. J. P. Palmer, J. E. Field, J. M. Huntley. Deformation, strengths and strains to failure of polymer bonded explosives. Proc. R. Soc. Lond. A. 1993, 440: 399-419.

[2] C. B. Skidmore, D. S. Phillips, P. M. Howe, et al. The evolution of micro structural changes in pressed HMX explosives. In proceeding: 11th International Detonation Symposium. 1998.

[3] P. W. Chen, H. M. Xie, F. L. Huang, et al. Deformation and failure of polymer bonded explosives under diametric compression test. Polymer Testing. 2006, 3(25): 333-341.

[4] P. W. Chen, F. L. Huang, Y. S. Ding. Microstructure, deformation and failure of polymer bonded explosives. J. Mater. Sci. 2007, 42(13): 5272-5280.

[5] P. J. Rae, S. J. P. Palmer, H. T. Goldrein, et al. White-light digital image cross-correlation (DICC) analysis of the deformation of composite materials with random microstructure. Optics and Lasers in Engineering. 2004, 41(4): 635-648.

[6] P. J. Rae, H. T. Goldrein, S. J. P. Palmer, et al. Moire interferometry studies of PBX 9501. Shock Compression of Condensed Matter. 2001, 825-828.

[7] P. J. Rae, S. J. P. Palmer, H. T. Goldrein, et al. Quasi-static studies of the deformation and failure of PBX 9501. Proc. R. Soc. Lond. A.2002, 458: 2227-2242.

[8] M. Li, J. Zhang, C. Y. Xiong, et al. Damage and fracture prediction of plastic-bonded explosive by digital image correlation processing. Optics and Lasers in Engineering. 2005, 43(8): 856-868.

[9] Z. W. Liu, H. M. Xie, K. X. Li, et al. Fracture behavior of PBX simulation subject to combined thermal and mechanical loads. Polymer Testing. 2009, 28(6): 627-635.

[10] A. L. Lewis, H. T. Goldrein. Strain measurement techniques in explosives. Strain. 2004, 40(1): 33-37.

[11] H. I. Goldrein, P. J. Rae, S. J. P. Palmer, et al. Construction of a high-resolution moiré interferometry for investigating microstructural displacement fields in materials. Phil. Trans. R. Soc. Lond. A. 2002, 360(1794): 939-952.

[12] H. M. Xie, H. Shi, P. W. Chen, et al. An experimental study on creep deformation of PBX with laser moiré interferometry method. Fracture and Strength of Solids. 2006, 306(6): 1037-1042.

[13] P. J. Rae, H. T. Goldrein, S. J. P. Palmer, et al. 12th International Detonation Symposium, 2002, 44-48.
[14] S. G. Grantham, J. E. Field. Speckle correlation methods applied to ballistics and explosives. Proc. of SPIE Vol. 4933, 27-32.
[15] S. G. Grantham, C. R. Siviour, W. G. Proud, et al. Speckle measurements of sample deformation in the split Hopkinson pressure bar. J. Phys. IV France. 2003, 110: 405-410.
[16] S. G. Grantham, C. R. Siviour, W. G. Proud, et al. High-strain rate Brazilian testing of an explosive simulant using speckle metrology. Meas. Sci. Technol. 2004, 15: 1867-1870.
[17] C. R. Siviour, D. M. Williamson, S. G. Grantham, et al. Split Hopkinson bar measurements of PBXs. Shock compression of condensed matter. 2003,706(2): 804-807.
[18] T. C. Chu, W. F. Ranson, M. A. Sutton, et al. Applications of digital image correlation techniques to experimental mechanics. Experimental mechanics. 1985, 25(3): 232-244.
[19] D. Lecompte, A. Smits, S. Bossuyt, et al. Quality assessment of speckle patterns for digital image correlation. Optics and lasers in Engineering. 2006, 44(11): 1131-1145.
[20] W. G. Proud, M.W. Greenaway, C. R. Siviour, et al. Characterizing the response of energetic materials and polymer bonded explosives (PBXs) to high rate loading. Mater. Res. Soc. Symp. Proc. Vol. 896. 2006, 0896-H08-02.1-12.
[21] C. J. Tay, C. Quan, Y. H. Huang, et al. Digital image correlation for whole field out-of plane displacement measurement using a single camera. Optics Communications, 2005, 251: 23~36.
[22] H. W. Wang, Y. L. Kang. An improved digital speckle correlation method and its application in copper thin film. Proc. SPIE Vol. 2002, 4537: 151-153.
[23] K. P. Chong, M. D. Kuruppu. New specimen for fracture toughness determination for rock and other materials. Int. J. Fract. 1984, 26, R59-62.
[24] K. P. Chong, M. D. Kuruppu. Fracture toughness determination of layered materials. Eng. Fract. Mech. 1987, 28(1): 43-54.
[25] P. D. Peterson, K. S. Mortensen, D. J. Idar, et al. Strain field formation in plastic bonded explosives under compressional punch loading. Journal of Materials Science, 2001, 36(6): 1395-1400.
[26] K. Li Study on quasi-static and dynamic mechanical behaviors of polymer bonded explosive. Master degree thesis. Beijing: Department of Mechanics, Beijing institute of technology. 2008. (in Chinese)
[27] J. Zhao Applicability of Mohr-Coulomb and Hoek-Brown strength criteria to the dynamic strength of brittle rock. International Journal of Rock Mechanics and Mining Sciences. 2000, 37(7): 1115-1121.
[28] D. Williamson, S. J. P. Palmer, S. G. Grantham, et al. Mechanical properties of PBS9501. American Institute of Physics. 2004, 706: 816-819.
[29] C. Liu, C. M. Cady, P. J. Rae, et al. On the quantitative measurement of fracture toughness in high explosive and mock materials. In proceeding: In proceeding: 14th International Detonation Symposium, 2010.
[30] S. J. P. Palmer, J. E. Field, J. M. Huntley. Deformation, strengths and strains to failure of polymer bonded explosives. Proc. R. Soc. Lond. A . 1993, 440: 399-419.

[31] P. W. Chen, H. M. Xie, F. L. Huang, et al. Deformation and failure of polymer bonded explosives under diametric compression test. Polymer testing, 2006, 25(3): 333-341.
[32] P. W. Chen, F. L. Huang, Y. S. Ding. Microstructure, deformation and failure of polymer bonded explosives. J. Mater. Sci. 2007, 42(13): 5272-5280.

Part 5

Modelling

19

Virtual Crack Closure Technique and Finite Element Method for Predicting the Delamination Growth Initiation in Composite Structures

Pietropaoli Elisa
Cira, Italian aerospace research center
Italy

1. Introduction

Even thought composite materials have been introduced in aircraft industries since the middle of the last century, only the quite recent decision of the most important aircraft suppliers to use extendedly these advanced materials for their new aircrafts (AIRBUS-A380 and BOEING-787) have made people aware on the great potentiality of composites in strategic fields. It is not rare to see in newspapers composite materials to be referred as "plastics", really, if composites were only "plastics" they would not be used for such strategic applications. Indeed, composite materials for aerospace structures are properly "Fiber Reinforced Plastics" being the great advantages associated to the use of composites brought by the combination on a macroscopic scale of two constituents, namely reinforcing fibers and matrix (polymeric for example).
Thus, the principal difference between composites and other materials obtained by combining more elements (such as metals alloys) lies in the fact that composite materials constituents differ at molecular level to each other and are mechanically separable (Jones R,1999)-(Mazumdar,2002).
It is well known that the same material has higher stiffness and strength in the fiber form than in the bulk one because of the reduced number of defects, such as dislocations, that it contains. Being a single fiber of microscopic diameter useless to realize any load-carrying structure, the basic idea is to join and keep fibers in the required positions by embedding them into a matrix (polymeric, metal, ceramic) in order to obtain a material whose properties could be improved with respect to the ones of the constituents.
Thus, within a composite material fibers are the load-carrying elements which provide the required stiffness and strength while the matrix material binds the fibers together and transfers the load between them.
Since composites are materials that "can be built", they can be designed to fulfil requested requirements in terms of both mechanical properties and corrosion and electrical behaviour.
Many advantages can be obtained by using composites instead of traditional engineering materials (such as improved specific stiffness and strength), however high costs and lacks of knowledge in their behaviour do not make the use of composite materials easy at all.
In terms of engineering analysis of the mechanical behaviour of composites the major concern is about their inherently anisotropy. For example, the application of a load in a

direction that is not principal for the material leads to coupling effects between shear and extension thus the application of a normal stress induces not only an extension in the direction of the stress and a contraction perpendicular to it but also a shearing deformation (Jones R,1999).

A lot of composite material types have been developed (i.e with short or long reinforcing fibres), however in the following only composites made of long and continuous fibers embedded in a polymeric matrix are addressed.

Furthermore, only macromechanics aspects of these materials are accounted for, thus assuming the material homogeneous and the effects of the constituents detected only as an averaged macroscopic properties of the composites.

As above said composites can be tailored to achieve specific requirements, for example in terms of strength and stiffness of the material itself. However, in terms of design of structures different laminae or ply with different fibers orientation of composites materials can be stacked and bonded together in order to obtain a laminate composite material whose properties meet definite design needs in particular directions without wasting of materials where stiffness and strength are not required.

Due to the inherent anisotropy of the material, the damage phenomenology of composite laminate is quite complex (Altenbach et al., 2004). Failure strongly depends on the stress distribution within the material which is surely associated to the intensity of the applied load but also on its direction and on the laminate stacking sequence.

Literature classified fracture modes (Pagano & Schoeppner, 2003) of composite laminates in:

- Intralaminar failure: fracture is located inside the lamina (i.e matrix crack, fiber breakage, matrix-fiber debonding, fiber kinking)
- Interlaminar failure: fracture occurs between two adjacent plies and lies in a plane parallel to that of the fibers (i.e delamination)
- Translaminar failure: fracture is oriented transverse to the laminate plate

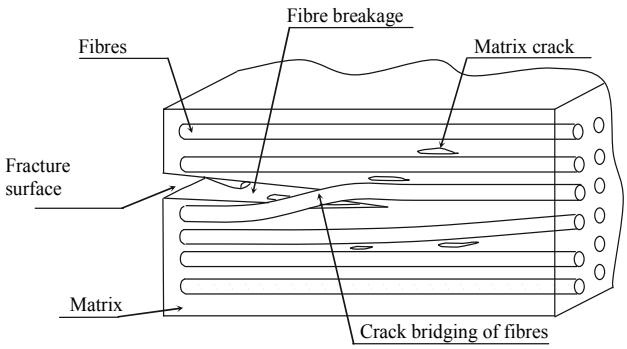

Fig. 1. Failure modes of unidirectional composites

A simplified sketch of failure modes in unidirectional composites was proposed by Pagano & Schoeppner (2003) as shown in Figure 1.

2. Interlaminar damage: Delaminations

Delaminations are probably the most critical and studied, failure mode of composite material. In the composites literature, delamination is generally assumed to take place at the

interface between adjacent plies and treated as a fracture process between anisotropic layers, rather than to consider it, more precisely, as a fracture between constituents or within one of the constituents (such as the material matrix) (Pagano & Pipes, 1971).
Delamination can onset due to manufacturing (drilling, residual thermal stress induced by the cure process) or to low velocity impact of dropping tools or runway debris. Furthermore delamination may be induced by interlaminar shear and normal stresses associated to some geometrical configurations such as free edges, curved sections as well as tapers and transitions. Whichever their cause is, delaminations may buckling and growth under service conditions thus leading to the premature collapse of the structure as well as to the premature buckling of the laminate, intrusion of moisture, stiffness degradation, and loss of fatigue life.
The through-thickness weakness of composite laminates results in poor response to impact damage. Impacts are generally classified based on impactor velocity or on their energy. Low velocity impacts are typically impacts in which a large object falls onto the structure with low velocity while high velocity impacts are impacts resulting in complete perforation of the target (Abrate, 1998).
A low velocity impact event usually results in a combination of failure modes including matrix crack, local fiber breaking at the front-face impacted surface, back-face ply splitting and fiber breaks, and multilevel delamination (Pagano & Schoeppner, 2003). All these damage cannot be detected during visual inspection therefore are defined Barely Visible Impact Damage (BVID) but they may reduce consistently the strength of the structure.
The amount of damage induced in the structure depends, also in this case, the laminate stacking sequence. It has been observed that delaminations occur only at interfaces between plies with different fiber orientation (Abrate, 1998) and in general are introduced at several interfaces within the same laminate. Furthermore, it has been found that the delaminated area has an oblong of "peanut shape" whose major axis is oriented in the direction of the fiber of the lower ply of the delaminated interface away from the impact surface.
Experimental non-destructive technique such as C-Scan and X-Ray provide a projection of these entire damaged surface on a single plane.
Thus, by overlaying the plan view of each of the individual interface delaminations, the resultant damaged area may appear to be a nearly circular or an elliptical continuous region.
The damage pattern is strongly influenced by the thickness of the impacted laminate that determines the laminate bending stiffness or the duration of the contact between the laminate and the impactor. Thin laminate subjected to impact tends to bend consistently, this results in large in-plane tensile stresses that exceed the transverse tensile strength of the plies near the back face of the laminate leading to matrix cracking and delamination (damage progress from the bottom therefore the damage pattern is referred as reversed pine tree as shown in Figure 2, a).
Thick laminates behave a low bending compliance that results in significant transverse normal and shear contact stress leading to matrix cracking in the contact region and delamination between the plies near the impacted surface (Pagano & Schoeppner, 2003 and Abrate,1998), pine tree damage pattern shown in Figure 2, b.
Two different considerations are generally used for the design of composite structures namely damage resistance and damage tolerance. The damage resistance can be defined as the measure of the capability of a material or structure to resist the initial occurrence of damage (Pagano & Pipes, 1971). Whereas, the damage tolerance is a measure of a damaged material or damaged structure to sustain load and/or maintain functional capability.

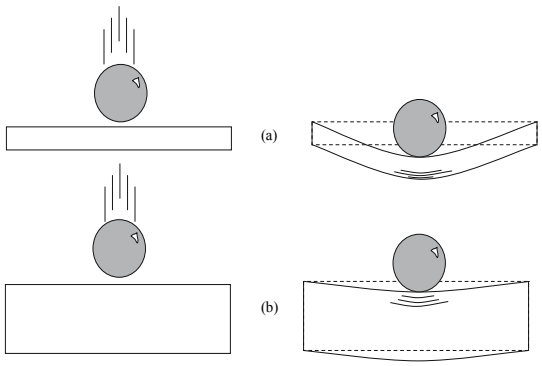

Fig. 2. Impact on thin (a) and thick (b) laminates

The damage resistance may be quantified by measuring the load at which damage initiates during a single impact event on an undamaged specimen. In literature a huge amount of works have been devoted to the analysis of the damage resistance determination in case of low velocity impact on composite laminates.

Worth of noting are, amongst the others, the works by Davies and Zhang (Davies & Zhang, 1995)-(Davies et al., 1994) devoted to the development of a theoretical method for the prediction of the threshold fracture load in low velocity impacts as well as the determination of the extent of the damaged area.

In order to improve the damage resistance of composite structure to the delamination onset, the design should be aimed at minimizing interlaminar stresses by avoiding critical shapes (curved sections, ply drop off and so on) and selecting opportunely the laminate stacking sequence.

Damage tolerance considerations are generally based on experimental investigations. The stiffness and strength reduction associated to the presence of a delamination in composite laminate plates is very strong especially in compression. A common measure of the damage tolerance of impacted laminates is obtained by performing compression after impact (CAI) tests. Within these tests, a damaged structure, is progressively loaded until the structural collapse is reached and the design allowables are determined accounting for the presence of undetected delamination or intralaminar damage.

Nowadays there is a wide demand of numerical tools capable to measure the damage tolerance of aircraft composite structures and this explains why many research activities are dealing with the development of numerical methodologies with predictive capabilities.

In order to generate experimental data to be used for validating numerical models dealing with delamination, experimental tests (CAI) are generally performed by creating an artificial debonding between two adjacent layers of a composite laminate through the insertion of a very thin film of Teflon (Kyoung & Kim, 1995).

Two edges of the structure are then clamped in a test machine and a compressive displacement is gradually applied. The composite laminate is subdivided by the delamination into a thin sub-laminate and a thick sublaminate or base sublaminate. Different kinds of configuration (local and global instabilities) may appear at different load levels and they can be monitored by following the out of plane displacement of two control points (U and L in Figure 3) placed on the two sub-laminates.The behaviour commonly observed during these tests can be described as follows (Riccio & Pietropaoli,2008). As the load increases the thin sublaminate buckles first. Afterwards, the buckling of the base

sublaminate is induced. In this case, depending on the thicknesses ratio of the two sub-laminates, the out of plane displacement of the base sublaminate can be of the same sign (Type I) or of different sign (Type II) with respect to the one of the thin sub-laminate. When the buckling is of Type II, an increase in applied load determines the condition known as global buckling: the thin sublaminate is dragged towards the base sublaminate but the delamination opening continues to be relevant.

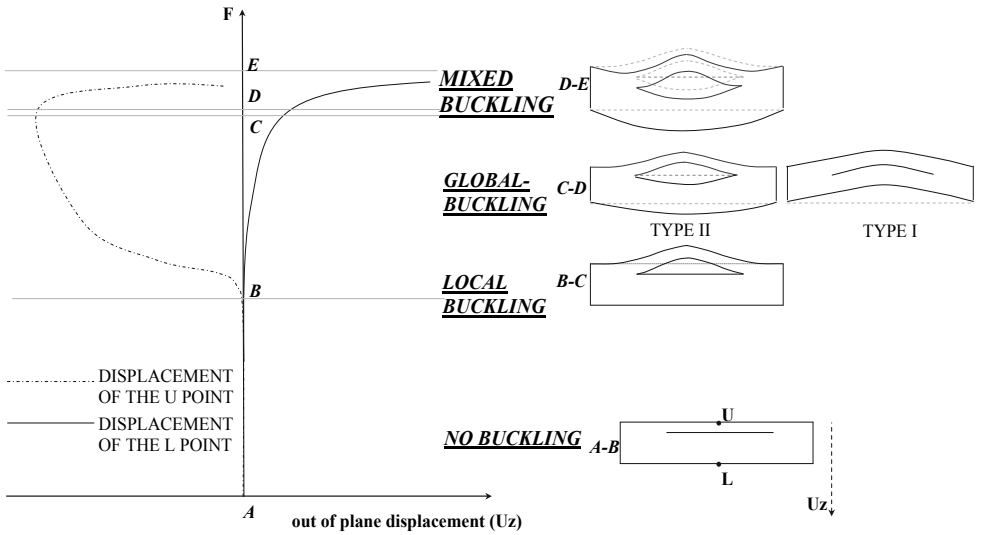

Fig. 3. Buckling configurations

3. Virtual crack closure technique

A delamination can be assimilated to a fracture process between anisotropic layers (interlaminar damage). Thus, fracture mechanics principles (Janssen et al., 2004) can be used to study the behaviour of composite structures in presence of interlaminar damage and to determine the conditions for the delamination growth initiation.

Under the assumption of considering the delamination growth process as a crack propagation phenomenon (Kachanov, 1988), fracture mechanics concepts can be generally transferred to the analysis of delaminated composite structures.

The propagation of a crack is possible when the energy released for unit width and length of fracture surface (named Strain Energy Release Rate, G) is equal to a threshold level or fracture toughness, characteristic for each material (Janssen et al., 2004).

Starting from the earlier analytical works by Chai et al., (1981) and Kardomates (1987), delamination in composites has been studied by evaluating the Strain Energy Release Rate. Nowadays, the G calculation is generally performed by means of techniques used in conjunction with the finite element method, such as the Virtual Crack Closure Technique.

According to the Virtual Crack Closure Technique, the evaluation of the Strain Energy Release Rate can be obtained starting from the assumption that for an infinitesimal crack opening, the strain energy released is equal to the amount of the work required to close the crack. Therefore, the work W required to close the crack can be evaluated by performing two analyses. The first analysis is needed to evaluate the stress field at the crack tip for a crack of

length a and the second one is aimed to obtain displacements in the configuration with the crack front appropriately extended from a to $a+\Delta a$ (Figure 4). The expression of the work W evaluated according to the two-steps Virtual Crack Closure Technique is given by Eq. (1).

$$W = \frac{1}{2}\left(\int_0^{\Delta a} \sigma_{yy}^{(a)}(x)\delta u_y^{(b)}(x)dx + \int_0^{\Delta a} \sigma_{yx}^{(a)}(x)\delta u_x^{(b)}(x)dx + \int_0^{\Delta a} \sigma_{yz}^{(a)}(x)\delta u_z^{(b)}(x)dx \right) \quad (1)$$

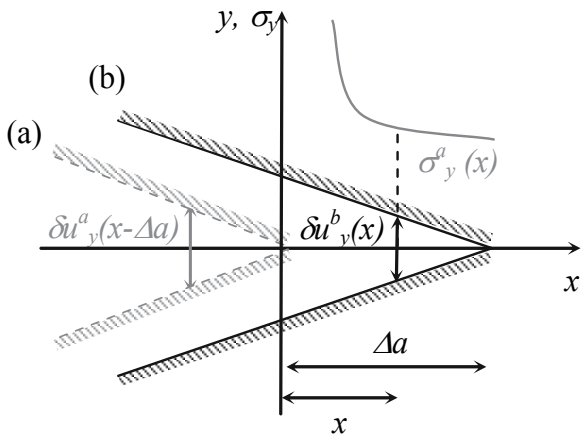

Fig. 4. Two-steps virtual crack closure technique: schematization of the two configurations before (a) and after the crack extension (b)

The quantities indicated in Eq. (1) with the apex (a) and (b) are evaluated in configuration (a) and (b) of Figure 4 respectively describing the crack tip status, before and after the crack propagation.

The calculation of the Strain Energy Release Rate can be simplified by adopting an alternative approach: the one step Virtual Crack Closure Technique (VCCT). The VCCT is based on the assumption that an infinitesimal crack extension has negligible effects on the crack front therefore both stress and displacement can be evaluated within the same configuration by performing only one analysis.

By adopting this technique, the expression of the work W required to close the crack becomes as in Eq. (2).

$$W = \frac{1}{2}\left(\int_0^{\Delta a} \sigma_{yy}^{(a)}(x)\delta u_y^{(a)}(x-\Delta a)dx + \int_0^{\Delta a} \sigma_{yx}^{(a)}(x)\delta u_x^{(a)}(x-\Delta a)dx + \int_0^{\Delta a} \sigma_{yz}^{(a)}(x)\delta u_z^{(a)}(x-\Delta a)dx \right) \quad (2)$$

where both displacements and stress are evaluated in the configuration (a) of Figure 4. According to the definition previously given, the Energy Release Rate can be written as in Eq.(3).

$$G = \lim_{\Delta a \to 0} \frac{W}{\Delta a} \quad (3)$$

Combining Eq.(2) and (3) it is possible to obtain the expression of the Strain Energy Release Rate for the three mutually orthogonal fracture modes: GI associated to the mode I or opening; GII to the mode II or in-plane shear, GIII to the mode III or antiplane shear. These three basic fracture modes are shown in Figure 5.

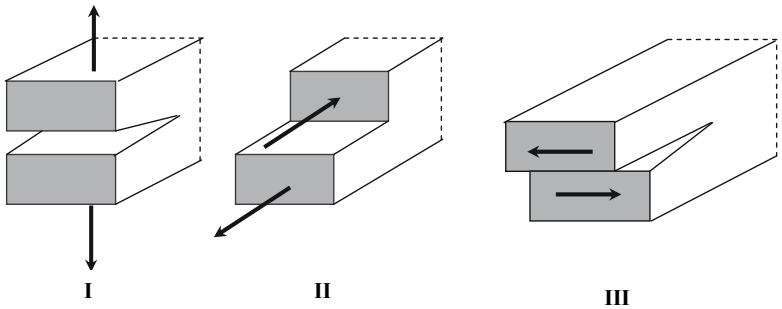

Fig. 5. VCCT schematization of the two configurations before (a) and after the crack extension (b)

3.1 Delamination growth criteria

In fracture mechanics, the Strain Energy Release Rate (G) is the quantity that, compared with the material fracture toughness (G_C), characterizes the state of the delamination (no growth, growth initiation, stable or unstable growth). As said before, G must be larger than Gc before crack growth occurs (Eq.4).

$$G > G_C \tag{4}$$

However, three different fracture modes can be defined associated to three orthogonal modes of loading (see Figure 5). For composites, it is extremely important to consider effect of the mode mixities on the delamination behaviour. Indeed, a delamination may be loaded in one of these modes or rather in some combination of these modes (Reeder, 2006).
Experimental tests are used to measure the critical fracture toughness but unfortunately, several different types of specimens are needed to generate delamination toughness data over a desired range of mixed-mode combinations (Reeder & Crews, 1990).
Results of these kinds of tests can be presented by plotting the mode I component of fracture toughness G_{IC} against the mode II component G_{IIC}.
Delamination growth criteria may be viewed as curve fit to fracture test data plotted in mixed mode diagrams. Thus, the accuracy of a failure criterion can be checked by seeking its capability to fit the material response when plotted on these diagrams.
Due to a late development of Mode III tests, most criteria available in literature, have been conceived taking into account only the first and the second interlaminar fracture modes. However, currently three dimensional criteria (Reeder, 2006) have been developed too.
One of the most used criterion is the power law Eq. (5) which may be used to represent a wide range of material responses by selecting opportunely the two exponents α, β.

$$\text{Power law criterion} \left(\frac{G_I^m}{G_{IC}}\right)^{\alpha} + \left(\frac{G_{II}^m}{G_{IIC}}\right)^{\beta} + \left(\frac{G_{III}^m}{G_{IIIC}}\right)^{\chi} = 1 \tag{5}$$

Another one is the Benzeggagh & Kenane (1996) criterion or B-K criterion, which requires the selection of only one fitting parameter η (Eq. (6)).

$$\text{B-K criterion} \quad \frac{G_T}{G_{IC}+\left[\left(G_{IIC}-G_{IC}\right)\frac{G_{II}^m}{G_T}+\left(G_{IIIC}-G_{IC}\right)\frac{G_{III}^m}{G_T}\right]\left(\frac{G_{II}^m+G_{III}^m}{G_T}\right)^{\eta-1}}=1 \tag{6}$$

It is clear that the proposed criteria are only mathematical expressions able to represent different material responses by varying the values assigned to the fitting parameters. Thus, the selection of these parameters requires that mixed-mode testing be performed during the characterization of the material.

3.2 Finite element models for computing the strain energy release rates by using the VCCT

Analytic computations of stresses and displacement at the crack tip are possible only in a few simplified cases ((Janssen et al., 2004)-(Chai et al., 1981), whereas numerical solutions may be found quite easily by using the Finite Element Method also for complex geometry. Indeed, the VCCT is generally used for the evaluation of the Strain Energy Release Rate in finite element analyses.

The first VCCT approach to compute Strain Energy Release Rates, starting from forces at the crack tip and relative displacements of the crack faces behind it, was proposed for four noded elements by Rybicki & Kanninen (1977).

After it was extended to higher order elements by Raju (1987) and to three-dimensional cracked bodies by Shivakumar et al. (1988). A comprehensive review of VCCT formulae for different element types was given by Krueger (2004). Whitcomb (1989) was one of the first to introduce the use of the VCCT to determine Strain Energy Release rate distributions for a circular delamination.

Since then, a lot of numerical analyses have been performed by using this technique: many of them dealing with delamination growth initiation (Mukherjee et al., 1994)-(Whitcomb,1992), others with growth evolution (Klug et al., 1996)-(Shen et al., 2001)-(Xie & Biggers, 2006)-(Pietropaoli & Riccio A., 2010a and 2010b) and skin-stringer debonding (Orifici et al., 2008)-(Wang & Raju 1996)-(Krueger & O'Brien, 2000).

When dealing with three-dimensional problems, the one-step Virtual Crack Closure Technique (VCCT) is generally used instead of the two-steps Virtual Crack Closure Technique in order to reduce the computational time requested for the analysis.

In the last years a wide spreading interest has been focused on cohesive elements (Camanho et al., 2003)-(Turon et al., 2004), because, based on both the strength of material formulation for crack initiation and fracture mechanics for crack propagation, they are able to overcome one important limitation of the VCCT: the need to define an initial delamination.

However, cohesive elements still pose problems in the definition of the constitutive model for interlaminar damage to be used.

Therefore, even if more rough in some aspects, the VCCT still continue to attract the attention, due to the simplicity of its theory and to its suitability for implementations in post-processing subroutines.

A delamination is merely a debonding between two adjacent parts of the same structure along the thickness. This debonding can be simulated in the finite element method by maintaining not merged nodes on two adjacent faces of the volumes or surfaces representing respectively two sublaminates (Figure 6).

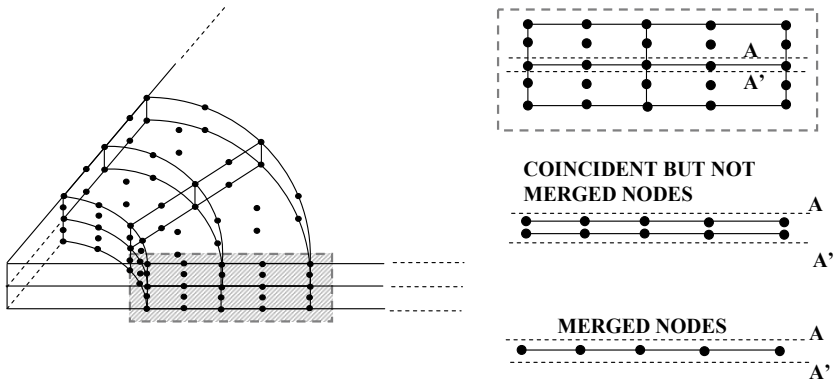

Fig. 6. A delamination can be simulated by maintaining not merged nodes with identical coordinates belonging to adjacent elements

Node pairs on adjacent interfaces can be connected by means of Multipoint constraints (Cook, 1995) or equivalently by relations between degree of freedom of these nodes. Indeed, node pairs in the debonded area are not connected but contact elements are introduced to avoid overlaps.
By proceeding in this way the evaluation of the Strain Energy Release Rate along the crack front, even if three-dimensional, can be obtained by using only nodal forces and displacements.
An example of application of the VCCT to a circular delamination is shown in Figure 7.

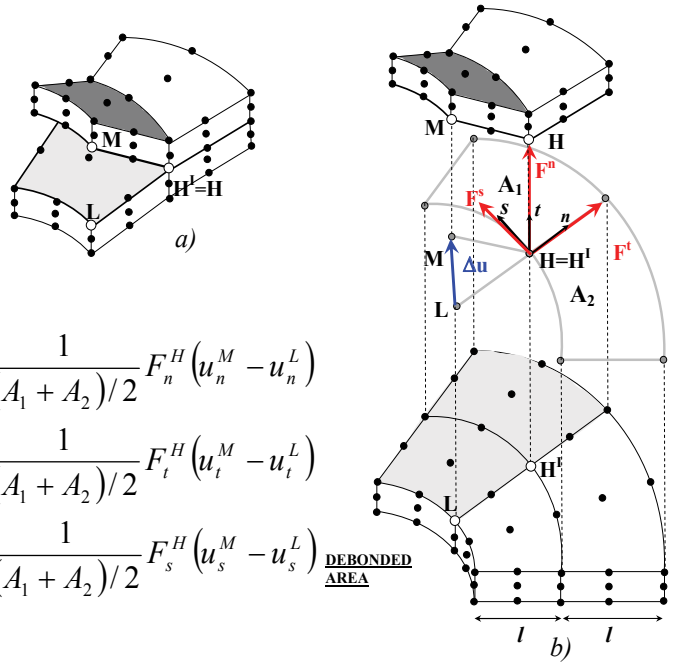

$$G_I^H = \frac{1}{2}\frac{1}{(A_1 + A_2)/2} F_n^H \left(u_n^M - u_n^L\right)$$

$$G_{II}^H = \frac{1}{2}\frac{1}{(A_1 + A_2)/2} F_t^H \left(u_t^M - u_t^L\right)$$

$$G_{III}^H = \frac{1}{2}\frac{1}{(A_1 + A_2)/2} F_s^H \left(u_s^M - u_s^L\right)$$

Fig. 7. Force at the crack tip (measure at the node H=H') and displacements (components of the vector connecting the nodes L and M)

The Eq. (7) can be used to compute Strain Energy Release rate components. It is worth noting that these components are referred to a local reference system (t,s,n).
The mesh in Figure 4 has been realised with elements of the same length (l) in the direction orthogonal to the delamination front.
Krueger (2004) has proposed corrections to VCCT formulae for elements with different lengths or widths at the crack tip.
Okada et al. (2005) proposed corrections for skewed and non-symmetric mesh arrangement at the crack front. The mesh of the finite element model can have edges parallel or orthogonal to the delamination front (as in Figure 6 and Figure 7), in this case it is called "orthogonal mesh", otherwise the mesh is "non orthogonal".
When orthogonal meshes are used, the delamination front can be easily individuated, otherwise algorithms for tracing the delamination front can be used (Xie & Biggers, 2006)-(Liu et al., 2011).

4. Application

The capabilities of the proposed approach to predict the delamination growth initiation has been verified on a test-case taken from literature (Sun et al., 2001).
The benchmark selected is a laminated composite plate characterized by the presence of an embedded elliptical delamination with semi axes of length 30 mm (in the applied load direction) and 15 mm (in the transverse direction).
Numerical data are available in literature (Sun et al., 2001) in terms of out of plane displacement versus load of two control points placed in the middle of the plate (respectively on the top of the thinnest sublaminate and on the bottom of the thickest or base sublaminate) and delamination growth initiation load. The specimen has a total length of 100 mm, it is clamped at four edges along the out of plane direction and a static compressive load is applied along the x-axis direction. The delamination is placed between the forth and the fifth ply over 32 plies. The laminate stacking sequence is $[(0°_2/90°_2]_{4S}$ with a nominal ply thickness of 0.127 mm. The material properties are reported in Table 1.

Longitudinal Young's Modulus	E_{11}	*134 GPa*
Transverse Young's Modulus	$E_{22} = E_{33}$	*10.2 GPa*
Shear Modulus	$G_{12} = G_{13}$	*5.52 GPa*
	G_{23}	*3.43 GPa*
Poisson's Ratio	$\nu_{12} = \nu_{13}$	*0.3*
	ν_{23}	*0.49*
Critical strain energy release rate for mode I	G_{IC}	*200 J/m²*
Critical strain energy release rate for mode II	G_{IIC}	*500 J/m²*

Table 1. Material properties

4.1 Analytical results

It is worth noting that for this geometrical configuration it is possible to obtain an analytical estimation of the critical values of the applied strain at which there are respectively the local buckling (ε_{CR}) and the delamination growth initiation (ε_{GR}). The analytical expressions proposed by Chai et al. (1981) are valid under the hypothesis that the material is isotropic, homogeneous and linear elastic. Even thought the benchmark selected is in composites,

being the plies oriented at 0° and 90° and the laminate symmetric, the material behaviour can be assumed to be equivalent to that of an isotropic material. The equivalent Young's modulus E_{eq} can be obtained by using the formulae of the Classical Lamination Theory (CLT) in Jones (1999) and Kollar & Springer (2007). By using the CLT an equivalent Young's modulus for the composite material under consideration has been found to be equal to 72GPa. The data needed for the application of the analytical expressions proposed by Chai et al. (1981) are summarized in Table 2. Looking at the values in Table 2, it is straightforward to admit that the ratio h/t is very small or rather that the delamination subdivides the structure in two parts: a base sublaminate whose thickness is 3.36mm and a thin sublaminate of thickness 0.64mm. In this case two analytical models can be used, the first called "thin film" (Figure 8) approximation in which the base sublaminate is assumed to be infinitely thick and the second the "thick column" in which the base sublaminate is of finite thickness but it is assumed to remain unbuckled (Chai et al., 1981).

Equivalent Young's Modulus	E_{eq}	*72GPa*
Plate Length in the load direction	L	*100mm*
Delamination length in the load direction	l	*60mm*
Thickness of plate	t	*4mm*
Thickness of the thinnest sublaminate	h	*0.64mm*
Equivalent Poisson Ratio	v	*0.3*

Table 2. Data needed for the application of the analytical model by Chai et al. (1981)

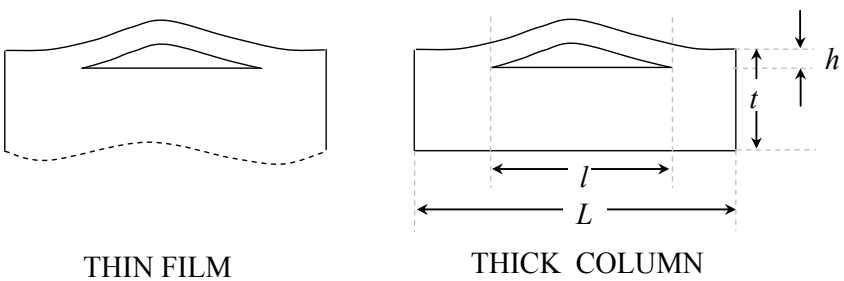

Fig. 8. Thin film and thick column delamination buckling models

The applied strain at which the delamination buckles (local buckling of the delamination) is given by the Eq. (7) (Chai et al., 1981). The expressions for the Strain Energy Release Rate at the strain ε_0 are given by Eq. (8) and Eq. (9-10) respectively for the "thin film" approximation and for the "thick column" approximation. Indeed, these analytical expressions were obtained by Chai et al., (1981) using a one dimensional modeling of the structure.

$$\varepsilon_{CR} = \frac{\pi^2}{3\left(1-\nu^2\right)}\left(\frac{h}{l}\right)^2 \tag{7}$$

$$G_a = \frac{E_{eq}h\left(1-\nu^2\right)}{2}\left(\varepsilon_0 - \varepsilon_{CR}\right)\left(\varepsilon_0 + 3\varepsilon_{CR}\right) \quad \text{"THIN FILM"} \tag{8}$$

$$\bar{G}_b = \frac{\pi^4 \bar{h}\left(1-\bar{h}\right)}{18k^2}\left(\bar{\varepsilon}_0 - \bar{\varepsilon}_{CR}\right)\left[\bar{\varepsilon}_0 + \bar{\varepsilon}_{CR}\left(3 + \frac{4\bar{h}\bar{l}}{1-\bar{h}}\right)\right] \quad \text{“THICK COLUMN”} \tag{9}$$

where

$$\bar{G}_b = \frac{G_b L^4\left(1-\nu^2\right)}{Et^5};\ \bar{h} = \frac{h}{t};\ \bar{l} = \frac{l}{L};\ k = 1-\bar{h}+\bar{h}\bar{l};\ \bar{\varepsilon}_{CR} = \left(\frac{\bar{h}}{\bar{l}}\right)^2;\bar{\varepsilon}_0 = \varepsilon_0 \frac{3\left(1-\nu^2\right)}{\pi^2}\left(\frac{L}{t}\right)^2 \tag{10}$$

The value of the applied strain at which the Strain Energy Release Rate equals the material fracture Toughness is the ε_{GR} (applied strain at which the delamination starts growing) can be determined by manipulating Eq. (8) and Eq.(9) imposing respectively that $G_a = G_{CR}$ (Thin film) and $\varepsilon_0 = \varepsilon_{GR}$ and $G_b = G_{CR}$ when $\varepsilon_0 = \varepsilon_{GR}$. By doing so, the results in Table 3 can be obtained.

Strain necessary to cause the local buckling (if l=60mm)	ε_{CR}	*410*με
Strain necessary to cause the local buckling (if l=30mm)	ε_{CR}	*1634*με
CASE I: G_{CR}=0.2N/mm (l=60mm)		
applied strain at which the delamination starts growing “THIN FILM”	ε_{GR-a}	*2785*με
applied strain at which the delamination starts growing “THICK COLUMN”	ε_{GR-b}	*2780*με
CASE II: G_{CR}=0.2N/mm (l=30mm)		
applied strain at which the delamination starts growing “THIN FILM”	ε_{GR-a}	*2867*με
applied strain at which the delamination starts growing “THICK COLUMN”	ε_{GR-b}	*2756*με

Table 3. Analytical results obtained by using the formulae by Chai et al. (1981)

Two values for the ε_{CR} are reported in Table 3: the first is referred to the case of a length of the delamination in the direction of the applied load equal to 60mm, the second to a length of the delamination in the direction of the applied load equal to 30mm. In the benchmark selected (Sun et al., 2001), the delamination is elliptical whereas the analytical model is one-dimensional. Therefore, an intermediate value between *410*με and *1634*με should be obtained for the elliptical delamination as strain necessary to cause the local buckling.

4.2 Numerical results

Since there are only 0° and 90° plies and both the boundary conditions and the applied load are symmetric, only one quarter of the plate has been meshed by using 20 node hexahedral layered elements. For this purpose, the faces AB and AD in Figure 9 have been constrained according to symmetry conditions (ux=0 on AD and uy=0 on AB) whereas on BC and DC has been imposed uz=0. The area AEH is the debonded zone. The load is applied on BC in the x direction.

A displacement controlled non-linear analysis has been performed (Pietropaoli & Riccio, 2010c) and the results obtained are shown in Figure 10 in terms of “applied displacement” versus “out of plane displacement” graph. The value of the ε_{CR} obtained by this graph (Leissa, 1987) is above 1370με, the one computed by Sun et al. (2001) was above 1350με. Therefore, there is a good agreement between the numerical results that fall in the range individuated by using the analytical model (Table 4).

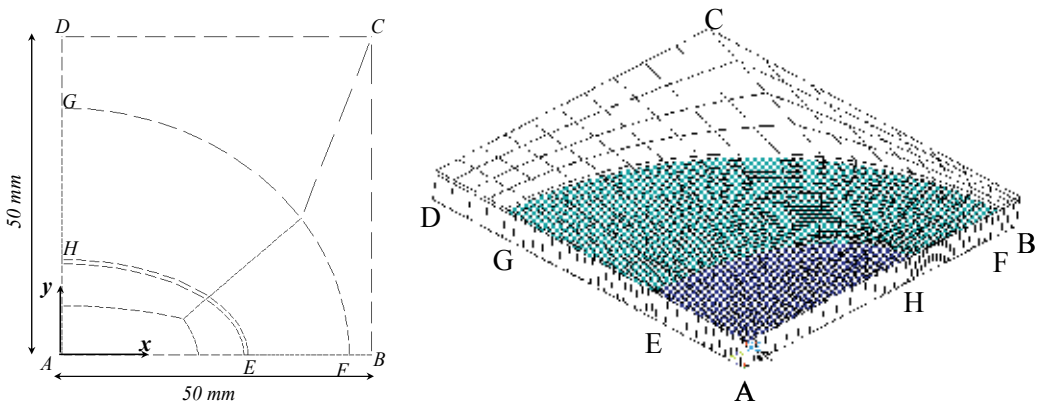

Fig. 9. Geometry and mesh of the plate with an elliptical embedded delamination

Strain necessary to cause the local buckling (analytical value)	ε_{CR}	*410-1643*με
Strain necessary to cause the local buckling (Sun et al., 2001)	ε_{CR}	*1350*με
Strain necessary to cause the local buckling determined by using Figure 7	ε_{CR}	*1370*με

Table 4. Strain necessary to cause the local buckling

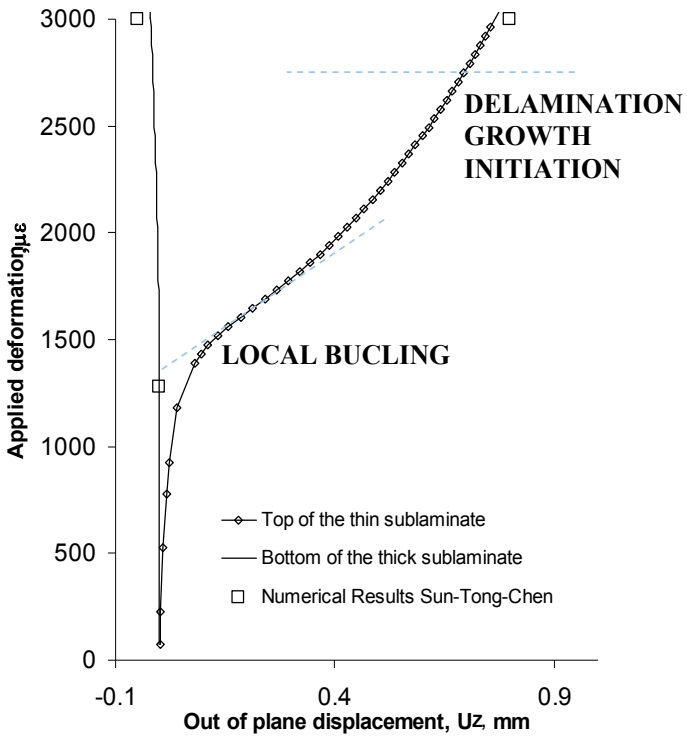

Fig. 10. Applied displacement versus out of plane displacement graph (no growth)

The Strain Energy Release Rate distributions at 2700με and 2750με obtained by using the VCCT are plotted in Figure 11 against the angle θ for the fracture modes I and II along the delamination front. The corresponding values of the failure index computed by using the power low criterion in Eq. (5) with $\alpha = 1, \beta = 1$ are shown in Figure 12.

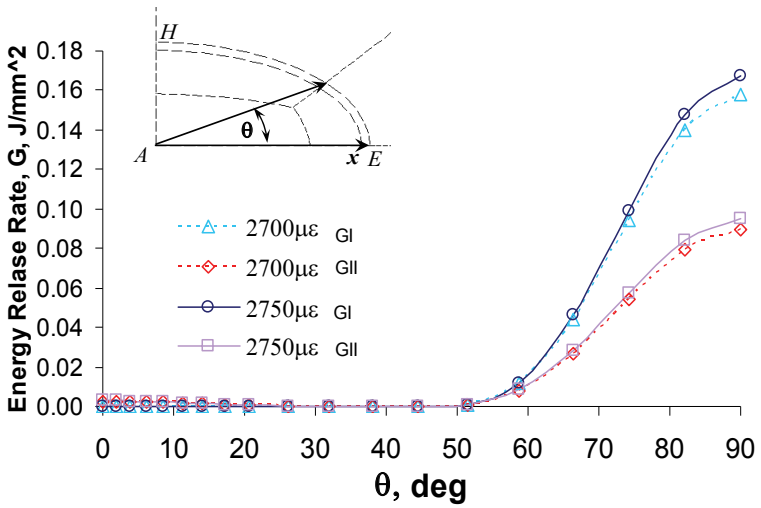

Fig. 11. Strain Energy Release Rate Distributions along the delamination front at 2700με and 2750με

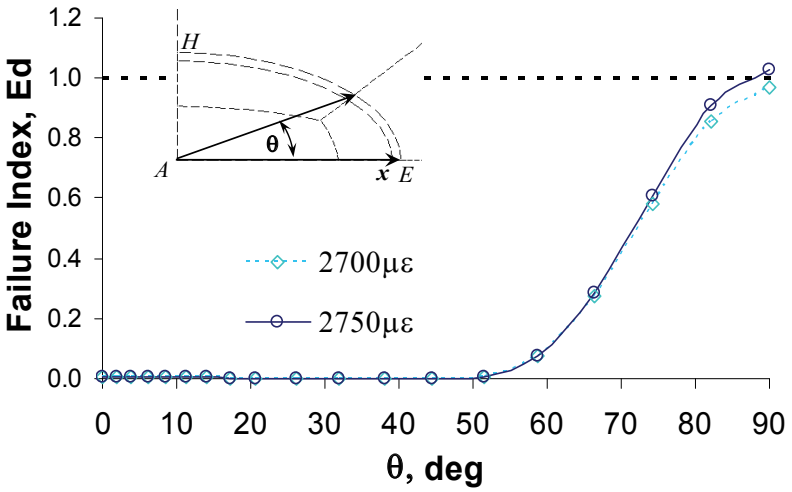

Fig. 12. Failure index distribution along the delamination front at 2700με and 2750με

The failure index becomes greater than 1 at an applied strain equal to 2750με in the range 87°<θ<90°. This means that the delamination starts growing in the direction orthogonal to the applied load and that the ε_{GR} is equal to 2750με.
In this case, two different values for the fracture toughness for the mode I and II have been considered, as reported in Table 1.

In the work by Sun et al. (2001), a Griffith type crack growth criterion was used (Eq. (4)) where the critical strain energy release rate was assumed to be equal to the one of the fracture mode I: $G_C = G_{IC}$. Furthermore, the finite element model by Sun et al., (2001) was based on the Reissner-Mindlin plate theory which neglects the transverse normal stress σ_{zz} and leads to an approximation of the shear stresses σ_{xz} and σ_{yz}. These choices have led Sun et al. (2001) to obtain an underestimated prediction of the ε_{GR} = 2000με.

applied strain at which the delamination starts growing (Sun et al., 2001)	ε_{GR}	2000με
applied strain at which the delamination starts growing (Figure 9)	ε_{GR}	2750με
applied strain at which the delamination starts growing (analytical model)	ε_{GR}	2756με-2867με

Table 5. Applied strain at which the delamination starts growing

It is straightforward to recognise in Table 5 the agreement between the numerical results obtained in this work 2750με and the range defined by the analytical model 2756με< ε_{GR} <2780με. This agreement demonstrates the effectiveness of the VCCT in predicting the delamination growth initiation.

5. Conclusion

Composites are material whose behaviour is difficult to predict by using numerical methods especially in presence of damage. However, the finite element method used in conjunction with the Virtual Crack Closure Technique (VCCT) can provide effective information in terms of global behaviour of the structure in presence of an interlaminar damage. The effectiveness of the VCCT has been proved in this Chapter through the determination the delamination growth initiation load for a composite plate with an elliptical delamination and the comparison of this value with reference results.

6. References

Abrate S. (1998), Impact on composite structures, Cambridge University Press, ISBN 9780521473897.

Altenbach, H., Altenbach, J., Kissing, W. (2004), Mechanics of Composite Structural Elements, Springer, ISBN 3540408657.

Benzeggagh, M. L., Kenane M. (1996), Measurement of Mixed-Mode Delamination Fracture Toughness of Unidirectional Glass/Epoxy Composites with Mixed-Mode Bending Apparatus. *Composites Science and Technology*, Volume 56, Issue 4, pp. 439-449,ISSN 0266-3538.

Camanho P. P., Davila C. G., De Moura M. F. (2003), Numerical simulation of Mixed-Mode Progressive Delamination in Composite Materials, *Journal of composite materials*, Volume 37, pp.1415-1438,ISSN 0021-9983.

Chai, H., Babcock, C.D.,Knauss, W. G (1981), One dimensional modelling of failure in laminated plates by delamination buckling, *International Journal of Solids and Structures*, Volume 17, pp. 1069-1083, ISSN 0020-7683.

Cook R.D. (1995), Finite Element Modeling for Stress Analysis, Wiley, ISBN 0471107743.

Davies G. A. O., Zhang X., Zhou G. and Watson S. (1994), Numerical modelling of impact damage, *Composites*, Volume 25, Issue 5, pp.342-350, ISSN 1359-835X.

Davies G. A. O., Zhang X. (1995), Impact damage prediction in carbon composite structures, *International Journal of Impact Engineering*, Volume 16, Issue 1, pp.149-170, Elsevier, ISSN 0734-743X.

Janssen M., Zuidema J. and Wanhill R.J.H. (2004), Fracture Mechanics, Spon Press Taylor & Francis, ISBN 0415346223.

Jones R. (1999), Mechanics of composite materials, Taylor and Francis, 156032712X

Kachanov L.M. (1988), Delamination buckling of composite materials, Kluwer Academic Publishers, ISBN 90247-37702.

Kardomates, G. A. (1987), Large deformation effects in the post buckling behaviour of composites with thin delaminations, *AIAA Journal*, Volume 27, pp.624-631, ISSN 0001-1452.

Klug, J., Wu, X. ,and Sun, C. T. (1996),Efficient Modeling of Postbuckling Delamination Growth in Composite Laminates Using Plate Elements, *AIAA Journal*, Volume 34, pp.178-184, ISSN 0001-1452.

Kollar L.P.,Springer G. (2007), Mechanics of composite structures, Cambridge University Press,ISBN 9780521801652.

Krueger R., O'Brien T. K. (2000), A shell/3D modeling technique for the analysis of delaminated composite laminates. NASA/TM-2000-210287.

Krueger R., (2004), The Virtual Crack Closure Technique: History, Approach and Applications, Applied Mechanics Reviews, Volume 57, Issue 2, pp.109-143, ISSN 0003-6900.

Kyoung W. M. and Kim C. G. (1995), Delamination buckling and growth of composite laminated plates with transverse shear deformation, *Journal of composite materials*, Volume 29, Issue 15, pp. 2047-2068, ISSN 0021-9983.

Leissa A. W. (1987), A Review of Laminated Composite Plate Buckling, *Applied Mechanics Reviews*, Volume 40, Issue 5, pp. 575-592, ISSN 0003-6900.

Liu Y. P., Chen C. Y., Li G. Q. (2011), A modified zigzag approach to approximate moving crack front with arbitrary shape, *Engineering Fracture Mechanics*, Volume 78, Issue 2, pp. 234-251, ISSN 0013-7944.

Mazumdar S. K. (2002), Composites manufacturing materials, product, and process engineering,CRC press, ISBN 0849305853.

Mukherjee, Y. X., Gulrajani, S. N., Mukherjee, S. and Netravali, A. N. (1994), A numerical and experimental study of delaminated layered composites, *Journal of composite materials*, Volume 28, pp.837-870, ISSN 0021-9983.

Okada H., Higashi M., Kikuchi M., Fukui Y., Kumazawa N. (2005), Three dimensional virtual crack closure-integral method (VCCM) with skewed and non-symmetric mesh arrangement at the crack front, *Engineering fracture mechanics*, Volume 72, pp.1717-1737, ISSN 0013-7944.

Orifici A. C., de Zarate Alberdi I. O., Thomson R. S., Bayandor J. (2008), Compression and post-buckling damage growth and collapse analysis of flat composite stiffened panels, *Composites Science and Technology*, Volume 68, pp. 3150–3160, ISSN 0266-3538.

Pagano N. J. and Schoeppner G. A. (2003), Delamination of polymer matrix composites: problems and assessment, Comprehensive composite materials, Elsevier Science, Volume 2, pp.433-528, ISBN: 978-0-08-042993-9.

Pagano N.J. and Pipes R.B. (1971), The influence of stacking sequence on laminate strength, *Journal of Composite materials*, volume 5, pp.50-57, ISSN 0021-9983.

Pietropaoli E., Riccio A. (2010a), A global/local finite element approach for predicting interlaminar and intralaminar damage evolution in composite stiffened panels under compressive load. *Applied Composite Materials*, DOI: DOI: 10.1007/s10443-010-9135-1, Springer, ISSN 1573-4897.

Pietropaoli E. Riccio A. (2010b), On the robustness of finite element procedures based on Virtual Crack Closure Technique and fail release approach for delamination growth phenomena. Definition and assessment of a novel methodology, *Composites Science and Technology*,Volume 70, Issue 8, pp. 1288-1300, ISSN 0266-3538.

Pietropaoli E., Riccio A. (2010c), Finite Element Analysis of the Stability (Buckling and Post-Buckling) of Composite Laminated Structures: Well Established Procedures and Challenges,*Applied Composite Materials*, DOI: 10.1007/s10443-010-9182-7, Springer, ISSN 1573-4897.

Raju I. S. (1987), Calculation of strain-energy release rates with higher order a singular finite element, *Engineering Fracture Mechanics*, Volume 28, pp. 251-274, 0013-7944.

Reeder J. R. and Crews J. H. (1990), Mixed-mode bending method for delamination testing, AIAA Journal, Vol.28,No.7, pp. 1270-1276, ISSN 0001-1452.

Reeder J. R. (2006), 3D Mixed-Mode Delamination fracture criteria-an experimental perspective, 17-20 Sep. 2006; American Society for Composites 21st Annual Technical Conference; Dearborn, MI; United States.

Riccio A., Scaramuzzino F., Perugini P. (2003), Influence of contact phenomena on embedded delaminations growth in composites, *AIAA Journal*, Volume 41, Issue 5, pp. 933-940, ISSN 0001-1452.

Riccio A., Pietropaoli E. (2008), Modeling damage propagation in composite plates with embedded delamination under compressive load, *Journal of composite materials*, Volume 42, Issue 13,pp.1309-1335, ISSN 0021-9983

Rybicki E. F., Kanninen M. F. (1997), A finite element calculation of stress intensity factors by a modified crack closure integral, *Engineering Fracture Mechanics*, Volume 9, pp. 931-938, ISSN 0013-7944.

Shen F., Lee K. H., Tay T. E. (2001), Modeling delamination growth in laminated composites, *Composites Science and Technology*, Volume 61, pp.1239-1251, , ISSN 0266-3538

Shivakumar K. N., Tan P. W., Newman J. C. Jr, (1988), A virtual crack closure technique for calculating stress intensity factors for cracked three dimensional bodies, *International Journal of Fracture*, Volume 36, R43-R50, ISSN 0376-9429.

Sun X., Tong L., and Chen H. (2001), Progressive failure analysis of laminated plates with delamination, *Journal of reinforced plastics and composites*, volume 20, pp.1370-1389, ISSN 0731-6844.

Turon A., Camanho P. P., Costa J., Dávila C. G. (2004), An Interface Damage Model for the Simulation of Delamination Under Variable-Mode Ratio in Composite Materials, NASA/TM-2004-213277

Wang J. T., Raju I. S. (1996), Strain Energy Release Rate Formulae for Skin-Stiffener Debond Modeled with Plate Elements, *Engineering Fracture Mechanics*, Volume 54, pp.211-228, ISSN 0013-7944.

Whitcomb J. D. (1989), Three-dimensional analysis of a postbuckled embedded delamination, *Journal of composite materials*, Volume 23, pp. 862-889, ISSN 0021-9983

Whitcomb J. D. (1992), Analysis of a Laminate with a Postbuckled Embedded Delamination, Including Contact Effects, *Journal of Composite Materials*. Volume 26,pp.1523-1535, ISSN 0021-9983

Xie D., Biggers S. B. (2006), Strain energy release rate calculation for a moving delamination front of arbitrary shape based on the virtual crack closure technique. Part I: Formulation and validation, *Engineering fracture mechanics,* 2006, Volume 73, Issue 6, pp.771-785, ISSN 0013-7944

Xie D., Biggers S. B. (2006). Strain energy release rate calculation for a moving delamination front of arbitrary shape based on the virtual crack closure technique. Part II: Sensitivity study on modeling details, *Engineering fracture mechanics*, Volume 73, Issue 6, pp. 786-801, ISSN 0013-7944

20

Experimental and Numerical Methods to Characterize Electrical Behaviour of Carbon Fiber Composites Used in Aeronautic Industry

Alexandre Piche, Ivan Revel and Gilles Peres
EADS Innovation Works
France

1. Introduction

Carbon Fiber Reinforced Plastic materials are widely used in aeronautic industry because of their high strength to weight ratio, to replace metallic parts. As these materials are not as conductive as metal, there is an increasing need to characterize their electromagnetic properties in order to understand and anticipate direct or indirect effects of lightning and functional current return. Multilayer composite materials present a strong anisotropy due to the different type of material properties and fibers orientation. This has for consequence to create privileged paths for current circulation and possible voltage drops inside the material. The level of accuracy needed on electrical property of a CFRP part strongly depends on the way the CFRP material is electrically solicited (direct current injection, induced effects, illumination…) and consequently on its location and its function inside the aircraft structure. In addition, this level of accuracy depends also increasingly of the development stage of the aircraft: foreground project, mature design, certification, maintenance. For the above reasons, the importance of having adapted and flexible means of characterization becomes crucial.
This chapter is divided in two main sections. The first section presents a general review of the main experimental techniques allowing electrical characterization of CFRP materials. The second starts by reporting existing numerical models of CFRP materials. Then, we present an original approach to simulate current distribution within the composite layup.

2. Electrical characterization of CFRP materials

We present in this part the main experimental techniques of electrical characterization of CFRP materials. Extracted electrical conductivity from measurements is sensitive to the technology of composite (orientation of plies, fiber to resin density ratio, percolation, manufacturing process…) but also to the measurement method itself. Indeed, the way to measure the electrical conductivity depends on the final objective. The most appropriate measurement technique is the one reproducing as close as possible the way the current circulates when the sample faces an electromagnetic excitation. We describe in the following the theoretical basis, the approximations/limitations and the standard use for the three main techniques:

- "Four points": extraction of equivalent conductivity from resistance measurement in selected directions.
- TEM cell: extraction of equivalent "radial" conductivity from shielding effectiveness measurement.
- Magnetic probe: extraction of equivalent "circular" conductivity from magnetic field attenuation.

2.1 "Four points" method

This method is based on a DC electrical resistance measurement consisting in injecting a constant current with a stabilized power supply. The injection is achieved by the way of electrodes in contact with the sample. To control the surface across the current is injected and minimize contact resistances, some metal deposition is done on the section. It shall be sufficiently conductive to be equipotential and have the lowest contact resistance with the CFRP surface. To improve that connection, it is possible to tighten the sample into a metallic vise.

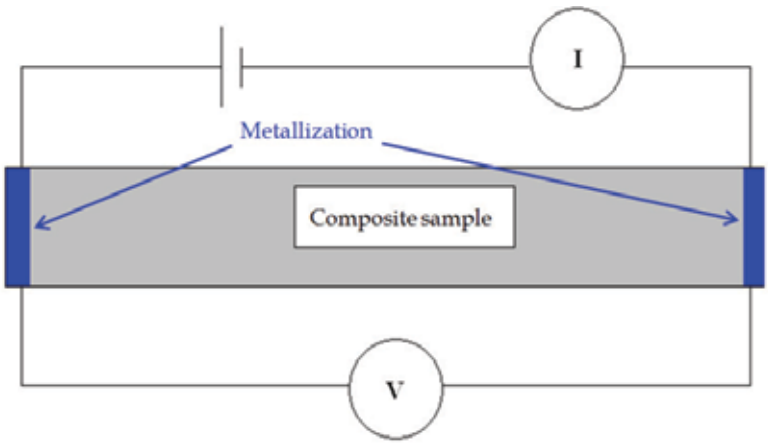

Fig. 1. "Four points" method

The measure of the voltage drop allows deriving the resistance, R=U/I. From this resistance, an electrical conductivity σ_u, corresponding to the effective conductivity in the direction u (defined as the axis of the sample from one metallization to another), is extracted considering a homogeneous material of thickness d and a section S:

$$\sigma_u = \frac{d}{RS} \tag{1}$$

This method is typically used to determine the conductivity along fibers (σ_x), the conductivity perpendicular to the fibers within plies (σ_y), and the conductivity between plies (σ_z). This requires manufacturing of specific samples with unidirectional plies at least for σ_x and σ_x extraction. To avoid manufacturing of dedicated samples, it is possible to combine measurement results with an analytical model [1-3] taking into account of the non-uniform current distribution in the sample in order to obtain the right conductivity in the required direction.

2.2 Transverse Electro-Magnetic (TEM) cell

The Transverse Electro-Magnetic Cell (TEM) is a coaxial structure which ensures the propagation of plane waves in the frequency band going from 100 kHz up to 1 GHz. It is a mean to characterize shielding effectiveness of materials and to extract equivalent "radial" conductivity. The term "Radial" denotes the fact that the device forces the current to circulate in the material from the internal to the external diameter of the cell, effectively in a radial way.

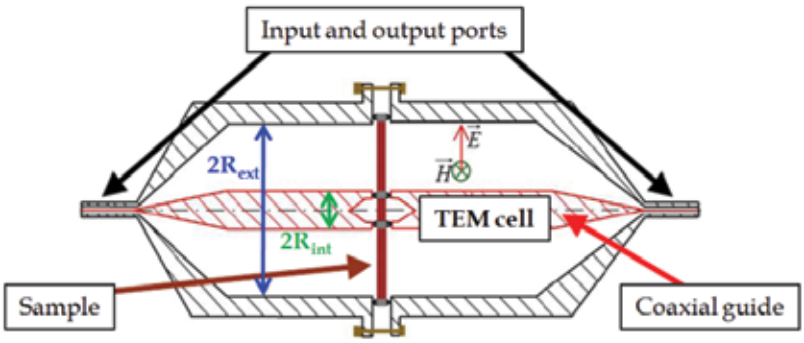

Fig. 2. TEM cell

The principle consists in measuring the insertion losses for a given material. We determine the S_{21} parameter with and without presence of the sample to take into account the imperfections of the cell. The sample connects the internal and the external metal conductors acting as a resistance in parallel (i.e. resistance R_L).

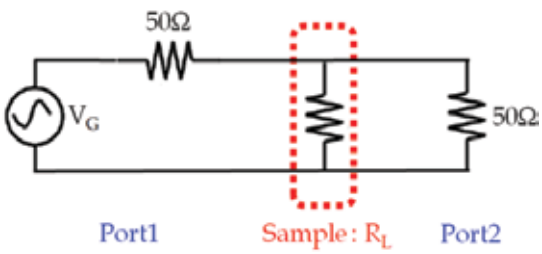

Fig. 3. Low frequency electric diagram of TEM cell

We determine the resistance R_L with the measurement of insertion losses (IL). If we note respectively P_{outA} and P_{outB} the transmitted power to the port 2 with and without presence of the sample, we have:

$$P_{outA} = \frac{V_G^2}{8 \times 50\Omega} \tag{2}$$

$$P_{outB} = \frac{1}{2 \times 50\Omega} \frac{V_G^2}{\left(2 + \frac{50\Omega}{R_L}\right)^2} \tag{3}$$

$$IL = \frac{P_{outB}}{P_{outA}} = \left(\frac{1}{1 + \frac{50\Omega}{2R_L}} \right)^2 \tag{4}$$

Assuming the composite homogeneous and the current uniformly distributed in the thickness d (i.e. no skin effect so $f << 1/d^2\pi\mu_0\sigma_{rad}$), we can deduce the conductivity σ_{rad} from the resistance R_L.

$$\sigma_{rad} = \frac{1}{2\Pi d R_L} \ln\left(\frac{R_{ext}}{R_{int}} \right) \tag{5}$$

This effective conductivity results from a complex combination between conductivities along fibers, perpendicular to the fibers within plies and between plies. Measurements with TEM cell are well adapted to address illumination threats as HIRF (High Intensity Radiated Fields).

2.3 Magnetic probe

This technique consists in measuring the normal magnetic field with and without the presence of the composite material via two loops.

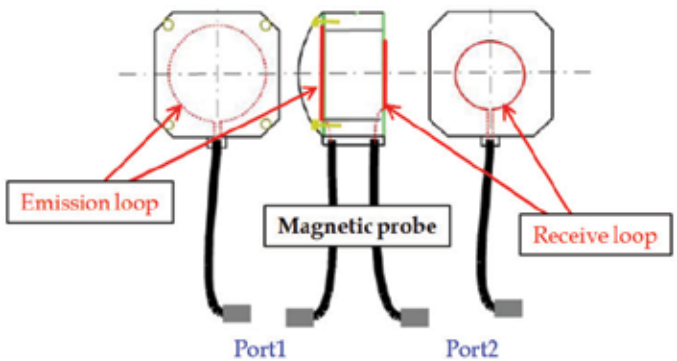

Fig. 4. Magnetic probe

A judicious configuration of the probe makes possible to write the attenuation of the normal H field as a first order low-pass filter whose cut-off frequency f_c at -3dB is inversely proportional to the "circular" conductivity σ_{cir}. The term "circular" denotes the fact that the device forces the current to circulate in the plan of the sample around a center coinciding with the center of the probe, effectively in a circular way. If we suppose that the composite is homogeneous and that the currents induced by the emission loop (of radius a) are uniform in the thickness d (no skin effect), we can write:

$$f_C = \frac{1.4}{\Pi\mu_0 a d \sigma_{cir}} \ll \frac{1}{d^2 \Pi \mu_0 \sigma_{cir}} \tag{6}$$

$$\sigma_{cir} = \frac{1.4}{\Pi\mu_0 a d f_C} \tag{7}$$

As for TEM extracted conductivity, the conductivity derived from magnetic probe results from a complex current flow along and perpendicular to the fibers and between plies. For standard CFRP materials, it is observed that both conductivities are similar and allow predicting with a good accuracy the resistance of any large quasi-isotropic sample whatever the excitation way (except in particular cases of injection versus layup). This is even true when dealing with CFRP covered with metallic lightning protection layer.

2.4 Synthesis

We summarize in the following table typical conductivity values of aeronautic composite materials.

Conductivity	Range (S/m)
σ_x	40000
σ_y	200
σ_z	0.1 / 10
σ_{rad}	5000 /20000
σ_{cir}	5000 /20000

Table 1. Standard conductivity values

Experimental approach for electrical characterization has two main drawbacks. First, the knowledge of the conductivity σ_x, σ_y and σ_z is most of the time insufficient to predict the resistance of different materials, layups and excitations because these conductivities are solicited in a complex manner. In addition, experimental characterization of CFRP is costly and needs many specific samples. For these reasons, numerical simulation appears to be an interesting way to support electrical characterization and moreover to understand electrical behaviour of CFRP material facing complex current distribution.

3. Modelling of CFRP materials

3.1 Existing models of CFRP materials

We first present a non exhaustive review of CFRP material models or modelling techniques published in the literacy. First, Lenning [4] describes an analysis technique to predict lightning current paths in a CFRP sample and voltage drops between plies. He has developed a quasi-static Finite Difference Time Domain method (FDTD) able to treat anisotropic materials. He is interested in the conductance mechanisms in thickness and highlights its non linear behaviour. A FDTD approach is also used by Kitaygorsky [5] in order to determine the current density into a composite.

Benzaid [6] presents a different method to model a thin multilayer composite panel in frequency domain. He uses an impedance matrix which connects the tangential components of magnetic and electric fields at each interface and he assumes a negligible conductivity in thickness.

Several works [1; 7-9] deal with the modelling of the electromechanical behaviour of CFRP materials under tensile loading. Indeed, mechanical deformation and electrical resistance of CFRP are coupled (i.e. carbon fibers are strained and broken gradually under mechanical loading inducing an increase of the electrical resistance). The material is inherently a sensor of its own damage state; its integrity could be estimated by monitoring the resistance change. In this context, Park [7] introduces the concept of "electrical ineffective length" δ_{ec}

which is the typical length over which a broken fiber regains its current-carrying capability due to electrical contacts between fibers (i.e. average distance between adjacent contact points). Then, Park uses a Monte Carlo technique to handle the random distribution of the contact points. Replacing them with contact resistors, the composite is thus modelled by a DC network circuit and solved with Kirchhoff's rules.

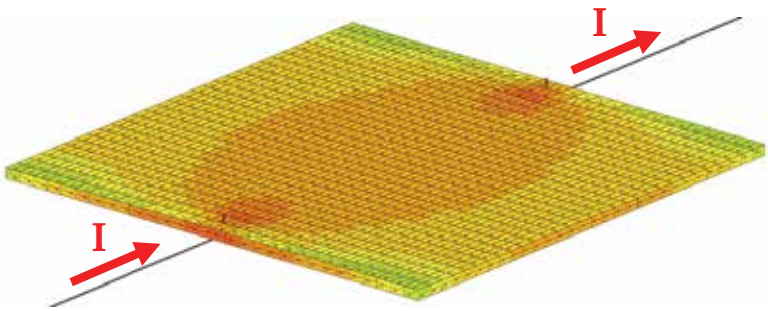

Fig. 5. Current density in a CFRP panel (FDTD approach)

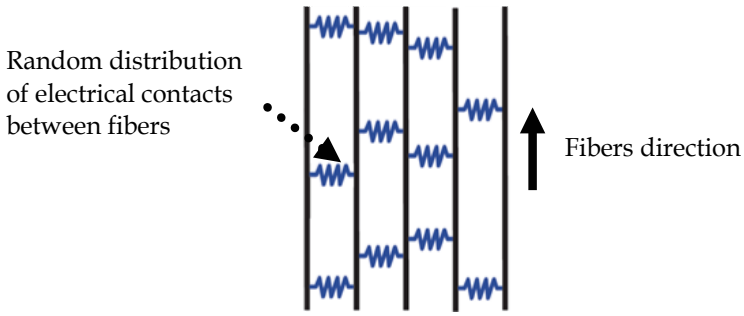

Fig. 6. DC network circuit of a carbon fiber layer

Finally, Zhang [10] studies the effective electrical properties of a conductive fibrous network consisting of short coated fibers. The methodology proposed can be used to predict electrical behaviour of fibrous materials including nanotubes. Short fibers are modelled as randomly distributed cylinders with thin conductive coating layers. The effective conductivity is deduced from a finite element discretization scheme. Monte Carlo simulations are performed to quantify the impact of the different material settings (fiber ratio, thickness of the coating layer, fibers orientation).

From our side, we have decided to develop a numerical model to better understand conduction mechanisms in CFRP and support material qualification process. This model that differs from those reported before is presented in the next section.

3.2 Numerical wired approach for modelling CFRP materials

3.2.1 General principle

Multilayer composite materials are made of different plies of carbon fibers with various orientations to achieve the required thickness and mechanical strength. The most common sequence of plies in aeronautic industry is 0°/45°/90°/-45°, the composite being then considered as quasi-isotropic (QI). We have developed a numerical approach to simulate the current distribution within the composite and assess the consecutive voltage drops between

plies. It consists in modelling the multilayer composite by a 3D network of thin wires, representing the fibers, the contacts between fibers and the contacts between plies. By convention, x-direction is associated to fibers direction, y-direction is perpendicular to the fibers within a ply and z-direction is according to the thickness. The electrical properties of the network are derived from DC measurements on dedicated samples. Such a model takes into account of the different orientations of each ply. The principle of the wired model is illustrated on the next figure:

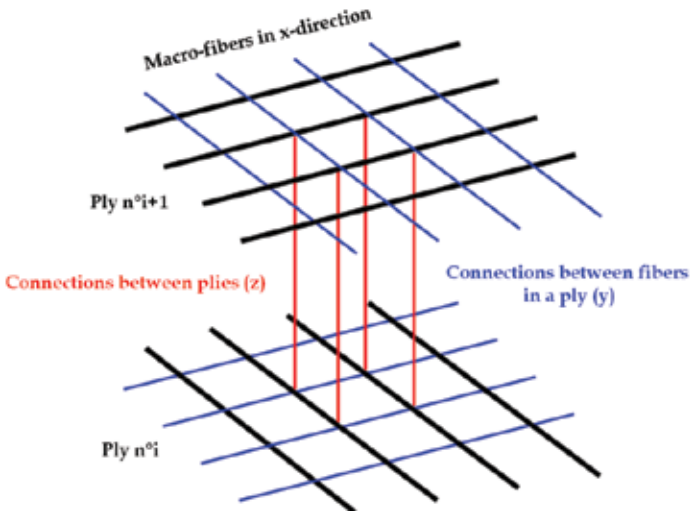

Fig. 7. 3D wired model of a composite

The numerical simulation is based on the Boundary Element Method in a frequency range comprised between the continuous up to few MHz (i.e. lightning spectrum).

3.2.2 Model of a ply

A ply is composed of carbon fibers (of few microns in diameter) impregnated in a dielectric resin. The conductivity along fibers, σ_x, is proportional to fibers conductivity and fibers-to-resin rate. Due to that large rate (around 60% - 70%), we model fibers by equivalent fibers, called macro-fibers, consisting in wires with distributed resistance derived from σ_x. The macro-fibers represent several fibers in parallel, the conductivity of the epoxy resin being neglected. The conductivity in y-direction is driven by local contacts between fibers. Consequently, it depends on the fibers conductivity, the fiber-to-resin rate and the fibers ripple and misalignment. To represent this, we consider electrical connections between macro-fibers by the way of thin wires. Properties of these wires are deduced from measurement of σ_y. We assume that the first ply is the reference at 0° (direction of the fibers is 0°). We split the plies in two families; those at 0° and 90°, those at 45° and -45°.

3.2.2.1 Model of plies at 0° and 90°

For such plies, the distance between adjacent macro-fibers and adjacent y-electrical connections, supposed identical, is noted d. In the model, this distance is set to a few mm to limit the number of unknowns in the problem to solve. The next figure presents an example of array of wires simulating a ply.

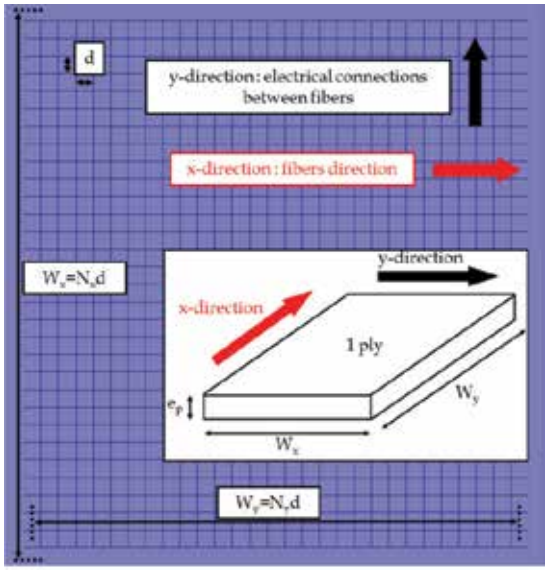

Fig. 8. Numerical model of a ply at 0° and 90°

The linear resistance of a ply in the fibers direction is given by $1/W_x e_p \sigma_x$, where W_x is the dimension of the sample in the y-direction and e_p is the thickness of the ply. Then, the distributed resistance (Ω/m) of a macro-fiber is:

$$R_x = \frac{N_x}{W_x e_p \sigma_x} = \frac{N_x}{N_x d e_p \sigma_x} = \frac{1}{d e_p \sigma_x} \tag{8}$$

The linear resistance of a ply perpendicular to the fibers direction is given by $1/W_y e_p \sigma_y$, where W_y is the dimension of the sample in the x-direction. Then, the distributed resistance (Ω/m) of a single connection between 2 macro-fibers is:

$$R_y = \frac{N_y}{W_y e_p \sigma_y} = \frac{N_y}{N_y d e_p \sigma_y} = \frac{1}{d e_p \sigma_y} \tag{9}$$

The electrical conductivities σ_x and σ_y are derived from DC measurements on unidirectional bar samples in which we force the current to flow respectively in the fibers direction and perpendicular to the fibers within a ply.

3.2.2.1 Model of plies at 45° and -45°

For such plies, the distance between adjacent macro-fibers and adjacent y-electrical connections, supposed identical, is equal to $d\sqrt{2}/2$. This choice is driven by the objective to create at the end z-connections the most simple and repetitive (purely vertical, parallel and equidistant) as possible. The next figure presents the modelling of a ply at 45° (or -45°).
For these plies, the distributed resistance of the macro-fibers, R_x, and the y-electrical connections between macro-fibers, R_y, becomes:

$$R_x = \frac{\sqrt{2}}{d e_p \sigma_x}, \quad R_y = \frac{\sqrt{2}}{d e_p \sigma_x} \tag{10}$$

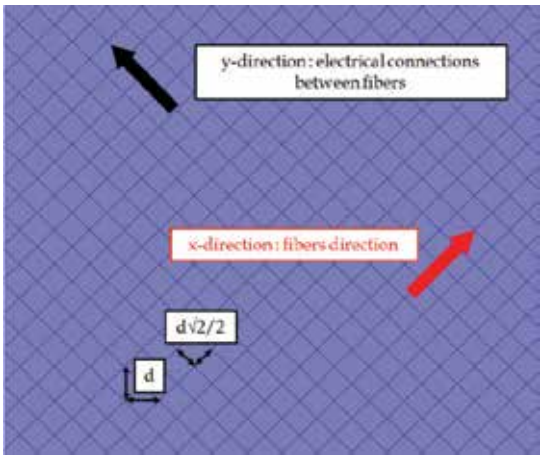

Fig. 9. Numerical model of a ply at 45° (or -45°)

3.2.3 Model of a multilayer composite

The different plies of the multilayer composite are connected by the way of thin wires with distributed resistance Rz to handle the electrical contacts between plies (driven whatever by percolation, added conducting inclusions, doped resin, partial discharges…). The next figure shows a 3D wire model of a composite sample.

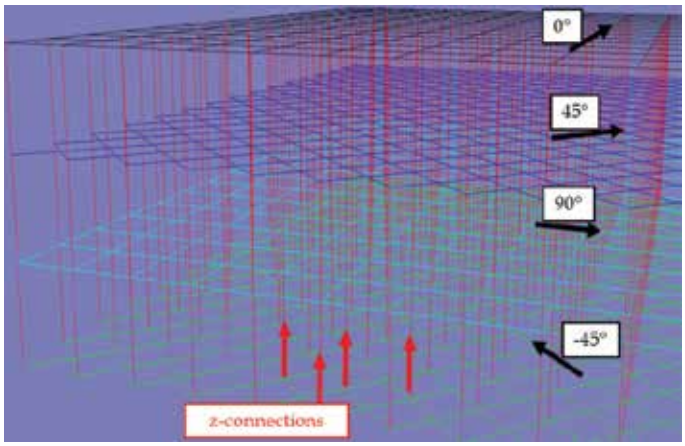

Fig. 10. z-connections in the 3D-wired model

Plies are modelled is such a way that electrical connections in thickness are parallel and uniformly distributed; the space between two adjacent z-connections in x and y-direction is d. The following figure shows a top view of the model.

Introducing N_x and N_y as the number of macro-fibers and of connections between macro-fibers in the 0° ply family, and considering that the linear resistance of the whole sample across thickness is $1/(W_x W_y \sigma_z)$, the linear resistance of a single z-connection is:

$$R_z = \frac{N_x N_y}{W_x W_y \sigma_z} = \frac{N_x N_y}{dN_x dN_y \sigma_z} = \frac{1}{d^2 \sigma_z} \tag{11}$$

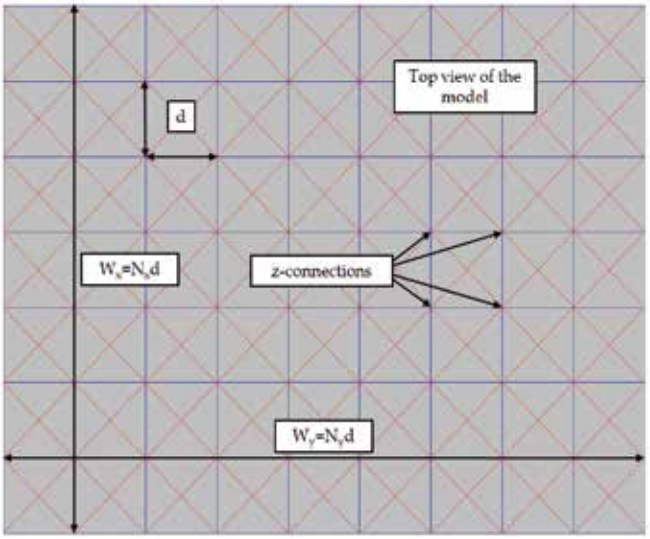

Fig. 11. Top view of the model

This relation is valid if the physical thickness of the sample, L_φ, is kept in the numerical model. The thickness of one ply is typically around 200µm (indeed between 120 and 260µm depending on the grade) and the distance between adjacent plies is of the order of few tens of µm. Consequently, the distance between adjacent plies is enlarged (typically 1mm) to ease the distinction for model building stage and for post-processing. If we note L_{num} the numerical thickness of the sample, the linear resistance of a single z-connection, R_z, becomes:

$$R_z = \frac{L_\varphi}{L_{num} d^2 \sigma_z} \tag{12}$$

We have checked that the artificial increase of the material thickness has no influence on the results until several MHz. It is important to underline two main assumptions on which the model is based. First, the extraction of the z-direction conductivity is based on the hypothesis that contacts between plies are distributed all over the surface. As a consequence, a model based on that conductivity could be not relevant if contacts in the σ_z characterization sample were few and inhomogeneous. Secondly, we do not take into account of non linear behaviour of electrical contacts between adjacent plies, due to pre-existing contacts improved by the current or to partial discharges initiated by voltage drops. As a consequence, σ_z is considered in the model as an equivalent or effective conductivity, constant whatever the current injected. Note however that this model can nevertheless be used to assess sensitivity of results with respect to these assumptions.

3.2.4 Validation of the model with experimental characterization

We present in this part some validations of the wired approach in both DC and frequency domain on a composite having 12 plies (sequence: 0/90/0/90/0/90/90/0/90/0/90/0).

3.2.4.1 Extraction of electrical conductivities

As explained, the model is built knowing electrical conductivities σ_x, σ_y and σ_z extracted thanks to the 4 points method on dedicated samples.

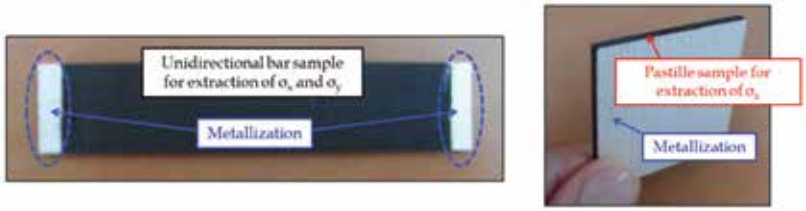

Fig. 12. Composite samples for extraction of σ_x, σ_y and σ_z

We use unidirectional bar samples (length L = 15cm, width W = 2cm, e = 3mm) to extract conductivities σ_x and σ_y by forcing the current to flow respectively in fibers direction and perpendicular to them. For σ_z, we use square samples (S = 4cmx4cm, e = 3mm), forcing the current to flow across the thickness. Conductivities obtained are reported below:

$$<\sigma_x>=\frac{L}{We<R_{Xmeas}>}=40490\ \mathrm{S/m} \tag{13}$$

$$<\sigma_y>=\frac{L}{We<R_{Ymeas}>}=200\ \mathrm{S/m} \tag{14}$$

$$<\sigma_z>=\frac{e}{S<R_{Zmeas}>}=1.3\ \mathrm{S/m} \tag{15}$$

These conductivities have been obtained with injected currents of the order of 100mA.

3.2.4.2 Validation in DC

The validation presented consists in a comparison between calculated and measured DC resistances of a rectangular composite sample (13cmx9.5cmx3mm, 12 plies). Several local metal depositions have been done on each edge to allow current injection and exit in various configurations. The metallization is done on the top, the lower part and the edge of the material. During these tests, the injected current is 100mA.

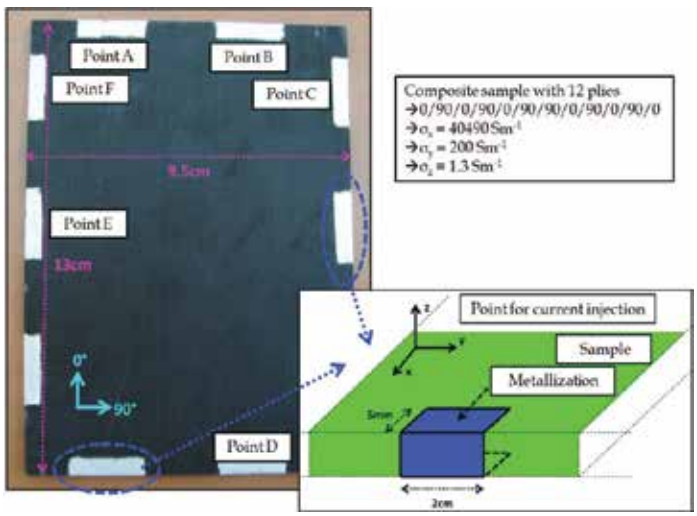

Fig. 13. Rectangular composite sample with local metallizations

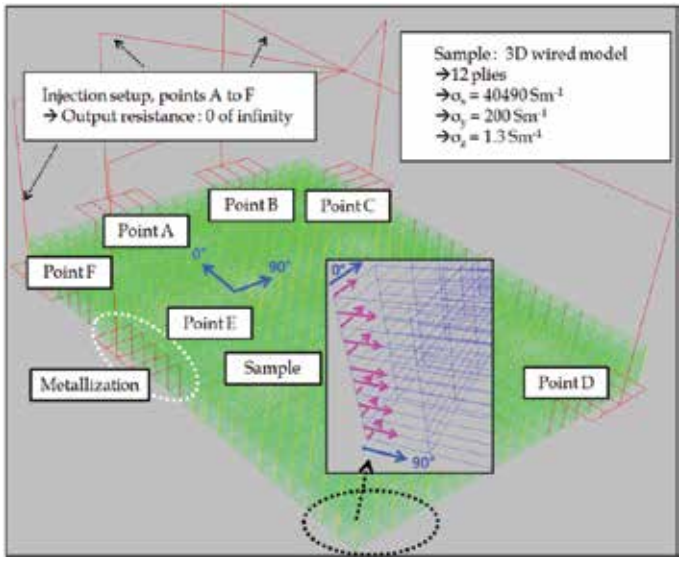

Fig. 14. Wired model of the composite sample

Calculated and measured resistances for several configurations are reported in the next table:

	Resistance (mΩ)		
Configuration	Calculated	Measured	Difference
point A – point D	49.7	57.4	7.7
point B – point D	47.7	54.6	6.9
point D – point E	45.6	52.6	7
point B – point E	40.2	45.9	5.7
point C – point F	37.8	43.9	6.1

Table 2. Comparison between measured and calculated resistances

We observe on average a difference of 15% between measurements and numerical results. This could be partly explained by the contact resistances (metallization and measurement setup).

3.2.4.3 Validation in frequency domain

We have also assessed relevance of numerical predictions in frequency domain for two different configurations. In the configuration 1, a bar sample (length L = 15cm, width W = 2cm, thickness e = 3mm, sequence 0/90/0/90/0/90/90/0/90/0/90/0) is powered by a voltage generator in a circuit loop (15cmx5cm). The current (a few mA) is injected by the way of a network analyser. The following picture presents the setup of the configuration 1.
We focus on the real part of the impedance seen from the source (Zin) because it is sensitive to the current repartition in the material only (when the imaginary part is controlled by the injection loop, what is not our concern in that case). Due to the sequence of plies, the sample geometry and the injection setup, the current flows only along the fibers of the 6 plies at 0° (that coincides with the sample axis and directly joins one metallization to the other). We compare the measured impedance to the calculated one using our model.

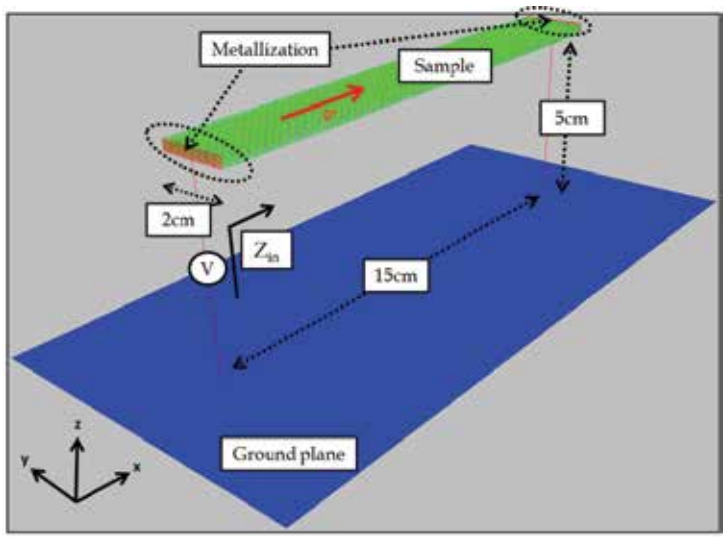

Fig. 15. Setup of the configuration 1

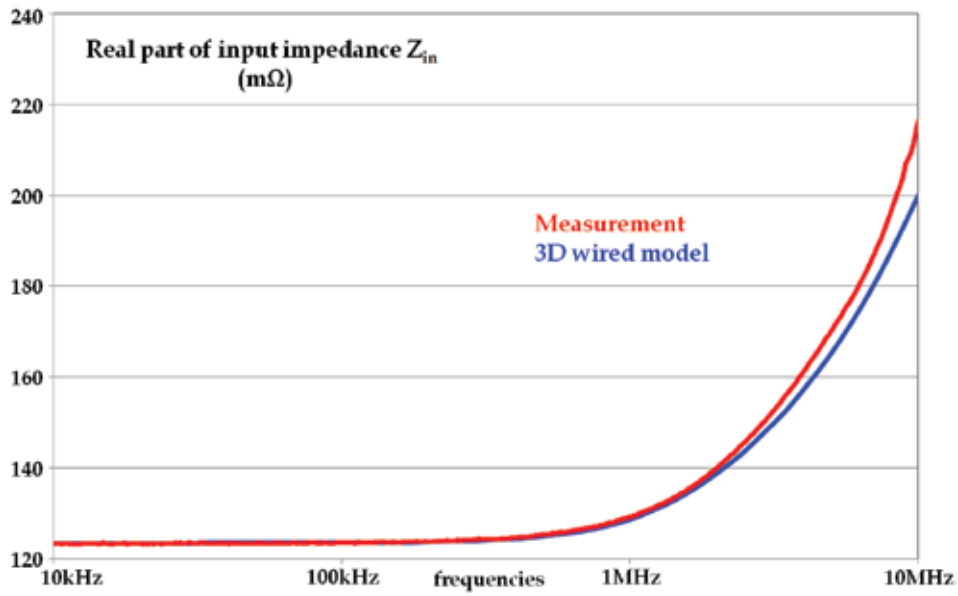

Fig. 16. Real part of the impedance (measurements vs simulation), configuration 1

We observe a very good correlation between calculation and measurement until few MHz. We note also a constant real part of the impedance up to few 100 kHz. Indeed, in DC the current is uniformly distributed in the whole section so the real part of the impedance is equal to the resistance of the sample ($R_{DC}=L/(6e_{ply}W\sigma_x)$ =123.5mΩ). When the frequency increases, the current concentrates on edges so the effective section of the material decreases and the real part (i.e. the equivalent resistance) increases. This is illustrated on the next figure where we present current cartography on the sample modelled using a thin surface.

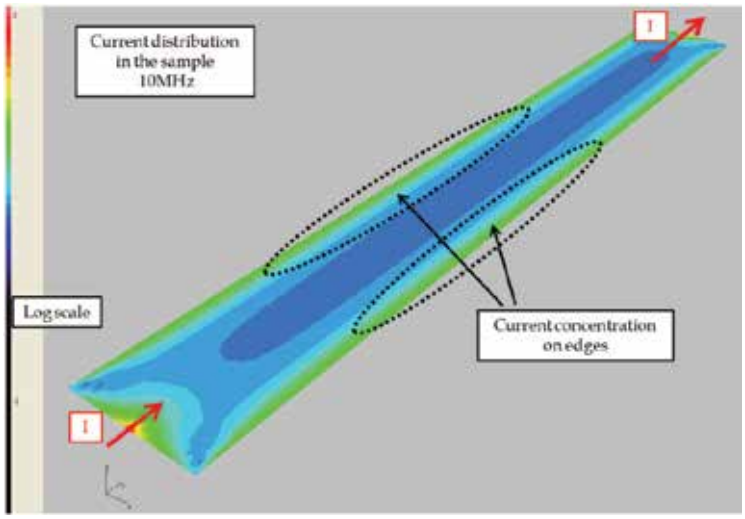

Fig. 17. Current distribution in the sample with a surface model at 10MHz

In configuration 2, we use the rectangular sample presented in figure 13. The current (a few mA) is also injected by the way of a network analyser.

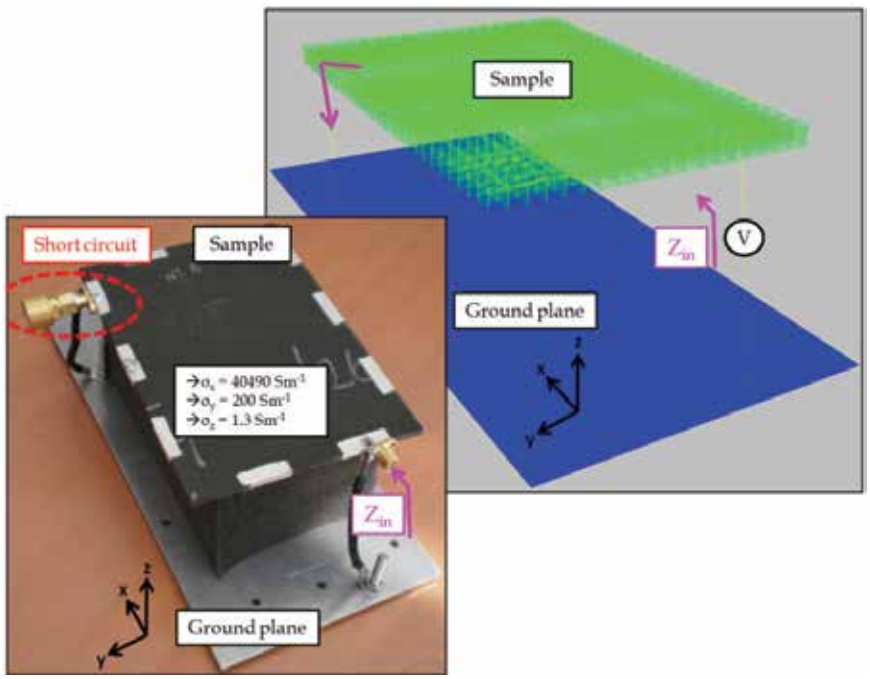

Fig. 18. Setup of the configuration 2

The current has to flow perpendicular to the fibers direction to join the exit point. We compare again the real part of the impedance seen from the source.

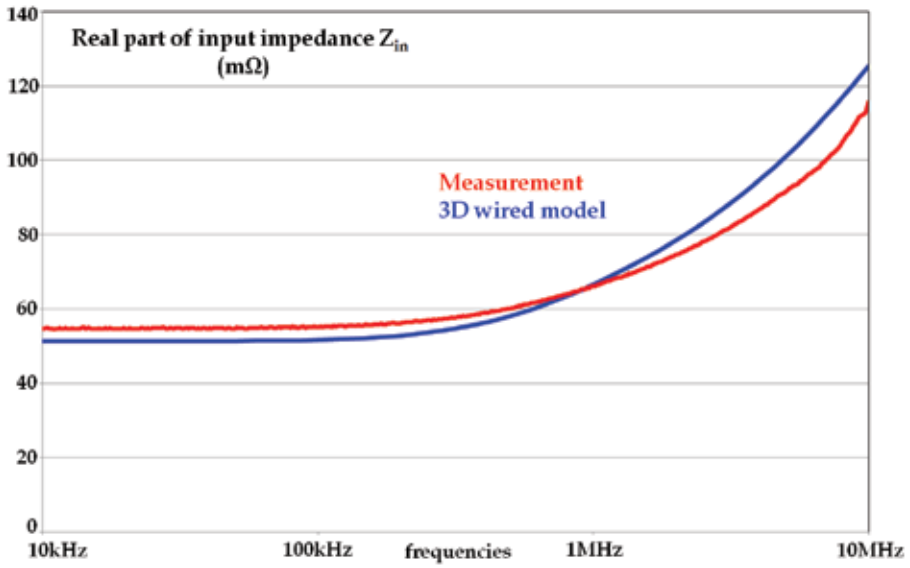

Fig. 19. Real part of the impedance (measurements vs simulation), configuration 2

The difference between measurements and numerical results at low frequency are discussed in section 3.2.4.2. In conclusion, the model developed is relevant until few MHz that suits with an application to lightning problems.

4. Conclusion

We have presented different experimental and numerical methods to characterize the electric behaviour of carbon fiber composites used in aeronautic industry. Standard experimental techniques allowing electrical characterization of CFRP materials have been described with their approximations. As extracted electrical conductivity depends on the measurement method itself, it is necessary to understand how the material is crossed by the current in order to select the appropriate method(s). Moreover, experimental characterization is sometimes not sufficient to understand how the material is solicited and moreover it is quite expensive when dealing with CFRP materials. The numerical model presented in that chapter has been initially developed to support test definition and material characterization [11]. Thus, this approach is well adapted to assess sensitivity of results (sample resistance, current distribution…) with parameters as the layup, the different conductivities or the hypothesis of contact homogeneity. More recently [12], this model has been used to support the understanding of the dynamical electrical behaviour of CFRP materials during a short circuit with objective to estimate current levels and to adapt protection devices.

5. References

[1] Park J. B., Hwang T. K., Kim H. G., Doh Y. D. "Experimental and numerical study of the electrical anisotropy in unidirectional carbon-fiber-reinforced polymer composite", Smart Mater. Struct. 16 (2007) 57-66.

[2] Busch R, Ries G, Werthner H, Kreiselmeyer G, Saemann-Ischenko G "New aspects of the mixed state from six-terminal measurements on Bi2Sr2CaCu2Ox single crystals", 1992, Phys. Rev. Lett. 69 522–5.

[3] J. L., Espinoza O. J. S., Baggio-Saitovitch E "Influence of the anisotropy in the c-axis resistivity measurements of high-Tc superconductors", 1999, Physica C 315 271–7.

[4] Lenning F. E. "Analysis of Lightning Current Flow in Anisotropic CFRP using Finite Differencing Methods" I03-50 CEM Proceedings, International Conference on Lightning and Static Electricity, September 16-19, 2003, Blackpool, England.

[5] Kitaygorsky J, Elliott J. R., Kamihara N, Satake K, Yamamoto K "Modeling the Effects of Anisotropic Material Properties on Lightning-Induced Current Flow in Structures Containing Carbon Fiber Reinforced Plastic", International Conference on Lightning and Static Electricity, September 15-17, 2009, Pittsfield, Massachusetts, USA.

[6] Bensaid S "Contribution à la caractérisation et à la modélisation électromagnétique et thermique des matériaux composites anisotropes", Thèse de Doctorat de l'Université de Nantes, 2006.

[7] Park J. B., Okabe T and Takeda N "New concept for modeling the electromechanical behaviour of unidirectional carbon-fiber-reinforced plastic under tensile loading", Smart Mater. Struct. 12 105–14.

[8] Xia Z, Okabe T, Park J. B., Curtin W. A. and Takeda N "Quantitative damage detection in CFRP composites: coupled mechanical and electrical models", Compos. Sci. Technol. 63 1411–22.

[9] Gillet A, Olivier P, Al Maghribi A, El Sawi I "Prediction of electrical properties of an aeronautic composite", JNC16, Toulouse, France (2009).

[10] Zhang T, Yi Y. B. "Monte Carlo simulations of effective electrical conductivity in short-fiber composites", Journal of applied physics 103, 014910 (2008).

[11] Piche A, Revel I, Peres G "Numerical modelling of multilayer composite materials for lightning problems in aircraft applications", EMC Europe 2010, September 13-17, 2010, Wroclaw, Poland.

[12] Piche A, Andissac D, Revel I "Dynamic electrical behaviour of a composite material during a short circuit", EMC Europe 2011, to be published.

21

Adaptive Composite Materials: Bionics Principles, Abnormal Elasticity, Moving Interfaces

Shilko Serge
V.A. Belyi Metal-Polymer Research Institute of NASB, Belarus

1. Introduction

Requirements imposed on artificial materials are constantly rising with time. Along with lately requisite properties, including stability of physical and mechanical characteristics, linearity of the equation of state and unambiguity of response to disturbance, there arose a problem of a complex active response to varying outer conditions. In other words, a tendency is observed of increasing number of material functions acquiring the features of intellectual systems.

So, obvious prototypes of these materials turn to be biosystems, from the one hand, and computer monitored technical systems able to reproduce intellectual behavior using sensor, processor and executive functions (including effector function and response action), from the other hand, plus feedforward and feedback. Although means of these properties realization can't be similar in artificial materials and above mentioned natural prototypes, generalizations obtained at the junction of the materials science, bionics and cybernetics allow to formulate the conceptual principles and to consider probable ways of the named interdisciplinary problem solution.

Recent reviews and terminological discussions in the field have confirmed actuality of the structural and functional analyses of smart composites, including functional nanomaterials [Bergman & Inan, 2004]. However papers, devoted to such materials (e.g., self-controlled membranes on hydrogel base [Galaev, 1995]) are commonly reduced to creation of sensors and actuators. Less attention have received principles and models of adaptive reactions in composites. The adaptive mode of reinforcing and self-assembling in smart materials [Schwartz, 2007] has been studied below in the form of phenomena caused unusual elastic properties of auxetic and multimodule materials. The development of adaptive composites allows us to hamper the failure process and promotes reliability and service life of products for different technical applications.

2. Adaptive composites in classification of materials

2.1 Classification of materials

The first stage of the present study is classification of materials with account of interrelations found between structure and functions as well as analysis and modeling of a subclass of

intellectual systems, namely adaptive composite materials (ACM). Some of the assumptions put forward by the authors are based on the theory of functional systems and synergism [Prigogine & Stengers, 1984]. Three generations of materials which can be discriminated in the proposed classification, are given in Table 1.

Generation of materials	Structural-and-functional characteristics	Means of property regulation	Factor determining optimum result
Traditional material	Monofunctional single-component material	Properties determined a priori by the origin of component material	Initial property of monocomponent
Composite material	Monofunctional polycomponental material with fixed boundaries between components	Properties are efficiently regulated technologically based on principles of additivity and synergism	Initial property of components and intermediate layers
Smart (adaptive) composites	Polyfunctional polycomponental material with movable boundaries between components	Self-regulation of structure based on sensor, processor and effector functions and feedforward and feedback channels	Efficiency of sensing extreme effects and elimination of refusals

Table 1. Evolution of structure and properties of materials

The first generation is traditional materials including monofunctional medium whose properties are determined by the nature and initial quality of a single component. The next are traditional composites with a prominent structural hierarchy, being also monofunctional. They are characterized by stability of inner and external boundaries, i.e. fixed structure of components, intermediate layers and the composite as a whole.

Adaptive materials with coordinated functions and active behavior belong to the third advanced generation of materials. These systems perceive outer effects at unchanged function owing to, presumably, structural self-organization. In this connection, the mobility of the component boundaries should be remembered as an indispensable property of smart materials, which is not present in traditional composites.

The qualitative transition of materials from the passive to active functioning is shown in Table 2. Naturally, prerequisites of such a transition are formed at the levels of two preceding generations. Thus, transformation of one physical field into another (e.g., piezo- or photo effects) is probable at the stage of monofunctional material. The creation of qualitatively new (emerged), including forecast properties, is a logical continuation of the additive and synergetic principles of composite production. This precedes the development of adaptive composites, being a subclass of smart systems with the dominating adaptive strategy.

The suggested classification makes it possible to forecast other unknown materials of the intellectual type, for example, capable of self-destruction "kamikaze", those ensuring partial or full restoration "regenerators" and materials offering programmed control of the environment ("cyber") and implicit ("incognito") ones. These subclasses constitute a new type of "ecophilous" materials which behavior supports homeostasis of the environment.

Functional evolution	Degree of activity	Degree of intellect	Functioning quality	Mode of behavior
mono-functional	passive	"trivial"	material	"predictable"
	active	"wit" (functional)		
poly-functional	active	smart (adaptive)	material = part	"indefinite"
				"egoist"
			material = system	"time-server"
		"wise" (ecophilous)	material = medium	"kamikaze"
				"regenerate"
				"cyber"
				"incognito"

Table 2. Systematization of materials by general criteria

2.2 Adaptive composites

Relative simplicity of ACM is due to their orientation aimed to fulfill only the adaptive function of the part or a system in contrast to a higher status of the material-medium subclass (Table 2). However the adaptive composite is formed rather in time than by a mechanical mixing of structural components, and evolutionizes as a specific unit by coordinating interrelated physical processes based on an imparted optimum criterion. In this case, the emergence of macrostructure is specified by origination of collective modes under the action of fluctuations, there competing and, finally, by selection of the most accommodated mode or their combination [Prigogine & Stengers, 1984]. The structures themselves could be described in physical terms as types of adaptation to outer conditions.

2.2.1 Self-organization of material structure

Reaction of a material due to mutual coordination of structural and functional parameters of microsystems characterizes it as an open self-regulating system. Selection of the mode of

behavior in response to outer effect does not arise from the principle of the least action, neither from the principle of compulsion (Gauss principle) nor from that of the utmost probability. Active response systems eliminate (or subordinate) contingency. This makes grounds to speak about a programmed behavior of the system, i.e. the decision is made according to the inner criteria determined by the structure itself and system parameters, which substantiates the necessity of direct and reverse connection channels.

It follows from the above said that to form a more complex processor function of ACM it is possible to use the universe phenomenon of self-organization, which is not limited to only systems of higher organization and functional complexity and isn't a monopoly of bio- or social systems. A self-organizing system is understood as a system capable of stabilizing parameters under varying outer conditions through directed ordering of its structural and functional relations aimed at withstanding entropic factors of the environment, which helps to preserve its characteristics as an integral formation [Prigogine & Stengers, 1984].

The material formed by combining its components acquires the characteristics of a composite structure, which is a notion nonequivalent to the structure of its constituents. This fact raises composite materials to a higher structural level and admits the probability of per layer differentiation of the functions in order to reach the integral control system. In our view, to realize adaptation mechanism to outer conditions in composite materials, it's worthwhile considering the combination of different scale physical processes, where we single out at least 4 structural levels: molecular, mesoscopic, macroscopic and polycomponental (Figure 1).

The molecular level is the basic one at programming material behavior. This is because its scale in polymer composites corresponds to cooperative effects of segmental mobility and conformal rebuilding that provide conditions for self-organization in high-molecular bodies. Just here the processor function is realized as a capacity for estimating variations due to outer effects and as a tool formulating the character and force of response based on stationary characteristics of the microsystem. Also, the effector function is fulfilled here for exciting reverse reactions by varying characteristics of the microsystem on a self-organization base.

The mesoscopic level performs the sensor function as an ability to perceive outer effects. Non-equilibrium processes are initiated at this level changing molecular structure and supporting the interaction of direct and reverse channels between the levels.

The macroscopic level makes provision for the mobile function as a reorganization of the initial subsystems (components) aimed at preserving the behavior model.

The mobile function is also realized at the polycomponental level, though intention in this case to provide the system (material = article) functioning as a whole.

To organize control, the processes relating to the mention levels should be coordinated using functional links between them.

It is to be remembered that polymer composites are potential carriers of intellectual properties. Namely, they are sensitive to physical fields, i.e. show a sensor function; make it possible to carry out the actuator function (shape memory of thermosetting resins, etc) and, finally, among all other artificial material media they most closely approach the living nature (biotissues are usually built of high-molecular compounds).

The study of synergetic phenomena in nonliving nature as a linking element between analogous processes in original objects will, in our opinion, provide a possibility to find structural-and-functional bioprototypes of adaptive composites.

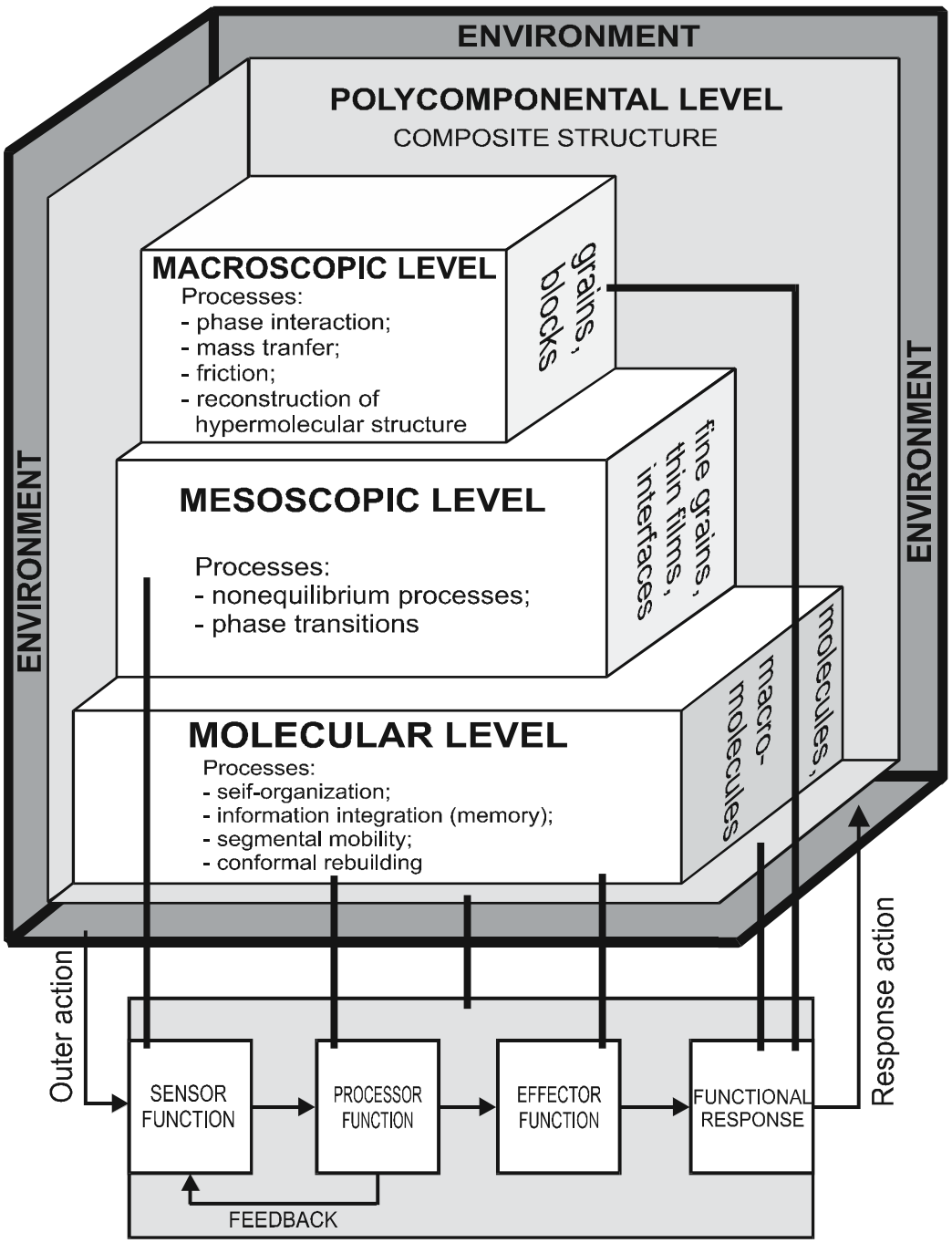

Fig. 1. Differentiation of structural levels at ACM development

3. Self-reinforcing in auxetic composites

The effort towards improving the performance of novel devices based upon realisation of non-linear and non-trivial (anomalous) deformation properties of materials is the aim of many current investigations. First, we shall consider the materials with a negative Poisson's ratio, ν, termed 'auxetics'. Data structuring, examination of the mechanisms of generating the negative Poisson's ratio and analysis of likely applications for auxetics have been discussed recently in [Wojciechowski et al, 2007] and reviewed particularly in [Koniok et al, 2004]. Poisson's ratio affects a very important mechanical property, i.e. compressibility of a material. Under a uniaxial stress, auxetics expand/contract at the direction perpendicular to the tension/compression direction, respectively as shown in Figure 2.

(a) (b)

Fig. 2. The deformation mode of an auxetic material under uniaxial stress: (a) compression, (b) tension. Initial configuration before loading has been shown by dashed lines

This property should influence stiffness and slip under contact loading, and in this way allow control over deformability and friction characteristics of composites and joints based on auxetics. As will be shown, the contact characteristics vary dramatically with variation of the sign of Poisson's ratio. In the classical elasticity theory for isotropic bodies [Landau & Lifshitz, 1986] Poisson's ratio $\nu = (3K - 2\mu)/(6K + 2\mu)$, where μ, K are the shear and volume moduli respectively, the Poisson's ratio of isotropic bodies can vary in the limits $-1 \le \nu \le 0.5$. The upper limit corresponds to incompressible materials, e.g. rubber, whose volume remains constant at significant shape variations, the lower one belongs to the materials preserving their geometrical form with changing volume.

Several natural and artificial auxetic materials have been described to date, but experimental and theoretical studies of the adaptive frictional and mechanical properties of these materials are not still well developed [Baughman & Galvao, 1993]. For example, there exists the possibility for realisation of self-reinforcing or self-locking effect in contact joints containing auxetic components. As a result, this effect would bring about a significant increase in the bearing capacity of frictional joints or shear strength of the fibre – matrix interface under mechanical or thermo-mechanical load.

Of specific interest here is the study of the self-locking effect under contact deformation of anisotropic auxetics based on directionally reinforced composites. This is because such materials may posses Poisson's ratios of much less than -1 ($\nu < -50$) and considerable strength due to their directional reinforcement.

The approaches available for creation of composites with $\nu < 0$ assume either the use of individual auxetic components or formation of an auxetic composite – a combination of

structural units of mesoscopic level (pores, granules, permolecular formations of polymers, etc). To study friction effects under contact loading the existing estimates of elastic properties of quasi-isotropic and anisotropic composites should be taken into account.

3.1 Auxetic inclusions (quasi-isotropic auxetics)

In [Wei & Edvards, 1999] the mechanical characteristics of a composite with ellipsoidal and spherical particles were calculated for the case of randomly distributed filler particles. Simulation results under different ratios of filler stiffness to matrix stiffness, for 45% volume fraction, are presented in Table 3.

Inclusion geometry	0.1	1.0	10
Disc (2D)	-0.3020	-0.2856	0.1216
Disc (3D)	-0.0385	-0.3575	-0.7387
Sphere	-0.0624	-0.2081	0.0650
Wedge (2D)	-0.2679	-0.2266	-0.0508
Needle (3D)	-0.0555	-0.1714	-0.0562

Table 3. Effective Poisson's ratio ν_c of the composite at $\nu = 0$

The possibility of obtaining auxetic composites using filled polymers has been considered in [Kolupaev et al, 1996]. The authors have obtained such composites using thermoplastic polyurethane with ultra-dispersed (0.3-1 μm) particles of tungsten, iron and molybdenum having $\nu \approx -0.2\text{-}0.4$. The composite possessed auxetic properties due to internal stresses σ_{in} produced by the inclusions in the matrix in the range $0.97\ \text{MPa} < \sigma_{in} < 7.11\ \text{MPa}$.

3.2 Non-auxetic inclusions (anisotropic auxetics)

Let us consider a composite formed by the oblique packing of fibres in an elastic incompressible elastomeric matrix (Figure 3a).

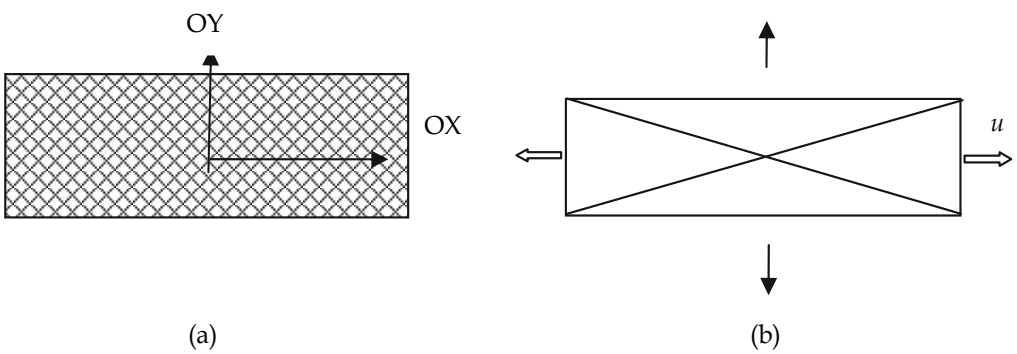

Fig. 3. Structure (a) and the mesofragment (b) of obliquely reinforced auxetic composite

At $E_2 << E_1$ we get $\nu_{xz} \approx 1 - ctg^2\theta$, where E_1, E_2 are Young's moduli of the fibres and matrix respectively. For small fibre packing angles, θ, Poisson's ratio ν_{xz} has negative values. The deformation results in a pantographic change in orientation of the fibres, which elongate insignificantly compared to the low-modulus matrix, thus promoting its contraction normal to the reinforcement direction. To this class of auxetics belong the laminates produced by the oblique superposing of the layers (Figure 3b). Investigations into laminates made of prepregs with carbon fibres and epoxy matrix have shown that ν_{xz} of the composite obtained at small packing angles of the layers (10^o-40^o) is negative.

3.3 Analysis of contact deformation of auxetic composites

The stress state parameters were determined for the double-lap type joint in conditions of initial compression δ_y and compression with shear δ_x (Figure 4a). The analysis of the auxetic element 1 interaction with two conjugated and located symmetrically non-deformable bodies 2 and 3 (Figure 4b) has been carried out using the finite element solution of contact problem with friction.

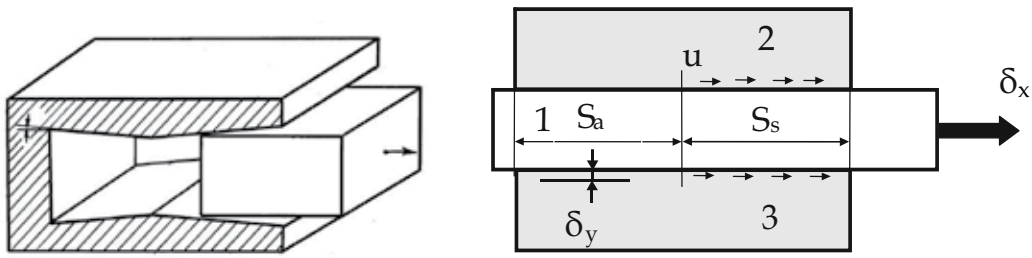

Fig. 4. General view (a) and calculation scheme (b) of a frictional joint with auxetic element

A peculiarity of this problem is a considerable nonlinear deformation brought about in conditions of unlimited shear by formation of the zones of adhesion S_a and slippage S_s with nonzero tangential contact displacements u (Figure 4b). Under compression of the joint the slippage zones are located symmetrically to the central zone of adhesion. Shear application leads to violations of this symmetry. The limiting load capacity of the joint is dependent on slippage onset over the whole contact area which, in its turn, is dependent upon the material compressibility.

For the case of a quasi-isotropic material Poisson's ratio was varied within theoretically acceptable values of the isotropic elastic medium, i.e. $-1 \le \nu \le 0,5$. The extreme values of the contact stresses tend to localise near to the right edge of the junction. The contact parameters vary insignificantly for the positive Poisson's ratios typical of isotropic materials, except for the limiting values characteristic for practically incompressible elastomers. Incompressibility (ν = 0.48-0.5) results in the elastic compression of the material and contact slippage. The stress strain state parameters including the maximal equivalent stress σ_{eqv}, contact pressure p, tangential stress τ and slippage u, have been studied as a function of Poisson's ratio for the quasi-isotropic materials and the reinforcement angle for the anisotropic ones (Figure 5).

An abrupt leap in the maximal contact parameters is observed when ν < 0, not seen with the positive Poisson's ratios. This increase is most marked when ν < -0.9. The adaptive mode of friction has been studied in the form of a self-locking effect under contact loading in

isotropic and anisotropic auxetic cases [Shilko et al., 2008a]. This effect suggests that the strength of such a joint rises with increasing shear load.

Similar calculations have been made for a joint with a deformable element of the anisotropic auxetic composite on the low-modular matrix base (see section 3.2, Fig. 3) under varying reinforcement angles that determine the elastic moduli E_x, E_y, E_z, ν_{xy}, ν_{yz}, ν_{xz}, G_{xy}, G_{yz}, G_{xz}. These elastic constants (Table 4) were calculated based on the volume fraction of the fibrous filler with $\mu = 0.1$, elasticity modulus and Poisson's ratio of the matrix and filler, respectively $E_m = 4$ MPa, $\nu_m = 0.5$, $E_f = 1.5$ GPa, $\nu_f = 0.4$ using the formulas

$$E_x = \frac{1}{a_{11}};\ E_y = \frac{1}{a_{22}};\ E_z = \frac{1}{a_{33}};\ G_{xy} = \frac{1}{a_{66}};\ G_{yz} = \frac{1}{a_{55}};\ G_{xz} = \frac{1}{a_{44}};$$
$$\nu_{xy} = -E_x a_{12};\ \nu_{yz} = -E_y a_{23};\ \nu_{xz} = -E_x a_{13}. \tag{1}$$

where a_{ij} are compliance coefficients of a unidirectional composite:

$$a_{11} = \frac{1}{\left(1+(n-1)\mu\right)E_m},\ a_{22} = a_{33} = \frac{\left(\mu + n(1-\mu)\left(1+(n-1)\mu\right) - \left(n\nu_m - \nu_f\right)^2 \mu(1-\mu)\right)}{\left(1+(n-1)\mu\right)E_f},$$
$$a_{12} = a_{13} = -\frac{\nu_m(1-\mu)+\nu_f\mu}{\left(1+(n-1)\mu\right)E_m},\ a_{23} = -\frac{\left(\nu_f\mu + n\nu_m(1-\mu)\right)\left(1+(n-1)\mu\right) + \left(n\nu_m - \nu_f\right)^2\mu(1-\mu)}{\left(1+(n-1)\mu\right)E_f}, \tag{2}$$
$$a_{66} = a_{55} = 2\frac{(1+\nu_m)\left(n(1+\nu_m)(1-\mu)+(1+\nu_f)(1+\mu)\right)}{\left(n(1+\nu_m)(1+\mu)+(1+\nu_f)(1-\mu)\right)E_m},\ a_{44} = 2\frac{(1+\nu_f)\mu + n(1+\nu_m)(1-\mu)}{E_f}$$

where $n = E_f / E_m$.

The minimal Poisson's ratio ν_{xz} = -2.142 is attained when the angle between the reinforcement direction and OY axis is 70° and deformation u is directed along OX axis (Figure 3).

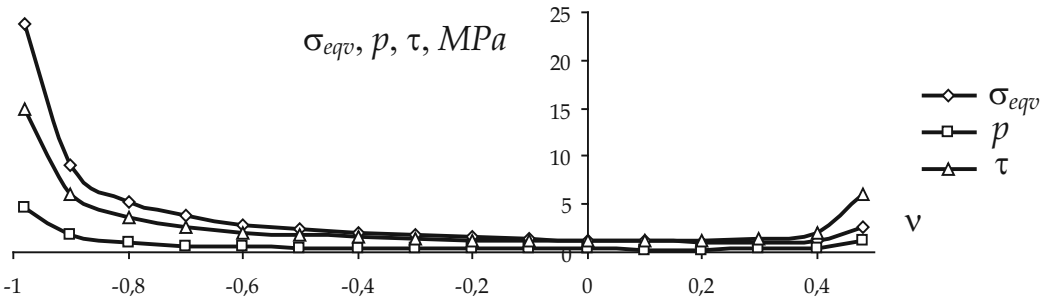

Fig. 5. Maximal values of equivalent stresses, contact pressures and tangential stresses as dependent on Poisson's ratio

The maximal contact parameters were determined for different surface geometries of the conjugated bodies, namely plane, cylindrical (curvature radius r = 100 mm) and wedge-like

(wedge aperture angle α = 174°). It is seen in Figs. 6-10 that the extreme dependence of contact stresses is characteristic for all geometries with a minimum at reinforcement angle 45°.

φ, degree	0	15	30	45	60	70	80	90
E_x, MPa	6.627	6.286	5.619	7.788	38.47	133.4	266.8	303.2
E_y, MPa	303.2	207.5	38.47	7.788	5.619	6.051	6.471	6.627
E_z, MPa	6.627	7.259	11.96	81.50	11.96	7.95	6.88	6.627
v_{xy}	0.010	0.082	0.336	0.945	2.242	2.793	0.912	-0.48
v_{yz}	0.480	-1.727	-1.316	0.048	0.662	0.858	0.958	0.989
v_{xz}	0.989	0.918	0.662	0.048	-1.316	-2.142	-0.743	0.48
G_{xy}, MPa	1.996	21.1	59.58	78.17	63.31	42.49	16.98	1.996
G_{yz}, MPa	1.996	2.285	3.181	3.754	2.753	2.521	1.771	1.666
G_{xz}, MPa	1.666	1.910	2.753	3.754	3.181	2.117	2.122	1.996

Table 4. Elastic constants for obliquely reinforced composite as a function of reinforcement angle φ

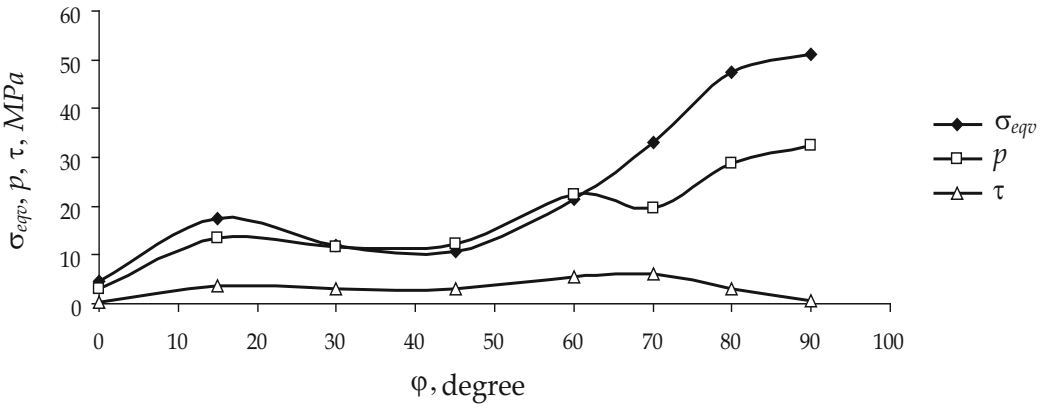

Fig. 6. Dependence of maximal values of equivalent stress, contact pressure and tangential stress on reinforcement angle at compression: δ_y = -1 mm (plane surface)

With a plane surface of the conjugated bodies (Figures 6, 7) the dependencies of stresses $\sigma_{eqv}(\varphi)$, $p(\varphi)$,$\tau(\varphi)$ have local maxima. Their location varies with increasing shear due to slipping.

For cylindrical conjugated bodies, the local minima are absent under pure compression of the auxetic section, although shear promotes their appearance in the region of large reinforcement angles (Figures 8, 9).

It is peculiar that the auxetic body in a junction with a wedge surface shows a rather weak shear effect upon the contact stress state. Similarly to the case of planar surfaces, the local

minima of maximal stress σ_{eqv} and contact pressure p correspond to the reinforcement angle of $\varphi = 15°$.

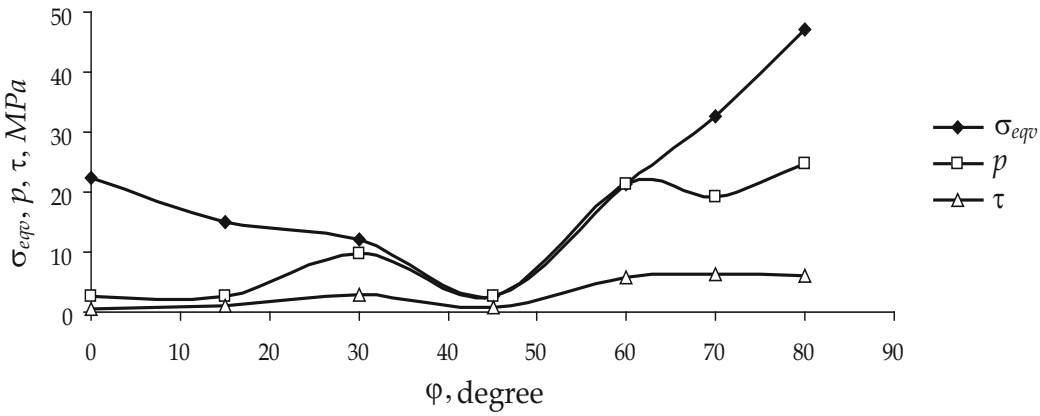

Fig. 7. Dependence of maximal values of equivalent stress, contact pressure and tangential stress on reinforcement angle at compression with shear: δ_y = -1 mm, δ_x = 5 mm (plane surface)

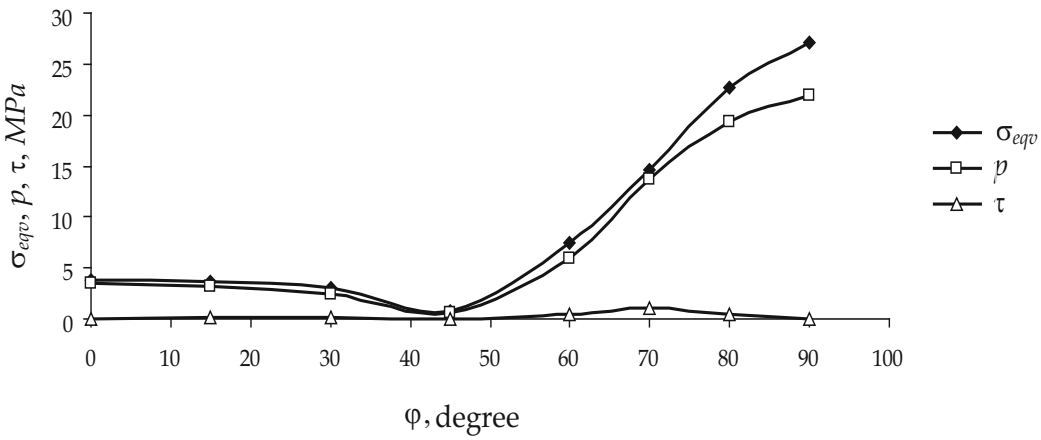

Fig. 8. Dependence of maximal values of equivalent stress, contact pressure and tangential stress on reinforcement angle at compression: δ_y = -1 mm (cylindrical surface)

So, promising functional materials with negative Poisson's ratios (auxetics) have been considered. The results reported here help to quantitatively evaluate the influence of Poisson's ratio (in the isotropic materials) and reinforcing angle (in the anisotropic composites) for compression and compression with shear contact interactions. The adaptive mode of friction has been studied in the form of self-reinforcing under contact loading in isotropic and anisotropic auxetics. This effect suggests that the bearing capacity of such a frictional joint rises with increasing shear [Shilko & Stolyarov, 1996]. It is shown that the use of auxetic materials is an efficient means of improving the mechanical and frictional characteristics of composites.

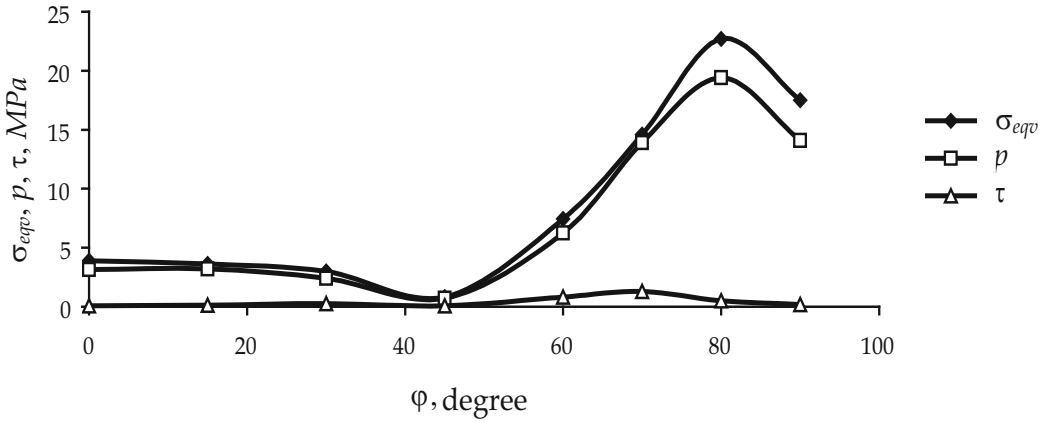

Fig. 9. Dependence of maximal values of equivalent stress, contact pressure and tangential stress on reinforcement angle at compression with shear: δ_y = -1 mm, δ_x = 0.1 mm (cylindrical surface)

4. Self-structuring of multimodule materials

As it was mentioned above, in contrast to traditional composites, which display stable interfaces between components determining invariability of technologically specified complex of properties (Table 1), the adaptive material admits mobility of interfaces.

As a consequence, description of able to regulate its structure ACM proceeding from the given optimal criterion presumes statement of the moving boundaries problem and use of methods for its solution. In this connection, let's turn to investigation results of elastic (reversible) remodelling of a physically nonlinear multimodular metals such as Fe, Al, Cu, Mg, etc [Bell, 1968] (particularly, in Figure 10 these data are given for Fe). Softening of bulk modulus near the volume phase transition has been observed in polymer gels too [Hirotsu, 1991]. In the paper [Baughman & Galvao, 1993] it has been shown that crystalline networks demonstrates unusual mechanical and thermal properties.

The hypothesis is to be introduced into the course of the model development according to which the adaptive reaction reduces is a specific transfer process to an optimum control over intrinsic to ACM moving boundaries.

Let a composite at the polycomponental level be formed by bonded elastic particles (Fig. 11a). Being initially homogeneous and isotropic, each particle is characterized under the force action by stress concentration in the contact zone with the neighboring particle (Fig. 11b). The role of the sensor function is presumed to be played by characteristic for a number of substances multimodule ability [Bell, 1968], that is, the presence of a set of n discrete values of Young's modulus E depending on stress σ, being in this case the control parameter. For numeric modeling of adaptation to extreme external loads, which are by far higher the acceptable one for the initial material, discretization of each particle by finite elements and block relaxation algorithm, are used. A system of inequalities is taken as a processor function of the multimodule composite, where the lower and upper estimates of stresses are corrected at model "exposure" proceeding from the optimum criterion, namely, the condition of the minimal equivalent stress σ_{eq}

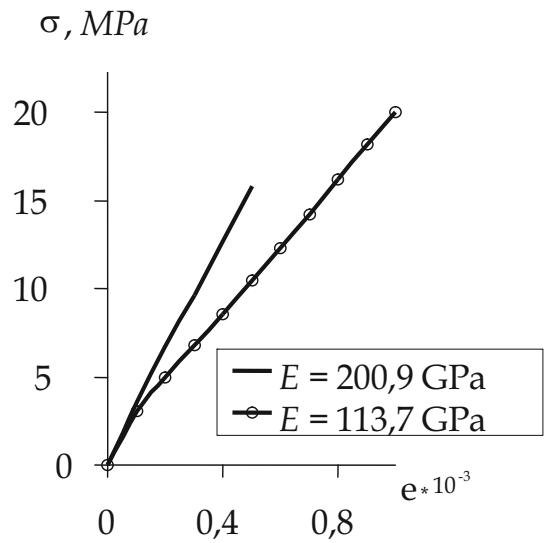

Fig. 10. Stress–strain curve of multimodule material (Fe) having two values of elastic modulus E

$$E = \begin{cases} E_1, \ \textit{if} \ \ \sigma^0 \le \sigma \ \le \sigma^1; \\ - - - - - - - - - - - - - \\ E_l, \ \textit{if} \ \ \sigma^{l-1} \le \sigma \ \le \sigma^l; \\ - - - - - - - - - - - - - \\ E_n, \ \textit{if} \ \ \sigma^{n-1} \le \sigma \ \le \sigma^n, \end{cases} \tag{3}$$

Simulation results prove that the adaptive reaction consists in transformation of the initial homogeneous structure into a reversible inhomogeneous one (Fig. 11c,d) ensuring perception of extreme loads through effective reduction of stress concentration due to dynamically optimal distribution of elastic modulus E.

So, the statement and systematic analysis of the problem of developing adaptive composites has enabled to trace evolution of structural organization of artificial materials, to clarify mechanisms of adaptation to external media and to disclose, to a certain degree, the effect of structure on formation of the optimum back reaction. In above considered example simulation of composite materials adaptivity is formulated as a problem on localizing moving internal boundaries, while differentiation of material functions is related to the changing scale level of the structure.

5. Self-assembling of auxetic porous composites with multimodular solid phase

Porous or cellular materials like «solid – gas» inhomogeneous systems are efficient composite structures in respect to optimizing strength and stiffness for a given weight.

These materials are useful for cushioning, insulating, damping, absorbing the kinetic energy from impact, packing, etc. Stiff and strong ones are preferable in load-bearing structures such as a lightweight core in sandwich panels. The term cellular is appropriate when the material contains polyhedral closed cells, as if it had resulted from solidification of a liquid foam.

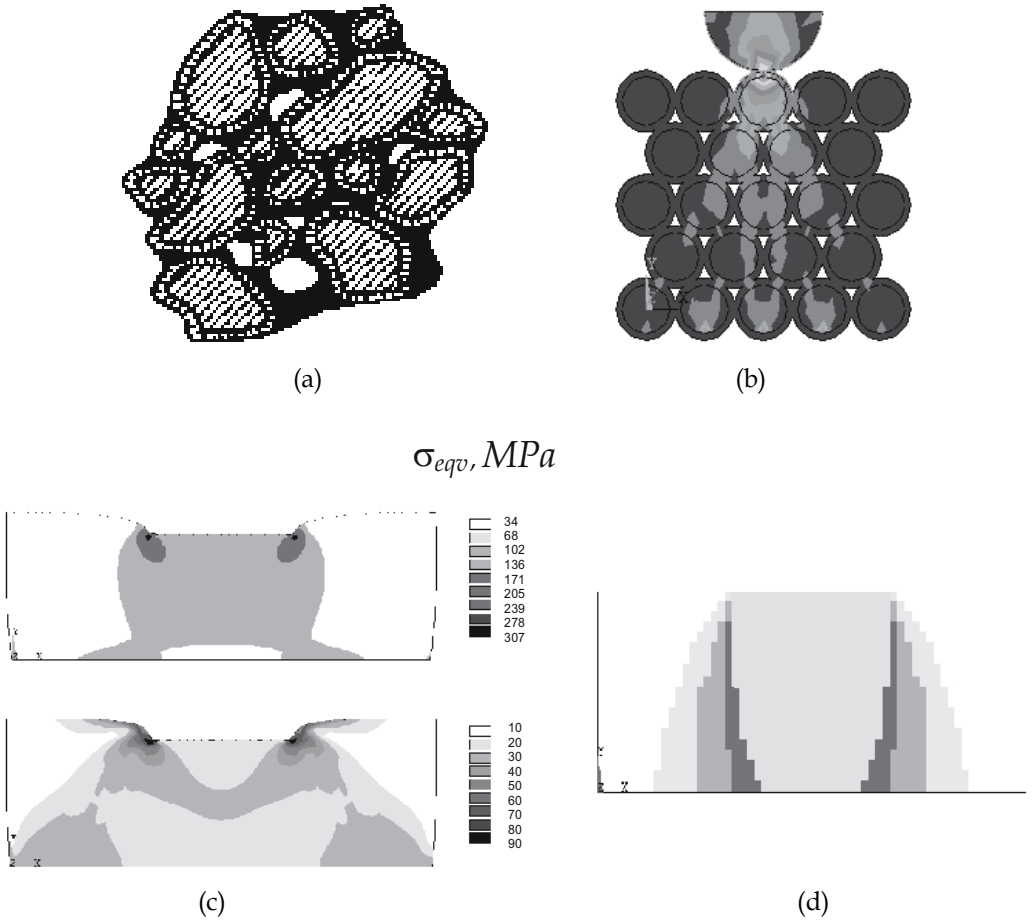

Fig. 11. ACM response after loading: typical composite structure (a); mesomechanical model (b); initial and final (after remodeling) distribution of equivalent stresses σ_{eq}. (c); dynamically optimal distribution of elastic modulus E (d)

A new means of improving the mechanical characteristics may be realized using abnormal deformation properties of auxetic porous materials having a negative Poisson's ratio ν [Lakes, 1987]. Auxetic porous materials, including auxetic porous nanomaterials (APN), having very high mechanical properties, are suitable for creating adaptive contact joints and for replacing natural materials such as damaged bone and tooth biotissues.

Examination of the mechanisms of generating a negative Poisson's ratio has been discussed and published in the last years, including special issues of *physica status solidi (b)* journal [Wojciechowski et al, 2007]. It is known that the inverted or re-entrant cell structure of

porous auxetics may be obtained by isotropic permanent volumetric compression of the conventional foam, resulting in non-reversible micro-buckling of the cell walls.
There is interest in compression-driven self-assembly as a means to create auxetic porous structures at the nanoscale. Below we predict the deformation behaviour of porous materials under uniaxial tension and compression (by an analytical method) and contact compression (by the finite element method).

5.1 Analytical determination of porous material elastic modulus

For open-cell flexible cellular materials, Poisson's ratio can be determined by a rod type structural unit with chaotically oriented cubic cells, as presented in Figure 12. It is worth mentioning that such a kind of unit cell model has been simulated in reference [Gibson & Ashby, 1982]. However, a cubic, not a spherical, structural unit had been used. Also, shear deformation of the rods had not been taken into account.

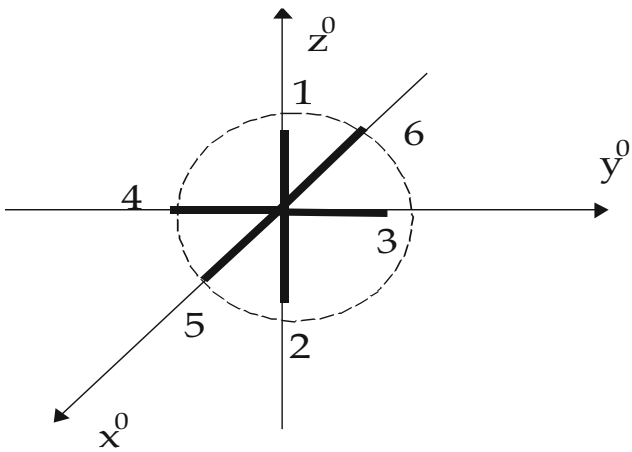

(a)

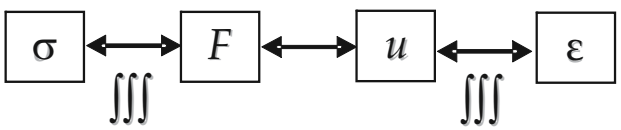

(b)

Fig. 12. Structural unit (a) and simulation procedure (b) of flexible cellular plastics: σ, ε are stress and strain tensor components; *F* is force acting on the rod end; *u* is displacement of force application point relatively to the rods; ∭ is averaged over direction

The rods of this structural unit are directed normally to the cubic planes. Symmetry of the element allows one to represent the displacement of the force application points (ends of rods) relatively to the rod joints through the deformation tensor components.

$$\Delta x_{L1} = x_{L1} - L = L\varepsilon_{z^0 z^0}, \quad y_{L1} = \frac{L}{2}\sqrt{\gamma_{x^0 z^{0^2}} + \gamma_{y^0 z^{0^2}}},$$
$$\Delta x_{L3} = x_{L3} - L = L\varepsilon_{y^0 y^0}, \quad y_{L3} = \frac{L}{2}\sqrt{\gamma_{x^0 y^{0^2}} + \gamma_{y^0 z^{0^2}}}, \tag{4}$$
$$\Delta x_{L5} = x_{L5} - L = L\varepsilon_{x^0 x^0}, \quad y_{L5} = \frac{L}{2}\sqrt{\gamma_{x^0 y^{0^2}} + \gamma_{x^0 z^{0^2}}},$$

where L is the structural unit rod length; x_{Li}, y_{Li} are the coordinates for the end of the i-th rod (i = 1..6) in the xy coordinate system; the x axis is directed longitudinally to the i-th rod in the non-deformed state (Figure 13).

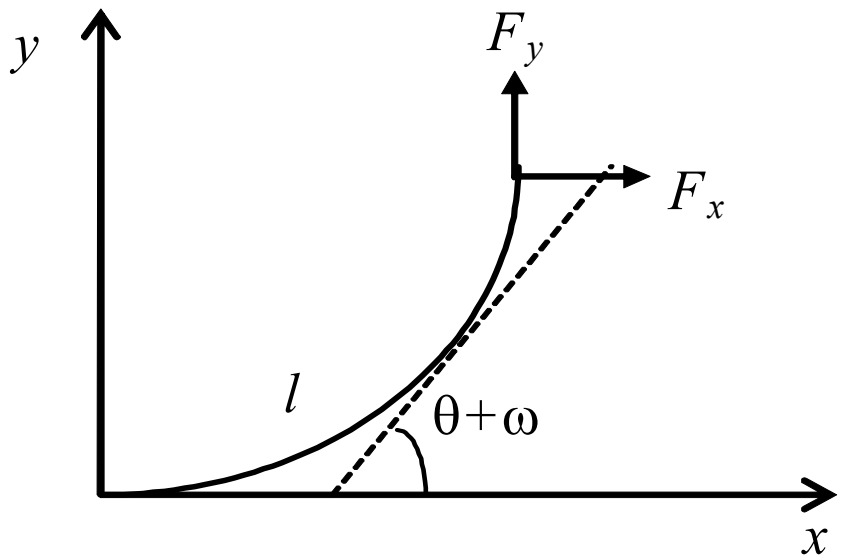

Fig. 13. Scheme of cantilever beam under large bending

Eq. (4) refers to deformations for which the Cauchy relations are satisfied. Here, the parameter L can be related to the solid state volumetric fraction by the following equation

$$V_f = \frac{V_m}{V} = \frac{9}{2\pi q^2}, \tag{5}$$

where V_m is the volume of rods in the structural unit; V is the structural unit total volume before deformation; q is the rod length L to its cross sectional side length r ratio. For simplification we neglected the volume of the nodes (rod joints) and assumed that the rods have a square cross-section. During further calculations we have estimated that the simulation results do not depend on the r value. So we may assume that r = 1, $L = q$.

Let us assume that in the coordinate system XYZ uniaxial strain is defined as $\varepsilon_{nm} = f(t)$ (other components of strain are equal to zero). The system XYZ position relative to the system $x^0y^0z^0$ is defined by Euler's angles β_1, β_2, β_3. Once the function $f(t)$ and Euler's angles are known, these define the deformation components in the $x^0y^0z^0$ system (Fig. 12). Then, the displacements (4) can be written as follows:

$$y_{Li} = \varepsilon_{nm}(t)\eta_i(\beta_1, \beta_2\beta_3), \quad \Delta x_{Li} = \varepsilon_{nm}(t)\xi_i(\beta_1, \beta_2\beta_3). \tag{6}$$

Here $\eta_i(\beta_1, \beta_2, \beta_3)$, $\xi_i(\beta_1, \beta_2, \beta_3)$ are the Euler's angle functions which are related by recalculating the tensor components under coordinate axis rotation. For the determination of forces $\vec{F}_i$ acting at the ends of the rods by the set deflections, it is necessary to solve a large flexure problem of a cantilever beam taking into account material viscosity. At the same time, to describe deformation of the low-density porous materials (V_f < 0.1) it can be assumed that the rod is deformed equally over all length L. The viscoelastic behaviour of the rod material is described by Rzhanitsyn's relaxation function

$$R(t) = Ae^{-\beta t}t^{\alpha-1}, \tag{7}$$

where t is time, s; and A, α, β are the kernel parameters.
The stress/strain relations are determined by the following equation

$$s_{\rho\chi} = 2G_f\left(\upsilon_{\rho\chi} - \int_0^t R(t-\tau)\upsilon_{\rho\chi}(\tau)d\tau\right), \quad \sigma = 3K_f\varepsilon. \tag{8}$$

where $s_{\rho\chi}$, $\upsilon_{\rho\chi}$, σ, ε are the deviatoric and spherical parts of the stress and strain tensors; G_f, K_f are the shear and bulk moduli of the material.
For the beam deformations, let us assume

$$\varepsilon_{ll} = \varepsilon_0(l) + \lambda\theta'(l), \quad \varepsilon_{\lambda l} = \frac{1}{2}\omega(l). \tag{9}$$

where l is the coordinate referred along the rod median in the deformed state; λ is the coordinate referred perpendicularly to l; θ is the rotation of the rod cross-section connected with flexural strain; θ' – θ is the derivative of the l coordinate; ω is the rod cross-section turning angle as a function of shear strain; ε_0 is the deformation of the centre line passing through the centre of gravity under tension or compression.
The allowance for flexural, shear and tensile-compression strains helps to describe deformation of "short" rods when their length is commensurable with the cross-sectional side length. For an arbitrary cross-sectional shape, the following expressions are valid

$$M = \iint_S \sigma_{ll}\lambda dS, \quad P = \iint_S \sigma_{ll}dS, \quad Q = \iint_S \sigma_{\lambda l}dS. \tag{10}$$

where M is the bending moment; Q, P are the transverse and longitudinal forces. Therefore, the equilibrium Eqs. for the cantilever rod for the large deflection case will take the form

$$\begin{aligned} Q &= F_y\cos(\theta+\omega) - F_x\sin(\theta+\omega), \\ P &= F_x\cos(\theta+\omega) + F_y\sin(\theta+\omega), \\ M &= F_y(x_L - x) - F_x(y_L - y). \end{aligned} \tag{11}$$

Substituting Eqs. (8) and (9) into (10) gives

$$\omega = \frac{-k}{G_f S}(F_x \sin(\theta+\omega) - F_y \cos(\theta+\omega)) + \int_0^t R(t-\tau)\omega(\tau)d\tau,$$
$$\varepsilon_0 = \frac{1}{E_f S}(F_y \sin(\theta+\omega) + F_x \cos(\theta+\omega)) + \int_0^t R(t-\tau)\varepsilon_0(\tau)d\tau,$$
$$\theta' = \frac{1}{E_f J}\left(F_y(L+\varepsilon_{nm}\xi - x) - F_x(\varepsilon_{nm}\eta - y)\right) + \int_0^t R(t-\tau)\theta'(\tau)d\tau, \quad (12)$$
$$x' = \cos(\theta+\omega),$$
$$y' = \sin(\theta+\omega).$$

where J, S are the second moments of the area and the cross-sectional area of the rod, correspondingly; E_f is Young's modulus of rod material; k is the coefficient complying with non-uniformity of tangential stress distribution over the cross-sectional area. In our calculations we assumed $k = 1$.

Therefore, a system of Eqs. was obtained for the five unknown coordinates l and time functions. Let us apply the following boundary conditions: $\theta(0,t) = x(0,t) = y(0,t) = 0$. In (12) η, ξ are constants. Solution of these combined Eqs. using the finite difference method allows us to obtain the coordinates of the free end of rod as a function of five variables, viz:

$$x_L = x(L,t) = f_x(F_x, F_y, \eta, \xi, t),$$
$$y_L = y(L,t) = f_y(F_x, F_y, \eta, \xi, t). \quad (13)$$

During computation of (12) it was taken into account that the l coordinate differentiation is made in the deformed state. Therefore, the increment of the l parameter was assumed equal to $dl = (1+\varepsilon_0)\frac{L}{n_0}$. Here, n_0 is a discretization number. The solution of (12) was carried out for a specified t. It should be mentioned that the structure of Rzhanitsyn's relaxation function (7) causes the integral terms in (12) to contain θ, γ and ε_0 functions which were defined during the previous steps.

The conditions for calculation of the required forces are of the type

$$\begin{cases} f_x(F_x, F_y, \eta, \xi, t) = L + \varepsilon_{nm}(t)\xi, \\ f_y(F_x, F_y, \eta, \xi, t) = \varepsilon_{nm}(t)\eta. \end{cases} \quad (14)$$

The solution of Eqs. (12) and (14) was obtained numerically with the help of MathCad® 7.0 software. The system of nonlinear Eqs. was solved using Newton's method. As the initial approximation we took the solution of the previous step. Therefore, we obtain the functions $F_x(\eta,\xi,t)$, $F_y(\eta,\xi,t)$ which can be presented as follows

$$F_x = C_{x1}\xi + C_{x2}\eta + C_{x3}\xi\eta + C_{x4}\xi^2 + C_{x5}\eta^2 +$$
$$+C_{x6}\xi^2\eta + C_{x7}\xi\eta^2 + C_{x8}\xi^3 + C_{x9}\eta^3 + C_{x10}\xi^2\eta^2. \quad (15)$$

At a given t, the coefficients C_{xj}, C_{yj} (j = 1..10) can be defined by standard regression procedures. The stress tensor components are related through the forces (15) as follows:

$$\sigma_{x^0x^0} = F_{x1}\frac{1}{\pi(L+\varepsilon_{nm}\xi_2)(L+\varepsilon_{nm}\xi_3)},$$
$$\sigma_{y^0y^0} = F_{x2}\frac{1}{\pi(L+\varepsilon_{nm}\xi_1)(L+\varepsilon_{nm}\xi_3)}, \tag{16}$$

$$\sigma_{z^0z^0} = F_{x3}\frac{1}{\pi(L+\varepsilon_{nm}\xi_1)(L+\varepsilon_{nm}\xi_2)},$$
$$\sigma_{x^0y^0} = F_{y1}\frac{1}{\pi(L+\varepsilon_{nm}\xi_2)(L+\varepsilon_{nm}\xi_3)}\frac{\varepsilon_{x^0y^0}}{\left(\varepsilon_{x^0y^0}{}^2+\varepsilon_{x^0z^0}{}^2\right)^{1/2}},$$
$$\sigma_{x^0z^0} = F_{y1}\frac{1}{\pi(L+\varepsilon_{nm}\xi_2)(L+\varepsilon_{nm}\xi_3)}\frac{\varepsilon_{x^0z^0}}{\left(\varepsilon_{x^0y^0}{}^2+\varepsilon_{x^0z^0}{}^2\right)^{1/2}}, \tag{17}$$
$$\sigma_{y^0z^0} = F_{y2}\frac{1}{\pi(L+\varepsilon_{nm}\xi_1)(L+\varepsilon_{nm}\xi_3)}\frac{\varepsilon_{y^0z^0}}{\left(\varepsilon_{x^0y^0}{}^2+\varepsilon_{y^0z^0}{}^2\right)^{1/2}}.$$

The stresses for the *XYZ* system were then redefined. Because of the chaotic orientation of the unit cells, the stress tensor components should be averaged over direction (Euler's angles)

$$\sigma_{nm} = \int_0^{\pi}\int_0^{2\pi}\int_0^{2\pi}\sigma_{nm}(\beta_1,\beta_2,\beta_3)\frac{\sin\beta_3}{8\pi^2}d\beta_1 d\beta_2 d\beta_3. \tag{18}$$

Therefore, for the known stress to time dependence, we defined time dependencies of the stresses in a representative volume of the material.

5.2 Calculation example: Uniaxial stress

As an example of using above technique, let us examine the stress-strain state of an elastic porous material based on high density polyethylene (HDPE). Experimental data for HDPE were obtained from [Goldman, 1979]: G_f = 237 MPa; K_f = 1402 MPa; A = 0.022 $s^{-\beta}$; β = 2.995 · 10^{-5} s^{-1}; α = 0.175.

Averaging in all possible loading directions (14) makes the simulated material isotropic at the macroscopic level. The $\tau(\gamma)$ function therefore characterizes the dependence of stress on strain deviator components $\tau(\gamma) = s_{nm}(2\upsilon_{nm})$. Thus, if functions $\tau(\gamma)$ and $p(\Theta)$ are known, it is possible to simulate isotropic material behaviour at an arbitrary homogeneous stress-strain state. Hence, for a uniaxial stress ($\sigma_{ZZ} \neq 0$) the following relations are true

$$2\upsilon_{ZZ} = \frac{4}{3}\varepsilon_{ZZ}(1+\mu);$$
$$\Theta = (1+\varepsilon_{ZZ})(1-\varepsilon_{ZZ}\mu)^2 - 1;$$
$$s_{ZZ} = \frac{2}{3}\sigma_{ZZ}; \tag{19}$$
$$\sigma = \frac{1}{3}\sigma_{ZZ}.$$

We introduce the transverse strain factor $\mu = -\frac{\varepsilon_{xx}}{\varepsilon_{zz}}$, which is analogous to Poisson's ratio in the linear elasticity region. Making allowance for a large bending flexure of the ribs where μ depends on strain ε_{ZZ}, this dependence is determined by the following Eq.

$$\tau\left(\frac{4}{3}\varepsilon_{ZZ}(1+\mu)\right) = 2p\left((1+\varepsilon_{ZZ})(1-\varepsilon_{ZZ}\mu)^2 - 1\right). \tag{20}$$

Under stretching, μ also decreases rapidly when the strain reaches ε_{cr}. In addition, the $\mu(\varepsilon_{ZZ})$ dependence rapidly passes on the horizontal plateau $\mu(\varepsilon_{ZZ}) = const = \nu^0$, where Poisson's ratio ν^0 is defined as

$$\nu^0 = \frac{3K - 2G^0}{6K + 2G^0}, \tag{21}$$

here K is the foam bulk modulus defined by the initial part of the $p(\Theta)$ curve; G^0 is the shear modulus defined by the $\tau(\gamma)$ curve.

It was found that the $\mu(\varepsilon_{ZZ})$ function does not depend on the strain rate. In Figure 14 the dependence of the factor μ on the longitudinal strain ε_{ZZ} at stretching (*a*) and compression (*b*) of an elastic cellular plastic based on HDPE (V_f = 0.01) is presented. Under compression the strain reaches some critical value ε_{cr} and μ rapidly decreases and becomes negative at ε_{ZZ} > 0.9%. Such an anomaly of the elastic behaviour was experimentally observed in polymer foams [Lakes, 1987]. Our investigations showed that this effect may occur in cellular materials with a tetrahedronal cell form when the cell ribs buckle inward or in a honeycomb microstructure.

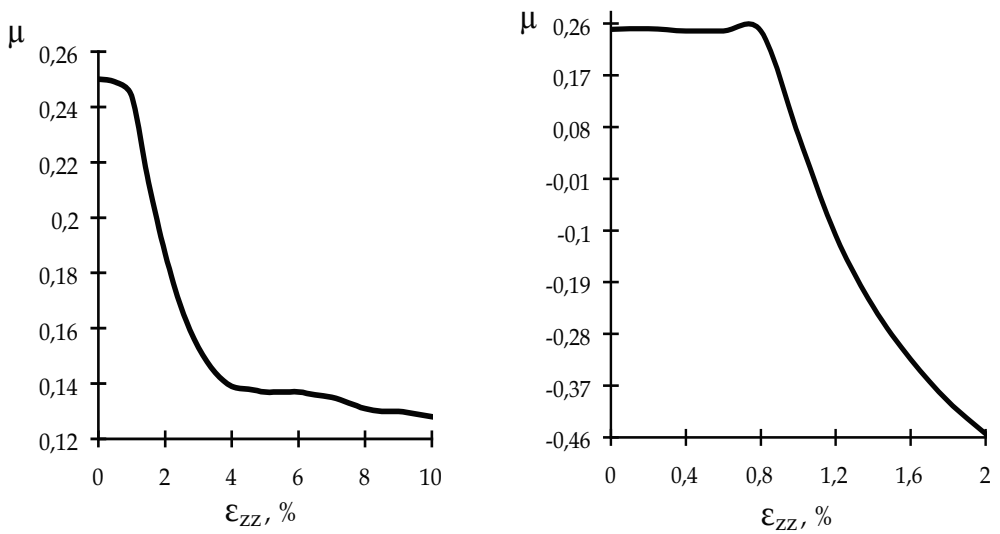

Fig. 14. Dependence of transverse strain factor μ on longitudinal strain ε_{ZZ} under stretching (a) and compression (b) of flexible cellular plastics

At small strains, μ remains constant and coincides with Poisson's ratio. Under compression the strain reaches some critical value ε_{cr} and μ rapidly decreases and becomes negative at ε_{ZZ} > 0.9%. Under stretching, μ decreases rapidly when the strain reaches ε_{cr} and $\mu(\varepsilon_{ZZ})$ dependence passes on the horizontal plateau.
By defining the $\mu(\varepsilon_{ZZ})$ function, the dependence of stress σ_{ZZ} on strain ε_{ZZ} can be obtained as

$$\sigma_{ZZ}(\varepsilon_{ZZ}) = \frac{3}{2}\tau\left(\frac{4}{3}\varepsilon_{ZZ}\left[1+\mu(\varepsilon_{ZZ})\right]\right). \tag{22}$$

At small strains, stability of μ allows us to determine the correlation between ε_{cr}, Θ_{cr} and γ_{cr}

$$\varepsilon_{\mathrm{cr}} = \frac{1}{1-2\nu}\Theta_{\mathrm{cr}}, \quad \gamma_{\mathrm{cr}} = \frac{4(1+\nu)}{3(1-2\nu)}\Theta_{\mathrm{cr}}. \tag{23}$$

5.3 Comparison with experimental data

To examine the applicability of the theoretical model for foam deformation properties, we compared the calculated and experimental values of the relative Young's modulus E/E_f and critical strains ε_{cr} proceeding from the following considerations: the majority of experimental data on deformation of elastic foams are based on their uniaxial compression behaviour; the calculated stress/strain dependence and the experimental behaviour are almost linear at $\varepsilon < \varepsilon_{cr}$. As it was shown in [Hilyard & Cunningham, 1987], $\sigma_{ZZ}(\varepsilon_{ZZ})$ dependence at $\varepsilon_{ZZ} > \varepsilon_{cr}$ to a certain degree is conditioned by inhomogeneity of the inner structure of the material.
During definition of Young's modulus E of an elastic cellular plastic, we considered that the rod cross-section turning angles are small ($\cos(\theta+\omega)\approx 1, \sin(\theta+\omega)\approx 0$) and we do not consider rod viscosity. In this case, the solutions can be obtained in the analytical form. For the relative Young's modulus, we have

$$\frac{E}{E_f} = V_f \frac{36 + V_f\pi(7+4\nu_f)}{216 + 3V_f\pi(9+8\nu_f)}, \tag{24}$$

where ν_f is the solid phase Poisson's ratio. In particular, for the elastic polymer material we assume that ν_f = 0.49. Equations (10) and (15) yield an approximate expression for the critical strain ε_{cr}

$$\varepsilon_{cr} = \frac{V_f\pi^3\left[72 + V_f\pi\left(9+8v_f\right)\right]}{72\left[36 + V_f\pi\left(7+4v_f\right)\right]}. \tag{25}$$

The dependence of the relative Young's modulus E/E_f on the relative solid volume fraction V_f for the elastic foam is presented in Figure 15.
In Figure 15, curve 1 corresponds to Eqs. (23). Curve 2 agrees with the results obtained in [Warren & Kraynik, 1987]. Curve 3 meets the results obtained in [Beverte & Kregers, 1987] using the semi-axes hypothesis. Curve 4 corresponds to the analytical expression

$$\frac{E}{E_f} = \frac{V_f}{3}\left(1 - 2\nu'\right) = 0,16V_f\,, \tag{26}$$

obtained in [Gibson & Ashby, 1982]. Here ν' is the Poisson's ratio of the material dependent on the number of rods in structural unit N. For simulation of mechanical behaviour of the rubber foam [Gibson & Ashby, 1982], we used a structural element with $4 < N < 8$, when $\nu' = 0.26$. Curve 5 in Figure 15 corresponds to the empirical relation for the relative Young's modulus of foam rubbers [Hilyard & Cunningham, 1987]

$$\frac{E}{E_f} = \frac{V_f}{12}\left(2 + 7V_f + 3{V_f}^2\right)\,. \tag{27}$$

The circles in Figure 15 reflect experimental data for the foam rubber [Lederman, 1971]. This comparison proves that the proposed technique makes it possible to predict quite accurately elastic properties of the material at $V_f < 0,15$.

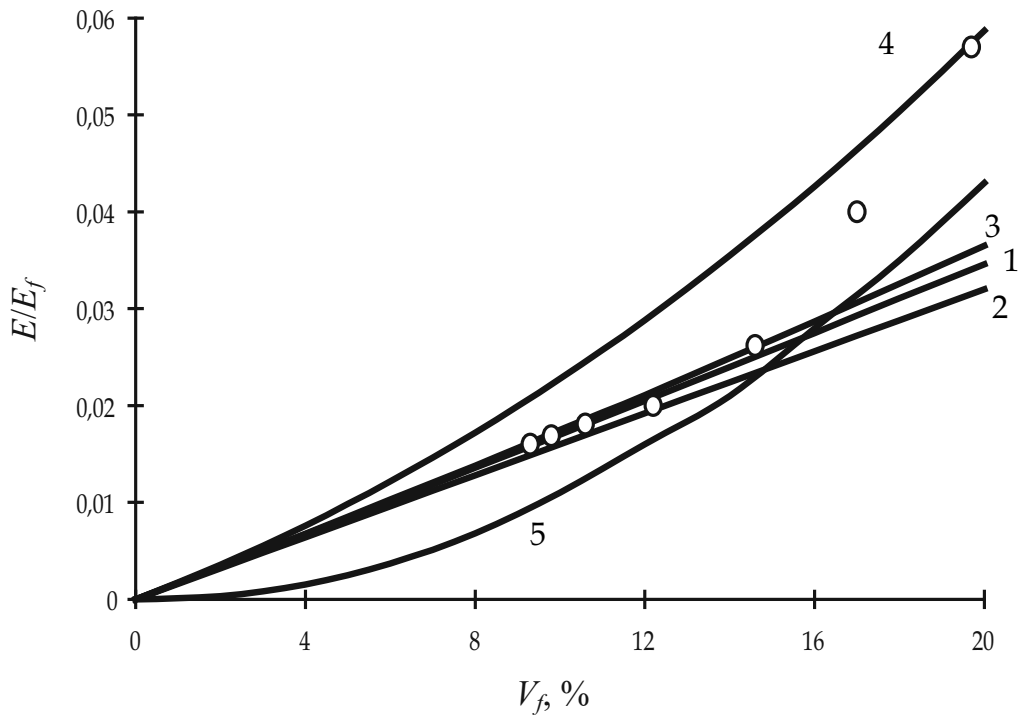

Fig. 15. The dependence of relative Young modulus E/E_f on the solid phase volumetric fraction V_f for the flexible foam: curve 1 corresponds to Eqs. (23); curve 2 corresponds to results obtained in [Warren & Kraynik, 1987]; curve 3 corresponds to results obtained in [Beverte & Kregers, 1987]; curve 4 corresponds to results obtained in [Gibson & Ashby, 1982]; curve 5 corresponds to results obtained in [Hilyard & Cunningham, 1987]; circles correspond to experimental data [Lederman, 1971]

5.4 Construction of the mesomechanical model

Mesomechanical (in the scale of the separate cells) description of cellular structure is time-consuming but a very informative method. A possibility for the determination of Poisson's ratio during special thermomechanical treatment of basic porous material when convex structural cells transform into concave ones as shown in Figure 16, is an advantage of the mesoscopic model.

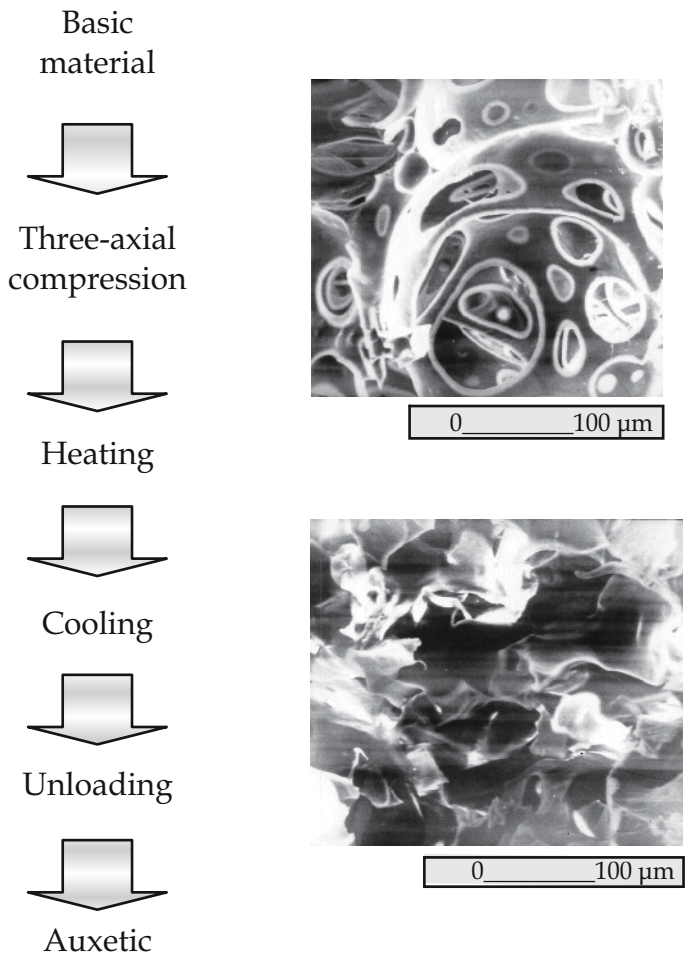

Fig. 16. A scheme of obtaining the auxetic material using transformation of ther basic structure into the inverted one with concave cells. Electron microscopy of a porous polyurethane fragment with magnification 50*

Previously, the determination of v as a function of the transverse and longitudinal strain was achieved for the case of compression of the sample made of a one-phase material with known values of Poisson's ratio (Figure 1a). The geometrical sizes of the rectangular sample are L_x = 50 μm, L_y = 250 μm; the compressive strain is ε_y = 0.5%. The calculated results are shown in Table 5. It should be noted that the technique has an acceptable accuracy which

increases as the friction between the sample and the plates decreases. This fact is explained by a free slip of the contact surfaces.

For calculation of the effective elastic characteristics of the porous material mesofragments we replace the real structure by a system of cells of regular polyhedrons. The transformation of the porous material into the auxetic one appears to be possible at bulk compression V_{in}/V_{tr} equal to 1.4÷4.8 where V_{in}, V_{tr} are the volume of the initial and transformed structure respectively. The best results are achieved at V_{in}/V_{tr} = 3.3÷3.7. This agrees with the data derived for foamed polyurethane and copper sponge.

The simulation allows us to describe cell transformation at the expense of free volume due to connection of structural units providing the required deformation mode.

The number of node	u_x, μm			
	f = 0.1		f = 0.5	
	Left side	Right side	Left side	Right side
1	-0.0507	0.0498	-0.0510	0.0493
2	-0.0507	0.0498	-0.0510	0.0493
3	-0.0507	0.0498	-0.0510	0.0494
4	-0.0507	0.0498	-0.0509	0.0494
5	-0.0506	0.0499	-0.0508	0.0495
6	-0.0506	0.0499	-0.0508	0.0496
7	-0.0506	0.0500	-0.0507	0.0498
8	-0.0506	0.0503	-0.0508	0.0503
9	-0.0504	0.0483	-0.0504	0.0499
10	-0.0373	0.0370	-0.0471	0.0405
u_x, average	-0.04929	0.04846	-0.05045	0.0487
u_x, total average	0.048875		0.049575	

Table 5. The calculation results of the transverse displacements

5.5 Mesomechanical analysis

According to the mesomechanical approach, some systems of regular polyhedrons, presented in Figure 17, were constructed for calculation of Poisson's ratio v during structural transformation under compression (Figure 16). In the numerical example, we give the following initial data for the solid phase of the porous material E = 1 GPa, v = 0.1; the sizes of the fragment 240*280 μm and the periodic cell 34*34 μm, the friction coefficient on the contacting surface with the rigid plates is f = 0.5.

Besides the linear elastic solid phase, we have assumed a physically nonlinear multimodular solid phase. In the last case, the stepwise dependence of Young's modulus on the stress component has been used (1).

We then simulated deformation of the initial structure with rectangular cells to analyse the formation of auxetic properties under compression of traditional porous material. To increase the accuracy, Poisson's ratio was determined by averaging the displacements for the left and right sides of the model structure fragment. According to Table 6, the results in the case of a multimodule solid phase seems to be more stable than for E = const and at less expressed auxetic properties (stability loss of the porous fragment made of multimodular material is absent at compression displacement u_y = 14.0 μm).

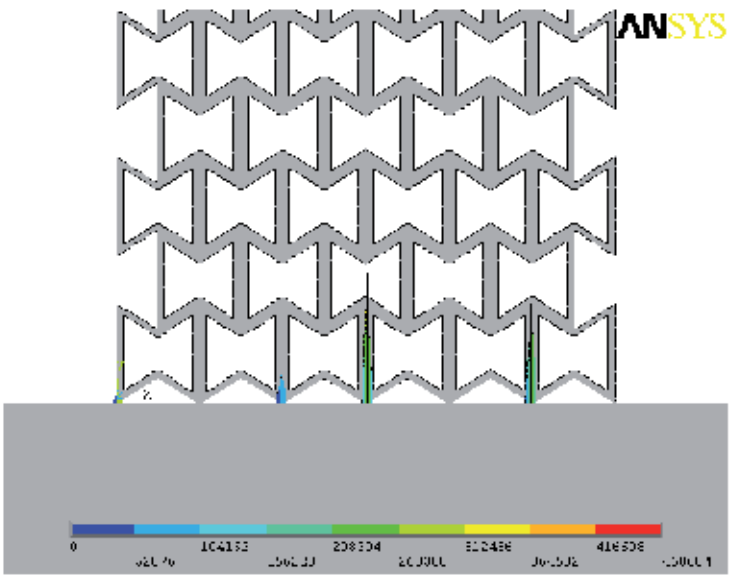

Fig. 17. Distribution of contact pressure under deformation of the porous structure (the vertical compressive displacement u_y = 0.1 μm)

u_y, μm	1.4	2.8	7.0	14.0*	21.0	28.0	35.0	42.0
E = const	-0.040	-0.054	-0.085	-0.49	-0.180	-0.222	-0.130	-0.291
$E = E(\sigma)$	-0.0146	-0.0195	-0.0340	-0.076	-0.080	-0.100	-0.118	-

*stability loss of porous material fragment.

Table 6. The calculation results of Poisson's ratio v

The dependences in Figure 18 were shown in a dimensionless form (compression level was taken as a ratio of normal displacements to the height of the porous material fragment u_y/b) for comparison under different conditions of loading. It can be seen from Figure 18 that instability of solution is observed at a step-by-step loading of the porous material with hexagonal cells at a deformation level 5%. The porous material with hexagonal cells and multimodule solid phase coincide closely. The solution is not converged for the porous material with square cells at deformation level more than 15% with local unstability in the range 2.5-7.5% and for multimodule solid phase at deformation level more than 10%. The solution is not converged at the deformation level more than 5% for the concave cells with

linear elastic and multimodular solid phase. According to the previous stress history the solution is not converged at the deformation levels greater than 7.5% and 3% for the square and concave cells respectively.

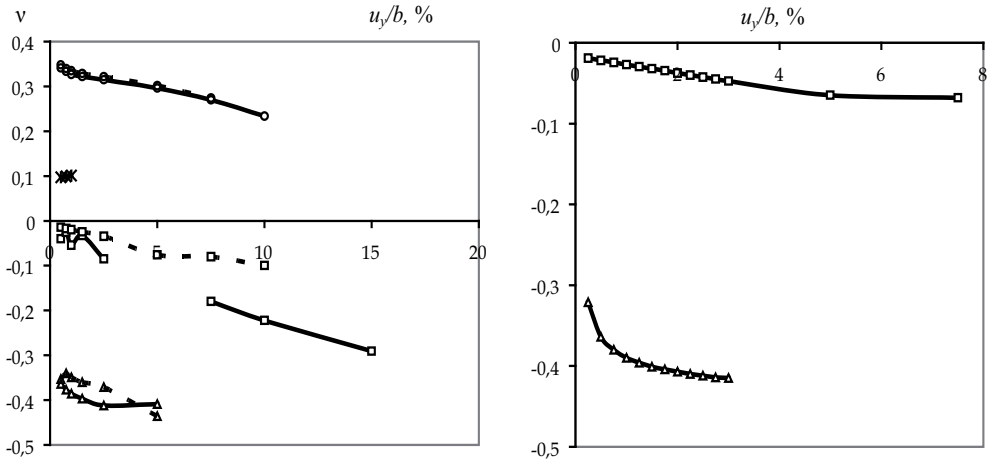

(a) (b)

Fig. 18. Dependence of Poisson's ratio on compression level: (a) step-by-step loading; (b) accounting the previous stress history for the porous material with square cells (squares), hexagonal cells (generated angle $\alpha = 60^0$) (triangles), circular cells (stars) and with multimodule solid phase (hatches)

The analysis of the stress-strain state of these cellular structures for various deformation levels shows that Poisson's ratio is near to zero at the initial stress state but decreases significantly under compression of the material, which its solid phase has a constant elasticity modulus. The predicted auxetic behaviour is due to generation of the concave cells at the determinative compression level. Poisson's ratio decreases for the structure with the given concave cells transferring into a plateau. At significant deformation, the solution is not converged due to closing of the cell edges.

At the macroscale the model of the cell structure is unstable. This may result in the a displacement of the fragment (in the given example this takes place at compression level u_y = 14 μm). For obtaining a stable solution, it is necessary to take into consideration the previous stress history of the contact friction process (Fig. 18b). The account of the previous stress history is also important for calculating the auxetic self-lock mode at the conditions of contact compression and shear [Shilko et al, 2008a].

5.6 Prediction of auxetic effects in porous materials with nano-sized cells

Self-assembling high-strength and rigid materials of small density are of great interest like Langmuir films. This may be reached by the auxetic porous material "construction" on the micro- and nano-size level. It is important that the value of adhesion forces F increases essentially at decreasing of the gap H between solid surfaces. The values of the adhesion force are shown in Table 3 for two pairs of polymers and three values of the gap H according to

$$F = \frac{A_{12}}{6\pi H^3}, \tag{28}$$

where A_{12} is the Hamaher constant and H is the distance between surfaces.
It is seen that a sharp increase of the adhesion force takes place in nano-sized cells of the porous material.

Material	F, MPa			A_{12}, Erg
	H = 10A	H = 5A	H = 4A	
Polytetrafluorethylene - Polyimide	7.38	51.1	115.3	$1.39*10^{-12}$
Polycaproamide - Polycaproamide	7.30	58.3	113.9	$1.37*10^{-12}$

Table 3. Estimation of adhesion forces in nano-sized cells on the basis of polymers

The calculations of the deformed state of the porous material subject to adhesion forces and multimodule effect simultaneously, show a possibility of self-assembling of a spontaneous, energetically preferable auxetic nano-sized structure as shown in Figure 19.
So, the auxetic porous materials with micro- and nano-sized cells, having good combination of density, deformational and strength properties, seem quite preferable for many technical and biomedical applications. Analytical and numerical modelling describes the cellular solid transformation resulting in microbuckling of the cell walls under certain loading conditions and providing the auxetic deformation mode.
Geometrically simple mesomechanical models of the porous material based on cubic, rectangular and concave structural units have been investigated in the present paper taking into account such important factors as large strains, history of loading, physical nonlinearities of solid phase, adhesive interaction and so on.
The limitations of the effective finite element simulation are caused by stability loss of the representative fragment of structure. The possibility of compression-driven self-assembly of nano-sized auxetics due to the increasing adhesion force between the cell walls has been predicted.

6. Conclusion

- The systematic analysis of the problem of developing adaptive composites has enabled us to trace evolution of structural organization of artificial materials, to clarify the mechanisms of adaptation to the external action, and to disclose, to a certain degree, the effect of structure on formation of the optimum back reaction.
- In above considered examples of composites, description of adaptive structures is formulated as a problem on localizing moving interfaces. The study of synergetic phenomena in the nonliving nature and analogous processes in biological objects will, in our opinion, provide a possibility to find structural-and-functional prototypes of adaptive composites.
- The proposed analytical and numerical models predict self-reinforcing in composites and joints made of auxetics under loading. The role of friction, previous stress history,

multimodule solid phase and adhesion forces acting between the walls of cells were shown in the formation of auxetic properties of the porous materials as the composites with the gas phase.

- The limiting values of compression deformation on the stability criterion of cellular structures under compression and the possibility of energetically preferable self-assembly of auxetic porous nano-sized materials have been predicted.
- It's seemed that realization of self-healing in composites made of auxetic and multimodule materials is a perspective goal of further studies.

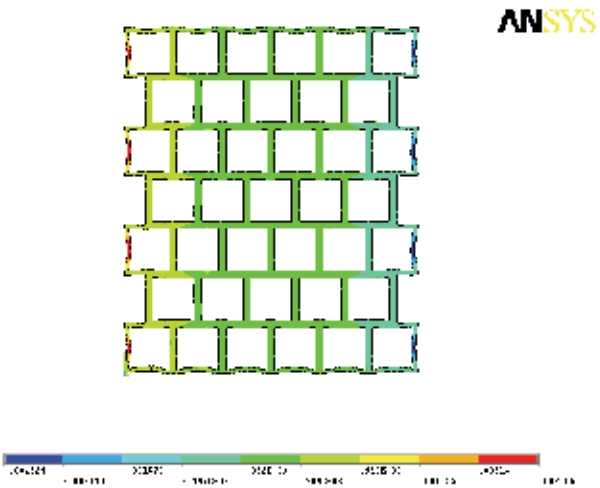

(a)

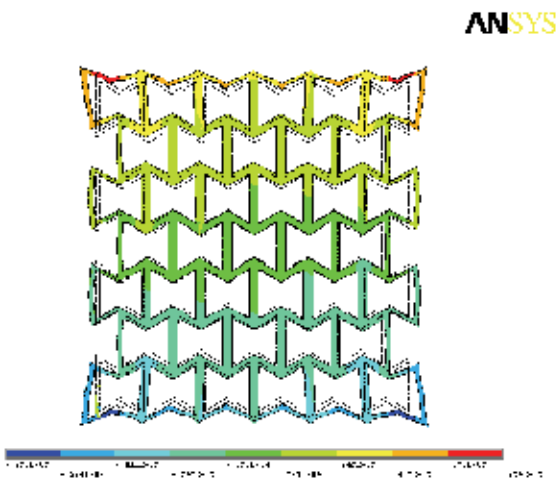

(b)

Fig. 19. Deformation modes of the porous material with initially rectangular (a) and concave (b) shape of the cells under the action of adhesion forces

7. Acknowledgement

The author is grateful for assistance to Prof. Yu. Pleskachevsky, Prof. R.D. Adams, Dr. D. Chernous and K. Petrokovets.

8. References

Anfinogenov, S.B. Kurek, M.F. Shilko, & S.V. Chernous, D.A. (2008). Mechanical and frictional properties of biological elastomers: Part 1: Description of human skin relaxation under tension. Russian Journal of Biomechanics, Vol. 12, No. 3, pp. 42–48, ISSN 1812-5123.

Baughman, R.H. Galvao, D.S. (1993). Crystalline networks with unusual predicted mechanical and thermal properties. Nature, Vol. 365, pp. 735-737, ISSN 028-0836.

Bell, J.F. (1968). The physics of large deformation of crystalline solids. Springer tracts in natural philosophy. Vol. 14, Springer, Berlin-Heidelberg-New York.

Bergman, D.J. Inan, E. (Ed(s)). (2004). Continuum models and discrete systems, Kluwer Academic Publishers, ISBN 1-4020-2314-6, Dordrecht-Boston-London.

Beverte, I.V., Kregers, A.F. (1987), Mechanics of Composite Materials. Vol. 23, No. 1, pp. 27-33).

Chernous, D.A. Shilko, S.V. Konyok, D.A. & Pleskachevsky Yu.M. (2003). Nonlinear viscoelastic behavior of flexible cellular plastics: refined rod model. *International Journal of Applied Mechanics and Engineering*, No. 1, pp. 27-41, ISSN 1425-1655.

Galaev, Yu.I. (1995). Smart polymers in biotechnology and medicine. Russian Chemical Reviews, Vol. 64, No. 5, pp. 505-524, ISSN 0036-021X.

Gibson, L.J. Ashby, M.F. (1982). The mechanics of three-dimensional cellular materials. Proceedings of the Royal Society A, Vol. 382, No. 3, pp. 43-59, ISSN 1364-5021.

Goldman, A.Ya. (1979). Strength of constructional plastics, Mashinostroenie, Leningrad (in Russian).

Hilyard, N.C. Cunningham, A. (1987). Low Density Cellular Plastics: Physical Basis of Behaviour, Chapman and Hall, London.

Hirotsu, S. (1991). Softening of bulk modulus and negative Poisson's ratio near the volume phase transition in polymer gels. Journal of Chemical Physics, Vol. 94, No. 5, pp. 3949-3957, ISSN 021-9606.

Kolupaev, B.S. Lipatov, Yu.S. Nikitchuk, V.I. Bordyuk, N.A. & Voloshin, O.M. (1996). Composite materials with negative Poisson coefficient. Journal of Engineering Physics and Thermophysics, Vol. 69, No. 5, pp. 542-549, ISSN 1062-0125.

Koniok, D.A. Voitsekhovsky, K.V. Pleskachevsky, Yu.M. & Shilko, S.V. (2004). Materials with negative Poisson's ratio. (The review). Journal on Composite Mechanics and Design, Vol. 10, No. 1, pp. 35-69, ISSN 1682-3532.

Lakes, R. (1987). Foam structure with a negative Poisson's ratio. Science, Vol. 235, pp. 1038-1040, ISSN 0036-8075.

Landau, L.D. Lifshitz, E.M. (1986). Theory of Elasticity. Vol. 7 (3rd ed.), Butterworth-Heinemann, ISBN 978-0-750-62633-0, Oxford.

Lederman, J.M. (1971). The prediction of the tensile properties of flexible foams. Journal of Applied Polymer Science, Vol. 15, No. 3, pp. 693-703, ISSN 0021-8995.

Prigogine, I. Stengers, I. (1984). Order out of Chaos: Man's new dialogue with nature, Flamingo, ISBN 0006541151, London.

Schwartz, M. (2007). Encyclopedia of Smart Materials, John Wiley & Sons, Inc. ISBN 0-471-17780-6, New York.

Shilko, S.V. Stolyarov, A.I. (1996). Friction of anomalously elastic bodies. Negative Poisson's ratio. Part 2. Calculation of self-locking parameters. Journal of Friction and Wear, Vol. 17, No. 4, pp. 23–29, ISSN 0202-4977.

Shilko, S.V. Petrokovets, E.M. & Pleskachevsky, Yu.M. (2008). Peculiarities of friction in auxetic composites. Physica status solidi B, Vol. 245, No. 3, pp. 591–597, ISSN 0370-1972.

Shilko, S.V. Petrokovets, E.M. & Pleskachevsky, Yu.M. (2008). Prediction of auxetic phenomena in nanoporomaterials. Physica status solidi B, Vol. 245, No. 11, pp. 2445–2453, ISSN 0370-1972.

Warren, W.E. Kraynik, A.M. (1987). The Winter Annual Meeting of the ASME, Boston, pp. 123–145.

Wei, G. Edvards, S.F. (1999). Effective elastic properties of composites of ellipsoids (II). Nearly disc– and nedle–like inclusions. Physica A, Vol. 264, pp. 404-423, ISSN 0378-4371.

Wojciechowski, K. Alderson, A. Alderson, K.L. Maruszewski, B. & Scarpa, F. (2007). Preface. Physica status solidi B, Vol. 244, No. 3, pp. 813–816, ISSN 0370-1972.

22

Mechanics of Composite Beams

Mehdi Hajianmaleki and Mohammad S. Qatu
Mississippi State University
USA

1. Introduction

A structural element having one dimension many times greater than its other dimensions can be a rod, a bar, a column, or a beam. The definition actually depends on the loading conditions. A beam is a member mainly subjected to bending. The terms rod (or bar) and column are for those members that are mainly subjected to axial tension and compression, respectively.

Beams are one of the fundamental structural or machine components. Composite beams are lightweight structures that can be found in many diverse applications including aerospace, submarine, medical equipment, automotive and construction industries. Buildings, steel framed structures and bridges are examples of beam applications in civil engineering. In these applications, beams exist as structural elements or components supporting the whole structure. In addition, the whole structure can be modeled at a preliminary level as a beam. For example, a high rise building can be modeled as a cantilever beam, or a bridge modeled as a simply supported beam. In mechanical engineering, rotating shafts carrying pulleys and gears are examples of beams. In addition, frames in machines (e.g. a truck) are beams. Robotic arms in manufacturing are modeled as beams as well. In aerospace engineering, beams (curved and straight) are found in many areas of the plane or space vehicle. In addition, the whole wing of a plane is often modeled as a beam for some preliminary analysis. Innumerable other examples in these and other industries of beams exist.

This chapter is concerned with the development of the fundamental equations for the mechanics of laminated composite beams. Two classes of theories are developed for laminated beams. In the first class of theories, effects of shear deformation and rotary inertia are neglected. This class of theories will be referred to as thin beam theories or classical beam theories (CBT). This is typically accurate for thin beams and is less accurate for thicker beams. In the second class of theories, shear deformation and rotary inertia effects are considered. This class of theories will be referred to as thick beam theory or shear deformation beam theory (SDBT).

This chapter can be mainly divided into two sections. First, static analysis where deflection and stress analysis for composite beams are performed and second dynamic analysis where natural frequencies of them are assessed. In many applications deflection of the beam plays a key role in the structure. For example, if an aircraft wig tip deflection becomes high, in addition to potential structural failure, it may deteriorate the wing aerodynamic performance. In this and other applications, beams can be subjected to dynamic loads. Imbalance in driveline shafts, combustion in crank shaft applications, wind on a bridge or a

structure, earthquake loading on a bridge or a structure, impact load when a vehicle goes over a pump are all examples of possible dynamic loadings that beam structures can be exposed to. All of these loads and others can excite the vibration of the beam structure. This can cause durability concerns or discomfort because of the resulting noise and vibration.

2. Stiffness of beams

Figure 1 shows a free body diagram of a differential beam element. Beams are considered as one dimensional (1D) load carriers and the main parameter for analysis of load carrier structures is stiffness.

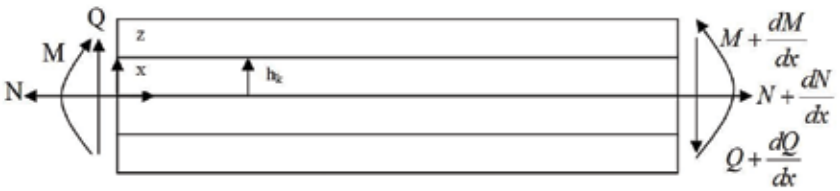

Fig. 1. Free body diagram of a differential beam element

In general for composite laminates, stiffness matrix composed of ABD parameters is used to relate the stress resultants to strains.

$$\begin{bmatrix} N_x \\ N_y \\ N_{xy} \\ M_x \\ M_y \\ M_{xy} \end{bmatrix} = \begin{bmatrix} A_{11} & A_{12} & A_{16} & B_{11} & B_{12} & B_{16} \\ A_{12} & A_{22} & A_{26} & B_{12} & B_{22} & B_{26} \\ A_{16} & A_{26} & A_{66} & B_{16} & B_{26} & B_{66} \\ B_{11} & B_{12} & B_{16} & D_{11} & D_{12} & D_{16} \\ B_{12} & B_{22} & B_{26} & D_{12} & D_{22} & D_{26} \\ B_{16} & B_{26} & B_{66} & D_{16} & D_{26} & D_{66} \end{bmatrix} \begin{bmatrix} \varepsilon_{0x} \\ \varepsilon_{0y} \\ \gamma_{xy} \\ \kappa_x \\ \kappa_y \\ 2\kappa_{xy} \end{bmatrix} \tag{1}$$

where regular ABD stiffness parameters for beams are defined as (Qatu, 2004).

$$A_{ij} = \sum_{k=1}^{N} b\overline{Q}_{ij}^{k}\left[\left(h_k - h_{k-1}\right)\right] \tag{2}$$

$$B_{ij} = \sum_{k=1}^{N} b\overline{Q}_{ij}^{k}\frac{\left(h_k^2 - h_{k-1}^2\right)}{2} \tag{3}$$

$$D_{ij} = \sum_{k=1}^{N} b\overline{Q}_{ij}^{k}\frac{\left(h_k^3 - h_{k-1}^3\right)}{3} \tag{4}$$

Note here that the above definitions are different from those used for general laminate analysis in the literature. The beam width is included in the definitions of these terms, while it is customary to leave this term out in general laminate analysis. In 1D analysis of beams, as we will see later, only parameters in x direction are considered and other parameters are

ignored. So instead of 6X6 stiffness matrix for general laminate analysis we will have a 2X2 matrix for CBT and 3X3 matrix for SDBT. This formulation has the disadvantage of not accounting for any coupling. To overcome this problem, we propose that instead of normal definition of A_{11}, B_{11}, and D_{11}, one can use equivalent stiffness parameters that include couplings. That is why we will deal with stiffness parameters first.

2.1 Equivalent modulus

One approach for finding equivalent modulus for the whole laminate was proposed by finding the inverse of the ABD matrix (J matrix) (Kaw, 2005). The laminate modulus of elasticity is then defined as

$$E = \frac{b}{I J_{44}} \qquad J = [ABD]^{-1} \tag{5}$$

where J_{44} is the term in 4th row and 4th column of the inverse of the ABD matrix of the laminate and I is the moment of inertia. If one wants to use this approach for finding parameters A_{11}, B_{11}, and D_{11} the following formulas derived by authors should be used.

$$A_{11} = \frac{b}{J_{11}} \tag{6}$$

$$B_{11} = \frac{1}{J_{14}} \tag{7}$$

$$D_{11} = \frac{b}{J_{44}} \tag{8}$$

2.2 Equivalent stiffness parameters by Rios and Chan

Another approach using compliance matrix can be done by the following formulation (Rios and Chan, 2010).

$$A_{11} = \frac{1}{a_{11} - \frac{b_{11}^2}{d_{11}}} \tag{9}$$

$$B_{11} = \frac{1}{b_{11} - \frac{a_{11} d_{11}}{b_{11}}} \tag{10}$$

$$D_{11} = \frac{1}{d_{11} - \frac{b_{11}^2}{a_{11}}} \tag{11}$$

where a_{11}, b_{11}, and d_{11} are relevant compliance matrix terms. Similar to previous section we have $a_{11}=J_{11}$, $b_{11}=J_{14}$, $d_{11}=J_{44}$.

2.3 Equivalent stiffness parameters by Vinson and Sierakowski

Finding equivalent modulus of elasticity of each lamina and using normal definition of ABDs leads to the following formulation (Vinson and Sierakowski, 2002).

$$\frac{1}{E_x^k}=\frac{\cos^4(\theta_k)}{E_{11}}+\left(\frac{1}{G_{12}}-\frac{2\upsilon_{12}}{E_{11}}\right)\cos^2(\theta_k)\sin^2(\theta_k)+\frac{\sin^4(\theta_k)}{E_{22}} \tag{12}$$

Equivalent A_{11}, B_{11} and D_{11} using these formulas would be

$$A_{11}=\sum_{k=1}^{N} bE_x^k\left(h_k-h_{k-1}\right) \tag{13}$$

$$B_{11}=\sum_{k=1}^{N} bE_x^k\frac{\left(h_k^2-h_{k-1}^2\right)}{2} \tag{14}$$

$$D_{11}=\sum_{k=1}^{N} bE_x^k\frac{\left(h_k^3-h_{k-1}^3\right)}{3} \tag{15}$$

3. Static analysis

In static analysis section we will consider composite beams loaded with classical loading condition and derive differential equations for displacements. Those equations would be solved with classical boundary conditions of both ends simply supported and both ends clamped. We will use the static analyses to find deflection and stress of composite beams under both CBT and SDBT.

3.1 Classical beam theory

Applying the traditional assumptions for thin beams (normals to the beam midsurface remain straight and normal, both rotary inertia and shear deformation are neglected), strains and curvature change at the middle surface are: (Qatu, 1993, 2004)

$$\varepsilon_0=\frac{\partial u_0}{\partial x},\ \kappa=-\frac{\partial^2 w}{\partial x^2} \tag{16}$$

where u, w are displacements in x and z directions, respectively. Normal strain at any point would be

$$\varepsilon=\varepsilon_0+z\kappa \tag{17}$$

Force and moment resultants are calculated using

$$\begin{bmatrix} N \\ M \end{bmatrix}=\begin{bmatrix} A_{11} & B_{11} \\ B_{11} & D_{11} \end{bmatrix}\begin{bmatrix} \varepsilon_0 \\ \kappa \end{bmatrix} \tag{18}$$

The equations of motion are

$$\frac{\partial^2 M}{\partial x^2}=-p_z \tag{19}$$

$$\frac{\partial N}{\partial x} = -p_x \tag{20}$$

where p_x and p_z are external forces per unit length in x and z direction, respectively. The potential strain energy stored in a beam during elastic deformation is

$$PE = \frac{1}{2}\int_V \sigma\varepsilon dV = \frac{1}{2}\int_0^l \left(N\varepsilon_0 + M\kappa\right) dx \tag{21}$$

writing this expression for every lamina and summing for all laminate we have

$$PE = \frac{1}{2}\int_0^l \left(A_{11}\left(\varepsilon_0\right)^2 + 2B_{11}\varepsilon_0\kappa + D_{11}\kappa^2\right) dx \tag{22}$$

substituting kinematic relations to equation (22) it will become

$$PE = \frac{1}{2}\int_0^l \left(A_{11}\left(\frac{\partial u_0}{\partial x}\right)^2 + 2B_{11}\left(\frac{\partial u_0}{\partial x}\right)\left(-\frac{\partial^2 w}{\partial x^2}\right) + D_{11}\left(-\frac{\partial^2 w}{\partial x^2}\right)^2\right) dx \tag{23}$$

The work done by external forces on beam would be

$$W = \frac{1}{2}\int_0^l \left(p_x u_0 + p_z w\right) dx \tag{24}$$

The kinetic energy for each lamina is

$$KE = \frac{1}{2} b\rho^{(k)} \int_0^l \int_{z_{k-1}}^{z_k} \left(\left(\frac{\partial u_0}{\partial t}\right)^2 + \left(\frac{\partial w}{\partial t}\right)^2\right) dx \tag{25}$$

where $\rho^{(k)}$ is the lamina density per unit volume, and t is time. The kinetic energy of the entire beam is

$$KE = \frac{I_1}{2}\int_0^l \left(\left(\frac{\partial u_0}{\partial t}\right)^2 + \left(\frac{\partial w}{\partial t}\right)^2\right) dx \tag{26}$$

where I_1 is the average mass density of the beam per unit length. These energy expressions can be used in an energy-based analysis such as finite element or Ritz analyses.

3.1.1 Euler approach

Inserting displacement relations in equations of motion will result in (Vinson and Sierakowski, 2002)

$$A_{11}\frac{\partial^2 u}{\partial x^2} - B_{11}\frac{\partial^3 w}{\partial x^3} + p_x(x) = 0 \tag{27}$$

$$B_{11}\frac{\partial^3 u}{\partial x^3} - D_{11}\frac{\partial^4 w}{\partial x^4} + p_z(x) = 0 \tag{28}$$

Solving these two equations for u and w will result in the following differential equations.

$$\left[\frac{A_{11}D_{11}-B_{11}^2}{A_{11}}\right]\frac{\partial^4 w}{\partial x^4}=p_z(x)-\frac{B_{11}}{A_{11}}\frac{\partial p_x(x)}{\partial x} \tag{29}$$

$$\left[\frac{A_{11}D_{11}-B_{11}^2}{B_{11}}\right]\frac{\partial^3 u_0}{\partial x^3}=p_z(x)-\frac{D_{11}}{B_{11}}\frac{\partial p_x(x)}{\partial x} \tag{30}$$

Stress in the axial direction in any lamina can be found by the following equation

$$\sigma_x=Q_{11}\left(\varepsilon_0+z\kappa\right)=Q_{11}\left(\frac{\partial u_0}{\partial x}-z\frac{\partial^2 w}{\partial x^2}\right) \tag{31}$$

Different loading and boundary conditions can be applied to these equations in order to find equations for u and w. These boundary conditions are

Simply supported: $w=0,\ M=0$

Clamped: $w=0,\ \frac{dw}{dx}=0$

Free: $V=0,\ M=0$

where V and M are shear force and bending moment and are linearly dependent on third and second derivative of w respectively. Here, we propose solution for both ends simply supported and both ends clamped with constant loading q_0. The reader is urged to apply other boundary conditions and find the equations for deflection. For specific case of simply supported boundary conditions at both ends and assuming $u_0(0)=0$ we have

$$\left[\frac{A_{11}D_{11}-B_{11}^2}{A_{11}}\right]w(x)=\frac{q_0 l^4}{24}\left[\left(\frac{x}{l}\right)^4-2\left(\frac{x}{l}\right)^3+\left(\frac{x}{l}\right)\right] \tag{32}$$

$$\left[\frac{A_{11}D_{11}-B_{11}^2}{B_{11}}\right]u_0(x)=\frac{q_0 l^3}{24}\left[4\left(\frac{x}{l}\right)^3-6\left(\frac{x}{l}\right)^2\right] \tag{33}$$

$$\sigma_x=\frac{q_0 l^2}{2\left(A_{11}D_{11}-B_{11}^2\right)}\left[\left(\frac{x}{l}\right)^2-\left(\frac{x}{l}\right)\right]Q_{11}\left(B_{11}-zA_{11}\right) \tag{34}$$

$$\tau_{xz}=\frac{1}{b}\int_h^z\frac{\partial\sigma_x}{\partial x}dz=\frac{q_0 l}{2b\left(A_{11}D_{11}-B_{11}^2\right)}\left[2\left(\frac{x}{l}\right)-1\right]\int_h^z Q_{11}\left(B_{11}-zA_{11}\right)dz \tag{35}$$

For clamped boundary conditions at both ends we have

$$\left[\frac{A_{11}D_{11}-B_{11}^2}{A_{11}}\right]w(x)=\frac{q_0 l^4}{24}\left[\left(\frac{x}{l}\right)^4-2\left(\frac{x}{l}\right)^3+\left(\frac{x}{l}\right)^2\right] \tag{36}$$

$$\left[\frac{A_{11}D_{11}-B_{11}^2}{B_{11}}\right]u_0(x)=\frac{q_0 l^3}{24}\left[4\left(\frac{x}{l}\right)^3-6\left(\frac{x}{l}\right)^2+2\left(\frac{x}{l}\right)\right] \tag{37}$$

$$\sigma_x = \frac{q_0 l^2}{2\left(A_{11}D_{11} - B_{11}^2\right)}\left[\left(\frac{x}{l}\right)^2 - \left(\frac{x}{l}\right) + \frac{1}{6}\right] Q_{11}\left(B_{11} - zA_{11}\right) \tag{38}$$

$$\tau_{xz} = \frac{1}{b}\int_h^z \frac{\partial \sigma_x}{\partial x} dz = \frac{q_0 l}{2b\left(A_{11}D_{11} - B_{11}^2\right)}\left[2\left(\frac{x}{l}\right) - 1\right] \int_h^z Q_{11}\left(B_{11} - zA_{11}\right) dz \tag{39}$$

One should note that for simply supported boundary condition the maximum moment and consequently maximum stress occurs at middle of the beam, while for the clamped case maximum stress occurs at two ends.

3.1.2 Matrix approach

Inserting the strain and curvature relations in the force and moment resultants equations and using those in the equations of motion, one can express the equations of motion in terms of displacements. Expressing those equations in matrix form we have

$$\begin{bmatrix} L_{11} & L_{12} \\ L_{21} & L_{22} \end{bmatrix} \begin{bmatrix} u_0 \\ w_0 \end{bmatrix} + \begin{bmatrix} p_x \\ -p_z \end{bmatrix} = \begin{bmatrix} 0 \\ 0 \end{bmatrix} \tag{40}$$

where $L_{11} = A_{11}\dfrac{\partial^2}{\partial x^2}$, $L_{22} = D_{11}\dfrac{\partial^4}{\partial x^4}$, $L_{12} = L_{21} = -B_{11}\dfrac{\partial^3}{\partial x^3}$.

The beam is supposed to have simply supported boundary condition. So we have on x=0, a.

$$w_0 = N_x = M_x = 0 \tag{41}$$

The above equations of motion as well boundary terms are satisfied if one chooses displacements functions as

$$\left[u, w\right] = \sum_{m=1}^{M} \left[A_m \cos(\alpha_m x), C_m \sin(\alpha_m x)\right] \tag{42}$$

where $\alpha_m = m\pi / a$ and a is the beam length. The external forces can be expanded in a Fourier series in x

$$\left[p_x, p_z\right] = \sum_{m=1}^{M} \left[p_{xm} \sin\left(\alpha_m x\right), p_{zm} \cos\left(\alpha_m x\right)\right] \tag{43}$$

Substituting these equations in the equations of motion we have the characteristic equation

$$\begin{bmatrix} C_{11} & C_{12} \\ C_{21} & C_{22} \end{bmatrix} \begin{bmatrix} A_m \\ C_m \end{bmatrix} + \begin{bmatrix} p_{xm} \\ -p_{zm} \end{bmatrix} = 0 \tag{44}$$

$$\begin{bmatrix} A_m \\ C_m \end{bmatrix} = \begin{bmatrix} C_{11} & C_{12} \\ C_{21} & C_{22} \end{bmatrix}^{-1} \begin{bmatrix} -p_{xm} \\ p_{zm} \end{bmatrix} \tag{45}$$

where $C_{11} = -\alpha_m^2 A_{11}$, $C_{22} = \alpha_m^4 D_{11}$, $C_{21} = -C_{12} = \alpha_m^3 B_{11}$. Stress in the axial direction would be found using the following procedure.

$$\begin{bmatrix} \varepsilon_0 \\ \kappa \end{bmatrix} = \begin{bmatrix} A_{11} & B_{11} \\ B_{11} & D_{11} \end{bmatrix}^{-1} \begin{bmatrix} N \\ M \end{bmatrix} \tag{46}$$

$$\sigma_x = Q_{11}\left(\varepsilon_0 + z\kappa\right) \tag{47}$$

3.2 Shear deformation beam theory

The inclusion of shear deformation in the analysis of beams was first made in early years of twentieth century (Timoshenko, 1921). A lot of models have been proposed based on this theory since then. In this chapter a first order shear deformation theory (FSDT) approach is presented to account for shear deformation and rotary inertia (Qatu, 1993, 2004).

$$u = u_0 + z\psi,\ w = w_0 \tag{48}$$

Strains and curvature changes at the middle surface are:

$$\varepsilon_0 = \frac{\partial u_0}{\partial x},\ \kappa = \frac{\partial \psi}{\partial x},\ \gamma = \frac{\partial w}{\partial x} + \psi \tag{49}$$

where ε_0 is middle surface strain, γ is the shear strain at the neutral axis and ψ is the rotation of a line element perpendicular to the original direction. Normal strain at any point can be found using equation 17. Force and moment resultants as well as shear forces are calculated using

$$\begin{bmatrix} N \\ M \\ Q \end{bmatrix} = \begin{bmatrix} A_{11} & B_{11} & 0 \\ B_{11} & D_{11} & 0 \\ 0 & 0 & A_{55} \end{bmatrix} \begin{bmatrix} \varepsilon_0 \\ \kappa \\ \gamma \end{bmatrix} \tag{50}$$

where for A_{55} we have (Vinson and Sierakowski, 2002).

$$A_{55} = \frac{5}{4}\sum_{k=1}^{N} b\overline{Q}_{55}^{k}\left[\left(h_k - h_{k-1}\right) - \frac{4}{3h^2}\left(h_k^3 - h_{k-1}^3\right)\right] \tag{51}$$

The equations of motion considering rotary inertia and shear deformation would be

$$\frac{\partial N}{\partial x} = -p_x \tag{52}$$

$$\frac{\partial Q}{\partial x} = p_z \tag{53}$$

$$\frac{\partial M}{\partial x} - Q = 0 \tag{54}$$

The potential strain energy stored in a beam during elastic deformation is

$$PE = \frac{1}{2}\int_V \sigma\varepsilon dV = \frac{1}{2}\int_0^l \left(N\varepsilon_0 + M\frac{\partial \psi}{\partial x} + Q\gamma \right) dx \tag{55}$$

Writing this expression for every lamina and summing for all laminate we have (Vinson and Sierakowski, 2002)

$$PE = \frac{1}{2}\int_0^l \left(A_{11}\left(\varepsilon_0\right)^2 + 2B_{11}\varepsilon_0\kappa + D_{11}\kappa^2 + A_{55}\gamma^2 \right) dx \tag{56}$$

substituting kinematic relations to equation (56) it will become

$$PE = \frac{1}{2}\int_0^l \left(A_{11}\left(\frac{\partial u_0}{\partial x}\right)^2 + 2B_{11}\left(\frac{\partial u_0}{\partial x}\right)\left(\frac{\partial \psi}{\partial x}\right) + D_{11}\left(\frac{\partial \psi}{\partial x}\right)^2 + A_{55}\left(\psi + \frac{\partial w}{\partial x}\right)^2 \right) dx \tag{57}$$

The work done by external forces on beam is found by equation (24). Finding the kinetic energy for each layer and then summing for all layers yield the kinetic energy of the entire beam.

$$KE = \int_0^l \left(I_1\left(\frac{\partial u_0}{\partial t}\right)^2 + I_1\left(\frac{\partial w}{\partial t}\right)^2 + 2I_2\left(\frac{\partial u_0}{\partial t}\right)\left(\frac{\partial \psi}{\partial t}\right) + I_3\left(\frac{\partial \psi}{\partial t}\right)^2 \right) dx \tag{58}$$

These energy expressions can be used in an energy-based analysis such as finite element or Ritz analyses.

3.2.1 Euler approach

Inserting displacement relations in equations of motion will result in

$$A_{11}\frac{\partial^2 u_0}{\partial x^2} + B_{11}\frac{\partial^2 \psi}{\partial x^2} + p_x(x) = 0 \tag{59}$$

$$A_{55}\left(\frac{\partial \psi}{\partial x} + \frac{\partial^2 w}{\partial x^2}\right) + p_z\left(x\right) = 0 \tag{60}$$

$$B_{11}\frac{\partial^2 u}{\partial x^2} + D_{11}\frac{\partial^2 \psi}{\partial x^2} - A_{55}\left(\psi + \frac{dw}{dx}\right) = 0 \tag{61}$$

Taking second derivative of equation (60) and solving for $\frac{\partial^3 \psi}{\partial x^3}$ from equations (59, 61) will result in following equations.

$$\frac{\partial^4 w}{\partial x^4} = \left[\frac{A_{11}}{A_{11}D_{11} - B_{11}^2}\right] p_z(x) - \frac{1}{A_{55}}\left[\frac{\partial^2 p_z(x)}{\partial x^2}\right] - \left[\frac{B_{11}}{A_{11}D_{11} - B_{11}^2}\right]\frac{\partial p_x(x)}{\partial x} \tag{62}$$

$$\frac{\partial^3 u_0}{\partial x^3} = \left[\frac{B_{11}}{A_{11}D_{11} - B_{11}^2}\right] p_z(x) - \frac{1}{A_{11}}\frac{\partial p_x(x)}{\partial x} \tag{63}$$

$$\frac{\partial^3 \psi}{\partial x^3} = \left[\frac{B_{11}}{A_{11}D_{11} - B_{11}^2}\right]\frac{\partial p_x(x)}{\partial x} - \left[\frac{A_{11}}{A_{11}D_{11} - B_{11}^2}\right] p_z(x) \tag{64}$$

For specific case of $p_z(x)=q_0$ with simply supported boundary conditions we have

$$w(x)=\frac{q_0 l^4}{24}\left(\frac{A_{11}}{A_{11}D_{11}-B_{11}^2}\right)\left[\left(\frac{x}{l}\right)^4-2\left(\frac{x}{l}\right)^3+\left(\frac{x}{l}\right)\right]+\frac{q_0 l^2}{2A_{55}}\left[\left(\frac{x}{l}\right)+\left(\frac{x}{l}\right)^2\right] \tag{65}$$

$$\psi(x)=\frac{q_0 l^3}{24}\left(\frac{A_{11}}{A_{11}D_{11}-B_{11}^2}\right)\left[1-4\left(\frac{x}{l}\right)^3+6\left(\frac{x}{l}\right)^2\right]+\frac{q_0 l}{2A_{55}} \tag{66}$$

$$\sigma_x=\frac{q_0 l^2}{2\left(A_{11}D_{11}-B_{11}^2\right)}\left[\left(\frac{x}{l}\right)^2-\left(\frac{x}{l}\right)\right]Q_{11}\left(B_{11}-zA_{11}\right)-\frac{2q_0 l^2 z}{A_{55}} \tag{67}$$

maximum deflection would occur at middle of the beam and it would be

$$w_{\max}=\frac{5q_0 l^4}{384}\left(\frac{A_{11}}{A_{11}D_{11}-B_{11}^2}\right)+\frac{q_0 l^2}{8A_{55}} \tag{68}$$

The first term in equation (68) is deflection due to bending and the second term is due to shear. For clamped boundary condition one can use the term due to bending from CBT analysis and add the term due to shear.

3.2.2 Matrix approach

Expressing equations of motion in terms of displacement we have in matrix form

$$\begin{bmatrix} L_{11} & L_{12} & L_{13} \\ L_{21} & L_{22} & L_{23} \\ L_{31} & L_{32} & L_{33} \end{bmatrix}\begin{bmatrix} u_0 \\ w_0 \\ \psi \end{bmatrix}+\begin{bmatrix} p_x \\ -p_z \\ 0 \end{bmatrix}=\begin{bmatrix} 0 \\ 0 \\ 0 \end{bmatrix} \tag{69}$$

where $L_{11}=A_{11}\frac{\partial^2}{\partial x^2}$, $L_{22}=-A_{55}\frac{\partial^2}{\partial x^2}$, $L_{33}=D_{11}\frac{\partial^2}{\partial x^2}-A_{55}$, $L_{13}=L_{31}=B_{11}\frac{\partial^2}{\partial x^2}$, $L_{23}=L_{32}=-A_{55}\frac{\partial}{\partial x}$, $L_{12}=L_{21}=0$. The following simply supported boundary conditions are used on x=0, a

$$w_0=N_x=\frac{\partial\psi}{\partial x}=0 \tag{70}$$

The above equations would be satisfied if

$$\left[u_0, w_0, \psi\right]=\sum_{m=1}^{m}\left[A_m\cos(\alpha_m x), C_m\sin(\alpha_m x), B_m\cos(\alpha_m x)\right] \tag{71}$$

Substituting these equations in the equations of motion we have the characteristic equation

$$\begin{bmatrix} A_m \\ C_m \\ B_m \end{bmatrix}=\begin{bmatrix} C_{11} & C_{12} & C_{13} \\ C_{12} & C_{22} & C_{23} \\ C_{13} & C_{23} & C_{33} \end{bmatrix}^{-1}\begin{bmatrix} -p_{xm} \\ p_{zm} \\ 0 \end{bmatrix} \tag{72}$$

where $C_{11} = -\alpha_m^2 A_{11}$, $C_{22} = \alpha_m^2 A_{55}$, $C_{33} = -\alpha_m^2 D_{11} - A_{55}$, $C_{31} = C_{13} = -\alpha_m^2 B_{11}$, $C_{23} = -C_{32} = A_{55}\alpha_m$, $C_{21} = C_{12} = 0$.

4. Dynamic analysis

To the knowledge of authors, there is no simple approach for dynamic analysis of composite beams considering all kinds of couplings. A review was conducted on advances in analysis of laminated beams and plates vibration and wave propagation (Kapania and Raciti, 1989. Another review was done on the published literature of vibrations of curved bars, beams, rings and arches of arbitrary shape which lie in a plane (Chidamparam and Leissa, 1993). Among FSDT works, some were validated for symmetric cross-ply laminates that have no coupling (Chandrashekhara et al., 1990; Krishnaswamy et al., 1992; Abramovich et al., 1994). In some other models, symmetric beams having fibers in one direction (only bending-twisting coupling) were considered (Teboub and Hajela, 1995; Banerjee 1995, 2001; Lee at al., 2004). Some FSDT models were validated for cross-ply laminates that have only bending-stretching coupling (Eisenberger et al. 1995; Qatu 1993, 2004).
Higher order shear deformation theories (HSDT) were also developed for composite beams to address issues of cross sectional warping and transverse normal strains. Some were validated for cross-ply laminates (Khdier and Reddy, 1997; Kant et al., 1998; Matsunaga, 2001; Subramanian, 2006). Other theories like zigzag theory (Kapuria et al. 2004) were used to satisfy continuity of transverse shear stress through the laminate and showed to be accurate for natural frequency calculations of beams with specific geometry and lay-up (symmetric or cross-ply laminates). Another theory was global-local higher order theory (Zhen and Wanji, 2008) that was validated for cross-ply laminates.
In this section, classic and FSDT beam models will be evaluated for their accuracy in a vibration analysis using different approaches for stiffness parameters calculation. Their results will be compared with those obtained using a 3D finite element model for different laminates (unidirectional, symmetric and asymmetric cross ply and symmetric and asymmetric angle-ply). The accurate model presented would then be verified for composite shafts.

4.1 Classical beam theory

Equations of motion for dynamic analysis of laminated beams would be

$$\frac{\partial^2 M}{\partial x^2} = I_1 \frac{\partial^2 w}{\partial t^2} - p_z \tag{73}$$

$$\frac{\partial N}{\partial x} = I_1 \frac{\partial^2 u}{\partial t^2} - p_x \tag{74}$$

where $I_1 = \sum_{k=1}^{N} b\rho^{(k)}\left(h_k - h_{k-1}\right)$. Expressing those equations in matrix form we have for free vibration

$$\begin{bmatrix} L_{11} & L_{12} \\ L_{21} & L_{22} \end{bmatrix} \begin{bmatrix} u_0 \\ w_0 \end{bmatrix} + \begin{bmatrix} -I_1 & 0 \\ 0 & I_1 \end{bmatrix} \frac{\partial^2}{\partial t^2} \begin{bmatrix} u_0 \\ w_0 \end{bmatrix} = \begin{bmatrix} 0 \\ 0 \end{bmatrix} \tag{75}$$

The equations of motion as well as simply supported boundary terms are satisfied if one chooses displacements as

$$[u,w]=\sum_{m=1}^{M}[A_m\cos(\alpha_m x),C_m\sin(\alpha_m x)]\sin(\omega t) \tag{76}$$

Substituting these equations in the equations of motion we have the characteristic equation

$$\begin{bmatrix}C_{11} & C_{12}\\ C_{21} & C_{22}\end{bmatrix}\begin{bmatrix}A_m\\ C_m\end{bmatrix}+\omega^2\begin{bmatrix}I_1 & 0\\ 0 & -I_1\end{bmatrix}\begin{bmatrix}A_m\\ C_m\end{bmatrix}+\begin{bmatrix}p_{xm}\\ -p_{zm}\end{bmatrix}=0 \tag{77}$$

The nontrivial solution for natural frequency can be found by setting the determinant of characteristic equation of matrix to zero.

One should note here that if the laminate is symmetric, the B_{11} term vanishes and the bending frequencies are totally decoupled from axial ones. As a result, the following well-known formula for the natural frequencies of a symmetrically laminated simply supported composite beam can be applied:

$$\omega_n=\left(\frac{n\pi}{\ell}\right)^2\sqrt{\frac{D_{11}}{\rho A}} \tag{78}$$

where ρ is density, ℓ is length and A is the cross section area of the beam. As we will see later it cannot be used for thick laminates and those that have any kind of coupling.

4.2 Shear deformation beam theory

The equations of motion considering rotary inertia and shear deformation would be (Qatu, 1993, 2004)

$$\frac{\partial N}{\partial x}=I_1\frac{\partial^2 u}{\partial t^2}+I_2\frac{\partial^2\psi}{\partial t^2}-p_x \tag{79}$$

$$-\frac{\partial Q}{\partial x}=p_z-I_1\frac{\partial^2 w}{\partial t^2} \tag{80}$$

$$\frac{\partial M}{\partial x}-Q=I_2\frac{\partial^2 u}{\partial t^2}+I_3\frac{\partial^2\psi}{\partial t^2} \tag{81}$$

where $(I_1,I_2,I_3)=\sum_{k=1}^{N}b\rho^{(k)}\left((h_k-h_{k-1}),\frac{1}{2}\left(h_k^2-h_{k-1}^2\right),\frac{1}{3}\left(h_k^3-h_{k-1}^3\right)\right)$. So by expressing equations of motion in terms of displacement we have in matrix form (for free vibration)

$$\begin{bmatrix}L_{11} & L_{12} & L_{13}\\ L_{21} & L_{22} & L_{23}\\ L_{31} & L_{32} & L_{33}\end{bmatrix}\begin{bmatrix}u_0\\ w_0\\ \psi\end{bmatrix}-\begin{bmatrix}I_1 & 0 & I_2\\ 0 & -I_1 & 0\\ I_2 & 0 & I_3\end{bmatrix}\frac{\partial^2}{\partial t^2}\begin{bmatrix}u_0\\ w_0\\ \psi\end{bmatrix}=\begin{bmatrix}0\\ 0\\ 0\end{bmatrix} \tag{82}$$

Equations of motion as long as simply supported boundary condition would be satisfied if

$$[u_0, w_0, \psi] = \sum_{m=1}^{M} [A_m \cos(\alpha_m x), C_m \sin(\alpha_m x), B_m \cos(\alpha_m x)] \sin(\omega t) \tag{83}$$

Substituting these equations in the equations of motion we have the characteristic equation

$$\begin{bmatrix} C_{11} & C_{12} & C_{13} \\ C_{12} & C_{22} & C_{23} \\ C_{13} & C_{23} & C_{33} \end{bmatrix} \begin{bmatrix} A_m \\ C_m \\ B_m \end{bmatrix} + \omega^2 \begin{bmatrix} I_1 & 0 & I_2 \\ 0 & -I_1 & 0 \\ I_2 & 0 & I_3 \end{bmatrix} \begin{bmatrix} A_m \\ C_m \\ B_m \end{bmatrix} + \begin{bmatrix} p_{xm} \\ -p_{zm} \\ 0 \end{bmatrix} = 0 \tag{84}$$

The nontrivial solution for natural frequency can be found by setting the determinant of characteristic equation matrix to zero.

5. Case studies

5.1 Rectangular beam

A rectangular cross section beam model having 1 m length, 0.025 m width, and 0.05 m height was considered and modeled in ANSYS® finite element code. Solid elements were used to apply 3D elasticity. A convergence study was done and the convergent model had 8 elements in thickness, 4 elements in width direction and 160 elements in length direction. Ratio of length to height of 20 was selected to be at the border of thin beams. Figure 2 shows the model.

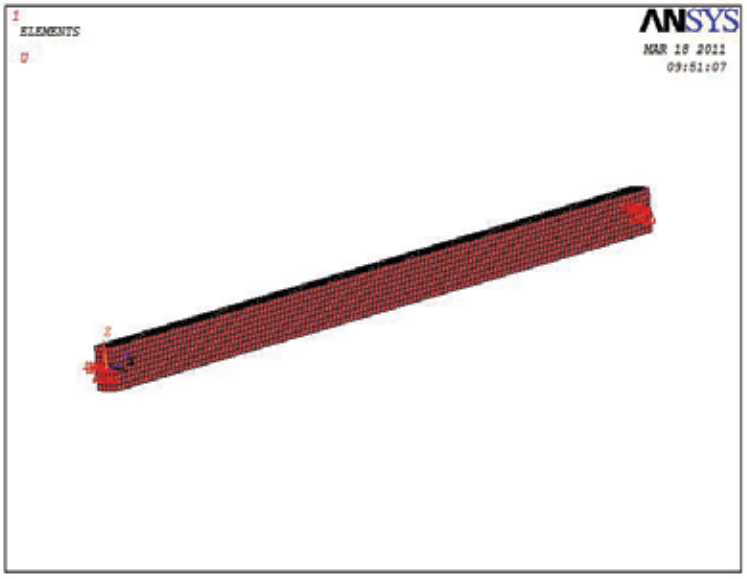

Fig. 2. 3D finite element model in ANSYS

The simply supported boundary condition was modeled by applying constraint on z direction at middle line of end faces. The material properties are E_1 = 138 GPa, E_2 =8.96 GPa, υ_{12}=0.3, G_{12}= 7.1 GPa, ρ =1580 kg/m^3.

Both static and modal analyses are done and the results of CBT and SDBT with different stiffness parameters are compared with 3D FEM in order to find the most accurate model.

5.1.1 Static analysis

A load of 250000 N/m were applied to the beam and the resulting deflection for cross-ply and angle-ply laminates were assessed using different models. The simply supported beam maximum deflection using Euler approach and matrix approach are given in Tables 1 and 2. Maximum normal stress is also presented in Table 3. Since the stress due to shear is low the results for CBT is not presented. The maximum deflection and stress in clamped beam are presented in Tables 4 and 5.

Laminate	CBT				SDBT				FEM
	(S_{11})	$(S_{11})_{VS}$	$(S_{11})_{Kaw}$	$(S_{11})_{Chan}$	(S_{11})	$(S_{11})_{VS}$	$(S_{11})_{Kaw}$	$(S_{11})_{Chan}$	3D
$[0]_4$	0.0901	0.0906	0.0906	0.0906	0.0988	0.0993	0.0993	0.0993	0.1000
$[0/90]_s$	0.1019	0.1026	0.1022	0.1022	0.1107	0.1113	0.1109	0.1109	0.1116
$[45]_4$	0.2753	0.7980	0.7980	0.7980	0.2840	0.8067	0.8067	0.8067	0.7824

Table 1. Maximum deflection of a SS beam (Euler aproach)

Laminate	CBT				SDBT				FEM
	(S_{11})	$(S_{11})_{VS}$	$(S_{11})_{Kaw}$	$(S_{11})_{Chan}$	(S_{11})	$(S_{11})_{VS}$	$(S_{11})_{Kaw}$	$(S_{11})_{Chan}$	3D
$[0]_4$	0.0908	0.0913	NA*	0.0913	0.1002	0.1008	NA	0.1008	0.1000
$[0/90]_s$	0.1028	0.1034	NA	0.1031	0.1123	0.1129	NA	0.1125	0.1116
$[45]_4$	0.2776	0.8046	NA	0.8046	0.2870	0.8140	NA	0.8140	0.7824

* Ill conditioning observed

Table 2. Maximum deflection of a SS beam (Matrix aproach)

Laminate	Maximum Stress			
	(S_{11})	$(S_{11})_{VS}$	matrix	FEM
$[0]_4$	3.000E+08	3.000E+08	3.000E+08	3.04E+08
$[0/90]_s$	3.397E+08	3.397E+08	3.397E+08	3.42E+08
$[45]_4$	3.000E+08	3.000E+08	3.000E+08	3.12E+08

Table 3. Maximum axial stress of a SS beam (at middle point)

Laminate	CBT				SDBT				FEM
	(S_{11})	$(S_{11})_{VS}$	$(S_{11})_{Kaw}$	$(S_{11})_{Chan}$	(S_{11})	$(S_{11})_{VS}$	$(S_{11})_{Kaw}$	$(S_{11})_{Chan}$	3D
$[0]_4$	0.01801	0.01812	0.01812	0.01812	0.02673	0.02684	0.02684	0.02684	0.02658
$[0/90]_s$	0.02039	0.02051	0.02044	0.02044	0.02911	0.02923	0.02916	0.02916	0.0286
$[45]_4$	0.05506	0.1596	0.1596	0.1596	0.06378	0.1683	0.1683	0.1683	0.1654

Table 4. Maximum deflection of a clamped beam (Euler aproach)

Laminate	Maximum Stress			
	(S_{11})	$(S_{11})_{VS}$	matrix	FEM
$[0]_4$	1.000E+08	1.00E+08	1.000E+08	1.00E+08
$[0/90]_s$	1.132E+08	1.132E+08	1.132E+08	1.16E+08
$[45]_4$	1.000E+08	1.00E+08	1.000E+08	1.00E+08

Table 5. Axial stress at middle of a clamped beam

The results show that Euler and matrix approaches have very close results. In general, using SDBT along normal ABD parameters can cause problems in laminates where coupling exists. However using equivalent ABDs from Vinson and Sierakowski or Chan's formulation one can get the most accurate results for deflection. This formulation is valid for any laminate having bending-twisting coupling.

5.1.2 Dynamic analysis

Different approaches for calculating the natural frequencies of the first 5 modes were evaluated. Five different stacking sequences were selected to cover different kinds of composite beams. These include unidirectional, symmetric cross-ply, asymmetric cross-ply, angle-ply and general laminates. The results are given in Table 6.

The results show that the classic beam model using normal ABD parameters is only valid for 1st mode of cross-ply laminates. The effective length becomes less on higher modes and the thin beam assumption no longer applies leading to inaccurate results. Although the $[45]_4$ laminate is symmetric; it has bending twisting coupling and using the normal ABD formulation leads to inaccurate results. The equivalent ABDs by equivalent stiffness parameters improve the classic approach for unsymmtric laminates but still not accurate enough for higher modes since the shear deformation is not included.

Using FSDT approach for thick beams (Qatu, 1993, 2004) along Vinson and Sierakowski equivalent modulus of elasticity for calculation of ABD parameters (Eqs. 13-15) one can reach accurate results for higher modes. This approach does not have coupling problems and accurate results for all laminate is achieved. The overall range of error is about 1 percent. The other equivalent parameters defined by compliance matrix are not as accurate as Vinson and Sierakowski and even do not have real results in some cases.

5.2 Tubular beam

Experimental results of a tubular boron/epoxy beam (Zinberg and Symonds, 1970) are used in this section to verify the accuracy of the model for tubular cross section. The laminate was $[90/45/-45/0_6/90]$ from inner to outer layers. The following equations were used for stiffness parameters.

$$A_{11} = \pi \sum_{k=1}^{N} E_x^k \left[\left(r_k^2 - r_{k-1}^2 \right) \right] \tag{85}$$

$$D_{11} = \frac{\pi}{4} \sum_{k=1}^{N} E_x^k \left[\left(r_k^4 - r_{k-1}^4 \right) \right] \tag{86}$$

$[0_4]$									
n	CBT				SDBT				FEM
	$(S_{11})^*$	$(S_{11})_{VS}$	$(S_{11})_{Kaw}$	$(S_{11})_{Chan}$	(S_{11})	$(S_{11})_{VS}$	$(S_{11})_{Kaw}$	$(S_{11})_{Chan}$	3D
1	9.898	9.869	9.869	9.869	9.431	9.406	9.406	9.406	9.373
2	39.593	39.477	39.477	39.477	33.413	33.343	33.343	33.343	32.978
3	89.084	88.824	88.824	88.824	64.529	64.428	64.428	64.428	63.28
4	158.372	157.909	157.909	157.909	98.109	97.996	97.996	97.996	95.77
5	247.457	246.733	246.733	246.733	132.196	132.082	132.082	132.082	128.67
$[0/90]_s$									
n	CBT				SDBT				FEM
	(S_{11})	$(S_{11})_{VS}$	$(S_{11})_{Kaw}$	$(S_{11})_{Chan}$	(S_{11})	$(S_{11})_{VS}$	$(S_{11})_{Kaw}$	$(S_{11})_{Chan}$	3D
1	9.302	9.275	9.291	9.291	8.910	8.886	8.901	8.901	8.873
2	37.207	37.098	37.163	37.163	31.931	31.861	31.903	31.903	31.651
3	83.716	83.472	83.618	83.618	62.369	62.266	62.327	62.327	61.51
4	148.829	148.394	148.653	148.653	95.659	95.540	95.611	95.611	93.91
5	232.546	231.865	232.271	232.271	129.705	129.583	129.656	129.656	126.88
$[0_2/90_2]$									
n	CBT				SDBT				FEM
	(S_{11})	$(S_{11})_{VS}$	$(S_{11})_{Kaw}$	$(S_{11})_{Chan}$	(S_{11})	$(S_{11})_{VS}$	$(S_{11})_{Kaw}$	$(S_{11})_{Chan}$	3D
1	4.688	4.674	NA	4.680	4.637	4.624	NA	4.630	4.609
2	18.718	18.663	NA	18.688	17.950	17.901	NA	17.924	17.651
3	41.990	41.867	NA	41.924	38.413	38.319	NA	38.362	37.251
4	74.337	74.120	NA	74.219	64.164	64.025	NA	64.088	61.354
5	115.526	115.188	NA	115.343	93.493	93.316	NA	93.397	88.302
$[45_4]$									
n	CBT				SDBT				FEM
	(S_{11})	$(S_{11})_{VS}$	$(S_{11})_{Kaw}$	$(S_{11})_{Chan}$	(S_{11})	$(S_{11})_{VS}$	$(S_{11})_{Kaw}$	$(S_{11})_{Chan}$	3D
1	5.6613	3.3251	4.5402	4.5402	5.5659	3.3033	4.4890	4.4890	3.3540
2	22.6450	18.1610	13.3005	18.1610	21.2317	12.9626	17.3840	17.3840	12.970
3	50.9513	40.8622	29.9262	40.8622	44.5592	28.3035	37.2377	37.2377	28.316
4	90.5801	72.6439	53.2021	72.6439	72.9229	48.4101	62.2926	62.2926	48.321
5	141.5314	113.5062	83.1283	113.5062	104.2553	72.3163	90.9410	90.9410	71.93
$[30_2/60_2]$									
n	CBT				SDBT				FEM
	(S_{11})	$(S_{11})_{VS}$	$(S_{11})_{Kaw}$	$(S_{11})_{Chan}$	(S_{11})	$(S_{11})_{VS}$	$(S_{11})_{Kaw}$	$(S_{11})_{Chan}$	3D
1	5.1433	3.4403	NA	4.8010	5.0735	3.4173	NA	4.7449	3.4830
2	20.5549	13.7558	NA	19.1791	19.5074	13.3998	NA	18.3329	13.458
3	46.1795	30.9295	NA	43.0585	41.3688	29.2239	NA	39.1346	29.222
4	81.9230	54.9322	NA	76.3072	68.4318	49.9103	NA	65.1941	49.857
5	127.6498	85.7212	NA	118.7286	98.7990	74.4320	NA	94.7571	73.97

Table 6. Nondimensional natural frequencies $\Omega = \omega a^2 \sqrt{12\rho / E_1 h^2}$ of rectangular simply supported beams. a/h = 20, b/h =0.5, Graphite/Epoxy, E_1/E_2 = 15.4, G_{12}/E_2 = 0.79, υ_{12} = 0.3 (subscript stands for formulation in deriving ABDs)

A number of researchers have worked on this beam with different beam and shell models and their results are shown in Table 7.

Author	Method used	Frequency (Hz)
Zinberg, Symonds, 1970	Measured experimentally	91.67
dos Reis et al., 1987	Bernoulli–Euler beam theory. Stiffness determined by shell finite elements	82.37
Kim and Bert, 1993	Sanders shell theory	97.87
	Donnell shallow shell theory	106.65
Bert and Kim, 1995	Bresse–Timoshenko beam theory	96.47
Singh and Gupta, 1996	Effective Modulus Beam Theory	95.78
Chang et al. 2004	Continuum based Timoshenko Beam	96.03
Qatu and Iqbal, 2010	Finite element analysis using ABAQUS	95.4
	Euler–Bernoulli beam theory	102.47
present study	Finite element analysis using ANSYS	95.89
	CBT using V-S	96.12
	SDBT using V-S	94.71

Table 7. Tubular Boron-epoxy beam fundamental natural frequencies (Hz) by different authors (E_{11} = 211 GPa, E_{22} = 24 GPa, $G_{12} = G_{13} = G_{23}$ = 6.9 GPa, υ = 0.36, density = 1967 kg/m^3), length = 2470 mm, mean diameter = 126.9 mm, thickness = 1.321 mm. (90, 45, -45,0,0,0,0,0,0,90) laminate (from inner to outer)

The results show that most of the models can predict the natural frequency of this beam with good accuracy. Only the models by dos Reis et al. predicted results that are far from those obtained by experiment. However the FSDT used in this paper is the most accurate model for this case.
The effect of ply orientation on reduction of stiffness and consequently natural frequency of a graphite-epoxy tube is presented in Table 8 (Bert and Kim, 1995).

Theory	Lamination angle						
	0	15	30	45	60	75	90
Sanders Shell	92.12	72.75	50.13	39.77	35.33	33.67	33.28
Bernoulli-Euler	107.08	89.88	71.15	52.85	38.20	31.42	30.22
Bresse-Timoshenko	101.20	86.82	69.95	52.38	37.97	32.90	30.05
Present FEM analysis	100.28	68.80	45.51	35.90	31.96	30.57	30.27
Present CBT approach	108.42	71.12	46.05	36.15	32.17	30.78	30.50
Present SDBT approach	104.43	70.50	45.91	36.06	32.09	30.70	30.36

Table 8. Effect of lamination angle on fundamental natural frequencies of tubular a graphite-epoxy beam. (E_{11} = 139 GPa, E_{22} = 11 GPa, $G_{12} = G_{13}$ = 6.05 GPa, G_{23} = 3.78 GPa, ν = 0.313, density = 1478 kg/m^3)

These results are for the first natural frequency of a graphite epoxy tubular beam with the same geometry of the previous one. Results of the present CBT, SDBT and FEM using shell elements are presented.
Results show a good agreement between this study and the previous ones. It shows the decrease in natural frequency by lowering stiffness and also bending twisting coupling.

6. Conclusion

Different approaches for static and dynamic analysis of composite beams were proposed and a modified FSDT model that accounts for various laminate couplings and shear deformation and rotary inertia was validated. The method was verified using 3D FEM model. The results showed good accuracy of the model for rectangular beams in static analysis for laminates having bending-twisting coupling and in dynamic analysis for all kinds of laminates. Also the model was verified for dynamic analysis of tubular cross section beams (or shafts) and the results were accurate compared to experimental ones and other models. This model provides an accurate approach for calculating the natural frequencies of beams and shafts with arbitrary laminate for engineers and scientists.

7. References

Qatu M. S. (2004). Vibration of Laminated Shells and Plates, Elsevier Academic Press, ISBN 978-0-08-044271-6, Netherlands.

Kaw A. K. (2005). Mechanics of Composite Materials. CRC Press, ISBN 978-084-9313-43-1, Boca Raton, USA.

Rios, G. & Chan, W. S. (2010). A Unified Analysis of stiffened Reinforced Composite beams. In: Proceedings of 25th ASC conference. Dayton, USA.

Vinson, J. R. & Sierakowski, R. L. (2002). The behavior of Structures Composed of Composite Materials, Kluwer Academic Publishers, ISBN 978-140-2009-04-4, Netherlands.

Qatu M. S. (1993). Theories and analyses of Thin and moderately Thick Laminated Composite Curved Beams,. International Journal of Solids and Structures, Vol. 30, No. 20, pp. 2743-2756, ISSN 0020-7683.

Timoshenko SP. (1921). On the correction for shear of the differential equation for transverse vibrations of prismatic beams, Philos Mag, Sec 6, No. 41 pp. 744–746. ISSN: 1478-6435

Kapania, R. K. & Raciti S. (1989). Recent Advances in Analysis of laminated beams and plates, PART II: Vibration and Wave Propagation, AIAA Journal, Vol.27, No.7, pp. 935-946, ISSN 0001-1452.

Chidamparam, P. & Leissa A. W. (1993). Vibrations of Planar Curved Beams, Rings, and Arches, Appl. Mech. Rev., Vol.46, No.9, pp. 467 -484, ISSN 0003-6900.

Chandrashekhara, K., Krishnamurthy, K. & Roy, S. (1990). Free vibration of composite beams including rotary inertia and shear deformation, Composite Structures, Vol.14, No.4, pp. 269-279, ISSN: 0263-8223.

Krishnaswamy, A., Chandrashekhara, K. & Wu, WZB. (1992). Analytical Solutions to vibration of generally layered composite beams, Journal of Sound and Vibration, Vol.159, No.1, pp. 85-99, ISSN: 0022-460X.

Abramovich, H. & Livshits, A. (1994). Free vibrations of non-symmetric cross ply laminated composite beams, Journal of Sound and Vibration, Vol. 176, No. 5, pp. 597-612, ISSN 0022-460X.

Abramovich, H., Eisenberger, M. & Shulepov, O. (1995). Vibrations of Multi-Span Non-Symmetric Composite Beams, Composites Engineering Vol.5, No.4, pp. 397-404, ISSN 1359-8368.

Teboub, Y. & Hajela, P. (1995). Free vibration of generally layered composite beams using symbolic computation, Composite Structures, Vol.33, No.3, pp. 123-134, ISSN: 0263-8223.

Banerjee, J. R. Williams F. W. (1995). Free Vibration of Composite Beams—an Exact Method Using Symbolic Computation, AIAA Journal of Aircraft, Vol. 32, No.3, pp. 636-642, ISSN 0021-8669.

Banerjee, J. R. (2001). Explicit analytical expressions for frequency equation and mode shapes of composite beams, International Journal of Solids and Structures, Vol.38, No.14, pp. 2415-2426, ISSN 0020-7683.

Li, J., Shen, R., Hua, H. & Jin, J. (2004). Bending–torsional coupled dynamic response of axially loaded composite Timosenko thin-walled beam with closed cross-section, Composite Structures, Vol.64, No.1, pp. 23–35, ISSN 0263-8223.

Eisenberger, M., Abramovich, H. & Shulepov, O. (1995). Dynamic stiffness analysis of laminated beams using a first order shear deformation theory. Composite Structures, Vol.31, No.4, pp. 265-271, ISSN 0263-8223.

Khdeir, A. A. & Reddy, J. N. (1997). Free And Forced Vibration Of Cross-Ply Laminated Composite Shallow Arches. Intl J Solids Structures, Vol.34, No.10, pp. 1217-1234, ISSN 0020-7683.

Kant, T., Marur, S. R. & Rao, G. S. (1998). Analytical solution to the dynamic analysis of laminated beams using higher order refined theory. Composite Structures, Vol.40, No.1, pp. 1-9, ISSN 0263-8223.

Matsunaga, H. (2001). Vibration and Buckling of Multilayered Composite Beams According to Higher Order Deformation Theories, Journal of Sound and vibration, Vol.246, No.1, pp. 47-62, ISSN 0022-460X.

Subramanian, P. (2006). Dynamic analysis of laminated composite beams using higher order theories and finite elements, Composite Structures, Vol.73, No.3, pp. 342-353, ISSN 0263-8223.

Kapuria, S., Dumir, P.C. & Jain, N. K. (2004). Assessment of zigzag theory for static loading, buckling, free and forced response of composite and sandwich beams. Composite Structures, Vol.64, No.3-4, pp. 317–27, ISSN 0263-8223.

Zhen, W. & Wanji, C. (2008). An assessment of several displacement based theories for the vibration and stability analysis of laminated composite and sandwich beams, Composite Structures, Vol.84, No.4, pp. 337-349, ISSN 0263-8223.

Zinberg, H. & Symonds, M.F. (1970). The development of an advanced composite tail rotor driveshaft. In: Proceedings of 26th annual forum of the American Helicopter Society, Washington, USA.

dos Reis, H. L. M., Goldman, R. B. & Verstrate, P. H. (1987). Thin-walled laminated composite cylindrical tubes. Part III––critical speed analysis, Journal of Composite Technology and Research, Vol.9, No.2, pp. 58–62, ISSN 0884-6804.

Kim, C. D. Bert, C. W. (1993). Critical speed analysis of laminated composite hollow drive shafts. Composite Engineering, Vol.3, No.7-8, pp. 633–43, ISSN: 1359-8368.

Bert, C. W. & Kim, C. (1995) Whirling of composite-material driveshafts including bending–twisting coupling and transverse shear deformation, Journal of Vibration and Acoustics, Vol.117, No.1, pp. 17–21, ISSN 1048-9002.

Singh, S. P. & Gupta, K. (1996). Composite shaft rotordynamic analysis using a layerwise theory, Journal of Sound and Vibration, Vol. 191, No. 5, pp. 739–56, ISSN 0022-460X.

Chang, M-Y., Chen, JK. & Chang, C-Y. (2004). A simple spinning laminated composite shaft model, International Journal of Solids and Structures, Vol.41, No.3-4, pp. 637–62, ISSN 0020-7683.

Qatu, M. S. & Iqbal, J. (2010). Transverse vibration of a two-segment cross-ply composite shafts with a lumped mass, Composite Structures, Vol.92, No.5, pp. 1126-1131, ISSN 0263-8223.

23

Asymptotic Expansion Homogenisation and Multiscale Topology Optimisation of Composite Structures

João A. Oliveira, Joaquim Pinho-da-Cruz and Filipe Teixeira-Dias
Departamento de Engenharia Mecânica, Universidade de Aveiro
Portugal

1. Introduction

Composite materials are among the most prominent materials today, both in terms of applications and development. Nevertheless, their complex structure and heterogeneous nature lead to difficulties, both in the prediction of its properties and on the achievement of the ideal constituent distributions. Homogenisation procedures may provide answers in both cases. With this in mind, the main focus of this chapter is to show the importance of computational procedures for this task, mainly in terms of the different applications of Asymptotic Expansion Homogenisation (AEH) to heterogeneous periodic media and, above all, composite materials. First of all, it is noteworthy that the detailed numerical modelling of the mechanical behaviour of composite material structures tends to involve high computational costs. In this scope, the use of homogenisation methodologies can lead to significant benefits. These techniques allow the simplification of a heterogeneous medium using an equivalent homogenous medium and macrostructural behaviour laws obtained from microstructural information. Furthermore, composite materials typically have heterogeneities with characteristic dimensions significantly smaller than the dimensions of the structural component itself. If the distribution of the heterogeneities is roughly periodic, it can usually be approximated by a detailed periodic representative unit-cell. Thus, the Asymptotic Expansion Homogenisation (AEH) method is an excellent methodology to model physical phenomena on media with periodic microstructure, as well as a useful technique to study the mechanical behaviour of structural components built with composite materials. In terms of computational implementation, the main advantages of this method are (i) the fact that it allows a significant reduction of the number of degrees of freedom and (ii) the capability to find the stress and strain microstructural fields associated with a given macrostructural equilibrium state. In fact, unlike other common homogenisation methods, the AEH leads to explicit mathematical equations to characterise those fields, that is, to perform a localisation.

On the other hand, topology optimisation typically deals with material distributions to achieve the best behaviour for a given objective. The common approach to structural topology optimisation uses a variety of compliance minimisation (stiffness maximisation) procedures and functions. When analysing composite materials, these strategies often lead to multiscale procedures, either as a way to relax the initial discrete problem or in an effort to attain both optimal global structure and optimal microstructure. In this sense, the integration of AEH

procedures in topology optimisation appears in different ways, either through simultaneous multiscale optimisation, or taking the influence of one of the scales and optimising the other. In this sense, this chapter shows the four main approaches to the integration of AEH in topology optimisation procedures: structure optimisation for a given composite microstructure; microstructure optimisation for a given structure; simultaneous optimisation of both scales (hierarchical approach); and material design. The problems are solved on a multiload multiobjective thermoelastic in-house developed computational platform.
The authors thus show the use of AEH procedures and equations both to evaluate homogenised composite materials and to find the ideal material distribution for a given problem. This chapter aims to provide a review of some of the main aspects of these methods and to present some illustrative examples.

2. Asymptotic Expansion Homogenisation

The Asymptotic Expansion Homogenisation (AEH) method is used to solve problems that involve physical phenomena on continuous media with periodic microstructures. It is a useful technique to study the behaviour of structural components built from composite materials, with some advantages over other methods. On one hand, it allows a significant reduction of the problem size and, on the other hand, it has the capability to characterise surface conduction heat flux, strain and stress microfields. AEH leads to specific equations that characterise these fields in a process called localisation, not found on most homogenisation methods. The localisation process is essentially the inverse of the homogenisation process.

2.1 Differential formulation of thermal and thermoelastic problems

A linear thermoelastic heterogeneous material fills a solid[1] $\Omega \in \mathbb{R}^3$ and has a microstructure defined by the periodic distribution of a Representative Unit-Cell (RUC) in the space Y (see Fig. 1). As periodic microstructure materials usually have a small relation $\varepsilon \ll 1$ between the characteristic dimensions of both domains, the thermomechanical response of these materials has periodic oscilations of the resulting temperature, displacement, conduction heat flux, stress and strain fields. These oscillations rise from the periodic heterogeneities and are seen in a neighbourhood ε of any point in Ω. It is thus natural to assume the existence of two separate scales $\mathbf{x}$ and $\mathbf{y}$ where the behaviour of the material on the macroscale and microscale, respectively, takes place. The variables associated to different fields are then functionally dependent of both systems $\mathbf{x}$ and $\mathbf{y}$, where

$$\mathbf{y} = \mathbf{x}/\varepsilon. \tag{1}$$

This functional dependence in $\mathbf{y}$ is periodic in the domain Y, a property usually referred to as Y-periodicity.
In terms of thermoelastic properties, Y-periodicity of the microstructural heterogeneity gives Y-periodic thermal conductivity $\mathbf{k}$, thermal expansion $\boldsymbol{\alpha}$ and elasticity $\mathbf{D}$ tensors. On the other hand, macroscale material homogeneity results in a non-direct dependency between these tensors and the macroscale coordinate system $\mathbf{x}$. In this context, these constitutive tensors are

[1] The open set $\Omega \in \mathbb{R}^3$ is limited by the boundary Γ.

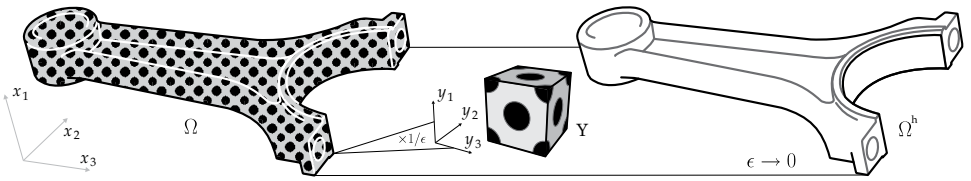

Fig. 1. Heterogeneous thermoelastic material Ω and representative unit-cell Y used in the microscale problem of the asymptotic expansion homogenisation, resulting, with $\varepsilon \to 0$, on the homogeneous material Ω^h.

defined as

$$k_{ij} = k_{ij}(\mathbf{y}), \tag{2}$$
$$\alpha_{ij} = \alpha_{ij}(\mathbf{y}) \quad \text{and} \tag{3}$$
$$D_{ijkl} = D_{ijkl}(\mathbf{y}), \tag{4}$$

respectively. On the macroscale coordinate system, $\mathbf{x}$, microstructural heterogeneities manifest over a period ε^{-1} times smaller than the characteristic dimensions of the space Y. Then, according to equation 1,

$$k^{\varepsilon}_{ij}(\mathbf{x}) = k_{ij}(\mathbf{x}/\varepsilon), \tag{5}$$
$$\alpha^{\varepsilon}_{ij}(\mathbf{x}) = \alpha_{ij}(\mathbf{x}/\varepsilon) \quad \text{and} \tag{6}$$
$$D^{\varepsilon}_{ijkl}(\mathbf{x}) = D_{ijkl}(\mathbf{x}/\varepsilon), \tag{7}$$

where the index ε states that $\mathbf{k}$, $\boldsymbol{\alpha}$ and $\mathbf{D}$ are εY-periodic in $\mathbf{x}$. In this sense, the thermal steady-state problem is described by the equilibrium equation and the Fourier's law for heat conduction (Cioranescu & Donato, 1999)

$$\frac{\partial q^{\varepsilon}_i}{\partial x^{\varepsilon}_i} - Q = 0 \quad \text{in} \quad \Omega \quad \text{and} \tag{8}$$
$$q^{\varepsilon}_i = -k^{\varepsilon}_{ij}\frac{\partial T^{\varepsilon}}{\partial x^{\varepsilon}_j} \quad \text{in} \quad \Omega, \tag{9}$$

for $i, j = 1, \ldots, 3$. q_i are the components of the surface conduction heat fluxes. Q it the rate of heat generation per unit volume and T the temperature field. The boundary of Ω is defined by the surfaces $\Gamma_{\mathrm{D_T}}$, $\Gamma_{\mathrm{N_T}}$ and $\Gamma_{\mathrm{R_T}}$. These are related to the Dirichlet, Neumann and Robin boundary conditions [2]

$$T^{\varepsilon} = \bar{T} \quad \text{in} \quad \Gamma_{\mathrm{D_T}}, \tag{10}$$
$$q^{\varepsilon}_i n_i = -\bar{q} \quad \text{in} \quad \Gamma_{\mathrm{N_T}} \quad \text{and} \tag{11}$$
$$q^{\varepsilon}_i n_i = h_{\mathrm{c}}(T^{\varepsilon} - T_{\infty}) \quad \text{in} \quad \Gamma_{\mathrm{R_T}}, \tag{12}$$

where $\Gamma_{\mathrm{D_T}} \cup \Gamma_{\mathrm{N_T}} \cup \Gamma_{\mathrm{R_T}} = \Gamma$ and $\Gamma_{\mathrm{D_T}} \cap \Gamma_{\mathrm{N_T}} = \Gamma_{\mathrm{D_T}} \cap \Gamma_{\mathrm{R_T}} = \Gamma_{\mathrm{N_T}} \cap \Gamma_{\mathrm{R_T}} = \varnothing$. $\bar{T}$ and $\bar{q}$ are prescribed temperature and surface conduction heat flux values, respectively. n_i are the components of an outward unit vector, orthogonal to the surfaces $\Gamma_{\mathrm{N_T}}$ or $\Gamma_{\mathrm{R_T}}$. h_{c} and T_{∞}

[2] Radiation processes are note considered in this work.

are the convection coefficient and ambient temperature, respectively. The temperature field is the solution to the thermal problem is the solution $T^\varepsilon \in \mathrm{V}_\Omega^0$ of the variational problem

$$\int_\Omega k_{ij}^\varepsilon \frac{\partial T^\varepsilon}{\partial x_j^\varepsilon}\frac{\partial v}{\partial x_i^\varepsilon}\mathrm{d}\Omega = \int_\Omega Qv\mathrm{d}\Omega + \int_{\Gamma_{\mathrm{N_T}}} \bar{q}v\mathrm{d}\Gamma - \int_{\Gamma_{\mathrm{R_T}}} h_\mathrm{c}\left(T^\varepsilon - T_\infty\right)v\mathrm{d}\Gamma, \quad \forall v \in \mathrm{V}_\Omega^0, \tag{13}$$

where V_Ω^0 is the set of continuous functions, sufficiently regular and zero-valued in $\Gamma_{\mathrm{D_T}}$.
The heterogeneous material is made of $n > 1$ homogeneous materials, making the thermal problem a set of n problems with equations equivalent to expression 8, having temperature and surface flux continuity conditions on every interface between subdomains (Lewis et al., 1996).
Assuming infinitesimal strains associated to a quasi-static process, the linear thermoelasticity problem is described by the following equilibrium equations, strain-displacement relations and constitutive relations (Duhamel-Neumann law) (Cioranescu & Donato, 1999)

$$\frac{\partial \sigma_{ij}^\varepsilon}{\partial x_j^\varepsilon} + b_i = 0 \quad \text{in} \quad \Omega, \tag{14}$$

$$\epsilon_{ij}^\varepsilon = \frac{1}{2}\left(\frac{\partial u_i^\varepsilon}{\partial x_j^\varepsilon} + \frac{\partial u_j^\varepsilon}{\partial x_i^\varepsilon}\right) \quad \text{in} \quad \Omega \quad \text{and} \tag{15}$$

$$\sigma_{ij}^\varepsilon = D_{ijkl}^\varepsilon \epsilon_{kl}^\varepsilon - \Delta T^\varepsilon \beta_{ij}^\varepsilon \quad \text{in} \quad \Omega, \tag{16}$$

respectively, where

$$\Delta T^\varepsilon = T^\varepsilon - T_0 \quad \text{and} \tag{17}$$

$$\beta_{ij}^\varepsilon = D_{ijkl}^\varepsilon \alpha_{kl}^\varepsilon = \beta_{ij}^\varepsilon(\mathbf{x}/\varepsilon). \tag{18}$$

σ_{ij} and ϵ_{ij} the components of the Cauchy stress tensor and strain tensor, respectively. b_i and u_i represent the components of the volume loads and displacements, respectively. T_0 is the reference temperature and β_{ij} are the components of the thermal moduli tensor. If $\Delta T^\varepsilon = 0$ or $\beta_{ij}^\varepsilon = 0$, the problem becomes the purely mechanical linear elastic problem. The boundary of Ω is defined by the surfaces $\Gamma_{\mathrm{D_u}}$ and $\Gamma_{\mathrm{N_u}}$. These are associated to Dirichlet and Neumann boundary conditions

$$u_i^\varepsilon = \bar{u}_i \quad \text{in} \quad \Gamma_{\mathrm{D_u}} \quad \text{and} \tag{19}$$

$$\sigma_{ij}^\varepsilon n_j = \bar{t}_i \quad \text{in} \quad \Gamma_{\mathrm{N_u}}, \tag{20}$$

respectively, where $\Gamma_{\mathrm{D_u}} \cup \Gamma_{\mathrm{N_u}} = \Gamma$ and $\Gamma_{\mathrm{D_u}} \cap \Gamma_{\mathrm{N_u}} = \varnothing$. $\bar{u}_i$ and $\bar{t}_i$ are prescribed displacement and surface load values, respectively. n_j are components of an outward unit vector, orthogonal to surface $\Gamma_{\mathrm{N_u}}$.
Solving the thermoelastic problem consists of determining the displacement field that is the solution $\mathbf{u}^\varepsilon \in \mathrm{V}_\Omega^0$ of the variational problem

$$\int_\Omega D_{ijkl}^\varepsilon \frac{\partial u_k^\varepsilon}{\partial x_l^\varepsilon}\frac{\partial v_i}{\partial x_j^\varepsilon}\mathrm{d}\Omega = \int_\Omega \left(T^\varepsilon - T_0\right)\beta_{ij}^\varepsilon \frac{\partial v_i}{\partial x_j^\varepsilon}\mathrm{d}\Omega + \int_\Omega b_i v_i \mathrm{d}\Omega + \int_{\Gamma_{\mathrm{N_u}}} \bar{t}_i v_i \mathrm{d}\Gamma, \quad \forall \mathbf{v} \in \mathrm{V}_\Omega^0, \tag{21}$$

where V_Ω^0 is the set of funcions, continuous, sufficiently regular and zero-valued in $\Gamma_{\mathrm{D_u}}$.
The heterogeneous material is made of $n > 1$ homogeneous materials, from which the linear thermoelasticity problem consists of n equations similar to equation 14, associated to displacement and surface load continuity conditions on the interfaces of the different material subdomains.

2.2 Homogenised thermal and thermoelastic problems

With the existence of two different scales, associated to behaviour levels over the macroscale Ω and microscale Y, the temperature and displacement fields are approximated using the respective asymptotic expansions in ε:

$$T^{\varepsilon}(\mathbf{x}) = T^{(0)}(\mathbf{x},\mathbf{y}) + \varepsilon T^{(1)}(\mathbf{x},\mathbf{y}) + \varepsilon^2 T^{(2)}(\mathbf{x},\mathbf{y}) + \cdots \quad \text{and} \tag{22}$$

$$u_i^{\varepsilon}(\mathbf{x}) = u_i^{(0)}(\mathbf{x},\mathbf{y}) + \varepsilon u_i^{(1)}(\mathbf{x},\mathbf{y}) + \varepsilon^2 u_i^{(2)}(\mathbf{x},\mathbf{y}) + \cdots, \tag{23}$$

where $T^{(r)}(\mathbf{x},\mathbf{y})$ and $u_i^{(r)}(\mathbf{x},\mathbf{y})$, with $r \in \mathbb{N}_0$, are Y-periodic functions in $\mathbf{y}$, classified as the r^{th} order temperature field correctors and displacement field correctors, respectively. According to equation 1, using the chain rule of function derivatives,

$$\frac{\partial \cdot}{\partial x_i^{\varepsilon}} = \frac{\partial \cdot}{\partial x_i} + \frac{1}{\varepsilon}\frac{\partial \cdot}{\partial y_i}. \tag{24}$$

In this context, including the temperature asymptotic expansion (Eq. 22) in the Fourier's equations for heat conduction (Eq. 9) and on the Duhamel-Neumann law (Eq. 16), and including the displacement asymptotic expansion (Eq. 23) in the linearised strain-displacement relations (Eq. 15), result in the linearised thermoelastic problem. The temperature field $T^{(0)}$ is the solution of the homogenised thermal problem

$$\frac{\partial \Xi_i}{\partial x_i} - Q = 0 \quad \text{in} \quad \Omega, \tag{25}$$

$$T^{(0)} = \bar{T} \quad \text{in} \quad \Gamma_{\mathrm{D_T}}, \tag{26}$$

$$\Xi_i n_i = -\bar{q} \quad \text{in} \quad \Gamma_{\mathrm{N_T}}, \tag{27}$$

$$\Xi_i n_i = h_{\mathrm{c}}\left(T^{(0)} - T_{\infty}\right) \quad \text{in} \quad \Gamma_{\mathrm{R_T}}, \quad \text{with} \tag{28}$$

$$\Xi_i = -k_{ij}^{\mathrm{h}}\frac{\partial T^{(0)}}{\partial x_j} \quad \text{in} \quad \Omega, \tag{29}$$

where Ξ_i are the components of the macrostructural homogenised superficial conduction heat fields and k_{ij}^{h} are the components of the homogenised thermal conductivity tensor, defined as

$$k_{ik}^{\mathrm{h}} = \frac{1}{|\mathrm{Y}|}\int_{\mathrm{Y}} k_{ij}(\mathbf{y})\left(\mathrm{I}_j^k - \frac{\partial \mathrm{Y}^k}{\partial y_j}\right)\mathrm{d}Y. \tag{30}$$

$\mathrm{I}_j^k = \delta_{jk}$ is the Kronecker delta and Y^k are the components of the thermal characteristic displacement field tensor (Pinho-da-Cruz, 2007). These are the solutions $\mathrm{Y}^k \in \widetilde{\mathrm{V}}_{\mathrm{Y}}$ of the auxiliary microstructural variational problem

$$\int_{\mathrm{Y}} k_{ij}\frac{\partial \mathrm{Y}^k}{\partial y_j}\frac{\partial v}{\partial y_i}\mathrm{d}Y = \int_{\mathrm{Y}} k_{ik}\frac{\partial v}{\partial y_i}\mathrm{d}Y, \quad \forall v \in \widetilde{\mathrm{V}}_{\mathrm{Y}}, \tag{31}$$

where $\widetilde{\mathrm{V}}_{\mathrm{Y}}$ is the set of Y-periodic continuous functions, sufficiently regular and with an average value[3] equal to zero in Y. The existence of average values equal to zero in Y for the

[3] The average value on a function $\Phi(\mathbf{x},\mathbf{y})$, Y-periodic in Y, is defined by $< \Phi >_{\mathrm{Y}} = \frac{1}{|\mathrm{Y}|}\int_{\mathrm{Y}} \Phi(\mathbf{x},\mathbf{y})\,\mathrm{d}Y$.

solutions of the equations 31 is an unicity condition for the thermal characteristic displacement field tensor $\mathbf{Y}$ (Sanchez-Hubert & Sanchez-Palencia, 1992).

Concerning the displacement field $u_i^{(0)}$, it is the solution of the homogenised thermoelasticity problem

$$\frac{\partial \Sigma_{ij}}{\partial x_j} + b_i = 0 \quad \text{in} \quad \Omega, \tag{32}$$

$$u_i^{(0)} = \bar{u}_i \quad \text{in} \quad \Gamma_{\mathrm{D_u}}, \tag{33}$$

$$\Sigma_{ij} n_j = \bar{t}_i \quad \text{in} \quad \Gamma_{\mathrm{N_u}}, \quad \text{with} \tag{34}$$

$$\Sigma_{ij} = D^{\mathrm{h}}_{ijkl} \frac{\partial u_k^{(0)}}{\partial x_l} - \left(T^{(0)} - T_0 \right) \beta^{\mathrm{h}}_{ij} \quad \text{in} \quad \Omega, \tag{35}$$

where Σ_{ij} are components of the macrostructural homogenised stress tensor. D^{h}_{ijkl} and β^{h}_{ij} are the components of the homogenised elasticity and thermal moduli tensors, respectively, defined as

$$D^{\mathrm{h}}_{ijmn} = \frac{1}{|\mathrm{Y}|} \int_{\mathrm{Y}} D_{ijkl}(\mathbf{y}) \left(\mathrm{I}^{mn}_{kl} - \frac{\partial \chi^{mn}_k}{\partial y_l} \right) \mathrm{d}Y \quad \text{and} \tag{36}$$

$$\beta^{\mathrm{h}}_{ij} = \frac{1}{|\mathrm{Y}|} \int_{\mathrm{Y}} \left[\beta_{ij}(\mathbf{y}) - D_{ijkl}(\mathbf{y}) \frac{\partial \Psi_k}{\partial y_l} \right] \mathrm{d}Y . \tag{37}$$

$\mathrm{I}^{mn}_{kl} = \delta_{km}\delta_{ln}$, where δ_{ij} is the symbol for the Kronecker delta. χ^{mn}_k and Ψ_k are the components of the mechanical characteristic displacement field tensor and thermomechanical characteristic displacement field tensor, respectively (Pinho-da-Cruz, 2007). These fields are the solutions $\chi^{mn}_k \in \widetilde{\mathrm{V}}_{\mathrm{Y}}$ and $\Psi_k \in \widetilde{\mathrm{V}}_{\mathrm{Y}}$ of the microstructural variational auxiliary problems

$$\int_{\mathrm{Y}} D_{ijkl} \frac{\partial \chi^{mn}_k}{\partial y_l} \frac{\partial v_i}{\partial y_j} \mathrm{d}Y = \int_{\mathrm{Y}} D_{ijmn} \frac{\partial v_i}{\partial y_j} \mathrm{d}Y, \quad \forall v_i \in \widetilde{\mathrm{V}}_{\mathrm{Y}}, \quad \text{and} \tag{38}$$

$$\int_{\mathrm{Y}} D_{ijkl} \frac{\partial \Psi_k}{\partial y_l} \frac{\partial v_i}{\partial y_j} \mathrm{d}Y = \int_{\mathrm{Y}} \beta_{ij} \frac{\partial v_i}{\partial y_j} \mathrm{d}Y, \quad \forall v_i \in \widetilde{\mathrm{V}}_{\mathrm{Y}}, \tag{39}$$

where $\widetilde{\mathrm{V}}_{\mathrm{Y}}$ is the set of Y-periodic functions, continuous and sufficiently regular, with an average value equal to zero in Y. Once again, the existence of average values equal to zero in Y for the solutions of the equations 38 and 39 is an unicity condition for the tensor $\boldsymbol{\chi}$ of the mechanical characteristic displacement field (Sanchez-Hubert & Sanchez-Palencia, 1992) and for the tensor $\boldsymbol{\Psi}$ of the thermomechanical characteristic displacement field, respectively.

Note that the usage of two scales in this application is based on the assumption of the existence of periodic oscillations os the resulting temperature and displacement fields that result from the periodicity of the microstructural heterogeneous detail. These oscillations should superimpose the macroscopic fields, where the heterogeneous details are not directly considered. Is this sense, for first-order approximations of the temperature and displacement fields, these oscillations can be seen as fluctuations around a macroscopic average value, as illustrated in figure 2.

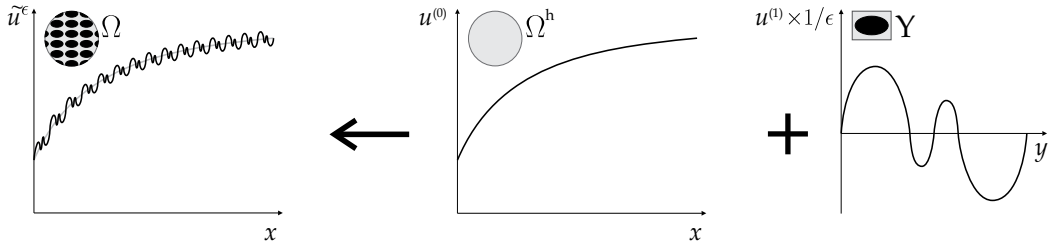

Fig. 2. Illustration of the asymptotic expansion homogenisation first-order approximation for the displacement field for a one-dimensional case. The displacement field in Ω is approximated adding the Y−periodic microscale first-order fluctuations to the homogenised macroscale Ω^{h} field.

2.3 Conventional methodologies

2.3.1 Conventional homogenisation

In practice, a significant part of structural applications based on periodic microstructure materials has a scale factor $\varepsilon \ll 1$. In this sense, first-order approximations for the temperature and displacement fields are adequate representations (see Eqs. 22 and 23). This simplifies the asymptotic expansion methodology, resulting in the conventional homogenisation methodology (Terada, 1996). This is a rigorous mathematical technique, in which the initial problems are approximated by a two-scale procedure. In this, the global problem becomes a conventional structural problem with a homogeneous material, using constitutive information taken from the solutions of the microscale problems. These, on the other hand, allow the study of the microstructural detail using a representative unit-cell. The homogenised properties are calculated from the solutions of the microscale problems with periodicity constraints (see Eqs. 31 and 30, 38 and 36, and 39 and 37).

In this sense, the numerical gains of this method are considerable, since the number of degrees of freedom associated to a detailed discretisation is significantly reduced. The microstructural details are instead defined on a single representative unit-cell, while the macrostructure is modelled as is it was a homogeneous medium.

2.3.2 Conventional localisation

Another advantage of the asymptotic expansion homogenisation is that it allows the characterisation of the microstructural surface conduction heat flux, strain and stress fields. In fact, contrary to the other usual homogenisation methods, this method provides mathematical expressions that define the microstructural levels of these fields. This process, opposite to the homogenisation, is called localisation (see Fig. 3).

Considering first-order approximations, the microstructural surface conduction heat flux field defined on the conventional localisation methodology is (Pinho-da-Cruz, 2007)

$$q_i^{(1)}(\mathbf{x},\mathbf{y}) = k_{ij}(\mathbf{y}) \left(\frac{\partial \Upsilon^k}{\partial y_j} - \mathrm{I}_j^k \right) \frac{\partial T^{(0)}}{\partial x_k} . \tag{40}$$

The localised microstructural strain field, on the other hand, is defined as

$$\epsilon_{ij}^{(1)}(\mathbf{x},\mathbf{y}) = \Im_{ij}^{kl} \left[\left(\mathrm{I}_{kl}^{mn} - \frac{\partial \chi_k^{mn}}{\partial y_l} \right) \frac{\partial u_m^{(0)}}{\partial x_n} + \frac{\partial \Psi_k}{\partial y_l} \left(T^{(0)} - T_0 \right) \right] , \tag{41}$$

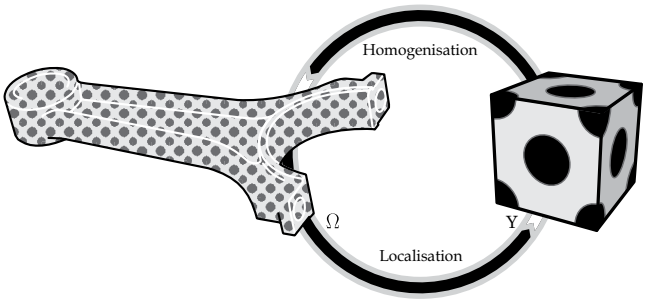

Fig. 3. Data flux between the macroscale Ω and microscale Y with the homogenisation and localisation procedures.

where

$$\Im_{ij}^{kl} = \frac{1}{2}\left(\delta_{ik}\delta_{jl} + \delta_{il}\delta_{jk}\right). \tag{42}$$

In turn, the localised stress field is defined as

$$\sigma_{ij}^{(1)}(\mathbf{x},\mathbf{y}) = D_{ijkl}(\mathbf{y})\left(\mathrm{I}_{kl}^{mn} - \frac{\partial \chi_k^{mn}}{\partial y_l}\right)\frac{\partial u_m^{(0)}}{\partial x_n} + \left[D_{ijkl}(\mathbf{y})\frac{\partial \Psi_k}{\partial y_l} - \beta_{ij}(\mathbf{y})\right]\left(T^{(0)} - T_0\right). \tag{43}$$

Equations 40, 41 and 43 allow, for a given point $\mathbf{x}$, the definition of the approximate values for the respective fields within the microstructural heterogeneities. On the other hand, the homogenised macrostructural heat flux, Ξ_i, and stress, Σ_{ij}, fields, being by definition the average of the microstructural heat flux $q_i^{(1)}$ and stress $\sigma_{ij}^{(1)}$ fields in Y, are unable to represent any microstructural fluctuations and lack detail.

For further details on the mathematical and numerical basis of the asymptotic expansion homogenisation method and its applications, please consult the references (Guedes & Kikuchi, 1990; Oliveira et al., 2009; Pinho-da-Cruz, 2007; Pinho-da-Cruz et al., 2008; 2009).

3. AEH and topology optimisation

In the context of topology optimisation aplications, the effective number of different homogeneous materials on the microstructure of a given heteregeneous material depends on the density distribution that results from the use of the SIMP (Solid Isotropic Material with Penalisation) method on the microscale. The homogenised constitutive tensors, $\mathbf{D}^{\mathrm{h}}$, $\boldsymbol{\beta}^{\mathrm{h}}$ and $\mathbf{k}^{\mathrm{h}}$ can be calculated using the AEH (see Eqs. 36, 37 and 30). However, their use in the topology optimisation procedures presented on the second part of this chapter requires a small change to the definition of the local properties within the microscale. Instead of having different base materials, the material in each point $\mathbf{y}$ is defined by the SIMP power-law method, thus affecting a single base material with different density values μ (Bendsøe & Sigmund, 2003), *i.e.*

$$\mathbf{D}_{e_y} = \mathbf{D}(\mu) = \mu^p \mathbf{D}^0, \tag{44}$$

$$\boldsymbol{\beta}_{e_y} = \boldsymbol{\beta}(\mu) = \mathbf{D}(\mu)\boldsymbol{\alpha}(\mu) = \mu^p \mathbf{D}^0 \mu^p \boldsymbol{\alpha}^0 = \mu^{2p}\boldsymbol{\beta}^0 \quad \text{and} \tag{45}$$

$$\mathbf{k}_{e_y} = \mathbf{k}(\mu) = \mu^p \mathbf{k}^0, \tag{46}$$

where the density $\mu = \mu(\mathbf{y})$ may vary continuously within[4] $0 \leq \mu \leq 1$ and p is an intermediate density penalisation factor, aimed at obtaining discrete results for the optimisation problem, with two well defined material phases. From this, equations 36, 37 and 30 are, respectively, slightly changed to

$$D^{\mathrm{h}}_{ijmn} = \frac{1}{|\mathrm{Y}|}\int_{\mathrm{Y}} D_{ijkl}(\mu)\left(\mathrm{I}^{mn}_{kl} - \frac{\partial \chi^{mn}_{k}}{\partial y_l}\right)\mathrm{d}Y\,, \tag{47}$$

$$\beta^{\mathrm{h}}_{ij} = \frac{1}{|\mathrm{Y}|}\int_{\mathrm{Y}} \left(\beta_{ij}(\mu) - D_{ijkl}(\mu)\frac{\partial \Psi_k}{\partial y_l}\right)\mathrm{d}Y \quad \text{and} \tag{48}$$

$$k^{\mathrm{h}}_{ik} = \frac{1}{|\mathrm{Y}|}\int_{\mathrm{Y}} k_{ij}(\mu)\left(\mathrm{I}^{k}_{j} - \frac{\partial \mathrm{Y}^{k}}{\partial y_j}\right)\mathrm{d}Y\,. \tag{49}$$

Equations 47 and 49 may as well be written in variational form (Bendsøe, 1995) as

$$D^{\mathrm{h}}_{ijmn} = \frac{1}{|\mathrm{Y}|}\int_{\mathrm{Y}} D_{pqkl}(\mu)\left(\mathrm{I}^{ij}_{pq} - \frac{\partial \chi^{ij}_{p}}{\partial y_q}\right)\left(\mathrm{I}^{mn}_{kl} - \frac{\partial \chi^{mn}_{k}}{\partial y_l}\right)\mathrm{d}Y \quad \text{and} \tag{50}$$

$$k^{\mathrm{h}}_{ik} = \frac{1}{|\mathrm{Y}|}\int_{\mathrm{Y}} k_{lj}(\mu)\left(\mathrm{I}^{i}_{l} - \frac{\partial \mathrm{Y}^{i}}{\partial y_l}\right)\left(\mathrm{I}^{k}_{j} - \frac{\partial \mathrm{Y}^{k}}{\partial y_j}\right)\mathrm{d}Y\,, \tag{51}$$

respectively.

Another aspect of the possible material distribution affects the desired bounds in terms of properties within the microscale. The presented SIMP format is usually applied for material interpolation between material and void. However, when working with composite materials, the bounds will be determined by two different constituent materials. One of the most straightforward ways to fulfil this requirement is slightly changing the power-law (Bendsøe & Sigmund, 1999; Sigmund, 2007). On one hand, the general material property P becomes

$$P(\mu) = \mu^p P_1 + (1-\mu^p)P_2 \tag{52}$$

where $P_1 > P_2$. This material interpolation scheme allows property P to vary between the bounds of material 1 and material 2. Furthermore, if $P_2 = P_{\min}$, it results in an interpolation between material and void. In either case, as used in this work, this power-law can be redefined as

$$P(\mu) = \mu^p P_1 + (1-\mu^p)d_m P_1 = \left[\mu^p + d_m(1-\mu^p)\right]P_1\,, \tag{53}$$

where $d_m = P_{\min}/P_1$. Alternatively, the modified SIMP (Bendsøe & Sigmund, 1999; Sigmund, 2007)

$$P(\mu) = P_{\min} + \mu^p(P_1 - P_{\min}) \tag{54}$$

has the same practical implications. Both in equations 53 and 54, $P_{\min}$ is the minimum value for the property P, different from zero to avoid singularities and numerical conditioning problems. Furthermore, these alternatives have some advantages over the original SIMP, most of all the fact that the minimum for P is now independent of the penalty exponent. They allow the use of multiphase materials, instead of the original cellular materials, and are more flexible for a wider variety of filtering techniques (Sigmund, 2007).

[4] In practice, it is usual to use a minimum value for the density $\mu \geq \mu_{\min} > 0$, in order to avoid numerical problems if $\mu = 0$.

4. Multiscale topology optimisation

Topology optimisation in structural mechanics consists of searching for the optimal material distribution within a certain admissible domain. This distribution, dependent on density variables, varies between high and low density regions. As a matter of fact, the initial definition of the problem is discrete, in which the variable can only take the values 1 (dense material) or 0 (void or soft phase). Among several others, one of the strategies for relaxing this problem is allowing the existence of intermediate densities and giving it physical meaning by association with coherent microstructures of cellular or composite material. This approach leads to multiscale procedures and is usually classified of homogenisation method, leading to several different implementations and using several methods to deal with the local problem (Allaire, 2001; Bendsøe & Kikuchi, 1988; Bendsøe & Sigmund, 2003; Diaz & Lipton, 1997; Guedes et al., 2006; Hassani & Hinton, 1999; Rodrigues et al., 2002; Theocaris & Stavroulakis, 1998; 1999).
In this sense, the authors show a multilevel or hierarchical methodology, for both thermoelasticity and heat conduction. A detailed description of the hierarchical methodologies applied to elasticity can be consulted in the references (Coelho et al., 2008; Rodrigues et al., 2002; Theocaris & Stavroulakis, 1998; 1999). The Asymptotic Expansion Homogenisation method is used in the local problem of this application, both in terms of constitutive analysis and sensitivity evaluation.

4.1 Hierarchical thermoelastic problem

Structural topology optimisation typically searches for the material distribution that minimize compliance (maximises stiffness). In its usual form, this is evaluated using the strain energy function as a measure of compliance or flexibility of the structure, defined as

$$S = \frac{1}{2}\int_{\Omega} \rho^p \boldsymbol{\varepsilon}(\mathbf{u}) : \mathbf{D}^0 : \boldsymbol{\varepsilon}(\mathbf{u}) \mathrm{d}\Omega \tag{55}$$

where $\rho = \rho(\mathbf{x})$ is the macrostructural density value, or using the work of exterior loads (*compliance*)

$$W = \int_{\Omega} \mathbf{b} \cdot \mathbf{u} \mathrm{d}\Omega + \int_{\Gamma_{\mathrm{Nu}}} \bar{\mathbf{t}} \cdot \mathbf{u} \mathrm{d}\Gamma \,. \tag{56}$$

$\mathbf{b}$ and $\bar{\mathbf{t}}$ are the volume and surface loads, respectively. These two functions can be used to define the total potential energy

$$P = S - W = \frac{1}{2}\int_{\Omega} \rho^p \boldsymbol{\varepsilon}(\mathbf{u}) : \mathbf{D}^0 : \boldsymbol{\varepsilon}(\mathbf{u}) \mathrm{d}\Omega - \left(\int_{\Omega} \mathbf{b} \cdot \mathbf{u} \mathrm{d}\Omega + \int_{\Gamma_{\mathrm{Nu}}} \bar{\mathbf{t}} \cdot \mathbf{u} \mathrm{d}\Gamma \right) . \tag{57}$$

According to the principle of minimum potential energy, the potential energy is minimised by the displacement field $\mathbf{u}$ that solves the equilibrium problem. This objective function gives an explicit definition of the hierarchical structure of the multiscale problem, which can be written as (Rodrigues et al., 2002; Theocaris & Stavroulakis, 1998; 1999)

$$\max_{\substack{\rho(\mathbf{x}) \\ 0 \le \rho(\mathbf{x}) \le 1 \\ \int_{\Omega} \rho(\mathbf{x}) \mathrm{d}\Omega \le V}} \min_{\substack{\mathbf{u}^l \in U \\ l=1,..,L}} \left[\frac{1}{2}\int_{\Omega} \Phi(\rho, \mathbf{u}^1, \ldots, \mathbf{u}^L) \mathrm{d}\Omega \right. \tag{58}$$

$$\left. - \sum_{l=1}^{L} w^l \left(\int_{\Omega} \mathbf{b}^l \cdot \mathbf{u}^l \mathrm{d}\Omega + \int_{\Gamma_{\mathrm{Nu}}} \bar{\mathbf{t}}^l \cdot \mathbf{u}^l \mathrm{d}\Gamma \right) \right] ,$$

where $\mathbf{u}$ is the equilibrium displacement field that minimises the potential energy function. This internal minimisation is done solving the equilibrium problem, which can alternatively be seen as an aditional equality constraint. The presented objective function states a multiload configuration with L load cases and corresponding weights w^l. The optimal energy density function $\Phi(\rho, \mathbf{u}^1, \ldots, \mathbf{u}^L)$ is the solution of the local (microscale) problem and is defined as

$$\Phi(\rho, \mathbf{u}^1, \ldots, \mathbf{u}^L) = \max_{\substack{\mu(\mathbf{x},\mathbf{y}) \\ 0 \leq \mu(\mathbf{x},\mathbf{y}) \leq 1 \\ \int_Y \mu(\mathbf{x},\mathbf{y}) \mathrm{d}Y = \rho(\mathbf{x})}} \sum_{l=1}^{L} w^l \left[D^{\mathrm{h}}_{ijkl}(\mu) \varepsilon_{ij}(\mathbf{u}^l) \varepsilon_{kl}(\mathbf{u}^l) \right] . \tag{59}$$

The multiload case was shown on this general definition of the problem but will be dropped for the remaining of this section. It will be recalled whenever necessary. The elastic problem can be extended to include the thermal expansion terms of the thermoelastic problem. In this sense, the strain energy can be updated using the generalised Duhamel-Neumman form of Hooke's law (Fung & Tong, 2005)

$$\sigma_{ij} = D_{ijkl} \varepsilon_{kl} - \beta_{ij} \Delta T \, , \tag{60}$$

rewriting equation 59, for a single-load case, as

$$\Phi(\rho, \mathbf{u}) = \max_{\substack{\mu(\mathbf{x},\mathbf{y}) \\ 0 \leq \mu(\mathbf{x},\mathbf{y}) \leq 1 \\ \int_Y \mu(\mathbf{x},\mathbf{y}) \mathrm{d}Y = \rho(\mathbf{x})}} \left[D^{\mathrm{h}}_{ijkl}(\mu) \varepsilon_{ij}(\mathbf{u}) \varepsilon_{kl}(\mathbf{u}) - 2\beta^{\mathrm{h}}_{ij}(\mu) \varepsilon_{ij}(\mathbf{u}) \Delta T \right] . \tag{61}$$

Note that the local problem results of a localisation process[5] where the local energy density function is maximised according to a macroscale strain tensor. This structure defines two different functionally dependent problems: the global problem, where equilibrium is achieved and the overall objective is evaluated, and a set of microstructural problems, where each of the local response is optimised and constitutive information is obtained. In the local problem, the local density variable $\mu(\mathbf{x}, \mathbf{y})$ is related to the global density variable through the local volume restriction as $\int_Y \mu(\mathbf{x}, \mathbf{y}) \mathrm{d}Y = \rho(\mathbf{x})$.
On a further notice, the global objective function and the overall definition of the hierarchical optimisation problem can also be defined as

$$\min_{\substack{\rho(\mathbf{x}) \\ 0 \leq \rho(\mathbf{x}) \leq 1 \\ \int_\Omega \rho(\mathbf{x}) \mathrm{d}\Omega \leq V \\ \mathbf{Ku} = \mathbf{f}}} \left[\frac{1}{2} \int_\Omega \Phi(\rho, \mathbf{u}) \mathrm{d}\Omega \right] , \tag{62}$$

treated in this case in terms of an equivalent strain energy function and being equivalent, at equilibrium, to the minimisation of the external load work (compliance). Note also that the factor $1/2$ can be simply omitted since it changes the value of the objective but nothing about the optimal solution (Arora, 2004). Furthermore, it is important to state that one of the advantages of the hierarquical structure is that the main procedure is independent of the material modelling. Homogenisation or material modelling may be done over independent modules, born from different methods and not restricted to the AEH used in this work.

[5] Localisation is a generic process where macroscale average values are used to render microstructural detail. The localisation methodology presented for the AEH is specific to that method.

4.2 Optimality conditions

To define the necessary conditions for the optimisation problem, it must be stated in a numerically compatible form. In this sense, according to Rodrigues *et al.* (Rodrigues et al., 2002), the augmented Lagrangian of the outer problem can be written as

$$\mathcal{L} = \min_{u \in U} \left[\frac{1}{2} \int_\Omega \Phi(\rho, \mathbf{u}) \mathrm{d}\Omega - \left(\int_\Omega \mathbf{b} \cdot \mathbf{u} \mathrm{d}\Omega + \int_{\Gamma_{\mathrm{Nu}}} \bar{\mathbf{t}} \cdot \mathbf{u} \mathrm{d}\Gamma \right) \right. \tag{63}$$

$$\left. - \frac{1}{2c} \left\{ \left[\max \left(0, \Lambda + c \left(\int_\Omega \rho \mathrm{d}\Omega - V \right) \right) \right]^2 - \Lambda^2 \right\} \right] ,$$

where c is the penalty parameter and $\Lambda \geq 0$ is the Lagrange multiplier associated to the global volume inequality restriction. Being $\tilde{\mathbf{u}}$ is the displacement field that fulfils global equilibrium, the stationary condition relative to the variable $\rho(\mathbf{x})$ is defined as

$$\frac{1}{2} \frac{\partial \Phi(\rho, \tilde{\mathbf{u}})}{\partial \rho} = \max \left\{ 0, \Lambda + c \left(\int_\Omega \rho \mathrm{d}\Omega - V \right) \right\} , \ \forall \mathbf{x} \in \Omega , \text{ with } \rho \in]0, 1[, \tag{64}$$

at point where ρ has intermediate values. At the extremes, this condition becomes an inequality ($\leq$ for $\rho = 0$ and $\geq$ for $\rho = 1$). Note, however, that these extremes are points where there's no need to solve the local problem. The stationary condition relative to the Lagrange multiplier, on the other hand, is

$$\Lambda = \max \left\{ 0, \Lambda + c \left(\int_\Omega \rho \mathrm{d}\Omega - V \right) \right\} . \tag{65}$$

Condition 65 implies the fulfilment of the global volume restriction. Condition 64 defines the stability of the Lagrange multiplier Λ at the equilibrium and for the optimal solution, meaning that the derivative of the energy density function at the optimum, relative to the global densities, should be constant at every $\mathbf{x}$ where $0 < \rho < 1$ (Coelho et al., 2008; Rodrigues et al., 2002).

The Lagrangian function for the local problem (Eq. 61) may be written as

$$\mathcal{L} = \left[D^{\mathrm{h}}_{ijkl}(\mu) \varepsilon_{ij}(\tilde{\mathbf{u}}) \varepsilon_{kl}(\tilde{\mathbf{u}}) - 2 \beta^{\mathrm{h}}_{ij}(\mu) \varepsilon_{ij}(\tilde{\mathbf{u}}) \Delta T \right] - \lambda(\tilde{\mathbf{x}}) \left[\int_{Y(\tilde{\mathbf{x}})} \mu \mathrm{d}y - \rho(\tilde{\mathbf{x}}) \right] . \tag{66}$$

This is defined for every $\tilde{\mathbf{x}} \in \Omega$ and the multiplier λ is relative to the local volume restriction, which compares the local density field μ with the global density value for a given point ($\rho(\tilde{\mathbf{x}})$). $\varepsilon_{ij}(\tilde{\mathbf{u}})$ are the strain components for the displacements $\tilde{\mathbf{u}}$ in point $\tilde{\mathbf{x}}$. Once again, the stationary condition relative to the optimisation variable is defined, in this case the microstructural density μ, as

$$\frac{\partial D^{\mathrm{h}}_{ijkl}(\mu)}{\partial \mu} \varepsilon_{ij}(\tilde{\mathbf{u}}) \varepsilon_{kl}(\tilde{\mathbf{u}}) - 2 \frac{\partial \beta^{\mathrm{h}}_{ij}(\mu)}{\partial \mu} \varepsilon_{ij}(\tilde{\mathbf{u}}) \Delta T = \lambda(\tilde{\mathbf{x}}) , \tag{67}$$

$$\forall \mathbf{y} \in Y(\tilde{\mathbf{x}}) , \text{ with } 0 < \mu < 1 ,$$

where

$$\frac{\partial D^{\mathrm{h}}_{ijkl}(\mu)}{\partial \mu} = \frac{1}{|Y|}\int_Y p\mu^{p-1} D^0_{pqrs}\left(\delta_{rk}\delta_{sl} - \frac{\partial \chi^{kl}_r}{\partial y_s}\right)\left(\delta_{pi}\delta_{qj} - \frac{\partial \chi^{ij}_p}{\partial y_q}\right)\mathrm{d}Y \tag{68}$$

and

$$\frac{\partial \beta^{\mathrm{h}}_{ij}(\mu)}{\partial \mu} = \frac{1}{|Y|}\int_Y \left(2p\mu^{2p-1} D^0_{ijkl}\alpha^0_{kl} - p\mu^{p-1} D^0_{ijkl}\frac{\partial \Psi_k}{\partial y_l}\right)\mathrm{d}Y \tag{69}$$

are the sensitivities of the homogenised tensors of elasticity, $\mathbf{D}^{\mathrm{h}}$, and thermal expansion moduli, $\boldsymbol{\beta}^{\mathrm{h}}$, respectively, to the variation of μ. As was the case for the global problem, these conditions become inequalities at the extremes. Condition 67 must be satisfied, for each $\mathbf{x}$ in Ω, at every $\mathbf{y}$ of the representative unit-cell.
The Lagangian 66 represents the local problem at the optimum, defined by the objective function $\Phi(\rho, \tilde{\mathbf{u}})$ (Eq. 61). From the definition of the Lagrange multiplier method, at the optimum $\tilde{\mathbf{x}}$,

$$\frac{\partial \Phi(\rho, \tilde{\mathbf{u}})}{\partial \rho} = \lambda(\tilde{\mathbf{x}})\,,\ \forall \tilde{\mathbf{x}} \in \Omega\,. \tag{70}$$

From this, according to equations 64 and 67, results

$$\frac{\partial D^{\mathrm{h}}_{ijkl}(\mu)}{\partial \mu}\varepsilon_{ij}(\tilde{\mathbf{u}})\varepsilon_{kl}(\tilde{\mathbf{u}}) - 2\frac{\partial \beta^{\mathrm{h}}_{ij}(\mu)}{\partial \mu}\varepsilon_{ij}(\tilde{\mathbf{u}})\Delta T = \lambda(\tilde{\mathbf{x}}) = 2\Lambda\,, \quad \forall \mathbf{y} \in Y(\tilde{\mathbf{x}})\,,\ \text{with}\ 0 < \mu < 1\,, \tag{71}$$

providing a conection between the optimal necessary conditions of both scales.

4.3 Hierarchical thermal problem

The presented hierarchical structure can be seamlessly adapted to the thermal problem. Note that both thermal and mechanical problems are formally identical. On one hand, both are defined by a typical conservation problem, with specific constitutive and compatibility relations and boundary conditions. On the other hand, both applications can have the objectives defined in terms of the maximisation of a constitutive constant, *i.e.* stiffness and conductivity. In this sense, as done for the objective definition of equation 62, the thermal compliance minimisation (or conductivity maximisation) can be defined for a thermal problem (see Eq. 13), ignoring convective and radiative terms ($Q = h_c = 0$), as

$$\min_{\substack{\rho(\mathbf{x}) \\ 0 \le \rho(\mathbf{x}) \le 1 \\ \int_\Omega \rho(\mathbf{x})\mathrm{d}\Omega \le V \\ \mathbf{K}_{\mathrm{T}}\mathbf{T} = \mathbf{q}}} \left[\frac{1}{2}\int_\Omega \Theta(\rho, \mathbf{T})\mathrm{d}\Omega\right]\,, \tag{72}$$

where

$$\Theta(\rho, \mathbf{T}) = \max_{\substack{\mu(\mathbf{x},\mathbf{y}) \\ 0 \le \mu(\mathbf{x},\mathbf{y}) \le 1 \\ \int_Y \mu(\mathbf{x},\mathbf{y})\mathrm{d}Y = \rho(\mathbf{x})}} k^{\mathrm{h}}_{ij}(\mu) T'_i T'_j\,, \quad \text{with} \quad T'_k = \frac{\partial T}{\partial y_k}\,. \tag{73}$$

Function Θ is equivalent to the strain energy density function of the thermoelastic problem for a thermal problem and is associated to the principle of virtual temperatures, which is in turn equivalent to the principle of virtual work (Bathe, 1996; Cook et al., 1989). It is a measure of thermal compliance, being used for the maximisation of the thermal conductivity for the macrostructural point $\mathbf{x}$ of Ω. T'_k and k^{h}_{ij} are the components of the temperature gradient and of the homogenised thermal conductivity tensor, respectively (see Eq. 30).
The definition of the optimisation problem and optimality conditions are equivalent to those of the previous section. It is however convenient to define the sensitivity of the homogenised thermal conductivity tensor to the variation of μ, given as

$$\frac{\partial k^{\mathrm{h}}_{ij}(\mu)}{\partial \mu} = \frac{1}{|\mathrm{Y}|}\int_{\mathrm{Y}} p\mu^{p-1}k^{0}_{rs}\left(\delta_{ri}-\frac{\partial \mathrm{Y}^{i}}{\partial y_r}\right)\left(\delta_{sj}-\frac{\partial \mathrm{Y}^{j}}{\partial y_s}\right)\mathrm{d}Y \tag{74}$$

Note that this problem can be solved independently or in a multiobjective approach. In this case, both thermal and mechanical objectives influence the objective function as (Challis et al., 2008; Chen et al., 2010; de Kruijf et al., 2007)

$$\min_{\substack{\rho(\mathbf{x})\\ 0\leq\rho(\mathbf{x})\leq 1\\ \int_\Omega \rho(\mathbf{x})\mathrm{d}\Omega\leq V\\ \mathbf{Ku}=\mathbf{f}\\ \mathbf{K}_{\mathrm{T}}\mathbf{T}=\mathbf{q}}} \quad w^{\mathrm{t}}\frac{F^{\mathrm{t}}}{F^{\mathrm{t}}_0}+w^{\mathrm{m}}\frac{F^{\mathrm{m}}}{F^{\mathrm{m}}_0}\,, \tag{75}$$

where F^{t} and F^{m} are the thermal and mechanical objective functions, respectively. F^{t}_0 and F^{m}_0 are normalisation terms, usually the respective objective values for the initial solution, and the values w^{t} and w^{m} are pondering weights for each objective. These weights can be used for the construction of Pareto fronts and are defined as $w^{\mathrm{m}} = 1 - w^{\mathrm{t}}$, with $w^{\mathrm{m}} \in [0,1]$ (Frischknecht et al., 2010).

5. Inverse homogenisation

The previous methodology, because of the clear separation of the problem in two distinct scales, provides a further utility. It is possible to sue the inner problem to perform local optimisation. Thus, ideal cellular or composite microstructures can be obtained as an optimal answer to a prescribed far-field. This is commonly called as local anysotropic problem or inverse homogenisation method.
The definition of this problem, equivalent to the local problems seen before within the hierarchical structure (see Eqs. 59 and 73), can be expressed as

$$\Phi(\mu,\overline{\varepsilon},\overline{\Delta T}) = \max_{\substack{\mu(\mathbf{y})\\ 0\leq\mu(\mathbf{y})\leq 1\\ \int_{\mathrm{Y}}\mu(\mathbf{y})\mathrm{d}Y=V}} \left[D^{\mathrm{h}}_{ijkl}(\mu)\overline{\varepsilon}_{ij}\overline{\varepsilon}_{kl} - 2\beta^{\mathrm{h}}_{ij}(\mu)\overline{\varepsilon}_{ij}\overline{\Delta T}\right]\,, \tag{76}$$

or

$$\Theta(\mu,\overline{\mathbf{T}'}) = \max_{\substack{\mu(\mathbf{y})\\ 0\leq\mu(\mathbf{y})\leq 1\\ \int_{\mathrm{Y}}\mu(\mathbf{y})\mathrm{d}Y=V}} \left[k^{\mathrm{h}}_{ij}(\mu)\overline{T'}_i\overline{T'}_j\right]\,, \tag{77}$$

as it concerns a thermomecanic or a thermal problem, respectivelly. $\bar{\varepsilon}$, $\overline{\Delta T}$ and $\overline{\mathbf{T}'}$ are strain, temperature difference and temperature gradient far-field prescribed values, respectively. The objectives of these problems are maximising the stiffness or thermal conductivity of the material. Once again, these problems can be solved within a multiobjective application.

6. Local approach

There are several approaches to solve material distribution problems for a given structural analysis application. In this work, as an alternative to the inverse homogenisation, a different strategy is also referred. Called by the authors optimisation local approach, it consists in the application of the typical single-scale topology optimisation problem to representative unit-cells, using specific periodic boundary conditions and asymptotic expansion homogenisation. The usual minimisation of the work of external loads or surface conduction heat fluxes (mechanical or thermal compliance) can be expressed as

$$\min_{\substack{0\leq\mu\leq 1 \\ \int_Y \mu(\mathbf{y})\mathrm{d}Y=\bar{\rho} \\ \mathbf{Ku}=\mathbf{f}}} \int_\Omega \Delta T\boldsymbol{\beta} : \boldsymbol{\varepsilon}(\mathbf{u})\mathrm{d}\Omega + \int_\Omega \mathbf{b}\cdot\mathbf{u}\mathrm{d}\Omega + \int_{\Gamma_{\mathrm{N_u}}} \bar{\mathbf{t}}\cdot\mathbf{u}\mathrm{d}\Gamma \tag{78}$$

or, using its practical implementation counterpart expressed in matrix notation (Sigmund, 2001), as

$$\min_{\substack{0\leq\mu\leq 1 \\ \int_Y \mu(\mathbf{y})\mathrm{d}Y=\bar{\rho} \\ \mathbf{Ku}=\mathbf{f}}} \int_\Omega \mathbf{u}^{\mathrm{T}}\mathbf{K}\mathbf{u}\,\mathrm{d}\Omega\,, \tag{79}$$

for the thermoelasticity problem, and

$$\min_{\substack{0\leq\mu\leq 1 \\ \int_Y \mu(\mathbf{y})\mathrm{d}Y=\bar{\rho} \\ \mathbf{K}_{\mathrm{T}}\mathbf{T}=\mathbf{q}}} \int_{\Gamma_{N_{\mathrm{T}}}} \bar{q}T\mathrm{d}\,\Gamma\,, \tag{80}$$

or, using its practical implementation counterpart expressed in matrix notation, as

$$\min_{\substack{0\leq\mu\leq 1 \\ \int_Y \mu(\mathbf{y})\mathrm{d}Y=\bar{\rho} \\ \mathbf{K}_{\mathrm{T}}\mathbf{T}=\mathbf{q}}} \int_\Omega \mathbf{T}^{\mathrm{T}}\mathbf{K}_{\mathrm{T}}\mathbf{T}\mathrm{d}\Omega \tag{81}$$

for the thermal problem (de Kruijf et al., 2007). The main difference to a typical macroscale topology optimisation problem resides on the use of boundary conditions. Using a far-field approach, the prescribed fields used in the inverse homogenisation are directly imposed in this case. Furthermore, not only strains and temperature gradients can be used in this case, but also stress and flux far-field states, applied as natural ou essential constraints. They are transformed in adequate boundary conditions to solve the finite element problems shown on the restrictions of the optimisation problem. These must enforce periodicity but in a broader sense than referred before. The periodicity boundary conditions used in the AEH restrict the overal deformation of the RUC, only allowing oscillations and maintaining an average

value equal to zero. In this case, the RUC is forced to deform according to the far-field values imposed, while still guaranteeing periodicity of the deformed state. In this case, not only two degrees of freedom are restricted in each boundary condition but three, using a control node to provide the adequate response of the RUC. After the convergence of the optimisation step, AEH is used to evaluate the constitutive properties of the obtained material.

7. Numerical details

The numerical approach to the presented procedures is dependent on several factors. In the context of this chapter, the authors make some general considerations over the finite element method (FEM) and clarify some aspects related to periodicity boundary conditions.
The general case of the optimisation problems shown here in the form of the hierarchical multiscale problem has a very high computational cost. Note that it requires two finite element models, each one discretising each scale. Moreover, the computational requirements are worsened from the fact that most of the time consumed in topology optimisation problem solving is spent on the finite element method equation solving (Bendsøe, 1995). The hierarchical structure needs, for each iteration, several FEM solutions. On one hand, the macroscale equilibrium problem. On the other hand, for each point on the macroscale (usually each finite element), an asymptotic expansion homogenisation problem is solved over the microscale discretisation. This, in itself, consists in several systems of equations to solve. Note that, for a two-dimensional problem, the elasticity problem requires three systems of equations, the thermal expansion one more and the thermal problem a further two. For the three-dimensional case, these values become six, one and three, respectively. Another aspect of these local problems, including the local approach, is related to conditioning problems, since the penalty method used here to enforce periodicity boundary conditions tends to unbalance the equations and to slow the convergence of the solver (Oliveira et al., 2010).
In what concerns the optimisation problem and variable update cycles, the authors use specific implementations of Optimality Criteria methods and Krister Svanberg's Method of Moving Asymptotes (MMA) (Bendsøe & Sigmund, 2003; Coelho et al., 2008; Svanberg, 1987).

7.1 Boundary conditions

At this point, it is important to clarify the use of periodicity boundary conditions, which are essential to the methodologies briefly shown in this chapter. Periodicity boundary conditions are imposed over the surface boundaries of the RUC (see Fig. 4) and shown here for a purely elastic case. Their usage for the thermal problem is almost seamless. The type of boundary condition used in this work is called Multi-Freedom Constraint (MFC), as opposed to the more usual Single-Freedom Constraint (SFC).
Starting with the periodicity boundary conditions used in the AEH, for a hexahedral unit-cell in $y_1 \in [0, y_1^0]$, $y_2 \in [0, y_2^0]$ and $y_3 \in [0, y_3^0]$ (see Fig. 4b), the boundary conditions can be defined, for the more general 3-D case, as

$$\begin{aligned} &\boldsymbol{\chi}(0, y_2, y_3) - \boldsymbol{\chi}(y_1^0, y_2, y_3) = \mathbf{0}\,, \\ &\boldsymbol{\chi}(y_1, 0, y_3) - \boldsymbol{\chi}(y_1, y_2^0, y_3) = \mathbf{0} \quad \text{and} \\ &\boldsymbol{\chi}(y_1, y_2, 0) - \boldsymbol{\chi}(y_1, y_2, y_3^0) = \mathbf{0}\,, \end{aligned} \tag{82}$$

where $\boldsymbol{\chi}$ is the corrector field for the elasticity homogenisation problem, which represents the mechanical characteristic displacement field tensor. In order to prevent rigid body motion,

displacements and rotations of an arbitrary point of the unit-cell must be locked or, since the MFCs are homogeneous (*i.e.* the independent value is equal to zero), the translation degrees of freedom of the vertices of the RUC must be restricted.

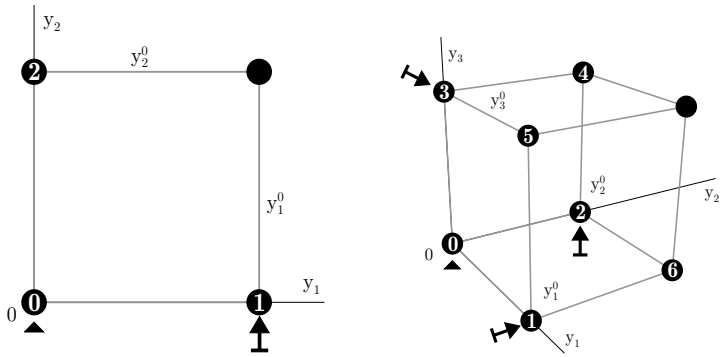

Fig. 4. Periodic RUC: (a) quadrilateral (2-D) and (b) hexahedral (3-D).

The second case in analysis is used on the local approach optimisation problem. This method allows the imposing of far-field stress or far-field strain. The imposing of a macroscale stress-state $\boldsymbol{\sigma}$ over the RUC (*e.g.* taken from a integration point of the main structure finite element mesh) may be done calculating the equivalent loads (**P**) over the RUC. This is done over the boundaries (Γ) of the unit-cell, where (Böhm, 1998)

$$\mathbf{P} = \int_{\Gamma} \bar{\mathbf{t}}_{\mathrm{a}}(\mathbf{y}) \mathrm{d}\Gamma, \quad \text{with} \quad \bar{\mathbf{t}}_{\mathrm{a}} = \boldsymbol{\sigma}_{\mathrm{a}} \cdot \mathbf{n}\,. \tag{83}$$

Here, $\bar{\mathbf{t}}_{\mathrm{a}}$ stands for the homogeneous surface traction vector corresponding to the applied (far-field) stress $\boldsymbol{\sigma}_{\mathrm{a}}$ at a given point on the cell's surface and $\mathbf{n}$ is the local surface outward unit vector. The numerical imposing of the equivalent loads involves multiplying a given stress component by the surface area of the boundary at a given element and distributing it to the connected boundary nodes. This equivalent load field must be antiperiodic for equilibrium to be fulfiled. On the other hand, in order to guarantee periodicity there must also be adequate MFCs. These are homogeneous, but, where the homogenisation application renders only oscillations around an average state, these must allow for the global deformation of the RUC. Thus, the vertices cease to be fixed and each MFC connects more than two nodes. The single-freedom constraints (SFCs) used are illustrated in figure 4, preventing rigid body motion by restricting 3 DOFs for the 2-D case and 6 DOF for the 3-D case. The MFCs use control vertices to pull the other nodes and guarantee periodicity. The resulting MFCs may be presented as

$$\begin{aligned} \mathbf{u}(y_1^0, y_2) &= \mathbf{u}(0, y_2) + \mathbf{u}_1 \quad \text{and} \\ \mathbf{u}(y_1, y_2^0) &= \mathbf{u}(y_1, 0) + \mathbf{u}_2\,, \end{aligned} \tag{84}$$

for the 2-D case, and

$$\begin{aligned} \mathbf{u}(y_1^0, y_2, y_3) &= \mathbf{u}(0, y_2, y_3) + \mathbf{u}_1\,, \\ \mathbf{u}(y_1, y_2^0, y_3) &= \mathbf{u}(y_1, 0, y_3) + \mathbf{u}_2 \quad \text{and} \\ \mathbf{u}(y_1, y_2, y_3^0) &= \mathbf{u}(y_1, y_2, 0) + \mathbf{u}_3\,, \end{aligned} \tag{85}$$

for the 3-D case.
For the last case, the macroscale strains $\boldsymbol{\varepsilon}$ are, as for the stress, imposed as a far-field state. The main difference to the previous case is that the RUC isn't deformed using Neumann boundary conditions, but only Dirichlet boundary conditions. The localisation is done forcing equivalent displacements that render an average strain equal to the macroscale strain. This is done, for the 2-D and 3-D cases, using the non-homogeneous conditions

$$\begin{aligned} \mathbf{u}(y_1^0, y_2) - \mathbf{u}(0, y_2) &= \mathbf{c}_1 \quad \text{and} \\ \mathbf{u}(y_1, y_2^0) - \mathbf{u}(y_1, 0) &= \mathbf{c}_2 \,, \end{aligned} \tag{86}$$

and

$$\begin{aligned} \mathbf{u}(y_1^0, y_2, y_3) - \mathbf{u}(0, y_2, y_3) &= \mathbf{c}_1 \,, \\ \mathbf{u}(y_1, y_2^0, y_3) - \mathbf{u}(y_1, 0, y_3) &= \mathbf{c}_2 \quad \text{and} \\ \mathbf{u}(y_1, y_2, y_3^0) - \mathbf{u}(y_1, y_2, 0) &= \mathbf{c}_3 \,, \end{aligned} \tag{87}$$

respectively. In this case, instead of the homogeneous three-node conditions used in equations 84 and 85, two-node non-homogeneous conditions are used, using the independent coefficients $\mathbf{c}$. These constants are calculated to match the imposed strain states. Yet another alternative configuration can be obtained with the same MFCs used in the stress-based case. Using the same homogeneous conditions to enforce periodicity, the Dirichlet condition can be imposed on the control vertices, rendering the same effect, *i.e.* adding the conditions

$$\begin{aligned} \mathbf{u}_1 - \mathbf{u}_0 &= \mathbf{c}_1 \,, \\ \mathbf{u}_2 - \mathbf{u}_0 &= \mathbf{c}_2 \quad \text{and} \\ \mathbf{u}_3 - \mathbf{u}_0 &= \mathbf{c}_3 \end{aligned} \tag{88}$$

to the homogeneous MFCs used before. Note that the third condition is used only for the 3-D case. Additionally, note that $\mathbf{u}_0 = \mathbf{0}$, which makes equations 88 correspond to single-freedom essential boundary conditions.

8. Examples

In the scope of this chapter, the authors show some representative examples of applications of the methods summed within the previous sections. In this sense, the Asymptotic Expansion Homogenisation is the main topic. As such, results of the associated AEH procedures are shown explicit or implicitly for most examples. Different applications and levels of multiscale optimisation are also shown. All of these examples were solved in a totally in-house developed code. This code, developed by the authors, uses the finite element method to solve 2-D and 3-D problems, with several different linear and quadratic elements, and a conjugate gradient iterative parallel solver. It solves problems in linear thermoelasticity with homogenisation and automatic degree of freedom association and periodicity boundary condition enforcing. Moreover, it is able to solve topology optimisation multiscale problems, using variations of power-law methods, optimality criteria and MMA (Svanberg, 1987).
The first example (Oliveira et al., 2009) shows a typical AEH application. In this linear elastic case, a given structure is subjected to a tensile stress. The material used to build this structure is represented using the discretisation shown in figure 5(a) and models an $AlSiC_p$ MMC with 30% volume fraction of SiC particles. The macroscale uses a structured hexahedra mesh and

the microscale an non-structured non-periodic tetrahedra mesh. Figures 5(b) to (g) show the 6 eigenshapes χ_{kl} associated to the characteristic displacements of the representative unit-cell, from which the oscillations that solve the local problem and allow the evaluation of the constitutive properties are processed. Furthermore, these oscillations are also used in the localisation procedure. In figure 6 it is possible to see the microscale stress field for a given element and Gauss point. As expected, the macroscale stress value sits within the microscale limits, as the material heterogeneities impose detailed stress oscillations (Oliveira et al., 2009).

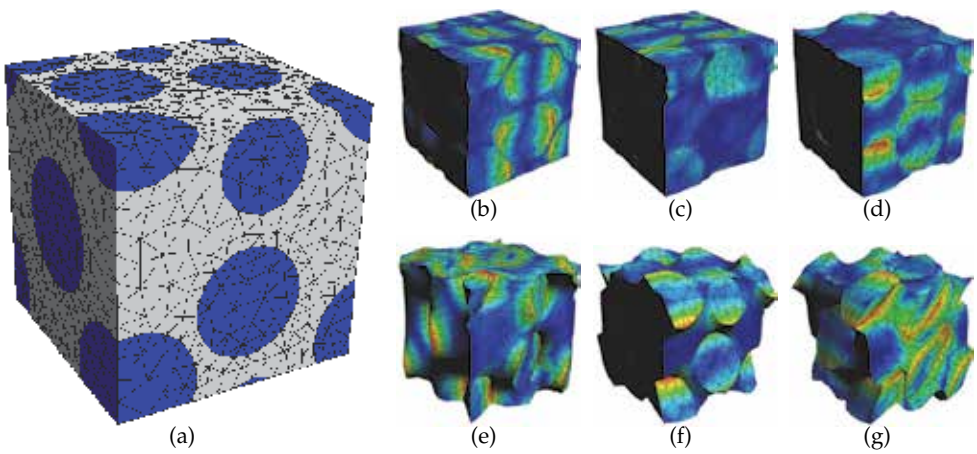

Fig. 5. Unstructured and non-periodic RUC finite element mesh (microscale). Characteristic displacements for the 30% reinforcement RUC: normal eigenshapes (a) χ_{11}, (b) χ_{22}, (c) χ_{33} and shear eigenshapes (d) χ_{12}, (e) χ_{23}, (f) χ_{13} (Oliveira et al., 2009).

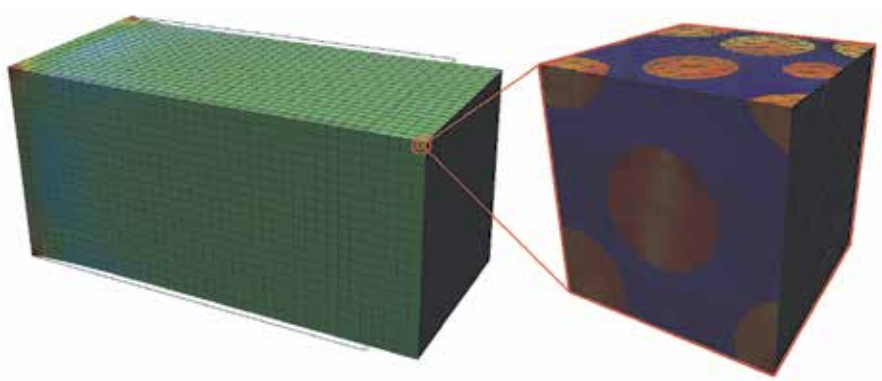

Fig. 6. Equivalent von Mises stress on the microscale, obtained with the localisation procedure on a Gauss point of a macroscale finite element (Oliveira et al., 2009).

As a second example, figure 7 shows the use of single-scale structural topology optimisation using different constitutive properties. In this case, a RUC of aluminium (Al) matrix reinforced with boron (B) continuous parallel fibres, with a reinforcement volume fraction of 47%, was used. Applying the asymptotic expansion homogenisation procedure led to an elasticity matrix for this three-dimensional composite material structure. Three different

bidimensional elasticity matrices were derived, each representing the material properties of the composite material for each of the three main orthogonal orientations. This resulted in the two orthogonal orthotropic and one cubic orientations illustrated in figure 7. These material properties were then used in the macroscale topology optimisation problem with the shown set of boundary conditions. It is clear that, for a constant reinforcement volume fraction, the microscale topology has a major influence on the optimal macrostructure design. Furthermore, the two orthotropic examples act as bounds for the isotropic case. It is also possible to verify the influence of the reinforcement orientation on the optimisation results.

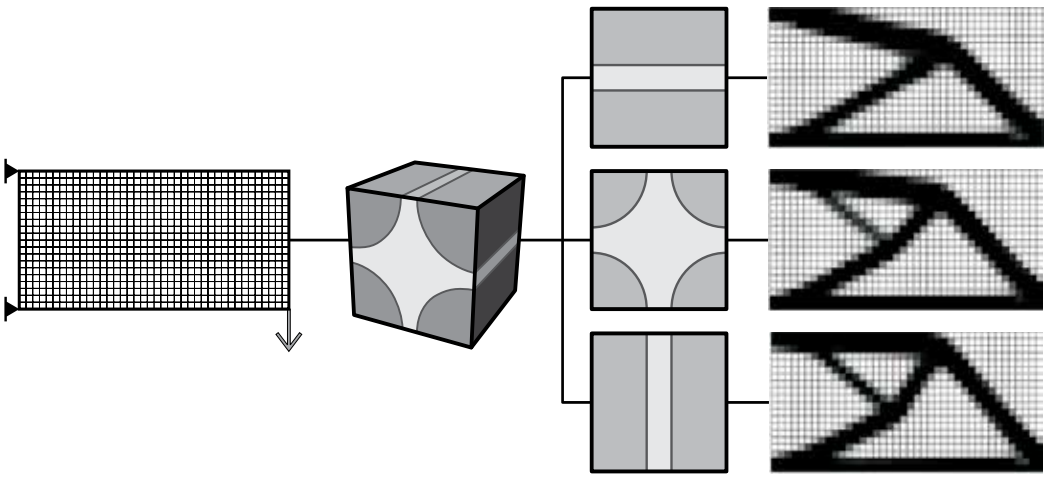

Fig. 7. Topology optimisation results using different reinforcement orientations.

A further application shows the multiobjective optimisation of simultaneously a mechanical and thermal problem. In this case, the local approach is applied to the compliance minimisation problem. The minimisation of these functions frequently results in conflicting objectives, as the resulting structures range from maximum stiffness to maximum heat dissipation (maximum conductivity). Figure 8 shows the Pareto front that arises from the maximisation of the stiffness of a 2-D RUC ($f_{\mathrm{v}} = 0.5$) over the vertical direction and the simultaneous maximisation of the thermal conductivity over a horizontal direction. The presented values are normalised, using each initial compliance. It is noteworthy that utopia solutions are different from Pareto optimal solutions, since objectives are conflicting. Figure 9 shows the characteristic fields (linear thermal expansion – $\mathbf{\Psi}$, thermal conductivity – $\mathbf{\Upsilon}$, and stiffness – $\boldsymbol{\chi}$), for a thermal problem weight of $w^{\mathrm{t}} = 0.4$. The same is shown for a 3-D RUC example, with $w^{\mathrm{t}} = 0.5$ and subjected to far-field stress ($\boldsymbol{\sigma} = \{1; 0; -1; 0; 0; 0\}$) and heat flux ($\mathbf{q} = \{0.5; 0.25; 1\}$) states.

An alternative to the local approach shown before is the use of the inverse optimisation. Figure 11 shows the optimal microstructure obtained when using this methodology for a mechanical problem, with a macroscopic strain of $\boldsymbol{\varepsilon} = \{0; 0; 0; 1; 1; 1\}$. Is is possible to see both the stiff and soft material phases. The composite material constituents have Young's moduli related as $d_{\mathrm{m}} = E_1/E_2 = 100$. A periodicity illustration is shown for this material distribution, showing that the method complies perfectly with this requirement. Furthermore, an anisotropy spherical plot shows the stiffness of this material along each direction, evaluated through the application of the AEH procedure. Once more, the characteristic displacements that result from the material distribution and the AEH methodology are also illustrated.

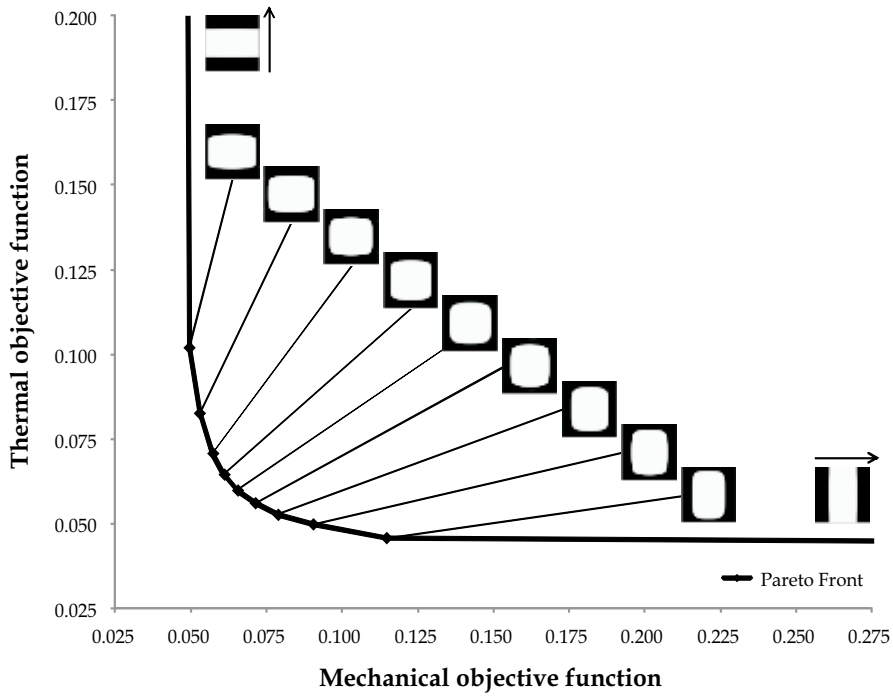

Fig. 8. Square RUC microscale optimisation results: Pareto front for a 2-D mechanical/thermal multiobjective problem.

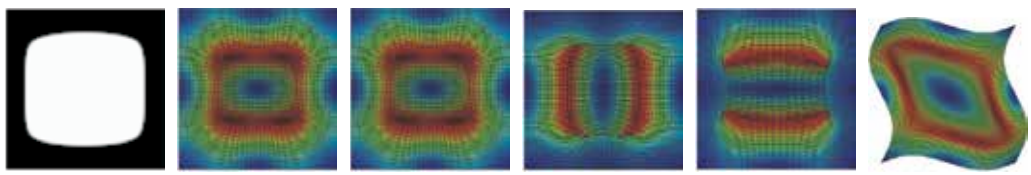

Fig. 9. Multiobjective topology optimisation, using the local approcah, for a 2-D RUC (w^t=0.4): (a) material distribution, (b) thermal expansion ($\mathbf{\Psi}$), (c) conductivity ($\mathbf{Y}$) and (d-e) χ_{11}, χ_{22} and χ_{12} characteristic displacement modes.

The previous example, in a hierarchical structure, can be used in applications as the following. In this case, for each iteration, a multiscale problem is solved. The global problem is solved on the macroscale, using constitutive information taken from the microscale. This problem leads to a strain field that can be used in different forms to control the microscale problem. In this first case, the strain field is averaged and pondered using the equivalent strain over the macroscale in a simplified hierarchical structure. All the macroscale is made of the same material, which constituent distribution in updated with the evolution of both the optimisation procedure and the macroscopic strain field. Figure 12 shows both the macroscale homogenenised problem and the optimal microscale solution that arises as a response to the global strains. The problem is a simultaneous bending and torsion test. The results show the results for both loads applied together (see Fig. 12(a)) or as part of a multiload case (see Fig. 12(b)).

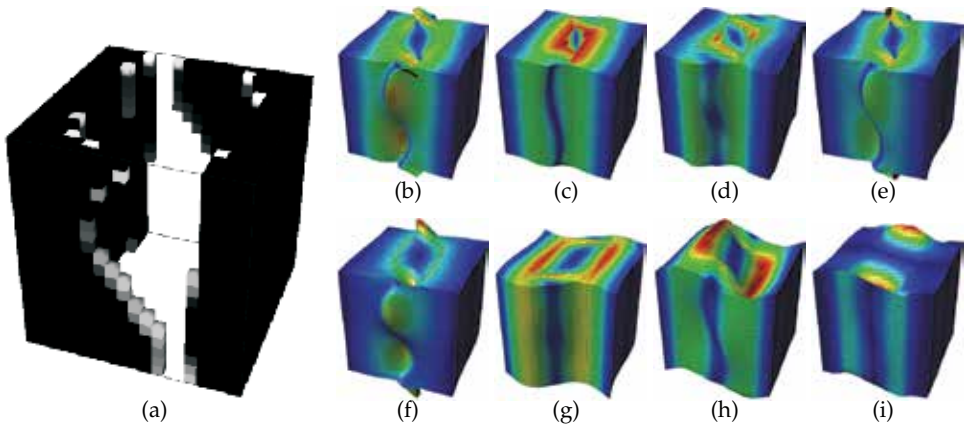

Fig. 10. Multiobjective topology optimisation, using the local approcah, for a 3-D RUC (w^{t}=0.5): (a) material distribution, (b) thermal expansion ($\mathbf{\Psi}$), (c) conductivity ($\mathbf{Y}$) and (d-i) χ_{11}, χ_{22}, χ_{33}, χ_{12}, χ_{23} and χ_{13} characteristic displacement modes.

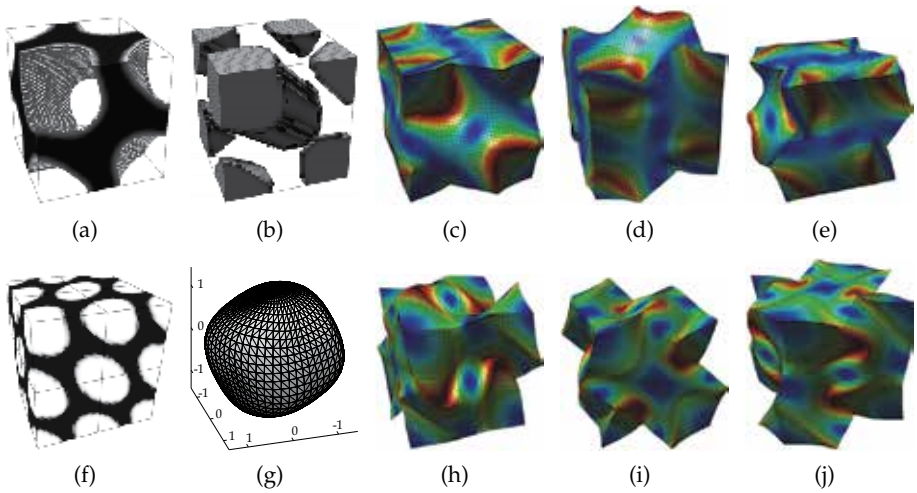

Fig. 11. Microscale topology optimisation, using the inverse homogenisation, for a 3-D RUC (ε={0;0;0;1;1;1}): (a) stiff and (b) soft material distributions, (f) periodicity illustration, (g) anisotropy plot, and (c-e,h-j) χ_{11}, χ_{22}, χ_{33}, χ_{12}, χ_{23} and χ_{13} characteristic displacement modes.

The general case of the previous examples is the application of the hierarchical procedure, with concurrent optimisation of the material distribution over the two scales. Figure 13 shows such an application. The presented 2-D example uses a typical bycicle wheel mechanical optimisation problem and adds a thermal problem, for a multiobjective strategy. Both the mechanical and thermal boundary conditions are represented and the weight of the thermal problem is $w^{\mathrm{t}} = 0.75$. Some of the local problem solutions are also presented, giving the notion of effective material distribution, as well of the shear dimension of the problem, even for a 2-D case. This multiobjective procedure needs normalisation of the objectives, acting on the objective function and the sensitivities. Note that, even for this relaxed and filtered

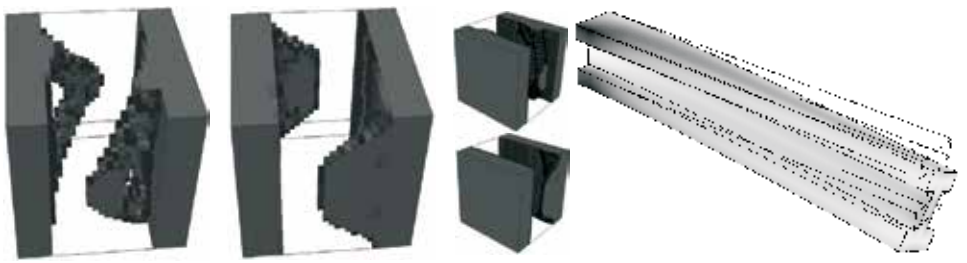

(a) (b) (c)

Fig. 12. Hierarchical problem with local topology optimisation: microscale optimal topology (stiff phase) for (a) bending and torsion and (b) bending and torsion as multiload cases, and (c) results with macroscale deformed state and stress isovalues.

solution, the macroscale density distribution still shows some checkerboard tendencies. This can be solved using higher-order finite elements but leads to an even higher computational cost.

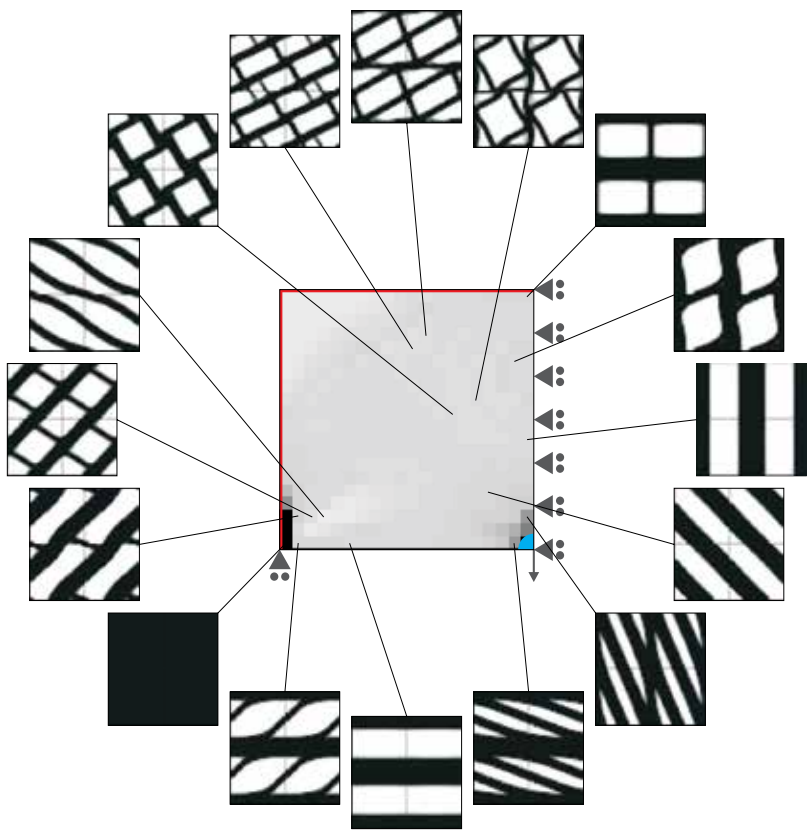

Fig. 13. Hierarchical multiobjective (thermal and mechanical) 2-D example (w^{t}=0.75), showing the macroscale density distribution and some local material distributions.

9. Final remarks

The main objective of this chapter was to give an overview of the Asymptotic Expansion Homogenisation, and its use both on the evaluation of effective properties of periodic structure composite and cellular materials and on the search for the optimal material for a given application. The procedures associated to these objectives are shown, for linear thermal an thermomechanical problems. Special emphasis is put on problem formulation and certain specific numerical details. Moreover, its usage in topology optimisation problems is shown to be varied, ranging from local optimisation to the full fledged hierarchical optimisation.
Nevertheless, in spite of the potential of these strategies, there are some shortcomings. First of all, the boundary conditions associated to these problems can become numerically problematic. On one hand, its implementation is not always straightforward. On the other hand, depending on the method used, they can lead to conditioning problems of the numerical equation systems and subsequent convergence problems and computational time increase. This is even more critical when considering optimisation problems. The varying local density distribution and the sometimes very high difference between numerical values within the systems of equations slows the problem solving down. If one adds this to the overall dimension of hierarchical multiscale problems, the problems rapidly approach limits that make them impossible to solve in conventional hardware.

10. Acknowledgements

The authors thank the financial support given by the Portuguese Foundation for Science and Technology (FCT – Fundação para a Ciência e a Tecnologia) and by the European Social Fund (FSE – Fundo Social Europeu) within the 3rd Community Support Framework.

11. References

Allaire, G. (2001). *Shape Optimization by the Homogenization Method*, 1st edn, Springer, New York, USA.

Arora, J. (2004). *Introduction to Optimum Design*, 2nd edn, Academic Press, San Diego, USA.

Bathe, K.-J. (1996). *Finite Element Procedures*, Prentice-Hall International Editions, Inc., New Jersey, USA.

Bendsøe, M.P. & Kikuchi, N. (1988). Generating optimal topologies in structural design using a homogenization method, *Computer Methods in Applied Mechanics and Engineering* 71(2): 197–224.

Bendsøe, M.P. (1995). *Optimization of Structural Topology, Shape, and Material*, Springer, Berlin, Germany.

Bendsøe, M.P. & Sigmund, O. (1999). Material interpolation schemes in topology optimization, *Archive of Applied Mechanics* 69(9-10): 635–654.

Bendsøe, M.P. & Sigmund, O. (2003). *Topology Optimization: Theory, Methods, and Applications*, Springer, Berlin, Germany.

Böhm, H.J. (1998). *A short introduction to basic aspects of continuum micromechanics*, CDL-FMD-Report, Christian Doppler Laboratorium für Mikromechanik der Werkstoffe, Institut für Leichtbau und Flugzeugbau, Technische Universität Wien, Vienna, Austria.

Challis, V.J., Roberts, A.P. & Wilkins, A.H. (2008). Design of three dimensional isotropic microstructures for maximized stiffness and conductivity, *International Journal of Solids and Structures* 45(14-15): 4130–4146.

Chen, Y., Zhou, S. & Li, Q. (2009). Multiobjective topology optimization for finite periodic structures, *Computers & Structures* 88(11-12): 806–811.

Cioranescu, D. & Donato, P. (1999). *An Introduction to Homogenization*, Oxford Lecture Series in Mathematics and Its Applications, Vol. 17, Oxford University Press, Oxford, United Kingdom.

Coelho, P.G., Fernandes, P.R., Guedes, J.M. & Rodrigues, H.C. (2008). A hierarchical model for concurrent material and topology optimisation of three-dimensional structures, *Structural and Multidisciplinary Optimization* 35(2): 107–115.

Cook, R.D., Malkus, D.S. & Plesha, M.E. (1989). *Concepts and Applications of Finite Element Analysis*, 3rd edn, John Wiley & Sons, New York, USA.

de Kruijf, N., Zhou, S., Li, Q. & Mai, Y.W. (2007). Topological design of structures and composite materials with multiobjectives, *International Journal of Solids and Structures* 44(22-23): 7092–7109.

Díaz, A. & Lipton, R. (1997). Optimal material layout for 3D elastic structures, *Structural and Multidisciplinary Optimization* 13(1): 60–64.

Frischknecht, B.D., Peters, D.L. & Papalambros, P.Y. (2010). Pareto set analysis: local measures of objective coupling in multiobjective design optimization, *Structural and Multidisciplinary Optimization* pp. 1–14. DOI: 10.1007/s00158-010-0599-2.

Fung, Y.C. & Tong, P. (2005). *Classical and Computational Solid Mechanics*, Advanced Series in Engineering Science, Vol. 1, World Scientific Publishing, Singapore.

Guedes, J.M. & Kikuchi, N. (1990). Preprocessing and postprocessing for materials based on the homogenization method with adaptive finite element methods, *Computer Methods in Applied Mechanics and Engineering* 83(2): 143–198.

Guedes, J.M., Lubrano, E. , Rodrigues, H.C. & Turteltaub, S. (2006). Hierarchical optimization of material and structure for thermal transient problems, *Proceedings of IUTAM Symposium on Topological Design Optimization of Structures, Machines and Materials: Status and Perspectives*, Springer, Bendsøe, M.P., Olhoff, N., Sigmund, O. (Eds.), Vol. 137, Rungstedgaard, Denmark, pp. 525-536.

Hassani, B. & Hinton, E. (1999). *Homogenization and Structural Topology Optimization: Theory, Practice, and Software*, Springer, London, United Kingdom.

Lewis, R.W., Morgan, K., Thomas, H.R. & Seetharamu, K.N. (1996). *The Finite Element Method in Heat Transfer Analysis*, John Wiley & Sons, Chichester, United Kingdom.

Oliveira, J.A., Pinho-da-Cruz, J. & Teixeira-Dias, F. (2009). Asymptotic homogenisation in linear elasticity. Part II: Finite element procedures and multiscale applications, *Computational Materials Science* 45(4): 1081–1096.

Oliveira, J.A., Pinho-da.Cruz, J., Andrade-Campos, A. & Teixeira-Dias, F. (2010). Stress- and strain-based multifreedom constraints for periodic media optimisation, *Proceedings of EngOpt2010 – 2nd International Conference on Engineering Optimisation*, APMTAC, Lisbon, Portugal, p. 148.

Pinho-da-Cruz, J. (2007). *Thermomechanical Characterisation of Multiphasic Materials Using Homogenisation Procedures*, PhD thesis (in portuguese), Universidade de Aveiro, Aveiro, Portugal.

Pinho-da-Cruz, J., Oliveira, J.A. & Teixeira-Dias, F. (2008). Homogenisation of composite materials in thermoelasticity: Formal mathematics and computational issues, *Proceedings of International Conference on Mathematics and Continuum Mechanics*, CIM, A.J.M. Ferreira, I.M.N. Figueiredo, J. Videman (Eds.), Vol. 30, Porto, Portugal, pp. 35-40.

Pinho-da-Cruz, J., Oliveira, J.A. & Teixeira-Dias, F. (2009). Asymptotic homogenisation in linear elasticity. Part I: Mathematical formulation and finite element modelling, *Computational Materials Science* 45(4): 1073–1080.

Rodrigues, H., Guedes, J. & Bendsøe, M.P. (2002). Hierarchical optimization of material and structure, *Structural and Multidisciplinary Optimization* 24(1): 1–10.

Sanchez-Hubert, J. & Sanchez-Palencia, E. (1992). *Introduction aux Méthodes Asymptotiques et à l'Homogénéisation: Application à la Mécanique des Milieux Continus*, Collection Mathématiques Appliquées pour la Maîtrise, Masson, Paris, France.

Sigmund, O. (2001). A 99 line topology optimization code written in Matlab, *Structural and Multidisciplinary Optimization* 21(2): 120–127.

Sigmund, O. (2007). Morphology-based black and white filters for topology optimization, *Structural and Multidisciplinary Optimization* 33(4-5): 401–424.

Svanberg, K. (1987). The method of moving asymptotes – a new method for structural optimization, *International Journal for Numerical Methods in Engineering* 24(2): 359–373.

Terada, K. (1996). *Global-Local Modeling for Composites by the Homogenization Method*, PhD thesis, University of Michigan, Ann Arbor, USA.

Theocaris, P.S & Stavroulakis, G.E. (1998). Multilevel optimal design of composite structures including materials with negative Poisson's ratio, *Structural and Multidisciplinary Optimization* 15(1): 8–15.

Theocaris, P. & Stavroulakis, G. (1999). Optimal material design in composites: An iterative approach based on homogenized cells, *Computer Methods in Applied Mechanics and Engineering* 169(1-2): 31–42.

Edited by Pavla Těšinová

Composites are made up of constituent materials with high engineering potential. This potential is wide as wide is the variation of materials and structure constructions when new updates are invented every day. Technological advances in composite field are included in the equipment surrounding us daily; our lives are becoming safer, hand in hand with economical and ecological advantages. This book collects original studies concerning composite materials, their properties and testing from various points of view. Chapters are divided into groups according to their main aim. Material properties are described in innovative way either for standard components as glass, epoxy, carbon, etc. or biomaterials and natural sources materials as ramie, bone, wood, etc. Manufacturing processes are represented by moulding methods; lamination process includes monitoring during process. Innovative testing procedures are described in electrochemistry, pulse velocity, fracture toughness in macro-micro mechanical behaviour and more.

ISBN 978-953-51-4440-3

Photo by tonymax / iStock

IntechOpen